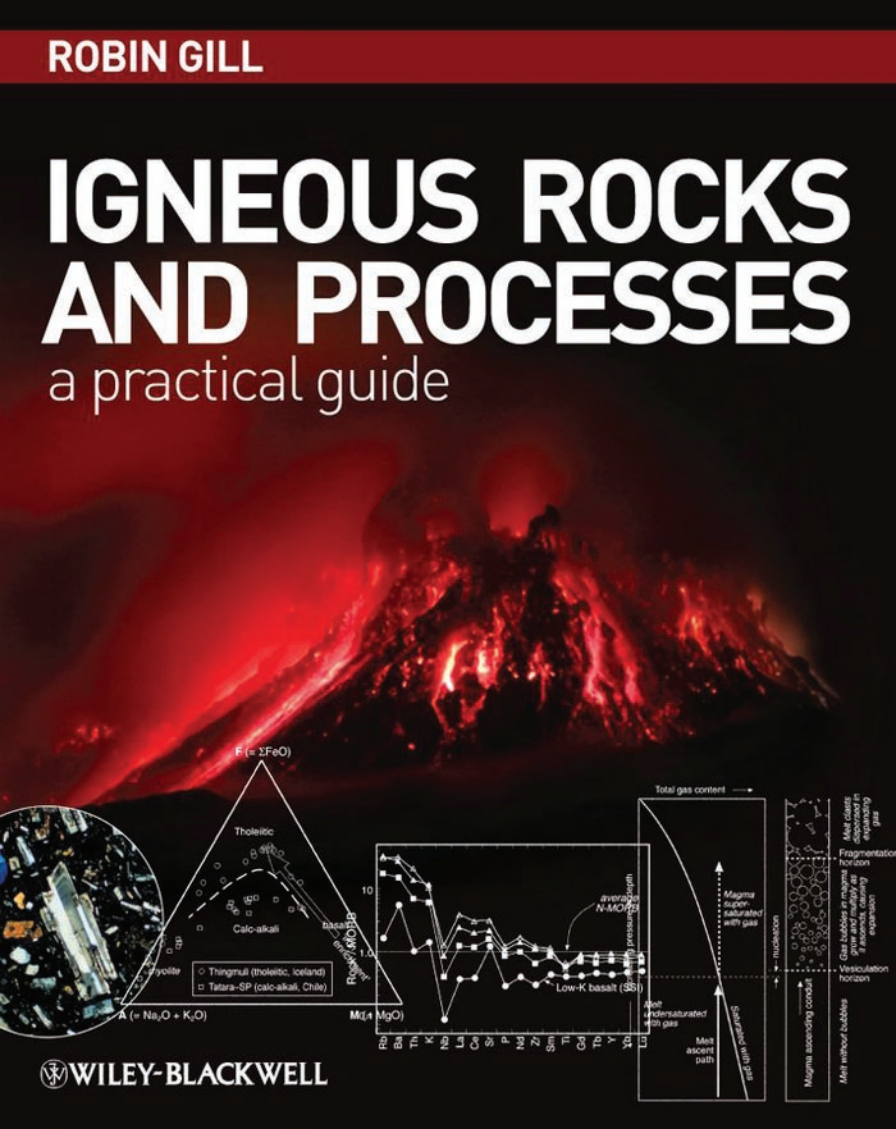
ROBIN GILL

IGNEOUS ROCKS AND PROCESSES

a practical guide



WILEY-BLACKWELL

Igneous Rocks and Processes

To Mary

Companion website

A companion website for this book is available at:

www.wiley.com/go/gill/igneous

The website includes figures from the book for downloading.

Igneous Rocks and Processes

A Practical Guide

Robin Gill

Department of Earth Sciences
Royal Holloway
University of London

WILEY-BLACKWELL
A John Wiley & Sons, Ltd., Publication

This edition first published 2010, © 2010 by Robin Gill

Blackwell Publishing was acquired by John Wiley & Sons in February 2007. Blackwell's publishing program has been merged with Wiley's global Scientific, Technical and Medical business to form Wiley-Blackwell.

Registered office: John Wiley & Sons Ltd, The Atrium, Southern Gate, Chichester, West Sussex, PO19 8SQ, UK

Editorial offices: 9600 Garsington Road, Oxford, OX4 2DQ, UK
The Atrium, Southern Gate, Chichester, West Sussex, PO19 8SQ, UK
111 River Street, Hoboken, NJ 07030-5774, USA

For details of our global editorial offices, for customer services and for information about how to apply for permission to reuse the copyright material in this book please see our website at www.wiley.com/wiley-blackwell

The right of the author to be identified as the author of this work has been asserted in accordance with the Copyright, Designs and Patents Act 1988.

All rights reserved. No part of this publication may be reproduced, stored in a retrieval system, or transmitted, in any form or by any means, electronic, mechanical, photocopying, recording or otherwise, except as permitted by the UK Copyright, Designs and Patents Act 1988, without the prior permission of the publisher.

Wiley also publishes its books in a variety of electronic formats. Some content that appears in print may not be available in electronic books.

Designations used by companies to distinguish their products are often claimed as trademarks. All brand names and product names used in this book are trade names, service marks, trademarks or registered trademarks of their respective owners. The publisher is not associated with any product or vendor mentioned in this book. This publication is designed to provide accurate and authoritative information in regard to the subject matter covered. It is sold on the understanding that the publisher is not engaged in rendering professional services. If professional advice or other expert assistance is required, the services of a competent professional should be sought.

Library of Congress Cataloguing-in-Publication Data

Gill, Robin, 1944–
Igneous rocks and processes : a practical guide / Robin Gill.
p. cm.
Includes bibliographical references and index.
ISBN 978-1-4443-3065-6 (hardcover : alk. paper) – ISBN 978-0-632-06377-2 (pbk. : alk. paper)
1. Rocks, Igneous. 2. Magmatism. I. Title.
QE461.G495 2010
552′.1–dc22
2009031380

A catalogue record for this book is available from the British Library.

Set in 11 on 12 pt Sabon by Toppan Best-set Premedia Limited

Printed and bound in Malaysia

1 2010

Contents

Preface vii
Acknowledgements ix

1. An introduction to magmas and magmatic rocks 1
2. Basalts and related rocks 20
3. Magma differentiation 65
4. Gabbroic rocks 93
5. Ultramafic and ultrabasic rocks 131
6. Andesite, dacite and rhyolite 161
7. How magmas erupt – an introduction to pyroclastic processes and products 209
8. Granitic rocks 241
9. Alkali rocks 291

Appendix A – Mineral identification using a polarizing microscope 347
Appendix B – Petrographic calculations 358
Appendix C – Symbols, units and constants used in this book 365
Glossary 367
Answers to exercises 382
Bibliography 396
Index 415
Colour plate section between pp. 214–215
Companion website for this book: wiley.com/go/gill/igneous

Preface

This book has grown from my experiences teaching a second-year igneous petrology course at Royal Holloway, University of London. At this intermediate level, one's primary goal is to help students to develop appropriate descriptive and interpretive techniques. An emphasis on skills dictates a different order of priorities to those that one would embrace in writing a book on petrogenesis. Faced with an intermediate rock of unknown provenance, a student should be encouraged to describe objectively the rock that they see, and to infer what they can from this information, rather than bend their analysis to fit a pre-conceived name, origin or tectonic association. The term 'andesite' should emerge from the student's examination, on the basis of the mineralogy they observe or the chemical data they are presented with, not because they happen to know that the rock comes from Japan (useful hint though that might be). Therefore, as I see it, the book that students need at this stage is one that can help them translate a set of observations (e.g. 'a rock consisting of abundant plagioclase and hornblende phenocrysts set in a fine-grained groundmass, mainly consisting of intermediate plagioclase + augite + opaques') into an informative, appropriate name ('plagioclase-hornblende-phyric andesite' – see Chapter 6). Intermediate students also need guidance in interpreting textures and geochemical data intelligently for themselves, in order to draw informed conclusions about magmatic processes. To support this practical student-led emphasis, most chapters in the book are devoted to major rock families (basalts, gabbroic rocks, granitic rocks, etc.); geotectonic environments are of course discussed, but they do not determine the structure of the book as they might in a text emphasizing magma genesis.

Once the nuts and bolts of igneous nomenclature have been introduced in Chapter 1, the order of chapters reflects a logical journey from the simplest, most abundant, least fractionated products of mantle melting (basalts, Chapter 2) and their plutonic equivalents (Chapters 4 and 5), through to more evolved magma types in Chapters 6 and 8. The final chapter examines the alkali rocks, whose diversity and mineralogical complexity challenge even the most dedicated student! Chapters 3 and 7 digress, at the points in the book where this is most pertinent, to examine experimental petrology (an invaluable laboratory window on magma evolution) and concepts of physical volcanology.

As to igneous nomenclature, I have aimed at what I hope is a judicious blend of traditional petrographic practice and current International Union of Geological Sciences (IUGS) convention (Le Maitre, 2002). The minerals observed in a rock are discussed here under four conceptual headings: *essential* minerals, *type* minerals, *accessory* minerals and *post-magmatic* minerals. 'Essential' and 'accessory' are familiar terms from traditional usage but assume slightly different meanings in this book, as the table shows:

Category of mineral (as developed in Chapter 1)	Traditional meaning	Meaning adopted in this book	Example
Essential mineral (or 'consists essentially of')	A mineral 'necessary to a rock's classification or nomenclature'[1]	A mineral whose presence is essential in determining the appropriate *root* name	Calcic plagioclase in basalt
Type mineral	–	A non-essential mineral used as a *qualifier*	Olivine in 'olivine basalt'
Accessory mineral	'A mineral occurring in small quantities in a rock whose presence does not affect diagnosis'[2]	Any magmatic mineral that is immaterial to the choice of root name or qualifiers	Magnetite in basalt
Post-magmatic mineral	–	A mineral filling voids ('hydrothermal') or replacing igneous minerals ('secondary')	Smectite in an altered basalt

[1] AGI Glossary of Geology, 2nd edition 1960.
[2] Holmes (1928).

The term 'type mineral' merely makes explicit a concept that we understand implicitly whenever we speak of 'olivine basalt'. It goes without saying that the same mineral may assume essential status in one rock type (nepheline in nephelinite), act as a type mineral in another (nepheline in alkali gabbro) or be present as an accessory in a third, according to abundance and context. The notion of 'post-magmatic mineral' is introduced to emphasize that a real igneous rock may in its current state contain minerals that never coexisted with the melt from which it originally formed.

In writing rock definitions, I have stuck to one cardinal principle: the definition of a rock type should be founded on purely descriptive criteria, free of genetic connotations. Accordingly the adjective 'volcanic' has been omitted from the definition of basalt and 'plutonic' from that of gabbro. Though this diverges from IUGS canon (Le Maitre, 2002, p 60[1]) I believe the logic is unassailable: a fine-grained sample from the chilled margin of a gabbroic intrusion, if found unlabelled in a drawer, would objectively be called a basalt, whereas the coarse-grained basic part of a thick komatiite lava would logically be called a gabbro (following, for example, Arndt et al., 1977). In other words, it should not be necessary to know where a rock comes from, or where it formed, in order to assign the appropriate name. To speak of a 'fine-grained gabbro' (MacKenzie et al., 1982, p12) is a logical contortion that ought to be queried by any intelligent student. The principles adopted here happen to be similar to the nomenclature adopted by the British Geological Survey (Gillespie and Styles, 1999).[2]

The 'practical' in the book's title highlights my aim to support students' own work in the petrology teaching lab or in research projects. Being a pragmatist, I have included outline optical data to allow simple mineral identification without recourse to a separate mineralogy text,[3] which (experience suggests) many students are reluctant to buy today; this summary optical information is given in Appendix A and in boxes at appropriate points in the body of the book. Appendix B covers various petrographic calculations, including a simplified CIPW norm scheme as an aid to understanding concepts like silica undersaturation. Appendix C summarizes the symbols and units used throughout the book. Figures and tables appearing in explanatory boxes are identified by numbers having *three* parts; so 'Fig. 1.3.1' identifies the first (or only) figure of Box 1.3 (which is of course the third box in Chapter 1). 'Fig. B3' refers the reader to Figure 3 in Appendix B. A general glossary is also provided to enhance the book's usefulness; terms defined in it are highlighted in **bold** where first mentioned in a chapter or section, or where cross-referenced in the glossary itself.

[1] Elsewhere, however (p3), the IUGS defines volcanic rock as 'an igneous rock with an **aphanitic** texture, i.e. a relatively fine-grained (<1 mm) rock …'. Rather than adopt this ambiguous usage, the term 'volcanic' is reserved in this book for its traditional genetic meaning, describing an igneous rock crystallized from magma that erupted at (or very close to) the surface.
[2] See www.bgs.ac.uk/bgsrcs/.
[3] The optical principles summarized in Appendix A are intended merely as a reminder, not as an introductory course.

Acknowledgements

The following organizations are thanked for permission to reproduce figures (the numbers in parentheses) or other material specified: American Geophysical Union (Figs. 5.3.1a,b,c; 6.4; 6.24; 9.13), American Journal of Science (Fig. 9.7b), Blackwell Science (Figs. 6.16; 8.23; 9.7c), British Geological Survey (Fig. 4.3e), Caribbean Helicopters (Fig. 6.3b), Elsevier (Figs. 2.13; 4.9; 4.14a; 5.4; 5.12; 5.13; 5.6.1; 6.17; 6.26a; 6.4.1; 8.7; 8.16; 8.18; 9.3; 9.14; 9.15; 9.18; Plate 2.10), Geological Society of America (Figs. 4.14b; 5.8a; 5.3.2; 6.7; 6.21b,c; 6.26b), Geological Society of Australia (Fig. 4.6.2), Geological Society of London (Figs. 4.4; 9.6; 9.8; 9.11; 9.16; 9.6.1 and a text extract from Guest et al., 2003), Geological Survey of Denmark and Greenland (GEUS) (Figs. 2.2d; 4.3; 4.6; 4.6.1; 8.3a; 8.8; 8.10a–c; 8.13b), Geologists' Association (Figs. 7.6; 8.5b), Getty Images (Fig. 7.9a), Integrated Ocean Drilling Program (Fig. 2.9a), Leicester Literary and Philosophical Society (Fig. 2.14), Mineralogical Association of Canada (Fig. 9.23), Mineralogical Society of America (Fig. 6.6), Montserrat Volcano Observatory (Fig. 7.4a and the front cover image), The Open University (Figs. 6.13; 6.21), Oxford University Press (Figs. 3.12; 4.4.1; 5.3; 5.8b; 5.11; 5.5.2; 6.18; 8.15; 8.19; 8.4.1; 9.7a; 9.20; 9.22), Penguin Books (text passage from Radice, 1963), Springer Business Media (Figs. 4.13; 5.9; 6.5; 7.17b; 9.4.1), Wiley Interscience (Fig. 2.5) and U.S. National Academy of Sciences (Fig. 5.4.1). The U.S. Geological Survey is warmly acknowledged as the source of many public-domain images used in this book (see captions); if only some other geological surveys were as generous.

The following people are warmly thanked for providing illustrations or giving permission to reproduce figures: J. Bédard (Fig. 4.3d); Smithsonian Institution of Washington DC (Figs. 6.3a & d); J. Blundy (Fig. 7.17b); A. Bussell (Fig. 8.10d); J.P. Davison (Fig. 2.5); C.H. Donaldson (Fig. 5.9); C.H. Emeleus (Fig. 4.3e); R. Greeley (Fig. 6.3e); D. Millward (Fig. 7.4b); I. Modinou (Fig. 2.2a); J.S. Myers (Fig. 4.6.3).

I thank the following colleagues for kindly providing samples or images for the following colour plates: D. Alderton (Plate 8.5)' F. Belton (9.18; 9.19), J.B. Dawson (9.10), C.M.H. Edwards (6.1; 6.2), J.G. Fitton (2.1), C.A. Goodrich (2.10), I.S. McCallum (4.9; 5.1; 5.2), E. McPherson (5.8; 5.9), M.A. Menzies (5.5), R.H. Mitchell (9.1; 9.2), I. Modinou (2.6), G. Stripp (4.11), R.N. Taylor (6.4; 6.5), C. Tiltman (7.2), B.G.J. Upton (9.9), P. Wallace (6.11), J. Walton (9.5), A. Zaitsev (9.4). Figure 2.9(c) was kindly provided by Integrated Ocean Drilling Program. I am most grateful to Eric Tomme and Jonathan Stone for providing Montserrat photographs. Other images are from my own collection or that of the Department of Earth Sciences, Royal Holloway, University of London. I am particularly grateful to Aubrey Lambert of Carl Zeiss (Germany) for giving me permission to reproduce the Michel-Levy chart.

Grazie mille to Giulia Kistruck for kindly translating a passage in Chapter 7 from Italian. Kevin D'Souza, Neil Holloway, Frank Lehane and Mark Longbottom are thanked for their skilled technical support over many years. I am grateful to Ian Francis and Kelvin Matthews of Wiley-Blackwell for their unstinting support.

Above all, I am very grateful to Dave Alderton, Grant Cawthorn, Godfrey Fitton,[1] John Gamble, Ray Macdonald, Colin Macpherson, Nick Petford and Anatoly Zaitsev for critically reviewing sections of the book, and to Richard Arculus and Jon Blundy for their many constructive comments on the complete manuscript. These perceptive contributions have added materially to the book's substance and accuracy. Its shortcomings of course remain my responsibility alone.

[1] who also improved algebraic rigour in Box 3.2.

Chapter 1

An introduction to magmas and magmatic rocks

WHY STUDY MAGMATIC ROCKS?

The purpose of this book is to stimulate the reader's interest in magmatic rocks and processes, to develop key skills of describing, classifying and naming such rocks, and to show how much we can learn about igneous processes from careful, informed interpretation of rock textures, mineralogy and geochemistry. The book is aimed primarily at the intermediate-level student of geology who already has a basic knowledge of igneous rocks, but anyone starting from scratch should find that the opening chapter and relevant boxes – together with the Glossary – provide the minimum introduction they require. The emphasis throughout the book will be on practical investigation, mainly by means of the polarizing microscope; basic mineral-identification data have therefore been included to provide – between one set of covers – all that the student needs during a typical igneous practical class.

The logical place to begin any 'ig. pet.' course is to ask what purpose the petrologist, geologist or volcanologist hopes to accomplish in studying igneous rocks. Why do we do it? What kinds of things do we hope to learn? What answers are we trying to find? Such questions should always engage the mind of a petrologist who embarks on a petrographic or geochemical study; petrological science has moved on a long way from the early days when merely describing an igneous rock was an end in itself. In real life, a petrologist may study a suite of igneous rocks with one or more objectives in mind, including:

- understanding eruptive *processes*;
- assessing from previously erupted products the *hazard* presented by a volcano to surrounding communities;
- investigating *magma evolution* in a subvolcanic magma chamber;
- documenting the *structure* and *formation* of oceanic or continental crust;
- inferring past *tectonic environments* (e.g. mid-ocean ridge, island arc) from the compositions of ancient igneous rocks;
- understanding the formation of economic *mineral deposits* associated with igneous rocks.
- establishing the *absolute age* of a succession of sedimentary and volcanic rocks (igneous rocks being easier to date isotopically than sedimentary rocks);
- identifying the *source* from which a magma has originated, and under what *conditions* melting occurred (i.e. investigating 'magma genesis');
- identifying from erupted magmatic rocks the character and distribution of *geochemical domains* in the underlying mantle, and their evolution in time.

In every such investigation, there is likely to be a role for carefully describing the igneous rocks involved, but the ultimate goal is usually to learn about magmatic processes, or the conditions under which those processes operate. That goal – of studying igneous rocks to learn about process – will come up again and again in this book, because understanding what goes on in magmatic systems is the modern petrologist's principal aim in life.

Igneous Rocks and Processes: A Practical Guide, 1st edition. By Robin Gill. Published 2010 by Blackwell Publishing

Igneous rocks can tell us not only about processes taking place on the Earth's surface at the present time, but also:

- about processes that have taken place earlier in Earth history, and
- about processes that operate in parts of the Earth that are not directly accessible to us, for example in a magma chamber that originally lay 5 km below an active volcano (but whose contents – or erupted products – are now exposed at the surface).

Today, anyone working with igneous rocks has to apply a range of skills, including the analysis of field relationships, hand-specimen identification in the field, the description and interpretation of thin sections, the allocation of informative rock names, the quantitative interpretation of rock and mineral analyses (often including trace elements and isotope ratios), and the interpretation of experimental equilibria and phase diagrams. This book provides a basic introduction to all but the first of these practical and interpretive skills. The book is not intended to take the place of advanced texts dealing with theories of igneous petrogenesis.

The remainder of this chapter is devoted to introducing the basic vocabulary that will be needed for a clear explanation of igneous rocks.

WHAT IS 'MAGMA'?

Igneous rocks are those that form from molten products of the Earth's interior. Petrologists use two words for molten rock. **Magma**[1] is the more general term that embraces mixtures of melt and any crystals that may be suspended in it. A good example would be flowing lava which contains **crystals** suspended in the melt (Fig. 1.1): the term magma refers to the entire assemblage, embracing both solid and liquid states of matter present in the lava. **Melt**, on the other hand, refers to the molten state on its own, excluding any solid material which might be suspended in or associated with it. The difference becomes clearer if one considers how one would chemically analyse the distinct chemical compositions of the magma and melt, once the lava flow had solidified (Fig. 1.1). The *magma* composition could be estimated by crushing up a sample of the solidified lava, including both phenocrysts and groundmass (ensuring they are present in representative proportions). Analysing the *melt* composition, however, would require the groundmass or glassy matrix – the solidified equivalent of the melt between the phenocrysts – to be physically separated out and analysed on its own.

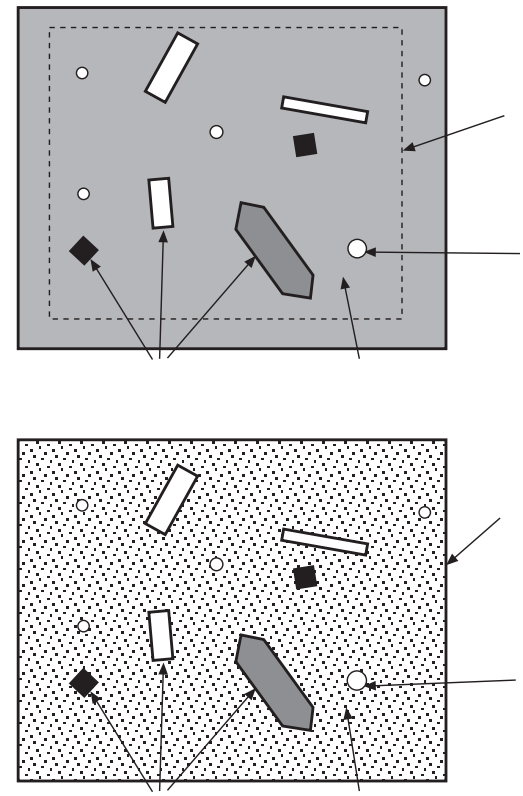


Fig. 1.1 Terminology used to designate the different constituents of (a) a molten lava and (b) the same lava in the solid state.

In fact, 'magma' may be used in a still broader sense. An ascending magma body, as it approaches the surface, commonly contains gas bubbles as well as phenocrysts, bubbles formed by gas that has escaped from the melt due to the fall in pressure that accompanies ascent (see Box 1.4). The term 'magma' is generally understood to embrace melt, crystals *and* any gas bubbles present (Fig. 1.1). Once erupted on the surface, on the other hand, and having lost some of its gas content

[1] Terms printed in **bold** are defined (and in some cases their etymology is explained) in the Glossary.

to the atmosphere, the molten material is more appropriately called 'lava'. Determining a representative chemical analysis of the original magma composition, including the gaseous component, would however be difficult: as the melt solidified and contracted on cooling, the gaseous contents of the vesicles would escape to the atmosphere (and they would in any case be lost during crushing of the rock prior to analysis). Determining the concentrations of these **volatile** magma constituents – from the solid rock that the magma eventually becomes – therefore requires a different analytical approach that will be discussed later.

Magmas are originally formed by melting deep within the Earth (Chapter 2). The initial melting event most commonly takes place in the mantle, though passage of hot magma into or through the continental crust may cause additional melting to occur there as well, adding to the chemical and petrological complexity of continental magmatic rocks. In oceanic and continental areas, mantle-derived magmas are liable to undergo cooling and partial crystallization in storage reservoirs (magma chambers) within the crust (Chapter 3), and such processes widen considerably the diversity of magma compositions that eventually erupt at the surface.

THE DIVERSITY OF NATURAL MAGMA COMPOSITIONS

What do we mean by magma (or rock) composition?

The overall composition of an igneous rock can be expressed in two alternative ways:

- as a quantitative geochemical analysis, giving the percentage by mass of each of the main *chemical* constituents (Box 1.1);
- as a list of the *minerals* present in the rock as seen under a microscope, perhaps including an estimate – qualitative or quantitative – of their relative proportions.

Though correlated, these two forms of analysis are not entirely equivalent in the information they convey. As a quantitative statement of chemical composition that can be plotted on graphs (e.g. Fig. 1.2) and used in calculations, a geochemical analysis provides the more exact information. The **bulk analysis** (also known as a **whole-rock analysis**) of a volcanic rock approximates closely – except for volatile components – to the composition of the magma from which it formed, considered at a stage before it had begun to crystallize. Careful analysis of geochemical data can reveal a lot about the *source* of the melt and the *conditions* (pressure, depth, extent of melting) under which the melt originally formed.

In some circumstances, however, other forms of rock analysis are of more practical use. Geochemical analyses, requiring elaborate laboratory facilities, are not usually available at the field stage of an investigation, when a geologist will normally find mineralogical and textural observations on hand-specimens a more practical way of characterizing, and discriminating between, the different rock types present in the area. Moreover, the occurrence in thin section of certain key indicator minerals – such as quartz, olivine, nepheline, aegirine–augite – provides immediate, key clues about the melt's chemical composition without resorting to the expense of geochemical analysis. The mineralogy of an igneous rock also provides information on *post-magmatic processes* (weathering, hydrothermal **alteration**) that may have made its chemical composition unrepresentative of magma composition (Box 1.4).

The study of a rock's mineralogical composition and texture – using a polarizing microscope to examine a thin section – is the science called *petrography*. A petrographic analysis of an igneous rock can range from a simple list of minerals seen (noting the textural relationships between them) to a full quantitative analysis of their relative volumes measured in a thin section. Qualitative petrographic examination is the normal prelude to geochemical analysis: it allows one to screen a suite of samples to eliminate unrepresentative or unsuitable specimens, and thereby avoid the expense of unnecessary chemical analyses. But a petrographic examination tells us a lot more about the rock than just its suitability for geochemical analysis: careful study of the rock's texture provides much information about the *eruption and crystallization history* of the magma.

It follows that a geochemical analysis and a petrographic (mineral-based) analysis give

Box 1.1 Chemical analyses of rocks and minerals

Most igneous rocks and minerals, and the magmas from which they form, fall into the class of chemical compounds called **silicates** – consisting of metals combined with silicon and oxygen.

The simplest way to visualize the chemical composition of complex silicate materials is as a mixture of oxides: silicon dioxide (SiO_2 – also known as 'silica') is usually the most abundant oxide in igneous rocks and minerals, and the oxides of titanium (TiO_2), aluminium (Al_2O_3), iron (Fe, both ferric Fe_2O_3 and ferrous FeO), manganese (MnO), magnesium (MgO), calcium (CaO), sodium (Na_2O), potassium (K_2O) and phosphorus (P_2O_5) are usually present in significant amounts as well. A typical silicate analysis, giving the *percentage by mass* of each of these oxides (traditionally referred to – inappropriately – as a 'weight percent' analysis), is shown in the table below.* The advantage of reporting an analysis in terms of *oxide* percentages is that it neatly introduces the right amount of oxygen into the analysis without the need to analyse it directly. The elements listed, whose oxides are normally found at levels greater than 0.1% by mass, are collectively referred to as the **major elements**.

Table 1.1.1 Analysis of a typical basalt.

SiO_2	48.3
TiO_2	2.591
Al_2O_3	13.03
Fe_2O_3 (ferric)	6.84
FeO (ferrous)	7.72
MnO	0.23
MgO	5.46
CaO	10.91
Na_2O	2.34
K_2O	0.51
P_2O_5	0.26
H_2O^+	1.41
CO_2	0.49
Total	100.1

Note that iron may be shown in the analysis as both ferric (trivalent) and ferrous (divalent) forms; the reason for doing so is that Fe^{3+} and Fe^{2+} ions behave differently in melts and mineral crystals, as explained in Box 2.6. Nonetheless, most modern analyses show only the total amount of iron oxide, expressed either as 'ΣFeO' or as 'ΣFe_2O_3' – the sigma symbol (Σ) denoting the summation; formulae for such calculations are given in Box 2.6.

The last two items in the analysis (Table 1.1.1) record the mass percentages of the two main **volatile** constituents of the rock (see Box 1.3). The analysis ends with a total percentage for all of the oxides determined, a cross-check which, in a good analysis, will normally lie between 99.5% and 100.5%.

Numerous other chemical elements are present in magmas, rocks and minerals at concentrations below 0.1%. These less abundant constituents are known as **trace elements**, and their concentrations are expressed in parts per million by mass ('ppm' = $\mu g\ g^{-1}$ = microgrammes of *element* per gramme of sample) or, in the case of the least abundant trace elements, in parts per billion (ppb = $ng\ g^{-1}$ = nanogrammes of element per gramme of sample). In spite of their low concentrations, trace elements provide important information about magma sources and conditions of formation.

Most rock analyses are prepared today either by inductively coupled plasma–atomic emission spectrometry ('ICP-AES') or by X-ray fluorescence spectrometry ('XRFS'); both are capable of determining major elements and selected trace elements in igneous rocks. Details of these and other methods – beyond the scope of this book – may be found in Gill (1997), which also describes the sample preparation required prior to analysis.

* Analyses of some non-silicate minerals (oxide, carbonate, phosphate and sulphate minerals) may be presented in the same way; SiO_2 will be a subordinate component in such cases.

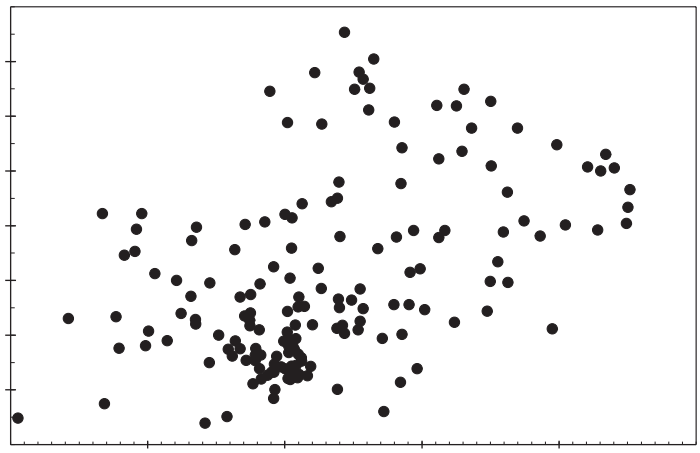


Fig. 1.2 Plot of total alkalis ($Na_2O + K_2O$) against SiO_2 (both in mass %) for a representative range of terrestrial volcanic rock analyses (representing igneous melt compositions). Data from Wilson (1989) with selected additions from Carmichael et al (1974) and Cox et al (1979). All data have been recalculated volatile-free (see Box. 1.3), except in the case of those analyses from Wilson (1989) for which no volatile data are given, which are assumed to have been volatile-corrected.

us complementary information about an igneous rock, and neither alone provides a complete understanding of the rock's origin and history.

How widely do natural magma compositions vary?

Figure 1.2 shows a large number of geochemical analyses of volcanic rocks from various geotectonic environments plotted in a **variation diagram**. The vertical dimension in this diagram depicts the sum of the Na_2O and K_2O contents (each, and their sum, expressed in mass per cent [mass %; see footnote[2]], i.e. grams of oxide per 100 g of rock) for each sample. The horizontal dimension shows the corresponding SiO_2 content (also in mass %), and each data point in the graph – that is, each pair of Na_2O+K_2O and SiO_2 co-ordinates – represents an individual rock analysis. In such diagrams, the rock analysis is taken to represent the original magma's composition. This particular plot is known as a 'total-alkalis *versus* silica' (or 'TAS') diagram and it is widely used for the geochemical classification of volcanic rocks (see Fig. 1.4).

The main purpose of showing this diagram here is to illustrate how widely natural silicate magmas can vary in their composition: SiO_2 contents range from 31% to 76%, and total alkali contents vary from 1% up to 15%. (This range is solely for silicate magmas: if natural **carbonatite** magmas were considered as well, the compositional range would become still greater.) This wide range of composition can be attributed primarily to four contributions that play a part in magma genesis:

- source composition and mineralogy (e.g. whether crust or mantle);
- depth of melting;
- extent (%) of melting;
- shallow magma-chamber fractionation processes, such as **fractional crystallization.**

The effects of these factors will be discussed in later sections of the book. The important conclusion to be drawn here is that natural volcanic rock (and magma) compositions lie scattered across a wide range of total alkali-SiO_2 space, with no obvious internal breaks

[2] In this book, the term 'mass percent' is used in preference to the traditional but less appropriate term 'weight percent'.

to divide up them into natural sub-groups. In other words, Nature creates within the Earth a *continuum* of potential magma compositions, and any categories or subdivisions we choose to erect (e.g. for the purpose of attaching names) are essentially arbitrary and man-made.

PARAMETERS USED TO CLASSIFY IGNEOUS ROCKS

Unless igneous petrologists are to communicate entirely in numbers, they need a consistent nomenclature that allows this wide compositional spectrum to be sub-divided into smaller fields, to which specific rock names can be applied, just as a state is divided for administrative purposes into named counties and districts.

Modern igneous nomenclature rests on three types of observation, each of which may influence the name given to a rock:

- *qualitative* petrographic observations (e.g. the presence or absence of quartz);
- *quantitative* petrographic data (e.g. the percentage of quartz in the rock);
- *chemical* composition (e.g. position in a TAS diagram – Fig. 1.4).

These can be illustrated further by considering three elementary ways in which we categorize igneous rocks.

Classification by qualitative criteria – grain size

Figure 1.3a shows how igneous rocks are divided into coarse-, medium- and fine-grained categories, based on a qualitative (or semi-quantitative) estimate of the average grain-size of the *groundmass* of the rock (N.B. *not* on the size of any phenocrysts present). This estimate may be based on hand-specimen observation or, more reliably, on thin section examination. According to the grain-size category in which it falls (fine, medium or coarse), a rock of basaltic mineralogy, for example, would be called a basalt, a dolerite (UK) or diabase (US),[3] or a gabbro.

[3] The IUGS *Subcommission on the systematics of igneous rocks* (Le Maitre, 2002) recommends the use of microgabbro in place of dolerite or diabase.

Another example of a qualitative observation used in rock classification is the presence of quartz or nepheline in the rock, indicating whether it is **silica-oversaturated** or **silica-undersaturated**.

Classification by mineral proportions – colour index

Familiar adjectives like 'ultramafic' and 'leucocratic' refer to the relative proportions of dark and light minerals in an igneous rock, where 'dark' and 'light' relate to the appearance of the minerals in hand-specimen, as indicated on the left of Fig. 1.3b. Dark minerals are known alternatively as **mafic** or **ferromagnesian** minerals; light minerals are also known as **felsic** minerals. The percentage of dark minerals is known as the **colour index** of the rock.

Quantitative measurements of mineral proportions in a thin section rely on a technique known as *point counting*. This entails mounting the thin section of interest in a special device attached to the microscope stage, which allows the slide to be advanced by regular small increments in both x and y directions by pressing relevant buttons. Starting near to one corner of the slide, the operator identifies the mineral under the cross-wires at each point as the thin section is stepped systematically across the stage, recording the number of 'hits' for each mineral present. Having acquired several hundred data points covering a significant area of the thin section, the percentage of each mineral is easily calculated. As the percentages calculated are proportional to the aggregate area of each minerals on the slide surface, such methods determine relative mineral proportions *by volume*, not by mass. As most dark minerals are significantly denser than the light minerals, this fact introduces a bias that must be borne in mind if mineral proportions determined in this way are compared with geochemical analyses (which are expressed in percentages *by mass*).

Strictly interpreted, all of the descriptors shown in Fig. 1.3b should be based on *quantitative* mineral proportions determined in this way, which is a time-consuming exercise. For most day-to-day purposes, however, the terms may be applied on the basis of a quick 'eyeball' estimate of dark and light mineral proportions.

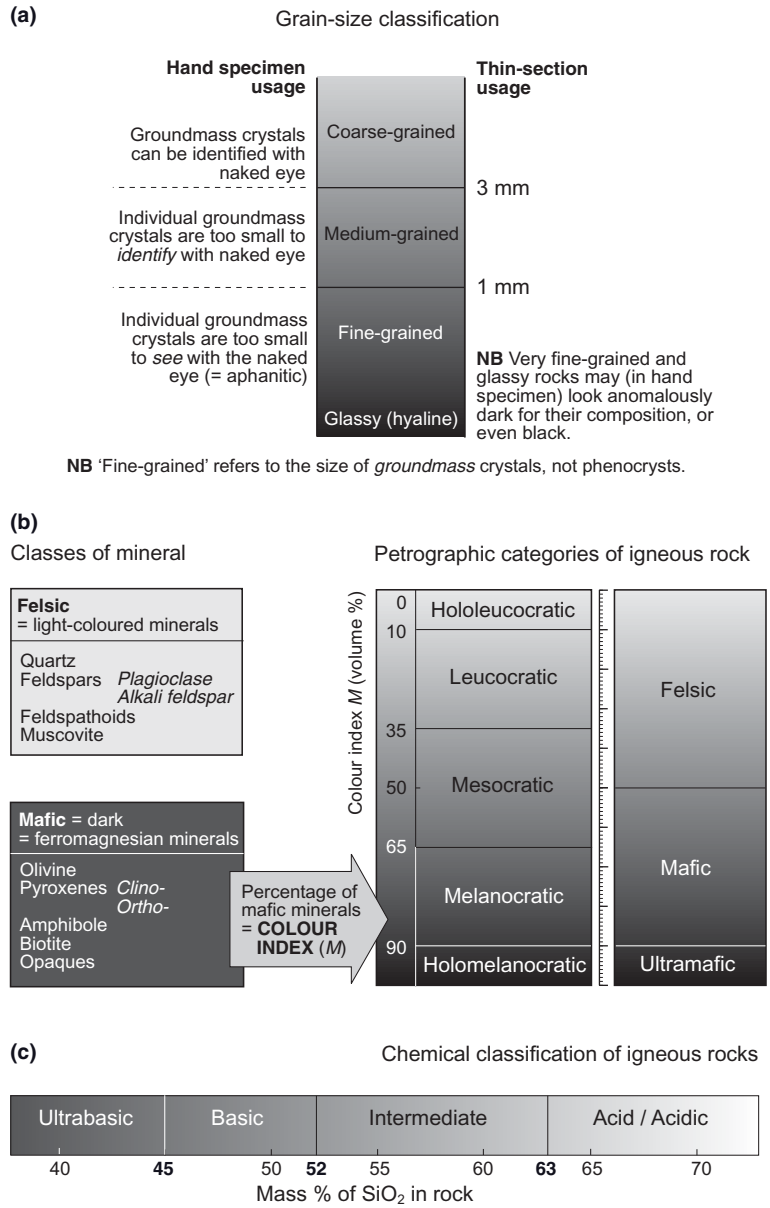


Fig. 1.3 Three simple ways in which igneous rocks may be categorized: (a) by grain size of the groundmass. The boundary between medium-grained and coarse-grained has been placed at 3 mm in conformity with Le Maitre (2002); other conventions (e.g. Cox et al., 1988) have used 5 mm; (b) by volume proportions of light (felsic) and dark (mafic) minerals observed under the microscope; (c) by silica content (requiring a chemical analysis). The boundary between intermediate and acid in (c) has been placed at 63% SiO_2 in conformity with Le Maitre (2002); previous conventions placed it at 65%. An analysis used to determine whether a sample is ultrabasic, basic, intermediate or acid should first be recalculated to a volatile-free basis (see Box 1.3).

It may help the reader to know the origins of words like **melanocratic** and **leucocratic:** they derive from the Greek roots *melano-* (meaning 'dark' as in *melan*oma and *melan*choly), *leuco-* (meaning 'light-coloured' as in *leuco*cyte – the medical term for a white blood cell), and *-cratic* (meaning 'ruled by', as in demo*cratic* and auto*cratic*). The term **meso-cratic** – though self-contradictory (since a rock cannot be dominated by something

between dark and light minerals!) – is the label applied to rocks having colour indices in the range 35–65.

Classification by chemical composition – acidic versus basic

The first classification of igneous rocks that most students encounter is the one that divides rocks into *ultrabasic*, *basic*, *intermediate* and *acid* categories. This classification is based on the SiO_2 content of the rock, as shown in Fig. 1.3c (based on values adopted by the International Union of Geological Sciences [**IUGS**]). The SiO_2 content, the first parameter in the geochemical analysis shown in Box 1.1, cannot be known until the sample has undergone laboratory analysis, and herein lies the main disadvantage of this classification: it cannot be used to describe rocks as they are being collected in the field or examined under the microscope.

It is important to draw a clear distinction between the silica content of a rock (which usually lies between 40% and 75%) and the quartz content (rarely more than 30%, and often zero): silica (SiO_2) is a chemical *component* present in all silicate minerals, whereas quartz (which has the same composition, SiO_2) is a *mineral* with a particular composition and crystal structure. Quartz represents surplus SiO_2, i.e. that left over after all the other silicate minerals have captured their share of the available silica in the melt.

The term 'silicic', a less precisely defined term widely used in North America, is broadly synonymous with 'acid'.

DEVISING A BASIC PETROGRAPHIC NOMENCLATURE FOR IGNEOUS ROCKS

The initial emphasis in this book will be on rock nomenclature based on qualitative petrographic observations, as these are most relevant to undergraduate practical classes and field work.

Most igneous rock names consist of a **root name** (such as *basalt*, *andesite*, *trachyte*) prefaced by one or more **qualifiers** that highlight any distinctive textural or compositional features that the rock in question may possess (e.g. *olivine* basalt, *plagioclase-phyric* andesite, *aphanitic* trachyte).

What is a basalt?

A well known dictionary of petrology defines 'basalt' as follows:

> *According to modern usage, basalt is a volcanic rock composed essentially of labradorite, pyroxene and iron ore, with or without interstitial glass or chlorite.*[4]

This definition, though recognizably referring to basalt, has a number of shortcomings that are worth highlighting in the interests of clarity:

1. As commonly understood, 'volcanic' is a *genetic* term (implying eruption on the Earth's surface) that may, in a few cases, be difficult to prove in the field. Though most basalts are indeed products of surface eruptions, petrologists prefer to base rock nomenclature on *descriptive* criteria relating to the individual sample, independent of field interpretation. In other words, it should be possible to give an appropriate name to an unlabelled rock sample pulled out of a drawer, without knowing the kind of body from which it was actually collected. The key descriptive characteristic that discriminates basalt from dolerite and gabbro is that it is the *fine-grained* member of this family. A fine-grained basic rock forming the chilled contact of a dyke (a hypabyssal rock), or even that of a major intrusion (a plutonic rock), qualifies as a basalt just as much as a basic lava flow. The centre of a thick basic lava flow may, on the other hand, be medium-grained (qualifying as dolerite) or in extreme cases even coarse-grained, in spite of its undoubtedly volcanic origin.
2. 'Pyroxene' is not specific enough: the pyroxene characteristic of basalt (and dolerite and gabbro) is high-Ca pyroxene, usually the variety known as augite (Box 2.1). Basalts *may* contain low-Ca pyroxene – enstatite – as well, but never without high-Ca pyroxene. A precise definition of basalt should therefore specify *augite* (or high-Ca pyroxene) as the essential pyroxene.

[4] Tomkeieff et al (1983).

3 'Labradorite' (An_{50}–An_{70} – see Box 1.2), on the other hand, is too restrictive. In some terrestrial basalts and gabbros, plagioclase cores fall within the more calcic range of bytownite (An_{70}–An_{90}), and lunar basalts even contain anorthite (An_{90}–An_{100}). Recognizing this wider range of plagioclase compositions in natural basalts, it is advisable simply to stipulate 'calcic plagioclase' (meaning any plagioclase whose anorthite content exceeds 50%) as the essential plagioclase in a basalt.
4 'With or without interstitial glass …' is redundant in a concise definition.
5 Chlorite is a hydrous sheet silicate mineral that never crystallizes directly from magma and is never found in fresh igneous rocks. Where it does occur in igneous rocks, it is invariably as a **secondary** product of the **hydrothermal alteration** of igneous minerals such as pyroxene, or as a constituent of hydrothermal veins. As the product of late-stage hydrothermal or low-grade metamorphic (i.e. post-magmatic) processes, affecting some basalts but not others, it has no place in the definition of an igneous rock.

A more accurate and succinct petrographic definition of 'basalt' is as follows:

> *Basalt is a fine-grained igneous rock consisting of the essential minerals calcic plagioclase and augite.*

How does one determine under the microscope whether a plagioclase is calcic or sodic? A simple technique is described in Box 4.1, but the practical details need not concern the reader at this stage.

'Essential', 'type', 'accessory' and 'post-magmatic' minerals

The above definition of a basalt rests on the presence of two key minerals: high-Ca pyroxene and calcic plagioclase. Any fine-grained igneous rock containing these two minerals qualifies to be known by the **root name** 'basalt'. However, petrologists routinely divide basalts into sub-groups according to other minerals they may contain. For instance, the occurrence of olivine in a basalt, in addition to augite and calcic plagioclase, places a basalt in the important sub-group called 'olivine basalt'. Not all minerals present in a rock are used in this way, however. For the purpose of giving rocks simple, informative names, it is helpful to consider the minerals a rock contains under four conceptual headings:

1 *Essential minerals:* those minerals whose presence in the rock determines the root name given to it. For example, the dominance of calcic plagioclase and augite in a *coarse-grained* rock leads unavoidably to the root name 'gabbro'. The absence of either of these essential minerals would invalidate the name: had olivine been present in place of augite, for example, the rock would be called a troctolite (Chapter 4).
2 *Type minerals:* minerals whose presence does not affect the root name, but does allow a rock type to be sub-divided by the use of **qualifiers**. For example, an *olivine gabbro* contains olivine in addition to calcic plagioclase and augite. The minerals selected to serve as type minerals usually tell us something about the composition of the rock: the presence of olivine, for example, indicates that a gabbro is somewhat SiO_2-deficient; the presence of aegirine in a syenite indicates that it is **peralkaline**.
3 *Accessory minerals:* minerals present in a rock (often in minor amounts) that tell us little about its key chemical characteristics and therefore have little to contribute to rock nomenclature. Examples are chromite, magnetite, apatite and ilmenite.
4 *Post-magmatic minerals:* minerals that formed *after* complete crystallization of the magma:
   - **hydrothermal** minerals filling veins and other voids (e.g. zeolite)
   - **secondary** minerals, replacing original minerals (e.g. epidote).

   As post-magmatic minerals are formed in late hydrothermal rather than igneous processes, they play no role in igneous nomenclature but, because their formation may have been accompanied by significant chemical changes, their presence should always be noted.

Box 1.2 Expressing the composition of a solid solution mineral

Olivine and plagioclase are two among many minerals that consist of **solid solutions**: any natural olivine, for example, is a mixture – on the molecular scale – of two compounds, Mg_2SiO_4 (forsterite, often abbreviated to Fo) and Fe_2SiO_4 (fayalite, abbreviation Fa).

Table 1.2.1 below shows a simplified olivine analysis, expressed in mass percentages of SiO_2, FeO and MgO (Box 1.1). A more concise way of stating the composition of a solid-solution mineral is as percentages of its **end-member** molecules, in this case Mg_2SiO_4 and Fe_2SiO_4. To see how this is done, it is helpful first to rewrite each formula in its alternative form, namely $(MgO)_2(SiO_2)$ and

Table 1.2.1 Calculating end-members for a simplified olivine analysis.

	Simplified olivine analysis, mass %*	Oxide **RMM**	Moles available per 100g of sample†	Moles allocated to $2FeO.SiO_2$‡	Moles allocated to $2MgO.SiO_2$	Total moles allocated	Residuals
SiO_2	39.58	60.09	0.6588	0.1157	0.5414	0.6571	0.0017§
FeO	16.63	71.85	0.2315	0.2315		0.2315	0.0000
MgO	43.66	40.32	1.0828		1.0828	1.0828	0.0000
Total	99.87		1.9731				
		Moles of X_2SiO_4:		0.1157	0.5414	0.6571	
		Molar % Fa and Fo#:		17.61%	82.39%	100.00	

* 'Oxide mass %' can be visualized as *grammes of each oxide per 100g of sample*.
† Each number in column 1 divided by the corresponding RMM in column 2 gives *moles per 100g of sample*.
‡ If n moles of FeO are available, they combine with $0.5n$ moles of SiO_2 to form $0.5n$ moles of fayalite.
§ The small excess of SiO_2 (amounting to 1 part in 400 of available SiO_2) may reflect analytical error or the fact that small amounts of CaO and MnO present in the original analysis have been neglected in the simplified version shown above.
= 100 * 0.1157 / 0.6571, etc.

It should be emphasized that a mineral that has essential status in one rock may serve as a type mineral in another, and as an accessory mineral in a third.

Examples of the essential minerals that define the common volcanic rock types are given in Table 1.1, together with the main type minerals upon which qualifiers may be based. This table is a simplification of the quantitative nomenclature spelled out in Le Maitre (2002). It is more common today, if a major element analysis is available, to derive a fine-grained rock's root name from its chemical composition plotted in Fig. 1.4, rather than from petrographic criteria. Since Fig. 1.4 has been based on a large compilation of petrographically well characterized volcanic rocks (Le Maitre, 2002), there is generally a good correlation between petrographic and chemical nomenclature.

A reader trying to memorize root names and their definitions can easily reduce each definition in Table 1.1 to a simple code. For example, nephelinite could be represented as 'cpx+ne'. The coarse-grained equivalent (e.g. ijolite, Table 9.3) could be specified by writing the same code in capitals.

Devising a full petrographic name

This hierarchy of minerals forms the basis for giving petrographic names to all igneous rocks. It provides for informative names such as *olivine gabbro*, *hornblende andesite* and *muscovite biotite microgranite*; in each of these compound names, a **root name** is prefaced by one or more **qualifiers**. The most important qualifiers indicate the type minerals present (which often provide clues about magma composition). A petrographic rock name has the general form:

(type mineral 3) (type mineral 2) (type mineral 1) … root name

$(FeO)_2(SiO_2)$. Doing so makes clear that *one* molecule of forsterite (Mg_2SiO_4), for example, is made by combining *two* molecules of MgO with *one* molecule of SiO_2. Such calculations become easier when the original analysis is expressed in numbers that reflect how many *molecules* (or moles) of each end-member are present, rather than how many *grammes*.

This transformation is accomplished by dividing each oxide percentage (mass % = *g of oxide per 100 g of olivine*) in column 1 by the relevant relative molecular mass ('RMM' in column 2). The result, in column 3, shows the number of *moles of each oxide per 100 g of olivine*. The 0.2315 moles of FeO can then be combined with 0.2315 ÷ 2 = 0.1157 moles of SiO_2 to produce 0.1157 moles of $(FeO)_2SiO_2$ (see table). Likewise 1.0828 moles of MgO can be combined with 1.0828 ÷ 2 = 0.5414 moles of SiO_2 to produce 0.5414 moles of $(MgO)_2SiO_2$. Dividing each of these numbers by their sum (0.6571) and multiplying by 100 gives the *molar percentage* of each **end-member** in this sample of olivine. The result shown in the Table can be written in the short-hand form Fo_{82}, the most concise way of expressing any olivine's composition.

Similar calculations allow plagioclase compositions to be expressed in terms of the molar percentage of the anorthite molecule (e.g. An_{56} for a plagioclase with 56 mole % of An and 44% Ab). The following names are widely used for specific ranges of composition:

anorthite	An_{100}–An_{90} (also refers to the pure end-member $CaAl_2Si_2O_8$)
bytownite	An_{90}–An_{70}
labradorite	An_{70}–An_{50}
andesine	An_{50}–An_{30}
oligoclase	An_{30}–An_{10}
albite	An_{10}–An_0 (also refers to the pure end-member $NaAlSi_3O_8$).

Solid solution in pyroxenes is more complex, so representing the composition of a pyroxene requires *three* compositional end-members: $Mg_2Si_2O_6$, $Fe_2Si_2O_6$ and $Ca_2Si_2O_6$ (as explained in Box 2.1). The presence of small amounts of Al_2O_3 and TiO_2 in most natural pyroxenes complicates matters a little, but for present purposes this can be ignored. Garnet compositions are still more complex and require *six* end-members (Box 5.2). Such 'formula calculations' are explained in more detail in Gill (1996, Chapter 8).

Note the convention (see Le Maitre, 2002) that, if several type minerals are listed in a rock name, the most abundant of them is listed last (i.e. closest to the root name). So a granite containing more biotite than muscovite would be called a *muscovite biotite granite*, not a biotite muscovite granite. The logic behind this convention is that muscovite serves here as a minor qualifier, indicating what kind of *biotite granite* we are dealing with.

The decision as to which minerals should be highlighted as type minerals is a matter of petrological judgement; experience, together with Table 1.1, will suggest which minerals have compositional significance in each case. One rule applies in all circumstances: no mineral that has the status of an essential mineral in a particular rock (one indispensable in determining the root name) can also feature as a type mineral. It would be a tautology to speak of an *augite basalt*, for instance, since the presence of augite is required by the root name basalt anyway, and needs no further emphasis.

Nonetheless, in dealing with an andesite, where the mafic mineral may be augite, low-Ca pyroxene, hornblende *and/or* biotite (Table 1.1), it *would* be appropriate to specify augite as a type mineral: whereas hornblende and biotite are characteristic of more **evolved**, lower-T, hydrous examples of andesite magma, the name *augite andesite* signifies that we are dealing with a relatively **primitive**, high-T or anhydrous andesite magma.

Appending type minerals to a rock name gives useful qualitative information (beyond what is available from the root name alone) about the chemical composition of the magma from which a rock crystallized, as will become

Table 1.1 Root names and essential minerals for the petrographic identification of the principal fine-grained igneous rocks. Where percentages are specified, these are estimates of volume % that may be based on qualitative visual assessment of a thin section. A number of minerals mentioned below may be unfamiliar at this stage (e.g. **feldspathoid**): they are introduced in later chapters. LCP, low-Ca pyroxene, including enstatite and pigeonite (see Box 2.1); plag, plagioclase; calcic plag, $An_{50–100}$; sodic plag, $An_{0–50}$; foid, **feldspathoid**.

Root name	Essential minerals required	Possible type minerals
basalt	augite + calcic plag	olivine, LCP (→ tholeiitic basalt[1]), minor nepheline (+ olivine → alkali basalt[1])
basanite	augite + calcic plag + foid (>10%) + olivine (>10%)	nepheline, leucite or analcite (according to the dominant foid)
tephrite	augite + calcic plag + foid (>10%) (olivine < 10%)	nepheline, leucite or analcite (according to the dominant foid)
nephelinite	augite + nepheline	olivine, melilite
leucitite	augite + leucite	olivine, melilite
trachybasalt	Calcic plag + augite + alkali feldspar *or* foid	
andesite	sodic plag[2] + a mafic mineral (pyroxene *or* hornblende *or* biotite)	pyroxene, hornblende or biotite (according to the dominant mafic mineral present)
latite	sodic plag + alkali feldspar	quartz (<20%)
trachyte	alkali feldspar[3] ± sodic plag	quartz (<20%), foid (<10%), aegirine-augite, biotite
phonolite	alkali feldspar[3] ± sodic plag + foid (>10%)	aegirine, riebeckite, biotite; It is also normal to specify the dominant foid if not nepheline, e.g. 'leucite phonolite'
dacite	sodic plag[4] + alkali feldspar + quartz (>20%)	hornblende, biotite
rhyolite[5]	alkali feldspar[3] ± sodic plag + quartz (>20%)	biotite, aegirine

[1] These types of basalt are usually distinguished according to chemical (rather than mineralogical) criteria. The concepts are explained in Chapter 2 (Box 2.4).
[2] Plagioclase phenocrysts, abundant in most andesites, are commonly zoned with calcic cores; the *mean* feldspar composition is however An <50.
[3] Alkali feldspar exceeds plagioclase
[4] Plagioclase exceeds alkali feldspar.
[5] Rhyolites commonly have a glassy groundmass.

apparent in later chapters. Type minerals provide one way for the petrologist to discriminate between otherwise similar rock types. The same is true of various other kinds of qualifier that may prove useful in specific circumstances, telling us about eruptive processes and crystallization history:

- It may be relevant to highlight textural features in a rock name if, for instance, differences in texture serve to discriminate between two sub-groups: similarities in eruption conditions or crystallization history may be shared by representatives of one batch of magma, but differ from those experienced by a second batch.
- Textural qualifiers such as **vesicular**, **porphyritic** (though see below), **seriate**, **spherulitic**, **welded**, **ophitic** and **poikilitic** provide key information about small-scale magma processes or conditions of crystallization.
- The identity of the phenocrysts present in a rock may be spelled out by prefacing the rock name with, say, *olivine-phyric* (if phenocrysts consist of olivine alone) or *olivine–augite–phyric* (if olivine *and* augite phenocrysts are present). An andesite containing plagioclase phenocrysts and hornblende in the groundmass would be referred to as a *plagioclase-phyric hornblende andesite*. Notice here that, although the mere presence of plagioclase is spelt out by the root name *andesite*, the fact that plagioclase occurs *as phenocrysts*

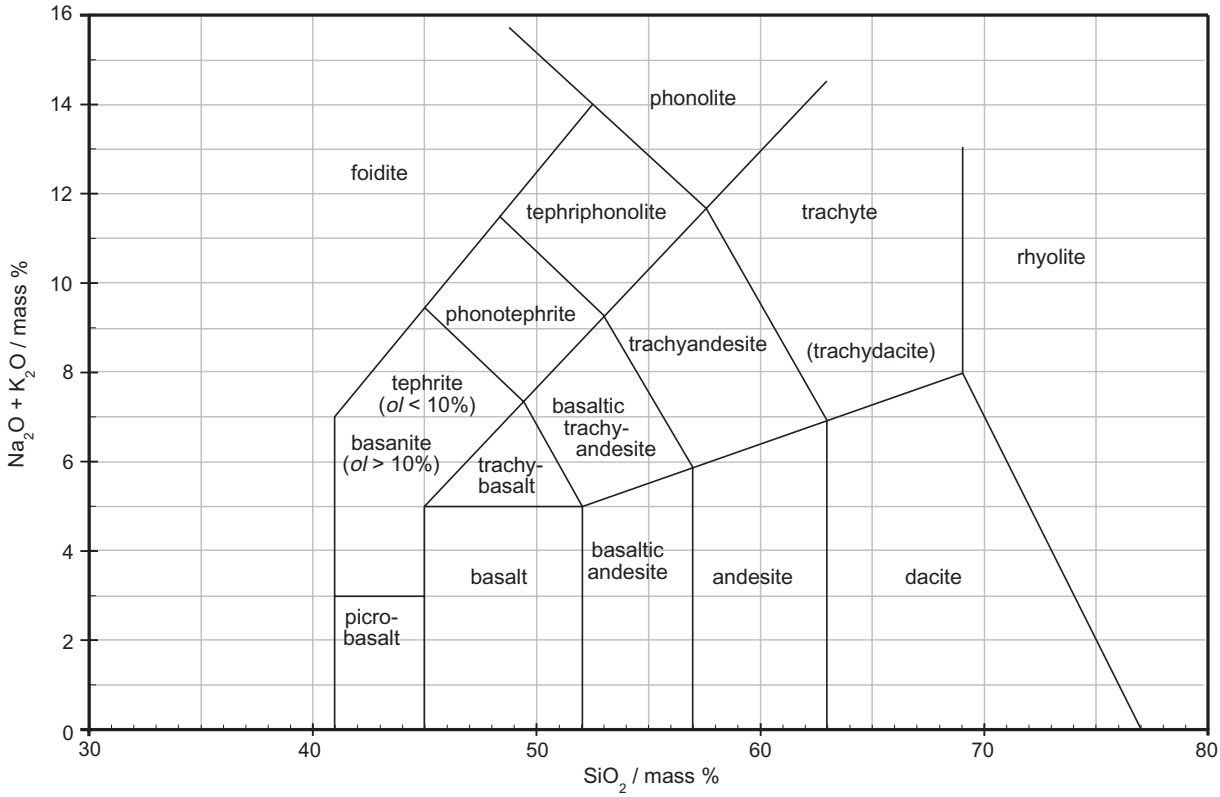


Fig. 1.4 TAS grid showing the fields for common rocks types designated by the *IUGS Subcommission on the Systematics of Igneous Rocks* (Le Maitre, 2002).* All analyses require correction for volatile content (Box 1.3) prior to plotting in this diagram.

* The symbol '*ol*' refers to **normative** olivine content (explained in Box 2.4). Rock compositions falling in the trachyte field may be given the name trachydacite if quartz amounts to more than 20% of the **normative** felsic minerals as a whole (quartz + feldspars). Such details need not concern the reader of Chapter 1.

needs emphasizing by means of the prefix 'plagioclase-phyric'.

- As Fig. 1.1 shows, the identity of the phenocrysts in a volcanic rock tells us which minerals had begun to crystallize prior to eruption (e.g. in a sub-volcanic magma chamber).
- Petrologists also use a variety of chemical qualifiers (e.g. low-K, high-K, peralkaline, peraluminous) to refine particular rock names. Such chemical parameters will be described in the following section.

CHEMICAL SUBDIVISION OF IGNEOUS ROCKS AND MAGMAS

There are certain circumstances in which petrographic nomenclature based on the polarizing microscope cannot work on its own. One example is where a rock contains a significant amount of glass. Most submarine basalts, for instance, consist of small amounts of olivine and plagioclase crystals (augite crystals are rarely seen) set in a glassy matrix. Volcanic glass represents melt that, for a variety of reasons (e.g. rapid chilling), has had insufficient time to crystallize. Consequently, a portion of the chemical components that *would* (under different conditions) have crystallized into recognizable mineral crystals – upon which a petrographic name could have been based – is held back in a glass phase whose composition cannot be determined under the microscope. For such a rock, or one whose groundmass crystals are too fine-grained to identify under the microscope, the rock name must be allocated on the basis of a geochemical analysis.

Not surprisingly, the mineralogical composition of a rock – on which petrographic rock nomenclature is based – correlates strongly with its chemical composition. One can therefore map the divisions between the petrographic rock types discussed above (and shown in Table 1.1) on to appropriate major element variation diagrams, and use these as an alternative basis for allocating root names. Figure 1.4 shows a TAS diagram upon which a grid of fields and boundaries has been constructed, according to the recommendations of the *International Union of Geological Sciences* (Le Maitre, 2002). The boundaries are drawn empirically so that they fit as closely as possible the distribution on this diagram of a large suite of petrographically identified rock samples (see Le Maitre, 1976). In plotting analyses on this diagram, it is important to ensure that they have been recalculated in volatile-free form to eliminate as far as possible any distorting effects due to alteration or weathering (Box 1.3).

Two reservations need to be made clear. The first is that the correlation between mineralogy and chemical composition is not perfect, and therefore a root name devised from Fig. 1.4 for a crystalline rock may in a few cases differ from its petrographic name. For this reason a rock name should be based on petrographic criteria where this is possible. The other reservation is that the alkali metals Na and K are among the most **mobile** elements in post-magmatic hydrothermal processes, and therefore their concentrations may change in such alteration processes (Box 1.4). This limits the reliability of Fig. 1.4 when applied to altered volcanic rocks, even when

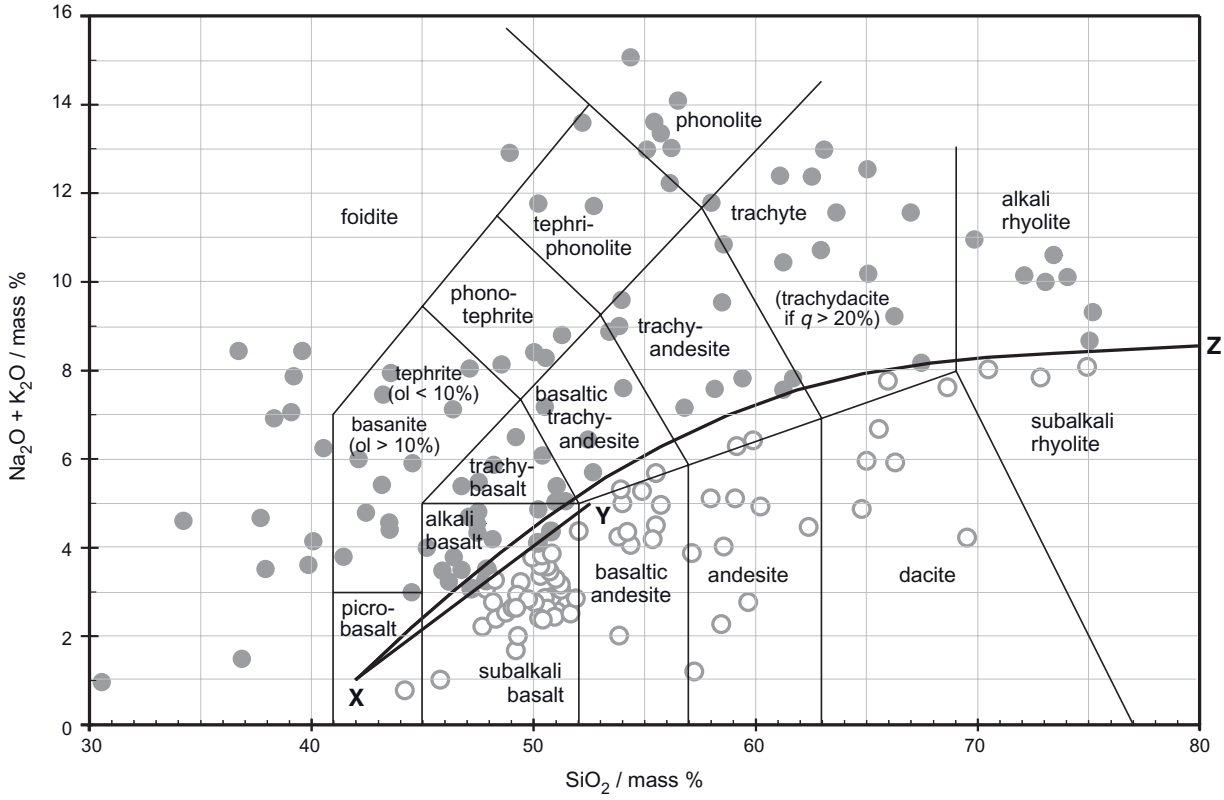


Fig. 1.5 TAS plot showing the division between **subalkali** and **alkali** series of volcanic rocks: the line X-Y shows the dividing line of Macdonald and Katsura (1964) for Hawaiian basalts, and the curve X-Z shows the dividing line of Miyashiro (1978) for a wider range of volcanic rocks. Basalts lying close to these boundaries are often called **transitional** basalts. The Fig. also shows the compilation of volcanic rocks depicted in Fig. 1.2: open symbols represent analyses of subalkali affinity, filled ones those of alkali affinity. Analyses require correction for volatile content (Box 1.3) prior to plotting in this diagram.

analyses have been recalculated volatile-free (Box 1.3).

This chemical approach is not used for naming coarse-grained rocks: there is no need to do so, as the essential and type minerals are usually present in large enough crystals to be readily identified under the microscope, or even in hand-specimen (Table 8.1). One should note that the mechanical sorting and selective accumulation of different types of crystals that may occur during slow crystallization (leading to the formation of **cumulate**

Box 1.3 Why recalculate volcanic rock analyses to eliminate volatiles?

Though igneous melts contain significant amounts of primary H_2O, CO_2, SO_2 and other dissolved gases at depth, these volatile constituents are effectively lost into the atmospheric-pressure surface environment on eruption. The contents of H_2O and other volatiles we measure in natural volcanic rocks are mostly due to the presence of hydrous minerals resulting from incipient hydrothermal alteration or weathering: they reflect post-magmatic changes in the mineralogy of the rock rather than original magma chemistry.

For the reasons discussed in Box 1.4, every effort should be made in the field to collect only the freshest material available for geochemical investigations, but in a representative collection of volcanic rocks some samples will unavoidably be more altered than others. In an analysis totalling 100%, the introduction of secondary volatiles depresses the concentrations of other constituents (Fig. 1.3.1), and it follows that some apparent differences between individual samples may arise simply from differences in the degree of alteration. Therefore, although a major element analysis should always include an estimate of total volatile content (e.g. a '**loss-on-ignition**' determination) as a means of monitoring alteration, it is normal practice to recalculate analyses into a volatile-free form before plotting geochemical data for volcanic rocks. This is done by multiplying each element or oxide concentration by the factor:

$$\frac{\text{analysis total \%}}{\text{analysis total \} - \text{volatiles \%}}$$

The reasoning behind this calculation is outlined in Fig. 1.3.1.

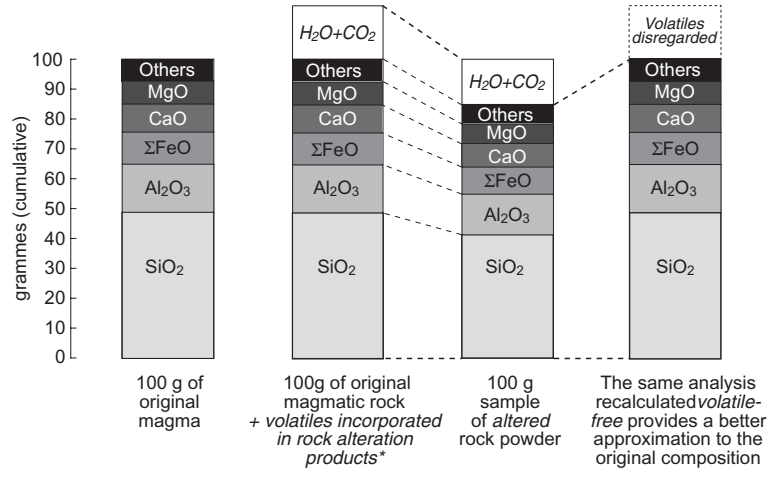


Fig. 1.3.1 Why rock analyses are re-calculated volatile-free before plotting.

rocks as discussed in Box 1.4) means that the chemical composition of a plutonic rock depends on the proportions of minerals that happen to have accumulated within it, and may be only indirectly related to the composition of the magma from which they crystallized.

Geochemical qualifiers

Figure 1.4 shows how a volcanic rock's geochemical composition can be used to allocate a root name (where a petrographic name would be difficult to determine). Rock geochemistry also provides a number of qualifiers that allow us to subdivide those rock types that embrace magmas from a number of sources. Basalts have for many years been divided into **alkali** and **subalkali** sub-groups. Various criteria have been devised for doing this; the simplest are shown in Fig. 1.5. The line XY shows the boundary drawn by Macdonald and Katsura (1964) to divide the subalkali basalts that form the bulk of Hawai`i (including shield volcanoes such as Kilauea) from the alkali basalts that have erupted at later stages of volcano development. To show how this can be applied, the analyses represented in Fig. 1.2 have been reproduced here, with the basalts symbolized in a manner reflecting whether they are alkali or subalkali basalts in the Macdonald and Katsura classification.

Petrologists have recognized for a long time that subalkali basalts tend to fractionate (evolve) towards low-alkali evolved melts

Box 1.4 Does an igneous rock analysis represent a magma composition?

In the quest to discover the origins of magmas and the conditions under which they form, extensive use is made of major element, trace element and isotopic analyses of *volcanic* rocks. The key assumption in doing so is that such analyses accurately represent the chemical compositions of the magmas from which the volcanic rocks crystallized. How widely can this assumption be justified, and what factors limit its application?

Degassing and volatile release

Magma confined at depth in the Earth contains gases dissolved in the melt. As load pressure is relieved during ascent toward the surface, this gas content will progressively come out of solution to form separate bubbles of gas (often apparent as **vesicles** in erupted lavas), which may escape from the magma into the atmosphere (Fig. 2.7). Such 'degassing' is common in all magmas held in shallow magma chambers or erupted on the surface. It follows that the volatile content measured in a fresh volcanic rock sample will generally be less than the true content originally dissolved in the melt at depth.

How can we determine the true pre-eruption 'magmatic' volatile contents of erupted volcanic rocks? One approach is to analyse the volatile content of minute *glass inclusions* (generally referred to loosely – even though no longer molten – as '**melt inclusions**' because they represent trapped melt) within individual phenocrysts, as illustrated in Plate 6.11. The tensile strength of the surrounding crystal effectively 'armours' the melt inclusion against rupture and gas escape as the host magma ascends towards the surface; micro-analysis of the 'trapped' volatile content of these glass inclusions provides the best available measure of that of the undegassed melt (see for example Hammer, 2006).

Hydrothermal alteration and low-grade metamorphism

Anhydrous minerals formed at melt temperatures such as olivine and plagioclase, if exposed to hydrous fluids at lower temperatures during cooling (for example, when fluids circulate through a thick volcanic succession), are prone to react and recrystallize into hydrous **secondary** minerals such as **smectite**, serpentine, chlorite and epidote. The analysis of a volcanic rock that has undergone such alteration or low-grade metamorphic reactions will therefore show elevated contents of H_2O and other volatile species, introduced by these post-magmatic reactions, that bear no relation to the

such as dacite and rhyolite, whereas alkali basalts fractionate toward more alkali-rich evolved melts such as trachyte or phonolite. It is therefore appropriate not only to divide *basalts* into alkali and subalkali classes, but to apply the same distinction to their respective families of residual melts as well. The curve XZ represents the dividing line introduced by Miyashiro (1978) for this purpose, and the more evolved melt compositions shown in Fig. 1.5 have also been symbolized according to which side of this line they lie on.

The broad division of Fig. 1.5 into alkali and subalkali fields, more or less according to Miyashiro's line, is not just an artefact of nomenclature but reflects a profound petrological distinction, as explained in Chapter 9. It is therefore no accident that the curve XZ lies close to the IUGS dividing lines between basaltic trachyandesite and basaltic andesite, between trachyandesite and andesite, and between trachyte and dacite. The curve also serves to divide the large field of rhyolite into subalkali and alkali varieties, which are characteristic of different tectonic environments.

A related diagram that is widely used to subdivide subduction-related volcanic rocks is shown in Fig. 1.6. In many island arcs, the potassium content of volcanic rocks increases in a systematic manner with distance of the eruption site from the trench or, more accurately, with the depth of the subduction zone below the point of eruption. Nomenclature is needed that reflects these variations, and therefore subduction-related basalts,

original volatile content of the magma. Allowance can be made for this secondary volatile content (see Box 1.3) but it is much harder to correct for any changes in the contents of relatively soluble non-volatile elements such as Na_2O, K_2O and CaO that may also have accompanied these reactions. For this reason geochemical work needs to be based on unaltered samples that show negligible amounts of such post-magmatic minerals under the microscope.

Crystal accumulation

In deep-seated magma chambers where the cooling rate is slow, crystals may sink or float in the melt according to their density and crystal size, and may then form deposits in which one mineral (or more than one) is selectively concentrated at particular horizons. Alternatively, one type of crystal may nucleate more efficiently on the chamber floor and walls than other minerals and thereby become selectively concentrated there. The possibility of such selective accumulation processes, operating on various scales, means that the composition of a plutonic rock hand–specimen will not accurately record the melt composition from which it crystallized. Moreover, accumulations of early crystals will generally have higher Mg/Fe (in the case of ferromagnesian minerals) or higher Ca/Na (in plagioclase) than the melt from which they separated (see Fig. 3.4).

Though crystal accumulation processes exhibit their most dramatic effects in large layered intrusions (Chapter 4), they are also known to occur in minor intrusions and even in thick lava flows (Chapter 2). Whereas in volcanic rocks the minerals that form can be seen as dictated by magma chemistry, in plutonic rocks where crystal sorting may have occurred the converse applies: the whole-rock chemical composition is in part a consequence of the minerals present and the proportions in which they happen to be combined.

Xenocrysts and xenoliths

Many igneous rocks contain foreign material in the form of **xenoliths** (Plate 5.3), torn from conduit walls during magma ascent, or present in a disaggregated state as individual *xenocrysts*. A bulk chemical analysis of the host rock will not faithfully represent the composition of the host magma if such exotic matter has not been carefully picked out during sample preparation. Even when obvious foreign bodies have been removed, the analysis may be distorted by chemical exchange between magma and xenoliths, especially in the case of slowly cooled plutonic host rocks.

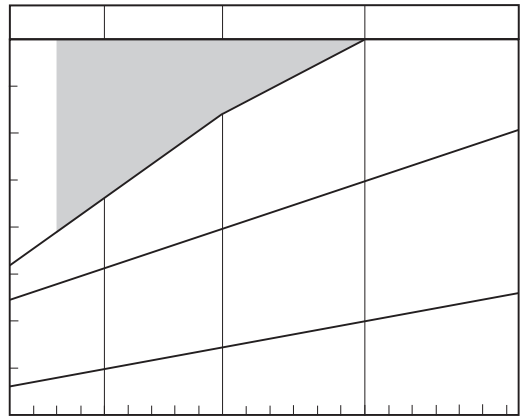


Fig. 1.6 K_2O *versus* SiO_2 diagram showing the boundaries used to subdivide subduction-related volcanic rocks. Analyses require correction for volatile content (Box 1.3) prior to plotting in this diagram. Boundaries shown are those defined by Le Maitre (2002), except for the one separating the shoshonite association which is from Peccerillo and Taylor (1976).

andesites and dacites are commonly allocated to low-K, medium-K or high-K magma series as defined in Fig. 1.6. Such divisions are not however applied to within-plate or constructive-margin volcanic rocks.

There are other examples of using geochemical qualifiers to refine rock nomenclature that will be discussed in later chapters (see for example Figs. 6.8b,c, 8.14, 8.19, 9.8.1 and 9.24).

REVIEW

Learning to study igneous rocks has much in common with learning a new language; success in both pursuits involves three essentials:

- vocabulary – learning a host of new words, both *nouns* (rock names) and *adjectives* (textural, mineralogical and geochemical qualifiers);
- grammar – learning the rules, conventions and structure (e.g. Le Maitre, 2002) upon which precise description relies;
- lots of practice, through which the learner gradually gains confidence and fluency (see exercises below).

This first chapter has introduced the basic syntax upon which the petrographic 'language' of igneous rock nomenclature is based. We have noted that the range of natural magma compositions represented by analyses of volcanic rocks from various settings is essentially a continuum. When straight lines are drawn on a diagram like Fig. 1.4 to define the domain of each rock name, we need to remember that – like fences on a prairie – their position is arbitrary, being determined by convenience and convention and not by any fundamental breaks in magma composition. Just as fences may be moved (and as words change their meaning with time), so petrological boundaries may shift as the details of nomenclature are refined in the light of new research. As an example, the boundaries shown in Fig. 1.6 have slightly different positions according to which paper you look at. This simply emphasizes the arbitrary nature of the boundaries in Fig. 1.4 rather than diminishing their validity.

On the other hand, the broad division of basalts and their diverse fractionation products in Fig. 1.5. into alkali and subalkali domains represents a fundamental petrological boundary that dictates the course of melt evolution, as discussed in detail in Chapter 9.

Adjectives like 'fine-grained', 'melanocratic' and 'ultrabasic' draw on a variety of qualitative and quantitative observations about a rock.

To clarify the underlying principles of igneous nomenclature, the minerals present in an igneous rock are segregated (in this book) into four conceptual categories: essential minerals (determining the rock's root name as in Table 1.1), type minerals, accessory minerals and post-magmatic minerals. This formulation is merely one way of codifying, or putting into explicit terms, an approach that all petrologists implicitly use in devising rock-names for igneous rocks.

EXERCISES

1.1 A thin section of an igneous rock contains phenocrysts ranging in size from 2–6 mm, and a groundmass consisting of crystals less than 0.05 mm in size. Should this rock be described as fine-, medium- or coarse-grained?

1.2 A coarse-grained rock sample consists of 40% augite (SiO_2 51.3%), 55% enstatite (SiO_2 50.9%) and 5% plagioclase (SiO_2 55.1%). Which of the following adjectives can be applied to this rock, and why? (a) ultrabasic, (b) ultramafic, (c) melanocratic, (d) holomelanocratic?

1.3 Determine appropriate rock names for volcanic rocks having the following compositions (given in volatile-free form):

	A	B	C
SiO_2	48.30	56.29	55.59
TiO_2	1.94	0.95	0.54
Al_2O_3	14.32	16.97	18.44
ΣFe_2O_3	10.45	8.09	8.09
MnO	0.15	0.13	0.27
MgO	10.00	3.83	0.57
CaO	9.50	8.02	2.64
Na_2O	3.20	2.52	7.96
K_2O	1.05	2.80	5.57
P_2O_5	0.39	0.40	0.33

1.4 Using Table 1.1, work out appropriate rock names (root names, with qualifiers as required) for fine-grained igneous rocks consisting of the following minerals:

(i) alkali feldspar + minor sodic plagioclase + minor biotite;
(ii) calcic plag + augite + nepheline (>10%);
(iii) calcic plag + alkali feldspar (in nearly equal amounts) + minor quartz;
(iv) nepheline + augite + minor olivine;
(v) sodic plag + hornblende (without quartz).

Chapter 2

Basalts and related rocks

Basalts are erupted in a wide variety of tectonic environments on Earth (e.g. mid-ocean ridges, island arcs, back-arc basins, intraplate oceanic islands, **large igneous provinces** and intra-continental rifts), and collectively they are found on the Earth's surface in greater volume than any other volcanic rock type. Basalts also occur on other terrestrial planets and the Moon and constitute an important class of meteorites (basaltic achondrites). Terrestrial basalt magmas are the products of melting in the Earth's mantle, and therefore their geochemistry, and the inclusions they sometimes contain, can tell us a great deal about the composition and mineralogy of the upper mantle and – many petrologists would argue – may provide information about the composition of the lower mantle too. Basalt magmas are parental to most of the more evolved magma types involved in continental and oceanic igneous activity, that develop through fractional crystallization in the crust (Chapter 3). In view of their parental role, and also because of their abundance and relatively simple mineralogy, basalts provide the most logical starting point for a systematic study of igneous rocks.

THE NOMENCLATURE AND MINERALOGY OF BASALTIC ROCKS

Definition

The simplest definition of a basalt is:

Basalt: a fine-grained,[1] mafic igneous rock consisting essentially of augite + calcic plagioclase.

Augite is a variety of high-Ca pyroxene (Box 2.1). 'Calcic plagioclase' refers to plagioclase crystals containing more anorthite ($CaAl_2Si_2O_8$) than albite ($NaAlSi_3O_8$) in molar terms (represented in symbolic form as An_{50}–An_{100}). How the composition of plagioclase may be determined under the polarizing microscope is explained in Box 4.1. The mineralogy of basalts is summarized in Table 2.1:

Table 2.1 Summary mineralogy of basalts. The optical properties of relevant minerals are summarized in Appendix A (Box A1).

Essential minerals	• augite • calcic plagioclase (An > 50 mol %)
Type minerals	• low-Ca pyroxene (enstatite or pigeonite – see Box 2.1); • olivine (see Box 2.2); • nepheline (or other feldspathoid). **NB** Low-Ca pyroxene and feldspathoid never coexist in basalts (see Box 2.4).
Common accessory minerals	• oxide minerals such as chromite, titanomagnetite or ilmenite (often reported simply as 'opaques' as they are not distinguishable in transmitted light); • apatite.
Common secondary (**alteration** or low-grade metamorphic*) minerals	• serpentine or **iddingsite** replacing olivine (see Box 2.2); • **smectite** replacing various minerals or glass; • chlorite* or **uralite** replacing pyroxene; • **sericite** or epidote replacing plagioclase.

* See text.

Igneous Rocks and Processes: A Practical Guide, 1st edition. By Robin Gill. Published 2010 by Blackwell Publishing

[1] A basalt need not always be a **volcanic** rock (in the sense of one erupted at the surface).

Many basalts are too fine-grained to permit confident microscopic identification of every mineral present, and may indeed have a glassy matrix from which one or more latent minerals have failed to crystallize. The mineral-based definition of 'basalt' given above is not easily applied to such rocks. Figure 2.1 shows an alternative – graphical – definition based on chemical composition, which can be used whenever a chemical analysis is available. Being **basic** rocks (Fig. 1.3c), basalts necessarily have SiO_2 contents within the range 45%–52%. Figure 2.1 also shows that the name 'basalt' is restricted to rocks with a total alkali content (Na_2O+K_2O mass %) less than 5%.

Basalts may be aphyric (devoid of phenocrysts) but more commonly contain phenocrysts or **microphenocrysts** of olivine, and of pyroxene and/or plagioclase as well in more evolved basalts. A basalt containing olivine phenocrysts would be termed an olivine-**phyric** basalt. Two other names are commonly used for olivine-rich basalts:

- *picrite*: a basaltic rock visibly enriched in olivine crystals, often as phenocrysts;
- *ankaramite:* a basaltic rock rich in olivine *and* augite phenocrysts (Plates 2.3–2.5).

In some picrites and ankaramites, the abundance of mafic phenocrysts may have been enhanced by gravitational accumulation (olivine and augite crystals being denser than basaltic melt). The definition of picrite (and picrobasalt) is discussed further in Box 5.5.

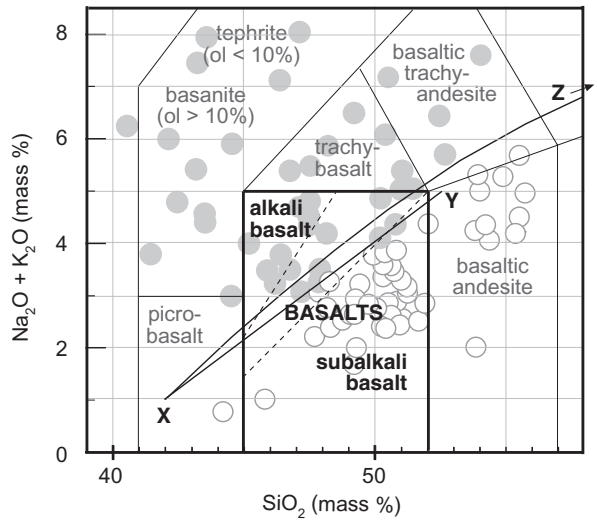


Fig. 2.1 Part of the TAS diagram shown in Fig. 1.5 emphasizing the compositional field that defines basalts according to **IUGS** (Le Maitre, 2002). The diagram also shows adjacent compositional fields (grey lettering), a selection of relevant analyses from Wilson (1989), Carmichael et al. (1974) and Cox et al. (1979), the dividing lines (X–Y and X–Z) commonly used to distinguish between alkali and tholeiitic basalts (for sources, see Fig. 1.5); the dashed lines delineate the region of overlap between alkali and subalkali basalts as defined by Le Maitre et al. (2002). Analyses require correction for volatile content (Box 1.3) prior to plotting in this diagram.

Subdividing basalts

On the basis of hand-specimen or thin-section examination, basalts can in principle be divided into several petrographic categories according to the type minerals they contain, following the principles outlined in Chapter 1. As Table 1.1 (column 3) anticipates, however, established basalt nomenclature does not fully conform to the logic of Chapter 1. By long-accepted historical precedent culminating in the seminal paper by Yoder and Tilley (1962), the term **tholeiite** is used today to describe a basalt containing a low-Ca pyroxene (enstatite or pigeonite), and the term **alkali basalt** is used in place of 'nepheline olivine basalt' (see Table 2.2). 'Tholeiite', representing the commonest type of basalt, is in effect used as a root-name in its own right (e.g. in 'olivine tholeiite').

Because the fine-grained or glassy matrix of basalts often makes it impractical to identify every mineral constituent, however, this petrography-based classification is rarely used today, and alternatives based on chemical composition are generally preferred. Figure 2.1 illustrates the simplest and most widely used discriminant diagram for subdividing basalts geochemically, based on the same diagram that is used for defining basalt. The diagram was first used in this way for subdividing the alkali basalts and tholeiitic basalts of Hawai`i, and Fig. 2.1 shows the alternative boundary lines of Macdonald and Katsura (1964, line X-Y) and Miyashiro (1978, line X-Z) as described in Chapter 1 (Fig. 1.5). If

Box 2.1 The structure and composition of pyroxenes – a refresher

The pyroxene family consists of chain silicates whose structural architecture is based on single chains of $(SiO_4)^{4-}$ tetrahedra, each tetrahedron sharing two oxygen atoms with its neighbours in the chain. The chains may be stacked together in two different ways, allowing pyroxene to crystallize in either the orthorhombic or monoclinic crystal system. Orthorhombic symmetry is confined to pyroxenes with low Ca contents (Fig. 2.1.1). In calcium-rich pyroxene, the large Ca^{2+} cation impedes the orderly stacking of chains characteristic of orthorhombic pyroxene: the distorted crystal structure crystallizes instead in lower-symmetry monoclinic form. Monoclinic pyroxene is the more common form, but in some basic igneous rocks both forms, known as orthopyroxene and clinopyroxene, may occur side by side.

Figure 2.1.1 summarizes the range of solid solution found in naturally occurring Ca-Mg-Fe pyroxenes (excluding sodic or alkali pyroxene which is discussed in Box 9.2). Pyroxene solid solutions are divided naturally into high-Ca and low-Ca families by a **miscibility gap** that exists between about 15 and 24 mol % $Ca_2Si_2O_6$ (see Box 4.5). Hardly any naturally occurring pyroxenes fall in this range of composition. The names used to identify the different domains defined by compositional and structural differences are shown in Fig. 2.1.1, which also summarizes how augite, pigeonite and orthopyroxene may be distinguished under the polarizing microscope (for techniques, refer to Appendix A). Older names for particular ranges of Fe–Mg solid solution, such as 'hypersthene', have not been adopted in this book (following Morimoto et al., 1988). Names such as enstatite may signify *either* a pure end-member (En, pure $Mg_2Si_2O_6$) *or* a range of solid solution (Fig. 2.1.1) approximating to it.

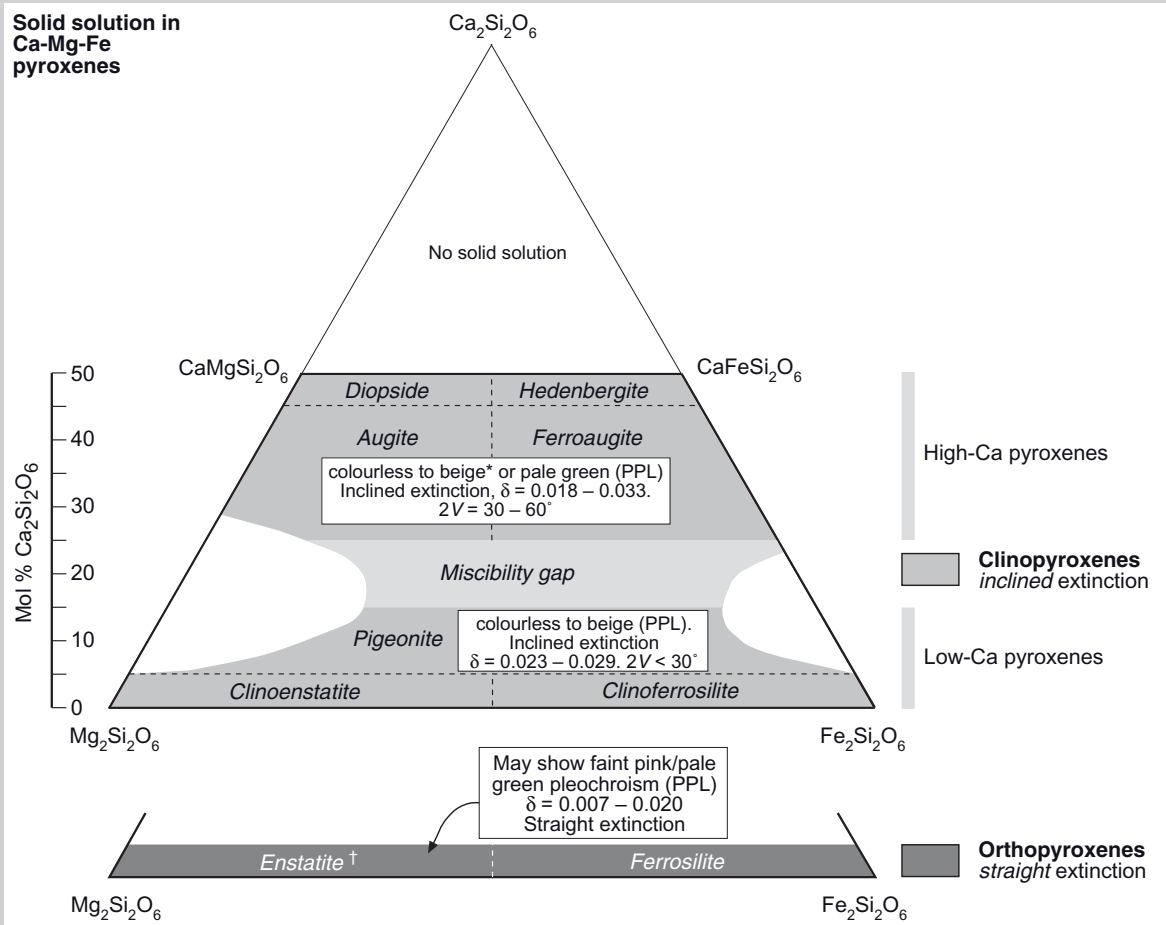
The equilibrium compositions of coexisting low-Ca and high-Ca pyroxenes are vary strongly with the temperature of equilibration, as indicated by the **solvus** curve discussed in Box 4.5.

Fig. 2.1.1 The range of solid solution in the Ca-Mg-Fe pyroxenes (shaded areas) and the names used to identify the various sub-series. The composition of a pyroxene solid solution is defined in terms of three chemical end-members ($Ca_2Si_2O_6$, $Mg_2Si_2O_6$ and $Fe^{2+}{}_2Si_2O_6$), but natural igneous pyroxenes rarely contain more than 50% $Ca_2Si_2O_6$. The compositional fields of high-Ca and low-Ca clinopyroxenes and the orthopyroxene series are highlighted. The diagram also summarizes key optical properties by which they may be distinguished in thin section.

a Hawaiian basalt analysis plotted above one of the dividing lines X-Y or X-Z in Figs. 1.5 and 2.1, it was called an *alkali basalt*, even if no actual nepheline could be identified in it. If on the other hand the analysis plotted below these lines, it was called a *tholeiite* or *tholeiitic basalt*, whether or not low-Ca pyroxene could be recognized in thin section. In adopting Fig. 1.5 as a tool for classifying a wider range of rock types, however, the International Union of Geological Sciences (IUGS) recognized that various subduction-related and other basalts would also plot in the lower part of the basalt field in Fig. 1.5, and so they introduced the more general term *subalkali basalt* for any rock whose analysis fell in this field. Subalkali basalt is a chemical category within which Hawaiian and other tholeiitic basalts (defined petrographically) are included.

The thinking that lies behind this important division of the basalt family into alkali and subalkali/tholeiitic will be explained later in the chapter.

Basalts are also categorized according to the tectonic environment in which they have erupted, 'mid-ocean ridge basalt' (often abbreviated to 'MORB') and 'ocean-island basalt' (OIB) being obvious examples. As we shall see later, these 'tectonic' categories of basalt differ in subtle aspects of their major and/or trace element composition, so geochemistry can often be used to discriminate between them, a technique that may shed light on the origins of older basalts whose original eruptive setting is no longer clear.



*Titanian augite (containing 3–6 mass % TiO_2, compared to 0.5–0.8% in most augites) usually shows pale-brown to lilac pleochroism. It is characteristic of alkali basaltic rocks.
†In older literature, the orthopyroxene solid solution series was divided into 6 ranges (enstatite, bronzite, hypersthene, *etc*).

Table 2.2 Petrographic subdivisions of basalt.

Type mineral present	Systematic name according to Ch. 1	Established nomenclature
low-Ca pyroxene (LCP)	enstatite (or pigeonite) basalt	tholeiitic basalt*
LCP + olivine	olivine enstatite (or pigeonite) basalt	olivine tholeiitic basalt
olivine	olivine basalt	olivine basalt
olivine + nepheline	nepheline olivine basalt	alkali basalt

* The IUGS Subcommission (Le Maitre, 2002) has recommended that the widely used term 'tholeiite' be replaced by 'tholeiitic basalt'.

Related rocks

The basalt field in Fig. 2.1 is surrounded by related fine-grained rock types which, though not basalts *sensu stricto*, may look similar. They are distinguished chiefly on chemical criteria, but there may be petrographic clues too:

- picrobasalts, having lower SiO_2 contents than basalts (they are ultrabasic in

composition), are more olivine-rich and contain little plagioclase;
- basaltic andesites have mafic minerals similar to basalts but contain plagioclase of more sodic composition (typically andesine – see Box 4.1);
- trachybasalts, basanites and tephrites usually contain recognizable alkali feldspar or feldspathoids (Box 9.1).

ERUPTIVE PROCESSES AND VOLCANIC FORMS

Basalt melts are characterized by having lower viscosity and lower gas content than more evolved magmas. Subaerial eruption may generate fountaining above the vent (typical of **hawaiian** eruptions) or may occur by quiet effusion. In either case the commonest product is lava flows of low **aspect ratio** (typically less than 1:50). Basalts may also erupt by low-explosivity pyroclastic processes of **strombolian** type. Basalts erupted in water form pillow lavas, with or without **hyaloclastite**, or sheet flows. Where molten basalt comes into contact with ground- or surface-water during ascent, the sudden expansion associated with conversion of water into steam generates **surtseyan** explosions that form craters or **maars**.

Subaerial lava flows

Voluminous eruptions of basalts invariably take the form of lava flows. Subaerial basaltic lava flows fall into two morphological categories:

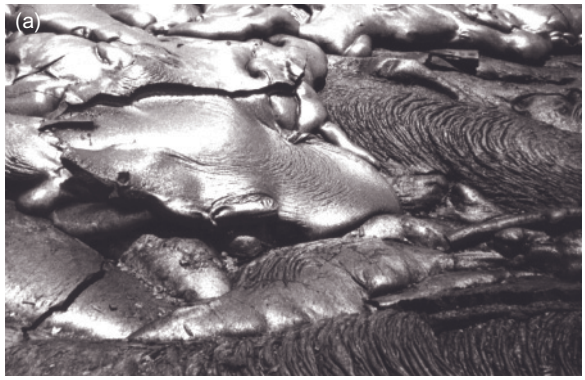
- **pahoehoe** flows;
- **a'a** flows.

A *pahoehoe lava* is characterized by a smooth, undulating or wrinkled surface (Fig. 2.2a) whose form indicates that the chilled skin forming on the surface of the molten lava remained **ductile** while the lava was in motion. The impression of plasticity is most marked with the wrinkled table-cloth-like form called *ropy pahoehoe* (Fig. 2.2a), which is formed when a section of ductile skin becomes anchored at the edges while the central portion continues to be carried forward by the drag of the lava advancing beneath. Though the most distinctive pahoehoe morphology, ropy lava is quite limited in extent. The more typical smooth or 'billowy' solidified lava surface (Fig. 2.2a) may conceal voids beneath a thin outer skin that can collapse beneath an unwary walker: such *shelly pahoehoe* is tiring and often painful to walk over. The interior of a pahoehoe lava is usually **vesicular**, often containing more than 20% vesicles by volume. Slowly moving pahoehoe flows advance by forming a succession of small lobes a few tens of centimetres across. Such subaerial *pahoehoe toes* rapidly become buried, and when later exposed by erosion (Fig. 2.2b) may be confused with subaqueous pillow lava; Fig. 2.5 summarizes criteria by which these two forms may be distinguished.

In contrast, the brecciated surface of an *a'a flow* (Fig. 2.2c) testifies to **brittle** behaviour of the chilled surface while the lava was in motion. Francis and Oppenheimer (2004) describe the surface of an a'a flow as 'a jumble of loose, irregularly shaped cindery blocks, often with razor-sharp asperities' and note that traversing such a surface can, understandably, be a 'miserable experience'. When seen in cross-section this rubbly, spinose upper layer, formed by brittle granulation of the deformed surface as the flow advances, passes down into a massive (though often vesicular) lava interior which may be crudely jointed. Being more viscous, basaltic a'a flows advance by internal **ramping**, and have steep flow-fronts that shed rubbly material in their own path. For this reason a'a lavas commonly exhibit rubbly material at the base as well as on top, and in some respects their mode of advances resembles that of a caterpillar-tracked vehicle.

It is common to see a lateral transition within a single lava flow from pahoehoe morphology into a'a morphology. The circumstances behind this transition are complex. The field evidence may be summarized as follows:

- proximal pahoehoe lava often passes down-flow into distal a'a lava, though in some cases a'a lava may be seen erupting directly from a vent;
- pahoehoe lava commonly changes laterally into a'a lava with increasing distance from the vent, but a'a lava is never seen to revert to pahoehoe;









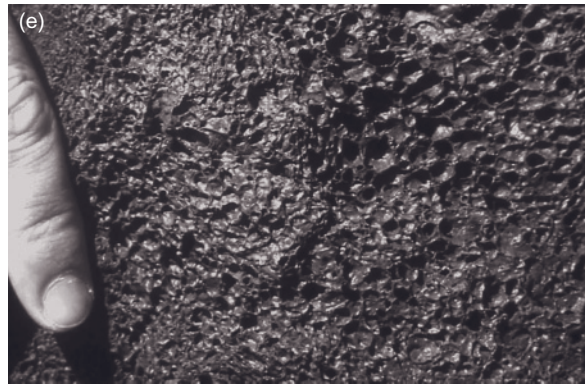


Fig. 2.2 (a) Smooth and ropy pahoehoe surfaces on basalt lava, Hawai`i. *Photo:* Ivvet Modinou. (b) Pahoehoe lava toes picked out by lighter-weathered margins, Gran Canaria; hammer 28 cm. (c) A'a flow top on 2001 basalt lava, Mt Etna, Sicily. (d) Trap featuring in Palaeogene basalts of the Geikie Plateau Formation, East Greenland; the eroded bench features are picked out by snow bands (photo by W.S. Watt from Larsen et al. (1989) reproduced by permission of the Geological Survey of Denmark and Greenland (copyright). (e) Scoria clast, Narices del Teide, Tenerife; note the fresh glassy sheen in this sample erupted in 1798 (cf. Plate 5.3).

- pahoehoe morphology is seen only on low-viscosity basalt lavas, whereas a'a surfaces are found on basalts *and* more evolved (more viscous) lava types as well;
- pahoehoe lava often transforms into a'a where it begins to flow down a steeper gradient.

In many areas of materials science, the transition between ductile and brittle responses to stress is mediated by two factors: temperature and strain rate. Ductile behaviour is favoured by high temperatures and/or low strain rates (slow deformation), whereas brittle deformation is favoured by cooler temperatures and/or higher strain rates. One may reasonably conclude that pahoehoe surfaces are associated with high near-vent temperatures, low lava velocity and/or low **effusion rates** (less than 5–10 $m^3 s^{-1}$), whereas a'a surfaces are favoured by cooling during transportation away from the vent and/or higher flow rates (e.g. lava cascading down a steep slope). Loss of volatiles from the advancing flow is also likely to play a part, as discussed in a later section.

Lava tunnels and tubes, where an insulating stationary crust or roof forms over flowing lava, are important features of basaltic lava **flow fields** (e.g. Hawai`i) because they facilitate lateral lava transport by cutting down radiant heat loss. Occasionally a tube roof may collapse locally, providing through the consequent 'skylight' a view of incandescent lava flowing beneath (Plate 2.6). Lava can flow in tunnels for many kilometres, under circumstances where, on the surface, it could flow only a few hundred metres owing to heat loss by radiant cooling. Tube-fed flows are one mechanism by which basaltic lavas can spread considerable distances even on the gentlest of gradients, producing the massive **shield volcano**es characteristic of ocean islands like Hawai`i and Réunion.

The plateau (or flood) basalts seen in places such as Skye and Mull (Hebrides, NW Scotland) and East Greenland, the Columbia River (western USA), the Deccan (India) and the Karoo (South Africa) represent higher effusion rates than the flow fields of Hawai`i. Individual flows, fed by extensive fissure systems, cover vast areas – tens of thousands of km^2 – with thick, almost flat-lying lava flows that in some cases can be traced for more than 750 km. Superposition of these flows can build up lava piles several kilometres thick. Rubbly flow tops erode back more rapidly than the massive (often columnar-jointed) interiors, and erosion of such terrains thus generates a characteristic stepped or 'trap' topography (from the Swedish *trappa*, stair) as shown in Fig. 2.2(d). To explain how individual lava flows can traverse such huge distances (sometimes over 100 km) before freezing, Self et al. (1996, 1998) have suggested that thick flood basalt flows are emplaced by inflation – the on-going injection of molten lava beneath an early-formed solidified skin that insulates the melt flowing beneath. Continued lava effusion, over periods of months or years, not only extends the flow laterally but progressively thickens the flow at a given distance from the vent.

Flood basalts frequently show well developed columnar jointing when exposed in cross-section. Such jointing is due to post-solidification thermal contraction of hot lava; being welded to the cooler rocks below, the lava cannot contract *en masse* and to accommodate contraction polygonal joints develop perpendicular to cooling isotherms, migrating inward from the lower margin. In well developed examples (Fig. 2.3a), a flow may be divided into a lower zone of regular vertical columns called the *colonnade*, and an upper zone of curved or highly irregular jointing called the *entablature*. Study of joint propagation (De Graff and Aydin, 1987; Lyle, 2000) suggests that the colonnade has formed by upward propagation of joints from the cool base of the lava, whilst the entablature represents downward propagation of joints from the flow's upper surface, with local water penetration contributing to the highly irregular isotherms to which the contorted jointing testifies. Another example of cooling joints forming perpendicular to a regular cooling surface is the radial jointing that may form around tree moulds (Fig. 2.3b) and in the interiors of pillow lavas (Fig. 2.4a).

Pillow basalts and subaqueous sheet flows

Basalt flows erupted under water differ in form from those erupted on land. The most easily recognized form is pillow lava

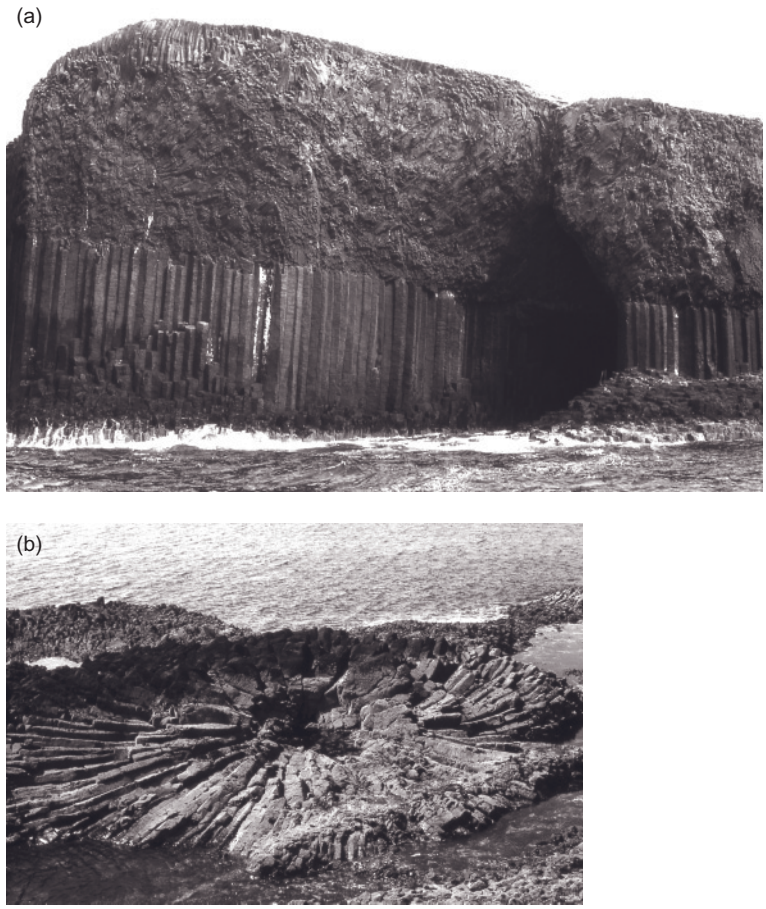


Fig. 2.3 (a) Colonnade and entablature in basalt lava, Isle of Staffa, Hebrides; (b) Rosette jointing in basalt lava surrounding a tree cast, Ardmeanach, Isle of Mull, Hebrides.

(Fig. 2.4a), the subaqueous analogue of pahoehoe. Though resembling piles of individual liquid-filled balloons, most pillow lavas are actually cross-sections of interconnecting lava tubes (Fig. 2.4b) that have advanced by repeated 'budding': each new lava lobe, chilled by the surrounding water, forms a ductile glassy envelope that inflates under the pressure of new lava being injected into it, until it becomes too cool and brittle to expand further, whereupon an incandescent crack forms from which molten lava breaks out to form the next pillow. The new pillow may have a smooth surface, or may exhibit corrugations engraved by irregularities along the crack from which it extruded – like mayonnaise squeezed out of a tube. Where a newly formed pillow settles into the junction between two underlying pillows, it forms a downward–pointing cusp which can provide a useful way-up indicator in deformed pillow-basalt terrains (Fig. 2.4a). When exposed in cross-section, pillow basalts may be recognized by the glassy skin and the radial cooling joints – perpendicular to the outer cooling surface – that they often display (Fig. 2.4a), indicating eruption under water (though not necessarily under the sea). Because such abrupt quenching of basaltic melt causes fine-scale fragmentation, pillow lavas are often intimately associated with deposits of fine, angular glassy detritus called **hyaloclastite** (from the Greek: 'glassy fragment' rock). Finely divided volcanic glass is intrinsically unstable and rapidly alters or weathers to a yellow or greeny-brown hydrated mass called *palagonite*, such as that filling the interstices in Fig. 2.4(a).

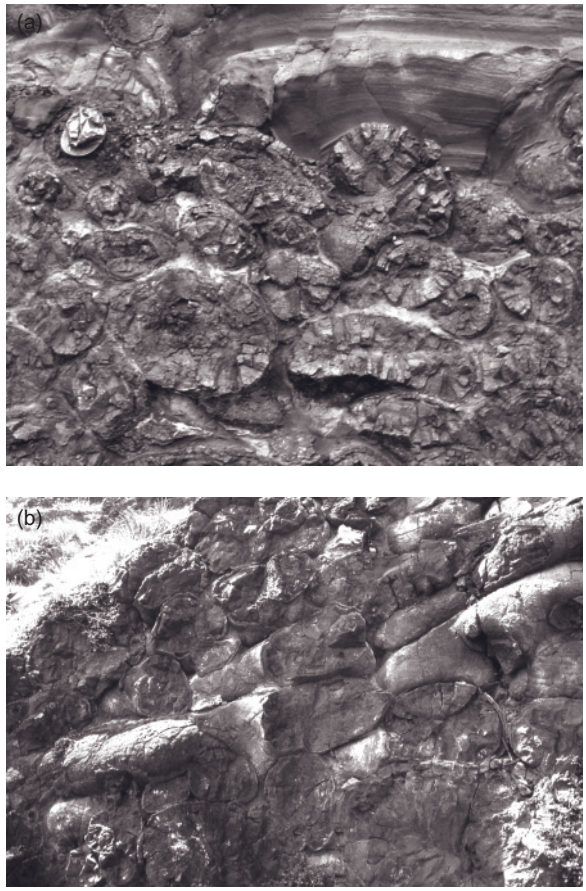


Fig. 2.4 (a) Pillow lava with associated hyaloclastite (Reykjanes peninsula, Iceland (Fig. 9.9); hat (top left) 25 cm. (b) Longitudinal view of pillow lava showing tube-like geometry, North Island, New Zealand; hammer (lower right) 28 cm.

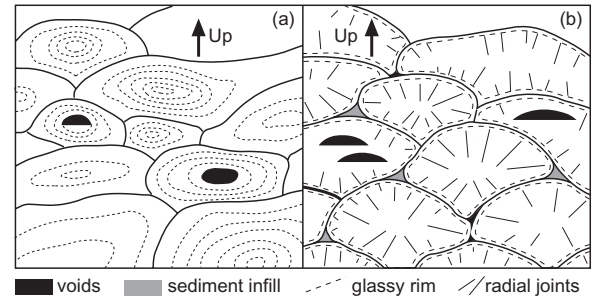


Fig. 2.5 Features that distinguish in cross-section between subaerial pahoehoe toes and subaqueous pillow lava, adapted from Macdonald (1967) by kind permission of J. Wiley and Sons Inc. (a) Pahoehoe toes showing characteristic concentric vesicle zones; black areas represent open tubes. (b) Pillow lavas showing characteristic radial jointing, chilled glassy selvages (dashed lines indicate the inner margins), interstitial sediment or hyaloclastite (grey), and voids within or between pillows (black).

Less distinctive, massive flows of submarine basaltic lava known as sheet flows are well known from deep-sea drilling in places such as the Galapagos rift in the eastern Pacific and the Nauru Basin in the southwest Pacific. They represent submarine eruption of basalt at higher **effusion rate**s (in the latter example, much higher) than those that generate pillow lavas.

Basaltic pyroclastic eruptions: scoria cones

The surface of the Earth in basaltic volcanic zones is commonly peppered with small cones built of successive beds of well sorted dark pyroclasts of highly vesicular basalt (or andesite) known as **scoria** (Fig. 2.2e and the host rock in Plate 5.3). Scoria cones (Fig. 2.6) are typical of slightly more explosive (volatile-rich) basaltic eruptions in which the vesiculating magma undergoes fragmentation on eruption and the clasts solidify before falling to ground around the vent. Such **strombolian** activity – named after the type locality, the island of Stromboli off the Italian coast – occurs as a series of discrete bursts probably related to the bursting of large gas bubbles in the conduit leading to the vent (see Chapter 7). When seen at night, strombolian explosions resemble firework shows as showers of glowing scoria clasts fall to earth and cascade down the outer flanks of the cone (Fig. 7.3d); daytime eruptions generate less photogenic bursts of ash and **lapilli** (Fig. 7.3c). Changes in explosivity may contribute to crude bedding in the cone-shaped fall deposit that forms around the vent (Fig. 2.6b). Such deposits are generally well sorted, with mean clast size decreasing with increasing distance from the vent.

HOW BASALT MAGMAS CRYSTALLIZE – EVIDENCE FROM TEXTURES

Microstructures and textures seen in hand-specimen and under the microscope tell us a

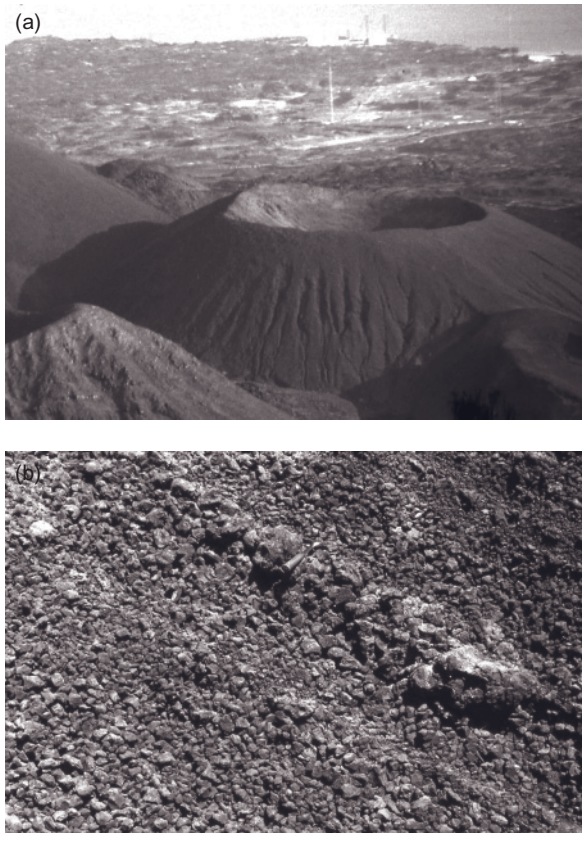


Fig. 2.6 (a) Scoria cone, Ascension Island, South Atlantic (photo J.P. Davidson). (b) Bedding in scoria, Tenerife; hammer (upper centre) 28 cm.

great deal about the processes by which, and the conditions under which, igneous melts crystallize. The textures of igneous rocks are known by a great variety of obscure-sounding terms (often derived from classical Greek) that the student geologist learns with some reluctance. Because textures have much to tell us about the process and conditions of crystallization of an igneous rock, however, these terms provide a useful shorthand for identifying different cooling histories, and some familiarity with them is therefore desirable. More detail on the nomenclature and interpretation of igneous textures may be found in the books by Shelley (1992) and Vernon (2004).

Vesicles and volatile solubility

Vesicles represent gas bubbles that form in molten lava that has become **supersaturated** with **volatiles** (primarily water vapour) following ascent from depth. Just as lager contains dissolved CO_2 that forms bubbles as soon as pressure is relieved on removing the cap (Zhang and Xu, 2008), so basaltic lava contains water and other volatiles that is wholly dissolved at depth but which **exsolves** to form bubbles as ascending lava encounters progressively lower confining pressure; unlike lager, however, many vesicles become frozen in as the lava solidifies. Figure 2.7a shows the process of vesiculation in relation to the solubility curve for water in molten basalt. Melt ascends along a decompression path, illustrated by the solid arrow, until it reaches a depth where it has become saturated with water: here it contains the maximum amount of dissolved water possible at the pressure concerned, and further ascent leads the magma into the supersaturated field, where excess water that the melt can no longer retain in solution **exsolves**. Much gas escapes to the atmosphere during eruption, but a proportion remains trapped in the magma as bubbles of steam. With continued ascent, the bubbles grow and multiply as shown in Fig. 2.7b, and are preserved as near-spherical voids when the lava solidifies.

The presence of dissolved volatiles in a basaltic melt lowers the temperature at which crystallization begins. The escape of gases during eruption ('degassing') can therefore initiate the formation of crystallites suspended in the melt, and this may be a factor in the transition from pahoehoe to a'a lava character noted above (Polacci et al., 1999).

Vesiculating melt must expand (the volatiles occupying greater volume in bubble form than when dissolved in the melt), and within an idealized cylindrical conduit of constant radius such expansion necessarily accelerates the melt upward; vesiculation in a volcano vent therefore promotes lava fountaining at the surface.

When seen in cross-section, pahoehoe lavas often show an upward concentration and enlargement of vesicles near to the top (Fig. 2.8a). This may reflect post-eruption vesiculation in response to the lower load pressure near the top of the flow, rather than flotation of bubbles formed at a deeper level (or an earlier stage) in the flow. Near-vertical

Box 2.2 How to distinguish olivine from augite in thin section

Olivine and augite are two minerals of similar relief and (superficially) similar interference colour that may be confused by the inexperienced observer. Below are some key features to look for in distinguishing between the two, those emphasized by *italics* being the most diagnostic.

	olivine in thin section	augite in thin section
Body colour in thin section (see Plate 4.1)	Colourless in PPL (Fe-rich varieties are pale yellow).	Usually a pale *beige* or grey colour in PPL (Plates 2.3 and 2.5); titanian augite has a pleochroic lilac tinge.
Fracture or cleavage	*Irregular curved fractures*, often emphasized by incipient alteration (see Plate 2.4).	Either one *cleavage* (in sections parallel to crystal elongation) or *two perpendicular cleavages* (in sections perpendicular to elongation).
Birefringence	0.035–0052 up to third–order colours.	0.018–0.033 up to second–order colours.
Extinction angle	Euhedral olivine* shows straight extinction relative to prism faces.	*Oblique extinction* relative to cleavage.
Alteration	*Susceptible to alteration* to: • red–brown **iddingsite**, or • serpentine (often colourless), or • green **bowlingite**. Relics of curved internal cracks – picked out by alteration products – often identify altered olivine.	More resistant. May undergo alteration to **uralite**.

*The lack of cleavage in olivine makes discrimination by extinction angle impractical for anhedral crystals.

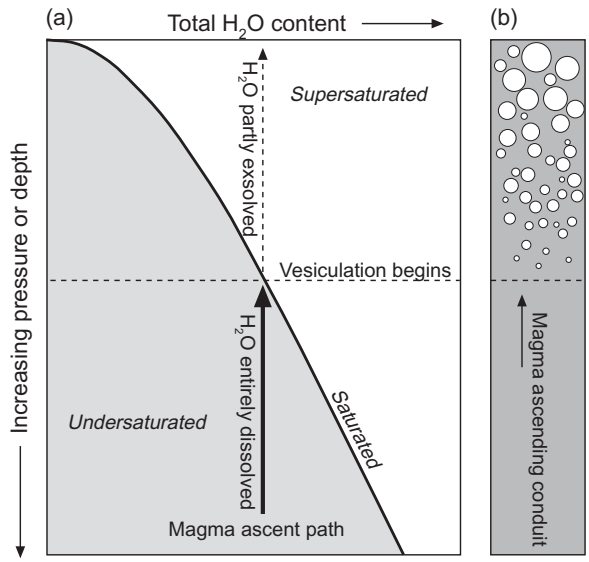


Fig. 2.7 (a) Solubility of a gas (in this case H_2O) in basalt melt as a function of pressure (i.e. depth). The form of the solubility curve is taken from Dixon et al. (1995). (b) Degree of vesiculation as a result of decompression as melt ascends a volcano vent towards the surface.

cylindrical vesicles may also form near the base of a lava flow; such *pipe vesicles* (Fig. 2.8b) result from the upward invasion of steam expelled from water-logged ground across which the lava has flowed. Because lava erupted under water experiences a load pressure related to water depth, submarine lava vesiculates less than subaerial lava of equivalent water content.

Hydrothermal circulation during burial of thick lava successions commonly leads to the deposition of low-temperature minerals in lava vesicles (typically zeolite, analcite or calcite in basalts). Filled or nearly filled vesicles are called **amygdales**. Sometimes amygdales may be filled with igneous minerals or glass in place of hydrothermal minerals, suggesting filling at much higher temperature.

Forms of basaltic glass

Basaltic glass may occur in various forms, all of them representing rapid quenching of melt

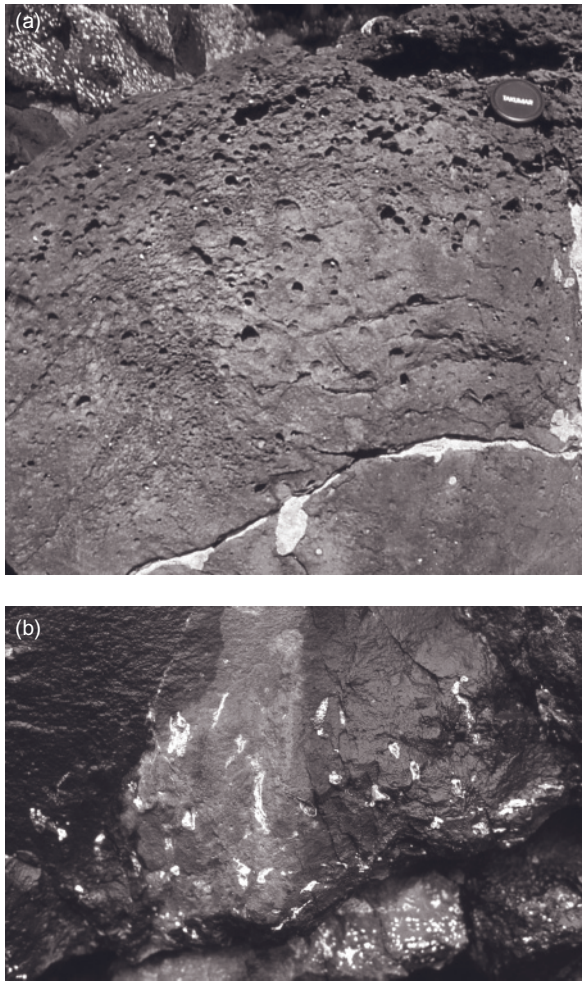


Fig. 2.8 (a) Upward increase in vesicularity in a basalt lava (Auckland, New Zealand). (b) Pipe **amygdales** at the base of a basalt lava in Skye; same scale as (a).

(Box 2.3). The most spectacular form, known as *Pele's hair* (after the Hawaiian goddess of volcanoes) consists of fine filaments of brown basaltic glass, less than 0.5 mm in diameter and up to 2 m long, drawn out from molten lava during fountaining or vigorous flow (Fig. 2.9a). Pele's hair is readily dispersed by the wind and is exclusively associated with subaerial **hawaiian eruptions**.

Basaltic glass commonly forms when melt is rapidly quenched by contact with liquid water, for example at the chilled margins of dykes or sills intruded into water-bearing sediment. When completely glassy, it is

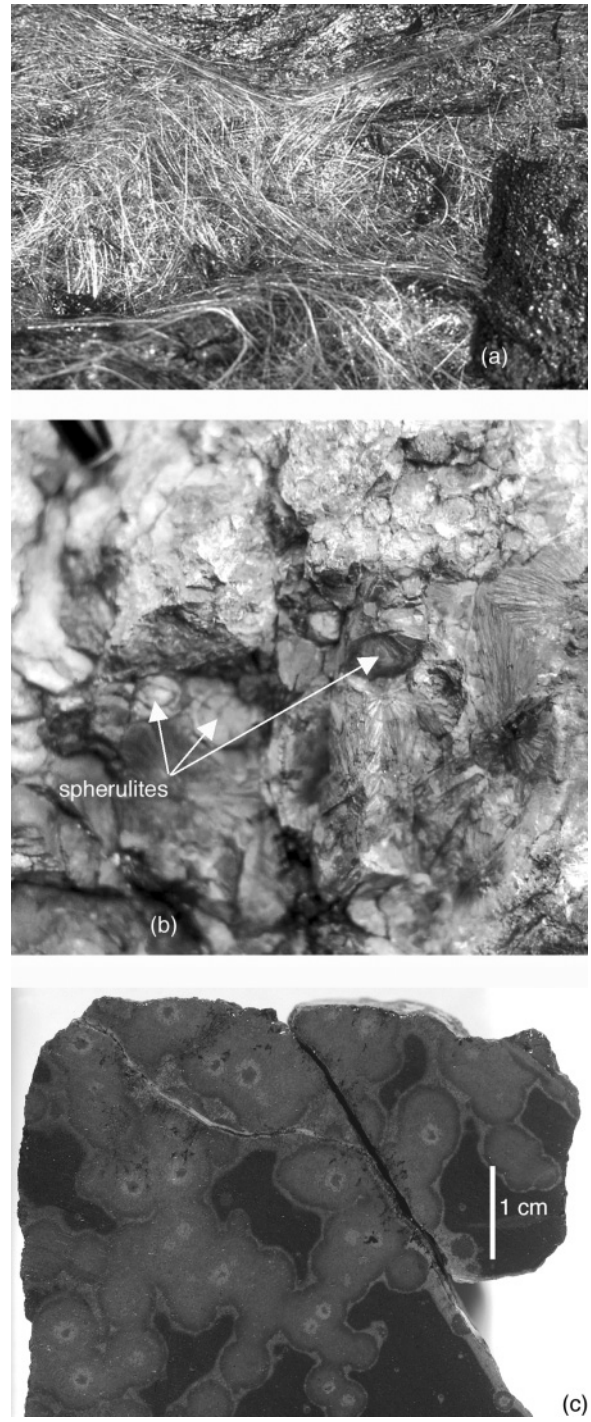


Fig. 2.9 (a) Pele's hair, Mauna Ulu, Hawai`i (photo D.W. Peterson, courtesy of U.S. Geological Survey*); (b) Devitrification **spherulites** in basaltic glass, Ardmeanach, Isle of Mull, Hebrides. Pen top (top left) ~1 cm wide. (c) Drill core showing spherulites formed around altered olivine crystals in an aphanitic basaltic pillow margin, Ontong Java Plateau (photo by Integrated Ocean Drilling Program/Texas A&M University).

* US Department of the Interior.

translucent and pale to reddish brown in colour, and is called *sideromelane*. The presence of submicroscopic crystals may however give the glass a black opaque appearance. Volcanic glass, owing to its **metastability** relative to the crystalline state, has limited durability on a geological time-scale, and commonly shows signs of slow, solid-state transformation into crystalline material, a process called devitrification. Spheroidal clusters of radiating fibrous crystals (Fig. 2.9b) called varioles or **spherulites** are sometimes a sign of devitrification, but may also form by supercooling of basaltic melt (see Fowler et al., 2002). In either case they represent crystallization under conditions in which growth rate greatly exceeds nucleation rate (Box 2.3). Spherulites sometimes form around pre-existing crystals (Fig. 2.9c).

Basaltic glass usually has a refractive index (RI) greater than that of balsam (1.54); glasses of more evolved composition tend to have RIs less than this (see Shelley, 1992, Fig. 1.24).

Textures involving variations in crystal size

Basalts, like other volcanic rocks, often contain two or more generations of crystals that differ in crystal size. In **porphyritic** (US **phyric**) texture, a clear distinction in size exists between **phenocrysts** – larger, **euhedral**, early-formed crystals of one or more minerals – and the finer-grained **groundmass** that surrounds them (Plates 2.1, 2.5). The minerals present as phenocrysts may be specified in the rock name by using adjectives such as 'olivine-phyric' or 'plagioclase-augite-phyric', as discussed in Chapter 1.

The contrast in grain size reflects a relationship between crystal size and rate of cooling (Box 2.3): when a basalt melt begins to crys-

Box 2.3 What determines grain size in igneous rocks?

Whether a magma crystallizes into a coarse- or fine-grained rock, or forms a glassy solid, depends on the cooling rate to which it is subjected. It is often said that slow cooling generates a coarse texture because there is time for large crystals to grow, whereas fine-grained rocks form when rapid cooling allows too little time for large crystals to grow. A sounder foundation for understanding grain-size differences in igneous rocks is shown in Fig. 2.3.1. Crystallization from a melt takes place in two stages:

- *nucleation:* the initial formation of minute embryonic crystals upon which further growth can occur;
- *crystal growth:* deposition of additional crystalline material on existing nuclei and crystals.

Both steps are impeded by free-energy barriers (Gill, 1996; Vernon, 2004), and consequently require some degree of **supercooling** or supersaturation before they can begin (typically several tens of °C). The relative efficiency of each process, as a function of the amount of supercooling ΔT (in °C), is illustrated by the curves in Fig. 2.3.1. Nucleation is energetically speaking the more difficult process, and therefore requires a greater degree of supercooling than crystal growth. This is the rate-determining step: no crystal growth can occur until the first crystal nuclei have formed.

Three ranges of supercooling are illustrated in Fig. 2.3.1:

1. Slow cooling generates a small degree of supercooling: the crystal growth rate (grey curve) is high at this point but the creation of new crystals is limited by a zero or low nucleation rate (black curve). Any crystal growth is therefore concentrated on relatively few crystals, leading to a coarse-grained texture typical of gabbro.
2. Rapid cooling leads to a greater degree of supercooling, favouring efficient nucleation (black curve) but the crystal growth rate is now much lower (grey curve). Thus large numbers of small crystals are formed, giving a fine-grained texture typical of many basalts.
3. Extremely rapid cooling (e.g. quenching in contact with water) brings about a degree of supercooling sufficiently high to suppress both nucleation and crystal growth: no crystals form, and the disordered melt state is 'frozen' in the form of glass.

tallize at depth, surrounded by warm wall-rocks, cooling is relatively slow, supercooling is modest and nucleation is sparse – conditions favouring the growth of large crystals. Were the melt to crystallize completely at this depth, the product would be a coarse-grained plutonic rock. If, on the other hand, partially crystallized magma escapes to the surface, evidence of the plutonic stage of crystallization will be preserved in the form of the suspended phenocrysts that it carries. Having grown surrounded by melt, they characteristically develop euhedral crystal form (though resorption during ascent may cause rounding or embayment). When phenocrysts exhibit **zoning**, it is a sign that the plutonic stage of crystallization has been sufficiently prolonged for significant evolution in melt composition to take place (though not long enough to allow complete equilibration). The accelerated cooling stage that follows eruption, on the other hand, will favour high supercooling and a large nucleation rate, generating a finer groundmass comprising large numbers of small crystals. **Intersertal** texture – when phenocrysts are surrounded by a glassy matrix (Plate 2.3) – represents an even faster final stage of cooling, perhaps due to interaction with water.

Thus porphyritic texture is normally an indication that magma ascent from the mantle to the surface was interrupted by a period of crystallization in a sub-volcanic (or deeper) magma chamber (Fig. 2.10a). Phenocrysts contribute to our understanding of magma evolution because they identify the minerals

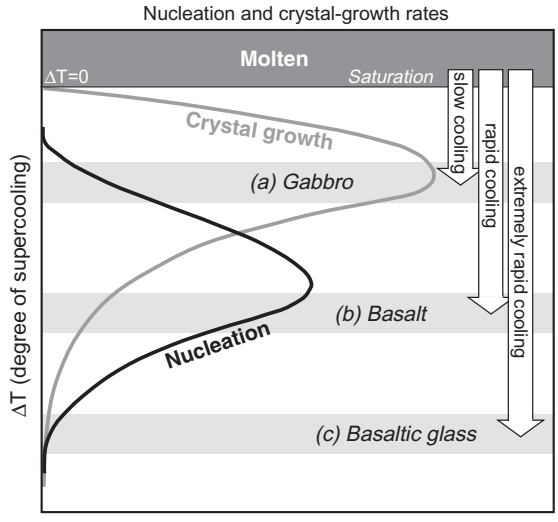


Fig. 2.3.1 Diagram showing the rates of crystal nucleation and crystal growth as a function of supercooling below the solidus temperature (after Dowty, 1980, based on data of Winkler). Three arbitrary ranges of supercooling (or cooling rate) are illustrated, producing coarse and fine crystal sizes and crystal-free glass.

Nucleation and crystal growth rates also depend on the diffusion rate in the melt. Because diffusion is slower in more siliceous melts (because they are more **polymerized**), glassy textures are more common in rhyolite than in basalt (Chapter 6).

In nature, crystallization of an igneous rock may occur in several stages, each characterized by a different degree of supercooling (or cooling rate) and nucleation rate. Multi-stage cooling histories may be inferred from the different grain-size ranges of early-, intermediate- and late-formed crystals (e.g. porphyritic texture – see Plate 2.1 and Fig. 2.10).*

*Lofgren (1980) argued that porphyritic texture might arise from a single-stage cooling process too, but the special circumstances implied by his experiments do not seem to be widely applicable in Nature.

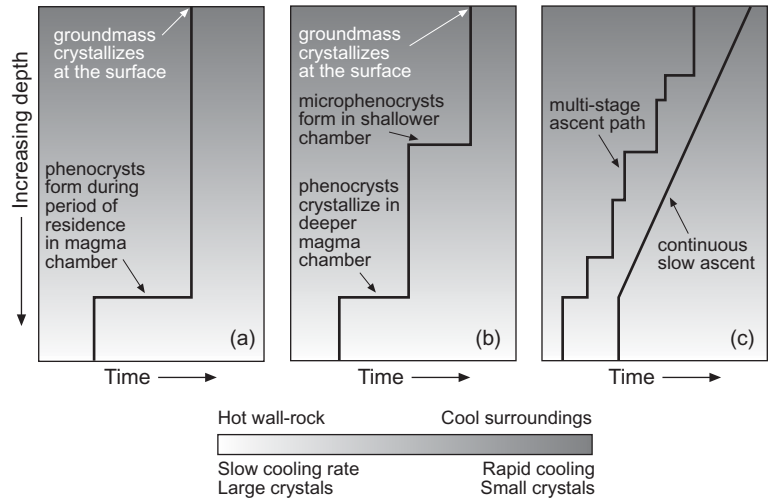


Fig. 2.10 Hypothetical magma ascent *versus* time paths to explain (a) porphyritic basalt and (b) the presence of two distinct generations of phenocrysts; (c) two alternative ascent paths to explain seriate texture. Real ascent paths are probably more complex than those shown.

that were crystallizing in the inferred magma chamber prior to eruption, and their compositions (readily determined by **electron microprobe**) can be used to model the changes in melt composition that accompany crystallization. The phenocryst minerals present may be specified in the rock name by the use of a qualifier such as 'olivine-augite-phyric' (for a basalt containing olivine and augite phenocrysts).

Textural variants on the porphyritic theme indicate more complicated cooling/ascent histories (Fig. 2.10):

- Some basalts contain two generations of phenocrysts (phenocrysts and microphenocrysts) as well as groundmass, indicating *two* stages of crystallization during ascent prior to eruption (Fig. 2.10b). Microphenocrysts in basalts may exhibit **intergranular** texture, in which equant olivine and pyroxene crystals fill spaces within a framework formed by tabular plagioclase microphenocrysts.
- Phenocrysts may aggregate into clusters (*glomerocrysts*) to form *glomeroporphyritic* texture (Plates 2.3, 2.4): according to Ikeda et al. (2002), clustering is advantageous in energy terms because crystals enjoy lower crystal-melt interfacial energy (the igneous analogue of a liquid's surface tension) in a cluster than when dispersed.
- A continuous gradation in crystal size from large, early-formed euhedral crystals to fine-grained matrix, with no sharp size distinction between phenocrysts and groundmass (Plate 2.3) is described as **seriate** texture. Crystallization of the largest crystals began at depth but, rather than undergoing sudden ascent and eruption, the magma followed a slow progress to the surface, crystallizing at progressively greater cooling rates (Fig. 2.10c). Seriate texture is more prominent in andesites than basalts (Plate 6.1).

When all crystals are too small to be distinguished by the naked eye, the texture is described as **aphanitic** (cf. **phaneritic**). Fine-grained rocks that lack phenocrysts are described as **aphyric** or simply *non-porphyritic*. The absence of phenocrysts suggests either that the melt has ascended directly from its source without being detained in a magma chamber en route, or that any phenocrysts that were formed have settled out by sinking or have been filtered or resorbed during subsequent ascent.

Basalts occasionally exhibit **ophitic** texture which is described and explained in Chapter 4.

ALTERATION AND METAMORPHISM OF BASALTS

Basaltic minerals crystallize at temperatures above 1000 °C (see Fig. 3.9) and are almost always **anhydrous** (amphiboles are rare in basalts). In a subaerial basalt that cools rapidly to ambient temperature and escapes later exposure to hot fluids, these primary minerals will be preserved. The hand-specimen will look almost black (except for a characteristic chocolate-brown weathered surface), and most phenocrysts will exhibit shiny crystal faces or cleavage surfaces; the thin section will be devoid of strongly coloured secondary minerals. Such a sample is described as *unaltered*.

When a basalt suffers prolonged exposure to hot circulating **fluids**, on the other hand, silicate minerals formed at magmatic temperatures may react to form new, **hydrous** minerals that are more stable under the new **hydrothermal** regime in which the rock finds itself. These reactions and their products are referred to under the general term of hydrothermal **alteration**. A new hydrous mineral that partially or completely replaces a **primary** igneous mineral crystal is referred to as an *alteration product* or *secondary mineral*. Common alteration products associated with basaltic mineralogy are summarized in Table 2.1. An alteration product may form a single, **optically continuous** crystal whose orientation in thin section may relate to that of the igneous crystal it replaces, but more commonly alteration products occur as aggregates or intergrowths of smaller crystals (Plate 9.15).

If the hydrothermal episode is relatively brief or the temperature attained is low, alteration may be arrested at an incipient stage and alteration products will then be confined to the margins of susceptible crystals (Plate 2.7), to mineral cleavages or, in the case of olivine, to internal cracks (Plate 2.8). Some minerals (notably olivine) are more prone to alteration than others (e.g. high-Ca pyroxene) and will succumb first. More pervasive alteration tends to affect a larger number of the minerals present, and the more susceptible minerals may be completely replaced by secondary minerals. In some cases, the alteration product(s) may preserve the outline of the original crystal – a euhedral phenocryst, for example – forming a recognizable **pseudomorph** (Plate 2.9) in thin section that may allow the identity of the original mineral to be inferred even if none of it remains.

In hand-specimen, an extensively altered basalt may take on a green or reddish tinge and have duller internal surfaces, and often breaks readily along a system of fractures (those that provided the channels for fluid penetration). In thin section, fine-grained alteration products will have replaced susceptible primary minerals, especially adjacent to fractures and veins.

Whereas incipient alteration causes relatively little change in the overall chemical composition of a basalt – apart from volatile components like H_2O (Box 1.3) – more pervasive alteration is often accompanied by *selective* changes in other major elements, especially the more **mobile** ones like Na_2O, K_2O and CaO (Box 1.4). Petrographic assessment of the degree of alteration and careful selection of the freshest samples available are therefore important preparatory steps before embarking on any geochemical study of magma composition, if the chemical signature of the magmatic processes being studied is not to be obscured by secondary chemical changes.

An ill-defined distinction is often drawn between *alteration*, whose intensity varies on a scale of metres, and *hydrothermal metamorphism* (Yardley, 1989) in which similar mineralogical changes are developed more pervasively on a regional scale. Alteration can be caused by fluids escaping up fractures and faults from deeper parts of the same magmatic system (**deuteric** alteration), or may reflect convective circulation of seawater or **meteoric** waters driven by magmatic heat sources below. Low-grade metamorphism of basalts often represents circulation of meteoric fluids during burial of thick volcanic sequences. In each case, the fluids responsible for mineralogical changes may also deposit new minerals such as epidote in amygdales and other cavities.

ANOTHER LOOK AT THE CHEMICAL SUBDIVISION OF BASALTS – NORMS

The division of basalts into *alkali basalts* and *tholeiitic basalts* is a fundamental one that sheds light on the degree of **silica-saturation** (or **-undersaturation**) in basic magmas. The

distinction was originally based on **modal** mineralogy: a basalt containing identifiable nepheline and olivine under the microscope was called an alkali basalt,[2] whereas one containing low-Ca pyroxene (with or without olivine) was called a tholeiite. Given the difficulty of recognizing small amounts of groundmass nepheline in a basalt – especially if the rock is altered or contains glass – petrologists today prefer to base such distinctions on chemical composition. To quantify silica undersaturation in an igneous rock composition, the rock's major element analysis may be used to calculate what is called the **norm** of the rock (sometimes the term 'CIPW norm' is used, in honour of its originators, the American petrologists W. Cross, J.P. Iddings, L.V. Pirsson and H.S. Washington, who published their groundbreaking work in 1902). Other variants of the norm have been proposed (e.g. by Niggli) but are no longer used.

What does the 'norm' of a rock mean? As Table 2.3 illustrates, a norm is simply the major element analysis of a rock translated into percentages of hypothetical ('normative') minerals with standardized compositions. The way the norm is calculated is illustrated graphically in Box 2.4 for the two analyses shown in Table 2.3; step-by-step instructions for carrying out a simplified norm calculation (with exercises) are given in Appendix B. Calculating a norm can be seen as a geochemical 'accountancy' exercise, enabling the petrologist to assess the silica 'budget' associated with each mineral present, and thereby to determine whether the rock composition as a whole is:

- 'in surplus' with regard to SiO_2: such a rock, with quartz among its normative minerals, is described as **silica-oversaturated**;
- 'in balance': a rock whose norm contains enstatite[3] and olivine but no quartz or nepheline is described as **silica-saturated**;
- 'in deficit' with regard to SiO_2: the oxide analysis *contains insufficient silica* to convert all of the Na_2O and K_2O into normative albite and orthoclase, requiring nepheline to be introduced in place of some or all of the alkali feldspar. Normative nepheline is the mark of a **silica-undersaturated** rock.

These concepts are summarized graphically in Fig. 2.11. The right-hand sub-triangle has the normative minerals quartz, albite and enstatite as its apexes, and any quartz-normative basalt will plot in this field (close to the albite–enstatite line, since basalts are never strongly quartz-normative) and qualify as silica-oversaturated. A basalt whose norm contains enstatite and olivine (i.e. olivine tholeiite) will plot in the middle, silica-saturated sub-triangle. Nepheline-normative basalts (alkali basalts) plot in the left-hand, silica-undersaturated sub-triangle.

The currently recognized definition of alkali basalt is 'a basalt whose norm contains nepheline', whereas a tholeiitic basalt is defined as one whose norm includes enstatite. Nepheline and enstatite are mutually incompatible prod-

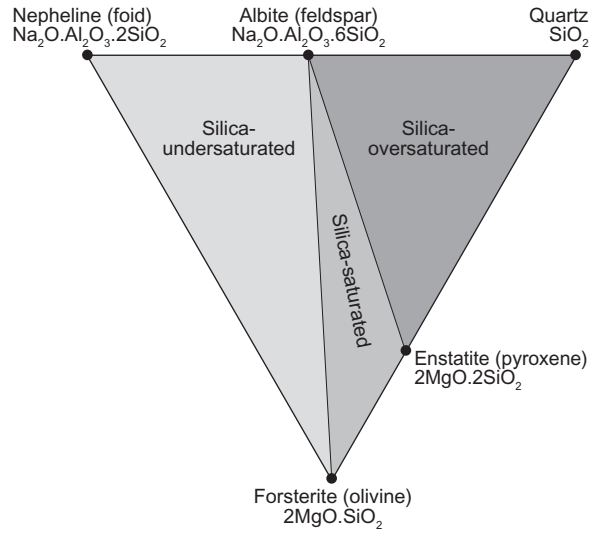


Fig. 2.11 Graphical representation of silica saturation in basalts in terms of the normative minerals present (shown in mass proportions). The dividing lines separate pairs of minerals that cannot occur together in a norm (Box 2.4): quartz/olivine, enstatite/nepheline and quartz/nepheline. This Fig. forms the base of the 'basalt tetrahedron' shown in Fig. 9.7(a).

[2] The original name was 'alkali olivine basalt', later condensed to 'alkali basalt'.

[3] The name 'enstatite' is used for low-Ca pyroxene here in compliance with modern mineralogical usage (Deer et al.1992). 'Enstatite-normative' here means the same as **hypersthene-normative** used in older literature (see Box 2.1).

Table 2.3 (a) Major element analyses of two basalts (from Le Maitre, 2002, Table C4, analyses 2 and 1 respectively) showing the recalculation from mass per cent of each oxide (which is g per 100 g of rock) to moles of each oxide per 100 g.

		Analysis A		Analysis B	
(a) Oxide analysis	*RMM (oxides)*	*mass %*	*mol/100g*	*mass %*	*mol/100g*
SiO_2	60.09	50.84	0.8461	47.37	0.7883
TiO_2	79.88	2.33	0.0292	1.69	0.0212
Al_2O_3	101.96	14.98	0.1469	15.26	0.1497
Fe_2O_3	159.69	4.08	0.0255	3.6	0.0225
FeO	71.85	8.32	0.1158	6.95	0.0967
MnO	70.86	0.18	0.0025	0.17	0.0024
MgO	40.32	7.53	0.1868	10.85	0.2691
CaO	56.08	9.59	0.1710	9.49	0.1692
Na_2O	61.98	1.75	0.0282	3.56	0.0574
K_2O	94.20	0.22	0.0023	0.84	0.0089
P_2O_5	141.94	0.16	0.0011	0.22	0.0015
Total		99.98		100.00	

(b) Norms calculated from the same analyses; columns 3 and 5 show the results in moles of each mineral per 100 g (note the correspondence with some numbers in part (a)), and columns 4 and 6 contain the same results expressed in mass %. The oxide-based mineral formulae used in the calculation are listed in column 2; a dot stands for 'combined with'. Blanks in columns 3, 4, 5 and 6 indicate where the calculation has bypassed the mineral concerned; zeroes indicate where the mineral has been eliminated by the silica deficit.

(b) Norm	*Normative mineral formulae*	*mol/100g*	*mass %*	*mol/100g*	*mass %*
quartz (q)	SiO_2	0.1283	7.71	0.0000	0.00
corundum (c)	Al_2O_3				
orthoclase (or)	$K_2O.Al_2O_3.6SiO_2$	0.0023	1.30	0.0089	4.96
albite (ab)	$Na_2O.Al_2O_3.6SiO_2$	0.0282	14.81	0.0574	22.26
anorthite (an)	$CaO.Al_2O_3.2SiO_2$	0.1163	32.37	0.0833	23.18
nepheline (ne)	$Na_2O.Al_2O_3.2SiO_2$			0.0150	4.26
leucite (lc)	$K_2O.Al_2O_3.4SiO_2$				
acmite (ac)	$Na_2O.Fe_2O_3.4SiO_2$				
diopside (Di)	$CaO.(FeO+MnO+MgO).2SiO_2$	0.0513	11.52	0.0807	17.92
wollastonite (wo)	$CaO.SiO_2$				
enstatite (En)	$(FeO+MnO+MgO).SiO_2$	0.1991	21.58	0.0000	0.00
olivine (Ol)	$2(FeO+MnO+MgO).SiO_2$			0.1219	18.46
magnetite (mt)	$FeO.Fe_2O_3$	0.0255	5.92	0.0225	5.22
ilmenite (il)	$FeO.TiO_2$	0.0292	4.43	0.0212	3.21
apatite (ap)	$3.33CaO.P_2O_5$	0.0011	0.37	0.0015	0.51
Total			100.00		99.99

Low-Ca pyroxene is represented here by the name 'enstatite' for consistency with current mineralogical usage (Deer et al., 1992); in other works on norm calculation (e.g. Cross et al., 1902, Cox et al., 1979, and Le Maitre, 2002) such pyroxenes are referred to by the obsolete name 'hypersthene'.

ucts of the norm calculation (Box. 2.4). As outlined above, the nomenclature in use today (Le Maitre, 2002) recognizes a wider category of **subalkali** basalt, which may be defined in normative terms as a basalt whose norm *contains no nepheline*. Subalkali basalts include a number of volumetrically important classes of tholeiitic basalt such as mid-ocean ridge basalt, as well as subduction-related basalt types.

The fundamental normative distinction between alkali basalt and tholeiitic basalt can

Box 2.4 Calculating the norm of an igneous rock

The calculation of a norm involves the following steps:

1. Recalculating the major-element analysis into volatile-free form (see Box 1.3). A norm involves *only anhydrous minerals*. Hydrous minerals are represented by anhydrous surrogates: hornblende, for example, is represented by pyroxene, and biotite by magnetite and orthoclase.
2. Dividing the weight per cent figure for each oxide (which is g oxide per 100 g of rock) by the relative molecular mass (RMM in g mole^{-1}) for the oxide concerned to express the analysis in the number of **moles** of each oxide per 100 g of sample;* this calculation is shown in Table 2.3(a) and the outcome for analysis A is represented graphically in Fig. 2.4.1a.

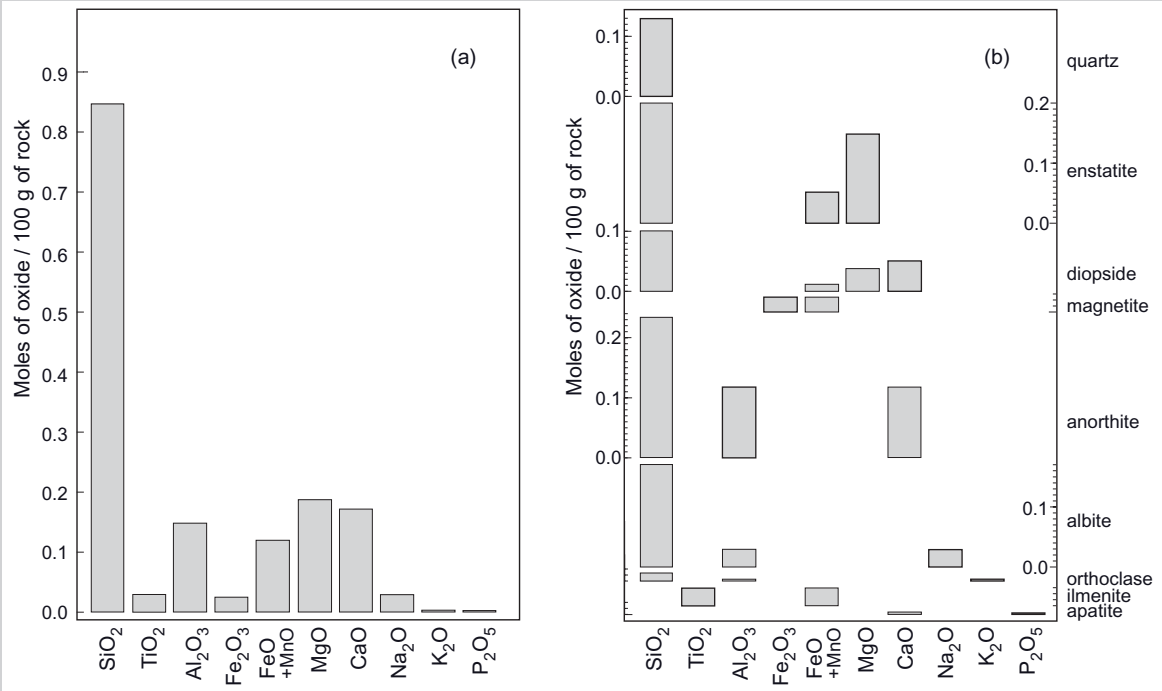


Fig. 2.4.1 (a) The analysis A in Table 2.2 depicted as moles of each oxide per 100 g of sample. The small amount of MnO present has been added to the FeO column as it occurs in the same minerals as FeO. (b) An 'exploded' version at the same scale showing how each oxide is divided among the various normative minerals. Allocation proceeds from bottom to top. Boxes with bold outlines identify the oxides whose (remaining) abundance regulates the amount of the normative mineral concerned. The graduated scale against each mineral indicates the calculated amount in moles per 100 g rock.

Note the appearance of quartz in the norm of this rock, indicating that Analysis A in Table 2.2 represents a **silica-oversaturated** magma.

*The logic here is analogous to dividing a bag of apples among children on a school trip: it is more useful to know the *number* of apples in the bag than their weight.

3 Combining relevant oxides in prescribed proportions to calculate how many moles of each normative mineral can be formed from the rock analysis, as illustrated for analysis A in Fig. 2.4.1b. For example, the familiar formula for albite ($NaAlSi_3O_8$) can be rewritten in the alternativeoxide-based form $Na_2O.Al_2O_3.6SiO_2$, which indicates that Na_2O, Al_2O_3 and SiO_2 need to be combined in the molar proportions 1:1:6 to form albite. The simplified mineral formulae used are shown in Table 2.3(b); norms are based on end-members and do not take into account complex solid solutions, such as in natural pyroxenes.
4 The 'minerals' in the norm are calculated in a prescribed order, starting at the *bottom* of Fig. 2.4.1b and working upward. The amount of each mineral is determined by the availability of the *least abundant* constituent (e.g. TiO_2 in the case of ilmenite), identified in Fig. 2.4.1b as boxes bordered by bold lines. More abundant oxides such as Al_2O_3 and particularly SiO_2 need to be partitioned between several normative minerals, as illustrated by the 'exploded' columns; SiO_2 is the last to be allocated, and the norm may need to be adjusted if too little SiO_2 is available (see Fig. 2.4.2).
5 Multiplying the molar amount of each normative mineral by the **RMM** of the mineral formula to yield a norm expressed in mass %. A norm should have a total approximating that of the original volatile-free analysis (allowing for rounding errors).

Analysis A in Table 2.3(a) contains over 50% SiO_2, and this is sufficient to meet the silica demands of all of the normative silicate minerals, leaving a small surplus expressed as normative quartz (Table 2.3b). This indicates a rock that is **silica-oversaturated**.

The norm of a silica-poor basalt

Analysis B in Table 2.3 shows a basalt with a lower silica content. When the norm of this analysis is calculated using the procedure outlined above, we discover that there is insufficient silica to satisfy the amount of enstatite (low-Ca pyroxene) implied by the FeO and MgO left over after forming diopside (Fig. 2.4.2a). The SiO_2 deficit can be diminished by converting all of the normative enstatite into the chemically similar – but silica-poor – mineral *olivine* (Fig. 2.4.2b), but a silica deficit (albeit smaller) still remains after this has been done. We need to be even more economical in our assignment of silica in this rock. A further 'saving' can be made by substituting the silica-poor **feldspathoid** nepheline in place of some of the albite (Fig. 2.4.2c); nepheline is a mineral that crystallizes naturally from silica-deficient melts. By introducing these silica-deficient minerals (highlighted by darker shading in Figs. 2.4.2b,c) in place of minerals with higher silica–demand, we can wipe out the deficit. That the norm calculation forces us to do this is a faithful reflection of what happens in Nature, and the appearance of quartz, enstatite, olivine and/or nepheline in a norm serves as a useful quantitative measure of the rock's state of silica oversaturation or undersaturation (Fig. 2.11).

Note that olivine is only introduced into the norm when a silica deficit arises. Quartz and olivine can therefore never appear together in a norm, in keeping with their mutual incompatibility in natural basic rocks. Likewise, because nepheline is only introduced into a norm when the analysis is sufficiently SiO_2-deficient to require all of the potential enstatite to be converted into olivine (see Fig. 2.4.1c), normative nepheline and enstatite can never coexist.

A simplified procedure for calculating norms is given in Appendix B. Details of a definitive computer package for such calculations are given by Le Maitre (2002).

Continued

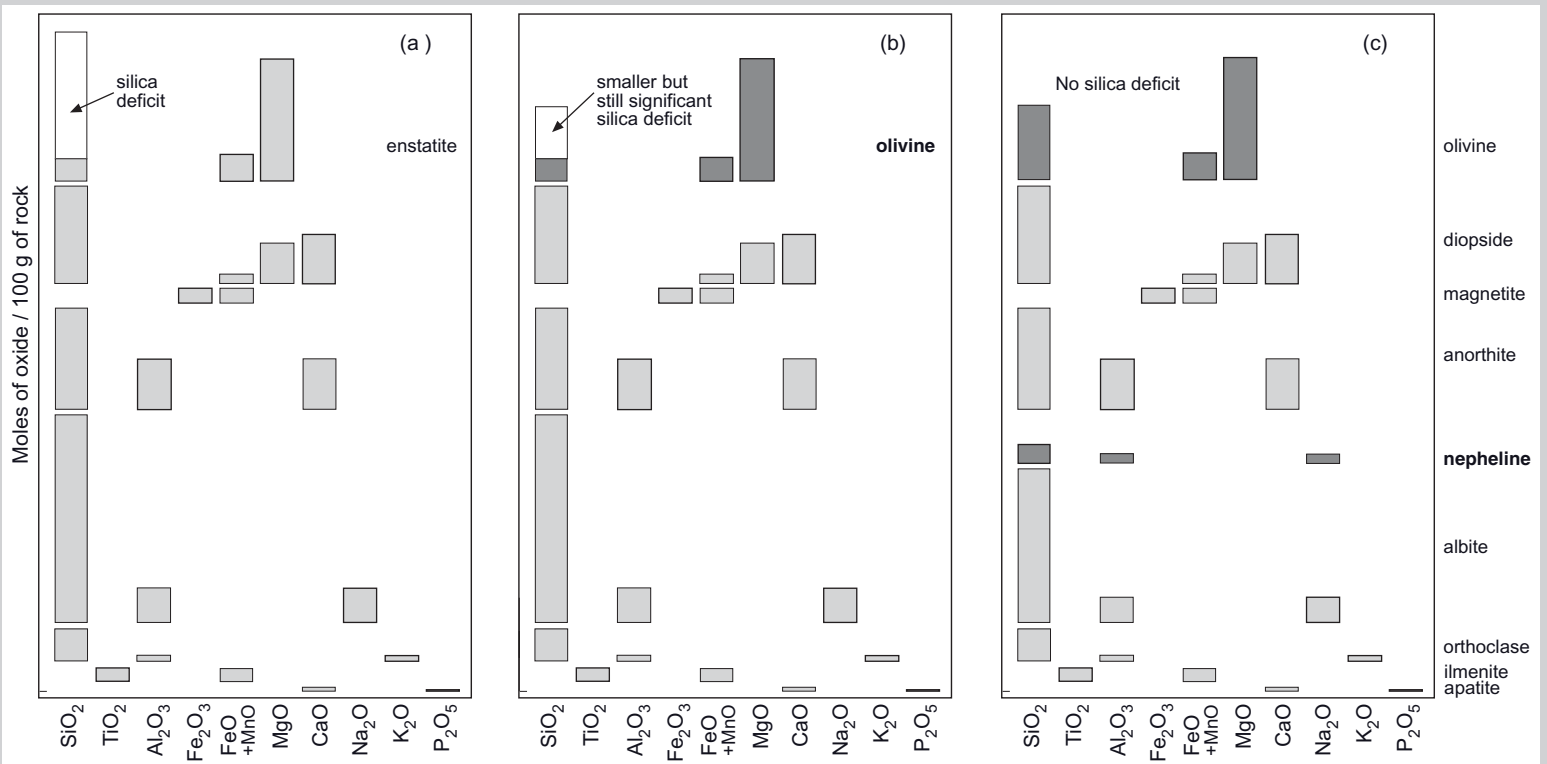


Fig. 2.4.2 Conceptual stages in the calculation of the norm of a **silica-undersaturated** rock (Analysis B in Table 2.3). The order of allocation proceeds from the bottom and works upward. Boxes with bold outlines identify the oxides whose (remaining) abundance regulates the amount of the normative mineral concerned. (a) Calculation carried out as in Fig. 2.4.1(b). The silica available in this analysis, however, proves insufficient to satisfy the amount of enstatite implied by the remaining (FeO + MnO) + MgO, leaving a silica deficit indicated by the blank part of the SiO_2 column. (b) Adjustment 1: recalculate some or all of the potential enstatite as olivine, which has a similar composition to enstatite but a lower silica demand (lower SiO_2:[FeO + MnO + MgO] ratio). Substituting olivine in place of all of the enstatite reduces the silica deficit but fails to eliminate it. Boxes with darker shading are those affected by silica adjustments. (c) Adjustment 2: recalculate some or all of the potential albite as the **feldspathoid** nepheline, which has a similar composition to albite but a lower silica demand (i.e. a lower SiO_2:[Al_2O_3 + Na_2O] ratio). Substituting nepheline in place of *some* of the albite, in addition to replacing enstatite with olivine in (b), is sufficient to eliminate the silica deficit completely. Boxes with darker shading are those affected by silica adjustments.

be projected on to a total-alkali versus silica (TAS) diagram like Figs. 1.5 and 2.1 to allow basalts to be classified without the need for norm calculations, though this does not result in a unique dividing line. The lines X–Y and X–Z are compromise lines for dividing nepheline-normative rocks from those with no normative nepheline (subalkali basalts). Because the norm involves oxides other than those plotted in the TAS diagram (Na_2O, K_2O and SiO_2), a small proportion of nepheline-normative basalts plot below the line X–Y, and a similar number basalts with no normative nepheline may plot above the line. The extent of this zone of ambiguity is illustrated by the dashed lines in Fig. 2.1, and basalts plotting in this region are commonly designated as **transitional basalts**.

Though the primary division between alkali and subalkali basalts is chemical, one or two petrographic clues allow us to distinguish them under the microscope, as described in Box 2.5.

WHERE BASALTS OCCUR

Basalt volcanism appears in a wide variety of tectonic environments on the Earth, as well as on other planets and their satellites. The chemical differences observed between basalts from different terrestrial tectonic settings, though relatively subtle, tell us a great deal about the processes by which basaltic melts are generated in the Earth's interior. The purpose of this section is to review the various settings in which basalts are found and to identify the petrological and geochemical signatures that characterize each of these settings. Volcanism is not exclusively basaltic in all of these environments; indeed in some, such as mature island arcs, basalts may be subordinate to more evolved rock types.

The main places in the world where basalts erupt are shown in Fig. 2.12. A full-colour map available at http://pubs.usgs.gov/imap/2800/ provides a useful supplement to this figure.

Mid-ocean ridge basalts (MORBs)

The Earth's mid-ocean ridge system (Fig. 2.12) – where new oceanic lithosphere is continually being created – has a total length of more than 60,000 km (Fowler, 2005), and overall it erupts basaltic lava on the surface at an average rate of around 3 km^3 $year^{-1}$ (Crisp, 1984). Most of the magma ascending from the mantle here is emplaced at depth, however, and the total melt production rate beneath mid-ocean ridges is probably nearer to 20 km^3 $year^{-1}$ (see Arculus, 2004).

The morphology of mid-ocean ridges varies according to spreading rate. Slow-spreading ridges like the Mid-Atlantic Ridge tend to exhibit a distinct fault-bounded median valley about 25 km wide, though topography varies considerably along the ridge: extension is continuous whereas magmatism is episodic (Fowler, 2005), so magma chambers are believed to be discontinuous in time and space beneath slow-spreading ridges. Volcanic output in eruptive sectors consists of small axial volcanoes – fed by individual pockets of ascending magma – that often coalesce to form axial volcanic ridges (Smith and Cann, 1993). Faster-spreading ridges like the East Pacific Rise, though similarly elevated above the abyssal plains (typically by ~2 km), usually show much smoother relief and lack a median valley: here volcanic output consists of extensive low-relief lava flows (sheet flows). Seismic evidence suggests that continuous crustal magma chambers underlie considerable lengths of fast-spreading ridges. All ridges – except some ultraslow ridges such as the Gakkel Ridge in the Arctic Ocean (Dick et al., 2003) – are divided into segments and offset by transform faults (Fig. 2.12), and in a few places basaltic lava erupts from these and their associated fracture zones (e.g. at St Paul's Rocks in the equatorial Atlantic).

The basalts erupted at mid-ocean ridges are olivine tholeiitic basalts that may be aphyric but more commonly contain phenocrysts of olivine ± chromite ± plagioclase ± augite (listed in their order of crystallization); though not first to appear, plagioclase phenocrysts are often the most abundant. Rapid quenching in cold seawater commonly results in a glassy matrix. The most distinctive aspect of mid-ocean ridge basalts (MORBs), however, is their chemical composition (Table 2.4). Basalts erupted from segments of the mid-ocean ridge system remote from **hot spots** ('N-MORBs' where 'N' stands for 'normal') vary little in composition, and are characterized by low contents of K_2O and other **incompatible elements** (Box 2.7). The distinctive

Box 2.5 Petrographic differences between tholeiitic and alkali basalts

Modal nepheline is rarely if ever observed in an alkali basalt under the microscope, but there are other petrographic clues that help to distinguish between alkali and tholeiitic basalts when no chemical analysis is available. In alkali basalts:

- augite crystals tend to have a faint lilac/mauve **body colour** owing to enrichment in titanium; such *titanian augites* (Box 2.1) often show slight pleochroism and more pronounced zoning than augites in tholeiitic basalts;
- augite usually appears as a phenocryst phase before plagioclase does: the usual order is olivine then augite then (in more evolved lavas) plagioclase.

In subalkali basalts:

- plagioclase usually appears as a phenocryst phase before augite (Plate 2.2). The usual order is olivine then plagioclase then (in more evolved lavas) augite.
- the occurrence of *low-Ca pyroxene*, either monoclinic *pigeonite* or orthorhombic *enstatite* (Box 2.1); low-Ca pyroxene may occur as phenocrysts, as groundmass crystals, and/or as overgrowths on olivine phenocrysts.

Traces of quartz may very occasionally be found in the groundmass of a tholeiitic basalt (leading to the term quartz tholeiite), crystallized from the most evolved dregs of **interstitial** melt. Macdonald and Katsura (1964) proposed that olivine in the groundmass served to discriminate alkali basalt, but more recent work shows that it can be found in the groundmass of nearly any Hawaiian basalt (M.O. Garcia, pers. comm.).

When mineral analyses are available, tholeiitic and alkali mafic rocks can be seen to differ also in the composition of high-Ca pyroxene present, as illustrated in Fig. 4.2.

trace element signature of N-MORBs can be seen most clearly in a graph in which incompatible element concentrations in a MORB are ratioed to those in a hypothetical 'primitive mantle' (Fig. 2.7.3[4]) and plotted on a logarithmic scale (Fig. 2.16); by convention, the elements are arranged from left to right in order of *decreasing* incompatibility (Box 2.7). N-MORB samples show a relatively smooth profile that is level for the least incompatible elements – those on the right – but becomes increasingly depressed for the most incompatible elements on the left. Basalts from ridge segments that happen to lie close to ocean islands or large seamounts (i.e. to hot spots) may on the other hand show almost level patterns, reflecting relative enrichment of highly incompatible elements ('E-MORB' where 'E' stands for 'enriched'), possibly by mixing with hot spot sources. Basalts from fast-spreading ridges such as the East Pacific Rise tend to be more **evolved** than those from slow-spreading ridges such as the Mid-Atlantic Ridge (though there is much overlap), a fact that probably reflects the more persistent magma chambers that are believed to exist beneath fast-spreading ridges.

Seawater permeates the pillow lavas of the ocean floor, and the high geothermal gradients characteristic of active spreading centres cause these pore waters to convect and interact chemically with the wall-rock basalts, such that:

- basalts undergo local hydrothermal metamorphism, leading to the replacement of igneous minerals by albite, epidote, chlorite and carbonate, with loss of SiO_2 and CaO and gain of FeO and MgO. These reactions, on approaching completion, produce a distinctive greenschist-facies metabasalt called **spilite**, found in many **ophiolite** belts.

[4] Figure 2.7.3 is the third figure in Box 2.7. Tables in Boxes are referred to in the same way.

Table 2.4 Major and trace element analyses of representative basalts from various tectonic settings. As the FeO/Fe_2O_3 ratio in a volcanic rock analysis rarely preserves the original magmatic value, FeO and Fe_2O_3 have been combined as 'total FeO' ('ΣFeO', actual FeO + [actual Fe_2O_3/1.11] – see Box 2.6). Some authors use ΣFe_2O_3 instead (ΣFeO × 1.11) and their analyses may result in low totals when presented in ΣFeO terms here. Blank spaces indicate elements that were not reported in the original publication.

NB The number of **significant figures** given here varies according to the **precision** of the analytical determination; the method and precision for a given element may differ from one analysis/laboratory to another.

Category	**Primitive mantle**	**N-MORB**		**OIB**		**Subduction-related volcanism**		**LIP-related volcanism**		**Continental rift**
Basalt type		**Tholeiitic basalt**	**Tholeiitic basalt**	**Tholeiitic basalt**	**Alkali basalt**	**Calc-alkali basalt**	**Low-K tholeiite**	**Low-K tholeiite**	**Subalkali basalt**	**Alkali basalt**
Location		**Mid-Atlantic Ridge**	**East Pacific Rise**	**Kilauea, Hawaii**	**Koloa, Kauai Is, Hawai`i**	**Honshu arc**	**South Sandwich Islands**	**Ontong Java plateau**	**Etendeka, Namibia**	**Kenya rift valley**
Data source	1	2	2	3	4	5	6	7	8	9
Mass % oxide										
SiO_2		50.48	49.30	49.28	45.64	50.77	50.88	49.47	50.07	47.18
TiO_2	0.217	1.19	1.68	2.61	1.84	1.59	0.50	1.08	3.19	3.63
Al_2O_3		16.87	14.40	12.56	12.49	16.21	18.24	14.05	12.68	14.75
ΣFeO		8.85	10.46	11.18	12.44	11.02	8.53	11.04	11.55	13.41
MnO		0.15	0.19	0.17	0.17	0.18	0.20	0.19	0.17	0.18
MgO		8.07	7.56	9.74	11.36	5.64	6.34	7.64	6.41	5.70
CaO		11.85	11.60	10.80	9.93	9.24	11.50	12.34	8.60	8.77
Na_2O		2.62	2.81	2.10	2.25	2.80	1.76	2.08	2.62	3.55
K_2O	0.030	0.10	0.13	0.48	0.67	0.93	0.10	0.12	1.48	1.31
P_2O_5	0.022	0.11	0.16	0.27	0.32	0.39	0.02	0.09	0.46	0.59
LOI		0.10	0.90		2.00		1.23	0.34	2.25	
Total		100.39	99.19	99.19	99.11	98.77	99.30	98.43	99.47	99.07

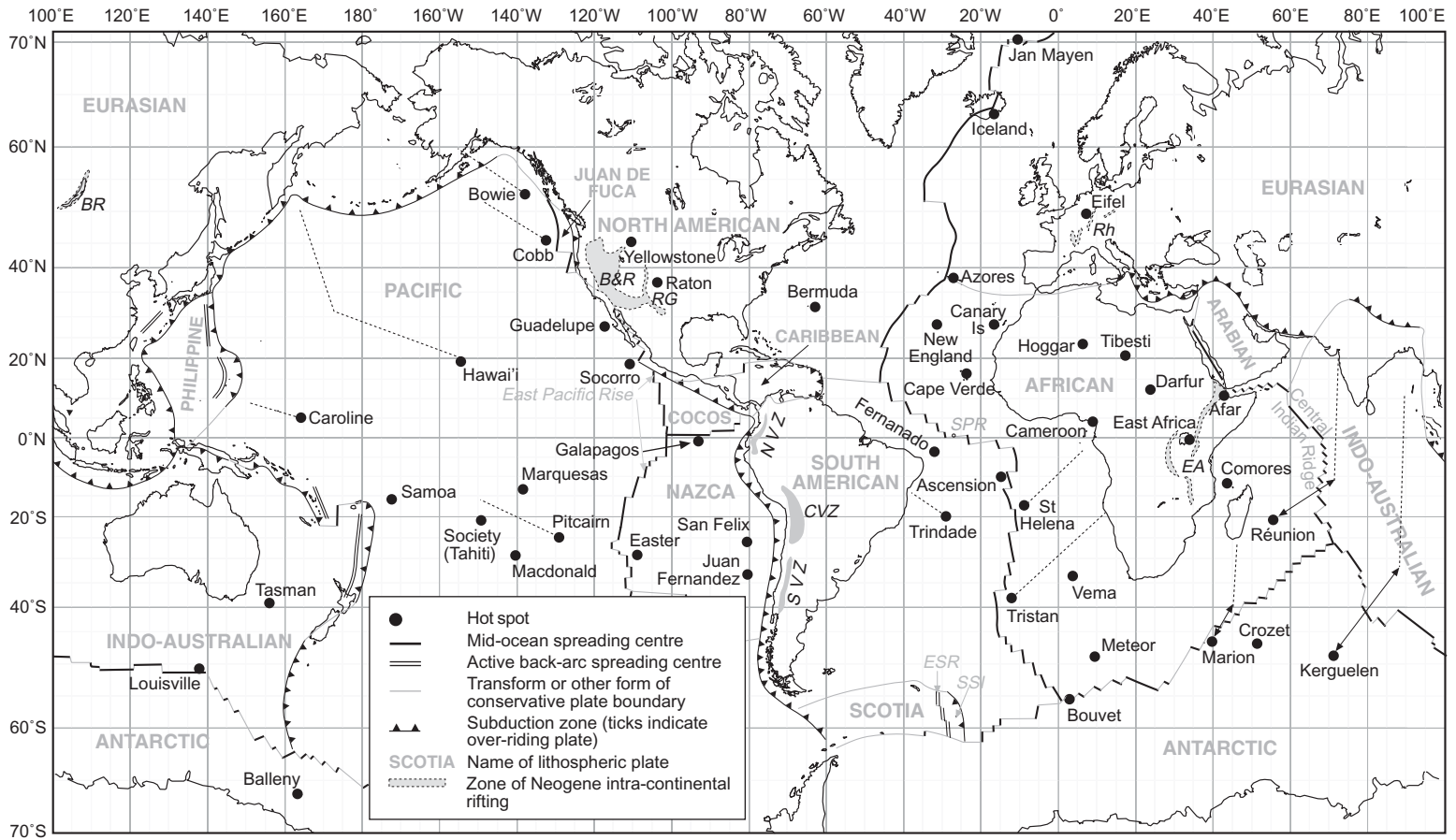


Fig. 2.12 Map of the world showing the principal lithospheric plates and **hot spots**, mid-ocean spreading centres, transforms, convergent margins and back-arc spreading centres, on a US Geological Survey base map. The hot spots shown are those listed by Steinberger (2000), to which Afar, Ascension, Bermuda, Bouvet and Crozet have been added; current geological opinion varies on the status and cause of individual hot spots. Dotted lines indicate the approximate orientation of seamount chains associated with selected hot spots; double-headed arrows in the Indian Ocean link seamount chains with their hot spots where they have been separated by seafloor spreading. *SPR* indicates the location of St Paul's Rocks, the product of volcanic activity at a 'leaky' transform. South Atlantic: *SSI* South Sandwich Islands (arc); *ESR* East Scotia Ridge. Intra-continental rifts: *BR* Baikal Rift, *B&R* Basin and Range province, *RG* Rio Grande rift, *EA* East African rift system, *Rh* Rhine and related western European rifts. *NVZ*, *CVZ* and *SVZ* refer to the northern, central and southern volcanic zones of the Andean cordillera.

Ppm by mass										
Rb	0.635	0.9	0.8	8.4	13	18.0	0.9	0.32	24.3	29
Ba	6.989	13.5	10	125	384	244	34	10.82	585	477
Th	0.085	0.191	0.171	1.14		1.39	0.12	0.247	4.14	5.62
Nb	0.713	2.5	3.1	24	31	3.3	0.19	3.3	28.3	63.0
La	0.687	3.08	4.06	14.6	20.3	10.13	0.90	2.92	38.6	52.2
Ce	1.775	8.71	12.3	36.5	35.3	25.21	2.81	8.14	86.3	107
Sr	21.1	126	142	368	478	391	108	118	626	933
Nd	1.354	7.91	11.3		25.5	18.8	2.84	6.91	45.8	51.3
Zr	11.2	78.3	100	141	110	132	21.3	61	280	227
Sm	0.444	2.53	3.92	5.55	6.30	5.04	1.11	2.19	9.34	9.32
Gd*	0.596	3.51	5.23			5.08	1.47	3.22	8.01	
Tb*	0.108			0.91	0.8	0.85	0.9	0.56	1.18	1.10
Y	4.55	26.9	37.0	22	24	30.0	11.9	22.7	29.9	25
Yb	0.493	2.53	3.67	1.90	1.30	2.86	1.40	2.20	2.33	1.80
Lu	0.074	0.40	0.57	0.27		0.43	0.22	0.36	0.33	0.26

* Which of these **REE** is reported depends on the analytical technique used in the original publication.

Data sources

1 Model primitive mantle composition compiled by Sun and McDonough (1989), used for normalizing as described in Box 2.7. Major elements other than TiO_2, K_2O and P_2O_5 were not included in the compilation.

2 Columbia University PetDB database at http://petdb.ldeo.columbia.edu, analyses DAR0057-022-002-1B and ODP0142.

3 Basaltic Volcanism Study Project (1981) analysis HAW-1 from the shield-forming subalkali suite of Kilauea volcano, Hawai`i.

4 Maaløe et al (1992) analysis 6 from the post-erosional volcanic suite of Koloa, Kauai, Hawaiian Islands.

5 Gust et al (1997) analysis 85-10-8-4.

6 Pearce et al (1995) analysis SSC35-4.

7 Fitton et al (2004) analysis 1183-9.

8 Ewart et al (2004) analysis KLS 554.

9 Macdonald et al (2001) analysis K93-1.

Box 2.6 Fe_2O_3, FeO and 'total iron oxide' – why and how?

The rock analysis in Box 1.1 showed separate entries for the two oxides of iron: Fe_2O_3 (ferric oxide) and FeO (ferrous oxide). The two entries highlight that iron may be present in silicate minerals in two oxidation states or – to express it another way – as two types of cation, Fe^{3+} and Fe^{2+}. Because these two ionic forms of iron possess different charge and ionic radii, they enter different cation sites in crystalline minerals (the octahedral site in olivine, for example, accepts Fe^{2+} ions but not Fe^{3+} ions) and behave differently in silicate melts. Accordingly, traditional major-element analyses show separate percentages for FeO (determined in a suitably prepared rock solution by measuring its capacity to reduce an oxidizing agent) and for Fe_2O_3 (which is calculated by subtracting FeO from the rock's 'total iron oxide').

In spite of these differences in chemical behaviour, most rock analyses published today no longer distinguish between FeO and Fe_2O_3, partly because FeO determination is slower than current analytical techniques for the other major oxides (so analyst time and costs are saved by omitting it), but chiefly because the FeO/Fe_2O_3 ratio measured on a cold igneous rock powder bears little systematic relationship to its value in the original hot magma. Instead, a typical modern analysis gives a combined figure for total iron oxide, as shown in Table 2.4.

Care needs to be taken when doing calculations involving FeO and Fe_2O_3, because the two oxides have different **RMM** values and Fe:O ratios:

	No of Fe atoms	No of oxygen atoms	Oxygens per Fe atom	RMM	RMM per Fe atom
FeO	1	1	1.0	71.85	71.85
Fe_2O_3	2	3	1.5	159.69	79.85

It is inappropriate simply to add or subtract FeO mass % and Fe_2O_3 mass %, since 1 kg of FeO represents more iron than 1 kg of Fe_2O_3. Conversely, because of the differences in RMM, 1.00 mass % of the element iron translates into ($\mathbf{RAM}_{Fe}$ + RAM_O) ÷ RAM_{Fe} = (55.85 + 16.00) ÷ 55.85 = 1.29% FeO or into (2 × 55.85 + 3 × 16.00) ÷ (2 × 55.85) = 1.43% Fe_2O_3 (Fig. 2.6.1). The ratio of these two numbers (1.4297 ÷ 1.2865 = 1.1113 ≈ 1.11) provides the conversion factor that must be taken into account in any calculation involving the notional transformation of the mass of one iron oxide into the other, or any summation of the two.

- by dissolving **mobile** elements, the hot seawater evolves into a fluid of higher **ionic strength**, rich in metal sulphides. Such fluids, on discharging into cold seawater at hydrothermal vents, precipitate clouds of dark sulphide sediment which are rich in elements like Cu, Zn and Pb; these discharging vents, associated with many active spreading centres, are called 'black smokers'.

Ocean island basalts (OIB)

The world's ocean basins are decorated by linear chains of intra-plate volcanic islands and seamounts (Fig. 2.12) – the Hawai`i-Emperor chain being the best known – in which the age of volcanism correlates with the island's position in the chain. Nonetheless by no means all intra-plate islands and seamounts are associated with such 'hot-spot tracks' (Wessel and Lyons, 1997). As a rule the elevation, composition, age and thicker crust of large intra-plate ocean islands are quite distinct from the abyssal plains upon which most of them stand. The submarine bulk of every intra-plate volcanic island greatly exceeds the volume exposed above the waves (Fig. 2.13). The largest stand as high above the surrounding sea floor as Everest rises above sea level: for instance, the altitude of Mauna Loa in Hawai'i is 4169 m above sea level and the

Total iron oxide may be expressed in two alternative forms:

$$\Sigma Fe_2O_3 = (1.11 \times FeO) + Fe_2O_3 \quad [2.6.1]$$

$$\Sigma FeO = FeO + (Fe_2O_3 \div 1.11) \quad [2.6.2]$$

FeO is more abundant than Fe_2O_3 in most fresh igneous rocks (see Carmichael et al., 1974; Wilson, 1989), so ΣFeO provides the more accurate picture and is the form quoted in all analysis tables in this book.* ΣFe_2O_3 is nonetheless widely quoted in many published analyses, though it over-represents the proportion of oxygen present (and raises the analysis total).

When FeO needs to be estimated from an analysis that lists only total iron oxide, e.g. for calculating norms of analyses in Table 2.4, a useful convention is to set $FeO_{est} = 0.9 \times \Sigma FeO$.

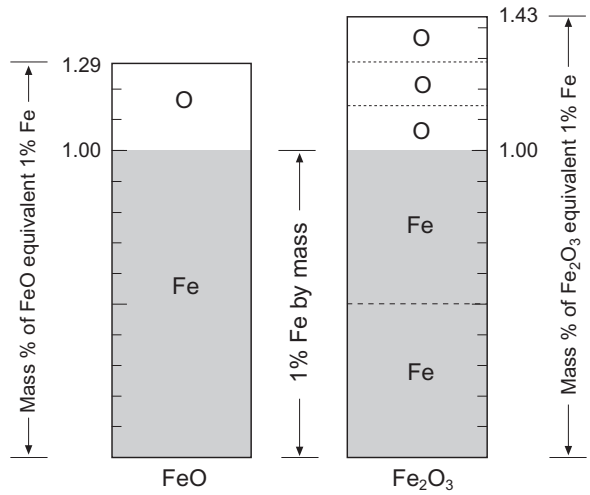


Fig. 2.6.1 Block diagram illustrating the make-up of FeO and Fe_2O_3 in mass terms; the shaded portion represents 1.00 mass % of Fe.

Some authors use alternative notations such as FeO or FeO_t.

surrounding abyssal plains are 5000 m deep.[5] Since the 1960s (Wilson, 1963) island-seamount chains, which trace the directions of plate motion, have been interpreted as the loci of stationary melting anomalies in the mantle (Fig. 2.12) over which lithospheric plates are migrating, though recent research suggests that hot spots may be less fixed than previously assumed (Christensen, 1998; Tarduno, 2007).

A **hot spot** is a localized source of magma supply whose output thickens the basaltic crust in its immediate neighbourhood (Fig. 2.13) by construction of a volcanic edifice on the sea floor, by intrusion of magma within the crust and by 'underplating' magma at the base of the crust. The crustal thickness beneath Ascension Island in the Atlantic is 12–13 km (Klingelhöfer et al., 2001), for example, and that of the Marquesas island chain in the Pacific is 15–17 km (Caress et al., 1995), compared to an average oceanic crustal thickness of 6–7 km. Compiling such data for 'hot-spot tracks' of known age allows melt production rates to be estimated: for example, White (1993) estimated the melt production rate (volcanic and plutonic) for Réunion in the Indian Ocean as 0.05 km^3 $year^{-1}$, and that for the Hawaiian chain about 0.18 km^3 $year^{-1}$.

[5] A 3D representation of the Hawaiian islands can be downloaded from http://pubs.usgs.gov/imap/2800/

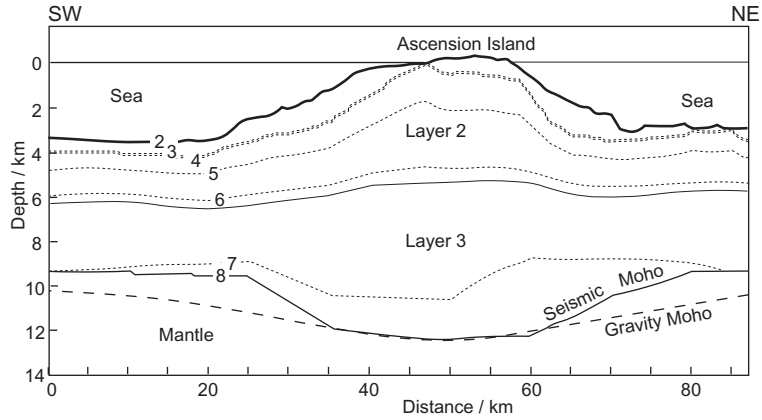


Fig. 2.13 Seismic cross-section of Ascension Island in the equatorial Atlantic (simplified from Klingelhöfer et al., 2001 Fig. 6A (copyright Elsevier 2001)). Dotted lines show the velocity model contours in km s^{-1}; the dashed line indicates the Moho depth from 3D gravity modelling.

The volcanic rocks that form the intra-plate islands and seamounts are overwhelmingly basaltic. Most oceanic islands develop in a similar way, starting with an early phase of voluminous growth lasting up to a million years that constructs a large, gently sloping, subaerial **shield volcano** (the 'shield-building stage'), followed by a hiatus during which erosion of the shield occurs, followed in turn by renewed, low-volume, more alkaline and more explosive volcanism (the 'post-erosional stage') in which **evolved** alkali magmas may be more prominent. In the Hawaiian islands the shield-building stage consists mostly of augite-plagioclase-olivine-phyric tholeiitic basalt, though it includes a late capping of transitional and alkali basalts; the post-erosional stage consists of more strongly alkali lavas, as well as occasional flows of more evolved products like trachyte (Fig. 9.8). The majority of ocean islands, however, are of alkali character throughout.

Intra-plate ocean island basalts constitute a well defined compositional magma type known as 'ocean island basalts' (OIBs). Figure 2.16(a) shows the incompatible element patterns for two examples of OIB. In spite of the differences between them, the OIB patterns exhibit consistently higher levels of enrichment of the more incompatible elements (by a factor of at least ten) than in MORB, but the OIB patterns cross over the MORB profiles to reverse this relationship on the right-hand side. This contrast in incompatible element fingerprints suggests that OIBs tap different mantle sources from those feeding mid-ocean ridges.

Iceland is a special case of an ocean island which happens to lie astride the Mid-Atlantic Ridge. Like many ocean islands it has well developed rift zones (Fig. 9.9), but here the geometry of the rifts has more to do with the oceanic spreading centre than with structural failure of an island edifice. The oldest basalts on Iceland – about 16 Ma old – are found at the NW and SE extremities of the island. Post-glacial volcanic activity has been concentrated in a λ-shaped feature – called the Neovolcanic Zone – transecting the centre of the island from SW to NE, connecting to the Reykjanes Ridge in the SW and the Tjörnes fracture zone in the NE. The intensity of lithospheric extension and associated volcanism occurring in the Neovolcanic Zone is indicated by dyke-fed fissure eruptions, non-eruptive fissures and local normal faulting, linear chains of cinder cones and craters (notably along the Laki fissure zone), and linear ridges ('mobergs') consisting of pillow breccia and hyaloclastites, marking where fissure eruptions have taken place beneath former ice sheets (Fig. 2.14). The bulk of Icelandic volcanism consists of subalkali basalts with a distinctive Fe, Ti-rich chemical signature showing both OIB and MORB affinities. More evolved subalkali rocks (including rhyolites) are associated with some volcanic centres (Chapter 6). Holocene alkali basalt volcanism is associated with the 'off-rift' Snaefellsnaes Peninsula in the west and the extreme southern end of the Eastern Fracture Zone, including the Vestmann islands (Fig. 9.9).

Box 2.7 Trace elements as 'fingerprints'

Basalts from different tectonic settings differ in chemical composition. Such differences throw light on the different ways in which basalt melts are formed, and help to identify the affinities of older basalts whose original tectonic setting has been obscured by subsequent events. **Trace elements** generally prove to be the most useful geochemical discriminants, because their concentrations vary more widely between settings than major elements.

Trace elements are subdivided according to their relative affinity for crystalline minerals and melt:

- **incompatible elements** are those which consistently favour the melt in preference to coexisting mineral crystals. Goldschmidt (1937) attributed this behaviour to having too large an ionic radius or too high an ionic charge (Fig. 2.7.1) to reside in the compact, highly ordered structure of most mineral crystals; such ions are more easily accommodated in the relatively disordered structure of the coexisting melt. Rb, Ba, La and U are good examples; the distribution of the main incompatible elements in the periodic table is summarized in Fig. 2.7.2.

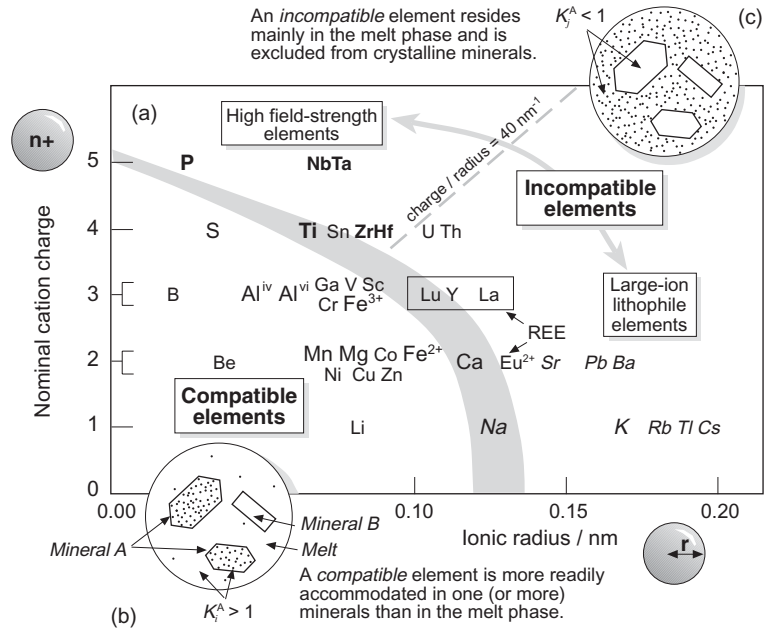


Fig. 2.7.1 Compatible and incompatible elements. (a) A plot of cation charge *versus* cation radius for **lithophile** elements (after Gill, 1996). Elements whose symbols overlap the fuzzy boundary between compatible and incompatible fields may fall into either group, depending on the lattice dimensions of the minerals crystallizing (or that are present during melting). Larger type indicates major elements; *italic type* indicates incompatible elements that are most prone to dissolution and mobility in aqueous fluids; **bold type** identifies incompatible elements whose concentrations are least mobile in such fluids. The box labelled 'REE' encloses the 15 **rare earth elements** from La to Lu (see Fig. 2.7.2) together with yttrium (Y) which behaves like an REE (see Fig. 2.7.2); europium (Eu) is unique among the REE in also having a divalent (2+) oxidation state. (b) Cartoon illustrating compatible behaviour, in which dots symbolize ions of a compatible element, and their density represents its equilibrium concentrations in coexisting crystal and melt. Note the element is compatible in one mineral A ($K_i^A > 1$) but not the other ($K_i^B < 1$). (c) Cartoon illustrating incompatible behaviour: the element has a higher concentration in the melt than in all coexisting crystals ($K_j^A < 1$).

Continued

- **compatible elements** are preferentially incorporated into one or more crystallizing minerals relative to the melt; for example, nickel is preferentially taken up by olivine.

Though ionic radius and charge are key factors in determining whether an element behaves compatibly or incompatibly, the lattice parameters of the host minerals also play a role (Blundy and Wood, 2003).

The affinity that an element has for a particular crystalline mineral can be expressed quantitatively in terms of the *partition coefficient* $K_i^{A/melt}$:

$$K_i^{A/melt} = \frac{\text{concentration of element } i \text{ in mineral A}}{\text{concentration of element } i \text{ in coexisting melt}}. \qquad [2.7.1]$$

In igneous applications, the presence of melt can be assumed and therefore '$K_i^{A/melt}$' can be abbreviated to 'K_i^A'. An incompatible element is one for which $K_i^A < 1.0$ (Fig. 2.7.1c). In the case of a compatible element, $K_i^A > 1.0$ for a specific mineral A: thus for the distribution of Ni between olivine and coexisting basalt melt, for example, $K_{Ni}^{olivine} \sim 14$.* It must be emphasized that such compatibility is highly dependent on the identity of the host mineral: though favoured by olivine, Ni is strongly *excluded* by feldspars ($K_{Ni}^{feldspar} \sim 0.01$) and therefore would behave as an incompatible element if feldspar were the only mineral crystallizing. The same point is illustrated by the **REE** in Fig. 6.6.1 (Box 6.6).

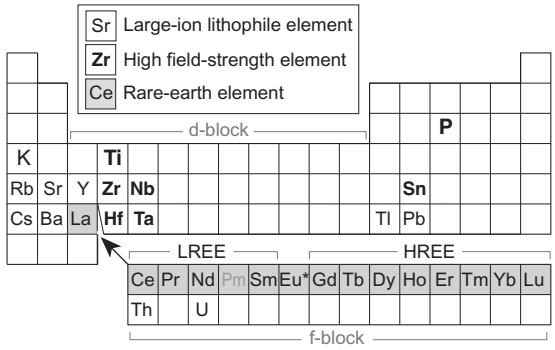


Fig. 2.7.2 Locations of incompatible lithophile elements in the periodic table; major elements are shown in **larger type**. The rare earth elements ('REE'), from lanthanum (La) to lutetium (Lu) inclusive, are chemically very similar to each other, and to yttrium (Y); the radioactive REE promethium (Pm, shown faint) is too short-lived to occur naturally on Earth.

Incompatible elements provide the most useful 'fingerprints' for distinguishing between different types of basalt. Fig. 2.7.3a shows one way to portray such information. The *x* axis shows a list of incompatible trace elements (and a few 'major' ones – K, P and Ti – that also exhibit incompatible behaviour) arranged from left to right *in order of decreasing incompatibility* (i.e. increasing K_i^A): those on the left are the most strongly excluded from all mantle minerals (olivine, enstatite, diopside, spinel and garnet) and therefore enriched in coexisting partial melt, while those on the right may be incorporated in selected mantle minerals, notably garnet if it is present. The *y* axis represents the concentration of each element in the sample(s) of interest, using a logarithmic scale in order to embrace a wide range of possible values.

The problem with this plot is that wide variations in natural abundance between individual trace elements generate a jagged appearance that obscures the differences between samples. Since these gross elemental abundance variations are common to all matter in the solar system, they can be smoothed out by plotting the ratio of each element's concentration in the sample of interest (an ocean island basalt in this instance) to its concentration in 'primitive mantle'. Fig. 2.7.3b shows

*Published values of partition coefficients for specific elements, minerals and melt compositions can be found in the GERM database (http://earthref.org/GERM/). Partition coefficients vary with the temperature and pressure at which melt and crystal equilibrate (see Blundy and Wood, 2003).

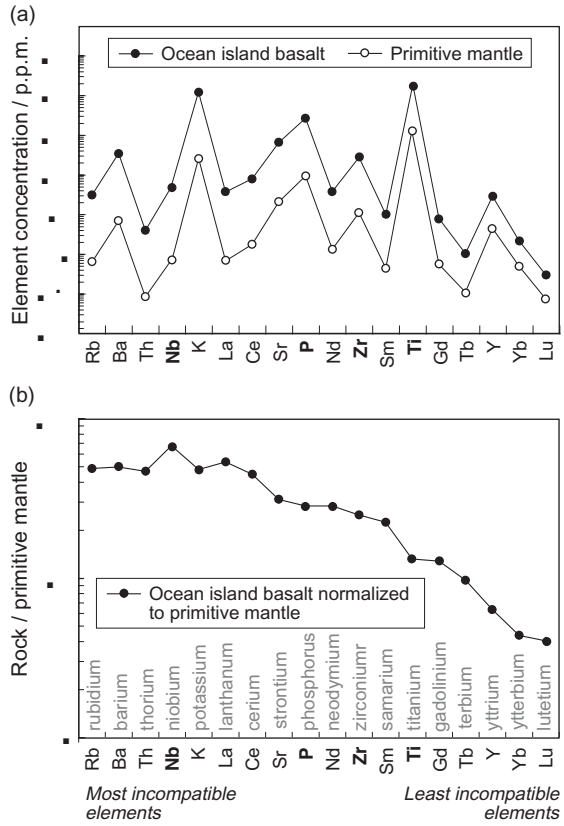


Fig. 2.7.3 Why normalize? (a) Raw concentrations in parts per million of incompatible elements plotted in order of decreasing incompatibility for typical ocean island basalt (OIB) and 'primitive mantle' (data for both from Sun and McDonough, 1989) plotted in order of decreasing incompatibility. (b) 'Normalized' incompatible element ratios for the same OIB data (i.e. the OIB/primitive mantle ratio for each element) in the same order. The data for hypothetical primitive mantle used for normalizing, from Sun and McDonough (1989), are listed in Table 2.4.

Chemical symbols shown **bold** indicate high field-strength elements (Fig. 2.7.1).

how this treatment generates a cleaner 'fingerprint', highlighting the selective enrichment in the melt of the most highly incompatible trace elements that is characteristic of OIB.

Figs. 2.7.3b and 2.15 show this kind of graph (sometimes called a '**spidergram**') in its simplest form. Many authors interpose additional incompatible elements (U, Ta, Pb, Hf and 'heavy' **REE** such as Dy and Er) but little advantage is gained by doing so.

As Fig. 2.7.1 shows, incompatible elements are often divided into:

- 'Large-ion **lithophile** elements' (LILE), having ionic radii too large to be accommodated in most rock-forming minerals;
- 'High field-strength elements' (HFSE), whose high charge:radius ratio creates an intense electrostatic field around each ion, making it unstable in an ionic silicate crystal.

LIL elements are more readily dissolved by aqueous fluids and are therefore relatively **mobile** during weathering, alteration and metasomatism (see Gill, 1996, p 207). HFS elements, on the other hand, resist dissolution and, being less mobile, serve as more reliable indicators of magma affinity in altered and metamorphosed basalts. This distinction is of key importance in considering the origins of subduction-related magmas (Chapter 6).

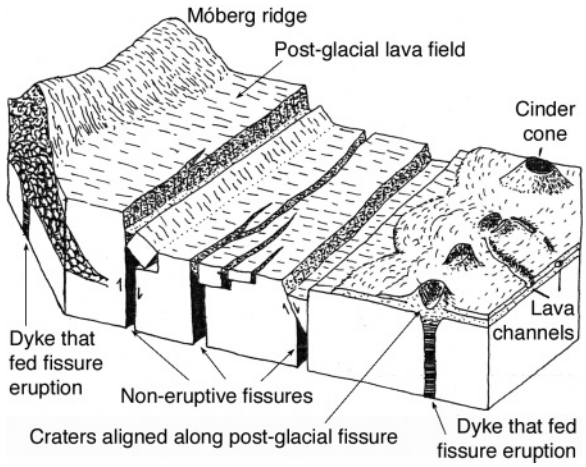


Fig. 2.14 Block diagram illustrating features of Neovolcanic Zone volcanism in Iceland (adapted from Walker (1965) by kind permission of the Leicester Literary and Philosophical Society, UK). *Móberg* is Icelandic for 'brown rock' (in this context meaning hyaloclastite): moberg ridges are linear ridges of accumulated pillow breccia and hyaloclastite formed during subglacial fissure eruptions.

Large igneous provinces (LIPs): oceanic plateaux and continental flood basalts (CFBs)

Across most of the ocean floor remote from hot spots, the basaltic crust has a uniform thickness of about 6.5 km, but ocean-floor bathymetry and geophysical studies in the past 25 years have revealed a number of enormous submarine basaltic plateaux (Fig. 2.15), rising to at least 1000 m above the surrounding abyssal plains, where the oceanic crust thickens to as much as 35 km (Mahoney and Coffin, 1997). Most are remote from spreading centres and exhibit no regular magnetic anomalies of the kind associated with mid-ocean ridges. These plateaux represent enormous *intra-plate* volcanic outpourings, each of which seems to have been emplaced in only a few million years. The largest is the Ontong Java Plateau (OJP) in the western Pacific which, taking account of related lavas in the adjacent Nauru Basin and the Solomon Islands, consists of about 60 million cubic kilometres of volcanic and plutonic rocks (Coffin and Eldholm, 1994) emplaced around 122 Ma ago (Fitton et al. 2004).[6] The basalts are dominantly olivine-plagioclase-phyric low-K tholeiites. Such voluminous oceanic plateaux and rises (Fig. 2.15) are oceanic examples of **large igneous provinces** (LIPs). Other examples are the Shatsky Rise in the Pacific and the massive Kerguelen Plateau in the Southern Ocean SW of Australia (Fig. 2.15; Coffin et al., 2002).

Their continental counterparts – **continental flood basalt** (CFB) provinces – were recognized much earlier, and their petrology and geochemistry have been studied in great detail in the last 50 years. Like oceanic plateaux, CFBs consist of great thicknesses (several km) of subalkali, usually olivine-plagioclase-phyric basalt lavas, though in some CFBs such as Etendeka and Yemen more evolved volcanics may also be volumetrically significant. There is commonly evidence of extensive domal uplift associated with early stages of CFB evolution, exemplified in Fig. 2.15 for the Afro-Arabian LIP of which the Yemen volcanics are a part. For some CFBs, like the North Atlantic Volcanic Province and the Deccan 'Traps' in India, the bulk of the volcanic output is now known to have been erupted in surprisingly brief intervals of time (as little as 0.5–2 Ma according to White, 1993, or less than 1 Ma according to Courtillot and Renne, 2003). The melt production rates during these short periods must have been colossal: for the Deccan alone, for example, the average melt production rate has been estimated at 5 km^3 $year^{-1}$ (White, 1993; Courtillot and Renne, 2003), greatly exceeding the present-day global hot spot output (~ 0.5 km^3 yr^{-1}) and falling not far short of the steady-state magma production rate of the entire mid-ocean ridge system (~20 km^3 yr^{-1}). Most CFBs, though not all (see Fig. 2.15), are found at passive margins where continental fragments have since separated, and many can be linked by means of island-seamount chains or aseismic ridges to present-day hot spots. Thus the Deccan CFB province (Fig. 2.15) is linked via the Maldive Ridge to the present Réunion hot spot, though the geographical correlation here has been

[6] Taylor (2006) suggests that the present OJP formed only a part of a still larger submarine plateau incorporating the Manihiki and Hikurangi plateaux (Fig. 2.15) as well, subsequently dispersed by Cretaceous seafloor spreading.

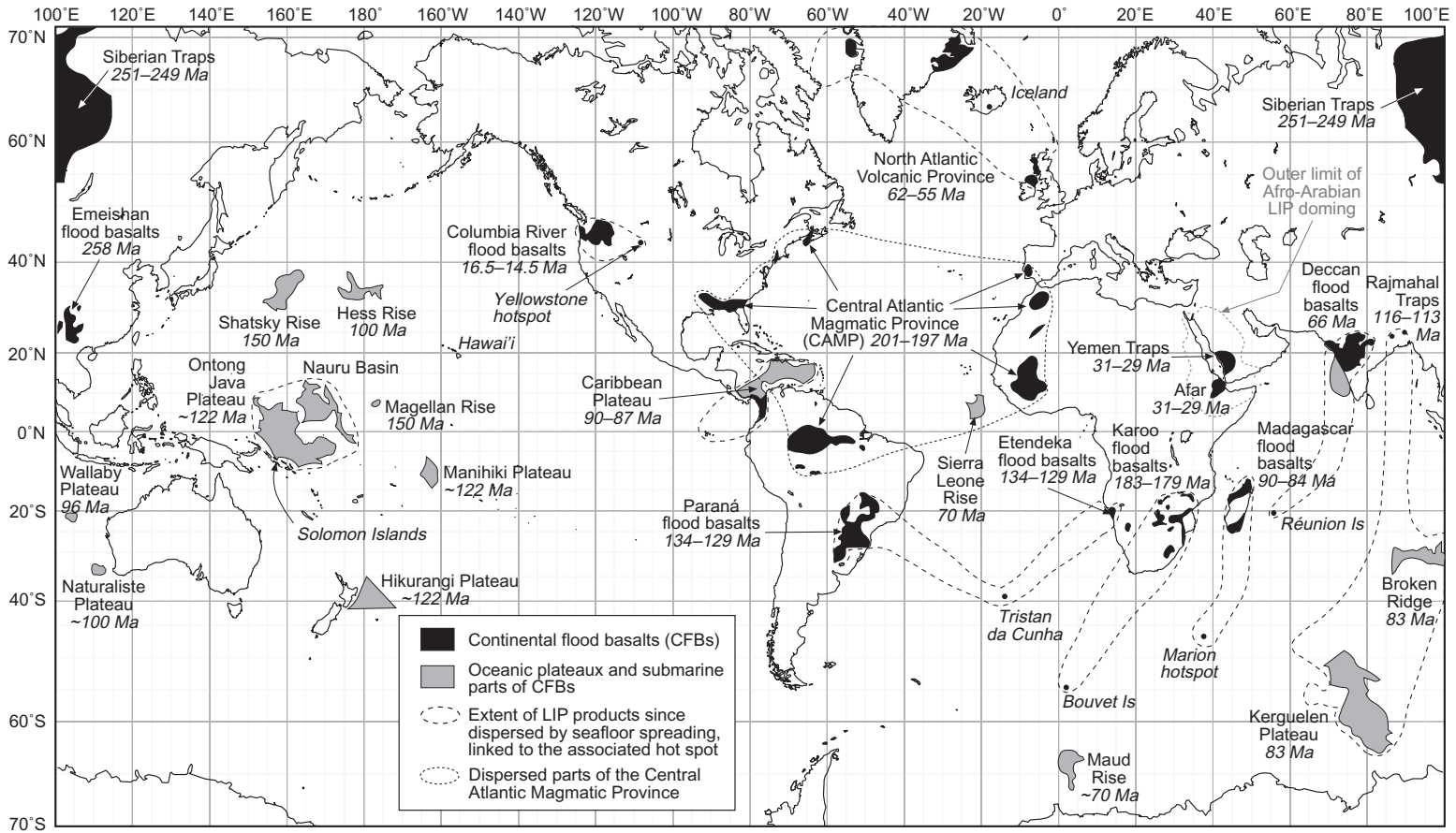


Fig. 2.15 The principal large igneous provinces (LIPs) formed in the past 260 Ma, with ages shown in italic. Continental and passive-margin flood basalts are shown in black; oceanic plateaux and major rises are shown in grey. Dashed outlines enclose volcanic provinces that have been dispersed by seafloor spreading since eruption, or link a LIP to a current hot spot believed responsible for it. Drawn from an on-line catalogue prepared by the IAVCEI* *Commission on Large Igneous Provinces* (www.largeigneousprovinces.org) from which the ages shown have been taken, on a base map prepared by the US Geological Survey (as in Fig. 2.12). The outcrop of Central Atlantic Magmatic Province basalts is from McHone (2000). The Ferrar LIP (183–179Ma), consisting of basalts and dolerite sills in Antarctica (Fig. 4.3d), Tasmania and New Zealand dispersed by the break-up of Gondwana, is not shown; it coincides in age with the Karoo LIP with which it appears to be cogenetic. Ages shown relate solely to the initial major volcanic outburst – many LIPs can be linked to a hot spot active today. The extent of doming associated with the ~30 Ma Afro-Arabian LIP (after Davison et al., 1994) is shown as a grey dashed line.

* International Association for Volcanology and the Chemistry of the Earth's Interior.

complicated by later seafloor spreading centred on the Central Indian Ridge (Fig. 2.12).

On the other hand, Ingle and Coffin (2004) have proposed that the Ontong Java oceanic plateau, the largest LIP on Earth in terms of volcanic output, may instead be the record of a bolide impact, on the grounds that it cannot be linked convincingly to any hot-spot track. This may explain why uplift at the time of eruption – as indicated in other submarine LIPs by the abundance of subaerial lavas in the volcanic sequence – appears to have been minimal: virtually all Ontong Java lavas so far sampled are clearly submarine (Fitton et al. 2004). Another LIP with no convincing link to any hot-spot track is the early Jurassic (200 Ma) Central Atlantic Magmatic Province (CAMP), whose products are dispersed on the margins of four continents (Fig. 2.15) as a result of the contemporaneous rifting and break-up of the Pangaea supercontinent. McHone (2000) argued that this LIP is not readily explained by a mantle plume; Coltice et al. (2007) instead attribute the volcanism to long-term shallow mantle heating associated with continent aggregation.

The largest CFBs are believed to have generated massive environmental crises at the time of their eruption, and some appear to be linked to biological extinctions (White and Saunders, 2005; Kelley, 2007). Controversy has raged for decades as to whether the major extinctions in the stratigraphic record arise from plume-related volcanic crises or from bolide impacts. White and Saunders (2005) suggest on statistical grounds that the end-Permian, end-Triassic and end-Cretaceous extinctions could result from bolide impacts that happened to coincide with LIP eruptions. The impact of oceanic plateau LIPs, erupted largely under water, appears to have been less severe.

Unlike the relatively uniform trace element patterns observed in MORB and OIB (Fig. 2.16a), incompatible element behaviour in LIPs is highly variable, both within and between individual provinces. Inter-provincial differences are illustrated in Table 2.4 and Fig. 2.16b by:

- a low-K basalt from the Ontong Java plateau; the pattern resembles N-MORB but has a more pronounced level portion and a steeper gradient among the most incompatible elements K, Th, Ba and Rb;
- an Etendeka flood basalt from Namibia; though tholeiitic, this basalt has an enriched incompatible element profile reminiscent of an OIB alkali basalt.

Factors like lithosphere thickness and – in continental areas – interaction with **sialic** crust, and the change of these factors with time as a province evolves, provide ample scope to explain these differences.

Intra-continental rift basalts

Basaltic volcanism is associated with intra-continental rifting in various circumstances:

- where extension is caused by doming above a sub-continental mantle hot spot, as in the *Kenya–Ethiopia rift system* in East Africa – illustrated in Fig. 9.3 – from 25 Ma BP to the present (Rogers et al., 2000);
- where extension occurs perpendicular to the compressive stresses behind a continental collision zone, illustrated by the Neogene volcanics of the *Rhine rift valley* of Germany (Fig. 2.12);
- in regions of post-subduction extension, as in the *Basin and Range Province* in the western USA ('*B&R*' in Fig. 2.12). Eastward subduction of the former Farallon Plate here in the Palaeogene produced calc-alkali magmatism (Chapter 6). All that remains of the Farallon Plate today are its NW and SE extremities, represented by the present Juan de Fuca and Cocos plates (Fig. 2.12); the portion in between – with the East Pacific Rise that generated it – has been subducting for the past 30 Ma, and this may be the cause of the elevated heat flow, uplift and widespread extension in the parts of the overriding plate directly above, extending as far east as the Rio Grande rift ('*RG*' in Fig. 2.12). Associated basaltic volcanism has occurred here since about 15 Ma ago, much of it SiO_2-undersaturated;
- other types of continental rift, like the *Baikal rift* in Eastern Siberia, whose tectonic origins are less clear.

Each of these examples is characterized by elevated heat flow (~100 mW m^{-2} within the rift and ~60 mW m^{-2} on the flanks) and a broad gravity low, consistent with thinned lithosphere. In each case the involvement of a mantle hot spot has been mooted but, except in the case of East Africa, it is generally accepted today that other tectonic mechanisms lie behind both extension and volcanism.

In Kenya the total volume of volcanic material erupted over the past 25 Ma amounts to about 200,000 km^3; if Ethiopia is considered too, the total mounts to about 500,000 km^3. In the other examples cited above, however, the magma productivity is at least an order of magnitude lower. Alkali and transitional basalts predominate in each case.[7] Basalts in most continental rifts form a continuum with more alkali and strongly undersaturated mafic rocks such as nephelinite and melilitite, and are accompanied by relatively large volumes of more evolved volcanics such as trachyte and phonolite (Chapter 9). It is therefore appropriate to discuss the petrography of continental rift basalts in the context of these more alkaline magmas in Chapter 9.

In terms of incompatible elements, the Kenya rift valley alkali basalt shown in Fig. 2.16(a) is barely distinguishable geochemically from an oceanic hot spot alkali basalt. The significance of this similarity is discussed in the final section of the chapter and in Chapter 9.

Subduction-related basalts

Subduction zones (Fig. 2.12), where oceanic lithosphere born at a mid-ocean ridge is interred back into the Earth's mantle, generate a wide variety of volcanic products. The most obvious aspect of this variability is reflected petrographically in the relatively large volumes of more **evolved** magmas erupted in many island arcs (andesites) and active continental margins (dacites and rhyolites) that will be described in Chapters 6 and 7. Though less obvious in the field and under the microscope, important variations also exist among the parental basalt magmas generated above subduction zones, as revealed by plotting their incompatible element profiles (Fig. 2.16c). We consider these basalts below under five headings, based partly on tectonic setting and partly on the geochemical divisions shown in Fig. 1.6.

Low-K or 'island-arc tholeiite' (IAT) arc basalts

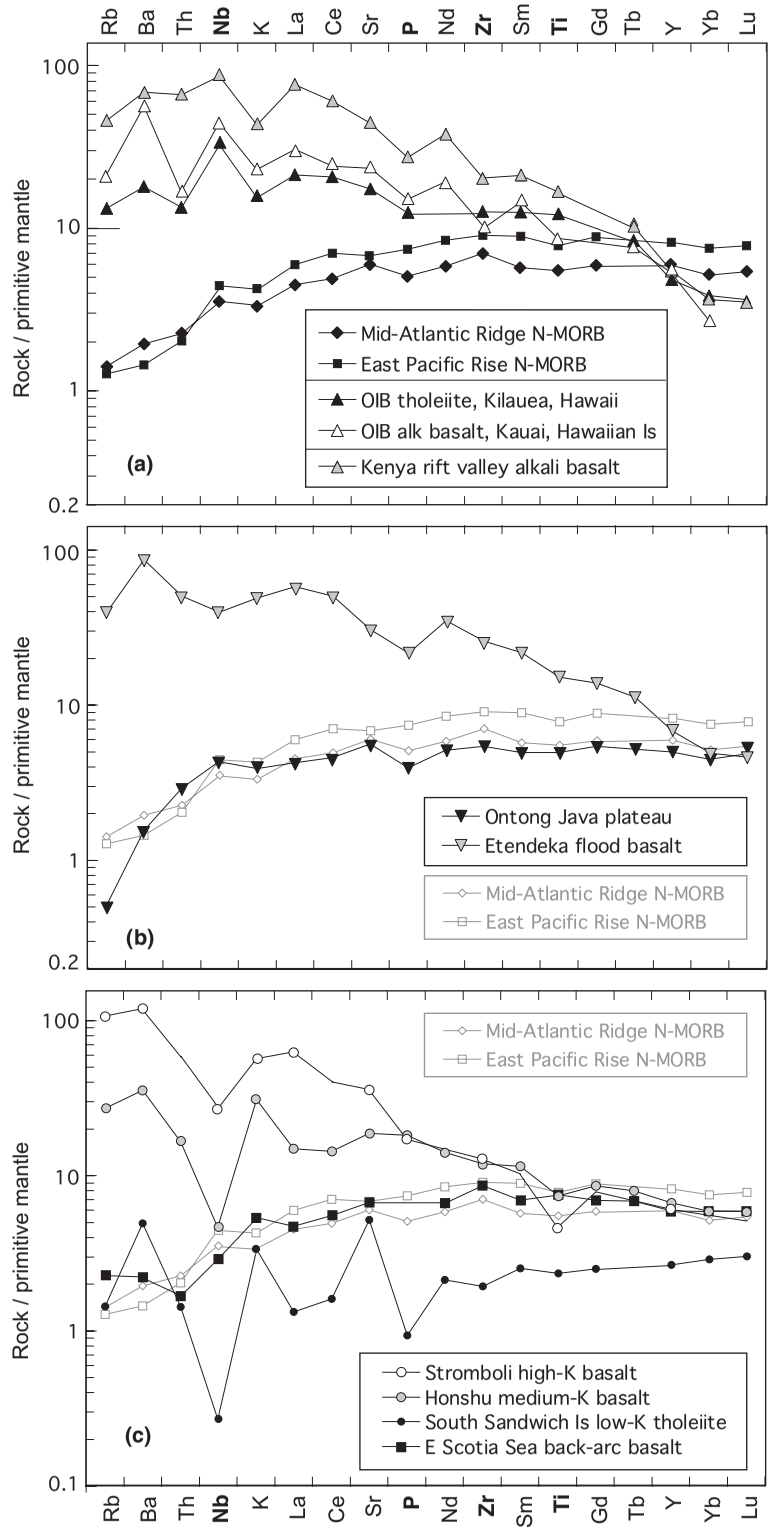
The association with the lowest K_2O content in Fig. 1.6, the 'low-K' or island-arc tholeiite association, is dominated by basalts, and is characteristic of immature oceanic island arcs such as the South Sandwich Islands, Tonga and the Izu Islands of Japan (Fig. 2.12). Lavas of this affinity probably also form the foundations of many more evolved island arcs. Unlike other subduction-related lavas, IAT basalts are often aphyric or only sparsely porphyritic, and consist of olivine, plagioclase and augite, sometimes accompanied by sparse orthopyroxene and/or magnetite.

The geochemistry of island-arc tholeiites is distinctive on account of their **depletion** in high field strength (**HFS**) incompatible elements but comparative enrichment in many large-ion lithophile (**LIL**) elements: these tendencies give most subduction-related magmas characteristically jagged profiles in primitive-mantle-normalized incompatible element diagrams. The IAT pattern in Fig. 2.16(c) is typical in having a relatively smooth, gently sloping right-hand portion that is depleted relative to N-MORB. This relatively smooth trend extends across to the 'lightest' rare earths, La and Ce (with a slightly lower La/Yb ratio than N-MORB), but the trend is interrupted by marked negative anomalies in the HFS elements P and Nb and positive anomalies in some **mobile** LIL elements (Sr, K and Ba). These characteristics point to a mantle source that is depleted overall relative to that of N-MORB (as indicated by Nb, P, rare-earth element (REE), Zr and Ti) but which has received an influx of mobile LIL elements by means of fluids expelled from the dehydrating slab, as discussed in Chapter 6.

Medium-K arc basalts

Rocks of the medium-K (Fig. 1.6) or '**calc-alkali**' association (Wilson, 1989) are the most characteristic products of mature island-

[7] Subalkali basalts predominate among lavas older than 5 Ma in the Basin and Range.


Rb
Ba
Th
Nb
K
La
Ce
Sr
P
Nd
Zr
Sm
Ti
Gd
Tb
Y
Yb
Lu
Rock / primitive mantle
100
10
1
0.2
0.1
(a)
Mid-Atlantic Ridge N-MORB
East Pacific Rise N-MORB
OIB tholeiite, Kilauea, Hawaii
OIB alk basalt, Kauai, Hawaiian Is
Kenya rift valley alkali basalt
(b)
Ontong Java plateau
Etendeka flood basalt
Mid-Atlantic Ridge N-MORB
East Pacific Rise N-MORB
(c)
Stromboli high-K basalt
Honshu medium-K basalt
South Sandwich Is low-K tholeiite
E Scotia Sea back-arc basalt

arc volcanism. Basaltic members of this association, sometimes referred to as **high-alumina basalts** (Kuno, 1960; see also Seth et al., 2002), are often notably porphyritic, containing phenocrysts of plagioclase, olivine, augite and magnetite, occasionally accompanied by hornblende. In many island arcs, however, strongly porphyritic medium-K andesites (Chapter 6) are more abundant than basalts.

Medium-K basalts are more variable in their incompatible-element geochemistry than low-K basalts but most share several common features. Figure 2.16(c) shows a medium-K basalt from central Honshu, Japan in which:

- all incompatible elements are present at higher concentrations than in IAT;
- highly incompatible elements (left-hand side), though variable, are more enriched than moderately incompatible elements;
- as in IAT, there is marked depletion in some high field-strength elements, notably niobium (Nb).

These are features common to many *supra-subduction zone* (SSZ) magmas in mature island arcs and convergent margins. They are believed to reflect intra-crustal magma fractionation superimposed on the signature of melting of mantle wedge peridotite metasomatized by slab fluids, as discussed in Chapter 6 and 11.

High-K arc basalts

Basalts of the high-K (Fig. 1.6) or 'high-K calc-alkali' association (Wilson, 1989, Fig. 6.15) are relatively scarce, usually being exceeded in volume by the andesites and more evolved members of the high-K association, both in island arcs and at active continental margins (e.g. the central volcanic zone of the Andes – Fig. 2.12). They typically contain phenocrysts of olivine and augite, sometimes accompanied by hornblende, magnetite and/or plagioclase.

Incompatible element patterns for high-K basalts tend to be more enriched in mobile LIL elements than in medium-K basalts (as one would expect since K is itself a LIL element). This is illustrated in Fig. 2.16(c) by a high-K basalt from the Aeolian island of Stromboli in the Mediterranean; note the negative Nb and Ti anomalies.

As in the case of Stromboli (Francalanci et al., 1999), basalts in the high-K category are often associated with potassic alkali lavas of trachybasalt type (Fig. 2.1) – members of the 'shoshonite association' – that are described in Chapters 6 and 9.

Basalts from back-arc basins

Rifting within an island arc may split the arc longitudinally and create between the 'front' and 'rear' fragments an extensional basin floored by oceanic crust that has running down its centre an oceanic spreading centre resembling a mid-ocean ridge. Spreading centres in such 'back-arc basins' (Figs. 2.12 and 6.18) erupt subalkali pillow basalts petrographically similar to N-MORB: phenocrysts are dominated by plagioclase and olivine with subordinate augite and opaques. Their compositions often share features with both IAT and N-MORB basalts. Figure 2.16(c) shows a basalt from the East Scotia Sea back-arc spreading centre behind the

Fig. 2.16 Incompatible element enrichment diagrams (**spidergrams**) for typical analyses of basalts. Note the vertical scale is logarithmic to allow a wide range of enrichment (relative to primitive mantle) to be depicted. (a) N-MORBs and OIBs, (b) LIPs, and (c) Subduction-related basalts, as tabulated in Table 2.4, with N-MORB samples shown faint for comparison in (b) and (c); the Stromboli high-K basalt and E Scotia Sea data in (c), not included in Table 2.4, are from Francalanci et al. (1999) and Fretzdorff et al. (2002) respectively.

For plotting, each analysis is (i) recalculated volatile-free (Box 1.3) where necessary, and (ii) divided element-for-element by the Primitive Mantle analysis given in Table 2.4 (as explained in Box 2.7). Where an element has been omitted from a published analysis (e.g. Gd or Tb), a straight line is drawn between the coordinates for neighbouring elements. Note the logarithmic scale of the vertical axis. Chemical symbols shown **bold** indicate high field-strength elements (Fig. 2.7.1).

South Sandwich Islands arc ('*ESR*' and '*SSI*' in Fig. 2.12) which has a MORB-like profile, but with a small negative Nb anomaly and positive K and Ba anomalies reminiscent of supra-subduction zone volcanic rocks.

Hydrothermal activity at back-arc spreading centres generates volcanogenic massive sulphide (**VMS**) deposits rich in Cu, Zn and Pb, analogous to those forming at mid-ocean ridges.

Basalts from active continental margins

Basalts covering the same range of composition seen in island arcs are also erupted above subduction zones at 'active' (or convergent) continental margins, though members of the low-K suite are poorly represented here. Basalts are also commonly insignificant in volume compared to more evolved magmas like andesites and dacites. In the Southern Volcanic Zone of the Andes, however, basalts and basaltic andesites (Fig. 2.1) predominate. Mineralogically and geochemically, basalts from active continental margins conform to the descriptions given above.

Extraterrestrial basalts

This chapter would be incomplete without brief mention of basaltic volcanism in other parts of the solar system.

Lunar basalts

The darker regions of the Moon's surface as seen from Earth (the *maria*) consist of rocks that have the petrographic attributes of basalt. Lunar basalts differ from their terrestrial counterparts, however, in several important ways:

- A proportion of lunar rocks qualifying as basalts mineralogically (Table 2.1) fall well outside the IUGS geochemical definition in Fig. 2.1, with SiO_2 contents in mare basalts extending as low as 38%. (The designation of these rocks as basalts predates the work of the IUGS Commission (Le Maitre, 2002) and seems to have been overlooked by them.)
- The lowest-SiO_2 mare basalts have spectacularly high TiO_2 contents (up to 13%). TiO_2 content is a key discriminant in distinguishing between different categories of lunar basalt (Basaltic Volcanism Study Project, 1981).
- Lunar basalts contain no detectable water and their iron minerals are highly reduced compared to terrestrial basalts (no ferric minerals are present and many samples contain traces of metallic iron).
- Alkali contents are much lower than most terrestrial basalts: Na_2O contents are usually less than 0.5% and K_2O usually below 0.1% (cf. Table 2.4).
- Pyroxene compositions vary widely in lunar basalts and in some samples, notably those from the Apollo 17 landing site, have metastable compositions lying within the miscibility gap in Fig. 2.1.1 (Basaltic Volcanism Study Project, 1981).

Basaltic meteorites and planetary surfaces

'Stony' **meteorites** (those consisting chiefly of silicate minerals with little metallic iron) are divided into two categories:

- *chondrites*, which have **primitive** ultramafic compositions (see Chapter 5) and usually contain distinctive mm-scale spherical aggregates of dendritic crystals and glass known as *chondrules* (from which the name 'chondrite' derives);
- *achondrites*, a smaller group of more differentiated compositions that contain no chondrules but have igneous textures (Plate 2.10): they are either basalts or more slowly cooled pyroxene or olivine cumulates.

The fine-grained igneous textures of the basaltic achondrites suggest they are products of volcanic processes operating on the surface of one or more celestial bodies, from which they have been ejected by an impact event. Various lines of evidence suggest that the commonest type of basaltic achondrite – called *eucrites* – are all ejecta from impacts on the surface of one of the largest known asteroids (known as 4 Vesta).

Other basaltic achondrites seem to derive from larger planetary bodies. An important group – known as shergottites (Plate 2.10) – show clear evidence of having been derived from the surface of Mars. Gas samples

extracted under vacuum from glassy inclusions in one example recovered from Antarctica are identical in composition to Viking analyses of the Martian atmosphere; the impact event that ejected the basalt fragments evidently generated impact melts that dissolved gases from the ambient Martian atmosphere. The young crystallization ages of the shergottites (165–450 Ma) also point to relatively recent volcanic processes that can only have occurred on a major planet. Another group of basaltic achondrites, with textures, compositions and older crystallization ages similar to Apollo lunar basalts, have clearly been derived from the Moon.

WHERE AND HOW ARE BASALT MAGMAS FORMED IN THE EARTH?

Source materials for basaltic melts

> *'The melting behaviour of basalts and eclogites indicates that both are partial melting products of a more primitive rock … presumed to be garnet peridotite.'*
>
> (Yoder and Tilley, 1962)

Basaltic magmas have low SiO_2 content (less than 52 mass %), relatively high MgO content (5%–15%) and less than 5% total alkalis. Though in theory such melts might form by the complete melting of source rocks of mafic composition, it is generally accepted that complete melting hardly ever occurs within the Earth – the only occasion being impact melting caused when the Earth is struck by high-velocity interplanetary debris. In all other circumstances, igneous melts are products of a process called partial melting (Box 5.4), in which melting stops short of completion and, once the partial melt has migrated upward, leaves behind in the source region a melt-depleted solid residue. In the partial melting of complex geological materials, the more fusible chemical components (mixtures of SiO_2, Al_2O_3, Na_2O, K_2O and H_2O) are preferentially concentrated in the melt, while more **refractory** components (notably MgO, Ni and Cr) are retained in the solid residue.[8] It follows that partial melts are more SiO_2-rich and MgO-poor than the source material from which they derive. Accordingly, in considering which regions of the Earth's interior might serve as sources of basaltic melts, one concentrates on domains that are SiO_2-poor and MgO-rich in comparison to basalt. The obvious candidates are the **ultrabasic** rocks that constitute the Earth's upper mantle. That basalt magmas are generated within the mantle is borne out by the occurrence of **peridotite** xenoliths with distinctive mantle textures (as explained in Table 5.4 and illustrated in Plates 5.3–5.8) in many alkali basalts and related rock types (though rarely in subalkali basalts). It is universally accepted among petrologists today that to understand why basalts erupt where they do, we need to investigate the thermal structure of the Earth's mantle.

[8] How major elements are partitioned between melt and residual solid is discussed in Chapter 5.

Conditions required for melting to occur in the mantle

Two lines of research contribute to current understanding of melting in the Earth's mantle:

1. Measurements of heat flow at the Earth's surface, from which the geothermal gradient at the surface can be calculated and the temperature distribution with depth in the Earth's interior – the '**geotherm**' – can be quantitatively modelled (see Fowler, 2005). Heat flow, gradient and geotherm vary widely according to geotectonic setting.
2. Laboratory experiments that determine the temperatures at which peridotites begin to melt, and how they vary with applied pressure (representing depth).

Figure 2.17 shows how such data can be combined to gain a general understanding of why melting occurs in the mantle. The diagram is divided into two principal domains: a grey area on the left indicating the conditions under which mantle rocks remain completely solid, and a white area representing the temperature and pressure domain where, according to laboratory experiments, melting is expected to occur. They are separated by a curve called the **solidus** which indicates the minimum temperature at which melting can

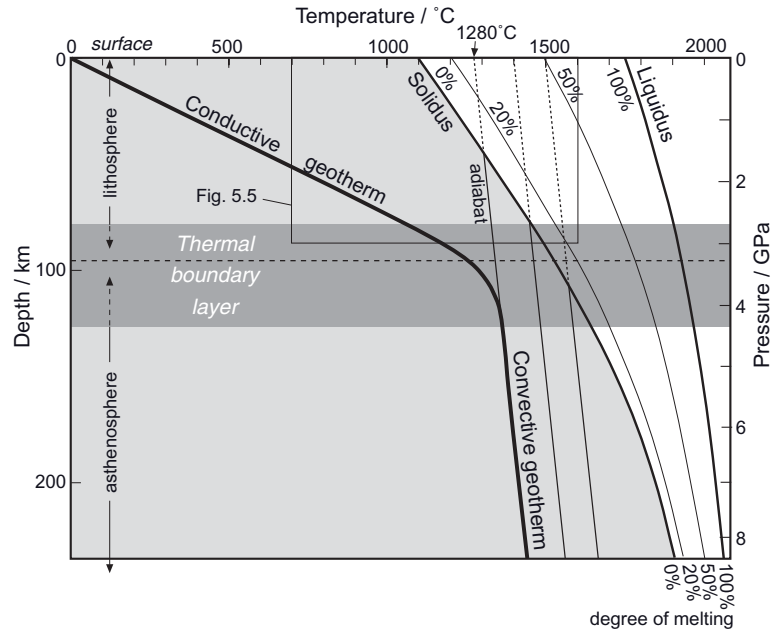


Fig. 2.17 Temperature versus depth diagram showing a representative oceanic geotherm and melting behaviour of mantle peridotite after McKenzie and Bickle (1988). The liquidus and solidus curves at higher pressures are as amended by Nisbet et al. (1993) to take account of 14 GPa melting experiments by Herzberg et al. (1990). Pressures corresponding to the depth scale are shown in the right-hand side.

begin in a mantle peridotite.[9] Sub-parallel curves show temperatures at which typical mantle peridotite will be 20% molten, 50% molten and 100% molten. These temperatures increase with depth: the deeper in the Earth, the higher the temperature required before melting can begin. (This generalization breaks down if H_2O is present, as we shall see later.)

The heavy curve in Fig. 2.17 shows a model geotherm typical of oceanic lithosphere remote from spreading centres. It consists of two linear portions linked by a curve. The upper linear domain represents the rigid outer shell of the Earth (crust and uppermost mantle) where – because rocks here are too cool to flow – heat is transported solely by thermal conduction: the linear temperature gradient is analogous to the steady-state temperature distribution in a steel rod with one end maintained at a higher temperature than the other. Geophysicists call this outer, rigid conducting layer the 'mechanical boundary layer'; it equates roughly, but not exactly, with the geologist's concept of 'lithosphere'.

The steeper linear portion of the geotherm, where temperature increases very slowly with depth, represents deeper mantle that is sufficiently hot and ductile (though still in the solid state) to convect readily over geological timescales: i.e. the asthenosphere. When it operates, convection redistributes heat more rapidly than conduction. A medium that is thoroughly mixed by convection – visualize a vigorously boiling pan of water – necessarily attains an essentially uniform temperature (and a uniform composition). Why, if that is true, is the geotherm not shown as a vertical line in this diagram at these depths, indicating a uniform temperature throughout this lower layer? To answer this we must recognize that mantle peridotite, like all rocks, is compressible: 1 kg occupies a slightly smaller volume at high pressure (at depth) than at lower pressure (shallower depth). Conversely, upward-convecting mantle undergoes slight expansion, and for this it must 'push aside' the surrounding mantle slightly. The mechanical work entailed in thus 'creating space' for expansion is accomplished at the expense of the

[9] In detail the solidus temperature varies with peridotite composition: Fig. 2.17 shows an average value after McKenzie and Bickle (1988) – see Fig. 2.16 caption.

peridotite's internal energy, and therefore its temperature falls slightly. Accordingly, ascending mantle – and the 'convective' part of the geotherm – both follow a steeply inclined, rather than vertical, P–T path called an **adiabat**.

In recognition of the *adiabatic expansion* experienced by upwelling mantle, it makes sense to express mantle temperatures (following the practice in meteorology) in terms of **potential temperature** T_p, which is the hypothetical surface temperature a deeply buried rock (at pressure $P_{initial}$ and temperature $T_{initial}$) *would* end up at if it were transported to the surface along the adiabat passing through $P_{initial}$, $T_{initial}$ *without melting*. It is now generally accepted, after McKenzie and Bickle (1988), that the asthenosphere has a uniform potential temperature (T_p) of about 1300 °C,[10] as shown by the 'convecting geotherm' in Fig. 2.17. Alternative adiabats are illustrated for potential temperatures of 1400 and 1500 °C, to which we shall refer later.

There is no sharp boundary between the convecting and conducting parts of the mantle. The darker horizontal band in Fig. 2.17 and the curved part of the geotherm represent a zone of gradual transition – designated the 'thermal boundary layer' – where, as temperature rises, rocks become progressively more ductile and begin to participate in convection. The base of the lithosphere or rigid 'plate' lies somewhere within this transition zone. It must be emphasized that the discussion of convection here carries no implication of melting or the presence of magma. Indeed, the location of the oceanic geotherm entirely within the grey sub-solidus area of Fig. 2.17 poses rather a paradox for a planet as volcanically active as the Earth: if the geotherm fails to intersect the solidus, how can we explain the partial melting that feeds volcanic eruptions at the surface?

Figure 2.18 illustrates three ways in which this paradox may be resolved within the Earth; the relevant geotectonic settings are cartooned in Fig. 2.18d. Mid-ocean ridges are currently looked upon as zones of passive extension. As the plates diverge, the asthenosphere beneath wells up to take their place. 'Upwelling' is represented by arrows from X to Y, both in Fig. 2.18d and Fig. 2.18a. Asthenosphere with a potential temperature of 1280 °C ascends along the 1280 °C adiabat as shown in Fig. 2.18a. Even though cooling slightly during ascent, upwelling asthenosphere traverses the pressure-dependent solidus at S and thus begins to melt. The degree of partial melting increases with continued upwelling and passes 20% melting before reaching Y. Partial melt separates over a range of depths to feed MORB volcanism or sub-ridge magma chambers in which gabbro crystallizes. The refractory solid residue that melting leaves behind accretes to the trailing edges of the diverging lithospheric plates. Similar mechanisms operate beneath back-arc spreading centres, though here there is evidence that slab H_2O also plays a role (Kelley et al., 2006).

Heating is thus not required to initiate mantle melting at mid-ocean ridges: the key factor is the opportunity afforded by plate divergence for *adiabatic upwelling* of asthenosphere that brings about *decompression melting*. Partial melting at intra-plate hot spots such as ocean islands, on the other hand, cannot be explained in this way, because the marked thinning of the lithosphere that characterizes mid-ocean ridges (Fig. 2.18d, left-hand side) does not occur here. The thicker basaltic crust found beneath ocean islands like Hawai`i and Ascension (Fig. 2.13) suggests a higher local mantle temperature, and most geophysicists[11] today attribute ocean island volcanism – at least that related to hotspot tracks shown in Fig. 2.12 – to the presence below an active island of a **mantle plume**. The term 'plume' denotes a mushroom-shaped convective upwelling from the lower-mantle that is hotter and less dense than the asthenosphere surrounding it (Fig. 2.18d). This thermal anomaly is represented in Fig. 2.18b by an elevated 'plume geotherm'. Having a higher potential temperature (an illustrative value of 1500 °C is shown in Fig. 2.18b), upwelling plume peridotite can intersect the solidus and begin melting at greater depth than in Fig. 2.18a, but the scope for continued upwelling is inhibited by the thick, relatively cool mechanical boundary layer ('MBL'

[10] The value originally estimated by McKenzie and Bickle was 1280 °C; this value has been retained in Fig. 2.16.

[11] But not all: see www.mantleplumes.org/

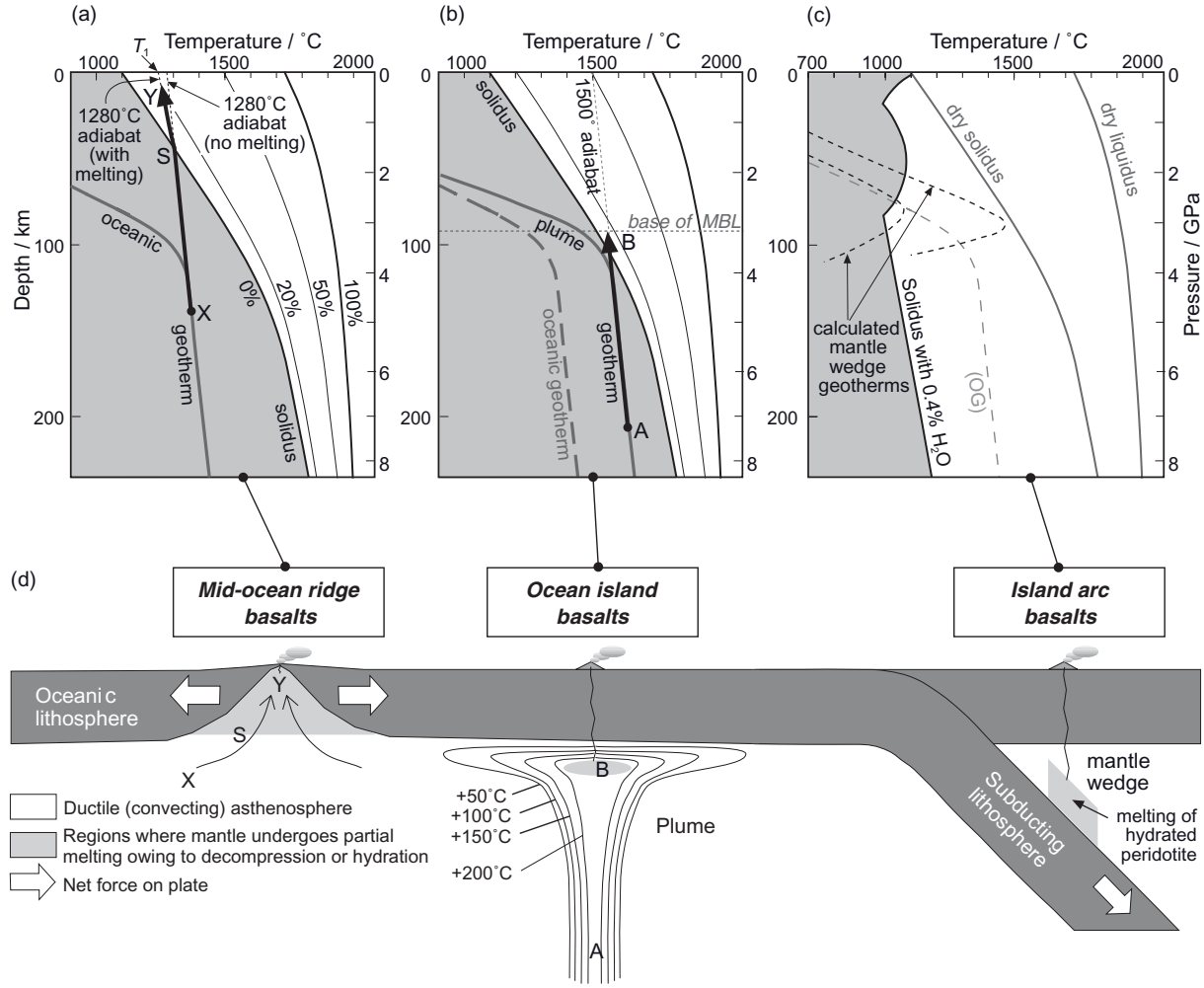


Fig. 2.18 Cartoons illustrating: (a) Melting by asthenosphere upwelling and decompression melting due to lithosphere extension at mid-ocean ridges; above S the upwelling mantle follows a slightly different adiabat (S–T_1) reflecting the greater compressibility of the melt present. (b) Decompression melting in an intra-plate mantle plume; here the degree of melting is restricted by the presence of thick lithosphere (dotted line) that inhibits further upwelling and decompression melting. Melts are tapped from this depth at lower degrees of melting than at Y in Fig. 2.18a. (c) Melting due to depression of the solidus in hydrous mantle wedge above a subduction zone. The peridotite solidus for 0.4% H_2O is from Wyllie (1981); the wedge geotherm models are from (lower T) Davies and Stevenson (1992) and (higher T) Furukawa (1993). The oceanic geotherm (OG) from Fig. 2.18a,b is shown merely for reference; it is not directly relevant in this context. (d) Geotectonic settings for (a), (b) and (c).

in Fig. 2.18b) present in this mid-plate region. For this reason, in spite of the elevated potential temperature, the degree of partial melting that occurs in a plume is generally lower than beneath a mid-ocean ridge and depends on lithosphere thickness (White, 1993). Where a plume happens to coincide with an oceanic spreading centre – as beneath Iceland – this constraint does not apply.

It cannot be assumed that all intra-plate volcanic islands in the oceans result from plumes with higher-than-normal potential temperatures. The majority of oceanic volcanic islands and seamounts are in fact unrelated to hot spot tracks, and some petrologists attribute them to fusible 'blobs' within the convecting asthenosphere (Fitton, 2007), the partial melting of which is due to a lower

solidus temperature rather than a thermal anomaly.

Plumes may be found beneath continental plates as well as in oceanic areas; the volcanism of the Kenya rift valley is generally understood to have a plume origin (Rogers, 2006), explaining why the Kenya rift valley alkali basalt shown in Fig. 2.16a is geochemically similar to an oceanic intra-plate alkali basalt. A more detailed discussion of East African volcanism and its origins is provided in Chapter 9.

Many (though not all) oceanic and continental intra-plate hot spots (Fig. 2.12) are considered to be products of mantle plumes operating in a 'steady-state' condition. Their total magma production rate (~0.5 $km^3 yr^{-1}$) is small relative to the output of the global mid-ocean ridge system. The birth-pangs of a *newly formed* plume may however be much more dramatic. Many petrologists and geophysicists (e.g. White and McKenzie, 1989) believe that the huge and often short-lived outpourings represented by LIPs and CFBs (up to 5 $km^3 yr^{-1}$ according to Courtillot and Renne, 2003) correspond to the initial arrival at the base of the lithosphere of a newly formed, hot plume-head. Such a 'starting plume' may be thought of as an upside-down analogue of the initial large blob that falls from a syrup-laden spoon, before the flow subsides to a more modest and sustained trickle. The geological evidence supporting this view is that many of the largest passive-margin CFBs like the Deccan and Paraná-Etendeka (Fig. 2.15) – ostensibly products of the initial impact of 'starting plumes' – are linked via progressively younging ocean-island chains to current intra-plate hot spots like Réunion and Tristan da Cunha (Fig. 2.15), interpreted as products of plumes operating in steady-state mode.

The agent that stimulates partial melting in the mantle wedge beneath an island arc (Fig. 2.18d, right-hand side) is neither lithospheric thinning nor an elevated geotherm, but the release of aqueous fluids by dehydration of the altered oceanic crust riding on the down-going slab as it heats up during subduction. The altered crust contains hydrous minerals like chlorite, serpentine and amphibole that have formed at the expense of original igneous minerals, chiefly early-on as a result of near-ridge hydrothermal circulation. Laboratory experiments show that the presence of small amounts of H_2O can substantially depress the peridotite solidus temperature in the overlying mantle wedge, as Fig. 2.18c illustrates. (The shape of the 'wet' solidus in this diagram is complicated by various factors beyond the scope of this chapter.) Figure 2.18c also emphasizes that the geotherm in the mantle wedge above a subduction zone is likely to exhibit a temperature maximum owing to cooling from below by the subducted slab (see Fig. 6.23). In spite of many uncertainties in thermal modelling of the mantle wedge, the projection of likely geotherms above the 'wet' peridotite solidus in Fig. 2.18c points to conditions in the mantle wedge favouring peridotite partial melting and the production of subduction-related basaltic melts. The ways in which basalt melts can be generated above subductions zones are discussed in more detail in Chapter 6.

Other settings for basaltic volcanism discussed in the previous section can generally be explained by one or other of these three melting scenarios. Basalts erupted in small volumes in continental rifts probably represent upwelling accompanying extensional thinning of continental lithosphere, but there may be a plume input too, as is believed to be the case for the voluminous volcanism of Kenya. Back-arc basaltic volcanism reflects high degrees of lithosphere extension attributed to 'roll-back' of the subducting slab – the lateral retreat of the subduction hinge-line away from the arc (as illustrated in Fig. 6.19).

REVIEW – WHAT INFORMATION CAN WE GLEAN FROM BASALTS?

Basalts are of interest for what they can tell us about internal processes inside the Earth, their magma sources, conditions of melting, past tectonic environments, magma evolution and eruptive processes. Their compositions allow us to investigate parts of the Earth that are inaccessible to us (e.g. the mantle), or internal and surface environments in the distant geological past. The principal conclusions from this chapter are:

- All basalt magmas are produced by partial melting of mantle peridotite.
- Mid-ocean ridge (and back-arc spreading centre) basalts are products of **decompression melting** of asthenosphere that wells

up owing to lithospheric plate divergence (Fig. 2.18a and d).
- Mid-plate hot spots, such as Hawai`i, are regarded by most petrologists and geophysicists as surface expressions of mantle plumes, localized convective features that are 150–300 °C hotter than the surrounding asthenosphere; ocean-island basalts are believed to be products of partial melting at elevated potential temperature, at high pressures dictated by a thick lithospheric 'lid' (Fig. 2.18b and d). Large igneous provinces are widely considered to record a vigorous infantile stage during the inception of a new plume. However a minority of Earth scientists question the current mantle plume orthodoxy.
- Most subduction-related basalt magmas are products of partial melting in the mantle wedge above a subduction zone, where aqueous fluids expelled from the slab promote melting by lowering the mantle **solidus** temperature (Fig. 2.18c,d).
- Basalts from these different geotectonic settings possess distinct geochemical signatures (Fig. 2.16) that in principle allow their recognition in ancient volcanic terrains.
- Phenocrysts (Plate 2.1) indicate that magma ascent from the mantle to the surface was interrupted by a period of crystallization in a sub-volcanic magma chamber (Fig. 2.10), and shed light on magma evolution by identifying the minerals that were crystallizing in the chamber prior to eruption. Magma differentiation during crystallization will be described in detail in Chapter 3.
- Though basalts may erupt by small pyroclastic explosions to form scoria cones (Fig. 2.6), the volcanology of basalts is dominated by lava flows (Figs. 2.2 and 2.3), the largest of which may flow for hundreds of kilometres. Laterally extensive lavas rely upon flow beneath the surface (through lava tubes) to minimize radiative heat losses.

Table 2.5 Major and trace element analyses of basalts for use in Exercises 2.1, 2.2 and 2.3. The analyses are provided in volatile-free form.

	C	D
	mass % oxide	
SiO_2	50.77	48.18
TiO_2	0.67	1.9
Al_2O_3	18.97	15.06
Fe_2O_3	1.55	1.87
FeO	7.95	9.55
MnO	0.19	0.19
MgO	6.32	6.97
CaO	11.8	12.15
Na_2O	1.69	2.76
K_2O	0.13	0.67
P_2O_5	0.03	0.29
	ppm element	
Rb	2.7	13
Ba	29	403
Th	0.3	2.31
Nb	0.21	25
La	1.1	22.4
Ce	2.84	43.6
Sr	120	460
Nd	2.97	24.5
Zr	19.2	110
Sm	1.06	5.17
Gd	1.52	
Tb		0.9
Y	13.3	29
Yb	1.41	2.51
Lu	0.2	

EXERCISES

2.1 Plot the basalt analyses given (volatile-free) in Table 2.5 in a TAS graph and comment on which categories of basalt they belong to.

2.2 Calculate norms for the basalt analyses given in Table 2.5, as described in Appendix B. In what key respect do they differ? Is this consistent with your answer in exercise 2.1?

2.3 Plot incompatible element enrichment diagrams ('**spidergrams**') for the analyses given in Table 2.5 and discuss the environments from which they might have been collected.

2.4 A rock analysis contains 1.56% Fe_2O_3 and 9.8% FeO by mass. Calculate values for ΣFe_2O_3 and ΣFeO.

Chapter 3

Magma differentiation

THE CAUSES OF MAGMA DIVERSITY

How does the wide diversity of natural magma compositions illustrated in Fig. 1.2 arise? This key problem exercised igneous petrologists for much of the twentieth century. Up to about 1960, research concentrated on the processes by which chemically diverse magma compositions might, in principle, be generated successively *from a single parental basalt melt*. Such processes – which are responsible for generating the most obvious form of diversity among igneous rocks, the spectrum between basic and acid melts – are referred to collectively as *magma differentiation*. Igneous petrologists today accept that fractional crystallization and crustal assimilation are the principal agents of magma differentiation, but other mechanisms may contribute in small ways or in particular circumstances (see Wilson, 1993). Because these processes, all related to magma crystallization, rely on cooling experienced by the magma at various stages on its ascent path, it is generally assumed that they take place within the crust (whether oceanic or continental), although in reality they almost certainly begin to operate while ascending magmas are still at mantle depths.

Our understanding of magma differentiation, the subject of the present chapter, has been derived primarily from:

1. laboratory experiments in which rock powders – or chemically equivalent synthetic preparations that equilibrate more quickly – are melted under controlled temperatures and pressures to investigate how crystallization proceeds, and what controls it;
2. geochemical and isotopic investigations on cognate suites of well preserved volcanic rocks (see Fig. 3.10);
3. field and laboratory studies on **cumulate** rocks in layered intrusions, which are discussed in Chapter 4.

The consequences of igneous differentiation manifest themselves on all scales, from the millimetre-scale plagioclase phenocrysts in an andesite lava – whose internal zoning bears witness to changing magma composition during crystal growth – to the granite batholiths that extend for hundreds of kilometres in mountain belts such as the Andes and the Himalaya.

Igneous differentiation processes, acting on a single 'parental' basalt magma, cannot by themselves generate *all* of the variability seen in Fig. 1.2. From the 1960s on, petrologists recognized that more subtle chemical variations observed among basic magmas themselves, as well as in their differentiates, must reflect variations in the conditions under which melts are originally formed in the mantle (or in some cases the crust): these conditions include the depth at which melting takes place, the extent of melting (what percentage of the original solid becomes molten), and the chemical and mineralogical composition of the mantle starting material or 'source'. These issues, falling under the general heading of *partial melting*, will be discussed in Box 5.4.

The distinct contributions that magma differentiation and partial melting make to magma diversity are illustrated in cartoon form in Fig. 3.1.

Igneous Rocks and Processes: A Practical Guide, 1st edition. By Robin Gill. Published 2010 by Blackwell Publishing

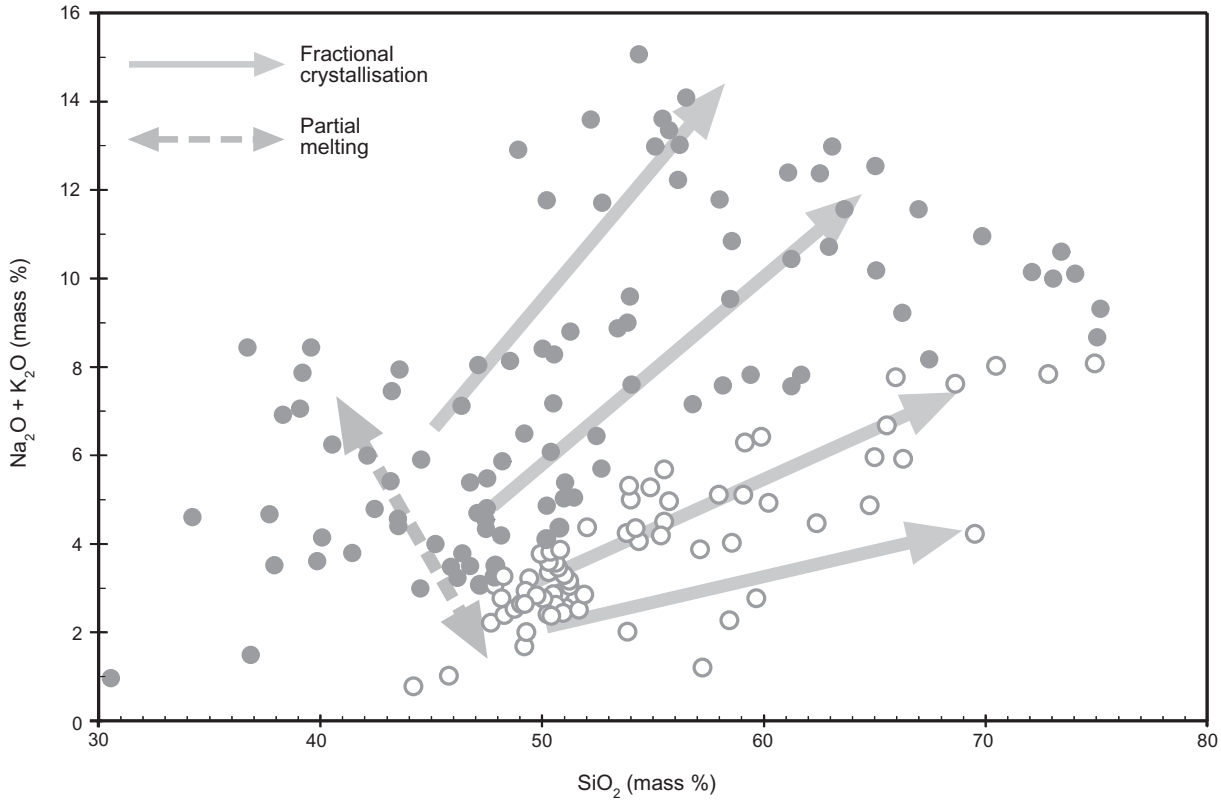


Fig. 3.1 Total-alkali versus silica (TAS) plot illustrating the contributions that magma differentiation (specifically, fractional crystallization) and partial melting make to overall magma diversity, adapted from Wilson (1989, Fig. 1.2a). Vectors are only intended to provide a qualitative indication of the direction of magma evolution; in detail, magma paths will not conform to straight lines on this diagram.

PHASE EQUILIBRIUM EXPERIMENTS

Melting and crystallization within the Earth involve equilibration at high temperatures between a silicate melt on the one hand, and one or more crystalline minerals on the other. Each of these coexisting, but physically and chemically distinct, forms of matter is designated by petrologists as a separate **phase**. In this chemical usage of the term, 'phase' may be defined as *a part of a solid or partially molten rock (or an experimental analogue) which has clearly defined physical and chemical characteristics that distinguish it from all other parts of the rock*.[1] A petrologist's understanding of the term can be illustrated by referring back to Fig. 1.1. The upper diagram shows five different phases:

- the 'white' crystals (representing plagioclase);
- the 'grey' crystals (representing, for example, olivine);
- the 'black' crystals (representing, for example, magnetite):
- the melt surrounding the crystals;
- the round bubbles of gas trapped or suspended in the melt.

Each phase is distinct from the others in its physical properties (e.g. density or refractive index), its chemical composition and its atomic structure. Moreover, the coexistence of these 5 phases could be inferred by studying the solidified rock (lower diagram), provided that we recognize the groundmass (whether glassy or crystalline) as

[1] All temporal connotations of the word 'phase' in its everyday usage are excluded from its petrological meaning.

representing an original melt phase, and the 'empty' vesicles as representing a gas phase. The crystals that were originally suspended in the melt can be identified from the phenocrysts present.

Much has been learned about magma evolution during melting and crystallization in the Earth by conducting carefully controlled laboratory experiments. Because such experiments involve studying chemical equilibrium between two or more phases (one usually being the melt), such experiments are called *phase equilibrium experiments* and the results are usually presented graphically in the form of **phase diagrams** (such as Figs. 3.2 and 3.3). The manner in which such diagrams are constructed is described in Box 3.1. This area of research is called *experimental petrology*.

The most important minerals to consider in the differentiation of basaltic melts are olivine, pyroxene, plagioclase and spinel. Much effort has been spent over the years in understanding their phase relations with basaltic melts and with each other. It is striking how general conclusions that we draw from simple experiments involving just these four minerals carry over into the natural world, allowing us to predict the course of melt evolution in natural magma systems.

Experiments with simplified compositions

Experimental petrology offers two avenues for studying crystallization. Perhaps the more intuitive approach is to take an actual volcanic rock (whose composition represents that of the magma from which it formed), to crush it into a fine powder, to melt the powder, and to observe how the resulting melt crystallizes at various temperatures (see Fig. 3.9). However, though such experiments shed light on the crystallization of individual rocks (see p.84), they provide little insight into magma differentiation *in general*. In the first place, experimenting with a single rock composition, or even several, allows little opportunity to vary melt composition systematically to see how it influences the course of crystallization. Secondly, natural rocks are chemically complex entities, consisting of at least ten major oxides (Box 1.1) and a still greater number of trace elements; unravelling how each of these chemical constituents individually affects melting and crystallization would be a hopelessly complex task.

The alternative to this 'real rocks' approach is to conduct crystallization experiments on chemically simple, laboratory-synthesized materials over whose compositions we can exert complete control. Working with just a small number of pure chemical components, mixed in carefully controlled proportions, allows us to see much more clearly the individual effect of each constituent on **liquidus** and **solidus** temperatures and on the course of crystallization. Figure 3.2 shows one of the simplest phase diagrams that we encounter in igneous petrology. It summarizes the melting and crystallization behaviour of simple mixtures of anorthite and diopside. The family of potential compositions that result from mixing pure $CaMgSi_2O_6$ and pure $CaAl_2Si_2O_8$ in various proportions constitutes what petrologists call 'the **system** $CaMgSi_2O_6$–$CaAl_2Si_2O_8$' or 'the system Di–An'. The word 'system' derives from chemical thermodynamics; it means simply a specified region of potential 'composition space' to which attention is currently confined, to the exclusion of other components. In the present context we are looking just at mixtures of $CaMgSi_2O_6$ and $CaAl_2Si_2O_8$, disregarding the effects of $NaAlSi_3O_8$, $CaFeSi_2O_6$, Mg_2SiO_4 or anything else.

We shall now examine the phase diagrams of several 'simple' (i.e. laboratory synthesized) silicate systems, to see what general conclusions about magma crystallization can be drawn from them.

In describing how melts crystallize, we need to take account of not only the *phases* involved in the process but also their chemical make-up. The composition of an olivine crystal, for example, can be expressed as percentages of *three* oxides, MgO, FeO and SiO_2 (Box 1.1). Taking account of the fixed proportions in which MgO and FeO combine with SiO_2 in olivine, however, we can express olivine composition more succinctly in terms of the molar percentages of just *two* end-members, Mg_2SiO_4 and Fe_2SiO_4 (Box 1.2). Olivine crystals can be considered to consist of just these two **components**. Plagioclase crystals, on the other hand, comprise two different components, $NaAlSi_3O_8$ and $CaAl_2Si_2O_8$. The number of components

Box 3.1 How are phase diagrams prepared?

A **phase diagram** such as Fig. 3.2 is usually the product of a series of laboratory experiments, in which carefully prepared compositions are heated one by one in a furnace, each to a pre-determined, carefully regulated temperature that is maintained for a sufficient period to allow the various phases to achieve chemical **equilibrium** with each other. The experimental **charge** is then **quenched**, (i.e. chilled to room temperature as rapidly as possible) and examined by various techniques to identify the phases present. The purpose of quenching is to prevent melt and crystals re-equilibrating with each other at lower temperatures.

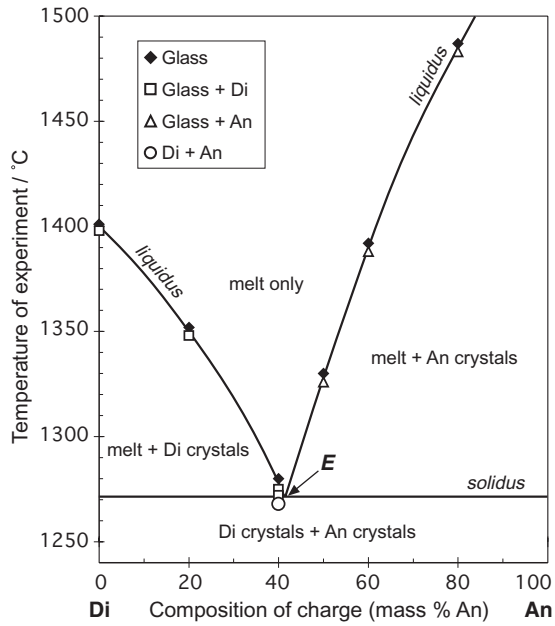


Fig. 3.1.1 Phase diagram for the system $CaMgSi_2O_6$–$CaAl_2Si_2O_8$ at atmospheric pressure, showing results from the individual experiments used to locate the boundaries (after Bowen, 1915). Different symbols are used to indicate the minerals/phases observed in the quenched charges (see key).

The strategy is illustrated in Fig. 3.1.1. This is a vertically stretched version of Fig. 3.2 that shows the original experiments from which this phase diagram was constructed; they were carried out by N. L. Bowen, the 'grandfather' of experimental petrology, and published in the *American Journal of Science* in 1915. Each point-symbol represents a separate experiment: it shows (as the *x*-coordinate) the particular mixture of diopside and anorthite crystals that formed the starting mixture, and

present is important in the context of the Phase Rule discussed in Box 3.3. The components of a system may be defined as *the minimum number of chemical species required to specify completely the compositions of all of the phases present*.[2]

[2] The distinction between system, phase and component is explained further in Gill (1996).

The system $CaMgSi_2O_6$–$CaAl_2Si_2O_8$: the geometry of a T–X *diagram*

This system provides the simplest possible laboratory analogue of a basaltic magma, and since basalt is the main product of partial melting in the mantle, it is a natural starting point for understanding magma fractionation in crustal magma chambers. As all possible

the exact temperature of the experiment as the *y*-coordinate. Each of these particular experiments was held at the required temperature for 30 minutes to allow equilibration between crystals and melt, before the charge was quenched by dropping it from the furnace into a bucket of water or mercury (a quenching method no longer used on safety grounds). Once cool, each charge was thin-sectioned and examined under a polarizing microscope to identify the **phases** that had formed at the temperature concerned: glass (representing quenched melt) ± plagioclase ± pyroxene.

The boundaries on the diagram are mapped out by plotting at each experiment's coordinates a symbol that is ornamented to show the phases found in the quenched charge: a black diamond shows the coordinates of an experiment that produced glass alone (indicating that the charge was completely molten at the temperature of the experiment); an open square represents an experiment in which the charge was found to contain glass *and* diopside, and so on as shown in the key. The open circle shows an experiment whose charge contained only crystalline diopside and anorthite: the absence of glass here indicated that no melting at all had occurred at this temperature, which must therefore lie below the **solidus** temperature for diopside–anorthite mixtures.

The temperature of the **liquidus** at each composition is demarcated by two data points: the black diamond shows a temperature at which the charge was found to be completely molten (all glass, $T > T_{liquidus}$), and the open symbol shows the slightly lower temperature of an experiment in which the charge contained glass *and* crystals ($T < T_{liquidus}$). By carrying out experiments at temperatures that *bracket* the liquidus in this way for each composition, the experimenter can pinpoint the liquidus curve with reasonable precision (within a few °C). The situation at 40% An is a bit more complicated:

Composition of charge	Temperature °C	Phases found
40% $CaAl_2Si_2O_8$	1280	glass
60% $CaMgSi_2O_6$	1275	glass + Di
	1272	glass + Di
	1268	Di + An (no glass)

Within this limited temperature interval, we pass from the *melt* field (quenched charge contains just glass), through the *melt + Di* field into the *Di + An* field, traversing through both the liquidus and solidus curves in a temperature interval of only 12 °C. That these two temperatures are so close to each other is a sign that this composition lies very close to the **eutectic** composition ***E***, at which the liquidus and solidus temperatures coincide.

The experiments in Fig. 3.1.1 were all run at atmospheric pressure in open platinum crucibles. In later decades, petrologists began to carry out melting experiments at progressively higher pressures in ever more elaborate high-pressure apparatus, allowing them to investigate melting and crystallization as they would occur at greater and greater depths within the Earth. Such experiments allow the construction of phase diagrams in P–T–composition space ('*P–T–X* diagrams'). The apparatus used need not concern us here; details can be found in the book by Holloway and Wood (1988).

compositions in Fig. 3.2 can be expressed as proportions of just two chemical components, $CaMgSi_2O_6$ and $CaAl_2Si_2O_8$, it is an example of a **binary** phase diagram. Such diagrams, showing relationships in temperature (*T*) – composition (*X*) space, are sometimes referred to as *T–X* diagrams.

The diagram consists of four fields:

- a 'melt' field at the top of the diagram (shown white) showing the range of temperatures and compositions within which $CaMgSi_2O_6$ + $CaAl_2Si_2O_8$ mixtures will be *entirely* molten;
- two lightly ruled fields depicting the circumstances under which melt coexists with *either* diopside crystals *or* anorthite crystals, depending on melt composition; these are the conditions in which $CaMgSi_2O_6$ + $CaAl_2Si_2O_8$ mixtures are *partially* molten;

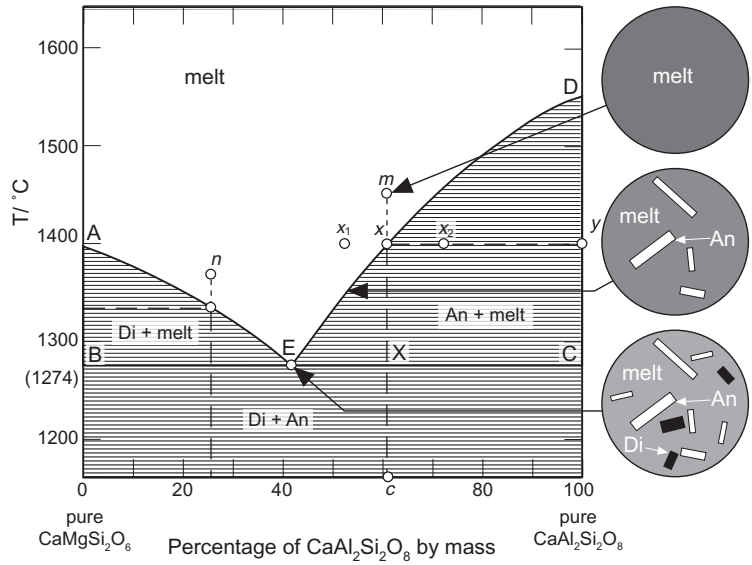


Fig. 3.2 Phase diagram for the pseudo-binary system $CaMgSi_2O_6$–$CaAl_2Si_2O_8$ at atmospheric pressure, showing the crystallization behaviour of melts consisting of mixtures of these two components. 'Di' and 'An' refer to the crystalline minerals diopside and anorthite. The roundels show how the experimental 'magma' would look under the microscope, if it were quenched at the various stages on the crystallization path indicated by the arrows, and illustrate the phenocrysts that would be seen in analogous natural volcanic rocks.

- a heavily ruled field showing the conditions under which $CaMgSi_2O_6$ + $CaAl_2Si_2O_8$ mixtures consist of crystalline diopside and anorthite, with no melt formed.

These fields are separated by two kinds of boundary:

- curved boundaries separating the 'melt' field from the 'melt + Di' and 'melt + An' fields. This curve (AED), called the **liquidus**, shows the temperature at which melts of different compositions *begin* to crystallize;
- a straight boundary separating the 'Di + melt' and 'An + melt' fields from the 'Di + An' field. This line BEC, called the **solidus**, marks the temperature at which crystallization reaches completion and melt ceases to exist.

The four fields all meet at a unique point in the diagram:

- the **eutectic** point E marks the sole melt composition and temperature at which melt can coexist with *both* diopside *and* anorthite.

Note the contrasting ways in which the two components mix together. In the crystalline state, diopside (a chain silicate) and anorthite (a framework silicate) have entirely different atomic structures, and as the two components cannot be tolerated within the same crystal structure they form no mutual solid solution at all.[3] Accordingly any point within the Di + An field must represent a physical mixture of separate crystals of diopside and anorthite (at the temperature in question). In the less ordered molten state, however, $CaMgSi_2O_6$ and $CaAl_2Si_2O_8$ melts are completely miscible with each other on the molecular scale. Therefore, as long as the temperature is high enough, homogeneous melts can be formed with any intermediate composition between 100% diopside and 100% anorthite. The composition of a melt such as *m* can be determined graphically by dropping a vertical to the baseline (e.g. *m*–*c*) and reading off the percentage of An dissolved in the melt.

What interpretation should one place on a point that lies within one of the melt-crystal fields (such as point x_2 in Fig. 3.2)? The dashed

[3] Natural pyroxenes do in fact contain small amounts of Al_2O_3 but the aluminous end-member is not $CaAl_2Si_2O_8$. See Morse (1980, p53) for a discussion of this minor complication.

horizontal line x–y passing through x_2 is called a **tie line**, because it links two phases coexisting in mutual equilibrium: x is the most $CaAl_2Si_2O_8$-rich melt that can exist at this temperature (1400 °C), and y represents pure anorthite at the same temperature. It follows that x_2 represents a mixture of melt and crystals. The proportions of this mixture can be calculated from the x-coordinate of x_2 by means of a useful geometrical tool called the **Lever rule**, which is explained in Box 3.2.

No homogeneous substance can have a composition lying within any of the ruled fields in Fig. 3.2; they represent areas of the diagram in which two separate phases (solid-solid or solid-melt) coexist, and are therefore referred to as **two-phase fields**. One can visualize them as being traversed by a mass of tie lines, which is what the horizontal ruling is intended to suggest.

x indicates the only melt composition that can coexist in chemical equilibrium with anorthite at 1400 °C and is said to be **saturated** with anorthite. If a melt at this temperature happened to be *more* $CaAl_2Si_2O_8$-rich (e.g. composition x_2), it would be unstable and would crystallize anorthite, thereby shifting the melt composition leftward until it reached x. If on the other hand a $CaAl_2Si_2O_8$-poor melt such as x_1 happened to coexist with anorthite crystals at 1400 °C, it would dissolve them until its composition had reached x (or until the anorthite was exhausted). Thus the liquidus curve, as well as indicating the temperature at which a cooling melt of a specified composition will begin to crystallize, also tells us the composition a melt must have if it is to coexist stably with crystals at a prescribed temperature.

How molten mixtures of anorthite and diopside crystallize

Having explored the architecture of Fig 3.2, let us see what light it sheds on magma crystallization. Consider a melt such as m. At its initial temperature of 1450 °C, it lies above the liquidus and must therefore be completely molten. Cooling (down the line m–x) will bring about no observable change until the liquidus is reached at point x (1400 °C). At the liquidus temperature, the melt begins to crystallize anorthite. $CaAl_2Si_2O_8$ is withdrawn from the melt to form the crystals, so the remaining melt necessarily becomes depleted in this component, and will shift slightly to the left. This shift, together with continued cooling, causes the melt to migrate down the univariant liquidus curve toward E, crystallizing more anorthite as it does so. If the melt should diverge momentarily from the liquidus, then the system will adjust (either crystallizing more An or redissolving it) to restore equilibrium. As crystallization advances, therefore, the melt's composition and temperature coordinates will together move down the liquidus towards E. The liquidus thus performs a third role in this diagram: it indicates the *crystallization path* in T–X space that is followed by the cooling melt.

What happens when the melt reaches the eutectic E? This is the one point where all four fields meet, and therefore a melt of this composition is in equilibrium with anorthite *and* diopside. Accordingly, when the melt reaches this composition (at 1274 °C), it will begin to crystallize diopside alongside anorthite. From this stage on, the two minerals crystallize in exactly the same proportions as the melt at point E (41% anorthite and 59% diopside), and the melt composition therefore remains constant. So, not surprisingly since this is an invariant point, does the temperature: the heat being lost by the system is matched by the heat of crystallization being released by the melt, so the temperature remains at 1274 °C until the melt has completely crystallized.

Melts whose compositions lie on the left-hand side of Fig. 3.2 behave in a similar way, but the order in which the minerals crystallize changes: diopside is the first mineral to crystallize from melt n (depleting the melt in the $CaMgSi_2O_6$ component), and anorthite appears only when the melt reaches the eutectic. Note that, regardless of the initial melt composition (except for the pure end-members), the composition of the final melt is the same.

The shape of the phase diagram in Fig. 3.2 is characteristic of mixtures of minerals that do not combine in mutual solid solution with each, and mix intimately only in the melt phase. Broadly similar phase diagrams involving eutectics exist for the systems Mg_2SiO_4–$Mg_2Si_2O_6$ (Fo–En), Mg_2SiO_4–$CaMgSi_2O_6$ (Fo–Di) and $CaMgSi_2O_6$–$NaAlSi_3O_8$ (Di–Ab).

Box 3.2 Estimating the composition of a mixture – the Lever rule

A tie-line is a line in a phase diagram linking two phases that are in chemical and thermal **equilibrium** with each other. Because thermal equilibrium means that the two phases are at the same temperature, a tie-line in a *T–X* diagram is always a horizontal line.

Any point whose coordinates lie *between* the ends of a tie-line represents a *physical mixture* of the two **phases** linked by the tie-line: either a solid–solid, a solid–liquid or (rarely in geology) a liquid–liquid mixture. The position of this intermediate point on a tie-line indicates the proportions in which the two phases are mixed. How can one calculate these proportions?

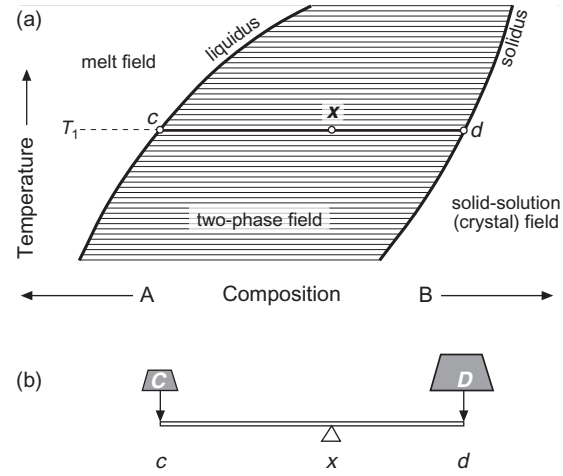


Fig. 3.2.1 (a) Part of a phase diagram (similar to Fig. 3.4) to illustrate the Lever Rule. (b) The beam-balance analogue.

Figure 3.2.1(a) shows part of a phase diagram (such as Fig. 3.4) in which complete solid solution exists between two compounds, A and B. The tie-line *c–d* depicts equilibrium at temperature T_1 between a melt of composition *c* on the liquidus, and a solid solution of composition *d* on the solidus; both *c* and *d* are expressed in mass % B. Composition *x* lies in the **two-phase field** between *c* and *d*, and must signify a physical mixture of these two phases. Let *C* and *D* represent the mass fractions (i.e. $C + D = 1.00$) in which *c* and *d* are mixed to form *x*. We can then express the composition of *x* as a weighted average of *c* and *d*:

Figure 3.2 illustrates a general principle of physical chemistry: mixtures of minerals invariably melt at (or remain molten to) lower temperatures than each pure mineral on its own. Pure anorthite crystallizes at about 1550 °C (point D) and pure diopside crystallizes at 1400 °C (point A), but mixtures of the two minerals are capable of melting at temperatures as low as 1274 °C. This principle also lies behind the use of salt to melt ice.

Adding olivine – the **ternary** *system An–Di–Fo*

A binary phase diagram like Fig. 3.2 can tell us only rather basic things about basalt crystallization. One of the obvious shortcomings of Fig. 3.2 is that olivine, a key constituent of many basalts, is not represented. Whilst it is a simple matter to add olivine – in the form of its magnesian end-member forsterite, Mg_2SiO_4 – to our experimental mixtures, the presence of the third chemical component, in addition to diopside and anorthite, requires the results to be plotted in a new kind of phase diagram. This takes the form of an equilateral triangle as shown in Fig. 3.3. How is it that the composition of a *three*-component mixture can be plotted in this *two*-dimensional diagram? The reason is that the three concentrations $c_1 + c_2 + c_3$ in each mixture necessarily

$$x = Cc + Dd \quad [3.2.1]$$

Since $C = 1 - D$, this can be rewritten:

$$x = (1 - D)c + Dd = c - Dc + Dd \quad [3.2.2]$$

Therefore

$$x - c = D(d - c) \quad [3.2.3]$$

leading to

$$D = \frac{x - c}{d - c} \quad [3.2.4]$$

Substituting $D = 1 - C$ into [3.2.1], we can show in a similar fashion that:

$$C = \frac{x - d}{c - d} = \frac{d - x}{d - c} \quad [3.2.5]$$

The mass ratio in which c and d are present in x is therefore given by:

$$\frac{C}{D} = \frac{d - x}{d - c} \Big/ \frac{x - c}{d - c} \text{ which (after cancelling denominators)} = \frac{d - x}{x - c} \quad [3.2.6]$$

In other words:

$$C(x - c) = D(d - x) \quad [3.2.7]$$

This is the equation that describes a balanced beam or lever, with the fulcrum at x and masses C and D at either end. In using this equation, it is immaterial whether $x - c$ and $d - x$ are expressed in mass % or in millimetres measured directly off Fig. 3.2.1: the results are the same in each case as the % / mm scaling factor cancels out.

Equation [3.2.7] is known as the 'Lever Rule', by which the composition of a mixture like x can be calculated from simple length measurements on a phase diagram. It can be applied to any compositional diagram in which all the variables appear in linear form, and in which all phases are homogeneous (i.e. not zoned). It can therefore be applied in binary (e.g. *T*–*X*) phase diagrams, ternary phase diagrams (e.g. in *X*–*X*–*X* diagrams such as Fig. 3.7 – see Exercise 3.4), and a wide range of **variation diagrams** too (e.g. Fig 3.10).

add up to 100%. The composition of each mixture is therefore completely defined by just *two* of the concentrations, say c_1 and c_2, the third concentrations being specified by $c_3 = 100 - c_1 - c_2$ rather than being a completely independent quantity.

The liquidus forms a surface in such a **ternary** (three-component) phase diagram, in contrast to the curve in Fig. 3.2. It takes the form of various curved 'hillsides' that meet each other along 'thermal valleys'. They can be portrayed either by a three-dimensional model constructed on a triangular base – see the inset in Fig. 3.3 – or by plotting the model in the form of a 'map' with temperature 'contours' as shown in the main diagram. Note, to begin with, that the left hand face of the model is the Di–An phase diagram that has already been discussed in Fig. 3.2, albeit in a back-to-front sense. In the main diagram the liquidus surface consists of four fields separated by gently curved boundaries. Each field represents the compositional domain within which one particular phase crystallizes first (analogous to each curved line in Fig. 3.2). The largest field is that in which forsterite is the 'liquidus phase'; the fields of diopside and anorthite are significantly smaller. (The spinel field is an anomalous feature of this particular diagram that need not concern us. A similar anomaly is encountered in Fig. 9.7b in Chapter 9, where the significance is discussed.)

Box 3.3 The Phase Rule

A distinction has been drawn in Fig. 3.2 between (i) the fields, (ii) the boundaries AE, ED and BC between those fields, and (iii) the unique point E in the diagram where fields and boundaries all meet. These features are the geometric expression of subtly differing categories of chemical equilibrium between the phases present in this system. Their significance can be appreciated by means of the *Phase Rule*, an elegant formula introduced by the nineteenth-century engineer J. Willard Gibbs, who fathered the science of thermodynamics:

$$\phi + f = C + 1^* \qquad [3.3.1]$$

ϕ represents the number of phases participating in a particular equilibrium and C is the total number of components required to describe their compositions. f, known as the *variance* or the number of *degrees of freedom*, represents the extent to which conditions (T, X) can be varied without disrupting the equilibrium. What does f tell us about the equilibria in Fig. 3.2?

Three phases are involved in Fig. 3.2: diopside, anorthite and melt. Diopside consists of pure $CaMgSi_2O_6$, anorthite consists of pure $CaAl_2Si_2O_8$, and the composition of the melt phase may, subject to temperature, consist of any combination of $CaMgSi_2O_6$ and $CaAl_2Si_2O_8$. These two components therefore suffice to account for the compositions of all three phases.

Consider an experiment being conducted under the conditions represented by point m in Fig. 3.2 (composition = c, $T \approx 1450\,°C$). Here the melt is the only phase present ($\phi = 1$) and (except at each edge of the diagram) it consists of 2 components ($C = 2$), therefore:

$$1 + f = 2 + 1 \;\therefore\; f = 2 \qquad [3.3.2]$$

Under these conditions, the melt state enjoys *two degrees of freedom*: we can vary either temperature, or melt composition, or both independently (within limits), without altering the one-phase character of this notional 'equilibrium'. This situation is described as *divariant*.

Compare this with the conditions represented by the point x in Fig. 3.2. Lying on the liquidus curve, it represents an equilibrium between coexisting melt *and* crystals of anorthite.

As $\phi = 2$,

$$2 + f = 2 + 1 \;\therefore\; f = 1 \qquad [3.3.3]$$

The only variation in T and X consistent with maintaining this two-phase equilibrium lies along the liquidus curve itself: raising the temperature independently to m, or changing melt composition to x_1 at constant temperature, for example, would eliminate anorthite and thus alter the two-phase essence of the equilibrium. Such an equilibrium, whose survival requires confinement to a one-dimensional boundary line, has only *one degree of freedom* and is described as a *univariant* equilibrium.

The melt composition and temperature indicated by point E represent a *three*-phase equilibrium between melt, anorthite *and* diopside $\therefore\ \phi = 3$.

$$3 + f = 2 + 1 \;\therefore\; f = 0 \qquad [3.3.4]$$

No variation at all in melt composition or temperature can be tolerated if all three phases are to remain in equilibrium: for example, moving up the boundary AE would eliminate anorthite, or allowing T to fall below $1275\,°C$ would eliminate melt. This equilibrium has *no degrees of freedom* and is described as *invariant*. Only the relative proportions of the phases can change without upsetting the three-phase character of the equilibrium. As we shall see, not all phase diagrams contain invariant points like E (e.g. Fig. 3.4).

*This is the version of the Phase Rule applicable to T–X phase diagrams. See Gill (1996) for a wider perspective.

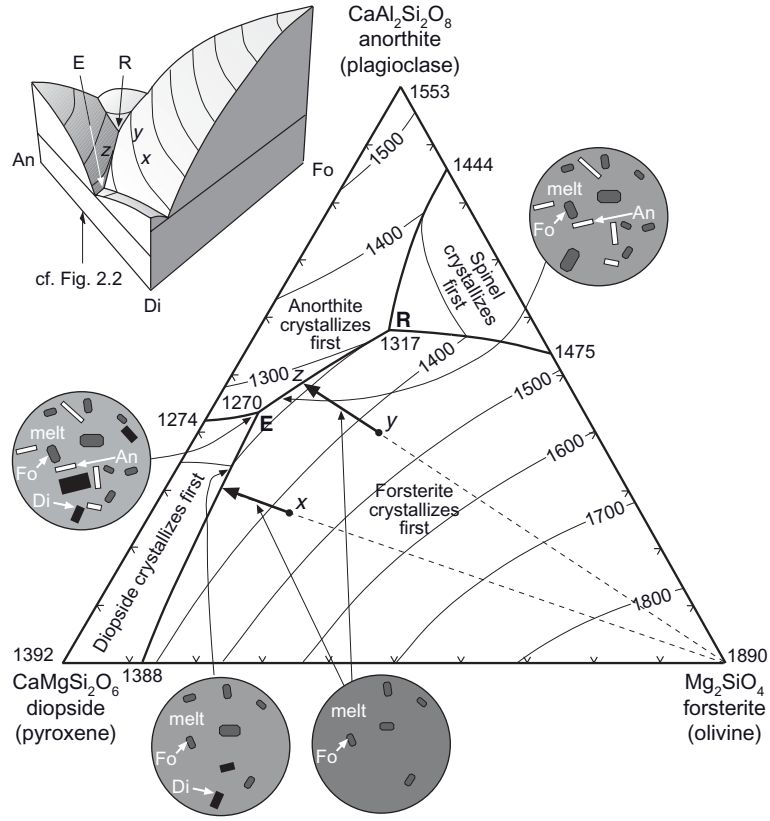


Fig. 3.3 Phase diagram for the ternary system $CaAl_2Si_2O_8$– $CaMgSi_2O_6$– Mg_2SiO_4 (An–Di– Fo) at atmospheric pressure after Osborne and Tait (1952) plotted in mass proportions. The inset shows the liquidus as a three-dimensional surface with temperature as the vertical axis. The main diagram shows the same liquidus topography indicated by temperature 'contours' graduated in °C. V-ticks mark 10% graduations in mass %. '*x*' and '*y*' are initial melt compositions discussed in the text. Roundels illustrate the phenocryst mineralogy at key stages along each crystallization path, showing how the phenocryst assemblage would vary according to the path that magma evolution followed. E represents a eutectic point (see text) and R represents a reaction point (see Box 4.3).

Consider the course of crystallization followed by the mixture labelled *x*. If it initially has a temperature above the liquidus (say 1500 °C), the first stage of its cooling path (sometimes called the *liquid line of descent* or LLD) simply involves cooling to the liquidus (at about 1430 °C). There, because this composition lies within the forsterite field, olivine will begin to crystallize; as no iron is present in this system, the olivine will be pure forsterite. Removing olivine in crystalline form causes the remaining melt to become depleted in the Mg_2SiO_4 component, which we represent on this diagram by drawing a line (dashed) from the Mg_2SiO_4 apex to the coordinates of *x*, then extending it beyond *x* (solid arrow). As cooling continues, the melt composition will migrate directly away from the forsterite apex, until it reaches the boundary between the forsterite and diopside fields. At this boundary, called a **cotectic**, diopside begins to crystallize alongside forsterite. The crystalline extract now being removed from the melt is a mixture of Di and Fo (see roundel), which must lie somewhere on the bottom edge of the diagram (the domain of An-free Di–Fo mixtures), and extracting it must drive the melt composition toward the An apex. In fact, because the Fo–Di boundary is a 'thermal valley', the melt composition must migrate along the cotectic toward the point E, as changing in any other direction would require a rise in temperature. Continued removal of Di + Fo eventually drives the melt composition to the point E where the three fields meet. Here anorthite begins to crystallize alongside

the forsterite and diopside. Note that, as crystallization advances, the number of solid phases crystallizing increases: in symbolic terms, the progression we are seeing (as shown by the roundels) can be written as

$$\text{melt} \rightarrow \text{melt} + \text{A} \rightarrow \text{melt} + \text{A} + \text{B} \rightarrow \text{melt} + \text{A} + \text{B} + \text{C} \quad [3.1]$$

where A, B and C represent different crystalline phases. Application of the Phase Rule (Box 3.3) to each of these stages shows they are respectively trivariant (variation of temperature together with compositional variation in two dimensions), divariant, univariant and invariant conditions. In chemically more complex natural systems (beyond the scope of a ternary diagram), this progression can extend to several more minerals. Note that 'melt' in equation 3.1 signifies a progression of evolving melt compositions from left to right, rather than a constant composition.

Melt *y* will follow a different path as it crystallizes but will arrive at the same final melt composition. Initial crystallization of forsterite drives melt *y* to intersect the An–Fo cotectic, at which point anorthite will begin to crystallize alongside forsterite; diopside will only appear when the melt has reached point E. This point represents (a) the composition at which the liquidus surface reaches its lowest temperature, and (b) the composition toward which all melts will converge as they crystallize, even melts whose initial compositions lie in the anorthite or diopside fields. It is called the **ternary eutectic** of this system. It is an invariant point like the binary eutectic in Fig. 3.2.

If we imagine Nature conducting these experiments in a leaky magma chamber, the magmas that periodically escape to the surface will bring with them a record of their chemical evolution (how much fractional crystallization they have undergone) in the form of suspended crystals, or 'phenocrysts' (as shown in the roundels). Initial liquids whose temperature exceeds the relevant liquidus temperature will contain no phenocrysts (they will be **aphyric**). Magmas that have crystallized a small amount and thereby undergone a modest change of composition will exhibit one type of phenocryst crystal (e.g. melt + olivine), whereas those magmas that have undergone greater degrees of fractionation will contain two or three (e.g. melt + olivine + pyroxene + plagioclase), or even more in complex natural magmas. It follows from these crystallization paths that how many different types of phenocryst a natural volcanic rock contains provides a good guide to how far the magma has fractionated: a wide variety of phenocrysts points to an **evolved** magma.

What general lessons can we learn from the systems studied so far? We can review them in terms of what happens both in laboratory experiments *and* in evolving natural magma chambers:

Laboratory experiments	Natural magma chambers
• Crystals that separate from a cooling silicate melt generally have a *different composition from the melt*: for example, melt *x* in Fig. 3.2 crystallizes anorthite that is richer in Al_2O_3 and poorer in MgO than the melt.	In a magma chamber, the first crystals to separate invariably differ in bulk composition from the melt. Rocks formed by segregation of these early-formed crystals (**cumulate** rocks) do not directly indicate the composition of the magma from which they crystallized (Chapter 4).
• The separation of crystals different in composition from the melt *causes the composition of the remaining melt to change*: melt *x* in Fig. 3.3, as it evolves, becomes progressively depleted in Mg_2SiO_4 and richer in $CaMgSi_2O_6$ and $CaAl_2Si_2O_8$ as it evolves down the liquidus surface.	As the melt in a magma chamber cools and crystallizes (forming cumulate rocks on the roof, sides and floor of the chamber), the melt continuously changes composition.
• The further crystallization progresses, the larger the number of minerals crystallizing at the same time. In Fig. 3.3, we see a progression from *melt x alone* → *melt* + *Fo* → *melt* + *Fo* + *Di* → *melt* + *Fo* + *Di* + *An*.	Cumulate rocks have the simplest mineralogy at the base of a layered intrusion, and become more complex in passing up through the intrusion (Chapter 4), reflecting the increase with time in the number of minerals crystallizing together.

To generalize, we have seen crystallization proceeding according to the following pattern:

$$\text{melt}_0 \rightarrow \text{melt}_1 + \text{A} \rightarrow \text{melt}_2 + \text{A} + \text{B} \rightarrow \text{melt}_3 + \text{A} + \text{B} + \text{C} \ldots \quad [3.2]$$

where melt_0 represents the initial melt, melt_1, melt_2, etc. represent melts at successive stages of evolution, and A, B and C represent minerals that crystallize from the evolving melt. This pattern of crystallization gleaned from laboratory experiments agrees with what we find in layered intrusions (Chapter 4, Fig. 4.8): as crystallization progresses, new minerals are added to the list of **cumulus** minerals, and the mineralogy of the cumulate rocks formed gets progressively more complex. But the study of layered intrusions also brings to light instances where a new cumulus mineral, rather than simply adding itself to the list, actually *takes the place* of a cumulus mineral already crystallizing:

$$\text{melt}_3 + \text{A} + \text{B} + \text{C} \rightarrow \text{melt}_4 + \text{A} + \text{B} + \mathbf{D} \quad [3.3]$$

Bowen (1922) was the first to recognize that the *disappearance* of a crystalline phase (C) in this way – not explained by the phase diagrams considered so far – is a sign of *reaction* between the mineral and a relatively evolved melt (in this case melt_3). The importance of this *reaction principle* will be dealt with in Chapter 4 (Box 4.3), in the light of the field evidence provided by layered basic intrusions.

How solid solutions melt and crystallize

As a guide to how basaltic magmas crystallize, Figs. 3.2 and 3.3 tell us only half of the story. Though no solid solution exists *between* diopside and plagioclase, for example, each of these minerals is itself one **end-member** of a solid solution series: anorthite belongs to the plagioclase series ($CaAl_2Si_2O_8$–$NaAlSi_3O_8$), and diopside forms solid solutions with other pyroxene end-members ($Mg_2Si_2O_6$, $Fe_2Si_2O_6$ and $CaFeSi_2O_6$). No experimental investigation of basalt crystallization would be complete without taking account of such solid solutions.

As an illustration, Fig. 3.4 shows the melting and crystallization behaviour of the plagioclase series, considered on its own. A plagioclase crystal is a solid solution consisting of two components mixed together: $NaAlSi_3O_8$ and $CaAl_2Si_2O_8$. The phase diagram consists of three fields:

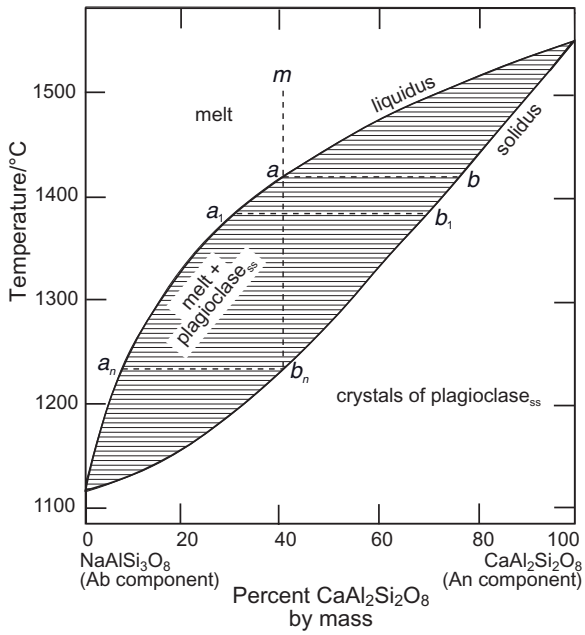


Fig. 3.4 The *T–X* phase diagram for the plagioclase feldspar series at atmospheric pressure (after Bowen, 1915). The 'ss' subscript is a reminder that plagioclase crystals belong to a solid solution, whose composition may vary continuously from An to Ab (though exsolution is encountered at lower temperatures over part of the range).

- a 'melt' field at the top of the diagram (white) showing the range of temperature-composition coordinates over which plagioclase is *completely* molten. Note that melts in this simple system are made up solely of $NaAlSi_3O_8$ and $CaAl_2Si_2O_8$ in various proportions; none of the other constituents of a basaltic melt (e.g. MgO) was present in these experiments.
- a 'two-phase' field (ruled) within which melt coexists with plagioclase crystals; here plagioclase is in a *partially* molten condition.
- a solid solution field ('plagioclase$_{ss}$') in which plagioclase exists wholly in a crystalline state and melt is absent. Unlike

Fig. 3.2, where the two chemical components formed a mixture of separate crystals at low temperatures, An and Ab are completely miscible at near-solidus temperatures, and therefore coexist within a single crystalline phase.

In this diagram, which in general layout illustrates the melting behaviour of many solid-solution minerals other than plagioclase, both the liquidus *and* the solidus are curved (cf. Fig. 3.2), and they pass smoothly from one end-member that exhibits a maximum melting temperature (in this case, anorthite) to the other end-member which melts at the minimum temperature in the system (albite). In contrast to Fig. 3.2, there is no unique **eutectic** point at an intermediate composition, toward which all crystallizing melts ultimately converge. The Phase Rule (Box 3.3) tells us why: no more than 2 phases can coexist in Fig. 3.4 ($\phi \leq 2$) and as there are two components ($C = 2$):

$$(1 \text{ or } 2) + f = 2 + 1 \quad \text{so } f = 2 \text{ or } 1 \qquad [3.4]$$

Thus only divariant and univariant equilibria exist in this phase diagram. There are no circumstances under which $f = 0$: a solid-solution phase diagram like this cannot contain an invariant point.

A **tie-line** such as a_1–b_1 links a melt composition a_1 on the liquidus with the unique composition of solid solution with which it can equilibrate at that temperature (on the solidus). As in Fig. 3.2, the liquidus curve here – in addition to indicating the temperature at which a cooling melt of a specified composition will begin to crystallize – also tells us the composition a melt must have if it is to coexist stably with crystals at that temperature. The solidus curve tells us the composition of the coexisting solid, which in this system is a solid solution.

Let us trace the course of crystallization of an arbitrary melt *m,* which happens to contain 41% by mass of the anorthite end-member. It will initially cool until it intercepts the liquidus (point *a*), at which temperature it begins to crystallize plagioclase. The composition of the first plagioclase formed is determined by drawing a *horizontal* tie-line (since both phases coexist at the same temperature) from *a* to the solidus curve, which it intersects at point *b*. The solid composition (76 mass % An[4]) is read by dropping a vertical from *b* to the composition scale.

Note the plagioclase *b* is more anorthite-rich than melt *a*. The structure of the diagram dictates that the crystals that form are enriched in the more **refractory** end-member, a conclusion that applies to all solid solutions. Removing crystalline plagioclase must therefore deplete the remaining melt in $CaAl_2Si_2O_8$, making it more albite-rich. Assuming crystallization is accompanied by continued cooling, the melt will progress down the liquidus curve, crystallizing more plagioclase as it cools. However, here we encounter another divergence from Fig. 3.2: the plagioclase composition will itself *change* as the temperature falls, because a tie-line such as a_1-b_1 tells us that melt a_1 is in equilibrium with plagioclase b_1, not the original *b*. So, as cooling continues, we can expect to see not only the *melt* composition changing, but that of the *plagioclase* crystallizing from it too.

But what of the crystals of composition *b* that formed when the melt first reached the liquidus? Will they retain their original composition as crystallization progresses, or will their composition change by on-going reaction with the evolving melt? This is a key question, the answer to which depends on how we conduct the experiment. For a crystal such as *b* to adapt its composition to b_1 (to remain in equilibrium with the more evolved melt a_1) requires the diffusion of Ca and Al ions from the crystal into the melt, and the diffusion of Na and Si ions from the melt into the crystal. The outcome will therefore depend on how diffusion rates for these ions through the crystal lattice (diffusion through melts is always more rapid) compare with the cooling rate of the experiment. If the experimental charge is subjected to very slow cooling, giving time for this diffusive exchange to occur, then the crystal composition has time to adapt continuously to the evolving melt composition. These conditions favour a regime that we call **equilibrium crystallization**. The crystal composition changes with

[4] The notation 'An_{76}' cannot strictly be used here as it implies molar % An (as measured optically – see Fig. 4.1.2). In practice, mass % ≈ mole % as $NaAlSi_3O_8$ and $CaAl_2Si_2O_8$ have similar relative molecular masses (**RMM**s).

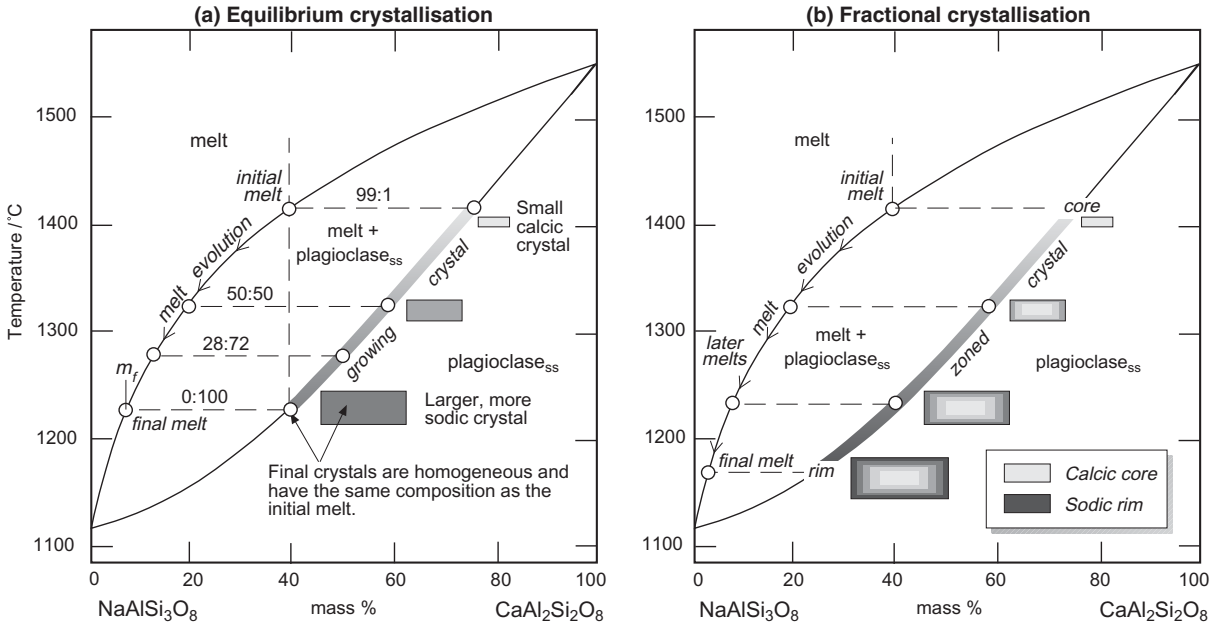


Fig. 3.5 (a) Equilibrium crystallization in the system $NaAlSi_3O_8$–$CaAl_2Si_2O_8$. The relative proportions of melt to crystals at each stage of crystallization can be calculated using the Lever Rule (Box 3.2): the proportions are shown above each illustrative tie-line. Note that crystallization reaches completion when the melt : crystal proportion becomes 0 : 100, at which point the crystals have just reached the composition of the original melt. The growing crystal, and its changing composition, are shown in cartoon form next to the solidus. (b) Fractional crystallization in the same system. The rate of crystal deposition outstrips re-equilibration between early crystals and later melts: the crystals are therefore not homogeneous as in equilibrium crystallization, but compositionally **zoned**.

time owing to continuous reaction with the liquid, but at any particular instant the entire crystal mass has a uniform composition. The final product will be homogeneous crystals identical in composition to the initial melt (Fig. 3.5a). N.L. Bowen (see Box 3.1) referred to this succession of compositions through which the crystal has passed – from 76 to 41 mass % An in Fig. 3.4 – as a *continuous reaction series*, a concept that has been linked to his name ever since.

The sceptical reader may wonder how, in a closed system whose overall composition cannot change, the melt and crystals can *both* become more sodic as the temperature falls. What we have so far taken no account of is the changing *proportions* of melt and crystals. At 1416 °C in Fig. 3.5a, at which crystallization has only just begun, the experimental charge consists almost entirely of melt, with only a tiny amount of crystals. At 1323 °C the melt: crystals ratio is about 50:50, whereas at 1227 °C only the merest trace of melt remains. The proportions of melt and crystals at each temperature can be calculated using the Lever rule described in Box. 3.2. In equilibrium crystallization, the melt is finally used up when the coexisting crystals have reached the composition of the initial melt. For this reason, when crystallizing under equilibrium conditions, the melt cannot evolve beyond the composition m_f.

If on the other hand the apparatus were allowed to cool rapidly, the growth rate of new crystalline material would outstrip the diffusional exchange of components between the earliest crystals and later melts. In the context of a laboratory experiment, this 'new crystalline material' will probably take the form of new growth layers rimming the original crystals. Rapid cooling prevents the early crystal cores from reacting and equilibrating chemically with later fractions of the changing melt. In such a regime, called **fractional**

crystallization, only the most recently deposited crystalline material (crystal rims) maintains equilibrium with the changing melt; the cores formed previously are unable to do so, and therefore more or less retain their original composition. Careful examination of crystal composition at the end of the experiment would reveal continuous compositional **zoning** within the plagioclase crystal (Fig. 3.5b). In true fractional crystallization, the crystal cores retain their original composition but the crystal mass as a whole is heterogeneous.

Because reaction between early cores and later melts is inhibited in fractional crystallization, the cores remain more calcic than would be the case in equilibrium crystallization (Fig. 3.5a). Though the rims continue to equilibrate with the evolving melt, the mass of crystalline material as a whole is enriched in the Ca end-member, and in a closed system such as this the melt as a whole must therefore become depleted in the Ca end-member. The outcome is that the melt is able to evolve to more extreme sodic compositions (Fig. 3.5b) than would be possible under equilibrium conditions – an important factor when considering the wide diversity of evolved melts in Fig. 3.1 – and the melt is no longer exhausted when the crystal rims reach the initial melt composition. Under extreme fractional crystallization the last melt can reach pure albite composition.

Exactly the same analysis can be applied to crystallization of molten olivine (the system Mg_2SiO_4–Fe_2SiO_4 shown in Fig. 3.6) and indeed to the crystallization of any binary solid solution.

How molten mixtures of diopside and plagioclase$_{ss}$ crystallize

Greater insight into the crystallization of basaltic magmas can be gained by considering Figs. 3.2 and 3.4 *together* in the framework of a single diagram (Fig. 3.7). The phase diagram for mixtures of diopside, anorthite and albite has a triangular form similar to Fig. 3.3 but, whereas in that diagram the three minerals exhibited no mutual solubility, here

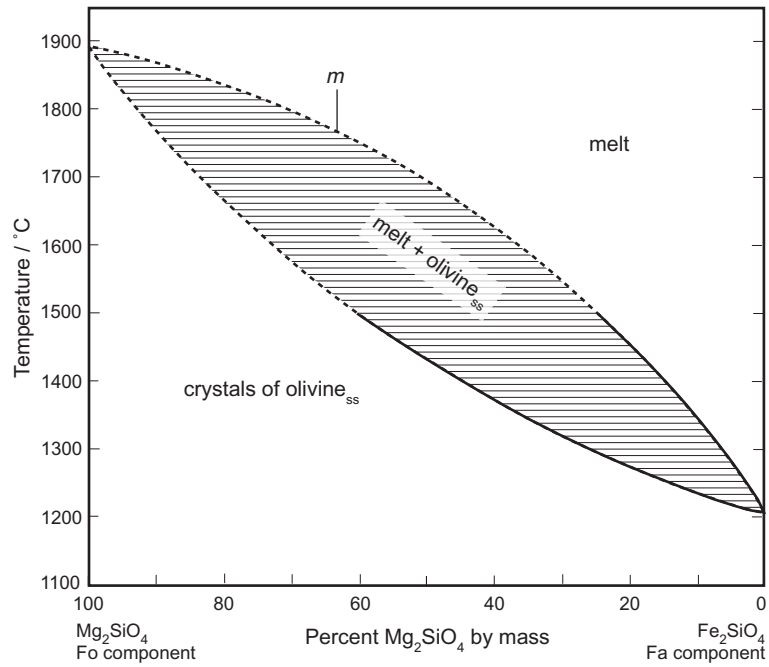


Fig. 3.6 The system Mg_2SiO_4–Fe_2SiO_4 after Bowen and Schairer (1932). As in Fig. 3.4, the subscript 'ss' is a reminder that olivine crystals are members of a continuous solid solution. (Dashed lines show where the liquidus and solidus curves have been interpolated from experimental data for pure Fo and experiments below 1500 °C.) The melt composition *m* relates to exercise 3.4.

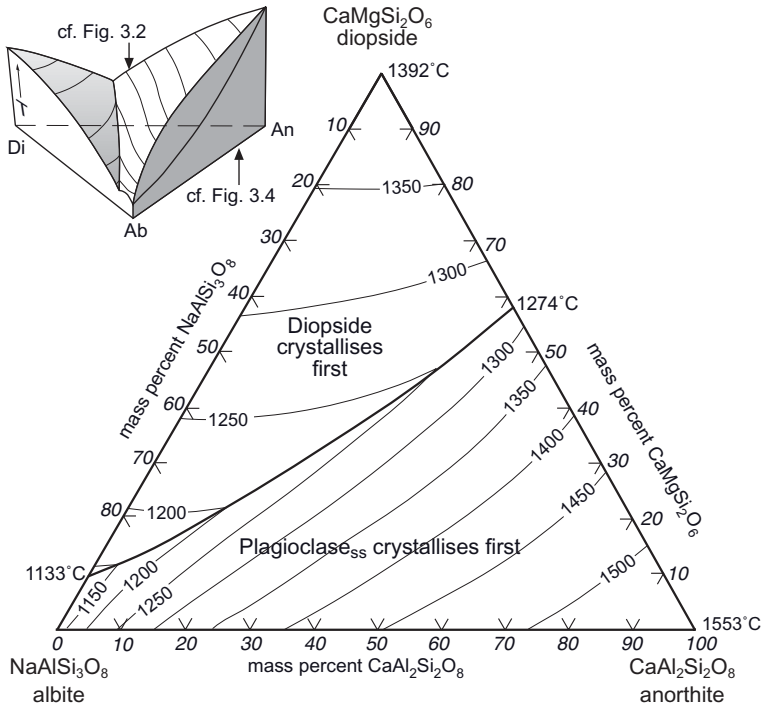
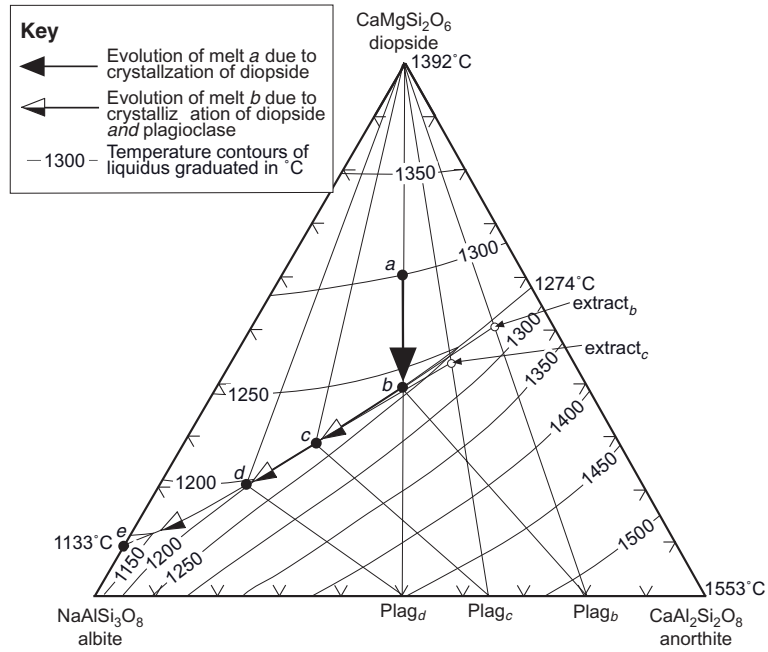


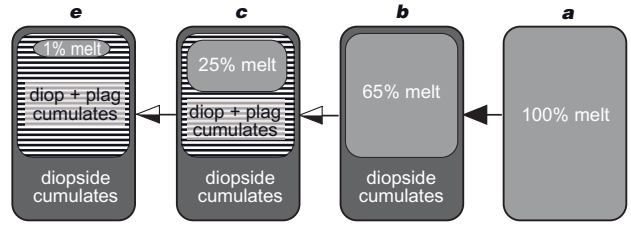
Fig. 3.7 Phase relations in the system $CaMgSi_2O_6$–$NaAlSi_3O_8$–$CaAlSi_2O_8$ (Di–Ab–An) at atmospheric pressure, plotted in mass proportions. The inset shows the liquidus surface as a three-dimensional model with temperature as the vertical dimension; it is divided into two sloping fields, in each of which one mineral will crystallize from the melt. The fields meet in a 'thermal valley' tracing melt compositions that can coexist with both solid phases. This topography is shown in the main Figure by temperature 'contours' graduated in °C. V-ticks along the edges of the triangle indicate 10% graduations (in mass %). The fields indicate the ranges of melt composition in which diopside and plagioclase respectively will crystallize first. The subscript 'ss' emphasizes that plagioclase crystallizes as a solid solution.

one of the sides of the triangle represents a solid solution. Consequently (by analogy with Figs. 3.4 and 3.6) Fig. 3.7 contains no **ternary eutectic**. The binary phase diagrams Di–An and Ab–An can be recognized forming the back and right-hand faces of the thumbnail cartoon in Fig. 3.7.

The geometry of the liquidus surface can be seen in the cartoon to consist of two 'hillsides' meeting along a plunging 'thermal valley'. Instead of terminating at a low point (ternary eutectic) within the diagram, the **cotectic** here descends continuously from the binary eutectic at 1274 °C in the Di–An system (right-hand side of the main diagram) to a another binary eutectic at 1133 °C in the system Di–Ab (left-hand side). The diagram contains only two fields, which define the domains of melt composition within which pure diopside (upper field) or plagioclase *solid solution* (lower field) will crystallize first.

The chemical evolution of crystallizing melts in this system is shown in more detail in Fig. 3.8. As melt *a* cools, it will encounter the liquidus at 1300 °C and, as it lies in the diopside field, will begin to crystallize pure diopside. By analogy with olivine in Fig. 3.3, removal of crystalline diopside drives the composition of the remaining melt directly away from the diopside apex of the triangle, down the black arrow. On reaching *b*, on the boundary between the diopside and plagioiclase$_{ss}$ fields, the melt will begin to crystallize plagioclase as well. What composition will the plagioclase have? As in Fig. 3.4, the melt composition can in principle be linked by a tie-line to the composition of the coexisting plagioclase '$plag_b$' at the temperature





Calculated mass % analyses of successive melts

	e	*c*	*b*	*a*
SiO_2	67.5	59.3	55.8	55.7
Al_2O_3	17.7	17.7	17.0	11.0
MgO	1.7	5.3	7.4	11.3
CaO	2.3	11.8	16.3	19.6
Na_2O	10.8	5.8	3.6	2.4

Fig. 3.8 Melt evolution arising from fractional crystallization of melt *a*. The cartoons below illustrate the progress of crystallization in a notional fractionating magma chamber at stages corresponding to melts *a*, *b*, *c* and *e*; the percentages of remaining melt are approximate for *c* and *e*. The table at the bottom shows the change in melt composition as crystallization progresses from *a* to *e*.

concerned (in this case about 1240 °C).[5] In keeping with Fig. 3.4, the crystalline plagioclase has a higher An : Ab ratio (i.e. lies further to the right) than the melt. Three phases now coexist in equilibrium (melt + diopside + $plag_b$), as highlighted by the *three-phase triangle* of tie-lines in Fig. 3.8. The composition of the crystalline extract now being removed from the melt ('$extract_b$') lies on the $plag_b$–diopside tie-line, and crystallization of this mixture causes the composition of the remaining melt to evolve along the cotectic in the down-temperature direction.

At point *c*, the melt is in equilibrium with $plag_c$ and diopside. The extract composition now lies on the diopside–$plag_c$ tie line at '$extract_c$'. The *c*–$extract_c$ tie-line is a tangent to the slightly curved cotectic *b*–*e* and there-

[5] In practice, the plagioclase compositions in equilibrium with ternary melts cannot simply be read off the diagram in the same way as in Fig. 3.4: the temperatures of plagioclase–melt equilibrium are lower in this ternary system than in the binary An–Ab system.

fore at *c* is slightly less inclined than the tie-line at *b*. As diopside and plagioclase continue to crystallize, the melt evolves toward composition *d*, but we must recognize that throughout this process the proportion of accumulating crystals has been increasing and the amount of remaining melt diminishing. This is illustrated in terms of a notional magma chamber in the boxes labelled *a*, *b*, *c* and *e* below the phase diagram. If crystals sink to the floor of the chamber as they are formed, the magma chamber would be floored initially by deposits of **cumulus** diopside crystals which, from stage *b* on, would be succeeded by cumulus deposits consisting of diopside *and* plagioclase.

Melt *d* is in equilibrium with diopside and plagioclase '$plag_d$'. Note that the tie-line between $plag_d$ and diopside passes through the original melt composition *a*. In other words, composition *a* can be expressed in terms of an entirely crystalline mixture of diopside and $plag_d$. This is a signal that, if crystallization has occurred under equilibrium conditions – i.e. slowly – the proportion of melt *d* has now fallen to zero: no melt is left and crystallization is complete. If however the experiment were being conducted under fractional crystallization conditions (faster cooling), then more anorthite would be locked away in early plagioclase cores, and enough of the albite component would remain in the melt to allow it to continue evolving down the cotectic, perhaps even as far as composition *e*, as shown in the cartoon magma chambers *a* to *e*.

This system is a good one for illustrating how effective fractional crystallization can be at changing melt composition. From the coordinates of compositions *a* to *e* in Fig. 3.8 and the formulae of Di, An and Ab, it is simple to calculate their compositions in terms of oxide mass % (see Exercise 2 at the end of the Chapter). These compositions are shown in the table at the bottom of Fig. 3.8. Even though we are dealing only with a simplified analogue of basalt composition in this phase diagram, the changes in composition mirror quite accurately those seen in a natural series of lava compositions: SiO_2 increases from 55.7% (a shade too high for real basalt) to 67.5%, MgO decreases from 11.3% to 1.7 %, CaO decreases from 19.6% to 3.3%, and Na_2O increases from 3.4% to 10.8%. Though within the confines of this system we cannot reproduce an entire evolutionary path from basalt to rhyolite, the experiments do generate dramatic changes in melt composition as crystallization proceeds. We shall draw comparison with chemical trends in real volcanic rocks in a later section.

The general lessons to be drawn from these solid solution systems can again be summarized in the context of both laboratory experiments and natural magma chambers:

Laboratory experiments	Natural magma chambers
• Most igneous minerals are solid solutions. Crystals of such minerals (e.g. olivine) that crystallize from a cooling silicate melt are *enriched in the more refractory end-member* (e.g. Fo).	Early cumulates near the base of a layered intrusion contain the most refractory mineral composition (e.g. the most Fo-rich olivine, as in Fig. 3.6).
• Crystallization depletes the remaining melt in this refractory component (e.g. An). Later fractions of melt and crystals become *progressively enriched in the lower-melting end-member* (Ab in Fig. 3.5).	The cumulate succession in a layered intrusion evolves from An-rich, early plagioclase crystals near the base to more Ab-rich, later crystals at the top. All solid-solution minerals show similar trends.
• Rapid crystallization favours *fractional crystallization*, in which crystal cores are chemically isolated from later fractions of melt and fail to re-equilibrate with them (producing *zoned* crystals). This leads to more extreme melt compositions.	Fractional crystallization may occur in large magma chambers because early cumulate deposits become isolated by burial beneath later deposits, and thus cannot continue reacting with later melt fractions.

In Figures 3.3 and 3.8 the crystallization path leads from melts rich in ferromagnesian components to later melts that are strongly depleted in these components. A series of rocks formed by fractional crystallization of basalt will therefore exhibit a progressive decrease in colour index.

Melting and crystallization experiments on real rocks

We have distilled a lot of useful petrological theory about magma differentiation from phase diagrams that are based on simplified, laboratory-synthesized compositions rather than complex natural melts. At this point it makes sense to carry out a 'reality check' to see how reliably such experiments predict the course of crystallization of actual volcanic rock samples and the melts prepared from them.

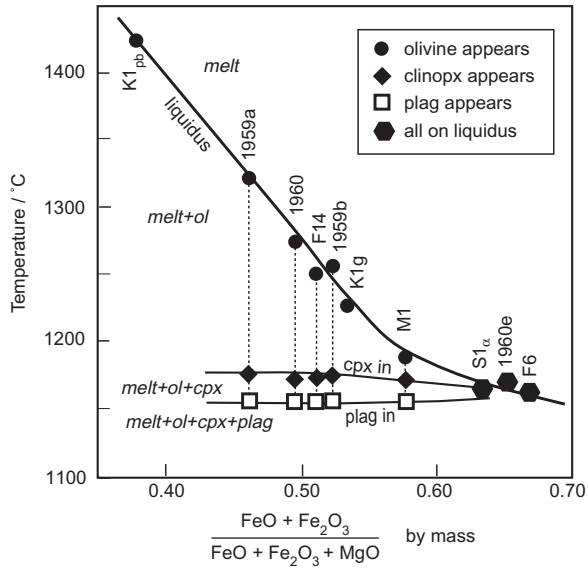


Fig. 3.9 Atmospheric-pressure crystallization behaviour of selected Kilauea lavas (data from Thompson and Tilley, 1969). The function $(FeO + Fe_2O_3)/(FeO + Fe_2O_3 + MgO)_{rock}$ is a measure of fractionation: low values signify primitive basaltic melts and high values more evolved melts. Each symbol indicates the temperature of first appearance of the mineral concerned (see key) as the molten sample is cooled: vertical dotted lines link results for the same lava. Olivine is the sole liquidus mineral for all samples except 1960e, $S1_\alpha$ and F6, in which all three minerals crystallize together. 'Cpx in' identifies the boundary at which clinopyroxene (cpx) crystals first appear.

Figure 3.9 shows the results of experiments carried out on a suite of Hawaiian basalt lavas by Thompson and Tilley (1969). The lava compositions span a range of major element compositions, suggesting they are products of different degrees of magma fractionation in the magma plumbing system beneath the summit of Kilauea. For each lava, finely ground powders were heated at atmospheric pressure until completely molten, and each was then allowed to cool to a different, carefully regulated temperature for several hours before being **quenched**. Each quenched sample was then sectioned to identify any crystals present. From these experiments it was possible to establish, for each lava, the temperatures at which (a) olivine, (b) clinopyroxene and (c) plagioclase began to crystallize. For most lavas, olivine appeared at a significantly higher temperature than clinopyroxene, and clinopyroxene began to crystallize about 20 °C above the first appearance of plagioclase. For the three most evolved samples, however, all three minerals began to crystallize at virtually the same temperature.

Compare the results in Fig. 3.9 with crystallization paths in Fig. 3.3. As olivine crystallizes first for most of the natural basalts, it is clear that their compositions fall within the natural analogue of the 'olivine field' in Fig. 3.3, similar to compositions *x* and *y*. Because clinopyroxene begins to crystallize in most of the Kilauea samples *before* plagioclase, it appears that *x* in Fig. 3.3 provides the better analogue for these natural basalts than *y*. Sample M1 evidently has a composition very close to a natural olivine–clinopyroxene cotectic analogous to that in Fig. 3.3, as olivine appears only just before clinopyroxene. The more evolved samples S1α, 1960e and F6 approximate to the eutectic in Fig. 3.3, as all three minerals appear at the same temperature rather than serially.

These experiments on real rocks show that the predictions of simple laboratory experiments mirror real melt behaviour surprisingly closely. We should, however, note some important differences. In the first place, the boundaries in the natural system occur at significantly lower temperatures than those in the synthetic system. For example, in the crystallization path of composition *x* in Fig. 3.3, plagioclase appears at 1270 °C, whereas in the natural crystallization paths in Fig. 3.9 it does not make an appearance until about

1150 °C. This difference should not surprise us, because the natural Fe-bearing ferromagnesian minerals and Na-bearing plagioclase in Fig. 3.9 inevitably have lower liquidus temperatures than the refractory end-members (Di, Fo and An) used in the synthetic experiments, as a glance at Figs. 3.4 and 3.6 will confirm.

The second difference is that the ultimate destination of melt evolution in Fig. 3.3 is a simple eutectic (E) at which all three minerals crystallize together. In natural systems, in which nearly all minerals crystallizing are intermediate members of solid solution series[6] rather than end-members, such a eutectic is transformed into a cotectic, just as the eutectic in Fig. 3.2 became one end of a cotectic in Fig. 3.7. Thus the three evolved samples in Fig. 3.9 merely mark the beginning of an olivine–clinopyroxene–plagioclase cotectic down which the melt can evolve further, rather than the end of the magma evolution line as Fig. 3.3 might suggest.

MAJOR ELEMENT VARIATION DIAGRAMS FOR NATURAL VOLCANIC ROCK SERIES

It is not feasible to conduct detailed laboratory experiments like those in Fig. 3.9 on every natural lava suite whose magma evolution is of interest. What other evidence can we find in magmatic rocks to shed light on magma chamber crystallization and to confirm that natural igneous melts broadly follow the principles of fractional crystallization discussed above?

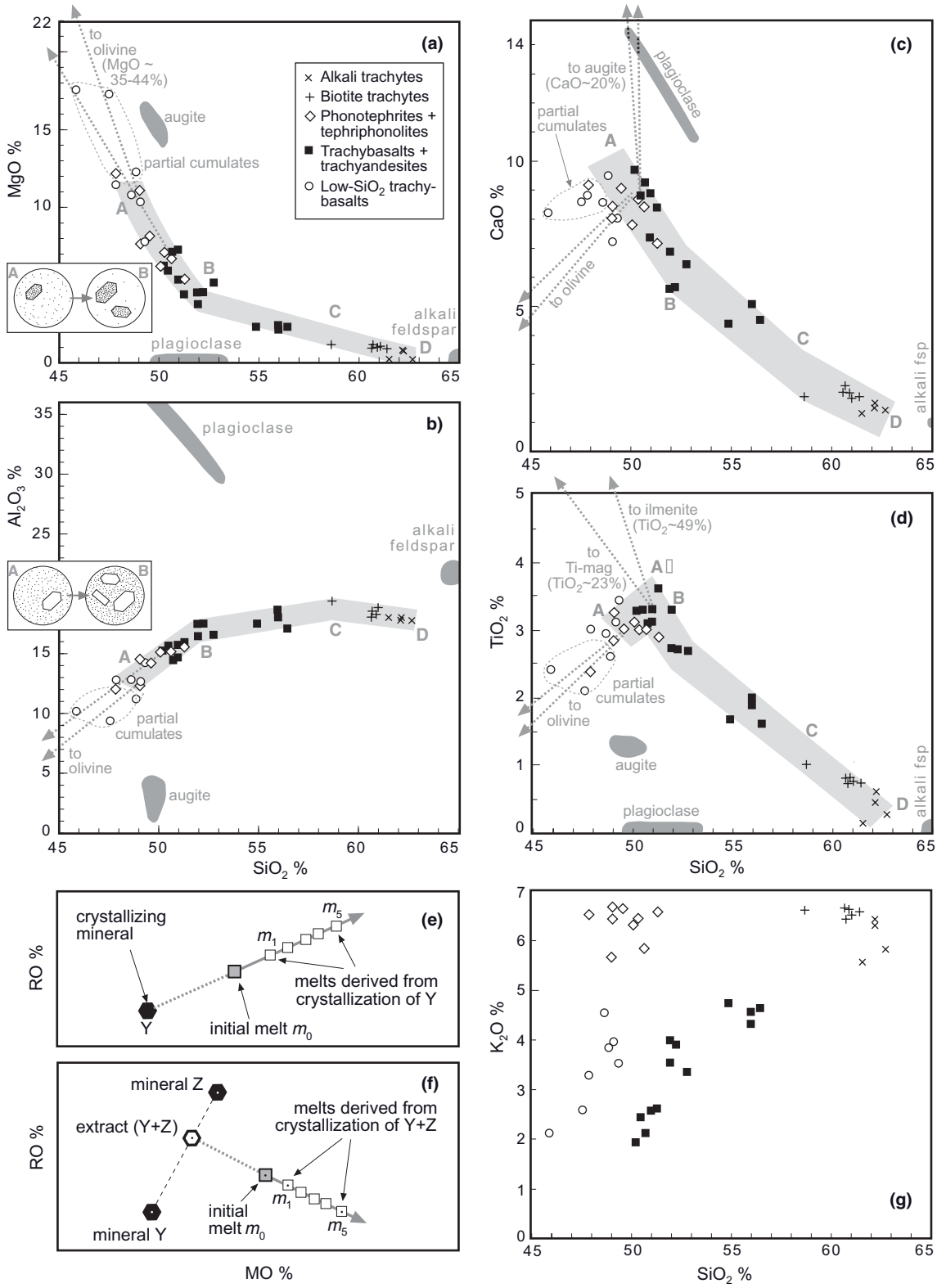
The chemical changes that accompany magma differentiation can be investigated by plotting analyses of the erupted rocks in **variation diagrams**. Examples of two-element variation diagrams (for major elements in volcanic rocks of Gough Island in the South Atlantic) are shown in Fig. 3.10. The unfamiliar volcanic rock names given in the key (Fig. 9.10a) may be treated simply as labels here; their significance is explained in Chapter 9. In each sub-diagram, the SiO_2 content is plotted on the x axis to serve as an index of advancing fractionation, from picrobasalts on the left hand side toward trachytes (evolved alkaline lavas; see Fig. 1.5) on the right. Each data point represents a single volcanic rock analysis, indicating magma composition in the chamber at the time of its eruption. Together the analyses define a trend of evolving magma composition – highlighted by the light grey band – that exhibits one or more abrupt changes of direction. To help interpret these features, analysed compositions of the main phenocrysts in the basalts (representing minerals crystallizing in the magma chamber) are shown as darker grey areas in each diagram; the compositions of olivine, augite, ilmenite and titanomagnetite – where they lie beyond the limits of the diagrams – are indicated by dashed arrows.

Figure 3.10a shows how the MgO content of the magma changed as it fractionated in the Gough Island magma system between 1 Ma and 100 ka ago. Initially the MgO content falls steeply from A to B, after which it declines more gently. Two arrows point toward the *range* of olivine compositions (Fo_{84}–Fo_{68}) found as phenocrysts in the trachybasalts. Because they are much more MgO-rich than the melt, their crystallization depletes the evolving melt in MgO (see the inset cartoon). The presence of augite phenocrysts in addition to those of olivine suggests that pyroxene was also crystallizing at this stage but, being less MgO-rich than olivine, this has less effect on MgO in the melt. Augite is however rich in CaO and its crystallization alongside olivine therefore causes a steep decline in the CaO content of the melt (A to B in Fig. 3.10c). According to Le Roex (1985), the most MgO-rich trachybasalts show textural evidence for partial **accumulation** of olivine and augite crystals, and their compositions are consistent with the *addition* of these minerals to (rather than removal from) the parental trachybasalt A in Figs. 3.10a,c.

Because olivine and augite are both aluminium-poor minerals, their crystallization concentrates Al_2O_3 in later fractions of melt (Fig. 3.10b), as illustrated by the inset cartoon. How this effect can be analysed graphically in a variation diagram is shown in Fig. 3.10e: the change in melt composition caused by removing a mineral Y from melt m_0 (by crystallization) is shown by extrapolating the line Y–m_0, as shown by the grey arrow.

At B in Figs. 3.10a–c there is an elbow in the trends. From B onward Al_2O_3 rises *less steeply* in Fig. 3.10b, suggesting that an aluminous mineral has begun to crystallize alongside olivine and augite, a conclusion supported

[6] Such as plagioclase, augite, olivine, low-Ca pyroxene, hornblende, biotite.


(a)
MgO %
to olivine (MgO ~ 35-44%)
augite
partial cumulates
plagioclase
alkali feldspar
Alkali trachytes
Biotite trachytes
Phonotephrites + tephriphonolites
Trachybasalts + trachyandesites
Low-SiO2 trachy-basalts
A
B
C
D
(b)
Al2O3 %
SiO2 %
(c)
CaO %
to augite (CaO~20%)
to olivine
alkali fsp
(d)
TiO2 %
to ilmenite (TiO2~49%)
to Ti-mag (TiO2~23%)
(e)
RO %
crystallizing mineral
melts derived from crystallization of Y
initial melt m0
(f)
mineral Z
extract (Y+Z)
melts derived from crystallization of Y+Z
mineral Y
MO %
(g)
K2O %

by the sudden abundance of plagioclase phenocrysts in rocks plotting close to B. An extract consisting of plagioclase + olivine + augite is Al_2O_3-rich and MgO-poor compared to olivine + augite alone, so the increase in Al_2O_3 and the decline in MgO in the observed trend both flatten out at B. How fractionation of Al-poor and Al-rich minerals *together* impacts on succeeding melts is illustrated in Fig. 3.10f. The appearance of alkali feldspar as a phenocryst mineral in the trachytes at C marks the involvement of a second aluminous mineral, causing the Al_2O_3 trend to dip gently downwards from C to D.

Minerals that differ markedly in composition from the melt have the strongest impact on the direction of melt evolution. This is illustrated in Fig. 3.10d, which shows an initial rise in TiO_2 content reflecting the crystallization of Ti-poor olivine and augite from A to A′, followed by a dramatic downturn where the Ti-rich oxide minerals ilmenite and titanomagnetite begin to crystallize at A′. Their impact is slightly diluted by the onset of plagioclase fractionation at B, causing the downward trend in TiO_2 to flatten out slightly. The elbows evident in Fig. 3.10, brought about by the crystallization of new phenocryst minerals, are a clear sign that fractional crystallization is the chief agent of magma differentiation: processes such as magma mixing are not capable of generating such marked discontinuities.

Figures 3.10e,f suggest that residual melts ought to undergo relatively smooth changes in composition (except where new minerals begin to fractionate). Why then do the data points in Figs. 3.10a–d, which appear to lie on a common trend, show such marked scatter (much greater than the analytical error)? It is likely that our simple notion of a homogeneous magma body undergoing uniform compositional change with advancing time is too naive: some parts of the magma may follow slightly divergent chemical paths owing to different local conditions, and the trends in Fig. 3.10 may even represent fractionation in a complex system of small magma batches – each evolving from a slightly different initial composition – rather than one big one.

On closer examination the illusory nature of the supposed 'unified trend' mooted above becomes more evident. Plotting K_2O contents (Fig. 3.10g) shows a distribution that is difficult to reconcile with fractionation of a single parent magma: the trachybasalts and trachyandesites define one trend, while the low-SiO_2 trachybasalts appear to lie on another (partly the result of accumulation) and the phonotephrites on a third; one cannot draw a single grey band through all of these groups. The single track of magma evolution that appears to emerge from Figs. 3.10a–d is misleading: when we consider *all* of the available data, we recognize a bundle of parallel trends of magma evolution, each beginning with a chemically distinct parental melt. This must be a contributory factor in the scatter seen in Figs. 3.10a–d.

MAGMA INTERACTION WITH THE CRUST

The laboratory experiments discussed earlier in the chapter were carried out in containers made of platinum or other noble metals,

Fig. 3.10 Variation diagrams illustrating magma evolution, exemplified by volcanic rocks of Gough Island in the South Atlantic; analyses (data from Le Roux, 1985, and Le Maitre, 1962) are plotted volatile-free (Box 1.3) as mass %; the key shows symbols representing the different rock types according to current nomenclature (Fig. 1.4). Dark grey fields and arrows represent relevant analysed phenocryst compositions in basalts and trachybasalts; the lighter grey band shows the inferred path of melt evolution. A, B, C and D mark discontinuities where new minerals appear to begin crystallizing. (a) MgO *versus* SiO_2; inset shows how growth of a high-MgO mineral depletes remaining melt in MgO. (b) Al_2O_3 *versus* SiO_2; inset shows how crystallization of low-Al_2O_3 mineral enriches remaining melt in Al_2O_3. (c) CaO *versus* SiO_2. (d) TiO_2 *versus* SiO_2. (e) Cartoon showing how changes in melt composition – due to crystallization of a mineral having the composition Y – appear in a two-element variation diagram as the extension of the line joining Y to the initial melt composition m_0; 'RO' and 'MO' represent arbitrary major-element oxides. (f) The effect of crystallizing *two* minerals (having compositions *Y* and *Z*) in specific proportions indicated by the **extract** composition. (g) K_2O *versus* SiO_2.

chosen for their high melting temperatures and chemical inertness, ensuring that the charge is not affected by metallic contamination even at melt temperatures. A magma chamber crystallizing at depth in the crust, particularly in the easily melted continental crust, does not enjoy this protection. There is abundant evidence that magmas can become contaminated by crustal components assimilated from the wall-rocks with which the magma comes into contact. This processes has relevance to the present chapter because assimilation and melting of **sialic** continental crust are believed to contribute significantly to the diversity of natural magmas in continental regions.

Though many geochemical properties of a magma can be affected by crustal assimilation, one of the clearest fingerprints often comes from **radiogenic isotopes** (Box 3.4). This is because chemical reactions like fractional crystallization have no effect on isotope abundance ratios, including those such as $^{87}Sr/^{86}Sr$ that involve a radiogenic isotope (in this case ^{87}Sr): in terms of their chemical behaviour two isotopes of the same element are identical. Such ratios may on the other hand be very sensitive to contamination by older rocks that are richer in the radiogenic isotope (especially if the magma contains a lower concentration of the element concerned than the crustal rocks surrounding it). Figure 3.11 shows a plot of **initial** $^{87}Sr/^{86}Sr$ ratio *versus* SiO_2 content for a series of related volcanic rocks from the Cantal volcano in the French Massif Central. The basic members of the series exhibit a narrow range of relatively low $(^{87}Sr/^{86}Sr)_0$ values – less than 0.7045 – reflecting their mantle source, but the more evolved lavas show a wider range that includes much higher values. The rocks exhibit a crude correlation between Sr initial ratio and SiO_2 content.

As crystal–liquid equilibria do not discriminate between the isotopes of heavy elements like Sr, crystals forming from a melt will contain Sr isotopes in exactly the same ratio as the melt, and it follows that fractional crystallization *acting on its own* cannot bring about a change in Sr-isotope composition in residual melts. So, although fractional crystallization can account for the SiO_2 range in Fig. 3.11, it cannot explain the high $(^{87}Sr/^{86}Sr)_0$ values present in the more evolved samples. The Cantal volcano stands on Variscan continental crust, and therefore contamination of the lavas by older crustal rocks – in which the decay of ^{87}Rb has over time produced higher $^{87}Sr/^{86}Sr$ ratios – provides an obvious explanation for the radiogenic strontium seen in the

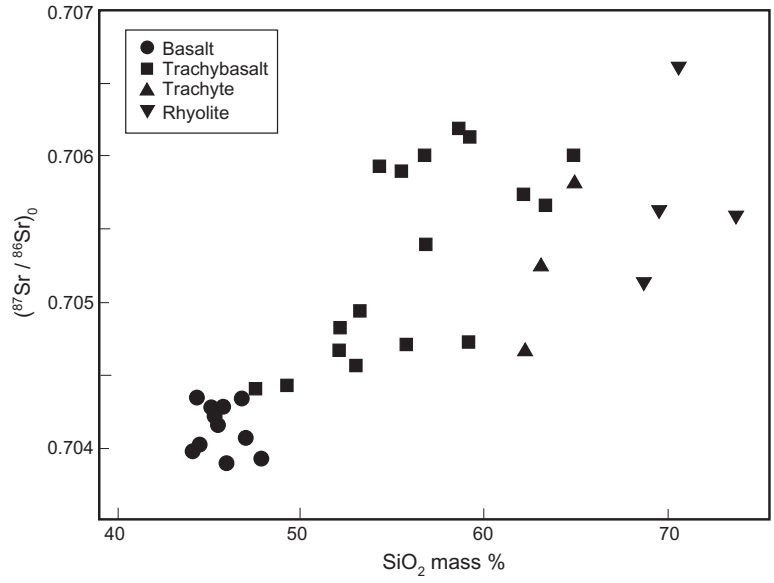


Fig. 3.11 **Initial** Sr-isotope ratios $(^{87}Sr/8^{6}Sr)_0$ of volcanic rocks from the Cantal volcano in central France plotted against their SiO_2 contents (after Downes, 1984).

high-SiO_2 samples. By numerical modelling of the effect of various possible contaminants, Downes (1984) was able to attribute the high Sr-isotope ratios in the evolved rocks to assimilation of lower crustal granulites, xenoliths of which – occurring in the lavas – gave $^{87}Sr/^{86}Sr$ values (corrected to the age of the lavas) ranging from 0.7058 to 0.7188.

The observation that the more evolved members of each series have the highest and most scattered $(^{87}Sr/^{86}Sr)_0$ ratios, while the basic members are confined to a narrow range of low values, suggests that crustal assimilation has taken place hand in hand with fractional crystallization. **Latent heat** released by crystallization passes into the country rock envelope in contact with the magma, where it promotes partial melting of the wall-rocks. Small melt fractions derived by partial melting of high-$^{87}Sr/^{86}Sr$ continental crust rocks become incorporated into the evolving magma body, raising $^{87}Sr/^{86}Sr$ to progressively higher values as crystallization progresses and more heat is released to the wall-rocks. This process, whose isotopic systematics were first described by De Paolo (1981), is known as 'assimilation with fractional crystallization' (**AFC**).

The extent to which crustal assimilation can alter the Sr isotope ratio in the fractionating magma depends on various factors, notably the $^{87}Sr/^{86}Sr$ ratios and the Sr contents (in parts per million, ppm) of the magma and contaminant: the effect will be maximized when the contaminant has much higher $^{87}Sr/^{86}Sr$ ratio – for example, through being much older (Box 3.4) – *and* a higher concentration of Sr than the magma. Small-degree partial melts of country rock are likely to have higher SiO_2 content than the magma, and therefore the latter will become slightly enriched in SiO_2 as well.

Crustal contamination may be detected using other radiogenic isotope systems, and also by means of oxygen isotopes (Box 3.4). Mantle rocks and magmas derived from them typically have $\delta^{18}O$ values between +5.4 and +5.8‰, whereas crystalline rocks of the continental crust that have not interacted with meteoric waters (which have very low $\delta^{18}O$) have average $\delta^{18}O$ values around +8‰; unaltered granites in particular lie in the range +6 to +9‰ (James, 1981), and sedimentary rocks may be as high as +20‰. Crustal contamination of mantle derived magmas is therefore indicated by whole-rock and mineral $\delta^{18}O$ values higher than the mantle range. As an example, Fig. 3.12 shows how $\delta^{18}O$ and $^{87}Sr/^{86}Sr$ increase together in successive zones of strongly zoned clinopyroxene phenocrysts in a magnesian basalt from the Yemen flood basalt province (Fig. 2.15), suggesting progressive crustal contamination of the host magma as the phenocrysts grew.

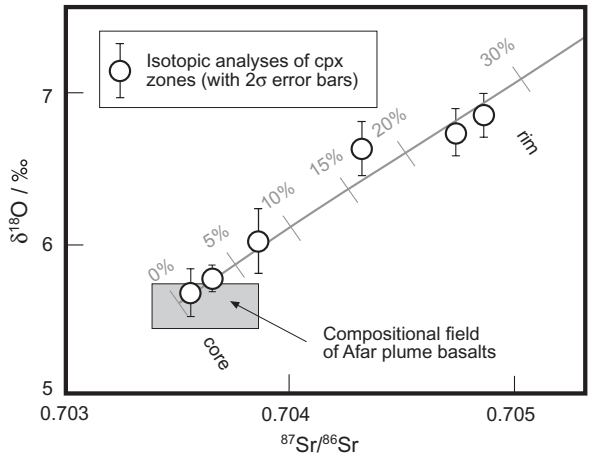


Fig. 3.12 Detection of crustal contamination using oxygen isotope ratios: correlation between $\delta^{18}O$ and $^{87}Sr/^{86}Sr$ in core-to-rim compositional zones of augite phenocrysts separated from a flood basalt from Yemen (from Baker et al., 2000 by permission of Oxford University Press). The grey line represents a numerically modelled crustal-contamination trajectory from primary basaltic magma ('0%', $\delta^{18}O$ = 5.6‰, $^{87}Sr/^{86}Sr$ = 0.7035, Sr 476 ppm) and continental crust ($\delta^{18}O$ = 10.6‰, $^{87}Sr/^{86}Sr$ = 0.7086, Sr 476 ppm); grey numbers represent mass percentages of crustal component.

REVIEW

The wide diversity of magma compositions found in Nature, illustrated in Fig. 3.1, can be attributed to:

1 variation in the conditions of melting and source composition in mantle source regions (illustrated by the dashed arrows in Fig. 3.1 and dealt with in Chapter 9), and
2 magma differentiation processes taking place in magma chambers probably

Box 3.4 Isotopes – the basics

Isotopes provide a powerful set of tools for testing theories of magma genesis and evolution. Isotope systems used to study igneous rocks fall into two categories:

1 *Radiogenic isotope systems.* The trace element rubidium (Rb, Z = 37) consists of two isotopes (Fig. 3.4.1): ^{85}Rb (72% of Rb atoms) and ^{87}Rb (28%). ^{87}Rb is a radioactive isotope (half life 48.8 Ga) and it decays slowly to ^{87}Sr, one of the four isotopes of the neighbouring trace element strontium (Sr, Z = 38), as shown by the grey arrow in Fig. 3.4.1. The proportion of ^{87}Sr relative to the other isotopes therefore increases with time in a given mineral or rock, in proportion to its Rb/Sr ratio (Fig. 3.4.2). For this reason ^{87}Sr is described as a ***radiogenic* isotope** (one that – at least in part – is *gen*erated by *radio*active decay). To highlight such changes when plotting cogenetic rocks of differing Sr content (Fig. 3.4.2), ^{87}Sr is by convention ratioed to the neighbouring non-radiogenic isotope ^{86}Sr, yielding the *strontium isotope ratio* ^{87}Sr/^{86}Sr. Because they change measurably over geological periods of time, radiogenic isotope ratios like ^{87}Sr/^{86}Sr, ^{143}Nd/^{144}Nd and ^{207}Pb/^{204}Pb are key parameters in isotope geochronology.

2 *Stable isotope systems.** The 3 isotopes of oxygen (^{16}O, ^{17}O and ^{18}O) are neither radioactive nor radiogenic and so their proportions do not vary with time. Nonetheless, because the difference in mass number (18 – 16 = 2) is relatively large in relation to the mean mass number (17), the ^{18}O/^{16}O ratio is detectably fractionated by geological processes such as crystallization and hydrothermal alteration. The minute natural variations in this ratio therefore serve as a useful tracer for detecting such processes. Since their isotope ratios (e.g. ^{18}O/^{16}O) do not change with time,

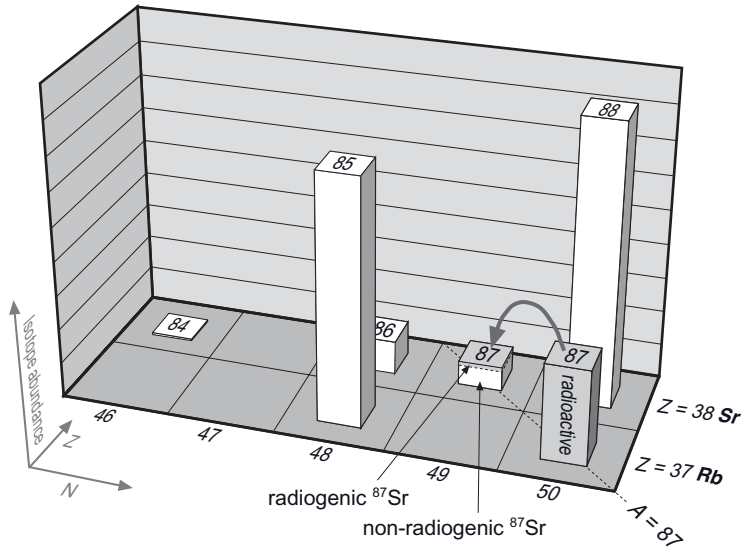


Fig. 3.4.1 Naturally occurring isotopes of the elements rubidium (Rb) and strontium (Sr). The height of each column represents the relative abundance of the isotope (shown here for equal amounts of the elements Rb and Sr); the number on the top of each column is the mass number $A = Z + N$ that serves to identify the isotope.

*The term 'stable' is a shade ambiguous: to a physicist it means simply non-radioactive, whereas in geochemical usage it implies *neither radioactive nor radiogenic* (i.e. unchanging with time). This meaning of the term has stuck because no better label has been found.

such systems are labelled 'stable isotopes'. Other stable isotope systems used to study geological processes and equilibria include $^{2}H/^{1}H$ (often written D/H where D stands for deuterium) and $^{34}S/^{32}S$.

Natural variations in the $^{18}O/^{16}O$ ratios of rocks and minerals are conventionally recorded using the $\delta^{18}O$ notation in order to eliminate inter-laboratory error.

Growth of radiogenic isotopes with time

When a rock or mineral contains very little Rb in relation to Sr, its $^{87}Sr/^{86}Sr$ ratio will increase only very slowly with time; in a sample with a high Rb/Sr ratio, on the other hand, the growth of $^{87}Sr/^{86}Sr$ is much more rapid. This is illustrated in Fig. 3.4.2. In mantle rocks, Rb is extremely low and the elemental Rb/Sr ratio in the mantle as a whole is only 0.028. In consequence the $^{87}Sr/^{86}Sr$ ratio in the mantle increases only very slowly with time, from 0.699 when the Earth formed 4.5 Ga ago to about 0.704 at the present time (Fig. 3.4.2). Present-day mantle-derived magmas have $^{87}Sr/^{86}Sr$ ratios – inherited from their mantle source-regions – close to this value. Because Rb is much more incompatible than Sr, rocks typical of the continental crust, especially those of the upper crust, have higher Rb/Sr values, and many granites have even higher values. It is evident that old continental crust (by virtue of both age and higher Rb/Sr ratio) will have much higher $^{87}Sr/^{86}Sr$ values than mantle-derived magmas do (Fig. 3.4.2), and therefore contamination of mantle-derived magmas by ancient sialic crustal rocks will lead to elevated $^{87}Sr/^{86}Sr$ ratios in the contaminated magma (Fig. 3.11).

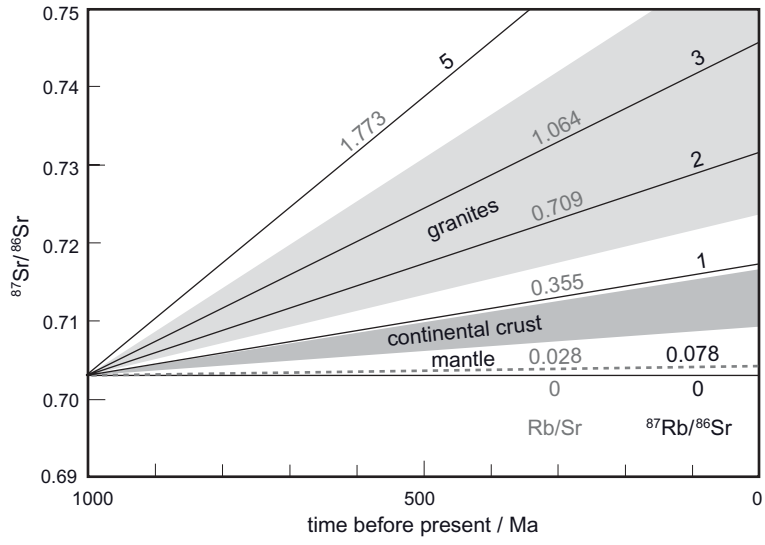


Fig. 3.4.2 Growth of radiogenic ^{87}Sr through time as a function of $^{87}Rb/^{86}Sr$ ratio (and the elemental Rb/Sr ratio shown in grey) in diverse rocks having an arbitrary age of 1 Ga; representative ranges of growth rate for mantle, continental crust and granites are shown (based on data from Taylor and McLennan, 1985).

The **initial isotope ratio** $(^{87}Sr/^{86}Sr)_0$ of a cogenetic suite of igneous rocks provides a guide to the identity of the source from which the parent magma was derived. The initial ratio may be determined from the *y*-intercept of an **isochron plot** (see Fig. 8.21a), or by applying a calculated age correction to an individual ratio based on the sample's age and Rb/Sr ratio.

located at crustal depths. These processes, illustrated by the full arrows in Fig. 3.1, have been the subject of this chapter.

The main agent of magma differentiation – fractional crystallization – can be understood in general terms from the study of phase diagrams for simple silicate systems prepared from laboratory experiments (Box. 3.1). Fractional crystallization usually proceeds from the crystallization of one mineral, then two minerals together, then three:

$$\begin{aligned} \text{melt} \rightarrow \text{melt} + \text{A} &\rightarrow \text{melt} + \text{A} + \text{B} \\ &\rightarrow \text{melt} + \text{A} + \text{B} + \text{C} \end{aligned} \quad \cdots \quad [3.1]$$

as illustrated by Fig. 3.3. At the same time, minerals that are solid solutions will initially form crystals rich in the refractory end-member (An, Fo, etc.) which thereafter, in parallel with changes in melt composition, become progressively depleted in that end-member as fractionation progresses (Fig. 3.4). Such processes cause parental magma compositions to evolve broadly along the solid arrows shown in Fig. 3.1. Reaction may also occur between early-formed crystals and later melts, but discussion of this complicating factor is deferred to Chapter 4, where it is discussed in the light of field evidence seen in layered gabbro intrusions.

Variation diagrams provide a powerful tool for examining actual magma evolution in suites of cognate volcanic rocks. Those illustrated in Fig. 3.10 employ SiO_2 content as the index of fractionation, but other parameters such as Zr content (in ppm) or MgO content are equally applicable (MgO decreases with advancing fractionation, so is often plotted in the opposite polarity to SiO_2: high values on the left, low values to the right). Abrupt bends in the trends signal the appearance of new fractionating minerals (e.g. ilmenite at A′ and plagioclase at B in Fig. 3.10) and provide a clear fingerprint of fractional crystallization in operation. Variation diagrams can be used to unravel the identities and proportions of minerals crystallizing in some detail (see Cox et al., 1979) but, as we have seen, misleading conclusions can be drawn if the data are not examined sufficiently carefully.

Magmas undergoing fractional crystallization in the continental crust are prone to assimilation of sialic contaminants, readily detected by means of radiogenic isotope and/or $^{18}O/^{16}O$ ratios (Figs. 3.11 and 3.12). Crustal assimilation increases the proportion of highly evolved residual melts in the magma chamber and among the eruptive products derived from it, and has played a key part in the genesis of many granite magmas (Chapter 8).

EXERCISES

3.1 The formulae of diopside and anorthite are $CaMgSi_2O_6$ and $CaAl_2Si_2O_8$ respectively. Calculate the ideal composition of each mineral expressed in mass % oxides.

Relative molecular masses in atomic mass units (**amu**): MgO = 40.32, Al_2O_3 = 101.96, SiO_2 = 60.09, CaO = 56.08.

3.2 Using the results from question 1, calculate in mass % oxides the compositions of initial melt *n* (26% anorthite) and eutectic melt E (41% anorthite) in Fig. 3.2.

3.3 (a) At what temperature does melt *y* in Fig. 3.3 begin to crystallize, and which mineral is the first to crystallize under these conditions? (b) What percentage of the melt must crystallize before the second mineral starts to crystallize, what is that mineral, and at what temperature does it appear?

3.4 In Fig. 3.6, what percentage of melt *m* will have crystallized at (a) 1700 °C, (b) 1600 °C and (c) 1550 °C under equilibrium crystallization, and what will be the composition of olivine coexisting with melt at each temperature (expressed as Fo_x)?

3.5 Use the Lever rule to calculate the composition of 'extract (Y + Z)' in Fig. 3.10(f) as mass percentages of Y and Z. Estimate the mass percentage of melt remaining when melt m_0 has fractionated (a) to composition m_1 and (b) to composition m_5

Chapter 4

Gabbroic rocks

Gabbros are coarse-grained igneous rocks equivalent in composition to basalts, representing basalt magma that has crystallized slowly at depth. If all gabbros were homogeneous intrusions, there would be little to say here that has not already been covered in Chapter 2, but homogeneity is not the rule. Larger gabbro intrusions normally exhibit an internal chemical and mineralogical architecture – called igneous **layering** – that preserves many details of the magma's crystallization history, and indirectly records the chemical evolution in melt composition that has been discussed from an experimental standpoint in Chapter 3. From studying igneous layering in the field – and the local variations in mineral proportions it entails – it is clear that differences in physical properties between the crystallizing minerals (notably their density, crystal habit and nucleation rate) are capable of segregating one mineral from another during crystallization or deposition. This leads to local concentration of particular minerals in layers, sometimes to the extent of producing virtually monomineralic rocks such as dunite and anorthosite. Such **cumulate** rocks require rock nomenclature to be extended to cover a wider range of mineralogical constitution than is found in basalts (Fig. 4.1).

Gabbroic rocks form in each of the geotectonic settings where basalts occur described in Chapter 2, though they become available for study in the field only when exhumed by uplift and erosion.

Igneous Rocks and Processes: A Practical Guide, 1st edition. By Robin Gill. Published 2010 by Blackwell Publishing

THE NOMENCLATURE OF GABBROIC ROCKS

Definitions

Gabbro: a coarse-grained igneous rock consisting essentially of augite (see Box 2.1) + calcic plagioclase (An > 50%).

Dolerite:[1] a medium-grained igneous rock (Fig. 1.3a) consisting essentially of augite + calcic plagioclase.

Other minerals that may be present in each rock type are listed in Table 4.1.

An optical technique for estimating plagioclase composition under the microscope is described in Box 4.1. A coarse-grained melanocratic or mesocratic rock containing *more sodic* plagioclase (An < 50%) is called a diorite rather than gabbro, especially if it contains hornblende in addition to (or in place of) pyroxene; such rocks are described in Chapter 8. Where the plagioclase content of a rock falls below 10%, the nomenclature of ultramafic rocks becomes applicable (Chapter 5).

Nearly all gabbros are found in plutonic bodies, but to restrict the term (as the International Union of Geological Sciences, IUGS, suggests) just to plutonic rocks is inappropriate, because gabbro – as defined descriptively above – may be found as a coarse-grained interior facies of certain thick lavas (see, for example, Arndt et al., 1977). It is better to base a rock definition on descriptive characteristics of the rock rather than how or where it was formed.

The adjective '**gabbroic**', as understood by most petrologists, embraces a wider variety of

[1] *diabase* in North America. IUGS recommends the synonym 'microgabbro' (Le Maitre, 2002).

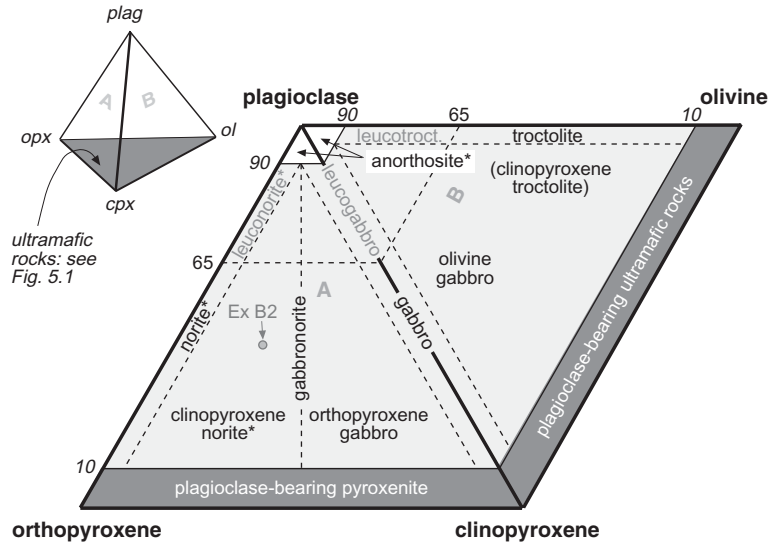


Fig. 4.1 Diagram showing the IUGS nomenclature for gabbroic rocks based on the modal proportions of plagioclase, olivine, clinopyroxene and orthopyroxene in the rock (Le Maitre, 2002). Faces A and B of the plag–opx–cpx–ol tetrahedron (inset) have been 'flattened out' to form the main diagram. 'Clinopyroxene troctolite' is shown in parentheses because, though it conforms to the logic of the IUGS nomenclature for gabbroic rocks, it does not appear explicitly in the IUGS scheme. The point labelled Ex B2 relates to Exercise 2 in Appendix B.

***NB** The requirement for plagioclase to be *calcic* (An > 50%) – as in the definition of gabbro *sensu stricto* – does not apply to norite, leuconorite or anorthosite.

Table 4.1 Summary mineralogy of gabbros and dolerites. The optical properties of relevant minerals are summarized in Appendix A.

Essential minerals	• augite • calcic plagioclase (An > 50 mol %) – see Box 4.1
Principal type minerals	• enstatite* (for identification, see Box 4.2) • olivine • nepheline, analcite (or another foid) • quartz • hornblende
Common accessory minerals	• opaques (chromite, magnetite, ilmenite, sulphide) • apatite, zircon
Common secondary (alteration) minerals	• serpentine or iddingsite replacing olivine (see Box 2.2) • chlorite or uralite replacing pyroxene • sericite replacing plagioclase and/or foids

* In older literature, magnesian orthopyroxenes were divided into enstatite ($En_{90–100}$), bronzite ($En_{70–90}$) and hypersthene ($En_{50–70}$); current usage includes all of these in the term 'enstatite' ($En_{50–100}$) as in Box 2.1.

coarse-grained gabbro-related rocks (norite, gabbronorite, troctolite and anorthosite, in addition to gabbro) than does the noun 'gabbro'. Norite, for instance, though it has a gabbro-like texture, consists essentially of plagioclase and *ortho*pyroxene (Fig. 4.1); clinopyroxene – if present at all – is subordinate. The justification for this more elastic usage of 'gabbroic' is that all of these rocks can in principle be formed by crystal segregation processes during the crystallization of a homogeneous melt of gabbro/basalt composition. The precise meaning of each of these names is based in the IUGS nomenclature on quantitative **modal** analyses, as shown in Fig. 4.1,[2] but the terms may also be applied infor-

[2] The inset figure shows a three-dimensional **quaternary** figure (a tetrahedron) in which the relative proportions of *four* minerals may in principle be plotted (disregarding the tricky question of how such a 3D plot could be portrayed). The main figure shows two faces of the tetrahedron (A and B) laid flat; each triangle shows the relative proportions of three different minerals shown at the apexes. The procedure for plotting modal data in such diagrams is described in Appendix B.

mally to qualitative visual analysis of a thin section; appropriate qualitative definitions in words are:

Anorthosite: a coarse-grained igneous rock consisting of more than 90% plagioclase.[3]
Troctolite: a coarse-grained igneous rock consisting essentially of calcic plagioclase + olivine.
Norite: a coarse-grained igneous rock consisting essentially of plagioclase + orthopyroxene.[3]
Gabbronorite: a coarse-grained igneous rock consisting essentially of calcic plagioclase + augite + enstatite (both pyroxenes being present in similar amounts).

The IUGS commends the term 'gabbroid' as a provisional field name for gabbro-like plutonic rocks, pending petrographic analysis under the microscope.

Subdividing gabbros and dolerites

Because coarse grain-size allows all minerals present to be identified with confidence (unless alteration has completely replaced one or more igneous minerals), the IUGS definitions of gabbro and related rocks are based entirely on modal proportions of minerals found in the rock (Fig. 4.1). Recourse to chemical variation diagrams – such as the total alkali–silica (TAS) plot – is no longer necessary, since the uncertainties associated with glass or fine grain-size in basalts are no longer an issue. Moreover, to the extent that the analysis of a coarse-grained rock may have been influenced by cumulate processes (Box 1.4), it does not reliably represent a magma composition and so plotting it in a TAS plot would be inappropriate.

Gabbros and the magmas from which they crystallized may be divided – like basalts – into tholeiitic and alkali categories:

- tholeiitic gabbro contains modal enstatite (orthopyroxene, identified as in Box 4.2) in addition to augite; minor **interstitial** quartz may also be seen, indicating a slightly silica-oversaturated melt, or alternatively olivine.
- alkali gabbro contains small amounts of a feldspathoid (nepheline or analcite – see Box A1 in Appendix A for identification) in addition to olivine, indicating crystallization from a silica-undersaturated magma. Minor hornblende and biotite may also be present.

These two types of gabbro differ in other ways too. The presence of two coexisting pyroxenes in a tholeiitic gabbro reflects the limited mutual solubility that exists between low-Ca and high-Ca pyroxenes. The two pyroxenes crystallize with compositions that reflect a temperature-dependent chemical equilibrium between them (discussed in more detail in Box 4.5): the enstatite is saturated with a high-Ca pyroxene component, and the augite is saturated with a low-Ca component. Tholeiitic gabbros contain augites whose compositions are constrained by this equilibrium to have relatively Ca-poor compositions. This mutual saturation relationship can often be seen under the microscope, because as the two pyroxenes cool slowly they become supersaturated with each other and develop microscopic intracrystalline **exsolution** lamellae or blebs (Box 4.5 and Plates 4.7 and 4.8). The augites found in alkali gabbros have no low-Ca pyroxene with which to equilibrate, follow a more Ca-rich trend (Fig. 4.2), are not saturated with the $Mg_2Si_2O_6$ component and therefore do not exsolve such lamellae on slow cooling. Alkali gabbro augites are usually of the brown-lilac-pleochroic titanian augite variety (Box 2.1).

Alkali gabbros and dolerites often contain distinctive accessory minerals such as the distinctive brown Ti-rich amphibole kaersutite.

THE SCALE AND EMPLACEMENT OF DOLERITIC AND GABBROIC INTRUSIONS

Minor intrusions

Dykes ('dikes' in N. America) are discordant intrusive sheets, near-vertical at the time of emplacement, that often occur in parallel (Fig. 4.3a) or radial swarms. Individual dykes range in scale from centimetres to several hundred metres in width, and may extend along strike for tens or hundreds of kilometres; some dyke swarms, however, extend for

[3] Note that the requirement for the plagioclase present to be calcic (An > 50%) is relaxed for norite or anorthosite, which may contain andesine instead.

Box 4.1 Estimating plagioclase composition

Plagioclase – at least at high temperature – can form homogeneous crystals having any composition between 100% anorthite ($CaAl_2Si_2O_8$) and 100% albite ($NaAlSi_3O_8$). For estimating the composition of plagioclase crystals in thin section, the most useful composition-dependent optical property is **extinction angle**. In albite-twinned plagioclase crystals (Fig. 4.1.1), individual twin lamellae will be seen to extinguish at an angle to the boundary plane* that separates them. The extinction angle has been calibrated relative to anorthite content, as shown in Fig. 4.1.2, and thus provides a means to determine composition under the polarizing microscope.

Figure 4.1.2 applies only to crystals whose albite-twin boundary planes (parallel to {010}) are accurately perpendicular to the plane of the thin section. Crystals having correct orientation can be identified by applying three tests (Deer et al., 1992), all of which have to be met for the determination to be reliable:

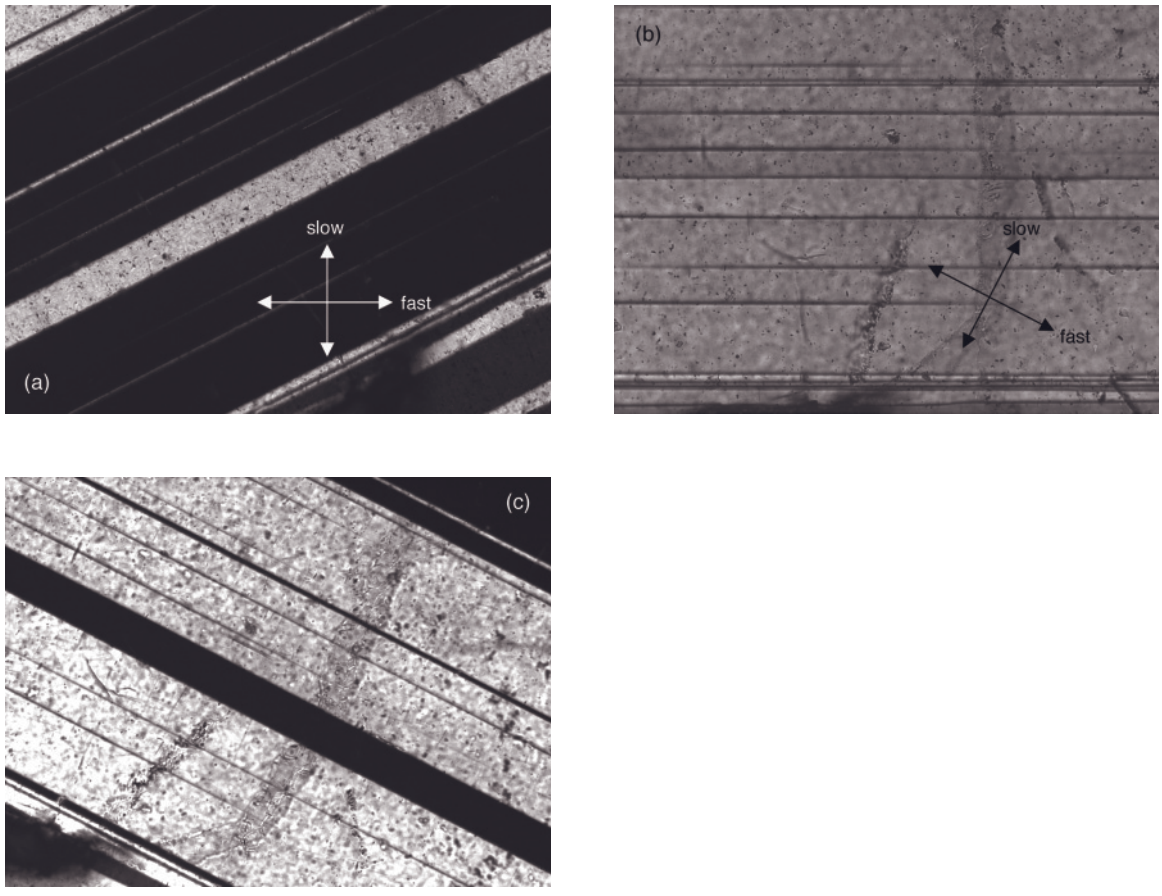


Fig. 4.1.1 (a) Picture of plagioclase in crossed polars (XP) showing albite twinning – the commonest in plagioclase – with one twin in extinction; the axes show the fast and slow vibration directions as determined using the sensitive tint plate (Box 9.2). (b) Picture of the same crystal in XP rotated 27.6° clockwise, the angle necessary to bring the boundary plane parallel to analyser; note the identity of tint across adjacent twins; (c) The same crystal with other twin in extinction position in XP (rotating the stage a further 27.3° clockwise). The sample is a gabbro from the Skærgaard Middle Zone.

*The term used by crystallographers for this boundary plane is *composition plane* (Cox et al., 1988; Deer et al., 1992). The term is not used here because, having nothing to do with chemical composition, it is potentially confusing.

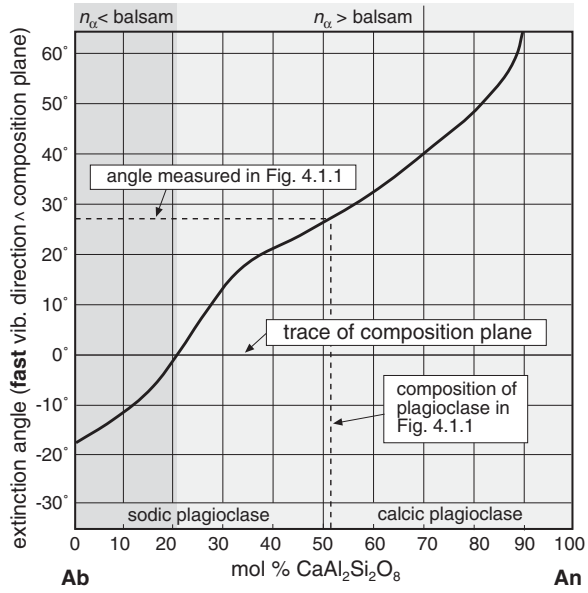


Fig. 4.1.2 Empirical curve for determining plagioclase composition from extinction angle for sections perpendicular to (010) – see below for selecting such sections. Plagioclases in the range An_0–An_{20} have extinction angles of similar magnitude to those between An_{20} and An_{38} but can be distinguished by having refractive index n_α less than balsam (see the darker zone in Fig. 4.1.2). The calibration shown applies only to 'low-temperature' plagioclases of hypabyssal and plutonic rocks (see Deer et al.,1992, Fig. 162). The extinction angle and estimated composition of the plagioclase crystal in Fig. 4.1.1 are shown for illustration.

1 the boundary plane should be sharp (Fig. 4.1.1b) and show no lateral movement with slight defocusing (any movement here implies a boundary plane *not* accurately perpendicular to the plane of the section);
2 neighbouring lamellae should give *identical* interference colours when the boundary plane is N–S or E–W (Fig. 4.1.1b);
3 adjacent lamellae should give the same extinction angle (in opposite directions) to within 5%. (Fig. 4.1.1a,c).

Having found a suitable crystal, rotate to a position in which one twin lamella is in exact extinction and measure the stage position using the stage micrometer. The vibration directions of the lamella are now parallel to the microscope's polarizer and analyser. It may be helpful to sketch the grain and mark on the two vibration directions (cf. Fig. 4.1.1a). Rotate through exactly 45° and use the sensitive tint plate (Appendix A1) to determine *which of the vibration directions is the fast* (lower–*n*) direction, and label it on your sketch. Return to the extinction position, and note whether the fast direction (α) is parallel to the horizontal or vertical cross-wire (polarizer or analyser direction respectively). Now rotate the stage to bring the boundary plane exactly parallel to the *same* cross-wire (Fig. 4.1.1b). Record the angle carefully and subtract it from the original reading to determine the extinction angle for the lamella of interest. Now rotate the stage to bring the adjacent lamella accurately into extinction (Fig. 4.1.1c), record the angle, and subtract the second reading from it to determine the complementary extinction angle. If the two difference measurements agree within a degree or two (disregarding sign), calculate their average; if not, find an alternative grain to measure.

Ideally, extinction angles should be measured in this way for about ten suitably orientated crystals and the *maximum value* obtained used in Fig. 4.1.2 to estimate plagioclase composition. For sodic plagioclases it may also be necessary to estimate the refractive index n_α (see caption to Fig. 4.1.2).

Box 4.2 Distinguishing between orthopyroxene and clinopyroxene

Extinction angle

The most widely used means of distinguishing between orthorhombic and monoclinic pyroxenes is extinction angle, but care must be taken to select appropriate crystal sections. In orthorhombic crystals, extinction is *parallel* to the prismatic {210} cleavage when viewed in prismatic or pinacoidal sections, but not in other sections. In monoclinic pyroxenes, extinction is *oblique* to the prismatic {110} cleavage except in sections parallel to the *y* axis.

The best general strategy for avoiding inappropriate sections that give misleading results is to select for the extinction test only those grains that exhibit:

1 a single cleavage (not two perpendicular cleavages, as seen in basal sections); *and*
2 the highest available interference colour (indicating proximity to an α–γ cross-section).

Figure 4.2.1 illustrates extinction behaviour of ortho- and clinopyroxenes in these circumstances.

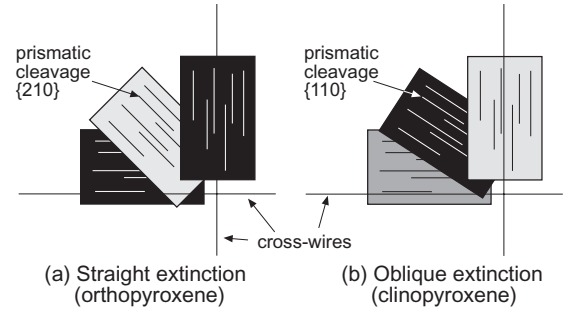


Fig. 4.2.1 The distinction in crossed polars between (a) straight or *parallel* extinction in an α–γ (100) section of an *orthopyroxene* such as enstatite, and (b) *inclined* extinction in an α–γ (010) section of a *clinopyroxene* such as augite.

Other differences

Three other clues provide confirmation as to whether a pyroxene is orthorhombic or monoclinic:

1 Some enstatites exhibit a weak but very distinctive pink-green pleochroism.
2 Orthopyroxenes have lower birefringence (first-order colours) than clinopyroxenes (second-order colours) – cf. Box A1 in Appendix A.
3 Orthopyroxenes never exhibit twinning whereas clinopyroxenes, including pigeonite, may do so.

more than 1000 km along strike, notably the Mackenzie giant dyke swarm in NW Canada (Fig. 4.13) which illustrates the radiating tendency of some large swarms. Basic dykes generally consist of dolerite at the centre (or gabbro in thicker dykes), but those emplaced at shallow depths commonly exhibit basalt chilled contacts (Fig. 4.3b). Sub-horizontal columnar jointing usually develops perpendicular to the dyke margins (Fig. 4.3a), which have acted as cooling surfaces. Dyke emplacement provides not only for upward transport of magma, possibly feeding surface fissure eruptions, but may also transport magma over considerable lateral distances too (Ernst et al., 1995).

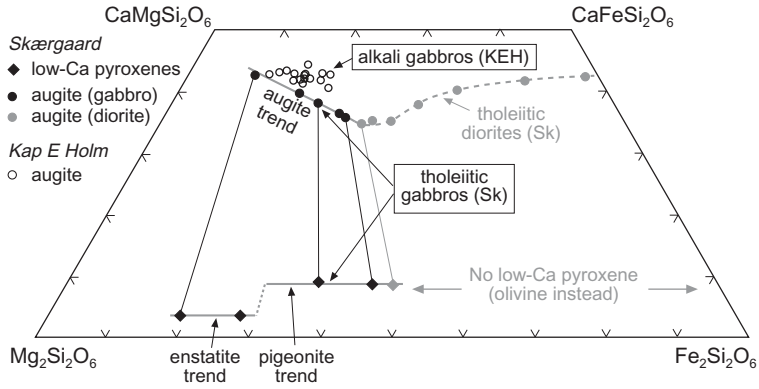


Fig. 4.2 Comparative plot of pyroxene compositions in typical tholeiitic gabbros (Skærgaard intrusion, solid black symbols) and alkali gabbros (Kap Edvard Holm complex, open symbols). Data are plotted in the 'pyroxene quadrilateral' introduced in Box 2.1. The augite trend differs between tholeiitic and alkali gabbro suites owing to equilibration with low-Ca pyroxene in the former (Box 4.5); when LCP ceases to crystallize, the augite trend changes direction (grey symbols representing more evolved Skærgaard diorites). Data from Wager and Brown (1968), Deer and Abbott (1965) and Elsdon (1971).

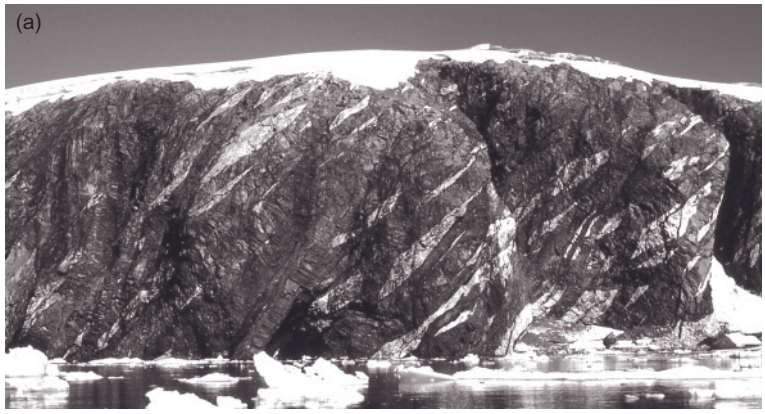
Sills are sub-horizontal sheet intrusions that are mostly concordant with bedding in the host country rocks (usually undeformed sedimentary or volcanic successions). Few sills are more than a hundred metres in thickness, but many of them are but individual sheets within sill complexes whose aggregate thickness may amount to several kilometres. The Jurassic Ferrar sills in the Transantarctic mountains (Fig. 4.3d), for example, together have a total thickness that in places reaches 2 km. Sills are often *transgressive*: traced laterally, they step up or down from one stratigraphic horizon in the host succession to another. Successive concordant and transgressive segments create a 'step and stair' geometry (Francis, 1982). In 3D, sills and sill complexes commonly develop a saucer- or bowl-shaped overall architecture. Computer-aided three-dimensional visualization of seismic reflection data for sill complexes (Thomson, 2004; Thomson and Schofield, 2008) reveals fascinating detail on how sill systems are emplaced, showing how individual sills advance laterally outward by extending finger-like lobes reminiscent of pahoehoe toes (Fig. 4.4a; cf. Fig. 2.2b and Plate 9.19), and how peripheral concentric dykes may transport magma from the central 'saucer' to an outer elevated rim in flat–ramp–flat style, in the form of a rimmed soup bowl (Fig. 4.4b).

Some sill complexes – like major dyke swarms – transport mafic magma laterally over huge distances in the crust: there is evidence that Ferrar sill magmas, for example, flowed laterally for as much as 4000 km from a single source, probably located in the Africa–Antarctica rifted margin (Storey and Kyle, 1997; Leat, 2008).

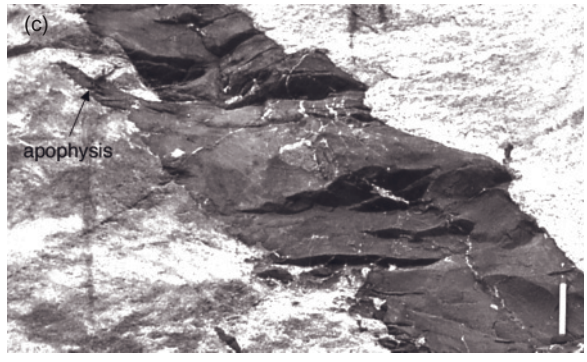
What factors determine whether basaltic magma is emplaced in the form of a dyke or a sill? A magma body in the crust will expand in the direction of least resistance. Figure 4.5(a) shows in cross-section the stresses acting at the tip of a propagating dyke. Upward extension of the tip (from z_1 to z_2) is propelled by the internal magma pressure P_m and resisted by (i) the least principal component σ_3 of the regional stress field, plus (ii) the tensile strength κ of the country rock (which has to be overcome before the crack can extend – typically ~50 MPa). The dyke will propagate upward only if:

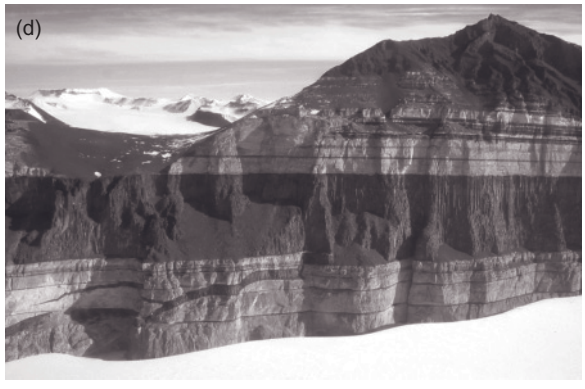
$$P_m > \sigma_3 + \kappa \qquad [4.1]$$

In rocks in which κ is independent of direction (i.e. in rocks with no bedding or strong fabric), the normal to a dyke surface approx-

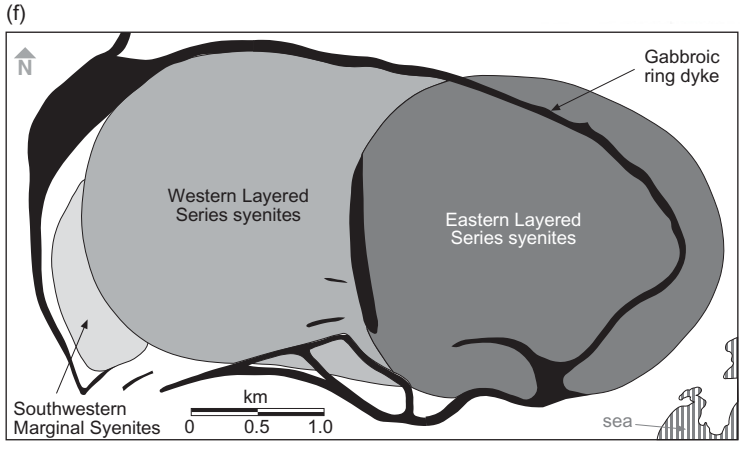

(a)


(b)
country rock
dyke
chilled margin


(c)
apophysis


(d)


(e)


(f)
N
Gabbroic
ring dyke
Western Layered
Series syenites
Eastern Layered
Series syenites
Southwestern
Marginal Syenites
km
0
0.5
1.0
sea

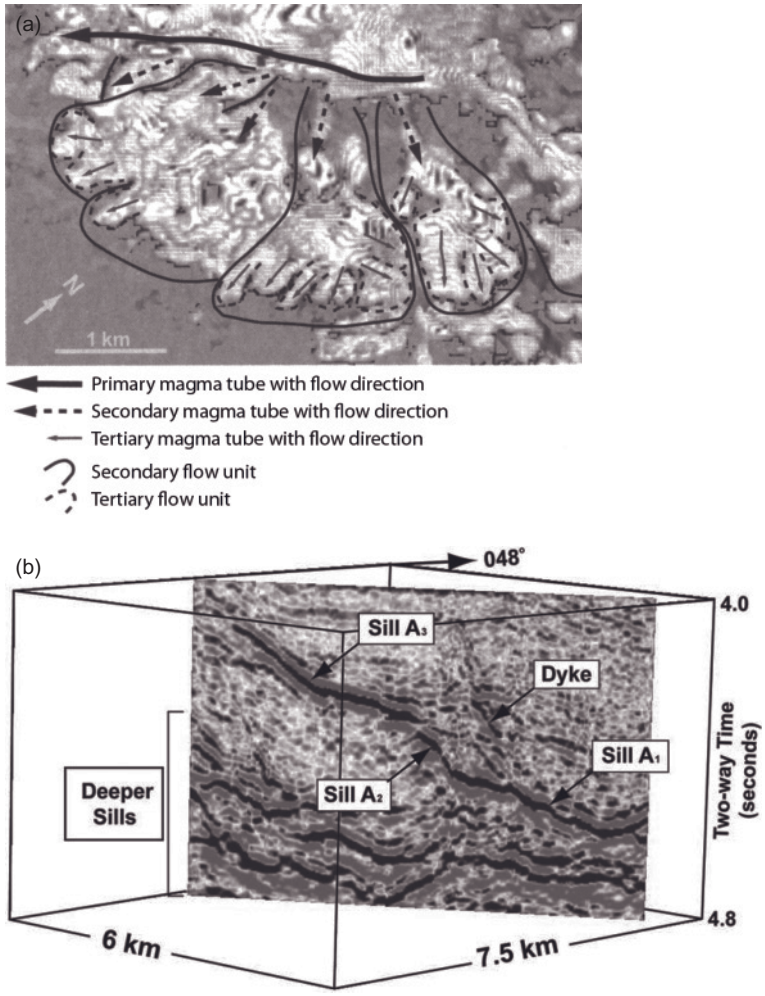


Fig. 4.4 (a) 3D seismic volume image of part of a primary flow unit within the hybrid sill complex beneath the North Rockall Trough. Secondary magma tubes, feeding secondary flow units, can be seen branching from the primary magma tube. Secondary flow units can also be seen to subdivide into lower-order flow units (reproduced from Thomson, 2004 by permission of the Geological Society of London). (b) Seismic section containing sills within the Flett Basin (NE of the Rockall Trough). Note that 'Sill A' can be shown to consist of three distinct segments producing a flat–ramp–flat morphology (reproduced from Thomson and Schofield, 2008 by permission).

Fig. 4.3 (a) Dense dolerite dyke swarm, E Greenland; earlier dykes (up to 1.5 m in thickness) have undergone post-emplacement tilting – younger dykes dip more steeply and exhibit clearer jointing.* (b) Chilled margin of a dyke; note the increasing grain-size towards the dyke interior (right) – 10 cm pen-knife for scale.* (c) irregular dyke showing **apophysis**; length of hammer 35 cm.* (d) Approximately 300 m-thick dolerite sill and discordant apophysis of the Ferrar sill complex cutting rift-margin sediments of the Beacon Supergroup in the Transantarctic Mountains, capped by comagmatic Kirkpatrick Basalts (photo J. Bédard, reproduced by permission); (e) Gently inclined dolerite cone sheets 1.5–2 m thick, west of Mingary pier, Ardnamurchan, Scotland; photo C.H. Emeleus from Emeleus and Bell (2005) reproduced by permission (IPR/103-27CA British Geological Survey © NERC. All rights reserved); (f) sketch map of a gabbroic ring dyke, Kûngnât intrusion, S Greenland (after Emeleus and Upton, 1976); white represents Proterozoic gneiss country rocks.

*Photo taken by the author during field work for the Geological Survey of Denmark and Greenland and reproduced by their permission.

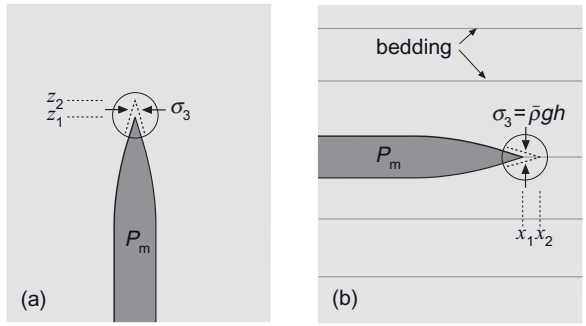


Fig. 4.5 Vertical sections showing stresses acting at the tip of (a) a propagating dyke and (b) an extending sill. σ_3 is the least principal compressive stress in the crust, $\bar{\rho}$ is the mean density of rocks overlying the sill (kg m^{-3}), g is the acceleration due to gravity (9.807 m s^{-2}), and h is the depth of emplacement equal to thickness of overburden (m).

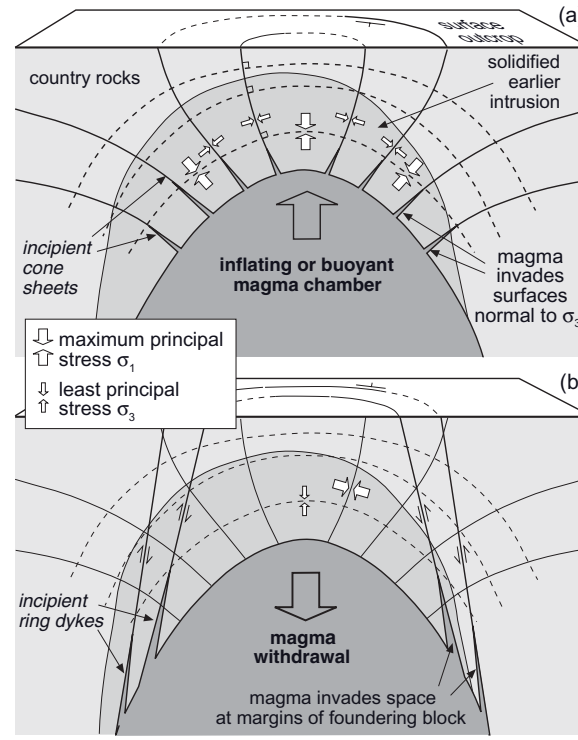


Fig. 4.6 Stress trajectories above a magma chamber; diagram following Anderson (1938) as amended by Jeffreys (1938). (a) Larger white arrows and dashed lines show the trajectories of maximum compression above an inflating magma chamber; smaller white arrows and solid lines directions of least compressive stress normal to σ_1. (b) On reduction in magma pressure, the stress field is reversed but extensional failure leads to ring fractures *oblique* to the principal stress directions.

imates to the direction of least principal compressive stress σ_3 at the time of emplacement, which must have acted in a horizontal direction and have been *less* than the vertical lithostatic load. When invading fractured rocks, dykes occasionally branch, or develop **apophyses** (Fig. 4.3c) or exploit ***en echelon*** fractures.

Sill emplacement, on the other hand, occurs at relatively shallow depths where the lithostatic load, acting vertically, constitutes the least principal stress (Fig. 4.5b). In these circumstances the requirement for lateral propagation (from x_1 to x_2) is:

$$P_m > \sigma_3 + \kappa = \bar{\rho}gh + \kappa \approx \bar{\rho}gh \qquad [4.2]$$

(symbols defined in the caption to Fig. 4.5). In shallow sedimentary rocks, steam generated by contact between magma and pore water may assist in overcoming the tensile strength κ of the wall-rocks, making it effectively zero. Sill propagation is likely to occur in these circumstances if the magma pressure simply exceeds the lithostatic load.

Minor intrusions that are centred on larger plutons usually adopt arcuate shape in plan view. Cone sheets are intrusive sheets that dip *inward* towards an intrusive complex (Figs. 4.3e, 4.5a), typically at a shallow angle, collectively forming an arcuate outcrop pattern. A **ring dyke** is an arcuate intrusive sheet, partially or wholly surrounding a pluton (Figs. 4.3f, 4.5b), that has vertical or steeply *outward* dipping contacts. Cone sheets and ring dykes usually cut (and therefore postdate) the upper parts of the plutonic complex with which they are associated, but they often extend into surrounding country rocks too (Fig. 4.3f). Cone sheets represent uplift and are formed when a magma chamber undergoes inflation. In Fig. 4.6(a), the fatter white arrows represent directions of maximum compression (σ_1) in these circumstances; smaller white arrows indicate trajectories of least compressive stress (σ_3), – perpendicular to σ_1 – which magma most readily invades. Ring dykes, on the contrary,

are associated with reduction of magma pressure (e.g. following surface eruption) and associated roof subsidence, as in Fig. 4.6(b): as often happens with extensional failure (Shaw, 1980), ring fractures are likely to form *obliquely* to the principal stress directions.

Gabbro plutons

Larger intrusions of gabbro (some with associated ultramafic or anorthositic components) range in scale from just a few kilometres in diameter to the vast 450 km east–west extent of the Bushveld Complex in South Africa. Determining an intrusion's shape in three dimensions is often made difficult by having to infer it through a sub-horizontal two-dimensional erosion surface and beneath cover rocks. Gabbro intrusions seem to exhibit a variety of geometries depending partly on the scale of the intrusion (Table 4.2). Moderate-size gabbroic intrusions may be broadly funnel-shaped (e.g. Skærgaard in E. Greenland;[4] Kiglapait in Labrador), bowl-shaped (e.g. Fongen-Hyllingen in Norway), giant dykes, or dyke-like with a funnel-shaped cross-section (e.g. the Great Dyke[5,6] in Zimbabwe; Muskox in Canada). The largest basic-ultrabasic intrusions tend to take the form of **lopoliths** (e.g. Bushveld[6] in South Africa). For a significant proportion of important mafic/ultramafic complexes, however, the original form has been obscured by faulting (e.g. Rum,[6,7] Hebrides), by tectonic deformation (e.g. Fongen-Hyllingen; Windimurra, W. Australia), by later intrusions (e.g. Cuillin,[6] Skye, Hebrides) or most commonly by cover (e.g. Stillwater[6] in Montana).

INTERNAL FORMS, STRUCTURES AND LAYERING

Minor intrusions

Most minor intrusions emplaced at shallow depths into cool country rocks form chilled margins (Fig. 4.3b) where crystal growth has been impeded by rapid cooling.

Some thick sills, for example the 125 m-thick alkali dolerite Shiant Isles Sill in the Hebrides (Gibb and Henderson, 2006) and the 300 m-thick tholeiitic Palisades Sill in New Jersey exhibit an olivine-rich layer near the base of the intrusion. Such *differentiated* sills were widely believed to reflect gravitational settling of early-formed dense minerals during slow cooling of an initially homogeneous magma body. However recent work suggests that the Shiant Isles Sill is the product of multiple intrusion (Gibb and Henderson, 2006), and that the basal olivine-rich zone of the Palisades Sill represents a separate injection of crystal-rich suspension (Husch, 1990; Gorring and Naslund, 1995). The Palisades Sill has a **pegmatitic** zone roughly two-thirds of the way up where final dregs of melt seem to have crystallized, suggesting that crystallization occurred downward from the roof as well as upward from the floor.

Some dykes and sills are *composite*: that is, their central parts have visibly different composition from the intrusion margins, suggesting that a second intrusion of different magma has exploited the same fissure or weak horizon, possibly before the first had completely solidified.

Igneous layering in gabbro plutons

Many gabbro plutons exceeding a few hundred metres in their smallest dimension exhibit igneous **layering**.[8] In its most obvious form, layering means the upward repetition of planar or shallow trough-shaped layers (centimetres to metres thick) that differ in relative mineral proportions (**modal** composition) to an extent that is obvious in the field. This can vary from a simple succession of thin bands richer in ferromagnesian minerals (Fig. 4.7a) to layers that are beautifully internally graded, from holomelanocratic (Fig. 1.3) at the base of each layer to mesocratic or leucocratic at the top, either stacked directly upon each other (Fig. 4.7b) or interspersed with homogeneous gabbro (Fig. 4.7c).

To form such layers in a plutonic rock requires some kind of crystal-sorting process

[4] The locations of these intrusions are shown in Fig. 4.13.
[5] A linear array of separate magma chambers at depth that merge at higher structural levels.
[6] Gabbros occur in association with ultramafic cumulates in these complexes.
[7] This is the currently preferred spelling; it appears widely as 'Rhum' in older literature.
[8] R.G. Cawthorn (pers. comm.) suggests layering may be found in intrusions as small as 300 m thick.

Table 4.2 Some important layered gabbroic intrusions: form, age, tectonic setting, associated rock types and mineral deposits. See Cawthorn (1996).

Form	Examples	Age/Ma	Tectonic setting	Rock types associated with gabbroic rocks	Mineral deposits (bold = producing)*	Recent description
Funnel-shaped	Skærgaard, E Greenland	55	Plume-related passive margin	Ferrodiorite	Au, PGE	Irvine et al. (1998), Andersen et al. (1998), McBirney (1996)
	Kiglapait, Labrador	1300	Anorogenic	Syenite		Yang and Morse (1992)
Lopolith or bowl- shaped	Fongen-Hyllingen, Norway	430	Synorogenic	Quartz syenite		Wilson and Sørensen (1996)
	Bushveld, South Africa	2060	Possible LIP Hatton, (1995)	Ultramafic cumulates, ferrodiorite	**PGE, Cr, V, Cu, Ni**	Eales and Cawthorn (1996), Cawthorn and Walraven (1998)
	Windimurra, W Australia	2800	Archaean greenstone belt	Ultramafic cumulates, leucogabbronorite etc.	PGE, V	Mathison and Ahmat (1996)
Giant dyke	Tugtûtoq, S Greenland	1163	Continental rift	Syenite (composite dyke)		Upton et al. (2003)
Dyke-like with funnel-shaped cross-section	Muskox, Canada	1270	Continental rift/LIP	Ultramafic cumulates	PGE, Cu, Ni, Cr	Roach et al. (1998)
	Great Dyke, Zimbabwe	2575	Continental rift/LIP	Ultramafic cumulates	**PGE, Cu, Ni, Cr**	Wilson (1996)
Other (form of intrusion less clear)	Eastern Layered Intrusion, Rum, Hebrides	60	Plume-related passive margin	Feldspathic peridotite		Emeleus et al. (1996)
	Stillwater, Montana	2700	Possibly subduction-related	Ultramafic cumulates	**PGE, Cu, Ni**, Cr	McCallum (1996)

* After Lee (1996) and Cawthorn (pers. comm.)

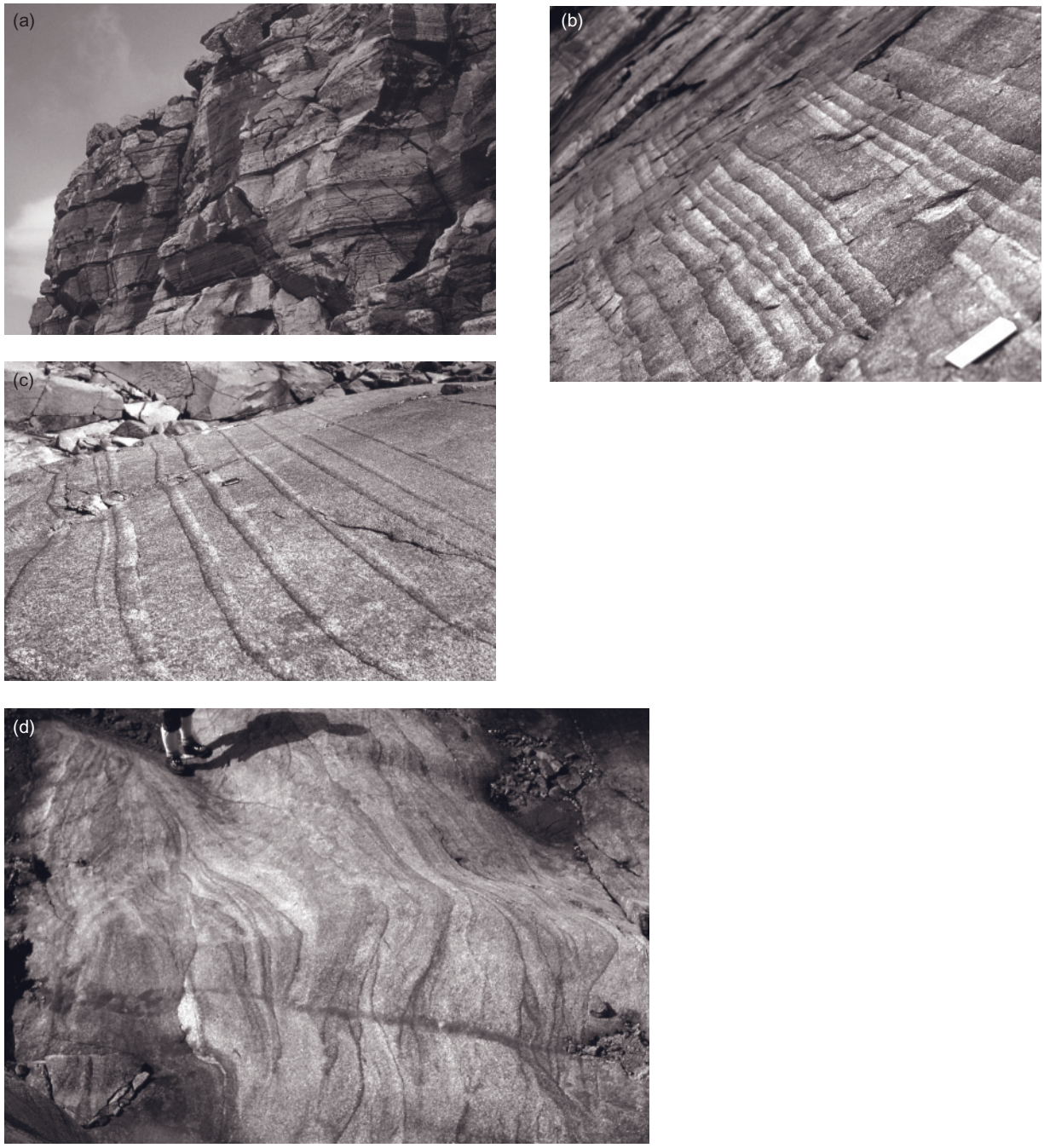


Fig. 4.7 (a) Mafic layers on various scales, Hallival, Rum, Hebrides; (b) stacked modally graded layers, MZ, Skærgaard intrusion (notebook 17 cm);* (c) modally graded layers alternating with homogeneous gabbro, MZ, Skærgaard (penknife 10 cm);* (d) cross-stratified layering, margins of the LZ, Skærgaard (the grey line across the bottom of the picture is silt deposited in a shallow gully).

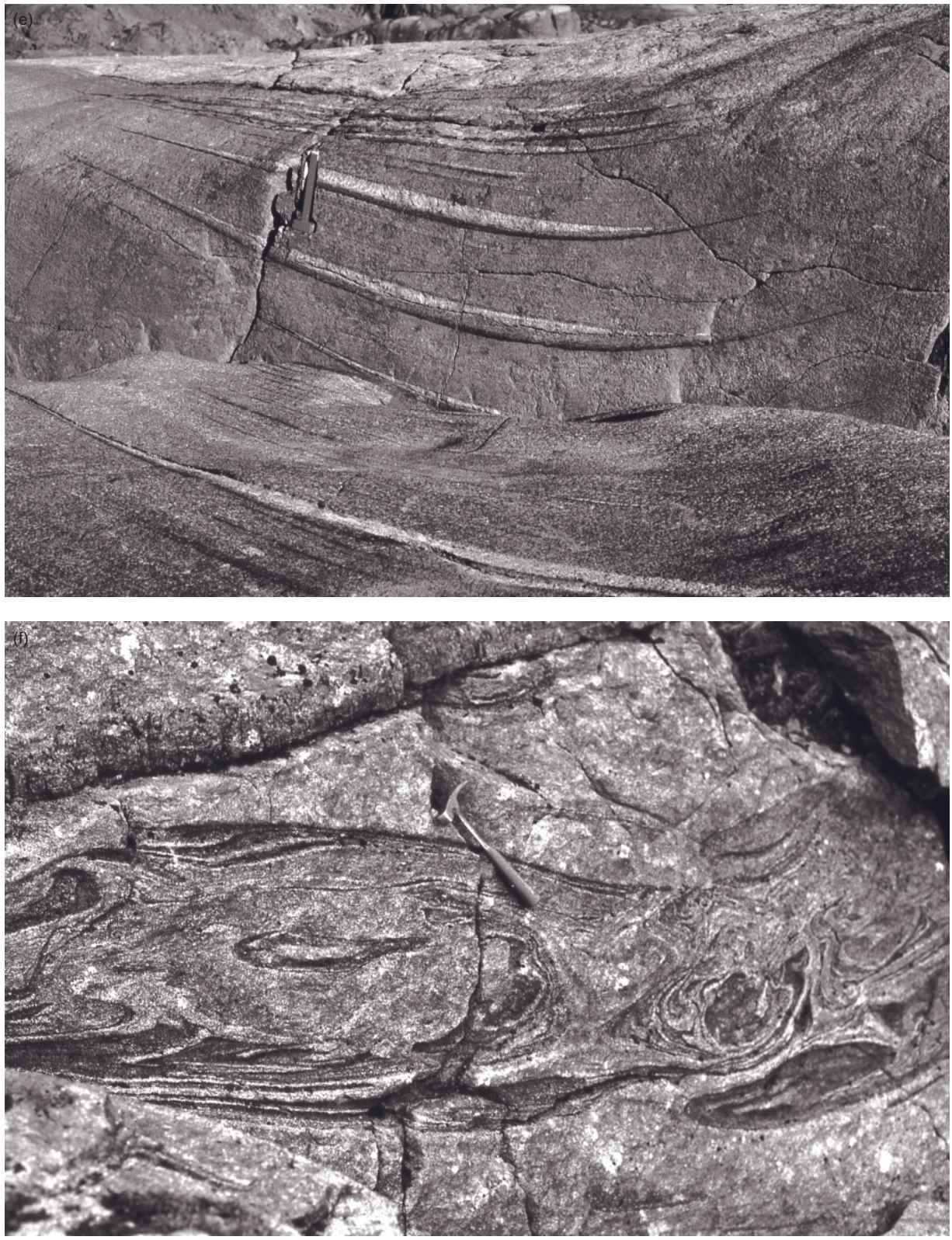


Fig. 4.7 *Continued* (e) trough layers, UZ, Skærgaard (hammer 35 cm) – when corrected for post-intrusion tilting, such troughs plunge toward the centre of the intrusion;* (f) slump structure, Hallival, Isle of Rum (hammer length 28 cm).

*Photo taken by the author during field work for the Geological Survey of Denmark and Greenland and reproduced by the Survey's permission. Figure 4.7(e) has been digitally retouched to minimize the visual impact of careless sampling.

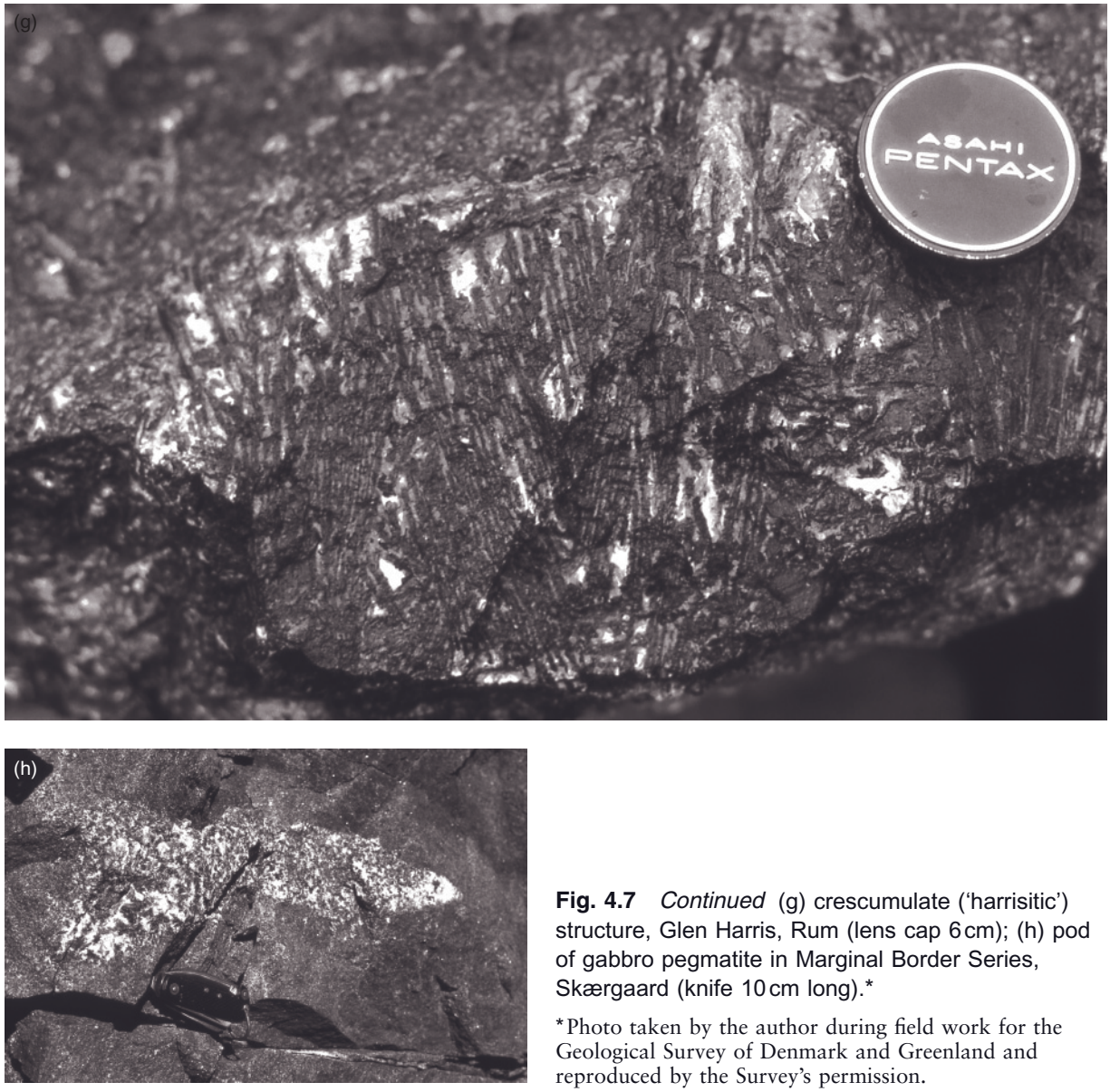


Fig. 4.7 *Continued* (g) crescumulate ('harrisitic') structure, Glen Harris, Rum (lens cap 6 cm); (h) pod of gabbro pegmatite in Marginal Border Series, Skærgaard (knife 10 cm long).*

*Photo taken by the author during field work for the Geological Survey of Denmark and Greenland and reproduced by the Survey's permission.

to have operated during crystallization and deposition. Usually the ferromagnesian minerals have accumulated preferentially at the base of each layer in Fig. 4.7b whereas felsic minerals are concentrated at the top. Plutonic rocks that are products of such mineral-selective processes – enriched in specific minerals relative to the melt composition – are called **cumulate**s. The distinction may be drawn in a cumulate rock between minerals that are believed to have accumulated by these processes (**cumulus** minerals) and those that have crystallized later from **interstitial** melt (**intercumulus** minerals). It follows that an analysis of a hand-specimen of a cumulate rock, unlike a volcanic rock, does not accurately record the composition of the melt from which it crystallized; only at a chilled margin, where cool wall-rocks have quenched the melt too rapidly for any accumulation to occur, can an estimate be made (not always reliably) of the initial melt or magma composition. Whereas in a volcanic rock mineralogy is dictated by melt composition,[9] the reverse is true in a cumulate rock: its chemical composition

[9] Mineralogy is also influenced by the conditions under which crystallization occurs.

depends primarily on the minerals it contains and the proportions in which they happen to be have accumulated (Box 1.4), which will vary from one horizon in a layer to another.

When describing layered intrusions, petrologists distinguish three types of igneous layering:

- *modal layering*:[10] layering defined by variation in the ***modal*** *proportions* of cumulus minerals with **structural height**, as seen in Fig. 4.7a; the variant shown in Figs. 4.6b,c is called *modally graded layering*;
- *phase layering:* layering defined by variation in the *identity* of the cumulus minerals with increasing structural height (Fig. 4.8b);[11]
- *cryptic layering:* layering defined by variation in the *compositions* of the cumulus minerals with structural height (Fig. 4.8b).

A few intrusions also exhibit *size-graded layering* of cumulus mineral crystals within layers, independently of modal proportions.

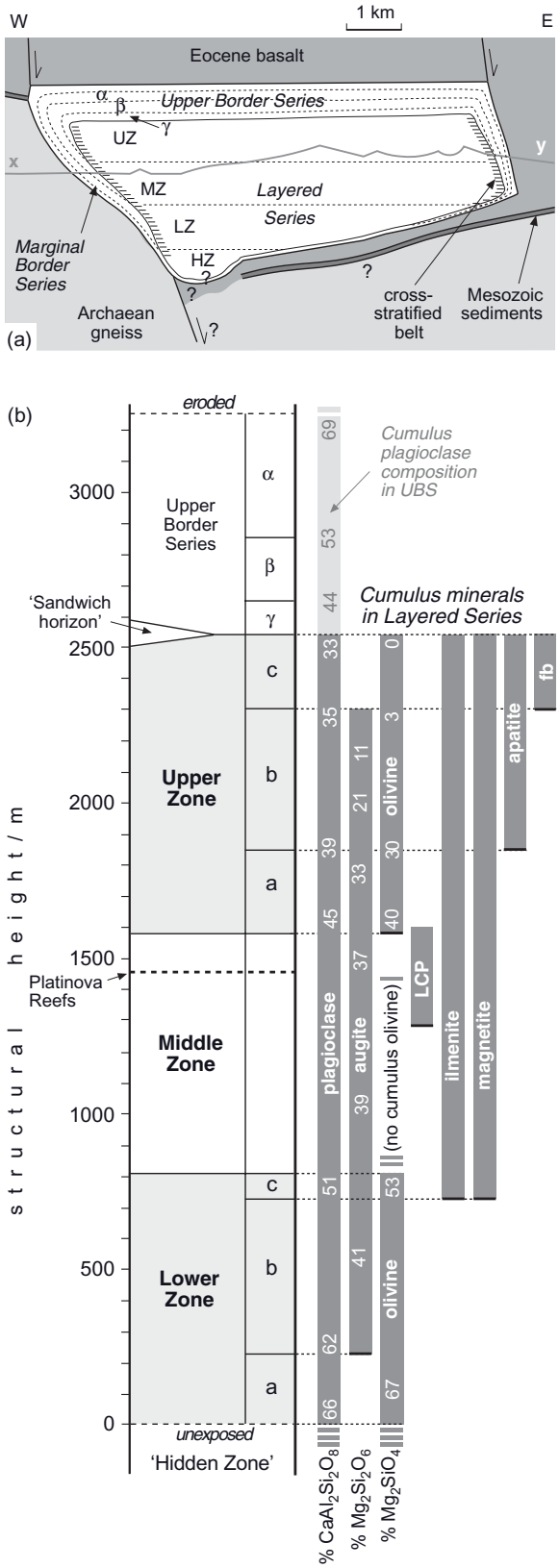
The different aspects of layering are best appreciated by studying a cross-section of a well exposed layered intrusion – the Skærgaard intrusion in E. Greenland shown in Fig. 4.8 – to illustrate the essential architecture of a layered gabbro body. Skærgaard is ideal for this purpose because it formed by closed-system crystallization of a single batch of magma, little disturbed by later magma injections that complicate many other gabbro plutons. Figure 4.8a shows the level at which the magma chamber was emplaced, close to the unconformity between Precambrian gneiss basement and cover (thin Cretaceous clastic sediments overlain by Eocene basalts). The line x–y shows the present level of exposure across the W–E section. Because the intrusion has been tilted to the SSE (not apparent in Fig. 4.8a) the present erosion surface in three dimensions actually exposes from NW to SE most of the vertical extent of the intrusion. A 'hidden zone' of unknown thickness remains concealed beneath the surface.

[10] The synonym 'rhythmic layering' is used in older literature.

[11] Irvine (1982) proposed 'crystallization layering' as a more appropriate name for this concept, but the term has not been widely adopted.

The Layered Series constitutes more than 90% of the volume of the intrusion (the remainder of the volume consisting of marginal and upper border series as shown in Fig. 4.8a). Modal layering – well developed throughout much of the Layered Series – provides a 'stratigraphic' framework in the field for documenting the order of deposition of the cumulate rocks as the intrusion crystallized, from earliest at the base to youngest at the top. The other forms of layering become apparent only from petrological study in the laboratory. The right-hand side of Fig. 4.8b shows that the cumulus mineral assemblage changes with increasing structural height. Such phase layering reflects how the set of minerals crystallizing from the melt at each stage changed as crystallization progressed; it provides the basis for dividing the exposed Layered Series into Lower, Middle and Upper Zones (LZ, MZ and UZ)(based on the initial presence, the disappearance, and then the reappearance of cumulus olivine), and for defining sub-zones where new cumulus minerals first appear, e.g. augite at the base of subzone LZb. By analogy with other layered intrusions (e.g. the Stillwater Complex in Montana), it is likely that the earliest cumulates to form, concealed in the unexposed 'Hidden Zone' (Fig. 4.8a), formed before plagioclase had begun to crystallize, and are therefore ultramafic in composition, though the volume of ultramafics may be small (see below).

Figure 4.8b also documents how the compositions of cumulus plagioclase, augite and olivine change progressively from bottom to top of the Layered Series. Being undetectable in the field, these systematic variations in mineral composition – recording, like phase layering, the evolution in melt composition as the magma chamber crystallized – were called 'cryptic layering' by Wager and Deer (1939). The variation in plagioclase composition has a bearing on rock nomenclature: whereas the LZ and MZ rocks fall within the definition of gabbro or troctolite, plagioclase composition in the UZ is too sodic (An < 50). The evolved rocks in this zone are properly called **diorite** and, because the mafic minerals present at this stage of cryptic layering are iron-rich, the term 'ferrodiorite' is widely used for these more evolved Skærgaard rocks.



The Layered Series is formed of crystals that accumulated on the contemporaneous floor of the solidifying magma chamber. The same changes in cumulus mineralogy are also recorded in Marginal and Upper Border Series that line the walls and roof of the intrusion (Fig. 4.8a). The Marginal Border Series (MBS) consists of two parts. The outer 'Tranquil Division' consists of homogeneous olivine gabbro that congealed immediately on to the cool walls of the chamber; chilled contacts against country rocks are preserved here and there, providing the only direct indication of initial melt composition. Inward from the Tranquil Division lies the 'Banded Division', marked by steep irregular stratification parallel to the walls, that records the same cumulate mineral 'stratigraphy', from outermost to innermost, as that seen from bottom to top of the Layered Series (Irvine et al., 1998).

The coarse plagioclase-rich gabbros of the Upper Border Series (UBS), lining the roof of the chamber, exhibit the same range of cryptic layering as the Layered Series (e.g. in plagioclase composition – Fig. 4.8b), but here it developed from the top downward. On this basis the UBS has been divided into α, β and γ zones corresponding to LZ, MZ and UZ respectively of the Layered Series. UBS rocks are also found as foundered blocks (autoliths) in the Layered Series, together with a few basaltic xenoliths from the roof above (Irvine et al., 1998). The fact that plagioclase is observed in all UBS rocks suggests that the proportion of any ultramafic rocks present in the Hidden Zone is small.

The boundary between the MBS and the Layered Series is marked by a spectacular belt of cross-stratified layering (Figs. 4.5d and

Fig. 4.8 (a) Simplified W–E cross-section of the Skærgaard intrusion, as interpreted by Irvine et al. (1998) and Nielsen (2004); the line x–y shows the present topography (a N–S section would show erosion to deeper structural levels). (b) Phase and cryptic layering in the Skærgaard intrusion (from Wager and Brown, 1968, as amended by Irvine et al., 1998) as a function of structural height (in metres); 'LCP' refers to low-Ca pyroxene (**inverted pigeonite**); 'fb' refers to the pyroxenoid ferrobustamite that takes the place of Fe-rich augites.

4.6a) that records the erosion, slumping and re-deposition of cumulus deposits at the break of slope where downward magma convection currents were deflected across the floor of the chamber. Cross-stratification adjacent to the walls is evidence for persistent, albeit fluctuating, large-scale convection currents throughout the crystallization history of the magma chamber. 'Trough bands' are stacks of synformal modally graded layers (Fig. 4.7e) that converge on the geographical centre of the intrusion. They hint at intense, though episodic and more localized, magma currents. They are most spectacularly developed in UZa, but less obvious examples occur quite widely (Irvine et al., 1998). The occurrence of igneous **lamination** in the Layered Series and the UBS is seen by many as further evidence for magma currents.

Cryptic layering, though the least evident in the field, is the easiest aspect of layering to explain. Figures 3.4 and 3.6 portray the course of crystallization of plagioclase and olivine solid solutions from laboratory melts. In each case, the earliest crystals to form are enriched – relative to the melt – in the more refractory end-member ($CaAl_2Si_2O_8$ and Mg_2SiO_4 respectively) and, as temperature falls, later crystals become richer in the less refractory end-member ($NaAlSi_3O_8$ or Fe_2SiO_4 respectively). The cryptic layering seen from bottom to top of the Skærgaard Layered Series is consistent with falling melt temperature as fractional crystallization advanced to more evolved melt compositions. Similar conclusions could be drawn for the changes in pyroxene composition. The continuity of cryptic layering in Fig. 4.8b is a hallmark of fractionation in a closed magma chamber. Some layered intrusions, on the other hand, exhibit abrupt reversals in mineral trends (e.g. olivine becomes more magnesian) that record influxes of fresh batches of primitive magma. Examples of intrusions where magma recharge is believed to have occurred include Rum, Muskox and Bushveld (see Chapter 5).

At the stage represented by the lowest exposed rocks of the Lower Zone, the Skærgaard melt seems to have been saturated with plagioclase and olivine, as these are the only cumulus phases here: other minerals present in these rocks crystallized later from the **intercumulus** melt. The melt composition here was analogous to point *z* in Fig. 3.3. As fractional crystallization advanced – recorded by higher levels in the Layered Series – first augite (point E in Fig. 3.3) then other minerals would have begun to crystallize as their concentrations in the melt exceeded saturation. In the Layered Series we are witnessing Nature's version of the sequence described in Equation 3.1. This aspect of *phase layering*, the progressive appearance of new cumulus minerals, is therefore consistent with experiments in simple eutectic systems.

But why does olivine *disappear* in the Middle Zone and then re-appear at the base of the Upper Zone? Explaining this entails an understanding of the Reaction Principle, as outlined in Box 4.3.

Paradoxically it is *modal layering* – the most conspicuous in the field – whose origins are most contentious. Wager and Deer (1939) proposed that igneous layering reflects the gravitational sorting and deposition of cumulus crystals – analogous to clastic sedimentation – under the influence of magma convection currents. They argued that most crystals nucleated near to the chamber roof where the country rocks bordering the intrusion were coolest and magma temperature was therefore lowest. Wager and Brown (1968) associated homogeneous gabbro layers (Fig. 4.7c) with slow steady currents (they suggested speeds of m day^{-1}) that transported crystals down the chamber walls and deposited them continuously as an accumulating crystal 'sediment' on the chamber floor. They postulated that modally graded layers (Fig. 4.7c), on the other hand, were deposited from more vigorous crystal-rich 'density currents' that surged intermittently down the walls of the intrusion (at speeds they estimated at km day^{-1}) and swept across the cumulate floor. Each density current episode delivered a carpet of suspended crystals that settled out according to density, the denser minerals settling out faster according to **Stokes' Law**[12] to produce a modally graded layer. In view of the striking quasi-sedimentary and erosional structures seen in Skærgaard (Fig. 4.7), many petrologists still envisage a role for the gravi-

[12] Modal layering suggests that Stokes' Law controls deposition in cumulates mainly through differences in crystal density (ρ_x), whereas in graded bedding in sediments (and size-layering in cumulates) grain radius *r* is the dominant parameter.

tational sorting and deposition of suspended crystals from convecting magma in generating modal layering (e.g. Sparks et al., 1993; Irvine et al., 1998), though their ideas diverge in detail from those of Wager and his coworkers.

However, an alternative school of thought explains layering in terms of *in situ* crystal nucleation and growth at the interface between the cumulate pile and the overlying melt – i.e. at the upwardly migrating 'floor' of the magma chamber (e.g. McBirney, 1996). One factor casting doubt on gravitational deposition is the possibility that plagioclase might *float* rather than sink in basaltic magma (Box 4.4). Supporters of *in situ* crystallization also argue that the adiabatic temperature drop experienced by upward-convecting melt is less than the drop in the liquidus temperature over the same depth range. Melt in the upper part of the chamber may thus be above the liquidus while that near the floor is below it, and therefore the floor is the most likely location for nucleation and crystal growth. They envisage a 'solidification front' migrating inward from the walls and upward from the base as the intrusion cools. They note that ferromagnesian minerals found at the base of each modally graded layer are characterized not only by higher densities than plagioclase, but also by simpler crystal structures (oxide, orthosilicate, chain silicate) that might nucleate more easily – and therefore earlier – than the framework-silicate plagioclase. It is therefore argued that modally graded layers are caused by differences in nucleation efficiency between minerals, as the solidification front sweeps past, rather than differences in settling rate. Some authors go further and interpret cryptic layering as evidence not of *evolution in time* of a homogeneous magma composition but of a *bottom-to-top chemical gradient in melt composition* that developed and persisted throughout the crystallization history of the magma chamber.

Some key differences between these two hypotheses are illustrated in Fig. 4.9. The divergence in current views on the mechanism of layering can be appreciated by scanning the papers by McBirney (1996) and Irvine et al. (1998) which, though addressing similar observations on the same intrusion, come to radically different conclusions. There is currently little sign of consensus or even

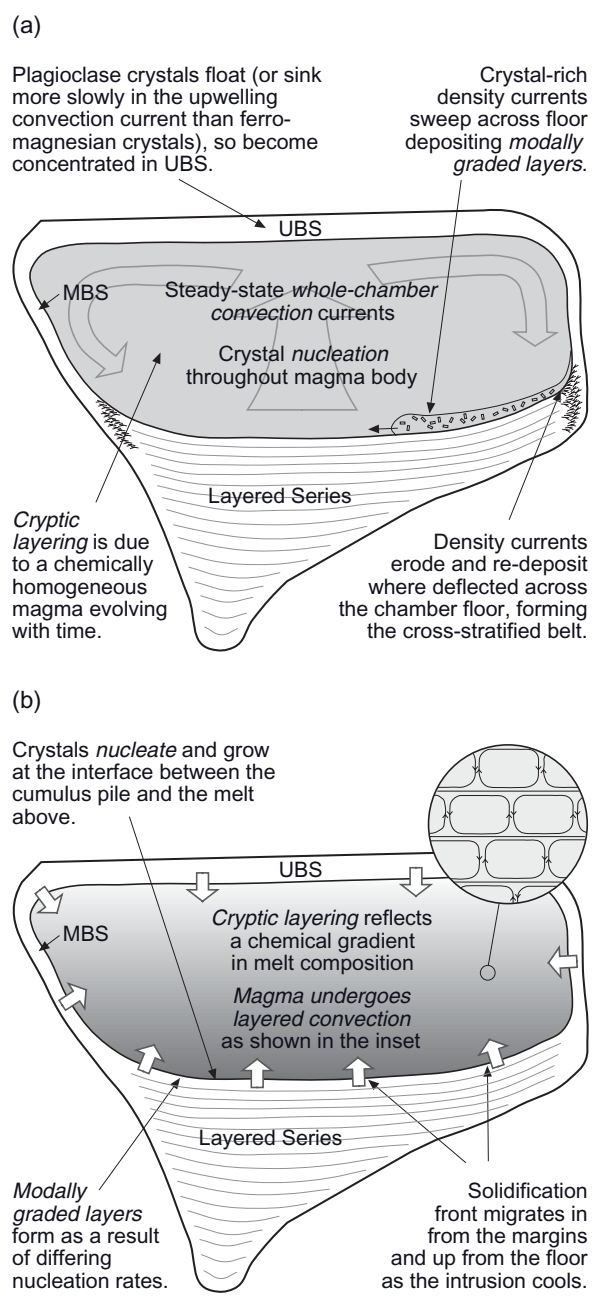


Fig. 4.9 Cartoons of a Skærgaard-type magma chamber summarizing alternative explanations of igneous layering: (a) crystal settling in a convecting magma with periodic density currents (e.g. Irvine et al., 1998); (b) in situ crystallization from a chemically stratified magma chamber (e.g. Wilson and Larsen, 1985). In (b) the inset illustrates the layered form that convection must adopt in such a zoned magma chamber (known as 'double-diffusive convection' because it entails diffusion of both heat and chemical components from one layer of cells to the next, in response to thermal and chemical gradients).

Box 4.3 The reaction principle

'In a eutectic system no mineral ever disappears. The first-formed mineral is simply joined by another, the pair by a third, and so on until all the minerals appear together in a final eutectic product (Equation 3.2). *Very different is the condition actually found, namely the disappearance of minerals … the very essence of the reaction series.'* N.L. Bowen (1922)

Why does olivine *disappear* as a cumulus mineral at the top of the Skærgaard Lower Zone and then *reappear* in the Upper Zone? The disappearance of olivine may be understood by reference to Fig. 4.3.1a, which illustrates how magnesian olivine becomes unstable in, and *reacts* with, more SiO_2-rich basaltic melts.

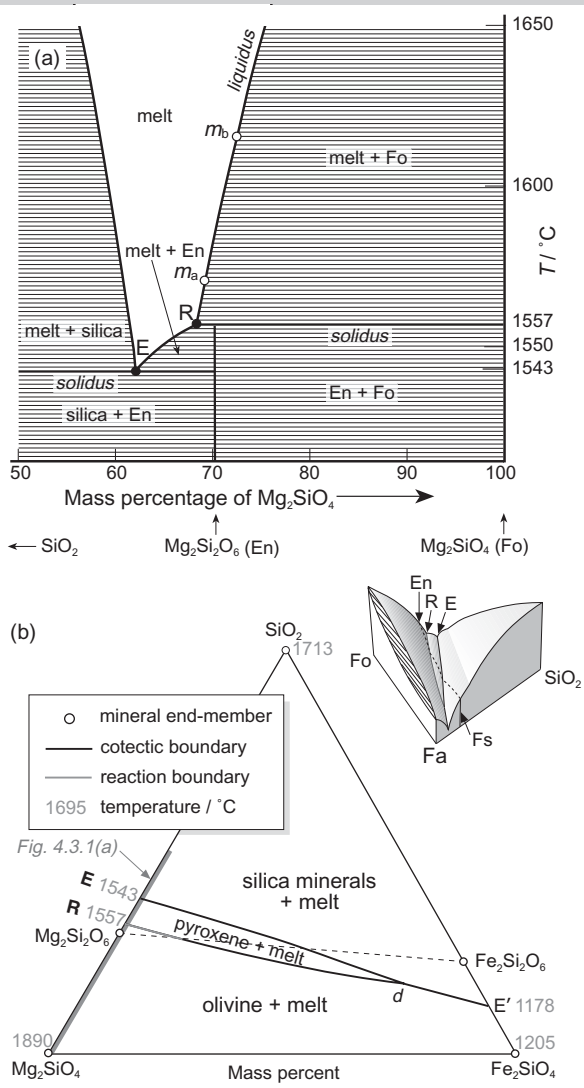


Fig. 4.3.1 (a) Part of the system Mg_2SiO_4–SiO_2 (after Bowen and Anderson, 1914) showing the reaction between melt and forsterite to form enstatite. Ruled areas represent **two-phase fields** (heavier ruling for solid-solid fields). (b) Liquidus boundaries in the system SiO_2–Mg_2SiO_4–Fe_2SiO_4 adapted from Bowen and Schairer (1935) seen in plan view. A thin dashed line marks the low-Ca pyroxene join between enstatite ($Mg_2Si_2O_6$) and ferrosilite ($Fe_2Si_2O_6$). The grey portion of the line R–*d* marks the limited region where pyroxene may form by olivine-melt reaction. The cartoon shows a perspective sketch of the liquidus surface.

Figure 4.3.1a shows the crystallization behaviour of melts whose compositions lie between forsterite (Mg_2SiO_4) and SiO_2. At first glance it resembles the binary eutectic system in Fig. 3.2 but there is one vital difference, emphasized by the *reaction point* R: this is a system having two **invariant** points. Consider melt m_a as it cools and crystallizes Fo (olivine). Its composition moves down the liquidus to the first invariant point R. This point lies at the intersection between the 'melt + Fo' field and a 'melt + En' field so an evolving melt reaching this composition coexists with both Fo *and* En (low-Ca pyroxene). Olivine ceases to be in stable equilibrium with the relatively SiO_2-rich melts to the left of R, therefore an evolving melt, on reaching R, *reacts* with olivine crystals already formed and converts them into enstatite:*

$$\underset{\text{forsterite}}{Mg_2SiO_4} + \underset{\text{melt R}}{SiO_2} \rightarrow \underset{\text{enstatite}}{Mg_2Si_2O_6} \qquad [4.3.1]$$

Under equilibrium conditions, only when every olivine crystal in contact with melt has been converted into enstatite can the melt resume its univariant evolution beyond R. From this point on, the melt will crystallize En directly until the eutectic E – the second invariant point – is reached. R can be regarded as the laboratory analogue of the boundary between LZ and MZ in Skærgaard, where olivine reacts out as a cumulus mineral and is replaced by low-Ca pyroxene.**

Why then does olivine *reappear* higher up in the Skærgaard cumulus sequence? Experiments show that the reaction relationship in equation 4.3.1 applies only to relatively Mg-rich olivine, as illustrated in Fig. 4.3.1b. The olivine series from Mg_2SiO_4 (Fo) to Fe_2SiO_4 (Fa) forms the base of the triangle, and the grey bar along the left-hand edge indicates the range of composition shown in Fig. 4.3.1a. The $Mg_2Si_2O_6$ (En) *point* in Fig. 4.3.1a appears here as one end of a *join* (shown by the dashed line) across to $Fe_2Si_2O_6$, representing solid solution in the low-Ca pyroxene series. The Fo–En reaction [4.3.1] operates only where the olivine + melt field *oversteps* this join, a phenomenon confined to the left-hand side of the diagram (where the liquidus boundary is shown grey). Tracing the detailed course of melt evolution and crystallization in this diagram involves many complexities (detailed by Bowen and Schairer, 1935). For the present purpose it is sufficient to note that the 'pyroxene + melt' field, representing the range of melt compositions capable of crystallizing low-Ca pyroxene (analogous to the MZ stage of Skærgaard melt evolution), has limited extent and pinches out at point *d*. The more Fe-rich stages of Skærgaard melt evolution (Fig. 4.2) that crystallized the olivine-bearing UZ cumulates (Fig. 4.8) corresponded to the region to the right of *d* in Fig. 4.3.1b.

Bowen's reaction principle

The reaction 4.3.1, involving the disappearance of one mineral and its replacement by a new one, is an example of what Bowen (1922) called the *reaction principle*. He saw this reaction as the first step in a *discontinuous reaction series* in which – as crystallization advances – olivine (reacting with melt) would be replaced by enstatite, then enstatite (reacting with more evolved melt) would be replaced by augite, then augite (reacting with cooler or more hydrous melt) would be replaced by hornblende, then hornblende by biotite.† Though the concept helps to explain why olivine crystals are sometimes seen rimmed by enstatite, enstatite crystals by augite (Plate 6.5) or augite crystals by hornblende, it lacks theoretical rigour and is seldom used today.

* Conversely, when enstatite melts it forms olivine + melt (an example of **incongruent melting**).

** Enigmatically the first appearance of cumulus low-Ca pyroxene is postponed to higher levels of the Middle Zone (Fig. 4.8b) according to Irvine et al. (1998).

† Bowen envisaged the discontinuous reaction series proceeding side by side with the *continuous reaction series* that occurs between plagioclase and the evolving melt in Figs. 3.4 and 3.5 (giving rise to cryptic layering).

Box 4.4 Will plagioclase sink or float?

Purely gravitational settling-out of cumulus crystals requires all cumulus minerals to be denser than basaltic melt. Ferromagnesian and oxide minerals clearly satisfy this requirement (Fig. 4.4.1) but plagioclase, owing to its relatively open, framework-silicate structure and low iron content, is much less dense. Is it sufficiently dense to sink in a basaltic liquid?

Figure 4.4.1 compares the measured density of plagioclase across its composition range (An to the left, Ab to the right) with the range of probable densities for basaltic melts: the full line shows how plagioclase density varies with composition at 25 °C, but thermal expansion will decrease the density at magmatic temperatures, as illustrated by the dashed line. Given the similarity in density between plagioclase and basaltic melt, the best answer to the question at the head of this box is 'neither': in a typical basic magma chamber, plagioclase will be almost neutrally buoyant ($\Delta\rho \sim 0$), will sink or float with minimal velocity (according to **Stokes' Law**), and in a convecting magma will tend to remain in suspension much longer than mafic minerals.

What mechanisms are available for depositing suspended plagioclase on the intrusion floor? One possibility is deposition from magma density currents which are collectively denser than the surrounding melt by virtue of the suspended crystals (mafic as well as felsic) that they carry. Another relevant factor is that the addition of even small amounts of H_2O can significantly lower the density of basaltic melts (Scoates, 2000), allowing the possibility that plagioclase may sink in more hydrous basaltic magma.

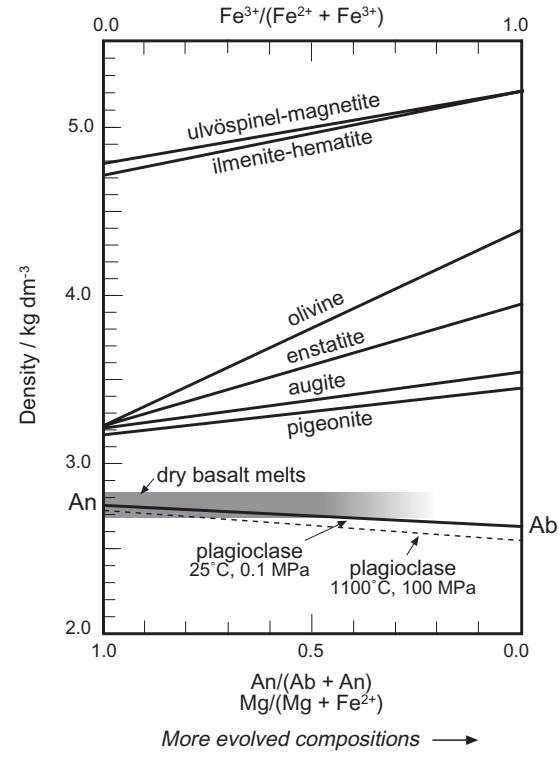


Fig. 4.4.1 Graph (after Scoates, 2000) comparing the density ranges of the main minerals in basic igneous rocks with calculated densities for basaltic melts; compositions are plotted in molar proportions. For plagioclase, the continuous line shows room-temperature density (Deer et al., 1992); the dashed line shows the density adjusted to 1100 °C and 3 km depth (using thermal expansivity and compressibility values from Gottschalk, 1997).

convergence between these two schools of thought. Another area of on-going contention concerns the chemical evolution of the melt. The change of cumulus mineral composition with advancing crystallization can be documented in great detail, but the parallel changes in *melt* composition can only be inferred indirectly since no unambiguous samples of it are available for analysis. Figure 4.10 illustrates the diversity of published melt evolution paths that different authors have proposed – which vary widely in the degree of iron- and silica enrichment inferred – and emphasizes how little we actually *know* about the Skærgaard melt composition and its evolution. Opinions vary even with regard to its initial composition (large symbols in Fig. 4.10).

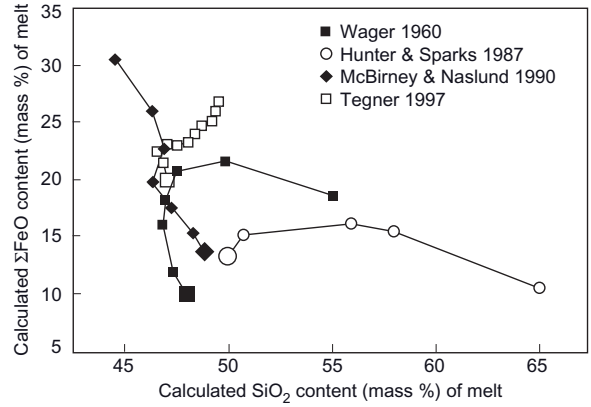


Fig. 4.10 Postulated melt evolution paths for the Skærgaard Intrusion, calculated according to the models of the authors listed, illustrated by a ΣFeO *versus* SiO_2 plot (adapted from Jang et al. 2001; copyright Elsevier). 'ΣFeO' represents the total iron content expressed as FeO. Larger symbols represent supposed initial melt compositions.

Metalliferous mineral deposits associated with layered mafic intrusions

Many layered mafic–ultramafic intrusions host important economic deposits of platinum group elements (PGE), chromite and/or base-metal sulphides. The world's supply of platinum, for example, is dominated by the huge Bushveld Complex of South Africa (Fig. 4.13 and Table 4.2). Precious metal deposits in layered intrusions tend to be highly concentrated at particular horizons in the cumulate sequence; mining geologists often refer to them as reefs. These horizons consist of – or are associated with – distinctive groups of cumulate layers that can be traced laterally for great distances. The renowned Merensky Reef in the norites of the Bushveld complex, for instance, can be traced along strike for about 180 km in the western limb of the complex and a further 120 km in the eastern limb. There are also a number of economically important **chromitite** layers, one of which (the Upper Group 2 chromitite) also contains important **PGE** reserves. The situation is similar in the Stillwater complex (Table 4.2): PGEs are concentrated in a horizon (here called the Johns-Manville or 'J-M' Reef) in layered norites some way above the horizon marking the first appearance of cumulus plagioclase, and they may be related to a major influx of fresh magma. In the Stillwater norites, however, chromite is largely absent, the major concentrations being confined to the lower ultramafic rocks.

Skærgaard, though smaller, shows parallels in its PGE distribution. The 'Platinova Reefs'[13] (Fig. 4.8b) consist of about ten PGE-rich zones – containing up to 4 ppm Au and 3 ppm Pd – that are associated with the 'Triple Group', a prominent trio of **macro-rhythmic** layers near to the top of the MZ (Fig. 4.8b). The precious metals are present here as minute grains of metal alloy associated with sulphides which clearly formed at magmatic temperatures (Nielsen, 2006). It is unclear, however, whether the alloy grains were precipitated from the melt directly, or initially as droplets of immiscible sulphide melt that subsequently decomposed (Andersen et al., 1998; Nielsen et al., 2005; Andersen, 2006).

HOW DOLERITES AND GABBROS CRYSTALLIZE – EVIDENCE FROM TEXTURES

Megascopic structures like phase and cryptic layering provide an archive of the fractional crystallization history of a magma chamber, telling us for example whether the chamber filled once with magma and thereafter remained essentially closed (e.g. Skærgaard) or whether the chamber was constantly being replenished with new batches of magma as

[13] Named after a former concession-holder, Platinova Resources Ltd.

crystallization progressed (e.g. Bushveld – Cawthorn and Walraven, 1998). This section, on the other hand, examines what can be learned from the *microscopic* textures in such rocks.

Grain size, nucleation and order of crystallization

Grain size in magmatic rocks depends on the degree of supercooling at which crystallization occurs, which in turn depends on the rate of cooling experienced by the magma (Box 2.3). In an intrusive body, magma cools most rapidly (and therefore fine- or medium-grained rocks are most likely to form):

1. near the margins of an intrusion (Fig. 4.3b), especially at shallow depth where wall-rocks are cooler;
2. in a small or tabular intrusion (large surface area/volume ratio) such as a dyke.

The finest-grained intrusive rocks are likely to be found where both of these factors work together. Coarse-grained rocks, on the contrary, form in the interiors of larger intrusions.

Overall grain-size can be influenced by factors other than cooling rate. Near to the margins of the Skærgaard intrusion, numerous patches of gabbro pegmatite are seen (Fig. 4.7h) in which crystals may grow up to 15 mm or more, significantly coarser than the host gabbro. They probably reflect the infiltration of water vapour from wall-rocks. As well as markedly lowering a melt's solidus temperature and the degree of supercooling, dissolved water promotes higher diffusion rates in the melt, promoting faster crystal growth so that coarser crystals result. An alternative explanation (Irvine et al., 1998) is that water-vapour infiltration may trigger re-melting of already-crystallized gabbro to form a coarser-grained assemblage.

The relative ease with which different minerals (a) nucleate and (b) subsequently grow from the melt lies behind a distinctive class of textures seen in many dolerites and related rocks. Plate 4.1 shows such a rock in which relatively large, *anhedral* crystals of augite have enveloped a profusion of smaller, randomly orientated, euhedral laths of plagioclase. The large size of the augite crystals arises from their inability to *nucleate* as efficiently as plagioclase (Box 2.3). This **ophitic** texture represents the growth of small plagioclase crystals on abundant nuclei, while the growth of augite was confined to the one or two nuclei available (within this field of view), resulting in far fewer but much larger pyroxene crystals. The intuition that plagioclase began to crystallize before augite here is not necessarily true (Vernon, 2004). The same interpretation applies to **sub-ophitic** texture, in which plagioclase is only partially enveloped by augite (Plate 4.2).

Ophitic and sub-ophitic textures are special cases (augite enclosing plagioclase) of a more general **poikilitic** texture, a term that embraces all instances of multiple crystals of one (or more) mineral(s) being enclosed by large crystals of another. Plate 4.3 illustrates another special case – poikilophitic texture – in which plagioclase *and* another mineral (in this case olivine) are enclosed by augite. The proliferation of names here is regrettable; there is much to be said for referring to *all* of these nucleation-mediated textures simply as 'poikilitic'.

Can we learn anything about order of crystallization from such textures? Note that in Plate 4.3 the enclosed plagioclase laths (and olivine crystals) tend to increase in size from the centre to the margins of the enclosing grain, whereas in Plate 4.1 no such spatial correlation exists. A possible reason for this difference is illustrated in Fig. 4.11. When an augite crystal *begins* to grow at the same time as plagioclase (Fig. 4.11a), early enclosure prevents subsequent growth of plagioclase laths that happen to lie near to the augite nucleus, whereas those further away have longer to grow before being incorporated (cf. Plate 4.3). When the augite begins to grow somewhat later than plagioclase (Fig. 4.11b), then no such systematic size variation develops (Plate 4.1).

Cumulate textures, zoning and changes in melt composition

'Cumulate' is a conceptual term rather than a descriptive one, and the main observational evidence pointing to cumulate origin (e.g. modal or cryptic layering) often occurs on a larger scale than a single hand-specimen, let alone a thin section. What features might characterize a cumulate in thin section? In

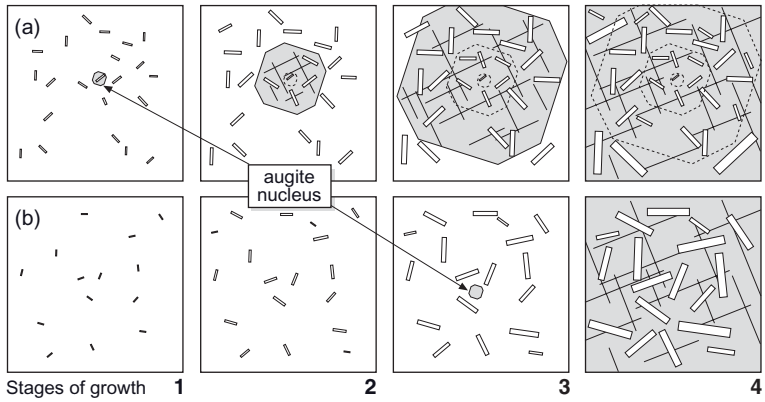


Fig. 4.11 Evidence for order of crystallization in ophitic/poikilitic texture. Each row of cartoons shows (from left to right) crystal development at 4 stages in the formation of ophitic texture, for two scenarios: (a) when augite and plagioclase begin to crystallize *together* – the smallest plagioclase laths mark the centre of growth of the augite oikocryst, where early enclosure prevented subsequent growth (based loosely on Shelley, 1992); (b) when augite begins to crystallize significantly *later* than plagioclase – the size of plagioclase crystals does not correlate with position in the augite crystal, because all had longer to grow prior to enclosure.

textural terms, the essence of a **cumulate** is a framework of touching crystals,[14] euhedral or subhedral in shape, that have been deposited by some crystal-sorting process – the **cumulus** minerals – with the spaces in between them filled by grains that have crystallized in situ from **intercumulus** melt (Irvine, 1982). Plate 4.4 shows an example from the Lower Zone of the Skærgaard Intrusion, in which euhedral plagioclase laths and equant olivine crystals constitute an obvious framework of cumulus minerals, with intercumulus augite oikocrysts[15] filling the interstices in between them. Whether the augite entirely postdates the olivine and plagioclase, or represents selective overgrowth on a limited number of cumulus augite nuclei formed at the same time, is unclear. A cumulate in which this distinctive framework of touching euhedral crystals is preserved, and which contains a significant proportion of several intercumulus minerals, is called an *orthocumulate* (Wager et al., 1960). In plagioclase-rich cumulates, euhedral feldspar laths may be deposited in a subparallel manner (Plate 4.5), producing a depositional foliation known as igneous **lamination**; because in this case the cumulus crystals are able to pack together more compactly, there is less void space between for intercumulus melt, and therefore less intercumulus matrix present.

However, the simple framework of touching euhedral crystals that identifies a cumulate in thin section (Plate 4.4) is often obscured by later modification, either at the late-magmatic stage or after solidification. Rather than forming isolated pockets, intercumulus melt may keep open diffusion or melt-migration channels to the main melt reservoir above, allowing re-equilibration. Crystallization of the intercumulus melt may then, instead of creating discrete intercumulus minerals, simply enlarge the existing cumulus crystals, forming overgrowths that in extreme cases completely fill the pore space between them, forming what is called an *adcumulate* (Wager et al., 1960). The original euhedral or subhedral outline of the cumulus crystals is thus obliterated; the texture now reflects crystal growth confined by nearest neighbours, yielding anhedral, often unzoned grains that may preserve little textural evidence of their cumulus beginnings.

Crystal shape may alternatively be modified by solid-state grain-boundary adjustment that occurs when magmatic rocks cool very slowly (Vernon, 2004): just as a liquid droplet minimizes its surface area under the influence of surface tension, so a hot polycrystalline

[14] One must remember that a thin section offers only a two-dimensional view of what in reality is a three-dimensional framework: minerals that actually touch in 3D may only 'nearly touch' in the plane of a single thin section.

[15] Opaque oikocrysts also occur outside the field of view.

assemblage will adjust crystal boundaries to minimize interfacial free energy. The hallmark of the resulting minimum-surface-area configuration is a polygonal arrangement of relatively straight crystal boundaries meeting at angles close to 120°. The ultimate example of such grain boundary adjustment is seen in many mantle peridotites (Plate 5.6). An example of such 'textural equilibration' in a cumulate rock is shown in Plate 5.2.

A particularly distinctive cumulate texture is illustrated in Fig. 4.7g and Plate 4.6. It consists of sub-parallel, plate-like olivine crystals (seen edge-on in Plate 4.6) that have grown perpendicular to the layering in parts of the Rum intrusion, notably in Glen Harris. Wadsworth (1961) attributed such olivine-crescumulate (or 'harrisite') textures to *in situ* growth of olivine upward from the floor of the intrusion into **supercooled** melt that was only gently convecting or had become stagnant. Crescumulates and **comb layering** indicate crystallization under conditions in which crystal growth rate G greatly exceeds nucleation rate N, though the cause is often unclear.

Intra-crystalline textures

Plutonic rocks not only crystallize slowly from the melt; they continue to cool slowly *after* crystallization is complete. Slow cooling allows time for individual minerals to transform into more stable crystallographic forms. In gabbros, it is the pyroxenes – with their temperature-dependent solid solutions and crystal symmetry – that illustrate such changes most clearly (Box 4.5).

Plate 4.7 illustrates a phenomenon known by two alternative names: unmixing or exsolution. The host crystal is a twinned augite that, at magmatic temperatures, contained a significant amount of low-Ca pyroxene (LCP) in solid solution (Fig. 4.5.1 in Box 4.5). At lower temperatures, however, low-Ca pyroxene is less soluble in augite and tends to **exsolve**. A rapidly cooled augite phenocryst in a volcanic rock would retain this LCP component in metastable solid solution, but when slowly cooled – as in this case – the crystal expels the excess of LCP in the form of lamellae of a distinct LCP (enstatite or pigeonite) phase. The lamellae pointing N–S in Plate 4.8 are in extinction, indicating that they consist of orthopyroxene (enstatite); monoclinic pigeonite would extinguish when the lamellae were oblique to the polars. Plate 4.9 shows a particularly fine example of orthopyroxene lamellae in augite.

Plate 4.7 shows a crystal of **inverted pigeonite** (A in extinction) with two generations of augite exsolution lamellae. The grain in extinction was originally pigeonite but is now enstatite. The thicker augite lamellae formed during inversion from the monoclinic crystal symmetry of pigeonite to the orthorhombic symmetry of enstatite (explained in Box 4.5); the thinner lamellae were exsolved during subsequent cooling of the enstatite.

The most distinctive internal feature of plagioclase is multiple twinning (Box 4.1), which may occasionally be coarse enough in some gabbroic rocks to be visible megascopically (Fig. 4.12).

Reaction textures

Augite crystals in some gabbros exhibit a rim or mantle of hornblende, which reflects the build-up of dissolved water (and **incompatible** components like K_2O) in the more evolved interstitial melt. This, together with falling temperature, enables hornblende – a hydrous mineral – to become stable (Box 6.2) and either replace the outer parts of the augite crystal or grow as a rim on it. Such a mantle is an example of a primary (magmatic) overgrowth.

In slowly cooled rocks like gabbro, reaction may also occur between adjacent crystals even after complete crystallization. Such solid-state (sub-solidus) reactions produce a **corona** reaction rim rather different from a primary overgrowth. The key difference is that the

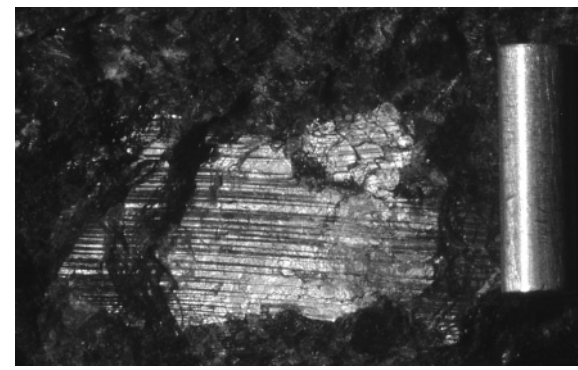


Fig. 4.12 Megascopic multiple twinning in plagioclase, anorthosite, Morin complex, Quebec; steel bar 1 cm long (photo K. D'Souza).

reaction products do not form a continuous rim around either crystal, but are found only at boundaries where the two reacting minerals are in mutual contact.

Sometimes grain boundaries in plutonic rocks are decorated by complex fine-grained, worm-like intergrowths of two minerals, called **symplectite** (Plate 4.10). Symplectites are conventionally regarded as products of metamorphic (sub-solidus) reactions between specific neighbouring minerals (Vernon, 2004). However, recent work on plagioclase–olivine–pyroxene symplectites seen in Skærgaard gabbros – bordering oxide grains (Plate 4.11) and occurring along grain boundaries and at triple junctions – suggests that these examples may have formed by reaction between the cumulus crystals and reactive residual melts percolating along grain boundaries during the final stages of crystallization (Stripp and Holness, 2006).

Other post-magmatic textures

Some textures in plutonic rocks develop at a very late stage. Plate 4.13 shows recrystallization of large strained plagioclase into subgrains at the boundaries of original crystals as a result of post-magmatic deformation. Such recrystallization – sometimes called 'core-and-mantle microstructure' (Vernon, 2004) – is typical of some massif-type anorthosites and related rocks (see the section entitled 'Anorthosites, norites and troctolites' below), and probably reflects strain generated during the emplacement process.

Alteration of magmatic minerals generates a diversity of textures, many of which will be illustrated in later chapters. One example appears in Plate 4.12, which shows a troctolite in which olivine has been partially altered to serpentine. This plane-polarized light (PPL) view emphasizes two distinctive textures associated with serpentinization:

- Alteration to serpentine is concentrated along the irregular cracks that are characteristic of olivine, here picked out by opaque material. Magmatic olivines contain FeO but serpentine accommodates practically none of it. Iron oxide expelled during serpentinization (represented approximately in equation 4.3) appears as finely disseminated opaque oxides associated with serpentine:

$$\underset{\text{typical gabbroic olivine}}{6(Mg_{0.75}Fe_{0.25})_2\,SiO_4} + \underset{\text{fluid}}{6H_2O} + 0.5O_2 \rightarrow \underset{\text{serpentine}}{3Mg_3Si_2O_5(OH)_4} + \underset{\text{magnetite}}{Fe_3O_4} \qquad [4.3]$$

- Close inspection reveals radiating systems of cracks traversing the surrounding plagioclase crystals, centred on each altered olivine crystal. Why have these cracks formed? The answer can be traced to the differing densities of olivine (3.22–4.39 $kg\,dm^{-3}$) and serpentine (2.55–2.60 $kg\,dm^{-3}$). Even allowing for the formation of dense magnetite (5.2 $kg\,dm^{-3}$), conversion of anhydrous olivine into serpentine (typically containing more than 12% H_2O) evidently entails expansion, and the cracks indicate that this expansion has been accommodated by brittle fracturing of the surrounding crystals.

WHERE DOLERITES AND GABBROS ARE FOUND

Many dolerites and gabbros are demonstrably sub-surface components of plumbing systems that have fed basaltic lava fields on the surface. It is therefore likely that such rocks exist beneath most of the basaltic provinces outlined in Chapter 2. Geochemical and petrological studies on basalts indicate that many are not primitive magmas in equilibrium with mantle assemblages, but have undergone some degree of fractionation in crustal magma chambers prior to eruption, and complementary cumulate deposits must therefore lie concealed at depth beneath the site of eruption. In this section we review the direct evidence for intrusions beneath the various settings where basalts are found.

Oceanic spreading centres

Ophiolite complexes, such as the Semail ophiolite in Oman (Fig. 4.13), typically include layered gabbroic and ultramafic rocks that represent cumulates formed in axial magma chambers beneath oceanic spreading centres, either at mid-ocean ridges or in back-arc basins above subduction zones (Box 5.3). Gabbro samples have also been recovered from some oceanic fracture zones and from oceanic extensional core complexes (Ildefonse et al., 2007).

Box 4.5 The pyroxene solvus and other complexities

Pyroxenes in slowly cooled plutonic rocks, when viewed in crossed polars, often display internal structures that highlight the sub-solidus complexity of the pyroxene family.

Inversion

Low-Ca pyroxene (LCP) may crystallize in either orthorhombic or monoclinic forms according to temperature and composition, as shown in Fig. 4.5.1 below. Magnesian LCPs crystallize directly as orthorhombic enstatite from basaltic melts such as m_1. More evolved melts such as m_2, however, crystallize monoclinic pigeonite first, which may then 'invert' (i.e. recrystallize in the solid state) into enstatite if the rock cools slowly enough (see **inverted pigeonites** below). In volcanic rocks, cooling is generally too rapid for this inversion to take place.

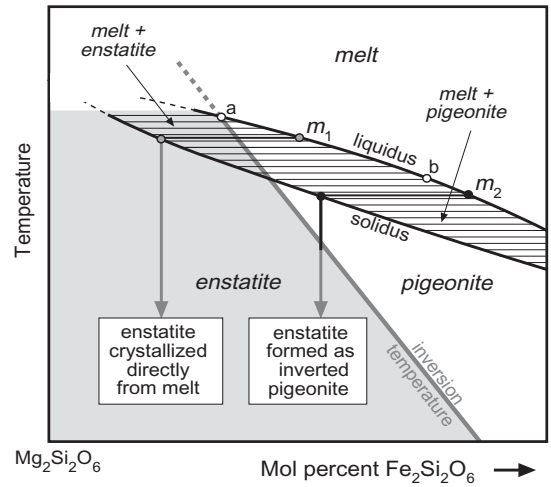


Fig. 4.5.1 Cartoon illustrating how the pigeonite-enstatite inversion temperature depends on composition. Also shown are notional liquidus and solidus lines for basaltic melts. Dashed lines represent metastable extensions of phase boundaries. (At atmospheric pressure, pure En melts incongruently to Fo + melt, not En + melt.)

Solvus and exsolution

High-Ca and low-Ca pyroxenes are separated by a **miscibility gap** (Box 2.1). The width of the gap varies with temperature, as shown for the magnesian (En–Di) end of the system in Fig. 4.5.2a below. The unornamented outer parts of the diagram denote enstatite, pigeonite or diopside solid solutions. The maximum contents of $Mg_2Si_2O_6$ that can be accommodated in diopside solid solution – and $CaMgSi_2O_6$ in pigeonite – at a given temperature are defined in such a phase diagram by a curve called the **solvus**. The ruled field inside the solvus shows the extent of the miscibility gap, where no homogeneous solid solution of intermediate composition is stable: all bulk compositions that plot in this field represent (under equilibrium conditions) *mixtures of two pyroxenes*.

y_1 represents a diopside crystal in equilibrium with an enstatite crystal x_1 at 1250 °C. On cooling it subsides into the ruled field (vertical arrow), indicating supersaturation with $Mg_2Si_2O_6$. It responds by precipitating *exsolution lamellae* of enstatite within the host crystal (see Plates 4.7–4.9). When the crystal has cooled to 1000 °C, the host crystal will have the composition y_2 with lamellae of composition x_2 (in mutual proportions represented by the open circle*). The coexisting enstatite

* See Box 3.2.

crystal x_1 responds to cooling in the same manner, exsolving diopside lamellae in smaller proportion. Inverted pigeonite, however, characteristically contains abundant augite lamellae or less regular 'blebs' because the host enstatite$_{ss}$ accommodates less $CaMgSi_2O_6$ in solid solution than the original monoclinic pigeonite (Fig. 4.5.2a); inversion is therefore accompanied by exsolution parallel to the (001) plane of the pigeonite. Subsequent slow cooling of the host crystal (now enstatite) may generate a second generation of exsolution lamellae parallel to the enstatite (100) plane (see Plate 4.7).

The solvus extends across the pyroxene quadrilateral as sketched in Fig. 4.5.2b. Slices 1–3 illustrate augite–pigeonite pairs of successively lower temperatures and more Fe-rich compositions.

The simplified diagrams in Fig. 4.5.2 suggest a continuous one-pyroxene field extending right across the solvus at T>1450 °C. When pyroxenes crystallize from basaltic melts, however, the uppermost part of the solvus is truncated by the basalt **solidus**, which is why separate crystals of augite and pigeonite/enstatite coexist in tholeiitic basalts and gabbros. Rare pyroxenes with homogeneous compositions in the 'forbidden zone' between HCP and LCP – as seen for example in some lunar basalts – have crystallized under disequilibrium conditions (e.g. very rapid cooling) and survive in a **metastable** state.

The composition of diopside coexisting with orthopyroxene (e.g. in mantle-derived peridotite xenoliths as shown in Plate 5.4 and 5.5) can be used as a **geothermometer** (see Fig. 9.22).

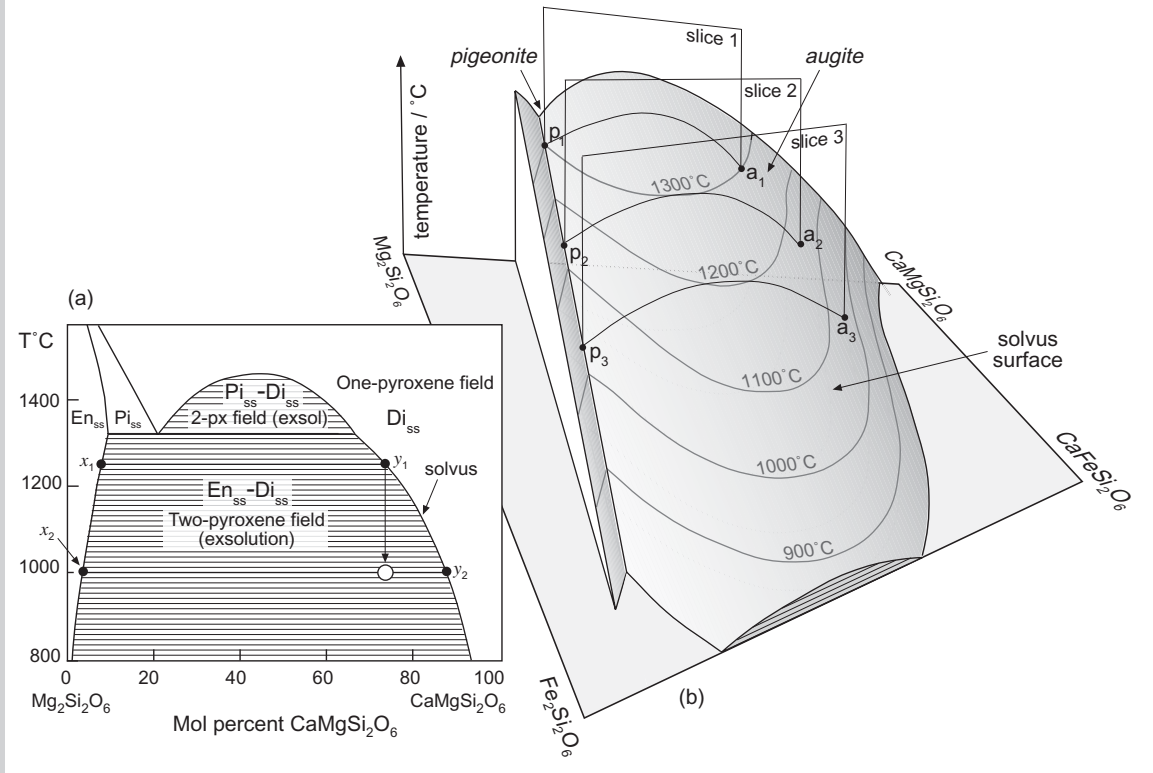


Fig. 4.5.2 (a) Simplified sub-solidus phase diagram showing the solvus between pure enstatite ($Mg_2Si_2O_6$) and pure diopside ($CaMgSi_2O_6$). Pi, pigeonite; En, enstatite; Di, diopside; the subscript 'ss' denotes a solid solution. Adapted from Lindsley (1983). (b) Simplified perspective view of the pyroxene solvus between pigeonite and augite. Temperature contours after Lindsley and Andersen (1983). The base (at 800 °C) consists of the pyroxene quadrilateral (Cf. Box 2.1).

NB these figures show only sub-solidus equilibria: melt evolution is not represented here and the solidus–solvus intersection has been omitted for clarity.

Oceanic islands

Gabbros are rarely if ever seen in situ on oceanic islands because the degree of erosion needed to expose them would submerge the edifice below sea level. That gabbroic rocks exist at depth within oceanic islands is nonetheless beyond doubt: gabbroic and ultramafic xenoliths with cumulate textures have been reported in lavas from many ocean islands. In basalts from the southern flank of Mauna Kea in Hawai`i, for example, gabbroic and ultramafic xenoliths have been found that exhibit modal, phase, cryptic and grain-size layering (Fodor and Galar, 1997), suggesting crystallization in a basaltic magma chamber large enough to form layered cumulates.

Large igneous provinces

Dense swarms of dolerite dykes are part and parcel of many large igneous provinces (LIPs), since fissure eruptions are required to accommodate the large effusion rates characteristic of such provinces. A prominent example is the 1.27 Ga McKenzie dyke swarm and associated sills and lavas which extend across at least 2.7 million km^2 of the Canadian Shield (Fig. 4.13). The Muskox layered intrusion in the NW Territories is a plutonic component of this province. Some older LIPs are represented only by a dyke swarm and intrusive complex as their surface volcanics have been entirely removed by erosion. The 2.06 Ga Bushveld Complex that crops out across 65,000 km^2 of South Africa has been interpreted as the intrusive analogue of a continental flood basalt province; the evidence points to many episodes of magma replenishment during its crystallization.

Sills may also account for an important fraction of the total magma volume of an LIP, as in the case of the 180 Ma Ferrar sills of the Transantarctic mountains and Tasmania. They were emplaced contemporaneously with the eruption of Karoo continental flood basalts in southern Africa and the Kirkpatrick basalts in Antarctica. The Ferrar sills account for 500,000 km^3 out of an estimated total magma production of 5 million cubic kilo-

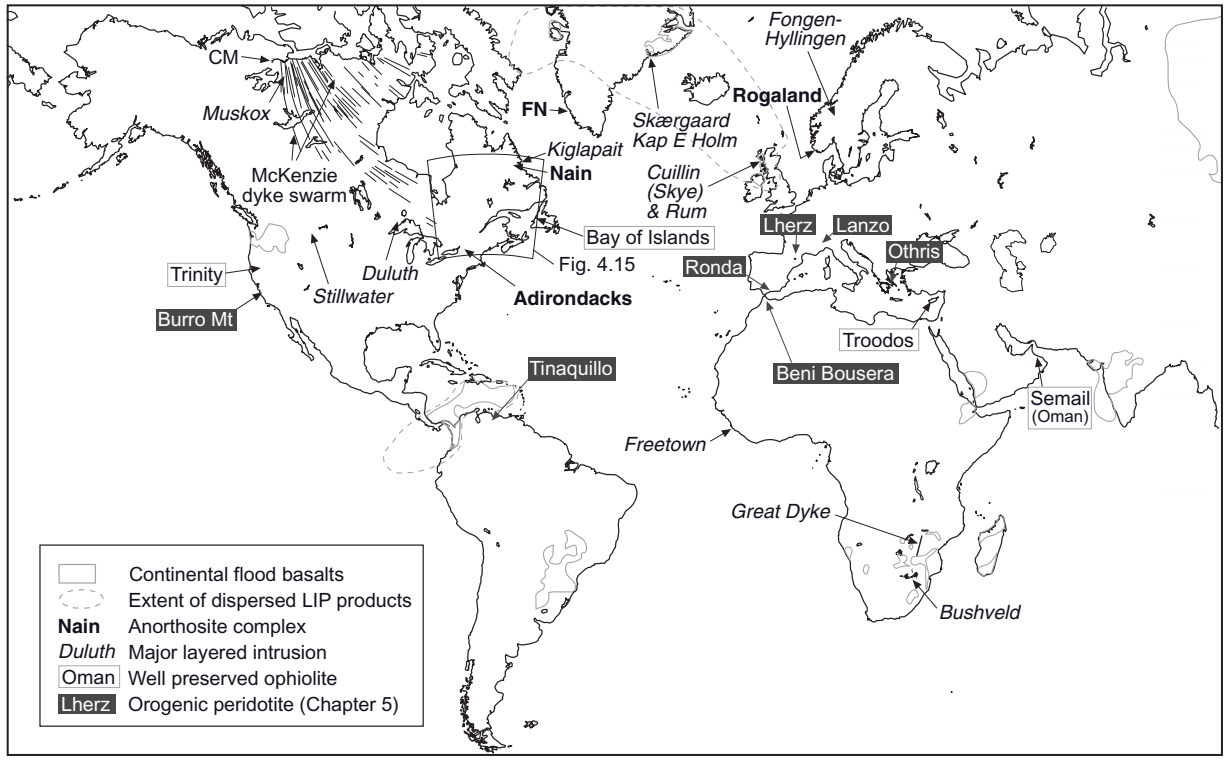


Fig. 4.13 Locations of the best known layered mafic/ultramafic complexes, anorthosite complexes, ophiolites and the McKenzie giant dyke swarm of northern Canada (Ernst et al., 1995). FN, Fiskenaesset complex, W Greenland; CM, Coppermine volcanics in NWT, Canada (a remnant of LIP volcanics believed to be cogenetic with the Muskox intrusion and the McKenzie giant dyke swarm).

metres[16] (Storey and Kyle, 1997). Their relative homogeneity, despite their outcrop spanning a major lithospheric boundary, suggests the magmas flowed laterally by as much as 4000 km from a single source (Storey and Kyle, 1997; Leat, 2008).

Intra-continental rift intrusions

An opportunity to inspect plutonic magmatism beneath a continental alkaline volcanic province associated with intra-continental rifting is provided by the 1300–1130 Ma Gardar province in S Greenland (Fig. 9.15; Upton et al., 1996, 2003). It consists of a number of doleritic and composite dyke swarms, some including giant dykes up to 800 m wide, and about a dozen large felsic central complexes ranging in composition from alkali granite to nepheline syenite. In addition to these intrusive bodies, a succession of continental sediments and basaltic volcanics is preserved in early down-faulted basins. The large volume of evolved plutons relative to mafic intrusions is reminiscent of some volcanic alkaline provinces such as Kenya (Chapter 2). The Gardar province will be discussed in more detail in Chapter 9.

The large Gardar felsic intrusions, many showing minimal isotopic evidence of crustal melting, indicate that considerable volumes of basaltic magma must have undergone extreme fractionation in deeper crustal magma chambers during the development of this alkaline province. This does not apply to all intracontinental alkaline magmatism, however: the occurrence of dense mantle-derived peridotite xenoliths in lavas from many small alkali basalt centres across the continents – e.g. Massif Central in France, Victoria in Australia (Plate 5.3), Rio Grande rift in New Mexico – is a sure sign that magmas have ascended direct from the mantle without being delayed in crustal magma chambers (where dense xenoliths would settle out).

Subduction-related complexes

Gabbroic cumulate xenoliths – some of them banded with adcumulate textures – have been reported from many tholeiitic and calc-alkaline volcanic rocks from island arc settings, notably the Lesser Antilles (Arculus and Wills, 1980), the Aleutians (Conrad and Kay, 1984; Bacon et al., 2007) and Arenal volcano in Costa Rica (Beard and Borgia, 1989). They indicate that layered gabbro plutons form at depth beneath island arc volcanoes, just as they do in other areas of basaltic volcanism. Not surprisingly, since subduction-related magmas tend to be richer in dissolved H_2O than other mantle-derived magmas, many of these xenoliths consist of hornblende gabbro. Here, as in subduction-related gabbros exposed *in situ* (e.g. Claeson and Meurer, 2004), hornblende is not a cumulus phase but typically forms prominent poikilitic oikocrysts enclosing chromite, olivine and clinopyroxene, and may be the product of reaction between these minerals and coexisting melt. Hornblende is markedly more abundant in plutonic gabbro xenoliths than it is as a phenocryst in basic volcanic rocks in the same island arcs: hornblende phenocrysts appear only in andesite lavas with SiO_2>54% (see Box 6.2).

Gabbros are also found in continental collisional zones, for example the Fongen-Hyllingen complex in the Caledonian mountains of Norway (Fig. 4.13, Table 4.2).

ANORTHOSITES, NORITES AND TROCTOLITES

Of the plutonic rocks that qualify as 'gabbroic', anorthosites are by far the most enigmatic. Since no volcanic rocks of equivalent composition are known, one must conclude that cumulate processes play a key part in their formation. On the small scale, anorthosite occurs as cumulate layers – notably forming the upper parts of modally graded layers – in many gabbroic layered intrusions like Skærgaard, but it also forms the main component of large intrusive bodies of Precambrian age, the largest of which compare in scale with granite batholiths; for example, the Lac Saint-Jean complex in Quebec (Fig. 4.15) has an outcrop area of 17,000 km^2. Anorthosite is present in these complexes in proportions much larger than would be expected from closed-system fractionation of basaltic magma. How can the preponderance of plagioclase-rich rocks be explained? The existence of this 'anorthosite problem' has been recognized for more than a century, but the manner in which the anorthosite masses were formed, sometimes on a huge scale, is still not fully understood.

[16] See www.largeigneousprovinces.org/record.html.

Terrestrial anorthosite occurrences fall into two categories whose characteristics are contrasted in Table 4.3 and Fig. 4.14.

Archaean calcic anorthosites

Metamorphosed anorthosites and associated leucogabbros constitute a small but highly distinctive component of most of the world's Archaean cratons. Many exhibit igneous layering similar to that seen in post-Archaean layered mafic intrusions such as Bushveld and Stillwater, but the Archaean anorthosites possess a coarse 'megacrystic' or porphyritic texture – consisting of large equant calcic plagioclase crystals (typically 1–5 cm but sometimes as large as 30 cm) set in a mafic matrix – that is never seen in younger gabbroic rocks. Plagioclase compositions lie in the An_{65}–An_{90} range (Fig. 4.14) but the more sodic of these compositions may reflect metamorphism or alteration: well preserved megacrysts usually lie between An_{80} and An_{90} (Ashwal, 1993). The anorthosite component is associated with leucogabbro and gabbro in these Archaean intrusive complexes, and ultramafic cumulates may also be present. The best known of these Archaean calcic anorthosite complexes, in the Fiskenaesset region of West Greenland, is profiled in Box 4.6.

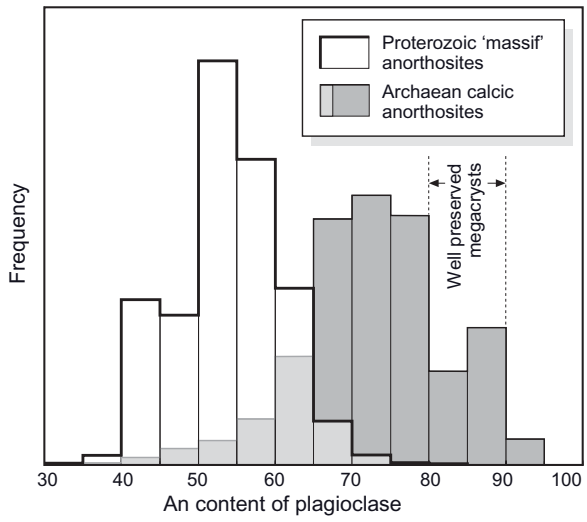


Fig. 4.14 Histograms comparing the ranges of plagioclase composition in the world's Proterozoic 'massif' anorthosites and Archaean calcic anorthosites (prepared from summary data in Ashwal, 1993); the frequency has been normalized to yield the same area for each histogram. The compositional range shown for well preserved (i.e. igneous) megacrysts in Archaean calcic anorthosites is also from Ashwal (1993).

Proterozoic 'massif' anorthosites

Massif anorthosites (spelt incorrectly as 'massive anorthosites' by some authors) owe their name to their tendency to form upland 'massifs' in many Precambrian terrains, for example the Adirondack Mountains of New York state (Fig. 4.15). They belong to a very distinctive igneous association that occurs – in contrast to the calcic anorthosites – almost exclusively in Proterozoic terrains and is characterized by plagioclase of intermediate composition (typically An_{40}–A_{60} (Fig. 4.14)). The dominant rock types (Table 4.3) are coarse-grained anorthosite, leucogabbro, leuconorite and leucotroctolite. In some intrusions the rocks may be relatively structureless whereas in others igneous layering is well developed.

Massif anorthosites are spatially associated with, and often cut by, distinctive orthopyroxene-bearing granitic rocks – **charnockite** and mangerite – and often **rapakivi** granites as well (whose significance is discussed in Chapter 8). The melanocratic and ultramafic rocks associated with Archaean calcic anorthosite complexes are largely absent. Terms such as 'Proterozoic anorthosite–mangerite–charnockite (AMC)[17] suite' are used by some authors to embrace the full range of magmatic rocks present in this association. The greatest concentration of intrusions of this kind in the world lies in a prominent belt more than 1000 km long – shown in Fig. 4.15 – from Labrador to Ontario and New York State, mostly in the Grenville Province of the eastern Canadian Shield. The intrusions vary in size, shape, degree of deformation and grade of metamorphism. Where least deformed, most are found to consist of numerous individual intrusions. Evidence that anorthosite-related magmatism of this age extended still further to the NE takes the form of abundant anorthosite xenoliths and plagioclase megacrysts that occur in basic and intermediate intrusions (the 'Big Feldspar Dykes') in the Proterozoic Gardar alkaline province in S Greenland.

[17] AMC stands for 'anorthosite–mangerite–charnockite'.

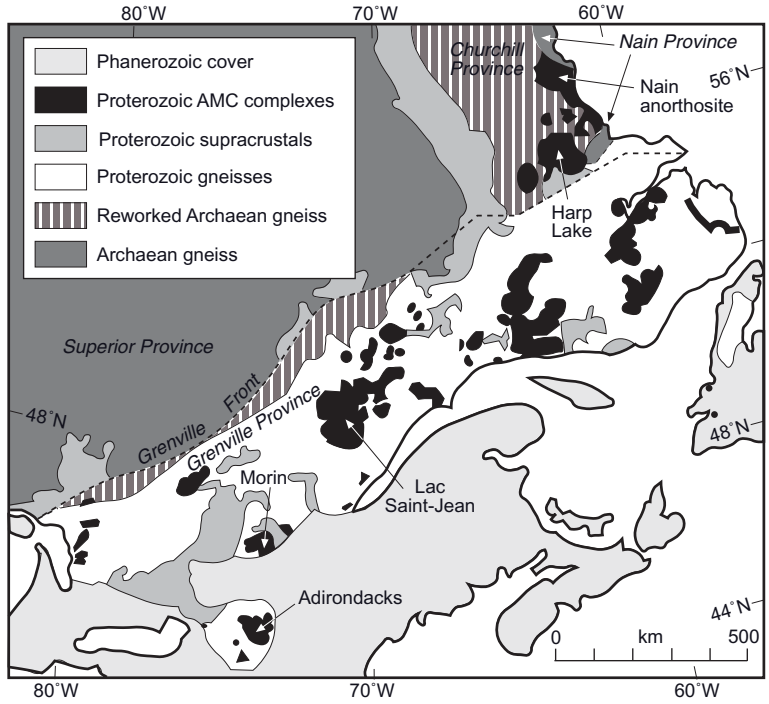


Fig. 4.15 Map of eastern Canada and the northeastern US showing the outcrop of Proterozoic anorthosite (AMC) complexes in black, after Ashwal (1993) with kind permission of Springer Science and Business Media.

Table 4.3 Distinguishing features of terrestrial anorthosite associations.

	Archaean calcic anorthosites	**Proterozoic 'massif' anorthosites**
Age range	2650–3730 Ma	930–2570 Ma (most between 1300 and 1800 Ma)
Surface outcrop	Most are smaller than 500 km^2. Often occur in dismembered form due to later intrusions and tectonism.	Up to 17,000 km^2
Typical plagioclase composition range	For pristine megacrysts ~ An_{80}–An_{90} but metamorphic plagioclase crystals show a wider range (see Fig. 4.14).	Mostly An_{40}–An_{60}
Associated mafic rocks	Gabbro and **leucogabbro** (often layered), ultramafic cumulates and chromitite (Box 4.6).	Leucogabbro, leuconorite and leucotroctolite in small volume. Ultramafic rocks are *absent*.
Associated felsic rock types	Tonalite, diorite (rare)	**Charnockite**, mangerite and other opx-bearing rocks, together with **rapakivi** granite
Examples	Fiskenæsset, W Greenland (Box 4.6) (Myers, 1975, 1981)	Rogaland complex , Norway (Fig. 4.16) (Bolle et al., 2003)

The geology of a well documented European AMC intrusion – the 0.93 Ga Rogaland igneous complex in SW Norway – is summarized in Fig. 4.16. It occurs at the SW extremity of the Sveconorwegian orogenic belt, the eastward extension of the Grenville orogen (Fig. 4.15). Figure 4.16a shows the disproportionately large volume of leucocratic rocks exposed at the surface – a key characteristic of Proterozoic anorthosite complexes. It is widely accepted that anorthosites form by *flotation* of plagioclase during crystallization of basaltic or andesitic magma, forming plagioclase-rich rocks as roof-cumulates. If that

Box 4.6 Profile of an Archaean calcic anorthosite complex: the Fiskenaesset complex of West Greenland

The Fiskenaesset Anorthosite Complex (FAC) in West Greenland (~150 km south of the largest town, Nuuk) is arguably the best exposed and most intensively studied Archaean anorthosite complex in the world. It probably formed as a single sill-like layered intrusion more than 2.8 Ga ago, but it has since been (i) disrupted by later granitoid intrusions; (ii) repeatedly deformed and folded with the host gneisses into complex interference patterns (Fig. 4.6.1); and (iii) metamorphosed to amphibolite and granulite facies (and locally retrogressed). The FAC now crops out over an area of 5000 km^2 as thin slices, trains of inclusions and some larger bodies – such as Majorqap Qâva (Fig. 4.6.1) – in a terrain of quartzo-feldspathic gneisses. Where original contacts are preserved, the FAC is seen to intrude metavolcanic amphibolites, some of which show relic pillow structures, suggesting original emplacement at shallow depths, possibly within oceanic crust (Myers, 1981). In spite of its complex post-crystallization history, the layered anorthosite complex preserves relict igneous textures and layering structures (Fig. 4.6.3) with stratiform chromite deposits over large parts of its outcrop, as well as a consistent internal igneous 'lithostratigraphy' (Fig. 4.6.2).

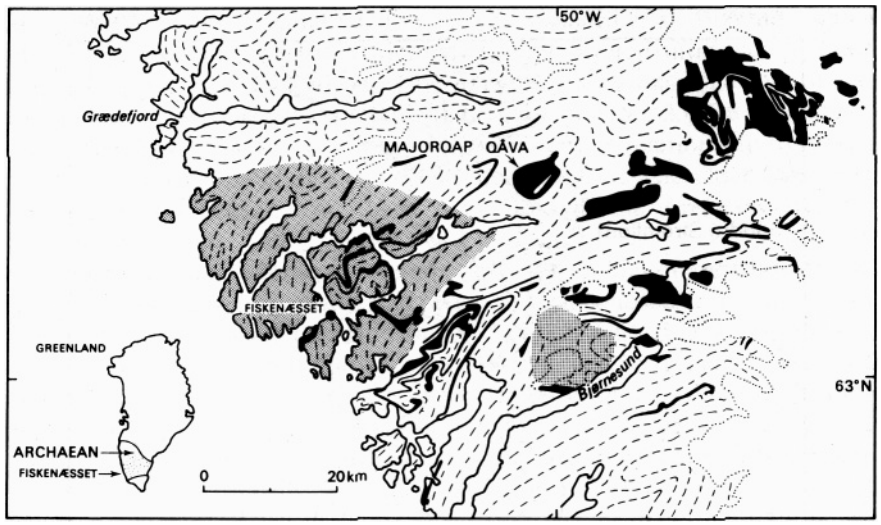


Fig. 4.6.1 Geological sketch map (reproduced with permission from Myers, 1975) showing the outcrop of the Fiskenaesset anorthosite complex (black), the trend of foliation in the host gneisses (dashed lines) and regions in which regional metamorphism reached granulite facies (shading). Dotted lines indicate the margins of inland ice cover. Reproduced by kind permission of the Geological Survey of Denmark and Greenland.

Although anorthosite is the dominant and most distinctive lithology (the anorthosite unit accounts for almost 50% of aggregate thickness), it is intimately associated in the FAC with gabbro, leucogabbro and ultramafic rocks, so 'anorthosite complex' is a less than an accurate description. As in other Archaean anorthosites, Fiskenaesset feldspars are notably coarse-grained (Fig. 4.6.3); size-grading is not uncommon – in the Upper Leucogabbro (Fig. 4.6.2), for example, plagioclase crystals increase in size upwards from 2 cm to 10 cm.

Most rocks in the FAC consist today of metamorphic plagioclase and hornblende, but original mineralogy is preserved sufficiently widely for the original cumulate minerals (olivine, enstatite, augite, plagioclase and chrome spinel) to be identified. Igneous plagioclase crystals are **normally zoned** from $An_{85–89}$ cores to $An_{79–84}$ rims, but metamorphic plagioclases cover a wider range.

The complex includes a much higher proportion of plagioclase-rich gabbroic rocks than more recent layered gabbro intrusions, the reason for which is unclear. The emplacement of a plagioclase-enriched mush initially formed in a deeper magma chamber is one possible explanation for the plagioclase-rich character and positive Eu anomalies (Box 8.5) of these rocks, as discussed for massif anorthosites below. The FAC rocks are recognizably cumulate; as to the composition of the original magma, however, there has been much debate though little consensus.

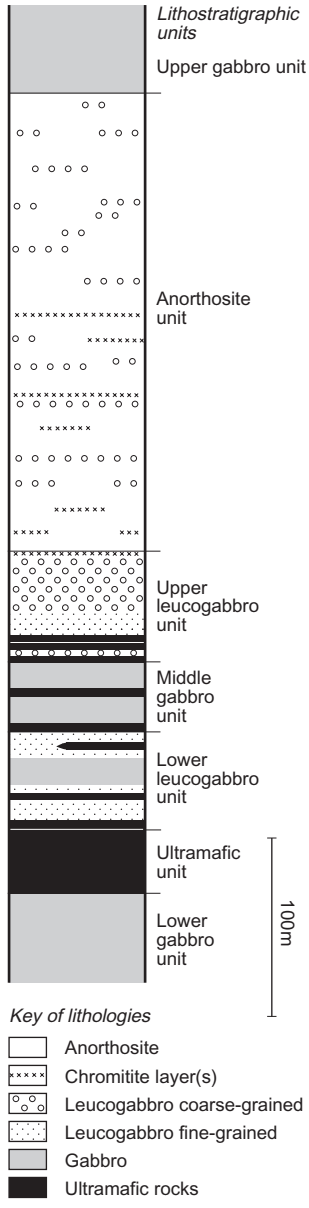


Fig. 4.6.2 A composite 'lithostratigraphic section' through the Fiskenaesset anorthosite complex, compiled by Myers (1981) from measured logs for a number of incomplete sections, reproduced by permission of the Geological Society of Australia.



Fig. 4.6.3 Field pictures of the Fiskenaesset anorthosite complex, West Greenland, kindly provided by J.S. Myers and reproduced with permission. (a) Megacrystic anorthosite (pen 13 cm); darker patches are richer in hornblende, probably after orthopyroxene oikocrysts. (b) Metaleucogabbro (hammer 28 cm long). (c) Plagioclase-chromite cumulate showing modal layering (hammer 28 cm long).

were the case, one would expect the complementary ultramafic and mafic floor-cumulates to lie directly beneath, and – even if not exposed – to be detectable in the form of a positive gravity anomaly. However, gravity surveys of the Rogaland igneous complex (Fig. 4.16b) show that such anomalies are confined to the relatively small volume of mafic rocks exposed at the surface (including those underlying the charnockites). No dense mafic or ultramafic accumulations appear to exist directly beneath the larger volume of anorthosite plutons, which differ little from country rocks in their gravity signature. Many (though not all) of the Canadian complexes show a similar deficit in high-density mafic–ultramafic cumulates.

The most widely accepted solution to this 'anorthosite problem' is to suppose that the parental magma chamber formed deep in the continental crust, close to the crust–mantle boundary. Dempster et al. (1999) proposed ponding of mantle-derived basaltic magma at the base of the crust, where interaction with Al-rich lower-crustal lithologies led to copious plagioclase crystallization. The parent melt may have originated in the underlying mantle or – as recent experimental data (Longhi et al., 1999; Longhi, 2005) suggest – by melting of lower-crustal mafic lithologies. According to Dempster et al., the magma chamber crystallized to form anorthositic roof-cumulates that became gravitationally unstable and ascended as a low-density crystal-mush diapir to shallower levels in the crust, leaving the denser mafic and ultramafic cumulates near the base of the crust (Ashwal, 1993, Fig. 3.39) where they remain undetectable by gravity survey owing to their great depth and their similarity in density to the underlying mantle. A similar model by McLelland et al. (2004) proposes initial anatexis of lower crustal rocks to form charnockite-suite magmas, leaving behind a plagioclase–pyroxene restite that can be remobilized as a plagioclase-rich mush by mantle derived basic magmas. The contact-parallel foliation seen in some anorthosite bodies (e.g. EO in Fig. 4.16a) is cited as evidence of diapir-style emplacement of crystal-rich mushes, though post-emplacement 'ballooning' (Chapter 8) seems a more viable explanation. Massif anorthosites commonly exhibit textural evidence of syn- or post-emplacement deformation (Plate 4.13). The associated orthopyroxene-bearing granitoids may be the product of melting of granulite-facies lower-crustal felsic rocks (see Chapter 8).

Lunar anorthosite

Anorthosite is also an important constituent of the lunar crust, being the principal component of the lunar 'highlands'. Though pristine coarse-grained 'igneous' anorthosites have been recovered in Apollo missions, nearly all of the highland surface consists of heavily impact-brecciated material. Plagioclase compositions fall mainly in the An_{85}–An_{97} range (see Ashwal, 1993, Fig. 7.3), significantly more calcic than nearly all terrestrial anorthosites. Lunar anorthosites are regarded as flotation cumulates that formed on the surface of an early 'magma ocean' thought to have covered the entire surface soon after the Moon's formation. Major impacts early in the Solar System's history disrupted this early anorthositic crust, allowing underlying basic magma to escape on to the surface to form the mare basalts.

REVIEW – WHAT CAN ONE LEARN FROM THE STUDY OF GABBROIC ROCKS?

Doleritic and gabbroic intrusions provide opportunities to study the magma plumbing systems that deliver magma through the crust to feed surface eruptions, and they help us to understand the mechanical and chemical controls that govern magma transport and evolution.

Minor intrusions

- The largest dyke swarms and sill complexes testify to past episodes of large-volume basalt magma production, the surface manifestations of which may have been mostly obliterated by erosion. Prominent examples, both linked to LIPs by many authors, are the 1.27 Ga McKenzie dyke swarm in NW Canada (Fig. 4.13) and the 180 Ma Ferrar sills in Antarctica.
- Minor intrusions provide a record of stress conditions in the crust during magma emplacement (Figs. 4.5 and 4.6).
- Changes in tectonic environment of emplacement may sometimes be discerned during the lifetime of a dyke swarm, as for example in the Tertiary coast-parallel dyke swarm in East Greenland (Fig. 4.3a),

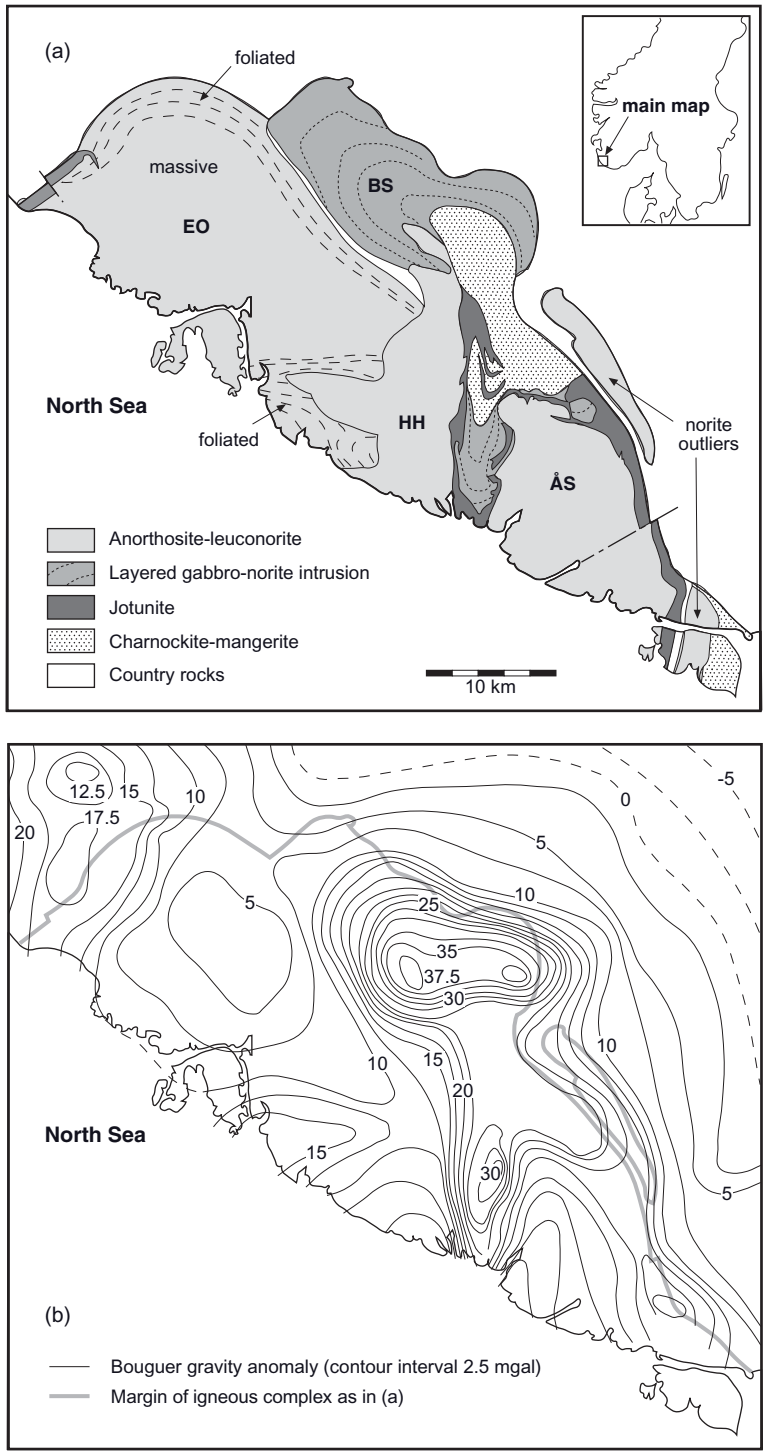


Fig. 4.16 (a) Simplified geological map of the Rogaland igneous complex, SW Norway (adapted from Bolle et al., 2003; copyright Elsevier). BS, the Bjerkreim-Sokndal layered intrusion (dotted lines indicate strike of layering); EO, the Egersund–Ogna anorthosite pluton (dashed lines indicate strike of foliation); HH, the Håland–Helleren anorthosite plutons; ÅS, the Åna–Sira anorthosite pluton. The names **charnockite**, mangerite and jotunite are defined in Fig. 8.2. (b) Bouguer gravity anomaly map for the Rogaland igneous complex (adapted from Smithson and Ramberg, 1979).

where late dykes have steeper dips than early ones owing to the progressive development of a flexural monocline (that tilted older dykes the most) throughout the period of dyke emplacement.
- Thick sills or dykes may reveal evidence for *in situ* fractionation during crystallization, e.g. olivine accumulation in the Palisades Sill, and layering in the Tugtûtoq giant dyke in S Greenland.

Layered intrusions

- The largest layered intrusions compare in scale to the volcanic outpourings associated with LIPs and continental flood basalts (CFBs), so are likely to have similar causes. For example, a plume origin has been proposed for the 2.06 Ga Bushveld complex in S Africa (Fig. 4.13).
- The 'stratigraphy' of layered gabbro/ultramafic intrusions documents in great detail the emplacement and crystallization history of basaltic magma in crustal magma chambers (Fig. 4.8b), and substantiates the experimentally derived principles of fractional crystallization and mineral-magma reaction discussed in Chapter 3.
- Cryptic layering in layered rocks (Fig. 4.8b) allows us to follow *changes* in magma composition as crystallization progresses, but the *absolute* magma composition at any stage is often hard to establish with confidence.
- Some intrusions (e.g. Skærgaard) exhibit an uninterrupted record of crystallization in a closed magma chamber. In others the record of cryptic layering is punctuated by abrupt reversals (e.g. the Tertiary Kap Gustav Holm complex in East Greenland – see Myers et al., 1993) that testify to influxes of fresh magma at several stages during the intrusion's crystallization history. In yet other intrusions virtually no cryptic layering is observed at all, e.g. Rum (Emeleus et al., 1996), suggesting that their chambers were open for a significant portion of their crystallization history, the melt being repeatedly replenished from below (and probably tapped from above) so that melt composition (and cumulus mineral compositions) remained more or less constant.
- 70 years of field and laboratory investigation have yet to yield a general consensus on whether cumulus crystals are deposited by gravitational sedimentation – having nucleated at higher levels in the intrusion – or are nucleated *in situ* on the magma chamber floor (Fig. 4.9). Layered intrusions therefore pose as many questions about magma chamber dynamics as they answer.
- Many layered mafic–ultramafic intrusions host important economic deposits of PGE, chromite and/or base-metal sulphides.
- Anorthosites record a voluminous basic to intermediate magmatic addition to the continental crust during Archaean (Box 4.6) and Proterozoic (Fig. 4.15) times. Though anorthosite genesis is still not fully understood, it is clear that cumulus processes lie behind the high proportion of leucocratic and hololeucocratic rocks in such complexes.

EXERCISES

4.1 Select appropriate petrographic names for plutonic rocks consisting of:
  (a) 30% enstatite, 25% augite, 45% plagioclase (An_{65}), minor opaques;
  (b) 75% calcic plagioclase, 22% olivine, 3% augite;
  (c) 46% plagioclase (An_{45}), 44% enstatite, 3% augite, 7% opaques;
  (d) 46% plagioclase (An_{45}), 44% enstatite, 9% augite, 1% opaques;
  (e) 55% plagioclase (An_{45}), 35% augite, 5% hornblende, 5% opaques;
  (f) 45% plagioclase (An_{65}), 40% augite, 10% analcite, 5% opaques.

4.2 (a) Use the Phase Rule to show that points R and E in Fig. 4.3.1a are invariant. (b) Describe what happens when a melt of composition m_b in Fig. 4.3.1a is allowed to undergo equilibrium crystallization, comparing the final outcome with the crystallization of melt m_a (Box 4.3).

4.3 Calculate in a spreadsheet the major-element analysis of a cumulate rock made up of 70% olivine having the composition given in Table 1.2.1 (Box 1.2) and 30% intercumulus matrix having the composition of analysis D in Table 2.5. Reference to Appendix B may be helpful.

Chapter 5

Ultramafic and ultrabasic rocks

Ultramafic and **ultrabasic** rocks, though not abundant at the Earth's surface, provide valuable insights into basalt magma genesis and mantle source domains. An igneous petrologist may encounter such rocks in three distinct settings:

- as early cumulates in layered intrusions exhumed by erosion; these are ultramafic cumulates that crystallized and accumulated from basic melts before they reached saturation with plagioclase;
- as samples of the Earth's peridotite mantle that have been transported to the surface by volcanic or tectonic processes;
- as lavas of ultrabasic composition erupted on the surface.

The first two categories, having formed at depth, are generally coarse-grained enough for all minerals to be identified (unless severely altered). This allows them to be described as ultramafic (**colour index** ≥90). They may or may not qualify as ultrabasic (SiO_2<45%) as well, depending on the relative proportions of olivine, spinel and pyroxene: magnesian pyroxenes usually have SiO_2 contents >50% and therefore a pyroxenite can be ultramafic without being ultrabasic.

The third category – consisting primarily of rocks called komatiites – was for many years a petrological enigma. The coarse platy olivine crystals that characterize these rocks, the usually pervasive alteration, the poor exposure in some Archaean terrains, and the difficulty of recognizing devitrified glass concealed their volcanic nature. That komatiites erupted as surface lavas only became widely accepted after publication of a seminal paper by Viljoen and Viljoen in 1969. The presence of olivine blades often 5 cm in length (Fig. 5.7) in a *volcanic* rock violates every petrological instinct about grain size and cooling rate, and points to very unusual conditions of crystallization that are discussed later in the chapter.

THE NOMENCLATURE OF ULTRAMAFIC ROCKS

Definitions

The names used to describe coarse-grained ultramafic rocks, and the ranges of modal composition they cover, are summarized in Fig. 5.1. Rocks with more than 40% olivine are known collectively as peridotites (from *peridot*, the name for gem-quality olivine). Figure 5.1(a), applicable only to rocks containing less than 10% by volume of felsic minerals (plagioclase), forms the base of the gabbro tetrahedron shown in Fig. 4.1. When no quantitative modal analysis is available, the following qualitative definitions may be used:

Dunite: a rock consisting almost entirely of olivine (named after Dun Mountain in New Zealand).

Lherzolite: a coarse-grained rock consisting essentially of olivine (>40%) + orthopyroxene + clinopyroxene (after Étang de Lherz[1] in the French Pyrenees).

[1] Most commonly spelt 'Lers' or 'Lhers' today.

Igneous Rocks and Processes: A Practical Guide, 1st edition. By Robin Gill. Published 2010 by Blackwell Publishing

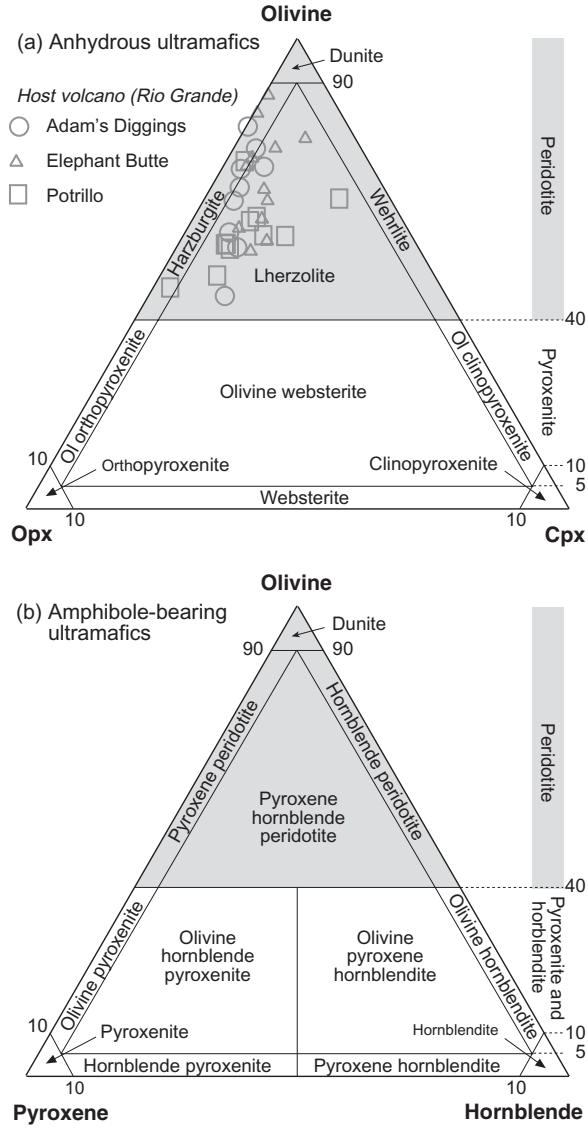


Fig. 5.1 Diagram showing IUGS nomenclature for coarse-grained ultramafic rocks based on the **modal** (i.e. volume %) proportions of olivine, clinopyroxene and orthopyroxene present (Le Maitre, 2002). The names apply only to rocks containing less than 10 modal % plagioclase (cf. Fig. 4.1). Representative natural compositions are illustrated (grey symbols) by mantle-derived spinel lherzolite and harzburgite xenoliths from basanite volcanoes associated with the Rio Grande Rift in New Mexico (Kil and Wendlandt, 2004).

Harzburgite: a coarse-grained rock consisting essentially of olivine (>40%) + orthopyroxene (after the town of Harzburg in the Harz Mountains of Germany).

Wehrlite: a coarse-grained rock consisting essentially of olivine (>40%) + clinopyroxene (named after a 19th century petrologist by the name of Wehrle, who produced the first analysis of such rock).

Websterite: a **pyroxenite** consisting of orthopyroxene + clinopyroxene (after Webster County, N Carolina). The presence of olivine (10% < olivine < 40%) as well leads to the name olivine websterite.

The definition of komatiite is covered in Box 5.5.

Given their origins in the mantle or as early cumulates from mantle-derived basaltic magma, these rocks – and the minerals they contain – are highly **magnesian**. This fact makes mineral identification a challenge in some ultramafic rocks, because the slight differences in body colour that serve to distinguish pyroxenes from olivine in basalt (Box 2.2) and gabbro derive from their iron content; low-Fe magnesian pyroxenes, on the other hand, have only the faintest body colour (and a relief similar to that of olivine). These difficulties are compounded in ultramafic xenoliths (hosted by basalts and kimberlites), in which the olivines may be extremely fresh – lacking the often-diagnostic alteration products – and pyroxene cleavage may be poorly developed. In these circumstances birefringence provides the main criterion for distinguishing olivine and pyroxenes:

Mineral	Birefringence
Enstatite	0.007–0.020
Diopside–augite	0.018–0.033
Magnesian olivine	0.035–0.040

Type minerals

In many mantle peridotites, the essential minerals shown in Fig. 5.1 are often accompanied by significant amounts of an aluminous phase: either plagioclase (rarely), Al-spinel (Box 5.1) or pyrope garnet (Box 5.2). Which of these is found in an ultramafic rock reflects the depth (pressure) range from which the rock originates (Fig. 5.5), and therefore it is informative to refer to spinel lherzolite or garnet lherzolite, whichever happens to be present (plagioclase lherzolite can form only at crustal

Box 5.1 Spinel minerals

Confusingly, the mineral name 'spinel' has three distinct meanings in mineralogy. It denotes:

- the entire *group* of oxide minerals of cubic symmetry that share the general formula $X^{2+}Y^{3+}_2O_4$, where X represents a divalent element (Mg or Fe^{2+}) and Y represents a trivalent element (Al, Fe^{3+}, Cr);
- one of three Mg–Fe^{2+} solid solution *series* (the one extending from $MgAl_2O_4$ to $FeAl_2O_4$ – see Fig. 5.1.1) within the spinel group;
- one *end-member* ($MgAl_2O_4$ – 'spinel *sensu stricto*') of the spinel series.

The three solid solution series of the spinel group are summarized in Fig. 5.1.1 and Table 5.1.1. Each apex of the triangular prism in Fig. 5.1.1 represents an end-member with a different trivalent ion (Fe^{3+}, Al^{3+}, Cr^{3+}); the front-to-rear (or left to right) dimension represents substitution between Mg and Fe as the divalent element. As well as solid solution within each Mg–Fe series, there is extensive mixing *between* the series, as illustrated by the shaded fields in Fig. 5.1.1. Many spinels also contain titanium, through incorporation of the end-member ulvöspinel ($Fe^{2+}_2TiO_4$ – not shown in Fig. 5.1.1).

Spinels are significant minerals in ultramafic and mafic rocks, but as most are opaque their diagnostic value in transmitted light is limited. The exception is the spinel series – typical of mantle-derived spinel peridotites (Table 5.1.1) – which is translucent green-brown in transmitted light (PPL); an example is shown in Plate 5.8. Being isotropic, such grains are black in crossed polars.

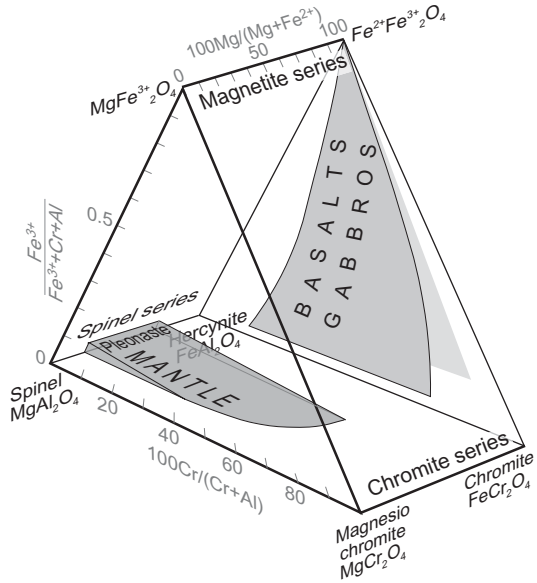


Fig. 5.1.1 The extent of naturally occurring spinel solid solutions depicted in a triangular prism (the 'spinel prism') with the spinel, magnetite and chromite series at its apices (adapted from Deer et al., 1992). The grey scales represent ratios commonly used for summarizing spinel composition: **Mg number**, 'Cr number' [= 100Cr/(Cr + Al)] and $Fe^{3+}/(Fe^{3+} + Al + Cr)$.

Table 5.1.1 Solid solution series and end-members of the spinel group.

Spinel series	Y^{3+}	Magnesian end-member	Ferrous end-member	Names for intermediate members	Opacity
Spinel	Al^{3+}	spinel $MgAl_2O_4$	hercynite $FeAl_2O_4$	pleonaste	brown to dark green in thin section*
Chromite	Cr^{3+}	magnesiochromite $MgCr_2O_4$	chromite $FeCr_2O_4$	–	opaque
Magnetite	Fe^{3+}	magnesioferrite $MgFe^{3+}_2O_4$	magnetite $Fe^{2+}Fe^{3+}_2O_4$	–	opaque

* See Plate 5.8.

Box 5.2 The garnet family

Garnets are a family of orthosilicate minerals embracing a wide range of solid solution (Fig. 5.2.1). The general formula is

$$X_3Y_2Si_3O_{12} \qquad [5.2.1]$$

where X represents divalent ions (Mg, Ca, Fe^{2+}, Mn) and Y represents trivalent ions (Al, Fe^{3+}, Cr^{3+}). Solid solution in the garnet family consists of two isomorphous series, each having three end-members (the two triangular fields in Fig. 5.2.1); there is extensive solid solution within each if these series, but little between them. The garnet that occurs in ultramafic rocks is a pyrope–almandine solid solution, with significant Cr substituting for Al.

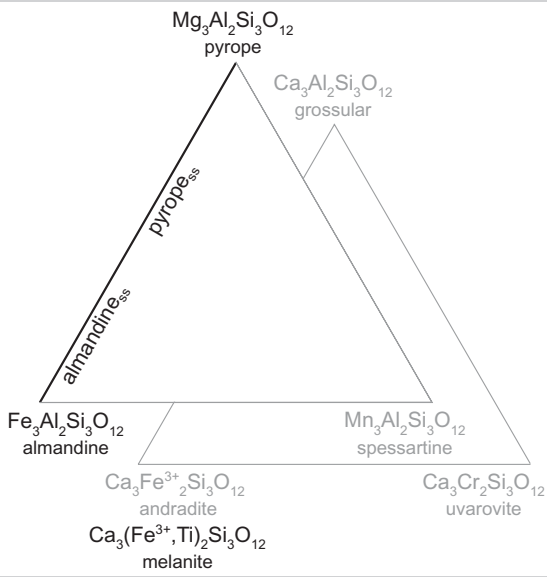


Fig. 5.2.1 Solid solution in the garnet mineral group. Garnets found in ultramafic and igneous rocks are largely confined to the $pyrope_{ss}$–$almandine_{ss}$ series ('ss' denotes solid solution) shown in black. Garnets with significant contents of the other end-members (shown grey) are restricted to metamorphic rocks, except for the titanian variety of andradite called *melanite* [$Ca_3(Fe^{3+},Ti)_2Si_3O_{12}$] which occurs in some alkali igneous rocks (Table 9.3).

Garnet belongs to the cubic crystal system and is thus isotropic between crossed polars (though larger garnets in metamorphic rocks may show appreciable birefringence). This characteristic – together with the high positive relief (RI ~1.71–1.83), lack of cleavage and equant, often rounded crystal shape – makes garnet unmistakable in thin section. $Pyrope_{ss}$ tends to be pinkish red (Plate 5.5) to purplish in hand-specimen (especially chrome-pyrope) but is virtually colourless in thin section; $almandine_{ss}$ on the other hand tends to a more brownish red in hand-specimen and may show a slight pink body colour in thin section.

depths). For rocks in which the aluminous phase constitutes less than 5%, International Union of Geological Sciences (IUGS) recommends the designation 'spinel-*bearing* lherzolite' or 'garnet-*bearing* lherzolite' (Le Maitre, 2002); the conclusions about depth of origin still apply.

Most fresh ultramafic rocks consist entirely of anhydrous minerals. When the hydrous mineral hornblende (calcic amphibole) occurs in an ultramafic rock (see Fig. 5.1b for nomenclature), it indicates that water was present (either in melt or as a vapour phase) during crystallization. Ultramafic rocks may also contain small amounts of other hydrous minerals such as **phlogopite** (Table 5.1).

Alteration

Ultramafic and ultrabasic rocks, whatever their origin, are very prone to hydrothermal alteration. Magnesian olivine and orthopyroxene react readily with hot aqueous fluids to form serpentine minerals. An ultrabasic

Table 5.1 Summary mineralogy of ultramafic rocks. The optical properties of relevant minerals are summarized in Appendix A.

Essential minerals	• olivine • orthopyroxene (enstatite) • clinopyroxene (diopside or augite) in lherzolite	
Principal type minerals	• plagioclase • spinel (pleonaste) • garnet	aluminous minerals
	• amphibole (hornblende) • mica (phlogopite)	
Common accessory minerals	• oxide minerals (chromite, spinel series)	
Common secondary (alteration) minerals	• serpentine or **iddingsite** replacing olivine (see Box 2.2) • chlorite or **uralite** replacing pyroxene	

rock in which most of the olivine has been altered to serpentine is called a *serpentinite*. Low-grade metamorphism of ultramafic rocks may result in serpentine or talc rocks.

Alteration of olivine crystals often leads to serpentine pseudomorphs which preserve traces of the olivine crystal's original conchoidal cracks in the growth pattern of the fibrous serpentine; evidently the cracks provided channels for fluid penetration into the crystal. For the same reason, primary fractures may also be picked out as trails of opaque iron oxide minerals (Plate 4.12): as serpentine accommodates little iron in its crystal structure, the iron present in the primary olivine is expelled during the alteration reaction (see equation 4.3).

Serpentinization of orthopyroxene leads to platy pseudomorphs that are distinctive in hand-specimen: the crystals take on a bronze- or honey-coloured metallic sheen, in which form the mineral is sometimes known by the special name *bastite*.

Given the propensity for mafic minerals to become altered, it is important to try to establish from alteration products the identity of the primary minerals present in the rock in order to infer the original rock type.

'STRATIFORM' ULTRAMAFIC CUMULATES IN LAYERED INTRUSIONS

Plagioclase is rarely the first mineral to crystallize from primitive basaltic magma, and the earliest cumulates to form in many gabbroic magma chambers are plagioclase-free and therefore of ultramafic composition (though minor plagioclase often appears in the solidified rock as an **intercumulus** mineral, as in Plate 5.2). Table 5.2 lists a number of layered intrusions in which ultramafic rocks form a prominent part of the exposed cumulate sequence. Because ultramafic cumulates – where present – are found at the base of the cumulate sequence, it is natural to regard them simply as initial cumulates from the basaltic magmas from which gabbroic layered rocks later crystallized. However, there is evidence from the Bushveld and Stillwater complexes that the ultramafic cumulates crystallized here from magmas with distinctly higher SiO_2 and MgO contents than those forming the overlying gabbros or norites (Eales and Cawthorn, 1996; McCallum, 1996). The likelihood (Table 5.2) that high-MgO melts have been involved in these and other complexes – such as Rum – is one reason for considering ultramafic cumulates separately in this chapter, rather than in Chapter 4.

Figure 5.2 compares the ultramafic cumulate divisions of three large Precambrian layered intrusions. In each case the rhythmically layered ultramafic cumulates are separated from the host country rocks by a variable border zone, known by a different name in each complex. The layered cumulate sequences are remarkably similar, even though the parallels are obscured by differing nomenclature. In each case, the ultramafic cumulates can be divided into two zones, the lower one consisting – at least in part – of olivine-bearing rocks, and the upper one comprising mainly pyroxenites. Layering, especially in the lower zones, takes the form of cyclic or **macro-rhythmic** units (Irvine, 1982), each of which grades from dunite or peridotite at the base (cumulus olivine ± chromite) up through harzburgite to pyroxenite at the top. Massive **chromitite** bands and/or disseminated chromite often

Table 5.2 Some layered intrusions in which ultramafic cumulates form an important part of the exposed layered series. Column 4 gives published estimates of the MgO content of the parent melt (see references cited).

Examples	Age/Ma	Tectonic setting	Estimated melt MgO	Recent description
Rum, Hebrides, Scotland	60	Passive margin	18–20%	Emeleus et al. (1996)
Semail ophiolite, Oman	95	Ophiolite (fast-spreading mid-ocean ridge *or* fore-arc spreading centre)	5–7%	Coogan et al. (2002)
Bay of Islands, Newfoundland, Canada	500	Ophiolite (subduction zone-MOR intersection)	'high-MgO high-SiO_2'	Kurth-Velz et al. (2004)
Duke Island, Alaska	110	Cordilleran thrust belt		Irvine (1974), Saleeby (1992)
Muskox, Canada	1270	Continental rift/LIP		Roach et al. (1998)
Bushveld, S Africa	2060	Possible LIP	14.9%	Eales and Cawthorn (1996)
Great Dyke, Zimbabwe	2575	Continental rift/LIP	16%	Wilson (1996); Oberthür et al. (2002)
Stillwater, Montana	2700	Possibly subduction-related	14.5%	McCallum (1996)

mark the base of each cyclic unit, sometimes in amounts worth mining. In Stillwater and Bushveld the pyroxenite zones overlying the lower peridotite zones are more uniform.

The most easily recognized cumulate textures in these rocks are those containing enstatite **oikocrysts** (Plate 5.1) or pockets of obviously intercumulus plagioclase (Plate 5.2). Many ultramafic cumulate rocks, however, exhibit a polygonal texture in thin section – reminiscent of that in mantle-derived ultramafic rocks (Plate 5.6) discussed below – that may reflect adcumulus overgrowth, but is more probably due to solid-state grain boundary readjustment promoted by very slow cooling (see Chapter 4; Vernon, 2004; Holness, 2005).

The repetition of macro-rhythmic units in the olivine-bearing zones – also prominent in the younger Muskox and Rum intrusions – has led to suggestions that the base of each such unit might mark the influx of a fresh batch of magma (e.g. Brown, 1956; Raedeke and McCallum, 1984). The lack of systematic cryptic layering through these units, or in some intrusions actual reversals in cryptic layering, has been cited in support of such 'magma rejuvenation' (e.g. Eales and Cawthorn, 1996). The 16 macro-rhythmic units of the Eastern Layered Series in the Rum complex have for many years been regarded as the signature of an open magma chamber periodically replenished by fresh magma (Brown, 1956; Emeleus et al., 1996). The prevailing view today is that in many intrusions – unlike Skærgaard, which appears to have evolved as a closed system – the progress of magma evolution and crystal accumulation on the chamber floor that leads to normal cryptic layering was punctuated by fresh injections of primitive (i.e. less evolved) magma from a larger, deeper reservoir. Such injections are detected in abrupt changes in the cumulus mineral assemblage and reversals in cryptic layering. The Rum cumulate series is also cut by thin peridotite sheets, and there is evidence that at least one of the main ultramafic units (Unit 9) originated as a minor intrusion of picritic magma rather than by cumulus processes (Holness, 2005).

What kinds of parental magma generated these voluminous ultramafic successions? Table 5.2 shows the best available estimates for the MgO contents of the parent melts for each of the ultramafic cumulate sequences. Many are higher than for typical basalts and – as we have seen from minor intrusions in Rum – fall in the **picrite** range (Fig. 5.5.1

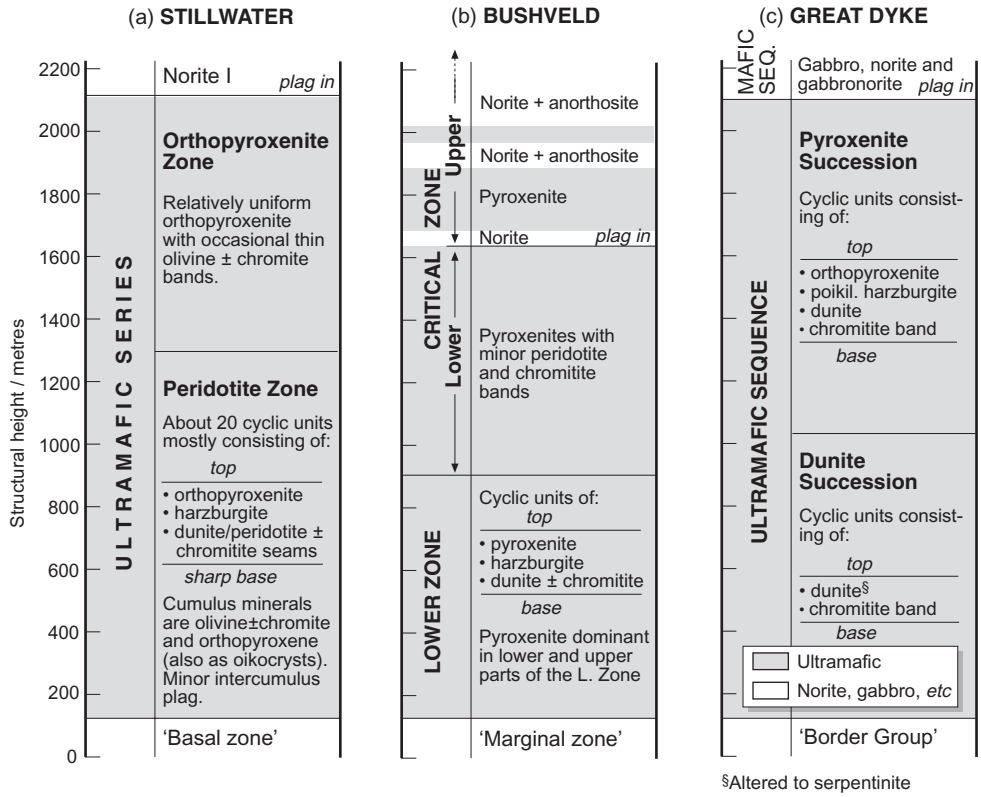


Fig. 5.2 Comparison of the ultramafic divisions of the Stillwater (Montana, USA), Bushveld (S. Africa) and Great Dyke (Zimbabwe) layered intrusions, after McCallum (1996), Eales and Cawthorn (1996) and Wilson (1996) respectively. See Fig. 4.13 for geographical locations. The original authors' nomenclature has been retained, except that 'orthopyroxenite' is used here in place of the obsolete rock name 'bronzitite' (a rock consisting essentially of orthopyroxene in the range $En_{70–90}$, a mineral formerly known as bronzite) widely used in Stillwater literature.

in Box 5.5). Parent-melt estimates for the Archaean and early Proterozoic intrusions shown in Fig. 5.2 also exhibit relatively high SiO_2 contents: 54% for Stillwater, 53% for the Great Dyke and 56% for Bushveld, values confirmed by the importance of cumulus orthopyroxene in the ultramafic cumulates. The conjunction of high MgO *and* high SiO_2 places these magma compositions into the boninite range (Chapter 6), a magma type also represented in some major Precambrian dyke swarms. Some authors have speculated that these large intrusions and dyke swarms represent plumbing systems for Precambrian large igneous provinces (**LIP**s), though it has to be said that boninite magmas play no obvious part in modern LIPs.

The ultramafic divisions of major layered igneous complexes contain seams of massive **chromitite** in the dunite member of each macro-rhythmic unit, providing rich sources of chromium. Bushveld, Stillwater and the Great Dyke also contain substantial deposits of platinum-group elements (**PGE**). In the Great Dyke the PGE-bearing sulphide deposits occur near the top of the ultramafic sequence, having been deposited prior to the first appearance of cumulus plagioclase, but in Bushveld and Stillwater they occur in the overlying noritic parts of the intrusions (Chapter 4).

Ultramafic cumulates in ophiolites

Table 5.2 emphasizes that ultramafic rocks are found in many **ophiolite** complexes (Box 5.3). Malpas (1978), describing the Bay of Islands ophiolite in Newfoundland, was the first to recognize that peridotites in ophiolite complexes have two fundamentally different origins:

Box 5.3 Ophiolites and the structure of oceanic lithosphere

The term ophiolite refers *not to a rock type*, but to an association of related rock types that are found as a consistent – though often incomplete – 'package' in many orogenic belts. The complete package is illustrated in Fig. 5.3.1a, together with profiles of a number of well known examples to emphasize that individual complexes may contain all, or often only some, of the complete sequence. The association of pelagic sediment, pillow basalt, sheeted dolerite dyke swarm, and mafic/ultramafic plutonic rocks is characteristic of oceanic crust formed initially at an oceanic spreading centre: the pillow basalts at the top of the section represent magma erupted on the ocean floor, the sheeted dyke swarm immediately below is a relic of the magma plumbing system by which magma supplied those spreading-centre eruptions, and the plutonic rocks are remnants of an axial magma chamber beneath, floored by mafic and ultramafic cumulates. The basal cumulates pass down into ultramafic tectonites that seem to represent the underlying mantle lithosphere: the harzburgitic and dunitic compositions of these deformed metamorphic rocks suggest residual mantle accreted on to the oceanic lithosphere after earlier magma extraction from upwelling asthenosphere (see Box 5.4).

The interpretation of ophiolites as samples of oceanic lithosphere is reinforced by the correlation between seismic refraction velocity profiles of in situ oceanic crust (Fig. 5.3.1b) and those of ophiolite cross-sections (Fig. 5.3.1c). The 'seismic Moho' marking the nominal base of the oceanic crust is defined by the sharp increase in seismic velocity between 6.5 and 7.5 km in Fig. 5.3.1b. Malpas (1978) suggested that this feature actually marks the boundary between mafic (plagioclase bearing)

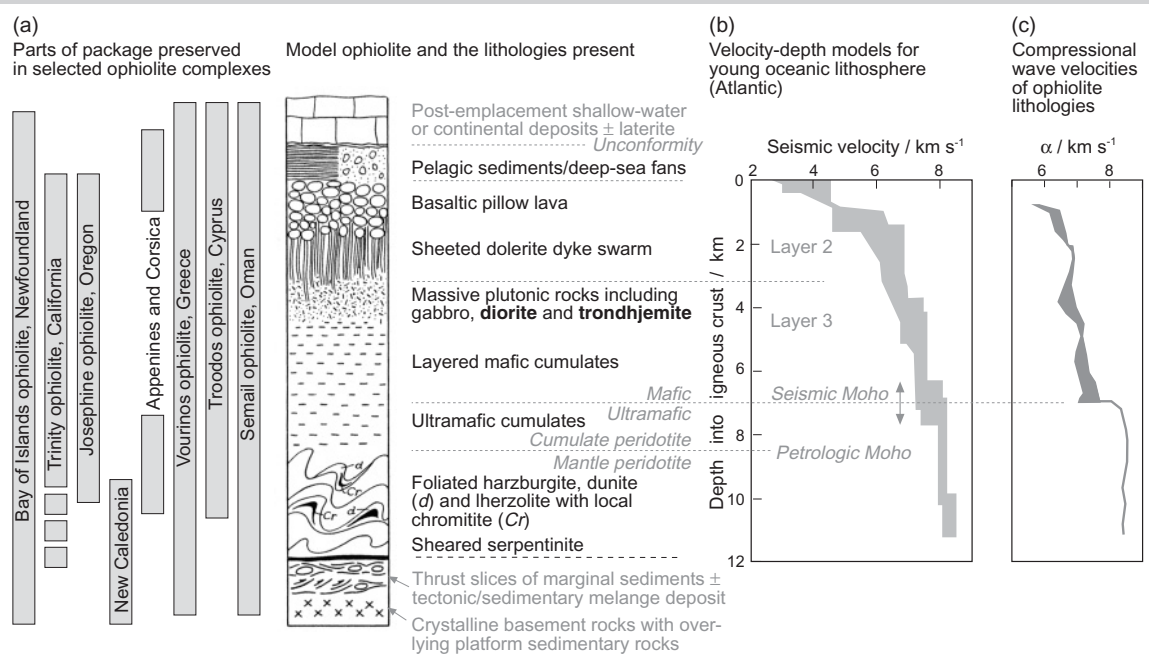


Fig 5.3.1 Composite diagram comparing: (a) A typical ophiolite package (adapted from Moores, 1982): the columns illustrate how much of the complete package is preserved in selected ophiolites around the world (see Fig. 4.11). 'Ophiolite' as traditionally defined embraces the lithologies printed in black to the right of the cartoon (reproduced from Moores (1982) courtesy of the American Geophysical Union); those in grey are additional units included in Moores' 'expanded' definition of an ophiolite complex; (b) A range of modelled seismic-refraction velocity-depth profiles for young oceanic lithosphere (Atlantic Ocean 0–7 Ma old; data from White et al.,1992) and scaled to part (a); and (c) Laboratory-measured compressional-wave velocities of lithologies of the Bay of Islands ophiolite (data from Salisbury and Christensen, 1978) plotted against structural height.

and ultramafic (plagioclase-free) cumulates in ophiolites, and the true base of the crust – where magma-chamber ultramafic cumulates pass down into mantle harzburgites – must lie deeper; he introduced the term 'petrological Moho' for this lower boundary (seen in ophiolites but not detectable seismically).

The deformed and often metamorphosed state of the rocks underlying many ophiolite bodies (see Fig. 5.3.1a) indicates that ophiolite bodies were emplaced into their present setting by tectonic rather than magmatic processes. Trains of ophiolite bodies adorn many of the world's orogenic belts (Fig. 5.3.2) and are believed to trace the exhumed continental suture zone where two converging continents have become welded together. This distribution suggests that ophiolites are fragments of oceanic lithosphere that formed the floor of a contracting ocean basin, which then became caught up in the ensuing continental collision zone.

In what geotectonic setting was the oceanic lithosphere preserved in ophiolites originally created? The dyke swarm and magma chamber suggest an oceanic spreading centre of some kind, but this could be at a mid-ocean ridge, in a back-arc basin or sometimes even in an intra-arc or fore-arc setting; all these possibilities have been proposed for different ophiolites. The Semail ophiolite in Oman, the largest and best exposed ophiolite, has been interpreted as the product of a fast-spreading mid-ocean ridge (Nicolas et al., 1994; Coogan et al., 2002), but formation at a fore-arc spreading centre in an immature arc setting above a subduction zone has also been proposed (Alabaster et al., 1982; Searle and Cox, 1999). Similar controversy surrounds the origin of the Troodos ophiolite in Cyprus. The geochemistry of the Bay of Islands ophiolite in Newfoundland suggests that it formed in a supra-subduction-zone (SSZ) environment (Jenner et al., 1991; Elthon, 1991) near an island arc–spreading ridge intersection (Kurth-Velz et al., 2004). No single tectonic context can account for all of the diverse ophiolite occurrences seen around the world. Dilek (2003) provides an up-to-date review of ophiolite origin and emplacement.

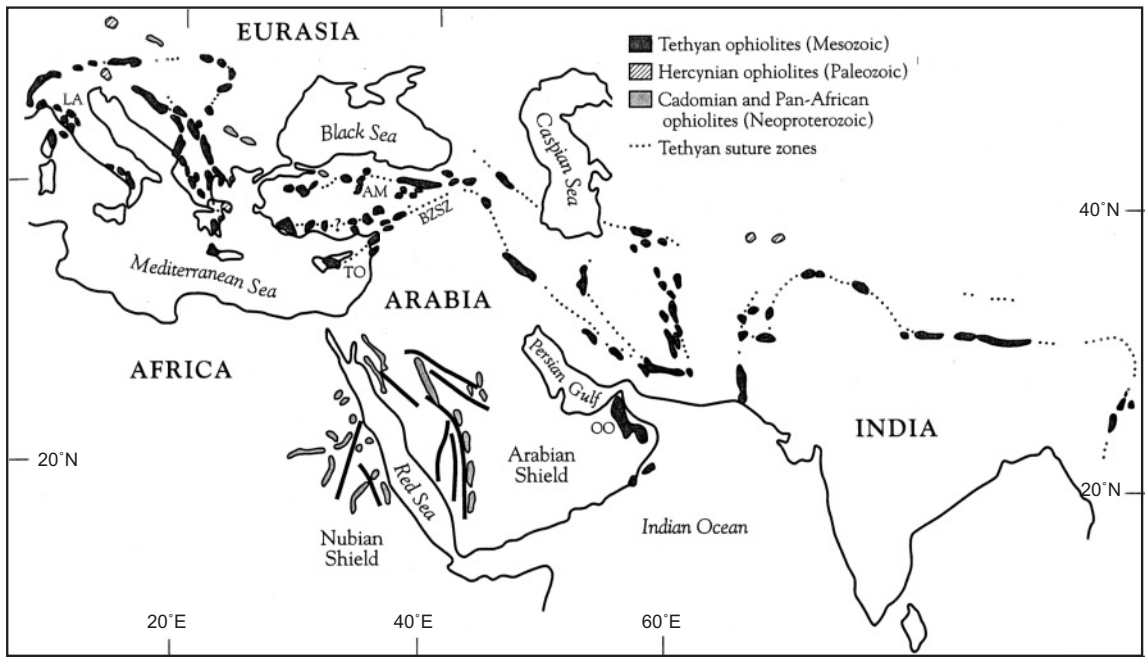


Fig. 5.3.2 Map showing the distribution of major Mesozoic (Tethyan), Palaeozoic and Neoproterozoic ophiolites bordering the Mediterranean, Black, Caspian and Red Seas and the Indian Ocean (adapted from Moores et al., 2000 courtesy of the Geological Society of America). LA, Ligurian ophiolites; AM, Ankara mélange; TO, Troodos ophiolite; BZSZ, Bitlis-Zagros suture zone; OO, Oman (Semail) ophiolite.

- an upper unit of dunites with chromitite bands and lenses, which appear to have formed as initial olivine (+ chromite) cumulates from basic magma in a magma chamber beneath an oceanic spreading centre (Box 5.3);
- a lower unit consisting mainly of harzburgites, showing tectonite fabrics attributable to solid-state deformation. Malpas recognized that the harzburgites could not be igneous cumulates (the reaction relationship between olivine and enstatite (Box 4.3) prevents these two minerals crystallizing in equilibrium from igneous melts at crustal depths), and concluded that they are deformed solid mantle rocks from the uppermost oceanic lithosphere. Their **depleted** composition (see Box 5.4) is consistent with this interpretation.

The sketch-section in Fig. 5.3 illustrates the same mantle-crust transition zone for part of the Semail ophiolite in Oman (shown as 'OO' in Fig. 5.3.2, Box 5.3). Light grey shading here signifies harzburgite tectonites, representing the lithospheric mantle forming the floor of an oceanic spreading centre magma chamber. This unit is host to numerous gabbroic and dunitic intrusive sheets, interpreted as relics of lithospheric magma plumbing systems that fed crustal magma chambers above. The unit shown white consists primarily of heterogeneous dunite, apparently of cumulus origin with chromitite lenses and pods reminiscent of continental layered intrusions (Fig. 5.2). In many places the dunites appear to have been subject to magma injection and percolation, indicated by gabbro sills and by zones of dunite 'enriched' with interstitial plagioclase and clinopyroxene (Boudier and Nicolas, 1995). The dunites are in turn overlain by layered gabbros, which are cut by intrusive sheets of troctolite and wehrlite. The cumulate succession from dunite to gabbro can be understood in terms of basaltic magma initially crystallizing only olivine (and minor chromite), then crystallizing plagioclase and augite in addition as the evolving melt became saturated with these minerals (cf. Fig 4.8).

The boundary between mantle harzburgite and cumulate dunite (the 'petrological Moho' of Malpas (1978) – see Box 5.3) is complex in the Semail ophiolite, with a lot of inter-

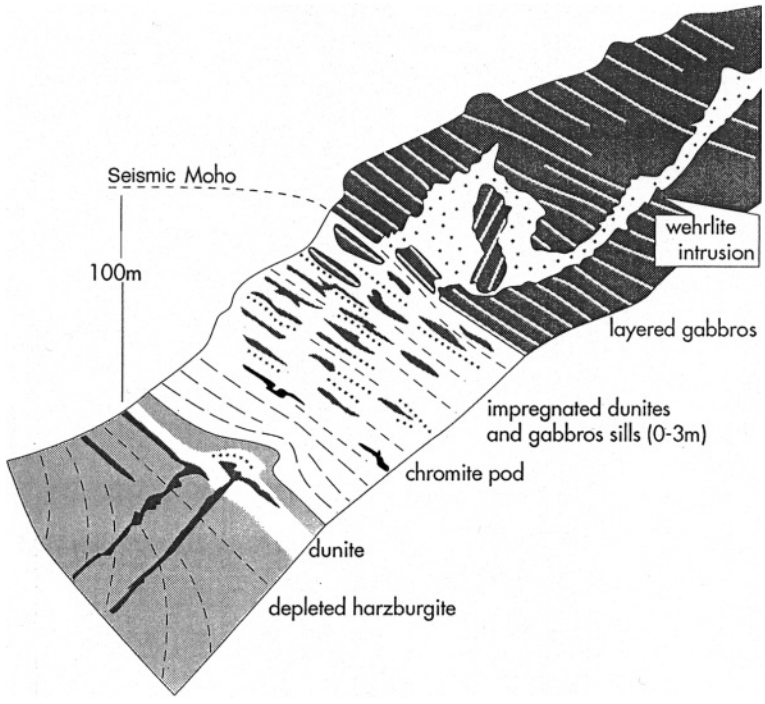


Fig. 5.3 Sketch section of the 'mantle transition zone' in the Semail ophiolite, Oman (Wadi Makhah section), showing depleted harzburgites of the mantle section (pale grey), ultramafic cumulates (white) containing chromitite pods (black), and overlying layered gabbros (dark grey; white bands depict layering); dashed lines indicate trace of foliation. Ultramafic rocks are cut by gabbro dykes and sills, and dots indicates dunites containing interstitial plagioclase and/or clinopyroxene resulting from magma percolation. Reproduced from Boudier and Nicolas (1995) by permission of Oxford University Press.

fingering of the two lithologies. Both possess planar and linear fabrics indicating high-temperature solid-state deformation which Boudier and Nicolas (1995) attribute to flow in the upwelling asthenosphere and accreting oceanic lithosphere beneath an ocean ridge; this deformation appears to have affected the early magma cumulates too. Such structural complexity is characteristic of nearly all ophiolites (Moores, 1982).

Ultramafic bodies of Alaskan type

More than 30 ultramafic complexes lie scattered along a 500 km long by 35 km wide linear chain extending from NNW to SSE along the south-eastern 'panhandle' of Alaska. Most are no more than a couple of kilometres in diameter. Some of the larger ones exhibit crude concentric zoning from a dunite core to hornblende pyroxenite margins, though the best described of them, the spectacularly layered Duke Island complex at the southern end of the chain (Irvine, 1974), is notable for lacking this pattern of zoning. These intrusions, the majority of which are unlayered but with distinctive cumulate textures, typify an association known as 'ultramafic complexes of Alaskan type'.

Alaskan-type ultramafic intrusions occur in many other parts of the world, notably in the Urals and the Siberian platform, in Colombia–Ecuador and in eastern Australia; the concentric architecture of one recently described Colombian example is illustrated in Fig. 5.4. In the Alaskan and Colombia–Ecuadorian cordilleras, such intrusions are located near boundaries between adjacent allochthonous terranes and some authors speculate that their genesis may be connected with terrane accretion. The concentric zonation characteristic of some bodies has been attributed to successive crystal-mush injections of cumulate fractions derived from a deeper-seated magma chamber (Tistl et al., 1994), and the unzoned, layered Duke Island intrusion may be a remnant of such a deeper chamber. The abundance of hornblende as a cumulus and post-cumulus mineral, and the injection of hornblende-plagioclase pegmatites and dykes into country rocks and contact breccias, point to a hydrous magma composition.

Like some major layered intrusions, Alaskan-type ultramafic bodies may contain

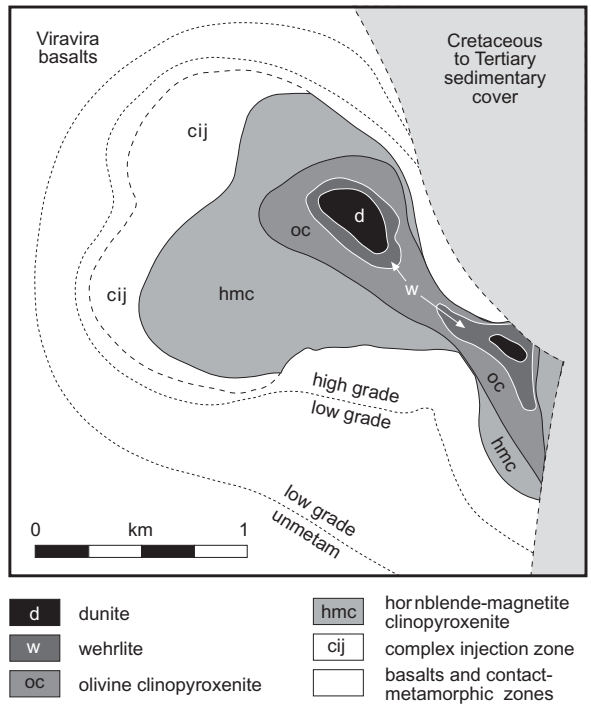


Fig. 5.4 Sketch geological map of a zoned ultramafic intrusion of Alaskan type: the 20 Ma-old Condoto intrusion in NW Colombia (SSW of Medellin), simplified from Tistl et al. (1994). The intrusion was emplaced into Viravira basalts which contain lenses of cognate peridotite cumulates. The 'complex injection zone' consists of metasomatized pyroxenites and magmatic breccias and is cut by hornblende-bearing dykes.

PGE deposits, associated with chromitite layers and segregations in the dunite core. Fourteen such complexes make up the 1000 km-long 'platinum-bearing belt' in the central and northern Urals, for example (Garuti et al., 1997). Placer deposits associated with such bodies often provide the best PGE prospects (e.g. Tolstykh et al., 2004).

MANTLE-DERIVED PERIDOTITES

Mantle xenoliths in basalts and kimberlites

It is not unusual to find continental **alkali** basalt or basanite lavas or plugs that contain distinctive fresh olive-green crystalline xenoliths (Plate 5.3), ranging in diameter up to a few tens of centimetres, consisting variously

of olivine, orthopyroxene, clinopyroxene and spinel. Typically the clinopyroxene in these xenoliths is a 'chrome-diopside' that has a vivid green colour in hand-specimen, as shown in Plate 5.4. The occurrence of orthopyroxene in inclusions hosted by alkali basalt suggests these are not **cognate** cumulates – formed from the host basalt itself at an earlier stage in its ascent through the crust – because low-Ca pyroxene would not be expected to crystallize from such SiO_2-poor melts at crustal depths. This conclusion is confirmed by the texture seen in thin section (Plate 5.6). There is no hint of cumulate textures like those shown in Plates 5.1 and 5.2. These xenoliths usually possess a polygonal or mosaic texture – in which most grain boundaries meet at 120° triple junctions – characteristic of advanced solid-state recrystallization; such rocks are best designated as metamorphic rather than igneous rocks. The spinel lherzolite and harzburgite xenoliths found in basalts are interpreted as samples of conduit wall-rock torn off and transported by magma that has ascended directly from the mantle. Typical compositions (as mineral proportions by volume) of such basalt-hosted 'mantle xenoliths' are illustrated in Fig. 5.1.

A more varied suite of mantle-derived xenoliths can be found in **kimberlite** diatremes and dykes (Chapter 9). In addition to spinel lherzolites, one may find garnet lherzolites (Plate 5.5), harzburgites, dunites, pyroxenites and **eclogites**, often accompanied by rock types of crustal provenance. Some of the diversity in mantle-derived xenoliths is attributable to the greater *depths* from which kimberlites appear to be derived (judging by the occurrence of diamond in some). Figure 5.5 shows a temperature-depth diagram similar to Fig. 2.17, in which the boundaries between plagioclase lherzolite, spinel lherzolite and garnet lherzolite stability fields are shown. The boundaries are inclined, indicating that the pressure (depth) at which garnet lherzolite (for example) would transform into spinel lherzolite depends on temperature, and therefore on the local geothermal gradient. Despite these sloping boundaries, it is broadly true that garnet lherzolite is stable at greater depth in the mantle than spinel lherzolite, and that plagioclase lherzolite is stable only in the crustal depth range (hence its rarity). Upwelling mantle that ascends along the ~1300 °C adiabat (cf. Fig. 2.17) will pass into spinel lherzolite field before reaching the solidus; the basaltic melts so formed encounter wall-rocks of spinel lherzolite, which dictate the dominant xenolith lithology found in such basalts. Only if mantle upwells along a higher-temperature geotherm (e.g. 1400 °C) will it melt enough at sufficient depth for the capture of garnet lherzolite xenoliths to be possible; spinel lherzolites may be entrained as well at shallower levels during later stages of magma ascent.

Another aspect of xenolith diversity relates to the *history* of the mantle domain 'sampled' by a xenolith. Box 5.4 explores the process of partial melting in polymineralic rocks such as lherzolite. 'Fertile' mantle – that from which no melt has previously been extracted

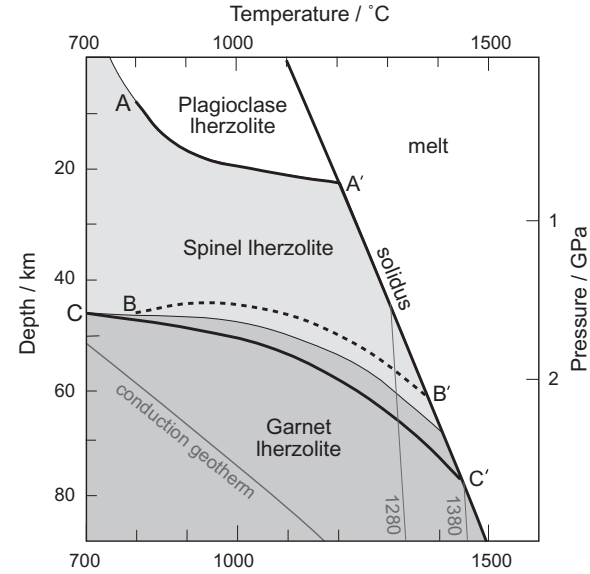


Fig. 5.5 Stability fields of plagioclase lherzolite, spinel lherzolite and garnet lherzolite on a temperature *versus* depth (pressure) plot. The plagioclase–spinel and spinel–garnet boundary curves A–A' and B–B' are from thermodynamic calculations by Saxena and Eriksson (1983); C–C' is an experimentally determined spinel–garnet boundary curve from O'Hara et al. (1971); the boundary between spinel and garnet lherzolite has been placed arbitrarily between curves B–B' and C–C'. The solidus curve and the lines marked '1280' and '1380' – the 1280 °C and 1380 °C adiabats respectively (cf. Fig. 2.17) – are from McKenzie and Bickle (1989).

– is represented here by simple lherzolite (disregarding spinel and garnet to simplify the discussion). Suppose the initial lherzolite has the composition 'M'. As melt (initial composition m_1) is extracted from M under equilibrium conditions, the residual solid assemblage becomes depleted with respect to m_1 and so migrates from M (lherzolite) to s_1 (harzburgite) then, if melt extraction continues, to s_2 (harzburgite) and s_3 (dunite). A volume of mantle that has experienced one or more episodes of melt extraction may therefore contain domains of harzburgite and dunite as well as lherzolite (Fig. 5.1), so it is not surprising to find such 'residual mantle' rock types represented in mantle xenolith suites hosted by basalts and kimberlites, which have presumably traversed such domains during their ascent.

Kimberlite xenolith suites have typically 'sampled' the thick mantle lithosphere that lies beneath Archaean cratons or the Proterozoic mobile belts that surround them (the two ancient crustal domains where kimberlites are typically found).

*Olivine composition in the mantle and the identification of **primary** melts*

Petrologists today accept that many basalts erupted at the Earth's surface (including most mid-ocean ridge basalts (MORBs)) have undergone some degree of fractional crystallization during their ascent; this may happen, for example, in an axial magma chamber underlying a fast-spreading mid-ocean ridge. In order to use basalt analyses as a geochemical 'window' into mantle source regions, it is important to eliminate more evolved basalts from consideration, those whose compositions are no longer in equilibrium with mantle mineralogy and may distort the conclusions drawn. To extract valid information about the mantle from basalt compositions, it is necessary to confine attention to **primary** melts – those which have undergone negligible fractionation since segregating from their mantle source. This requirement begs an important question: how can primary basalts be identified?

One simple, qualitative approach is to consider only those basalts that contain xenoliths of obvious mantle origin. When a magma spends time fractionating in a crustal magma chamber, any such xenoliths entrained in it – having densities ($\geq 3.2\,kg\,dm^{-3}$) well above that of the host melt (typically 2.65–$2.70\,kg\,dm^{-3}$) – will sink to the floor of the chamber and thereby escape later transportation to the surface. The presence of mantle-derived xenoliths is therefore an indication that the host lava has passed from the mantle to the surface *without* being detained in a magma chamber, and therefore with little opportunity for melt composition to fractionate significantly.

Mantle xenoliths, however, tend to be restricted in their distribution. A more widely applicable test of primary character is based on a lava's **Mg number** (often abbreviated to 'Mg #'). The principle is illustrated in Fig. 5.6. Olivines in mantle-derived peridotite xenoliths tend to have compositions lying in the range Fo_{88}–Fo_{92}. This range is shown as a vertical band on the left of Fig. 5.6.[2] Tracing tie-lines (from where these compositions intersect the solidus) horizontally across the two-phase (ruled) field to the liquidus indicates the range of melt compositions in this system that can coexist in equilibrium with mantle olivine – they are indicated by the right-hand vertical band. The melts in this phase diagram are simplified laboratory preparations – containing only Mg_2SiO_4 and Fe_2SiO_4 – that show little similarity to real basalts. Nonetheless a systematic relationship does exist between the composition of a natural basalt and the olivine with which it can equilibrate. In its simplest form (devised by Roeder and Emslie, 1970), this relationship may be written:

$$\frac{(Fe^{2+}/Mg)^{olivine}}{(Fe^{2+}/Mg)^{melt}} \approx 0.3 \qquad [5.1]$$

where Fe^{2+} and Mg represent the **atomic proportions** of ferrous iron and magnesium in

[2] Because olivine composition (e.g. Fo_{92}) is expressed in ***mole*** percentages of Mg_2SiO_4 whereas the composition (horizontal) axis of Fig. 5.6 is plotted – according to convention for such diagrams – in *mass* %, the left and right boundaries of the mantle-olivine band do not coincide with 92 and 88% on the composition axis of the figure. Similar reasoning explains why the right-hand boundary of the band of primary melts (Mg # = 68) does not plot at 68 in this diagram.

Box 5.4 How do rocks melt? Origins of 'fertile' and melt-depleted mantle

Figure 5.4.1 below presents two perspectives on the process of partial melting in a polymineralic rock such as lherzolite. On the left are views of the lherzolite as it might appear in thin section, shown at three stages of partial melting as the temperature is raised. On the right are sketches of the phase diagram for the laboratory system $CaMgSi_2O_6$(diopside)–Mg_2SiO_4(forsterite)–$Mg_2Si_2O_6$(enstatite), in which the progress of melting can be followed (see caption for explanation). The point M illustrates one possible composition for the initial solid (lherzolite) assemblage that undergoes partial melting: one simplified model for 'fertile mantle'.

The first melt to appear when M is heated to sufficient temperature (middle tier) necessarily forms in chemical equilibrium with *all* of the three minerals present. The only melt composition that can satisfy this requirement (m_1) lies at the junction of the three mineral stability fields (right-hand diagram), at the **eutectic** point E. This is the initial melt composition that would form from *any* mixture of diopside, forsterite and enstatite (whether M or N, for example). The location of E – within the triangle – tells us that *all three minerals participate in partial melting* and contribute to the initial melt, though in different proportions to those in the original solid.

Where will the first pockets of melt form in the rock? If all three minerals are required to contribute, it follows that such pockets (shown black in the left-hand diagram) can form only at Di–Fo–En grain intersections where *all* of the chemical components are available. Fo–En–En, Fo–Fo–En and Fo–Di–Fo grain intersections initially produce no melt. As partial melting progresses, the melt composition is initially buffered at m_1 by the presence of the three coexisting minerals. m_1 is richer in diopside than M and, as the proportion of melt m_1 increases (assuming that none escapes), the remaining solid mixture therefore suffers depletion in Di and migrates from M to s_1.

Mixture s_1 lies on the Fo–En edge of the diagram, and marks the stage at which $CaMgSi_2O_6$ has just disappeared from the solid residue and now resides entirely in the melt phase. Further melting (lower tier) can draw on only the two solid minerals remaining (Fo and En), and therefore the melt composition, hitherto constant, must begin to change. While it remains in equilibrium with Fo and En, it is constrained to migrate up the **cotectic** between the 'melt + olivine' and 'melt + opx' fields,* as the residual solid mixture migrates in composition from s_1 toward Fo: melt m_2, for example will coexist with residual solid s_2. When the melt reaches m_3, it coexists with a residual solid s_3 that consists solely of forsterite; enstatite has now disappeared from the solid residue. If melting continues, the melt will evolve from m_3 directly toward M.

Though the phase diagram shown only approximates to natural mantle mineralogy (it contains no iron – normally present in mantle olivine, orthopyroxene and clinopyroxene – and it lacks an aluminous phase), two useful lessons about partial melting can be drawn. Firstly, all of the minerals present in lherzolite *begin to melt together*, rather than one after the other as one might initially suppose. Secondly, as partial melting advances, first clinopyroxene becomes exhausted, leaving a Fo + En ('harzburgite') solid residue, then orthopyroxene disappears leaving a solid residue consisting only of Fo ('dunite' in Fig. 5.1).

Because we have been considering a closed system, the overall composition remains at M, but it consists in turn of melt m_1 + solid s_1, $m_2 + s_2$, $m_3 + s_3$, and eventually (if melting runs to completion) a melt of composition M.

* The olivine–enstatite reaction relationship shown in Fig. 4.3.1(b) does not apply at mantle pressure.

each phase (or the **molar proportions** of their oxides FeO and MgO). For day-to-day use, however, it is more common to express the Fe : Mg proportions in a rock in terms of its Mg-number:

$$\text{Mg number} = \left[\frac{100\,\text{Mg}}{\text{Mg} + \text{Fe}^{2+}}\right]_{\text{atomic}} = \frac{100(\text{MgO}/40.32)}{(\text{MgO}/40.32) + (\text{FeO}/71.85)} \qquad [5.2]$$

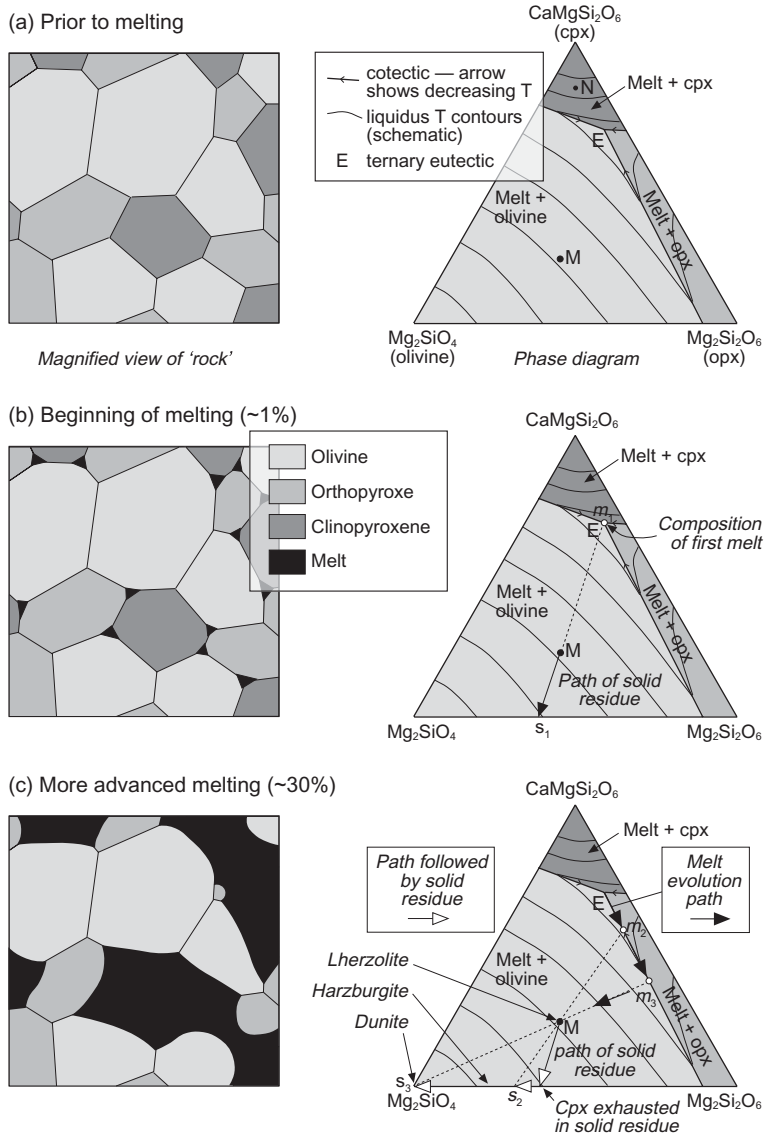


Fig. 5.4.1 Progression of melting in a lherzolite as temperature is raised from (a) below the solidus to (b) just above it to (c) substantially above it. The phase diagram on the right is a schematic representation of the anhydrous system Di–Fo–En at upper mantle pressures (~2 GPa) after Yoder (1976) courtesy of the National Academy of Sciences. Each field indicates the range of melt compositions that can exist in equilibrium with the *single* mineral indicated (tints correspond to relevant minerals in the left-hand diagram); the contours showing liquidus temperature are purely illustrative. Between the fields are **cotectic** boundaries marking melt compositions that coexist in equilibrium with *two* minerals. The point E (**eutectic**) where the three boundaries meet marks the sole melt composition that can exist in equilibrium with *all three* minerals.

where 40.32 and 71.85 are the relative molecular masses (**RMM**s) of MgO and FeO respectively and oxide amounts are expressed in mass %. The Mg number (ranging from 0 to 100) has high values for primitive melts and low values for more evolved (Fe-rich) melts. If we accept that mantle olivine compositions generally lie in the range Fo_{88}–Fo_{92} (Fig. 5.6), equation 5.1 can be used to show that primary melts – those in equilibrium with

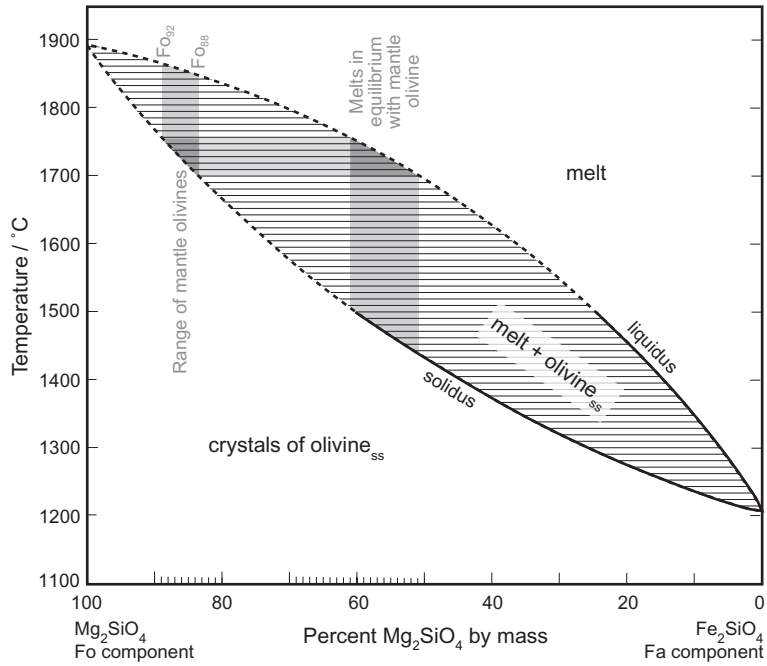


Fig. 5.6 The system Mg_2SiO_4–Fe_2SiO_4; as in Fig. 3.6, the subscript 'ss' denotes solid solution. The range of olivine compositions found in mantle-derived xenoliths is indicated by the left-hand vertical grey bar; note that 'Fo_{92}' and 'Fo_{88}' do not plot at 92 and 88 on the horizontal axis because it is graduated in mass %, not mole %. The horizontal grey bar indicates the bundle of tie-lines linking these olivine compositions to the range of melt compositions that can coexist with them (right-hand vertical grey bar).

mantle olivine – will have Mg numbers in the range 68–77 (see Exercise 5.2). Having an Mg-number value in excess of 68 is therefore a condition for a primary magma (some authors relax this requirement to Mg # >65).

Note that equations 5.1 and 5.2 involve FeO but not Fe_2O_3 (Fe^{3+} behaves differently from Fe^{2+} on account of its higher ionic charge and lower ionic radius, and cannot enter olivine). It is common when presenting basalt analyses, however, to list only the total of the iron oxides, as ΣFeO or ΣFe_2O_3 (see Table 2.4 and Box 2.6). In such cases, it is conventional to assume that 10% of the iron present in the melt is Fe^{3+} and the remaining 90% as Fe^{2+}. The 'FeO' used for calculating the Mg number is therefore set to $0.9 \times \Sigma FeO$ or $(0.9 \times \Sigma Fe_2O_3 \div 1.11)$.

Orogenic peridotite massifs

The spatial and temporal relationships between different mantle lithologies are difficult to study in volcanic-hosted xenoliths because *composite* xenoliths are relatively scarce, and their size (tens of cm in diameter) restricts the scale on which such relationships can be studied, compared say to a field outcrop. 'Orogenic' peridotites[3] provide an alternative setting for studying mantle rocks which, though not strictly in situ, preserves vital spatial relationships between different lithologies. Orogenic peridotites are lenses of shallow mantle material – varying in scale from <30 m to >20 km – that have been tectonically incorporated into the roots of continental collision zones like the Pyrenees and the Alps, later to be exhumed – often in association with high-grade crustal metamorphic rocks – by post-orogenic uplift and erosion. The intimate association with high grade metamorphic rocks of crustal origin such as granulites, charnockites and kyanite–almandine gneisses suggests a derivation from continental mantle lithosphere, rather than the oceanic lithosphere sampled by ophiolites. In some cases, for example the Lanzo and Othris peridotites (see Fig. 4.13), the involvement of subcontinental asthenosphere as well has been mooted.

Among the most extensively studied orogenic peridotites are those of the North Pyrenean Metamorphic Zone, including the eponymous Étang de Lherz massif (one of about 40 such bodies on the northern margins of the Pyrenees), and others in the Betic and Rif mountain belts that straddle the western Mediterranean (see Fig. 4.13). These ultramafic bodies consist chiefly of foliated,

[3] Known alternatively as 'alpine peridotites'.

metamorphosed spinel lherzolite, with subordinate spinel and garnet pyroxenites and/or harzburgite defining a compositional banding on the scale of metres that is concordant with the foliation. The rocks are commonly serpentinized. In some massifs the layered rocks are cut by discordant veins or dykes of amphibole-bearing pyroxenite and/or hornblendite that provide direct evidence of basic melt migration in the uppermost mantle; the intrusive relations have allowed the chemical interactions between such melts and their mantle wall-rocks to be investigated.

The processes responsible for the emplacement of orogenic peridotite bodies into the lower continental crust remain unclear. Some form of tectonic emplacement associated with shear zones, possibly during lithosphere extension, seems to be a major factor for some, while others appear to have ascended in diapiric form; the southern part of the Lanzo peridotite in the Italian Alps, for example, has been interpreted as an asthenospheric diapir emplaced during the opening of the Liguro-Piemontese ocean basin (Bodinier et al., 1991).

Textures in xenolithic and orogenic peridotites

The textures of ultramafic xenoliths in basaltic host-rocks and kimberlites have much in common with orogenic peridotites, a fact that is hardly surprising given that both associations derive from the sub-continental mantle. The least deformed examples in both suites possess a coarse crystalline texture (Plate 5.4) which, in thin section (Plate 5.6), can be seen to consist of interlocking anhedral grains whose polygonal boundaries meet at triple junctions with interfacial angles close to 120° (Plate 5.6). This polygonal texture is the hallmark of metamorphic rocks held at high temperatures for long periods. In three dimensions, it resembles the texture of froth formed from a soap solution, and the cause is the same: the reduction in interfacial free energy (surface tension in the case of the foam) that the system achieves through minimizing the total grain-boundary (or soap-film) area. The necessary grain-boundary adjustments are achieved by local solid-state recrystallization at grain boundaries, assisted by the high ambient temperatures in the mantle.

This least deformed configuration (Plate 5.6) is known as *protogranular* texture (the prefix 'proto-' signifying an original state). Another example is shown in Plate 5.7 from Lherz, in which original mineral grains are cut by mineralized fractures, probably formed during tectonic emplacement of the massif into the Pyrenean orogenic belt. A spectrum of more deformed textures is seen both in xenoliths and in orogenic massifs. Deformation within the mantle is dominated by ductile mechanisms. In the commonest deformed texture, two generations of olivine and orthopyroxene crystals can be distinguished:

- larger, often elongated or strained crystals ('porphyroclasts');
- smaller polygonal strain-free crystals ('neoblasts') or finer sheared material.

An example of this *porphyroclastic* texture with a sheared matrix is shown in Plate 5.8. More extreme deformation leads to a finer-grained equigranular or mosaic texture, which some authors believe may record derivation from the ductile asthenosphere.

Abyssal peridotites from the ocean floor

Peridotites have been dredged, drilled or recovered by submersible from numerous sites on the walls of fracture zone valleys and from rift-valley mountains of slow-spreading ridges like the Mid-Atlantic and Indian Ocean ridge systems (Dick et al., 1984), or at intersections such as St Paul's Rocks (Fig. 2.12). Commonly such *abyssal peridotites* are severely serpentinized and weathered, but they retain sufficient mineralogical and textural evidence for many authors to correlate them with 'lithospheric' alpine peridotites. In terms of their primary mineralogy, they vary in composition from spinel lherzolite to dunite. They are widely interpreted as residual mantle (remaining after the extraction of mid-ocean ridge basalt) that has accreted to the trailing edge of the extending oceanic lithosphere. Abyssal peridotites can be thought of as complementary in composition to MORB through the decompression partial-melting processes that feed mid-ocean ridge volcanism, and they retain a chemical record of these processes (Baker and Beckett, 1999).

Box 5.5 Definitions of 'komatiite' and 'picrite': consensus *versus* convention

Most published definitions of komatiite incorporate genetic, textural and compositional strands, broadly as follows:

- komatiite is generally understood to be a volcanic rock (recognized from field evidence such as chilled lava tops, pillows, hyaloclastite breccias, amygdales), but occasionally it may also form high-level sills and other minor intrusives (Beresford and Cas, 2001, Arndt et al., 2004);
- komatiite lavas – and sills – exhibit **spinifex** texture, though only in the upper portion (see Fig. 5.8);
- mineralogically speaking, komatiites are ultramafic/peridotitic in composition: plagioclase is very rare in Archaean komatiites (Nisbet et al., 1993);
- komatiites are chemically distinctive in being highly magnesian (typically 18% < MgO < 32% volatile-free).

In terms of chemical composition, komatiite lavas have much in common with **picrite**s, another type of high-Mg lava (Chapter 2). Picrites are basalts (or dolerites) containing an unusual abundance of (**polyhedral**) olivine phenocrysts, and often have MgO contents in the 15%–30% range, similar to komatiites. In some cases the high MgO content is the result of olivine crystals accumulating in basaltic magma, but some picrite lavas appear to have erupted as highly magnesian melts (e.g. Holm et al., 1993). The essential petrographic difference between picrite and komatiite lies in the presence or absence of spinifex olivine: in a komatiite lava, spinifex texture is present whereas in a picrite the olivine adopts only the more familiar polyhedral habit. Picrites often contain a small amount of plagioclase too.

The IUGS sought to draw a distinction between komatiite and picrite on purely chemical criteria (Le Bas, 2000; Le Maitre, 2002 Fig. 2.13). Their intricate compositional definitions are represented in simplified graphical form in Fig. 5.5.1. Kerr and Arndt (2001) challenged this approach: they demonstrated that more than half of the spinifex-textured komatiites described from Gorgona Island had compositions falling in the IUGS picrite field in Fig. 5.5.1, while all of the non-spinifex Gorgona picrites fell in the IUGS komatiite field (Fig. 5.5.2). They emphasized the need for nomenclature to take into account the key *textural* difference between picrite – in which olivine occurs solely as polyhedral crystals – and spinifex-textured komatiite. The practical distinction between komatiite and picrite remains contentious.

KOMATIITES, PICRITES AND RELATED HIGH-MGO VOLCANIC ROCKS

Though it is clear that peridotites with igneous textures can crystallize from igneous melts, most are coarse-grained and clearly plutonic in origin. As with all cumulate rocks, doubt surrounds the composition of the *melt* from which they crystallized. Can all peridotites with igneous textures be explained as cumulates from *basic* melts – the ultramafic composition being a consequence of selective crystallization or concentration of mafic minerals – or might some examples have crystallized from melts that were themselves *ultrabasic* in composition? The possible existence of ultrabasic melts was much debated between the mid-1920s and the late 1960s. Vogt (1926) and Hess (1938), for example, took the view – albeit cautiously – that peridotite melts could exist in Nature and might in some circumstances erupt at the Earth's surface. Bowen (1928), in his seminal book *The Evolution of the Igneous Rocks*, took the opposite stand, regarding all plutonic ultra-

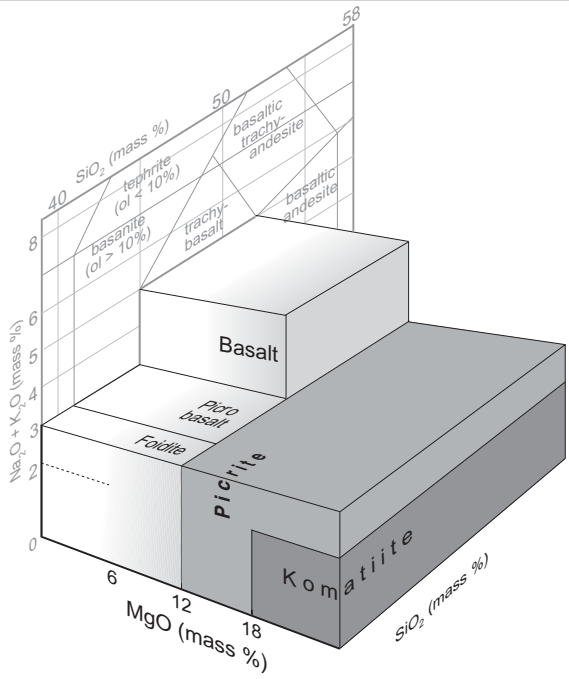


Fig. 5.5.1 A simplified graphical representation of the compositional fields of komatiite and picrite, according to their IUGS definitions (Le Maitre, 2002). The 3D diagram is based on the TAS plot in Fig. 2.1 (back plane), adding MgO as a third dimension. No upper limit for the MgO content is specified.

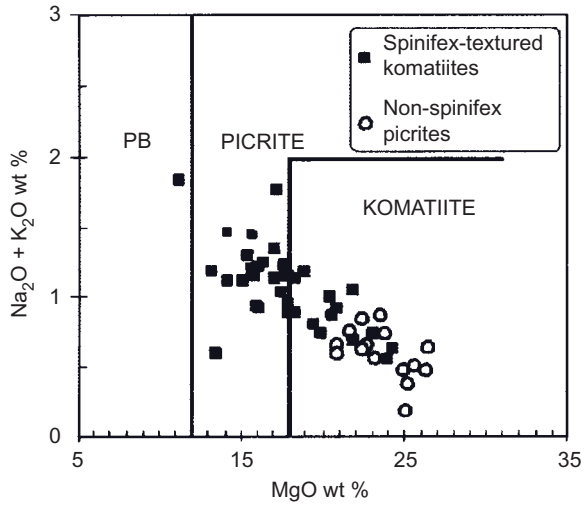


Fig. 5.5.2 Compositions of Gorgona Island komatiites (black symbols) and picrites (open symbols) plotted in a total-alkalis *versus* MgO plot; the fields marked are from IUGS (Le Maitre, 2002). Reproduced from Kerr and Arndt (2001) by permission of Oxford University Press.

mafic rocks as products of crystallization of basaltic magmas.[4] As with the explanations for massif anorthosites (Chapter 4), the existence of minor intrusions having peridotitic average composition could be explained through emplacement of crystal-enriched mushes remobilized from deeper chambers.

The proponents of peridotite melts faced two hurdles in getting their hypothesis accepted. The first was the lack – at least in the international geological literature of the time – of compelling field evidence for ultramafic *volcanic* rocks that could unambiguously represent melts of peridotitic composition. The second hurdle was that any peridotite melt would be highly magnesian in chemical composition and, from the experimental evidence already emerging (e.g. Fig. 3.6), could be expected to melt only at exceptionally high temperatures: the range 1500–1600 °C was mooted by both Vogt and Bowen. Most petrologists of the time regarded the accumulation of mafic minerals from *basaltic* melts as the more credible explanation for magmatic ultramafic rocks.

[4] See the brief review of this debate by Arndt and Nisbet (1982, pp. 1–3).

That prevailing view changed dramatically with the publication by Viljoen and Viljoen (1969)[5] of field research carried out in the Archaean Barberton Mountain Land of South Africa under the aegis of the 'International Upper Mantle Project'. The Viljoens' work demonstrated beyond reasonable doubt the existence, in the Komati River valley, of peridotitic lavas with MgO contents sometimes exceeding 30%: in the words of Viljoen and Viljoen (1982)

> '*(volcanic) features such as once-glassy chilled lava-tops, hyaloclastite breccias and amygdales were noted from the Barberton ultramafic lavas*',

and they coined the name 'komatiite' (after the Komati River) for these evidently effusive peridotite lavas. The term originally embraced both peridotitic lavas and chemically related basalts ('basaltic komatiites') with which they were associated, but today the term is reserved for high-Mg ultrabasic lavas (Box 5.5).

The most distinctive feature of the type-komatiites in the field was the presence of blade-like olivine crystals several centimetres in length, either randomly orientated or forming sheaves of sub-parallel or divergent crystals (Fig. 5.7); in thin section the olivine blades are often seen to have skeletal form (Plate 5.9). This texture, now universally known as 'spinifex texture' (alluding to a spiky Australian grass, *Triodia spinifex*, which it superficially resembles – see Nesbitt, 1971), was interpreted by the Viljoens as a **quench** texture, formed as a result of very rapid cooling – another pointer to surface eruption. Current explanations for the texture are reviewed in the following section.

Spinifex-textured komatiite lavas have since been recognized in all of the world's well preserved Archaean **greenstone** belts (Box 5.6); ironically they include some ultramafic lavas that had been recognized as such prior to 1969 but whose petrological significance had lain hidden in geological survey reports (examples are cited by Viljoen and Viljoen, 1982). Figure 5.8 illustrates the internal structure and thickness of typical komatiite lavas from the Munro Township locality in NE Ontario. The diagram emphasizes that spinifex texture is confined to the upper, more quickly cooled part of a komatiite lava (and blade size may vary considerably with depth below the surface of the flow); the lower part of the flow contains olivine with normal **polyhedral** habit. In other words, komatiite flows are *texturally zoned* and may for that reason be difficult to recognize where poorly exposed.

Though spinifex-textured komatiites are overwhelmingly of Archaean age, younger examples are known from Gorgona Island off the west coast of Colombia, where

[5] For a more accessible historical review, see Viljoen and Viljoen (1982).

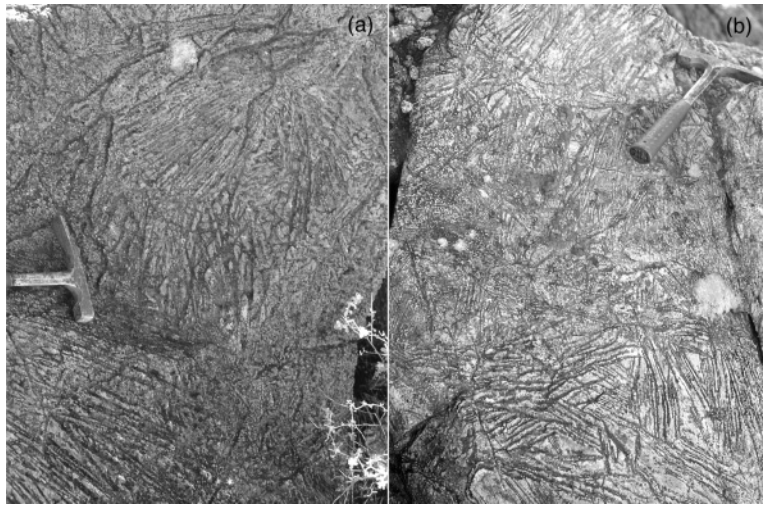


Fig. 5.7 Field photos (weathered surface) of spinifex-textured komatiites from the Kalgoorlie area, Western Australia. Dark features mark out the altered olivine blades; lighter material between represents altered interstitial pyroxene and glass.

Box 5.6 Greenstone belts

Greenstone belts are important components of many of the world's Archaean cratons. They consist of thick volcanic and sedimentary successions deposited on the Earth's surface between 3.6 Ga (or possibly earlier) and 2.5 Ga before present (BP) and subsequently modified by folding, thrusting and greenschist-facies metamorphism. Seminal examples are the 3.5 Ga Barberton greenstone belt in the Kaapvaal craton of South Africa (the type area for komatiites), the exquisitely preserved 2.7 Ga Belingwe greenstone belt in Zimbabwe (Renner et al., 1994) and the 2.7 Ga Norseman-Wiluna belt in the Yilgarn craton of Western Australia.

The lower parts of most greenstone-belt successions are dominated by komatiite and tholeiitic basalt lavas and associated minor intrusions, interbedded with ironstones and other chemical sediments; many workers regard this stage as representing Archaean sea-floor spreading (Bickle et al., 1994). At higher stratigraphic levels, andesitic and silicic stratovolcanoes and terrigenous clastic sediments and volcaniclastics assume greater prominence, suggesting the emergence of ancient island arcs.

Greenstone belts are preserved today in *greenstone–granite terrains*. In some classic examples (Kaapvaal in South Africa; Pilbara in Western Australia) the greenstone belts form elongated, apparently synformal in-folded basins between dome-like granitoid masses (Fig. 5.6.1), a relationship some attribute to the disruption of a laterally continuous volcanic succession by granite diapirism (e.g. Van Kranendonk et al., 2004). Elsewhere the greenstone–granite relationship is much more complex, and horizontal tectonism – either compressional thrusting or the extensional exhumation of deep crustal rocks – is seen as having played an important role, and such ideas have been applied to Kaapvaal and Pilbara too (de Wit, 1998).

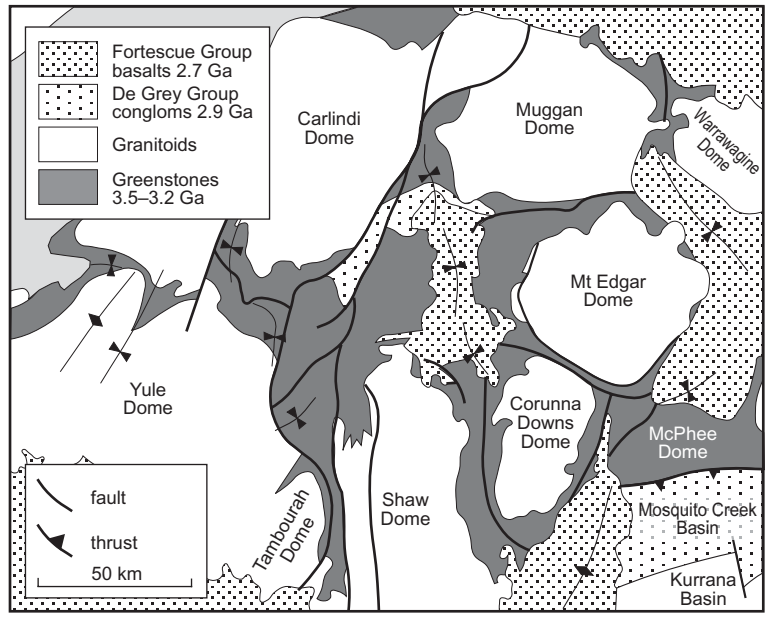


Fig. 5.6.1 Simplified map of the East Pilbara craton (after Van Kranendonk et al., 2004 by permission of Elsevier) illustrating the dome-basin architecture of the terrain. The granitoid complexes shown include components of the 3.5–3.5 Ga orthogneisses as well as younger potassic granites varying in age from 3.3 – 2.8 Ga.

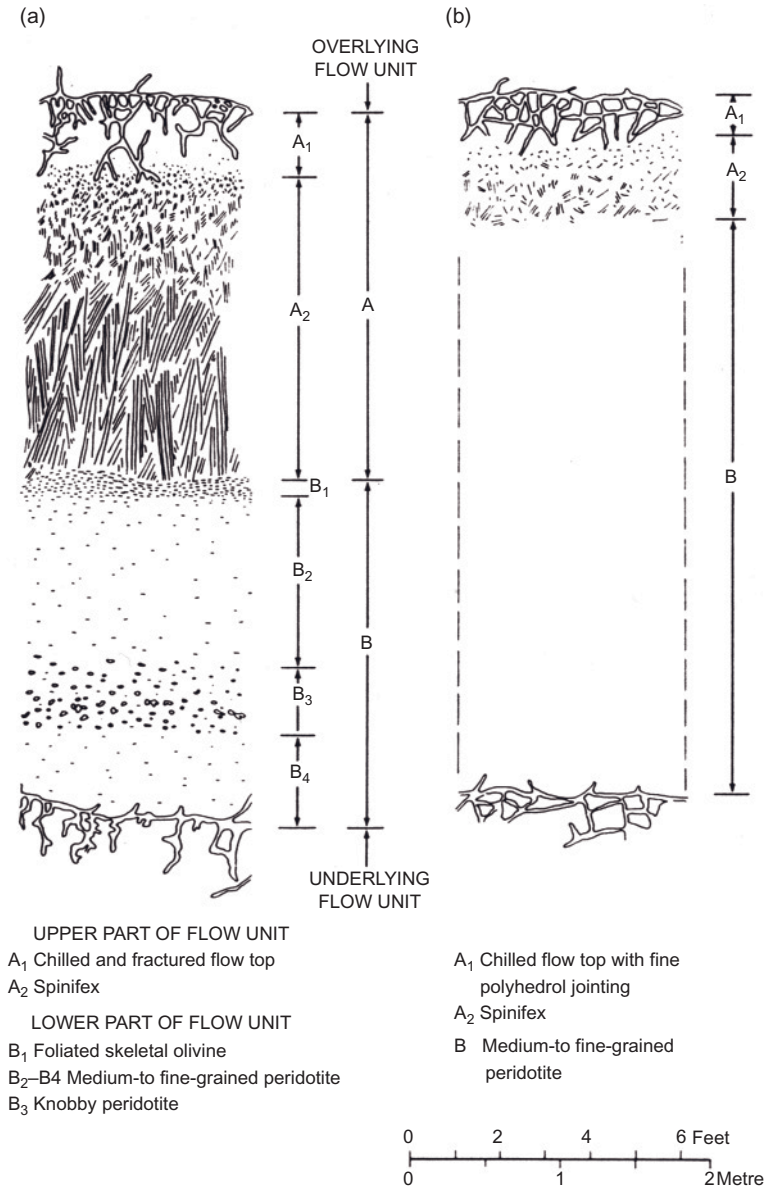


Fig. 5.8 Cross-sections of two types of komatiite flow in Munro Township, Ontario, simplified from Pyke et al. (1973) and Arndt et al. (1977) by permission of the Geological Society of America and Oxford University Press: (a) a flow with a well developed upper spinifex zone; (b) a flow with limited spinifex texture. More than half of the peridotite lava flows from this locality exhibit no spinifex texture at all.

late Cretaceous komatiites occur in association with **picrites** and basalts (Aitken and Echeverria, 1984; Kerr et al., 1996). Many geologists associate their eruption with the huge Caribbean–Colombian LIP (Fig. 2.15) formed by the ancestral Galapagos plume, though recent palaeomagnetic evidence suggests that Gorgona Island may instead be the product of another hotspot to the south.

Detail and significance of spinifex texture

Distinctive features of spinifex texture are illustrated in Plates 5.9–5.11. Plate 5.9 shows large, sub-parallel plates of colourless olivine (partly altered to serpentine + iron oxide) in PPL interspersed with brownish zones representing quenched melt in between. The field of view shows the massive central portions of several olivine plates sideways-on, but on the left several slender olivines exhibit branching forms near their terminations. The intervening brownish 'melt' zones have crystallized to feathery, fern-like or sometimes **dendritic** pyroxene, more clearly discerned in crossed polars (Plate 5.10). The brown zones also contain delicate dendrites of opaque chromite (Plate 5.11).

The dominance of platy olivines, together with skeletal and dendritic crystal habits, makes spinifex-textured komatiites unique among terrestrial igneous rocks. In explaining why such textures are seen in komatiites but not in basaltic lava flows, Donaldson (1976, 1982) showed experimentally that olivine habits similar to those in komatiites were favoured by unusually rapid crystallization (brought about in his experiments, if not in Nature, by rapid cooling). With increasing cooling rate, the dominant olivine habit (Fig. 5.9) changed from polyhedral (a), through 'equant hopper' (see caption) to 'elongate hopper' (e) and platy (not shown in Fig. 5.9). Donaldson compared this experimental sequence with the textural changes seen in passing from zones $B_{2–4}$ (interior, polyhedral olivine) to upper A_2 (spinifex olivine) in a thick komatiite flow (Fig. 5.8), a correlation he attributed to increasing crystallization rate near to the flow margin.

Why should rapid crystallization favour skeletal, hollow and platy habits? During very rapid crystallization of supercooled melt, crystal growth outstrips chemical diffusion in the surrounding melt, leaving a growing crystal surrounded by a zone of melt depleted in Mg_2SiO_4 relative to other melt constituents (Fig. 5.10). Depletion in Mg_2SiO_4 inhibits further growth on crystal faces but growth may still occur at surface irregularities and projecting corners (Fig. 5.10a), from where whiskers or fingers of new crystal may develop (Fig. 5.10b), the first step in developing a skeletal crystal form. Growth of the finger may itself become inhibited, whereupon a secondary finger may develop (Fig. 5.10c) from some favourable point on the surface of the primary finger. It is not difficult to understand

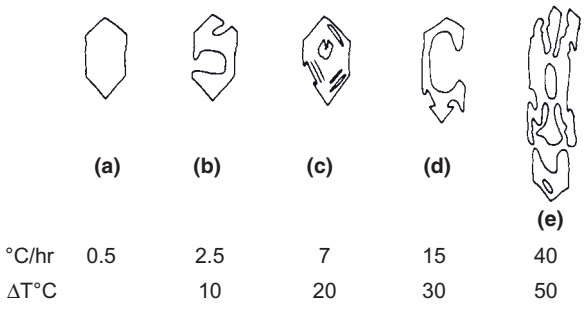


Fig. 5.9 Typical morphologies of olivine crystallized experimentally from ultrabasic melts as a function of cooling rate (in °C per hour) adapted with permission from Donaldson (1976,1982). 'ΔT °C' indicates the degree of supercooling below the liquidus at which olivine began to form. The normal polyhedral form of olivine (a) gives way at higher cooling rates to hollow forms often referred to as 'hopper' olivine (b)–(d), then to 'elongate hopper' form (e). Plate olivines (not shown) occur at slightly higher cooling rates. More extreme cooling rates produced other morphologies (e.g. 'chain' and 'feather' olivines) that are not seen in natural komatiites.

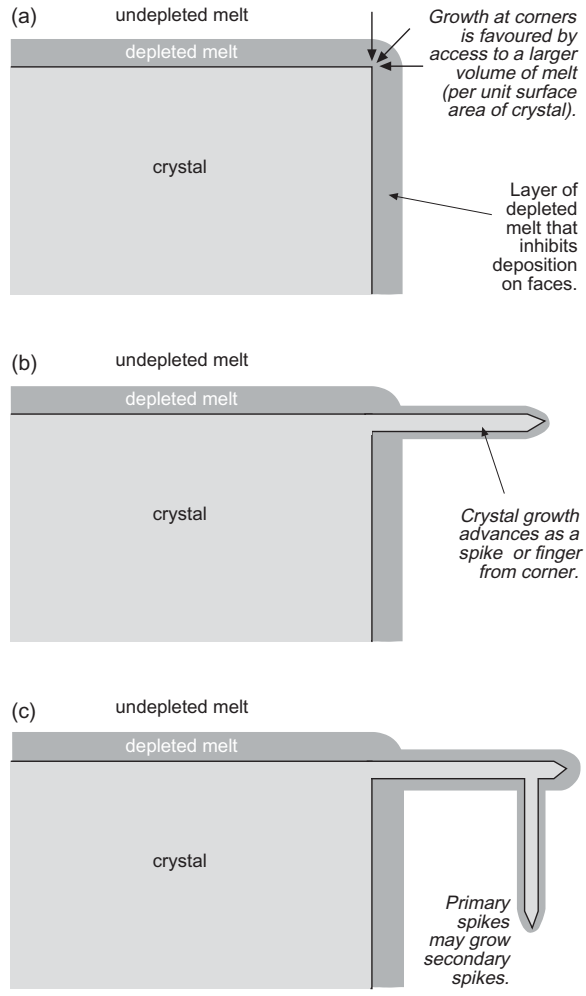


Fig. 5.10 Cartoon illustrating the formation of dendritic and similar crystal morphologies where normal growth of faces is inhibited by a zone of depleted melt surrounding the crystal (based loosely on Vernon, 2004).

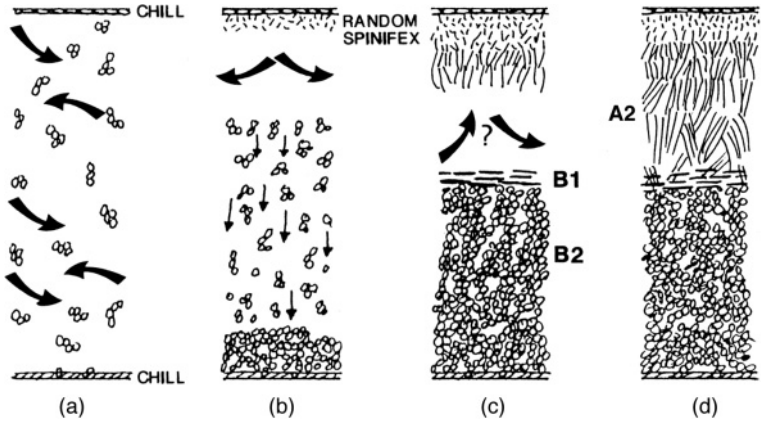


Fig. 5.11 Schematic diagram illustrating the crystallization history of a komatiite flow (from Renner et al., 1994 by permission of Oxford University Press): (a) Flow emplacement with polyhedral olivine phenocrysts suspended in the flowing lava; arrows represent magma convection. (b) Olivine settles out as spinifex zone starts to form; top of flow continues to convect. (c) Cumulate zone formed by settling olivines, but interstitial melt remains still unfrozen; spinifex zone extends downward from roof. (d) Flow has completely frozen. 'A2', 'B1' and 'B2' relate to Fig. 5.8.

how repetition of this process leads to the dendritic and other exaggerated forms seen in komatiite (best illustrated in Plates 5.10 and 5.11 by the dendritic pyroxene and chromite crystals).

Donaldson (1982) considered it unlikely that high cooling rates comparable to those in Fig. 5.9 could be achieved throughout the spinifex layer of a thick komatiite flow (A_2 in Fig. 5.8, which may be as much as 20 m thick in thick flows). He supposed instead that the large content of dissolved olivine in komatiite melts led to greater olivine supersaturation for a given ΔT compared to basic melts, and it was this that drove the rapid crystallization. Shore and Fowler (1999), on the other hand, considered that a high cooling rates *could* operate, even in thick komatiite flows. They suggested that spinifex olivines nucleated at the top of a komatiite lava (where cooling rate may have been enhanced by interaction with overlying water[6]), from where they grew rapidly downward under a strong temperature gradient. In their view, very rapid cooling would also have been promoted by high radiative heat loss from the flow surface – favoured by the uniquely high temperature of a komatiite melt – and by the notably high thermal conductivity of olivine crystals (especially in the *a* axis direction) relative to the surrounding melt. Anchoring of olivine crystals to the upper surface may therefore account for rapid internal cooling, the large crystal size and the sub-parallel disposition of the olivine plates. Olivine crystals suspended within the deeper, flowing interior lacked this 'heat sink' and grew more slowly to produce **polyhedral** crystals, which sank to form intra-flow cumulates (Fig. 5.11).

[6] At least some komatiites exhibit pillow structures suggesting sub-aqueous eruption (e.g. Renner et al., 1994).

Magma genesis of komatiites and picrites

Primary basalts erupt with MgO contents between 8% and 15% (Table 2.4). Typical komatiites, on the other hand, have MgO contents between 20% and 33% (Table 5.3). **Fertile** mantle rocks have MgO contents between 37% and 42%, and intuition suggests that komatiites, being closer in composition to mantle rocks than basalts are, must have incorporated a greater proportion of their mantle source and therefore represent a higher degree of mantle melting than do basalts. Komatiite volcanism occurred on a vast scale during Archaean times (Hill et al.,

Table 5.3 Major-element analyses of selected ultramafic rocks (tabulated volatile-free). A. Mantle-derived peridotites and estimated mantle composition. B. Komatiite analyses selected by Nisbet et al. (1993) as providing the best approximations to primary melt composition – unaffected by intra-flow olivine fractionation and accumulation – for each of the areas indicated.

	A. Mantle peridotite compositions			B. Komatiite melt compositions			
Description and location	**Kettle River peridotite, BC, Canada**	**Average mantle peridotite**	**Harzburgite**	**Gorgona Is, Colombia (87 Ma§)**	**Belingwe, Zimbabwe (2.7 Ga)**	**Alexo, Ontario (2.7 Ga)**	**Barberton, S. Africa (3.45 Ga)**
Source of data	**Walter (1998)**	**Herzberg (1993)**	**BVSP* (1981)**	**Nisbet et al. (1993) from sources cited in their paper**			
SiO_2	44.90	44.3	43.59	46.0	47.78	46.1	47.11
TiO2	0.15	0.09	0.03	0.53	0.37	0.23	0.36
Al_2O_3	4.30	2.36	1.27	11.1	6.82	7.4	3.93
Cr_2O_3	0.41	0.43	0.43				0.42
ΣFeO	8.09	8.31	5.71	11.3	11.13	10.6	11.67
MnO	0.13	0.13	0.07		0.19	0.17	0.19
MgO	37.65	41.64	48.39	20.6	25.68	28.1	28.95
NiO	0.24	0.27	0.31				0.20
CaO	3.48	2.20	0.21	9.3	7.00	6.9	6.74
Na_2O	0.22	0.23	0.06	0.84	0.98	0.2	0.15
K_2O	–	–	0.07	0.03	0.05	0.08	0.01
Total	99.57	99.96	100.14	99.7	100.00	99.8	99.73
Estimated T (°C) of eruption	–	–	–	1400 ± 15	1520 ± 10	1560 ± 5	1580 ± 70

* BVSP, Basaltic Volcanism Study Project; § See Kerr et al. (1996).

1994), and many have suggested that the high degrees of melting they represent require a steeper geothermal gradient and higher potential temperature in the immature Earth's mantle. Can this assertion be tested?

Nisbet et al. (1993) used komatiite analyses to estimate the potential temperatures required to generate such magnesian melts. Because olivine sinks rapidly in low-viscosity komatiite melts, olivine-accumulation may bias the composition of individual komatiite hand-specimens and yield misleading results. The first task of Nisbet and his co-authors was therefore to compile the best available estimates of parental komatiite *melt* compositions from Gorgona (Columbia), Belingwe (Zimbabwe), Alexo (Ontario) and the Barberton Mountain Land (the komatiite type-area in South Africa). These were used to estimate eruption temperatures for komatiite lavas (Table 5.3). Nisbet and his co-authors extrapolated these results to calculate the potential temperatures necessary to produce komatiite melts by partial melting of mantle peridotite. Their conclusions are summarized in the form of melting and ascent paths in Fig. 5.12.

Curve *a–b–c* represents the melting and ascent path predicted for the Cretaceous Gorgona Island komatiite melt shown in Table 5.3. Decompression melting appears to have begun at about 120 km depth (point *a* at ~4.5 GPa pressure) and would have progressed as adiabatic upwelling advanced into the partial melting field (thick solid line *a–b*). Nisbet et al. (1993) assumed that decompression melting would have extended only up to the base of the lithosphere (*b*), which acted as a cool 'lid' preventing mantle upwelling to shallow depths; the depth *b* represents the global mean thickness of the lithosphere (*b–c*) during Cretaceous time (87 Ma) as estimated by Bickle (1986). At *b*, melt would have sepa-

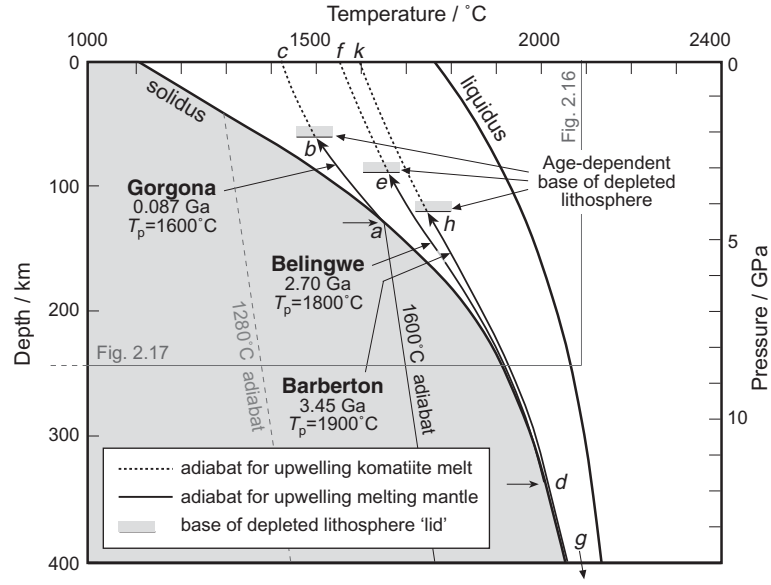


Fig. 5.12 Schematic temperature-depth diagram (cf. Figs. 2.16 and 2.17) showing melting and ascent paths applicable to the generation of komatiite melts. Figure adapted from Nisbet et al. (1993; copyright Elsevier); *a–b–c*, *d–e–f* and *g–h–k* represent the melting and ascent paths for parental komatiite melt compositions (Table 5.3) from Gorgona Island, Belingwe and Barberton respectively. Bars at *b*, *e* and *h* represent the base of the lithosphere (after Bickle, 1986) where upwelling and decompression melting cease. The boundaries of Fig. 2.17 and the 1280 °C adiabat are shown for comparison; sources of solidus and liquidus curves are as in Fig. 2.17.

rated from the solid residue and continued to the surface, erupting at about 1400 °C. Each segment of the adiabatic ascent path – solid up to *a*, melt + solid 'mush' from *a* to *b*, and melt only from *b* to *c* – has a different gradient, owing partly to the differing compressibilities of solid and melt (cf. Fig. 2.17) and partly to the increasing proportion of melt from *a* to *b*; the gradient is also affected by the latent heat of melting. The point where melting begins (*a*) coincides with the 1600 °C mantle adiabat (Fig. 5.12), suggesting a potential temperature T_p of 1600 °C in the mantle source region from which the Gorgona komatiites originated. The associated high-MgO Gorgona picrite parent melts (Fig. 5.5.2) probably formed at similar or slightly higher potential temperatures (Herzberg and O'Hara, 1998, 2002).

But Archaean parental komatiites are significantly more magnesian than their younger relative on Gorgona Island (Table 5.3). They are represented in Fig. 5.12 by Belingwe (2.7 Ga in age, melting/ascent path *d–e–f*) and Barberton (3.45 Ga, *g–h–k*). Intuition suggests that such magnesian melts must have been products of still higher degrees of mantle partial melting than the Gorgona komatiites, and this expectation is confirmed by the higher potential temperatures (1800 °C and 1900 °C respectively) that emerge from both the calculations of Nisbet et al. (1993) and an independent review by Herzberg and O'Hara (1998). The melting responsible for the Archaean komatiites also appears to have begun at much greater depths (*d* and *g* in Fig. 5.12).

The higher mantle potential temperatures implied by Archaean komatiite volcanism are not surprising: it is natural to expect that temperatures within the early Earth would be higher than today because less time had elapsed after the intense heating involved in planetary accretion. Richter (1988) calculated a secular cooling curve (potential temperature *versus* time) for the Earth's mantle which is shown in Fig. 5.13. The potential temperatures implied by komatiite magma genesis, as calculated by Nisbet et al. (1993), plot on

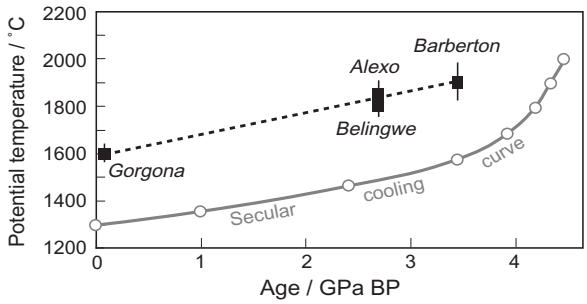


Fig. 5.13 Mantle potential temperatures inferred from komatiite parental melt compositions (Fig. 5.12) plotted as a function of age, after Nisbet et al. (1993; copyright Elsevier); the Gorgona age is shown here as 87 Ma (Kerr et al., 1996) in place of the 160 Ma age assumed by Nisbet et al. Error bars indicate the uncertainty associated with potential temperature estimates. The results are about 300 °C higher than the secular cooling model for the Earth's mantle developed by Richter (1988).

average 300 °C higher than this ambient-mantle cooling curve. This temperature anomaly resembles that inferred to exist beneath many current volcanic hot spots (cf. Fig. 2.18b and d), and it led Nisbet et al. (1993) and Herzberg and O'Hara (1998) to conclude that the high-MgO komatiites characteristic of many Archaean greenstone belts were products of Archaean mantle plumes similar to (though hotter than) those that lie beneath Hawai`i and Iceland today.

Are exceptionally high melting temperatures the only way to account for highly magnesian melts like komatiite? One school of thought (e.g. Parman et al., 1997, Grove and Parman, 2004) believes such high potential temperatures could never have been reached even in the early Earth, and argues instead that the high degrees of melting that komatiites require were the result of melting under H_2O-rich conditions (cf. Fig. 2.17c). This 'wet melting' hypothesis was however refuted by Arndt et al. (1997).

Mineral deposits associated with komatiites

Some komatiites host important Ni–Cu–**PGE**-bearing massive sulphide deposits, most notably at Kambalda (Beresford et al., 2002) and Black Swan (Barnes, 2004) in the Yilgarn craton in Western Australia but also, for instance, in the Reliance Formation komatiites of Zimbabwe (Prendergast, 2003) and the Alexo, Texmont and Hart komatiites in the Abitibi greenstone belt of Ontario (Lahaye et al., 2001). Most of these ore deposits have been deformed and metamorphosed and so reconstruction of the original magmatic sequence of events is often difficult. Nonetheless it appears that the massive sulphides in all of these examples are concentrated in troughs at the base of thick (~50 m) komatiite lavas that appear to have scoured down into the underlying rocks. The temperature of komatiite lava was evidently high enough to cause local melting in the rocks over which it flowed, generating *thermal erosion* channels in places where rates of flow and heat delivery were greatest.

The channels frequently invade inter-lava sulphide-bearing metasediments, and Huppert et al. (1984) suggested that the nickel-rich sulphide deposits have formed as a direct result of ingestion of these sediments. Ni is abundant in ultramafic lavas (Table 5.3) and, in the absence of sulphur, is incorporated as a compatible trace element in separating olivine crystals (see Fig. 2.7.1.in Box 2.7). On the other hand, Ni and Fe also exhibit a marked **chalcophile** tendency. In an initially sulphide-poor komatiite melt, the injection of sulphide by sediment or wall-rock contamination could lead to rapid separation of highly insoluble (Fe,Ni)S, probably as droplets of immiscible sulphide melt which – being much denser than komatiite melt – would sink and accumulate to form ponds of molten sulphide on the channel floor. This model of ore genesis is still widely supported (e.g. Lahaye et al., 2001; Dowling et al., 2004). It has however been challenged on isotopic grounds (Foster et al., 1996).

REVIEW – WHAT CAN ONE LEARN FROM THE STUDY OF ULTRAMAFIC ROCKS?

Ultramafic rocks of interest to the igneous petrologist are found in three main geological settings. Their characteristics, and the means by which rocks of the three associations may be distinguished, are summarized in Table 5.4.

Table 5.4 Summary of structural, textural and mineralogical characteristics of peridotites from three associations.

	Ultramafic cumulates	Mantle peridotites	Komatiites and other high-MgO lavas
Distinctive megascopic structures	Macro-rhythmic *layering*	'Orogenic' peridotites are typically *foliated* and show a concordant lherzolite-harzburgite *compositional banding*.	Some well preserved komatiite lava tops preserve evidence of glassy chills, amygdales and cooling joints.
Distinctive textures	Some form of cumulate texture may be present (e.g. enstatite *oikocrysts* (Plate 5.1)); adcumulate growth or solid state grain-boundary adjustment may obscure cumulate textures and produce polygonal outlines similar to mantle xenoliths.	Basalt- or kimberlite-hosted peridotites commonly exhibit *protogranular* texture with grain boundaries meeting at ~120° (Plate 5.6). Some xenoliths and many orogenic peridotites exhibit *sheared* textures (Plate 5.8).	***Spinifex*** texture in the upper part of a komatiite lava (Plate 5.9, Fig. 5.8). Olivine generally has **polyhedral** morphology in the lower part of a komatiite lava, and in picrite lavas.
Distinctive aspects of mineralogy	Interstitial (intercumulus) *plagioclase* (Plate 5.2). Hornblende is characteristic of some Alaskan-type peridotites.	*Spinel* or *garnet* usually present (Plates 5.4, 5.8 and 5.5). Clinopyroxene, if present, is typically *Cr-diopside* (vivid green in hand specimen (Plate 5.4)).	
Typical oxide minerals	Euhedral or subhedral *chromite* (opaque)	Magnesian *spinel* (brown body colour, translucent, isotropic)*– see Plate 5.8.	*Quench chromite* (dendritic, opaque – see Plate 5.11).
Associated mineral deposits	chromite, PGE-bearing sulphides (e.g. Great Dyke)		Ni sulphide, PGE (e.g. Kambalda, W Australia).

* However chromitite lenses occur in dunite tectonites of some ophiolites (Moores, 1982 and Fig. 5.3.1).

Ultramafic cumulates

- A number of major layered intrusions, emplaced in various tectonic settings (Table 5.2), contain significant volumes of ultramafic cumulates. They include both continental complexes and those emplaced beneath oceanic spreading centres that are now preserved in the form of ophiolite complexes.
- Ultramafic cumulate sequences in large Precambrian layered intrusions consist of a series of macro-rhythmic units, each comprising dunite (± chromitite) at the base, harzburgite in the middle portions and pyroxenite at the top (Fig. 5.2). Some regard them as products of repeated injections of fresh magma into a crystallizing magma chamber. The parent magmas for some of these intrusions appear to have been picritic or boninitic rather than basaltic.
- Ultramafic rocks in ophiolite sequences are of two different types (Box 5.3): a lower unit of harzburgite tectonites representing deformed upper lithosphere, and an overlying unit of dunites interpreted as the initial cumulus products of an axial magma chamber originally located beneath an oceanic spreading centre.
- Petrologically zoned ultramafic bodies of Alaskan type may reflect successive intrusion (at the level currently exposed) of crystal mushes remobilized from a deeper magma reservoir. Many contain valuable PGE and Au deposits.
- Ultramafic cumulate sequences commonly contain exploitable chromitite bands.

Mantle peridotites

- Mantle-derived ultramafic rocks are delivered to the surface as xenoliths in many alkali basalts (spinel peridotite) and in kimberlites (garnet and spinel peridotite and eclogite).
- Pyrope garnet crystallizes at greater pressure than magnesian spinel (Fig. 5.5), suggesting that kimberlites that host garnet peridotite xenoliths are derived from greater depths than the alkali basalts/basanite magmas that host only spinel peridotite xenoliths.
- Larger-scale samples of mantle rocks are furnished by orogenic peridotite massifs that are tectonically emplaced in the roots of continental collision zones such as the Pyrenees.
- Mantle-derived peridotite textures record their deformation history. The least deformed 'protogranular' examples show a coarse-grained polygonal metamorphic texture (Plates 5.6 and 5.7). In more deformed examples, larger crystals (porphyroclasts) are interspersed with smaller, less strained crystals (Plate 5.8).
- Lherzolite, harzburgite and dunite lie on a spectrum of progressively greater degrees of lithosphere depletion by magma removal (Box 5.4).

Komatiites and picrites

There is abundant evidence that lavas of ultramafic composition have erupted on the Earth's surface, at least during early chapters of its history. Such komatiite lavas are distinguished by the presence of large blade-shaped olivine crystals in their upper portions, a feature known as spinifex texture.

Spinifex texture is a product of extremely rapid crystallization of strongly supercooled high-MgO melt.

The compositions of komatiites suggest that potential temperatures in the mantle were higher in Archaean times (1800–1900 °C) than today. The Cretaceous komatiites and picrites of Gorgona Island imply an intermediate potential temperature of 1600 °C.

Many komatiites host important Ni–Cu–PGE-bearing massive sulphide deposits.

EXERCISES

5.1 Express in the form Fo_x the composition of the olivine crystal whose analysis is given below:

	Olivine analysis (mass % oxides)
SiO_2	39.93
FeO	13.97
MnO	0.19
MgO	45.67
CaO	0.04
Total	99.80

Relative atomic masses (RAMs): O, 16.00; Mg, 24.32; Si, 28.09; Ca, 40.08; Fe, 55.85; Mn, 54.94.

5.2 Use equations 5.1 and 5.2 to calculate the minimum Mg number for a primary mantle melt. Assume that mantle olivine compositions lie in the range Fo_{88} – Fo_{92}.

5.3 (a) Calculate the Mg number for the N-MORB analysis from the East Pacific Rise in Table 2.4. Does this basalt represent a primary melt? (b) Calculate Mg numbers for the two analyses from Hawai`i in Table 2.4. Have the magmas represented by these two rocks fractionated to significantly different degrees?

5.4 Calculate the Mg number for the arc-related low-K tholeiitic basalt (analysis 6) in Table 2.4. Could this melt be the product of partial melting of altered oceanic crust in a subduction zone? (Experiments show that partial melting of basalt in the presence of H_2O produces melts with Mg numbers in the range 25–45 (Helz, 1976)).

Chapter 6

Andesite, dacite and rhyolite

Included in the range of natural magma compositions shown in Fig. 1.5 is a collection of subalkali volcanic rocks whose compositions extend rightwards from the basalt field in the total-alkalis versus silica (TAS) diagram. These data points are representatives of a continuum of evolved magma compositions that may be found in association with subalkali basalts in various tectonic settings. For descriptive purposes, petrologists find it convenient to divide this continuum into andesite, dacite and rhyolite, as shown in Figs. 1.5 and 6.1a and discussed in more detail below. From what has been learned in Chapter 3 about the evolution of basaltic magmas in crustal magma chambers, it would be natural to regard these intermediate and acidic magmas simply as products of the fractional crystallization of basalt, as in some cases they may be. On the other hand, the relative abundance of dacite and rhyolite is significantly greater in mature island arcs and continental arcs than is seen in immature intra-oceanic island arcs, suggesting that **sialic** continental crust may have influenced the relative abundance of these more evolved magmas, in ways discussed later in the chapter.

Andesite, dacite and rhyolite are distinctive products of supra-subduction-zone (**SSZ**) volcanism, but they are not confined to this environment. They are formed in significant volumes in some continental large igneous provinces (LIPs) (e.g. Yemen) and rift zones. They are also erupted in small though significant amounts at a few oceanic spreading centres such as Iceland and the Galapagos spreading centre (Fig. 6.12).

Igneous Rocks and Processes: A Practical Guide, 1st edition. By Robin Gill. Published 2010 by Blackwell Publishing

THE NOMENCLATURE OF INTERMEDIATE AND ACID VOLCANIC ROCKS

Definitions

The names andesite, dacite and rhyolite are applied in slightly different ways according to the kind of information being used:

- A petrologist making *qualitative petrographic observations* of minerals and textures would use a scheme along the lines of Table 6.1.[1]
- When a *chemical analysis* of a fresh volcanic rock is available, names may be applied according the International Union of Geological Sciences (IUGS) fields in a TAS plot (Fig. 6.1a).
- When a quantitative ***mode*** is available (from 'point-counting' minerals in a thin section – see Chapter 1), dacite and rhyolite may be defined according to the relative proportions of quartz, alkali feldspar and plagioclase using the 'QAP plot' shown in Fig. 6.1(b). One weakness of this IUGS approach is that andesite and basalt fall in the same field; a **colour index** lower than 35 is therefore used to distinguish andesite (Le Maitre, 2002, p. 30).

The simplest definitions in words are:

Andesite: a fine-grained,[2] usually **mesocratic** igneous rock consisting essentially of plagioclase + one or more mafic minerals; typically andesites are plagioclase-phyric (Plate

[1] How to distinguish between plagioclase and alkali feldspar is summarized in Box 6.1.

[2] Andesite need not necessarily be a **volcanic** rock (in the sense of magma erupted on the surface).

Table 6.1 Mineralogy of andesite, dacite and rhyolite.

	Andesite	Dacite	Rhyolite
Essential minerals	• plagioclase* • one or more mafic minerals	• sodic plagioclase • quartz • alkali feldspar *plagioclase > alk fsp*[$]	• alkali feldspar • quartz • sodic plagioclase *alk fsp > plagioclase*
Type minerals	• augite[§] • enstatite[§] • olivine • hornblende	• hornblende • biotite • garnet (rare) • pyroxene	• hornblende • biotite • pyroxene
Colour index	Usually **mesocratic**	**Leucocratic**	Difficult or impossible to determine (glass)
Texture	Markedly plagioclase-phyric (except boninite)	Often strongly quartz- and feldspar-phyric Groundmass usually crystalline	Quartz- and feldspar-phyric. Matrix usually glassy (spherulitic) or microcrystalline
Common secondary minerals	• chlorite or **uralite** replacing pyroxene, hornblende or biotite • **sericite** or epidote replacing feldspars (turbid appearance in PPL) • serpentine or **iddingsite** replacing olivine (see Box 2.2)		

* Usually oscillatory-zoned: compositions may range from bytownite to andesine.
§ Andesite containing *both* augite and enstatite is often called simply 'two-pyroxene andesite'.
$ For the distinction between alkali feldspar and plagioclase under the microscope, see Box 6.1.

6.1), and the plagioclase phenocrysts often show **oscillatory zoning** (Plate 6.2).

Dacite: a fine-grained (usually plagioclase-phyric) **leucocratic** igneous rock consisting essentially of sodic plagioclase + quartz; alkali feldspar[1] if present is subordinate to plagioclase (Plate 6.6).

Rhyolite: a leucocratic igneous rock consisting essentially of quartz + alkali feldspar (usually as phenocrysts) in a glassy or microcrystalline groundmass (Plate 6.9).

Andesites are (after basalts) the second most abundant volcanic rock type on the Earth (Gill, 1981). Less evolved andesites may sometimes be difficult to distinguish from basalts in thin section (Plate 6.3); clues to look for are oscillatory-zoned plagioclase phenocrysts and significant amounts of orthopyroxene. Moreover, being intermediate rocks that are chemically more evolved than basalts (Fig. 6.1a), andesites have lower liquidus and solidus temperatures that may permit hydrous mafic minerals such as hornblende and biotite to crystallize in addition to – or in place of – pyroxene (Box 6.2); the identity of the mafic mineral may be used as a qualifier (hence the listing as type minerals in Table 6.1). Hydrous mafic minerals stand out immediately through being more strongly coloured (and pleochroic) in plane-polarized light (PPL) than olivine and pyroxene.

The petrographic distinction between dacite and andesite is the presence of abundant quartz in dacite; the dominant mafic mineral may be hornblende and/or biotite (Plate 6.6). Rarely, dacite may also contain garnet (Plate 6.8), reflecting **anatexis** of continental crust as discussed in Chapter 8. Alkali feldspar may be seen but is subordinate to plagioclase (Fig. 6.1b). Rhyolite, on the other hand, is distinguished from dacite by the dominance of alkali feldspar over plagioclase, and often by the glassy nature of the groundmass, emphasized by such features as **perlitic cracks** and **spherulites** (Fig. 6.2). Evolved rocks similar to rhyolite but containing less quartz are known as quartz latite (A ≈ P in Fig. 6.1b) and quartz trachyte (A > P).

The TAS plot in Fig. 6.1a is the most widely used basis for the nomenclature of intermediate and acid volcanic rocks. Its use is appropriate when a major-element analysis is available, the rock analysed is relatively fresh (feldspar alteration may by accompanied by significant changes in whole-rock alkali content), and the analysis has been recalculated volatile-free (Box 1.3). The IUGS nomenclature based on the TAS diagram differentiates the lower-SiO_2 part of the andesite

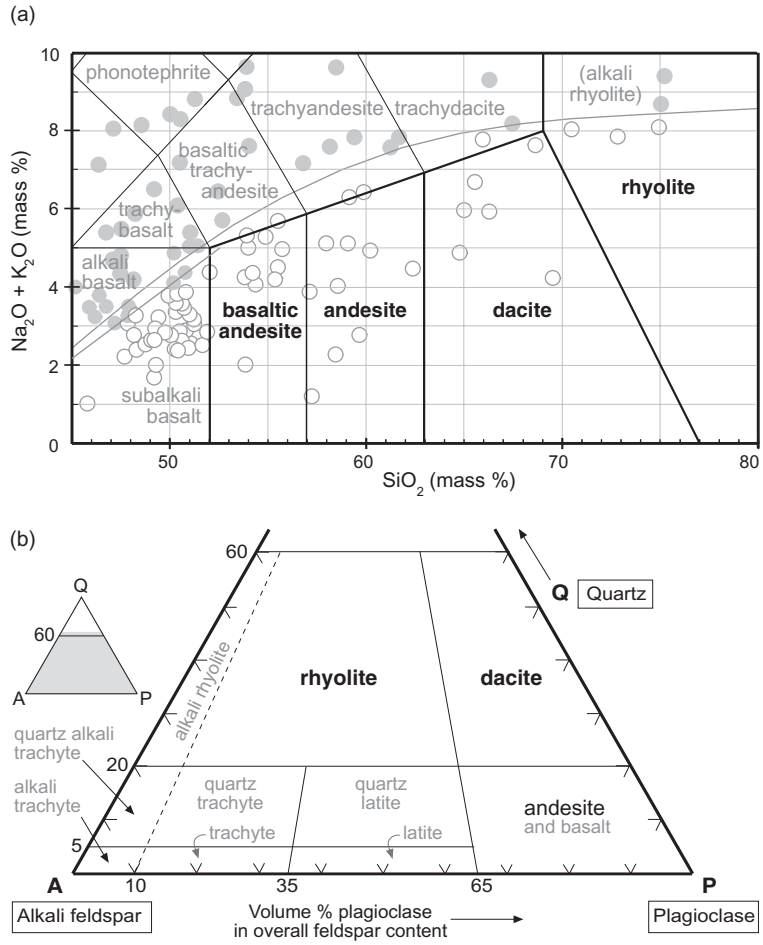


Fig. 6.1 (a) TAS plot showing the compositional fields of basaltic andesite, andesite, dacite and rhyolite recognized by the IUGS (Le Maitre, 2002, Fig. 2.14); the illustrative rock compositions shown are as in Fig. 1.5. The curved line (from Miyashiro, 1978) divides alkali from sub-alkali associations. (b) The lower portion (see inset) of a QAP plot showing the relative modal (volume) proportions of quartz (Q), alkali feldspar (A) and plagioclase (P) used for the IUGS modal definition of dacite, rhyolite and associated fine-grained igneous rocks, after Le Maitre (2002, Fig. 2.11);* v-marks indicate 10% divisions. Lines radiating from the Q apex are boundaries at which plagioclase/total feldspar is equal to 10%, 35% and 65% (by volume). For plotting modes in this figure (see Exercise 6.1), scale up the modal proportions of quartz, alkali feldspar and plagioclase so that they add up to 100% exclusive of other minerals, as explained in Appendix B. IUGS defines 'plagioclase' as feldspar with >5% An and 'alkali feldspar' as having <5% An.

* The simpler names alkali trachyte, quartz alkali trachyte and alkali rhyolite have been used in place of longer names like alkali *feldspar* trachyte, etc. proposed by IUGS.

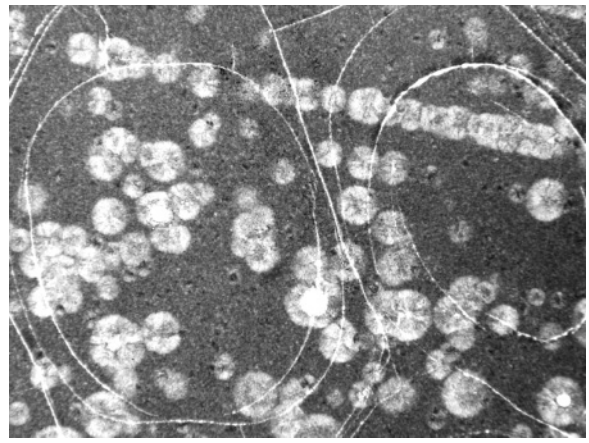
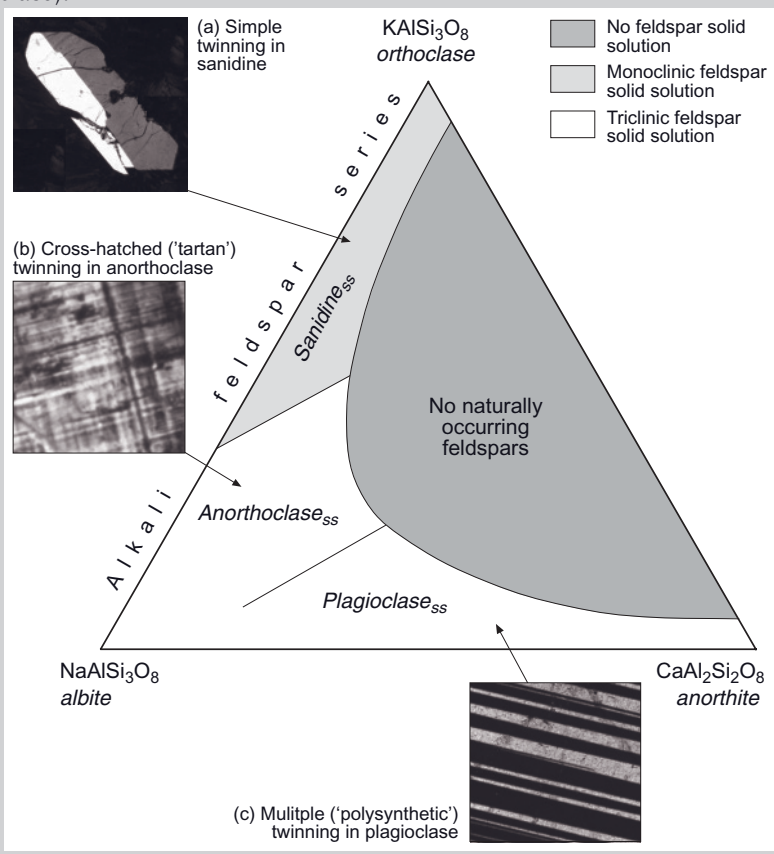


Fig. 6.2 Thin section showing **perlitic cracks** (large elliptical marks) in glassy lava. The small circular features are **spherulites** (centres of devitrification). PPL, width of field 2.7 mm.

Box 6.1 Distinguishing between types of feldspar in volcanic rocks

Figure 6.1.1 shows a ternary diagram indicating the range of natural feldspar solid solution at magmatic temperatures. Along the base of the triangle is the **plagioclase** solid-solution series. The left-hand margin of the triangle represents the **alkali feldspar** solid-solution series which, at magma temperatures (and low P_{H_2O}), extends continuously from $NaAlSi_3O_8$ to $KAlSi_3O_8$ (the end-member known as orthoclase).



spectrum as 'basaltic andesite' (Table 6.2), though this chemical distinction is not recognized in petrographic definitions (Table 6.1 and Fig. 6.1b).

Note that there is no simple SiO_2 threshold that separates dacite and rhyolite in Fig. 6.1, since the boundary recognized by the IUGS is diagonal, not vertical.

Andesite, dacite and rhyolite are arbitrary divisions of what is in essence a continuum of possible magma compositions. In view of the different types of data used in Figs. 6.1a,b, samples plotting near field boundaries in Fig. 6.1a may end up with different names in Fig. 6.1b and vice versa. Fine-grained rocks with higher alkali content than andesite and dacite are termed trachyandesite and trachydacite (Fig. 6.1a and Chapter 9).

Composition, grain-size and colour in hand-specimen

The colour of a hand-specimen varies with composition, degree of weathering *and* grain size. The generalization that felsic rocks are lighter-coloured in hand-specimen than mafic rocks is true only to a degree: the finer-grained a rock is, the darker it will appear regardless of its composition. A conspicuous example of this grain-size dependence is **obsidian** which, even when rhyolitic in composition (not always the case), is jet black in a fresh hand-specimen (Fig. 6.3d) on account of its glassy state.

For volcanic rocks, the colour of the weathered crust may be a more reliable guide to composition than a freshly exposed interior surface. Sub-aerially weathered basalts tend

The style of twinning seen between crossed polars – reflecting the crystal's symmetry and structural state – provides the principal distinction between plagioclase and alkali feldspar under the polarizing microscope. The simplest style is shown by the monoclinic mineral sanidine (Fig. 6.1.1a and Plate 6.9): a typical crystal is divided into a pair of twin individuals that extinguish at different rotations, a situation most simply referred to as simple twinning; several configurations of simple twinning are possible – the commonest is known as Carlsbad twinning – but such details rarely concern the petrologist.

In contrast, plagioclase crystals usually exhibit repeated parallel twins (Fig. 6.1.1c), known variously as multiple, lamellar or albite twinning, which incidentally provides a basis for estimating the composition of a plagioclase crystal (Box 4.1). Plagioclase may in addition exhibit Carlsbad simple twins, but this has no diagnostic value. Care needs to be taken when working with plagioclase crystals that are too small to develop more than two twin lamellae (and may therefore be identified incorrectly as sanidine); should confirmation be needed, most plagioclase crystals show a refractive index (RI) slightly greater than the mounting medium, whereas for alkali feldspars it is lower. Multiple twinning may occasionally be absent in plagioclase, or may be hidden in a particular crystal by being oriented almost parallel to the plane of the section.

Anorthoclase – a triclinic mineral like plagioclase – characteristically exhibits multiple twinning in *two* perpendicular directions at once (Fig. 6.1.1b; Plate 9.6). A similar style of twinning is exhibited by the K-feldspar microcline (Box 8.1), but this forms only during slow cooling and so is not seen in volcanic rocks.

Rapid cooling ensures that feldspars in volcanic rocks retain their high-temperature structural state to low temperatures. Structural changes that occur during slow cooling complicate the optical characteristics of feldspars in plutonic rocks, as explained in Box 8.1.

Fig. 6.1.1 The extent of natural solid solution in the feldspars (see key), and the compositional ranges to which individual mineral names apply (after Deer et al., 1992). The mineral names shown for the alkali feldspars are the high-temperature minerals found in volcanic rocks ('ss' signifies solid solution); they differ from the alkali feldspars occurring in plutonic rocks (see Box 8.1). The panels illustrate actual examples (under crossed polars) of the distinctive twinning of (a) sanidine, (b) anorthoclase and (c) plagioclase.

to form a chocolatey brown weathered surface, andesites weather red, grey or green, while rhyolites commonly form a white- or creamy-weathering surface, in marked contrast to the darker interior (Fig. 6.3f).

Boninites

Most andesites, being more evolved than basalts, have MgO contents below 5% (Table 6.2). An important exception is the andesite sub-group known as high-Mg andesite or *boninite* (Crawford, 1989). An example of a thin section from the type locality (the Bonin Islands in Japan) is shown in Plate 6.4. Most of the crystalline material consists of prismatic orthopyroxene phenocrysts and microphenocrysts, which are set in an almost colourless glassy matrix. Some of the orthopyroxene phenocrysts may be rimmed by overgrowths of clinopyroxene (cpx) (see Plate 6.5). Being devoid of plagioclase, the rock fails to meet either of the petrographic definitions of andesite but with an SiO_2 content of 57.6%[3] it falls squarely within the andesite field in a TAS plot. The most widely accepted definition of boninite embraces both petrographic *and* geochemical criteria (adapted from Taylor et al.,1994 and Le Maitre, 2002):

- *Boninite:* a fine-grained igneous rock containing abundant orthopyroxene phenocrysts or microphenocrysts but no

[3] Table 6.2.

Box 6.2 Why hornblende and biotite crystallize only from more evolved melts

The identity of the mafic phenocrysts in volcanic rocks changes in progressing from basaltic to more evolved magmas: in basalts olivine and augite predominate, whereas orthopyroxene, hornblende and biotite become progressively more widespread in andesites, dacites and rhyolites (Fig. 6.2.1). The cross-over in olivine and orthopyroxene trends reflects the reaction relationship between magnesian olivine and evolved melt to form orthopyroxene, already noted in Box 4.3. The later appearance of hornblende and biotite, however, relates to the limited high-temperature stability characteristic of all **hydrous** minerals (Fig. 6.2.2).

The formulae of hornblende and biotite include OH^- ions:

Hornblende (calcic amphibole): $(Na,K)_{0–1}Ca_2(Mg,Fe,Al)_5Si_6Al_2O_{22}(\mathbf{OH})_2$
Biotite (mica): $K_2(Mg,Fe^{2+})_{6–4}(Fe^{3+},Al,Ti)_{0–2}Si_6Al_2O_{20}(\mathbf{OH})_4$

Hydrous minerals such as these undergo **dehydration** at high temperatures; for example:

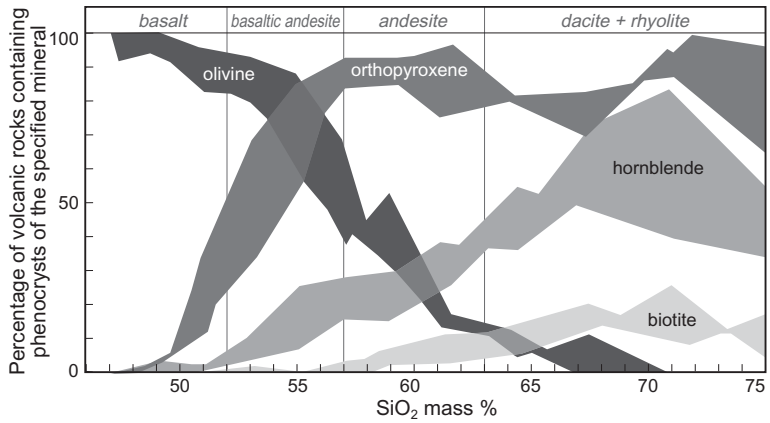


Fig. 6.2.1 Frequency curves for the occurrence of selected mafic minerals as phenocrysts in calc-alkali lavas from the west Pacific and Aleutians island arcs and the Cascades, as a function of whole-rock SiO_2 content (data from Ewart, 1982). The vertical axis represents the percentage of all volcanic rocks (within a given SiO_2 interval) that contain phenocrysts of the specified mineral; the width of each trend represents the divergence between different provinces (NW Pacific, SW Pacific, Aleutians and Cascades). Augite and Fe–Ti oxides (not shown) are also important phenocryst minerals across a wide range of composition.

plagioclase, whose composition meets the following geochemical criteria: (a) SiO_2 >52%; (b) 25%>MgO>8%; (c) TiO_2 <0.5%.[4] Many boninite lavas have a glassy matrix (Plate 6.4) and may contain clinoenstatite (Box 2.1) and/or olivine phenocrysts in addition to orthopyroxene.

Boninites – in spite of their high SiO_2 contents – represent primitive magmas, as their lack of plagioclase and their high MgO and low TiO_2 contents testify (Table 6.2). Most boninites have Mg numbers within the range for equilibration with mantle olivine (see the discussion of **primary** melts in Chapter 5). True boninites undergo fractionation leading to a 'boninite series' of more evolved volcanic rocks (often associated with them in the field) that share some but not all of the above characteristics.

[4] The IUGS definition refers only to the geochemical aspects of this definition.

$$\underset{\text{biotite (simplified)}}{KFe^{2+}{}_3Fe^{3+}AlSi_3O_{10}(OH)_2} \xrightarrow{O_2} \underset{\text{sanidine}}{KAlSi_3O_8} + \underset{\text{magnetite}}{Fe_3O_4} + \underset{\text{vapour}}{H_2O} \qquad [6.2.1]$$

For a given hydrous mineral, dehydration will occur at a well defined temperature that increases with water-vapour pressure (Fig. 6.2.2) and varies with melt composition. The form of such 'dehydration curves' has two important implications for the crystallization of hydrous minerals from igneous melts:

- Hornblende or biotite can crystallize as a stable mineral only at temperatures *below* the relevant dehydration curve. Only melts *more evolved than basalt* have solidus temperatures low enough for hydrous minerals to crystallize, which is why hornblende phenocrysts first appear in andesites, and why biotite phenocrysts are found only in evolved andesites, dacites and rhyolites (Fig. 6.2.1).
- Under low-pressure (near-surface) conditions, dehydration temperatures approach solidus temperatures (even for andesite and dacite). In volcanic rocks, therefore, hydrous minerals occur *only as phenocrysts* (crystallized at depth where they can be stabilized by high P_{H_2O}) and not as groundmass minerals: crystallization under surface conditions yields only anhydrous minerals.

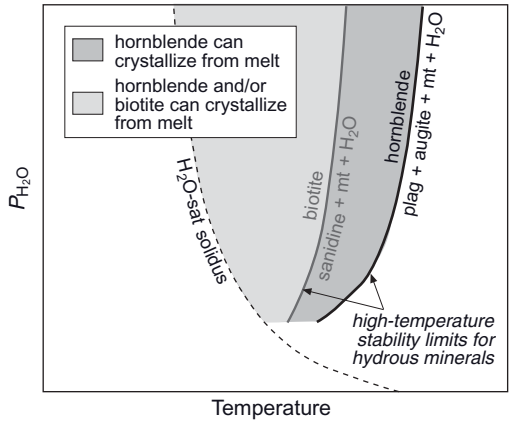


Fig. 6.2.2 Schematic P_{H_2O}–T dehydration curves for biotite and hornblende. In each case, the conditions favouring crystallization of the hydrous mineral lie on the low-temperature side of the dehydration curve, and those favouring the anhydrous breakdown products lie on the high-temperature side. (Abbreviations: plag, plagioclase; mt, magnetite: 'H_2O' represents vapour.) The dashed curve represents the water-saturated solidus for dacite (see Fig. 6.4.1 in Box 6.4 for source); the shaded areas illustrate the restricted P_{H_2O} conditions where hornblende and biotite are able to crystallize from melt (NB not to scale).

Related rocks

Andesites and dacites are unambiguously subalkali magmas; all lie below the Miyashiro curve in Fig. 6.1a. Rocks of broadly similar composition but with higher alkali contents (plotting above the Miyashiro line) fall in the trachyandesite and trachydacite fields, which are discussed in Chapter 9.

Rhyolites falling above the Miyashiro curve in the TAS plot correspond broadly to the alkali rhyolite field shown in Fig. 6.1b.

ERUPTIVE PROCESSES AND VOLCANIC FORMS

Andesite lava flows

Many andesite lava flows and flow fields look similar to basalt flows, but there tend to be quantitative differences. Andesite melts are more **polymerized** (Box 6.3) than basalts on

Table 6.2 Major and trace element analyses of representative andesites, dacites and rhyolites from various tectonic settings. Iron data are presented as 'total FeO' ['ΣFeO' = actual FeO + (actual Fe_2O_3/1.11)] as in Table 2.4. Blank entries indicate components that are not given in the published analyses. Values in brackets were not tabulated in the original publication but have been interpolated from neighbouring REE. The rare earth element europium (Eu) included in this table is discussed in Chapter 8.

Rock type	Boninite	Basaltic andesite	Andesite			Dacite	Adakite	Rhyolite
Tectonic setting	Emergent fore-arc	Intra-oceanic island arc	Intra-oceanic island arc	Intra-oceanic island arc	Andean CVZ	Intra-oceanic island arc	Island arc	Continental back-arc extension
Location	Chichijima Bonin Is, W Pacific	South Sandwich Islands	South Sandwich Islands	Montserrat, Lesser Antilles	Volcan Ollagüe Chile-Bolivia	Plat Pays complex, Dominica	Mindanao, Philippines	Taupo, New Zealand
Reference	1	2	3	4	5	6	7	8
Mass % oxide								
SiO_2	55.09	53.31	58.07	59.95	61.4	63.4	60.85	74.24
TiO_2	0.07	0.73	0.73	0.65	0.84	0.52	0.59	0.31
Al_2O_3	7.85	16.44	17.51	17.24	16.6	16.6	17.46	13.63
ΣFeO	8.47	9.86	6.66	6.67	5.2	5.78	4.3	2.33
MnO	0.19	0.20	0.16	0.18	0.07	0.15	0.09	0.10
MgO	16.97	5.11	3.82	2.96	2.6	2.26	2.7	0.35
CaO	6.86	10.38	7.91	7.37	5.1	5.78	4.57	1.72
Na_2O	1.12	2.57	2.93	3.34	3.8	3.41	5.32	4.42
K_2O	0.31	0.44	0.84	0.77	2.9	1.46	2.54	2.82
P_2O_5	0.02	0.10	0.12	0.14	0.24	0.12	0.3	0.05
LOI	1.93	#	0.29	–0.06	0.64	0.3	1.14	#
Total	98.89	99.14	99.04	99.21	99.39	99.78	99.86	99.97
Ppm								
Rb	8.1	9.5	18.7	17.03	87	40	47	95
Ba	23.5	96	180	199	769	267	537	634
Th		0.83	1.68	2.39	7.9	4		10
Nb	<1	0.91	1.96	3.00	9	3.1	4.4	5.7
La	0.67	3.07	6.19	9.97	34.2	10	16.6	24
Ce	1.36	8.82	14.88	22.66	66.6	19	33	53.8
Sr	51	145	197	286	505	218	992	155
Nd	0.75	7.13	10.53	12.49	34.0	11	18	25.8
Zr	10.8	48.2	81.5	86.5	193	97	65	217
Sm	0.22	2.21	2.78	2.86	6.18	2.6	(3.3)	5.6
Eu	0.08	0.76	0.95	1.00	1.32	0.8	0.9	1.25
Gd*	0.25	2.66	3.15	3.26	(5.42)	2.6	(2.5)	(6.0)
Y	1.8	20.5	24.8	21.4	22	17	9.4	34.1
Yb	0.32	2.05	2.72	2.34	1.69	2.1	0.75	3.3
Lu	0.06	0.31	0.4	0.38	0.24	0.33		
Sc	36.3	36.2	26.3	14.5	10.6	14	9	7
Cr	1659	17	31	0.25	23		66	6
Ni	323	17	16	2.03	5	3	45	5

#The published analysis is volatile-free. * Where not given in original paper, Gd has been interpolated from Sm and Tb.

Data sources

1 Taylor et al. (1994) analysis 780/23 (enstatite–microphyric boninite).
2 Pearce et al. (1995) analysis SST 7-1 (enstatite–olivine–phyric basaltic andesite, Thule Is).
3 Pearce et al. (1995) analysis SSL 12-1 (plag–phyric two-pyroxene andesite, Leskov Is).
4 Zellmer et al. (2003) analysis MVO 47 (hornblende–enstatite–phyric andesite lava, Soufrière Hills volcano).
5 Feeley and Davidson (1994), analysis OLA9024 (plagioclase–opx–cpx–phyric andesite lava, Volcan Ollagüe).
6 Lindsay et al. (2005), analysis D-JL-46 (from the Patates dacite lava dome).
7 Sajona et al. (1993), analysis Q90-68 (plag–hornblende–biotite–phyric adakitic andesite).
8 Price et al. (2005) analysis P1174 (Taupo rhyolite, Taupo Volcanic Zone. North Island).

account of their higher SiO_2 contents and thus have higher viscosity. Furthermore, the abundance of phenocrysts in andesite adds to its resistance to flow through an increase in the lava's **yield strength**. Andesite lava therefore tends to move at lower velocity and the resulting flow has a higher **aspect ratio** than a typical basalt lava. Andesite lavas never develop pahoehoe morphology: spiny **a'a** surfaces are common but the most typical form associated with andesite is blocky lava (Fig. 6.3a), whose surface consists entirely of large smooth-sided disoriented blocks formed by **autobrecciation**. Such blocks cascade down the flow front (sometimes tens of metres high) and become re-incorporated in the base of the flow as the lava advances over them.

Andesite *sensu lato* covers a wide range of SiO_2 content, and more evolved andesites – especially those that have crystallized to an advanced degree prior to or during eruption, as in the post-1995 eruptions of the Soufrière Hills volcano on Montserrat (Fig 6.2b) – may be sufficiently viscous to form a thick lava dome instead of a tabular lava flow. Such a form is more typical of dacites and rhyolites and is therefore discussed below.

Andesites may also erupt explosively to form scoria cones or other pyroclastic deposits that are discussed in the following chapter.

Dacite lava domes and spines

The higher level of SiO_2 present in dacite and rhyolite melts (Fig. 6.1), together with their lower temperatures of eruption, increases the viscosity of such melts relative to that of andesite (Box 6.3), especially when crystallization has progressed to an advanced degree prior to eruption (Plate 6.6). Because of these factors, dacite lavas erupt as thick domes constructed directly over the vent rather than more laterally extensive lavas typical of andesite.

Exogenous and endogenous lava dome growth

Lava domes vary in size and shape depending upon the volatile content and rheology of the lava. They also vary in the manner in which they grow. Some domes grow by the accumulation of new lobes of lava *extruded* from summit vents. As well as covering the top of the dome, such lobes may ooze down the steeper flanks, forming **coulée**s (French: 'lava flow') whose surfaces are pleated by distinctive arcuate ridges – called *ogives* – resembling large-scale pahoehoe (Figs. 6.6e and 9.10). This extrusive style of dome growth is described as *exogenous* (Latin: 'growing on the outside').

On the other hand, many lava domes grow by inflation when fresh magma is *intruded* into the dome interior without breaking out on the surface. Such *endogenous* dome growth (Latin: 'growing from within') leads to the development of blocky or spiny tops and steep sides covered with talus shed from the over-steepened slopes above (Fig. 6.3b). It is not uncommon for a lava dome to grow by both endogenous and exogenous mechanisms. At Mount St Helens between 1980 and 1986, 15 episodes of dome emplacement occurred, each beginning with an endogenous phase that led to eventual break-out of lava on the surface as exogenous lobes (Fink et al., 1990). At Unzen volcano in Japan between 1991 and 1993, on the other hand, the dome grew initially by exogenous lobe formation, but as discharge rate declined endogenous intrusion became the dominant growth mechanism (Kaneko et al., 2002).

Sometimes magma pressure within an active dome forces up a spine of solidified lava through the summit. The most renowned example is probably the one erupted following the 1902 eruption of Mt Pelée in Martinique, but similar phenomena have been observed in recent years on the Soufrière Hills lava dome in Montserrat and at Mt St Helens (Fig. 6.3c). In the latter case the spine and a smooth 'whaleback' feature – also extruded in solid form – together constitute a new lava dome that has developed since late 2004; by June 2005, the smooth-sided spine had risen 160 m above the crater floor.

Instead of erupting on the surface, andesite or dacite magma may on occasion be emplaced as a shallow level intrusion within a volcano edifice, leading to a doming up of the overlying rocks. An infamous example of such a *cryptodome* is the one whose emplacement into the northern flank of the pre-1980 volcano led to the landslide that initiated the 18 May 1980 plinian eruption of Mt St Helens in Washington State, USA.

Rhyolite magmas usually erupt explosively, often with the production of voluminous

Box 6.3 Factors that affect a magma's capacity to flow

Melt structure

The **viscosity** of a silicate melt depends on two melt properties (Fig. 6.3.1):

1 temperature: a given melt becomes more viscous at lower temperature;
2 composition: acid melts are many times more viscous than basic ones at the same temperature.

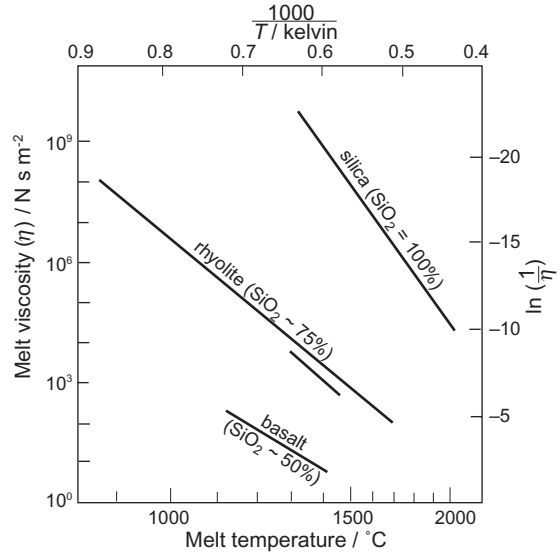


Fig. 6.3.1 Experimental data illustrating that silicate melt viscosity *decreases* with increasing melt temperature, and *increases* with melt SiO_2 content (from basalt to rhyolite to pure molten silica). Note that the viscosity and temperature scales are both non-linear ($\log_e$ viscosity^{-1} in fact varies linearly with T^{-1} where T is expressed in kelvins). Adapted from Gill (1996, Fig. 3.8) based on data from Scarfe (1977).

Silicate melts consist on the atomic scale of metal cations dispersed among a variety of more complex silicate anions. The architecture of these molecular anions has a critical influence on the ease with which the melt can flow. In basaltic melts the anionic structures, being relatively small and simple [SiO_4^{4-}, $Si_2O_7^{6-}$, $(SiO_3)_n^{2n-}$ …], readily nudge and jostle past each other and therefore obstruct melt flow the least, giving basalt a low viscosity at a given temperature. In SiO_2-rich melts like dacite and rhyolite, on the other hand, the anionic units form much larger three-dimensional networks (resembling those found in mica and feldspar crystals) that more readily tangle up with each other, and this more **polymerized** structure greatly inhibits a melt's capacity to flow, as manifest in the melt's

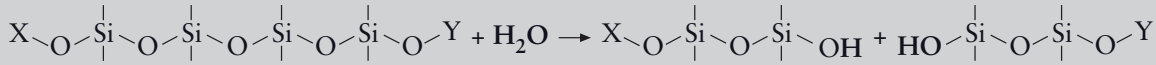
pyroclastics: one huge example is the 26 ka-old Oruanui eruption in the Taupo region of New Zealand, which produced 430 km^3 of fall deposits and an ignimbrite sheet exceeding 320 km^3 in volume according to Wilson, 2001). **Effusive** eruptions are relatively rare. Where rhyolite lavas do erupt, they form domes in a similar style to dacite. A delicate 'bracelet' of late rhyolite domes has for example formed within the walls of the 1.1 Ma Valles caldera in New Mexico, probably the result of leakage of degassed rhyolitic magma up the caldera ring–fracture system (see Figs. 7.19c and 7.20b).

When a cross-section through a young dacite or rhyolite lava dome is exposed, it not uncommonly exhibits *flow banding*, an interbanding of visually distinct layers of differing crystallinity or vesicularity (though not necessarily differing chemical composition); the banding may be coarse enough to see in the field (Fig. 6.3d,g), or may occur on a sub-mm

high viscosity. Imagine a thought experiment with two buckets, one filled with cotton buds and the other with cotton-wool balls – which will be easier to 'pour' out?

Volatile content

Volatiles affect a magma's ability to flow in two radically different ways. When *dissolved* in the melt, they influence its polymerization. Dissolved H_2O tends to *depolymerize* a melt:



polymerized melt | dissolved water | less polymerized melt

[6.3.1]

CO_2, on the other hand, tends to promote polymerization, but is present in most intermediate and acid magmas at concentrations 1–2 orders of magnitude lower than H_2O. The overall effect of dissolved volcanic gases is to *reduce* viscosity.

However, as soon as an ascending magma become supersaturated with volatiles and gas bubbles begin to form (Fig. 2.7), an opposite effect begins to assert itself. The presence of *exsolved* gas in the form of bubbles diminishes a liquid's capacity to flow by increasing its **yield strength** (think of stiffly beaten egg-white). Exsolved gas in the form of vesicles therefore tends to *increase* a melt's effective viscosity.

Crystal content

The presence of a significant crystal suspension in a magma, like the presence of bubbles, increases its yield strength relative to that of the melt alone.

Combined effect of magma ascent and decompression

These different influences reinforce each other when a magma ascends from depth. Under high pressure (at depth), volatiles are stabilized in solution, thus keeping viscosity relatively low. High P_{H_2O} also lowers the solidus and thus inhibits crystallization. Ascent of the magma toward the surface, however, leads to decompression that reduces the solubility of dissolved volatiles, which eventually begin to vesiculate as gas bubbles. The reduction in *dissolved* volatile content increases melt viscosity, while the appearance of *bubbles* increases the yield strength of the bubble-charged magma. The reduction of dissolved volatile content through vesiculation and degassing also raises the solidus, promoting crystallization with a consequent further rise in yield strength. Adiabatic cooling during ascent also acts to increase melt viscosity slightly.

These effects therefore combine, especially in the case of more evolved magmas whose intrinsic viscosity inhibits the escape of gas bubbles, to produce a magma that is highly explosive at shallow depth.

scale (fine examples are illustrated in Vernon, 2004). The bands represent pockets of physical or chemical heterogeneity in the viscous lava that have been sheared out and attenuated by laminar flow during extrusion (and sometimes deformed into folds); any phenocrysts present may also exhibit *flow foliation*. The banding is evidence of magma **mingling** in subvolcanic magma chambers. Seaman et al. (1995), for example, inferred the involvement of three compositionally distinct magmas and two mingling events (Fig. 6.4) to explain the particular features of flow banding seen in the Aliso lava dome on southern Arizona.

Streaky pumices in some pyroclastic deposits probably derive from similar magma mingling in the sub-volcanic plumbing system. On the other hand, some examples of flow banding or flow lamination in rhyolite bodies have a pyroclastic origin, where **ignimbrite** has become so strongly **welded** that it

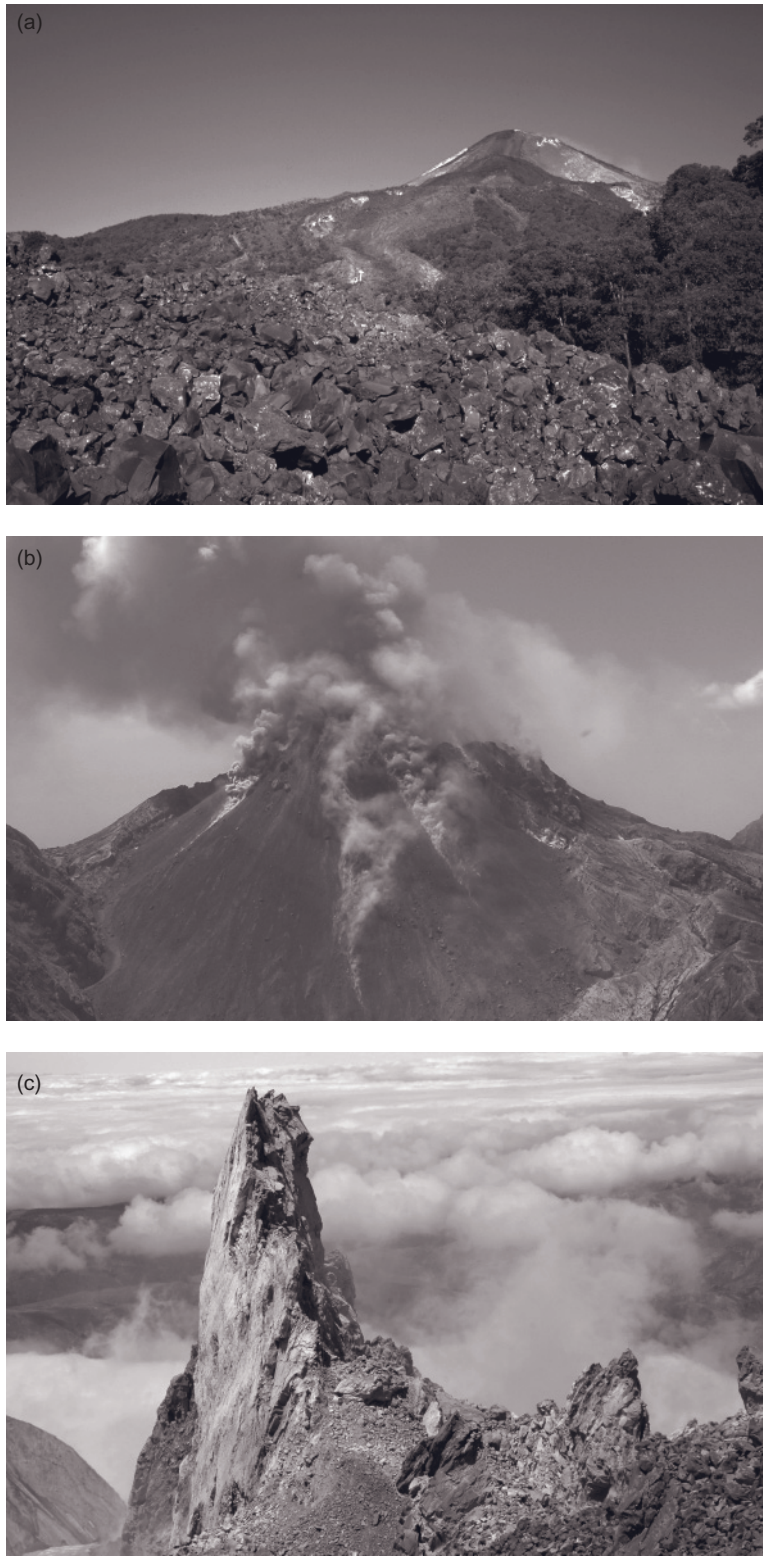
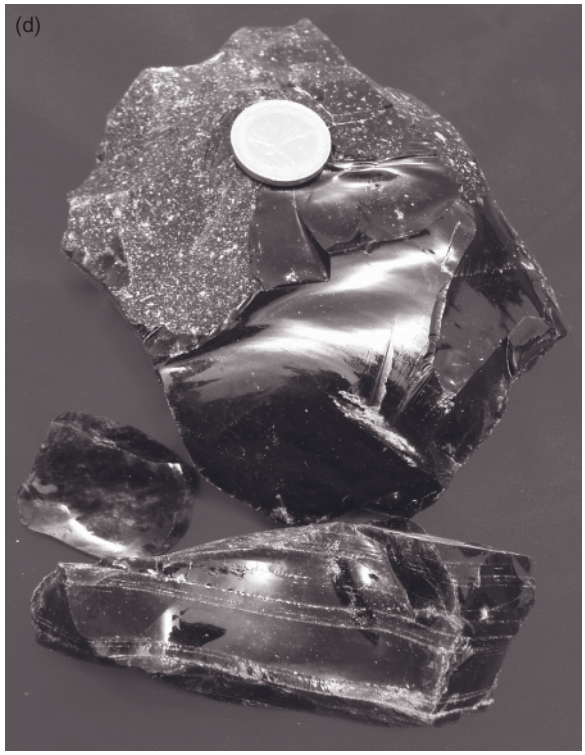


Fig. 6.3 (a) Blocky andesite lava flow surface, from the 1975/6 eruption of Colima volcano, Mexico (photo by Jim Luhr, Smithsonian Institution, reproduced by permission). (b) Endogenous andesite lava dome filling the crater of the Soufrière Hills volcano in Montserrat in June 2000 showing craggy summit and talus slopes (picture courtesy of Caribbean Helicopters). (c) Lava spine projecting from the dacite lava dome in the crater of Mt St Helens, viewed from the south on 12 May 2005 (photo by Steve Schilling, reproduced courtesy of USGS Cascades Volcano Observatory); by late June the spine had risen 160 m above the surrounding terrain.





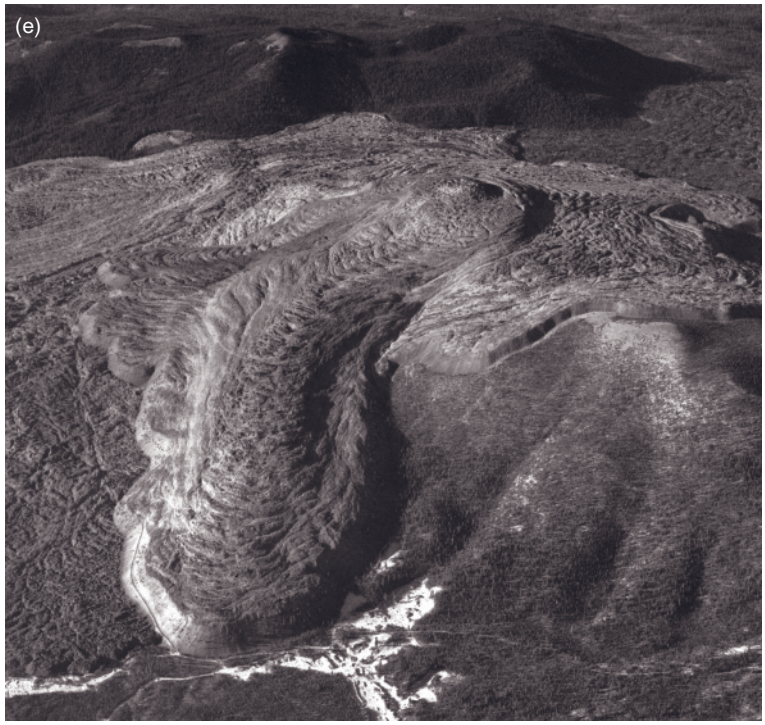


Fig. 6.3 ***Continued*** (d) Fragments of rhyolitic obsidian (from the Roche Rosse flow), Monte Pilato, Lipari, Aeolian Islands (coin 2.3 cm in diameter); the speckled area is a fracture surface. (e) Oblique aerial photo (courtesy of Ronald Greeley, Arizona State University) of an obsidian coulée at Glass Mountain, Medicine Lake volcano, California. The dirt road at the foot of the picture provides scale. Note the eruption vent at the summit and the pleated surface (ogives). (f) White weathering-crust on rhyolite from English Lake District.



Fig. 6.3 ***Continued*** (g) Flow banding in latite lava flow, Gourougou, Morocco; hammer length 75 cm.

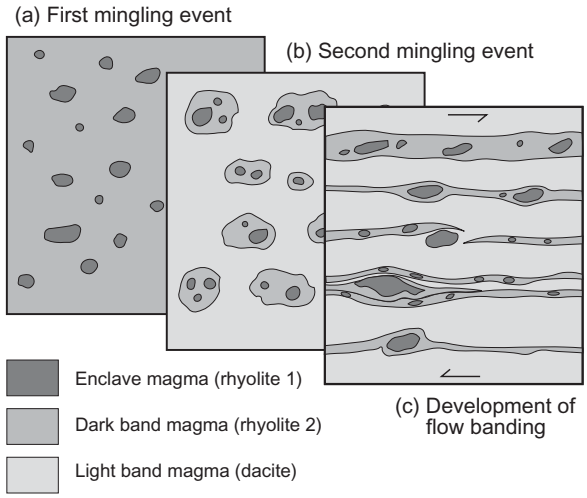


Fig. 6.4 Formation of flow banding by the mingling of discrete magma compositions, as inferred for the Aliso lava dome in southern Arizona (adapted from Seaman et al., 1995 courtesy of the American Geophysical Union).

flows and looks like lava (Kokelaar and Moore, 2006).

Pyroclastic eruptions

Lava flows and domes – examples of **effusive** volcanism – are characteristic of magmas that are relatively poor in **volatile** content. The largest-scale dacite and rhyolite eruptions, on the other hand, are those in which elevated dissolved volatile contents (4%–8%) have led to highly **explosive** eruptions, creating extensive blankets of **tephra** that may be traced for hundreds or even thousands of kilometres. Such **pyroclastic** eruptions and their deposits are the subject of Chapter 7.

HOW ANDESITES, DACITES AND RHYOLITES CRYSTALLIZE – TEXTURAL EVIDENCE

Textures involving variations in crystal size and groundmass crystallinity

Andesites and dacites are often richly porphyritic (Plates 6.1 and 6.6): common phenocryst minerals include plagioclase, orthopyroxene, clinopyroxene, hornblende, biotite, Fe–Ti oxides, apatite and quartz (or tridymite). The ordered sequence in which phenocrysts appear and change their relative proportions in a series of intermediate to acid lavas or pyroclastics (Box 6.2) is testament to advancing fractional crystallization. This may occur in large, long-lived magma chambers that become established and remain at a fixed depth in the crust. Crystallization at depth under such isobaric conditions results from cooling, and occasional leakage of magma to feed surface eruptions will produce lavas with a sharp distinction in grain size between phenocrysts and groundmass.

Many andesites and dacites are on the other hand **seriate**-textured (Plates 6.1 and 6.6), which suggests polybaric crystallization during magma ascent (see Fig. 2.10c). Crystallization during magma ascent is strongly influenced by the presence of volatile components, as explained in Box. 6.4. For a volatile-poor magma, the liquidus and solidus temperatures *decrease* as the magma ascends (Fig 6.4.1, Box 6.4), and therefore crystallization can only occur if cooling at the conduit walls outpaces the rate of ascent. The solidus temperature for water-rich melts, on the other hand, rises rapidly as the melt ascends; in these circumstances, crystallization can occur purely as a consequence of decompression (or possibly due to degassing, which reduces P_{H_2O}), as illustrated by point *z* in Fig. 6.4.1. Water-saturated magmas are thus likely to solidify completely before they can reach the surface.

Blundy and Cashman (2001) reconstructed the crystallization history of dacites erupted from Mt St Helens in Washington (US) between 1980 and 1983. Their conclusions are summarized in Fig. 6.5. In order to illustrate upward magma-migration paths realistically, the figure is shown with pressure (and depth) increasing downward, an orientation inverted relative to Fig. 6.4.1 (Box 6.4). In the lower part of the diagram, a magma with an inferred water content of 6 mass % is H_2O-undersaturated, but on ascending it will traverse the saturation boundary (broad grey dashed line), become supersaturated with respect to H_2O and begin to vesiculate. Arrowed black lines illustrate the ascent paths of batches of magma that fed different surface eruptions. Blundy and Cashman suggest that phenocryst crystallization began at about 10 km depth and continued up to about 4 km.

Field *cd* represents conditions in the shallow cryptodome that formed beneath the northern flank of Mt St Helens in the spring of 1980. The groundmass glass of cryptodome samples is packed with feldspar **microlites** and occasional quartz **oikocrysts** (Figs. 6b & e of their paper). The inferred temperature in the cryptodome was barely lower than the deeper segments of the ascent path, and Blundy and Cashman concluded that matrix crystallization in these samples was the product of slow ascent and decompression under water-saturated conditions rather than by cooling. Feldspar microlites formed as the magma ascended from 4 km to 1 km; the poikilitic quartz crystals nucleated as the almost solid magma passed across the quartz-saturation boundary ('Qz in') in Fig. 6.5. Such 'ascent-driven crystallization' is a consequence of the marked rise in the melt's solidus temperature as pressure (P_{H_2O}) falls. It may actually cause the magma to get hotter as it ascends, owing to release of latent heat of crystallization (Blundy et al., 2006).

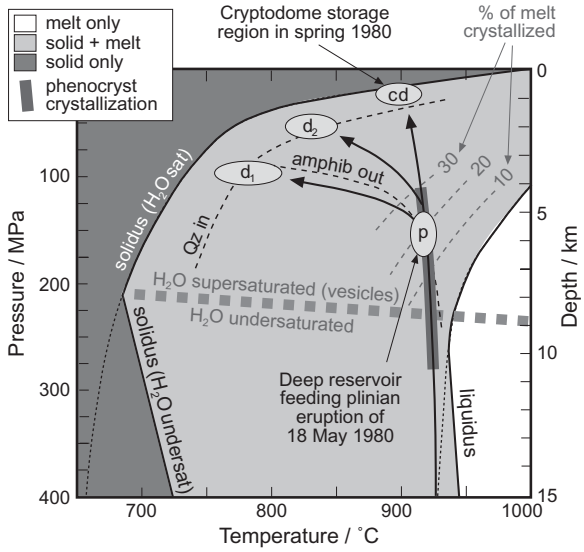


Fig. 6.5 Inferred ascent and crystallization paths for various Mt St Helens 1980 dacite magma batches, after Blundy and Cashman (2001) with kind permission of Springer Science and Business Media. The vertical axis represents pressure (left-hand scale) and depth (right-hand scale), both increasing downwards. Solidus and liquidus curves are those inferred for an assumed water content of 6% (cf. Fig. 6.4.1 in Box 6.4, shown the other way up). The ellipse *p* represents the inferred conditions in the magma reservoir that fed the plinian eruption (18 May 1980). Ellipse *cd* indicates the approximate conditions in the cryptodome that developed during the spring of 1980 prior to this eruption; d_1 and d_2 represent the storage conditions for amphibole-phyric and amphibole-free dacites that erupted as effusive domes in February 1981 and early 1983 respectively. The dashed line 'Qz in' shows the degree of crystallization required before quartz appears. The line 'amphib out' represents the inferred low-pressure stability limit for hornblende in dacite melts.

The field *p* represents P–T conditions in the deeper magma reservoir which fed the subsequent plinian eruption on 18 May 1980. Pumice samples from 18 May plinian fall deposits contain about 30% phenocrysts by volume (mainly hornblende, plagioclase and orthopyroxene) but the groundmass between the vesicles consists entirely of glass with no feldspar microlites or quartz. Evidently decompression and chilling during this explosive eruption occurred too rapidly for groundmass crystals to nucleate.

The explosive eruptions of 1980 were followed by a series of effusive dome-forming dacite eruptions, both endogenous and exogenous, that continued until 1986. The dacite lava erupted in February 1981 contains both hornblende and quartz, whose coexistence is only feasible (according to Fig. 6.5) at temperatures of around 780 °C and depths around 4 km. This suggests supply from a shallow magma reservoir (d_1) that had undergone significant cooling. The dome eruption in February–March 1983 contains quartz but no amphibole, suggesting derivation from a reservoir at depths too shallow to permit amphibole to form. The puzzle is to explain how such cool magmas managed to reach the surface, since during ascent they would encounter the solidus (and should then freeze) at depths of 1–2 km.

Ascent-driven crystallization can only occur under H_2O-saturated conditions when solidus and liquidus temperatures (and the intervening crystallinity contours in Fig. 6.5) rise dramatically as the surface is approached. Adiabatic ascent under H_2O-undersaturated conditions may even lead to resorption of phenocrysts, as discussed below.

Intra-crystalline textures

Twinning is a prominent feature of both plagioclase and alkali feldspars (Box 6.1), but is of little interest to the petrologist except as a means of mineral identification.

Zoning and resorption textures are more relevant for what they tell us about crystallization history.

Oscillatory zoning

Among the most striking – but least understood – features of many intermediate and acid volcanic rocks viewed under crossed polars is the **zoning** seen in plagioclase phenocrysts. Zoning is a systematic radial variation in composition of a crystal, which occurs in many minerals but is more easily detected in plagioclase through the associated change in extinction angle (Box 4.1) and interference colour. Two kinds of zoning are relevant to plagioclase phenocrysts in andesites and dacites:

Box 6.4 Crystallization and melting with and without water

The **liquidus** and **solidus** temperatures at which melts crystallize depend on pressure and on the availability of water. Figure 6.4.1 shows experimentally determined liquidus and solidus curves for a simplified (Mg- and Fe-free) dacite composition. The crystallization behaviour of the melt in the absence of water is shown by the 'dry solidus' and 'dry liquidus' lines on the right; as in other P–T diagrams such as Fig. 2.17, the dry liquidus and solidus temperatures increase with pressure (and depth). The solidus and liquidus are closer together for this evolved composition than they would be for basalt.

Adding water changes things radically, but its effect depends on *how much* is added. Water may be present in this system in two forms: as H_2O dissolved in the melt and, if water is present *in excess of* the amount that is soluble in the melt at the pressure concerned, as a separate H_2O vapour **phase** too. Water could theoretically reside in hydrous minerals as well, but none happen to crystallize at these temperatures in the absence of iron and magnesium (elements that are required for biotite and hornblende to form).

Experiments in the presence of *excess* water show a dramatic *drop* in solidus temperature with increase in pressure (negative d*T*/d*P*), as shown by the curve marked 'H_2O-saturated solidus' in Fig. 6.4.1. Under these conditions, cooling melt at depth can persist to much lower temperatures than it could at the surface. The presence of a gas phase is possible when $P_{H_2O} \geq P_{total}$. However, although melts might be produced at relatively low temperatures under such conditions, their capacity to ascend through the crust is restricted by the solidus: the ascent path of a partial melt produced at *z*, for example, would soon intersect the melt's solidus, causing it to solidify again without making significant progress toward the surface.

What happens when only a *limited amount* of water is present? The amount of H_2O that can dissolve in melt increases with pressure (cf. CO_2 in a fizzy drink). Imagine a series of melting experiments in which the total amount of water in the system is fixed at (say) 5%. Gradually raising the applied pressure will transfer an ever greater proportion of the 5% from the gas phase into the melt, and experiments at points *a*, *b* and *c* in Fig. 6.4.1 will reveal a progressively lower solidus temperature (negative d*T*/d*P*). Eventually a pressure will be reached ('*s*' in Fig. 6.4.1) where the entire 5% has dissolved in the melt, eliminating the gas phase. Further raising the total pressure now takes the system into an H_2O-*under*saturated regime in which P_{H_2O} increases no further; accordingly the solidus temperature undergoes no further depression. The solidus under these new conditions (*s*–*s*′) resumes a positive slope in *P*–*T* space (positive d*T*/d*P*), similar to the dry solidus but at a substantially lower temperature. The *P*–*T* conditions where dacite can be partially molten in the presence of 5% water are shown by the shaded area in Fig. 6.4.1.

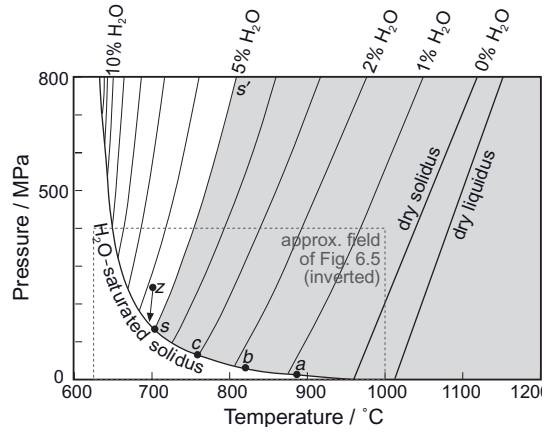


Fig. 6.4.1 P–T melting diagram showing the melting behaviour of synthetic dacite under varying hydration conditions (modified from Holtz et al., 2001; copyright Elsevier). Two lines on the right show the solidus and liquidus temperatures as a function of pressure in the absence of H_2O ('dry'). The curve on the left shows the solidus under water-saturated conditions (i.e. with excess H_2O present as a gas phase at all pressures). The lines in between show how the solidus is depressed with increasing water content (expressed as mass %) under H_2O-*under*saturated conditions; the grey area shows the P–T conditions under which dacite would be partially or wholly molten in the presence of 5 mass % H_2O.

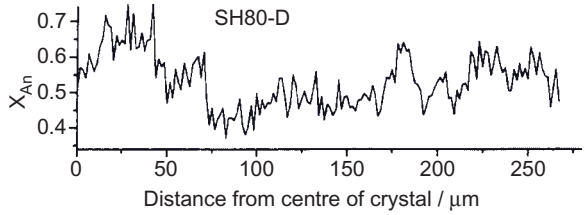


Fig. 6.6 Variation in composition from core to rim of a Mt St Helens plagioclase phenocryst (reproduced by permission of the Mineralogical Society of America from Holten et al., 1997 Fig. 9 upper). X_{An} signifies the mole fraction of anorthite in the plagioclase.

- *normal* zoning, in which composition varies in one direction from an An-rich core to a less An-rich rim, with corresponding progressive change in extinction angle;
- *oscillatory* zoning, in which the composition varies cyclically from core to rim (Fig. 6.6), producing concentric rings of lower and higher extinction angle (Plate 6.2) and interference colour. Fluctuations of the order of 30% in An content are not unusual (Nixon and Pearce, 1987).

Smooth normal zoning reflects a crystal's continuing re-equilibration to changing melt composition as the host magma evolves during the growth history of the phenocryst in a magma chamber; it can be thought of as the small-scale analogue of cryptic layering in the layered series of a major intrusion.[5] Explanations for oscillatory zoning, on the other hand, are necessarily more complex, and divide into two schools of thought:

1 *Extrinsic mechanisms:* oscillatory zoning is seen as a crystal's response to *fluctuating* external conditions. Bowen (1928), for example, attributed it to recycling of plagioclase phenocrysts through zones of cooler, more evolved melt and hotter, more primitive melt in a convecting magma chamber. Others have interpreted it as a record of a crystal's reaction to repeated influxes of fresh magma and its mixing with more evolved resident magma. Recent research shows that the An content of plagioclase may fall during eruption-related decompression[6] in a magma chamber and rise again during subsequent magma repressurization (Blundy et al., 2008).
2 *Intrinsic mechanisms:* oscillatory zoning might alternatively arise as a consequence of self-organization during crystal growth, e.g. some form of oscillating feedback between crystal growth rate (which depletes the boundary layer of melt surrounding the crystal) and solute diffusion rates (which restore the depleted layer by exchange with surrounding melt).

Oscillatory zoning is not confined either to plagioclase or even to magmatic systems (Shore and Fowler, 1996) and may therefore have more than one cause.

Melt inclusions

Rapid phenocryst growth may trap pockets of contemporaneous melt within a phenocryst which are preserved as glass inclusions in the crystal interior (Plate 6.11). Such inclusions, known slightly confusingly as **melt inclusions**, provide a means of analysing the composition of the melt from which the phenocryst crystallized. Because the surrounding crystal 'armours' the inclusion against decompression during ascent and eruption, analysis of melt inclusions often provides the best way of determining the true volatile content of the magma at depth, prior to degassing during ascent and eruption. Primary H_2O contents of arc magmas range up to 8% (Fig. 6.14). Other volatiles are found at much lower levels; CO_2, for example, is generally present in melt inclusions at concentrations below 2500 ppm (Wallace, 2005).

Resorption, overgrowth and sieve texture

Phenocrysts may undergo partial **resorption** in a host melt for one of several reasons:

- A drop in pressure owing to **adiabatic** ascent may bring the temperature of a water-undersaturated magma closer to its liquidus temperature.

[5] A *sudden* shift from calcic to more sodic plagioclase may on the other hand reflect decompression associated with eruption.

[6] The rise in solidus temperature as P_{H_2O} falls can cause the rapid crystallization of alkali feldspar.

- A drop in pressure or P_{H_2O} may cause the stability field of one phenocryst mineral to expand at the expense of another. Magma *m* in Fig. 6.7 lies on the cotectic between the stability fields of alkali feldspar$_{ss}$ and quartz at 200 MPa H_2O and thus may contain phenocrysts of both minerals. If P_{H_2O} is reduced suddenly to 50 MPa, the same melt composition will lie within the alkali feldspar field, making quartz unstable and prone to resorption, as noted by Whitney (1988) and Blundy and Cashman (2001). The resorbed quartz crystal in Plate 6.9 may reflect such a change.
- Mixing of the host magma A with a more primitive (higher-temperature) magma B may lead to the resorption or reverse zoning of phenocrysts originally in equilibrium with A.

Petrographic evidence for resorption can be seen in Plate 6.6, where the large plagioclase crystal just above the centre shows a rounded 'internal outline' picked out by a zone of small inclusions, upon which a new euhedral overgrowth has subsequently developed. The rounded outline results from resorption of the outer parts of a plagioclase phenocryst, probably as a result of mixing of its host melt with hotter, more primitive melt, leading to partial resorption of the crystal; the dust zone consists of material that adhered to the corroded surface before renewed plagioclase deposition formed the superimposed overgrowth.

Resorption can lead to internal as well as external corrosion of phenocrysts, leading to deep embayments and channels, as illustrated by the corroded quartz phenocryst in Plate 6.9. Subsequent rapid overgrowth may trap pockets of melt in such voids, giving rise to the **sieve texture** seen in some plagioclase phenocrysts (Plate 6.7). Sieve-textured plagioclase has been attributed by Nelson and Montana (1992) to rapid decompression rather than magma mixing. Rapid eruption may preserve melt inclusions like those in Plates 6.7 and 6.11 as pockets of glass within phenocrysts.

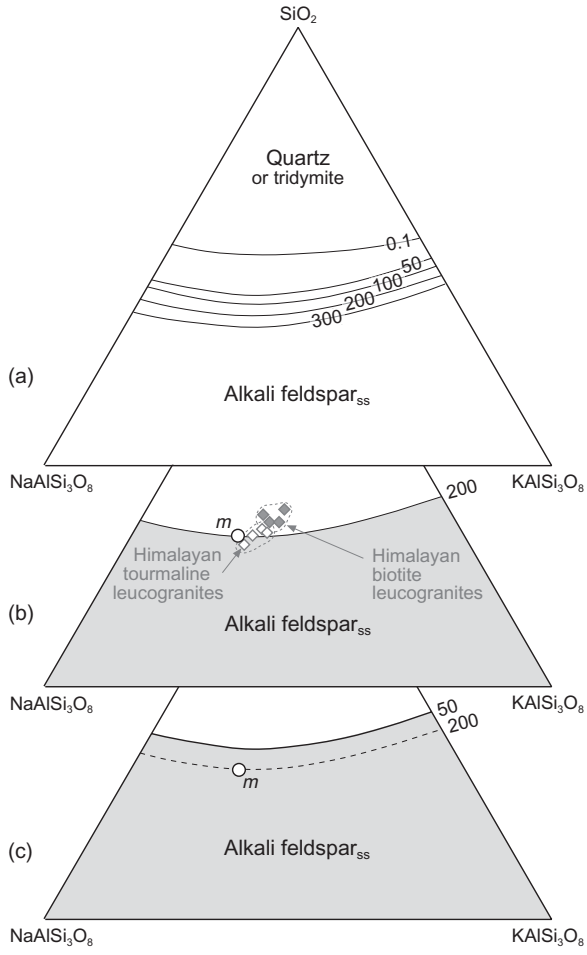


Fig. 6.7 Alkali feldspar and quartz stability fields in system SiO_2–$NaAlSi_3O_8$–$KAlSi_3O_8$ (in mass proportions) under water-saturated conditions, after Tuttle and Bowen (1958) courtesy of the Geological Society of America. The position of the cotectic curve varies with P_{H_2O} (expressed in MPa); 0.1 MPa represents atmospheric pressure (dry experiments). A melt *m* in equilibrium with alkali feldspar *and* quartz at P_{H_2O} = 200 Mpa (Fig. b) falls within the enlarged alkali feldspar field P_{H_2O} = 50 Mpa (shaded, Fig. c), quartz crystals will be unstable, and they will tend to be resorbed. The grey diamonds in (b) show norms of 8 Himalayan leucogranites (calculated from analyses given by Ayres and Harris, 1997) referred to in Chapter 8.

Volcanic glass, devitrification and related textures

High-SiO_2 melts like rhyolite are highly **polymerized**. Their complex molecular structure (Box 6.3) inhibits not only physical flow but chemical diffusion and crystal growth as well. Rhyolite lavas therefore tend to be glassy. The most distinctive form is **obsidian**, the name given to jet-black, aphyric volcanic glass, which is usually (though not always) of rhyolitic composition. Its glassy nature is

apparent both from the vitreous lustre (Fig. 6.3d) and from its conchoidal fracture: broken surfaces[7] are smooth but puckered on a millimetre scale by arcuate wave-like ridges. Obsidian was valued and traded across Europe in Neolithic times for the manufacture of sharp tools; tracing its provenance by comparing geochemical analyses provides useful avenues for archaeological research on trade routes. Classic examples of obsidian include the obsidian lavas of Lipari (Fig. 6.3d) in the Aeolian Islands and the magnificent Glass Mountain coulée at Medicine Lake, California (Fig. 6.3e). Obsidian typically contains bands of pale pumiceous material.

Pitchstone is another form of glassy volcanic (or high-level intrusive) rock, differing from obsidian in containing more crystals, as **microphenocrysts** (Plate 6.10) and as **microlites** or crystallites. The crystal content imparts a less vitreous lustre than seen in obsidian. Pitchstones vary in composition from andesite to rhyolite but acidic compositions are commonest; they tend to contain higher volatile contents than obsidian (Shelley, 1992).

As it contracts, volcanic glass commonly forms diagnostic spheroidal fractures that may be seen as arcuate **perlitic cracks** in thin section (Fig. 6.2) and on fracture surfaces.

Volcanic glass – representing melt that has failed to crystallize – constitutes a metastable state, and over long periods of geological time (Castro et al., 2008) it tends to undergo slow solid-state crystallization, a process known as **devitrification**. Signs are easily seen under crossed polars, where originally isotropic glass can be seen to have transformed into birefringent crystalline material (framed area in Plate 6.9). The incipient crystals commonly nucleate on solid impurities and grow as sheaves or **spherulites** (Fig. 6.2) radiating out from the original 'seed' particle. Because the individual crystals are oriented radially, complete spherulites generally show a cruciform extinction pattern under crossed polars, formed by those crystals whose vibration directions happen to lie nearly parallel to polarizer or analyser; the cross does not move as the stage is rotated. Davis and McPhie (1996) summarize several ways in which spherulitic structures may form, but in acidic glasses devitrification is the commonest.

[7] Obsidian shatters into razor-sharp glass shards when hammered and precautions are needed to avoid injury – especially to the eyes – when collecting.

CHEMICAL SUBDIVISION OF ANDESITES, DACITES AND RHYOLITES

The association of andesites, dacites and rhyolites falls unambiguously in the subalkali field in Figs. 1.5 and 6.1. Given that these volcanic rocks occur in diverse geotectonic settings, is there any chemical subdivision that reflects these different environments?

The concept of a 'calc-alkali' path of magma evolution

Most andesites and dacites erupted in volcanic arcs at convergent plate margins follow a direction of magma evolution quite distinct from their relatives in other tectonic settings. This distinction is illustrated in Fig. 6.8.

The top diagram shows (as filled circles) analyses from the Thingmuli volcano in eastern Iceland – as far away from a subduction zone as one can get – plotted in a ternary diagram with total alkalis, ΣFeO and MgO forming the apexes (generally known as an 'AFM plot'). The trend of black circles from basalt to rhyolite leads initially toward the ΣFeO apex before swinging leftwards and downwards toward the $Na_2O + K_2O$ apex. The initial trend towards the ΣFeO apex (highlighted by the grey arrow) reflects a marked decrease in the MgO content of the evolving melt (from 8.6% to about 4.0% in the case of Thingmuli), accompanied by a smaller relative rise in ΣFeO content (from 11.5% to 15%). This so-called 'iron-enrichment trend' is attributable to the early fractionation of magnesian olivine and other MgO-rich mafic minerals (together with calcic plagioclase). As crystallization advances and fractionating crystals of the mafic minerals themselves become more iron-rich (Fig. 3.6), the trend veers round to one of decreasing MgO *and* ΣFeO with increasing alkalis. Thingmuli volcano in eastern Iceland (filled circles) is a classic example of the elbow-shaped 'tholeiite trend'[8] characteristic of subalkali basalt evolution in settings remote from subduction. Andesite members of such asso-

[8] Sometimes called the 'Fenner trend' after Fenner (1931) who first identified it.

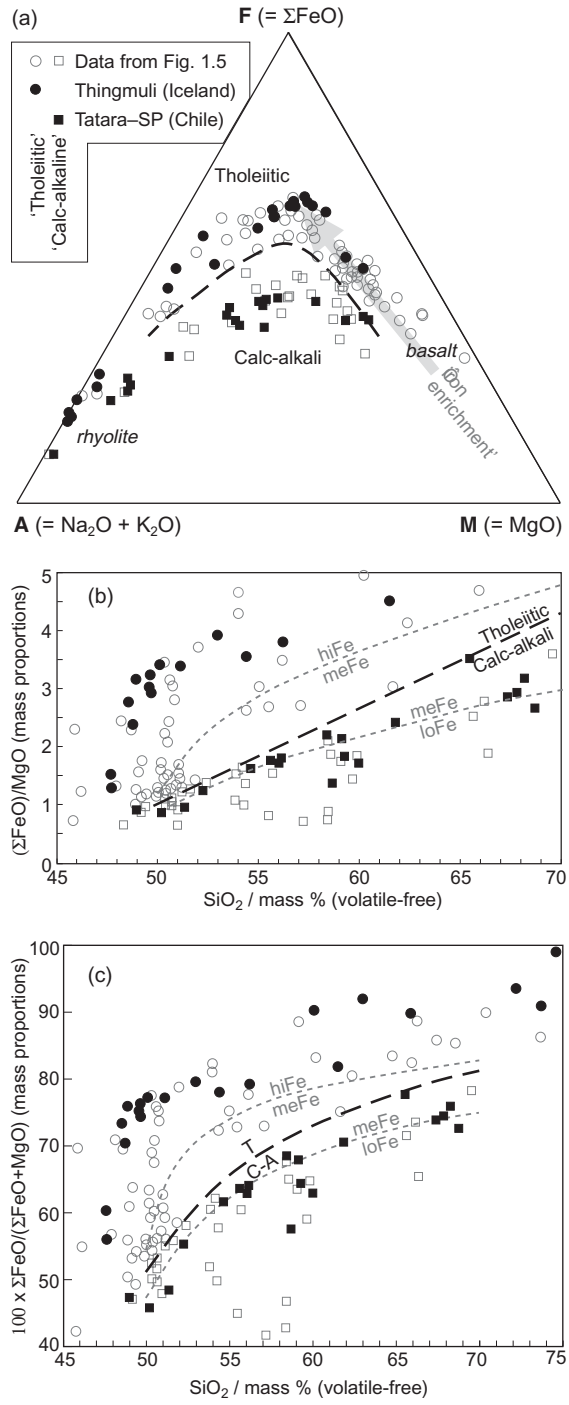


Fig. 6.8 (a) An 'AFM' (Alkalis–ΣFeO–MgO) plot showing tholeiitic and calc-alkali fields and the dividing line between them (heavy dashed line) proposed by Irvine and Baragar (1971). Filled symbols represent selected analyses from Thingmuli volcano in eastern Iceland (Carmichael, 1964) and from the Tatara/San Pedro volcanic complex (Dungan et al. 2001). Grey open symbols represent subalkali compositions from the database plotted in Figs. 1.5 and 6.1. The grey arrow illustrates the general direction of iron enrichment initially followed by tholeiitic magma series (e.g. Thingmuli). (b) The same analyses plotted in a plot of (ΣFeO)/MgO versus SiO_2, an alternative diagram for discriminating between calc-alkali and tholeiitic magma trends; symbols as in (a). The heavy dashed line separating tholeiitic and calc-alkali fields is from Miyashiro (1974). The grey dashed curves show the boundaries between low-, medium- and high (ΣFeO)/MgO suites proposed by Arculus (2003). Evolved Thingmuli samples with low MgO contents (<1.0 %) plot beyond the ranges of ΣFeO/MgO and SiO_2 shown. (c) A revised form of Fig. 6.8(b) that is less susceptible to distortion at low MgO values. Note the larger number of evolved samples that are represented within this plot.

ciations are commonly referred to as *icelandites*, though similar trends can be found in lavas from other oceanic spreading centres and passive continental margins.

Most subduction-related magma series, however, follow a markedly different trend, illustrated in Fig. 6.8(a) by the Tatara-San Pedro volcano in the Chilean Andes (filled squares). The Tatara trend strikes more directly across the triangle with less curvature. A dividing line is shown in Fig. 6.8a, separating tholeiitic magma series that exhibit iron-enrichment trends from subduction-related suites in which this tendency is suppressed. Figure 6.8b shows an alternative diagram often used for making the same dis-

tinction. Magma suites that plot below the dividing lines in Figs. 6.7a and b have for many years been described as **calc-alkaline** ('calc-alkalic' in North America), a term originally defined by Peacock (1931). The precise distinction he sought to draw through introducing this term has long since slipped into obscurity but, as a geochemical descriptor of magma series characteristic of subduction-related settings, 'calc-alkali' continues to be a widely used adjective.

Though the distinction between tholeiitic and calc-alkali magma series is a pivotal one in igneous petrology, the adjective 'calc-alkali' itself is increasingly regarded as an unfortunate misnomer, on the grounds that the prime discriminant of the 'calc-alkali' trend in Fig. 6.8a and b – the (ΣFeO)/MgO ratio – has little to do with either calcium or the alkalis! For that reason,

> *'calc-alkaline has come to mean various things to various people'*

according to Sheth et al. (2002). Arculus (2003) proposed a subdivision of subalkali magma lineages into more sensibly named low-, medium- and high-ΣFeO/MgO categories ('loFe', 'meFe' and 'hiFe' in Fig. 6.8b)[9] to replace the 'calc-alkali' *versus* 'tholeiitic' subdivision. Note that the Tatara-San Pedro trend straddles the meFe/loFe boundary, making it difficult to allocate in this three-fold classification. Arculus (2003) also suggested confining the use of 'calc-alkali' to the original sense proposed by Peacock (1931). Only time will tell whether the Arculus scheme gains acceptance among petrologists, or whether the 'calc-alkali' concept – regardless of its name – proves too entrenched in the literature to be easily abandoned.

The ΣFeO/MgO ratio takes on high scattered values when MgO falls to low values (<1.0%) in more evolved members of tholeiite series; the most evolved Thingmuli samples, for example, have ratios between 8.7 and 113, plotting well beyond the limits of Fig. 6.8b. A more appropriate way of plotting the Arculus diagram that overcomes this problem is shown in Fig. 6.8c.

[9] Arculus (2003) proposed boundary lines that are curves in Fig. 6.8b rather than straight lines, to accommodate magma evolution trends like that of Thingmuli.

The effect of water on magma evolution

> *'Variations in the order of appearance of phases occur with changes in water pressure. The first silicate phase to appear on the liquidus changes with water pressure. … Plagioclase is usually the last major phase to crystallize at elevated water pressure.'*
>
> (Yoder and Tilley, 1962)

Nomenclature aside, why do the tholeiitic and calc-alkali trends develop such different degrees of iron-enrichment when both appear to evolve by fractionation of subalkali basalt? The two trends of black points appear very distinct in Figs. 6.8a and b, though the distribution of grey points in these figures cautions us that they might belong to a fan of divergent trends with intermediate degrees of iron enrichment, rather than a clear-cut dichotomy. The mechanism by which Nature generates this divergence of trends in different tectonic settings from a relatively restricted range of subalkali basalt compositions needs explaining.

The evolutionary path followed by a melt undergoing fractional crystallization depends on (a) the initial melt composition, (b) which minerals crystallize from it, (c) the order in which they first appear, and (d) the proportions in which they crystallize. Osborn (1959) explained the tholeiitic 'iron-enrichment' trend as the product of crystallization under shallow, anhydrous conditions (favouring early crystallization of mafic silicate minerals and plagioclase), whereas in his view the calc-alkali trend reflected deeper crystallization under oxidizing conditions which he attributed to the presence of significant H_2O in the melt. These conditions, he argued, would bring about early crystallization of magnetite (Fe_3O_4) which, by depleting the melt in ΣFeO at an early stage, would suppress iron-enrichment; it would also (as magnetite is a non-silicate) elevate SiO_2 content in later melts.

The Osborn magnetite-fractionation theory, though influential for a time, foundered on the simple observation (see for example Carmichael et al., 1974) that many basalts and basaltic andesites associated with calc-alkali volcanoes – including those of the Cascades (Fig. 6.12) to which Osborn specifically refers – do *not* contain magnetite as an early phenocryst phase, which they should

do if magnetite fractionation were the key factor behind their distinctive chemical trend. More recent work suggests that Osborn, like Kennedy (1955) before him, was nonetheless right to highlight the role of H_2O in the evolution of the calc-alkali rocks, though it affects melt evolution in a way rather different from the one he imagined.

The striking effect that H_2O under pressure can exert on magma evolution is demonstrated by the laboratory crystallization experiments illustrated in Fig. 6.9. The starting compositions used in these experiments – the enlarged symbols in Fig. 6.9 – ranged from basalt (A and B) to basaltic andesite (C). The molten charge in each experiment was allowed to equilibrate at a predetermined temperature below the liquidus, before being **quenched**. The composition of the glass (i.e. quenched melt) obtained in each experiment was analysed by **electron microprobe**, and the array of glass compositions derived from successive experiments on the same starting material defines the compositional path followed by the evolving melt as crystallization progresses. The results, for experiments carried out at three controlled H_2O-vapour pressures, are illustrated in the form of Al_2O_3 and ΣFeO *versus* MgO **variation diagrams** in Fig. 6.9. The least evolved (high-MgO) melt compositions lie to the *right-hand side* of these diagrams, and the array of data points to the left represents successive melt compositions as crystallization progresses.

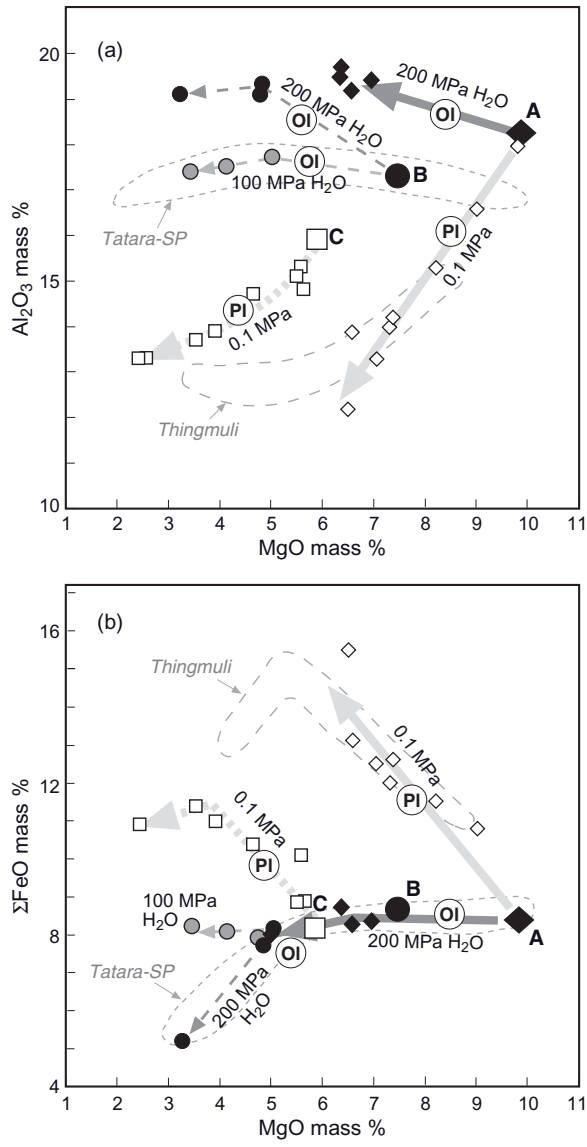


Fig. 6.9 Experimentally determined melt evolution paths as a function of P_{H_2O} (based on data of Grove et al., 1982 and Sisson and Grove, 1993a,b) illustrated for (a) Al_2O_3 and (b) ΣFeO. Each symbol represents the glass composition obtained for a separate experiment: circles, squares and diamonds relate each experiment to the relevant starting composition (larger symbols). Atmospheric pressure (0.1 MPa) experiments (open symbols) were conducted in air without added water. 100 MPa and 200 MPa experiments (grey and black symbols respectively) were conducted under H_2O-saturated conditions at pressures equivalent to 3 and 6 km depth. Starting materials: A and B are basalt; C is basaltic andesite. The fields outlined in grey show the distribution of lava analyses from Thingmuli and Tatara-San Pedro volcanoes (from the sources cited in Fig. 6.8) for reference. Circular labels indicate the dominant early mineral crystallizing in each series of experiments.

The data, though somewhat scattered, define clearly divergent trends. Experiments on rocks A and C conducted at atmospheric pressure in the absence of water (open symbols, pale grey arrows, '0.1 MPa') define melt evolution trends of falling Al_2O_3 and rising ΣFeO contents. In contrast, the experiments on basalts A and B at elevated P_{H_2O} (grey or black symbols, darker grey arrows) produce melt evolution paths leading to higher or near-constant Al_2O_3 contents and lower or near-constant ΣFeO contents. The marked contrast in the direction of melt evolution in response to differing P_{H_2O} is particularly clear from the two series of experiments on basalt A. The distribution of analyses from Thingmuli in Iceland (the grey dashed field) is broadly consistent with the atmospheric-pressure experimental trend, in keeping with Osborn's interpretation of shallow-depth fractionation, whereas the distribution of Tatara-San Pedro analyses (the grey dotted field) is consistent with fractional crystallization at higher P_{H_2O}, possibly in magma chambers at greater depth.

Why does melt evolution vary so markedly with P_{H_2O}? The answer relates to the main minerals crystallizing. Yoder and Tilley (1962) recognized that water under pressure delays plagioclase crystallization to a later stage of melt evolution (Table 6.3): plagioclase crystallizes from basalt melt earlier in atmospheric-pressure anhydrous experiments, whereas it makes its first appearance significantly later when crystallization occurs at high P_{H_2O} (compare arrows A and B in Fig. 6.10). The profound influence that P_{H_2O} has in determining the order and proportions in which different minerals crystallize is confirmed by the circular labels in Fig. 6.9. Calcic plagioclase is a high-Al_2O_3, low-SiO_2 mineral, and its early crystallization from basalt melts at low P_{H_2O} depletes them in Al_2O_3 and elevates ΣFeO (as well as raising their SiO_2 content), leading to a Thingmuli-like trend. At high P_{H_2O}, on the other hand, plagioclase is subordinate to olivine (± cpx) among the early minerals crystallizing from basalt melts (Sisson and Grove, 1993a,b), so Al_2O_3 largely remains in the melt where its concentration rises with advancing fractionation until plagioclase appears at a later stage.

At first sight this explanation is difficult to reconcile with the ubiquity of plagioclase phenocrysts in nearly all subduction-related volcanic rocks including basalts. However there is evidence (Annen et al., 2006) that the phenocrysts in many hydrous magmas grow during ascent and storage at relatively shallow depths, and they are not necessarily the same as the minerals driving the main fractionation trend in deeper, high-P_{H_2O} magma reservoirs.

Low-K, medium-K and high-K associations

Arc-related volcanic rocks vary widely in their K_2O contents, which often correlate with the stage of arc development and with geographical location relative to the arc axis. For this reason it is often useful to divide them into low-K, medium-K and high-K geochemical associations as shown in Fig. 6.11. This diagram is less effective than Fig. 6.8 in discriminating between subduction and non-subduction settings, as the extensive overlap here between Thingmuli and Tatara-San Pedro volcano trends illustrates. The K_2O–

Table 6.3 Crystallization sequences in experiments on a Kilauea subalkali basalt (Fig. 6.10); data from Holloway and Burnham (1972, Table 3).

	Crystallization sequence at atmospheric pressure (cooling path A in Fig. 6.9)	**Crystallization sequence at elevated P_{H_2O} (equivalent to cooling path B in Fig. 6.9)**
Sequence of crystallization	ol	ol
	ol + cpx	ol + cpx
	ol + cpx + plagioclase	ol + cpx + magnetite
	ol + cpx + plag + magnetite	ol + cpx + magnetite + amph
	(No amphibole found)	ol + cpx + magnetite + amph + plagioclase

ol, olivine; cpx, clinopyroxene; plag, plagioclase; amph, amphibole.

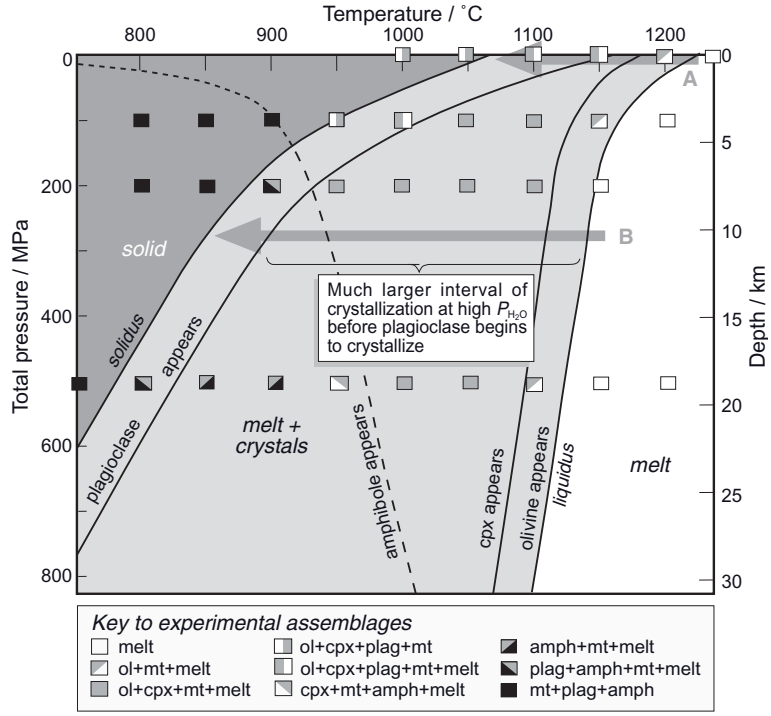


Fig. 6.10 Phase diagram summarizing the results of crystallization experiments on a Kilauea tholeiitic basalt in the presence of excess H_2O ($P_{H_2O} = P_{total}$) by Yoder and Tilley (1962). Each small rectangle represents the *P–T* conditions of a separate experiment and its ornamentation shows the minerals formed in the experiment (see key). Curves show as a function of pressure the approximate temperatures at which olivine, augite and plagioclase begin to crystallize as temperature falls. Arrows A and B show cooling paths that illustrate the pressure-dependence of plagioclase crystallization.

SiO_2 diagram is therefore applied only to subduction-related magmas. Most calc-alkali rocks plot within the medium-K and high-K fields.

The highest K_2O contents of all belong to the shoshonite-latite association. Shoshonites are a potassic variety of trachyandesite (Fig. 9.2) which, in keeping with their mildly alkali character, will be discussed again in Chapter 9. Because they are associated with propagating rifts in both intra-oceanic (e.g. Izu–Bonin–Mariana – Fig. 6.18) and continental arcs (e.g. Cascades), they merit occasional mention in the current chapter too.

WHERE ANDESITES, DACITES AND RHYOLITES OCCUR

Andesites, dacites and rhyolites may in principle form as products of fractional crystallization of subalkali basalt in any of the environments where it occurs (discussed in Chapter 2), but they occur in greatest abundance above subduction zones.

The main places in the world where andesites, dacites and rhyolites erupt are shown in Fig. 6.12. The full-colour map that can be downloaded from http://pubs.usgs.gov/imap/2800/ provides a useful supplement.

Island arcs

Complementary to the mid-ocean rift system (where new oceanic lithosphere is continually being created) is the worldwide system of subduction zones, the convergent plate boundaries where lithosphere formed at ocean ridges returns to the mantle. The intra-oceanic island arcs and active continental margins that form above these subduction zones are where the largest volumes of andesite, dacite and rhyolite are erupted. Most of these 'magmatic arcs' are located in the so-called 'Ring of Fire' that borders the Pacific Ocean on its western and

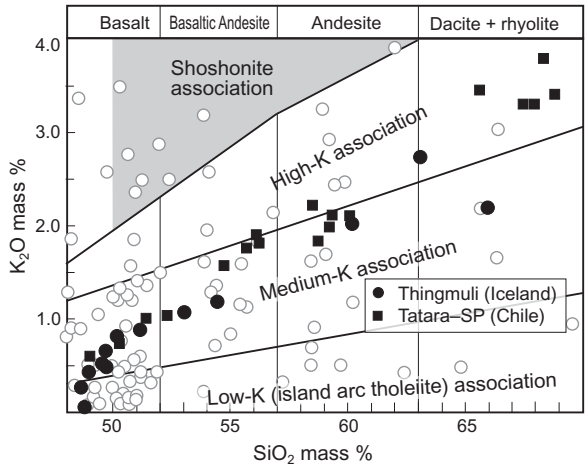


Fig. 6.11 K_2O versus SiO_2 plot showing how basalts, andesites, dacites and rhyolites may be subdivided geochemically into low-K, medium-K and high-K associations (boundary lines from Le Maitre, 2002). The boundary dividing the shoshonite association from the high-K association is that of Peccerillo and Taylor (1976). The boundary distinguishing dacite from rhyolite in Fig. 6.1 cannot be represented as a unique line in this diagram, so the fields are combined. The filled symbols are from the sources cited in Fig. 6.8, and the open data points are from the sources given in Fig. 1.5. **NB** Analyses need to be recalculated volatile-free (Box 1.3) before being plotting in this diagram.

northern margins – where the arcs are intra-oceanic – and on its eastern margin where subduction occurs beneath an active continental margin (Fig. 6.12).

The global output rate of subduction-related volcanism has been estimated by Crisp (1984) to be in the region of 0.4–0.6 km^3 $year^{-1}$, almost an order of magnitude lower than that produced by the mid-ocean ridge system (about 3 km^3 $year^{-1}$).[10] However, as at ocean ridges, the volume erupted at the surface is likely to be outweighed (by perhaps 5–10 times) by the proportion of magma emplaced at depth within the crust, and so total melt production rates above subductions zones probably exceed 2.5 km^3 $year^{-1}$. Arculus (2004) quotes estimates in the range 1.2–7 km^3 $year^{-1}$.

The main features of an intra-oceanic subduction system are illustrated in the cross-section shown in Fig. 6.13. The most obvious topographic features are (a) the ocean trench where the subducting plate begins its descent into the mantle, and (b) the volcanic arc constructed on the overriding plate, running parallel to the trench and typically displaced about 50–150 km from it. Between them lies the *fore-arc* region. The example shown in Fig. 6.13 is an *accretionary margin,* because sea-floor sediments scraped off the downgoing slab pile up at the leading edge of the overriding plate. This leads to:

1 a wedge-shaped body of accreted sediment that grows with time. Owing to the shear stress associated with downward movement of the underlying slab, the dominant structures in this *accretionary prism* are folding and thrust faulting, often combining to form a chaotic *mélange*; the base of the prism is marked by a highly sheared décollement. Accretionary prisms commonly build up to form a *fore-arc high* (Fig. 6.13).
2 the *fore-arc basin* between the fore-arc high and the island arc, filled with coarser clastic sediments shed by subaerial erosion of the adjacent arc.

Examples of accretionary fore-arcs are found in the Aleutian, Lesser Antilles and Indonesian arcs (Fig. 6.12). Many other fore-arcs (probably the majority) are on the other hand *erosional* rather than accretionary: i.e. more material is removed from the overriding plate (and carried to deeper levels in the subduction zone) than is deposited there. Examples are associated with the Mariana, Peruvian and Tonga–Kermadec trenches (Clift and Vannucchi, 2004).

For a typical arc-trench system, gravity is lowest at the trench (Fig. 6.13) owing to the depth of water and thickness of low-density sediment within it. As it enters the trench, the subducting slab first bends downward at the 'hinge' and then straightens out. Some seismologists attribute the double seismic zone detected within some slabs (Fig. 6.13) to the stresses associated with straightening-out of the flexed slab (Fowler, 2005). Subduction

[10] Subduction-related volcanic output includes a major proportion of often highly vesicular pyroclastic ejecta. In order to use volumes of pyroclastic material to estimate magma production rates, one must recalculate volumes to **dense rock equivalent** (DRE) to eliminate distortion due to vesiculation.

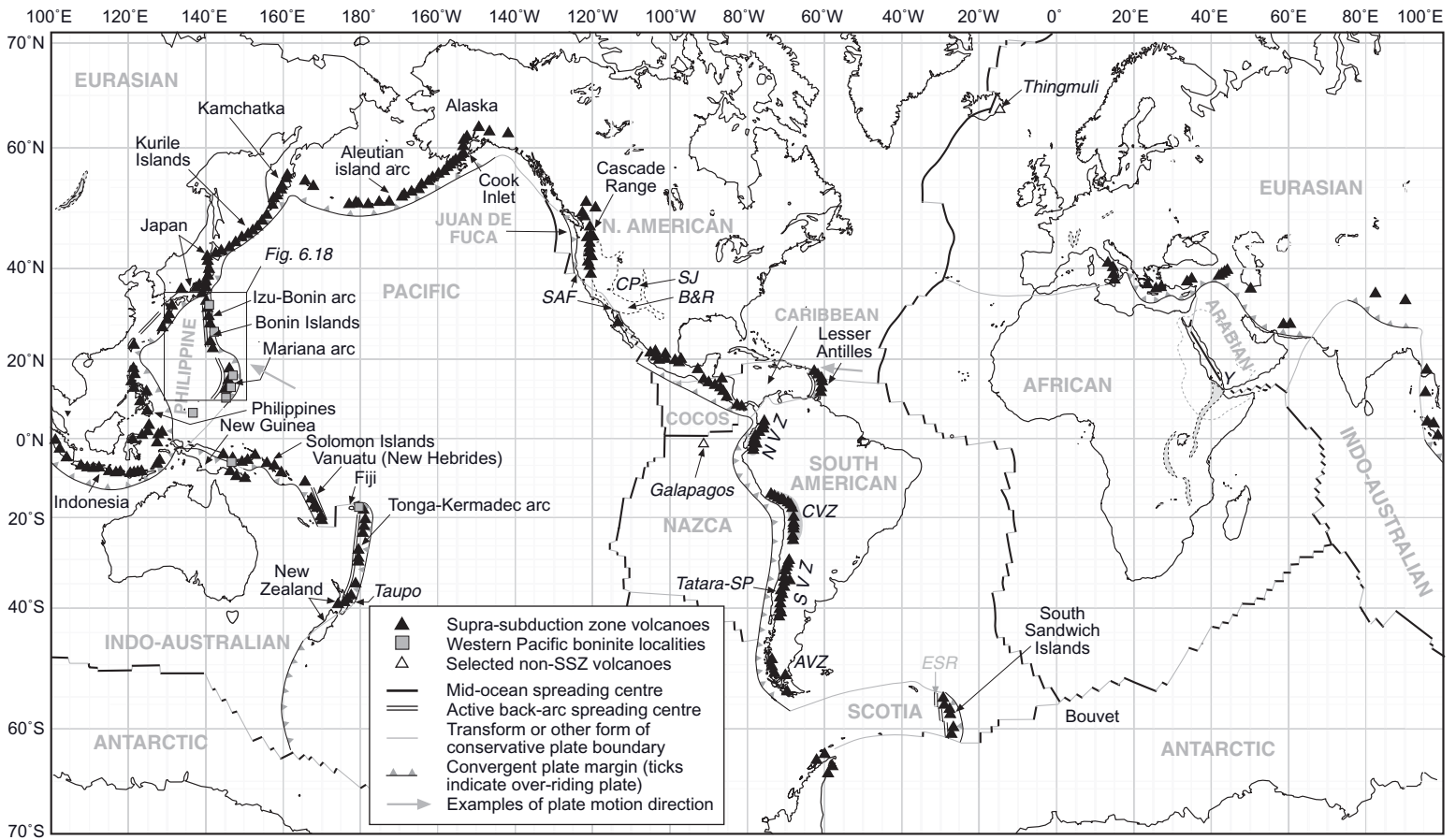


Fig. 6.12 A map of the world showing active oceanic island arcs and continental volcanic arcs, on a US Geological Survey base map (cf. Fig. 2.12). The distribution of supra-subduction zone (SSZ) volcanoes is represented by black triangles (volcanoes are too numerous to be shown individually). The 'Ring of Fire' surrounding the Pacific Ocean can be traced clockwise from New Zealand to the southern tip of South America. *ESR*, East Scotia Ridge; *B&R*, Basin and Range Province; *CP*, Colorado Plateau; *SJ*, San Juan volcanic field; *SAF*, extent of the San Andreas Fault. *NVZ*, *CVZ, SVZ* and *AVZ* refer to the northern, central, southern and Austral volcanic zones of the Andean cordillera. '*Y*' indicates Yemen. The area of the western Pacific enlarged in Fig. 6.18 is indicated by a box.

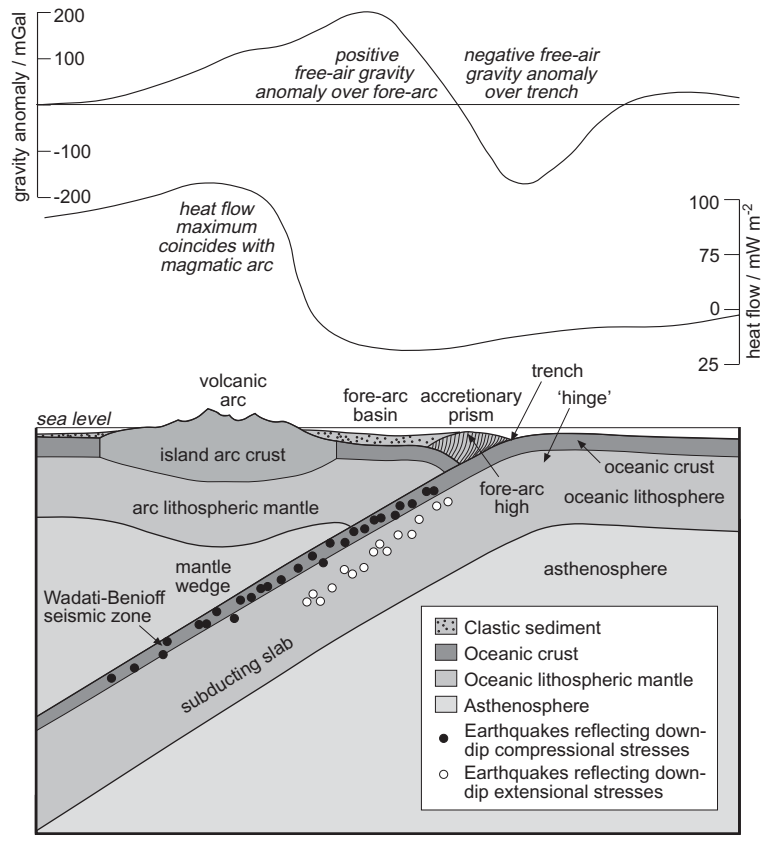


Fig. 6.13 Observational aspects of a typical island arc (adapted from Blake and Argles, 2003 by permission of the Open University). The lower part of the figure shows a cross-section of a typical intra-oceanic subduction system to depths of about 300 km. Circles show earthquake foci in the down-going slab (many others originate in the overriding slab). The graphs above are sketches of representative free-air gravity and heat flow profiles across the section. The gravity profile shows a marked negative anomaly reflecting the low density of water and sediment occupying the trench and a positive anomaly over the fore-arc region (a consequence of the cold dense subducted slab beneath). Heat flow is low over the fore-arc region (subducting slab is cooler than surrounding mantle) and reaches a maximum over the volcanic arc (reflecting shallow magmatic heat sources there) and the back-arc region.

zones vary significantly in the dip of the subducting plate: most dip at angles between 40° and 70° to the horizontal, but more extreme values are known: beneath Honshu (northern Japan), for example, the Pacific plate dips at only 25°, whereas the same plate subducting beneath the Izu–Bonin–Mariana arc further south steepens with depth to become almost vertical.

Note that the surface plate motion of a subducting plate is not necessarily perpendicular to the plate margin and the associated island arc beneath which it subducts. Indeed, given the arcuate geometry of many island arcs, orthogonality cannot apply universally, and many instances are known of oblique subduction, e.g. the northern Mariana arc (Fig. 6.18) and the northern Lesser Antilles arc (Fig. 6.12). In extreme cases, such as the western end of the Aleutian arc, the plate boundary ceases to be convergent and becomes strike-slip.

The Japanese arc is unusual in consisting of two chains of active **stratovolcanoes** running parallel to the trench (Tatsumi and Eggins, 1995). The 'trench-side chain' of volcanoes is located at a distance from the trench where the **Wadati–Benioff zone** has reached a depth of 100–120 km; the 'arc-trench gap' measured at the surface will obviously vary

inversely with subduction dip. The less active 'back-arc side-chain' lies further away from the trench, at a distance corresponding to a Wadati–Benioff zone depth of 160–200 km. The high heat flow through the arc crust (Fig. 6.13) reflects the presence of magma at shallow depths.

The basement on which arc volcanoes stand varies from one arc to another. Young arcs like the South Sandwich Islands and the Mariana and the Tonga–Kermadec arcs (Fig. 6.12) are built on relatively thin crust (15–20 km thick), whereas more mature arcs typically sit on 30 km-thick crust (Fowler, 2005) with a seismic structure resembling continental crust; the plutonic emplacement of arc magmas and their differentiation products has contributed significantly to crustal thickness here (discussed in Chapter 8). The crustal structure of the Japan arc is more complex still owing to the accretion of Paleozoic and Mesozoic terranes and continental arcs at the margins of the Asian craton, from which Japan became detached only 25 Ma ago. Near-complete cross-sections of palaeo-island arc crust are occasionally preserved in accreted terranes or continental sutures, such as the 210–180 Ma Talkeetna arc section in south-central Alaska (e.g. Greene et al., 2006) and the Kohistan section in NW Himalaya (Petterson and Treloar, 2004). Thick cumulate sequences in such deeply eroded sections suggest that a lot of differentiation takes place at the base of the crust (Annen et al., 2006).

The range and categories of magma composition associated with island arcs and other subduction systems are summarized in Fig. 6.11. In young island arcs the dominant volcanics tend to be basalts and basaltic andesites of the low-K association (alternatively known as the 'island arc tholeiite' association), as many volcanoes in the South Sandwich arc – initiated less than 3 Ma ago – illustrate. Low-K basalts and related basaltic andesites are often aphyric but may contain phenocrysts of plagioclase, augite, olivine, enstatite and opaques but no hornblende. It is reasonable to suppose (though unproven) that similar low-K magma products form the early foundations of more mature island arcs.

The present-day volcanoes of mature arcs, on the other hand, erupt mainly andesitic and dacitic products belonging to the medium-K and high-K associations in Fig. 6.11 (broadly rocks of **calc-alkali** affinity), as instanced by the central sector of the Lesser Antilles and many western Pacific arcs such as Japan. In the former, andesites predominate (phenocrysts of plagioclase, augite, hornblende, enstatite and opaques) but basalts and dacites both occur and there are rare rhyolites too; information on fractionating minerals can also be gained from studying cumulate inclusions that often occur in the volcanics, consisting of the same minerals along with olivine, magnetite, biotite, ilmenite, quartz and apatite.

Subduction-generated magmas generally possess higher volatile contents than those from other tectonic settings. The most compelling – albeit qualitative – evidence for this lies in the fact that most of the world's highly explosive volcanoes lie around the Pacific 'Ring of Fire' and along the Indonesian arc where the Indo-Australian plate subducts beneath the Eurasia plate (Fig. 6.12). The correlation between explosivity, viscosity and volatile content is explained in Box 6.3. Quantitative measurements of magma volatile content in pre-eruption magma reservoirs can be obtained by analysing minute melt inclusions trapped within phenocrysts during crystal growth, which in most minerals retain the pre-eruption volatile content of the melt unaffected by degassing of the host magma during its ascent (see Box 1.4). Figure 6.14 compares the pre-eruption dissolved water contents of selected subduction-related basic magmas (island-arc tholeiites and boninites) with those from other tectonic settings, which are much lower.

The highest range of H_2O content in Fig. 6.14 is populated by more evolved subduction-related magmas involved in a number of major Quaternary eruptions, in which H_2O and K_2O have been further enriched by fractional crystallization or other fractionation processes. Such analyses suggest that magmas responsible for the most violent pyroclastic eruptions commonly have pre-eruption water contents in the range 4%–7%.

Subduction-related magmas also possess a very distinctive trace element fingerprint, as illustrated by the incompatible element profiles shown in Fig. 6.15a. As noted in Chapter 2 (see discussion of Fig. 2.16c), these profiles are made more complex – compared to mid-

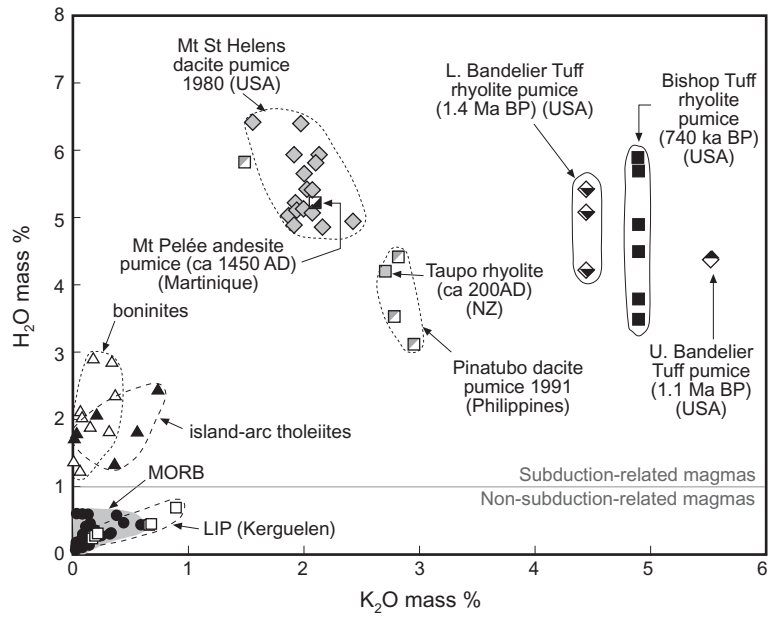


Fig. 6.14 Pre-eruption water contents plotted against K_2O content for selected subduction-related magmas, measured using melt inclusions in phenocrysts. Analyses for MORB glasses (recovered from depths where pressures are high enough to prevent volatile loss by degassing) and melt inclusions from one LIP (Kerguelen oceanic plateau) are shown for comparison. Data from Barclay et al. (1996), Belkin et al. (1998), Blundy and Cashman (2005), Danyushevsky et al. (2000), Dunbar and Kyle (1993), Dunbar and Hervig (1992), Gerlach et al. (1997), Martel et al. (1998), Sobolev and Chaussidon (1996) and Wallace (2002).

ocean ridge basalt (MORB) and ocean island basalt (OIB) lavas – by the presence of positive and negative 'spikes' in the patterns. Nonetheless the following generalizations can be made:

- Abundances increase from basic to acid compositions, most notably for the most strongly incompatible elements (left-hand side);
- Profiles generally become steeper (i.e. higher Rb/Yb ratios) for the more acid rocks;
- There are prominent negative anomalies for the high field strength elements (**HFSE**) niobium (Nb), phosphorus (P) and titanium (Ti) though not for zirconium (Zr);
- The magnitude of the negative spike for Nb remains roughly the same for all rock types whereas the anomalies for P and Ti tend to increase from basaltic andesite to rhyolite;
- Excepting Nb, the elements to the left of La are abruptly more abundant than lanthanum (La) and the elements to the right of it.

In summary, subduction-related magmas are geochemically distinctive in having higher volatile contents and higher large-ion lithophile element/rare-earth element (**LILE/REE**) and LILE/HFSE ratios than magmas from other tectonic settings. These observations provide the key to understanding the petrogenesis of arc magmas, as discussed in the following section of the chapter.

For many island arcs, magma composition correlates broadly with the distance of the volcano from the trench, or – to put it another way – with the vertical depth *h* of the Wadati–Benioff zone beneath the volcano. The best known example is the tendency for the K_2O content of volcanic rocks to increase from trench-side to back-arc-side volcanoes, sometimes called the '*K-h* relationship' (Dickinson, 1975). This is illustrated in histogram form in Fig. 6.16. In these cases, parallel correlations against *h* often exist for other geochemical

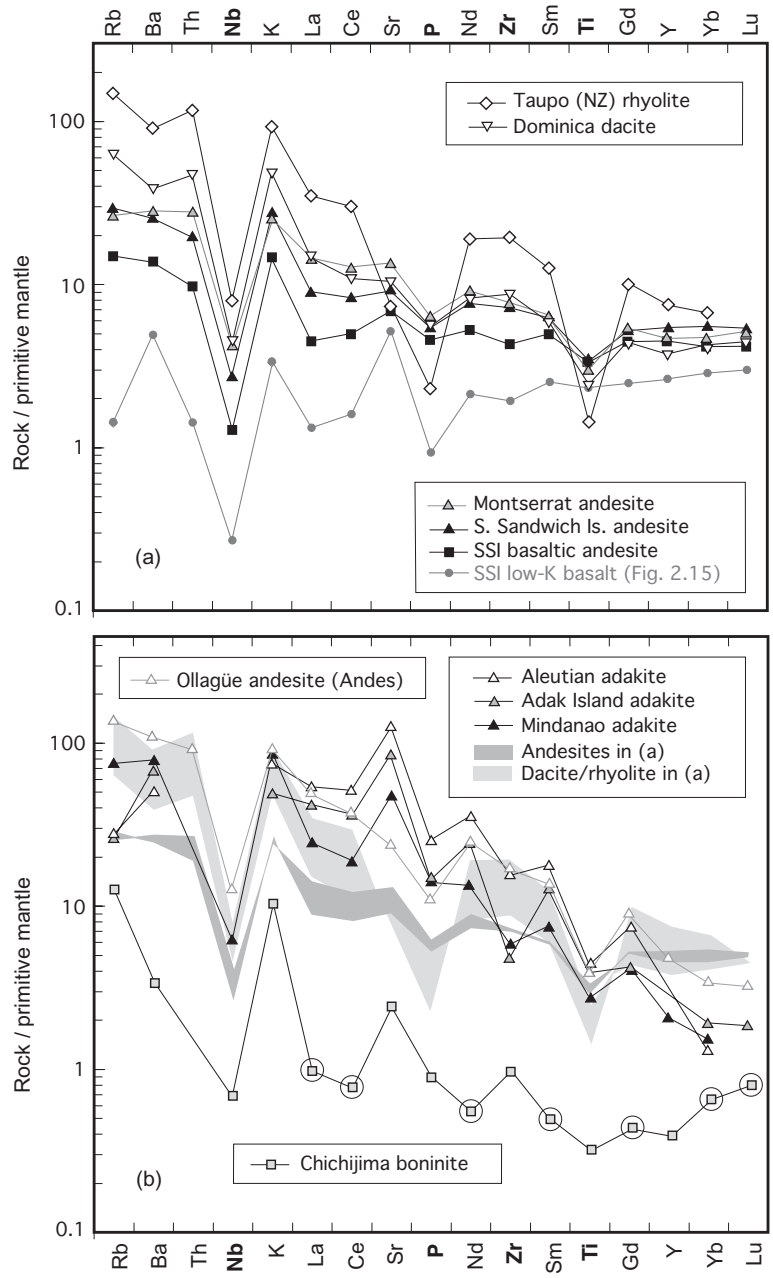


Fig. 6.15 Incompatible element enrichment diagrams for island arc-related volcanic rocks tabulated in Table 6.2. (a) Typical andesites, dacite and rhyolite, together with (in grey) a low-K tholeiitic basalt from the South Sandwich island arc (see Table 2.4) for comparison. (b) A boninite, three adakites and an andesite from the Central Volcanic Zone of the Andes; analyses are from Table 6.2 (except the Aleutian adakites, from Kay (1978)). Shaded fields in (b) show the andesite and dacite + rhyolite fields from Fig. 6.15a for comparison. The **rare earth element** abundances in the boninite have been circled to emphasize the characteristic upwards-concave shape of boninite REE patterns.

Chemical symbols shown **bold** indicate high field-strength elements (**HFSE**, see Fig. 2.7.1). Normalizing data (from Sun and McDonough, 1989) are tabulated in Table 2.4.

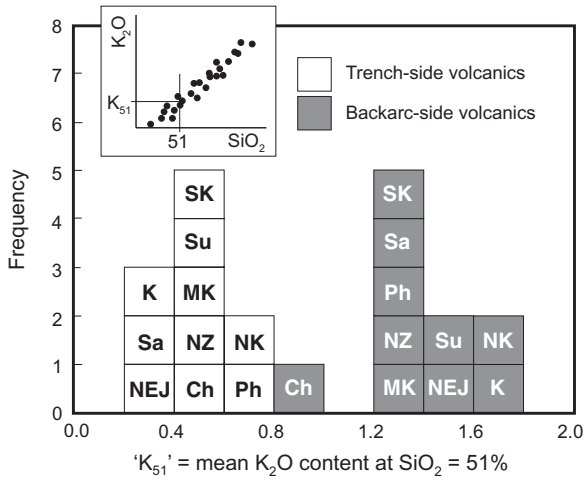


Fig. 6.16 Variation of K_2O contents of arc volcanic rocks with distance from the trench. Each box represents a particular arc volcanic association, and its position along the horizontal axis (K_{51}) represents its mean K_2O content measured at the point on a K_2O–SiO_2 variation diagram where SiO_2 = 51.0% (see inset cartoon) – a device to eliminate differences due solely to varying degrees of fractionation. Adapted with permission from Tatsumi and Eggins (1995) Fig. 3.13 courtesy of Blackwell Publishing. Ch, Chile; K, Kamchatka arc; MK, Middle Kurile arc; NEJ, NE Japan; NK, North Kurile; NZ, New Zealand; Ph, Philippines; Sa, Sangihe (Indonesia); SK, South Kurile arc; Su, Sulawesi (original data sources are listed by Tatsumi and Eggins). The cartoon illustrates the derivation of K_{51}: each data point represents the analysis of an individual volcanic rock from the province in question.

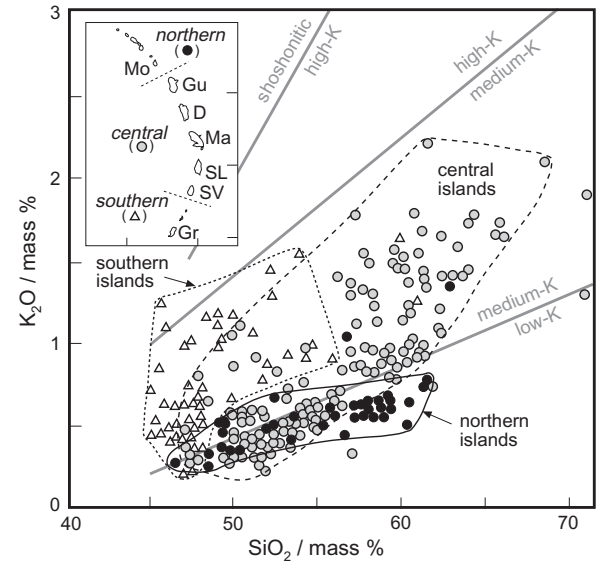


Fig. 6.17 Chemical zonation along the length of the Lesser Antilles volcanic arc, adapted from Macdonald et al. (2000; copyright Elsevier); the inset map shows the division of the arc into the northern central and southern divisions adopted in that paper (Mo, Montserrat; Gu, Guadeloupe; D, Dominica; Ma, Martinique; SL, St Lucia; SV, St Vincent; Gr, Grenada). To make the zonation clearer, the envelopes in the main figure exclude a few outlying data points. The IUGS low-, medium- and high-K boundaries as in Fig. 6.11 are shown in grey.

parameters such as the La/Yb ratio. One or two island arcs fail to conform to a direct *K-h* correlation, however: in the Vanuatu/New Hebrides arc, for example, the relationship even seems to be reversed (Barsdell et al., 1982).

One or two island arcs exhibit systematic *longitudinal* variation in magma composition. The best known example is the Lesser Antilles arc (Figs. 6.12 and 6.17), where the currently active volcanoes define a single 10 km-wide volcanic zone, too narrow to exhibit meaningful cross-arc geochemical variation. Figure 6.17 shows one aspect of the longitudinal zonation, based on the three-fold geographical division of the arc used by Macdonald et al. (2000). Though the three populations overlap considerably, the shift in geochemical character from north to south is clear: the northern islands produce mostly low-K magmas, the central islands (eruptively the most prolific) produce low- and medium-K magmas covering the widest range of SiO_2 content, while Grenada and the Grenadines in the south produce medium-K basalts and basaltic andesites, some being SiO_2-undersaturated.

Back-arc extension and related volcanism

Passing southward along the Izu–Bonin–Mariana arc-trench system (Figs. 6.12 and 6.18), one encounters a point ('A' in Fig. 6.18) where the active Izu–Bonin volcanic arc divides into the active Mariana volcanic arc to the east, and an older submarine 'remnant arc' of extinct volcanoes (the West Mariana Ridge – Fig. 6.18) to the west. The active and remnant volcanic arcs are separated by an

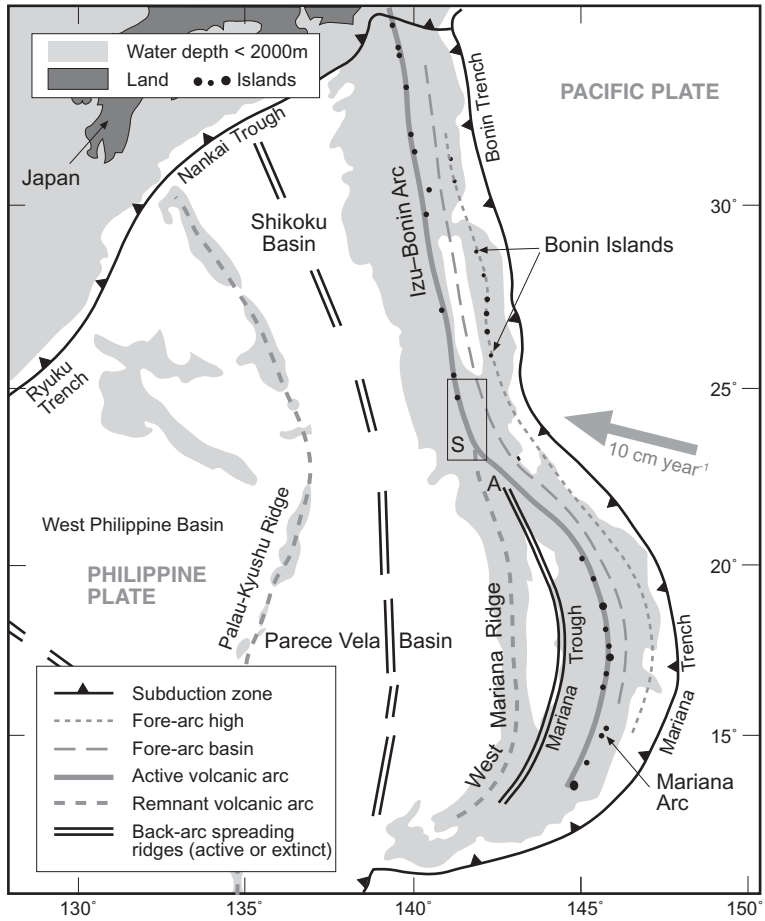


Fig. 6.18 The Izu–Bonin–Mariana arc system and associated back-arc basins, adapted from Taylor et al. (1994) by permission of Oxford University Press. White areas represent water depths exceeding 2000 m. The rectangle marked S shows the main area of current shoshonite volcanism.

extensional basin, the Mariana Trough, which is floored by oceanic crust. Magnetic lineations and bathymetry indicate that active sea-floor spreading has been taking place in this basin for about 5 Ma, forming a young *back-arc basin* that is steadily separating the West Mariana Ridge from the Mariana Arc. Incipient rifting in the arc crust north of A suggests that the spreading axis is propagating in that direction (Yamazaki et al., 2003), progressively 'unzipping' the Izu–Bonin arc northward. Geophysical evidence suggests that the Parece Vela and Shikoku basins to the west (Fig. 6.18) also originated as an earlier back-arc basin, rifting beginning about 30 Ma ago and subsequent sea-floor spreading separating the Palau-Kyushu Ridge from the pre-5 Ma Mariana Arc (Sdrolias et al. 2004). With the onset of spreading in the Mariana Trough, the Parece Vela–Shikoku basin became inactive, though high heat flow remains as a legacy of earlier spreading and magma input.

It is perhaps counter-intuitive to find *extensional* basins associated with a *convergent* plate boundary. Would we not expect convergence to generate compressional tectonics rather than extension? This seeming paradox is less strange if we take account of the Jurassic age of the Pacific plate where it subducts beneath the Mariana arc: being old, cold and therefore dense, the plate lacks buoyancy and is susceptible to *slab roll-back*, in which the subducting plate sinks into the mantle faster than it converges with the overriding plate. The 'hinge line' – instead of being fixed like the roller supporting a conveyor belt – retreats away from the over-riding plate (Fig. 6.19). As a result, the unsupported arc lithosphere collapses laterally where it is hottest and weakest, at the volcanic front. Extensional

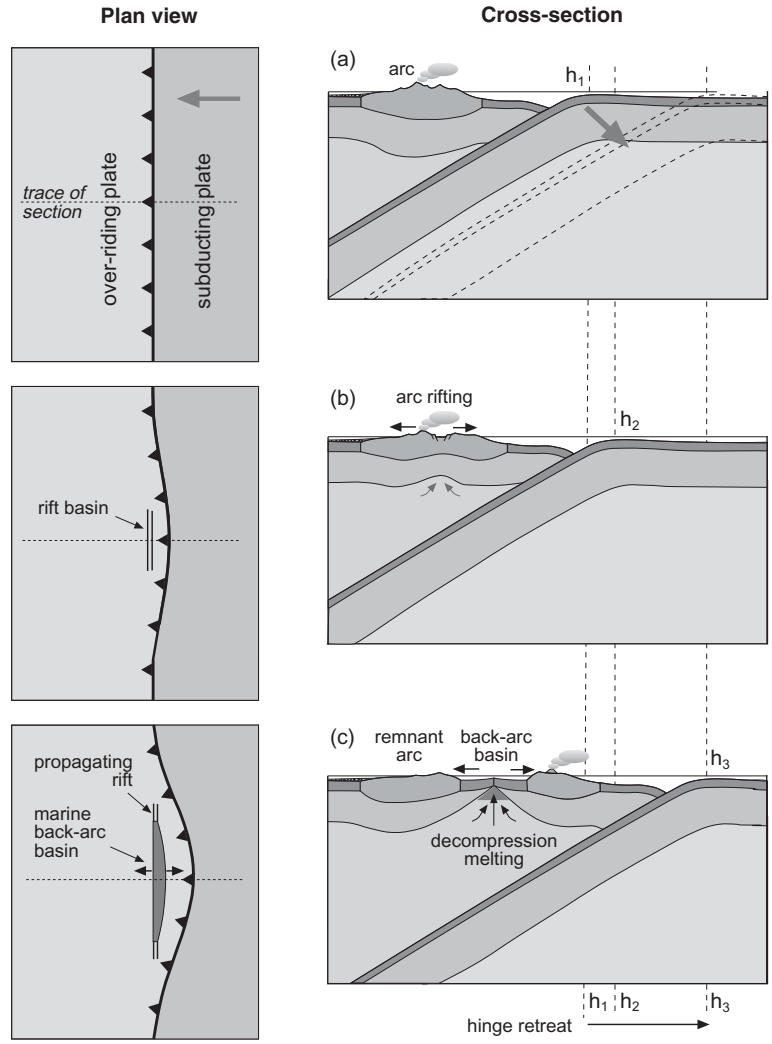


Fig. 6.19 Initiation of an intra-oceanic back-arc basin by slab roll-back. (a) Plan and cross-section of the initial subduction zone as in Fig. 6.13. 'h_1' indicates the hinge of the subducting slab. The grey arrow and the dotted lines show the extent of arc roll-back in passing from stages (a) to (c). (b) Incipient roll-back causing lithospheric extension in the overriding slab; 'h_2' indicates the new position of the slab hinge. (c) roll-back sufficient to bring about inception of a back-arc basin floored by oceanic crust; h_1, h_2 and h_3 indicate how far the hinge has retreated from (a) to (c). Arc volcanic activity is confined to the trench-side arc fragment; back-arc ridge volcanism is supplied by upwelling of asthenosphere as at mid-ocean ridges.

thinning of the lithosphere allows upwelling of asthenosphere, which undergoes decompression melting, leading to initiation of MORB-style basaltic volcanism and hydrothermal activity at the back-arc spreading centre. SSZ volcanic activity on the trench-side portion of the arc continues, but ceases in the remnant arc. Similar back-arc basins and remnant arcs occur in other parts of the world, associated with for example the Lesser Antilles, South Sandwich and Tongan arcs (Fig. 6.12). Not all such basins 'unzip' progressively like the Mariana example, and breakup is not always centred at the volcanic front; these complexities are summarized in the well illustrated review by Martinez et al. (2007).

The incipient stages of rifting that lead to a back-arc basin formation often involve **shoshonite** volcanism (Fig. 6.11), as seen in

the Izu–Bonin–Mariana arc (Fig. 6.18) at the present time and as occurred in the Fiji arc between 5.5 and 3 Ma ago. The main phase of back-arc spreading generates N-MORB-like basalts with varying degrees of arc geochemical signature as outlined in Chapter 2.

Continental arcs

The circum-Pacific ring of subduction-related volcanoes (Fig. 6.12) consists not only of discrete island arcs marking where one oceanic plate subducts beneath another, but also of magmatic arcs formed at active continental margins where oceanic plates are overridden by *continental* plates. Examples of the latter situation include the Andes where the Nazca plate subducts beneath South America, the Cascade Range where the Juan de Fuca plate subducts beneath North America, and the Alaskan peninsula and Cook Inlet where the Aleutian island arc adjoins the North American continent (Fig. 6.12).

The subduction process beneath active continental margins is the same in essence as occurs beneath island arcs (Fig. 6.13), but several differences in detail need emphasizing:

- Slabs subducting beneath continental plates tend to dip less steeply (on average 20° less) than slabs subducting beneath oceanic plates (Lallemand et al., 2005). For example, slab dip beneath Chile, Colombia and Japan is in the range 30–50°, whereas slabs subducting beneath the Izu–Bonin, New Hebrides, Tonga–Kermadec and West Aleutian arcs have dips between 50° and 70°.
- Magmas erupting in continental volcanic arcs ascend through crust of greater thickness, lower density and more easily melted composition than is true for typical island arcs and, moreover, erupt at higher elevation (up to 6000 m above sea level in the Andes, for example). These factors favour more advanced fractional crystallization during ascent, accompanied by greater degrees of crustal assimilation, so dacite and rhyolite are more prominent in most active-margin volcanic arcs (Fig. 6.20).
- In addition to a shift to the right in Fig. 6.11, continent-margin arcs tend to plot higher up in this diagram (i.e. more K_2O rich compositions for a given SiO_2 content): low-K magmas are less in evidence and there is a greater abundance of high-K and shoshonite types. Contents of other incompatible elements are similarly elevated: the Andean andesite in Fig. 6.15b, for example, shows incompatible element enrichment more in keeping with the Taupo rhyolite than island-arc andesites, though heavy rare-earth elements (HREEs) are somewhat lower.

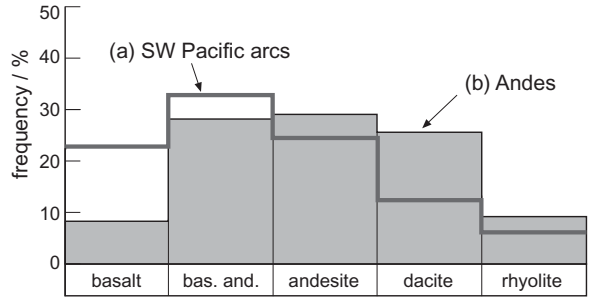


Fig. 6.20 Comparison of the approximate relative proportions of volcanic rock types in (a) intra-oceanic island arcs of the SW Pacific ocean; and (b) the Andes, estimated from relative numbers of analyses of each rock type in the geochemical database of Ewart (1979, 1982).

The Andes illustrate several key links between the geometry of subduction and the magmatism that accompanies it. Along two sectors of the Andes, the Nazca plate is currently subducted at an exceptionally shallow angle (e.g. the upper cross-section in Fig. 6.21c), and no current volcanic activity occurs there. These 'flat-slab zones' occur between the northern and central volcanic zones (traverse a–a' in Fig. 6.21a,c), and between the central volcanic zone (CVZ) and southern volcanic zone (SVZ). The non-volcanic zones lie close to where the Nazca and Juan Fernandez aseismic ridges impinge upon the subduction zone, suggesting that the thicker (up to 18 km) oceanic crust forming these ridges – by bestowing enhanced buoyancy in the lithosphere – influences the geometry of subduction and dictates the exceptionally shallow angle of the downgoing slab. Section a–a' shows that the mantle wedge present beneath active arcs is absent or greatly diminished

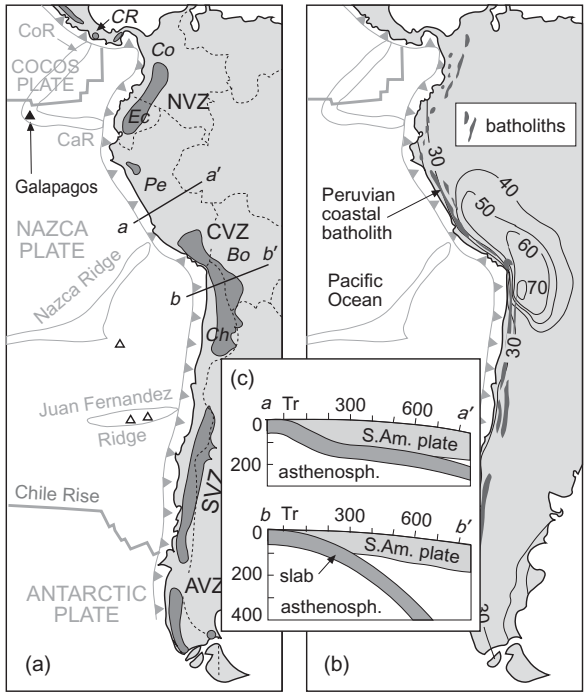


Fig. 6.21 (a) Map of South America showing in darker shading the northern, central, southern and austral volcanic zones (*NVZ*, etc.), the traces of the cross-sections a–a' and b–b' shown in (c), and relevant submarine plate boundaries and aseismic ridges (CaR, Carnegie Ridge; CoR, Cocos Ridge). Triangles represent off-shore, off-ridge volcanic centres from the Global Volcanism Project of the Smithsonian Institution. *Bo*, Bolivia; *Ch*, Chile; *Co*, Colombia; *CR*, Costa Rica; *Ec*, Ecuador; *Pe*, Peru. (b) The same map showing isopachs of continental crustal thickness (km) from Baranzangi and Isacks (1971); Cordilleran batholiths are also shown in dark grey. (c) Cross-sections showing differing angles of subduction along traverses a–a' and b–b' in section (a), adapted from Barazangi and Isacks (1971); Tr, trench; distances and depths in km. Figure adapted from Blake and Argles (2003) by permission of The Open University.

here, and this must be one factor in explaining the volcanic gaps in Fig. 6.21a.

Another aseismic ridge, the Carnegie Ridge ('CaR' in Fig. 6.21a), impinges on the Ecuador section of the South American subduction zone, causing flat subduction but *without* an associated 'volcanic gap'. A distinctive element of the Ecuador volcanoes – as indeed in Costa Rica ('CR'), where the equivalent Cocos aseismic ridge ('CoR') collides with the Latin American trench (Fig. 6.21a) – is the eruption of **adakite**[11] lavas. Whether or not adakites are in some way related to shallow subduction, or the proximity of the Galapagos Ridge, is discussed in the final section of the chapter.

The CVZ coincides with a region where the continental crust underwent significant thickening (Fig. 6.21b) during an episode of crustal shortening 10–12 Ma ago; the consequent high elevation of the cordillera here, dictated by isostasy acting on a crustal thickness of up to 70 km, is reflected in its name – the Altiplano. The CVZ differs from other Andean volcanic zones in the exceptionally high proportion of silicic volcanic rocks, often as huge dacitic **ignimbrite** sheets that cover an area well in excess of 50,000 km^2.

An impressive example of a large-volume rhyolite eruption is the Taupo volcano in the North Island of New Zealand. This has produced 9 eruptions exceeding 10^3 km^3 in output in the past 60 ka. The largest was the climactic 26.5 ka Oruanui eruption, which ejected a total of 530 km^3 of rhyolite magma (Wilson, 2001). A Taupo analysis is given in Table 6.2 and Fig. 6.15.

Oceanic spreading centres

Oceanic crust consists overwhelmingly of basalt, but more evolved magmas are erupted at several locations on the global ocean ridge system, notably where a ridge runs above or close to a hot spot. Iceland, where rhyolites in fact account for 10%–12% of the surface rocks, is a prime example. The volcano Krafla, a central volcano in Iceland's axial rift zone (Fig. 9.9), is particularly well known for its **bimodal** suite of basalts (with a few icelandites) and rhyolites. Thingmuli (Fig. 6.12) illustrates the potential in Iceland for generating a complete magma series from basalt through icelandite (tholeiitic andesite) and dacite to rhyolite (Figs. 6.8 and 6.11) by fractional crystallization.

Evolved lava types also occur in the Galapagos Islands (Fig. 6.21a). Volcan Alcedo on Isabela Island is an active basaltic volcano that erupted ~1 km^3 of rhyolite about 120 ka ago, both as pumice and as lava issuing from the caldera floor (Geist et al., 1995). Andesites and dacites are known elsewhere on the

[11] Named after Adak Island in Alaska.

Galapagos Islands, and are also associated with a propagating rift tip of the nearby Galapagos Ridge.

Continental LIPs

Many continental flood basalt provinces are overwhelmingly basaltic, but a small number have developed a marked bimodal character, with significant volumes of silicic volcanics being present (Fig. 6.22). Prominent examples are:

- the Afro–Arabian flood basalt province (Figs. 2.14 and 6.12) where, in northern Yemen alone, ~5000 km^3 of rhyolitic pyroclastics and lavas were erupted in a short interval about 29 Ma ago (Peate et al. 2005; Baker et al., 1996);
- the Paraná-Etendeka flood basalts in Brazil and Namibia (Fig. 2.15) where large volumes of silicic volcanics were erupted around 132 Ma ago (Ewart et al. 2004b).

Continental rifts

Prior to 30 Ma ago, Tertiary volcanism in the western USA was of calc-alkali andesite–dacite type, associated with the subduction of the former Farallon plate beneath North America; rhyolites were relatively rare. However about 30 Ma ago the subduction zone consumed a stretch of the East Pacific Rise – equivalent in length and latitude range to the present San Andreas fault ('*SAF*' in Fig. 6.12) – and a marked change took place in the tectonic regime in the parts of the North American plate directly above: elevated heat flow, uplift and extension developed across a wide area known as the Basin and Range Province ('*B&R*' in Fig. 6.12). Extension-related volcanism here (since 15–20 Ma) has been predominantly basaltic (Chapter 2), but some volcanoes have erupted bimodal suites consisting of basalt (or trachybasalt) with associated high-silica rhyolite (SiO_2 72%–76%) that is geochemically distinct from subduction-related rhyolites. The San Juan volcanic field in Colorado ('*SJ*' in Fig. 6.12) exemplifies the transition from calc-alkali to extension-related basalt-rhyolite magmatism with time.

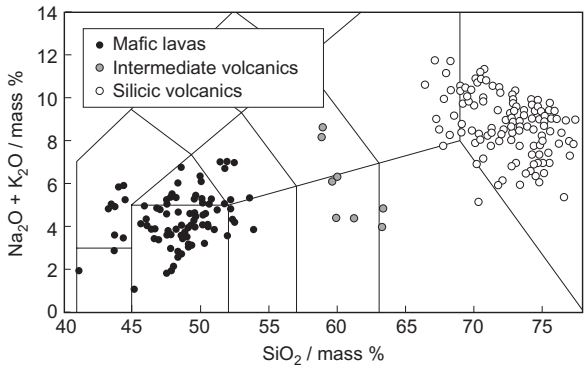


Fig. 6.22 TAS diagram for Afro-Arabian Oligocene flood volcanic rocks of northern Yemen (data from Peate et al., 2005) illustrating their bimodal distribution; note the low abundance of intermediate rocks. The boundaries are the same as in Fig. 2.1 and Fig. 6.1.

Large-scale rhyolite eruptions

Yellowstone National Park, in Wyoming in the western USA (Fig. 2.12), has been the focus of some of the largest volcanic eruptions known to have occurred in recent geological time anywhere on the Earth's surface. The Yellowstone Plateau volcanic field (YPVF) is made up of the products of three huge, caldera-forming eruptions (Table 6.4 and Chapter 7) erupted in Pliocene and Quaternary times from a magmatic system that – judged by its seismicity, intense hydrothermal activity and on-going uplift/subsidence episodes – undoubtedly remains active (Lowenstern and Hurwitz, 2008). Each eruption produced a rhyolitic ignimbrite sheet covering thousands of km^2. The total magma output in

Table 6.4 Large-volume rhyolite eruptions from the Yellowstone caldera system, USA (data from Christiansen, 2001).

Eruption	Age / Ma	Area of deposit / km^2	Magma volume erupted / km^3
Lava Creek Tuff	0.64	7500	1000
Mesa Falls Tuff	1.3	2700	280
Huckleberry Ridge Tuff	2.1	15,500	2450*

* A single pyroclastic **cooling unit** believed by Christiansen (2001) to have been erupted in a few hours or days.

the last 2 Ma amounts to about 6000 km^3. Volcanic systems capable of eruptions on this vast scale are called supervolcanoes (see Wilson, 2008, for a recent review).

The Yellowstone eruptions are a further example of a bimodal magmatic system but, unlike others where basalt predominates or basalt and rhyolite are of approximately equal volume (e.g. Yemen), rhyolites here make up 95% of the volcanic output (Christiansen, 2001); basalts (mainly low-K tholeiites) occur only around the margins of the plateau, though most of the voluminous volcanics of the (slightly older) Snake River Plain immediately to the south-west are basalts. The YPVF is thus the latest product of a bimodal volcanic system whose focus (the 'Yellowstone hotspot') has propagated 450 km north-eastward during the past 12–15 Ma.

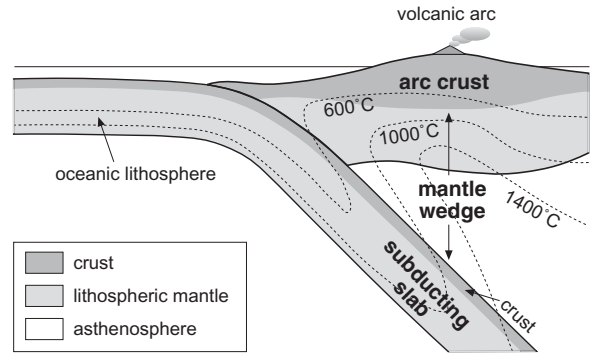


Fig. 6.23 Cartoon cross-section of an intra-oceanic subduction zone emphasizing in bold the *a priori* regions where melting might occur. Oceanic and arc crusts are shown shaded. Isotherms are based loosely on Tatsumi and Eggins (1995) and Furukawa (1993).

HOW ARE INTERMEDIATE AND ACID MAGMAS FORMED IN THE EARTH?

Arc volcanism

Source materials – where does melting initially occur?

Figure 6.23 shows three domains of a subduction system that could participate in partial melting:

- the downgoing slab, consisting of sediment and basaltic oceanic crust 6–7 km thick (hydrothermally **altered** to varying degrees) riding on oceanic lithospheric mantle (peridotite, locally serpentinized) up to 100 km thick;
- the 'mantle wedge'[12] beneath which the slab is subducting, comprising asthenosphere and sub-arc mantle lithosphere (both peridotite in composition);
- the arc crust above the mantle wedge, consisting of gabbro, diorite and (especially at active continental margins) more evolved plutonic and basement rocks.

In discriminating between these potential source regions for arc volcanism, it is vital to recall that the most **primitive** magmas erupted in typical island arcs are *basalts* (e.g. Table 2.4 analyses 5 and 6): it is these – rather than the andesites and dacites discussed in this chapter – that indicate most about the source from which arc magmatism ultimately derives. Producing basalt by partial melting requires a peridotite source (Chapter 2, penultimate section). The slab contains peridotite but, as the isotherms in Fig. 6.23 illustrate, it mostly forms the cool interior of the slab. The most easily melted part of the slab is the upper basaltic layer of oceanic crust, which is hotter (Fig. 6.23), has a lower solidus temperature than peridotite, and contains hydrous minerals (as alteration products) that lower the solidus still further. Melting this would however produce not basalt but more evolved melts (see Exercise 5.4) with SiO_2 contents in the range 55%–70% (Helz, 1976). Similar reasoning rules out the arc crust as a source for subduction-related basalts. These arguments, by eliminating alternatives, point firmly to the mantle wedge as the crucible where subduction-related melting primarily occurs. This conclusion is confirmed by seismic tomography of the Japanese arc (Fig. 6.24a) which highlights regions of low S-wave speed – strongly suggesting partial melting – in the mantle wedge but not in the slab beneath.

What causes melting in the mantle wedge?

The clues that provide petrologists with the answer to this question lie in the geochemistry of arc volcanic rocks. The first clue is the high pre-eruptive volatile contents found in many subduction-related magmas (Fig. 6.14), and the characteristically explosive eruptions to

[12] Wedge-shaped in three dimensions but appearing as a triangle in cross-sections like Fig. 6.23.

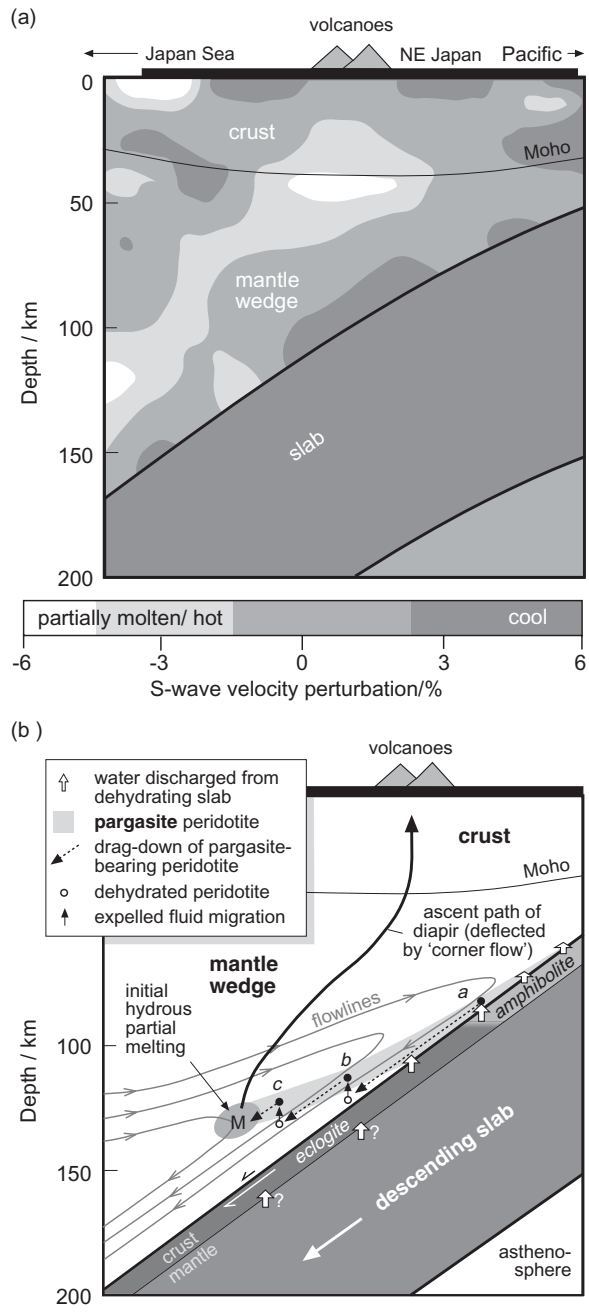


Fig. 6.24 (a) Monochrome sketch of a seismic tomography section (after Nakajima et al., 2001a courtesy of the American Geophysical Union) through the subduction zone beneath NE Japan, showing regions of low S-wave velocity (recording partial melting) in the mantle wedge and crust but not in the descending slab. (b) Cartoon summarizing one view of how slab dehydration brings about hydrous melting in the overlying wedge to produce an inclined melt-ascent path consistent with (a). Flowlines for supposed slab-induced convection in the wedge (grey lines) are from Furukawa (1993). The grey band *a*–M depicts the *T*-depth stability field of pargasite peridotite (Davies and Stevenson, 1992). The H_2O flux from slab to wedge – arising from breakdown of hydrous metamorphic minerals such as lawsonite, chlorite and amphibole in the slab – is continuous to about 90 km depth (Schmidt and Poli, 1998).

which they often give rise. Has the water content (and that of other volatile species) of the mantle source region been supplemented in some way – and, if so, from where?

The second clue resides in the distinctively 'spiky' incompatible-element enrichment profiles possessed by all subduction-related magmas (Fig. 6.15). One can gain a sharper insight by plotting Figs. 2.16 and 6.15 in a slightly different form. What we want to know is how the *source region* of subduction-related basalts differs in composition from the MORB *source region* (the asthenosphere). To answer this question it makes sense to plot analyses of SSZ volcanic rocks ratioed to average N-MORB rather than to primordial mantle; differences introduced by the melting process then cancel out (to a first approximation). Pearce (1983) first advocated 'MORB-normalized' incompatible element plots for this purpose. Figure 6.25a shows the South Sandwich Islands low-K basalt of Table 2.4 (and Fig. 2.16c) replotted in a variant of his diagram; the normalizing factors are listed in

the caption. Note how the 'spikes' in Fig. 6.25a correlate with sub-groups of incompatible elements distinguished in Fig. 2.7.1a:

- the most enriched elements Rb, Ba, Th, K and Sr are all **LIL** elements, most of which are relatively soluble and so are susceptible to aqueous transport (see Fig. 2.7.1a);
- the most depleted elements relative to MORB – the elements Nb, P and Zr which fall below the dashed line – are (together with Ti) **HFS** elements that are highly immobile in aqueous fluids (see Fig. 2.7.1a);
- the **REE** and Y (which mimics **HREE**) form a sub-horizontal array in between (highlighted by the dashed line).

The latter two groups plot in Fig. 6.25a below the MORB reference line. One school of thought explains this depletion by supposing that a refractory mineral that readily accommodates these elements (i.e. one in which they are compatible) remained behind in the source during melting, restricting their take-up in the low-K basalt melt. A more widely held view today is that the magma source tapped by the South Sandwich Island low-K basalt had become more depleted in these elements than the MORB reservoir, owing to a more complex history of partial melting and melt extraction in the source region. The extent of this depletion is most marked for the HFSE, especially Nb. This pattern is now accepted by most petrologists as the geochemical signature of peridotites in the mantle wedge above a subduction zone, defining what is termed the 'wedge component' contributing to the compositions of arc volcanics. Negative Nb anomalies are characteristic of magmas derived by subduction-related melting of the mantle wedge in SSZ settings.

Pearce and Parkinson (1993), among others, recognized that the HFSE depletion is most extreme in arcs associated with back-arc spreading centres. The low-K basalt in Fig. 6.25a is from the South Sandwich Islands arc in the south Atlantic, and the strong depletion of HFS elements here, particularly of Nb, probably derives from a domain in the mantle wedge affected by decompression melting beneath the associated East Scotia Rise back-arc spreading centre (*ESR* in Fig. 6.12).

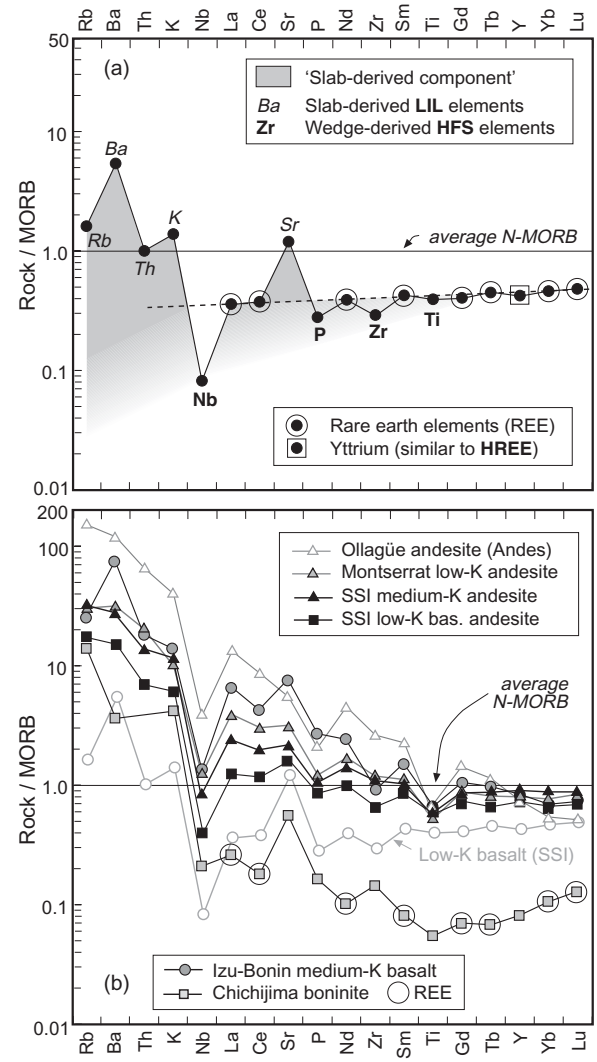


Fig. 6.25 MORB-normalized plots of SSZ volcanic rocks (after Pearce et al. (1995)). (a) low-K basalt from the South Sandwich Islands (Table 2.4); (b) Other island-arc volcanic rocks in Table 6.2 (except the medium-K Izu–Bonin basalt where the analysis is from Sun and Stern, 2001); note the vertical scale extends to higher values than in (a).

The N-MORB normalizing values used are (in ppm) Rb 0.56, Ba 6.3, Th 0.12, Nb 2.33, K 1079 (as K_2O 0.13%), La 2.5, Ce 7.5, Sr 90, P 314 (as P_2O_5 0.072%), Nd 7.3, Zr 74, Sm 2.63, Gd 3.68, Ti 7600 (as TiO_2 1.27%), Tb 0.67, Y 28, Yb 3.05, Lu 0.455 (Pearce and Parkinson, 1993 after Sun and McDonough, 1989).

The LIL elements Rb, Ba, K and Sr, on the other hand, are *enriched* relative to MORB: in other words, they plot *above* the 'average N-MORB' line in Fig. 6.25a. Given that most

of these enriched elements are highly incompatible (plotting on the left side of the diagram), the earlier melt-extraction process inferred above to explain the depleted HFSE trend would have depleted the wedge source in these LIL elements too. That the LILE are present in the South Sandwich Islands low-K basalt at *higher* levels than in MORB is widely understood to be a signal of later re-enrichment of the source with LIL elements, prior to the melting that produced the low-K basalt. The aqueous mobility of these elements (Fig. 2.7.1a) suggests that the agent of re-enrichment was probably a hydrous fluid which, at some stage, **metasomatized** the wedge source region. Given that subducting lithosphere contains hydrous minerals (formed during near-ridge hydrothermal alteration of sea-floor basalts) that will dehydrate as the descending slab heats up, it is not a huge leap to suppose that this LILE-bearing fluid emanates from the slab. The excess of mobile LIL elements (together with the light REEs La, Ce, Nd and Sm, which also show small degrees of enrichment) over the HFS elements defines what is called the 'slab-derived component' introduced into the wedge peridotites by these fugitive hydrous fluids. The slab component is symbolized by the grey area in Fig. 6.25a; the fuzzy lower boundary highlights our lack of precise knowledge on the original contents of these elements in the depleted wedge prior to fluid-borne LILE re-enrichment.

The slab-derived aqueous fluids, whose fingerprint survives in the LILE trace element patterns of nearly all subduction-related volcanic rocks (Fig. 6.25b), are in fact the very agent that causes melting in the wedge. In the words of Davies and Stevenson (1992),

> *'the fundamental paradox of subduction zone volcanism is the presence of melt and high heat flow adjacent to an enormous heat sink, the cold subducting slab'*

(see the heat flow profile in Fig. 6.13 and the isotherms in Fig. 6.23). Figure 2.18c showed that calculated mantle wedge geotherms fall short of intersecting the dry peridotite solidus. What makes melting possible here is the marked depression of the peridotite solidus caused by a small proportion of introduced water. Even the depleted peridotite source inferred for the low-K basalt in Fig. 6.25a – from which easily fused fractions must have been removed by previous episodes of melt extraction – could succumb to melting when fluxed with aqueous fluids from the slab.

Figure 6.25b shows MORB-normalized patterns for (i) more evolved volcanics from the South Sandwich arc (shown in black); and (ii) subduction-related rocks from other arcs. The South Sandwich Islands basaltic andesite and andesite share many features in common with the South Sandwich Islands low-K basalt in Fig. 6.25a, but they are more enriched in the LIL elements, have higher La/Yb ratios and are less depleted in HFS elements. These differences may be ascribed to intra-arc variations in wedge depletion, degree of melting and extent of fractional crystallization. The samples from other arcs illustrate the highly variable degrees of enrichment seen in SSZ volcanics around the world; note particularly how much more enriched in all elements the Izu–Bonin medium-K basalt is than any of the South Sandwich Islands rocks. Nonetheless most share the distinctive high LILE/HFSE imprint of arc magmatism: relative to the REE which form a regular line or curve in each pattern, the LIL elements tend to be enriched, whereas the HFS elements tend to form negative spikes.

In a few arc systems two distinct slab contributions can be identified. Volcanic rocks in the Mariana arc (Fig. 6.18), for example, exhibit an isotopic signature attributable to a subducted sediment component, thought to have been transported from slab to mantle wedge by migration of small-volume silicic partial melts (Elliott et al., 1997). In most arcs, however, hydrous fluids seem to be the dominant agent for metasomatizing the wedge.

How is water transported into the wedge? The role of wedge dynamics

The oceanic crust forming the upper part of the subducting slab consists of hydrothermally altered basalt, deep-sea sediment, and sometimes arc/continent-derived clastic sediment too. A large proportion of the water carried down in the hydrated crust, especially in the sedimentary component, is expelled at too shallow a depth ($\ll 50$ km) to participate in arc magma genesis. As the slab penetrates to deeper and hotter levels, the hydrous greenschist-facies assemblages in the altered basalts

are transformed first into amphibolite-facies mineralogy. Eventually, at depths around 60–90 km beneath the fore-arc region (Fig. 6.24b), amphibolite dehydrates further to form **eclogite**.[13] The water released in this succession of metamorphic dehydration reactions passes continuously up into the wedge above (Poli and Schmidt, 2002). Dehydration of serpentinized slab peridotites may also contribute to the subduction-related volatile flux invading the wedge (Rüpke et al., 2004).

Petrologists once assumed that invasion of fluid from the dehydrating slab caused immediate partial melting of the wedge peridotites directly above, but the tomographic section shown in Fig. 6.24a suggests that the true picture is more complex. In the first place, the peridotites directly overlying the subducting slab (where it dehydrates to eclogite) are cooler than the interior parts of the wedge – as shown by the isotherms in Fig. 6.23 – and even in the presence of water vapour are too cool to melt *in situ*. Secondly, numerical modelling (e.g. Furukawa, 1993; Kelemen et al., 2003) suggests that, far from being a static mass, the wedge peridotites convect in response to (i) the cooling effect of the descending slab; and (ii) the down-dip frictional drag it exerts on the wedge, as illustrated by the flowlines in Fig. 6.24b. This figure shows one model explaining the pattern in Fig. 6.24a, in which slab-derived hydrous metasomatism converts peridotite pyroxenes in the wedge into **pargasite**. Pargasite-bearing peridotite formed at *a* is carried by convective flow down to *b*. Here, having exceeded the pargasite breakdown temperature, it dehydrates and the fluid released migrates upward and metasomatizes peridotite vertically above. The pargasite peridotite consequently formed at *b* is the next stage in a series of similar cycles, whose net effect is to transport fluid (together with its 'slab component' of dissolved LIL elements) toward the hotter interior of the wedge, where metasomatized peridotite can eventually undergo partial melting (at M). Chlorite may also play a significant role in the onset of hydrous melting (Grove et al., 2006).

The upwelling route of partially molten peridotite may be deflected trench-ward by the convective 'corner flow' in the wedge, as shown in Fig. 6.24b. This deflection explains the inclined (rather than vertical) zone of low S-wave velocity – representing hot, partially molten mantle – observed by seismic tomography beneath NE Japan (Fig. 6.24a). Calculations by Pearce and Peate (1995) suggested that as little as 10% of the partial melting beneath arcs is specifically attributable to volatile transfer from the slab, the remainder being due to decompression melting as the partially molten wedge mantle ascends along the curved arrow in Fig. 6.24b.

Tatsumi and Eggins (1995) attributed the trench-side volcano chain to melting accompanying the breakdown of pargasite (amphibole) in the mantle wedge, as outlined above. Some of the pargasite may however react with orthopyroxene to form **phlogopite** (mica) which resists dehydration to greater depth. The back-arc chain of volcanoes in Japan may be the result of deeper melting associated with phlogopite breakdown.

Why are the proportions of andesite, dacite and rhyolite higher in mature arcs?

The preponderance of more evolved magmas in mature arcs may reflect the difficulty that dense basic magma experiences in ascending through thicker crustal sections. Devine (1995) argued that the upper arc crust acts as a density filter favouring the transport of more evolved (i.e. less dense) magmas to the surface; parental basaltic magmas, on the other hand, will – being denser (Box 6.5) – have a greater tendency to stagnate and fractionate at mid-crustal levels, eventually yielding more evolved magmas whose lower densities favour resumed ascent. Eruptions of calc-alkali magmas vary in style from lava effusion to highly explosive pyroclastic eruptions, according to the volatile content of the magma approaching the surface and the extent of degassing prior to eruption. The biggest pyroclastic eruptions may result in the formation of large calderas owing to the evacuation of magma from a voluminous underlying magma chamber, as discussed in Chapter 7.

To the more fundamental questions as to why maturity of an island arc brings a shift from low-K to calc-alkali magma affinity, with higher La/Yb and less depletion of HFS incompatible elements (Fig. 6.25b), and why this character becomes more marked further from the trench, there is no simple, universally applicable answer.

[13] The high density of eclogite contributes to the 'subduction pull' force on a subducting plate.

Box 6.5 Melt and magma density

The density of an igneous melt depends mainly on:

- the temperature – a given mass of melt expands on being raised to higher temperature, and its density thus decreases;
- the melt's chemical composition and structure – high concentrations of components like Na_2O and SiO_2 reduce the density of a melt, whereas components like MgO and particularly ΣFeO act in the opposite direction. (The same is true of silicate minerals: mafic minerals like olivine and pyroxene are denser than felsic ones like feldspar and quartz. Oxide minerals rich in Fe are densest of all.)

Of these, the second factor is the dominant one. Fig. 6.5.1 shows typical melt densities for the main volcanic rock types calculated for 1250 °C. As a rule, the more evolved the melt, the lower its density becomes.

Mafic minerals have densities greater than all of the melt densities in Fig. 6.5.1, so when mafic crystals are suspended in a melt, the bulk density of the magma (melt + crystals) increases. Felsic minerals, on the other hand, have densities much closer to the melts in which they are suspended and exert little influence on magma density.

Vesicles, consisting of gas, lower the density of any magma of which they form a part. This is illustrated most dramatically by the exceptionally low density of **pumice** (often low enough to float on water).

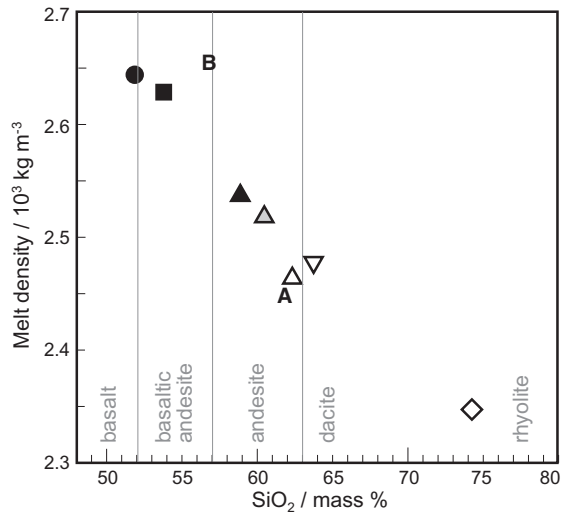


Fig. 6.5.1 Calculated anhydrous silicate melt densities at 1250 °C as a function of SiO_2 content, for the analyses given in Table 6.2 and the low-K tholeiite tabulated in Table 2.4; symbols as in Fig. 6.15 except that: B, Chichijima **b**oninite; and A, Mindanao **a**dakite. Calculations based on data of Bottinga and Weill (1970).

Role of crustal melting

The association of silicic volcanism in the Andean CVZ with the thickest crust in South America (Fig. 6.21a,b is no coincidence: it seems that the high geothermal gradient caused by Andean subduction-related magmatism, superimposed on the heating arising from mid-Miocene crustal thickening, has caused extensive melting and assimilation of

continental crust, thus accounting for the over-abundance of silicic products here (de Silva, 1989). The effects of crustal assimilation also make their mark among less evolved magmas in the CVZ too. The Ollagüe stratovolcano on the Chile-Bolivia border consists dominantly of andesitic and dacitic lavas, illustrated by the andesite shown in Table 6.2 and in Figs. 6.15 and 6.25. We have already noted its incompatible element enrichment is much greater than in arc andesites and has more in common with arc dacites and rhyolites. Feeley and Davidson (1994) attributed magma compositions here to crystal fractionation 'coupled with large amounts of crustal assimilation'. Though the impact of crustal assimilation is less prominent in the northern volcanic zone (NVZ) and SVZ, it can be detected in many Andean volcanic rocks and it must make a contribution to the higher abundance of evolved magmas here compared to oceanic island arcs.

Other large-scale SSZ rhyolite eruptions are likely to involve crustal melting too. An example is Taupo in New Zealand. The Taupo Volcanic Zone in the North Island is a region of rapid extension and high heat flow, with several prominent andesite volcanoes. Nonetheless rhyolite accounts for 80% of total volcanic output. To quote Price et al. (2005):

> *'As crustal extension and thinning proceed, rising geotherms result in large scale crustal melting, with earlier formed andesitic systems being recycled and progressively overwhelmed and extensive rhyolitic storage systems formed at relatively shallow depths in the crust.'*

Adakites: do they imply slab melting?

The dominant volcanics in Ecuador belong to a subset of intermediate and acid volcanic rocks called **adakites**. Typical compositions are illustrated in Fig. 6.15b and Table 6.2. Adakites have SiO_2 ≥56% and Na_2O ≥3.5% but there is little in their mineralogy to distinguish them from normal calc-alkali andesites and dacites. What sets them apart are conspicuous positive Sr spikes in incompatible-element enrichment diagrams like Fig. 6.15b, and unusually low contents of the **HREE** and yttrium (Y). These two characteristics are readily combined into a useful index for identifying adakites – the Sr/Y ratio – which typically has values >40 for adakites, whereas normal calc-alkali lavas have Sr/Y ratios less than 40.

The relatively high SiO_2 contents and moderate **Mg numbers** of adakites (in the range 45–60) suggest that they could originate from the partial melting of *basaltic* source rocks rather than peridotites (cf. Fig. 5.6). The low content of HREE and the high La/Yb ratios in these rocks are a sure sign that such source-rocks contain garnet, which – if it remains as a residual mineral after melting – would retain most of the HREE and Y in the source (Box 6.6), thereby depleting the escaping melts in these elements. Adakites could alternatively result from fractional crystallization of basaltic parent magma at depths where garnet would be one of the minerals crystallizing. (The lack of HREE depletion in 'normal' arc volcanics suggests, on the other hand, that they originate from depths where spinel, rather than garnet, is the dominant aluminous phase.)

Adakites in Ecuador and Costa Rica share a geotectonic setting in which young oceanic lithosphere of the Nazca and Cocos plates subducts at a relatively shallow angle, probably due to subduction of the Carnegie and Cocos aseismic ridges ('CaR' and 'CoR' in Fig. 6.21a). When first described, adakites were explained as being products of partial melting of metabasalts in the down-going slab (Defant and Drummond, 1990). During subduction, altered basalts of the oceanic crust pass through greenschist and amphibolite metamorphic facies (Fig. 6.24b) before dehydrating to form **eclogite**, a garnet-bearing basic rock. Normal subduction conditions do not permit significant slab melting, but modelling suggested that where very young (<5 Ma) oceanic lithosphere is being consumed, its temperature may still be high enough for dehydration melting (see Box 8.4) to occur under eclogite facies conditions in the metamorphosed oceanic crust, producing HREE-depleted intermediate melts (Defant and Drummond, 1990; Martin, 1999).

Not all known adakite localities meet this criterion, however. Adakites have now been recognized in arcs where the lithosphere being subducted may be as old as 45 Ma, too old for residual ridge heat to promote slab melting. Gutscher et al. (2000) proposed the key factor

Box 6.6 What can **rare-earth elements** (**REE**) tell us about source mineralogy?

The rare earth elements (REE – see Fig. 2.7.1) form a series of closely related trace elements that occupy their own row in the Periodic Table (Fig. 2.7.2). Their chemical properties vary little – they all form 3+ ions, for example – and what variation does occur correlates smoothly with position in the row, as illustrated by their M^{3+} ionic radii, for example, which decrease continuously from lanthanum (La^{3+} = 12.7 pm*) to lutetium (Lu^{3+} = 10.5 pm). The trivalent element *yttrium* (Y) has a very similar radius to the **HREE** (Fig. 2.7.1) and is often shown in REE and similar plots. The REE and Y are incompatible with respect to the main liquidus minerals of basic igneous magmas (e.g. olivine in Fig. 6.6.1): early fractionation of such melts merely elevates the whole REE pattern in diagrams such as Fig. 2.7.3, with only slight changes in La/Y, La/Yb or La/Lu ratio.

Some igneous processes nonetheless discriminate between light rare-earth elements (**LREE**) and HREE. The LREE behave incompatibly with respect to all major rock-forming minerals, whereas the HREE are less incompatible in some minerals like hornblende, and strongly compatible in garnet (Fig. 6.6.1). If garnet is present in a source rock undergoing partial melting, the melt produced will be *depleted in HREE and yttrium* (Y) relative to melts produced in the absence of garnet. This is because melt–garnet equilibrium favours the garnet which retains HREE at the expense of the melt, *provided* garnet survives as a residual mineral after partial melting. If the garnet were completely consumed during melting, on the other hand, its HREE content would be liberated into the melt.

The degree of HREE and Y depletion in a basalt carries information about the depth from which it derives. Upper mantle lherzolites contain an aluminous mineral whose identity varies with depth: spinel is stable at relatively shallow mantle depths, but garnet is more stable deeper down (Fig. 5.5). Basalts whose **melting column** is rooted at depth in garnet lherzolite will show depletion in HREE (and higher La/Yb ratios) compared to basalts that originate from shallower depths where melting is confined to spinel lherzolite facies. Prominent examples are the kimberlite and lamproite patterns shown in Fig. 9.18.

The adakites shown in Fig. 6.15b have lower HREE and Y than comparable arc magmas because – according to current thinking – they result either from the melting of garnet-bearing basic rocks (in the metamorphosed oceanic crust of the subducting slab or in the lower continental crust) or from the fractional crystallization of garnet from basic magmas.

The element europium (Eu) is unique among the REE in forming not only Eu^{3+} ions but also (under appropriately reducing conditions) Eu^{2+} ions. The petrological applications of 'Eu anomalies' arising from this behaviour are discussed in Box 8.5.

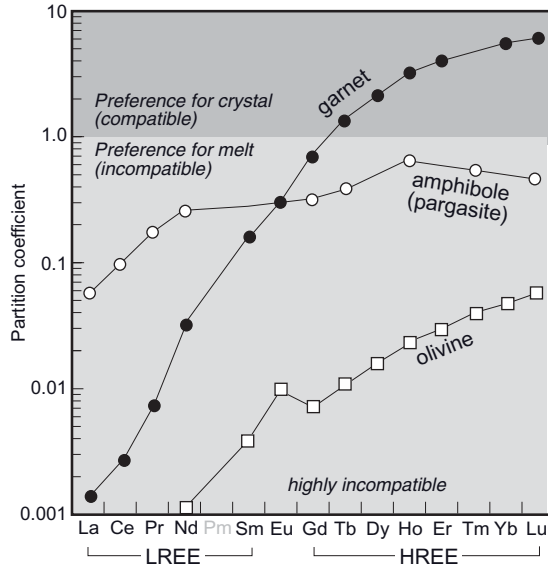


Fig. 6.6.1 Illustrative mineral–melt partition coefficients $K_i^{\text{mineral/melt}}$ (where *i* = an individual rare earth element – see Box 2.7) for the distribution of the trivalent rare earth elements between garnet, amphibole, olivine and basic silicate melts (data from Green et al., (2000), Latourrette et al., (1995) and Bedard (2005) respectively); note that published olivine data vary widely. The partition coefficient axis is logarithmic to span four orders of magnitude in a single plot. Note that the HREE (except Gd) are compatible in garnet, whereas the lightest REE are highly incompatible.

* pm, picometre (10^{-12} m).

in promoting adakite magma genesis by slab melting was not the age of the slab but very low angle ('flat-slab') subduction. Other authors consider that some adakite magmas (e.g. Peru's Cordillera Blanca batholith discussed in Chapter 8) derive from deep-crustal melting of garnet-amphibole-bearing basaltic rocks, the result of 'underplating' by relatively dense basic magmas (Atherton and Petford, 1993; Peacock et al., 1994; Bryant et al., 2006). However a growing consensus now considers that adakite magmas are formed by deep fractional crystallization of garnet from hydrous, wedge-derived arc basalt magmas near the base of the arc lithosphere (see for example Macpherson et al., 2006).

Many Archaean gneisses have **trondhjemite** compositions very similar to adakites. The implications for subduction and magma genesis during the first third of Earth history are discussed in Chapter 8.

Boninites – melting strongly depleted mantle wedge or slab?

In a number of places in the western Pacific arc system (shown by grey squares in Fig. 6.12), the fore-arc basement – which is exposed on land in the Bonin Islands – contains a substantial proportion of boninite lavas of mid-Eocene age. The primitive character indicated by their high Mg-numbers and lack of plagioclase is confirmed by extreme depletion in REE and HFS elements, illustrated by the Chichijima boninite in Table 6.2 and Figs. 6.15b and 6.25b. This, together with the shallow U-shape of its REE pattern and the combination of *positive Zr* and *negative Ti* spikes relative to the REE, is peculiar to boninites. The shape of the pattern in Fig. 6.25 suggests – as for other arc magmas – melting of an HFSE-depleted mantle source enriched with slab-derived LIL elements, but the degree of source depletion in elements on the right of the diagram seems to have been much greater in the boninite than in the South Sandwich low-K basalt, for example. Many petrologists regard them as products of the melting of residual harzburgitic peridotite remaining after the extraction of MORB, of the kind found in oceanic mantle lithosphere (Figs. 5.3 and 5.3.1).

The uniquely large volume of Izu–Bonin–Mariana (IBM) boninite volcanism and its simultaneous eruption along thousands of kilometres of young arc (Fig. 6.12) in mid-Eocene times point to a combination of circumstances unmatched in more recent arc volcanism. Four requirements need to be met to explain the chemical attributes of boninite seen in Fig. 6.25:

1 an extreme degree of depletion in the wedge source (Fig. 6.25), probably indicating the melting of mantle lithosphere rather than depleted asthenosphere;
2 high mantle temperatures, in order to accomplish the partial melting of refractory (possibly harzburgitic) lithospheric mantle;
3 hydrous fluxing to introduce LILE enrichment;
4 a source of the uniquely high Zr/Sm and Zr/Ti ratios noted above.

Taylor et al. (1994) sought to explain the last feature through the incorporation of small fractions of melt from amphibolite facies metabasalts in the descending slab – amphibole can accommodate REE and Ti and therefore retain them in the slab source, whereas it does not accept Zr – but more recent work has ruled out slab melting and instead attributes the high Zr/Sm and Zr/Ti to melting of mafic veins or domains in the wedge mantle lithosphere. Macpherson and Hall (2001) argued that the mid-Eocene volcanism in the IBM arc system may have developed its boninitic character because subduction was being initiated in a region where a starting plume (Chapter 2) was already active and generating anomalously high mantle temperatures.

Boninite lavas are also found in a number of ophiolite complexes of various ages (e.g. the Cretaceous Troodos ophiolite of Cyprus ('TO' in Fig. 5.3.2 in Box 5.3)) suggesting that the conditions required for the formation of such melts were not confined to the Eocene west Pacific. Chapter 5 noted that the inferred parent magma compositions for a number of large Proterozoic mafic intrusions, as well as major Proterozoic dyke swarms, also lie in the boninite range.

Origins of non-arc intermediate-to-acid volcanism

Rhyolites account for about 10% of the surface rocks in Iceland. Opinions are divided as to the manner in which the rhyolite melts

are formed: Nicholson et al. (1991) considered they are derived from basalt mainly by fractional crystallization, though with a contribution from assimilation of altered wall-rock (assimilation with fractional crystallization, **AFC**), whereas Jonasson (1994) regarded them entirely as the products of the partial melting of altered basalts. Thingmuli (Fig. 6.12) constitutes the classic example of fractional crystallization from basalt through icelandite (tholeiitic andesite) and dacite to rhyolite (Figs. 6.8 and 6.11), yet no recent work has assessed the contribution from crustal assimilation.

Evolved lava types also occur in the Galapagos Islands and along the Galapagos ridge. In their study of the Volcan Alcedo volcano on Isabela Island, Geist et al. (1995) regarded the 120 ka-old rhyolites as the product of advanced fractional crystallization of basalt, ruling out an origin by crustal **anatexis**.

Why a few LIPs contain large volumes of silicic volcanics (sometimes as abundant as the accompanying basalts, as in northern Yemen) is not fully understood. The bimodal composition distribution in Yemen (Fig. 6.22) and Paraná-Etendeka suggests either:

- that magma access to the surface was highly composition-dependent and biased against the intermediate products of fractional crystallization while favouring the parental basic magmas and their extreme silicic differentiates; or
- that the silicic melts in Fig. 6.22 are the product not of fractional crystallization of the basic magmas but of partial melting of the crust through which they passed (and within which large hot magma mafic chambers – capable of partially melting wall- and roof-rocks – may have resided); rhyolites are the first melts to form in the partial melting of crustal silicate rocks (see Chapter 8).

Isotopic data (Baker et al. 2000) do not support melting of Pan-African crustal rocks observed at the surface as the origin for the Yemen rhyolites, though partial melting of **underplated** basaltic material related to the flood basalt episode remains a possibility. The origins of the Etendeka-Paraná silicic volcanics are equally enigmatic (Ewart et al., 2004).

Explaining the voluminous outpourings of rhyolite from the Yellowstone calderas in the past 2 million years, as part of a bimodal magmatic system biased toward silicic magmas, is equally challenging and requires careful analysis of isotopic compositions of Sr, Nd, Pb and O in volcanic and basement rocks. As with other major rhyolites, like Taupo in New Zealand, one can postulate an origin *either* by extreme fractionation of mantle-derived basaltic magma deep in the crust, *or* by partial melting of continental crust initiated by the emplacement of large volumes of hot mantle-derived basic magma at depth, but in reality rhyolite magma genesis on this huge scale often appears to involve a complex interplay between these two simple concepts (Hildreth et al., 1991; Charlier et al., 2005). Most petrologists attribute Yellowstone uplift and volcanism to an underlying Yellowstone mantle plume, though some demur (Christiansen et al., 2002). The plume explanation is supported by recent seismic tomography experiments (Yuan and Dueker, 2005) which have demonstrated the existence of a P-wave low velocity anomaly ~100 km in diameter that can be traced from the present Yellowstone caldera down to a depth of 500 km. The velocity anomaly is consistent with a 'plume-like' excess temperature relative to surrounding mantle of 150–200 °C.

REVIEW – WHAT CAN WE LEARN FROM ANDESITES, DACITES AND RHYOLITES?

Andesites, dacites and rhyolites are found in diverse tectonic circumstances, but they occur in greatest abundance in supra-subduction zone (SSZ) settings – in island arcs and at active continental margins – and their compositions here shed light on internal processes at these convergent margins.

The main conclusions from this chapter are:

- SSZ volcanism arises from partial melting that occurs mainly within the ultramafic *mantle wedge* above a subduction zone, rather than in the descending slab below or the arc crust above.
- Phenocryst-poor low-K basalt is the dominant magma type in immature intra-oceanic island arcs, whereas in more established island arcs and active continental margins surface eruptions consist chiefly of highly porphyritic calc-alkali andesite and dacite; resorption and over-

growth textures and oscillatory zoning testify to long and complex magma fractionation histories.

- Various lines of evidence indicate that H_2O plays the key role in subduction-related magma genesis. Dehydration of hydrous metamorphic minerals in the downgoing slab as it heats up creates a flux of volatiles into the mantle wedge above, where it brings about partial melting by depressing the peridotite **solidus** (Fig. 2.18c,d). The high explosivity of many volcanoes around the 'Ring of Fire' can thus be traced ultimately to seawater recycled through subduction zones.
- The distinctive 'spiky' trace-element signature of SSZ magmas (Figs. 6.15a and 6.25a) may by divided into (i) a 'slab-derived component' enriched in LILE, transported from the slab by hydrous fluids; and (ii) a variably HFSE-depleted 'wedge component' (Fig. 6.25a) representing the composition of peridotite source rocks in the mantle wedge prior to slab-derived enrichment.
- Continental arcs are characterized by a higher proportion of silicic volcanics – like the dacitic pyroclastics of the Andean CVZ – and greater enrichment in incompatible elements such as K_2O (illustrated to an extreme degree by the CVZ andesite in Fig. 6.15b).
- Boninites seem to represent melting of ultra-depleted harzburgite, probably in the wedge lithosphere (Fig. 6.23). Eocene boninites in the western Pacific (Fig. 6.15) may be products of subduction-related magmatism assisted by unusually high temperatures associated with a contemporaneous starting plume.
- Rhyolites (and other silicic magmas) are found in several non-subduction settings. The most impressive take the form of large-scale ignimbrite sheets in bimodal association with basalt, like those associated with successive Yellowstone calderas formed in the past 2 million years.

It is instructive to reflect on how delicately the Earth's internal processes at convergent margins depend on the conditions at its surface: if Earth-surface temperatures happened to lie *outside* the narrow range within which liquid water is stable at atmospheric pressure (0 °C–100 °C), there would be no oceans, negligible hydration of 'oceanic' crust would occur, hydrous fluids could not be released from subducted crust, melting in the mantle wedge would be confined by the dry solidus to much greater depths, and island arcs as we know them could not form.

EXERCISES

6.1 Select appropriate *names* for fine-grained rocks consisting of:
   (a) 45% plagioclase (An_{25}), 8% alkali feldspar, 30% quartz, 5% hornblende, 8% biotite and 4% opaques (modal proportions);
   (b) 51.5% SiO_2, 2.5% Na_2O, 1% K_2O, loss-on-ignition (**LOI**) 2.5% and analysis total 99.7%;
   (c) 59.5% SiO_2, 2.6% K_2O and **LOI** 0.2%;
   (d) 59.5% SiO_2, 3.0% ΣFeO, 2.1% MgO and **LOI** 0.2%.

6.2 Outline the key observations that discriminate between each of the following pairs:
   (a) andesite and dacite;
   (b) andesite and trachyandesite;
   (c) basaltic andesite and shoshonite;
   (d) calc-alkali and tholeiitic fractionation paths;
   (e) calc-alkali dacite and adakite;
   (f) boninite and low-K basalt;
   (g) dacite and rhyolite under the microscope.

6.3 A Yellowstone rhyolite has the following trace element contents (in ppm): Rb 221; Ba 722; Th 32; K 42,280; Nb 56; La 94; Ce 180; Sr 5; P 140; Nd 71; Zr 321; Sm 16; Ti 1100; Gd 13; Tb 2.5; Y 64; Yb 8; Lu 1.1.

   Plot a MORB-normalized profile and discuss (a) the amount of subduction signature in the light of Fig. 2.16, and (b) the evidence for apatite crystallization during magma evolution.

Chapter 7

How magmas erupt – an introduction to pyroclastic processes and products

The high viscosity and often volatile-rich compositions of the silicic melts discussed in Chapter 6 make them liable to erupt explosively. Indeed, the largest and most damaging eruptions of such magmas are invariably pyroclastic eruptions, as the voluminous rhyolitic ignimbrite sheets of Taupo, Toba and Yellowstone illustrate. Such phenomena are not confined, however, to the SiO_2-oversaturated magmas discussed in Chapter 6; evolved alkaline and SiO_2-undersaturated magmas such as **trachyte** and **phonolite**, though not in the same erupted-volume league as Yellowstone, are just as liable to generate major pyroclastic eruptions capable of distributing tephra over a wide geographical area. Examples are provided by the phonolitic pumices of Tenerife in the Canary Islands, of Laacher See in the Eifel region of Germany, and the initial AD 79 white pumice layer of Vesuvius in Italy. The present chapter deals with the subject of physical volcanology, emphasizing the mechanics of pyroclastic eruptions and the physical character of the deposits they produce rather than the petrological affinity of the magmas involved.

Magmas and magmatic processes rarely attract public and media attention except when volcanoes erupt. It has been estimated that as many as 500 M people (about 7.5% of the world's population) live in areas at risk from active volcanoes. This unfortunate fact of human settlement results from several influences: the fertile soils that often form on volcanic ash, the long repose times (often centuries) between successive major eruptions which dim communal awareness of the volcano nearby, population pressures on available land, and the perverse growth of large conurbations close to some potentially lethal volcanoes, as the sprawling suburbs of Naples – encroaching on the slopes of Vesuvius itself – illustrate. A petrologist who takes no interest in eruptive processes therefore misses an opportunity to engage a wider public.

For accessible reading on volcanology, the books by Francis and Oppenheimer (2004) and – at a simpler level – Rothery (2001) are recommended.

THE NOMENCLATURE OF VOLCANIC ERUPTIONS AND DEPOSITS

Effusive versus explosive volcanism

It is convenient to distinguish straight away between *effusive* volcanic activity – the main product of which is fluid lava – and *explosive* activity, which ejects mainly pyroclastic material. Useful though these adjectives are, one should recognize they are 'end-members' of a continuum; the effusion of **silicic** lava domes, for example, is often accompanied by explosions (sometimes even large enough to demolish the growing edifice). Moreover, activity at a given vent may change from one style to the other – in either direction – during the course of an eruptive episode: the eruption of Mt St Helens that began on the 18 May 1980, for instance, was primarily explosive – **plinian** – in nature but the eruption concluded with the relatively quiet effusion of a succession of lava domes in the crater left by the initial paroxysmal stage.

Igneous Rocks and Processes: A Practical Guide, 1st edition. By Robin Gill. Published 2010 by Blackwell Publishing

Whether magma is expelled effusively or explosively depends on two inter-related properties, both of which are consequences of magma composition:

- Magma viscosity, which depends on magma temperature and SiO_2 content (Fig. 6.3.1 in Box 6.3): viscous magma (or one of high **yield strength**) is less able to dissipate applied stresses by quiet flow, and is therefore more likely to fail in a brittle, violent manner. In particular, gas bubbles escape less readily from viscous silicic lava than from basalt lava.
- Magma volatile content: gas-rich magma is more likely to erupt explosively, because massive vesiculation and expansion will occur as load pressure is relieved (Fig. 7.1).

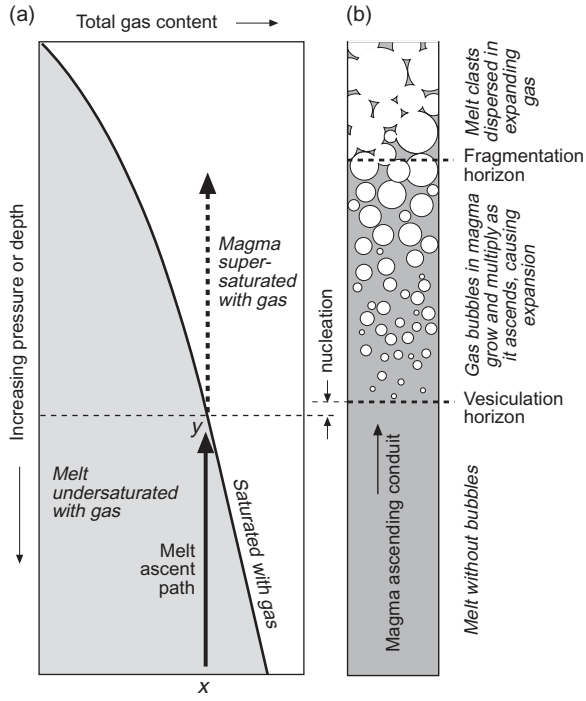


Fig. 7.1 (a) Solubility of gas in a silicate melt as a function of pressure (cf. Fig. 2.7); melt with a dissolved gas content of *x* % becomes saturated with gas at *y*. (b) Progress of melt up a volcanic conduit; above the vesiculation horizon (shallower than *y* as bubble nucleation is not instantaneous), the presence of a gas phase leads to progressive expansion – and therefore upward acceleration – as load pressure is relieved during ascent. The fragmentation horizon marks where froth transforms into spray.

The effect of dissolved gas content in ascending magma is illustrated in Fig. 7.1. At depth the gases will be entirely dissolved in the melt, but at some point the ascending magma will cross a saturation boundary (at *y* in Fig. 7.1a, equivalent to the broad dashed line in Fig. 6.5), and bubbles of a separate gaseous **phase** will begin to appear.[1] Continued ascent and decompression above the 'vesiculation horizon' leads to expansion of existing bubbles and the formation of new ones. If we imagine the conduit to be a pipe of uniform radius (Fig. 7.1b), it is easy to see that this gas-driven expansion unavoidably accelerates the magma upward – the only direction in which expansion is possible.

Effusive activity is favoured by hot, fluid (low SiO_2) magma like basalt that has a low dissolved volatile content. Upward acceleration due to bubble expansion may contribute to lava fountaining as seen in Hawaiian eruptions, but eruptive activity here falls short of being seriously explosive. The fluidity of basalt lava leads to the construction of extensive lava plateaux (Fig. 2.2d) or of gently sloping shield volcanoes (Fig. 7.2a). At the other extreme, cooler, more viscous, evolved (higher SiO_2) magma, if it is also gas-rich, is most likely to erupt explosively. The changes in melt structure arising from decompression and vesiculation during ascent will accentuate this tendency (Box 6.3). Effusion of such magmas can only occur if ascent is slow enough (or is stalled) to allow gas to leak away through conduit walls. Volcanoes prone to explosive eruptions often build up stratovolcanoes consisting of alternations of lavas and pyroclastic layers (Fig. 7.2b).

Styles of volcanic eruption

Volcanoes vary widely in their styles of eruption, and indeed eruptive characteristics may differ between one eruption and another at the same volcano. Volcanologists divide eruptions into a number of categories that reflect the dominant physical phenomena observed during the course of a given eruption. This

[1] Vesiculation begins *above* the saturation horizon in an ascending body of melt (Fig. 7.1) because the nucleation of bubbles, like that of crystals (Box 2.3), requires a degree of supersaturation.

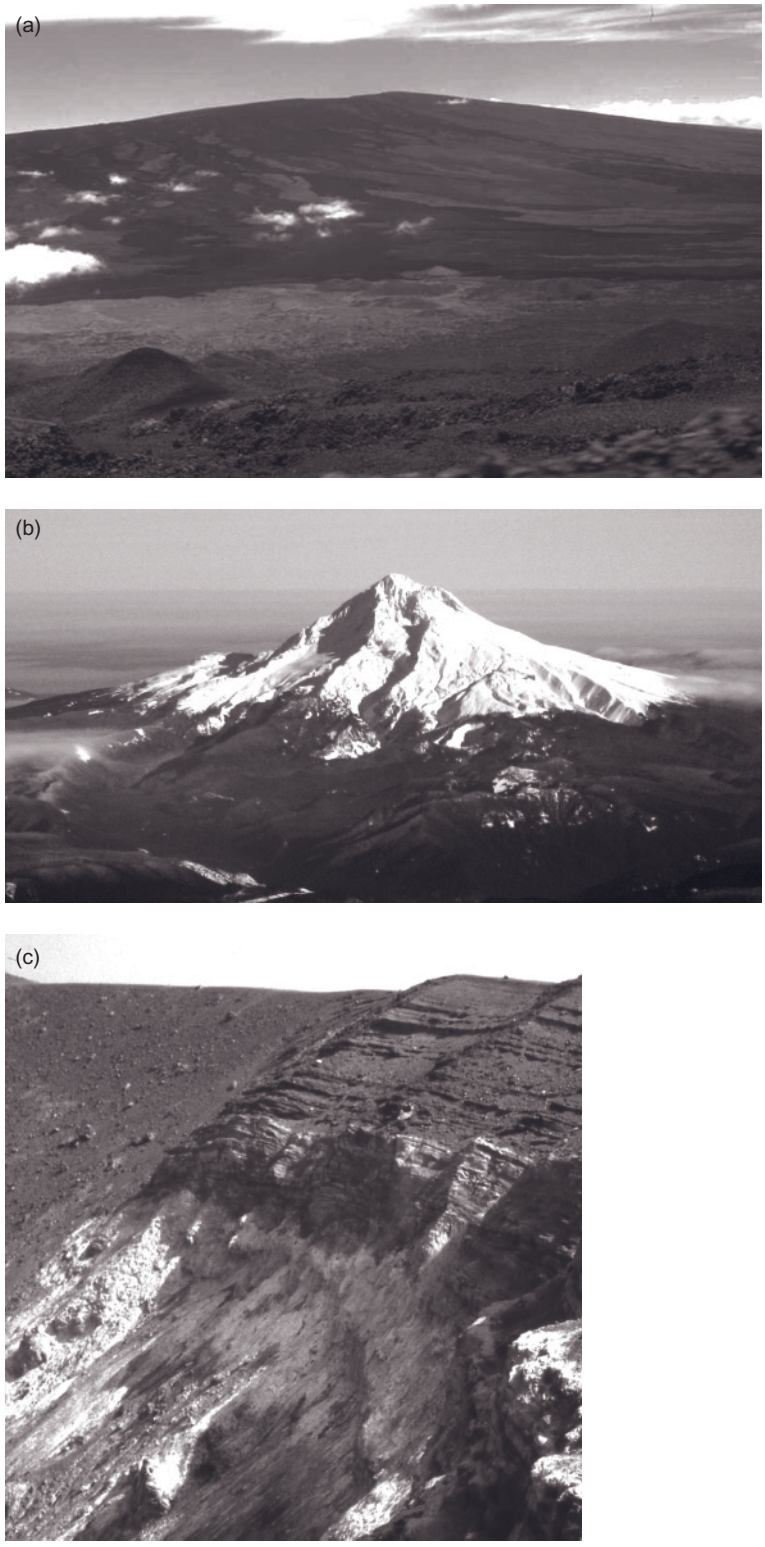


Fig. 7.2 (a) Shield volcano: view of Mauna Loa volcano from Mauna Kea, Hawai`i (US Geological Survey photo by D. Little). (b) Stratovolcano: aerial view of Mount Hood, Oregon from the west (US Geological Survey photo by M. Doukas). (c) Crater of Fossa volcano, Vulcano; the darker beds exposed in the upper wall are the products of the 1888–90 vulcanian eruptions. Photographs (a) and (b) are reproduced courtesy of the US Geological Survey.

approach – and the adjectives used, such as hawaiian and vulcanian (usually written today without initial capitals) – were first introduced by the Italian volcanologist Giuseppe Mercalli in a book published in 1907. The main categories are reviewed below (in order of increasing explosivity) using eye-witness accounts. The differences between these styles of eruption and the landforms associated with them are summarized in Table 7.1.

Hawaiian eruptions

The active volcanoes of Hawai`i have been a magnet to inquisitive tourists for at least two centuries. Among the earliest published accounts presented to the scientific community was one by a missionary, Joseph Goodrich, who wrote in the *American Journal of Science* of a visit (probably to Mauna Loa)[2] in 1824:

> *'The crater appears to be filling up* [with lava]. *In the middle of the crater it was still spouting. I crossed the bottom in several places.... Dense sulphurous fumes are ascending from all parts of the bottom; the gases are very suffocating, so much so that the crater is impassable in many places. The escape of the gaseous substances makes a tremendous roaring, like the steam jet from the boiler of a steam train. On the night of the 22nd of December 1824 a new volcano* [vent] *broke out at the bottom of the large crater; as soon as it was sufficiently light, I descended near to the spot where the lava was both spouting up and boiling like a fountain; some of the lava was thrown forty or fifty feet into the air* [cf. Fig. 7.3a]. *It was one of the most awful scenes that I have ever witnessed, to see such a mass of lava, red hot, boiling and running like water, although it was not so liquid as water. ... On my visit there six weeks after* [missionary workload seems to have been light!] *I found it had formed a lava mound, upwards of 60 feet above the bottom of the crater. ... Capillary volcanic glass* [a reference to Pele's hair – see Fig. 2.9a] *is in great abundance in some places on the bottom to the depth of 2–3 inches; and some is to be seen 15 or 20 miles from the crater, drifted by the wind and lodged in the crevices of the lava.'.*

[2] Hawai`i has two currently active volcanoes capped by calderas: Mauna Loa at 4169 m (Fig. 7.2a) and Kilauea at 1200 m. The highest point is Mauna Kea (4206 m), an inactive shield volcano similar to Mauna Loa.

Here in Goodrich's words we have the essence of hawaiian activity: fountaining of fluid,[3] red-hot basaltic lava – later accounts even record lava fountaining as high as 800 feet (250 m) – and the construction of a *spatter cone* around the active vent where the still-molten lava lands. In these circumstances molten lava often accumulates to the extent of forming a lava lake (Fig. 7.3b), which may then magically drain away over a period of days or weeks. Hawaiian eruptions are essentially effusive, and therefore produce only tiny volumes of pyroclastic material, chiefly in the form of Pele's hair. Other characteristics of such eruptions (lava tubes, etc.) have been discussed in Chapter 2.

Strombolian eruptions

A contemporary account by a Signor Monticelli of an 1822 flank eruption of Vesuvius gives a vivid impression of what volcanologists mean today by a strombolian eruption:

> *'The cone, lit at its summit, presents a magnificent spectacle: a column of fire stood tall in the sky, amid thick swirls of smoke. It seemed like a big beacon ... but looking closer it showed the observer an uninterrupted shower of* [glowing] *stones, violently thrown out of the volcano's mouth, falling down with parabolic trajectories out to varying distances* [from the vent]. *Imagine one of the fountains in St Peter's Square in Rome squirting not water but glowing stones: picture the fountain thousands of times bigger, and you'll get a feel for the display of fireworks the eruption provided.'*[4]

Seen in daylight, strombolian eruptions such as this are (from a distance) rather unimpressive: periodic explosions noisily eject clouds of basaltic ash and lapilli (Table 7.2 and Fig. 7.3c) up to heights of a few hundred metres above the vent, and showers of solid black **scoria** (gobs of vesicular magma chilled in the air) patter down on the surrounding scoria cone and the crater at its centre. Only the vent itself glows red, and this will be hidden from anyone not standing on the very lip of the crater. As Monticelli's account makes clear, however, a strombolian eruption

[3] Fluid enough to flow a distance of 40 miles to the sea.
[4] Kindly translated from the Italian by Giulia Kistruck.

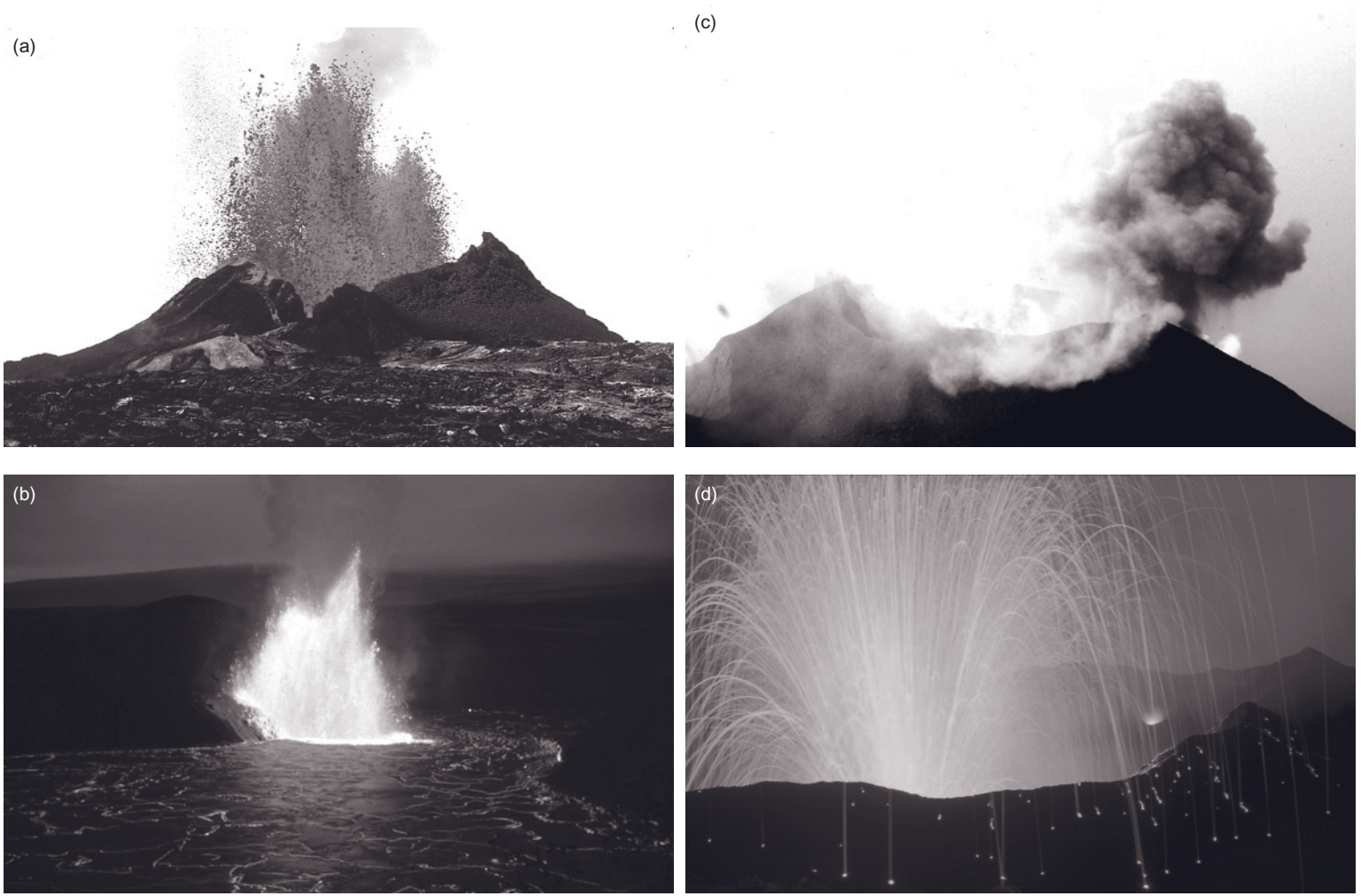


Fig. 7.3 (a) Hawaiian lava fountaining at Pu'u 'O'o, Kilauea, Hawai`i, in September 1983 (photo by J.D. Griggs); the fountain itself and the light-coloured lava drape in the foreground are glowing red; the vent is surrounded by a spatter cone which in due course built up into a much larger edifice. (b) Lava fountain seen across the December 1959 lava lake in Kilauea Iki crater, Hawai`i; note the glowing cracks in the solidified lava skin covering the lake (photo by J.P. Eaton). (c) Small strombolian eruption column, Stromboli volcano; note the fuming cone in the foreground. (d) Strombolian eruption at night, Stromboli; a second, more distant erupting crater can be seen on the right (photo by B. Chouet). Photographs (a), (b) and (d) are reproduced courtesy of the US Geological Survey.

Table 7.1 Styles of eruption and their observed characteristics.

	Commonly observed phenomena	Pyroclastic deposits (Composition)	Typical volcanic landforms
hawaiian	fire fountains ≥100 m high (Fig. 7.3a), lava lake (Fig. 7.3b), lava tubes	small amounts of Pele's hair/tears (Basalt)	basaltic **shield volcano** (Fig. 7.2a), summit caldera, spatter cone, lava flows (pahoehoe, a'a), levées
strombolian	periodic explosions emitting **scoria**/ash clouds (Fig. 7.3c,d)	well sorted scoria beds (Basalt or basaltic andesite)	scoria cone (Fig. 2.6)
vulcanian	discrete explosions, short-lived eruption column 5–10 km high (Fig. 7.4a)	thin beds of ash (Fig. 7.2c), bread-crust bombs (Fig. 7.4b), lithics (Juvenile component usually intermediate/acid)	crater (e.g. Fossa, Fig. 7.2c)
sub-plinian	sustained eruption column 10–20 km high, PDCs*	(a) widespread pumice fall blanket	**stratovolcano** (Fig. 7.2b) and crater; however, larger plinian eruptions often have no associated positive edifice, and may eject enough magma to cause caldera subsidence (Fig. 7.18)
plinian and ultraplinian	sustained eruption column 20–50 km high and umbrella (Fig. 7.4c,d), PDCs*	(b) pumiceous lapilli tuff/**ignimbrite** (Usually dacite, rhyolite or phonolite)	
hydrovolcanic	repeated explosions, 'cock's tail' ash cloud (Fig. 7.9a), expanding base-surge cloud	thin beds of juvenile ash (often basalt) *and/or* country-rock lithics; cross-stratified base-surge deposits	tuff (or ash) ring; crater or **maar** (Fig. 7.9b)

* PDC = **pyroclastic density current** (Fig. 7.4e).

seen at night resembles a spectacular firework display (Fig. 7.3d): red-hot pyroclasts of scoria (barely glowing by daylight) trace graceful parabolic paths up and down through the air, and they may glow for a while after landing on (and tumbling down) the flanks of the cone. A relatively regular timing of explosions (every 30 minutes to several hours) is characteristic of strombolian eruptions. The type volcano, forming the island of Stromboli in the Italian Aeolian Islands,[5] has been erupting in this way (interspersed with occasional larger explosions and episodes of lava effusion) for thousands of years; the glow at its summit has provided a natural lighthouse for nocturnal mariners since classical times. Most examples of strombolian activity, however, produce **monogenetic** scoria cones on a smaller scale. The associated deposits and landforms are summarized in Table 7.1.

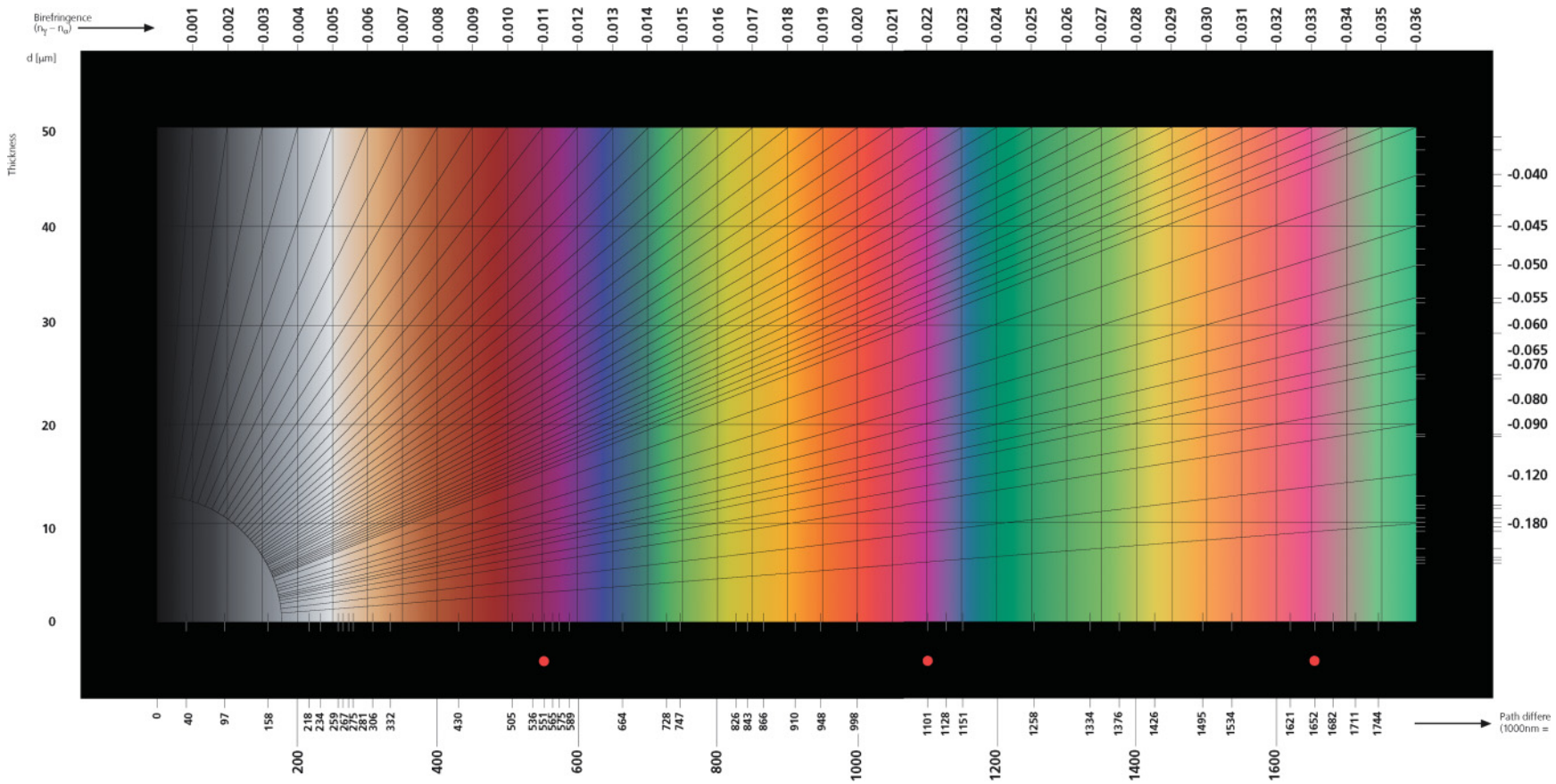
Whereas in hawaiian eruptions the fountaining lava remains molten until it has fallen to the ground, strombolian scoria have generally solidified before they reach the ground – though they may remain incandescent for a while. The difference is attributable to the degree of fragmentation – large squirts of melt can retain heat more effectively than the fist-sized (or smaller) gobs of magma that form typical scoria.

Vulcanian eruptions

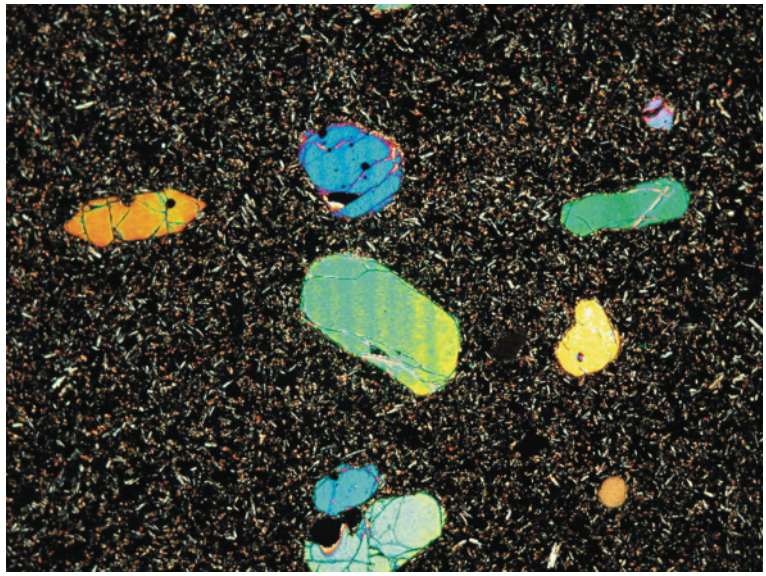
Another of the Aeolian Islands, the eponymous island of Vulcano,[6] provides the type locality for vulcanian eruptions – those characterized by irregular 'cannon-like' explosions. The Fossa cone on Vulcano erupted in this manner between 1888 and 1890, and Guest et al., (2003) have pieced together the

[5] Isole Eolie in Italian.

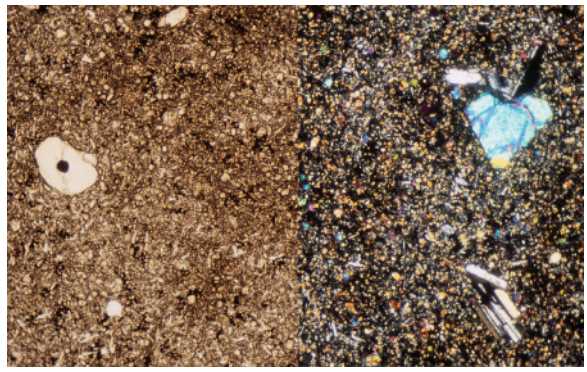
[6] **NB** the island's name and that of the science derived from it (volcanology, -ist) are spelt differently.



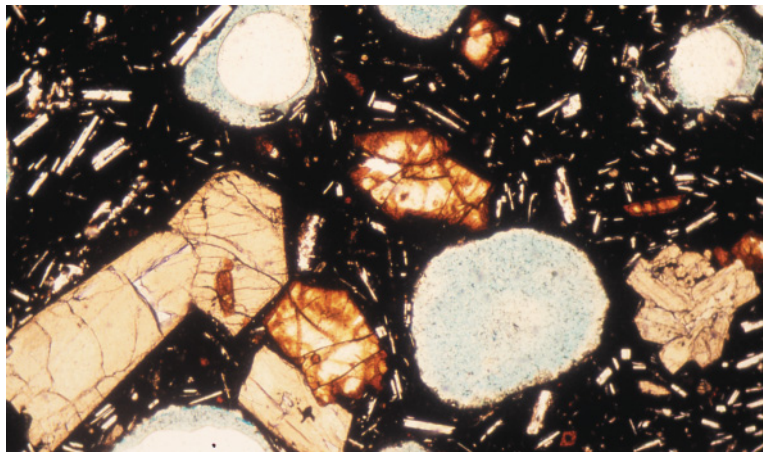
1 Michel-Lévy chart The Michel-Lévy chart of interference colours, reproduced courtesy of Carl Zeiss, Germany (colour PDF available from www.zeiss.de/C12567BE0045ACF1/allBySubject/A30F2861A5385EBCC1256D52004AD6DF).



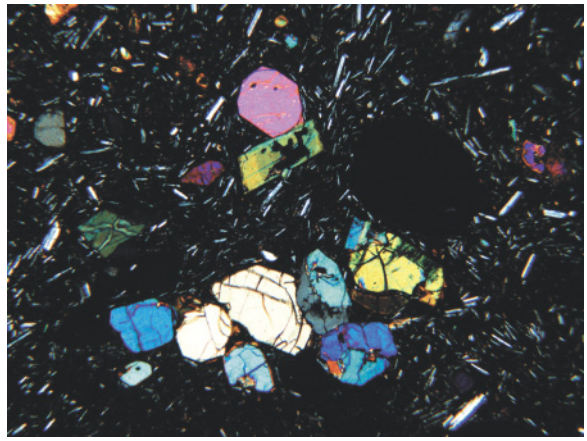
2.1 Olivine-phyric basalt from Waikoloa, island of Hawai`i (image courtesy of J.G. Fitton); Width of field 3.5 mm.



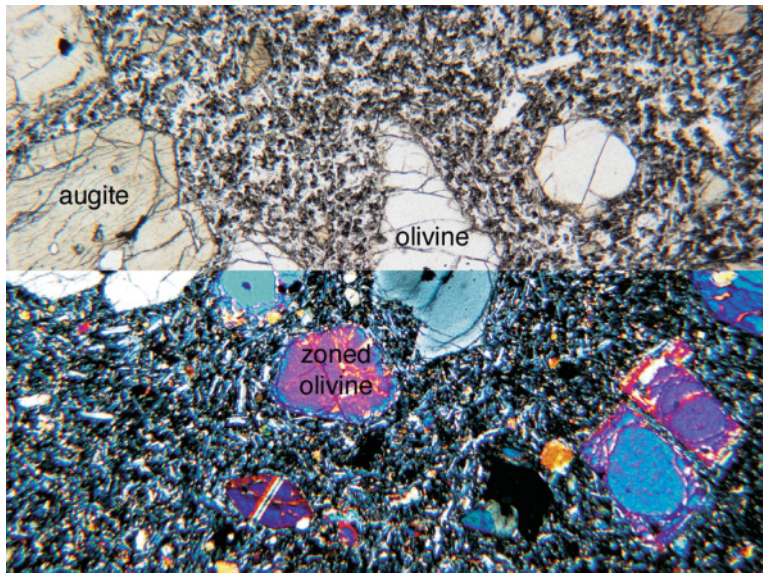
2.2 Holocrystalline basalt with microphenocrysts of olivine and plagioclase (Preshal Mohr, Isle of Skye); left PPL, right XP. As the appearance of plagioclase phenocrysts without augite phenocrysts suggests, this basalt has tholeiitic composition. Width of field 3.2 mm.



2.3 Scoriaceous lava in PPL showing (i) **seriate** texture; (ii) phenocrysts of colourless olivine (with red **iddingsite** alteration) and beige augite; (iii) microphenocrysts of plagioclase, altered olivine and sparse augite; (iv) glassy groundmass rendered opaque by submicroscopic inclusions of oxide minerals; (v) a **glomeroporphyritic** cluster of augite crystals (right); (vi) vesicles (tinted blue owing to mounting medium). Width of field 1.3 mm. (ankaramite from Agde, Hérault, France).



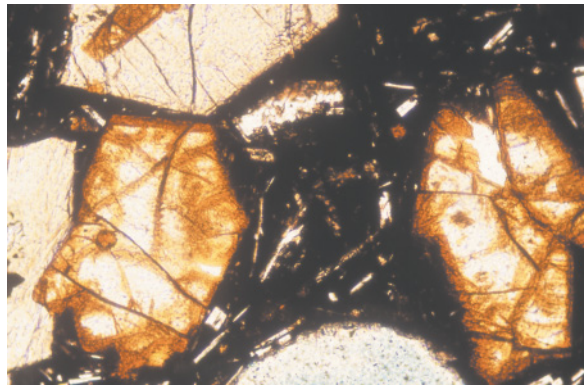
2.4 Glomeroporphyritic cluster of olivine crystals under crossed polars. The circular black area lacking plagioclase microlites is a vesicle (ankaramite from Agde, Hérault, France. Width of field 2.7 mm).



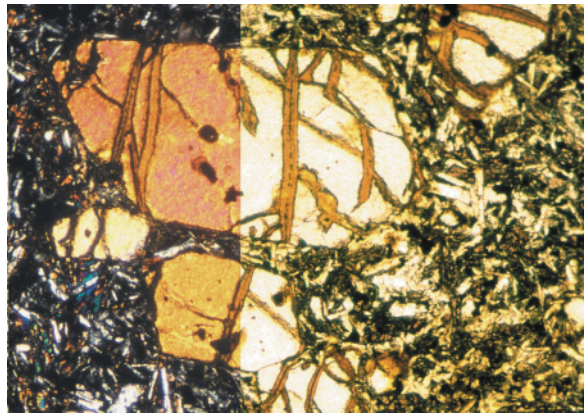
2.5 Olivine-augite-phyric ankaramite (Aoba Island, Vanuatu, SW Pacific. Upper portion PPL, lower portion crossed polars. Width of field 2.7 mm).



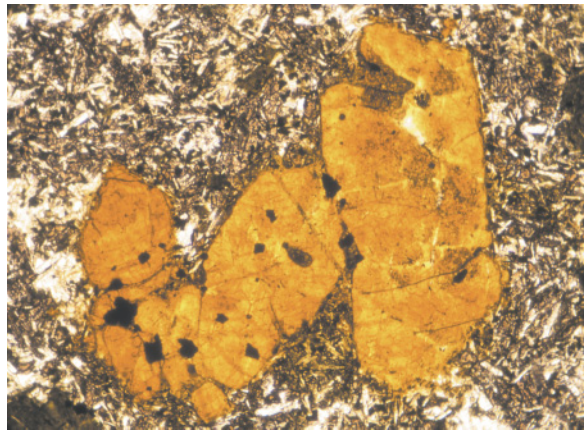
2.6 Skylight in pahoehoe lava flow, Hawai`i (photo Ivvet Modinou, reproduced with permission).



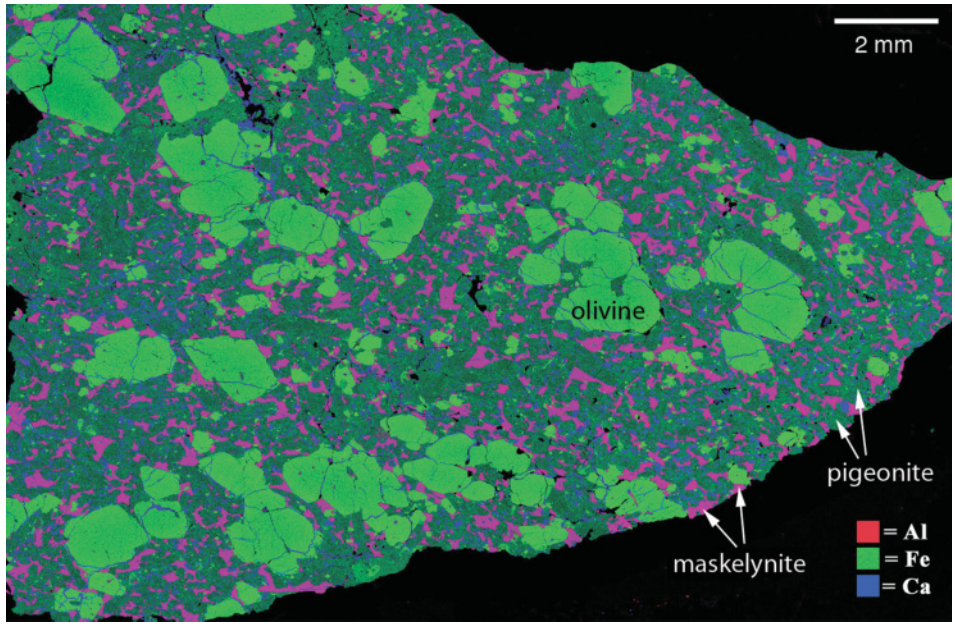
2.7 Iddingsite alteration concentrated at the margins (and along some cracks) of olivine phenocrysts in PPL (width of field 1.4 mm); note the difference in body colour between colourless olivine (where unaltered) and beige augite.



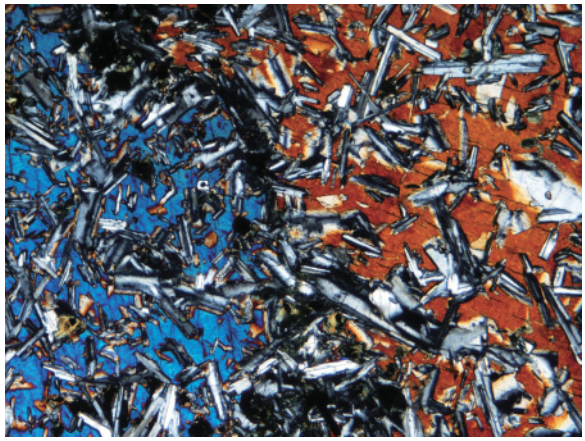
2.8 Incipient serpentinization along internal cracks in olivine phenocrysts; XP left, PPL right (width of field 0.9 mm).



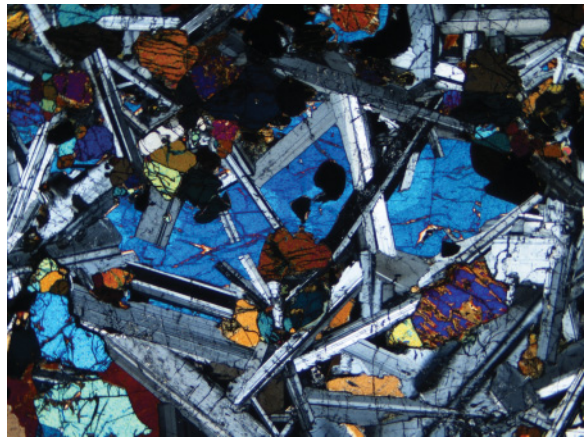
2.9 Iddingsite **pseudomorph** after euhedral olivine phenocrysts in PPL (width of field 3.2 mm).



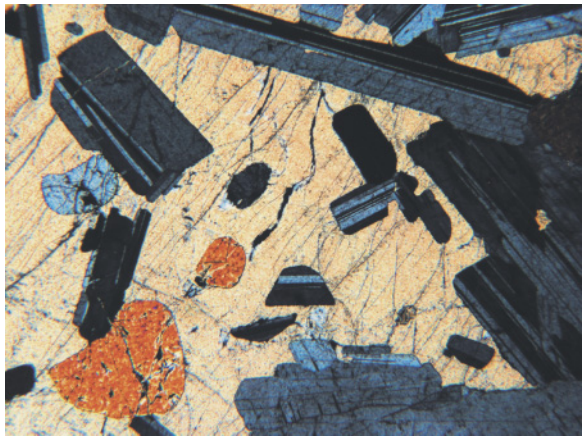
2.10 An X-ray element map of an olivine-phyric shergottite (a basaltic achondrite meteorite originating from Mars). The map was made by scanning an **electron microprobe** beam across an area of polished sample surface and mapping points from which X-ray spectra of Al, Ca and Fe were emitted; the distribution of each element is indicated by the colours shown in the key. The colours allow individual mineral grains to be mapped by their distinct compositions: olivine glomerocrysts (clusters of phenocrysts) contain iron and appear light to medium green, groundmass pigeonite is darker green, and maskelynite (glass produced by isochemical shock-melting of plagioclase) appears lilac as it contains both Ca (blue) and Al (red). Original image courtesy of C.A. Goodrich; reproduced slightly modified from Goodrich (2003) by permission of Elsevier.



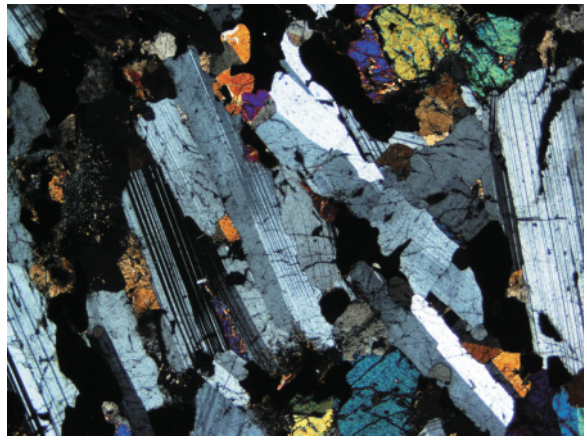
4.1 **Ophitic** texture in basalt (crossed polars): euhedral multiply twinned plagioclase laths (grey interference colours) are enclosed by two augite oikocrysts with first-order orange and second-order blue interference colours. Width of field 1.3 mm. (Loch Scridain, Isle of Mull.)



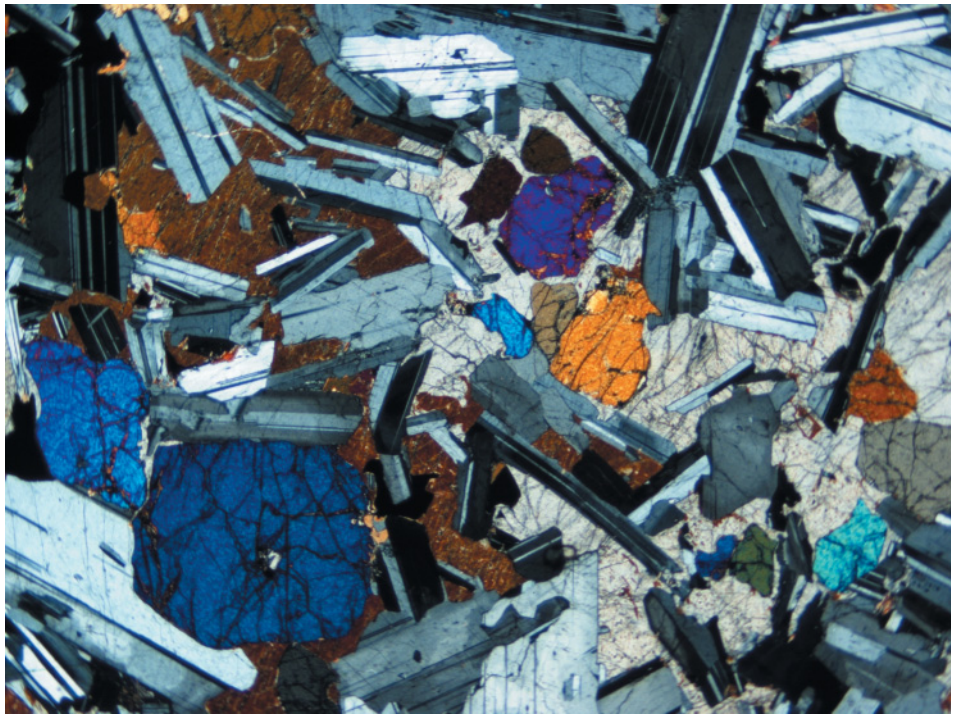
4.2 Sub-ophitic olivine dolerite (crossed polars): the texture resembles ophitic texture except that plagioclase laths are generally not completely enclosed by augite (cf. Plate 4.1). (Olivine analcite dolerite from the Clauchlands Sill, Isle of Arran, field of view 5.4 mm wide.)



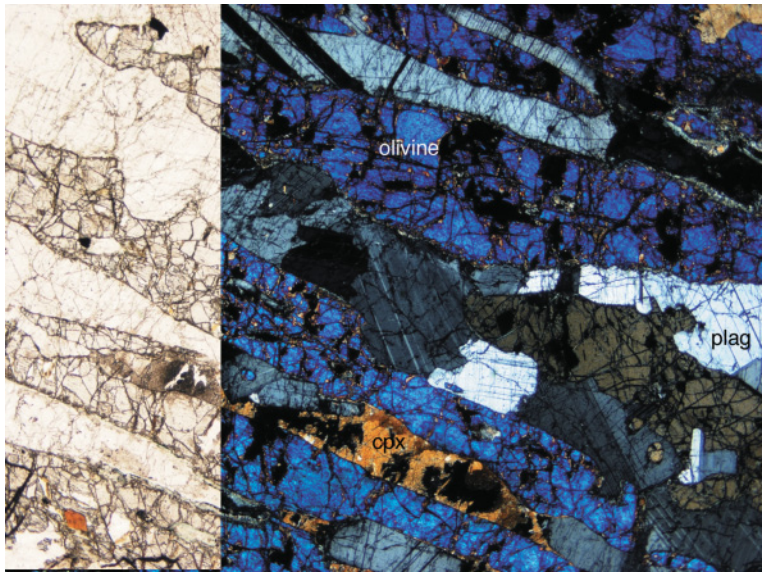
4.3 Poikilophitic texture in gabbro (crossed polars; field of view 2.7 mm wide): olivine crystals in addition to plagioclase laths are enclosed by the augite oikocryst. Note that the size of included crystals increases from the centre to the rim of the oikocryst (gabbro, location unknown).



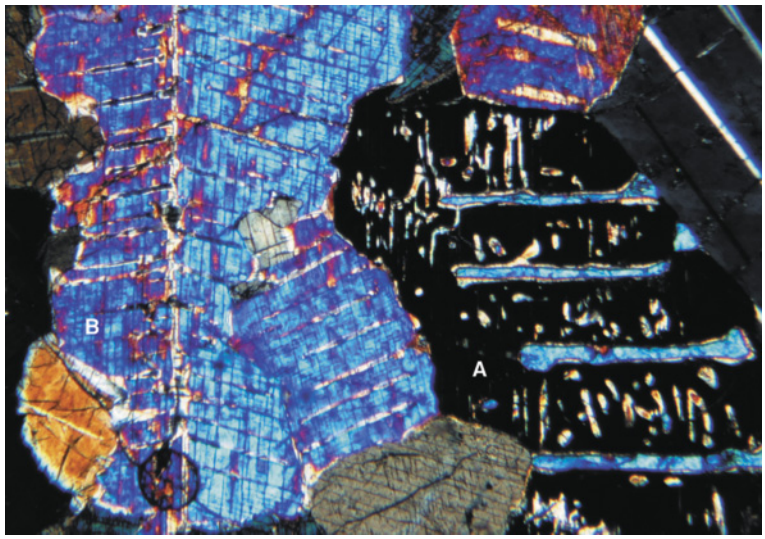
4.5 Igneous lamination in feldspathic gabbro (crossed polars; field of view 5.4 mm wide); subparallel cumulus plagioclase crystals are interspersed with cumulus olivines and sparse interstitial augite and opaques (UZ, Skærgaard intrusion, East Greenland).



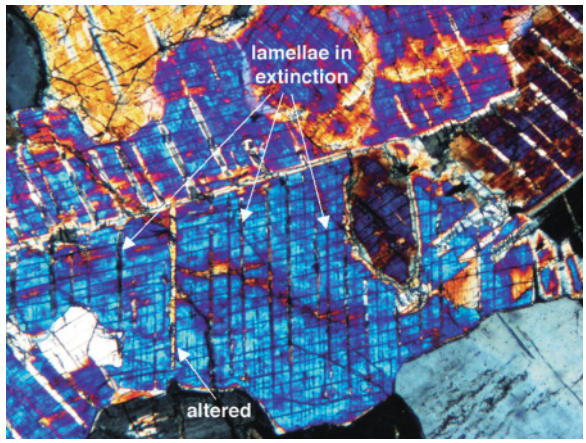
4.4 Olivine-plagioclase cumulate in gabbro (crossed polars; field of view 5.4 mm wide): LZ, Skærgaard intrusion, East Greenland.



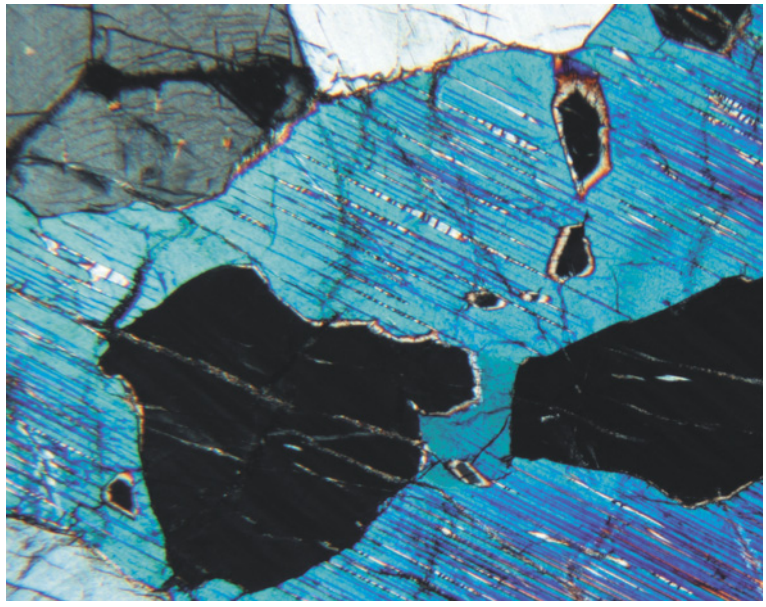
4.6 Olivine crescumulate (narrow diagonal crystals with blue interference colour) with intercumulus augite and plagioclase crystals in olivine gabbro (PPL on left, XP on right; field of view 5.4 mm wide): Glen Harris, Isle of Rum, Hebrides).



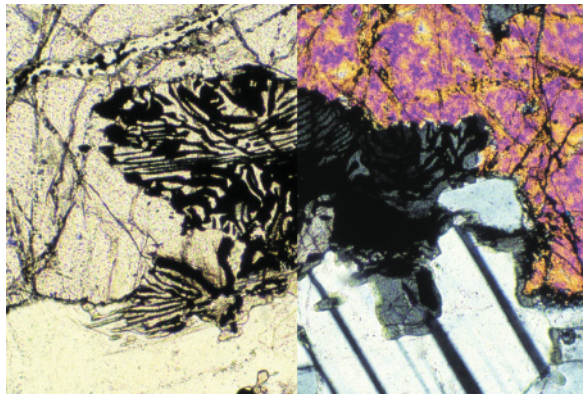
4.7 Inverted pigeonite (crystal A, in extinction) with two generations of exsolution lamellae: broad augite lamellae parallel to pigeonite (001) – formed during inversion – and finer augite lamellae parallel to enstatite (100) formed during subsequent cooling. An adjacent twinned augite crystal (crystal B) shows enstatite exsolution lamellae parallel to (001). Norite, Bushveld Complex (field of view 2.7 mm wide).



4.8 Twinned augite crystal (grain B in Plate 4.7) showing exsolution lamellae of orthopyroxene in gabbro (crossed polars); the lower part of the twinned augite host shows orthopyroxene lamellae extinguishing parallel to the (100) plane of the lamellae (except for one that has undergone alteration). Field of view 2.7 mm wide.



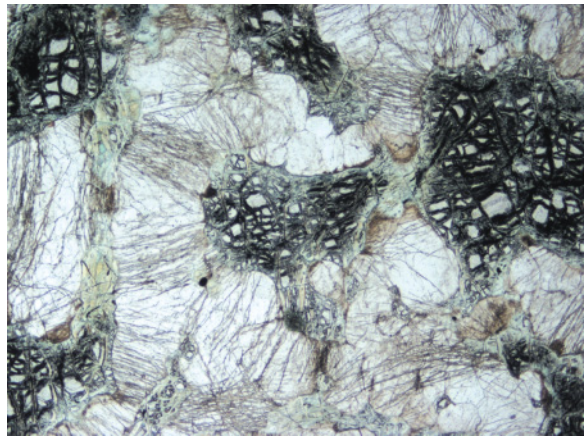
4.9 Augite oikocryst enclosing cumulus orthopyroxene, the augite also showing exsolution lamellae of orthopyroxene parallel to (100) emphasized by their cleavage; peridotite zone of the Stillwater Complex, Montana (crossed polars, field of view 1.5 mm wide). Thin section courtesy of I.S. McCallum, University of Washington, Seattle.



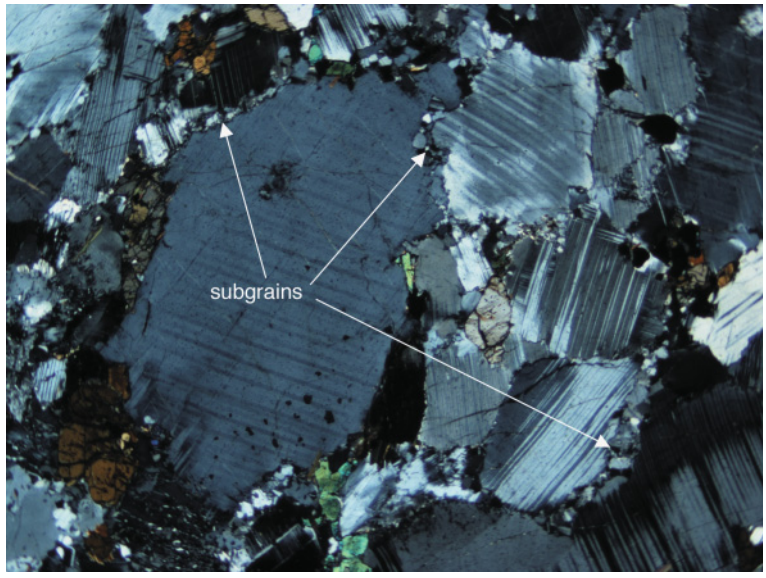
4.10 Orthopyroxene-opaque symplectite formed at the boundary between grains of olivine (top) and plagioclase; PPL on left, XP on right (troctolite from Ben Buie intrusion, Isle of Mull, field of view 0.5 mm wide).



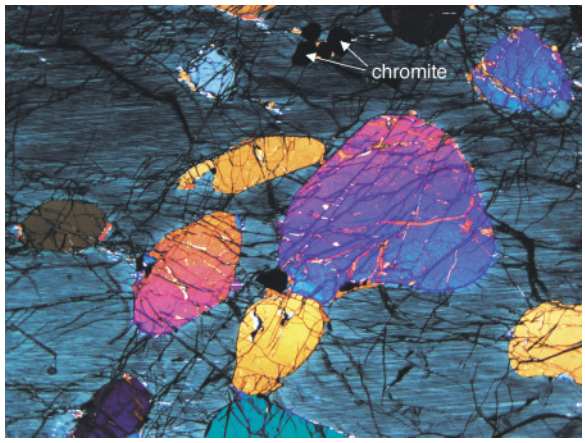
4.11 Olivine-plagioclase symplectite growing outward from the margin of a cumulus Fe–Ti oxide grain into the neighbouring cumulus plagioclase grain. Skærgaard Intrusion Middle Zone (photo courtesy of Gemma Stripp, University of Cambridge). Crossed polars, field of view 0.7 mm wide.



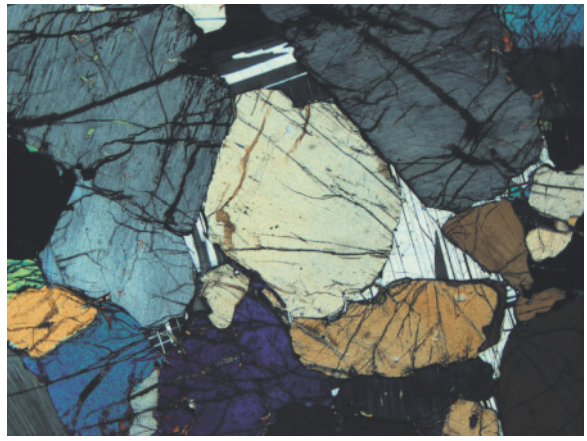
4.12 Expansion cracks in plagioclase radiating from serpentinized olivine crystals owing to the expansion that accompanies alteration. (Troctolite, Aberdeenshire, UK, field of view 2.7 mm wide.)



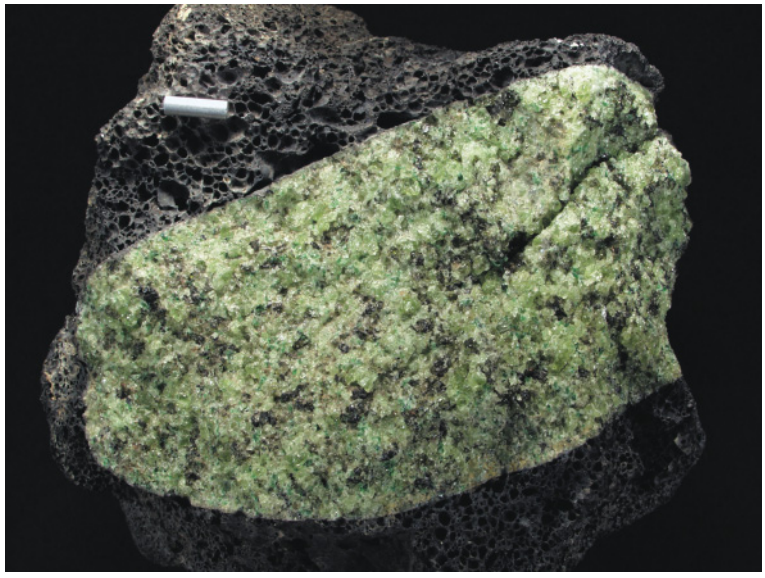
4.13 Massif-type anorthosite (in crossed polars): note that original plagioclase crystals have become strained (e.g. slight curvature of twin lamellae in some crystals) and have recrystallized along boundaries into smaller sub-grains in response to post-crystallization stress (Morin complex, Quebec, Canada; field of view 5 mm wide).



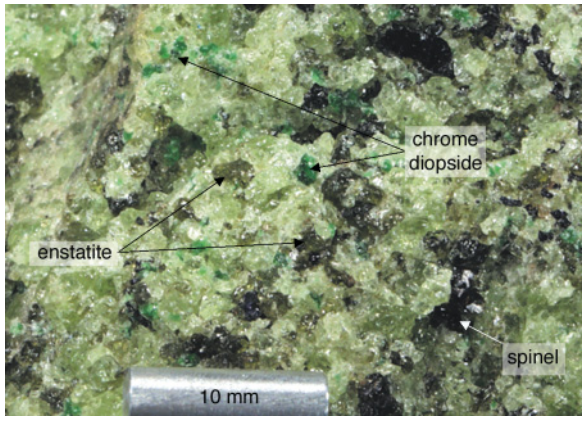
5.1 Partially resorbed cumulate olivine crystals embedded in an enstatite oikocryst: olivine–chromite cumulate from the peridotite zone of the Stillwater Intrusion (crossed polars; field of view 5.4 mm wide); thin section courtesy of I.S. McCallum, University of Washington, Seattle.



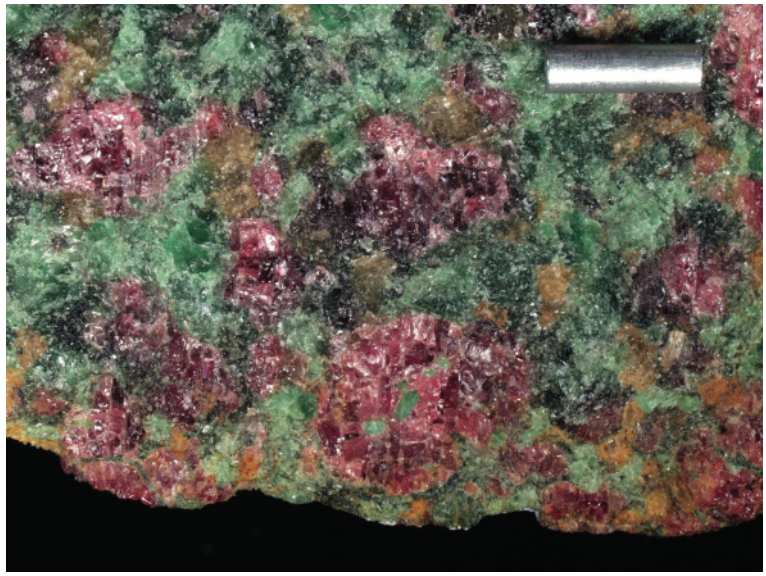
5.2 Olivine–enstatite cumulate with intercumulus plagioclase (multiple twinning) from the peridotite zone of the Stillwater Intrusion, Montana, (crossed polars; field of view 5.4 mm wide); note local grain boundary re-adjustment to ~120° close to the lower half of the left-hand margin. Thin section courtesy of I.S. McCallum, University of Washington, Seattle.



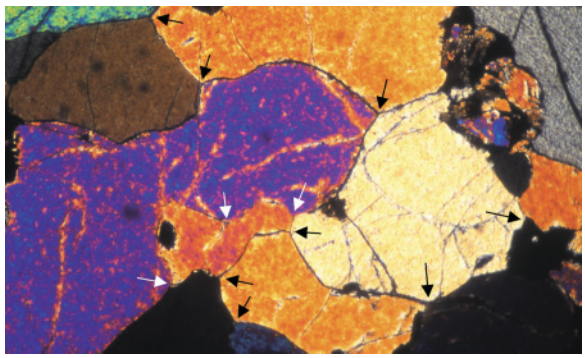
5.3 Spinel lherzolite nodule, Leurat volcano, Victoria, Australia (metal rod 1 cm long). Note the xenolith's rounded outline in contact with the basaltic scoria host (top of the picture). Photo K. d'Souza.



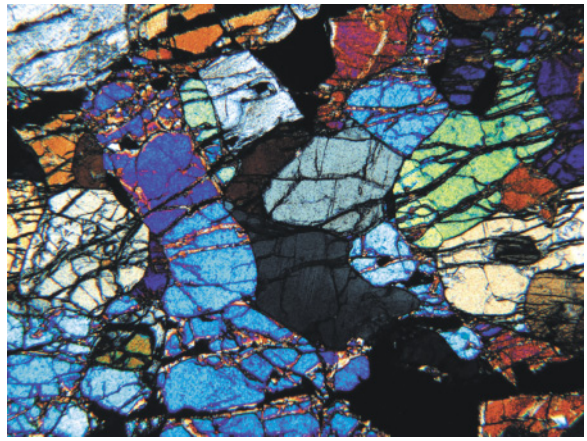
5.4 Close-up of Plate 5.3 showing chrome diopside and other individual minerals (1 cm rod for scale). The dominant lighter green mineral is olivine. Photo K. d'Souza.



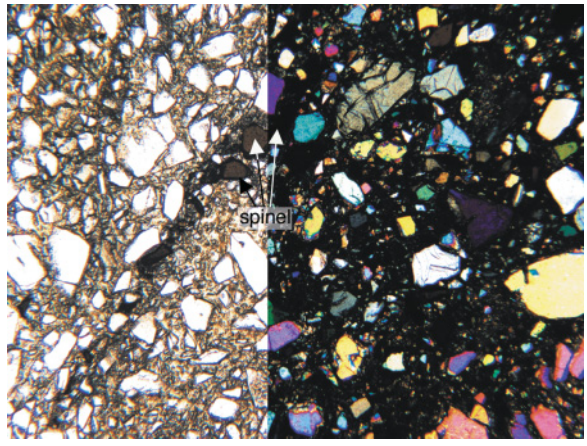
5.5 Hand-specimen of protogranular garnet lherzolite xenolith from a kimberlite (locality unknown). Chrome diopside as in Plate 5.4; yellow mineral is enstatite; garnet is red; olivine is paler green (metal rod 1 cm long). Sample courtesy of M.A. Menzies, University of London. Photo K. d'Souza.



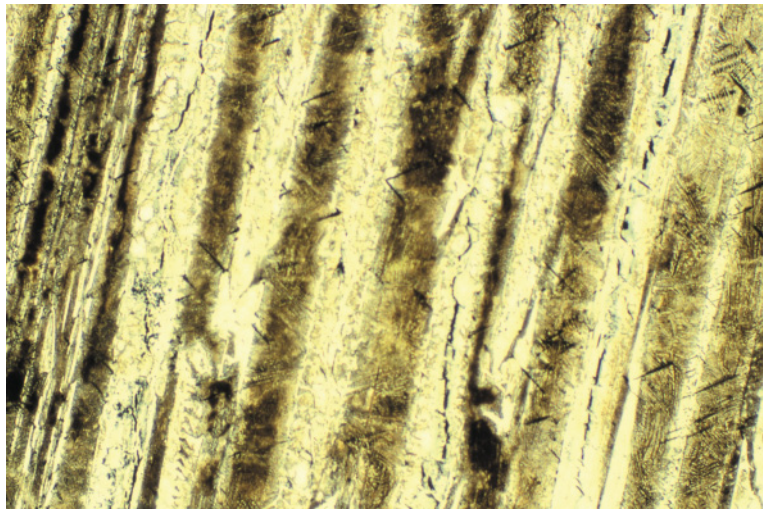
5.6 Protogranular texture in a mantle harzburgite (xenolith in basalt from the Massif Central, France, crossed polars, field of view 2.7 mm wide); the arrows highlight triple junctions with interfacial angles close to 120°.



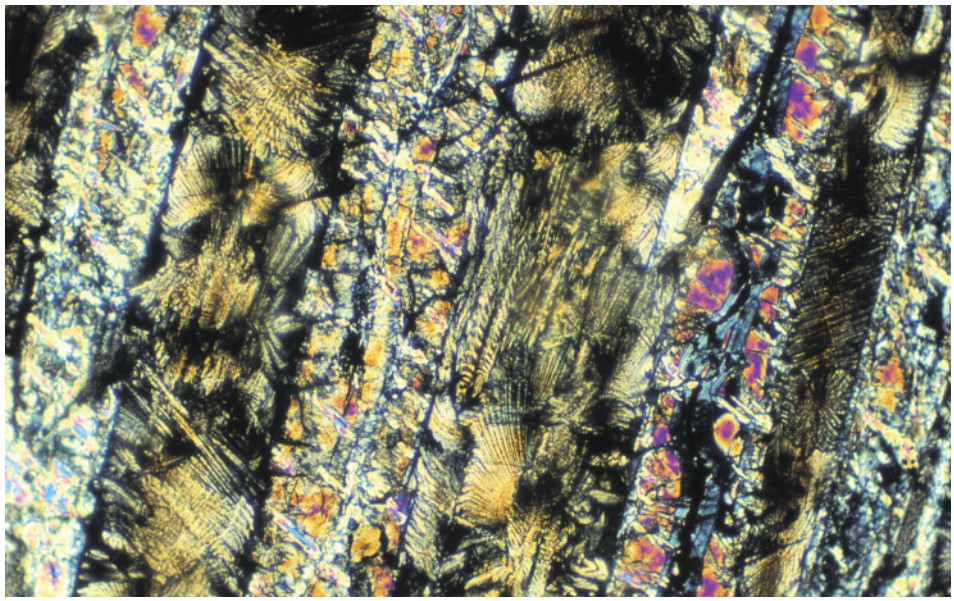
5.7 Protogranular spinel lherzolite from Lherz (Fontete Rouge borehole); crossed polars, field of view 2.7 mm wide. Thin section courtesy of E. McPherson, Open University.



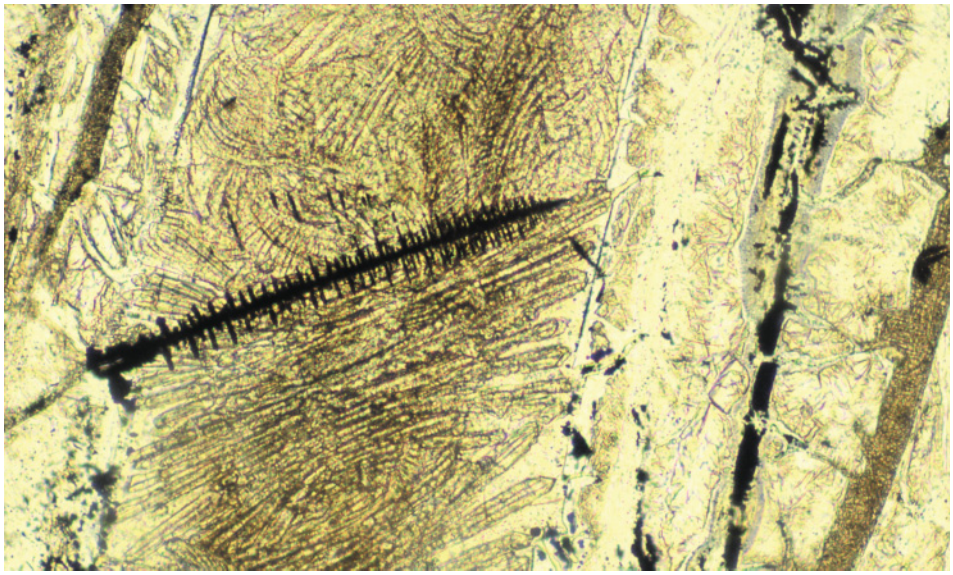
5.8 Porphyroclastic ('sheared') spinel lherzolite from Lherz (from a shear zone intercepted by the Fontete Rouge borehole); total width of field of view 2.7 mm. The arrowed isotropic grains with brown body colour are spinel. Thin section courtesy of E. McPherson, Open University.



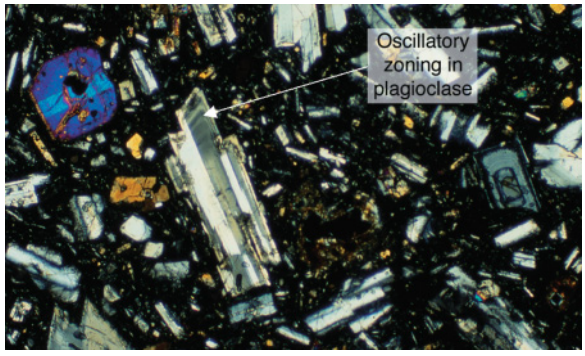
5.9 Spinifex texture in a komatiite flow, Munro Township, Ontario, seen in PPL. The white bands are olivine plates seen in cross-section; skeletal forms and forked terminations can be seen on the extreme left. Straight narrow black crystals are primary chromite dendrites (cf. Plate 5.11). Partial serpentinization of olivine has also precipitated internal opaque trails of secondary iron oxide (cf. Plate 4.9 and equation 4.3). The intervening brown bands consist of feathery pyroxene crystals (most easily discerned on the right and in Plates 5.10 and 5.11) crystallized from interstitial melt. Field of view 1.4 mm wide.



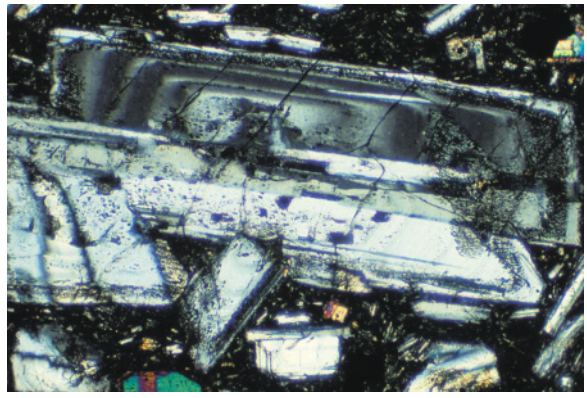
5.10 The same komatiite viewed at higher magnification between crossed polars. Bands showing the higher interference colours are **optically continuous** olivine plates (partly serpentinized – grey interference colours). Bands between the olivines consist of fine plumose, fern-like and dendritic pyroxene crystals precipitated rapidly from interstitial melt. (Munro Township, Ontario; field of view 0.56 mm wide)



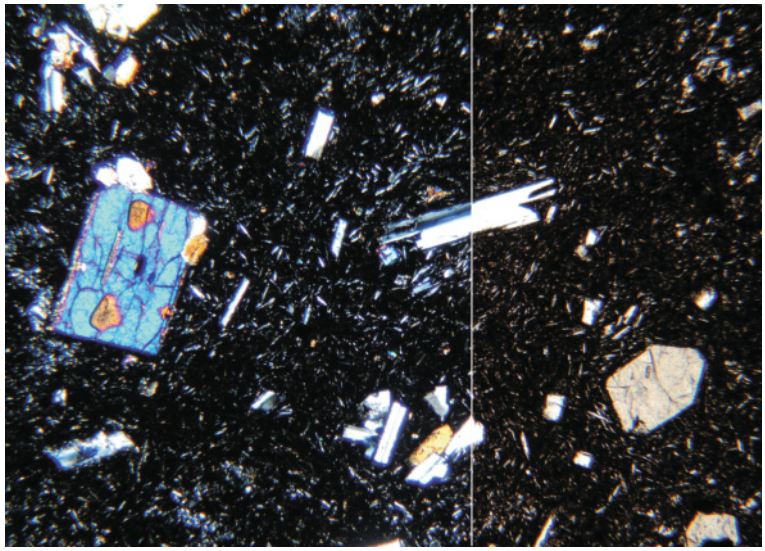
5.11 'Christmas tree' dendrite of chromite in an interstitial 'melt' zone (plumose crystal outlines of pyroxene are visible) in komatiite seen under high magnification (PPL); oriented chromite branches detached from the main 'tree' probably connect with it in the third dimension. In the paler olivine plate on the right, opaque iron oxide expelled during serpentinization forms a less regular central band (komatiite flow from Munro Township, Ontario; field of view 0.28 mm wide).



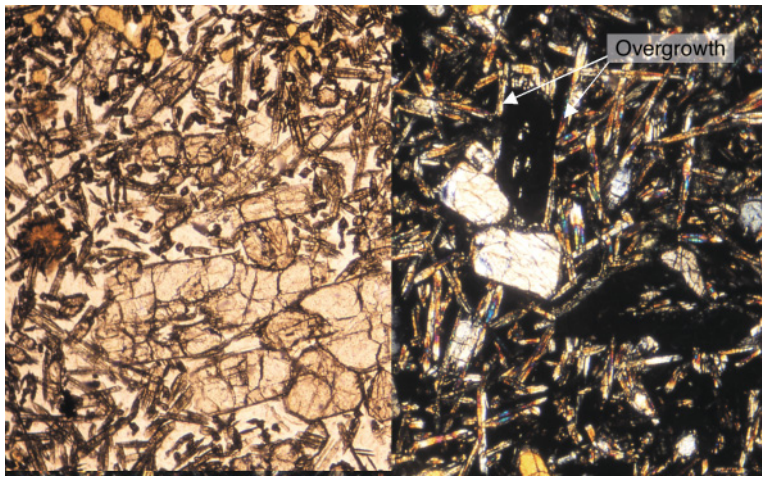
6.1 Plagioclase-phyric pyroxene andesite with seriate texture, from Cereme volcano, Java; feldspar phenocrysts exhibit oscillatory zoning. Field of view 1.3 mm wide. Sample courtesy of C.M.H. Edwards.



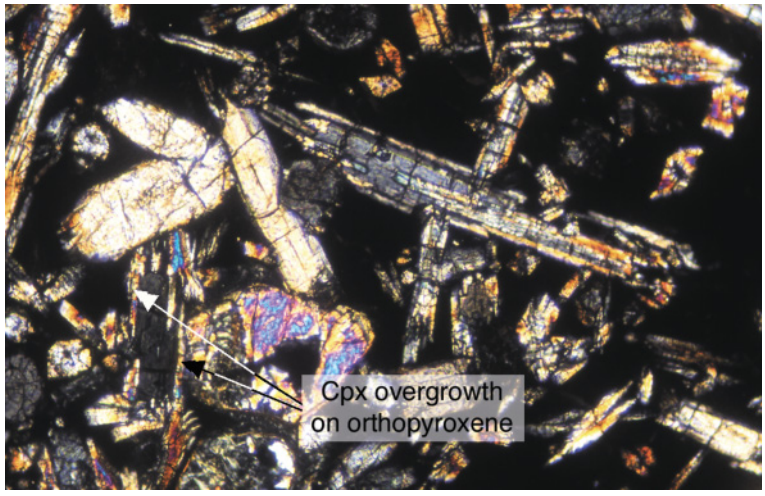
6.2 Close-up of oscillatory zoning in a complex plagioclase phenocryst (clearest in top half) from Cereme andesite lava. Crossed polars, field of view 0.5 mm wide. Courtesy of C.M.H. Edwards.



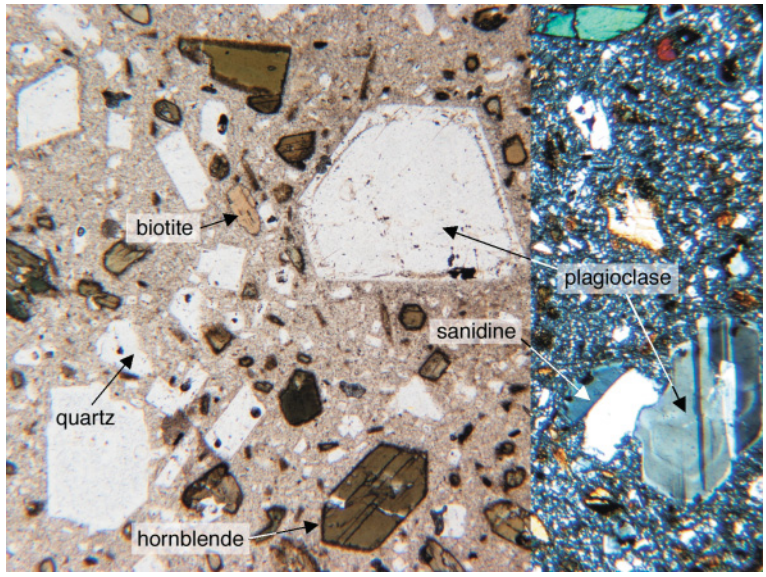
6.3 Basaltic andesite (Tanna, Vanuatu). Right PPL, left XP, field of view 2 mm wide. Note the swallowtail terminations of the plagioclase crystal (centre). The high-birefringence crystal (left) is olivine.



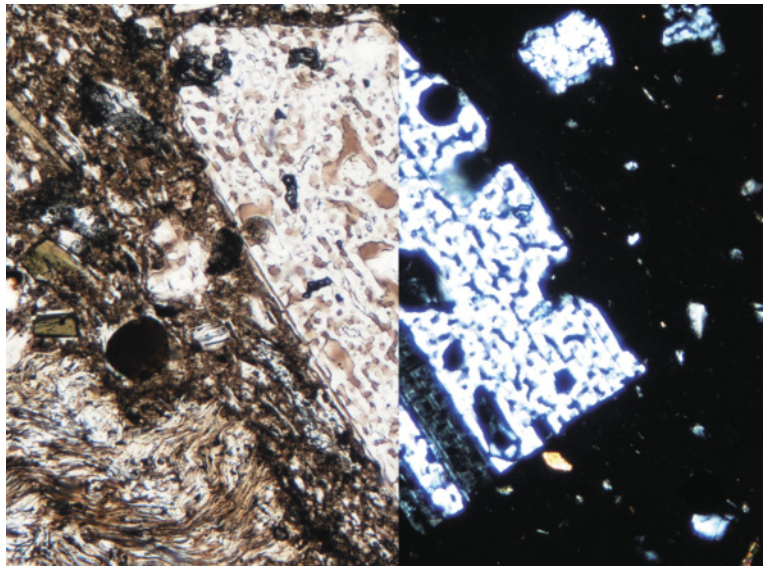
6.4 Enstatite-microphyric boninite lava from Chichijima, Bonin Islands, Japan; field of view 1.4 mm wide in total (PPL on left; XP on right). Thin section courtesy of R.N. Taylor, Southampton Oceanographic Institute, UK.



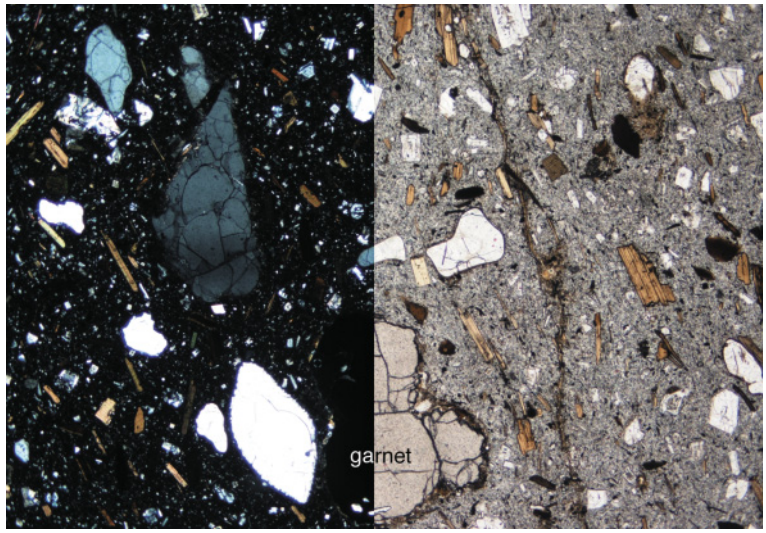
6.5 Overgrowth of clinopyroxene on an enstatite crystal (in extinction) in the same thin section as Plate 6.4. Crossed polars, field of view 0.55 mm wide. Thin section courtesy of R.N. Taylor, Southampton Oceanographic Institute, UK.



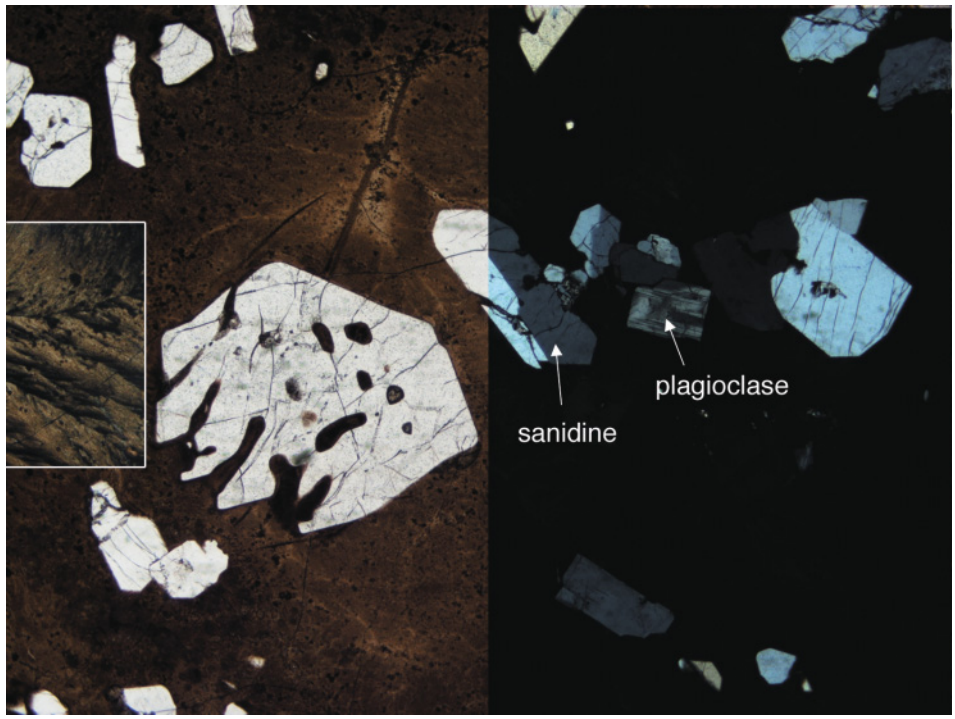
6.6 Plagioclase-phyric biotite hornblende dacite lava (Northland, New Zealand). Note the oscillatory zoning in the plagioclase phenocryst right (cross polars), and the overgrowth delineated by a zone of small inclusions in the large central plagioclase phenocryst. Field of view 2.7 mm wide in total.



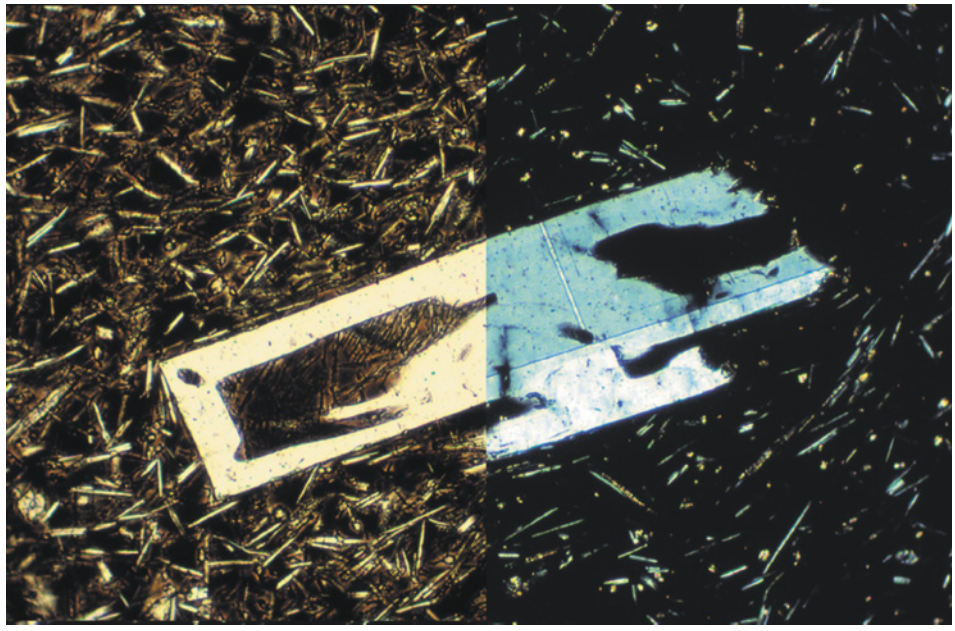
6.7 Relatively coarse **sieve texture** (abundant light brown 'melt' (glass) inclusions PPL) in a plagioclase clast in a welded rhyolitic lapilli tuff, Battleship Rock, Valles Mts, New Mexico (left PPL, right XP): note also the crystal's embayed outline. Field of view 0.9 mm wide.



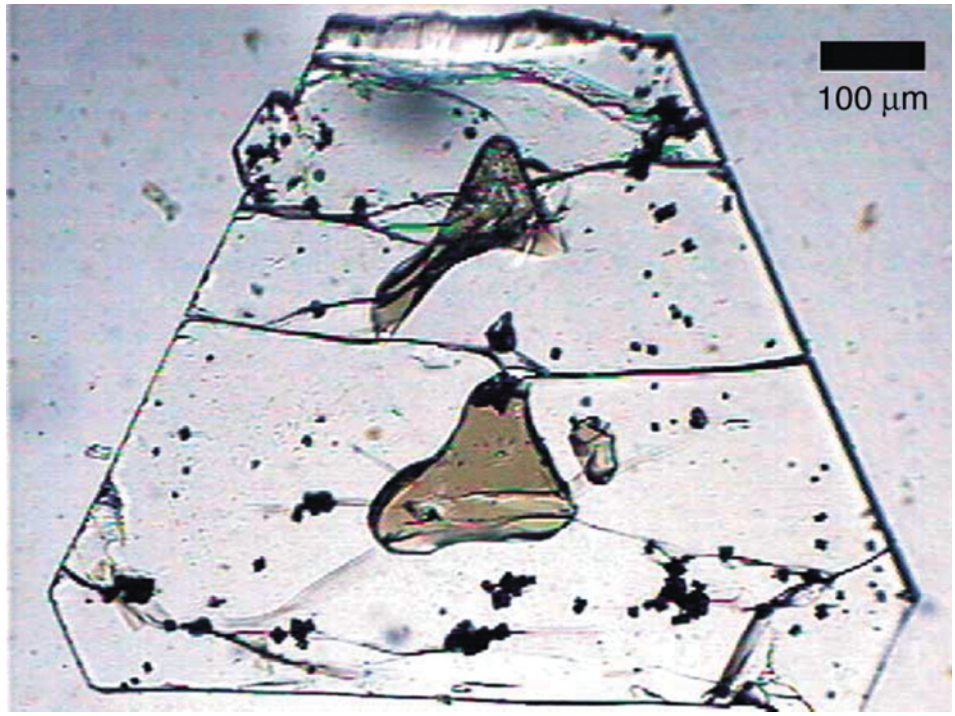
6.8 Garnet-bearing biotite dacite from the Miocene Cerro de Hoyazo volcano in SE Spain (right PPL, left XP). Field of view 5.4 mm wide.



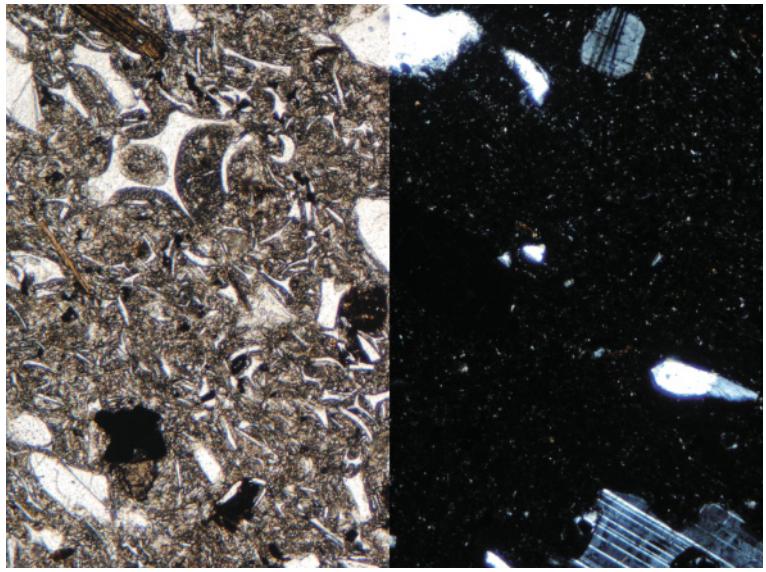
6.9 Rhyolite showing a simple-twinned sanidine crystal, a multiply twinned plagioclase crystal and a partially resorbed quartz phenocryst (Taylor Creek Rhyolite, New Mexico; field of view 5.4 mm wide). Left PPL, right XP; the framed area on the extreme left is shown in crossed polars, over-exposed to emphasize the birefringence associated with spherulitic devitrification of the glassy matrix.



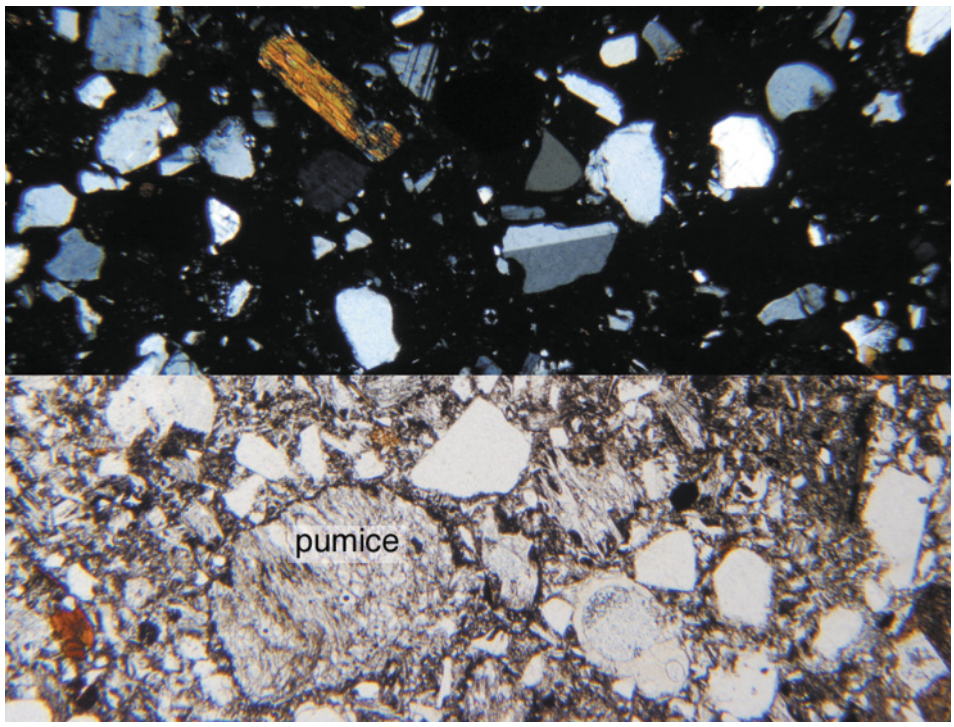
6.10 Pitchstone showing a skeletal sanidine microphenocryst and feldspar microlites in a glassy matrix. (Sill from Ross of Mull, Hebrides, Scotland; Left PPL, right XP, field of view 0.54 mm wide in total.)



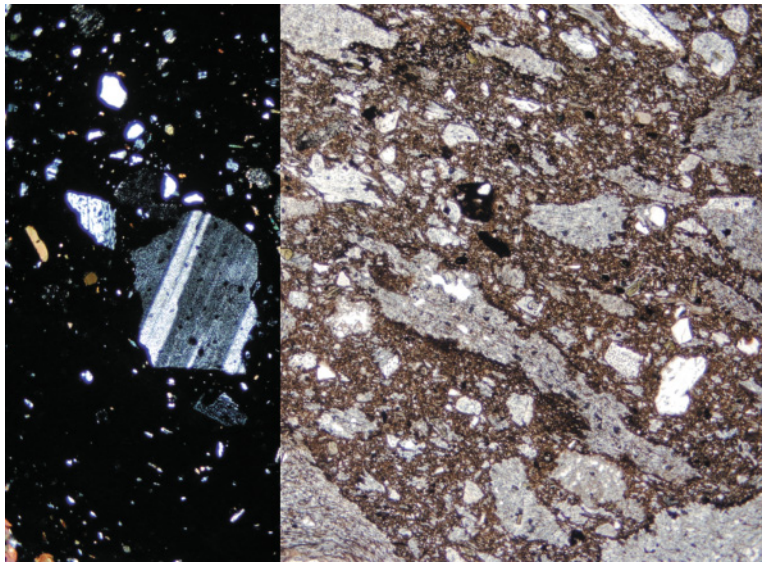
6.11 Melt inclusions in an olivine crystal separated from a basaltic clast from Blue Lake Maar, Oregon: image courtesy of Paul Wallace (Metrich and Wallace, in press).



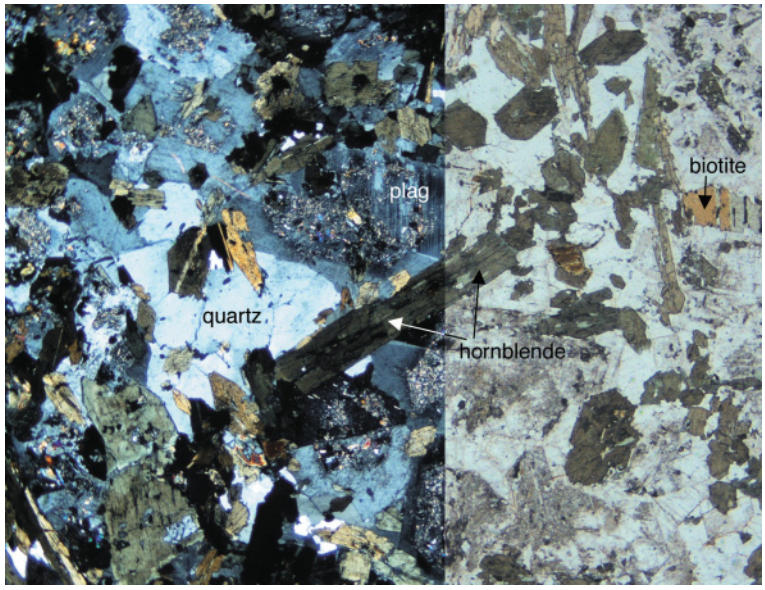
7.1 Toba Tuff from the 74 ka BP eruption, showing crystal fragments of plagioclase, sanidine, quartz, biotite and opaques and cuspate glass shards (left PPL, right XP). Field of view 1.3 mm wide. Sample courtesy of C. Tiltman, SE Asia Research Group, University of London.



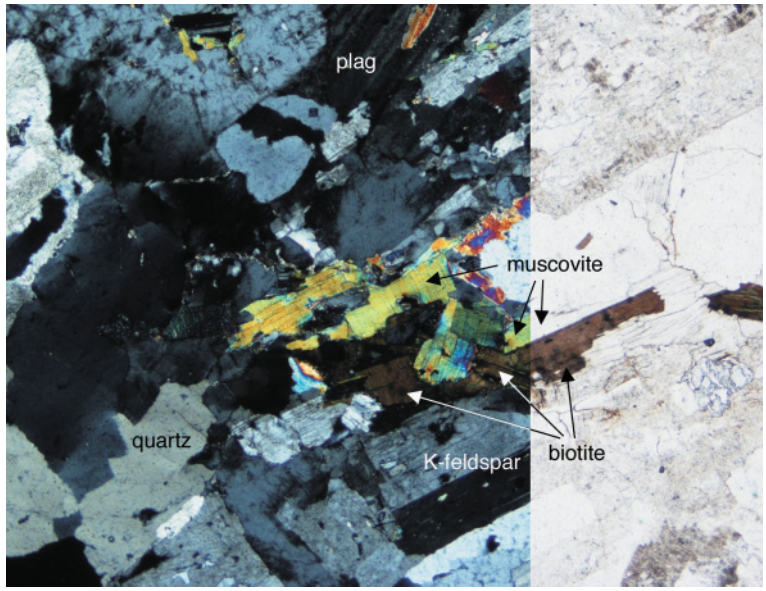
7.2 Unwelded lapilli-tuff (Kneeling Nun ignimbrite), New Mexico (lower part PPL, upper XP). Undeformed, smooth and ragged pumice clasts (textured particles in PPL) and irregular grains of sanidine, plagioclase, quartz, biotite and opaques of all sizes are set in a matrix of glass shards. Field of view 2.7 mm wide.



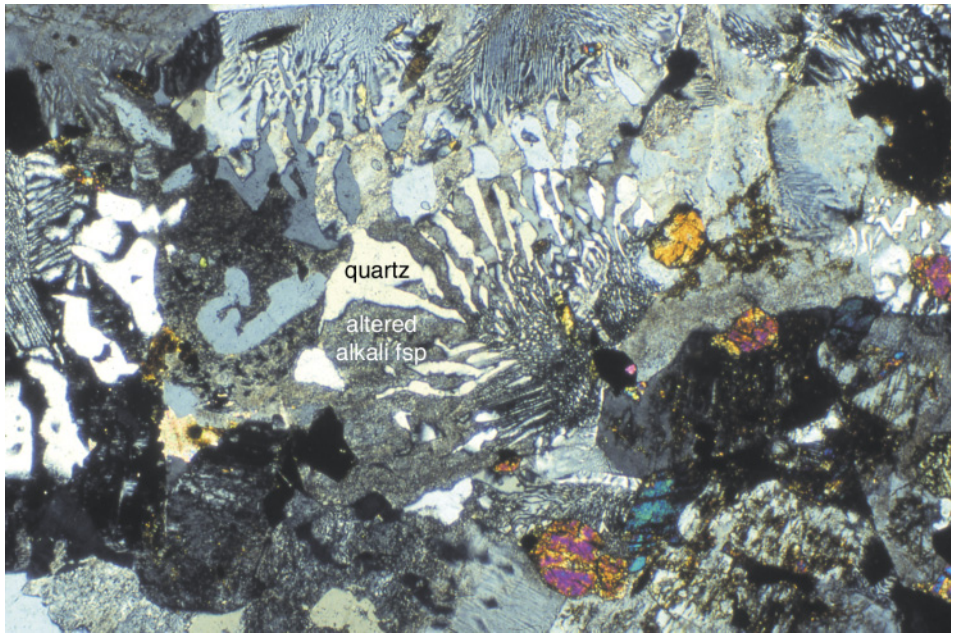
7.3 Eutaxitic texture in welded lapilli-tuff (Battleship Rock ignimbrite), Jemez Mountains, New Mexico (left XP, right PPL). Flattened pumice lapilli (fiamme) define a foliation oblique to the edges of the picture; they and broken crystals of plagioclase, sanidine, biotite and glass shard are set in an altered brown ash matrix. Field of view 5.3 mm wide.



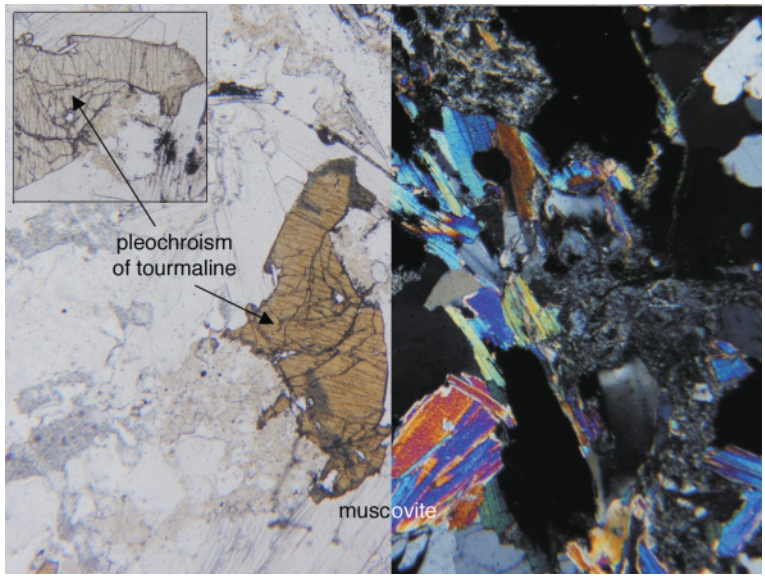
8.1 Hornblende quartz diorite (left crossed polars, right PPL; field of view 4.8 mm wide); plagioclase is extensively **sericitized**, making it speckly in crossed polars and turbid in PPL. Minor intrusion, Ardara pluton, Ireland (slide courtesy A. Hall).



8.2 Subsolvus two-mica granite, Albtal, Schwarzwald, Germany (crossed polars left, PPL right; field of view 3.8 mm wide). Note the dark spots (pleochroic haloes surrounding U,Th-rich accessory mineral inclusions) in biotite crystals.



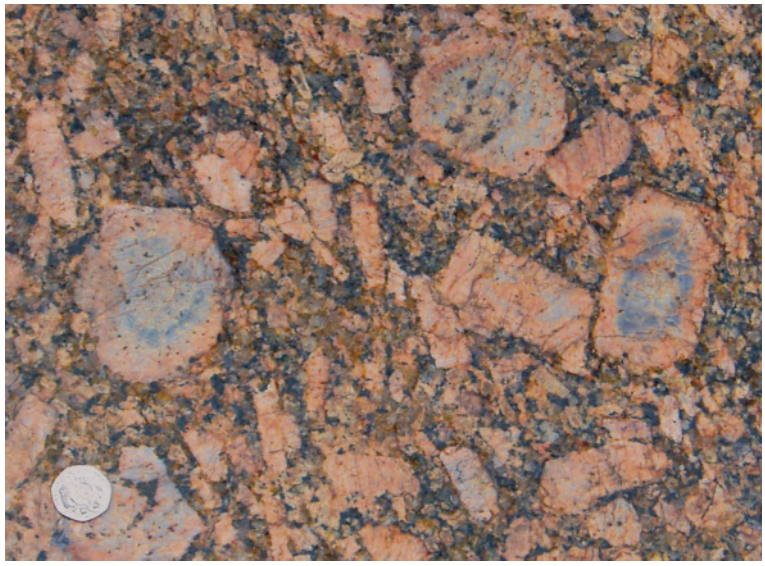
8.3 Micrographic texture in granophyre, Isle of Mull, Scotland; the small grains with second-order interference colours are altered mafic minerals (crossed polars; field of view 1.3 mm wide).



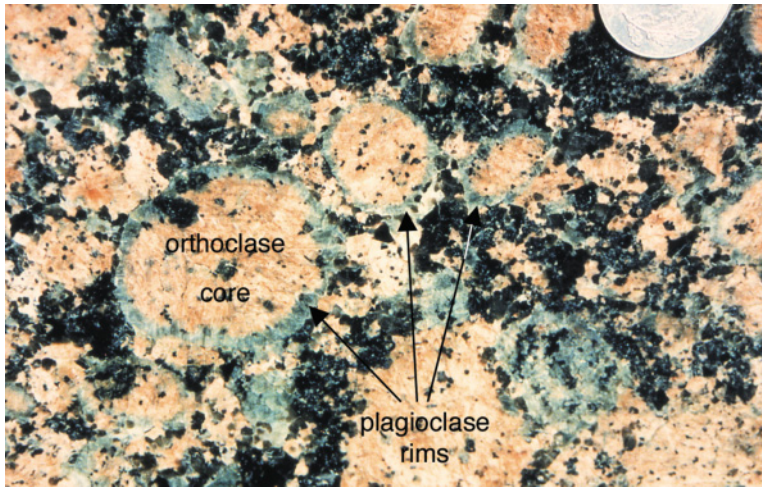
8.4 Tourmaline muscovite granite: left PPL (inset shows tourmaline crystal rotated to demonstrate pleochroism), right XP. Cornwall, UK (section courtesy of D. Alderton).



8.5 Polished slab of orbicular diorite (origin unknown); inset shows one orb in detail. Pen 14 cm long, 1.2 cm wide. Note how the middle layers of several orbs are defined by the radial growth of black acicular crystals; this is present though less conspicuous in the outer layer of the enlarged orb too. Large black crystals in the core also show partial radial arrangement.



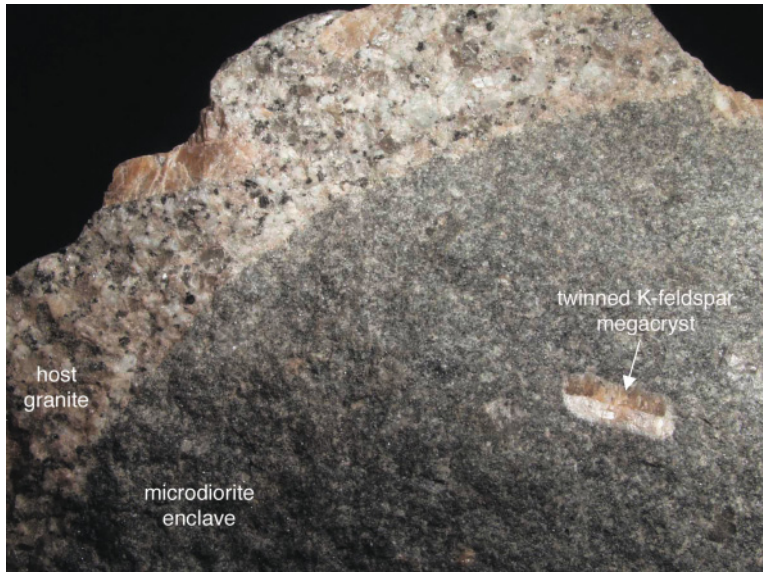
8.6 Mantled plagioclase texture in polished granite slabs (origin unknown; ornamental paving, Grosvenor Square, London). 20p coin 1.2 cm in diameter.



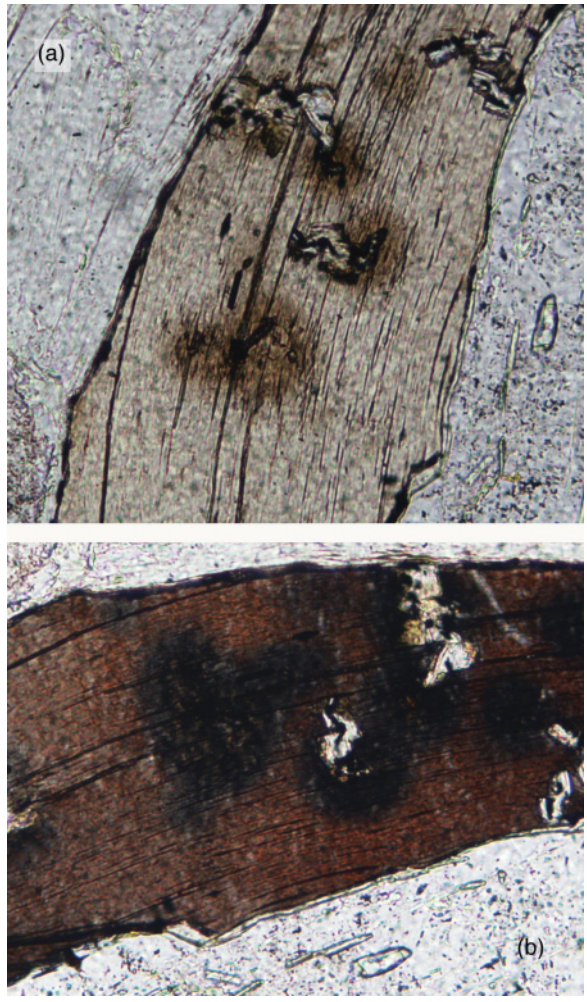
8.7 Polished surface of rapakivi granite slab (origin unknown) in the forecourt of the Geological Museum, Copenhagen; coin approx 1.5 cm in diameter. Corroded megacrysts of K-feldspar (pink) are mantled by greyish plagioclase.



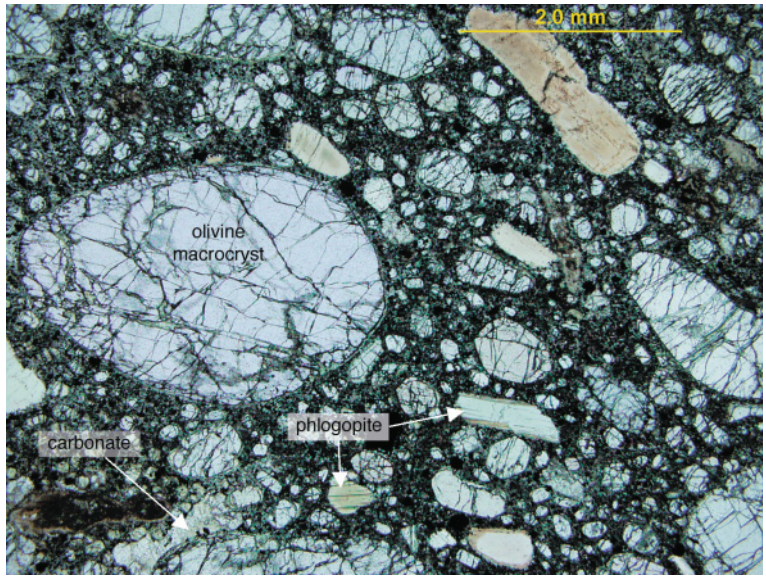
8.8 K-feldspar megacryst in microdiorite enclave in a hand-specimen of Shap granite, UK; the simple twinning is discernible in hand-specimen owing to differential reflection from the two twin individuals. Steel bar 1 cm long (photo K. D'Souza).



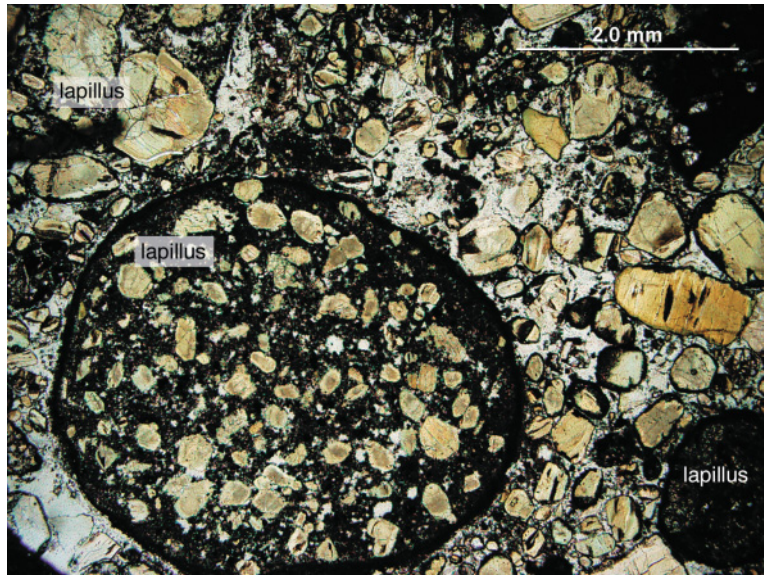
8.9 Margin of microdiorite enclave in hand-specimen of Shap granite; K-feldspar megacryst in the enclave is about 1.7 cm long (photo K. D'Souza).



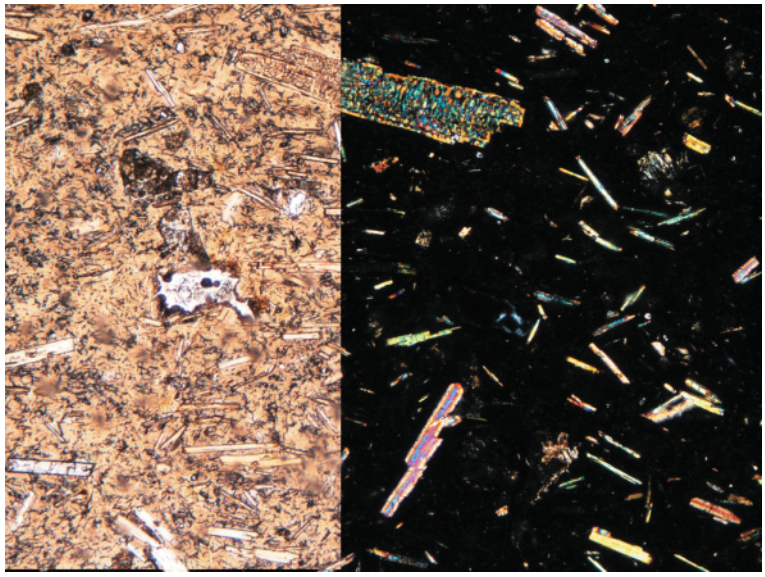
8.10 Pleochroic biotite crystal containing inclusions surrounded by **pleochroic haloes** resulting from radiation damage.



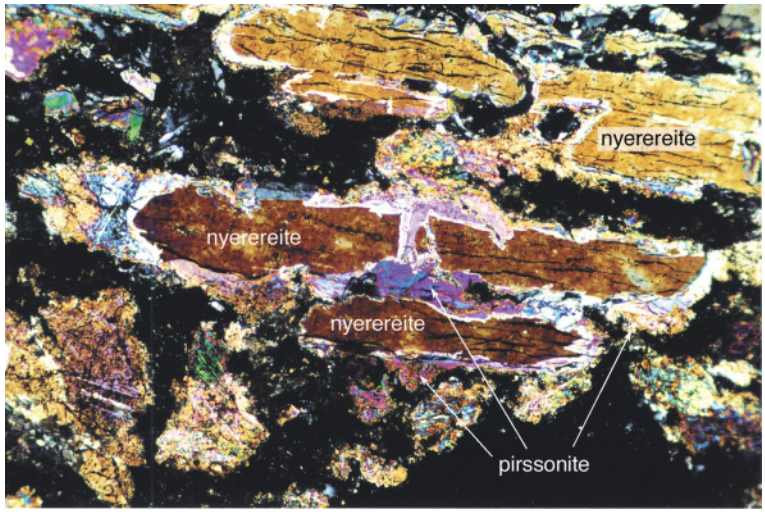
9.1 Hypabyssal kimberlite from Wesselton Mine, South Africa, consisting of rounded olivine macrocrysts of various sizes, together with crystals of phlogopite (arrowed). Apart from patches of carbonate, the groundmass minerals are too fine-grained to identify. PPL, field of view 7 mm wide. Image courtesy of R.H. Mitchell.



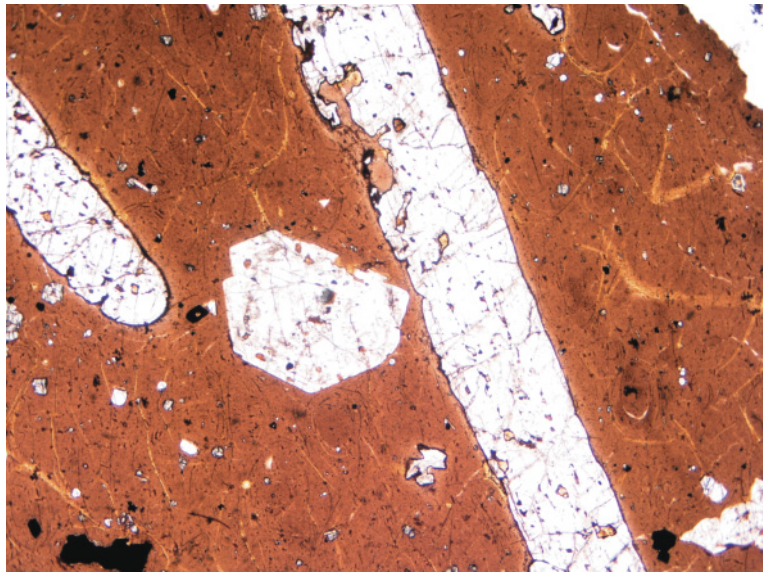
9.2 Tuffisitic or 'massive volcaniclastic kimberlite' (MVK, Sparks et al., 2006) from Kao diatreme in Lesotho, southern Africa. The rounded object lower centre with a texture similar to Plate 9.1 – though olivine macrocrysts within are smaller and more serpentinized – is a juvenile pelletal lapillus. It is surrounded by smaller lapilli in a matrix of macrocrysts and crystal fragments. PPL, field of view 7 mm wide. Image courtesy of R.H. Mitchell.



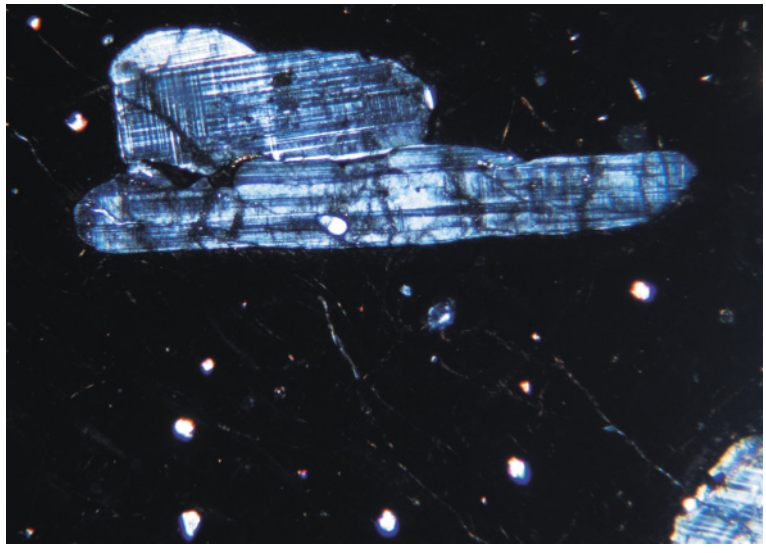
9.3 Phlogopite **hyalo**-lamproite lava from La Ciudad, Almeria, SE Spain. The speckly microphenocryst near the top and most of the smaller crystals in this field of view are mildly pleochroic phlogopite; its straight extinction is illustrated by the horizontal crystal at the centre of the image traversing the PPL/XP boundary. PPL (left) and crossed polars (right); overall field of view 1.3 mm wide.



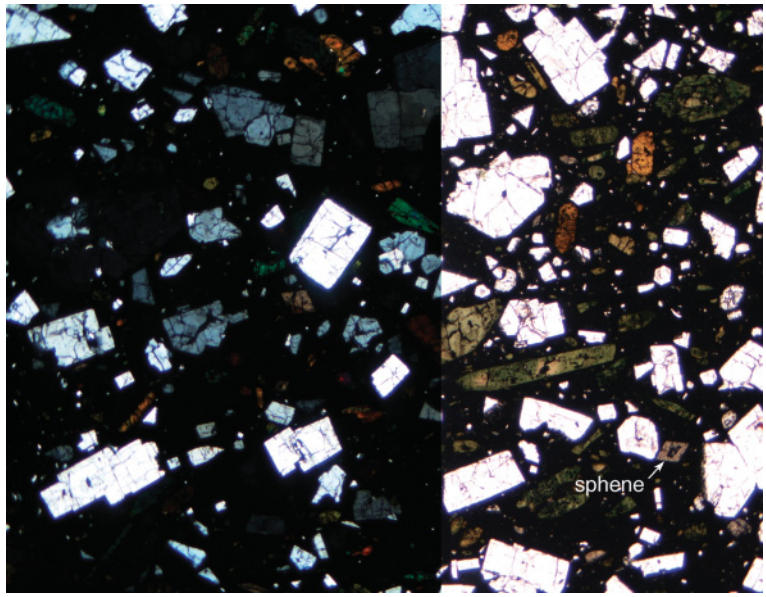
9.4 Elongate phenocrysts of primary nyerereite [$Na_2Ca(CO_3)_2$] rimmed by the hydrous alteration product pirssonite [$Na_2Ca(CO_3)_2.2H_2O$] in natrocarbonatite lava from Oldoinyo Lengai erupted in 2000, reproduced from Zaitsev and Keller (2006) with kind permission of the authors and Elsevier. The dark areas are groundmass (consisting of fluorite with magnetite, sulphides and apatite) and holes in the slide where soluble minerals (such as gregoryite and sylvite) have dissolved during weathering. Crossed polars, field of view 1.37 mm wide.



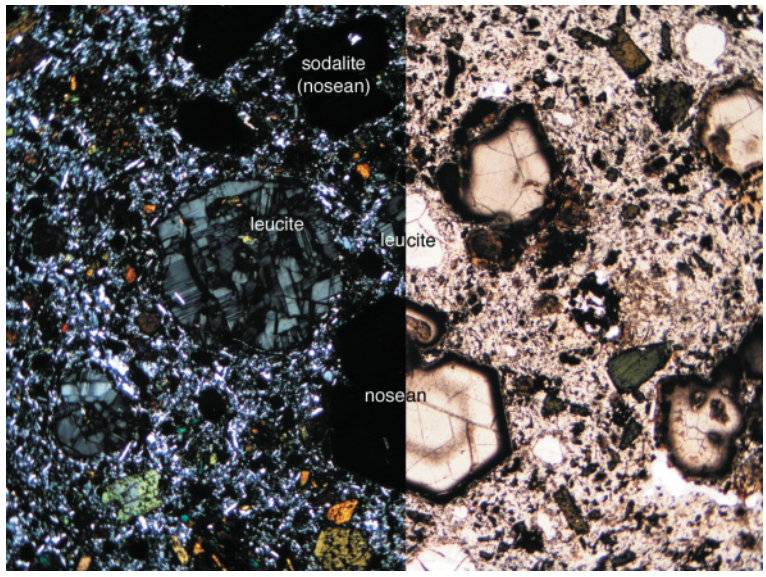
9.5 **Hyalo**-phonolite lava, Mt Kenya. Large phenocrysts of anorthoclase (here partially resorbed and with dark borders) and equant nepheline in a brown glassy matrix showing incipient **perlitic** cracks. Note the embayment into anorthoclase near the top of the image where melt has locally redissolved the crystal; pools of glass within crystals may result from similar embayment from above or below the plane of section. PPL; width 5 mm. Sample courtesy of Jamie Walton.



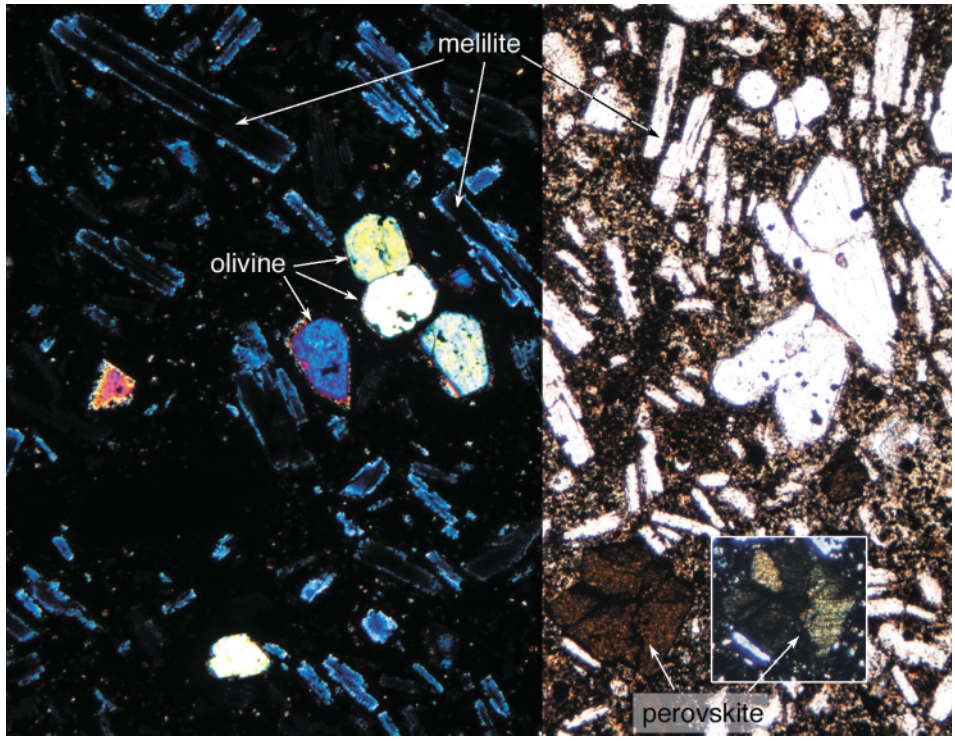
9.6 Fine-scale cross-hatched multiple twinning characteristic of anorthoclase in the phonolite lava shown in Plate 9.5 – see Box 6.1. Crossed polars, width of field 1.8 mm.



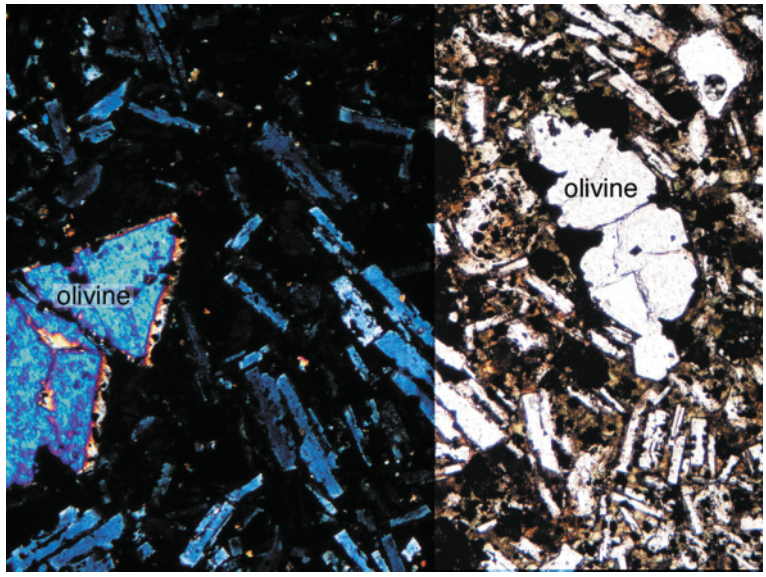
9.7 Seriate-textured nephelinite (locality unknown) containing low birefringence rectangular (occasionally 6-sided) nepheline, green-brown sodic pyroxene (pleochroic aegirine–augite, Box 9.1), and one diamond-shaped brown sphene crystal (right) in a dark glassy groundmass. The rock is devoid of feldspar. Crossed polars (left) and PPL (right), field of view 5 mm wide.



9.8 Leucite sodalite phonolite, Reiden, Germany. Leucite forms the large rounded phenocrysts having low relief and low birefringence, and exhibiting complex multiple twinning. Sodalite (variety nosean; Fig. 9.1.1) forms higher-relief euhedral isotropic phenocrysts, here with distinctive brownish rims (and occasional internal growth zones). The green micro-phenocrysts are sodic pyroxene (Box 9.2). The holocrystalline groundmass consists of the same minerals plus feldspar microlites too fine to show diagnostic twinning. Crossed polars (left) and PPL (right), field of view 5 mm wide.



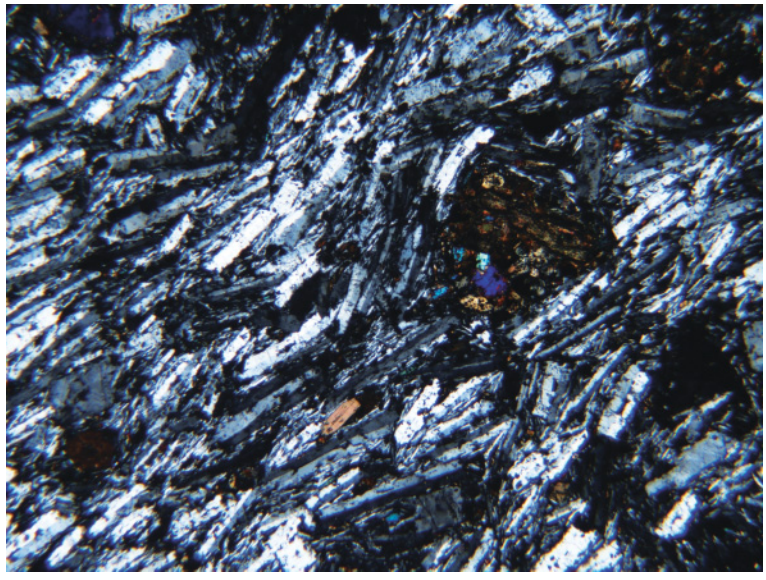
9.9 Olivine melilitite from Bufumbira, Western Rift, Uganda (thin section courtesy of B.G.J Upton): laths of melilite showing anomalous blue-grey interference colour at the margins, equant olivine crystals and one crystal of perovskite are surrounded by brown glassy groundmass. The inset shows perovskite multiple twinning in crossed polars. Crossed polars (left), PPL (right): width of field 1.3 mm.



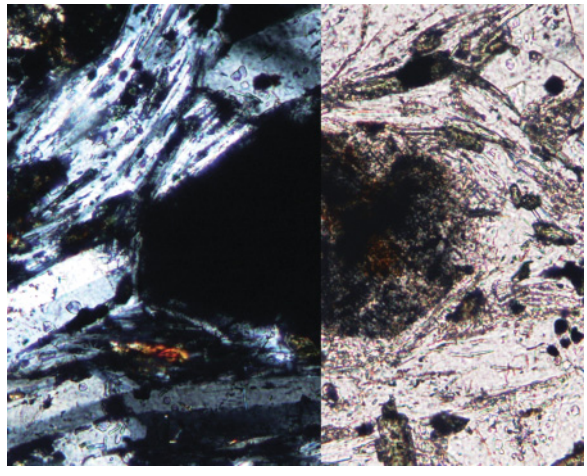
9.10 Olivine melilitite lava from Armykon Hill in northern Tanzania (thin section courtesy of J.B. Dawson). Melilite laths and olivine crystals are set in a groundmass of the same minerals, opaques and altered glass. Crossed polars (left), PPL (right): width of field 1.3 mm.



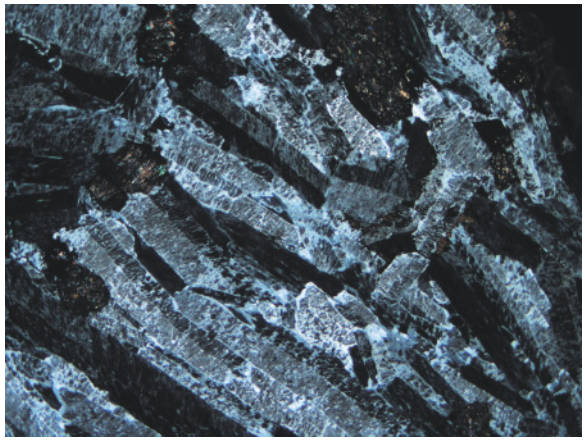
9.11 Hawaiite lava, Canary Islands. Note oscillatory zoning in lower plagioclase phenocryst. Circular features in PPL are vesicles. Crossed polars (left), PPL (right): width of field 5.2 mm.



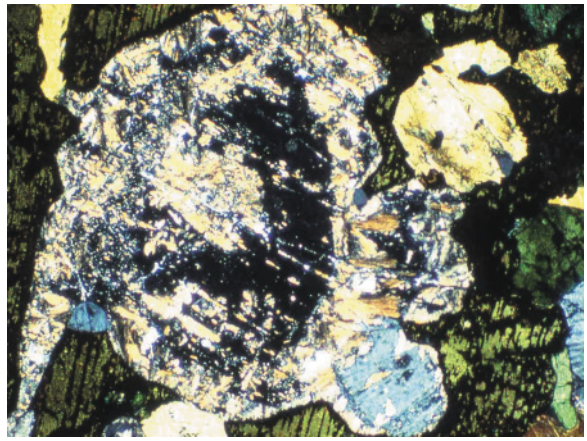
9.12 Trachytic texture in a phonolite lava from Puy Griou, Cantal, France. Note how the sub-parallel sanidine laths sweep around the larger crystal. Crossed polars, field of view 2.7 mm wide.



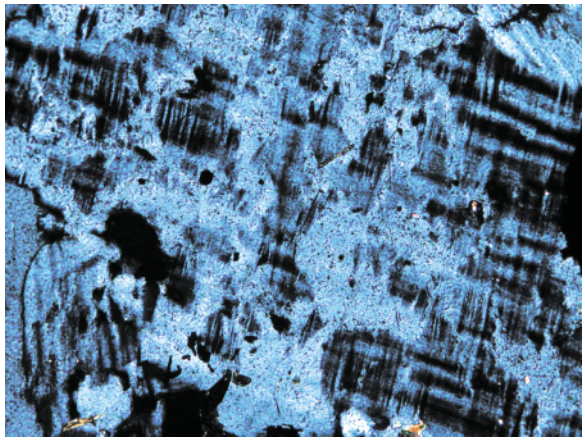
9.13 A crystal of nosean in the phonolite shown in Plate 9.12. Crossed polars (left), PPL (right); width of field 0.53 mm. The isotropic crystal is packed with opaque inclusions, except for a clear rim.



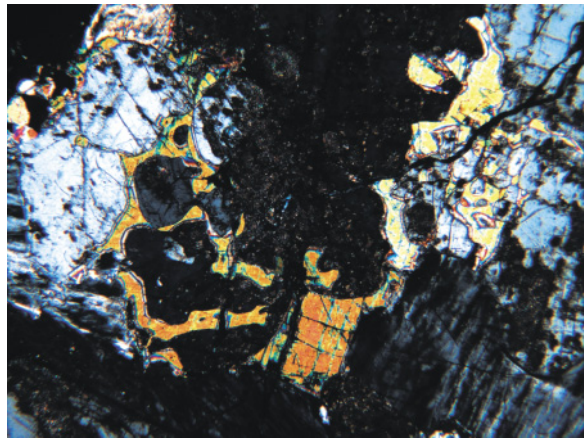
9.14 Igneous **lamination** in a **hypersolvus** syenite (consisting of simple-twinned **perthite** crystals). Grønnedal-Íka complex, South Greenland. Crossed polars, field of view 5 mm wide.



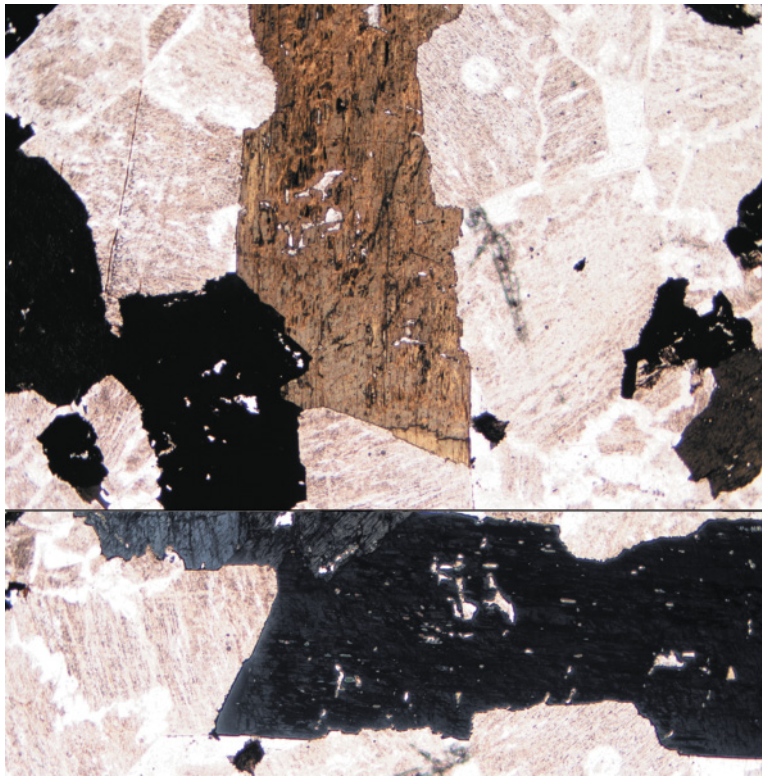
9.15 Crystals of nepheline (one in extinction position) partially altered to **sericite** in nepheline syenite, Grønneda-Íka complex, South Greenland, associated with sodic pyroxene (green), altered biotite (green with opaques along cleavage) and perthite (grey on extreme right). Crossed polars, field of view 0.7 mm wide.



9.16 Wispy albite lamellae in a tartan-twinned microcline host of perthite in nepheline syenite. Crossed polars, field of view 0.5 mm wide.



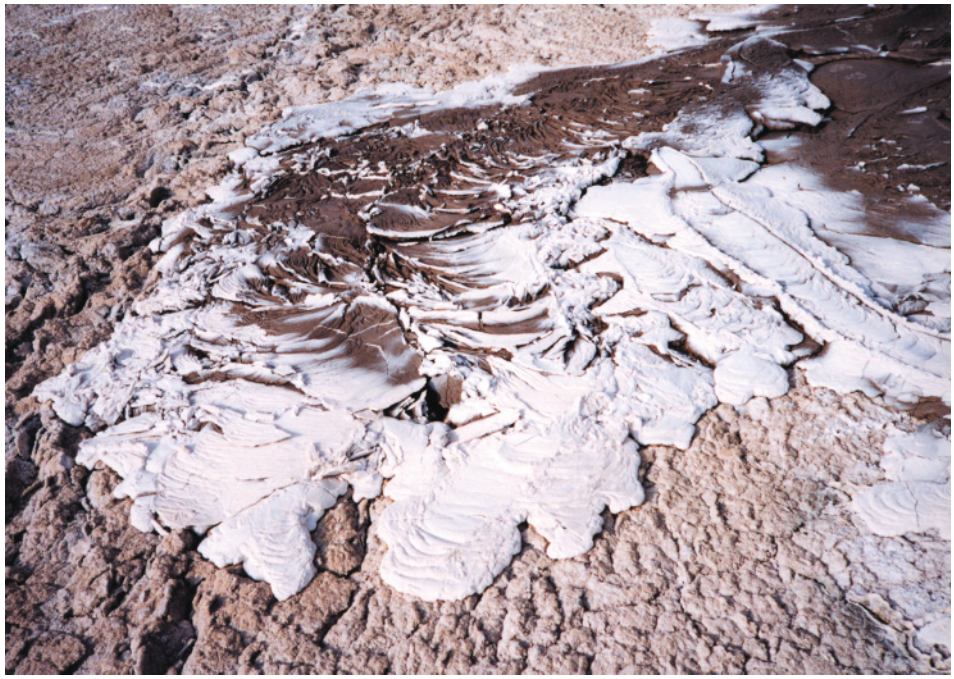
9.17 Cancrinite (higher interference colours) formed by late-stage reaction of nepheline with carbonate-bearing melt in a nepheline syenite; Grønneda-Íka, S Greenland.



9.18 Beige-to-inky blue pleochroism of riebeckite in syenite, Kûngnât complex, S Greenland; width of view 5.4 mm. The two views show the same grain rotated through 90°.



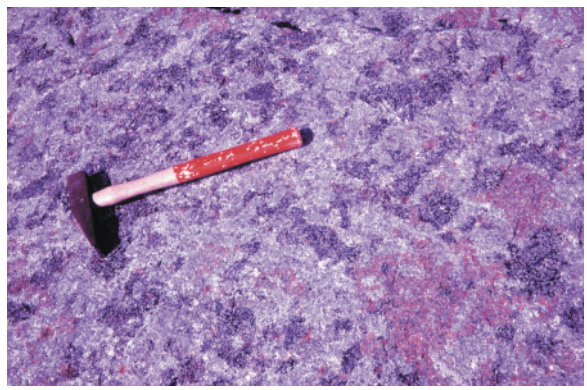
9.19 The fairytale world of the Oldoinyo Lengai crater, northern Tanzania. A thin flow of fresh black natrocarbonatite lava spreads across white crater floor consisting of altered natrocarbonatite, beside steep-sided carbonatite spatter cones in August 1998 (photo Fred Belton, reproduced by kind permission).



9.20 A thin lobe of **pahoehoe** natrocarbonatite lava undergoing the characteristic transition from the initial dark appearance of fresh lava to the white hydrated state, progressing from the margins to the centre. Oldoinyo Lengai crater, Tanzania, August 1998 (photo Fred Belton reproduced by kind permission). Field of view approximately 2 m left to right.



9.21 Black (arfvedsonite-rich), pink (eudialyte-rich) and white (nepheline- and alkali feldspar-rich) layers in peralkaline nepheline syenite cumulate rock ('kakortokite') in the lower exposed part of the Ilímaussaq complex, S Greenland. Macrorhythmic layering can be seen in the cliffs behind. Hammer shaft 45 cm.



9.22 Eudialyte (pink), arfvedsonite (black) and alkali feldspar (white) oikocrysts surrounding smaller cumulus sodalite crystals (grey-blue) in peralkaline nepheline sodalite syenite ('naujaite'), Ilímaussaq complex, S Greenland.

following account of this eruption from contemporary accounts:

> *'The eruption started on 3 August 1888. For the first 3 days only old material, stripped from the conduit walls, was erupted; in other words, the Fossa's throat was being cleared. … The ejected material was hot, as it is reported to have set fire to hedges. However during the next 13 days the amount of fresh magma increased until it became the dominant material ejected. By this time there were large masses of plastic ejecta, rounded in form, elongated or flattened, typically showing a breadcrust surface texture* [Fig. 7.4b]. *It was clear to the geologists observing the activity that the introduction of new magma to the system was causing the eruption. Despite this, there has been argument since about the role of primary magma. … The situation is confused by the fact that a high percentage of non-juvenile material was ejected during this eruption, lithic fragments (often) being coated by a layer of fresh lava. …*
>
> *The rate and violence of the explosions were variable. They could be as frequent as one every minute or two, throwing up columns of ash as high as 5000 m or more. … There were three paroxysmal explosive events, on 4 August 1888, 26 December 1889 and 15 March 1890.'* In the last instance, *'a violent explosion accompanied by an enormous bang occurred in the evening … the sky glowed red for some 3 minutes after the explosion. Clearly this explosion had removed the plug of chilled lava at the top of the magma column in the conduit, exposing fresh magma which over the next few minutes was cooled … to develop a new crust.'*[7]

Vulcanian eruptions are commonly described as 'throat-clearing eruptions' because, as in the case of the Fossa eruptions, they eject a high proportion of **lithic** material (pre-existing solidified rock blocking the vent) as well as **juvenile** (new magmatic) tephra. They form small-volume (<1 km^3) but widely dispersed, thinly bedded deposits (Fig. 7.2c; Wright et al., 1980). The juvenile material is commonly intermediate to acidic in composition, and such ejecta continue vesiculating during and after flight: the on-going expansion cracks the chilled skin, creating the 'breadcrust' effect. Figure 7.4(a) shows the eruption column of a vulcanian explosion at the Soufrière Hills volcano on Montserrat, one of a series of explosions that occurred in 1997 at approximately 10 hour intervals, lofting ash up to 12 km into the air.

Plinian eruptions

Whereas hawaiian, strombolian and vulcanian eruptions are named after volcanic islands or individual volcanoes, plinian eruptions are named after Pliny the Younger, whose account of the AD 79 eruption of Vesuvius provides the oldest surviving description of such an eruption. In August of that year, he was staying at the villa of his uncle, Caius Plinius ('Pliny the Elder', himself a prolific writer), in Misenum on the western side of the Bay of Naples, 30 km west of Vesuvius. He wrote:[8]

> *'On 24 August, in the early afternoon, my mother drew his* [Caius Plinius's] *attention to a cloud of unusual size and appearance … It was not clear at that distance from which mountain the cloud was rising (it was afterwards known to be Vesuvius); its general appearance can be best expressed as being like an umbrella pine,*[9] *for it rose to a great height on a sort of trunk and then split off into branches, I imagine because it was thrust upwards by the first blast and then left unsupported as the pressure subsided, or else it was borne down by its own weight so that it spread out and gradually dispersed. Sometimes it looked white, sometimes blotched and dirty, according to the amount of soil and ashes it carried.'*
>
> Later in his account Pliny refers to a courtyard nearer to the volcano being '*full of ashes mixed with pumice stones*' and '*the danger of falling pumice stones, even though these were light and porous. … As a protection against them,* [people] *put pillows on their heads tied down with cloths. … Soon afterwards the cloud sank down to earth and covered the sea. Ashes were falling* [on Misenum] *and … a dense black cloud was coming up behind us, spreading over the earth like a flood*.'

[7] Reproduced here by kind permission of the publisher, the Geological Society of London.

[8] translated from the Latin by Radice (1963); reproduced here by permission of Penguin Books Ltd.

[9] *Pinus pinea* (US 'stone pine'), an umbrella-shaped tree common in southern Italy; see Fig. 7.4g.

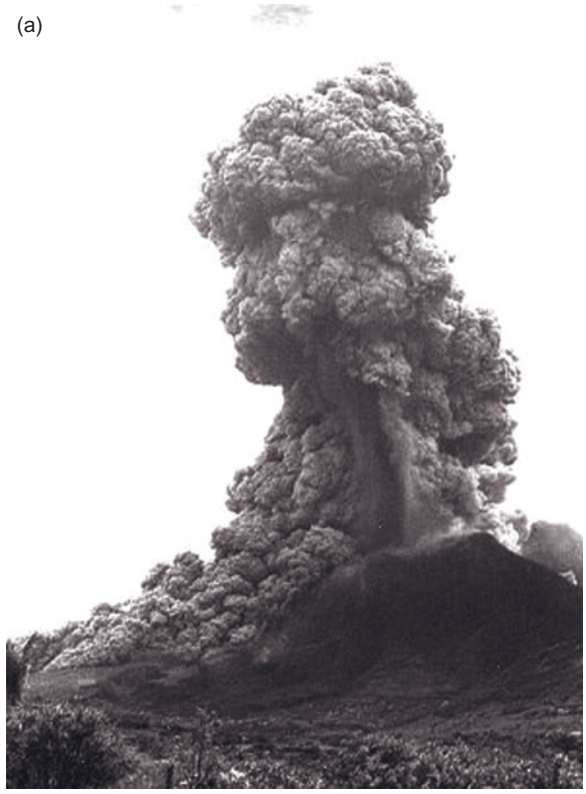






Fig. 7.4 (a) Vulcanian eruption at the Soufrière Hills volcano, Montserrat in October 1997 (photo by kind permission of the Montserrat Volcano Observatory). (b) Breadcrust bomb on the flanks of Vulcano, Aeolian Islands (photo D. Millward; hammer 35 cm). (c) 18 May 1980 plinian eruption of Mount St Helens, Washington, USA (photo by Austin Post, Cascades Volcano Observatory).





Fig. 7.4 *Continued* (d) Plinian eruption column of Pinatubo volcano seen from former Clark Air Base, Philippines in 12 June 1991 (photo by Dave Harlow). (e) Pyroclastic density current descending from the 7 August 1980 plinian eruption column of Mt St Helens (photo by P.W. Lipman).





Fig. 7.4 *Continued* (f) Dacite lava dome in August 1981 in the post-May 1980 crater of Mount St Helens (photo by Lyn Topinka). (g) Umbrella pine like that referred to in Pliny's account of Vesuvius 79AD. Photographs (c), (d), (e) and (f) are reproduced courtesy of the US Geological Survey.

Pliny's account aptly summarizes what we recognize today as the key features of a plinian eruption:

- a sustained explosive eruption continuing for many hours, initially producing a buoyant **eruption column** that extends to a high altitude (Fig. 7.4c,d) – commonly 15–40 km – and is capped by an 'umbrella' or anvil (Fig. 7.6a), marking the altitude at which the ash cloud is no longer buoyant – here it spreads out laterally rather than rising further (hence the reference to the umbrella pine);
- the dominance of pumice and ash in the tephra raining from the cloud;

- the tendency for the cloud to collapse and form ground-hugging density currents.

Plinian eruptions, being highly explosive, are characteristic of evolved magmas (dacite, rhyolite, phonolite) that possess the highest volatile contents. They differ from vulcanian eruptions in being sustained eruptions with higher eruption columns (>15 km), producing copious volumes of pumice that – in the largest eruptions – represent the ejection of hundreds or even thousands of cubic kilometres of magma during the course of a few hours.

Nomenclature of pyroclasts and pyroclastic deposits

Pyroclasts are solid fragments of magma or magma-derived material (rock, crystals, pumice) formed by fragmentation at high (though not always magmatic) temperatures. Most pyroclasts form as hot **juvenile** products of explosive eruptions, the high magma volatile contents lying behind such eruptions being manifest in the form of a high vesicle content. Vesiculation reaches a maximum in **pumice**, which may have a bulk density low enough for it to float on water[10] (until it becomes water-logged). Pumice is typically intermediate to acid in composition. **Scoria** is the term used for vesicular pyroclasts of basaltic or andesitic magma.

Pyroclast grade and pyroclastic deposits

The terminology used to describe pyroclasts is based on the same size ranges as those used to characterize epiclastic sedimentary deposits (Table 7.2).

For describing rocks made up of pyroclastic material, the International Union of Geological Sciences (IUGS) (Le Maitre, 2002) uses the nomenclature of Fisher (1966) shown in Fig. 7.5.

[10] Rafts of pumice, sometimes kilometres in diameter, occasionally form on the ocean surface as a result of submarine or island eruptions. Recent examples of pumice rafts formed in association with a submarine eruption at Home Reef volcano near to the Tongan island of Late in August 2006.

Table 7.2 Nomenclature of pyroclasts.

Pyroclasts		*Diam. / mm*	*Φ*	*Epiclastic equivalent*
blocks or bombs*	coarse			boulders
		256	-8.0	
	fine			cobbles
		64	-6.0	
lapilli				pebbles
		2	-1.0	
ash	coarse			sand
		1/16	+4.0	
	fine			silt

* Bombs are pyroclasts in this size-range with a distinctive form related to flight or impact.

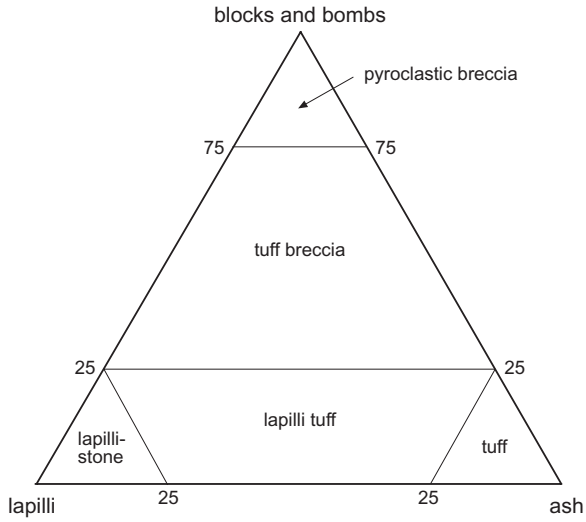


Fig. 7.5 Descriptive nomenclature for pyroclastic rocks after Fisher (1966).

Fall versus *current*[11] *deposits from plinian eruptions*

Figure 7.6 illustrates two radically different ways in which solid particles in a plinian eruption column are delivered to the ground during the course of such an eruption:

[11] 'Pyroclastic current deposit' as used here embraces both 'flow' and 'surge' deposits distinguished in older terminology.

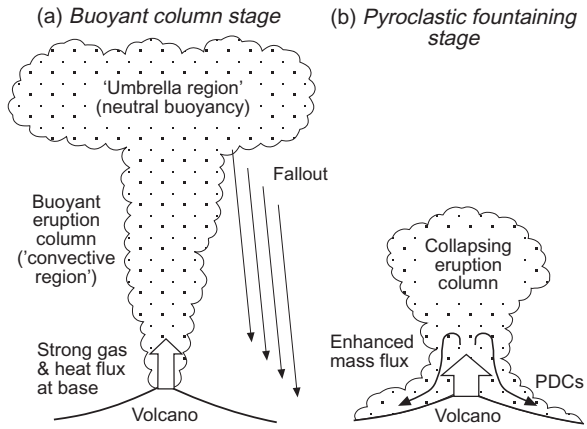


Fig. 7.6 (a) The buoyant-column stage of a plinian eruption when pyroclastic fall deposits form. (b) The collapsing-column or 'fountaining' stage of a plinian eruption when the column is no longer buoyant, and its contents are carried to the ground by pyroclastic density currents (PDCs). Adapted from Gill and Thirlwall (2003) courtesy of the Geologists' Association.

1 In the early stages of the eruption, the eruption column – being hot, buoyant and thrust upward by a sustained gas jet – achieves its maximum height (Fig. 7.6a). Pumice clasts shower down individually from the column and umbrella, covering the ground to form a *pyroclastic fall deposit* (Fig. 7.7a).
2 Towards the climax of a plinian eruption, various factors (increased mass flux, vent widening, etc.) cause the eruption column to become denser than the surrounding air, whereupon it collapses downward en masse (faster than the settling rate of individual clasts) in a process called *column* (or *fountain*) *collapse*: the cloud – lapilli, ash and gas – behaves like a hot dense fluid, sweeping rapidly down the flanks of the volcano as a series of ground-hugging **pyroclastic density currents** (PDCs).[13] The unsorted deposit of pumiceous lapilli-ash that a PDC leaves in its wake is called an **ignimbrite** (one of several classes of *pyroclastic current deposit*).

[12] The concentrated part of a PDC is hidden beneath a billowing, advancing ash cloud (Fig. 7.4e).

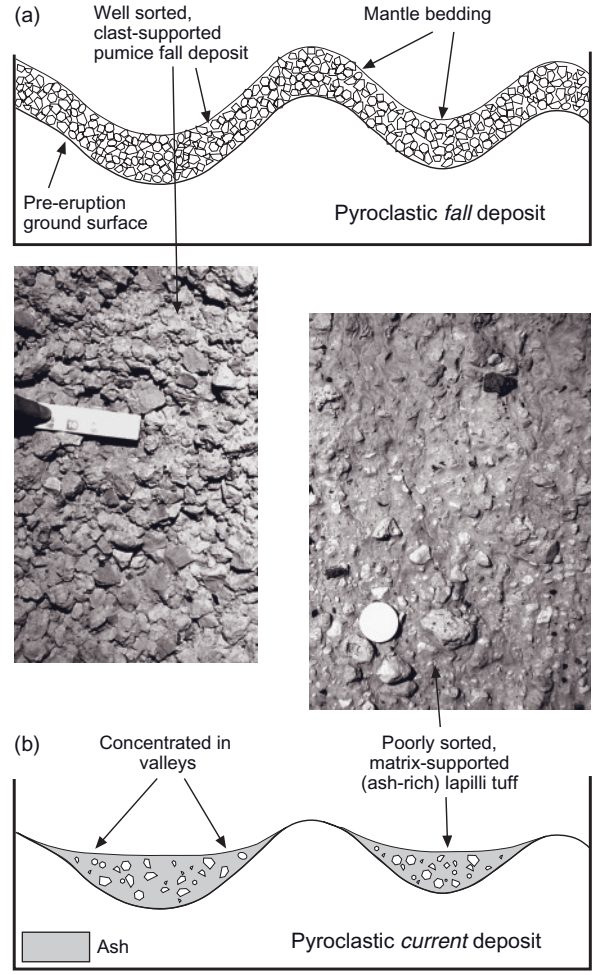


Fig. 7.7 Characteristics of plinian pyroclastic fall and current deposits in the field. (a) A pumice fall deposit shows mantle bedding and consists of well sorted pumice lapilli as shown in the picture (ruler 10 cm in length). (b) a pyroclastic current deposit (ignimbrite) tends to be concentrated in valleys and consists of ash-rich lapilli-tuff (coin 2.3 cm diameter).

The distinction between pyroclastic *fall* and *current* deposits associated with plinian eruptions is summarized in Fig. 7.7 and elaborated below. Fall deposits, formed of pumice particles that have settled through several tens of kilometres of air, are characteristically well sorted and clast-supported, the lack of finer ash giving exposed surfaces a characteristic rough gravel-like appearance (Fig. 7.7a). Fall deposits mantle the volcano and the surrounding terrain with a tephra blanket of

relatively even thickness – so-called 'mantle bedding' (Fig. 7.11a) – which, like mean clast-size, decreases with increasing distance from the volcano. Any ambient wind at the time of the eruption causes the deposit to be extended downwind (Fig. 7.8 inset). The fall deposit from a major plinian eruption may cover many thousands of km^2 (Fig. 7.8).

Ignimbrites deposited by PDCs, on the other hand, are characteristically poorly sorted, consisting of lapilli of pumice dispersed in a matrix of ash (Fig. 7.7b), for which the descriptive term is lapilli-ash or – when lithified – lapilli-tuff (Fig. 7.5); the ash gives exposed surfaces a more even though knobbly appearance when compared to a fall deposit. The distribution of ignimbrite is often dictated by the ground-hugging nature of a PDC: it tends to concentrate in ravines and valleys and thins out over higher ground in between (Fig. 7.7b), though on flat ground a large ignimbrite will form a thick sheet extending across a wide area. The total volume of an ignimbrite sheet often exceeds that of the associated fall deposit upon which it rests.

The phenomenon of pyroclastic density currents is not confined to plinian eruptions. The internal structures of ignimbrites and the other types of pyroclastic current deposits – and the processes they record – are considered in a later section.

Identifying eruptive style from pyroclastic deposits

> '*Explosive eruptions are evanescent phenomena. The presence of a trained observer on the scene is often fortuitous, and conditions are frequently such as to preclude close observation anyway. Fewer than 10% of the explosive eruptions of the present* [twentieth] *century have been reasonably well documented scientifically*.'

These words were written by the eminent volcanologist G.P.L. Walker in 1973 at the beginning of a paper in which he introduced a new approach to characterizing volcanic eruptions, based not on eye-witness accounts like those above (valuable those these may be) but on the dimensions of the deposits they leave behind. Walker's classification – the standard one used today – is based on two measurable attributes of a *pyroclastic fall deposit* (Fig. 7.7):

1. the degree of fragmentation *F* (a surrogate for the intrinsic 'explosiveness' of the eruption); and
2. the area across which the deposit is dispersed – as represented by the dispersal index *D* in km^2 – reflects the height of the eruption column.

The definitions of *F* and *D* are given in Fig. 7.8 and its caption. The higher the eruption column, the more widely the tephra will be dispersed, and therefore the dispersal index – measured in a way that is insensitive to wind speed – serves as a general guide to column height. The fragmentation index is a measure of the explosive intensity of the eruption.

Hawaiian eruptions of fluid basaltic lava – hardly explosive at all, producing tiny volumes of pyroclastic material – appear as one end-member of the 'main *F–D* trend' (the shaded band) in Fig. 7.8. Strombolian eruptions, responsible for innumerable basaltic scoria cones in volcanic areas all over the world, are explosive enough to disperse their products over distances of a kilometre or so, but the degree of fragmentation remains low; the black squares in Fig. 7.8 show the *F–D* co-ordinates of a number of well characterized strombolian eruptions documented by Walker. His main trend of eruption styles continues with increasing dispersal index (and column height) through sub-plinian to plinian. Many plinian deposits exhibit significantly greater fragmentation (open circles in Fig. 7.8), and the 'main trend' lifts off to higher values of *F* as the violence of the eruption increases. In the most powerful eruptions of all – for which Walker (1980) suggested a separate 'ultraplinian' category – it rises as high as 90%, for instance in the 1.8 ka BP Taupo eruption in the North Island of New Zealand shown by the large circle in Fig. 7.8. What we see from Fig. 7.8 is that the eye-witness eruption categories described above form parts of a continuum of eruption violence, and the boundaries that divide the categories are relatively arbitrary.

Walker attributed the shaded trend in Fig. 7.8 to 'open-vent' eruptions of magmas. whose volatile content and viscosity increase from left to right. Tephra from vulcanian eruptions, on the other hand, have higher fragmentation indices and their *F–D*

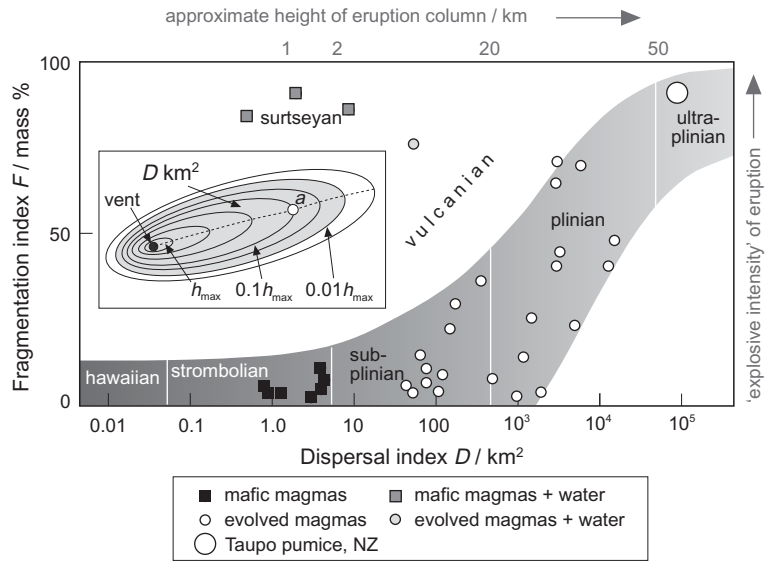


Fig. 7.8 Classes of pyroclastic eruption mapped on to a plot of fragmentation index *F* versus dispersal index *D* (after Walker, 1973, and Wright et al., 1980); the data points shown for illustration are from Walker (1973, 1980). The shaded field represents the 'main trend' where most eruption coordinates plot; data for vulcanian, surtseyan and phreatoplinian categories are too scattered to delineate clear boundaries (Wright et al., 1980).

The inset explains the meaning of *D*. The ellipses represent **isopachs** mapping the thickness of the pyroclastic *fall* deposit produced by the eruption (as a proportion of its value where the deposit is thickest, h_{max}); *D* is the land area in km^2 lying within the 1% h_{max} isopach. The dashed line shows the dispersal axis. *F* (the mass percentage of tephra finer than 1 mm) is measured on a single sample collected at *a* (open circle) where the axis intersects the 0.1 h_{max} isopach; the clast size-distribution is measured by granulometric analysis (sieving and weighing size fractions).

coordinates, though scattered, lie above the shaded trend in Fig. 7.8. The reason may be that the vent has become blocked by a plug of cold solidified material, and the build-up of gas and magma pressure required to clear the blockage leads to greater fragmentation on its release.

The classes of eruption considered so far derive their explosiveness from the ascending magma's own *intrinsic* volatile content, which vesiculates and expands as the magma decompresses on approaching the surface (Fig. 7.1). In these circumstances the fragmentation is due, in Walker's words, to

> '*the tearing apart of … magma which results from the movement, expansion and escape of gas bubbles*'.

The effect is similar to the frothing of champagne when decompression is achieved by removing the cork. Very different results are obtained when magma interacts with *extraneous* water, as the following section explains.

Hydrovolcanic eruptions

In the early hours of 14th November 1963, Icelandic fishermen noted the first signs of the volcanic activity that led over the following months to the formation of a new island, Surtsey (named after the 'fire giant' of Icelandic mythology), southwest of the Vestmann Islands which lie off the southern coast of Iceland (Fig. 9.9). By mid-morning the fishermen were reporting explosions and '*black jets of tephra*' and '*pillars of smoke and ash*' rising from the sea. Thorarinsson et al. (1964) summarized the distinctive eruption style of the succeeding months: '*After each explosion*

a black tephra-laden mass rushes up, and out of it shoot numerous bombs, each with a black trail of tephra. … The black curved tephra fingers turning white [as invisible superheated steam condenses to white clouds of water droplets] *are very typical. The vertical black jets have occasionally reached a height of half a kilometre*.' This kind of eruption, illustrated here by a similar eruption off the coast of Tonga in Fig. 7.9a, is typical of basaltic magma when it erupts into shallow water. Intimate mingling of water with melt transforms the water instantly into steam, creating repeated explosions that throw out bombs and ash. The distinctive ash trails that mark the trajectories of disintegrating projectiles were vividly described as 'tephra-fingers' by Thorarinsson et al. (1964); other authors refer to the 'cock's-tail' appearance of the ash cloud. This style of eruption, reflecting explosive interaction between molten basalt and surface water, soon became known as 'surtseyan' (Walker and Croasdale, 1972). The associated tephra (where they can be measured onshore) form a thinly bedded ash- or tuff-ring or cone around the vent and are

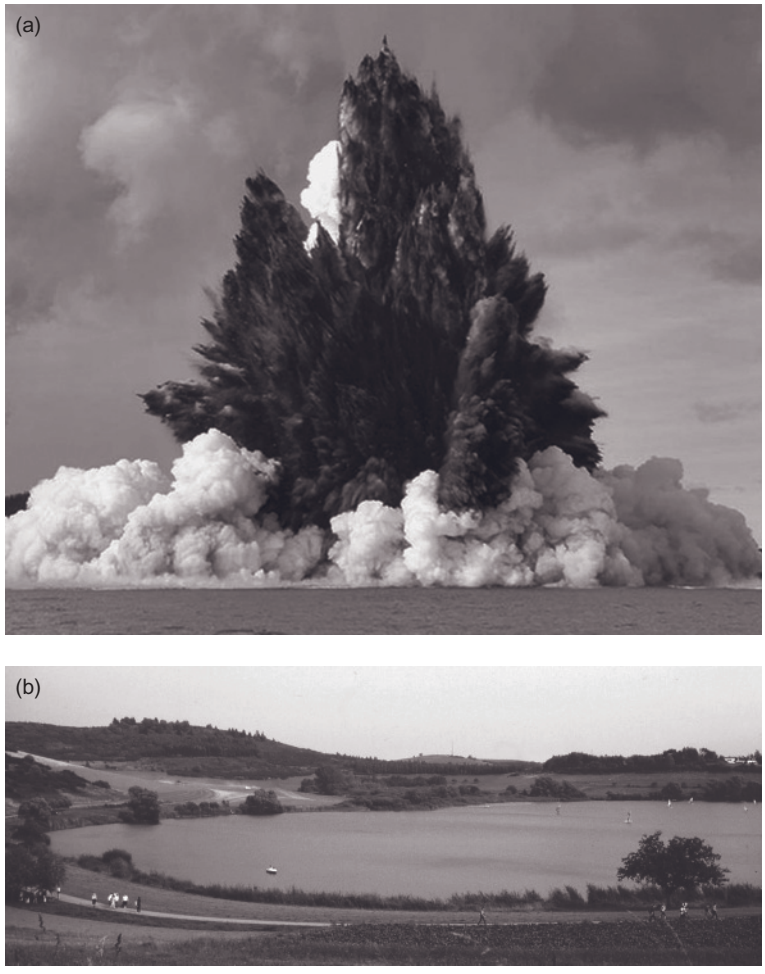


Fig. 7.9 Hydrovolcanic eruptions: (a) Surtseyan eruption of an undersea volcano off the coast of Nuku'Alofa, Tonga, on 18th March 2009 (photo by Dana Stephenson, reproduced by permission of Getty Images); note the ash-and-vapour trails behind the disintegrating ballistics, giving the cloud a characteristic "cock's tail" appearance; the white ring at the base represents an incipient base-surge density current. (b) Schalkenmehrener **maar**, Eifel, Germany, an explosion crater formed by a Pleistocene **phreatomagmatic** eruption.

characteristically finely fragmented; accordingly they plot near to the top of the *F–D* plot (Fig. 7.8). The distinctively high *F*-values reflect the intense shattering caused by thermal shock when molten lava undergoes rapid quenching by the cold water (Walker, 1973).

Similarly violent steam-generating explosions occur on land, either when magma erupts into a lake or when it encounters groundwater during its ascent toward the surface; in the latter case, the rocks overlying the seat of the explosion are blasted out to form a crater surrounded by a low ring of ejecta. This occurred in Pleistocene times at numerous locations in the Eifel region of Germany, and many of the craters have since filled with water to form near-circular lakes as much as a kilometre across, known locally as **maar**s (Fig. 7.9b); the term has been adopted in volcanology for any hydrovolcanic explosion crater. Such explosions are described as **phreatic** when the ejecta consist solely of country-rock (indicating interaction between water and heated *wall-rocks* rather than the magma itself), and **phreatomagmatic** when a juvenile magmatic component (e.g. basaltic tephra) is also present – evidence of direct contact between *magma* and groundwater (i.e. **meteoric** water).

Why do underwater eruptions in some circumstances generate violent surtseyan blasts producing voluminous tephra, while in others – as we saw in Chapter 2 – they lead to relatively gentle effusion of pillow lavas, the only tephra produced being hyaloclastite? Two factors come into play in determining how explosive a magma/water interaction might be:

1 *Pressure:* surtseyan explosions are violent because of the large volume-increase when liquid water is transformed suddenly into gaseous steam. Because steam is compressible, the volume change becomes progressively smaller at higher pressure (i.e. greater depth) and reaches zero at water depths of a kilometre or two.
2 *Water : melt ratio:* experiments show that the explosive efficiency of water/melt interactions (expressed in terms of conversion from thermal into kinetic energy) and the degree of clast fragmentation (Φ) reach a maximum when the water-to-magma mass ratio lies in the range 0.3 to 10 (Fig. 7.10).

Surtseyan and phreatomagmatic eruptions therefore seem to represent interaction between magma and water: (a) at shallow depth; and (b) at water : magma ratios favouring maximum explosivity (the shaded range in Fig. 7.10). In the presence of higher proportions of water the interaction is likely to be much less explosive, favouring pillow and sheet lavas.

The term 'hydrovolcanic' conveniently embraces all of these eruption styles involving surface water or groundwater.

INTERNAL STRUCTURES OF PYROCLASTIC DEPOSITS

Pyroclastic fall deposits

Pyroclastic fall deposits, whether they consist of basaltic scoria or more evolved pumice, share the characteristic of being well sorted,

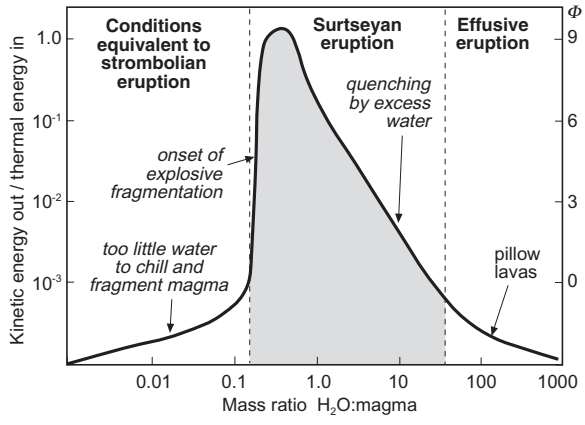


Fig. 7.10 Experimental energy-conversion curve for water-magma interaction in shallow water, after Wohletz and McQueen (1984). The vertical axis shows the explosive efficiency (i.e. the ratio of output kinetic energy to input thermal energy, normalized to a maximum value). The scale on the right hand side represents the grain size parameter Φ (as shown in Table 7.2), reflecting the finer fragmentation when explosive efficiency is high.

with clast size decreasing at greater distances from the vent. Strombolian eruptions produce only low degrees of fragmentation and therefore little fine ash is formed. When seen in cross-section (e.g. in a quarry face) scoria deposits may exhibit crude outward-dipping bedding picked out by coarser and finer lapilli (Fig. 2.6b); this may be due to fluctuating explosiveness in the vent or may reflect cascading of coarser proximal lapilli down an unstable slope.

In plinian fall deposits the high degree of sorting (proximal fall deposits are virtually ash-free) reflects prolonged settling through the air, providing the opportunity for smaller lapilli and ash to be dispersed to greater distances from the vent. Plinian fall deposits are usually massive but may sometimes show a degree of stratification (Fig. 7.11a).

It is common to cite the total volume of tephra as a guide to the scale of a plinian eruption. In order not to exaggerate the volume of magma ejected, one routinely compensates for the vesiculation-driven inflation of tephra by expressing the total volume as km^3 **dense rock equivalent** ('DRE').

Pyroclastic current deposits

Ignimbrites – products of plinian column collapse

Ignimbrites vary considerably in their internal structure. Many consist of massive **lapilli-tuff** (conveniently abbreviated to 'mLT') as illustrated in Fig. 7.11(b), but others may show internal stratification of composition or maximum clast size (Fig. 7.11c). Some ignimbrites exhibit vertical grading of pyroclasts, and it is not uncommon to see in one ignimbrite normal grading of lithic clasts alongside inverse grading of pumice lapilli. Horizons rich in lithic clasts provide another example of vertical heterogeneity seen in some ignimbrites, e.g. in the Bandelier tuff in New Mexico.

In some ignimbrites, pumice lapilli are lensoid rather than equant in shape and they then tend to lie sub-parallel to each other, defining a foliation (Fig. 7.11d and Plate 7.3), which suggests they were still ductile enough to deform at the time of deposition and perhaps for some time afterwards. Lithic clasts incorporated in the ignimbrite, on the other hand, being crystalline, resist such deformation The flattened pumices, given their flame-like appearance in outcrop, are given the Italian name **fiamme**. The foliation picked out by the fiamme, observable both in hand-specimen (Fig. 7.11d) and in thin section (Plate 7.3), is termed **eutaxitic** texture, and the deformation that lies behind it is called *welding*. Lapilli-tuffs in which pumice lapilli retain their original equant, uncompacted shape (Plate 7.2) are described as *unwelded*; those in which eutaxitic foliation has developed are described as *welded*. Strongly welded ignimbrites are hard rocks and they commonly adopt some of the characteristics of lava, e.g. columnar jointing (Fig. 7.11e). The eruption conditions favouring welded and unwelded ignimbrites are discussed in a later section.

Though all agree that ignimbrites result from the collapse of a plinian eruption column, the manner in which PDCs transport and deposit their load has been controversial for decades. The former 'standard model' of ignimbrite emplacement, introduced by Sparks et al. (1973), envisaged the collapsing column passing through a 'deflation' stage, in which the diffuse cloud condenses into a concentrated 'avalanche' of pumice, lithics, ash and gas, moving over the ground by laminar flow aided by intense shearing at the base (Fig. 7.12a and Table 7.3); ignimbrite emplacement equates with this avalanche simply coming to rest. Any vertical heterogeneity seen in the ignimbrite (e.g. reverse grading of pumice lapilli) must in this hypothesis be inherited from *instantaneous* gradients that had developed within the flowing avalanche. In this collapse–deflate–avalanche–stop model, the billowing ash cloud above the PDC reflects the elutriation of fines from the avalanche by escaping gases.

In the past decade, a new concept of ignimbrite emplacement has been proposed by Branney and Kokelaar (1992, 2002). Rather than being emplaced as a single moving package that eventually comes to rest, they view ignimbrite as being deposited *progressively* at the base of a sustained density current passing above, a process they call 'progressive aggradation'. A snapshot cross-section at any one location during deposition would show: (i) at the base, the stationary deposit that has accumulated up to the moment of the

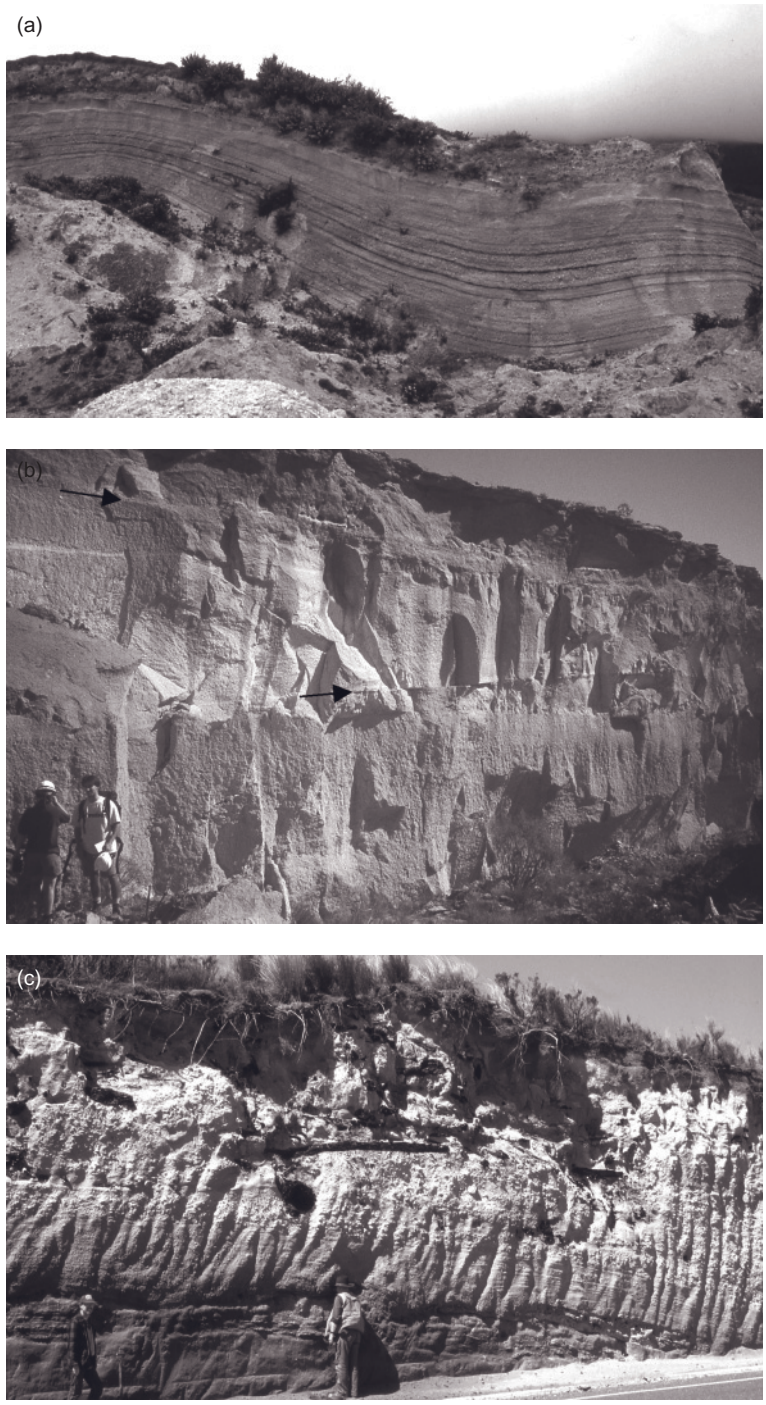


Fig. 7.11 (a) Mantle bedding in a plinian fall deposit, Okareka quarry near Rotorua, New Zealand. (b) Massive lapilli-tuff exposed in a quarry face, part of the Granadilla ignimbrite in Tenerife; note internal boundaries (arrowed). (c) Roadcut in 1.8 ka BP Taupo ignimbrite, Waihohonu stream, New Zealand, 50 km from its source; note the stratified lower portion and the carbonized tree trunks that were carried along by the current.

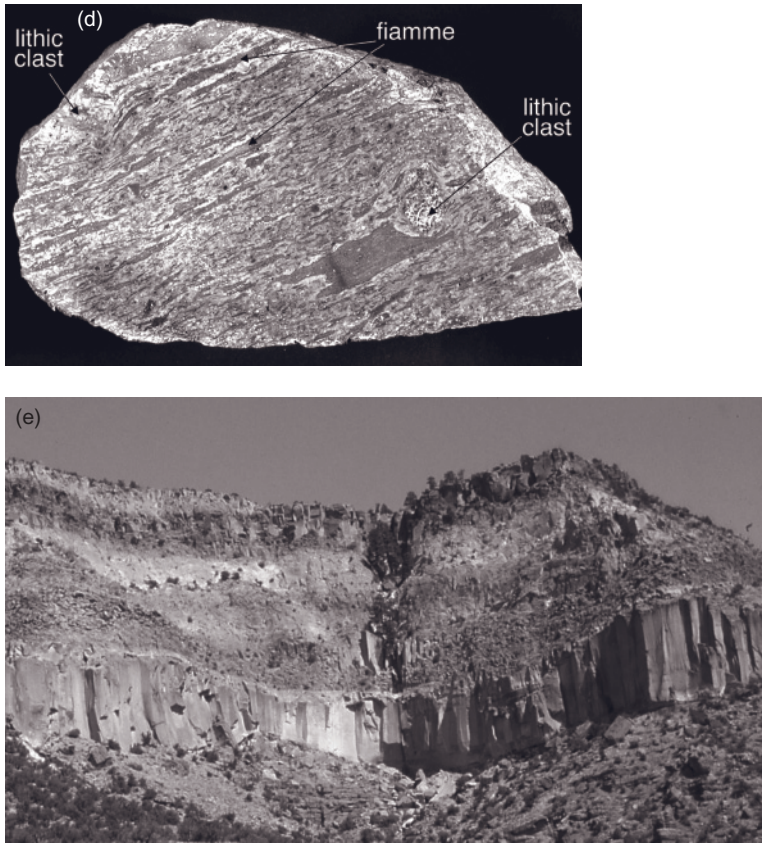


Fig. 7.11 *Continued* (d) Polished surface of Ordovician welded lapilli-tuff from Sty Head, English Lake District; width of field 27 cm; note the stronger compaction of matrix around the lithic clasts, which have themselves remained undeformed. (e) Jointing in welded Lower Bandelier ignimbrites (overlain by Upper Bandelier tuff) in the west wall of San Diego Canyon, Jemez Mountains, New Mexico.

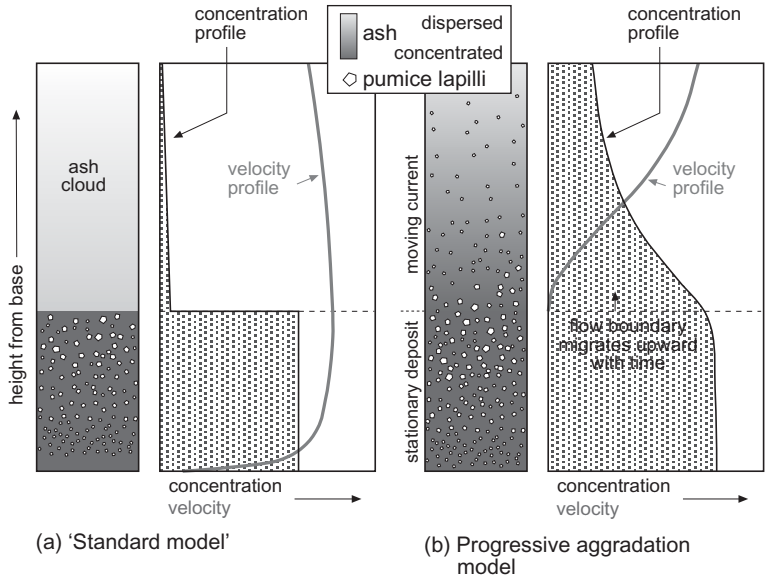


Fig. 7.12 Cartoons illustrating (a) the 'standard model' of ignimbrite emplacement (Sparks et al., 1973); and (b) the progressive aggradation model of Branney and Kokelaar (1992, 2002).

Table 7.3 Mechanisms of PDC transport and ignimbrite deposition.

Feature	Explanation in the 'standard model'	Explanation in the progressive aggradation model
Nature of the density current	Column collapses and 'deflates' to form a concentrated, laminar semi-fluidized 'avalanche' above a basal shearing layer.	Column collapses as a sustained density current which develops internal stratification, with a dilute turbulent cloud at the top grading down into a concentrated current at the base.
Deposition of ignimbrite	Deposition occurs when the current comes to rest.	Deposit 'aggrades' at the current's lower boundary throughout the life of the current.
Interpretation of ash cloud	Due to elutriation of ash by escaping gas.	Upper dilute part of PDC.
Vertical clast grading	Segregation within laminar-flow current during transport producing stratified current.	Size of depositing clasts varies with time due to current unsteadiness or changing eruption conditions.
Compositional zoning	Hard to explain.	Eruption taps progressively deeper, less fractionated levels within feeder magma chamber with time.
Lithic horizons	Hard to explain.	Discrete episodes of vent widening cause wall-rock brecciation, introducing packets of lithics into the collapsing column.

snapshot; (ii) a flow boundary where aggradation is currently taking place; and (iii) the still-moving density current above, concentrated at the base but becoming more dilute at higher levels (Fig. 7.12b and Table 7.3). As interpreted in this model, vertical heterogeneity in an ignimbrite (e.g. grading of lapilli) records *changes in time* during the deposition process, reflecting either varying conditions at the vent, or unsteadiness in current velocity and carrying power. Progressive aggradation explains the compositional zonation seen from the bottom to the top of some large ignimbrite sheets (as a record of the eruption tapping progressively deeper levels of a zoned magma chamber with time), and accounts for abrupt variations in the proportion of lithic clasts (recording episodes of brecciation, e.g. associated with vent widening). The visually dominant 'phoenix' ash cloud is interpreted simply as the more dispersed, turbulent upper portion of the density current itself.

The same PDC can deposit material at one place while eroding substrate at another, and this behaviour may vary through the life of a sustained current. A single ignimbrite sheet may therefore consist of several layers (Fig. 7.11b), each package thickening or thinning along or across the current direction. Such layers have previously been interpreted as individual 'flow units' separated in time, but (in the absence of weathered horizons between them) the progressive aggradation model views them as products of a single sustained current whose velocity waxes and wanes – sometimes in a complex manner – through the course of a single eruption.

A complete plinian deposit typically consists of a pumice fall bed at the base, overlain by pumiceous lapilli-tuff, indicating that the eruption progressed from an initial buoyant eruption column (pumice fall) to a collapsing column (ignimbrite). The magma erupting at this latter stage is commonly less volatile-rich than during the initial buoyant-column stage (see Bishop Tuff data in Fig. 7.13). Not uncommonly, the close of plinian activity is marked – as at Mt St Helens in 1980 – by the extrusion of a lava dome or domes, similar in composition (except in terms of volatile content) to the plinian tephra. The dome represents on-going leakage of gas-poor magma from the underlying magma plumbing system whose volatile content has been depleted (Fig. 7.13). Such 'degassing' occurs either because upper, more volatile-rich fractions of magma

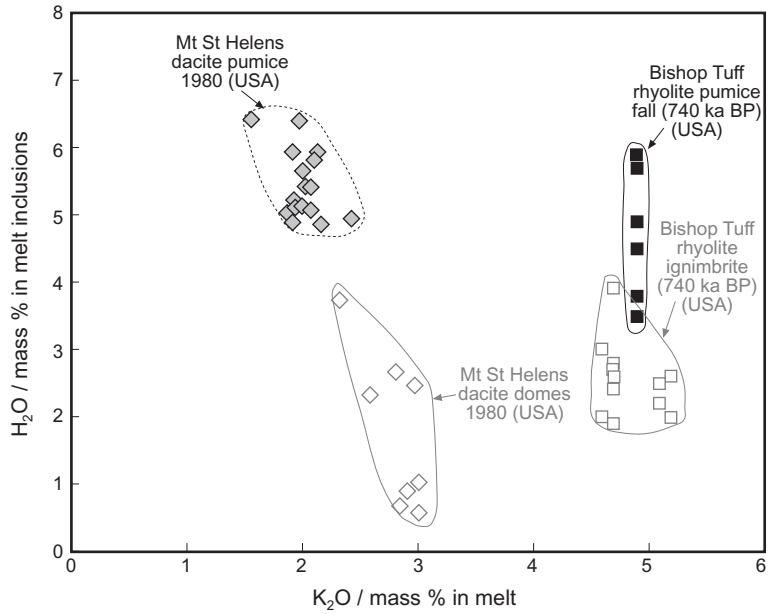


Fig. 7.13 Pre-eruption H_2O contents of various Mt St Helens and Bishop Tuff magmas (cf. Fig. 6.14) to illustrate – for the Bishop Tuff – the change in volatile content between buoyant-column (pumice) and collapsing-column (ignimbrite) stages of a plinian eruption, and – for Mt St Helens – the extent of magma degassing between magma erupted at the early plinian stage and magma forming the post-plinian dacite dome. Data from Dunbar and Hervig (1992) and Blundy and Cashman (2005).

were expelled during the explosive phase of the eruption, or because of leakage of volatiles through the walls of the conduit as time and wall permeability allow.

Though most characteristic of plinian eruptions, PDCs may occur in any eruption which forms a significant eruption column. Figure 7.4a, for example, shows a PDC (in the left-hand side of the figure) forming by collapse of a vulcanian eruption column at the Soufrière Hills volcano, Montserrat (Lesser Antilles) in October 1997.

Block and ash deposits – products of lava-dome collapse

A very different type of pyroclastic density current occurred in 1902 on another Caribbean island, Martinique (see Fig. 6.17 inset), as described soon after the event by Lacroix (1904):

> *'On the morning of 8 May, the sky was clear; a tall vertical vapour plume of striking regularity was rising from the crater* [of Mont Pelée volcano in the north of the island], *when suddenly at 08.02 there occurred the terrifying event that, within a few minutes or even less, destroyed the capital St Pierre and its 28,000 inhabitants. Several witnesses … heard violent detonations, then saw a black cloud, sparkling with flashes of lightning, rolling down over the terrain and overwhelming the town with furious rapidity. Having enveloped St Pierre, it abruptly came to rest just to the north of the village of Le Carbet* [about 5 km SE of St Pierre]. *When an opposing wind swept it back, the few survivors on board those ships in the harbour that had not been sunk, and those held fast to floating wreckage, could see that nothing remained of the town except a pile of burning ruins. All vegetation and dwellings in the area between the crater, le Morne Folie and la Petite Anse du Barbet had disappeared, being covered now by a thick shroud of grey ash.'*

Eye-witnesses described a tremendous blast of searing hot gas passing over the town, capable of capsizing large ships in the harbour and setting fire to anything flammable in its path.

Lacroix coined the term '*nuée ardente*' (French: 'glowing cloud') for this particularly lethal type of eruption, because – especially

when seen around dusk – such clouds do glow a dull red.[13] Surprisingly, the hot ash cloud that proved so devastating for St Pierre and its citizens was no more than a peripheral – if deadly – part of the PDC causing the havoc. The main course of the PDC on 8 May actually lay some 3 kilometres to the NW of St Pierre in the valley of the Rivière Blanche, as Lacroix discovered in the following days:

> *'All of the region between the crater, Peres Rive and Lamarre Point was found to have been levelled by a thick layer of hot debris, among which (north of Rivière Sèche) are blocks of lava more than 100 m^3 in size drowned in a matrix of ash, lapilli and stones of every size.'*

This eloquently describes the bulk of the deposit left behind by what today is called a *block-and-ash flow*. This type of PDC results from the gravitational disintegration of an endogenous lava dome, whose swelling creates unstable, over-steepened sides (e.g. Fig. 6.3b) that readily collapse. If the dome is perched at the top of a sufficiently steep slope or ravine – as was true of the dome growing on Mont Pelée in May 1902 – the material it sheds (often including still-incandescent rock from the dome interior) breaks up on repeated impact with the ground to form a mixture of lava blocks, lapilli and ash-grade material with sufficient momentum to continue flowing rapidly down the steep slope. It evolves into a hot, ground-hugging pyroclastic density current consisting not of pumice but of dense juvenile lava debris. Much of the finest ash component is borne aloft by heated air to form the familiar billowing ash cloud (Fig. 7.14a), and it was the lateral spread of this searingly hot ash cloud and the associated intense winds that wiped out St Pierre and its population. Those who have more recently survived encounters with the fringes of such PDCs report 'burning of the air passages', and this in more intense form was probably the cause of most fatalities in St Pierre in 1902. Similar *nuées ardentes* were observed from Mont Pelée in July and December of the same year and again in 1929; the phenomenon is often referred to as *Peléean* activity.

Much new scientific understanding of block-and-ash flows has been gleaned from the volcanic activity in progress at the Soufrière Hills volcano in Montserrat since 1995. A succession of endogenous andesite lava domes (Fig. 6.3b) has formed in English's Crater, giving rise to numerous episodes of dome collapse; block-and-ash flows (not to be confused with the vulcanian column-collapse PDC on Montserrat illustrated in Fig. 7.4a) have repeatedly cascaded down the Tar River Valley to the north-east, culminating in a catastrophic series of PDCs that removed virtually all of the dome on 22 May 2006.

In some cases, dome collapse seems to be solely the work of gravity, as illustrated by most Montserrat PDCs since 1995, whereas in other instances – like Mont Pelée in May 1902 – the collapse appears to have been initiated by one or more explosions

> ('*Several witnesses … heard violent detonations …*').

In either case the block-and-ash deposits are much the same: a chaotic jumble of dense lava blocks of all sizes – some several metres in diameter – in an ashy matrix (Fig. 7.14b). Sometimes inverse grading is seen among the larger clasts. The high temperature origin of the deposit may sometimes be inferred from distinctive prismatic jointing in larger clasts and from oxidative reddening.

Base surge deposits related to hydrovolcanic eruptions

Hydrovolcanic eruptions often create their own kind of pyroclastic density current. In addition to the darker "cock's tail" ash cloud, Fig. 7.8(a) reveals a basal cushion of white vapour. This represents the incipient stage of a radially-expanding, doughnut-shaped ground-hugging ash cloud called a *base surge*. Such clouds are a feature of many eruptions involving explosive magma-water interaction, and result from the gravitational collapse of a short-lived eruption column associated with each explosion. Base surges are a form of pyroclastic density current, but they are more dilute than those that form ignimbrites and, owing to the involvement of water, are cooler and

[13] Describing a similar eruption one evening in July that year, Anderson and Flett (1903) recorded that '*(the cloud) was dull red and in it were brighter streaks which we thought were large stones as they seemed to give off tails of yellow sparks*'.

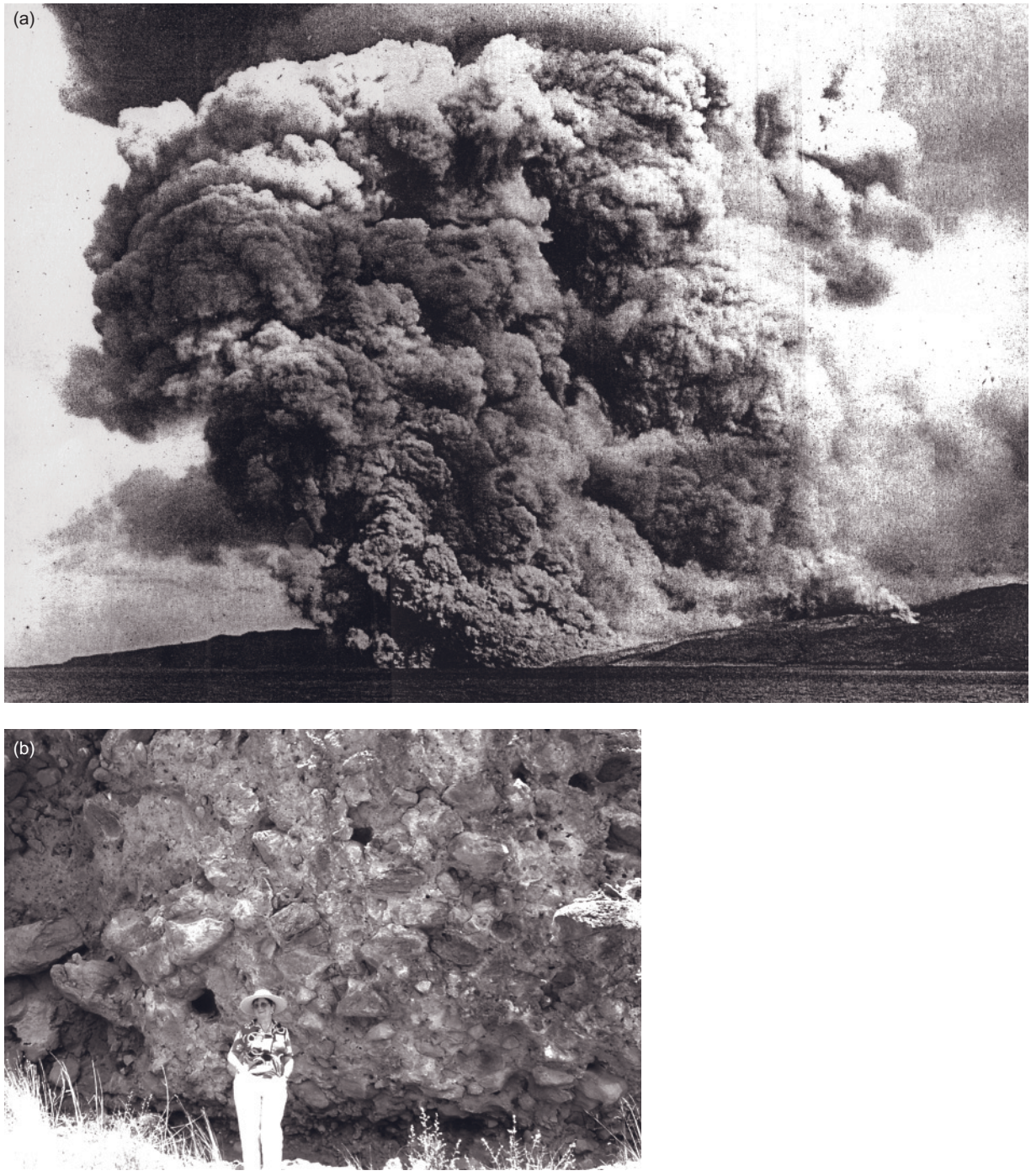
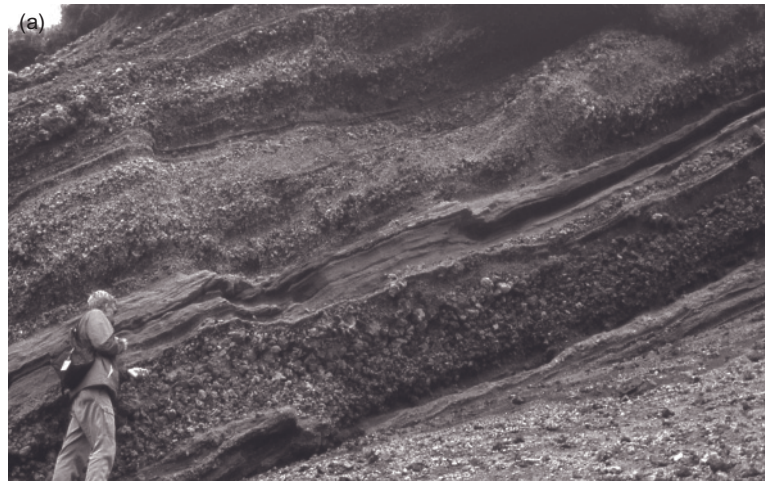


Fig. 7.14 (a) *Nuée ardente* from Mont Pelée reaching the sea on 16 December 1902 (from Lacroix, 1904). (b) Typical section of a block-and-ash deposit (Old Horse Springs, New Mexico, USA).

moister. The violent, gusting, centrifugal winds associated with these turbulent surges deposit poorly sorted but distinctively laminated and cross-laminated ash beds accounting for much of the tuff ring that builds up from repeated explosions; dune forms are common, typically accreting on the up-current side (forming anti-dunes). When current-direction indicators are mapped out, they point radially out from the seat of the explosions.



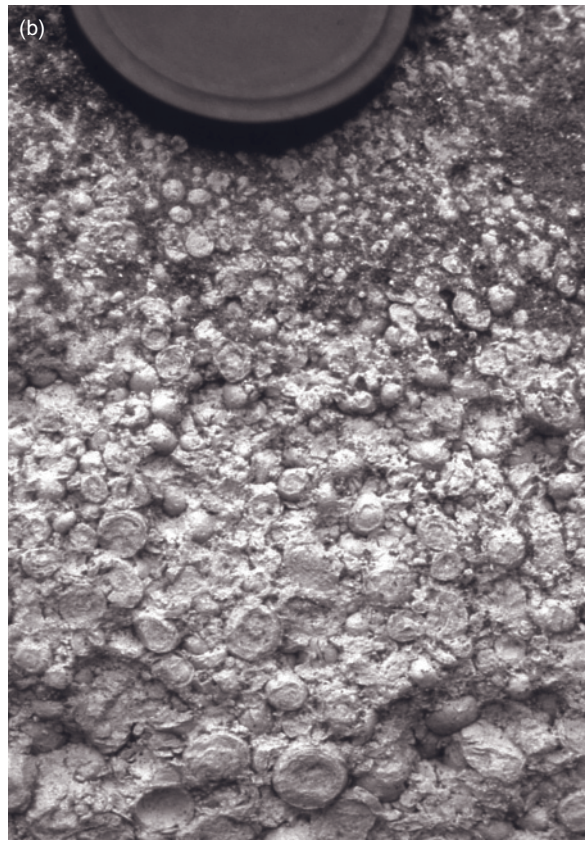


Fig. 7.15 Products of hydrovolcanic eruptions: (a) Alternating juvenile andesitic scoria beds and laminated base-surge beds at the Pukeonake scoria cone, Tongariro National Park, New Zealand. (b) Accretionary lapilli of Oruanui rhyolitic ash, New Zealand; lens cap diameter 6 cm.

The maar-forming interaction between ascending basaltic magma and an aquifer in its path commonly produces alternating beds of strombolian and base surge deposits (Fig. 7.15a). An initial series of phreatomagmatic explosions disrupts the aquifer and allows magma direct access to the surface where it feeds a period of strombolian activity. A pause in magma supply may allow water to percolate back into sedimentary or pyroclastic beds over a period of months or years, and the cycle may be repeated a number

of times with the arrival of new batches of magma (Fig. 7.15a).

Accretionary lapilli are another common product of phreatomagmatic eruptions; these are spheroidal lapilli with a concentric internal structure (Fig. 7.15b), formed by successive accretion of fine ash on to seed particles in a damp ash cloud; they may also form when ignimbrites enter the sea.

Edifice Instability

Nuées ardentes derived from perched lava domes are just one indication of the intrinsic instability of many volcanic edifices. In engineering terms, volcanoes are pretty shoddy structures, and they succumb to gravity in a variety of other ways. Firstly, many volcanoes are prone to *sector collapse* (sometimes without any associated eruption), when a large mass of the volcano fails and the detached material tumbles down as a cold *debris avalanche* (a rapidly moving mass of blocks, boulders and gravel). The precipitating factor leading to failure may be seismicity, or oversteepening of the flanks resulting from shallow magma intrusion (both of these factors played a part in initiating the May 1980 eruption of Mt St Helens in Washington, USA), or the overloading of unstable flanks by new volcanic deposits, or (in the case of ocean islands) 'de-buttressing' of the sub-aerial edifice by wave action. A debris avalanche deposit has many attributes of a block-and-ash deposit, but there are two critical differences: debris avalanche deposits contain no evidence of high temperature emplacement (Fig. 7.16), and the debris usually includes a range of volcanic rock types (in contrast to the juvenile uniformity of a block-and-ash deposit). The hummocky surface of a debris avalanche deposit (Fig. 7.17) may conceal 'megablocks' up to 1 km in size that have slid with their internal stratigraphy more or less intact.

A second hazard relates to the presence on many stratovolcanoes of large volumes of unconsolidated ash. When mixed with water – derived perhaps from sudden melting of summit snow and ice, from emptying of a crater lake, or during heavy rain – and accelerated by gravity, the ash becomes highly mobile and forms a devastating volcano-related mudflow known by the Indonesian term *lahar* (Fig. 7.16). Though confined by the drainage systems down which they flow, lahars may travel rapidly – as far as 100 km from their source – dragging up trees, large rocks, soil and other debris as they go; their carrying power is phenomenal. They may also erode the banks of waterways they follow. Lahars flowing down the canyons of Nevado

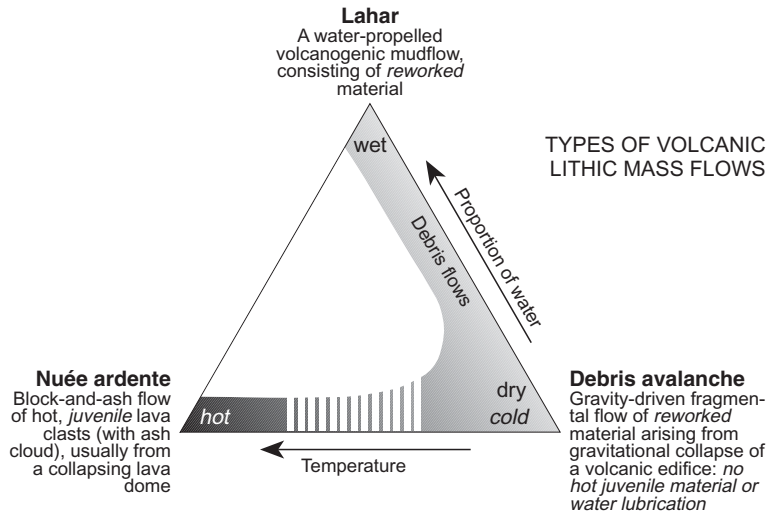


Fig. 7.16 Summary of the relationship between hot block-and-ash flows, cold volcanic debris avalanches and flows, and lahars.



Fig. 7.17 Hummocky terrain marking the surface of an exceptionally large debris avalanche deposit (covering an area of 675 km^2) derived 300 ka ago from Mt Shasta, California (the prominent peak on the skyline 20 km to the south). Photo Harry Glicken, reproduced courtesy of USGS/Cascade Volcano Obseratory.

del Ruiz volcano in the Colombian Andes following a minor eruption in 1985 overwhelmed the valley town of Armero, killing 25,000 people there. Lahar deposits are unsorted and '*contain fragments of all sizes from fine mud to boulders as big as houses*' (Francis and Oppenheimer, 2004); compared to a debris avalanche, the larger clasts tend to be more widely spaced amid a matrix of finer mud.

MICROSCOPIC TEXTURES

Much of the evidence upon which we base our understanding of pyroclastic processes is derived from field observation of outcrop-scale structures (sorting, grading, cross-lamination and so on). The polarizing microscope makes a relatively minor contribution, yet the examination of thin sections can shed light on magmatic processes before and during eruption.

Pumice

The principal and most distinctive product of a plinian eruption is the highly vesicular form of volcanic glass that we call **pumice**. Careful examination under a hand lens (Fig. 7.18a), in thin section and under an electron microscope (Fig. 7.18b) shows that pumice is vesicular across a whole range of scales, from micrometres up to millimetres, sometimes even centimetres. The larger vesicles in a given piece of pumice probably nucleated first and grew by diffusion of supersaturated gas through vesicle walls while molten; coexisting smaller vesicles nucleated later so had less opportunity to grow before the surrounding melt froze into glass. Pumice usually contains a high volume proportion of vesicle voids (sometimes as high as 80%),[14] and this high vesicularity often gives it a density low enough to float on water.[15] Some vesicles may be elongated or flattened (Fig. 7.18a), indicating stretching or shear deformation of the inflating pumice prior to vitrification. Pumice may contain phenocrysts formed at depth, and if the melt's ascent path brought it closer to its solidus (Fig. 6.5) – e.g. as a result of volatile loss – it may be crowded with minute crystal microlites formed at this late stage (Fig. 7.18b).

Plate 7.1 shows a sample of tephra from the 74 ka BP eruption of Toba volcano in Sumatra, Indonesia; the ash layer from this colossal eruption (probably the largest eruption in human history) can be traced as far

[14] See Wright et al. (2003).
[15] Rafts of pumice lapilli from the Krakatau 1883 eruption in Indonesia remained afloat long enough to drift across the Indian Ocean as far as the coast of Africa.

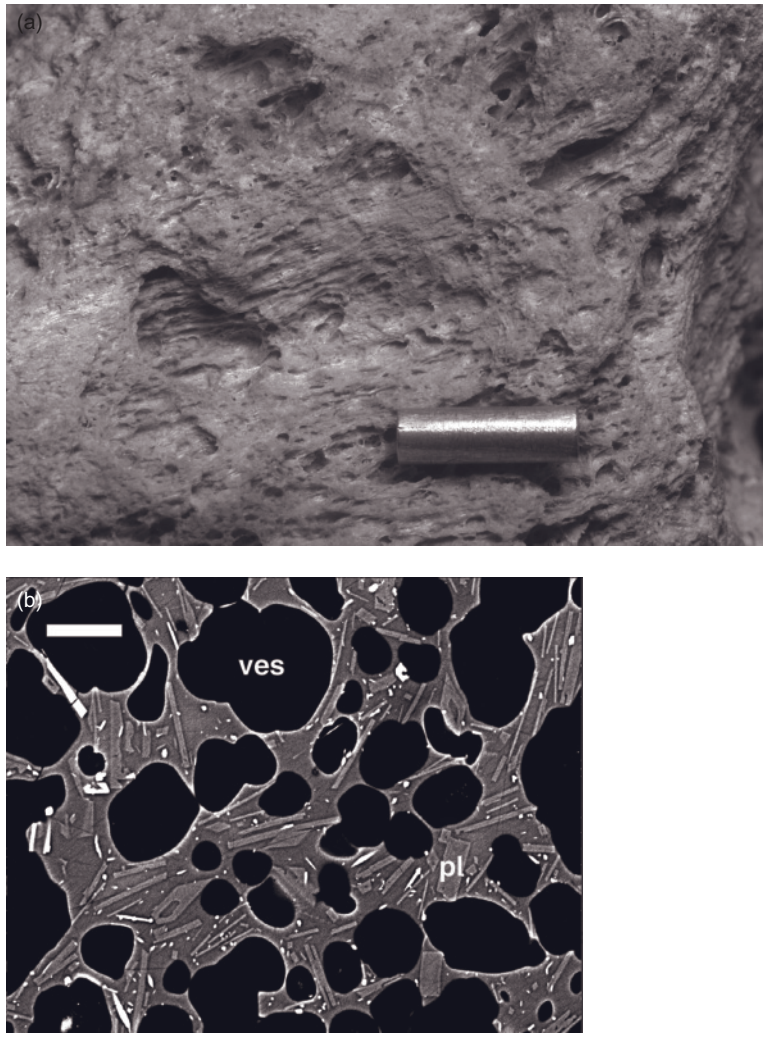


Fig. 7.18 (a) Close-up of a pumice lapillus from Tenerife (photo K. D'Souza); scale bar 1 cm long. Note the elongation of bubbles. (b) Back-scattered electron micrograph of 18 May 1980 Mt St Helens pumice, showing μm-scale vesicles (ves) and intervening glass crowded with plagioclase **microlites** (pl) formed during ascent (reproduced from Blundy and Cashman, 2001, Fig. 6b by kind permission of Springer Science and Business Media); scale bar represents 10 μm.

away as NW India. The sample contains numerous crystal fragments of biotite, feldspar and quartz up to 1.5 mm in size and sparse pumice clasts, but its most distinctive feature is the matrix made up of curved, often **cuspate** shards of isotropic volcanic glass. Some of these shards curve in the same sense on opposing sides, suggesting they are wall fragments from single bubbles of frothing melt. Others represent disrupted films of melt that divided two or more adjacent bubbles; the shape of one shard (top left) even suggests the junction of five bubbles. These shards record bubble expansion beyond the tensile strength of the intervening melt. Similar pumiceous ash forms the matrix of many ignimbrites (Plate 7.2 and 7.3), though rarely as well preserved as this.

A volcanic ash like that in Plate 7.1 that has been lithified into a coherent rock is called a **tuff**. Depending on the dominant constituent, the name may be refined to *crystal tuff*, *vitric tuff* (meaning it contains glass shards as

in Plate 7.1) or, if clasts of crystalline rock predominate, *lithic tuff*. Combinations of these qualifiers are possible, e.g. crystal-lithic tuff.

Lapilli-tuff

Plate 7.2 shows a rock containing a jumble of pumice clasts, crystal fragments and occasional lithic clasts in an isotropic matrix made up of glassy ash. The fragmentary nature of the assemblage is clear from the broken crystals (several show irregularly truncated twinning), and the fine lithified glassy matrix qualifies this rock as a tuff. Pumice clasts show no common foliation consistent with post-depositional deformation.

The hand-specimen of this rock contains pumices up to 3 cm in diameter, and its poorly sorted character is encapsulated by the name *lapilli-tuff*:

Lapilli-tuff: a tuff containing clasts of lapilli size in an ash-grade matrix.

More specifically this is a *pumice lapilli-tuff* (the lapilli could alternatively consist of lithic clasts). Taking account of the field setting in which this rock was found, one may conclude that it is the product of a pumice-rich pyroclastic density current resulting from the collapse of a plinian eruption column, an origin indicated by the genetic term *ignimbrite*. Nonetheless, until the evidence pointing to this origin has been amassed, it is good practice to use simply the descriptive term lapilli-tuff. Note that neither term – lapilli-tuff or ignimbrite – implies anything about the rock's chemical or modal composition. In the case of Plate 7.2, the presence of quartz and biotite crystals indicates an evolved composition. This example is in fact a rhyolite, but ignimbrites of evolved andesite (Pinatubo), dacite (Mt St Helens and Fish Canyon Tuff, Colorado), **trachyte** (Campanian ignimbrite, Italy), **phonolite** (Tenerife) and even basalt (Masaya volcano, Nicaragua) composition are also known.

Welded lapilli-tuff

The pumice that constitutes the juvenile component of an ignimbrite consists of highly vesicular glass (Plate 7.2) which remains ductile at the emplacement temperatures of some ignimbrites (~550 °C). In the earlier stages of a plinian eruption (Fig. 7.6a), when the ejecta are lofted to high altitude, there is time for pumice lapilli to cool almost to atmospheric temperature before they reach the ground as fall or current deposits; in these circumstances, lapilli mostly retain their shape in spite of the load pressure of overlying deposits. As the eruption reaches its climax, however, the eruption column becomes denser and ejecta become incorporated almost immediately in PDCs (Fig. 7.6b). Pumice may in these circumstances be deposited while still hot and ductile enough to deform. As hot pumice is buried deeper in an accumulating pile of hot ignimbrite, it readily flattens to form sub-parallel **fiamme** (Plate 7.3). Crystal and lithic fragments, on the other hand, resist this compaction. Proximal fall deposits occasionally exhibit welding too.

Ignimbrites and the associated pumice fall beds thus provide a sensitive stratigraphic record of the evolution of a plinian eruption. The initial buoyant plume produces a widespread pumice fall blanket, later column collapse leads to the development of pyroclastic density currents and the ignimbrites they deposit, and at the climax of the eruption – when vent enlargement or other factors maximize magma discharge rates – the likelihood of welded ignimbrites reaches its peak. Many major ignimbrite sheets show variation in the density of welding from bottom to top (Fig. 7.11e) that records – if progressive aggradation is accepted – the fluctuating state of the eruption column.

CALDERAS

The largest plinian and ultraplinian eruptions erupt colossal volumes of evolved magma into the atmosphere, more rapidly than magma can be re-supplied from below to the subvolcanic magma chamber. Though it is unlikely that the chamber supplying an eruption is ever completely emptied, sufficient magma is discharged for the chamber roof to become critically under-supported, resulting in failure and vertical subsidence of the roof rocks into the partially emptied chamber below. The topographic depression resulting from magma

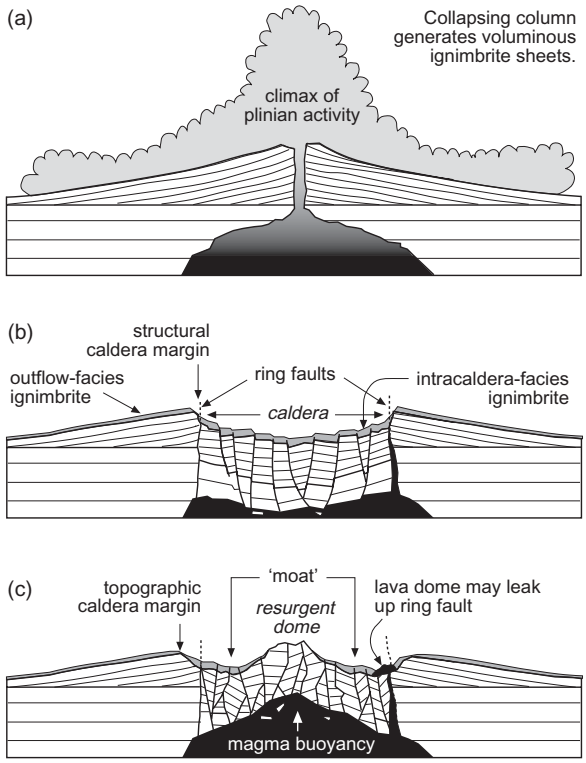


Fig. 7.19 Cross-sections showing stages in the evolution of a caldera, incorporating ideas of Howel Williams (see Francis and Oppenheimer, 2005, Fig. 11.5) and Kokelaar and Moore (2006): (a) climactic ignimbrite-forming stage of a large-scale plinian eruption; (b) collapse of the unsupported chamber roof; (c) uplift of a resurgent structural 'dome' owing to the buoyancy and magma pressure of the magma reservoir beneath.

chamber roof collapse is called a **caldera** (Fig. 7.20a). Subsidence is often, but not always, accommodated by vertical or outward-dipping ring faults, presumably located near to the periphery of the unsupported area of the roof (Fig. 7.19b).

Calderas are characteristic of many volcanoes involved in large-volume plinian eruptions (e.g. that associated with the 1883 eruption of Krakatau, Indonesia). Repeated episodes of subsidence may lead to a *caldera complex* (Cole et al., 2005) containing a number of nested or overlapping calderas. In the case of the largest eruptions, some or all of any pre-existing volcanic edifice founders within a larger caldera leaving a net depression in the ground surface, as happened for example at Yellowstone (Wyoming) 650 ka ago (Table 6.4), in the Oruanui eruption at Taupo (New Zealand) 26.5 ka ago, and at Crater Lake (Oregon) 7.7 ka ago. The scale of such caldera-forming eruptions is summarized in a recent paper by Hildreth and Wilson (2007):

> *'The Bishop Tuff, product of one of the world's greatest Quaternary eruptions, was released at 760 ka BP during an episode about 6 days long from the Long Valley magma chamber in eastern California. Fallout remnants are preserved from the Pacific Ocean to Nebraska over an area exceeding 2.5 × 10^6 km^2 … Long Valley caldera collapsed along a 12 km × 22 km elliptical ring-fault zone that became active only after half or more of the* [600 km^3] *erupting* [rhyolite] *magma had escaped from the chamber.'*

Though 760 ka sounds a long time ago, this vast eruption was the culmination of a 4 Ma history of activity. The caldera has been the site of post-caldera eruptions and hydrothermal activity, and is the focus of current volcano-seismic unrest. The Long Valley caldera undoubtedly remains alive today.

Eruptions on the colossal scale of Yellowstone (Table 6.4), the 760 ka Bishop Tuff event, and the 74 ka BP eruption of Toba – referred to as super-eruptions (Bachmann and Bergantz, 2008) – have global environmental consequences, as elaborated by Self and Blake (2008). The largest documented pyroclastic eruption is represented by the 28 Ma-old Fish Canyon Tuff, a silicic ignimbrite ~5000 km^3 in volume that erupted from the 100 × 32 km^2 La Garita caldera in the San Juan mountains of Colorado (Bachmann et al., 2002).

Most calderas evolve by a combination of collapse mechanisms, often piecemeal or in several stages (Cole et al., 2005; Kokelaar and Moore, 2006). Ring faults may not operate equally on all sectors of the periphery, leading to what is termed 'trapdoor collapse'; in 'downsag' calderas, there appear to be no ring faults at all (or they fail to reach the surface). Once formed, a fault-controlled caldera

wall erodes back quite rapidly, so that the topographic feature (the *topographic caldera margin* – Fig. 7.19c) retreats outward with time relative to the position of the ring faults responsible for its formation (the *structural caldera margin* – Fig. 7.19b). Hildreth and Wilson (2007) note that the Long Valley caldera – originally 12 km × 22 km in extent – has been enlarged to a depression that today measures 17 km × 32 km

> *'by syneruptive slumping and secular erosive recession of the walls'.*

The location of the ring fault system may be highlighted at the surface by the extrusion of lava domes lying inward of the topographic wall (Fig. 7.19c), as illustrated most elegantly by the ring of such domes in the Valles caldera of New Mexico (Fig. 7.20b); the youngest of these domes is the Banco Bonito **coulée**, whose ogives (surface wrinkles) are suggested in the figure. Mineralization or alteration of caldera-fill pyroclastics may also mark the location of a ring fault system below.

The continuing presence and/or resupply of low-density evolved magma in the magma chambers beneath large calderas often leads to structural doming of the central parts of a caldera floor (Fig. 7.19c); uplift-driven erosion may remove intracaldera plinian tephra from the up-domed area, exposing older rocks beneath (Figs. 7.19c and 7.20b). The positive domal feature is described as a *resurgent dom*e (a structural feature not to be confused with a lava dome), and the annular depression encircling it within the caldera is called a *moat* (Figs. 7.19c and 7.20b). Similar resurgence and the eruption of 'moat rhyolites' have occurred in the Long Valley caldera too. Bachmann and Bergantz (2008) illustrate a nice example of a resurgent dome and moat at Creede caldera in the San Juan volcanic field, Colorado.

Calderas also occur on the summits of some large effusive basaltic shield volcanoes such as Mauna Loa and Kilauea in Hawai`i. In this context, subsidence is usually due to the draining of magma from a summit chamber into dilating dyke systems radiating out from it, which may feed flank eruptions at lower altitudes. A few basaltic volcanoes have however formed calderas as a result of explosive eruptions, an example being Masaya volcano in Nicaragua (see Cole et al., 2005).

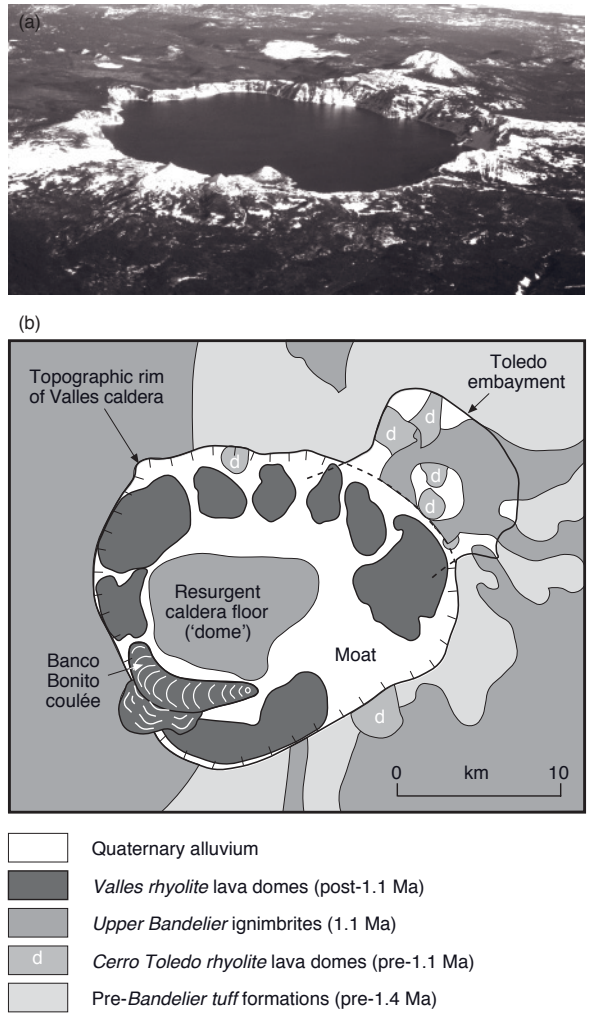


Fig. 7.20 (a) Aerial view of the 7.7 ka BP Crater Lake caldera, Oregon, from the west (US Geological Survey photo by M. Doukas); caldera diameter approx 10 km. Several small cones have since formed within the caldera, including the Wizard Island scoria cone in the foreground. (b) Too good to be true? – a sketch map of the Valles caldera in New Mexico showing the remarkable 'bracelet' of post-caldera ('Valles') rhyolite domes marking the probable location of the ring fracture (caldera structural margin); the Toledo embayment is a subsidiary caldera intermediate in age between the Lower and Upper Bandelier tuff eruptions.

REVIEW – THE SIGNIFICANCE OF PYROCLASTIC ERUPTIONS

Major pyroclastic eruptions occur when evolved, volatile-rich magmas rise to shallow depths where the dissolved-gas pressure in the melt exceeds the load pressure imposed by overlying rocks or magma. Plinian eruptions may occur regardless of whether the magma is silica-oversaturated (e.g. the dacite of Mt St Helens in 1980 or the rhyolites of Taupo 26.5 and 1.8 ka ago) or silica-undersaturated (like the phonolitic pyroclastics of Vesuvius AD 79 and Tenerife over the past 600 ka); the main requirement is a high dissolved volatile content in the magma.

The principal conclusions from this chapter are that:

- It is convenient to divide eruptions broadly into *effusive* and *explosive* categories. The explosivity of an eruption depends primarily on the dissolved volatile content of the magma involved and its viscosity (which increases with SiO_2 content – Box 6.3), though interaction with meteoric water may contribute to explosivity, as happened in the 26.5 ka BP Oruanui eruption at Taupo in New Zealand.
- The categories used in describing volcanic eruptions (plinian, etc.) were originally founded on eye-witness accounts (after Mercalli, 1907), but today the objective categorization of large-scale pyroclastic eruptions is based mainly on clast-size analysis of their fall deposits (Fig. 7.8).
- It is important to use terminology in a way that distinguishes between pyroclastic *processes* on the one hand – terms such as PDC and block-and-ash flow – and the *deposits* they leave on the ground – lapilli-tuff or ignimbrite (if the PDC is pumiceous), and block-and-ash deposit (if it is not).
- The pyroclastic deposit produced by a plinian eruption typically comprises an initial *fall bed* consisting of well sorted pumice (reflecting the initial buoyant state of the eruption column), then one or more units of poorly sorted pumiceous *lapilli-tuff* (ignimbrite representing a denser, non-buoyant eruption column undergoing collapse). The ignimbrite may be succeeded by a closing phase in which *lava domes* of similar composition to the plinian tephra are erupted; such domes are generally considered to represent magma from the same reservoir that has undergone 'de-gassing' during the course of the plinian eruption. Examples are provided by the dacite domes that erupted in the crater of the May 1980 plinian eruption of Mt St Helens (Washington) and by the ring of rhyolite domes in the Valles caldera in New Mexico (Fig. 7.20b).
- Hydrovolcanic eruptions – involving interaction between magma and *external water* – produce tephra with higher degrees of fragmentation (Fig. 7.8) producing fine ash and a high proportion of glass. Accretionary lapilli are often formed in such eruptions.
- *Nuées ardentes* (Fig. 7.14a), consisting mainly of juvenile dense lava clasts and ash (forming block-and-ash deposits – Fig. 7.14b), are hot PDCs that originate in the collapse of perched lava domes.
- Base surges (Fig. 7.9a) are dilute, cool PDCs that migrate radially outward from a hydrovolcanic explosion and deposit distinctively laminated ash beds (Fig. 7.15a).
- Large pyroclastic eruptions are often accompanied by the formation – or renewed subsidence – of a caldera (Figs. 7.19, 7.20). The largest such eruptions may have global environmental consequences (e.g. the 74 ka BP Toba eruption).

EXERCISES

7.1 Devise an appropriate descriptive name for the rock shown in Plate 7.1 reflecting the components present. Comment on the grade of pyroclasts present.

7.2 Explain the differences in meaning between the following sets of terms:
- lapilli-tuff and ignimbrite;
- plinian and vulcanian;
- pumice-rich PDC and ignimbrite;
- resurgent dome and lava dome;
- column collapse, dome collapse and sector collapse;
- caldera and crater;
- lahar and debris avalanche.

7.3 The sequence below summarizes a pyroclastic deposit exposed in a quarry face.

(a) Summarize the sequence of beds in words using appropriate descriptive terminology.

(b) Interpret this stratigraphic record in terms of successive eruptive processes.

5.	6 m bed similar to 3, but pumice clasts show marked flattening in the central portion
4.	0.15 m pumice-ash layer notably richer in lithic clasts
3.	5 m bed of lithified unsorted pumice clasts and ash, with small, sparse lithic clasts
2.	1.5 m bed of well sorted pale pumice clasts (≤2 cm), fining slightly towards the top
1.	Poorly sorted lithified pumice clasts and ash with weathered upper surface (base not exposed)

Chapter 8

Granitic rocks

'Granitic' rocks – embracing the coarse- and medium-grained counterparts of andesite, dacite and rhyolite (Chapter 6) – are the most abundant igneous rocks of the Earth's continental crust. They are found in various geotectonic settings, from orogenic and continent-collision zones such as the Andes and the Himalaya to anorogenic intraplate settings, and they even occur in small volumes at mid-ocean ridges and in ophiolite complexes. The thermal and volatile fluxes in the roof zones of granitic plutons and **batholith**s are a key engine of hydrothermal mineralization, by which important metalliferous mineral deposits are formed. Granitic rocks – and the continents of which they form an important part – are features that make the Earth unique among the planets of the solar system (Campbell and Taylor, 1983).

THE NOMENCLATURE OF INTERMEDIATE AND ACID PLUTONIC ROCKS

Definitions of granitic rock types

Petrologists apply the adjective 'granitic' more widely than the noun 'granite'. It embraces diorite, granodiorite and granite, which are broadly the coarse-grained analogues of andesite, dacite and rhyolite respectively. Unlike their volcanic counterparts – where latent mineralogy may be concealed by glass, or fine grain-size may defeat reliable identification – the grain size in granitic rocks is sufficient for the constituent minerals to be identified with confidence under the microscope. Most are also readily distinguishable in hand-specimen (Table 8.1). Accordingly the International Union of Geological Sciences (IUGS) recommends a purely modal (petrographic) basis for naming granitic rocks, without resort to the total-alkalis versus silica (TAS) plot discussed in Chapter 6. Note that the IUGS scheme – summarized in Fig. 8.1 – includes more categories for plutonic rocks than Fig. 6.1 did for volcanic ones.

In practical terms, the manner in which names are allocated to intermediate and acid plutonic rocks depends on the information available:

- When a *quantitative* ***mode*** is available, granite and granodiorite are distinguished according to the relative proportions of alkali feldspar and plagioclase using the QAP plot shown in Fig. 8.1.[1] In this diagram, diorite falls in the same field as gabbro; the distinction between them is drawn on the basis of *plagioclase composition* – calcic (An > 50) for gabbro, sodic for diorite (Le Maitre, 2002, p.24). Anorthosites fall in this field too, but have a colour index $M < 10\%$ (see Fig. 1.3b).
- A petrologist making *qualitative petrographic observations* of minerals and textures would use a scheme such as Table 8.2.[2]

[1] The dividing lines in Fig. 8.1 are arbitrary boundaries for dividing up a continuum of plutonic rock compositions; they do not signify any compositional breaks between natural rock populations.

[2] Distinguishing between plagioclase and alkali feldspar in plutonic rocks is summarized in Box 8.1.

Igneous Rocks and Processes: A Practical Guide, 1st edition. By Robin Gill. Published 2010 by Blackwell Publishing

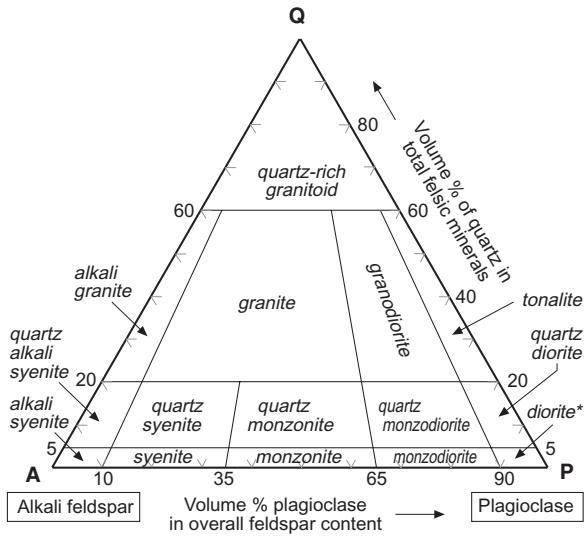


Fig. 8.1 A ternary QAP plot showing the relative modal proportions of quartz (Q), alkali feldspar (A) and plagioclase (P) defining the IUGS fields for granitic rocks, after Le Maitre (2002, Fig. 2.11);** v-marks indicate 10% divisions. Lines radiating from the Q apex are boundaries at plagioclase/total feldspar = 10, 35, 65 and 90% (by volume). For plotting a rock **mode** in this figure, scale up the proportions of quartz, alkali feldspar and plagioclase so that they sum to 100% exclusive of other minerals (see Fig. B1b, Appendix B). For guidance on the petrographic distinction between alkali feldspar and plagioclase in plutonic rocks, see Box 8.1. IUGS defines 'plagioclase' as feldspar with >5% An and 'alkali feldspar' as having <5% An.

*diorite if the plagioclase is sodic (An < 50%), gabbro if the plagioclase is calcic.
**As in Chapter 6, the simpler terms alkali syenite, quartz alkali syenite and alkali granite have been substituted for alkali *feldspar* syenite, etc.

Simple definitions expressed in words are as follows:

Diorite: a coarse-grained, usually mesocratic igneous rock consisting essentially of sodic plagioclase and one or more mafic minerals; an abundance of hornblende usually serves to distinguish diorite from gabbro (Plate 8.1).

Tonalite: a coarse-grained, mesocratic or leucocratic igneous rock consisting essentially of sodic plagioclase and quartz, accompanied by one or more hydrous mafic minerals [10 < *M* < 40].

Granodiorite: a coarse-grained, leucocratic igneous rock consisting essentially of sodic plagioclase, potassium feldspar (including **perthite**) and quartz, accompanied by one or more hydrous mafic minerals; distinguished from granite by the *predominance of plagioclase* [5 < *M* < 25].

Granite:[3] a coarse-grained, leucocratic igneous rock consisting essentially of quartz, potassium feldspar (including perthite) and plagioclase; a *predominance of alkali feldspar* distinguishes it from granodiorite [5 < *M* < 20].

Alkali granite: a coarse-grained, leucocratic igneous rock consisting essentially of quartz and potassium feldspar (including perthite) with *negligible plagioclase*; commonly confirmed by the presence of distinctive alkali pyroxene or alkali amphibole (see Chapter 9) [*M* usually <20].

All of these rock types are embraced by the general field (or hand-specimen) term **granitoid.** The prefix 'leuco' may be attached to tonalite, granodiorite or granite to identify unusually leucocratic specimens (whose colour indices *M* fall below the ranges indicated).

These names apply to coarse-grained intermediate and acid rocks. The prefix 'micro' may be used to denote equivalent medium-grained rocks: 'for example, microdiorite' signifies a rock of diorite mineralogy and composition which happens to be medium- rather than coarse-grained.[4]

Two varieties of tonalite earn themselves specific names on account of distinctive geotectonic connotations. **Trondhjemite** is a **leuco**tonalite (i.e. consisting essentially of plagioclase and quartz – Fig. 8.1), usually also containing minor biotite. Trondhjemites were the igneous protoliths from which many gneiss complexes of the Archaean cratons formed, and many Archaean gneisses share geochemical attributes with modern adakite

[3] This is the *sensu stricto* meaning of 'granite'. The name is also sometimes used *sensu lato* to embrace all of the granitic rocks.
[4] This established usage (e.g. Cox et al., 1988) is preferred to that suggested by Le Maitre (2002, p.21).

Table 8.1 Identifying the main rock-forming minerals of granitic rocks in hand-specimen.

Mineral	Colour	Habit	Cleavage, etc	Notes
Quartz	colourless/grey	usually anhedral	no cleavage	white when in h/thermal veins
alkali feldspar	pink or white	lath-shape, tabular	poor, 2 sets at 90°	simple twins often visible
plagioclase	white (rarely green or black)	lath-shape, tabular	poor, 2 sets at ~90°	rarely see multiple twins
pyroxene	black to dark green or brown	4- or 8-sided prisms	two good sets at ~90°	
Amphibole (hornblende)	black to dark green	lozenge-shaped prisms	two good sets at ~120°	
biotite	black to dark brown	dark shiny flakes (6-sided)	one excellent cleavage	
muscovite	colourless	silvery flakes (6-sided)	one excellent cleavage	
tourmaline	usually black	elongate 3-sided prismatic/needles	no cleavage	lack of cleavage distinguishes from hornblende

Table 8.2 Mineralogy of typical granitic rocks.

	Diorite	Tonalite	Granodiorite	Granite[¶]	Alkali granite
Essential minerals	• plagioclase • one or more mafic minerals as below	• plagioclase • quartz	• sodic plagioclase • quartz • alkali feldspar *plag > alk fsp*[$]	• alkali feldspar • quartz • sodic plagioclase *alk fsp ≥ plag*	• alkali feldspar • quartz
Type minerals	• quartz • hornblende • biotite • augite	• hornblende • biotite[@]	• hornblende • biotite[@]	• hornblende • biotite[§ @] • muscovite[§] • tourmaline • garnet (almandine) • cordierite • andalusite	• riebeckite or other alkali amphibole • aegirine-augite (These alkaline minerals are discussed in Ch. 9)
Colour index	Melanocratic or mesocratic	Mesocratic*	Mesocratic or leucocratic	Leucocratic	Leucocratic
Common secondary minerals	• chlorite, **uralite** or **iddingsite** replacing pyroxene, hornblende or biotite • **sericite** or epidote replacing feldspars (Quartz is not susceptible to alteration.)				

[$] For the distinction between alkali feldspar and plagioclase in plutonic rocks under the microscope, see Box 8.1. **Perthite**, when present, is included with alkali feldspar; **antiperthite** is counted as plagioclase.
[§] The name 'two-mica granite' is often used for a granite containing *both* biotite and muscovite (Plate 8.2).
* A leucocratic variant of tonalite, consisting essentially of sodic plagioclase and quartz with biotite, is given the name **trondhjemite**.
[¶] The terms (quartz-) monzonite and (quartz-) syenite designate quartz-poor equivalents of sodic and potassic granites (see Fig. 8.1).
[@] Often contains inclusions of radioactive accessory minerals like zircon that give rise to pleochroic haloes (Plate 8.10).

Box 8.1 Distinguishing between types of feldspar in plutonic rocks

Figure 6.1.1 (Box 6.1) showed the range of Or–Ab–An solid solutions that occur in natural feldspars at magmatic temperatures. In volcanic rocks, although phenocrysts may *grow* at slow cooling-rates, the rapid chilling associated with eruption ensures that feldspars are 'frozen' in the high-temperature forms shown in Fig. 6.1.1. During the slow cooling experienced by a plutonic rock, however, alkali feldspar crystals have sufficient time to **invert** to structures that are stabler at low temperatures. Accordingly, plutonic rocks exhibit intra-crystalline textures in **alkali feldspar** crystals that are not seen in volcanic rocks. These are illustrated in Fig. 8.1.1 below, using a three-dimensional figure formed by adding a temperature dimension to the ternary diagram shown in Fig. 6.1.1.

The top surface of Fig. 8.1.1 is identical to Fig. 6.1.1 (though seen here in perspective); lower regions illustrate the complexities that develop only in slowly cooled feldspars. The ruled areas signify regions of compositional space where no homogeneous solid solutions exist in nature: the ruling is a visual reminder that any composition falling within these areas represents a *mixture* of two feldspars whose compositions lie at each end of a **tie line**. Note, on the $KAlSi_3O_8$–$NaAlSi_3O_8$ face of the figure, the 2-feldspar field demarcated by the **solvus**. This embraces a range of Or–Ab solid solutions which, though stable as a homogeneous phase at high temperature, **exsolve** into two distinct phases as temperature falls below the solvus (cf. Fig. 4.5.2 in Box 4.5). An example of exsolution texture is shown (in crossed polars) in Fig. 8.1.1c: dark blebs and lamellae of Na-feldspar (almost at extinction) form a herringbone pattern dictated by the symmetry of the simple-twinned K-feldspar host (light shade in lower part of field; mid-grey in upper). Alkali feldspars showing such structures are called **perthites**. Exsolution – being a relatively slow process – does not occur during rapid cooling, and high-*T* homogeneous feldspars therefore survive in a **metastable** state in volcanic rocks. Many of the sanidine and anorthoclase phenocrysts present in evolved volcanic rocks would have exsolved to form perthite and **antiperthite** intergrowths respectively (Fig. 8.1.1), had their slow cooling not been interrupted by eruption.

When a K-rich sanidine experiences slow cooling, it inverts first to an alternative **monoclinic** form called orthoclase, then to **triclinic** microcline. Inversion is a slow process suppressed by rapid cooling. Like its fellow triclinic alkali feldspar, anorthoclase, microcline exhibits crossed multiple twinning (Fig. 6.1.1b), widely known as 'tartan' twinning. These two alkali feldspars might be difficult to distinguish were it not for the different cooling regimes required to form them: microcline occurs only in slowly cooled (i.e. coarse-grained) rocks like granite (Plate 8.2), whereas anorthoclase is confined to volcanic rocks (Plate 9.6).

In hand-specimen, alkali feldspar in plutonic rocks forms white or pink tabular crystals, in which simple twinning can sometimes be recognized with the naked eye or under a hand lens (Plate 8.8). Plagioclase forms elongated tabular crystals, usually white in colour; simple twinning is less common.

volcanics (see 'Archaean **TTG** suite' below). Plagiogranite is a petrographically similar intrusive rock that occurs in small volumes at ocean ridges and in many ophiolite sequences (see Table 8.4).

Related rocks

In the modal classification shown in Fig. 8.1, granite and granodiorite are bordered on the quartz-poor side by quartz syenite, quartz monzonite and quartz monzodiorite. These are transitional rocks types between granitoids and their SiO_2-saturated or SiO_2-undersaturated alkaline analogues syenite, monzonite and monzodiorite, which are discussed in Chapter 9. They share many of the textural and mineralogical characteristics of granitoids, and are not uncommonly associated with them in the field.

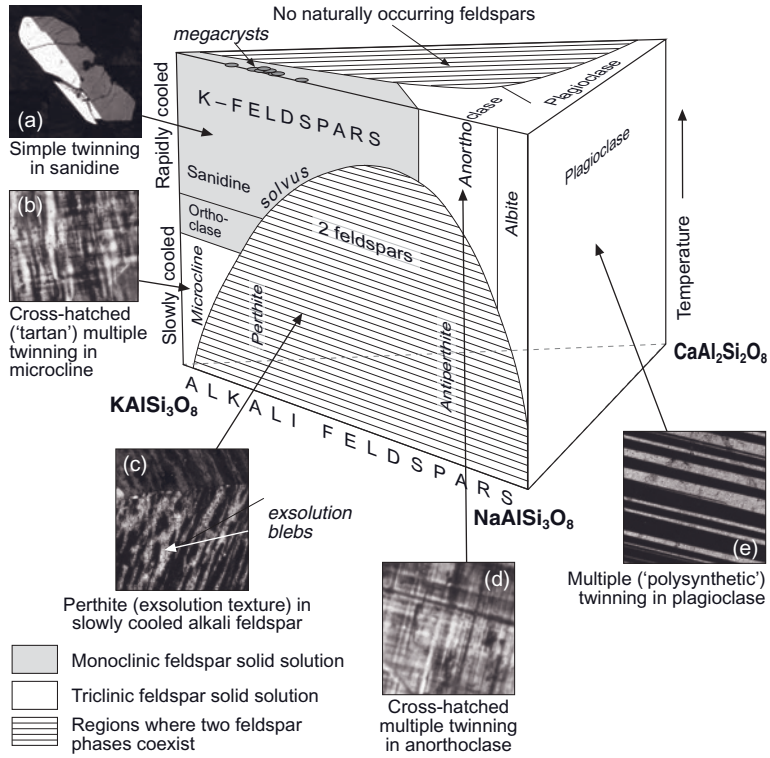


Fig. 8.1.1 Extent of natural solid solution in feldspars as a function of temperature; the triangular base of the figure is the same as that in Fig. 6.1.1 and the vertical dimension represents temperature. The panels illustrate (under crossed polars) examples of the twinning and exsolution characteristic of each range of solid solution: (a) simple twinning in high-*T* sanidine; (b) coarse 'tartan' twinning in low-*T* microcline; (c) exsolution and simple twinning in low-*T* **perthite**; (d) fine cross-hatched multiple twinning in high-*T* anorthoclase, and (e) planar multiple twinning in high- *and* low-*T* plagioclase. The ellipses labelled '*megacrysts*' show the compositions of K-feldspar megacrysts in granites, as compiled by Vernon (1986).

Orthopyroxene granites

Hydrous minerals like hornblende and biotite are ubiquitous in all of the rocks discussed above. They reflect crystallization of evolved, hydrous magmas under plutonic conditions of relatively high P_{H2O} in which solidus temperatures are lower than those at which such minerals dehydrate (Fig. 6.2.2 in Box 6.2). Some granitic melts, however, crystallize in circumstances where pleochroic orthopyroxene takes the place of hornblende, and the only hydrous mineral present is minor biotite. Orthopyroxene-bearing rocks of granitic and monzonitic composition – known respectively as **charnockites** and mangerites (Fig. 8.2) – are often (though not invariably) associated with massif-type anorthosite complexes (Fig. 4.15). Their origin and significance are discussed later.

FORM AND SCALE OF GRANITIC INTRUSIONS

Individual plutons

Individual granite plutons vary in surface outcrop from <10 km^2 to more than 1000 km^2.

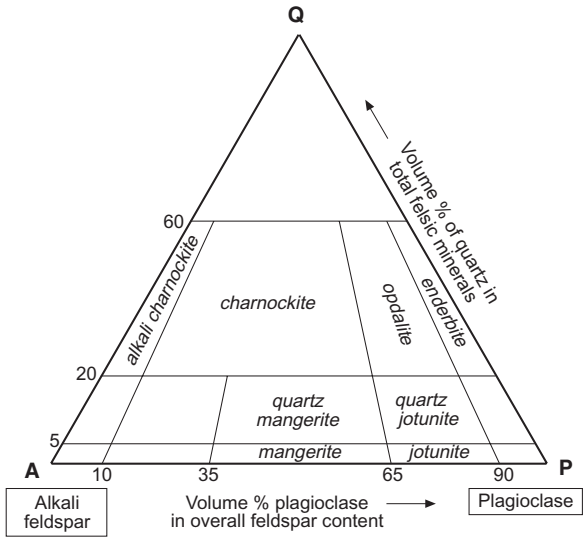


Fig. 8.2 A ternary QAP plot showing the relative modal proportions of quartz (Q), alkali feldspar (A) and plagioclase (P) defining the IUGS fields for *orthopyroxene-bearing* granitic rocks, after Le Maitre (2002, Fig. 2.11). Lines radiating from the Q apex are boundaries at plagiocl ase/total feldspar = 10, 35, 65 and 90% (by volume).

Until recently our understanding of their shape was relatively unconstrained by facts. Granite exposed at the surface usually constitutes only the unroofed uppermost dome of a body whose deeper architecture is seldom observed in the field; it is unusual for granite plutons to be exposed in sections more than a kilometre or two in vertical extent, and the floor of such intrusions is almost never seen (e.g. Rosenberg et al., 1995). Because granite outcrops are often bounded by circular or elliptical outward dipping contacts (Fig. 8.3a), the intrusion beneath has traditionally been assumed – for want of direct three-dimensional observation – to take the form of a vertical cylinder, or stock. This conventional view was reinforced by the concept of buoyant granite **diapirs** ascending through surrounding denser crust developed by Ramberg (1981).

Most of what we know about the overall shape and volume of granite plutons comes from geophysical investigations. Granites often have lower density than surrounding country rocks, and so their concealed form can be investigated using the associated negative **Bouguer** gravity anomaly. Examples are the granitoid intrusions of the English Lake District investigated by Bott (1974). Figure 8.4 shows the Bouguer anomaly (a) and the preferred density interpretation (b) for the northern part of the granite mass comprising the Eskdale Granite and the overlying Ennerdale Granophyre (shown in dark grey in the inset map). The density models Bott devised to account for the gravity data are consistent with a steep-sided, internally zoned granite stock (Fig. 8.4b), but such models are never uniquely determined by gravity data and alternative interpretations may be found to explain the data; for example, the Bouguer anomaly trend in Fig. 8.4(a) could alternatively be explained by a homogeneous intrusion whose base becomes shallower in the north than in the south (Bott, 1974).

Does our mental image of the Eskdale granite as a continuous solid mass represent the truth? Seismic reflection surveys – capable of picking up finer internal detail than gravity studies – provide an alternative geophysical tool that yields new insights into the architecture of granite intrusions, as illustrated by the work of Evans et al. (1993) on the same pluton (Fig. 8.4). Evans et al. (1993) discovered in their WSW–ENE seismic line – perpendicular to Bott's gravity traverse – numerous horizontal reflectors located *within* the concealed part of the granite pluton, down to depths of 4 km (the depth limit of their data). The reflectors were concentrated in distinct depth bands 100–250 m thick, separated by unreflective layers up to a kilometre thick. Evans et al. (1993) concluded that the supposedly solid mass of the granite pluton actually consists (at least in the upper, western portions they investigated) of a stack of granite sheet intrusions – forming the non-reflective layers – interfingering with reflective slivers of sedimentary country rocks (Skiddaw Group, Fig. 8.4c), which in their words

> '*give the steep western margin of the granite complex a cedar-tree profile*'.

Though one should be cautious about extending this analysis to the Eskdale pluton as a

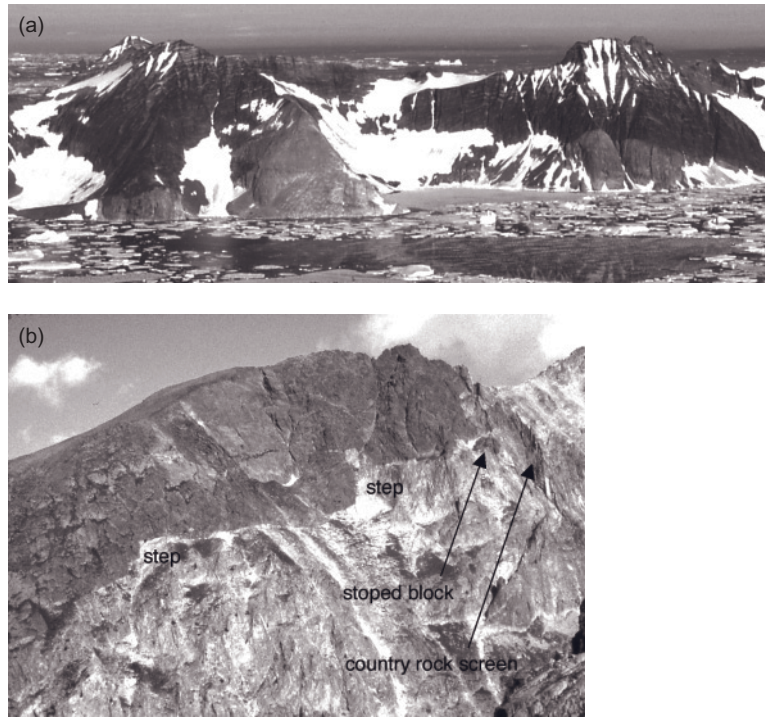


Fig. 8.3 (a) Steep outward-dipping eastern margin of a granite pluton intruding diorite, Kialineq plutonic centre, East Greenland; note the light-coloured, sub-horizontal granite sheets intruding the roof zone (island peaks).* (b) Stepped roof contact of granite pluton, Argentera massif, Italian Alps; a stoped roof block and country-rock screen can be seen on the right.

*Photograph taken by the author during fieldwork carried out under contract to what is now the Geological Survey of Denmark and Greenland; reproduced here with their kind permission.

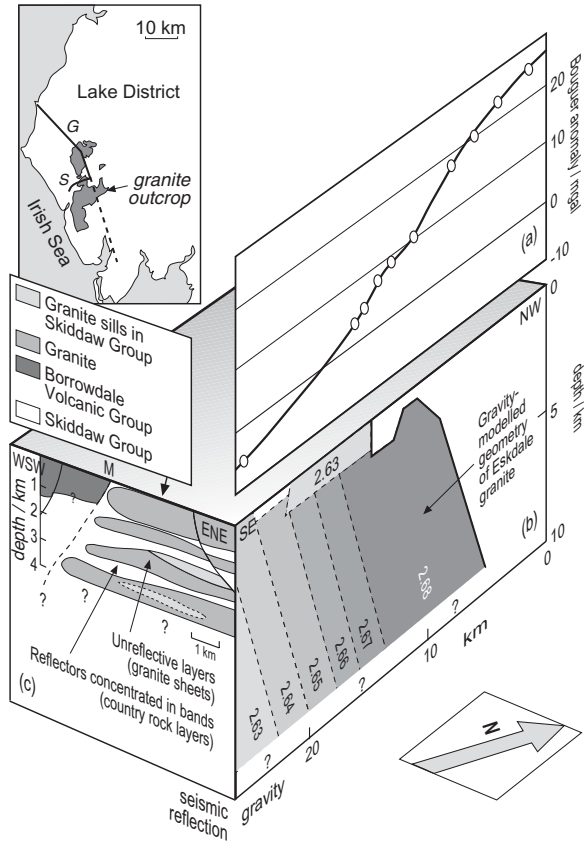


Fig. 8.4 Alternative geophysical views of a granite pluton. Pane (a) of the three-dimensional model shows the **Bouguer anomaly** across the northern half of the Eskdale and Ennerdale granite complex (English Lake District – see index map), while face (b) beneath it shows a model SE–NW section through the granite body (shades of grey), showing the rock-density distribution that best accounts for the Bouguer anomaly; the inferred densities of the granite are given in kg dm^{-3} (data and interpretation from Bott, 1974). Face (c) shows an ENE–WSW cross-section through the western margin of the granite body, based on the seismic reflection study of Evans et al. (1993), showing the granite as consisting of stacked sheet intrusions; the dashed line 'M' marks the overall western limit of the granite mass. The index map shows the lines of the gravity (G; only the solid portion is shown in (a) and (b)) and seismic (S) surveys.

whole, it accords with a current shift in thinking which views most granite plutons as near-horizontal tabular bodies rather than vertical cylinders extending to depth. This perspective is also relevant on the **batholith** scale, as discussed in the following section.

Some granitoid plutons take the form of ring intrusions (Table 8.3), emplaced around the periphery of a foundered crustal block; they are often closely related to an overlying volcanic caldera system and therefore represent high-level intrusions. A well known example is the Glencoe ring intrusion in Scotland (Fig. 8.5a), discussed below under the heading of 'Cauldron subsidence'. Sometimes a succession of mutually invasive arcuate intrusions may be formed, as in the western Red Hills centre in Skye (Fig. 8.5b), suggesting successive episodes of cauldron subsidence.

Batholiths

The high cordilleras of western North America are dominated by vast areas of Mesozoic granitoids, where numerous individual granitic plutons have congregated to form compound masses called **batholiths** (Fig. 8.6). The period over which a batholith develops by successive phases of intrusion may last for 50–100 Ma. In many batholiths – like the Sierra Nevada – newer plutons invade older plutons, creating a complex, mutually intrusive history. In others – like the Peninsular Ranges Batholith in Baja California – individual plutons are separated from each other by a network of intervening country rocks (Johnson et al., 2003). Batholiths are found in continental magmatic arcs, orogenic belts and suture zones of all ages around the world (see for example Fig. 6.21b). They vary in linear scale from the modest Lake District-Weardale Batholith in northern England (of which the Eskdale–Ennerdale pluton featured in Fig. 8.4 forms a part) – traceable from its gravity signature for 100 km to the ENE (Bott, 1974) – to the gigantic Trans-Himalayan batholith which extends for nearly 1500 km along the southern margins of the Tibetan plateau; indeed, if the Karakorum batholith to the west is included, the length of this Trans-Himalayan plutonic system increases to over 3000 km.

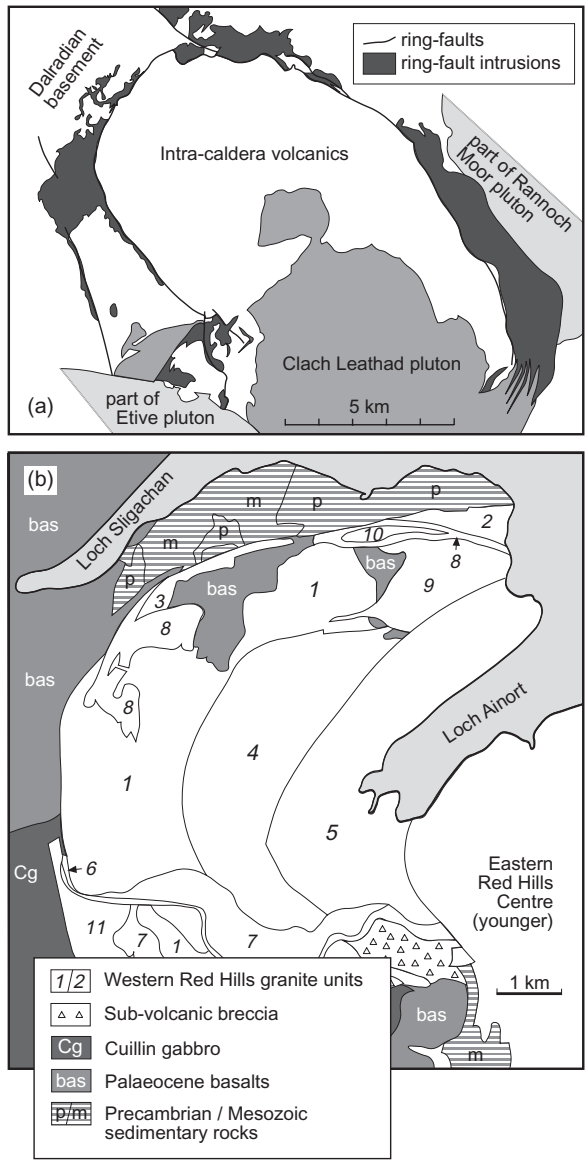


Fig. 8.5 (a) Ring faults, fault-intrusions and the Clach Leathad cauldron-subsidence pluton, Glencoe centre, Scotland (simplified from Kokelaar and Moore, 2006); the ring faults dip nearly vertically in the SW and NW but radially outward at 50–80° in the NE. 'Dalradian' refers to Neoproterozoic metasediments of the Dalradian Supergroup. (b) Successive annular acid intrusions in the Eocene Western Red Hills Centre (WRHC), Isle Skye, Scotland (from Bell, 1976, by permission of the Geologists' Association); numbers indicate the order of emplacement of the WRHC units.

Table 8.3 Some examples of granitoid intrusions: form, age, tectonic setting, associated rock types and mineral deposits.

Apparent form	Example	Age/Ma	Size	Tectonic setting	Associated igneous rock types	Recent description
Stock	North Arran granite, Scotland	60	10 km in diameter	Plume-related passive margin	–	England (1992)
Tabular	Quernertoq rapakivi granite, SE Greenland	~1745 Ma	20 km long	Ketilidian orogen	Microcline granite	Grocott et al. (1999)
Tabular/ lopolith	Ljugaren granite[§], central Sweden	~1700 Ma	$12 \times 12\,km^2$	Postdates 1.9–1.8 Ga Svecofennian orogen	Other granites	Cruden (1998)
Ring intrusion	Glencoe ring intrusion, Scotland (Fig. 8.5a)	~410 Ma	Ring 8 km in diameter Ring intrusion ≤1.5 km wide	435-425 Ma Scandian phase of Caledonian orogen	Intra-caldera calc-alkaline lavas and ignimbrites. **Appinite** bodies are associated with many Caledonian granites	Kokelaar and Moore (2006)
Dyke-like intrusions	Great Tonalite Sill plutons, Alaska*	~65 Ma	Composite body, extends $800 \times 25\,km^2$	Deep shear zone in an accreted terrane	Gabbro, diorite, granodiorite, hornblendite; synplutonic dykes; microdiorite enclaves	Ingram and Hutton (1994)
Batholith	Coastal batholith of Peru	100 to ~60 Ma	$1600 \times 65\,km^2$	Andean cordillera	Marginal-basin basaltic volcanics; diorite, tonalite, granodiorite; andesitic synplutonic dykes	Haerderle and Atherton (2002); Cobbing (1999)

* Despite its name, the Great Tonalite Sill is a 'multiple-dyke-like' structure (Ingram and Hutton, 1994).
§ A good example of a granite body formerly regarded as having diapiric form but now interpreted as a sheet intrusion.

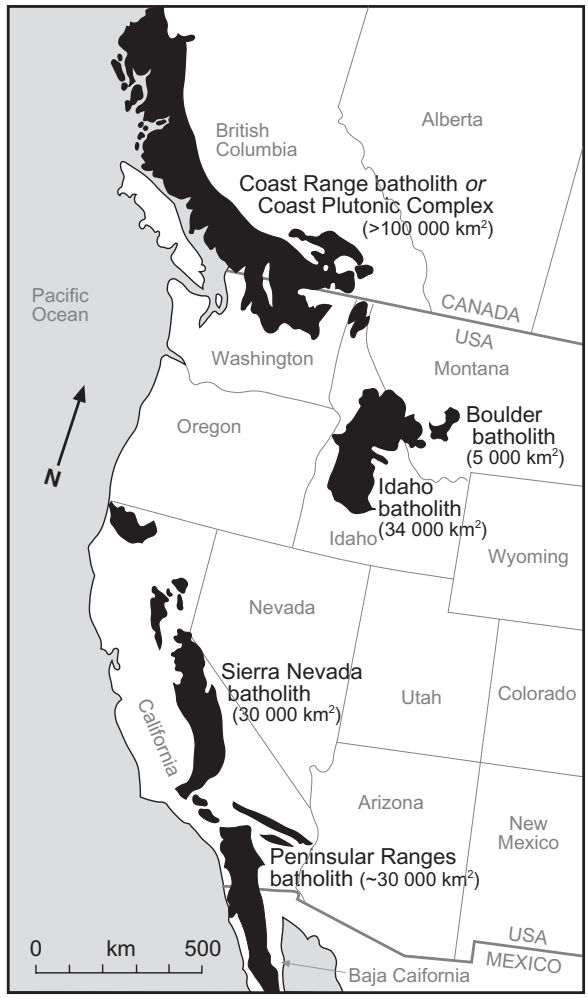


Fig. 8.6 Mesozoic granitoid batholiths of western North America, showing approximate outcrop areas in km².

Though it is natural to imagine such huge intrusive masses having deep crustal roots, there are increasing indications that – like many individual plutons – batholiths may be sheet-like in form (Cruden, 1998; Vigneresse, 1995; Petford et al., 2000; Taylor, 2007). Figure 8.7 shows the results of a gravity traverse of the Coastal Batholith of Peru by Haerderle and Atherton (2002). Field relations show that most of the batholith was intruded into marginal-basin volcanic rocks (Fig. 8.16), chiefly of basaltic composition and thus of relatively high average density. The gravity signal suggests that the batholith has the geometry of a flat slab, extending to no greater depth than 3 km below sea level, except where it is 'anchored' along the western margin by a deeper root zone only 4 km wide (Fig 8.7). Individual plutons in the batholith vary between 1.0 and 5.6 km in thickness, averaging at about 2.6 km and suggesting **aspect ratios** that average around 5. Thus, as Haerderle and Atherton (2002) conclude,

> '*on a crustal scale, it is clear that the batholith forms a thin veneer at the top of the continental crust*'.

It seems likely that most of the world's granitic **batholiths**, contrary to what the Greek meaning of the word suggests, are relatively shallow tabular bodies.

An increasingly powerful technique for investigating pluton shape, complementary to gravity inversion, is to conduct field surveys of the anisotropy[5] of magnetic susceptibility (AMS) across an intrusion, which provide petrofabric information related to the geometry of magma flow during emplacement. In the Dinkey Creek pluton in the Sierra Nevada batholith in California, for example, AMS fabrics provide evidence both for the tabular configuration of the intrusion and for a NNW-trending feeder dyke at depth (Cruden et al., 1999).

EMPLACEMENT OF GRANITIC INTRUSIONS: THE 'SPACE PROBLEM'

> *'In spite of much discussion, there is still no consensus on how space is made for magmas in the continental crust. A major problem involves the three-dimensional shape/geometry and in particular evidence of the floors of plutons which are curiously rarely observed.'*
>
> Haerderle and Atherton (2002)

Accounting for the 'space' currently occupied by a large intrusion is – on the face of it – a key element in understanding the emplace-

[5] Preferred (not random) orientation, in this case of magnetic mineral crystals in an intrusive body.

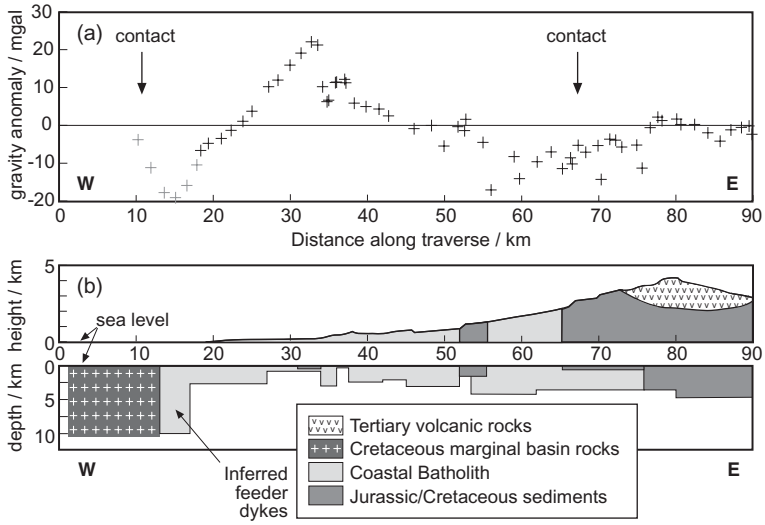


Fig. 8.7 (a) Residual gravity anomaly (after removal of linear regional fields); and (b) the preferred two-dimensional gravity model for the Casma–Huarez gravity traverse across the Coastal Batholith of Peru (Fig. 8.16), after Haerderle and Atherton (2002; copyright Elsevier); note the difference in height-depth scales above and below sea-level in (b). Grey crosses in (a) represent data from parallel traverses.

ment mechanism: a large granite intrusion must have taken the place of an equivalent volume of pre-existing crustal rocks, so to where have those rocks been removed? If something was 'here' before that is no longer here, where is it now? Though this 'space problem' is not confined to granite intrusions, the larger granite batholiths like the Sierra Nevada of California and the Trans-Himalayan batholith highlight it on the most spectacular scale.

Forming granite in situ: 'granitization' and migmatite

One way to circumvent the space problem is to suppose that the granite was not introduced at all, but has formed in situ. Nineteenth-century French geologists developed a notion called 'granitization', which remained popular during the 1930s and 1940s, invoking

> '*a process by which solid rocks are transformed to rocks of granitic character without passing through a magmatic stage*'

(Read, 1957), a change mysteriously accomplished by 'permeating fluids'.

> '*One of the difficulties in proving granitization is that nearly all criteria are subject to alternative interpretations*',

wrote Buddington in 1959. Since that time, the magmatic view of granites has re-asserted its dominance: as Pitcher (1997) observes, the concept of

> '*granitization can now be recognized as one of those blind alleys into which scientific thought is prone to drift*'!

Migmatites, on the other hand, provide direct evidence that granite *can* form more or less in situ. A migmatite (from the Greek for 'mixture') is an intimate outcrop-scale mixture of two components: quartzo-feldspathic layers, pods or veins of granitic composition that cut or are interlayered with darker gneisses (Fig. 8.8). They are found in regional metamorphic terrains that have developed to sufficiently high grade to initiate the partial melting – **anatexis** – of deep-crustal

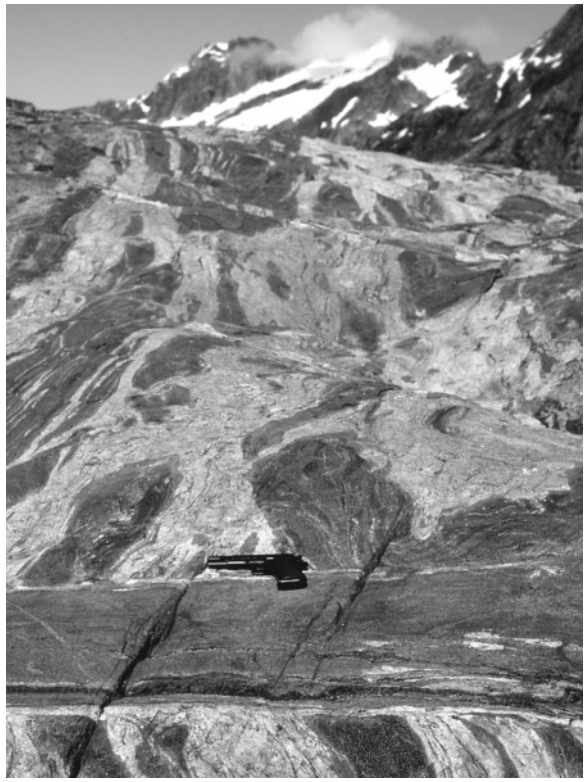


Fig. 8.8 Migmatite in metasedimentary gneiss, Depotfjord, East Greenland (cut by an amphibolite dyke; revolver 22 cm).*

*Photograph taken by the author during fieldwork carried out under contract to what is now the Geological Survey of Denmark and Greenland; reproduced here with their kind permission.

(often metasedimentary) rocks. The lighter veins or layers (which constitute the 'leucosome'[6] component) are interpreted as migrating partial melt frozen while still close to the site of melting; the host gneiss ('mesosome') may develop darker selvages ('melanosome') along the contact with leucosome, which some interpret as the complementary solid residuum left behind by melt extraction; the mesosome is regarded as source rock that has yet to melt.

Are migmatites anything more than a local curiosity – do they have any wider bearing on the source of granite melts? Mehnert (1968) highlighted granitoid massifs in the Black Forest of southern Germany where a transition is observed from a homogeneous magmatic granodiorite core, through increasingly heterogeneous, 'streaky' granodiorite margins that grade out into a migmatite zone, beyond which lie normal quartz-feldspar-biotite gneisses. The implication is that migmatites mark the initial stage of a crustal fusion process deep in the crust that can lead to the accumulation of significant bodies of homogeneous granitic melt. On the other hand, Zeng et al. (2005) cited a migmatite in the southern Sierra Nevada batholith in California which appears to have solidified before it managed to migrate any significant distance. This may often be the case, because most migmatite melts probably form close to the water-saturated solidus (e.g. point *z* in Fig. 6.4.1 in Box 6.4) and any decompression accompanying ascent is likely to cause almost instant solidification; indeed some authors dismiss migmatites as examples of 'failed granites'.

The great majority of granitoid plutons lack any trace of associated migmatite (though many contain inclusions of country rock – see below), and in these cases one must conclude that the magma has migrated to significantly shallower depths than its place of origin, so that space once again becomes an issue. One may conclude that such melts – if anatectic in origin – are likely to have formed in H_2O-*under*saturated conditions (Fig. 6.4.1).

Stoping

Where the roof zone of a shallow granite or other felsic intrusion is well exposed, one may sometimes see the roof rising or falling in steps, and angular blocks of roof rock may be seen suspended in the granite beneath (Fig. 8.3b). These observations are evidence of a style of magma ascent called *stoping*, in which space is created for magma ascent by the detachment and sinking of roof blocks varying in scale from metres to hundreds of metres: magma and roof thus 'change places' incrementally as each block subsides into magma beneath. Stoping requires the upward propagation into the roof rocks of cracks and fissures along which magma can penetrate (Fig. 8.9a), and such brittle behaviour suggests that stoping can operate only in high-level intru-

[6] Greek meaning 'pale body', as distinct from melanosome ('dark body').

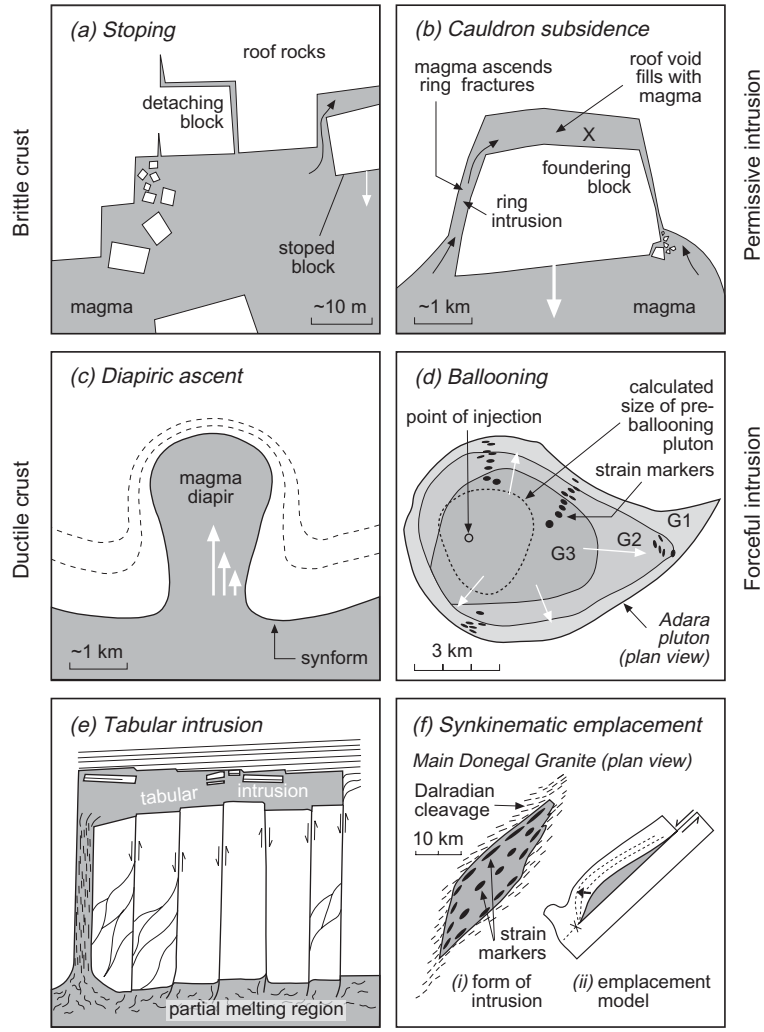


Fig. 8.9 Models and criteria for the ascent and emplacement mechanisms for granitic magma. The scales shown are only illustrative. (a) Stoping. (b) Caldron subsidence. (c) Diapiric up-welling (adapted from Ramberg, 1981). (d) Ballooning: the Ardara pluton is a Caledonian intrusion in the NW of Ireland; internal contacts divide it into 3 intrusive stages: G1, G2 and G3. The inferred point of injection and estimated extent of the initial intrusion prior to ballooning (dashed line) are from Molyneux and Hutton (2000). The steep tangential foliation in the granite increases toward the periphery of the pluton, as indicated by the flattening of enclaves which act as strain markers (black ellipses, after Holder, 1979). (e) Emplacement of a tabular pluton via a dyke root zone, according to Haerderle and Atherton (2002) and Cruden (1998); the intrusion begins as a concordant sill but inflates chiefly by floor depression; stoping modifies the roof profile. (f) Cartoon representing the emplacement of the Donegal Main Granite into a sinistral transcurrent shear zone, after Hutton (1982, 1988).

sions whose roof rocks are relatively cool. Undoubtedly stoping modifies the roof profile of many felsic intrusions, but there is little evidence that piecemeal stoping contributes in a major way to the ascent of granite plutons (Glazner and Bartley, 2006).

Cauldron subsidence

Ring and arcuate intrusions (Fig. 8.5) indicate, on the other hand, that the foundering of much larger crustal blocks – by means of steep ring faults – can provide important channels for the ascent of acidic magma in the

upper crust. The term **cauldron subsidence** was introduced by Clough et al. (1909), in their classic work on Glencoe in Scotland, to describe the piston-like sinking of a ring-fault-bounded block into a magma body beneath (Fig. 8.9b), with complementary ascent of magma up the ring fractures to fill the potential roof-void above, forming a 'bell-jar'-shaped intrusion. In some cases, as in Glencoe (darker units in Fig. 8.5a), the ring faults invaded by the granitic magmas clearly correlate with the margins of a surface caldera, though in more deeply exhumed systems little proof of this association may survive. According to Kokelaar and Moore (2006), the Clach Leathad pluton (medium-grey in Fig. 8.5a)

> '*represents the roof zone of the intrusion where magma welled up to replace foundered crustal blocks of Dalradian metasedimentary rocks and Glencoe igneous rocks*',

as symbolized by point X in Fig. 8.9(b).

Cauldron subsidence may occur repeatedly at the same igneous centre, later intrusions sometimes being offset relative to earlier ones as seems to have occurred in the Western Red Hills granite centre in Skye (Fig. 8.5b) and most spectacularly in the Ras ed Dom syenite-granite ring complex in Sudan (Fig. 8.18). Pitcher (1997) argued that major batholiths may be built up by

> '*nested arrays of multiple plutons extending downwards as a stack of foundering blocks and interconnecting cauldrons*'.

Stoping and cauldron subsidence operate in shallow-level intrusions where the relatively cool country-rock envelope is susceptible to brittle failure. These mechanisms are described as *permissive* because subsidence simply allows crustal rocks and magma to exchange places.

Diapiric upwelling

Under hotter conditions deeper in the crust, the contrast in viscosity or ductility between viscous magma and the solid country-rock envelope may be substantially less than near the surface. Grout (1945) and Ramberg (1981) were among many to argue that, once the viscous drag between magma and wall-rocks is reduced sufficiently, buoyant magma could well up as a viscous **diapir** resembling a salt dome, the up-flow being compensated by a peripheral down-flow of heated (and thus ductile) country-rocks surrounding the diapir. Any bedding or other original fabric in the surrounding medium is downwarped to form a peripheral synform (Fig. 8.9c) owing to removal of material from the source layer into the diapir, as can be seen to happen around salt diapirs.

The concept of diapiric upwelling, born more of laboratory experiment than field observation, has been influential in sustaining a long-established view of cylindrical granite plutons with deep roots, which has however been seriously challenged in the past 20 years. Grout and Ramberg assumed in their models that granite magmas had high viscosities not markedly below that of solid rock, whereas modern measurements suggest that much lower granite melt viscosity values would apply in practice (e.g. Clemens and Petford, 1999). Even allowing for the effect of crystal content (Box 6.3), such measurements undermine the physical basis for diapirism. Moreover, according to Grocott et al. (1999),

> '*the hypothesis for the emplacement of granites as diapirs can no longer be sustained for mid- to high crustal levels because re-examination of plutonic contacts previously thought to be diapiric has failed to reveal critical diagnostic structures* [pointing to diapirism] *in the intrusive and host rocks*'.

A few plutons, notably the North Arran outer granite in Scotland, do however show structural features that are hard to explain without invoking diapiric uprise (England, 1992).

Ballooning

Magma ascending through the crust becomes cooler and more viscous, and its upward progress may therefore stall. Deeper fractions of the same magma stream – retaining their higher temperature – continue to ascend and invade the cooler mass above. This can lead to up-doming and radial inflation of the stalled magma body. The distinctive attribute of this process, known as *ballooning* (Fig. 8.9d), is that it causes a concentric flattening foliation to develop, both in the outer zones of the pluton itself – as indicated by the flat-

tening of xenoliths and other strain markers – and in the surrounding country-rock envelope, reflecting the outward-directed compression imposed by the expanding core of the magma body. A widely cited example of ballooning is the Caledonian Ardara pluton in the NW of Ireland (Molyneux and Hutton, 2000). A similar mechanism has been invoked to explain the tangential foliation near the margins of the Tarçouate Laccolith in Morocco (Pons et al., 2006).

The notion of ballooning remains controversial; other authors have for example attributed the phenomena at Ardara and similar intrusions elsewhere to multistage diapirism (Paterson and Vernon, 1995). Since space is created by radially compressing pre-existing country rocks, diapiric upwelling and ballooning are classed as *forceful* emplacement mechanisms, as distinct from the *permissive* mechanism of cauldron subsidence.

Emplacement of tabular plutons and batholiths

We concluded in a previous section that many granite plutons and batholiths, notwithstanding their sometimes domed upper surfaces with outward dipping contacts, are actually tabular in overall three-dimensional form with a total thickness of 5–6 km or less (Figs. 8.4 and 8.7). Understanding how such sheet intrusions might form requires answers to two questions:

1. How is *magma transported* from the source to the level of the pluton?
2. How is *space made* to accommodate the magma that filled the pluton?

There is an increasingly strong case for arguing that most granitic magmas ascend through the crust not as classic cylindrical diapirs but by means of dyke systems, which in many cases seem to exploit pre-existing faults. Many Andean batholiths lie close to, or are bordered by, major fault systems, and gravity studies suggest that the Coastal Batholith of Peru, for example, has a narrow, steep-sided 'root-zone' extending to at least 10 km depth at its western margin (Fig. 8.7) which seems likely to be the expression of a dyke feeder system. Other examples of such root zones are cited by Cruden (1998). Petford et al. (1993) estimated that the flow of viscous granitic magma up a dyke 6 m wide, resulting either from buoyancy or from magma pressure, could be sufficiently rapid to fill a major batholith (their calculations were based on the Cordillera Blanca in Peru) in a period no longer than a few hundred years.

Upward propagation of a magma-filled dyke may be arrested in a number of ways – such as by intersection with a freely slipping horizontal fracture, or a ductile or fracture-resistant horizon – at which point magma will spread out laterally as a thin sill or sheet. Given sustained magma pressure, this sill will then inflate vertically – in much the same manner as discussed for thick basaltic lava flows in Chapter 2 – to form a voluminous tabular intrusion limited only by the continued supply of magma.

> '*Emplacement occurs when mainly vertical flow switches to predominantly horizontal flow and vertical inflation*'

(Brown, 2007). Inflation may be accomplished by up-doming of the roof (forming a **laccolith**) at shallow crustal levels, or by floor depression (forming a **lopolith**); in the latter case the floor of the intrusion

> '*can be viewed as foundering into a deflating layer of partial melt*'

(Cruden, 1998) at a deeper crustal level, as shown in Fig. 8.9(e), so that

> '*the rates of melt production, extraction, ascent and emplacement ultimately are balanced at the crustal scale*'

(Brown, 2007). Cruden (1998) and Haerderle and Atherton (2002) favour floor depression as the dominant mechanism for the majority of granite plutons, whereas Grocott et al. (1999) and Stevenson et al. (2007) argue that roof uplift also has a role to play. Brown (2007) argues that roof uplift will dominate at shallow levels in the crust, whereas deeper in the crust where overburden pressures are much higher floor depression will prevail.

Synkinematic plutons

Granite magmatism is closely associated with orogeny, and the form of many granite plutons

reflects the tectonic forces that controlled their emplacement. Tectonism may play a part in creating the space occupied by a granite. An example is the Main Donegal Granite in NW Ireland (Fig. 8.9f), whose emplacement was re-investigated by Hutton (1982, 1988). The granite intruded a sinistral shear zone whose transcurrent displacement is demonstrably greater in the NE than in the SW (illustrated in Fig. 8.9f[ii] by imagining that the shear zone is pinned in the SW at the point shown by a cross). According to Hutton, differential shear displacement caused the NW side to bend outward and create the space now filled by the granite, which was emplaced synchronously with shear zone development. The granite has itself been strongly deformed by on-going transcurrent shear, the strain being most marked toward the contacts and toward the narrower NE end (Fig. 8.9f).

Space for granitic magma may also be created within local sites of dilation in shear zones, in extension structures, and in thrust settings.

INTERNAL STRUCTURES IN GRANITIC INTRUSIONS

Inclusions

Many granitoids – like their gabbroic counterparts (Chapter 4) – host a diverse suite of inclusions, often referred to in European circles as **enclaves** (from the French word for 'enclosure'). Both terms embrace small bodies, centimetres to metres across, that show an obvious contrast in grain-size or composition compared to the granite that envelops them. Such inclusions may have several origins:

1 As xenoliths of country rock torn from the chamber or conduit walls or foundered from the roof, in various stages of digestion or disintegration from pristine (with sharp boundaries – Fig. 8.10a) to partly assimilated (diffuse boundaries).
2 As rounded globules or trains of blebs of contrasting magmatic material – often finer grained and darker – suggesting injection of new magma of different composition while the granite was still molten (Fig. 8.10c; Plate 8.9). This new magma, if more mafic and therefore initially hotter, may appear to quench to a fine-grained solid when chilled by contact with cooler granitic magma (see below).
3 As **schlieren** of **cognate** cumulates picked up by an influx of new magma (e.g. Reid et al., 1993), sometimes called **autoliths**.
4 As fragments of refractory solid residue from the melting process – known loosely as *restite* – or disaggregated crystals of restite minerals.

Igneous layering

Modal layering of the kind seen in gabbro intrusions (Chapters 4 and 5) is less well developed and more enigmatic in acidic intrusions. Examples have however been described from a number of granitic and syenitic plutons. A recently cited example is the Tarçouate Laccolith, a shallow-level, composite, calc-alkaline pluton of Proterozoic age in the Anti-Atlas ranges of Morocco (Pons et al., 2006). It consists of an outer, foliated but homogeneous biotite granodiorite surrounding an inner hornblende granodiorite that is rich in melanocratic (monzodiorite) inclusions; the hornblende granodiorite core exhibits pervasive **modal layering** (variation in the proportion of biotite and hornblende) accompanied by cross-stratification and trough-banding reminiscent of similar features in gabbro intrusions like Skærgaard (Fig. 4.6d,e). The occurrence of well developed layering correlates with the abundance of microgranular monzodiorite inclusions (type 2 in the classification outlined above), leading Pons et al. (2006) to suggest that convective crystal settling and the formation of inclusion trains both occur as consequences of episodic injection of more mafic (monzodiorite) magma during the crystallization of the hornblende granodiorite.

Comb and orbicular layering

Close to the margins of quartz monzonite, diorite and granodiorite plutons – for example those making up the Sierra Nevada batholith in California – it is not uncommon to see a distinctive form of banding in which each layer is made up of elongated crystals (often of plagioclase and hornblende) oriented perpendicular to the plane of layering; the resemblance to the teeth of a comb has led to the

term *comb layering* (Moore and Lockwood, 1973). The crystals tend to broaden or to branch as they grow toward the intrusion interior, suggesting crystallization under conditions in which growth rate G greatly exceeded nucleation rate N. Indeed the nucleation rate within the melt must have been effectively zero, as the elongate crystals seem to have grown on the solid substrate provided by the chamber walls, floor or roof (a process termed 'heterogeneous nucleation'), rather than on new crystal nuclei forming from the melt itself ('homogeneous nucleation'). Vernon (1985) argues this may be brought about by local **superheating** of the melt,[7] which would purge the melt of the crystal nuclei upon which homogeneous nucleation depends. Abruptly introducing water into the magma – thus lowering the liquidus temperature (Fig. 6.4.1) – is one way by which superheating may arise (though the cause of any such water ingress remains speculative).

What processes operate to generate the rhythmic banding is a harder question to answer. It could be that fluctuations in the P_{H_2O} of the magma column, due for example to repeated eruption or degassing at the surface, cause periodic raising and lowering of the liquidus temperature (Box 6.4) and concomitant fluctuation in the degree of supercooling/ supersaturation, so that periods of rapid growth alternate with negligible growth. Alternatively the boundary between one layer and the next may merely mark where depletion in the dissolved constituents required for crystal growth ('nutrients') has reached a critical cut-off value; growth would then cease until melt circulation or diffusion restored the critical supersaturation for a new stage of heterogeneous nucleation and growth.

Solid inclusions suspended within the magma body – often abundant near the pluton margins – provide an alternative substrate upon which comb layering could develop, and this may lie behind the striking phenomenon called **orbicular layering** (Plate 8.5). The orbs in question are ovoid bodies, typically a few centimetres or tens of centimetres in diameter. In cross-section they exhibit delicate internal modal banding, often with radial development of elongate crystals (Plate 8.5 inset). In some examples the banded structure consists of successive growths of crystals on what appear to be pre-existing crystalline inclusions that happened to be suspended in the magma (e.g. MacKenzie et al., 1982, Fig. 1.05); in other cases the cores on which the crystals nucleated are more variable, even over a few centimetres (Plate 8.5), and their origins are less clear. The striking variety of orb geometry and constitution is illustrated by Elliston (1984). Orbicular and comb layering are sometimes closely associated in the field.

[7] Superpheating can be expected where magma ascends adiabatically, e.g. up a dyke system.

Evidence of multiple phases in injection

Few granite intrusions are formed by a single pulse of magma. In many plutons there is evidence for a succession of intrusive episodes, each of which disrupts, intrudes or replaces all or part of the products of the preceding phases of intrusion. Large-scale examples of this are provided by the Palaeogene Western Red Hills Centre, illustrated in Fig. 8.5b, and the 236 Ma Ras ed Dom granite-syenite ring complex in Sudan (Fig. 8.18). The successive pulses of magma that solidify to form successive intrusive units may differ in composition and mineralogy (Fig. 8.18), or they may be distinguishable only in terms of differing grain size or other textural attributes. The field contacts between successive intrusions may, or may not, be chilled or finer-grained. The relative age of two units may often be inferred at a well exposed mutual contact from **apophyses** of the younger unit into the older one (though back-veining may confuse the issue) or by inclusions of the older lithology in the younger unit, or by minor intrusions that cut one unit but are truncated by a (later) neighbouring one.

Net veining

On a smaller scale, the relatively cool solidified envelope of a silicic pluton may crack open in a brittle manner in response to the inflating tendency of pressurized magma ascending from deeper levels. The result is a three-dimensional network of cracks invaded by a later granite or microgranite magma; the crazed appearance later exposed by erosion, most obvious when the two components differ in composition and sometimes resembling on

a two-dimensional erosion surface the regularity of a fishing net (Fig. 8.10b), is known as *net veining*. Net vein complexes or 'intrusion breccias' (Emeleus and Bell, 2005) such as that in Fig. 8.10b sometimes show lateral or vertical transition into massive granite having a similar composition to the net veins, suggesting that net veining may represent an incipient stage of *stoping* (discussed above).

Synplutonic dykes

Well exposed granitoid outcrops are commonly transected by semi-regular bodies of finer-grained darker rock that, despite being broken up into discrete angular fragments, retain a dyke-like form and coherence (Fig. 8.10d). Such bodies are disrupted by back-veining of the host (or related pegmatite veins) along what appear to be brittle fractures, and they may be truncated by later intrusive phases of the host granitoid. Field observations like these suggest that basic magma was intruded at a stage when the host granite had cooled sufficiently to fail in a brittle manner yet before it had cooled to the point where re-melting was no longer possible. The term *synplutonic dyke* is widely used to describe such bodies, which sometimes occur in discernible swarms. A severe degree of disruption may reduce a synplutonic dyke to a train of angular enclaves.

Magma mingling

One indication of the contemporaneous availability of melts of differing composition is the widespread occurrence in many granitoids of dark rounded **aphanitic** blebs (see 'Inclusions' above). More dramatic evidence of such *magma **mingling*** is impressively exposed in several granite-syenite intrusions of Palaeogene age in East Greenland. Figure 8.10c shows an example where microsyenite magma has been injected into an angular fracture in a coarser-grained, older syenite. Rounded pillow-like lobes of darker andesite or microdiorite, here and there showing **cuspate** margins, form a near-continuous train within the microsyenite. The dark lithology is nowhere in direct contact with the older coarse-grained syenite, and most petrologists would interpret these relationships as indicating that the dark andesite was intruded into the pale microsyenite dyke while the latter was still molten. The sharp margins in Fig. 8.10c suggest minimal chemical mixing between the two melts, but in other examples the magma 'lobes' have diffuse margins, suggesting significant assimilation.

Similar relationships are seen (though rarely as well exposed) in a number of granitic complexes. In Centre 2 of the Ardnamurchan Central Complex in NW Scotland (Blake et al., 1965; Emeleus and Bell, 2005) lobate dolerite intrudes microgranite but is also net-veined by it.

Appinite and lamprophyre minor intrusions

> *'Of all the many associations of acid and basic rocks, perhaps that of granitic rocks with appinite (and lamprophyre) is the most enigmatic but may be the most instructive'* (Atherton and Ghani, 2002).

Appinites are small to medium-sized bodies of medium- to coarse-grained hornblende-rich intrusive rocks that were first described in association with late Caledonian granites in northwest Scotland; they are named after the Appin district of Argyll. They occur as inclusions, as clusters of minor intrusions and pipes – often satellitic to granite plutons but clearly associated with them in space and time – and as explosion breccias. In petrographic terms, appinites are extremely diverse, but are generally mesocratic to melanocratic in composition. The most typical facies of the appinite suite is a coarse-grained hornblende-phyric meladiorite, thin sections of which show brown or green hornblende crystals set in a groundmass of plagioclase and K-feldspar in roughly equal proportions (Fowler and Henney, 1996), but this rock may grade into ultramafic, phlogopite-bearing or pyroxenite variants. The mineralogy and brecciation common in appinites suggest that high volatile pressures play a key role in their formation and emplacement, and the common association of late-stage sulphides and carbonates supports this conclusion.

Granites are also cut by mafic dykes that are distinctively porphyritic in mafic minerals alone. Typical phenocryst phases may be augite, hornblende or biotite; the dykes may contain plagioclase or K-feldspars (confined to the groundmass) while others are



Fig. 8.10 (a) Composite crustal inclusion in granitoid, Ammassalik district, E Greenland.* (b) Net-veining of microgranite in diorite, Kialineq intrusive centre, E Greenland; hammer for scale, lower centre.* (c) Lobes of andesite magma emplaced into still-molten microsyenite net-vein cutting earlier syenite, Nualik plutonic centre, East Greenland; note: (i) that the andesite lobes are always separated from the older syenite by microsyenite; and (ii) back-veining of microsyenite into andesite.* (d) Field sketch of synplutonic microdiorite dykes in a typically disrupted state cutting an undeformed granodiorite host (shown white) on Cortes Island, British Columbia, Canada, from Pitcher and Bussell (1985) by permission of M.A. Bussell; the coarser-stippled areas represent metasomatized portions of the dykes.

*Photograph taken by the author during fieldwork carried out under contract to what is now the Geological Survey of Denmark and Greenland; reproduced here with their kind permission.

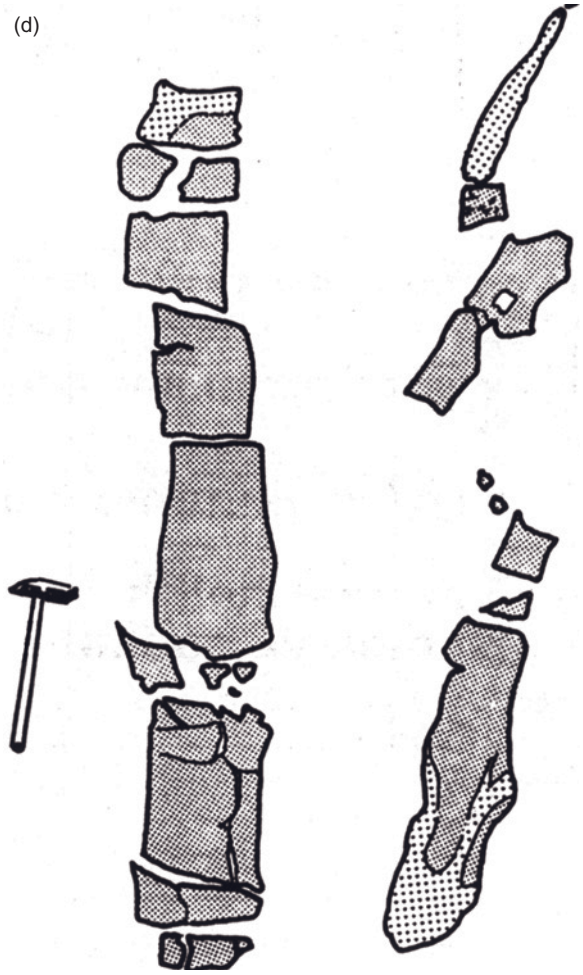


Fig. 8.10 *Continued*

feldspathoidal. The collective term used for these distinctive dyke rocks – whether associated with granite or not – is **lamprophyre** (Box 9.6). Numerous varietal names exist to identify different mineralogical types of lamprophyre (for example, a biotite orthoclase lamprophyre may be called a *minette*), but the simple use of type minerals – as in this example – provides an easier and more systematic nomenclature. In their mineralogy and geochemistry, many lamprophyres cutting granitoids have a lot in common with the more melanocratic appinites. The genesis of these rocks is discussed in Chapter 9.

Miarolitic cavities (vugs)

Granites emplaced within a few kilometres of the surface – 'high-level granites' or 'epigranites' (a contraction of 'epizonal granites') – may contain dissolved volatiles at a pressure (principally P_{H_2O}) exceeding the confining pressure acting on the magma. In these circumstances the dissolved gases begin to exsolve in a similar manner to vesiculating basalt lava. At the time of its final emplacement, however, such a granite may already have reached an advanced stage of crystallization, and therefore the gas bubbles that form – constrained partly by the high viscosity of the magma and partly by the faces of surrounding crystals – may adopt highly irregular shapes, in contrast to the dominantly spheroidal form of basalt vesicles (dictated by surface tension). These centimetre-scale voids – known as *vugs* or *miarolitic*[8] *cavities* – are lined with euhedral crystals of rock-forming minerals like quartz, feldspar, mica, but often include more exotic minerals such as topaz, beryl and fluorite.

Mineral fabric

Crystallization of granitic magma generally leads to rocks with randomly orientated crystals. The mechanisms that sometimes give rise to igneous **lamination** in gabbroic plutons seem not to operate in the more viscous magmas from which granites crystallize, and therefore no magmatic mineral fabric develops. When a granite does exhibit preferred mineral orientation (foliation – as in Fig. 8.11 – or lineation), the fabric may represent differential flow (shearing) within a still-mobile crystal mush on the point of final solidification, or it may be the product of post-crystallization deformation. The latter can arise in two ways:

1 If magma continues to flow into a crystallizing high-level pluton from a deeper reservoir, the chamber must inflate (push back its margins) in order to provide space for the incoming magma. Such *ballooning* may cause the outer shell of already-crystallized granite to undergo flattening. The result will be a concentric mineral foliation sub-parallel to the margins of the chamber. The Ardara pluton summarized in Fig. 8.9(d) is an obvious example.

[8] From an Italian collectors' term *miarole* for a crystal-lined cavity in granite or pegmatite.

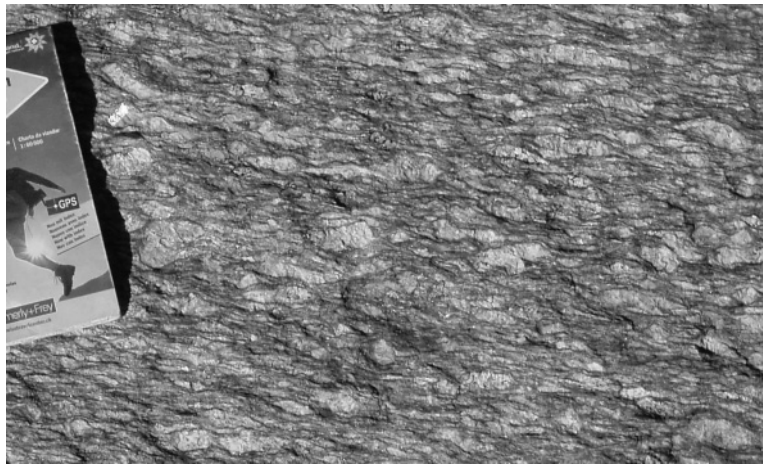


Fig. 8.11 Planar foliation in a granitoid (Bregaglia, Switzerland). Length of map 20 cm. Note the lensoid shape of many K-feldspar megacrysts.

2 A granite pluton emplaced early in an orogeny may undergo deformation during later regional tectonism (Fig. 8.11). In this case the foliation in the granite will be broadly concordant with that in the surrounding country rocks. Such internal deformation (or lack of it) allows the timing of different plutons in an orogenic belt to be categorized as *syn-tectonic* or *post-tectonic*.

HOW GRANITIC MAGMAS CRYSTALLIZE – TEXTURAL EVIDENCE

Variations in crystal size: **K-feldspar** megacrysts

Many granitic rocks contain abundant, euhedral K-feldspar crystals – pink or white in colour – that are conspicuously larger than the groundmass surrounding them; lengths up to 5 cm are common, but in some cases K-feldspar crystals may range up to 20 cm in length. It is natural to regard them as giant **phenocrysts**, but an alternative school of thought has for many years interpreted these crystals as post-magmatic **porphyroblasts** formed as a product of **metasomatism**. Recognizing the need for a descriptive term free of genetic connotation, most petrologists refer to them as 'K-feldspar megacrysts'.

The belief that such crystals are porphyroblasts – formed after the host rock had solidified – derives from their occurrence not only in the host granites but *sometimes also in some of the enclaves they contain* (Plate 8.9); some megacrysts have even been described as cutting across the boundary between enclave and granite host. The literature suggests that some megacrysts occur in hornfelsed sedimentary enclaves, where by definition they could not be phenocrysts but could only have formed by metasomatism. In his thorough review of the problem, however, Vernon (1986) noted that the so-called hornfelsed sedimentary inclusions are poorly described and illustrated, and are more readily interpreted as finer-grained co-magmatic igneous rocks (cognate xenoliths or mafic inclusions). He assembled compelling evidence in favour of a true phenocryst origin for K-feldspar megacrysts, including the following:

- Megacrysts in granites commonly exhibit euhedral shape (when allowance is made for irregular overgrowths); K-feldspar porphyroblasts known to have formed in metamorphic rocks, on the other hand, are rarely if ever euhedral.
- Euhedral mineral inclusions (plagioclase, biotite, etc.) within the megacrysts themselves are arranged in growth zones and tend to be oriented parallel to K-feldspar growth faces; if a growing porphyroblast were to envelop pre-existing grains of other minerals, the inclusions would be anhedral, randomly distributed and randomly orientated, like those observed in the surrounding groundmass.

- Mineral inclusions in the megacrysts are generally smaller than equivalent crystals in groundmass, consistent with their growth being terminated earlier than in the groundmass; inclusions in a post-magmatic porphyroblast would on the other hand be similar in size to groundmass crystals outside (unless the inclusions were partially resorbed by the enveloping host).
- Simple twinning is common in megacrysts in granites (and enclaves – Plate 8.8) but much less so in metamorphic or metasomatic K-feldspars.

The exceptional size of many megacrysts compared to phenocrysts in volcanic rocks, and their presence in some granites but not in others, must be related to nucleation. Vernon (1986) attributes the large size of K-feldspar megacrysts to a high growth-rate G combined with a low nucleation rate N for the mineral[9] in H_2O-undersaturated granitic melts. This causes efficient growth to be concentrated on the few centres where nucleation has succeeded, leading to the formation of very large crystals. In granites lacking megacrysts, the $N:G$ ratio was presumably higher, allowing larger numbers of smaller K-feldspar crystals to develop and grow. Megacryst-bearing granites may be identical in major element composition to adjacent non-porphyritic or seriate granites (Bateman and Chappell, 1979), so that the factors that determine the $N:G$ ratio remain unclear. Since megacrysts are so common in granites, it is puzzling that phenocrysts of similar size should be so rare in volcanic rocks of comparable composition; one explanation may be that K-feldspar phenocrysts do not grow to megacryst size until the host magma has acquired too high a crystal content to reach the surface (C.R. Bacon, cited by Vernon, 1986).

Instinct suggests that the mineral forming the largest phenocrysts in an igneous rock must have been the first to begin crystallizing, but the K-feldspar megacrysts illustrate the fallacy of this assumption. As Vernon (1986) points out, in experiments on typical granite melts K-feldspar often begins crystallizing *after* the appearance of the mafic minerals and plagioclase. This reinforces the conclusion that the megacrysts' dramatic size is due to their inefficient nucleation, which concentrates all of the K-feldspar growth on a small number of crystals, and not to their early appearance.

[9] Though not so low as to suppress homogeneous nucleation entirely.

Overgrowths

The formation of mineral overgrowths is frequently seen in granitic rocks. In diorites, it is common to see augite mantled by hornblende – an example of a reaction rim formed as the conditions (T, P_{H_2O}) changed during magma crystallization from those favouring the anhydrous (augite-bearing) assemblage to the hydrous (hornblende-bearing) assemblage. Had cooling been sufficiently slow, augite might have been completely transformed into hornblende: a reaction rim is evidence of incomplete reaction. Biotite may sometimes be seen mantling orthopyroxene. Plate 8.6 shows a granitoid in which plagioclase in mantled by orthoclase.

Rapakivi granite

A distinctive overgrowth seen in many Proterozoic granitoids, frequently associated with anorthosites and charnockites, is the formation of white oligoclase rims on large rounded (partially resorbed) pinkish[10] K-feldspar megacrysts, as illustrated in Plate 8.7. Such rocks are known as rapakivi granites: the type localities are in central and southern Finland, where 'rapakivi' simply means 'rotten rock' (a reference to weathered exposures in this area). The Finnish localities form part of a belt of mid-Proterozoic magmatism that extends from the Ukraine to the mid – western USA (Frost et al., 1999) via Fennoscandia, southern Greenland and Labrador; other examples of rapakivi granitoids occur in southern China, Australia and Amazonia. Rapakivi texture is not confined to Precambrian rocks however: rapakivi granites of Miocene age have recently been reported from Death Valley in California and elsewhere in the western USA (Calzia and Rämö, 2005).

The formation of this visually intriguing texture in hornblende-biotite granites and monzonites is enigmatic. The overgrowth suggests an abrupt change in magma compo-

[10] This texture is best seen in hand-specimen.

sition or conditions during crystallization, and the conventional view (Hibbard, 1981) is that mixing occurred between (i) an evolved magma crystallizing K-feldspar megacrysts (under the conditions discussed above); and (ii) a hotter, more basic magma undersaturated with respect to K-feldspar. Hybridization of the two melts leads to partial resorption of the K-feldspar megacrysts – causing the rounding noted above – but the sudden cooling experienced by the more basic melt causes rapid deposition of oligoclase crystals (initially skeletal) that build up a rim on the K-feldspar. Other authors have attributed rapakivi texture to exsolution or to shifts in the plagioclase–K-feldspar cotectic with falling P_{H2O} during ascent, but such explanations are less widely accepted today.

The formation of abrupt rims of more calcic composition on plagioclase crystals is another sign of magma mixing during granitoid crystallization.

Intergrowths

Plate 8.3 shows in crossed polars a granite consisting mainly of **alkali feldspar** and quartz; the alkali feldspar is turbid owing to alteration (whereas the quartz, not being susceptible to alteration, remains clear). The striking feature is the intricate intergrowth in which the quartz forms what appear to be irregular patches arranged within a feldspar host; the patches seem to grow radially out from a pre-existing crystal surface. Patches in proximity share the same interference colour and, when the slide is rotated between crossed polars, they extinguish at the same position, suggesting that in three-dimensions they must all be parts of one **optically continuous** crystal that has grown in a highly convoluted intergrowth with a K-feldspar crystal (which also shows optical continuity). The shared orientation and complex shape of some of the larger quartz patches creates the appearance of primitive writing, hence the use of the term *micrographic*[11] to describe this texture. A porphyritic granite exhibiting this groundmass texture between alkali feldspar and quartz is called a **granophyre**.

[11] The texture is termed 'graphic' when discernable by the naked eye; 'micrographic' when visible only under the microscope.

How does this remarkable texture arise, and what does it tell us about the conditions of crystallization? The texture seems to represent coincidence of three circumstances:

1. A mostly crystallized magma with an evolved **interstitial** melt composition which lies on the alkali feldspar-quartz cotectic (Fig. 6.7) close to the minimum melt composition; the melt is virtually exhausted in the components of the mafic minerals, as they are absent from the intergrowths.
2. Rapid crystallization ($G >> N$) under conditions favouring **heterogeneous** rather than homogeneous nucleation: new crystals find it easier to nucleate on pre-existing crystals than to form fresh nuclei.
3. Crystal growth proceeds faster than 'nutrient' ions can diffuse through the melt to replenish the depleted melt zone close to the crystal surfaces (cf. Fig. 5.10): feldspar and quartz thus grow opportunistically, exploiting pockets of melt of favourable composition and forming a convoluted intergrowth rather than discrete crystals.

For such intergrowths to form in a coarse-grained rock requires a high degree of supercooling of evolved granitic melt, but under plutonic conditions this cannot be due to rapid cooling. One possible explanation for this counter-intuitive combination would be if a magma that had crystallized to a relatively advanced degree under near-water-saturated conditions (depressing the solidus – Fig. 8.12b) experienced a sudden loss of water vapour pressure (e.g. by failure of roof rocks, releasing confined gases to the atmosphere). The drop in P_{H2O} would cause the solidus temperature to shoot up to values well above the actual melt temperature (Fig. 8.12a), creating 'instant' supercooling.

Intra-crystalline textures

Exsolution textures

The propensity for alkali feldspar crystals to **exsolve** internally into **perthite** or **microperthite** was outlined in Box 8.1. The cause of exsolution is the solvus that divides the $KAlSi_3O_8$–$NaAlSi_3O_8$ solid-solution series.

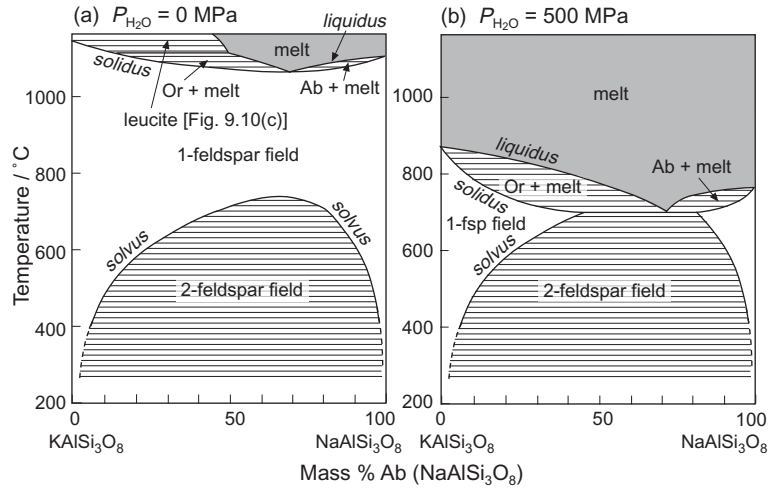


Fig. 8.12 Crystallization and exsolution in the alkali feldspar series (ruled areas represent **two-phase fields**). (a) At low or zero water-vapour pressure, complete solid solution exists at T > 700 °C between $KAlSi_3O_8$ (Or) and $NaAlSi_3O_8$ (Ab): crystallization of melt under these conditions generates a single homogeneous feldspar phase of intermediate composition, which exsolves to form **perthite** or **antiperthite** as it cools through the **solvus** into the 2-feldspar field, characteristic of **hypersolvus** granites. Leucite is a feldspathoid (Box 9.1). (b) High P_{H_2O}, depresses the alkali feldspar solidus to the point where it intersects the solvus: under these conditions no 1-feldspar field exists and therefore no homogeneous intermediate alkali feldspars can form; two separate feldspar species (one K-rich and one Na-rich) crystallize directly from the melt (as in **subsolvus** granites). Data from Tuttle and Bowen (1958) and Morse (1970).

Its shape (Fig. 8.12) makes the degree of solid solution between orthoclase and albite highly temperature-sensitive: mutual solubility increases with temperature until, at temperatures above 700 °C, solid solution spans the entire compositional range. This means that (at low water-vapour pressures) melts of granitic composition can crystallize a homogeneous alkali feldspar in the sanidine-anorthoclase range (Fig. 8.1.1 in Box 8.1). The homogeneous **hypersolvus** feldspar persists down to 700 °C or beyond, but – during slow cooling – as it crosses the solvus it will begin to unmix internally into microscopic lenses or patches of Na-rich feldspar dispersed in a K-feldspar host, or vice versa (Fig. 8.1.1c). The equilibrium compositions of the two coexisting feldspars are given by the two limbs of the solvus at the temperature concerned; the compositions will diverge as temperature falls. The result will be a granite having a *single population* of perthite or microperthite crystals (as exemplified by a syenite in Plate 9.14), described as a *hypersolvus granite*. A typical example would be a granite or syenite emplaced at a very shallow level in the crust, having lost most of its volatile content by decompression during ascent.

The outcome is different when the feldspar crystallizes from melt under high P_{H_2O} (Fig. 8.12b), for example when a volatile-rich magma crystallizes at depth. The solvus changes little in response to P_{H_2O} but the liquidus and solidus drop markedly at high P_{H_2O}. At P_{H_2O} = 500 MPa, they have fallen to such low enough temperatures that they intersect the solvus, eliminating the hypersolvus region of complete solid solution. The solid-solution gap means that feldspars forming under these conditions crystallize as separate Or-rich and Ab-rich crystals (Plate 8.2). Granites containing two distinct populations of potassic and sodic feldspars are referred to as *subsolvus granites*.

Twinning

The distinctive forms of twinning seen in granitoid feldspars have been outlined in Box 8.1.

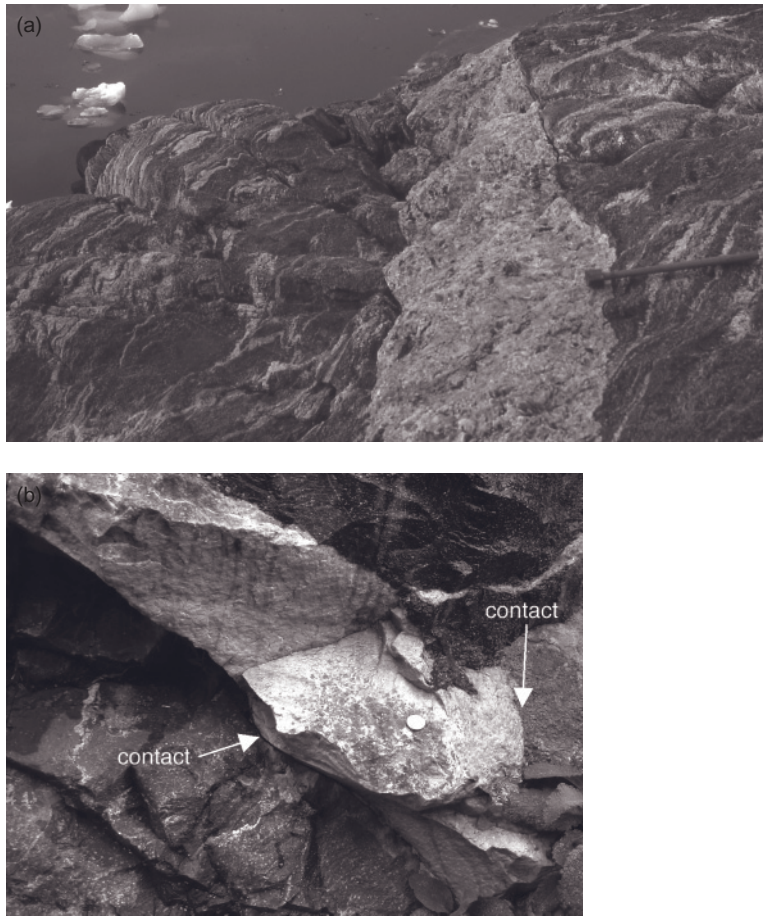


Fig. 8.13 (a) Metre-wide transgressive granite pegmatite sheet cutting Precambrian gneiss, Ammassalik district, E Greenland.* (b) Small discordant aplite vein cutting country rock close to the contact of the Dartmoor Granite, SW England; coin 2.2 cm in diameter.

*Photograph taken by the author during fieldwork carried out under contract to what is now the Geological Survey of Denmark and Greenland; reproduced here with their kind permission.

LATE-STAGE PROCESSES, ALTERATION AND MINERALIZATION ASSOCIATED WITH GRANITOIDS

Pegmatite and aplite

Many granite plutons contain lenses, veins or sheets of a markedly coarser-grained facies granite that is given the name **pegmatite**. In a few pegmatites, individual crystals may achieve extraordinary proportions – metres or even tens of metres in length and tonnes in weight – but interlocking crystals 1–5 cm in size are much more common. The simplest pegmatites differ little in composition from the normal granite surrounding them – consisting of just feldspars, quartz, muscovite and perhaps tourmaline (Plate 8.4) – while others include a number of more exotic minerals such as beryl ($Be_3Al_2Si_6O_{18}$), spodumene ($LiAlSi_2O_6$), topaz [$Al_2SiO_4(OH,F)_2$], pyrochlore [$(Na,Ca)_2(Nb,Ta)_2O_6(OH,F)$], cassiterite ($SnO_2$) and monazite [$(Ce,La,Th)PO_4$]. Pegmatites often (though not always) contain rare and valuable minerals such as these, whose presence, suggesting a high level of geochemical enrichment in rare elements (F, Li, Be, B, Nb, Sn, **REE** Th), makes complex pegmatites of this kind of great interest to economic geologists.

Pegmatites form bodies a few metres to a hundred metres or so in size. Most occur close to the margins of granitic intrusions, and may extend as veins or dykes into surrounding country rocks (Fig. 8.13a). They are most

commonly associated with granites and syenites, but gabbro pegmatites are found near the margins of some mafic intrusions too (see Fig. 4.7h). Granite pegmatites vary from simple – differing from the host granite only by virtue of grain size – to zoned types that are internally differentiated in terms of grain size and mineralogy, usually in a concentric arrangement and sometimes with large vugs in the core. In zoned bodies, pegmatite is often intimately associated with a finer grained, **phaneritic** rock of similar composition called **aplite** (another distinctive late-stage product of granite magmatism – see Fig. 8.13b and quartz veins. Some aplites contain rare minerals comparable to those in pegmatites.

How are pegmatite and aplite formed? The reasons for the large size of crystals in pegmatite remain controversial. Beyond doubt, pegmatite and aplite are 'late-stage' phenomena, associated with the last dregs of melt in a slowly crystallizing pluton, a view reinforced by their high and sometimes economic incompatible-element contents (Nb, Sn, REE, Th). Since a small internal pegmatite body must cool at the same rate as the surrounding pluton (or possibly faster in the case of transgressive pegmatites), the large crystal size cannot be due to slower cooling, and – like other textures discussed earlier in this chapter – must reflect difficulty in nucleation and therefore a low $N:G$ ratio. Vernon (2004) relates poor nucleation to a build-up of dissolved water in the residual melt. Water depolymerizes the melt (Box 6.3), making it harder for **polymerized** crystals such as feldspar and quartz to nucleate. The delay in nucleation causes a high degree of super-saturation to develop, so that once nucleation is achieved crystal growth may occur rapidly, leading to the crystallization of pegmatite. The high water concentration present during pegmatite formation depresses the solidus temperature considerably, and if water should escape from the residual melt the sudden rise in solidus temperature would render it highly supercooled, and extremely rapid nucleation in such circumstances probably lies behind the relatively fine grain-size characteristic of aplite.

Contraction taking place as a result of crystallization may play a role in pegmatite formation, as shrinkage cracks would draw in H_2O-saturated interstitial melt from the surrounding crystal mush (J. Blundy, pers. comm.).

Alteration

> *'Hydrothermal alteration is a chemical replacement of the original minerals in a rock by new minerals, where a hydrothermal fluid delivers the chemical reactants and removes the aqueous reaction products.'* Reed (1997)

The build-up of volatile species in late-stage granitoid magmas, to saturation and beyond, leads to the fluxing of the solidified upper parts of an intrusion, and the roof rocks above them, by **hydrothermal** fluids. Such fluids are supplemented by convecting fluids from other sources (e.g. meteoric water), which may be volumetrically more important. Magmatic minerals that may persist metastably under relatively dry sub-solidus conditions become unstable in the presence of hydrous fluids, and recrystallize into new (mostly hydrous) minerals – called alteration products – that are stable in this new hydrothermal regime. An example is the alteration of K-feldspar to **sericite:**

$$\underset{K\text{-}feldspar}{3KAlSi_3O_8} + \underset{fluid}{2H^+} \rightarrow \underset{sericite\,(mica)}{KAl_2AlSi_3O_{10}(OH)_2} + \underset{fluid}{2K^+} + \underset{quartz}{6SiO} \qquad [8.1]$$

This equation makes clear that the aqueous fluid consists not only of H_2O but also contains ionic solutes that play an important role in alteration reactions. This example is a **hydrolysis** reaction in which H^+ in the fluid is exchanged for K^+ in the feldspar. The net effect is that the mineral crystal gains H^+ (which becomes hydroxyl) and loses potassium, thereby changing its identity into the new minerals sericite and quartz. Other important alteration reactions involve cation metasomatism, in which metals (e.g. K, Na, Ca) are added to the rock to form new minerals. Such chemical changes serve as a reminder of the importance of taking alteration into account when studying the geochemistry of igneous rocks (Box 1.3).

The nature of the alteration assemblage formed in a given granitoid depends on various factors, such as temperature, the fluid's composition (e.g. pH, salinity) and the water : rock ratio. The pervasiveness of alteration depends largely on the rock's microstructure, e.g. on grain size, mineral cleavage and the intensity of fracturing in the rock (which assists fluid penetration). At relatively low temperatures, alteration of igneous rocks may resemble low-grade (greenschist facies) metamorphism, with the appearance of minerals like epidote and chlorite. These factors generate considerable variety in the type and intensity of alteration in granitic intrusions. Common alteration products seen in granitoids, and the minerals from which they usually form, are summarized in Table 8.2. Alteration is not confined to anhydrous minerals: for example, both hornblende and biotite are susceptible to chloritization. Note on the other hand that not all new alteration products are hydrous, as illustrated by the quartz in equation 8.1.

Mineralization

> '*The predominant volatile in virtually all felsic magmas in the Earth's crust is H_2O. Evidence is found in the abundance of hydrous minerals such as amphiboles and micas in felsic igneous rocks, and in analyses of volcanic gases, glass inclusions in phenocrysts and fluid inclusions. … Other volatiles in relatively small amounts, such as HCl, HF, H_2S, SO_2, H_2 and CO_2, play highly important roles … especially at the stage when an aqueous phase – the hydrothermal fluid – separates from a crystallizing magma.*'
>
> Burnham (1997)

As we noted above, hydrothermal fluids escaping from granitoid complexes contain solutes. Na^+, K^+, Ca^{2+} and Mg^{2+} are among the most abundant cations, but economically important metals like Cu, Mo, Ag and even Au are usually present too; though their concentrations in the fluid are low, a large volume of hydrothermal fluid fluxing through the roof of a crystallizing granite body may be sufficient to deposit a significant tonnage of ore. Perhaps the best known type of hydrothermal mineral deposits associated with granitic rocks is the so-called 'porphyry copper' type. Porphyry copper deposits are associated with relatively shallow, porphyritc (hence the name) granite intrusions, which exsolve boiling saline ore fluids at sufficient pressures to fracture the solidified upper margins of the intrusion and the overlying roof rocks, allowing the fluids to deposit copper and other sulphides in the permeable carapace to form a large, low-grade disseminated ore body.

Another important type of hydrothermal mineral deposit is associated with 'greisen', an old miners' name for a typically coarse-grained alteration assemblage of muscovite, quartz, topaz and fluorite, often with tourmaline. Greisen, sometimes capped by pegmatite, forms near the roof of some granite plutons, and commonly hosts workable – though not always currently economic – Sn-W-Mo ore bodies.

The type of metal deposit correlates closely with the type of granite and the source rocks from which the magma formed (Box 8.3). Some, notably the Zr-Nb deposits associated with some intraplate granites (Table 8.3.1), are concentrated by primary magmatic processes rather than secondary hydrothermal fluid circulation.

GEOCHEMISTRY AND THE CHEMICAL SUBDIVISION OF GRANITOIDS

Table 8.2 and Fig. 8.1 summarize the petrographic differences that allow names to be given to the main rock types recognized within a given granitic pluton or batholith. Diorites are the least evolved of the granitoid family, whilst granites are the most evolved. Diorite, granodiorite and granite can be viewed as successive stages on the differentiation path of a granitic magma, though magma mixing, crustal contamination and crustal melting are equally important contributors to the compositional range of many granitoid plutons.

Granitoids are found in a variety of tectonic settings around the world. When the chemical trends of granitoid suites in different settings are examined carefully, a number of correlations with geotectonic environment emerge. The usefulness and significance of such 'geotectonic indicators' will be discussed later in the chapter. For the time being, attention is confined to chemical parameters that are useful in describing compositional differences between different suites of granitoids.

The first question to ask is how closely *rock* analyses of granitoids can be expected to

reflect the *magma* composition from which they crystallized. Chapter 4 showed that gabbro rock analyses may differ substantially from the compositions of the parent magmas owing to the cumulus processes operating during crystallization. Does this 'cumulate effect' apply to whole-rock analyses of granitoids too? Modal layering is indeed recorded in some granitoids (see 'Internal structures in granitic intrusions' above), particularly near to pluton margins, but it plays a less significant role in evolved acid intrusions than in gabbros; the higher viscosity and lower diffusion rates of siliceous melts (relative to mafic ones – Box 6.3) probably militate against crystal settling and other crystal segregation processes. Moreover the main variation between layers will be in the proportion of mafic minerals, and since these proportions are low in more evolved granitoids the potential for 'cumulate bias' here is slight, though it may affect diorite analyses. The analysis of a relatively homogeneous granite may therefore be taken, at a first approximation, to represent the composition of the magma from which it crystallized (except for the volatile constituents).

Three terms (introduced by Shand, 1951) are useful in summarizing a key aspect of the major element chemistry of granitoids and its mineralogical outcome:

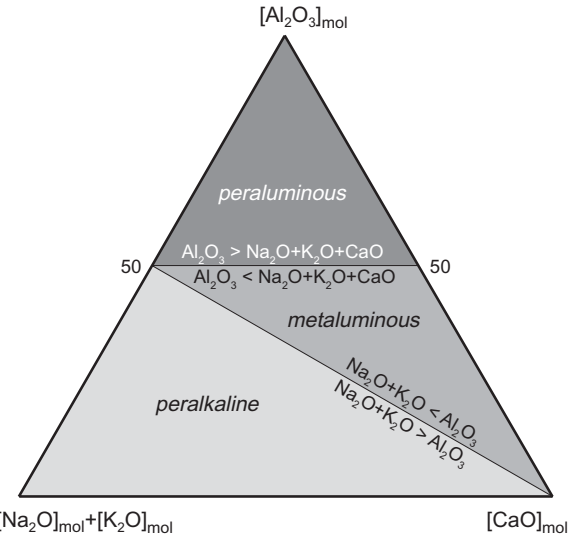


Fig. 8.14 Peraluminous, metaluminous and peralkaline fields shown in a ternary plot of whole-rock Al_2O_3, Na_2O + K_2O and CaO contents (in molar proportions). To plot an analysis in this figure, Al_2O_3, Na_2O, K_2O and CaO mass percentages need to be (i) divided by their respective **RMM** values (see Table 2.3); and (ii) scaled up so that the total of the four molar amounts equals 100% (Appendix B).

Box 8.2 Aluminous minerals in granitoids and related rocks

Peraluminous granitoids generally contain one or more distinctively aluminium-rich minerals, as listed in Table 8.2.1 below. All except tourmaline are close to colourless in plane-polarized light (PPL), though garnet may have a pink-red tinge and cordierite may exhibit yellow **pleochroic haloes** (radiation damage) around inclusions of apatite or zircon.

As cordierite and andalusite form chiefly during metamorphism of argillaceous sedimentary rocks, their occurrence in granite is commonly attributed to contamination by pelitic metasediments or direct partial melting of such material (as in the case of the High Himalayan leucogranites discussed below).

Table 8.2.1 Distinctive aluminium-rich minerals

	Mineral	*Formula*
Isotropic mineral	garnet (almandine)	$(Mg,Fe^{2+})_3\mathbf{Al}_2Si_3O_{12}$
Anisotropic minerals	muscovite	$K_2\mathbf{Al}_4[Si_6\mathbf{Al}_2O_{20}](OH,F)_4$
	cordierite	$(Mg,Fe^{2+})_2[Si_5\mathbf{Al}_4O_{18}](H_2O)_n$
	tourmaline	$Na(Fe,\mathbf{Al})_3\mathbf{Al}_6B_3Si_6(O,OH)_{30}$
	andalusite	$\mathbf{Al}_2SiO_5$
	topaz	$\mathbf{Al}_2SiO_4(OH,F)_2$

* Almandine is usually completely isotropic, though other

peraluminous:

$$[Al_2O_3]_{mol} > [Na_2O]_{mol} + [K_2O]_{mol} + [CaO]_{mol} \quad [8.2]$$

peralkaline:

$$[Na_2O]_{mol} + [K_2O]_{mol} > [Al_2O_3]_{mol} \quad [8.3]$$

metaluminous:

$$[Na_2O]_{mol} + [K_2O]_{mol} < [Al_2O_3]_{mol} < [Na_2O]_{mol} + [K_2O]_{mol} + [CaO]_{mol} \quad [8.4]$$

where $[CaO]_{mol}$, for example, represents CaO expressed in molar proportions, i.e. the mass percentage of CaO in the major element analysis divided by the relative molecular mass (**RMM**) for CaO (56.08). The meaning of peraluminous, metaluminous and peralkaline is shown diagrammatically in Fig. 8.14.

The prefix 'per-' signifies an abundance or excess of the element in question. Calculating the **norm** (Box 2.4) of a peraluminous rock brings to light an excess of alumina over the amount required to combine with Na_2O, K_2O and CaO to form feldspars: this surplus Al_2O_3 emerges in the norm of a peraluminous rocks as the normative mineral *corundum* (Table 2.3), and such analyses may be described as *corundum-normative*. Moreover no CaO remains to form any diopside (Box 2.4). A peraluminous granitoid is usually characterized in modal terms by the presence of muscovite[12] (usually alongside biotite) and possibly other Al_2O_3-rich minerals too, such as topaz, almandine garnet, andalusite or cordierite (Box 8.2). Granitoids with this mineralogical signature are often designated as 'S-type' in view of their probable derivation by partial melting of basement rocks of ultimately sedimentary origin (Box 8.3).

At the other extreme, peralkaline granitoids are aluminium-*deficient* and plot in the lower-left field in Fig. 8.14. In calculating the norm of a peralkaline granitoid, aluminium becomes exhausted before all of the alkalis ($Na_2O + K_2O$) have been allocated to alkali feldspar. This has two consequences. Firstly no Al_2O_3 is left over to combine with CaO to form anorthite; all of the CaO in the analysis (after calculating apatite) is therefore allocated to diopside (Box 2.4). Secondly the excess of sodium left over after alkali feldspar (Or + Ab) combines with Fe_2O_3 to form the alkali pyroxene end-member called acmite ($NaFeSi_2O_6$ – see Table 2.3). The outcome in terms of modal mineralogy may take the form of green-tinted pleochroic sodic pyroxenes of the aegirine–augite series (Box 9.2), or blue-green pleochroic sodic amphiboles of the arfvedsonite and riebeckite series (Box 9.4). Granites having this mineralogical fingerprint are characteristic of anorogenic settings, and form part of an association called 'A-type' granitoids (Box 8.3).

[12] Muscovite is a strongly aluminous mineral, as its formula ($K_2O.3Al_2O_3.6SiO_2.2H_2O$) indicates when compared say to orthoclase feldspar ($K_2O.Al_2O_3.6SiO_2$). Muscovite itself never appears in a norm because the norm calculation involves only **anhydrous** minerals (Box 2.4); corundum is its anhydrous surrogate in the norm.

that occur in some granitoids.

Birefringence	*Colour in PPL*	*Other diagnostics*
0*	Colourless to pink	High relief ($n \sim 1.8$).
0.036–0.049	Colourless	Speckly straight extinction in non-basal sections, basal cleavage, low relief.
0.008–0.018	Colourless	Dusted with fine opaque inclusions. May show yellow pleochroic haloes around inclusions of apatite or zircon. Sometimes exhibits lamellar twinning.
0.017–0.035	Colourless-yellow	Pleochroic (Plate 8.4, Box A1).
0.009–0.012	Colourless, pink or green	Moderate relief ($n \sim 1.63$). –ve. $2V_\alpha$ = 73–86°
0.008–0.011	Colourless	Moderate relief ($n \sim 1.63$). +ve. $2V_\gamma$ = 48–68°

varieties of garnet may show slight birefringence.

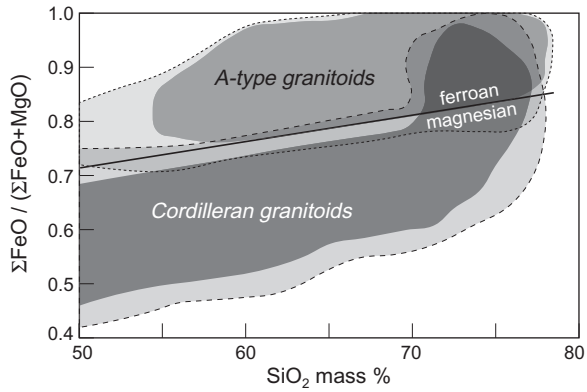


Fig. 8.15 Plot of '*Fe*-number' [ΣFeO/(ΣFeO + MgO)] versus SiO_2 content (volatile-free) for (i) intrusive rock compositions associated with Mesozoic batholiths in North America ('Cordilleran granitoids'); and (ii) A-type granitoids worldwide, after Frost et al. (2001) by permission of Oxford University Press. The darker fields encompass 95% of each population; the dashed and dotted fields enclose all data points. Also shown is the dividing line between 'ferroan' and 'magnesian' granitoid fields (*ibid*).

Metaluminous granitoids (the majority) fall between these extremes (Fig. 8.14). Hornblende and/or biotite are typical mafic minerals.

A more comprehensive descriptive basis for chemically subdividing granitoids, also founded on major-element geochemistry, was introduced by Frost et al. (2001). Figure 8.15 illustrates one of the three parameters used in their descriptive classification, the so-called *Fe*-number (whole-rock ΣFeO/[ΣFeO + MgO]).

WHERE GRANITIC MAGMAS OCCUR

Granitoids, being the plutonic counterparts of andesites, dacites and rhyolites, may be emplaced in any of the geotectonic environments where such volcanics are found erupting. Indeed, where the roof zones of high-level granitoid plutons are preserved, granites are commonly found to be invading volcanic successions of similar affinity, for example in Glencoe (Fig. 8.5a) and the Andes. Exhumation by uplift and erosion takes time, and many of the most intensively studied and best understood granitoid complexes are of Mesozoic or older age, notably the batholiths of the western USA (Fig. 8.6) and the coastal batholith of Peru (Figs. 8.7 and 8.16) which are considered below.

Table 8.3 summarizes the shape, size and tectonic setting of a number of representative granitoid intrusions. Table 8.4 provides representative analyses of granitoids from different settings, whose incompatible element profiles are plotted in Fig. 8.20.

Volcanic arcs

Granitoids are found in oceanic island arcs wherever sufficiently deep erosion has occurred to expose them, but they are usually subordinate to mafic plutonic and volcanic rocks. Examples occur in the Aleutian and Kurile arcs, the Caribbean, the Philippines and the Solomon Islands (Pitcher, 1982). The granitoids here are low-SiO_2 quartz diorites and tonalites; in the Aleutian arc, for example, gabbro often forms the peripheral zone of zoned plutons with quartz diorite in the core. The Tanzawa plutonic group, exposed where the northern end of the Izu–Bonin–Mariana (IBM) arc is colliding with Japan (Fig. 6.18), consists predominantly of tonalites emplaced in the IBM middle crust (Tatsumi et al., 2008).

Active continental margins

The scale and longevity of plutonic activity that can arise when prolonged subduction takes place beneath an active continental margin are illustrated by the Coastal Batholith of Peru (Fig. 8.16), the most intensively studied sector of a chain of vast granitic batholiths running down the Andean active margin of South America (Pitcher et al., 1985). The Cretaceous–Palaeogene Coastal Batholith extends in segmented style for about 1600 km from Arequipa in the south ('*A*' in the inset of Fig. 8.16) to beyond Trujillo in the north ('*T*') and is made up of nearly 1000 individual plutons that vary between 1.0 and 5.6 km in thickness. Many are elongated parallel to the batholith trend, have flat roof zones and steep margins with sharp contacts, and are zoned with felsic cores. Some plutons form ring dykes that pass upward into tabular intrusions above (Haerderle and Atherton, 2002), probably representing instances of sub-volcanic cauldron subsidence similar to Glencoe (Fig. 8.5a). Intervening country rocks are rarely deformed and the intrusive regime

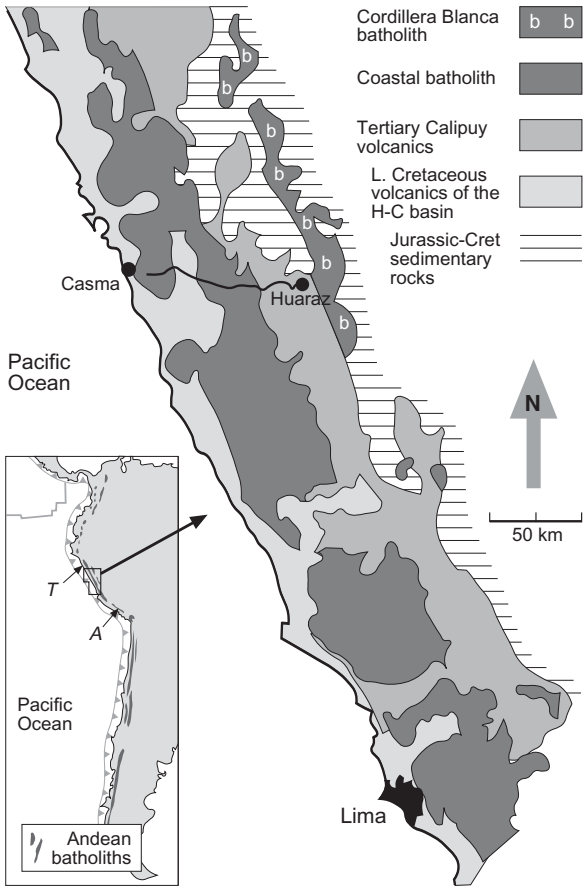


Fig. 8.16 Sketch map of the central section of the Coastal Batholith of Peru and the later Cordillera Blanca batholith, after Haerderle and Atherton (2002; copyright Elsevier); 'H-C basin' in the key stands for the Lower Cretaceous Huarmey-Cañete basin. The line from Casma to Huaraz marks the line of the gravity traverse shown in Fig. 8.7.

– evidently exploiting pre-existing fracture patterns – appears to have been permissive.

Along the central 70% of the batholith's length, plutons were emplaced at shallow level into mainly volcanic host rocks filling a Lower Cretaceous marginal basin (the Huarmey–Cañete basin), the extensional origins of which are indicated by the basaltic dyke swarm underlying it (Haerderle and Atherton, 2002). The granitoids are themselves cut by swarms of synplutonic dykes of andesite composition (similar to that shown in Fig. 8.10d), most trending NNW–SSE, suggesting on-going extension during crystallization. North of Trujillo, the batholith – here in somewhat attenuated form – invades sedimentary formations of the adjacent Chicama basin, whereas 200 km south of Lima (in the 'Arequipa segment') it passes into basement rocks of the Arequipa massif and their volcanic and sedimentary cover.

The plutons making up the Coastal Batholith were mostly emplaced between 100 and 60 Ma BP (Cobbing, 1999), though one or two give dates as young as 30 Ma. The rock types represented (disregarding early gabbros) include quartz diorite (SiO_2 ~57%), quartz monzodiorite, granodiorite and granite (SiO_2 ~77%), but the dominant rock type is tonalite (~60% SiO_2). The main mafic minerals are hornblende and biotite, and on this account the rocks of the batholith are described as I-type granitoids (Box 8.3); magnetite and apatite are important accessories. The granitoid-associated mineralization consists chiefly of Cu-Mo-W-bearing skarns, porphyry-type disseminated Cu-Mo sulphides and Au-Ag-bearing veins.

Since about 50 Ma, the focus of granitoid magmatism has shifted progressively eastward. In mid-Cenozoic times there were large outpourings of andesitic volcanics (the Calipuy volcanics) along the eastern margin of the coastal batholith in what is sometimes called the 'inner arc', accompanied by emplacement of sparse high-level granitoid plutons (not shown in Fig. 8.16) between 50 Ma and 20 Ma in age.

The most recent – and most easterly – phase of batholith emplacement in Peru formed the late Miocene Cordillera Blanca batholith (ornamented 'b' in Fig. 8.16), which extends for more than 200 km NNW to SSE in the High Cordillera region where the Andean crust currently attains its greatest thickness (about 50 km at this latitude). The rock types vary from older quartz diorites, quartz monzodiorites and tonalites (intruded between 13 and 10 Ma, around the time of crustal thickening – see Chapter 6) to younger leucogranodiorites with >70% SiO_2, emplaced through thickened crust around 5 Ma BP. Leucogranodiorite is the most abundant rock type – amounting to about 85% of the volume of the batholith. In contrast to the coastal batholith, there are no synplutonic dykes. The main mafic minerals of the granitoids are again hornblende and biotite so the batholith is I-type (Box 8.3). Deformed granites close to the Cordillera Blanca fault system (which defines the western margin of the batholith) are peraluminous, though the muscovite they

Box 8.3 Inferring source protolith: I-type, S-type and A-type granitoids

'Granites of the major batholiths in the Tasman Orogenic Zone of eastern Australia are of two contrasting types which are of widespread occurrence and which may be distinguished by chemical, mineralogical, field and other criteria. We interpret these granites as being derived by partial melting of two different types of source material – igneous and sedimentary. Differences in the derived granites are inherited from the source rocks so that we recognize an I-type and an S-type [of granite] *respectively.'*

Thus began a short but very influential paper published by B.W. Chappell and A.J.R. White in 1974, establishing a fundamental petrogenetic division among the Palaeozoic granitoids of eastern Australia that has since been adopted worldwide. The distinctions they drew between 'I-type' and 'S-type' granitoid magmas are summarized in Table 8.3.1.

Table 8.3.1 Characteristics of I-type, S-type and A-type granitoids.

	I-type granitoids	S-type granitoids	A-type granitoids
Major element composition	Metaluminous*	Peraluminous*	Metaluminous to peralkaline; High ΣFeO/MgO (see Fig. 8.15)
Normative minerals	Normative diopside	Normative corundum	Normative diopside ± acmite
Range of rock types represented	Plutons commonly include a wide range of rock types from basic to acid (SiO_2 56%–77%)	Generally confined to high-SiO_2 leucogranite (SiO_2 64%–77%). No associated mafic rocks.	Typically high-SiO_2 granitoids (often associated with syenite)
Type minerals	Hornblende and biotite	Muscovite (usually with biotite) ± other Al-rich minerals (Box 8.2)	Mafics are Fe-rich biotite or alkali pyroxene/amphibole
Range of $(^{87}Sr/^{86}Sr)_0$	0.704–0.706	0.708–0.765	0.702–0.717§
Xenolith lithologies	Mafic hornblende-bearing xenoliths of igneous appearance	Metasedimentary xenoliths	Various
Associated economic deposits	Porphyry Cu, Mo sulphides ± Ag-Au-bearing pyrite veins	Sn, W , U (Li, Be, B) (see Fig. 8.3.1)	Zr, Hf, Nb, Ta, Y, **REE**, U, Th (**HFS** elements – see Fig. 2.7.1)

* Chappell and White (1974) placed the I-type/S-type boundary at $Al_2O_3/(Na_2O + K_2O + CaO)_{mol} = 1.1$ rather than 1.0.
§ The range for the White Mountain magma series of New Hampshire is an exception, extending up to 0.736 (Eby, 1990).

contain and their S-type character are considered to be secondary in origin (Atherton and Petford, 1993).

Mesozoic granitoid batholiths are a prominent feature of western North America too (Fig. 8.6), though here their distribution is less linear. Pitcher (1982) amongst others has highlighted a crude zonation from I-types nearer to the Pacific coast (e.g. Sierra Nevada) to S-types further east (e.g. Idaho batholith). A similar zonation in relation to the continental margin is seen in the Palaeozoic Tasman orogenic belt of eastern Australia, where the division into I- and S-type granites was first established (Box 8.3): S-type granitoids mostly lie 'in-board' of the coastal zone of I-type batholiths.

Continental collision zones

Granitoid plutonism is a prominent feature of the Himalayan ranges and the southern margin of Tibet, where India and Eurasia have been undergoing continent-continent collision beginning about 55 Ma ago, and where about 1000 km of crustal shortening

It should be emphasized that the distinction between I-type and S-type, though founded on observational criteria, is in essence a genetic and conceptual one: 'I-type' granitoids are so named because they are interpreted as products of the partial melting of meta-*igneous* crustal rocks, whereas 'S-type' granites are presumed to owe their peraluminous composition to the anatexis of pelitic metamorphic protoliths of argillaceous *sedimentary* origin (though this may not always be the case). As a framework for petrogenetic debate, the division of orogenic granitoids and their associated ore deposits (Fig. 8.3.1) into 'I-type' and 'S-type' has proved valuable, but it falls short of being an objective classification applicable to all granitoids.

One shortcoming is that many granite plutons emplaced after orogenic movements have ceased, or in continental rifts and other regions remote from orogenic belts, are not catered for. Some of these are metaluminous and overlap in composition with I-type granites, but others have peralkaline composition and mineralogy. This observation led M.C. Loiselle and D.R. Wones in 1979 to propose (in an even shorter conference abstract) a third category which, referring to their *anorogenic* conditions of emplacement, they called 'A-type' granites. Their chemical characteristics include high ΣFeO/MgO (Fig. 8.15) and high concentrations of **HFS** trace elements (Table 8.4), to the extent that economic Zr, Nb, Y and REE deposits are associated with some A-type granites. Mineralogically they are notable for being **hypersolvus** granites, suggesting crystallization under lower-pressure or drier conditions (Fig. 8.12) than typical subsolvus I- and S-type granites (Eby, 1990).

A second pitfall of the I-, S- and A-type granite subdivision is the impression it gives that each class of granites is derived from a single source, readily identified from a magma composition. In reality, granitoid magmas are hardly ever derived from a single source but represent mixtures of mantle-derived melts intermixed with crustal melts of various compositions (Frost et al., 2000).

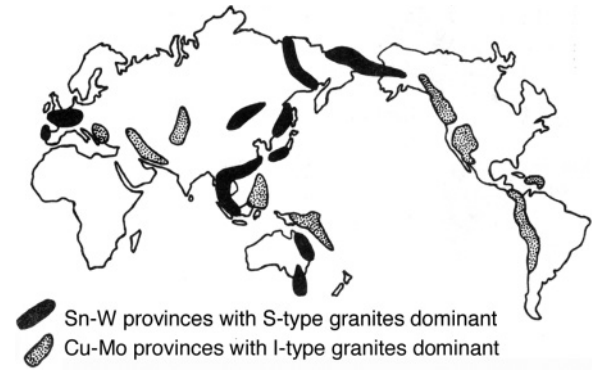


Fig. 8.3.1 Mineral deposits associated with I- and S-type granitoids worldwide (after Beckinsale, 1981).

has occurred in that time. The plutonic activity in this region divides into several belts of contrasting character.

The most voluminous of the Himalayan magmatic suites consists of the 2500 km long Trans-Himalayan Batholith and its western counterpart, the Karakorum Batholith, that run along the SW margin of the Tibetan plateau (Fig. 8.17) about 200 km NE of the highest Himalayan ranges. The Trans-Himalayan Batholith lies directly NE of the Tethyan suture zone where the Indian craton on the SW side abuts the Eurasian plate on the NE. Further to the NW, this suture divides into two (Fig. 8.17): (i) a northern strand separating the Eurasian plate from the Kohistan-Ladakh terrane[13] – a fossil island arc that docked with the Eurasian landmass prior to the collision of India; and (ii) a southern branch of the suture (mapped as the 'Main

[13] The North American spelling 'terrane' takes precedence over the English 'terrain' in this context, as the concept of allochthonous terranes was first developed by North American geologists. The English spelling is retained in this book for the more general meaning of the word.

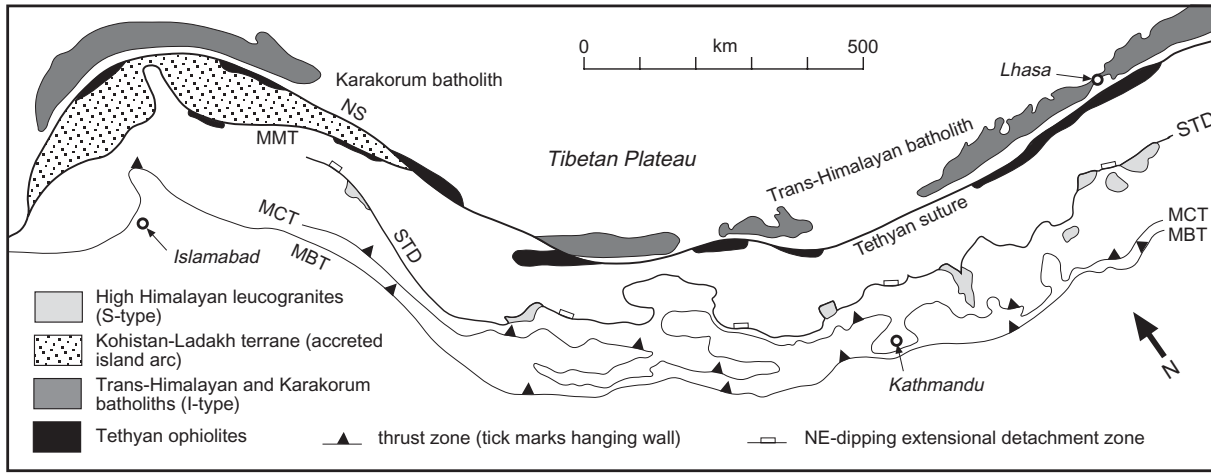


Fig. 8.17 Sketch map of suture zones, thrust tectonics and granitoid batholiths of the Tibet– Himalaya region. STD, South Himalayan detachment (normal fault zone); MCT, Main Central Thrust; MBT, Main Boundary Thrust; NS, Northern Suture; MMT, Main Mantle Thrust (the suture zone between the Indian continent and the Kohistan-Ladakh terrane).

Mantle Thrust' or MMT) where the Indian craton collided with the Kohistan arc. The granitoid mass of the Karakorum Batholith lies to the north of the northern suture.

The batholiths forming this chain consist of numerous discrete plutons of I-type hornblende and biotite granodiorites and granites. They were intruded, mostly into Tethyan metasedimentary rocks, between 100 and 40 Ma ago. Since they mostly predate the India–Tibet collision, they must have formed in circumstances analogous to the Mesozoic Andean batholiths, above a subduction zone that had consumed oceanic lithosphere over a prolonged period.

Another, much younger magmatic belt – the High Himalayan leucogranites – comprises a discontinuous chain of S-type, often tourmaline-bearing, 2-mica leucogranite sheet intrusions dispersed along the highest ranges of the Himalaya (Fig. 8.17); indeed they form some of the highest of the Himalayan peaks, including Everest itself. Most lie close to the footwall of the South Tibetan Detachment (STD), a system of low-angle extensional shear zones and normal faults thought to contribute to the extensional collapse of the Himalayan orogen. The leucogranites have ages in the range 24–19 Ma and possibly even younger. They are confined within the tectonic wedge of high-grade metasedimentary rocks, known as the Greater Himalayan Sequence, lying between the STD and the Main Central Thrust zone ('MCT' in Fig. 8.17) to the SW of it. At least some of the leucogranite bodies are concordant and sill-like or laccolithic in form, and one view is they have been emplaced as sills after significant lateral magma transport from the NE along the STD (Searle, 1999).

Two other belts of S-type granitoid plutonism crop out along the Himalayan chain. The North Himalayan plutonic belt lies midway between the Trans-Himalayan and High Himalayan belts and includes plutons of similar age to the High Himalayan belt, though much less voluminous. The Lesser Himalayan plutonic belt to the south is of Palaeozoic age and therefore unrelated to India-Eurasia collision (Debon et al., 1986).

Granitoid plutons of both I- and S-type occur in abundance in many older collisional orogens, such as the Caledonian/Appalachian orogeny on the NW margins of Europe and the eastern USA, the Variscan orogeny of Europe (e.g. western Iberia), and the Tasman fold belt of eastern Australia.

Intraplate granitic rocks

Granitoid magmatism is not confined to active continental margins or convergent plate boundaries. A glance at the geology of ancient continents like Africa throws up numerous

examples of granitic and syenitic complexes that have nothing to do with orogeny, or that were intruded into orogenic belts long after tectonism ceased. Pearce et al. (1984) divided such *intraplate* or *within-plate* granitoid magmatism into three categories:

1 Granitoids emplaced into continental crust of close to normal thickness, such as: (i) the granites of Nigeria; (ii) the granites and syenites of Sudan (Fig. 8.18); and (iii) the granites of the Permian Oslo graben in Norway.
2 Granites (and associated monzonites and syenites) intruded into continental crust thinned significantly by passive-margin extension, such as the Palaeogene granites of E Greenland and NW Scotland. Pearce et al. (1984) based the dividing line between categories 1 and 2 on the absence or presence respectively of a significant unidirectional dyke swarm (a simple measure of the degree of crustal attenuation).
3 Granitoids emplaced into oceanic islands, notably Ascension Island in the south Atlantic and Réunion in the Indian ocean.

A fourth category, distinguished by Sylvester (1989), consists of:

4 Alkaline granites in post-orogenic continental settings, typically 25–75 Ma after a collision event, as exemplified by Precambrian/Cambrian granitoids of the Arabian–Nubian shield, late Devonian A-type granitoids of the Lachlan fold belt in SE Australia (which postdate the associated I- and S-type plutonism), and Cretaceous granitoids of western Alaska.

All of these settings fall within the A-type or *anorogenic* category of granitoids (Box 8.3, Table 8.3.1). The granites are metaluminous to peralkaline and in each case are commonly associated with syenites (Fig. 8.18). The mafic minerals include biotite and hornblende in the metaluminous granites and syenites, or fayalite, ferroaugite (Fig. 2.1.1 in Box 2.1), aegirine–augite (Box 9.2) and sodic amphiboles such as riebeckite and arfvedsonite (Box A1) in the peralkaline examples.

Intraplate A-type granitoids have significantly higher *Fe*-number values than typical Cordilleran granitoids (Fig. 8.15) and accordingly fall in the 'ferroan' granitoid category of Frost et al. (2001). They also stand out on account of the higher concentrations of high field-strength (**HFS**) incompatible trace elements like Zr, Nb (Table 8.4 and Fig. 8.19) and also Ga.

Ocean spreading centre 'plagiogranites'

Associated with the upper plutonic units in many ophiolite complexes are small bodies of leucocratic quartz microdiorite or microtonalite that either interdigitate with cumulate gabbro layers or exist as small plugs or dykes within the sheeted dyke swarm. Being confined within the ophiolite itself, they appear to be formed contemporaneously by fractionation of subalkali basaltic magmas (as distinct from post-obduction anatectic granites that cut some ophiolites, for example the Oman ophiolite (Searle and Cox, 1999). A few examples of similar acidic rocks have also been dredged from the ocean floor, for example on the Mid-Atlantic Ridge at 45 °N (Table 8.4) and from the inner wall of the Tonga trench. These oceanic microgranites seem to have formed at mid-ocean ridges or other oceanic spreading centres.

These rocks are generally medium- to fine-grained and consist primarily of quartz and plagioclase; hornblende is the main ferromagnesian mineral. As they contain negligible K-feldspar, the name 'oceanic plagiogranites' was proposed by Coleman and Peterman (1975) and is still widely in use.

Geochemical discriminants and tectonic association of granitoids

There have been several attempts to distinguish between the different granitoid associations reviewed above – and the geotectonic environments into which they were emplaced – using geochemical (usually trace element) discriminant diagrams. The potential value of such schemes is that they may shed light on the palaeotectonic setting of ancient granitoid magmatism in cases where unambiguous geological (field) evidence has proved difficult to obtain. The most widely cited scheme is that devised by Pearce et al. (1984), two of whose discriminant diagrams are illustrated in Fig. 8.19.

The diagrams are based on a database of 600 analyses of granitoids emplaced in

Table 8.4 Major and trace element analyses of representative granitic rocks from various tectonic settings. Iron data are presented as 'total FeO' ['ΣFeO' = actual FeO + (actual Fe_2O_3/1.11)] as in Table 2.4. Blank entries indicate components that are not given in the original published analyses.

Rock type	**Quartz diorite**	**Tonalite**	**Granodiorite**		**Granite**			**Charnockite**
Tectonic setting	**Cordillera**	**Archaean craton**	**Cordillera**	**Cordillera *I type***	**Collisional thrust belt *S type***	**Intraplate postorogenic *A type***	**Mid-ocean ridge**	**Proterozoic granulite terrain**
Location	**Sierra Nevada, California**	**Average of Archaean TTG**	**Sierra Nevada, California**		**Langtang Nepal Himalaya**	**Wallagga, Ethiopia**	**MAR 45° N plagiogranite**	**Fishtail pluton, Bunger Hills E Antarctica**
Reference	**1**	**2**	**3**	**4**	**5**	**6**	**7**	**8**
Mass % oxide								
SiO_2	55.27	70.2	62.78	71.65	75.01	77.26	72.47	64.00
TiO_2	0.94	0.33	0.70	0.24	0.15	0.35	0.33	1.25
Al_2O_3	17.39	15.74	15.74	14.87	14.99	11.01	14.17	13.92
ΣFeO	7.04	2.56	5.08	1.58	1.18	2.22	2.85	7.63
MnO	0.14	0.04	0.09	0.04	0.03	0.02	0.08	0.15
MgO	3.80	1.09	2.50	0.38	0.37	0.04	1.39	1.19
CaO	7.13	3.17	4.80	1.87	0.77	0.18	1.48	3.59
Na_2O	3.59	4.87	3.25	3.98	3.25	4.38	5.55	2.30
K_2O	1.51	1.88	3.22	4.19	3.85	4.26	0.24	4.16
P_2O_5	0.24	0.12	0.18	0.08	0.12	0.01	0.06	0.47
LOI[§]	2.28		1.42	0.88	0.79	0.13	1.00	0.78
Total	99.33	100.00	99.76	99.76	100.51	99.86	99.62	99.44

Ppm								
Rb	88	50	134	158	236	152	<2	100
Ba	440	746	745	1170	354	75	149	1973
Th	12.2	5.98	31.8	16.8	9	8.1	3.4	1
Nb	7	5.4	8	9	11	23	42	20
La	25.6	29.84	26.6	29.3	15.97	53.2	43.8	46.4
Ce	48	51.63	50	58	30.51	180	81.7	94.8
Sr	616	495	478	484	127	18	89	294
Nd	19	19.92	22	15	15.49	58.2	35.1	51.0
Zr	86	149	143	138	72	357	285	351
Sm*	*4.7*	2.79	*5.8*	*2.5*	3.75	13.1	7.7	9.28
Eu*	*1.2*	0.91	*1.1*	*0.85*	0.85	0.36	1.62	3.12
Gd*	*3.8*	2.04	*5.8*	*2.5*	4.52	11.3	8.8	
Tb*		0.25			0.68	1.47	1.3	1.17
Y	18	6.8	26	8	22	63	55	31
Yb	1.9	0.46	2.4	0.65	1.34	4.48	6.9	1.99

* Data in *italics* (not tabulated in the original paper) have been estimated from published REE plots (Frey et al., 1978); Gd, by graphical interpolation.
§ **Loss-on-ignition**.

Data sources

1 Bateman and Chappell (1979) and Frey et al. (1978), analysis 0 (quartz diorite, Tuolumne intrusives).
2 Drummond et al. (1996), analysis 3 (average Archaean high-Al **TTG** suite).
3 Sources as for column 1, analysis 4 (granodiorite, Tuolumne intrusives),
4 Sources as for column 1, analysis 21 (granite porphyry, Tuolumne intrusives).
5 Inger and Harris (1993), analysis KG208 (biotite-muscovite-leucogranite, Langtang valley, Nepal Himalaya.
6 Kebede and Koeberl (2003), analysis TK060 (Horna granite, Wallagga area, western Ethiopia).
7 Pearce et al. (1984) 'oceanic' analysis (c) (oceanic plagiogranite, Mid-Atlantic Ridge at 45° N).
8 Sheraton et al. (1992) analysis 86286060 (orthopyroxene granite, Fishtail pluton, Bunger Hills, E Antarctica).

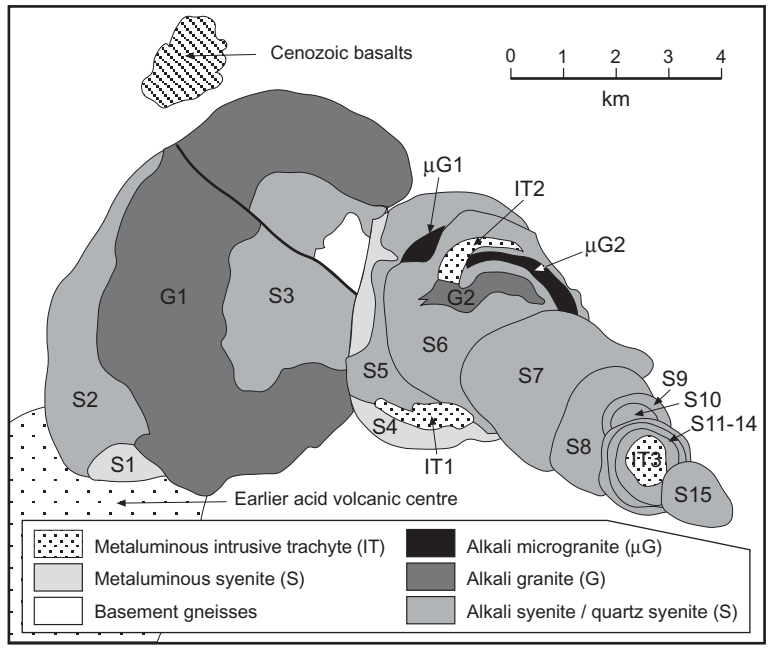


Fig. 8.18 Sketch map of the 236 Ma-old Ras ed Dom granite-syenite ring complex (adapted from O'Halloran, 1985; copyright Elsevier), one of a score of such complexes in the Bayuda desert of Sudan. Units of each type are numbered in order of intrusion. The size of successive intrusions here decreases with time and their centres migrate first to the NE then to the SE.

tectonic settings that are well understood. Pearce et al. (1984) showed it was possible to distinguish geochemically between 4 broad tectonic categories (roughly equivalent to the headings above): volcanic arc granitoids, syn-collisional granitoids, within-plate (anorogenic) granitoids, and ocean spreading centre (and intra-ophiolite) granites. Analyses of granites from each of these associations are plotted with different symbols in Figure 8.19, and empirically they define distinct compositional fields in each of the two diagrams. The Rb *versus* (Y + Nb) diagram largely succeeds in discriminating between the four categories, but volcanic arc and syn-collisional granitoids cannot be separated from each other in the Nb *versus* Y plot. The boundaries shown are those defined by Pearce et al. (1984) as the best straight-line fits to their data; as often happens with such diagrams, a few peripheral analyses plot on the wrong side of most boundaries.

Such diagrams undoubtedly have their uses in studying magmatism in geologically complex areas, but they need to be used with caution. Nb and Y are relatively **immobile** elements whose primary concentrations in silicate rocks are relatively robust in the face of moderate degrees of alteration and metamorphism, but the same cannot be said of the **mobile** element Rb; for Fig. 8.19b to be reliable, it is vital to ensure that only analyses of fresh unmetamorphosed rocks are plotted.

The reader should also recognize that the compositional differences that emerge from Fig. 8.19 actually have more to do with differing source compositions and crystallization histories than with tectonic setting *per se* (Frost et al., 2001).

Archaean TTG suite

The world's Archaean cratons comprise terrains of two contrasting types. One consists of greenstone belts (see Box 5.6) interspersed with granitic bodies, which together make up what are called ***greenstone-granite terrains***, like those found in the Yilgarn and Pilbara blocks of Western Australia and the Kaapvaal craton of South Africa. The second kind – known as *high-grade Archaean terrains* and typified by the Lewisian gneiss complex of NW Scotland, the Amîtsoq/Itsaq gneiss

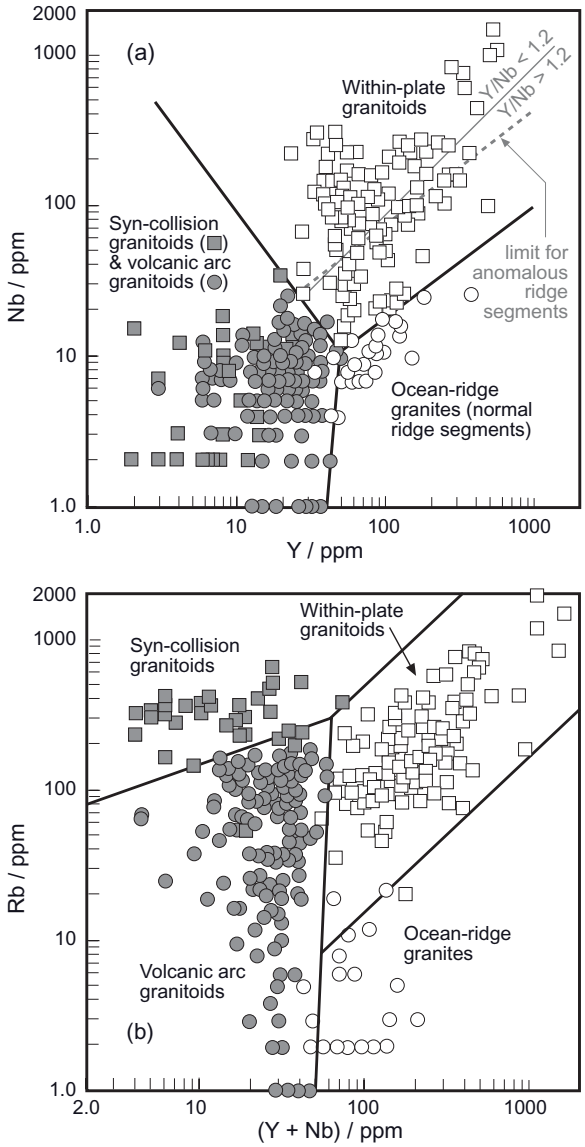


Fig. 8.19 Two of the discriminant diagrams devised by Pearce et al. (1984, reproduced by permission of Oxford University Press) showing analyses of granitoids from clearly defined tectonic environments: (a) Nb ppm *versus* Y ppm; the dashed line indicates the upper limit for granites from anomalous (E-MORB) ridge segments; the significance of the Y/Nb ratio (Eby, 1990) is discussed later in the chapter. (b) Rb ppm *versus* (Y + Nb) ppm. The clustering of low Nb and Rb values in horizontal arrays arises because these values (being close to the analytical detection limits) are quoted to only one **significant figure**, an effect magnified by the use of logarithmic scales. **NB** Analyses need to be recalculated volatile-free before plotting in these figures (Box 1.3).

complex of West Greenland (Nutman et al. 1996) and the Limpopo belt of southern Africa – is dominated by banded, upper amphibolite- to granulite-facies, quartzofeldspathic gneisses. They contain lenses, layers or irregular inclusions of older supracrustal lithologies (both metavolcanic and metasedimentary). The gneisses in this second setting have low K-feldspar contents – hence the widely used field term 'grey gneisses' reflecting the lack of pink feldspar – and have evidently formed from plutonic igneous protoliths of tonalitic, trondhjemitic and granodioritic composition. Together they constitute what is called the Archaean tonalite–trondhjemite–granodiorite (**TTG**) suite.

In addition to the K-poor character implied by their petrography (Fig. 8.1), Archaean TTG terrains, representing the Earth's oldest continental crust, are distinguished by gneisses with steep REE patterns and heavy rare earth element (HREE) enrichment barely higher than 2× chondrite. In this respect they are similar to modern **adakite** lavas (Table 8.5 and Chapter 6). The other trace element characteristic that sets adakites apart from normal arc volcanics – a Sr/Y ratio above 40 – is also observed in the Archaean TTG association (Table 8.5). One may fairly conclude that available sources and melting conditions within the Archaean Earth bore some similarity to those that generate adakite magmatism today, and the implications are discussed in the final section of this chapter.

Normal K-rich granites also occur in Archaean terrains, but – judging from the compositions of Archaean sedimentary rocks – accounted for less than 10% of the surface areas exposed to erosion in early Archaean times (the bulk being TTG), though they became the dominant granite type after about 2500 Ma (Taylor and McLennan, 1985).

Proterozoic anorthosite–mangerite–charnockite (AMC) suites

In Chapter 4 mention was made of 'massif' anorthosites and their distinctive association with orthopyroxene-bearing granitoids **charnockite** and mangerite (the anorthosite–mangerite–charnockite (AMC) – suite).

Charnockite and related orthopyroxene-bearing granitoids (Fig. 8.2) are characteristic of medium- to high-pressure granulite terrains;

Table 8.5 Comparison between average Archacan TTG, modern adakite and modern arc dacite analysis (data from Martin, 1999).

	Modern arc dacites	Modern adakites	Modern adakitic plutons	Archaean TTGs
Mass percent oxide				
SiO_2	68.22	64.66	67.30	69.79
TiO_2	0.46	0.51	0.54	0.34
Al_2O_3	14.63	16.77	15.78	15.56
ΣFeO	3.86	3.78	3.00	2.81
MnO	0.09	0.08	0.05	0.05
MgO	1.22	2.20	1.96	1.18
CaO	2.88	5.00	3.67	3.19
Na_2O	4.15	4.09	4.19	4.88
K_2O	3.37	1.72	2.15	1.76
P_2O_5	0.21	0.17	0.12	0.34
ppm element				
Ni	5	24	24	14
Cr	8	36	46	29
Sr	380	706	280	454
La	48.1	19	17.7	32
Y	47	10	17	7.5
Yb	4.4	0.93	1.1	0.55
$(La/Yb)_N$	7.5	14.2	11.0	39.7
Sr/Y	8.1	68.7	16.5	60.5

the type locality is the Madras area of southern India. Intrusive relations sometimes indicate magmatic emplacement of the protolith, but debate has raged as to whether the orthopyroxene now present in these rocks crystallized directly from water-depleted magma, or is the product of post-magmatic dehydration metamorphism of normal hornblende-bearing granite (many charnockites show signs of deformation and recrystallization). Kilpatrick and Ellis (1992) have argued for a distinctive 'C-type' granitoid magma type capable of crystallizing magmatic orthopyroxene.

HOW ARE GRANITOID MAGMAS FORMED?

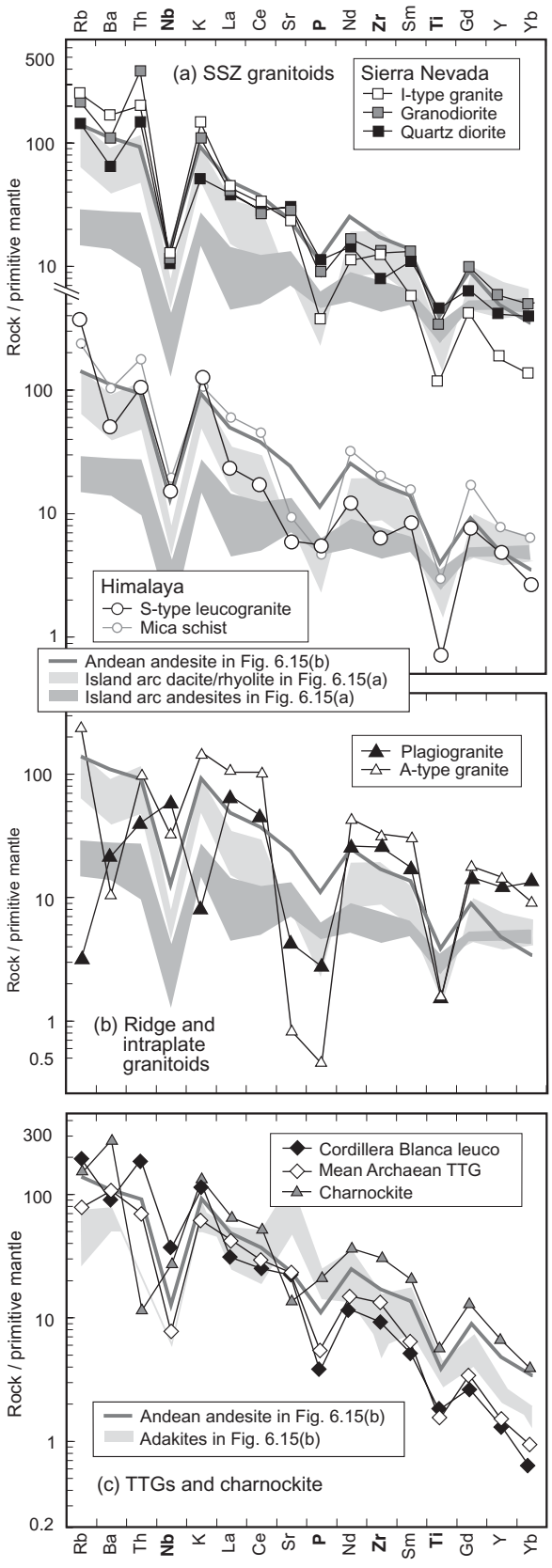
Though homogeneous granite exposures often present the illusion of a simple genesis, the great diversity of structures and textures reviewed in preceding sections of this chapter reminds us that granitoid petrogenesis is often a complex, multistage process. Moreover the details of magma genesis – insofar as they are known – seem to vary considerably from one tectonic setting to another: as H.H. Read famously remarked

'*there are granites and granites*'.

Delving deeply into the evolving complexities of granite magma genesis (and the many tools that petrologists use to investigate it) lies beyond the scope of this book, but Chapter 8 would be incomplete without a summary of the current state of understanding. Traditionally granite magma genesis has been viewed in terms of an interplay between two contrasted processes: (i) extended fractional crystallization of mantle-derived basic magma; and (ii) partial melting of old sialic continental crust, leading either to the formation of anatectic plutons or to the contamination of mantle-derived magmas. Increasingly, however, the evidence suggests that additional processes also have to be taken into account.

Plagiogranites

Granitoids emplaced in the ocean basins, where magma evolves in the absence of continental crust as a potential contaminant, have the simplest origins. Oceanic plagiogranite is formed from mid-ocean ridge basalt by



spreading-centre fractionation processes, the foremost of which is likely to be fractional crystallization. Figure 8.20b shows the **spidergram** of an oceanic plagiogranite from the mid-Atlantic ridge (see analysis in Table 8.4). The pattern is notable for:

- relative depletion in the most highly incompatible large-ion lithophile (LIL) elements Rb, Ba and K, consistent with derivation from mid-ocean ridge basalt (MORB) (Fig. 2.16b), though further loss may have occurred through alteration;
- greater enrichment in Th, Nb and light rare earth elements (LREE) than for HREE [$(La/Yb)_N \sim 4.5$], consistent with MORBs from this anomalous 45 °N sector of the mid-Atlantic Ridge;
- prominent negative anomalies in P and Ti, symptomatic of advanced fractional crystallization of accessory minerals apatite [$Ca_5(PO_4)_3(OH,F)$] and Fe–Ti oxides, which deplete the residual melt in P and Ti.[14] The low level of Sr records the frac-

Fig. 8.20 Incompatible element enrichment profiles for selected granitoid analyses, including those in Table 8.4 (sources listed there), normalized to primitive mantle as tabulated in Table 2.4. The contaminated Ollagüe Andean andesite from Fig. 6.15b and fields for the arc andesites and dacites in Fig. 6.2a are shown for reference in panels (a) and (b). (a) Subduction-related granitoids from the Sierra Nevada batholith and a post-collision leucogranite from the High Himalaya association; a mica schist viewed as a possible source material for the leucogranite (Inger and Harris, 1993, analysis RM202) is also shown for comparison. (b) Mid-Atlantic Ridge plagiogranite (from 45 °N) and an anorogenic granite from western Ethiopia. (c) a leucogranodiorite from the Cordillera Blanca in Peru (Fig. 8.16, analysis from Petford and Atherton, 1996), the mean composition of Archaean **TTG**, and a magmatic charnockite from Antarctica. The shaded field in (c) represents the adakites shown in Fig. 6.15b. Bold typeface highlights **HFS** elements.

[14] These characteristics are also consistent with formation of granite melt by partial melting of MORB-related gabbros, if apatite and ilmenomagnetite remain behind in the solid residue.

tionation of feldspar, in which Sr is mildly compatible.

There is no hint of a negative Nb anomaly, setting the plagiogranite apart from supra-subduction zone (SSZ) lavas and plutonics shown in Fig. 6.15 and 8.20a.

Cordilleran granitoids

Fractional crystallization has been proposed as the prime factor behind observed compositional variations in the Mesozoic Coastal Batholith of Peru. Atherton and Sanderson (1985) found they could model[15] the observed chemical trends by starting with a parental diorite magma and subtracting (i.e. 'crystallizing') plagioclase + hornblende + biotite ± pyroxene ± magnetite from it in varying proportions. Their calculated chemical evolution matched the observed trends without necessitating any assimilation of upper continental crust. Initial Sr isotope ratios from the Lima segment of the batholith – where it intrudes the Cretaceous Huarmey-Cañete Basin volcanics – fall within the range expected for the fractional crystallization of mantle-derived magmas (Fig. 8.21), confirming that negligible assimilation of older continental crust had occurred. The higher initial ratios in the Arequipa and Toquepala segments, on the other hand, where the batholith is in contact with the Precambrian Arequipa massif, suggest that significant crustal contamination has affected some intrusive units here (Fig. 8.21b).

Atherton and Sanderson (1985) supposed that the parental diorite magma was the product of a two-stage process in which: (i) basic magmas originating by partial melting of metasomatized mantle wedge accumulated and crystallized at the base of the continental crust; then (ii) underwent partial melting to form the parental diorite magma. Melts produced by this 2-stage process would inherit low $^{87}Sr/^{86}Sr$ ratios, because the basic rocks from which they formed were still young when they underwent partial melting (Box 3.3); sufficient time would not have been available to allow significant growth of ^{87}Sr relative to ^{86}Sr in spite of moderately high Rb/Sr.

[15] i.e. duplicate mathematically.

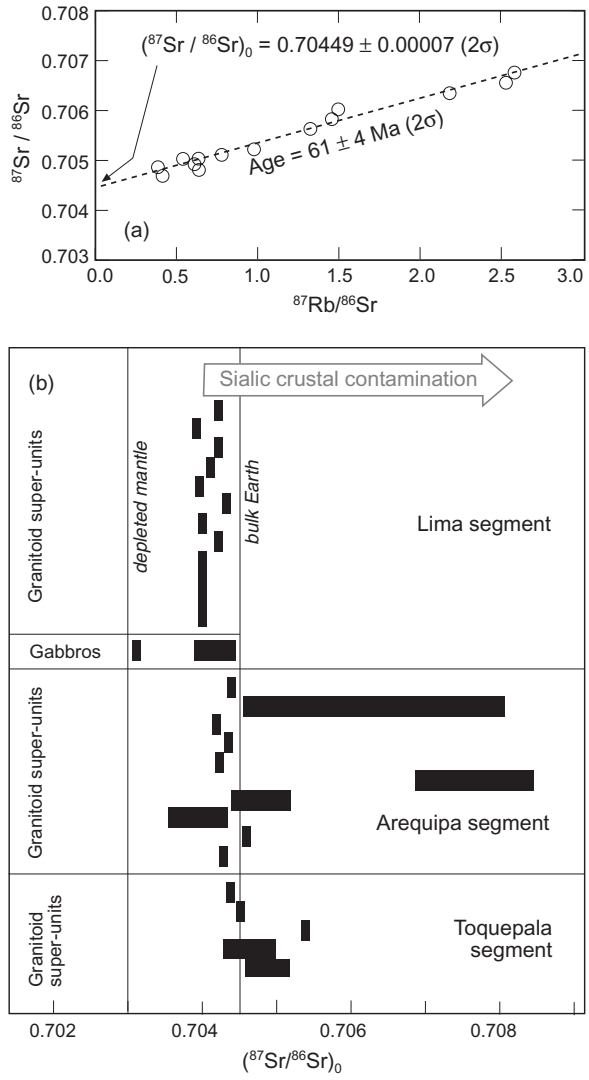


Fig. 8.21 Sr isotope trends in the Coastal Batholith of Peru. (a) An Sr **isochron** plot for the Yarabamba 'super-unit', illustrating the gradient (from which age is calculated) and the *y* axis intercept, which indicates the initial Sr isotope ratio $(^{87}Sr/^{86}Sr)_0$ at the time of emplacement. (b) Summary of initial Sr isotope ratios obtained for different super-units and segments of the batholith, showing the elevated crustal contamination in the Arequipa and Toquepala segments (after Beckinsale et al., 1985).

Fractional crystallization also seems to have played a role in the northern and southern sectors of the Mesozoic Sierra Nevada batholith in California, though here the evidence for assimilation of sialic continental crust is much stronger. Figure 8.20a shows spidergrams for three granitoids from the

Tuolumne pluton in the northern Sierra Nevada. Note the following features:

- The granitoids share several features of island-arc volcanic rocks in Fig. 6.15 (summarized here by shaded fields), notably the large negative Nb anomaly.
- Nevertheless the elevated level of enrichment and the profile slope have more in common with the contaminated Andean andesite (grey line) than with the arc volcanics, suggesting a significant degree of crustal assimilation (cf. Feeley and Davidson, 1994).
- The differences between individual granitoid patterns are relatively slight, but Rb, Ba, Th, Nb and K increase consistently from diorite to granodiorite to granite, consistent with fractional crystallization.
- The negative P and Ti anomalies also increase in magnitude progressively from diorite to granite, consistent with fractionation of accessory apatite and Fe–Ti oxides.

Figure 8.22a shows that $(^{87}Sr/^{86}Sr)_0$ ratios for plutons in the northern and southern Sierra Nevada (filled symbols) increase crudely with SiO_2 content. The simplest interpretation of this kind of trend is that it represents assimilation of older continental crust by normal mantle-derived basic magmas during the course of fractional crystallization. The notion of assimilation linked to fractional crystallization (De Paolo, 1981), often referred to as **AFC**, was introduced in Chapter 3. The factors controlling the relative contribution of basalt crystallization *versus* crustal melting in lower-crustal 'hot zones' have been discussed quantitatively by Annen et al. (2006).

The open symbols in Fig. 8.22b, on the other hand, represent intrusive suites from the central Sierra Nevada, which follow quite different trends. They exhibit essentially no correlation between initial ratio and silica content: the gabbroic and dioritic members of each series have $(^{87}Sr/^{86}Sr)_0$ values as high as the more evolved granites. Coleman and Glazner (1997) attributed the high initial ratios of the mafic rocks here (0.706–0.7075) not to input of older crust – which would have correlated $(^{87}Sr/^{86}Sr)_0$ with SiO_2 as in Fig. 8.22(a) – but to melting of highly enriched, ancient subcontinental mantle lithosphere.

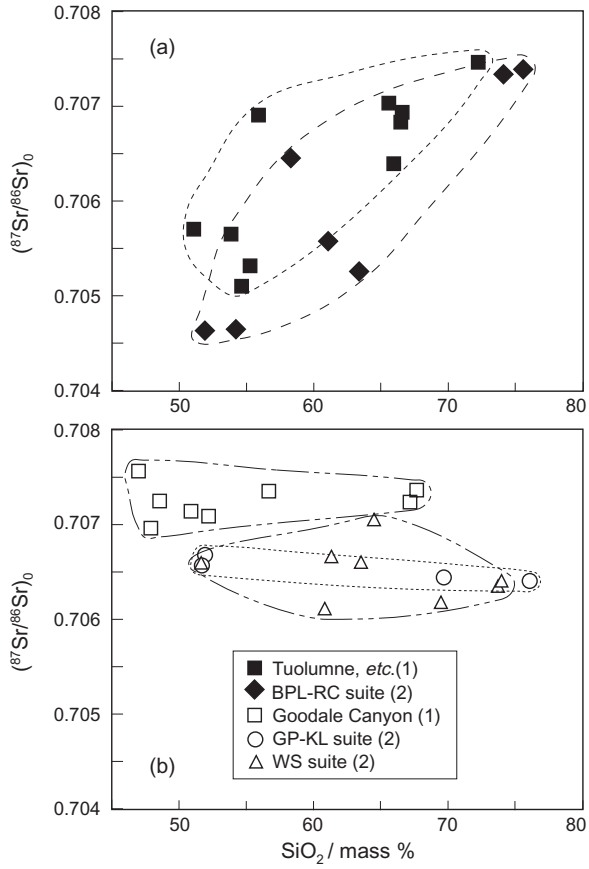


Fig. 8.22 Correlations between initial Sr isotope ratio and whole-rock SiO_2 content for granitoid suites in the Sierra Nevada batholith, California. Data from Coleman and Glazner (1997, '1') and Wenner and Coleman (2004, '2'); abbreviations as in Wenner and Coleman, 2004). (a) Intrusive suites from northern and southern segments ('Tuolumne, etc.' includes Mount Whitney and Rock Creek suites); (b) Intrusive suites from central segment. Field boundaries highlight the distribution of samples from each intrusive suite.

There is plentiful evidence for the enriched nature of the lithospheric mantle underlying parts of western USA from mantle xenoliths found in basaltic volcanics across the region. Wenner and Coleman (2004) summarized the diversity of granitoids in the central Sierra Nevada as follows:

> '*Trends in initial Sr … isotope ratios reveal little variation within a wide range of rock types in the same suite, but significant spatial and isotopic variation among individual*

suites of rocks. These observations are consistent with the interpretation that granites in the [central] *Sierra are generated by partially melting juvenile, mantle-derived diorites and mixed with penecontemporaneous mantle melts. … There is little evidence that ancient continental crust was involved in the generation of the central Sierra Nevada batholith. Instead, isotopic trends from east to west in this study indicate that the majority of granites in the central Sierra Nevada are likely juvenile crust.*'

The same theme of re-melting of juvenile mafic rocks underplating the continental crust emerges from the late Miocene Cordillera Blanca batholith in the eastern cordillera of Peru (Fig. 8.16). As in the central Sierra Nevada, $(^{87}Sr/^{86}Sr)_0$ here varies within a relatively narrow envelope (0.7041–0.7057) for intrusive rocks ranging from quartz diorite to leucogranodiorite that span a wide range of SiO_2 content (55%–72%). Even though the magmas ascended through 50–60 km of thickened continental crust, Petford et al. (1996) concluded that little contamination by mature continental basement had occurred. The high-Na leucogranodiorites of the Cordillera Blanca are notable for their adakite-like characteristics, such as relatively high Sr/Y and La_N/Yb_N ratios and low $HREE_N$ compared to most calc-alkaline magmas (Fig. 8.20c); indeed the leucogranodiorite pattern is steeper and shows greater depletion in HREE than for present-day volcanic adakites. Petford and Atherton (1996) interpreted these features as the signature of partial melting of juvenile mafic rocks underplating the continental crust. Given the thickened overlying crust (≥50 km) at the time of leucogranodiorite emplacement (~5 Ma BP), the mafic 'underplate' that had accumulated from normal SSZ processes would have passed from plagioclase-stable to deeper garnet-stable conditions, favouring retention of HREE in the source during melting. Even though subduction beneath this sector of the Andes at the end of the Miocene times was shallow – favouring adakite magma genesis by slab melting – Petford and Atherton (1996) consider partial melting of garnet-bearing mafic rocks underplating the continental crust as the most likely explanation for the adakitic affinity of the Cordillera Blanca batholith.

Archaean TTG suite

Archaean trondhjemitic (TTG) gneisses have high-Na major element compositions and incompatible-element signatures broadly similar to modern adakites in general (Fig. 6.15) and to the Cordillera Blanca granitoids in particular (Fig. 8.20c) so the igneous protoliths of these gneisses may have formed by similar processes. Martin (1986, 1999) attributed the incompatible-element characteristics of Archaean TTG gneisses (Fig. 8.20c) to slab melting in the garnet stability field, as proposed for modern adakites. Nutman et al. (1999) and Smithies (2000), on the other hand, consider that partial melting of garnet-bearing mafic rocks at the base of a tectonically thickened crust[16] or partial melting of a thick, hydrothermally altered basaltic pile are equally feasible explanations. What is beyond doubt is the presence of garnet in the source region and its role as a residual phase in buffering HREE in the melts formed.

A complementary insight into the difference between Archaean and post-Archaean granitoid formation is afforded by the REE europium (Eu), a sensitive monitor of plagio-

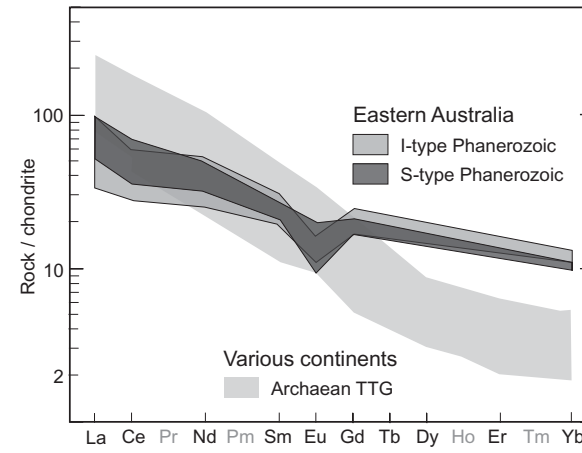


Fig. 8.23 Comparison of REE patterns for (a) Archaean TTG gneisses from West Greenland, Swaziland and the Pilbara block, Western Australia, and (b) I- and S-type granitoids from the Palaeozoic New England Batholith of eastern Australia (after Taylor and McLennan, 1985, by permission of Blackwell Publishing). Elements shown in grey are intervening REE not plotted in this diagram.

[16] Note that the TTG pattern in Fig. 8.20c bears more resemblance to Cordillera Blanca than to adakites with respect to Sr/Y and La/Yb.

clase fractionation (Box 8.5). Typical Proterozoic and Phanerozoic K-rich granites exhibit negative Eu anomalies (Fig. 8.23), indicating either that plagioclase was present in the source where partial melting took place, or that plagioclase fractionation occurred during magma evolution. Archaean K-poor TTG gneisses, on the other hand, are distinguished not only by their steeper patterns and low HREE, but also by a lack of any Eu anomaly, suggesting partial melting at depths too great for plagioclase to be stable where garnet would fractionate in its place.

Collision-related leucogranites

The I-type granitoids of the Trans-Himalayan and Karakorum batholiths (Fig. 8.17), emplaced respectively in the intervals 100–40 Ma and 110–70 Ma ago, formed above a long-lived subduction zone prior to the collision between India (or the Kohistan arc) and Eurasia. Their petrogenesis can therefore be expected to have much in common with Andean batholiths (such as the Coastal Batholith of Peru discussed above) and those of the western USA. The younger, collision-related S-type leucogranites that make up the discontinuous High Himalayan and North Himalayan belts, on the other hand, have a very different origin.

The High Himalayan collision-related leucogranites have several distinctive features:

- they are pale granites with a limited range of composition: unlike Cordilleran I-type batholiths, the intrusions are devoid of diorites and other intermediate granitoids;
- silica contents are uniformly high (SiO_2 70%–77%);
- the leucogranites are strongly peraluminous (Exercise 8.3) and contain key aluminous minerals (Table 8.2.1); inclusions of metasedimentary lithologies are not uncommon;
- the leucogranites have high $(^{87}Sr/^{86}Sr)_0$ ratios in the range 0.743–0.762[17] (Inger and Harris, 1993; Harris et al., 1995);
- compared to Cordilleran granitoids, Himalayan leucogranites are enriched in Rb and K but are depleted in Sr, Zr and LREE (Fig. 8.20a).

[17] Excluding an anomalous sample with $(^{87}Sr/^{86}Sr)_0 = 0.736$.

These characteristics all point to formation of leucogranite melts by anatexis of high-grade meta**pelites** (Box 8.3) of the 'High Himalaya crystalline sequence'. Early researchers proposed that dehydration reactions in deeper-seated metamorphic rocks had provided a hydrous fluid flux sufficient to induce H_2O-saturated anatexis of overlying muscovite-bearing pelites, but current thinking favours fluid-absent (i.e. H_2O-undersaturated) 'dehydration melting' of muscovite as the cause of anatexis (Box 8.4). Isotopic analysis shows that, at the time of leucogranite emplacement (~20 Ma BP), the pelites had $^{87}Sr/^{86}Sr$ ratios in the range 0.749–0.761, similar to the $(^{87}Sr/^{86}Sr)_0$ values of the leucogranites themselves, whose initial isotope ratios could therefore have been inherited from the pelites.

Fig. 8.20a compares the incompatible element profile of a High Himalayan leucogranite with that of a mica schist from the same area (Langtang valley). The obvious similarities between these two lithologies, particularly with respect to the most incompatible elements Rb, Ba, Th, Nb and K and the negative anomalies for Sr, P and Ti, broadly support the pelite anatexis model.

Intraplate granites

The chemical diversity of A-type granites and the range of tectonic settings in which they occur make it unlikely that a single petrogenetic model will account for all of them. Eby (1990) divided A-type granites into two categories according to their Y/Nb ratios:

> '*There is a group of A-type granitoids which have low Y/Nb ratios* [<1.2 – see Fig. 8.19a] *and generally low initial* $^{87}Sr/^{86}Sr$ *ratios. These suites are differentiates of basaltic magmas directly derived from OIB-like* [plume] *mantle sources, which may have undergone some crustal interaction. There is a second group of A-type granitoids characterized by higher Y/Nb ratios (1.2–7) and highly variable initial* $^{87}Sr/^{86}Sr$ *ratios. On a suite-by-suite basis, this* [second] *group shows a complex petrogenetic history, some suites having a significant mantle component whereas others may be totally of crustal origin.*'

Box 8.4 Dehydration (or fluid-absent) melting

Hydrous minerals possess limited stability at high temperature: minerals like muscovite and biotite are characterized by well defined, pressure-dependent breakdown temperatures (Box 6.2) at which they decompose into anhydrous minerals plus an H_2O vapour. These relations allow mica to form in medium-grade metamorphic rocks like schists, but not as a rule in granulites.

Under mid-crustal conditions in orogenic belts, muscovite dehydration plays a key role in crustal melting. Figure 8.4.1 shows solidus curves for the anatexis of muscovite-bearing **pelites** like those of the High Himalayan metasedimentary sequence. In the presence of excess water, the pelite solidus falls to temperatures as low as 600 °C at depth, although melts formed under these 'wet' conditions – in which $[dT/dP]_{solidus}$ is negative (dashed curve) – cannot ascend far before re-crossing the solidus and solidifying. If only a limited amount of H_2O is present, however, $[dT/dP]_{solidus}$ becomes positive (solid line) as explained in Box 6.4, enabling any melts formed to ascend to shallower levels without immediately solidifying. Melting under these conditions can be summarized by:

$$\underset{\substack{\textit{hydrous}\\\textit{mineral}}}{\textit{muscovite}} + \underset{\text{anhydrous minerals}}{\text{plagioclase} + \text{quartz}} \rightarrow \underset{\substack{\textit{hydrous}\\\textit{melt}}}{\textit{melt}} + \underset{\text{anhydrous minerals}}{\text{K-feldspar} + \text{sillimanite (or kyanite)}} \qquad [8.4.1]$$

The limited H_2O present resides solely in the muscovite on the left-hand side of equation 8.4.1 and in the melt on the right-hand side (italicized for emphasis): there is no excess to form a separate H_2O fluid phase. Melting like this that involves the disappearance of a hydrous mineral, producing melt and anhydrous crystalline products, is called dehydration melting or fluid-absent melting. Experiments show that partial melting of Al-rich pelites produces high-SiO_2, peraluminous melts similar in composition to the High Himalayan leucogranites.

The grey curved arrow in Fig. 8.4.1 shows a possible scenario for dehydration melting followed by ascent and emplacement of leucogranite magma, as envisaged by Inger and Harris (1993) for Himalayan leucogranites. Melting begins in the kyanite stability field and is aided by decompression arising from extension across the South Tibetan Detachment (Fig. 8.17), followed by deformation-enhanced melt segregation. Leucogranite melts ascend from the source area through dyke systems (as observed in migmatites beneath the emplacement horizons) before lateral injection as sills and laccoliths.

Dehydration melting is also relevant to production of adakite magmas by slab melting.

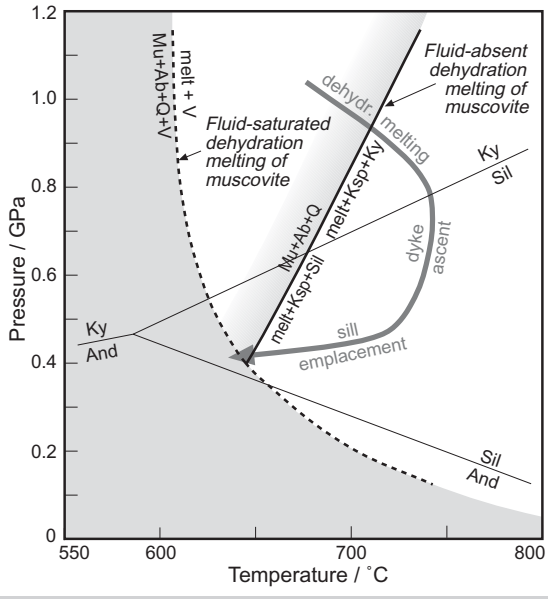


Fig. 8.4.1 Cartoon illustrating the muscovite-dehydration melting of metapelite to form leucogranite (after Inger and Harris,1993, by permission of Oxford University Press). The heavy dashed curve shows a H_2O-saturated pelite solidus; the solid line shows the pelite solidus in H_2O-undersaturated conditions (cf. Fig. 6.4.1). The phase boundaries for the three Al_2SiO_5 polymorphs are shown for reference as thin lines. Mineral abbreviations: Mu, muscovite; Ab, albite (plagioclase); Q, quartz; V, vapour (H_2O in fluid phase); Ky, kyanite; Sil, sillimanite; And, andalusite; Bi, biotite; Ksp, K-feldspar. The grey arrowed curve illustrates a possible *P–T–t* path leading from anatexis through ascent to leucogranite sill emplacement.

Box 8.5 Europium anomaly and plagioclase fractionation

Europium is unique among rare earth elements in having a stable 2+ oxidation state in addition to the 3+ state characteristic of REE as a whole (Fig. 2.7.1). Under the relatively reducing conditions obtaining in most magmas, Eu will be present mainly as Eu^{2+} ions whereas all other REE will exist as M^{3+} ions. As a result, Eu will partition between minerals and melt differently from the other REE. Compared to them, the Eu^{2+} ion has a lower charge and a larger ionic radius that make it rather similar to the Sr^{2+} and Ca^{2+} ions (Fig. 2.7.1). Its radius is slightly too large to allow substitution for Ca^{2+} in dense ferromagnesian minerals like augite and garnet, but like Sr^{2+} it readily takes the place of Ca^{2+} in the open framework structure of plagioclase, in which it substitutes preferentially (i.e. is mildly compatible). As a consequence the fractionation of plagioclase will deplete a melt in Eu relative to other REE (which are incompatible in plagioclase).

The effect of plagioclase fractionation on the REE pattern is illustrated in Fig. 8.5.1. The middle pattern shows the REE pattern of a primitive lunar basalt, in which the REE define a level pattern at about 10× chondrite. The pattern of a more evolved lunar basalt (top) is similar except that: (i) the overall enrichment is about 10× greater owing to fractionation; and (ii) Eu is less enriched than the other REE, giving what is referred to as a negative Eu anomaly. This is due to the selective extraction of Eu by plagioclase crystallization during fractionation under the exceptionally reducing conditions characteristic of the Moon's interior (favouring high Eu^{2+}/Eu^{3+}). Supporting evidence for this interpretation is provided by the pattern for a lunar highlands anorthosite. The anorthosite formed as a plagioclase cumulate on the surface of a magma ocean early in the Moon's history, and confirms the preferential incorporation of Eu into plagioclase.

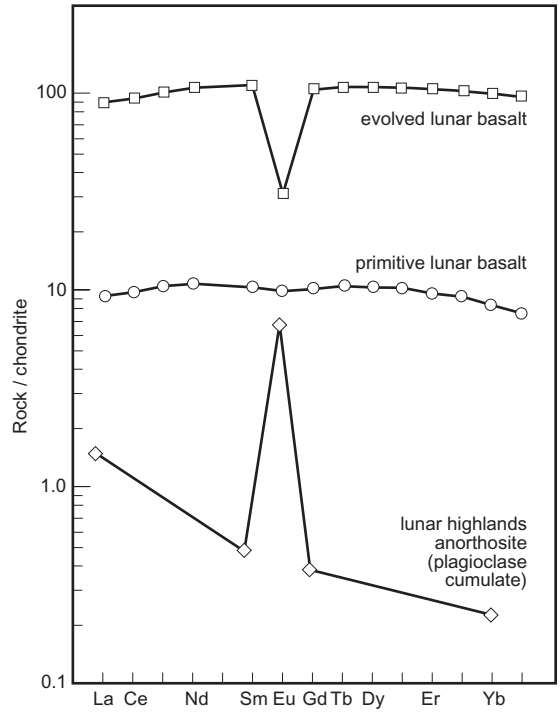


Fig. 8.5.1 REE patterns for three lunar rocks. The patterns are similar in principle to incompatible element enrichment profiles (Fig. 2.16, Fig. 8.20), but the diagram is confined to the REE (shown in atomic-number order). For historical reasons, the abundances in a REE plot are normalized not to primitive Earth mantle but to the average composition of chondrite meteorites (numerically there is little difference). Adapted from Gill (1997) and Taylor (1982).

The incompatible element profile of the A-type granite listed in Table 8.4 is shown in Fig. 8.20b. Like that of the plagiogranite, it has hallmarks of advanced degrees of fractional crystallization (high overall level of enrichment, marked negative anomalies for Sr, P and Ti). However Rb, Th and K are higher than in the plagiogranite, consistent with derivation from an ocean island basalt (OIB)-type basaltic parent rather than from ridge basalt (Fig. 2.16a). The moderate negative Nb anomaly and the relatively high Y/Nb ratio (2.7) that results from it suggest a significant degree of contamination by old continental crust.[18]

Charnockites and the AMC suite

Has the orthopyroxene that characterizes the charnockite–mangerite-jotunite association (Fig. 8.2) crystallized directly from a water-depleted magma, or is it the product of post-magmatic dehydration metamorphism of hornblende-bearing granite during deformation and metamorphism? One view is that 'charnockitization' of hydrous granitoids may result as much from metamorphic exchange with CO_2-rich fluids ascending from greater depths in the crust or mantle (Friend, 1981) as from high metamorphic temperatures *per se*. Kilpatrick and Ellis (1992), on the other hand, take the view that intrusive charnockites are sufficiently distinct in geochemical terms (high TiO_2, P_2O_5, Zr: see Table 8.4) to be regarded as a distinct 'C-type' granitoid magma type – from which magmatic orthopyroxene crystallizes directly – which they propose formed by partial melting of a deep-crustal granulite-facies (i.e. dehydrated) mafic source. They cite latite and dacite analyses which they regard as volcanic equivalents of such C-type magmas as evidence for their existence.

The common association of Proterozoic charnockitic intrusives with massif anorthosites (the AMC suite discussed in Chapter 4) tends to support the notion of magma derived by melting of granulite-facies rocks deep in the crust. There is a broad consensus that

> *'small ferrodioritic (jotunitic) to monzonite (mangeritic) intrusions* [associated with anorthosite] *appear to have formed from liquids residual to either the crystallization of the anorthositic masses, or the more primitive (deep-crustal) mafic intrusion. … Most workers ascribe the formation of the associated granitoids (quartz monzonite, charnockite) to melting of the lower crust'*. (Longhi et al., 1999).

Is granite peculiar to the Earth?

From space, Earth stands out from other terrestrial planets orbiting the Sun in two ways: (i) its blue oceans of liquid water; and (ii) the brown-green continental regions where the Earth's surface is sufficiently elevated to project above sea level. Campbell and Taylor (1983) and Taylor and McLennan (1995) pointed out that these two key Earth features may be interlinked.

The Earth's surface in continental regions is isostatically elevated above the ocean basins because continental lithosphere, taken as a whole, is less dense than oceanic lithosphere. The buoyancy of continental lithosphere resides almost entirely in the crust: the continents consist of thick sialic crust with an average density of $2.8 \times 10^3\,kg\,m^{-3}$, whereas the basaltic oceanic crust has an average density of $2.9 \times 10^3\,kg\,m^{-3}$ (Fowler, 2005) and is too thin to impact significantly on oceanic lithosphere density. The distinctive low density of continental crust derives mainly from the voluminous granitic rocks that have accumulated there through magmatic processes over geological time. It has had huge influence on Earth history through elevating the continents (contributing to erosion, sediment production and prevailing climate) and by preventing their subduction.

As much as 60% of the present volume of the continents was probably already in existence by the end of the Archaean (Taylor and McLennan, 1995). Our knowledge of the processes by which Archaean continents formed remains sketchy, but it seems likely that, as in post-Archaean crustal accretion, some form of subduction played a vital part. Whether

[18] Most additions to the continental crust throughout Earth history have been products of subduction-related magmatism and bear its telltale negative Nb anomaly. Assimilation of continental crust into non-subduction magmas introduces the assimilant's Nb anomaly into the hybrid magma (see Exercise 8.5).

melting occurs in the downgoing slab (adakites, TTG), in the mantle wedge (island arcs) or in basic to intermediate material underplating the continents (Cordillera Blanca), water subducted in hydrated oceanic crust plays a key role in initiating subduction-related melting. Without oceans on the Earth, the continents could not have developed in their present form. Campbell and Taylor (1983) concluded their paper in the following words:

> *'Our main thesis is simple. Water is essential for the formation of granites, and granite in turn is essential for the formation of stable continents. The Earth is the only planet with granite and continents because it is the only planet with abundant water.'*

Since their paper was published, however, the possible existence of silicic igneous rocks on other planets has been mooted by various authors, notably in relation to the 'pancake domes' detected by Magellan radar imagery on the surface of Venus (though no direct chemical data exist to support their supposed silicic composition).

Rosing et al. (2006) floated the startling notion that photosynthesis may be another Earth-surface process that has contributed to terrestrial granite magmatism and continent formation.

REVIEW – WHAT CAN WE LEARN FROM GRANITIC COMPLEXES?

Like their volcanic counterparts, granitoids are found in a variety of tectonic settings but occur in largest volumes at convergent plate boundaries, above subduction zones (as in the case of the Andean chain) and where continents collide (the Himalaya).

The principal conclusions from this chapter are:

- Granitoid plutons vary widely in form, scale and tectonic setting. Increasingly, the traditional assumption that most granite plutons have the form of a deep-rooted stock emplaced as a diapir is breaking down in the face of geophysical evidence suggesting a sheet-like architecture for many granitoid bodies (Figs. 8.4 and 8.7).
- Batholiths on the scale of 1000 km or more may be emplaced over periods exceeding 50 Ma, as in the case of the Coastal Batholith of Peru. Gravity data suggest that it has a slab-like form, apparently fed by a dyke-like root on the western side. Calculations suggest that granitic magmas may ascend to high crustal levels through feeder dyke systems.
- 'Bell-jar' plutons in which a central block of roof rock has foundered – allowing ascent of magma up its periphery – are products of cauldron subsidence, as in Glencoe where ring fractures clearly correlate with the structural margin of a surface caldera.
- Crystallization of granitoid melts may lead to a wide variety of distinctive textures, many attributable to subtle interplay between nucleation and crystal-growth rates.
- Variations in the geochemistry and mineralogy of granitoids support classifications that correlate with supposed source region (Box 8.3), with fractionation history and thus with tectonic environment (Fig. 8.19).
- Granite magma genesis involves: (a) intracrustal fractional crystallization of mafic or intermediate, mantle-derived magmas; (b) anatexis or assimilation of old, upper crustal acid rocks recognized by high $(^{87}Sr/^{86}Sr)_0$; and/or (c) re-melting of juvenile mafic to intermediate, mantle-derived rocks underplating the continental crust. Melting of shallow-subducting slab rocks has been proposed for high Sr/Y Archaean TTG (Martin, 1999) and analogous younger tonalitic batholiths, but re-melting of garnetiferous basic rocks underplating the crust offers an equally credible explanation.
- Charnockites and related orthopyroxene-bearing granitoids (Fig. 8.2) have been explained as products of dehydration due to fluxing of CO_2 during high-grade regional metamorphism of granitic intrusive, but there seems to be little doubt that some charnockites – notwithstanding later deformation and recrystallization – are truly magmatic in origin, and indeed may have eruptive equivalents (Kilpatrick and Ellis, 1992).

EXERCISES

8.1 Select appropriate *names* for rocks with the following characteristics:
   (a) Coarse-grained, 40% plagioclase, 28% alkali feldspar, 12% quartz, 8% hornblende, 8% biotite and 4% opaques (modal proportions);
   (b) Medium-grained leucocratic rock made up mainly of plagioclase, alkali feldspar and quartz in more or less equal amounts, with a small amount of biotite and opaques;
   (c) Coarse-grained rock consisting of perthite and quartz (with negligible plagioclase), together with small amounts of arfvedsonite (alkali amphibole).

8.2 Outline the key observations that discriminate between each of the following pairs:
   (a) granite and granodiorite;
   (b) granite and quartz monzonite;
   (c) tonalite and trondhjemite;
   (d) diorite and anorthosite;
   (e) monzonite and mangerite;
   (f) S-type and A-type granites.

8.3 Determine whether each of the analyses in Table 8.4 is peraluminous, metaluminous, or peralkaline. Use the RMM data given in Table 2.3(a).

8.4 Plot the analyses of Table 8.4 in Fig. 8.19.

8.5 Test the effect on Th_N, Nb_N and K_N of contaminating the Etendeka flood basalt in Table 2.4 with 5, 10 and 25 mass % of Sierra Nevada I-type granite in Table 8.4. Plot the results in a primitive mantle-normalized diagram.

Chapter 9

Alkali rocks

Alkali[1] rocks can be defined in various ways, but broadly speaking they form the population of rock compositions situated above the alternative dividing lines X–Y and X–Z in Figs 1.5 and 9.1. The alkali category encompasses a wide spectrum of colour index, from ultramafic to **felsic**. Alkali rocks fall a long way short of subalkali rocks in their overall volume: alkali basalt lava plateaux never match the largest subalkali large igneous provinces (LIPs) in scale, for example, and syenite provinces almost never compare in size with the largest granitic batholiths. In fact, in volume terms alkali rocks constitute no more than 1% of all igneous rocks exposed on the Earth's surface.

The fascination of alkali rocks lies chiefly in their composition and mineralogy:

- SiO_2 deficiency may lead to the crystallization of various feldspathoids (Box 9.1) in place of feldspars;
- familiar mineral families like pyroxenes and amphiboles often appear in alkali rocks in unfamiliar guises, such as the sodic clinopyroxene aegirine–augite which is a pleochroic green mineral in plane-polarized light (PPL) (Box 9.2) that superficially resembles hornblende. The sodic amphibole riebeckite has a distinctive indigo-to-light brown pleochroism (Box 9.4; Plate 9.18);
- the high concentrations of incompatible elements in many alkali magmas may lead – at least in evolved plutonic **peralkaline** rocks – to the occurrence of rare accessory minerals (e.g. Plate 9.21 and 9.22).

The diversity of feldspathoids present in undersaturated rocks unfortunately makes the nomenclature of alkali rocks complex and unnecessarily challenging (Table 9.1). The nomenclature used here involves some judicious simplification. Varietal names and other complexities not discussed here can be looked up in Le Maitre (2002).

Basic and ultrabasic alkali magmas, especially potassic ones, are also of petrological interest because – judging from their content of ultramafic xenoliths – they ascend rapidly from considerable depths in the mantle. Such mantle-derived xenoliths provide an invaluable opportunity to study directly the petrology of the deeper parts of the sub-continental lithospheric mantle (**SCLM**) through which the host magmas have ascended. Kimberlite and lamproite, for example, often contain lherzolite and other mantle-derived xenoliths and xenocrysts – including diamonds – that shed important light on the thermal state and composition of the thick sub-cratonic continental lithosphere.

The term 'acid' is less useful as an expression of magma fractionation for alkali rocks than it is for subalkali rocks. The reason is that, as Fig. 9.1(a) shows, some highly evolved alkali rocks such as phonolite

[1] 'Alkali' is the adjective favoured by IUGS (Le Maitre, 2002). It supersedes 'alkaline' hitherto used in the UK and Europe and 'alkalic' used in North America.

Igneous Rocks and Processes: A Practical Guide, 1st edition. By Robin Gill. Published 2010 by Blackwell Publishing

Box 9.1 Feldspathoid minerals and melilite

Feldspathoids ('foids' for short) are the key minerals that identify silica-undersaturated rocks. Those that occur in igneous rocks (i.e. disregarding scapolite) have compositions that can be thought of as silica-deficient variants of the alkali feldspar series, $NaAlSi_3O_8$–$KAlSi_3O_8$. Their compositions are presented graphically (and their diagnostic optical properties summarized) in the silica-deficient part of the system SiO_2–$NaAlSiO_4$–$KAlSiO_4$ in Fig. 9.1.1.

Nepheline, the sodalite minerals and kalsilite crystallize only from silica-undersaturated melts. The hydrous feldspathoid analcite crystallizes from such melts under relatively high P_{H2O} conditions, but most of the analcite found in igneous rocks has formed as a post-magmatic hydrothermal mineral

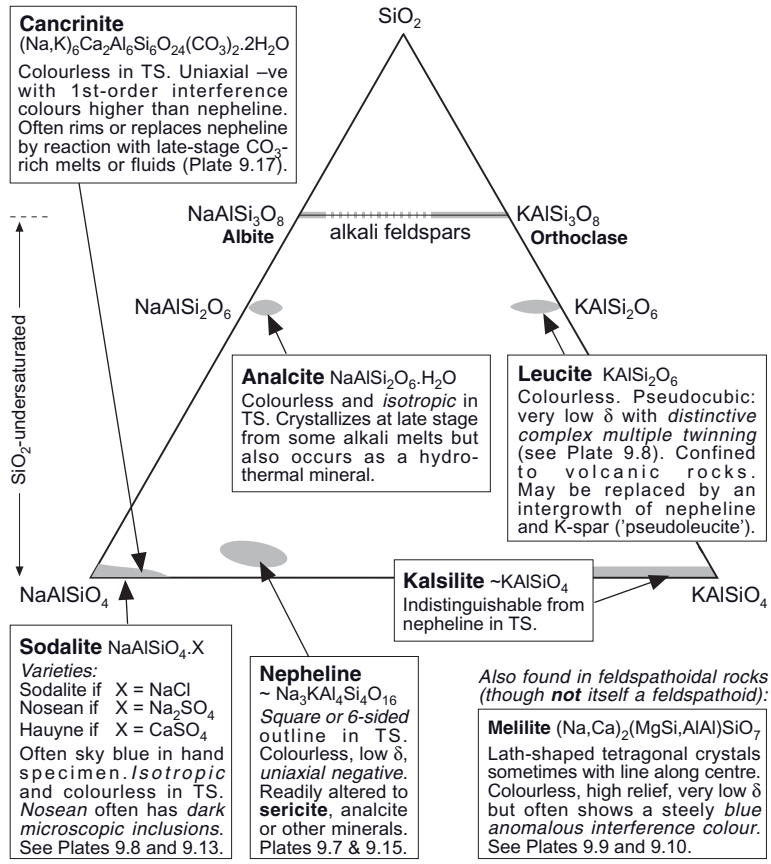


Fig. 9.1.1 How different feldspathoids relate compositionally to each other and to the alkali feldspars (shown in molar proportions). Summary optical data are given for each feldspathoid mineral (and for melilite, a non-foid mineral that stands in for plagioclase in strongly undersaturated rocks). TS, thin section. See Boxes 6.1 and 8.1 for alkali feldspar identification.

actually fall in the 'intermediate' rather than 'acid' range of SiO_2 content. In practical terms, **felsic** (Fig. 1.3) or **salic** are more appropriate descriptors of relative differentiation among alkali rocks.

The petrography and field occurrence of the commoner alkali rocks are summarized below, beginning with volcanic examples and proceeding to their plutonic counterparts.

filling vesicles. Leucite, though itself undersaturated, may crystallize from saturated or oversaturated melts (Fig. 9.7c).

Melilite (not a foid) is another mineral characteristic of strongly SiO_2-deficient igneous rocks (Plates 9.9 and 9.10). It can be thought of as 'standing in' for plagioclase in such rocks.

Nepheline or quartz? **optic sign** as a diagnostic tool

Nepheline is a low-birefringence colourless mineral (Plate 9.7) that in anhedral form could be confused with quartz (Table 9.1.1).

Both are uniaxial low-birefringence minerals. They may be distinguished by their different optic sign as follows:

1 Select a crystal that is orientated to show the *minimum* interference colour for all stage positions (rotate the stage to check).
2 Select the high-power objective and focus carefully; select a clean part of the crystal.
3 With polars crossed, raise the sub-stage assembly and introduce the Bertrand lens.

A dark cross should be seen in a grey field – the interference figure of a uniaxial mineral. Determine the mineral's sign from the colour change on introducing the sensitive-tint (gypsum) plate as summarized in Fig. 9.1.2.

Nepheline's lower birefringence and its susceptibility to alteration provides other clues.

Table 9.1.1 Comparative optical properties of nepheline and quartz.

	Nepheline	Quartz
Body colour (PPL)	colourless	colourless
Relief	low	low
Cleavage	poor	none
Birefringence	0.003–0.005	0.009
Indicatrix	uniaxial	uniaxial
Sign	negative	positive
Alteration	susceptible	unaltered

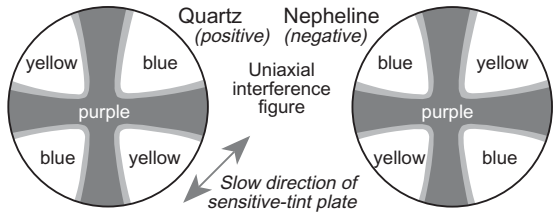


Fig. 9.1.2 Using a uniaxial interference figure (Fig. A3 in Appendix A) to determine optic sign.

THE NOMENCLATURE OF FINE-GRAINED ALKALI ROCKS

Definitions for sodic and mildly potassic rock types

As with subalkali rocks, appropriate names may be attached to sodic alkali rocks in different ways according to the kind of information available:

- A petrologist making *qualitative petrographic observations* of minerals and textures would use Table 9.1.
- When a *chemical analysis* of an unaltered fine-grained rock is available, names may be applied according the International Union of Geological Sciences (IUGS) fields in a total-alkalis versus silica (TAS) plot (Figs. 9.1a and 9.2). **Norm**s calculated

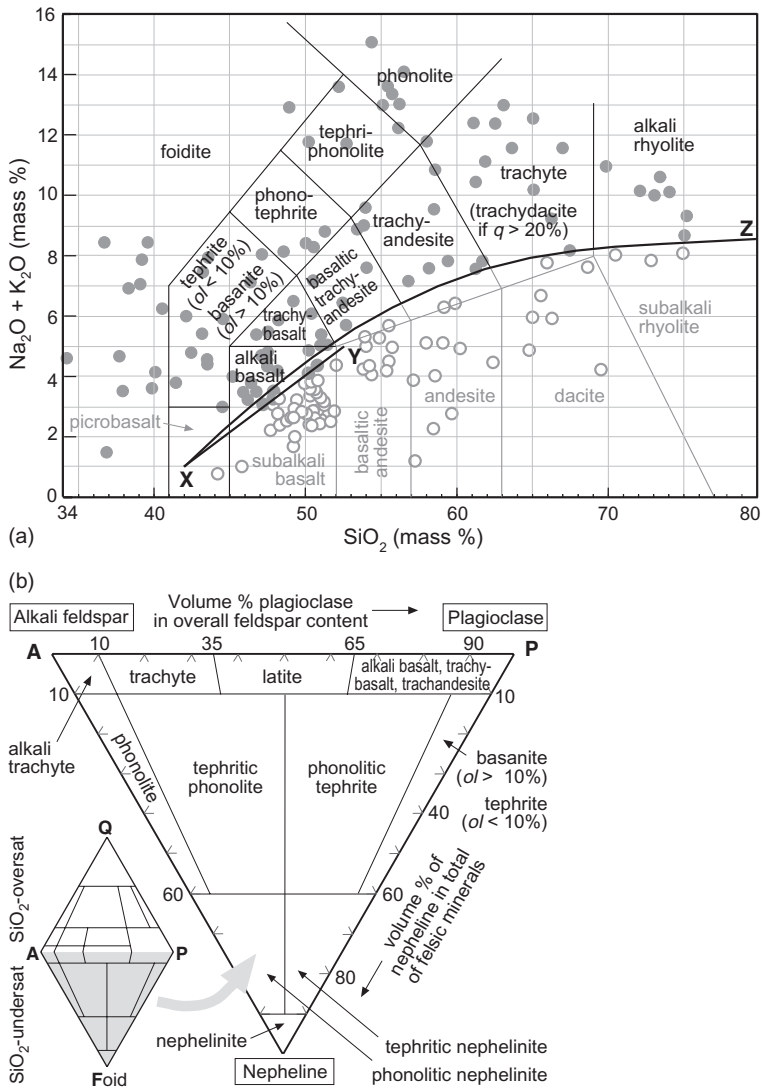


Fig. 9.1 (a) TAS plot showing the compositional fields of fine-grained alkali rocks recognized by the IUGS (Le Maitre, 2002, Fig. 2.14); rock compositions and boundary lines are as in Fig. 1.5 (where the sources are listed). Analyses need to be recalculated volatile-free (Box 1.3) before being plotted in this diagram. '*ol*' refers to normative olivine (Box 2.4); '*q*' represents quartz as a percentage of all felsic minerals in the norm. (b) The undersaturated portion of the QAPF quadrilateral (see inset – the 'Foid' apex represents the total feldspathoids present) showing the nomenclature of fine-grained undersaturated alkali rocks according to modal IUGS definitions (after Le Maitre, 2002). The larger triangle shows the nomenclature used when nepheline is the dominant foid. The modal proportions of nepheline, alkali feldspar and plagioclase need to be scaled up to sum to 100% exclusive of other minerals (see Fig. B1b, Appendix B). IUGS defines 'P' as feldspar with >5% An and 'A' as feldspar having <5% An.

from the analysis may also be useful (e.g. in discriminating between basanite and tephrite).

- When a quantitative *mode* is available (from point-counting a thin section – see Chapter 1), more evolved alkali rocks may be named according to the relative proportions of foids, alkali feldspar and plagioclase using the 'QAPF plot' shown in Fig. 9.1b.

Simple definitions of these rock types in words are:

Foidite: family name for fine-grained melanocratic igneous rocks consisting essentially of clinopyroxene + a feldspathoid ('**foid**'). This generic term embraces the individual rock types nephelinite (Plate 9.7), leucitite, analcitite and kalsilitite (name reflects the dominant feldspathoid present).

Melilitite: fine-grained melanocratic igneous rock consisting essentially of clinopyroxene + melilite (Fig. 9.1.1 in Box 9.1). See Plate 9.9 and 9.10.

Basanite: a fine-grained melanocratic igneous rock consisting essentially of calcic plagioclase + augite + nepheline + *olivine* (>10%); it differs from alkali basalt by having a higher nepheline content (>5%).

Tephrite: a fine-grained melanocratic igneous rock consisting essentially of calcic plagioclase + augite + nepheline; *olivine*, if present, is only a minor constituent (<10%).

Trachybasalt: a fine-grained, melanocratic to mesocratic igneous rock consisting essen-

Table 9.1 Petrography of some fine-grained alkali rocks.

	Nephelinite*	Basanite	Tephrite	Trachybasalt	Trachyandesite	Trachyte	Phonolite
Essential minerals	• nepheline • cpx	• calcic plag • cpx • foid • olivine (>10%)	• calcic plag • cpx • foid (ol < 10%)	• *calcic* plag • cpx • sanidine or anorthoclase§	• sodic plag • cpx • sanidine or anorthoclase#	• sanidine &/or anorthoclase#	• sanidine or anorthoclase# • nepheline or another foid
Type minerals	• olivine • melilite • leucite	• leucite§ • analcite§	• leucite§ • analcite§	• olivine	• hornblende† • biotite†	• quartz • biotite† • aegirine-augite • riebeckite†	• leucite§ • analcite§ • aegirine • riebeckite†
Colour index	Melanocratic	Melanocratic	Melanocratic	Melanocratic to mesocratic	Mesocratic	Leucocratic	Leucocratic
Textures					Oscillatory zoning common in plagioclase phenocrysts	May be porphyritic. Groundmass commonly shows **trachytic texture**	Often porphyritic. Groundmass may show trachytic texture

* Leucitite, analcitite and melilitite are other feldspar-free rock types defined in an analogous way. The names are somewhat misleading: these are *not* monomineralic rocks consisting simply of nepheline, leucite, etc. (cf. pyroxenite, hornblendite).
§ Here the type mineral specifies *which* essential feldspathoid is present (assumed to be nepheline if not specified).
To distinguish between alkali feldspars and plagioclase under the microscope, see Box 6.1.
† Hydrous mineral present in phenocrysts only.

Box 9.2 Sodic pyroxenes

Pyroxenes that crystallize from alkali-rich magmas have sodic compositions lying outside the range of Mg-Fe–Ca solid solutions found in subalkali rocks (Box 2.1). When monovalent Na^+ substitutes

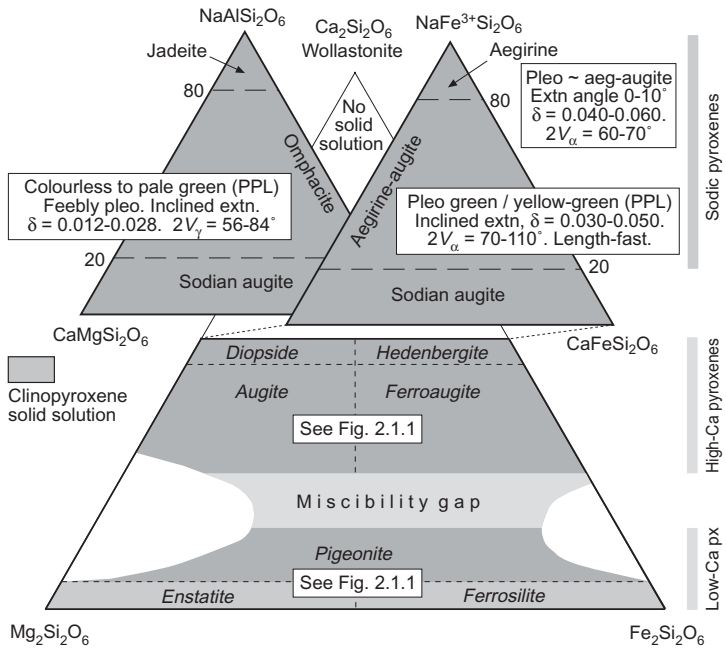


Fig. 9.2.1 How sodic pyroxene solid solutions relate to Ca–Mg–Fe pyroxene end-members (Box 2.1). The right-hand triangle upper shows aegirine–augite and aegirine solid solution characteristic of pyroxenes in many alkali rocks, extending from the $CaMgSi_2O_6$–$CaFe^{2+}Si_2O_6$ join to the end-member $NaFe^{3+}Si_2O_6$. (The left-hand triangle represents NaAl pyroxenes of the high-pressure omphacite–jadeite series found in eclogites.)

tially of *calcic* plagioclase + augite + alkali feldspar. See Plate 9.11.

Trachyandesite: a fine-grained, mesocratic igneous rock consisting essentially of *sodic* plagioclase + alkali feldspar + augite.

Trachyte: a fine-grained igneous rock consisting essentially of alkali feldspar.[2] If quartz is present the rock is called quartz trachyte.

Latite: a fine-grained igneous rock consisting essentially of alkali feldspar + sodic plagioclase in approximately equal proportions.

Phonolite: a fine-grained igneous rock consisting essentially of alkali feldspar + nepheline (and/or other feldspathoids). See Plate 9.5 and 9.8.

These definitions, and the divisions shown in Fig. 9.1, are merely convenient ways of dividing up a continuum of rock compositions.

Mildly potassic rocks

Trachybasalt and trachyandesite are sometimes subdivided into two series according to the value of Na_2O–K_2O in mass % (Fig. 9.2):

[2] Groundmass feldspar laths may be aligned in a swirly pattern, known as **trachytic texture** (Plate 9.12).

Table 9.2.1 Optical distinction between augite, aegirine–augite and aegirine.

	Augite $Ca(Mg,Fe^{2+})Si_2O_6$	*Aegirine-augite* $(Na,Ca)(Fe^{3+},Fe^{2+},Mg)Si_2O_6$	*Aegirine* $NaFe^{3+}Si_2O_6$
Birefringence	0.018–0.033	0.030–0.050	0.040–0.060
Body colour and pleochroism	Colourless to beige:* weakly pleochroic*	Strongly pleochroic: green including yellow-green tinges	Strongly pleochroic: green often including emerald green

* Except for titanian augite (Fig. 2.1) which has a distinctive pale purple-brownish pleochroism.

for one of the divalent ions Mg^{2+}, Fe^{2+} or Ca^{2+} in pyroxene, charge balance is preserved through coupled substitution of a trivalent ion (Fe^{3+} or Al^{3+}) for a neighbouring divalent ion. The sodic pyroxenes found in alkali rocks involve the substitution of $[Na^{+}Fe^{3+}]$ for $[(Mg,Fe)^{2+}Ca^{2+}]$, giving rise to aegirine and the aegirine–augite solid solution series as shown in Fig. 9.2.1 below. Both exhibit a distinctive pleochroism in shades of green.

Green pleochroic aegirine–augite could be mistaken for hornblende. These two minerals are distinguished by a simple test based on the fact that alkali pyroxenes are length-fast: waves vibrating parallel to the crystal length experience the lowest refractive index. The stage is rotated so that the length of the crystal in question runs NE to SW. Note the interference colour in the thinner parts of the crystal. Now insert the sensitive-tint plate (usually itself length-slow):

- If the resulting interference colour is *increased* (giving second- or higher-order colours) the crystal is length-slow (hornblende).
- If the new interference colour is *lower* than that of the crystal on its own, the crystal is length-fast (sodic pyroxene).

Aegirine and aegirine–augite are distinguishable from other clinopyroxenes by their strong greenish body colour and pleochroism, and higher birefringence (Table 9.2.1). Distinguishing *between* aegirine and aegirine–augite is less easy because their pleochroic schemes differ only subtly; aegirine has the highest birefringence (Table 9.2.1) though strong body colour makes this difficult to estimate.

- if $Na_2O–K_2O > 2.0$ mass %, the rock is *sodic* and belongs to the hawaiite-mugearite-benmoreite-trachyte series characteristic of intraplate (Hawai`i) and constructive margin (e.g. Hebrides[3]) environments.
- a trachyandesite for which $Na_2O–K_2O < 2.0$ mass % belongs to the *mildly potassic* shoshonite–latite series characteristic of some island-arc and collisional environments.

Potassic and ultrapotassic rocks

There is an important – though volumetrically subordinate – division of mafic and ultramafic alkali rocks in which K_2O exceeds Na_2O. The adjectives use to describe such rocks are:

Potassic: when K_2O mass % > Na_2O mass %.
Ultrapotassic: when K_2O mass % > $2 \times Na_2O$ mass %.[4]

The K-rich chemical character is expressed mineralogically in the appearance of sanidine ($KAlSi_3O_8$) in silica-saturated rocks, or of the potassic feldspathoids leucite ($KAlSi_2O_6$) and/or kalsilite ($KAlSiO_4$ – see Box 9.1) in silica-undersaturated rocks, often accompanied by

[3] Mugeary in Skye and Ben More in Mull are type localities (both in Scotland).

[4] This is the definition adopted by Foley et al. (1987); other authors place the threshold at $K_2O/Na_2O > 2.5$ or >3.0.

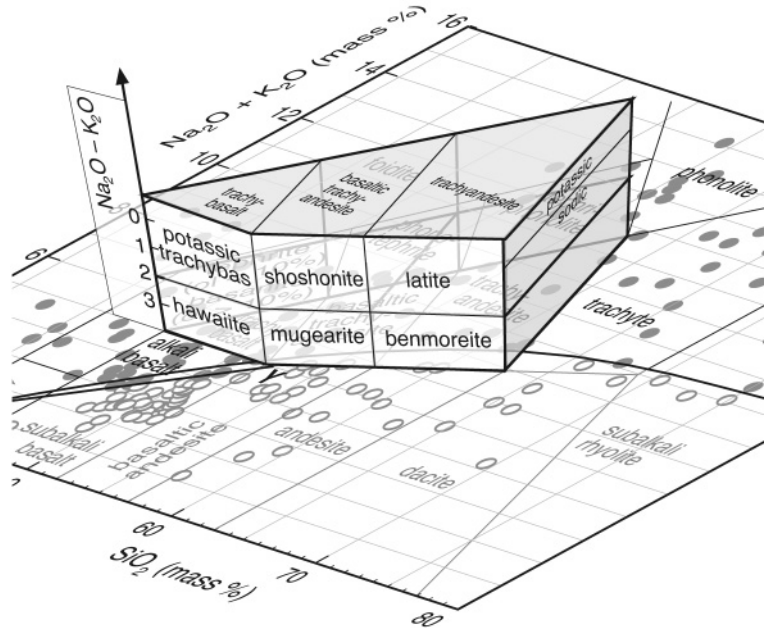


Fig. 9.2 Perspective view of the TAS diagram for alkali rocks (Fig. 9.1) showing how trachybasalts and trachyandesites are divided into shoshonite–latite (mildly potassic) and hawaiite-mugearite–benmoreite (sodic) series, according to whether Na_2O–K_2O (mass %) is numerically less or greater than 2.0. NB: compositions are described as 'potassic' only when $K_2O > Na_2O$, i.e. when Na_2O–$K_2O < 0$ (Table 9.2).

K-rich mafic minerals such as phlogopite mica or K-richterite (Box 9.4).

Leucitite and kalsilitite are foidites that comply with the definition given above. The other members of the potassic family – kimberlite, kamafugite and lamproite – are less straightforward to define and are described in Boxes 9.7 and 9.8.

Starting afresh, unencumbered by historical legacy, one could undoubtedly devise a simpler nomenclature for alkali rocks than the one described above. The IUGS scheme described here is the best rationalization of an arcane terminology that developed piecemeal over more than a century (some names – such as tephrite – even date from classical times).

Alkalinity and K_2O/Na_2O among fine-grained mafic and ultramafic rocks

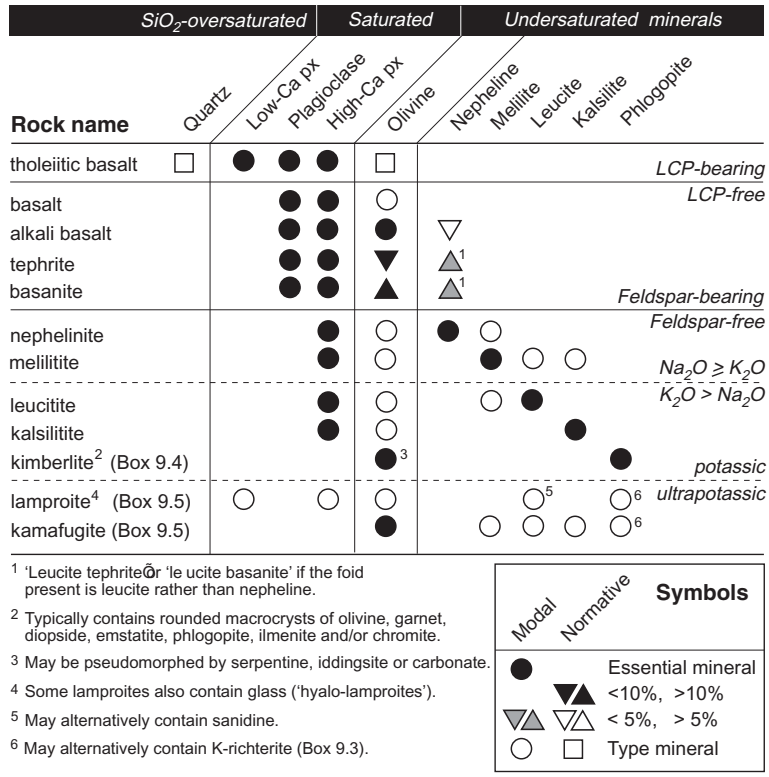
The logic behind alkali rock nomenclature may be easier to understand by looking at Table 9.2, which shows how the *mafic* and *ultramafic* alkali rocks can be laid out systematically according to petrography and major-element composition. Subalkali or tholeiitic basalts, characterized by the presence of low-Ca pyroxene (in mode or norm – see key), appear at the top of the table. With an increase in alkali content (and decrease in SiO_2 content), low-Ca pyroxene (**LCP**) disappears and its place may be taken by olivine (olivine basalt). When small amounts of nepheline appear in the norm as well, the rock is called an alkali basalt, but if significant nepheline is visible in thin section the rock is called a tephrite or a basanite, according to how much olivine is present. Further increasing the alkali content and reducing the silica content makes the composition so undersaturated that feldspars no longer form, leading to feldspar-free rocks such as nephelinite or melilitite.

The lower half of Table 9.2 shows the key mineralogy of potassic and ultrapotassic rocks (Boxes 9.7 and 9.8).

Associated rock types

Perhaps the most remarkable rock type associated with alkali rocks is *carbonatite*, an igneous

Table 9.2 Grid summarizing the key mineralogy (minerals divided into SiO_2-oversaturated, -saturated and -undersaturated categories from left to right) of fine-grained mafic and ultramafic rock types. Rock-types become progressively more alkali and potassic from top downwards: solid dividing lines mark where rocks (a) lose low-Ca pyroxene and (b) become feldspar-free; dashed lines delineate progressively more potassic character. The grid simplifies a complex and evolving field of igneous nomenclature.



rock consisting essentially of carbonate minerals which, according to textural evidence (euhedral carbonate phenocrysts – as in Plate 9.4 – or the presence of vesicles in the rock, for example), have crystallized directly from a carbonate-dominated melt. Carbonatites may take intrusive, effusive or pyroclastic forms. The definition and mineralogical make-up of carbonatites are discussed in Box 9.3.

Lamprophyre dykes (Box 9.6) are also associated with a number of alkali complexes.

ERUPTIVE PROCESSES AND VOLCANIC FORMS

Most alkali magmas erupt in ways similar to their subalkali analogues, which have been outlined in Chapters 2, 6 and 7. Alkali basalts and basanites, for example, erupt to form lava flows or cinder cones indistinguishable in physical form to those associated with tholeiitic basalt eruptions. Intraplate **peralkaline** rhyolites and phonolites may erupt in explosive plinian style similar to subduction-related dacite magma, or – when degassed – may form lava domes and coulées (Fig. 9.10) similar in appearance to the rhyolite dome of Glass Mountain (Medicine Lake, California – see Fig. 6.3e). Rather than revisit information covered elsewhere in the book, the present section concentrates on examples where the eruptive style of certain alkali melts diverges significantly from the behaviour of subalkali magmas.

The eruption of foidite magmas – the lesson of Nyiragongo 2002

> *'On 17 January 2002 several lava flows originated along a 10 km fissure system* [extending] *from the summit area of Mount Nyiragongo (3649 m a.s.l.) to the suburbs of Goma town. … At 08.30 local time the pre-existing North Shaheru fissure (2600–2800 m a.s.l.) generated a "curtain of fire", and, in the following hours, the fissure system propagated southward, reaching the outskirts of Goma (1550 m a.s.l.) at about 16.00. Two large lava flows erupted from different vents entered the town, one of them reaching Lake Kivu at night. By that time, approximately 15% of the town was covered by lava, one third of the airport runway was destroyed, and about 120 000 people found themselves homeless.'*
>
> (from Giordano et al., 2007)

Mount Nyiragongo is a **stratovolcano** forming part of the Virunga Volcanic Chain that runs NE–SW across the western branch of the East African rift, from the Democratic Republic of Congo into Rwanda (Fig. 9.3). Mt Nyiragongo is known both for the longevity of its lava lake (which was active for 50 years prior to 1977) and for the extreme fluidity of its melilite leucite nephelinite lavas. The rapidly moving flows of Nyiragongo's previous major eruption, in 1977, had devastated a number of villages located close to the fissure zone, but had stopped 2 km short of the town of Goma on the north shore of Lake Kivu, about 20 km to the south of the volcano, without serious threat to its 20,000 inhabitants. In 2002, however, lava erupted from a number of vents along the N–S fissure. That issuing from near-summit vents was observed to flow at speeds of several tens of km h^{-1}. The low viscosity which this implies is confirmed by the form of the solidified lava, preserved today as proximal pahoehoe flows no more than 5–15 cm thick. It was fortunate, however, that the lava erupting from vents nearer to Goma flowed at slower speeds, estimated at between 0.1 and 1.0 km h^{-1}.

Modelling suggests that the lava issuing from the higher sections of the fissure system emerged at a temperature of about 1370 °C (significantly above its liquidus temperature) and with a viscosity in the region of 60 Pa s, virtually the lowest ever measured for any natural silicate magma (Giordano et al., 2007). This extreme fluidity points to an exceptionally low degree of polymerization (Box 6.3) in silica-poor melts such as these (see Table 9.5 for analysis), and its fluidity was doubtless promoted by the absence of crystals in the **superheated** melt. Had this very hot lava issued from fissure sectors closer to Goma, the inundation of the town and the death toll would have been much more severe. The lava erupting from vents closer to Goma, however, had already cooled to around 1320 °C during southward fissure-propagation in the weeks or months preceding the eruption. Its lower temperature and greater crystal content raised the lava's apparent viscosity, resulting in lower flow velocities and less devastation of the town. The thicker flow units (>2 m), their a'a surfaces and a greater abundance of scoria testify to the greater viscosity of these cooler, locally derived lavas.

The oft-quoted maxim that 'lava flows constitute a hazard to property but not to life' (since they generally advance at speeds slow enough to allow escape on foot) evidently cannot be relied upon for alkali-rich ultrabasic magmas like those of Nyiragongo. In the event the death toll in 2002 was limited to about 60 (most caused by the explosion of a fuel tank) but could have been a lot higher had serendipity not directed the hotter, more highly mobile lava to erupt from higher vents, distant from the centre of population.

Eruption of carbonatite – the unique case of Oldoinyo Lengai

> *'The vent* [was] *filled with heaving black liquid and was surrounded by an asymmetric cone. Another small flow took place from the breach in the western flank of the vent-cone. … The new lava was again a black lava and even when semi-liquid it showed no sign of the red-hot glow as has been described from other* [silicate] *lava flows. … A noticeable feature of the flows was that, although they were jet-black when first extruded, the lava started to turn white within 24 hours.*
> (from Dawson, 1962)

For the past 15,000 years, the imposing cone of Oldoinyo Lengai has towered 2200 m above the southern shores of Lake Natron in the Gregory rift valley (Fig. 9.3), periodically ejecting nephelinite and carbonatite tephra.

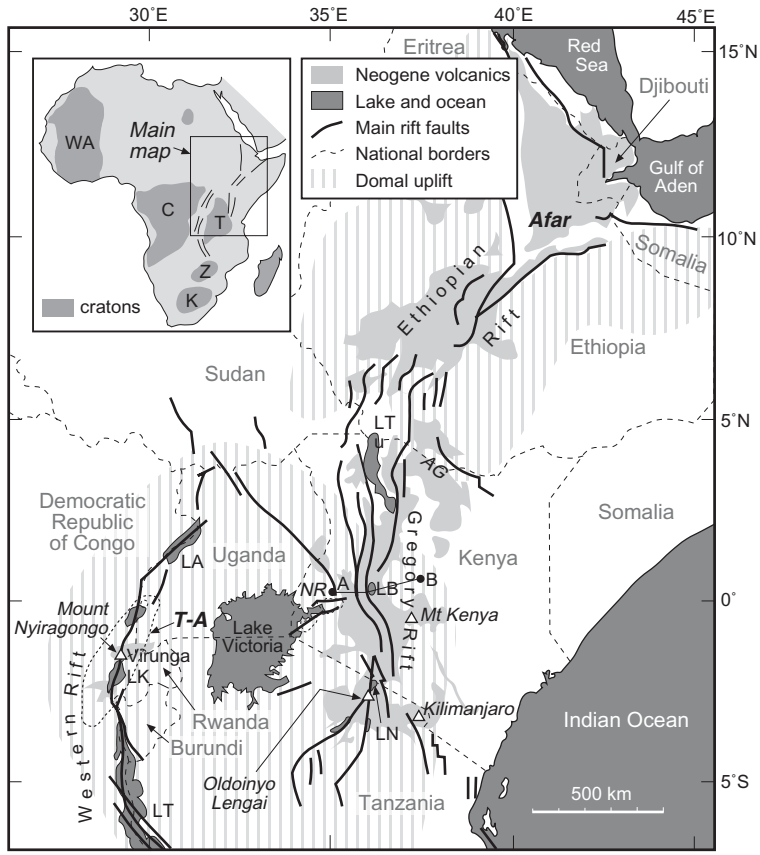


Fig. 9.3 Map of the East African rift system showing the eastern (Gregory), western and Ethiopian rifts. Thick black lines show the main extensional faults, light grey areas indicate the extent of Neogene rift-related volcanics (both after Chorowicz, 2005 with permission from Elsevier), and feint vertical ruling indicates the extent of domal uplift above 1200 m (the Ethiopian and East African Plateaux). ***T-A*** = Toro Ankole volcanic province. Subsidiary rift and graben: *AG*, Anza Graben; *NR*, Nyanza Rift (formerly 'Kavirondo Rift'). Rift lakes: LA, Lake Albert; LB, Lake Baringo; LK, Lake Kivu; LN, Lake Natron; LT, Lake Tanganyika; LTu, Lake Turkana. The thin black line A–B west of Mt Kenya shows the location of the gravity traverse represented in Fig. 9.14. The inset map shows how the rift system relates to the main cratons of Africa: C, Congo; K, Kaapvaal; T, Tanzanian; WA, West African; Z, Zimbabwean.

The current edifice is the product of two main cone-building phases, the first phonolitic in composition and the later one consisting chiefly of nephelinite (Klaudius and Keller, 2006). Oldoinyo Lengai first captured worldwide attention in the 1960s when Dawson (1962) published the first report in an international journal of active carbonatite volcanism there; it remains the only volcano in the world where carbonatite eruptions have been observed in progress. Effusions of remarkably fluid natrocarbonatite lava on the floor of the summit crater occurred continuously between 1983 and 2007 and were exhaustively photographed during frequent visits (see Plates 9.19 and 9.20, and www.mtsu.edu/~fbelton/lengai.html).

The 2950 m-high Oldoinyo Lengai crater has a bizarre, other-worldly appearance. Steep-sided natrocarbonatite spatter cones loom over the crater floor like shrouded monks, issuing thin flows of black vesicular lava on to the surrounding white crater floor (Plate 9.19), or ejecting strombolian showers of bombs, lapilli and ash tens of metres into the air. The cones are ephemeral and the

Box 9.3 What are carbonatites?

Carbonatite is an igneous rock consisting essentially of carbonate minerals. That carbonate rocks could have a magmatic origin was initially disputed by influential petrologists of the early 20th century such as Shand, Daly and Johannsen, but the existence of carbonatite magmas is now beyond doubt. Primary carbonate minerals found in carbonatites include calcite, dolomite, siderite, ankerite and – uniquely at Oldoinyo Lengai and nearby vents – sodium carbonate minerals such as nyerereite.

The proportions of carbonate and silicate minerals present in a carbonatite body – especially a plutonic one – often vary considerably in the field, even over short distances, and the precise definition of 'carbonatite' is therefore contentious. The IUGS definition (Le Maitre, 2002) embraces plutonic and volcanic rocks that contain more than 50 modal % of primary magmatic carbonate minerals. Recognizing, however, that a homogeneous carbonatite melt may at depth crystallize cumulate rocks with a range of individual carbonate:silicate ratios, Mitchell (2005) advocated relaxing this definition of carbonatite *sensu lato* to include any rock with more than 30 modal % of igneous carbonate minerals, adding type-mineral qualifiers as appropriate (e.g. phlogopite dolomite carbonatite).

Among carbonatites so defined, Mitchell (2005) draws a distinction between:

1. Primary magmatic carbonatites (*sensu stricto*), chiefly associated with nephelinite, melilitite or their (feldspar-free) plutonic equivalents: examples occur at Tororo and Napak in Uganda, Shombole and Kizingiri in Kenya, and analogous plutonic complexes at Fen in Norway and Oka in Quebec.
2. A diverse suite of other carbonate-rich igneous rocks – often enriched in Ba, Sr and REE minerals – that are associated with evolved plutonic rocks such as syenites (Fig. 9.4) leading some to suggest they may be residual products of advanced fractional crystallization.

In most instances, carbonatite is preserved as a high-level, intrusive body (Fig. 9.6) or as a **diatreme** (Box 9.7) in a subvolcanic alkali ring complex (e.g. Polino in Italy), but more than 50 examples of extrusive carbonatite are also known, taking the form of tuff-rings, lavas, pyroclastics and stratocones (Woolley and Church, 2005). Indeed there is evidence (Bailey et al., 2005; 2006) that carbonatite volcanism may be much commoner than hitherto recognized, tuffaceous carbonatite breccias having in the past been misidentified as being sediment-hosted. Some carbonatite diatremes and pyroclastics – belonging to category (1) above – contain mantle xenoliths, testifying to derivation and rapid ascent from mantle depths. Indeed a few mantle xenoliths have been found to contain carbonate glasses (quenched melts) which may represent carbonatite in the making.

The only carbonatite volcano known to be currently active – Oldoinyo Lengai in Tanzania – erupts lavas (Fig. 9.5) and tephra of *natrocarbonatite*, in which the main primary carbonate minerals are nyerereite [ideal formula $Na_2Ca(CO_3)_2$] and gregoryite [ideal formula Na_2CO_3].

Carbonatite magmatism is primarily an intraplate igneous phenomenon, though rare carbonatites have been reported from orogenic zones, such as Pakistan, where they have been emplaced along Himalayan thrust belts (Tilton et al., 1998). Carbonatites have been reported from Fuerteventura (Canary Islands), the Cape Verde islands in the central Atlantic, and the Kerguelen archipelago in the Southern Ocean (Woolley and Church, 2005), but these are the only instances known in the ocean basins.

Carbonatites furnish economic concentrations of rare minerals and metals, such as REE minerals at Mountain Pass in California. 99% of the world's niobium (Fig. 2.7.2) comes from pyrochlore [$(Ca,Na)_2Nb_2O_6(OH,F)$] extracted from carbonatite complexes in Brazil and Canada.

appearance of the crater can change markedly from year to year.

Natrocarbonatite lava erupts at a temperature of about 590 °C (Norton and Pinkerton, 1997), sufficiently hot to glow red in the dark but – unlike fast-flowing basaltic lavas (Plate 2.6) – the glow is too feeble to be visible in daylight. By comparison with silicate melts it has extremely low viscosity (about 1–5 Pa s, even less viscous than Nyiragongo nephelinite) and typically forms pahoehoe flows a few centimetres thick, sometimes with markedly ropy surfaces. Nonetheless a substantial flow with an a'a surface formed in July 2000. Freshly erupted natrocarbonatite lava is black in colour (Plate 9.19), and contains phenocrysts of nyerereite [ideal formula $Na_2Ca(CO_3)_2$] and gregoryite [ideal formula Na_2CO_3] in a groundmass of fluorite (CaF_2) and sylvite (KCl) with traces of magnetite, apatite and sulphides. On exposure to the air, the water-soluble alkali carbonate minerals are rapidly altered to white hydrated variants such as pirssonite [$Na_2Ca(CO_3)_2.2H_2O$] and gaylussite [$Na_2Ca(CO_3)_2.5H_2O$] as illustrated in Plate 9.4. As a result, the fresh black lava goes white in a matter of hours or days (Plate 9.20), a transition elegantly recorded in Fig. 2(a) of Zaitsev and Keller (2006); the transformation takes even less time when rain is falling.

An explosive eruption in early September 2007, big enough for the ash cloud to be visible on satellite imagery and to deposit ash on the village of Ngare Sero (18 km to the north) for a period of 12 hours, may have concluded the period of quiet effusive natrocarbonatite activity that has characterized Oldoinyo Lengai since 1983. The volcano now erupts ash of extremely undersaturated hybrid composition (Mitchell and Dawson, 2007).

NOMENCLATURE OF COARSE-GRAINED ALKALI ROCKS

The nomenclature for coarse-grained alkali rocks is far from straightforward. Traditional nomenclature is cluttered with geographically derived varietal names, while the IUGS rationalization – though more systematic – seems unduly challenging for the novice through its introduction of forbidding new names like 'foid monzodiorite'. The nomenclature used here involves some simplification.

How names are allocated to coarse-grained alkali rocks depends on the information available:

- A petrologist making *qualitative petrographic observations* of minerals and textures would use a scheme such as Table 9.3.
- If a *quantitative* ***mode*** is available, IUGS assigns names according to the relative proportions of alkali feldspar and plagioclase using the QAPF plot shown in Fig. 9.4.[5] As noted in relation to Fig. 8.1, diorite falls in the same field as gabbro in this diagram, and the distinction between them is based on plagioclase composition – calcic (An>50) for gabbro, sodic for diorite.

In order to keep names as succinct as possible, established varietal names are used here where possible (e.g. 'essexite' in place of 'nepheline monzogabbro' in Fig. 9.4).

Simple definitions for the commonest coarse-grained alkali rock types, expressed in words, are given below. The range of colour index applicable to each root name (after Le Maitre, 2002, Fig. 2.8) is given in square brackets.

Ijolite: a coarse-grained, mesocratic igneous rock consisting essentially of nepheline + clinopyroxene [$30 < M < 70$]. (Cf. nephelinite).

Theralite: a coarse-grained melanocratic rock consisting essentially of calcic plagioclase + augite + nepheline [$35 < M < 65$]; i.e. gabbro containing essential nepheline.

Essexite: a coarse-grained, melanocratic igneous rock consisting essentially of calcic plagioclase + clinopyroxene + nepheline + alkali feldspar [$20 < M < 60$].

Monzonite:[6] a coarse-grained, leucocratic or mesocratic igneous rock consisting essen-

[5] The dividing lines in Fig. 9.4 are arbitrary boundaries for dividing up a continuum of plutonic rock compositions; they do not imply any compositional breaks between natural rock populations.

[6] The variety *larvikite*, widely used as a decorative facing stone on shop-fronts in Britain on account of the distinctive sheen of its 'schiller' feldspars, is probably the most familiar example of monzonite to European readers.

Table 9.3 Petrography of some coarse-grained alkali rocks.

	Ijolite[*]	Theralite	Essexite	Monzonite	Syenite	Nepheline syenite
Essential minerals	• nepheline • clinopyroxene[¶]	• calcic plag • augite[§] • nepheline	• calcic plag • augite[§] • nepheline • alkali feldspar *plag > alk fsp*[$]	• sodic plag • alkali feldspar *plag ~ alk fsp*[$]	• alkali feldspar • sodic plag *alk fsp > plag*[$]	• alkali feldspar • nepheline *alk fsp > plag*[$]
Type minerals	• olivine • melilite • phlogopite • garnet[#]	• olivine	• olivine	• quartz • augite • hornblende	• quartz • olivine (Fa) • augite or aegirine-augite[‡] • hornblende or sodic amphibole[‡] • biotite[‡]	• analcite • aegirine-augite[‡] • riebeckite or other sodic amphibole[‡]
Common accessory minerals (other than opaques)	sphene, apatite perovskite wollastonite	biotite hornblende or kaersutite apatite		May be foid-bearing. sphene, apatite, zircon[‡]		eudialyte[‡], astrophyllite[‡] zircon[‡], sphene, apatite
Colour index	Mesocratic*	Melanocratic	Melanocratic to mesocratic	Mesocratic to leucocratic	Leucocratic	Leucocratic
Systematic IUGS name	Nepheline foidolite	Nepheline gabbro	Nepheline monzogabbro (nepheline monzodiorite if plag is sodic)			
Alteration	Nepheline is frequently altered to sericite (Plate 9.14), analcite, cancrinite or zeolite.					

* The melanocratic variant is called 'melteigite', and the leucocratic variant is called 'urtite' (Fig. 9.5).
[¶] The pyroxene may be sodian augite, aegirine-augite or aegirine (Fig. 9.2.1) and it is often strongly zoned.
[§] The augite present is typically *titanian augite* with a pleochroic lilac tinge in PPL (Boxes 2.1 and 2.5).
[$] See Box 8.1 for the practical distinction between alkali feldspar and plagioclase in plutonic rocks under the microscope. **Perthite**, when present, is included with alkali feldspar (**antiperthite** is counted as plagioclase).
[‡] As a rule, aegirine-augite, sodic amphibole, eudialyte & astrophyllite crystallize from melts of **peralkaline** composition. Augite, hornblende, biotite & zircon crystallize from **metaluminous** melts.
[#] The garnet occasionally found in foidolites is the *melanite* variety of andradite (see Box 5.2).

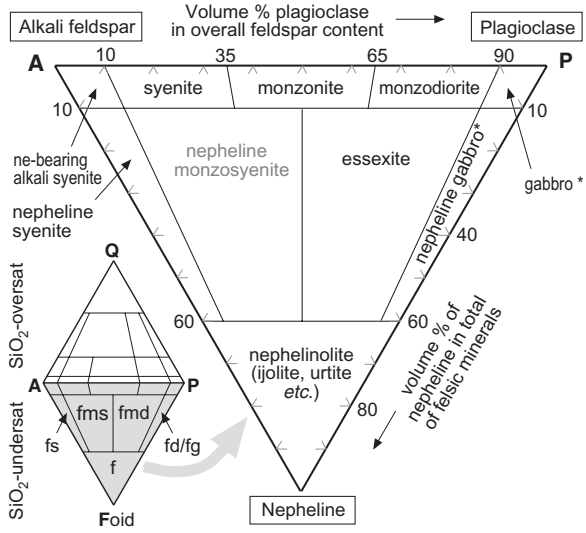


Fig. 9.4 The cartoon shows the generalized IUGS nomenclature for coarse-grained alkali rocks, based in the undersaturated portion of the QAPF quadrilateral (f, foidolite; fmd, foid monzodiorite; fg, foid gabbro; fms, foid monzosyenite; g, gabbro; m, monzonite; md, monzodiorite; s, syenite). The main figure shows the modal nomenclature applied to rocks in which *nepheline* is the dominant foid. Rocks such as monzodiorite and syenite with less than 10% foid may be described as 'foid-bearing' or 'nepheline-bearing'. For plotting in these diagrams, the modal proportions of nepheline, alkali feldspar and plagioclase are scaled up to sum to 100% exclusive of other minerals (see Fig. B1b, Appendix B). IUGS defines 'P' as feldspar with >5% An and 'A' as feldspar having <5% An. The optical distinction between plagioclase and alkali feldspars in plutonic rocks is summarized in Box 8.1.

*When the mean plagioclase composition is sodic (An < 50) 'diorite' is used in place of 'gabbro'.

tially of sodic plagioclase + potassium feldspar[7] in roughly equal proportions, together with mafic minerals [15 < *M* < 45]. (Cf. latite)

Syenite: a coarse-grained, leucocratic igneous rock consisting essentially of alkali feldspars [10 < *M* < 35]. (Cf. trachyte)

Nepheline syenite: a coarse-grained, leucocratic igneous rock consisting essentially of alkali feldspars + nepheline [*M* < 30]. (Cf. phonolite)

[7] Including **perthite**.

Sövite: Coarse-grained calcite-rich carbonatite.

The mafic minerals present in more evolved rock types like syenite (fayalitic olivine, sodic pyroxene, sodic amphibole, biotite) serve as type-minerals highlighting differences in magma composition: the sodic pyroxene aegirine–augite (Box 9.2) and the sodic amphibole riebeckite (Box 9.4) crystallize from peralkaline melts, whereas biotite is more characteristic of metaluminous syenites. For reasons discussed in Chapter 6 and 8, amphiboles are more prevalent in plutonic rocks than volcanic ones (where they occur only as phenocrysts).

As with other plutonic rocks where mineral proportions are sensitive to cumulus processes, the prefix 'leuco' may be attached to a rock name to signify an atypical leucocratic specimen (one whose colour index *M* falls *below* the range indicated after each root-name above). Adding the prefix 'mela', on the other hand, denotes a rock with a *higher*-than-usual colour index (*above* the range given beside each rock name above).

Unfortunately specific names are sometimes used in place of these prefixes for rocks with the same essential mineralogy but differing mineral proportions. Thus the leucocratic variant of ijolite is known as *urtite*, whereas a the melanocratic variant is called *melteigite*. A nepheline syenite particularly rich in aegirine–augite is called either *malignite* if mesocratic, or *shonkinite* if melanocratic (Fig. 9.5).

These names apply to coarse-grained alkali rocks. As in Chapter 4 and 8, the prefix 'micro' may be used to denote analogous medium-grained rocks: e.g. 'microsyenite' signifies a rock of syenite mineralogy and composition which happens to be medium- rather than coarse-grained. Medium-grained sövite is sometimes called *alvikite*.

INTRUSIVE FORMS AND PROCESSES IN ALKALI PLUTONS

Diatreme-hypabyssal systems

Highly alkaline tuff-ring volcanoes are typically underlain by **diatremes** and, beneath them, by dykes and sills. This high-level intrusive architecture is illustrated in Fig. 9.7.1 (Box 9.7).

Box 9.4 Sodic amphiboles

The amphiboles characteristic of alkali-rich igneous rocks, like pyroxenes, have sodic compositions quite distinct from the hornblendes found in subalkali rocks. Solid solution in the amphibole family can be understood by reference to the general formula $A\ B_2\ C_5\ T_8\ O_{22}\ (OH)_2$, where A, B, C and T represent cation sites of different sizes in the crystal structure (which therefore accommodate different cations):

- A is a large site that may accommodate Na^+ or K^+ or may be partially or completely vacant (a vacant A-site is represented by '□' as in the riebeckite formula in Fig. 9.4.1).
- B sites are relatively large octahedral sites accommodating Na^+, Ca^{2+}, Mg^{2+} or Fe^{2+}.
- C sites are smaller octahedral sites accommodating Mg^{2+}, Fe^{2+}, Al^{3+} and/or Ti^{4+}.
- T sites are tetrahedral sites accommodating Si^{4+} (and also a proportion of Al^{3+} in some amphiboles).

The amounts of each ion present in each site are determined by routine calculation from the major-element analysis of the crystal of interest, in a manner analogous to the formula calculation for olivine shown in Table 1.2.1 in Box 1.2 (see Gill, 1996, Table 8.4 for details of the calculation applied to amphibole).

The International Mineralogical Association (IMA) (1997) subdivides amphiboles into 4 families according to which ions occupy the B site, as shown in Fig. 9.4.1. The hornblendes typical of andesites and granitoids fall in the calcic category. The formulae and optical properties of the distinctive amphiboles found in alkali rocks are summarized in the boxes in Fig. 9.4.1. The characteristic pleochroism of each readily distinguishes them from common hornblende. The beige-to-inky blue pleochroism of riebeckite is illustrated in Plate 9.18.

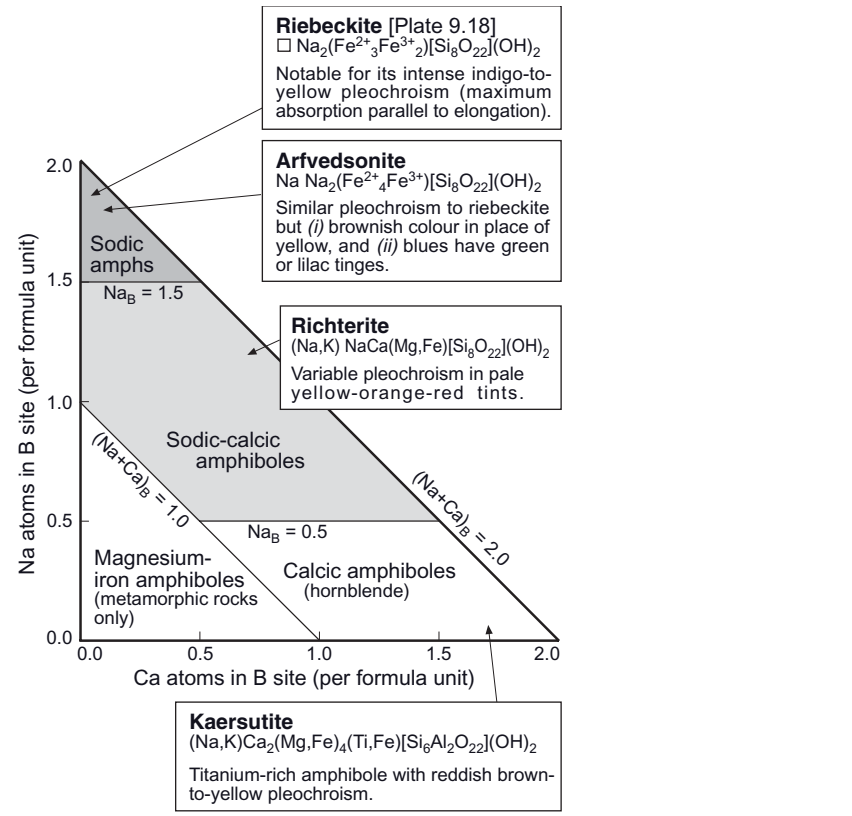


Fig. 9.4.1 Summary of amphibole subdivisions and optical properties of the main amphibole types found in alkali rocks. '□' denotes a vacant A site.

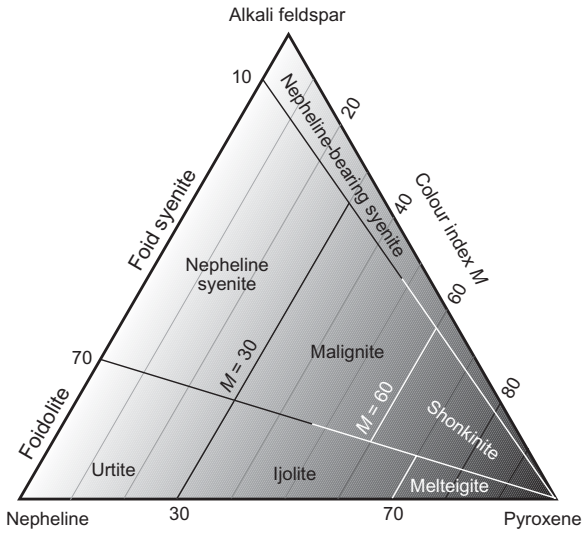


Fig. 9.5 Fields for nepheline syenite, malignite, shonkinite, urtite, ijolite and melteigite in a modal alkali feldspar–nepheline–pyroxene diagram, adapted to comply with current IUGS nomenclature (Le Maitre, 2002, Figs. 2.4 and 2.8) from a similar diagram by Le Bas (1977).

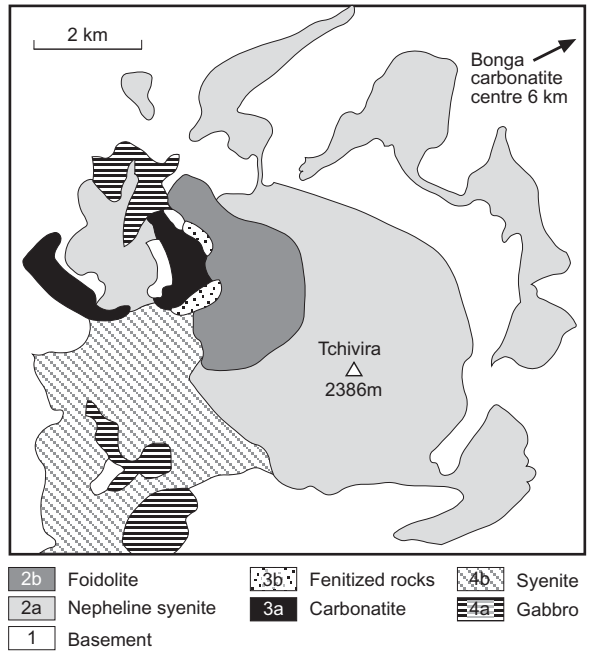


Fig. 9.6 Sketch map of the Cretaceous Tchivira ijolite–nepheline syenite–carbonatite ring complex in Angola, based on a 1973 map by F.E. Lapido-Loureiro (reproduced from Woolley, 2001, courtesy of the Geological Society of London) amended by Coltorti et al. (1993).

Ring intrusions

Figure 9.6 shows a geological sketch map of the Tchivira complex in SW Angola, a *circa* 130 Ma-old ijolite-nepheline syenite-carbonatite *sensu lato* intrusive centre – representing the roots of a Cretaceous nephelinite-phonolite-carbonatite volcano – that forms a prominent mountain rising 1400 m above the surrounding Precambrian basement. The complex exhibits a concentric ring structure so well developed as to be discernible on aerial photographs (Woolley, 2001). Arcuate intrusions of carbonatite (with associated feldspathic breccia) and heterogeneous foidolite (mainly ijolite and urtite) are arranged concentrically about a central body consisting of nepheline syenite, which also forms inner and outer arcuate intrusions to the east (Fig. 9.6). Contrasting compositionally with these silica-undersaturated lithologies are the gabbro and syenite units that have subsequently been emplaced to the north and south of the central nepheline syenite (Coltorti et al., 1993). The complex is cut by numerous basalt, tephrite and phonolite dykes.

Enclosed between the eastern margin of the carbonatite and the foidolite unit, and intimately associated with screens of country rock, are arcuate lenses of coarse-grained syenitic rocks rich in K-feldspar. Contact rocks of this kind – which typically contain metasomatic sodic pyroxenes or amphiboles in addition to K-feldspar, and which appear to have formed by carbonatite-related alkali metasomatism of country rocks – are a feature of many intrusive carbonatite complexes. They are called **fenites** after the Fen carbonatite complex in Telemark, southern Norway, where W.C. Brögger first described such rocks in 1921. Further evidence for the metasomatizing power of carbonatite melts is provided by mineral deposits that may occur within the fenitization haloes of carbonatites, for example the fluorite deposits at Amba Dongar in India (Williams-Jones and Palmer, 2002). Expulsion of alkali-rich aqueous and/or carbonic fluids seems to be

part and parcel of carbonatite ascent, and may in part explain the enigmatic discrepancy between natrocarbonatite erupting today at Oldoinyo Lengai and the relatively alkali-poor compositions of older intrusive carbonatites (Table 9.4).

Similar complexes to Tchivira, of comparable age, occur in a corresponding position on the other side of the Atlantic Ocean, notably the Jacupiranga and Juquiá complexes in SE Brazil. Arcuate intrusions and concentric ring-intrusion architecture are seen in alkali complexes of less extreme composition too, notably the Okenyenya complex discussed in a later section.

Lopoliths

The Lovozero intrusion in the Kola Peninsula of north-western Russia is the largest of the world's peralkaline syenite intrusions, with an outcrop area of about 650,000 km^2. It was emplaced into Archaean granite gneisses in the form of a **lopolith**, with a broad feeder dyke system in the south-western part (Kogarko et al., 1995, 2006). Its shape and scale thus resemble the Peruvian coastal batholith (Figs. 8.7 and 8.16). Rather than being made up of many individual plutons, however, the complex was emplaced in three main plutonic stages, each magma more evolved than the one before (Kogarko et al., 2006). Just as ideas are changing in relation to granite emplacement (Fig. 8.9), it may be that other syenite complexes – previously regarded as having dome-like form – will in due course prove to be tabular in shape.

Igneous layering in alkali intrusions

Igneous modal layering occurs widely in alkali intrusions, from the layered gabbros of the Mesozoic Okenyenya ring intrusion in NW Namibia (Le Roex et al., 1996) and the Cenozoic Lilloise intrusion in East Greenland (Chambers and Brown,1995), to the beautifully exposed layered syenites and nepheline syenites of the Gardar province in S Greenland (Fig. 9.15; Plate 9.21). Layering may be accompanied by other textural attributes of layered gabbros, such as igneous lamination (Plate 9.14).

Table 9.4 Comparison of (a) carbonatite rock from the Kalkfeld complex in Namibia with (b) the composition of a natrocarbonatite melt/fluid estimated from fluid inclusions trapped in associated metaquartzites (from Bühn and Rankin, 1999). The authors conclude that the inclusions represent a late-stage metasomatizing fluid rather than pristine carbonatite melt.

	KF54 sövite (carbonatite, whole rock)	KF113 carbonatite melt/fluid (calculated comp)
mass %oxide		
SiO_2	5.53	
TiO_2	0.32	1.1
Al_2O_3	0.49	
ΣFeO	23.92	4.1
MnO	2.61	0.6
MgO	4.05	1.0
CaO	19.40	16.3
Na_2O	0.13	21.3
K_2O	0.04	7.0
P_2O_5	7.05	
H_2O	0.50	[20]
CO_2	19.20	[20]
F	0.53	0.6
Cl	<0.01	5.0
ppm metal		
Rb	1	1066
Ba	500	3816
Th	53	411
Nb	12000	190
La	3176	3361
Ce	5695	4172
Sr	25000	11467
Nd	1777	1055
Zr	11	
Sm*	225	162
Eu	63	32
Gd*	152	152
Y	435	771
Yb	26	27
Lu	4	2

[ ] = assumed values

The 50 Ma-old Lilloise complex is believed to have formed by crystallization of an alkali picrite parent magma. The lowest 600 m of the cumulate sequence consist of ultramafic olivine–high-Ca pyroxene (**HCP**) cumulates, passing upward into >400 m of alkali gabbro (plag-HCP-olivine) cumulates, which are in turn succeeded by 500 m of hornblende- and

kaersutite-plagioclase cumulates. Modal layering is well developed in the cumulate units, most noticeably in the Middle (gabbro) Zone, where it varies from cm-scale to **macro-rhythmic** layering. Modal layering is accompanied by both phase and cryptic layering. Lilloise therefore has much in common with Skærgaard (Chapter 4). There are, however, obvious differences in mineralogy (the absence of LCP and the presence of hornblende and kaersutite). Moreover, unlike the undisturbed Skærgaard intrusion, Lilloise experienced extensive post-deposition deformation related – according to Chambers and Brown (1995) – to 'piston-like subsidence' of the intrusion, which has markedly disturbed the layering both at the margins and in the interior; near vertical modal layering is not uncommon here.

Like the Lovozero intrusion mentioned above, several syenite plutons of the Gardar province in SW Greenland (Fig. 9.15) exhibit modal layering, of which the Ilímaussaq complex is visually – and in mineralogical terms – the most spectacular. The lowest exposed part of this intrusion consists of evolved floor cumulates that crystallized at temperatures in the 700–800 °C range. The exposed cumulates consist of a series of 29 macro-rhythmic layers, each enriched in black arfvedsonite at the base, pink to brownish-red eudialyte[8] in the middle, and – much the thickest – white nepheline + alkali feldspar at the top, forming a layered sequence 280 m thick (Plate 9.21) that is laterally continuous over a distance of 4 km. The local name 'kakortokite' continues to be used for these spectacular layered rocks in recognition of their unusual mineralogy. Larsen and Sørensen (1987) calculated that the high-level floor cumulates currently exhumed would have crystallized from the last 2% of a postulated parental alkali basalt magma body, assuming that enrichment were the result of fractional crystallization alone. This estimate would not however apply if the cumulates had crystallized from a compositionally stratified magma body. Either way, the implication is that the exposed layered kakortokites are only the uppermost fraction of a much thicker cumulate pile below, the denser mafic component of which is confirmed by large gravity and magnetic anomalies centred on the complex.

Complementing these late-stage floor cumulates are roof cumulates (structurally equivalent to the Skærgaard Upper Border Series – Fig. 4.8a) that preserve a more complete record of the magma chamber's crystallization history, beginning with a relatively high temperature (800–900 °C) anhydrous cumulus assemblage of alkali feldspar, fayalite, hedenbergite, Ti-magnetite and apatite, later joined by nepheline and sodalite. Phase layering evolves downward from syenite through layered nepheline syenite and sodalite syenite to a remarkable sodalitolite (local name 'naujaite') in which myriads of small sodalite crystals are surrounded by large oikocrysts of eudialyte, arfvedsonite, alkali feldspar and nepheline (Plate 9.22). Between the sodalitolite and the underlying floor cumulates lies a 'sandwich horizon' (cf. Fig. 4.7b) of laminated **subsolvus** sodalite nepheline syenites (local name 'lujavrite') rich in all of the same minerals plus analcite and aegirine. The last dregs of this extremely volatile- and incompatible-element-enriched magma, the most evolved in the complex, formed a significant uranium deposit at Kvanefjeld.

There is as much uncertainty over the mechanisms that produce layering in evolved alkali complexes like Ilímaussaq as there is for the major mafic and ultramafic subalkali layered intrusions discussed in Chapter 4. Current hypotheses range from gravity accumulation in a convecting foid syenite magma (Kogarko et al., 2006) to *in situ* crystallization of a compositionally stratified, stagnant foid syenite magma (Larsen and Sørensen, 1987; Bailey et al., 2006).

TEXTURES – MINERAL IDENTIFICATION AND CRYSTALLIZATION PROCESSES

As alkali magmas undergo similar crystallization processes to those discussed in Chapters 2, 6 and 8, alkali rocks share many of the textures featured there. As explained in those chapters, rock textures shed important light

[8] Eudialyte is a rare silicate mineral with the formula $Na_5FeZr(Si_3O_9)_2(OH,Cl)$. Its occurrence in peralkaline syenites is discussed in a later section on chemical attributes of alkali rocks.

on crystallization processes, but in alkali rocks intra-crystalline textures also provide important clues for mineral identification.

Textures involving variations in crystal size and matrix crystallinity

Many volcanic alkali rocks are conspicuously porphyritic (Plate 9.3, 9.4, 9.5 and 9.11) or seriate-textured (Plate 9.7 and 9.8), reflecting magma ascent histories of the kinds outlined in Fig. 2.10.

Not all large crystals in alkali volcanic and hypabyssal rocks, however, can necessarily be interpreted in this way. Hypabyssal kimberlites (Box 9.7) contain rounded crystals significantly larger than surrounding matrix material (Plate 9.1) whose origin is enigmatic; some may indeed have originated as cognate phenocrysts, but others are sufficiently ambiguous to require use of the non-genetic term 'macrocrysts'.

Intra-crystalline textures and mineral identification

The dominant feldspar in many evolved sodic volcanic rocks is *anorthoclase*, whose most diagnostic feature is a fine-scale version of the cross-hatched multiple twinning (Box 6.1) characteristic of all triclinic feldspars. This is illustrated in Plate 9.6. The anorthoclase crystals in this section, though originally euhedral, have been rounded off by **resorption**, probably during magma ascent under water-undersaturated conditions (cf. Fig. 6.5), and this process may also explain the appearance of glass in crystal interiors, presumed to represent local embayment of melt into the crystal from above or below the plane of the thin section.

Complex multiple twinning in alkali volcanic rocks is not restricted to alkali feldspars. *Leucite* exhibits very low birefringence, but distinctive multi-directional multiple twinning can nonetheless usually be seen (Plate 9.8) in phenocrysts, though rarely in groundmass leucite. Multiple twinning is also seen in the accessory mineral perovskite (Plate 9.9).

A dense population of sub-microscopic inclusions is diagnostic of sodalite mineral *nosean* (Fig. 9.1.1). Plate 9.8 shows – in addition to leucite – several euhedral crystals of nosean with distinctive dark brown margins reminiscent of *crème caramel,* and one crystal exhibits a similar internal growth zone; this appearance is attributed to sub-microscopic iron oxide inclusions (MacKenzie et al., 1982). Nosean may alternatively take on the appearance of a wire pot-scourer in PPL (Plate 9.13) owing to exsolution of minute opaque filaments. In the absence of such features, the sodalite end-members (all of which are isotropic) cannot be distinguished by optical means alone.

Normal and oscillatory zoning may be discerned in plagioclase and/or pyroxene phenocrysts, for example in trachybasalts and trachyandesites (Plate 9.11). The possible origins of this feature in plagioclase have been discussed in Chapter 6.

Feldspars in plutonic alkali rocks of evolved composition typically share the attributes of A-type **hypersolvus** granites (Box 8.3 and Fig. 8.12). Rather than the separate K-feldspar and plagioclase crystals of subsolidus granites, the two solvus end-members coexist as exsolution lamellae and host within a single population of perthite crystals (Box 8.1; Plate 9.14). The K-feldspar host may be orthoclase or tartan-twinned microcline (Plate 9.16).

Groundmass textures

Holocrystalline trachytes and phonolites commonly exhibit a groundmass fabric of aligned alkali feldspar microlites – known as *trachytic texture* – which may swirl distinctively around phenocrysts and inclusions (Plate 9.12), suggesting an origin by late-stage laminar flow of crystal-rich pseudo-viscous magma.

Plates 9.3, 9.5, 9.9 and 9.11 illustrate alkali rocks in which groundmass nucleation has been completely inhibited, resulting in a glassy matrix.

Reaction and alteration textures

Cancrinite (Fig. 9.1.1) sometimes forms as a reaction product between nepheline and either

calcite or late-stage carbonate-bearing melts or fluids (Plate 9.17).

Nepheline is also commonly altered (Plate 9.15), especially in plutonic alkali rocks. Typically a fine-grained alteration product is formed, consisting variously of **sericite**, analcite, sodalite or fibrous zeolite.

Leucite is not always as well preserved as shown in Plate 9.8. In some volcanic rocks it is partially or wholly **pseudomorphed** by a fine secondary aggregate consisting chiefly of alkali feldspar and nepheline, known as *pseudoleucite*. Similar examples, often with less well defined morphology, are found in a number of alkali syenites (e.g. at Magnet Cove, Arkansas). Textural and experimental evidence suggests that pseudoleucite has formed from primary magmatic leucite, though the details of the process remain poorly understood.

CHEMICAL ATTRIBUTES AND THE SUBDIVISION OF ALKALI ROCKS

Alkalinity: peralkaline *versus* metaluminous

The concept of 'alkalinity' can be quantified by comparing the total alkali content of a volcanic rock with its Al_2O_3 content in molar proportions. The rock may be described as *peralkaline* or *metaluminous* according to formulae 8.2 and 8.3 given in Chapter 8:

peralkaline $[Na_2O]_{mol} + [K_2O]_{mol} > [Al_2O_3]_{mol}$

metaluminous $[Na_2O]_{mol} + [K_2O]_{mol} < [Al_2O_3]_{mol} < [Na_2O]_{mol} + [K_2O]_{mol} + [CaO]_{mol}$

where $[Na_2O]_{mol}$, for example, represents Na_2O expressed in molar proportions, i.e. the mass % of Na_2O in the major element analysis divided by the relative molecular mass (**RMM**) for Na_2O (i.e. 61.98). The relationship between peralkaline and metaluminous is shown graphically in Fig. 8.14 (alkali rocks rarely fall into the peraluminous category).

Whether a melt is peralkaline or metaluminous has an important influence on ferromagnesian mineralogy, as explained in normative terms in Chapter 8. Peralkaline rocks are characterized by distinctive green sodic pyroxenes like aegirine–augite (Box 9.2) and/or sodic amphiboles like riebeckite (Box 9.4). In metaluminous alkali rocks, on the other hand, the dominant mafic minerals are biotite, hornblende and titanian augite (Box 2.1). Which of these minerals occurs is, by the same token, a clue to magma composition.

Peralkalinity also influences the accessory minerals present. Metaluminous melts crystallize the mineral zircon ($ZrSiO_4$), and its limited solubility in such melts and its relatively early crystallization during fractional crystallization buffer the Zr contents of such melts at modest levels of a few hundred parts per million (**ppm**) (Table 9.5). In peralkaline melts, however, Zr atoms become involved in molecular complexes with sodium and iron, and their enhanced stability in the melt suppresses zircon crystallization and allows much higher concentrations of Zr to accumulate in the melt as an incompatible element (Table 9.5, analyses 2 and 8). The Zr minerals that eventually crystallize are complex Na-Zr silicates like eudialyte [$Na_5FeZr(Si_3O_9)_2(OH,Cl)$] and catapleiite [$Na_2Zr(Si_3O_9).2H_2O$]. Nepheline syenite intrusions like Ilímaussaq in Greenland (Fig. 9.15) and Lovozero (Kola peninsula, N.W. Russia) owe their exotic mineralogy – and the unusually high whole-rock concentrations of rare elements like Zr, Nb, U, Th and **REE** they contain – partly to the peralkalinity of the magmas from which they crystallized. Peralkaline nepheline syenites rich in eudialyte or similar minerals are sometimes described as *agpaitic*,[9] after the Ilímaussaq locality Agpat (now written Appat).

Silica undersaturation

Alkali rocks – defined as those lying above the line X–Z in Fig. 9.1a – span a compositional range from silica-oversaturated (e.g. alkali rhyolite) to silica-undersaturated (e.g. nepheline syenite or melilitite). The concept of silica saturation was introduced in Chapter 2. The normative basis for expressing degrees of saturation is summarized in Box 2.4 and is set out as a systematic procedure in Appendix B.

Greater insight into the meaning of silica saturation can be gained by studying Fig. 9.7a, devised by Yoder and Tilley (1962)

[9] 'Agpaitic' relates to mineralogy and is not merely a synonym for peralkaline.

Table 9.5 Major and trace element analyses of representative volcanic and hypabyssal alkali rocks from various tectonic settings. Iron data are presented as 'total FeO' ['ΣFeO' = actual FeO + (actual Fe_2O_3/1.11)] as in Table 2.4. Blank entries indicate components that are not given in the published analyses.

Rock type	Nephelinite	Lamproite	Basanite	Tephrite	Mugearite	Shoshonite	Trachyte	Phonolite
Tectonic setting	Continental rift	Anorogenic	Oceanic hotspot	Oceanic hotspot	Oceanic hotspot	Intra-arc rift	Continental rift/hotspot	Oceanic hotspot
Location	Nyiragongo, DR Congo	Gaussberg, Antarctica	Pico Teide, Tenerife, Canary Is	Pico Teide, Tenerife, Canary Is	Haleakala crater, Hawaii	N Hiyoshi, northern Mariana arc	Menengai, Kenya rift	Pico Teide, Tenerife, Canary Is
Reference	1	2	3	4	5	6	7	8
Mass % oxide								
SiO_2	36.49	50.85	44.89	48.99	51.19	55.78	62.68	58.97
TiO_2	3.01	3.42	3.73	2.97	2.31	0.63	0.81	0.68
Al_2O_3	11.12	9.86	15.72	16.74	17.67	17.69	14.40	18.82
ΣFeO	11.17	6.00	11.46	8.93	9.11	6.51	6.41	3.41
MnO	0.22	0.09	0.19	0.19	0.25	0.15	0.30	0.20
MgO	8.64	7.95	5.39	3.8	2.84	2.89	0.36	0.40
CaO	17.41	4.63	10.76	8.15	6.57	6.52	1.50	0.84
Na_2O	3.40	1.65	4.02	5.45	5.73	3.72	6.66	9.80
K_2O	2.88	11.61	1.66	2.22	2.17	4.11	5.33	5.43
P_2O_5	1.77	1.48	0.92	1.17	0.99	0.35		0.10
LOI	2.89	1.22	#	#	#	0.87	0.18	0.38
Total	99.00	98.76	98.74	98.61	98.83	99.24	98.88	99.03
ppm								
Rb	70	315	34	53	50	123	75	179
Ba	1412	5550	465	640	849	836	54	54
Th	15.7	36	10	8	6.0	18.1	8	30
Nb	150	90	85	108	72	14.8	84	254
La	147	145	48.8	72.6	64.4	60.3	91.2	98.7
Ce	278	263	104.1	146.6	141.1	107	189	176.7
Sr	1176	1808	1130	1177	1015	941	2.9	4
Nd	109	84	45.2	57.6	65.0	43.1	79.4	50.4
Zr	298	1004	292	380	445	326	317	1084
Sm	16.0	10.8	8.36	10.0	13.15	7.51	14.23	8.08
Eu	4.6	3.0	3.00	3.36	3.97	2.00	1.68	1.59
Gd	11.6	6.8	7.64	9.88	10.03[$]	6.39	10.35	6.89
Y	40	18	35	41	43	29.2	61	46
Yb	2.3	1.20	1.64	2.28	3.21	2.48	6.05	3.26
Lu	0.32	0.1	0.25	0.31	0.45	0.40		0.58
Cr	254	306	33	24	2	1.81		7
Ni	112	233	14	2	4	9.43		5

[#] The published analysis is volatile-free.

Data sources

1 Platz et al. (2004) analysis 96-606 (olivine-cpx-leucite-melilite-phyric melilite nephelinite).
2 Sheraton and Cundari (1980), mean analysis (leucite-olivine-augite-phyric lamproite); whole-rock REE contents have been calculated from mineral and glass analyses given by Foley and Jenner (2004) using modal proportions in Sheraton and Cundari (1980).
3 Ablay et al. (1998), analysis T-1909 (historic olivine-cpx-magnetite-plagioclase-apatite-phyric basanite).
4 Ablay et al. (1998), analysis TV-23-7 (olivine-cpx-magnetite-plagioclase-kaersutite-phyric phono-tephrite).
5 West and Leeman (1993) (2003) analysis HK-37 (sparsely plagioclase-olivine-hornblende-phyric mugearite lava).
6 Sun and Stern (2001), analysis D53 (plagioclase-olivine-phyric shoshonite lava with glassy groundmass).
7 Macdonald et al. (1994), analysis W2 RJK9 (welded trachytic ignimbrite, Menengai volcano, Kenya).
8 Ablay et al. (1998), analysis T1-17-2 (feldspar-cpx-biotite-magnetite-apatite-phyric phonolite).

for classifying basalts according to their normative minerals. The figure shows a regular tetrahedron[10] – with normative diopside, nepheline, olivine and quartz at its apexes – in which basalt norms can in principle be plotted. This figure, universally referred to as the 'basalt tetrahedron' and taking Fig. 2.11 as its base, is divided into three sub-volumes reflecting different outcomes of the norm calculation for basalts. A few relatively SiO_2-rich basalts contain enstatite and small amounts of quartz in their norms and would plot in the silica-oversaturated volume '1'. A basalt having enstatite and olivine in the norm (thus ruling out quartz) would plot in the wedge-shaped silica-saturated volume '3', whereas a strongly SiO_2-deficient basic rock with normative nepheline and olivine would plot in the silica-undersaturated volume '5'. The two essential normative minerals of all basalts – diopside (representing modal augite) and plagioclase (represented in this system by albite) – lie on a line on the rear face that is common to all three volumes. Albite lies on the rear edge intermediate between nepheline and quartz, because its formula ($NaAlSi_3O_8$) is equivalent to one nepheline molecule ($NaAlSiO_4$) combined with two SiO_2 molecules. Enstatite lies on the front olivine-quartz edge, reflecting its reaction relationship to Mg-rich olivine and SiO_2.

These sub-volumes are separated by two interior planes (marked '2' and '4'). Yoder and Tilley (1962) referred to the Di–En–Ab plane ('2') as the 'plane of silica saturation' and it separates the oversaturated volume '1' from the saturated volume '3'. The 'critical plane of silica undersaturation' ('4'), as Yoder and Tilley's name suggests, has greater significance for low-pressure basalt magma fractionation, since it divides the basic melt compositions in volume '5' that fractionate to form undersaturated residual melts (e.g. phonolite) from those in other parts of the tetrahedron that fractionate towards oversaturated residual melts like rhyolite. To see how this works, consider the experimental phase relations in the ternary system $CaMgSi_2O_6$–$NaAlSiO_4$–SiO_2 forming the rear face of the basalt tetrahedron, as shown in Fig. 9.7b.

[10] The familiar ternary diagram is a tool for plotting 3 components in 2 dimensions. Petrologists use a tetrahedron as an analogous concept for plotting 4 components in 3 dimensions (see Appendix B)

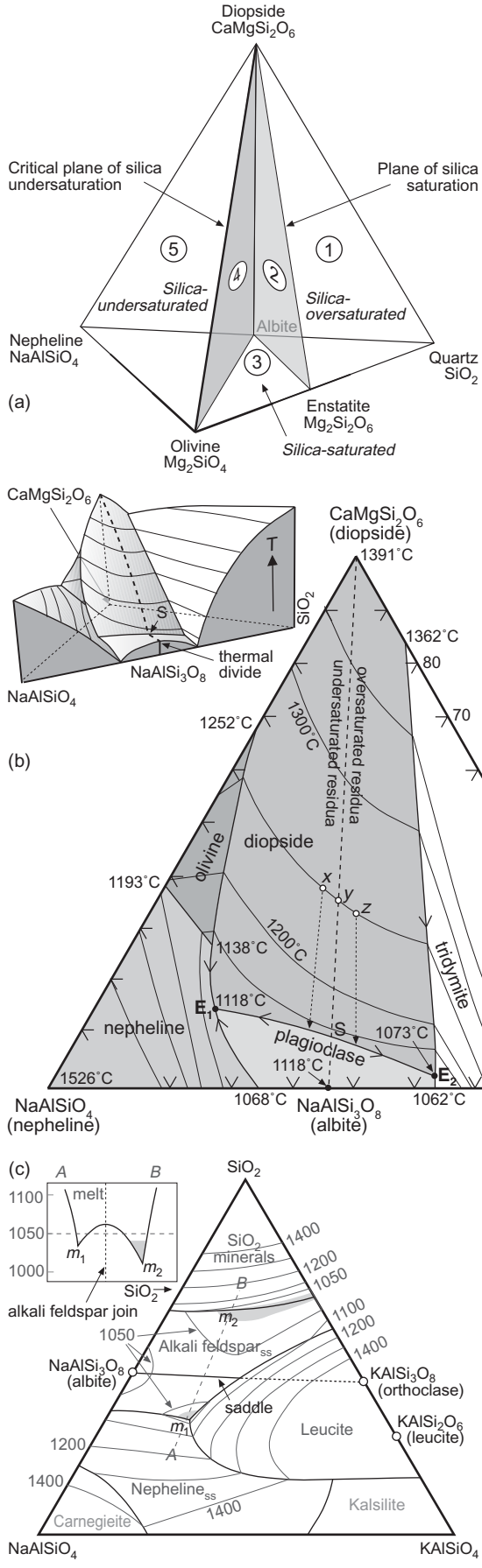
Fractional crystallization of alkali basic magmas

Figure 9.7b is a ternary diagram depicting the three-dimensional geometry of the $CaMgSi_2O_6$–$NaAlSiO_4$–SiO_2 liquidus surface by means of temperature 'contours' (isotherms) which can be read like an everyday topographic map; some readers may find the three-dimensional thumbnail sketch helpful (inset). The liquidus surface comprises four main fields, showing the ranges of melt composition from which nepheline, diopside, albite and silica minerals will each crystallize *first*.[11] The fields are separated by **cotectic**s which form plunging 'thermal valleys' leading towards two ternary **eutectic**s, E_1 and E_2. All melt-fractionation paths lead ultimately to one or other of these eutectics. A residual melt arriving at E_1 would crystallize albite, diopside and nepheline (a silica-undersaturated assemblage), whereas a melt evolving to E_2 would crystallize the silica-oversaturated assemblage albite–diopside–tridymite (the last being a high-temperature silica mineral).

The two eutectics are separated by a low 'thermal saddle' (S) in the liquidus surface (clearest in the inset cartoon) at 1140 °C. This temperature barrier prevents any melt evolving by natural fractional crystallization from E_1 to E_2 or from E_2 to E_1, since either traverse requires an initial rise in temperature, something that cannot happen in a cooling magma chamber. In fact, the dashed line stretching from diopside to albite divides the diagram into two halves, between which no equilibrium melt-evolution paths can lead. To see what this means, consider melts with initial compositions *x*, *y* and *z*. As they cool, each begins to crystallize diopside at the same temperature (1250 °C), but their subsequent paths are very different. Crystallizing diopside from *x* causes the melt to evolve down the left-hand dotted arrow,[12] meeting the diopside-albite cotectic to the *left* of the saddle. Crystalliza-

[11] A small olivine field also exists in this phase diagram, even though olivine is not one of the end-members defining this system. It tells us that this is not strictly a **ternary** phase diagram (involving only 3 components). The olivine field (like the spinel field in Fig. 3.3) is a reminder that this phase diagram can only be understood fully as part of the more complex Mg_2SiO_4–$CaMgSi_2O_6$– $NaAlSiO_4$–SiO_2 (quaternary) system. For present purposes we can ignore this complication.

[12] Obtained by drawing a line from the diopside apex to *x* and extrapolating it.


Diopside
CaMgSi2O6
Critical plane of silica undersaturation
Plane of silica saturation
5
4
2
1
Silica-undersaturated
Silica-oversaturated
Albite
Nepheline
NaAlSiO4
Quartz
SiO2
3
(a)
Enstatite
Mg2Si2O6
Olivine
Mg2SiO4
Silica-saturated
CaMgSi2O6
T
S
SiO2
thermal divide
NaAlSi3O8
NaAlSiO4
CaMgSi2O6 (diopside)
1391˚C
1362˚C
80
70
60
50
40
30
20
10
Mass % CaMgSi2O6
1252˚C
1300˚C
oversaturated residua
undersaturated residua
(b)
olivine
diopside
1193˚C
x
y
z
1200˚C
1138˚C
tridymite
E1
1118˚C
nepheline
S
1073˚C
plagioclase
1118˚C
E2
1697˚C
1526˚C
1068˚C
NaAlSi3O8
(albite)
1062˚C
SiO2
NaAlSiO4
(nepheline)
(c)
A
B
1100
1050
1000
melt
m1
m2
SiO2
alkali feldspar join
SiO2
SiO2 minerals
1400
1200
1050
B
m2
1100
1200
1400
1050
Alkali feldspar ss
NaAlSi3O8
(albite)
KAlSi3O8
(orthoclase)
saddle
m1
Leucite
KAlSi2O6
(leucite)
1200
A
1400
Nepheline ss
Kalsilite
Carnegieite
1400
NaAlSiO4
KAlSiO4

tion of diopside and albite *together* (in proportions approximating to the coordinates of S) will now drive the melt composition *leftward*, away from the saddle towards the undersaturated eutectic E_1 where nepheline will begin to crystallize as well. Crystallization of diopside from melt *z*, on the other hand, will drive it down the right-hand dotted arrow, meeting the cotectic to the *right* of the saddle, from where diopside + albite crystallization will drive it towards the oversaturated eutectic E_2; here tridymite (a silica mineral) will start to crystallize as well. Crystallization of diopside from melts *x* and *z* – initially so close in composition – leads down divergent paths that end up with residual melts of radically different composition. On account of this divergence, the line $CaMgSi_2O_6$– $NaAlSi_3O_8$ is said to act as a *thermal divide* between distinct undersaturated and oversaturated domains in the phase diagram. The term is a shade misleading here as it conjures up a more pronounced temperature 'ridge' than actually exists (except around S); in truth, the Di–Ab join is acting more as a *chemical* watershed.

Though it is hard to demonstrate in 3 dimensions, the plane of critical undersaturation ('4') in Fig. 9.7a acts in the same way, preventing a melt in volume 5 from evolving by low-pressure fractional crystallization towards a saturated or oversaturated residual melt. Likewise a melt in volumes 1–3 cannot fractionate to an undersaturated residual melt. As Yoder and Tilley (1962) concluded,

> *'in general, under equilibrium conditions, no one liquid can produce both nepheline-bearing products and silica-bearing products if only major phases* [minerals] *are considered. On these grounds it must be concluded that a single* [parental] *basalt magma cannot produce both a tholeiite trend and an alkali basalt trend solely by fractionation'*.

In other words, a single parent magma cannot at low pressures[13] fractionate to form both phonolite and rhyolite residual melts. The degree of SiO_2 saturation in melts that fractionate at shallow crustal depths is largely inherited from differences that their basic or ultrabasic parent magmas bring with them from the mantle, as seen in the alkali magma associations of the East African Rift for example (Figs. 9.11 and 9.12).

These arguments do not of course take account of the possible effects that assimila-

[13] At high pressures basalt mineralogy (plag + augite) gives way to **eclogite** mineralogy, and fractionation of garnet and jadeite-rich pyroxene generates different evolutionary trends.

Fig. 9.7 (a) Normative diagram based on the 'basalt tetrahedron' of Yoder and Tilley (1960) showing the *plane of SiO_2 saturation* (dividing the volume containing quartz-normative rock compositions from that of quartz-free compositions) and the *critical plane of SiO_2-undersaturation* (dividing the volume containing nepheline-normative rock compositions from that of nepheline-free compositions). The diagram is not to scale. (b) A ternary phase diagram (mass proportions) showing phase relations in the system $CaMgSi_2O_6$–$NaAlSiO_4$–SiO_2 at atmospheric pressure, plotted in mass proportions (after Schairer and Yoder, 1960; reprinted by permission of the American Journal of Science). The liquidus stability fields of plagioclase, nepheline, diopside and olivine have been differentially shaded for clarity; the unshaded field relates to SiO_2 minerals tridymite and (at higher temperatures) cristobalite. Arrows, showing the temperature gradients of cotectics, point down-temperature. E_1 and E_2 are under- and over-saturated eutectics respectively, separated by a thermal 'saddle' at S. The inset shows a three-dimensional sketch of the liquidus surface, illuminated from the left. (c) Phase relations in the 'residua' system SiO_2–$NaAlSiO_4$–$KAlSiO_4$ (mass proportions) at atmospheric pressure after Schairer (1957) by permission of Wiley-Blackwell, showing the 'thermal minima' m_1 and m_2 in the liquidus surface (shaded) on either side of the 'saddle' on the alkali feldspar join $NaAlSi_3O_8$– $KAlSi_3O_8$. Temperatures are shown in °C. Open circles indicate the compositions of end-member albite, orthoclase and leucite. (The diagram covers the same compositional space as Fig. 9.1.1 but differs in appearance through being plotted in mass rather than molar proportions.) The inset shows a sketch cross-section of the alkali feldspar saddle along the dashed line *A–B* in the main figure.

tion of sialic crust might have on the relative SiO_2 saturation of evolved continental alkali magmas (cf. Figs. 3.11 and 3.12).

Silica saturation in phonolites, trachytes and rhyolites

How the two eutectics E_1 and E_2 and the thermal divide in Fig. 9.7b influence the evolution of **salic** alkali magmas can be understood in greater depth in Fig. 9.7c. This ternary system can be seen as an expansion (by adding $KAlSiO_4$) of the bottom edge of Fig. 9.7b, and it shows the phase relations for residual melts (phonolite, trachyte, rhyolite) remaining after extended fractionation of plagioclase and mafic minerals has eliminated from the melt all of the MgO, FeO and CaO originally present. The liquidus surface is divided into 6 fields separated by 'thermal valleys'. They indicate the melt-composition ranges over which silica minerals, alkali feldspar solid solution, leucite and nepheline solid solution each crystallize first from the melt (the fields of kalsilite and carnegieite – an artificial form of $NaAlSiO_4$ – are not relevant in the present discussion).

The liquidus surface falls to its lowest temperatures at two 'thermal minima' (not strictly eutectics in this system) towards which evolving melts fractionate. The norms of many natural phonolites and nepheline syenites, when plotted in this ternary diagram, congregate close to the undersaturated minimum m_1, whereas alkali rhyolites and granites generally plot close to the oversaturated minimum m_2 (cf. Fig. 6.7), suggesting that natural phase relations do not differ much from those in this simplified laboratory system. The two minima are separated by a modest temperature 'saddle' which, as in Fig. 9.7b, prevents crystallizing melts evolving during cooling from m_1 to m_2 or vice versa. The norms of natural trachytes and syenites plot across the saddle region; such melts could in principle evolve to phonolite or to rhyolite by alkali feldspar fractionation, depending on whether the melt composition lies below or above the $NaAlSi_3O_8$–$KAlSi_3O_8$ join in Fig. 9.7c.

The large field where leucite crystallizes first is a low-pressure feature. The fact that it extends over the composition of orthoclase ($KAlSi_3O_8$) indicates **incongruent melting**: when pure $KAlSi_3O_8$ is heated in the laboratory at atmospheric pressure it melts to form coexisting leucite ($KAlSi_2O_6$) and melt, rather than $KAlSi_3O_8$ melt alone. Experiments under higher pressures in the presence of water vapour (cf. Fig. 8.12), however, show that the leucite field contracts and eventually disappears at high P_{H_2O}. This partly explains the limited occurrence and instability of leucite in plutonic alkali rocks, in which it is generally replaced by pseudoleucite.

WHERE ALKALI ROCKS OCCUR

The compositional variety of the alkali rocks is matched only by the diversity of geotectonic environments in which they are found. They attain their largest volume in a few continental rifts like the East African Rift System (EARS), the system of rift valleys running from the Red Sea to Tanzania, but they occur – often in small volumes – in a host of other settings too, both oceanic and continental. Indeed the array of alkali volcanoes of the 'Cameroon Line', extending from northern Nigeria through Cameroon into the Gulf of Guinea (Fig. 9.16), traverses the boundary between the continental and oceanic domains.

Ocean islands

The bulk of the island of Hawai`i (and other islands in the Hawaiian chain) consists of mildly olivine-phyric tholeiitic basalts erupted rapidly during what is called the *shield-building stage* of each volcano. This subalkali stage accounts for more than 95% of the volume of each edifice, but is both preceded and succeeded by small volumes of alkali rocks. Fig. 9.8 shows how the development of each island has been divided into four discrete phases (Clague, 1987). The first, *'pre-shield' stage* is observed only in Loihi Seamount – the youngest edifice in the linear Hawaiian–Emperor volcanic chain – situated 30 km off the SE coast of Hawai`i. It consists of early olivine-augite-phyric alkali basalt and basanite lavas succeeded by transitional and olivine ± augite ± plagioclase-phyric tholeiitic basalts, all erupted relatively slowly. It is reasonable to suppose that this infant edifice will in due course become completely hidden beneath a much larger tholeiitic shield volcano, and on these grounds it is generally accepted that most if not all of the Hawaiian islands and Emperor seamounts probably incorporate a hidden pre-shield alkali stage in their development.

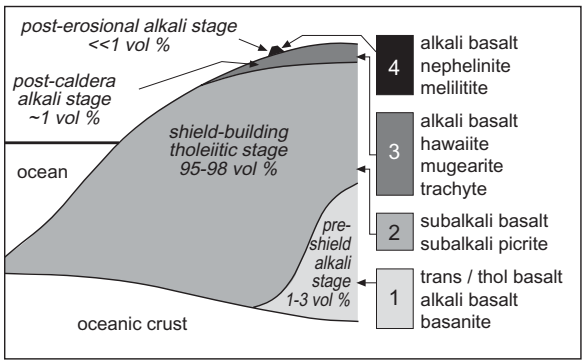


Fig. 9.8 A notional cross-section through a typical Hawaiian island showing the four magmatic stages in its construction (after Clague, 1987, courtesy of the Geological Society of London).

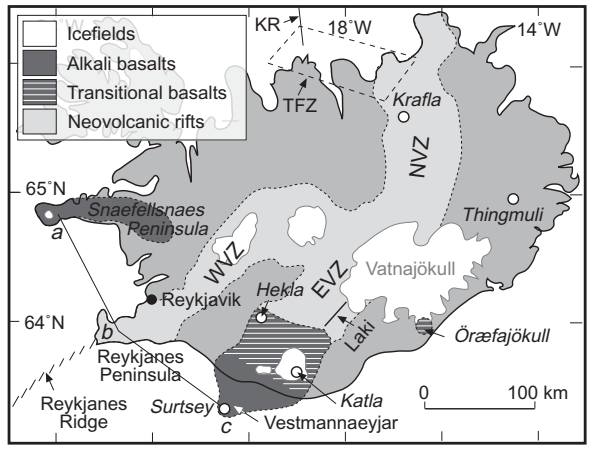


Fig. 9.9 Geological sketch map of Iceland showing Holocene 'off-rift' alkali basalt fields of the Snaefellsnaes Peninsular and south central Iceland. Öræfajökull, Thingmuli, Hekla and Katla volcanoes and the Laki fissure zone are also shown. WVZ, EVZ and NVZ refer respectively to the western, eastern and northern sectors of the neovolcanic zone; KR, Kobeinsey Ridge; TFZ, Tjörnes Fracture Zone (after Gudmundsson, 2007). The line *a–b–c* shows the trace of the sketch cross-section shown in Fig. 9.20.

Lavas of the '*post-caldera' stage* ('3') form a thin, discontinuous cap of alkali basalts, hawaiites, mugearites (Table 9.5) and smaller amounts of ankaramite, trachyte and phonolite. Eruption of these lavas commonly follows the collapse of a summit caldera, and the vents (like Hualalai and Haleakala volcanoes) tend to be concentrated in the caldera area or along rift zones emanating from it; most of the lavas and scoria cones formed at this stage lie within the caldera. Because the post-caldera alkali stage succeeds the shield-building stage, it has yet to develop on the relatively young volcanoes of Mauna Loa, Kilauea and, of course, Loihi.

The *post-erosional stage* of alkali volcanism ('4'), as the name suggests, follows a period of dormancy – lasting 1–2 Ma – during which deep erosional valleys are incised in the tholeiitic shield edifice. Small volumes of alkali basalts or more strongly alkali lavas like basanite and nephelinite erupt very slowly from satellite vents that seem unrelated to the main rift architecture of the island. Xenoliths of spinel lherzolite, dunite and, in some localities, garnet lherzolite are a common feature of lavas of this stage (such as the Honolulu Volcanics of the Koolau shield on the island of Oahu).

A similar constructional history – dominated by mafic volcanics – applies to oceanic islands around the world, though in many the shield-building stage itself also consists of alkali basalts (Carmichael et al., 1974). Some island groups or chains express a chemical provinciality in ocean island basalt (OIB) composition. For example the basalts on islands in the South Atlantic (Tristan da Cunha and Gough Island) and Kerguelen in the southern Indian Ocean (Fig. 2.12) are noticeably more potassic and highly incompatible trace element (**HITE**)-rich than OIBs elsewhere.

Carbonatites have been reported on Fuerteventura (Canary Islands) and Cape Verde islands in the central Atlantic and on Kerguelen (Woolley and Church, 2005), but these are the only instances known in the ocean basins.

Iceland

In volume terms the great bulk of Icelandic basalts are of subalkali composition. In two 'off-rift' areas of Holocene activity on either side of the main rift zone, however, alkali basalts predominate. The more extensive one is the Snaefellsnaes peninsula in western Iceland (Fig. 9.9); its eastern counterpart is the volcano Öræfajökull (actually the largest active volcano in Iceland) which exhibits a

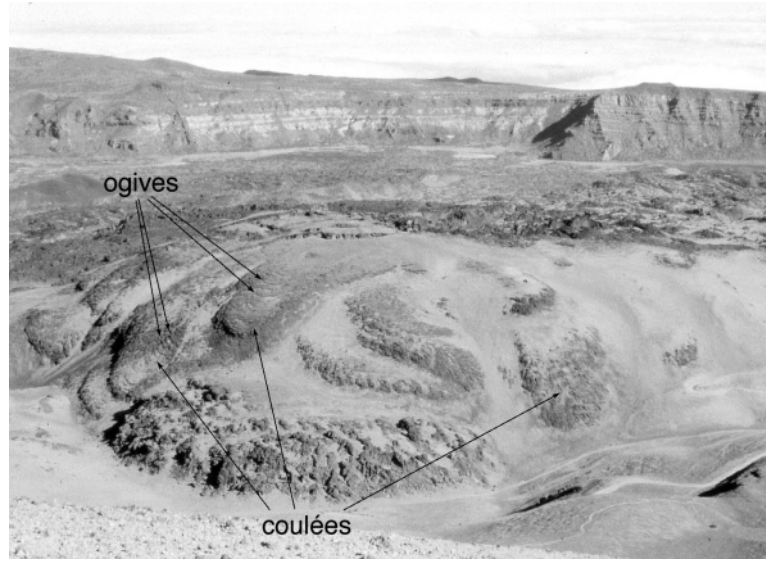


Fig. 9.10 Exogenous phonolite lava **coulées** on the flanks of Montaña Rajada, a post-caldera dome complex in the Las Cañadas caldera of Tenerife (Canary Islands). The resemblance to ropy pahoehoe is due to arcuate ogives on the coulée surface (partly obscured by later pumice fall). The topographic Cañadas caldera wall – capped by historic cinder cones – can be seen in the background.

transitional–alkali compositional trend. More advanced fractionation products like hawaiites, mugearite and trachytes occur in each of these areas, and moreover Öræfajökull has erupted large volumes of rhyolite, giving it a **bimodal** abundance distribution. Alkali lavas are also found at the southern tip of the southward-propagating eastern rift, notably on the islands called Vestmannaeyjar (Fig. 9.9). Basalts from volcanoes marginal to this southern alkali basalt area, like Hekla and Katla, are of transitional character.

Tenerife

Tenerife, one of the Canary Islands off the Atlantic coast of North Africa, is unusual among ocean islands on account of the relatively high proportion of evolved alkali rocks that characterize the post-erosional stage of the island's development. After a shield-building stage from 11 to 4.2 Ma that formed the basaltic and basanitic foundations of the island, a new post-erosional stratovolcano – the 'Cañadas' volcano – grew in the centre of the island, rising to 2500 m above the shield basement. Large volumes of magma evidently accumulated within this edifice, and slow cooling within a large magma chamber (or chambers) led in due course to the eruption of as much as 100 km^3 of peralkaline phonolites in a succession of large plinian eruptions whose deposits are preserved today as pumice fall deposits and ignimbrites on the south-eastern, south-western and northern flanks of the island. These voluminous eruptions occurred between 1.5 and 0.17 Ma ago and led to the progressive development of a spectacular summit caldera (Fig. 9.10).[14] The outflow pyroclastics (Fig. 7.19b) are generally unwelded, though the proximal facies preserved on the caldera rim contain intensely welded airfall deposits thought to have formed by late-stage fire fountaining as the intensity of each eruption declined.

Near to the NW margin of the caldera, a new cone – the imposing 3718 m-high Pico Teide – has developed, together with two satellite centres (Pico Viejo and Montaña Blanca). Teide and Pico Viejo have basanitic foundations (Table 9.5) upon which each has built

[14] A minority of geologists interpret the caldera feature as an arcuate landslide scarp associated with repeated lateral collapse of the northern flanks of the island. Though multiple sector collapse has undoubtedly affected the physiography of Tenerife, its role in forming the 'caldera' is conjectural.

Box 9.5 How to identify a primary melt

'**Primary** melt' is the term used for a natural melt whose composition is consistent with derivation by direct partial melting of fertile mantle peridotite, with negligible fractional crystallization during ascent.

Chapter 5 reviewed the major element composition of mantle peridotites and concluded that mantle olivines have compositions in the range Fo_{90}–Fo_{92} (Fig. 5.6). It follows that any melt formed directly by partial melting of mantle peridotite must equilibrate with olivines of this composition range (equation 5.1), constraining the Mg number of primary melts to values greater than 68. Many petrologists accept a less stringent value of 65 as the minimum value for a volcanic rock analysis to qualify as representing a primary melt.

Melts initially in equilibrium with mantle olivine commonly crystallize olivine and chromite during ascent, reducing the concentration of Ni (strongly compatible in olivine) and Cr in the melt composition that reaches the surface. Ni content thus provides an alternative criterion for identifying a primary melt: basaltic melts with Ni ≥ 250 ppm are generally considered primary, whereas those with Ni < 250 ppm have probably undergone fractionation of olivine (depleting the melt in Ni) ± other minerals. Both of these criteria presume that the erupted magma's composition has not been affected by near-surface olivine accumulation or alteration.

In the field, the presence of mantle-derived xenoliths suggests that the host magma was close to primary composition: as the magma evidently ascended from the mantle too rapidly for these dense xenoliths to settle out before eruption, it is unlikely that individual crystals could have settled out, but instead remain suspended as phenocrysts so that the bulk host-rock analysis should preserve a primary magma composition (with regard to non-volatile elements).

its own edifice of intermediate and felsic lavas and pyroclastics. The most recent output from Teide consists of summit-fed feldspar-phyric phonolite lava flows[15] with a distinctive black glassy matrix, which form prominent levéed features on the southern and eastern flanks. The later phases of eruption from the nearby Montaña Blanca centre, on the other hand, produced phonolite lava domes and coulées with distinctive exogenous features (Fig. 9.10). Like the voluminous Cañadas pyroclastics, they illustrate volcanological styles that evolved silica-undersaturated, alkali volcanics share with silicic volcanics from island arc and cordilleran settings.

Continental rifts

East African Rift System

The alkali volcanic province of Ethiopia, Kenya and northern Tanzania (Fig. 9.3) has evolved hand in hand with the East African rift system, itself a response to the extensive post-Eocene up-doming of the Ethiopian and East African plateaux (Fig. 9.3). The plateaux flanking the rift rise to 3000 m above sea level (a.s.l.), and it is on these plateaux that Africa's highest peaks are found – the stratovolcano Kilimanjaro (5895 m a.s.l.) and the shield volcano Mt Kenya (5200 m). By contrast, some sectors of the rift floor lie at sea-level or even below it.

The structural development of the Kenya (Gregory Rift) part of the rift system has been divided into three phases (Baker, 1987):

4–0 Ma BP:	Full graben stage
12–4 Ma BP:	Half-graben stage (major normal faults on western margin, monocline on the east)
30–12 Ma BP:	Pre-rift stage

Volcanism has been associated with each of these stages. How its character has varied both in time and with location relative to the developing rift can be seen in Fig. 9.11. Four volcanic associations are recognized (see the key in Fig. 9.11), each seeming to represent magmas lying on a distinct fractionation path

[15] An analysis is given in Table 9.5.

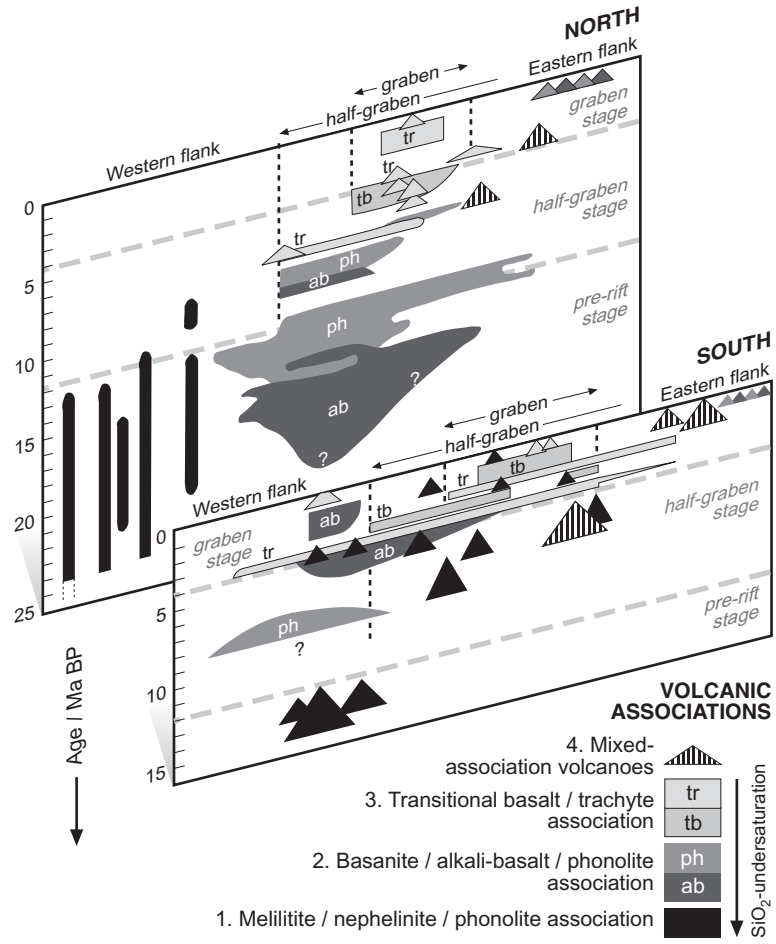


Fig. 9.11 Age profiles across northern and south sectors of the Kenya Rift Valley (after Baker, 1987, reproduced by permission of the Geological Society of London). The lateral extent of lava fields and central volcanoes (triangles) of each volcanic association is shown approximately, as are the locations of half-graben and graben boundary faults.

(Fig. 9.12). The most strongly silica-undersaturated association (1) consists of melilitites, nephelinites, phonolites and occasional carbonatites (note that the mafic rocks of this association are feldspar-free). The second association (2) comprises basanites, alkali basalts, tephrites and phonolites. The least undersaturated association (3) is made up of transitional basalts, mugearites, benmoreites, trachytes and occasional alkali rhyolites. The fourth association includes a number of central volcanoes in which these associations are intermingled. The coherence of these associations – more undersaturated derivatives being consistently associated with the most SiO_2-poor parent magmas – suggests a number of parallel magmatic lineages, as illustrated in Fig. 9.12. While some mafic and ultramafic rocks in association 1 are primitive enough to be **primary** mantle melts (Box 9.5), the basanites and transitional basalts of associations 2 and 3 are generally too evolved to represent primary melts (Macdonald and Upton, 1993).

From Fig. 9.11 a number of generalizations can be made about the temporal and spatial distribution of these associations, in both the northern and southern sectors of the Kenya rift:

- Volcanism began earlier, and has been more voluminous, in the north than in the south.
- There is a general tendency in the north for more undersaturated magmas to be erupted on the flanks of the rift at each stage, while more silica-saturated magmas

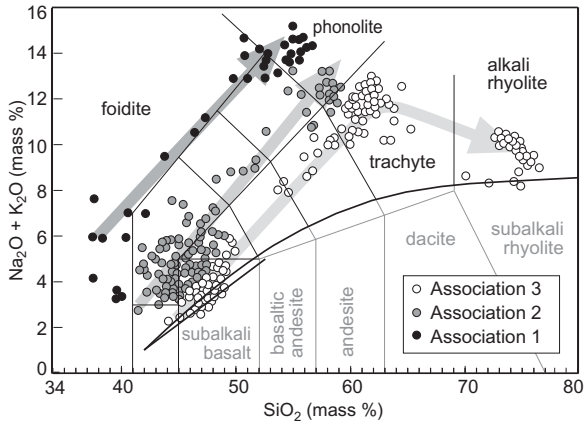


Fig. 9.12 Analyses of selected Kenya rift volcanic rocks plotted in a TAS plot (cf. Fig. 9.1a). The shade-coding and the parallel fractionation paths of the three magma associations defined in Fig. 9.11 are only illustrative.

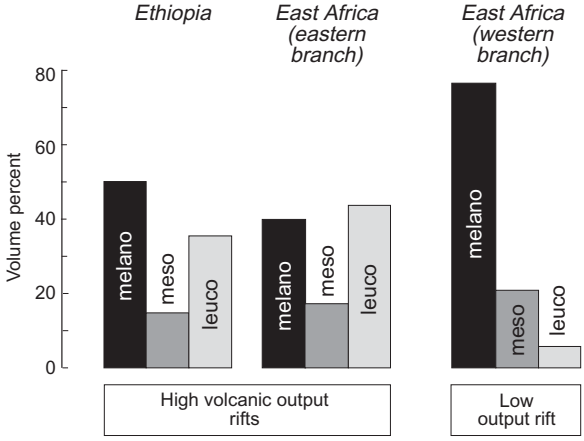


Fig. 9.13 Volume proportions of melanocratic, mesocratic and leucocratic volcanic rocks in high- and low-volcanic-output continental rift zones (adapted from Barberi et al., 1982 by kind permission of the American Geophysical Union). Note that the volume distributions of the two high-volcanic output provinces are bimodal.

are erupted in the rift/graben. However, association 1 is more widely distributed in the south.

- At any one location, magmatism tends to become less undersaturated as time advances.
- The earliest volcanism appeared to the west of the present graben, and later centres show a general eastward migration, especially in the north.
- Mixed-association volcanoes lie in the east of each section.

An important feature of the volcanism of the Gregory (eastern) rift in East Africa is the bimodal volume distribution of magma composition, in which leucocratic volcanic rocks like trachyte and phonolite constitute as much as 50% of the total volcanic output (Fig. 9.13), equalling or exceeding the volume of melanocratic volcanics like nephelinite and basalt. This is a characteristic of a number of high-volcanic-output continental rifts, and contrasts with low-volcanic output rifts like the western branch of the East African rift system (Fig. 9.13) as well as with the majority of continental flood basalt provinces, in which mafic rocks strongly predominate.

How can this overabundance of felsic volcanics in high-volcanic output rifts be explained? Karson and Curtis (1989) estimated that magma fractionation of the 22,900 km^3 of trachytic and phonolitic volcanics erupted in the rift between the equator and 2° S from the Miocene to the present (omitting central volcanoes) required the existence of 35,000 km^3 of ultramafic cumulates and 95,000 km^3 mafic cumulates within the crust. Gravity studies across the rift (Fig. 9.14a) show that the East African rift is characterized by: (i) a broad negative **Bouguer** anomaly indicating anomalously low densities at mantle depths; upon which is superimposed (ii) a narrower, smaller positive Bouguer anomaly representing an axial region of anomalously *high* densities within the crust directly beneath the rift, consistent with the presence of cumulates complementary to the evolved volcanics. Whether the dense bodies in the crust are laterally extensive intermediate-density intrusions or swarms of dyke-like higher-density bodies is unclear from the gravity and seismic profiles.

Accumulation of dense magmatic material in the crust indicates periods when magma supply from the mantle exceeded the rate of magma eruption at the surface, during which fractionating magma may deposit dense cumulates at depth and emerge at the surface as seemingly disproportionate volumes of evolved magma. Continental crust may thus

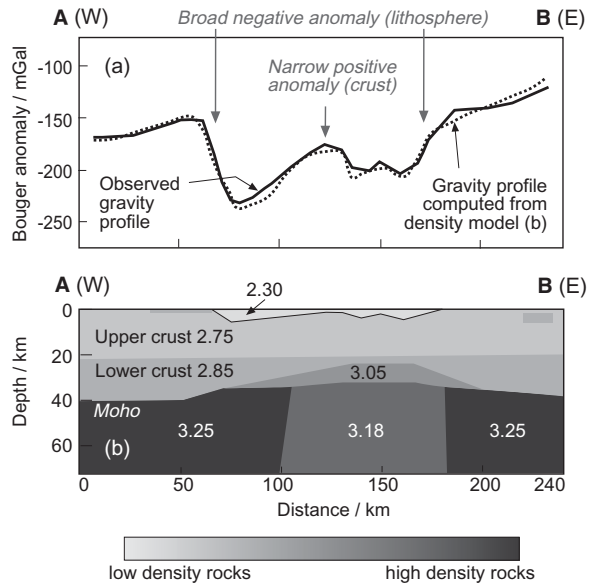


Fig. 9.14 Gravity profile and composite interpretation across the Kenya Rift Valley, adapted from Mariita and Keller (2007) with permission of Elsevier. (a) Gravity profile from W to E across the Kenya rift valley and its flanking plateaux in the region of Lake Baringo (see thin black line A–B west of Mt Kenya in Fig. 9.3); the dashed curve shows a computed gravity profile based on the density model shown in (b). (b) A simple density model for the upper mantle and crust beneath East Africa providing the best fit to the gravity profile shown in (a). Numbers indicate model densities in kg dm^{-3}.

act as a density filter favouring the preferential transport of lower-density salic magmas to the surface (Gill, 1973). Alternatively the large volumes of trachyte and phonolite volcanics could be products of partial melting of the deep mafic intrusions of alkali basalt composition (Hay and Wendlandt, 1995). The latter hypothesis accounts for the bimodal abundance distribution, but is silent on the cause of the supposed reheating and re-melting.

The broad negative anomaly in Fig. 9.14 is consistent with lithospheric thinning beneath the rift, which allows upwelling of hotter, lower-density mantle to shallower depths. Thinning is attributable partly to stretching of the lithosphere over the areas of domal uplift shown in Fig. 9.3, and partly to the cause of that uplift: the invasion of a column of exceptionally hot mantle ascending from deeper in the mantle. Low seismic velocities observed in the mantle beneath the Kenya rift are consistent with 3%–5% of partial melt in this low-density column (Mechie et al., 1997). The contribution of mantle plumes to the structural and magmatic evolution of East Africa is discussed later in this chapter. A similar correlation of uplift, extension and volcanism (dominantly basaltic in this case) is observed in the Basin and Range Province and related areas in the western USA (‘*B&R*’ in Fig. 2.12), where – as in East Africa – uplift of up to 3000 m is symmetrically distributed on either side of the Rio Grande rift (‘*RG*’ in Fig. 2.12). Around 80% of the Basin and Range volcanics are like East Africa nepheline-normative. Whether Basin and Range volcanism reflects a mantle plume (Fitton et al., 1991) or can be attributed to subduction of a segment of the East Pacific Rise over the past 30 Ma (Chapters 2 and 6) remains a matter of contention.

All of the alkali volcanic rocks of the Gregory Rift and its flanks are of sodic affinity (Na_2O–K_2O > 2.0 mass %), a picture that contrasts markedly with the volcanics of the western branch of the rift system.

Western Rift

The narrower Western Rift of East Africa coincides with the western margin of the Tanzanian craton, and emphasizes the control that crustal and lithosphere structure exerts on the location of continental rifting. The volcanic output associated with the Western Rift is far less extensive and voluminous than in the Gregory rift, and is notable for its potassic silica-undersaturated affinity over the past 3 Ma (though between 11 and 6 Ma BP tholeiitic and sodic alkali volcanics were erupted here – see Kampunzu et al., 1998). The ultrapotassic kamafugites characteristic of recent volcanism in the western rift are described in Box 9.8. Erupted carbonatites are known from Fort Portal in the north.

The plutonic Gardar alkali province in South Greenland

The magma plumbing and intrusions likely to underlie a continental alkali volcanic province

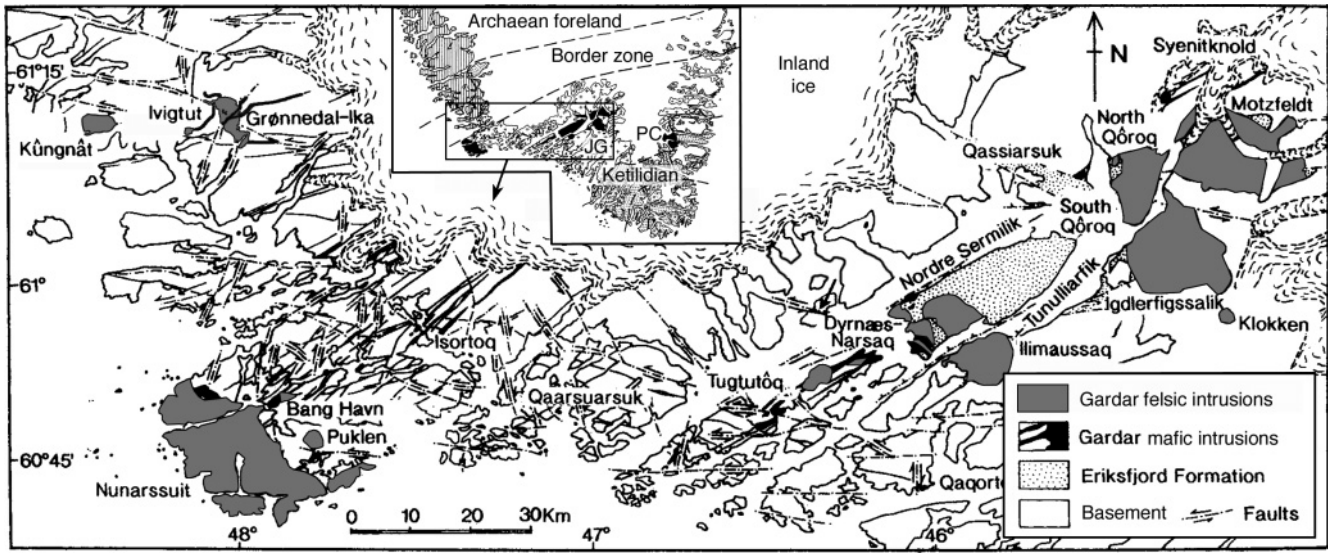


Fig. 9.15 Map of the mid-Proterozoic Gardar alkali province in South Greenland (see inset map) adapted from Upton et al. (2003), showing the distribution of the downfaulted Eriksfjord Formation of subaerial lavas and sediments, the Gardar dyke swarms and the mafic and felsic plutons. Gardar magmatism is concentrated in three SW–NE zones: (i) Ivigtût-Grønnedal, (ii) Nunarssuit-Isortôq and (iii) Tugtutôq-Motzfeldt. The inset map shows the location of the Gardar Province in relation to the Archaean craton and the 1850–1600 Ma Ketilidian orogen; JG, Ketilidian Julianehåb Batholith; PC, Paatusoq Complex (a newly discovered syenite pluton of Gardar age – others may lie beneath the intervening icecap.).

such as the Gregory Rift today can be appreciated by examining older, exhumed plutonic provinces of similar compositional affinity, such as the mid-Proterozoic Gardar alkali province in South Greenland (Upton et al., 2003) or the Permian Oslo province in southern Norway. The Gardar province, now superbly exposed by glaciation, was emplaced during three episodes of magmatism that took place between 1350 and 1140 Ma BP. Figure 9.15 shows that it consists of:

1 a fault-bounded basin preserving a 3-km-thick sequence of subaerial alkali basalt/hawaiite lavas and clastic sediments (the Eriksfjord Formation);
2 three NE–SW zones of mainly mafic dyke swarms, including a number of massive composite dykes as much as 800 m in width;
3 plutons with circular or elliptical surface outcrop concentrated within these zones, consisting largely of syenite or granite, probably emplaced 5 ± 2 km below the surface.

Comparing the Gardar plutonic province to the volcanics of the Gregory Rift and surrounding areas highlights numerous points of similarity (Macdonald and Upton, 1993), including:

- The location of the Gardar rift and most of the associated magmatic province – within a Proterozoic orogen bordering the Archaean craton of Greenland (Fig. 9.15) – resembles the distribution of Cenozoic rifts bordering the Tanzanian craton in East Africa (Fig. 9.3).
- The mildly alkali mafic dykes and the high volume percentage of felsic rocks in the Gardar Province are reminiscent of the transitional basalts, mugearites, benmoreites, trachytes and occasional alkali rhyolites of association 3 in the Gregory Rift.
- Sparse ultramafic lamprophyres (Box 9.6) and related lavas, sometimes containing mantle xenoliths and associated with carbonatite, are analogous to the nephelinite-carbonatite association of EARS.

Box 9.6 Lamprophyres

Lamprophyres make up a diverse, polygenetic rag-bag of *porphyritic dyke rocks** that share a name on account of one distinctive unifying attribute easily recognized in the field: they have phenocrysts of solely mafic minerals (usually biotite or amphibole), with feldspars and/or feldspathoids confined to the groundmass. Owing to the common association of lamprophyres with granitoid plutons, they were mentioned briefly in Chapter 8 (along with appinites). Minor intrusions of lamprophyre affinity are common in other settings too, however, and – since most have alkali compositions (Fig. 9.6.1) – it is appropriate to review their petrology and occurrence from a wider standpoint here. Lamprophyres have been described by Rock (1987) as being

'*among the most widespread of alkaline rocks*'.

Interpreted in the broadest sense, the lamprophyre family extends from holomelanocratic to mesocratic in mineralogical constitution. Lamprophyres are typically intruded at a late stage in igneous centres where they occur (Rock, 1977). Though they overlap in chemical composition with other igneous rock types (Fig. 9.6.1), they cannot be dismissed as mere textural variants of the plutonic or volcanic rocks with which they are associated in the field. Common (though not universal) characteristics by which they stand out include:

- a banded or zoned internal structure within the dyke, suggesting flow differentiation or multi-stage intrusion;

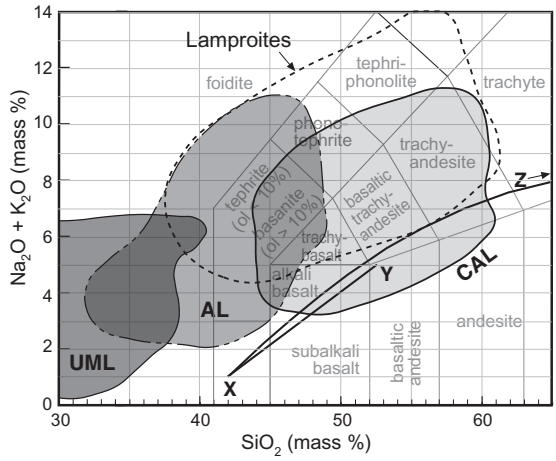


Fig. 9.6.1 Compositional fields of ultramafic lamprophyres (UML), alkali lamprophyres (AL) and calc-alkaline lamprophyres (CAL) after Rock (1987), mapped on to an IUGS TAS plot emphasizing (i) the alkali character of nearly all lamprophyres, (ii) the extent of overlap between established lamprophyre groups; (iii) their overlap in TAS space with lamproites (dashed line) and other igneous rock types. Boundaries (reproduced here by permission of the Geological Society of London) were drawn by Rock (1987) to enclose 95% of the available analyses of each group, avoiding outlying (and possibly inaccurate) data.

*Lamprophyres also occur more rarely as sills, plugs and stocks; associated breccias are common.

- centimetre-scale globular **ocelli** of carbonate or silicate composition, seemingly formed as droplets of immiscible melt separated from the host magma;
- evidence of high magma volatile content in the form of primary calcite, zeolites or other hydrous minerals normally considered to have a hydrothermal origin;
- Selective alteration is common: if mafic minerals are altered, the felsic minerals are often fresh, and vice versa (Rock, 1987).

On the basis of mineralogy, composition and tectonic association, Rock (1987) distinguished three groups of lamprophyres:

- *calc-alkali lamprophyres* (CAL in Fig. 9.6.1) characterized by *biotite* or *hornblende* phenocrysts with alkali feldspar or plagioclase in the groundmass (foids are absent). CALs are associated with granitoid plutons in orogenic belts.
- *alkali lamprophyres* (AL) characterized by *kaersutite* (Fig. 9.4.1) or zoned *titanian augite* (Box 2.1) phenocrysts in a groundmass containing feldspars and foids. ALs are associated with syenite-gabbro or alkali rock-carbonatite complexes in continental rift valleys and cratons.
- *ultramafic lamprophyres* (UML) characterized by the presence of phenocrysts of phlogopite, olivine and/or augite in a groundmass containing *perovskite*, *carbonate* and/or *melilite*; varieties with SiO_2 contents as low as 20% are transitional to carbonatite. UMLs are less common than other lamprophyres and are associated with alkali ultramafic-carbonatite centres and syenites in continental rifts (e.g. Downes et al., 2005).

Most UMLs have SiO_2 contents less than 36% whereas most CALs have SiO_2 contents above 46% though there are significant overlaps between groups (Fig. 9.6.1). Rock (1987) included lamproites and kimberlites within a broader 'lamprophyre clan' but this association is not recognized by IUGS (Le Maitre, 2002).

Lamprophyre nomenclature suffers from a profusion of varietal names as outlined in Table 9.6.1.

Table 9.6.1 Varietal names for lamprophyres. Group names are from Rock (1987) – see Fig. 9.6.1). Inequalities refer to relative abundance: thus 'biotite > hornblende' stands for 'biotite is more abundant than hornblende'. 'Ti-augite' refers to titanian augite described in the caption to Fig. 2.1.1.

Group	Lamprophyre name	Main phenocryst minerals	Felsic mins in groundmass
CAL	minette	biotite > hornblende	alkali feldspar > plag
	vogesite	hornblende > biotite	alkali feldspar > plag
	kersantite	biotite > hornblende	plag > alkali feldspar
	spessartite	hornblende > biotite	plag > alkali feldspar
AL	sannaite	kaersutite ± Ti-augite	(alkali fsp > plag) >foid
	camptonite	kaersutite ± Ti-augite	(plag > alkali fsp) >foid
	monchiquite	kaersutite ± Ti-augite	analcite ± glass
UML	alnöite	phlog ± olivine ± augite	melilite ± perovskite ± calcite
	aillikite	oliv ± HCP ± amph ± phlog	calcite ± perovskite
	damkjernite*	biotite ± Ti-augite	nepheline ± calcite ± alk fsp

* This is the established name, albeit based on a mis-spelling of the Norwegian type locality 'Damtjern'.

- The Tugtutôq-Motzfeldt NE–SW dyke zone in the Gardar exhibits a narrow axial gravity high – implying a complementary mass of dense mafic igneous rocks lying at greater crustal depths – similar to that associated with the Gregory Rift in East Africa (Fig. 9.14). No broader negative anomaly is seen beneath the Gardar, however, in keeping with its much greater age and thicker lithosphere.

Macdonald and Upton (1993) have drawn a parallel between the Tugtutôq-Ilímaussaq dyke zone in the Gardar province (where extension – represented by the down-faulted block and subsequent intense dyke emplacement – was followed by emplacement of central plutons) and the Erte'Ale range in the Danakil Depression of Ethiopia, where basaltic fissure eruptions in the rapidly extending axial zone of the Ethiopian Rift were succeeded by the construction of trachytic and rhyolitic central volcanoes and related caldera complexes, whose roots may resemble the Gardar central plutons.

A notable difference between the two provinces, however, is that Gardar basaltic rocks possess higher Al_2O_3/CaO ratios than the transitional basalts of East Africa, a magma characteristic thought to lie behind the abundance in mafic Gardar dykes of plagioclase megacrysts (Macdonald and Upton, 1993). These 'Big Feldspar Dykes' have no volcanic analogue in East Africa, but suggest the presence at deeper crustal levels beneath the Gardar of Proterozoic anorthosite complexes similar to those in contiguous parts of eastern North America and the Baltic Shield (Figs. 4.13 and 4.14).

Continental anorogenic provinces less clearly associated with rifting

Cameroon–Gulf of Guinea

The 'Cameroon Line' is a prominent 1600-km-long volcanic chain that extends north-east-wards from Pagalú Island in the Gulf of Guinea almost as far as Lake Chad, alongside the NW margin of the Congo craton (Fig. 9.16). It consists of both volcanic islands and seamounts in the Gulf of Guinea and continental volcanoes – including four large central volcanoes in Cameroon and extensive lava plateaux in Cameroon and Nigeria (Fitton, 1987; Déruelle et al., 2007). Early anorogenic intrusive ring complexes of granite and syenite are associated with the lineament and range in K-Ar age from 66 to 30 Ma (with a few dates of around 10 Ma near Mount Cameroon). K-Ar ages of the volcanic rocks, on the other hand, range from 35 Ma to the present. There is no correlation between age and geographical location that might suggest Pacific-style plate migration over a fixed hot spot. Mount Cameroon (4095 m high, West Africa's highest mountain) is still active – erupting 6 times between 1868 and 2000 – and several other volcanoes exhibit morphologically recent scoria cones. The volcanic rocks of the chain are predominantly of alkali type, varying in composition from transitional basalt to nephelinite at the primitive end of the differentiation spectrum, and at the evolved end from alkali rhyolite (dominant in the continental part of the chain) to phonolite (prevalent in the oceanic sector).

The petrological range of the Cameroon line volcanic rocks is similar to those of the Kenya rift, yet here

> '*no rift faulting or graben structures have been observed along the continental sector … and most of the magmatism has been associated with central rather than fissure volcanoes*'

(Fitton, 1987), though according to a more recent study (Déruelle et al., 2007)

> '*the continental sector is a succession of horsts and grabens*'.

Fitton (1987) noted that the Y-shaped distribution of continental Cameroon Line volcanism (Fig. 9.16) resembles the shape of the Benue Trough (a Cretaceous rift with its own scattered volcanic suite erupted in three periods of 147–106 Ma, 97–81 Ma and 68–49 Ma according to Coulon et al. (1996), forming part of an extended system of rifts that spread across central Africa during the Cretaceous), though any connection is still poorly understood.

Kimberlites and cratons

Kimberlite is virtually the only Phanerozoic magma to ascend through and be emplaced

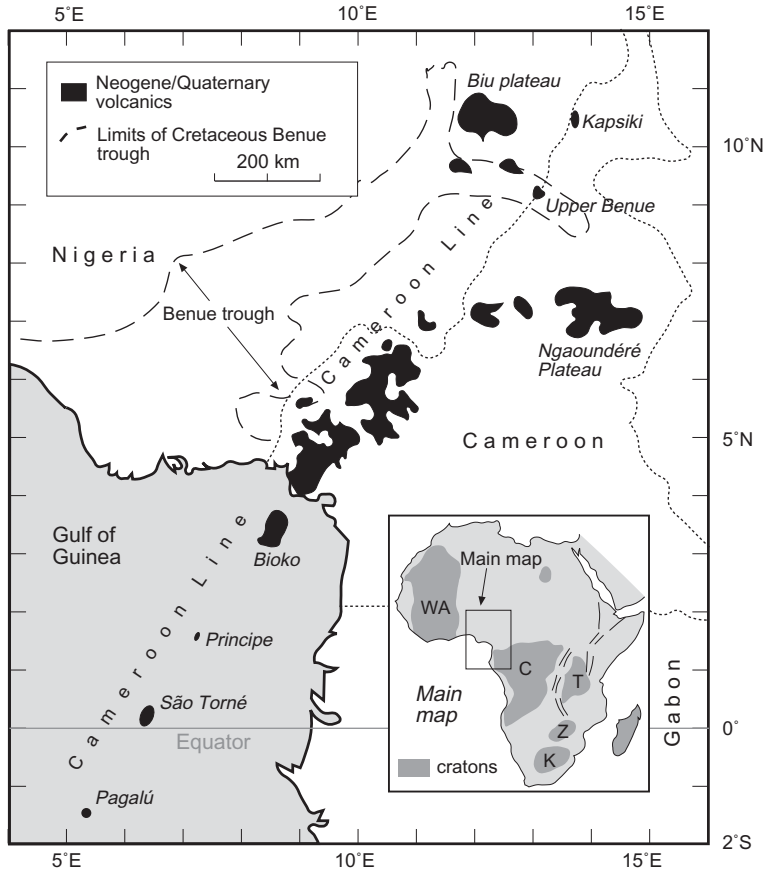


Fig. 9.16 Map of west-central Africa showing the distribution of Neogene–Quaternary volcanic rocks of the 'Cameroon Line' and related centres (after Fitton, 1987*). The location of the main map area is shown in the index map, as are Archaean cratons (see Fig. 9.3 caption for abbreviations).

*By permission of the Geological Society of London.

within stable cratons. The distribution of kimberlite intrusions and their economically important diamond content correlate with Archaean cratons and the Proterozoic mobile belts that form their margins, as described in Box 9.7.

Subduction-related alkali rocks

As mentioned in Chapter 6, small volumes of high-K alkali volcanic rocks are associated with a number of island arcs and continental arcs, usually being found on the back-arc side away from the trench (Fig. 6.16). Some other examples of subduction-related high-K alkali rocks are considered below.

Potassic volcanic rocks of Italy

> *'Italian volcanism is one result of the collision between the African and Eurasian tectonic plates. The complex nature of the collision is masked by the apparently simple arrangement of Italy's volcanoes along a front extending from … Monte Amiata in Tuscany, past the Campanian volcanoes and Etna, to the tiny island of Pantelleria* [Fig. 9.17]. *In detail however this front consists of interacting segments that can be distinguished by the age, clustering and chemistry of its component volcanoes.'* (Kilburn and McGuire, 2001)

The Quaternary has seen volcanoes erupting at various times along the length of the Italian peninsula and beyond, from Tuscany in the north to Sicily and Pantelleria in the south. The volcanoes exhibit a remarkable diversity of magma type for such a small geographical area. Some volcanoes like Etna and centres on the island of Pantelleria have sodic alkali

affinity (see black triangles in Fig. 9.17): thus Etna currently erupts mainly hawaiites,[16] while Pantelleria is the type-locality for *pantellerite* – a peralkaline variety of alkali rhyolite – which has erupted on the island both as ignimbrites during large caldera-forming pyroclastic eruptions (producing some Tenerife-like welded fall deposits too) and as lava flows. The majority of Italian volcanoes, however, are to varying degrees potassic in composition.

The Aeolian arc of seven volcanic islands and a similar number of seamounts, lying just north of Sicily, is mostly younger than 1 Ma and includes the archetypes Vulcano and Stromboli (Fig. 9.17) whose names today are synonymous with styles of eruption (Fig. 7.8). Most of the magmas erupted from Vulcano belong to a single high-K basalt to high-K rhyolite trend (Fig. 6.11), though the island has exhibited a rich repertoire of eruptive style from simple stratovolcano, to caldera formation and filling with lava domes, to the vulcanian style characteristic of the present Fossa cone (see Chapter 7). Stromboli, on the other hand, has erupted a variety of magma types during its history (calc-alkaline, high-K, shoshonitic and potassic), both as lavas and pyroclastics. Its current strombolian style of eruption (interspersed with occasional larger explosions, and with episodes of lava effusion as seen in 2002–3 and in March 2007) has persisted for thousands of years.

[16] The initial volcanism from Etna – erupted between 500 and 200 ka ago – consisted of tholeiitic basalts. Between 30 and 20 ka it erupted hawaiite, mugearite and trachyte.

Box 9.7 Kimberlite

Kimberlite is an ultramafic (and ultrabasic) rock defined according to textural as well as compositional attributes. An unaltered kimberlite consists of relatively large, rounded-to-anhedral crystals (0.5–10 mm in size) of olivine and other mafic minerals, set in a finer-grained matrix (Plate 9.1). Whether the larger crystals are **cognate** (i.e. phenocrysts) or not is often unclear, and as they are sometimes evidently fragments of larger crystals they are referred to as *macrocrysts*, a descriptive term deliberately free of genetic implications (Mitchell, 1986). The macrocrysts are chiefly of olivine, but may also include phlogopite, garnet, diopside, enstatite, magnesian ilmenite and/or chromite. The matrix of a kimberlite typically includes (in addition to olivine, phlogopite, perovskite, spinel and apatite) primary carbonates and serpentine, suggesting that it has crystallized from a volatile- (chiefly CO_2-) rich magma. Many kimberlites contain rounded-to-subangular xenoliths of mantle lithologies (e.g. lherzolite, harzburgite, eclogite) and related xenocrysts, as well as xenoliths of lower crustal origin such as granulite and gneiss. Some kimberlites are of economic interest for containing diamond xenocrysts; typical yields from productive diatremes are about 25–50 carats per 100 tonnes.

Kimberlite typically occurs as tabular dykes or sills at deeper levels that pass upward into a near-surface horn-shaped **diatreme** filled by volcaniclastic debris (Fig. 9.7.1). The hypabyssal facies found in minor intrusions consists of hard, fresh, dark grey/green/black rocks with a macrocryst texture (Plate 9.1), known as *hypabyssal kimberlite* (HK). Diatreme facies kimberlite consists of angular-to-rounded country-rock xenoliths, kimberlite clasts and *pelletal* ***lapilli*** – distinctive rounded pellets containing serpentinized olivine and other macrocrysts, set in a finer matrix of microcrystalline diopside and serpentine (Plate 9.2). This vent assemblage is widely known as *tuffisitic kimberlite breccia* (TKB), though the term *massive volcaniclastic kimberlite* (MVK) is now preferred (Mitchell, 1986; Sparks et al., 2006). At most kimberlite localities the overlying crater facies has been removed by erosion.

The occurrence of kimberlites is restricted to ancient continental cratons, where lithosphere tends to be at least 150–200 km thick. Clifford (1966) was the first to note that diamond-bearing kimberlites in Africa are confined to the Archaean cores of these cratons (regions that have been stable for more than 2.4 Ga, according to Mitchell, 1986); kimberlites found in the surrounding Proterozoic mobile belts, on the other hand, are barren of diamond.

Most kimberlites are Palaeozoic or Mesozoic in age.

Compared to the arc-like character of Aeolian Island volcanism, Quaternary volcanism further north on the Italian mainland has been more alkaline and generally of potassic and/or ultrapotassic character. Thus the volcanoes of the Roman province (e.g. Vulsini) include a wealth of leucite-bearing lavas and ignimbrites, and the province also includes the **kamafugite** volcanoes at Cupaello and San Venanzo (Box 9.8). The Campanian volcanoes around Naples erupt shoshonites (see below), leucite basanites and leucitites.

The shoshonite suite

Shoshonites and latites are mildly potassic trachybasalts and trachyandesites (Fig. 9.2). They are found in three tectonic settings (see literature cited by Gill et al., 2004):

- propagating rifts in intra-oceanic island arcs and back-arc basins, such as the Izu–Bonin–Mariana arc system (see the box marked 'S' in Fig. 6.18), the Tabar-Lihir-Tanga-Feni islands in NE Papua New Guinea and in Fiji, usually in association with calc-alkaline volcanism.
- rift-zones in continental magmatic arcs such as the Cascades in the western USA, in association with low-, medium- and high-K calc-alkaline volcanics.
- post-collisional settings such as the Tibetan plateau and the Alps, where an elevated orogen may undergo gravity-controlled extensional collapse and associated litho-

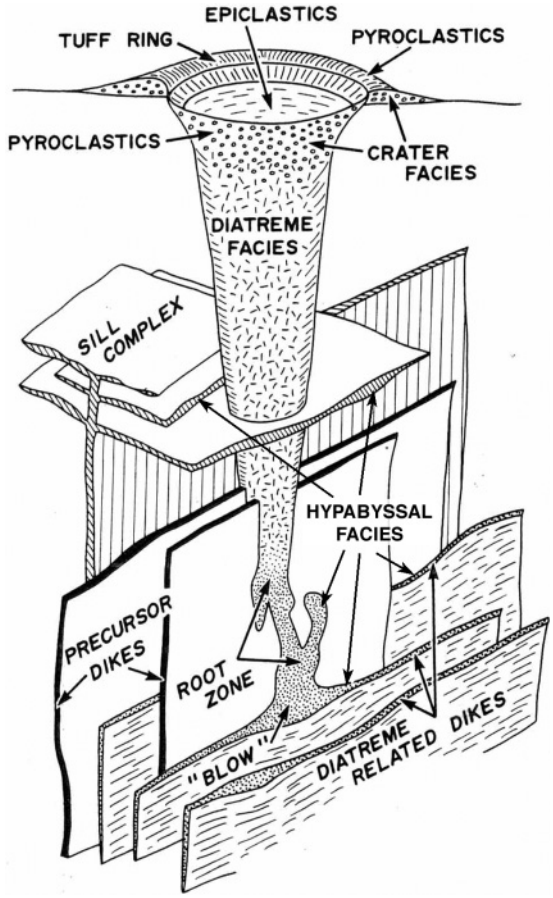


Fig. 9.7.1 Model of an idealized kimberlite plumbing system (after Mitchell, 1986, by kind permission of the author and Springer Science and Business Media). The vertical dimension is between 1 and 3 km.

Box 9.8 Ultrapotassic rocks

The lowest division of rocks in Table 9.2 consists of diverse continental volcanic rocks that share the distinction of being **ultrapotassic**. They fall into two broad categories that differ in silica content:

- *Kamafugites** are ultrabasic volcanic rocks (Fig. 9.8.1) found in some continental rifts, notably the western branch of the East African rift system;
- *Lamproites* are basic to intermediate lavas and hypabyssal rocks that occur in various post-orogenic settings.

The term *kamafugite* embraces a range of rare mafic volcanic rocks consisting essentially of olivine ± melilite ± leucite ± kalsilite (Plates 9.9 and 9.10). As the mineralogy implies, they are thoroughly silica-undersaturated and have ultrabasic compositions (Fig. 9.8.1). The type-kamafugites occur in the active Toro-Ankole volcanic province, lying to the north and south of Lake Kivu in the western rift valley** of East Africa (Fig. 9.3). Similar volcanics are also found in a few other parts of the world, where the tectonic context is less clear, such as the Quaternary San Venanzo and Cupaello volcanoes of central Italy (*SanV* and *C* in Fig. 9.17).

Most *lamproite*s, on the other hand, have basic to intermediate compositions. They share some features with kimberlite, often containing depleted dunite and harzburgite xenoliths and sometimes diamond xenocrysts too; in fact the yield of diamonds from lamproites is usually richer than in kimberlite diatremes (~500 carats/100 tons as compared to 20–80 carats/100 tons, according to Mitchell and Bergman, 1991). Lamproites are mafic to ultramafic but few are ultrabasic (Fig. 9.8.1). In mineralogical terms lamproites are highly diverse and thus difficult to define by petrography alone: they may contain olivine, diopside, enstatite, phlogopite (Plate 9.3), K-richterite (Fig. 9.4.1), leucite and/or sanidine as major minerals (Table 9.2), plus a host of other minerals as accessories. They do *not* contain plagioclase, melilite or kalsilite. Many lamproites have a glassy (Plate 9.3) or very fine-grained matrix. Their mineralogical diversity and scattered occurrence have spawned a plethora of redundant varietal names (Le Maitre, 2002) that are best abandoned in favour of systematic names: for example, 'diopside-phlogopite-leucite lamproite' – being more informative – is preferable to 'wyomingite'. The unifying feature is that all lamproites are ultrapotassic in composition while being relatively SiO_2-rich (Fig. 9.8.1). In contrast to kimberlites, they contain more H_2O^+ than CO_2. Rock (1987) suggested a relationship between lamproites and certain types of lamprophyre (Box 9.6), but such a link is conjectural.

*This odd-sounding name, introduced by Sahama (1974), is a contraction of the older rock names katungite, mafurite and ugandite (whose individual meanings need not concern the reader).
**The volcanic rocks of the western branch of the East African rift system (Fig. 9.3) are more potassic than those of the eastern 'Gregory' rift.

spheric thinning. Granitoid intrusions of similar composition in older collisional belts such as the Fennoscandian shield reflect analogous magmatism in older orogens.

The Campanian shoshonites mentioned in the preceding section are most easily regarded as falling in the third of these environments.

Lamproites and the aftermath of continental collision

The tectonic context for lamproite volcanism is sometimes hard to identify (Box 9.8), but it most commonly occurs in a post-collisional setting, and may (as in southern Tibet) be related to late extension associated with the gravitational collapse of the orogen (Gao et al., 2007).

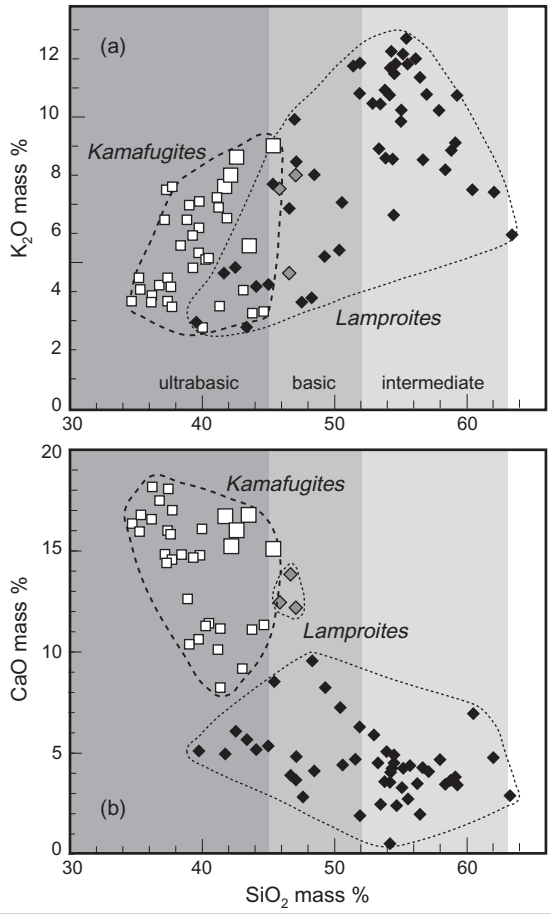


Fig. 9.8.1 Major-element comparisons between kamafugites and lamproites. Kamafugite data are for Toro Ankole in East Africa ('***T-A***' in Fig. 9.3; small squares, El Hinnawi, 1965) and San Venanzo and Cupaello volcanoes in central Italy (larger squares, from Gallo et al., 1984). The lamproite data, taken from several continents, are from Mitchell and Bergman (1991); the grey diamonds represent anomalous examples with phlogopite oikocrysts from Leucite Hills in Wyoming. (Analyses require recalculation to volatile-free form for plotting in these diagrams.)

Lamproites may occur as lava flows, dykes, volcanic pipes or tuff rings. They occur in a variety of continental settings, for example as a late event in orogens that have undergone extensional collapse, as in southern and northern Tibet and SE Spain. In other cases the tectonic setting is more enigmatic; the Leucite Hills lamproites in the western USA, for example, lie close to the boundary between the Wyoming Archaean craton and the Colorado Plateau, where the Cretaceous Laramide orogeny represents the most recent tectonism (Mirnejad and Bell, 2006). All major lamproite occurrences are Cenozoic in age.

HOW ARE ALKALI MAGMAS FORMED IN THE EARTH?

Alkali rocks pose major challenges to our understanding of magma genesis owing to their compositional diversity and the range of environments in which low-volume alkali magmatism may occur. For some classes of alkali rocks (such as shoshonites), petrologists still lack a plausible, comprehensive explanation.

One may reasonably suppose that the melting processes and conditions within the Earth that generate the spectrum of basic and ultrabasic alkali melts shown in Fig. 9.1a are qualitatively similar to those proposed for generating basaltic melts in the final section of Chapter 2 (see Fig. 2.18). In making this assumption, however, we need to explain why, in the present context, mantle processes give rise to alkali and often silica-undersaturated parent magmas – like those of the East African rift – rather than the subalkali basalts that characterize mid-ocean ridges, LIPs and the larger ocean islands like Hawai`i. We begin by discussing some geochemical clues.

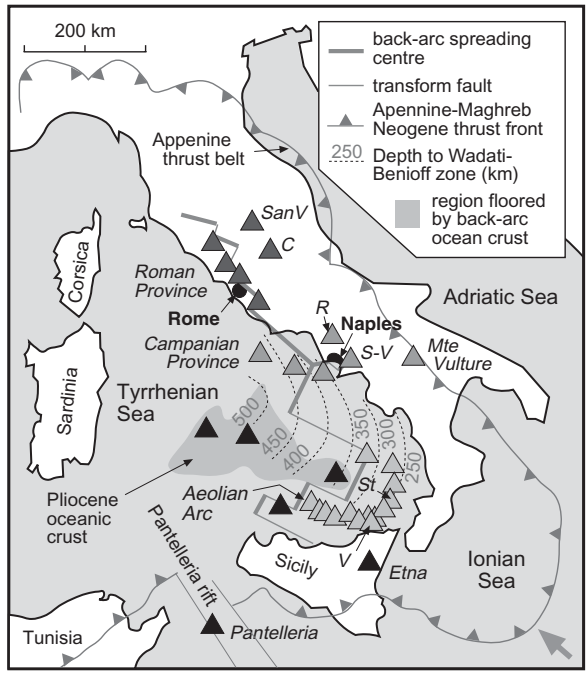


Fig. 9.17 Map showing Quaternary volcanoes of Italy (triangles). *C,* Cupaello; *R,* Roccamonfina; *SanV,* San Venanzo; *St,* Stromboli; *S–V,* Somma–Vesuvius; *V,* Vulcano. Black triangles signify sodic alkali basalt–trachyte volcanoes; other triangles are shaded according to the province to which each volcano belongs. The Appenine–Maghreb thrust front (suture zone) and the inferred back-arc spreading centres and transform faults in the Tyrrhenian Sea back-arc basin and in western Italy are from Turco and Zuppetta (1998). The zone of intermediate and deep focus earthquakes beneath southern Italy is shown by depth contours in km (after Panza and Suhadolc, 1990).

Geochemical evidence

SiO_2 content of mantle partial melts – undersaturation and depth of melting

Partial melting experiments on mantle peridotites summarized in Fig. 9.18 show that the silica contents of melts formed are sensitive to the pressure under which the experimental melting is carried out. The relatively large scatter in the data points in Fig. 9.18 arises partly from the use of two different peridotites as starting materials, and partly from the fact that melting experiments at each pressure were conducted at several temperatures (i.e. over a range of melt %). The underlying trend is nonetheless clear: melts formed in equilibrium with peridotite at high pressure have significantly lower SiO_2 contents than analogous melts formed at low pressure. One explanation for the SiO_2-undersaturation characteristic of many mafic alkali rocks, therefore, could be that they represent magmas formed by partial melting at higher pressures (i.e. at greater depths – Fig. 9.18 top scale) than subalkali magmas. Many basic alkali magmas are erupted from volcanoes located on relatively thick lithosphere, where the depth of melting in the asthenosphere beneath may be controlled by the thickness of the overlying, more refractory lithosphere.

The degree of silica-saturation of basic and ultrabasic magmas, as we have seen, exerts an overriding influence on the character of the evolved magmas that form from them by high-level fractional crystallization (Figs. 9.7b and 9.12).

Incompatible element enrichment and degree of melting

A key characteristic of basic and ultrabasic alkali magmas is their enrichment in highly incompatible trace elements (HITE) compared to most subalkali basic magmas. This is illustrated in general terms in Fig. 9.19, where the Rb, Ba and Th contents of alkali rocks extend from 40× to almost 1000× primitive mantle. A more specific illustration of this difference may be obtained by comparing the two OIB patterns – both from the Hawaiian islands – shown in Fig. 2.18(a). The post-erosional Hawaiian alkali basalt from the island of Kauai (Table 2.4 column 4) contains consistently more Rb, Ba, Th, Nb, K, La, Ce, P and Nd than the Hawaiian tholeiite from Kilauea (Table 2.4, column 3). The difference cannot be attributed to differing degrees of fractional crystallization, since the two samples have very similar Mg numbers (64.4 and 63.3 respectively – see exercise 5.3b).

One way to explain differing levels of HITE enrichment in magmas likely – as here – to be derived from similar sources is to postulate that the more enriched alkali basalt magma was the product of a *lower degree of partial*

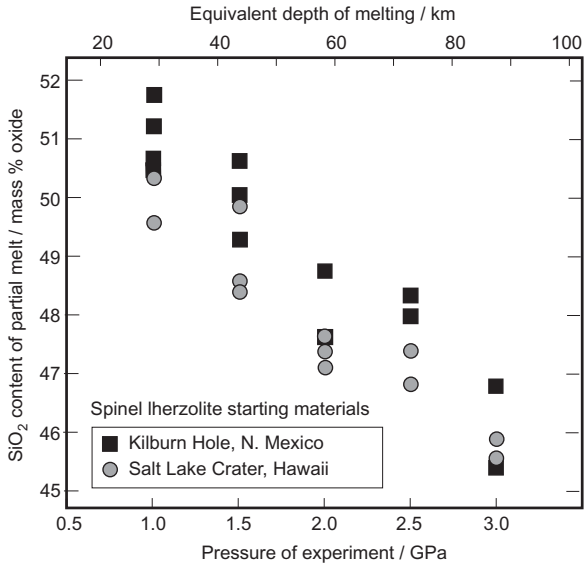


Fig. 9.18 Pressure-dependence of melt SiO_2 content in partial melting experiments on two natural spinel lherzolites (from Hirose and Kushiro, 1993) with permission of Elsevier. The high-pressure experimental charges included aggregates of small diamond crystals to provide void space into which low-degree partial melts could segregate; after **quenching**, melt compositions were determined by **electron microprobe** analysis of the chilled glass trapped between the diamonds. This allows reliable analysis of smaller melt fractions than conventional techniques.

melting, since low-degree melts are more enriched in such elements than higher degree melts (Box 9.9). Note however that the OIB alkali basalt has very similar HREE enrichment to the OIB tholeiite (Yb is actually slightly lower). The OIB's higher La/Yb ratio may reflect residual garnet in the alkali basalt mantle source, buffering the HREE and Y concentrations of the parental primary melt (Box 6.6).

Both the lower SiO_2 content of basic and ultrabasic alkali magmas and the lower degree of melting they seem to represent, are consistent with melting beneath thick lithosphere. Figure 2.17 shows how, for a given potential temperature, the degree of melting increases as asthenospheric mantle upwells to shallower depths. A thick lithosphere, generally assumed to have a refractory major-element composition resistant to partial melting, inhibits this upwelling and therefore dictates that melting is confined to greater depth, where only relatively small degrees of melting are possible. The applicability of this explanation for alkali magmatism in various settings is evaluated below.

Incompatible element enrichment from continental lithosphere?

The spidergrams for alkali basalts, basanite, mugearite and tephrite from Hawai'i, Tenerife and Kenya form a relatively coherent grouping (reproduced as the grey band in Fig. 9.19b), and much of the limited variation among them can be explained by varying degrees of fractional crystallization (since it correlates with Mg number). The fact that continental alkali basalts and alkali rocks from ocean islands have similar trace element signatures suggests a common ultimate derivation for such magmas from *sub-lithospheric* sources of similar composition: the differences between oceanic and continental lithosphere composition seem to have had relatively little impact on the character of these alkali magmas.

The picture is strikingly different for some of the other alkali rocks featured in Fig. 9.19. The Wesselton kimberlite, the Nyiragongo leucite nephelinite (Fig. 9.19a), the Gaussberg lamproite and the Cupaello kamafugite (Fig. 9.19b) all show substantially greater HITE enrichment. Though one could appeal to even lower degrees of melting of the same sub-lithospheric sources to explain these patterns, there comes a point where the proportion of melt formed would be so small that physically extracting it from the source is not feasible. It is also significant that all of these highly enriched examples come from continental regions having an extended geological history, and petrologists increasingly take the view that such high levels of enrichment testify to interaction of melt with subcontinental lithospheric mantle (**SCLM**) during ascent, or even to partial melting of the SLCM itself.

Detailed study of mantle xenoliths in kimberlites and some lamproites during recent decades has made clear that old SCLM has a

Box 9.9 Incompatible elements in partial melting

A highly incompatible trace element cannot be accommodated in crystals of the main rock-forming minerals present in the upper mantle (olivine, LCP, HCP, spinel and garnet). Atoms of such elements (Rb, Ba, Th, Nb, etc.) presumably reside in minute crystals of accessory minerals located along grain boundaries between, or as inclusions within, the major mineral crystals. This situation is illustrated in cartoon form in Fig. 9.9.1(a).

When partial melting begins, highly incompatible element atoms are extracted from grain boundaries into the small pockets of melt that form at appropriate grain intersections (Fig. 9.9.1b: cf. Box 5.4). As all incompatible element atoms are confined within these small pockets of melt, they are present at high concentration. As partial melting progresses, the same atoms become diluted in a larger volume of melt (Fig. 9.9.1c).

Thus when a given mantle source rock is partially melted and the products erupt at the surface, the initial melt delivered by small degrees of melting will be characterized by high concentrations of highly incompatible elements. Magmas representing higher degrees of melting will contain lower concentrations of these elements owing to dilution. This behaviour is described mathematically by the *partial melting equation*:

$$C_i^{\text{melt}} = \frac{C_i^0}{D_i + F(1 - D_i)} \qquad [9.9.1]$$

where C_i^{melt} is the concentration (ppm) of trace element i in the melt, C_i^0 is the bulk concentration (ppm) of trace element i in the pre-existing solid, F is the melt fraction (between 0 and 1) and D_i is the bulk distribution coefficient for trace element i in the solid mineral assemblage:

$$D_i = x^{\text{A}}K_i^{\text{A}} + x^{\text{B}}K_i^{\text{B}} + x^{\text{C}}K_i^{\text{C}} + x^{\text{D}}K_i^{\text{D}} + \ldots \qquad [9.9.2]$$

where x^{A} is the mass fraction of the mineral A in the solid mineral assemblage (A + B + C + D + …) undergoing melting, and K_i^{A} is the partition coefficient for trace element i between mineral A and melt.

For a highly incompatible element for which $K_i^{\text{A,B,C,D}} \approx 0.0$ and therefore $D_i \approx 0.0$, the partial melting equation reduces to the simpler form:

$$C_i^{\text{melt}} \approx \frac{C_i^0}{F} \qquad [9.9.3]$$

For complete melting, $F = 1$ And therefore $C_i^{\text{melt}} = C_i^0$.

complex chemical evolution. There is general acceptance today that parts of the SCLM have been progressively 'metasomatized' by the slow percolation of carbonate or hydrous fluids and/or low-volume silicate melts that leave behind a net local enrichment in incompatible elements. The veins and dykes seen in orogenic peridotites (Chapter 5) may be a different aspect of the same story. Magmas that subsequently ascend through thick metasomatized SLCM are liable to assimilate this 'metasomatic' component in otherwise depleted peridotite, and this 2-stage process is believed to explain the extreme enrichment in incompatible elements in the four rocks listed above. Note that the Wesselton kimberlite and Nyiragongo nephelinite patterns have high Nb values. The Gaussberg lamproite and the Italian kamafugite, on the other hand, both show marked enrichment of HITE *combined with negative Nb anomalies*, suggesting a subduction-related contribution to the metasomatic enrichment of their lithospheric mantle sources (Chapter 6).

Hot spot-related oceanic alkali basalts and related rocks

Hawai`i and other intraplate islands

Hawai`i and the other Hawaiian islands stand on a broad topographic swell about 1200 km

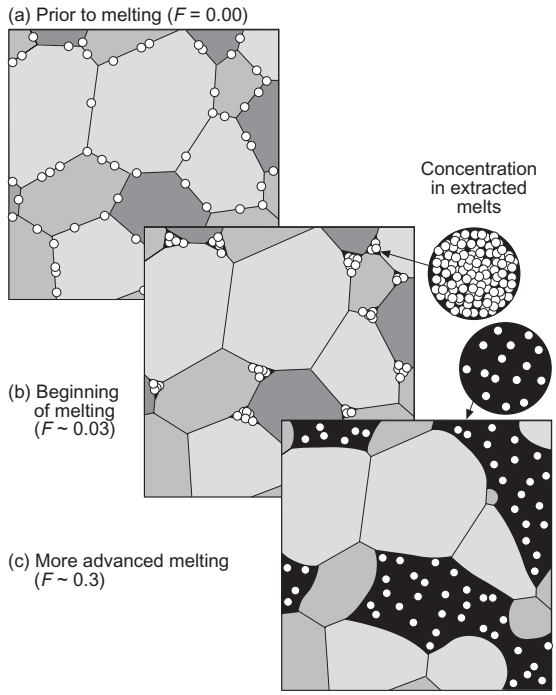


Fig. 9.9.1 Cartoons illustrating the distribution of atoms of a highly incompatible element (white circles) in a simplified mantle lherzolite undergoing partial melting as described in Box 5.4. The number of atoms shown is the same in each diagram; black represents melt. (a) Before melting begins incompatible element atoms, being excluded from rock-forming minerals, reside along grain boundaries. (b) At low degrees of melting, all incompatible element atoms are present (at high concentration) in small pockets of melt at appropriate grain boundary intersections. (c) As melting advances, the same number of atoms undergoes dispersal through a larger volume of melt (i.e. diluted to a lower concentration).

wide (SW–NE) and 3000 km long that rises as much as 1500 m above the surrounding abyssal plains, peaking 200–300 km to the NW of Kilauea (Zhong and Watts, 2002). The most widely accepted explanation for this feature is dynamic support by buoyancy forces deriving from a hot upwelling mantle plume below (Ribe and Christensen, 1999). Immediately surrounding the main island of Hawai`i is a more local moat-like depression of the sea floor, most marked on the NE, caused by flexural loading of the lithosphere by the island's weight.

In the development of individual Hawaiian islands, alkali basalts and other silica-undersaturated basic lavas (stage '1' in Fig. 9.8) seem to be erupted *prior* to the main tholeiitic shield-building phase (*viz.* Loihi), and also after it in the post-caldera and post-erosional stages ('3' and '4' in Fig. 9.8). As the island is carried by Pacific plate motion across the hot spot, this succession may relate to distance from the centre of the plume. One explanation (after Valbracht et al., 1996 and others) involves three stages of interaction between plume and oceanic lithosphere, described here from the perspective of one small volume element in the upwelling plume beneath a Hawaiian island as it is carried by convection up

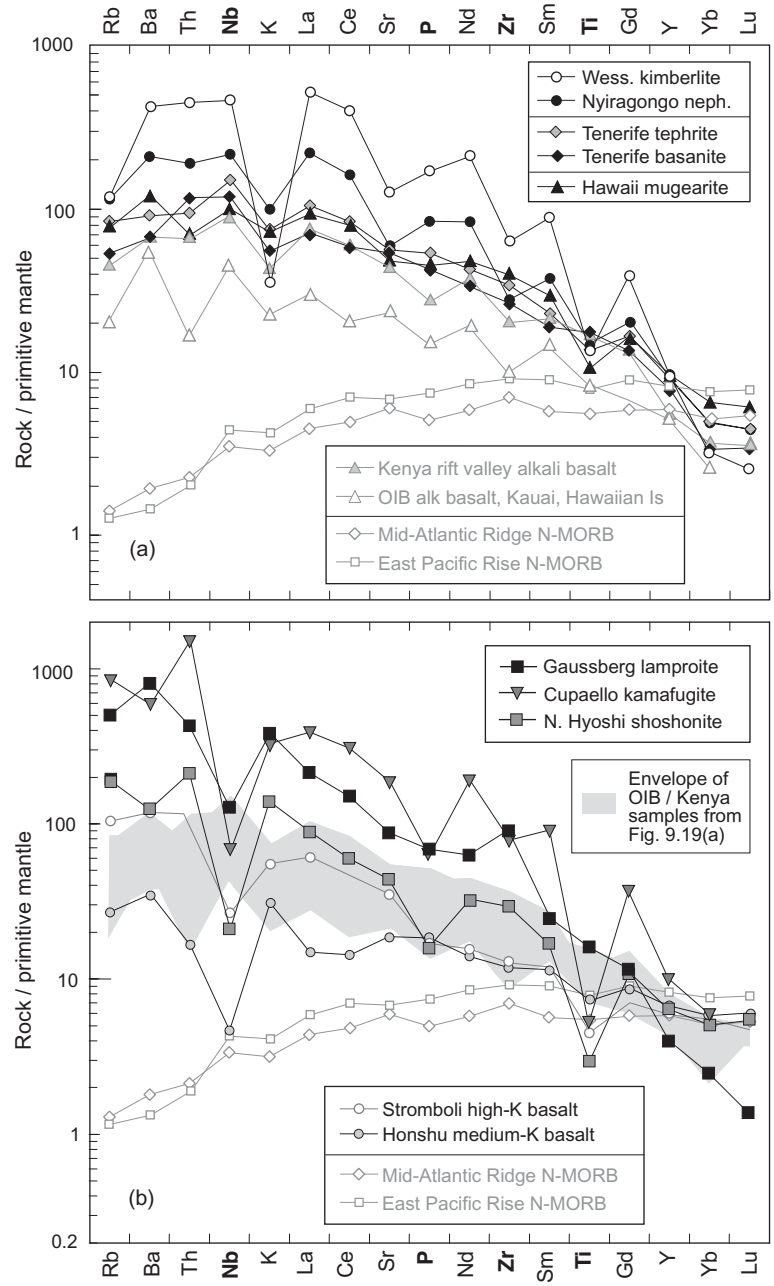


Fig. 9.19 Incompatible element enrichment diagrams for selected basic and ultrabasic alkali rocks (including most listed in Table 9.5). The primitive mantle normalizing factors (after Sun and McDonough, 1989) are tabulated in Table 2.4. Element symbols in **bold** signify **HFSE**. (a) Wesselton aphanitic kimberlite sill (data from Le Roex et al., 2003), Nyiragongo leucite melilite nephelinite, Tenerife basanite and teprite, and Haleakala mugearite from Hawai`i; MORB and alkali basalt patterns from Fig. 2.16 are shown (in grey) for comparison. (b) Patterns for potassic shoshonite from North Hiyoshi (northern Mariana arc), ultrapotassic Gaussberg lamproite (Antarctica) in Table 9.5, and a kamafugite from Cupaello (Fig. 9.17, data from Conticelli and Peccerillo, 1992) compared to medium- and high-K basalts and MORB from Fig. 2.16; the grey band summarizes the OIB and Kenya rift alkali basalt patterns from Fig. 9.19(a) for reference.

the plume stem and laterally into the plume head:

1 Ascending plume material initially undergoes incipient melting at depth, and volatile-rich[17] low-fraction melts escape from the plume volume element and permeate the overlying lithosphere, in which they initiate lithospheric melting to form the alkali and tholeiitic basalts characteristic of Loihi seamount.
2 The same plume volume-element, having ascended to shallower depths, undergoes more advanced decompression melting in the plume's hot axial zone, generating large volumes of shield-building subalkali magma. The post-caldera alkali volcanics may represent a waning phase of this stage as melting retreats to greater depths and lower degrees of melting in peripheral parts of the plume.
3 Low-volume melting supplying the post-erosional alkali magmas (which erupt after a significant hiatus) seems, according to isotopic data, to involve melting of a MORB component, either entrained into the plume itself (Valbracht et al., 1996) or present as invasive pyroxenite veins in the overlying lithosphere (Lassiter et al., 2000). Numerical experiments modelling the interaction between a buoyant plume and a moving lithospheric plate above show a second melting region 300–500 km 'downstream' of the plume axis (Ribe and Christensen, 1999) which may explain the post-erosional stage.

Oceanic island chains where the shield-building stage is formed of alkali basalts rather than tholeiites may (i) have formed on thicker lithosphere than Hawai`i; or (ii) be products of less vigorous (lower-potential temperature) plumes. Because the thickness of oceanic lithosphere increases with age up to about 60 Ma then increases only very slowly thereafter, it is unlikely to become substantially thicker than the 85 Ma-old lithosphere beneath Hawai`i, so (ii) seems the more acceptable explanation for alkali shields.

The Hawaiian plume model is applicable to large oceanic islands like Réunion and Tristan da Cunha (Fig. 2.12) that belong to age-progressive island chains, but it does not work for all intraplate ocean islands. The Canary Islands (including Tenerife) off the NW coast of Africa, for example, lack several of the attributes of the Hawaiian chain: there is no large-amplitude topographic 'swell' like that associated with the Hawaiian hot spot (testifying to a plume beneath), individual islands remain volcanically active for longer than Hawaiian islands and seamounts (all but one of the Canary Islands have been active in the past 5 ka) and melt productivity rates are lower. These differences are difficult to reconcile with the operation of a vigorous steady-state plume beneath the Canary Islands, and other magma genesis mechanisms may be at work, about which there is little consensus.

Many islands and seamounts in the ocean basins are unrelated to age-progressive island chains like Hawai`i, and one cannot reasonably postulate a mantle plume beneath every one. The concept of small-scale fusible 'blobs' within the convecting asthenosphere was mentioned in Chapter 2 as one possible explanation (Fitton, 2003) for the scattered volcanic centres in ocean basins.

Iceland

No volcanic region in the world has been more intensively studied than Iceland yet, in spite of the wealth of geochemical and isotopic data now available, how the origins of the 'off-rift' alkali basaltic and related volcanism differ from the olivine tholeiites and picrites of the main rift zones remains poorly understood. One recent model is illustrated in Fig. 9.20. It shows in cartoon form a cross-section beneath Iceland from Snaefellsnaes to Vestmannaeyjar (*a–b–c* in Fig. 9.9). These points lie at approximately equal radial distances from the supposed plume centre beneath the Vatnajökull ice-sheet. The white area depicts the hot, radially expanding plume-head, with asthenosphere beneath and lithosphere above. The vertical bars represent the melting columns that feed volcanism at *a*, *b* and *c* (in

[17] This characteristic is postulated to explain the primitive He-isotope composition of Loihi lavas, but the details need not concern us here.

three-dimensional these columns may incline toward the plume centre), truncated by lithosphere of varying thickness.

According to Kokfelt et al. (2006), isotopic and trace element data point to two dominant source compositions contributing to post-glacial volcanism: (i) a relatively enriched pyroxenite lithology containing 3%–6% garnet, and (ii) a depleted lherzolite source with less than 2% garnet. In their model both are present within the heterogeneous Iceland plume. The different depths at which these two lithologies *begin* to melt in the adiabatically upwelling plume are suggested by dashed lines in Fig. 9.20. Because the Vestmannaeyjar lie slightly closer to the hot plume centre (Fig. 9.9), melting is shown as beginning somewhat deeper there than beneath Snaefellsnaes. Melting beneath Snaefellsnaes is confined – by the relatively shallow beginning of melting and by the thick refractory lithosphere above – to a narrow depth interval between 80 and 50 km, and it draws mainly on the pyroxenite source which produces enriched alkali basalts. Melting beneath Vestmannaeyjar is subject to the same controls but here the melting interval extends from 100 to 40 km, allowing a greater proportion of melt to be derived from the depleted lherzolite component. Beneath the Reykjanes Peninsula (*b*), however, thin lithosphere permits a substantially greater degree of melting to occur at shallow depth, and here the subalkali magma composition is dictated by more advanced melting, mainly of the depleted lherzolite source.

Plume-related continental rift magmatism

Figure 9.3 shows that East African Neogene volcanism has been associated with the development of two broad topographic 'swells' (regions of domal uplift), one bordering the Ethiopian rift and the other centred on Lake Victoria. Uplift to an elevation of ~3000 m a.s.l. across such wide areas implies dynamic support by a column of anomalously low-density, upwelling mantle beneath each swell – the dimensions are not dissimilar to those of the swell associated with the Hawaiian plume described above. Moreover, during the Neogene, 10^5–10^6 km^3 of volcanic products have been erupted along the length of the Kenya rift (Baker, 1987) and a similar volume is associated with the Ethiopian rift (Rogers, 2006). Volcanic output on this scale, taking into account the correspondingly large volume of high-density magma also intruded into the crust (Fig. 9.14), implies elevated potential temperatures in the mantle below. Uplift and magmatism together point unambiguously to the presence of a hot convective mantle plume upwelling beneath eastern Africa. Seismic tomography suggests that anomalously low-velocity mantle extends to depths of at least 400 km beneath northern Tanzania (Nyblade et al., 2000).

The Ethiopian and East African plateaux appear distinct in Fig. 9.3 and so, if it is accepted that they have a plume origin, it is relevant to ask whether both have formed in response to *the same* plume, or whether each plateau is the product of a separate mantle plume. Ebinger and Sleep (1998) argued that both uplift-related volcanic provinces, together with a number of other uplifted centres of Neogene alkali volcanism scattered across northern Africa (Hoggar, Tibesti, Darfur, Cameroon Line), are all manifesta-

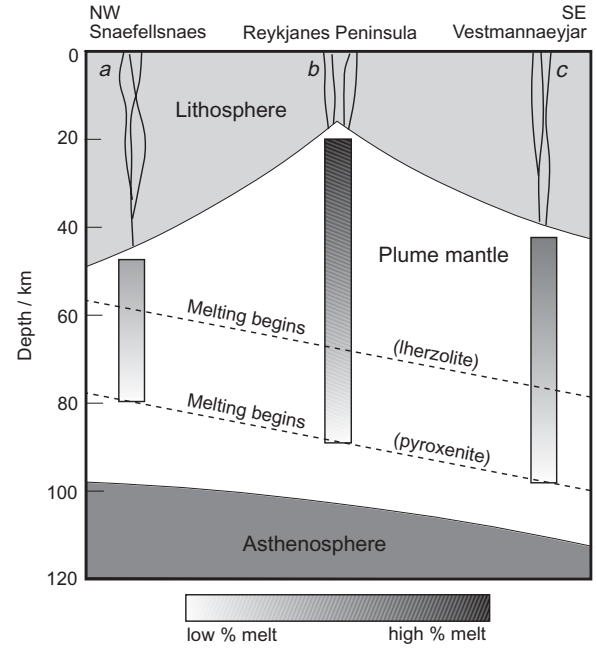


Fig. 9.20 Sketch cross-section of the melting region in the plume-head beneath Iceland along the line *a–b–c* shown in Fig. 9.9, adapted from Kokfelt et al. (2006) by permission of Oxford University Press.

tions of a single large plume beneath the Ethiopian Plateau, whose head has spread laterally outward where facilitated by favourable underside topography of the African lithosphere (i.e. by 'corridors' of somewhat thinner lithosphere). This model is not notably successful, however, at predicting the distribution of volcanism in the more southerly parts of the Kenya–Tanzania rift or in the Western Rift (cf. Fig. 9.3). Other authors, most recently Rogers (2006), argue that the region of uplift and rift volcanism centred on Lake Victoria (Fig. 9.3) is the product of a separate 'Kenya plume', which has isotopic and geochemical attributes quite distinct from the Afar plume (Rogers et al., 2000). Thermal modelling of a two-plume scenario by Lin et al. (2005) predicts the distribution of volcanic rocks in Kenya and northern Tanzania better than a single-plume model, and suggests that two plume heads would be separated by a 'stagnation streamline' that prevents mixing between them and preserves their separate geochemical and thermal (uplift) signatures.

The local onset of volcanism in East Africa has migrated southwards with time, from 35 Ma BP in Turkana ('LTu' in Fig. 9.3), 30 Ma BP in northern Kenya, 15 Ma in central/southern Kenya (Fig. 9.11) to ~10 Ma in northern Tanzania, a trend which Rogers (2006) attributes to southward migration of the Kenya plume[18] through time. It may be that the Eocene Amaro basalts of southern Ethiopia represent the earliest and most northerly volcanic manifestation of this plume, implying that it began its life as long ago as 45 Ma BP, 15 Ma before the first volcanic activity associated with the Afar plume.

The basalts, basanites and nephelinites of the Gregory rift in Kenya and northern Tanzania are geochemically similar (Fig. 9.19a) to OIBs. It is therefore reasonable to regard them primarily as products of melting of sub-lithospheric plume mantle, similar to that available beneath hot-spot-related oceanic islands (Macdonald et al., 2001), though in parts of East Africa the system is constrained to lower degrees of melting at greater depth by thicker continental lithosphere. Radiogenic isotope ratios nevertheless differ between basalts erupted through the edge of the Tanzania craton on the one hand and through Proterozoic mobile belts on the other (Rogers et al., 2000), and this correlation with crust/lithosphere age suggests the basalts have picked up an age-dependent isotopic contribution from the continental lithosphere too.

The distinctively potassic character of the lavas erupting in the Western Rift, accompanied by high concentrations of other incompatible elements such as Rb, Ba, Th, Nb and LREE (Fig. 9.19a), is generally attributed to the presence in the mantle source of a potassium-rich mineral, either amphibole or phlogopite. There is no counterpart of this highly potassic affinity in oceanic islands. Rogers (2006) therefore interprets the present-day volcanism of the Western Rift as derived essentially by partial melting of sub-continental lithospheric mantle that has previously been metasomatically enriched in incompatible elements, as discussed earlier in this chapter. As **HFSE** (including Nb) are as enriched as large-ion lithophile elements (**LILE**s) (Fig. 9.19a), he argues that the metasomatic agent is likely to have been an alkaline silicate melt (rather than hydrous fluids of the kind that fractionate LILE relative to HFSE in subduction-related settings). Radiogenic isotopes indicate that the incompatible element enrichment dates from ~1 Ga ago, when the lithosphere stabilized following the Kibaran orogeny in this part of Africa.

Carbonatites

> *'Petrologists have no real idea of the mineralogical and compositional character of any carbonatite-forming magma except that it must contain some Si, Mg, Fe, P and alkalis to account for the common presence of mafic silicates, oxides, and phosphates. Consequently, current petrogenetic schemes are rife with unconstrained speculation.'* (Mitchell, 2005)

Given this uncertainty over magma composition, how carbonatite magmas are formed remains an enigma. Carbonatites *sensu stricto* (Box 9.3), like the accompanying nephelinites and melilitites, are undoubtedly formed from mantle-derived magmas; lherzolite xenoliths

[18] Perhaps more appropriately called the 'Tanzania plume' in view of its supposed current location.

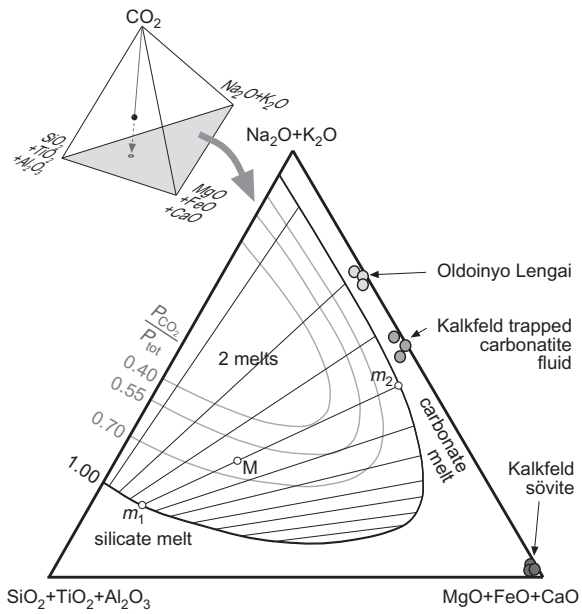


Fig. 9.21 Conceptual **isothermal** phase diagram (mass %) illustrating the **solvus** separating immiscible silicate and carbonate melts for CO_2-saturated (black curve) and CO_2-undersaturated (grey curves) conditions at 2.5 GPa and 1250 °C, based loosely on Brooker (1998). Co-ordinates in the quaternary system CO_2–(Na_2O + K_2O)–(SiO_2 + TiO_2 + Al_2O_3)–(MgO + FeO + CaO) are ***projected*** (Appendix B) from the CO_2 apex on to the ternary CO_2-free base (shaded in inset) shown in the main figure. The radiating fine lines are notional **tie lines** linking coexisting silicate (e.g. m_1) and carbonate (m_2) melts. The compositions of Oldoinyo natrocarbonatite, Kalkfeld 'trapped carbonatite fluid' (Table 9.4) and Kalkfeld sövite are from Bühn and Rankin (1999).

reported from a number of eruptive carbonatites (Woolley and Church, 2005) confirm this. One possible magma genesis model is that coexisting carbonatite and silicate magmas may evolve as complementary immiscible melts that separate from a common parental carbonate-silicate magma. Such a relationship is supported by field observation of carbonate **ocelli** in a nephelinite lava (Kjarsgaard and Peterson, 1991) and by several experimental studies (reviewed by Brooker, 1998). Figure 9.21 shows a possible solvus and the 'miscibility gap' it encloses, at mantle pressures and temperatures.[19] According to Brooker, the 2-melt immiscibility field is small when melts are undersaturated with CO_2 (grey solvus curves) but expands as CO_2-saturation is approached (black curve). Radiating **tie lines** link compositions on opposite sides of the solvus that are in mutual equilibrium: a composition such as M, for example, forming a homogeneous melt under CO_2-undersaturated conditions (e.g. $P_{CO_2}/P_{total} \sim 0.5$), unmixes into separate silicate and carbonate melts (m_1 and m_2) as pressure relief leads to CO_2-saturation. Note the solvus does not extend to alkali-poor edge of the diagram, so the unmixing phenomenon is therefore restricted to relatively alkali-rich melts. On the face of it calcite-rich sövites such as those from Kalkfeld (Table 9.4) cannot be products of immiscibility, unless – as inferred from **fenite** aureoles – sövite is merely a volatile-depleted residue of carbonatite magma originally much richer in alkalis.

Homogeneous carbonated silicate melts might alternatively be driven across the solvus by (i) cooling, which widens the miscibility gap; or (ii) through fractionation of silicate minerals. Carbonatite magmas could alternatively originate by direct partial melting of carbonated mantle peridotite. Bell et al. (1998) and Mitchell (2005) argued that primary magmatic carbonatites are of several types (to adapt H.H. Read's granite maxim, there are 'carbonatites and carbonatites'), and therefore no single model is likely to account for them all.

Other continental rifts and alkali provinces

In East Africa there is a clear causal association between uplift, rifting, volcanism and an underlying mantle plume. Involvement of a plume is more difficult to demonstrate for alkali provinces that are no longer active. In the Gardar alkali province in South Greenland, for example, the geology provides a clear record of late Proterozoic extension, rift-related subsidence and alkali magmatism (see above), but no evidence has been preserved for

[19] The existence of a solvus is well established though details vary from one study to another.

major regional syn-magmatic uplift – like that in East Africa today – that could confirm plume involvement. Petrological comparisons, together with the axial gravity high in the Tugtutôq-Motzfeldt dyke zone, establish a close parallel with the tectonomagmatic setting of the EARS (Upton et al., 2003), but direct evidence for plume activity at the time is lacking.

Some rift-related continental alkali provinces seem to form without any plume involvement at all. The Carboniferous Midland Valley rift of Scotland produced OIB-like volcanism for 70 Ma but there appears to have been no plume-generated updoming like that seen in East Africa and the Basin and Range (see Fitton, 2003). In cases such as this, magmatism was probably due to decompression melting that accompanied passive upwelling of asthenosphere in response to extension-related lithospheric thinning. Why such a process – given its similarity to upwelling at mid-ocean ridges – should yield OIB-like rather than MORB-like (asthenospheric) magmas here is puzzling: this is another aspect of Fitton's (2003) 'OIB paradox'.

The origins of Cameroon Line magmatism, which has continued intermittently from 66 Ma BP to the present day in west-central Africa (Fig. 9.16), are not fully understood. Basalts from volcanoes in the oceanic and continental sectors of the line are geochemically identical, ruling out significant involvement of lithospheric sources (since oceanic and continental mantle lithosphere would introduce distinct geochemical signatures) and placing the source of magmatism in the convecting mantle below. There is no correlation between age and geographical location among the volcanic and plutonic centres that could account for the linear geographical trend in terms of Hawaiian-style migration of lithosphere over a sub-lithospheric point-source beneath. If a mantle plume were invoked to explain the distribution of the volcanoes, their ages and their OIB-like composition, it would need to take the form of a vertical sheet and to remain stationary with respect to the African plate for 66 Ma (Fitton, 2003). Meyers et al. (1998) and Déruelle et al. (2007) have proposed a convective 'hot line' having these characteristics in the mantle below the region, but the cause of this unusual plume configuration – if it exists – is far from clear.

Unlike the Cameroon Line basalts, which are indistinguishable between oceanic and continental sectors, clear differences emerge for the salic magmas of the province: virtually all of the evolved volcanics from the continental sector are trachytes and alkali rhyolites, whereas all but two of the evolved rocks from the oceanic sector are phonolites. As Fitton (1987) put it:

> '*progressive crustal contamination of the fractionating magmas provides the simplest explanation for the dominance of oversaturated salic rocks in the continental sector*'.

Kimberlites

> *Kimberlite constitutes a rare, highly alkaline* volatile-rich *rock type that has in many ways attracted more attention than its relative volume might suggest that it deserves. This is largely because it serves as a carrier of diamonds and garnet peridotite mantle xenoliths to the Earth's surface. Furthermore, its probable derivation from depths greater than any other igneous rock type, and the extreme magma composition that it reflects in terms of low SiO_2 content and high levels of incompatible trace element enrichment, make an understanding of kimberlite petrogenesis important*. Le Roex et al. (2003)

That kimberlite magmas are sourced from deeper in the Earth's mantle than any other magma type is clear not only from the occurrence of diamond in many (a property shared with some lamproites), but also from analysis of the garnet lherzolite and harzburgite xenoliths that kimberlites typically contain. Such xenoliths are fragments of conduit wall-rock detached by kimberlite magma during its rapid ascent[20] through the lithosphere, and they place useful constraints on where and under what conditions the kimberlite melt

[20] Sparks et al. (2006) estimate that kimberlite magmas ascend at speeds of 4–20 $m\,s^{-1}$.

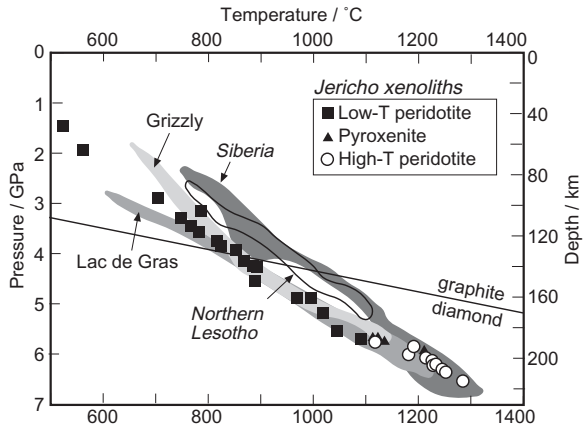


Fig. 9.22 *P–T* estimates from mantle xenoliths from the Jericho kimberlite pipe in the Slave craton, NWT, Canada, adapted from Kopylova et al. (1998) by permission of Oxford University Press. Each symbol represents a single xenolith. Comparative *P–T* fields for xenolith populations from other pipes in the Slave craton (Grizzly, Lac de Gras) and from kimberlites in Siberia and northern Lesotho (southern Africa) are also shown (sources given by Kopylova et al., 1998), as is the boundary defining stability fields of graphite and diamond.

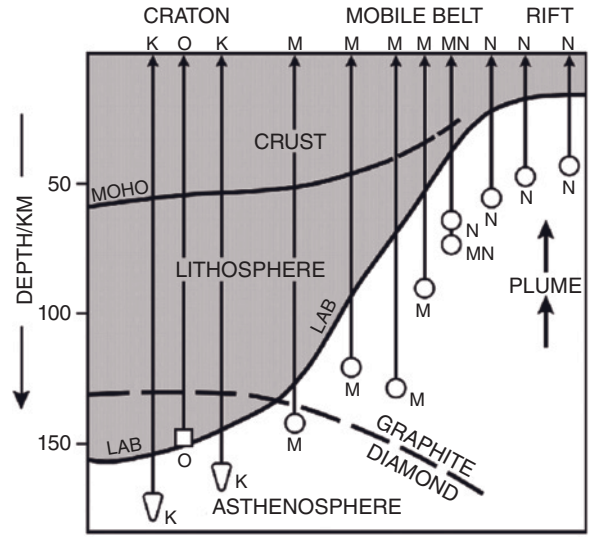


Fig. 9.23 Cartoon from Mitchell (2005, by permission of the Mineralogical Association of Canada) linking the origins of kimberlite (K), melilitite (M) and nephelinite (N) to lithosphere thickness and plume input. LAB, lithosphere–asthenosphere boundary; MN, melilite nephelinite.

formed. The Al_2O_3 content of orthopyroxene crystals coexisting with garnet is known – from laboratory experiments – to vary with the pressure at which the equilibrium was established (MacGregor, 1974). Potentially therefore **electron microprobe** analysis of Al_2O_3 in natural orthopyroxenes in garnet peridotite xenoliths allows their *depths* of residence in the mantle (i.e. depth of origin of the xenolith) to be estimated. The *ambient temperature* experienced by the xenolith immediately prior to its entrainment by kimberlite magma can likewise be estimated by geothermometry based on the CaO content of clinopyroxene coexisting with orthopyroxene (Box 4.5). Figure 9.22 shows estimates of the depths and ambient temperatures at which mantle xenoliths – recovered in this example from the Jericho kimberlite pipe in the Slave craton of northern Canada – had equilibrated before being caught up in the ascending kimberlite magma. The data points define a 'shield geotherm' through Slave craton lithospheric mantle. As the kimberlite must have originated from depths greater than the deepest-sourced xenolith it contains, this plot indicates that the Jericho kimberlite originated more than 220 km below the surface. Xenoliths from other kimberlites from the Slave Province and elsewhere suggest derivation from similar depths.

We can therefore conclude that kimberlite magma genesis is characterized by very low degrees of partial melting within metasomatized **SCLM** (to explain the extreme enrichment in HITE shown in Fig. 9.19) which takes place at considerable depths (to explain the pressure range recorded by the xenoliths shown in Fig. 9.22 and sometimes confirmed by the presence of diamonds) as illustrated in Fig. 9.23. The occurrence of kimberlites in and around ancient cratons, rather than associated with younger rifts, is consistent with this picture.

A distinction is sometimes drawn for South African kimberlites between:

- 'Group I' kimberlites, which have high Nb contents (like Wesselton in Fig. 9.19) and initial Sr isotope ratios similar to OIB; and

- 'Group II' kimberlites (called 'orangeites' by Mitchell, 1986), which tend to be more phlogopite-rich, have negative Nb anomalies, and possess more radiogenic Sr.

The distinction between these categories is chiefly geochemical; mineralogical differences are slight. Becker and Le Roex (2006) proposed that Group I kimberlite magmas are the result of melting **SCLM** that has previously been enriched by OIB-like (i.e. plume-derived) melts or fluids. Group II kimberlites, on the other hand, exhibit a Nb deficiency reminiscent of supra-subduction zone (**SSZ**) magmatism, attributed in Becker and Le Roex's (2006) model to melting of

> *'Archaean and Proterozoic lithospheric mantle source regions metasomatized by melts or fluids associated with ancient subduction events unrelated to mantle plume upwelling. The upwelling of mantle plumes beneath southern Africa during the Mesozoic, at the time of Gondwana break-up, may have acted as a heat source for partial melting of the SCLM and the generation of both Group I and Group II kimberlite magmas.'*

Whether partial melting to form kimberlite magma is initiated within the SLCM – as inferred above – or in the asthenosphere below it (Fig. 9.23) is open to debate, but few doubt the impact that ancient shield lithosphere has on the composition of kimberlites.

Subduction-related alkali rocks

The arc-like volcanism of the Aeolian islands of Italy has been attributed (e.g. Guest et al., 2003) to on-going NW subduction of the African plate beneath the Ionian Sea where the subduction zone remains active (see the grey arrow and the Wadati–Benioff zone contours in Fig. 9.17). The potassic provinces of central Italy have previously been interpreted as products of such subduction as well, but they are located in a region of Italy – west of the Apennine mountains – that has experienced rifting and block faulting from the upper Miocene to the present. Indeed, parts of the neighbouring Tyrrhenian Sea are floored by new oceanic crust (Fig. 9.17) and thus have some characteristics of an extensional back-arc basin (cf. Fig. 6.19). Most recent models attribute the central Italian potassic volcanoes to this episode of extensional tectonics behind the Apennine–Maghreb thrust front, and to the lithospheric thinning that has accompanied it (Turco and Zuppetto, 1998 – see Fig. 9.17). There are a few, however, who regard the Quaternary Italian volcanoes as plume-related (Bell et al., 2006).

The shoshonite suite

Extensional tectonics within a convergent-margin environment also seem to play a key part in the genesis of the shoshonite suite (Fig. 9.2) and some high-K calc-alkali volcanics associated with them. A subduction connection is clear from the negative Nb anomaly shown by most shoshonites, which is often accompanied by a similar anomaly for Ti (e.g. Fig. 9.19b). Shoshonites generally show significantly higher large-ion lithophile (LIL) element enrichment (100–1000×) than associated calc-alkaline volcanics.

For the intra-oceanic Mariana shoshonites, Sun and Stern (2001) concluded that – notwithstanding the Nb anomaly – slab-derived hydrous fluids played a less important role in shoshonite magma genesis than for the associated calc-alkali and tholeiitic magmas. Instead they attributed the distinctive shoshonite incompatible-element enrichment (Fig. 9.19b) to the involvement of subducted oceanic sediment in the back-arc spreading centre mantle source; they showed that the negative Nb anomaly could have been inherited from the subducted sediment.

Shoshonites from continental magmatic arcs (e.g. the Cascades of the western USA) and post-collisional settings (Tibet, Alps) generally have much steeper REE patterns than those from intra-oceanic arcs like the Marianas, as shown by their Ce/Yb ratios in Fig. 9.24. The high Ce/Yb values probably reflect the presence of residual garnet in the mantle source. The figure also emphasizes the much greater enrichment of Ce (and by analogy other LREE) in shoshonites from collisional settings like Tibet. Turner et al. (1996) attrib-

uted the Tibet shoshonites to melting of SCLM previously metasomatized by ancient subduction processes. Their model hinges on a specific interpretation of extensional orogenic collapse, in which the lower part of the thickened lithosphere becomes detached and sinks, exposing the cooler lithosphere interior to asthenospheric temperatures sufficient to initiate lithospheric melting.

These disparate models do not currently explain the common characteristics that shoshonites share in nearly all of the settings where they occur. A unifying hypothesis is required that embraces all of these diverse extensional, subduction-related environments.

Lamproites

Lamproites are sometimes associated in the field with shoshonites in post-collisional tectonic settings, as for example in Tibet and the NW Alps (Fig. 9.24).

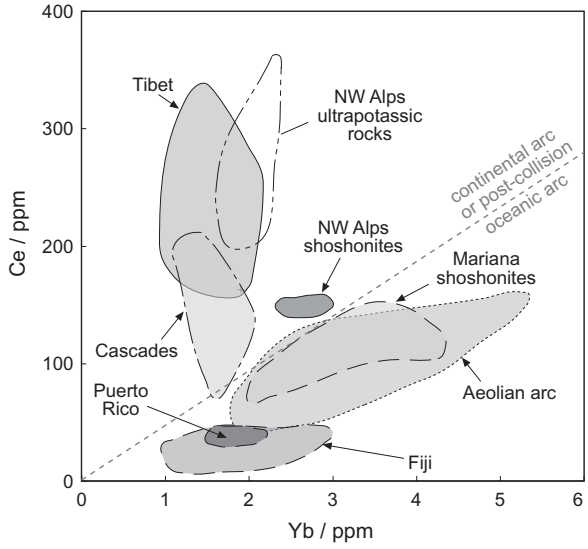


Fig. 9.24 Ce–Yb fields for shoshonites from various parts of the world, after Gill et al. (2004) and Sun and Stern (2001) using data sources cited there. Solid lines enclose shoshonite data fields for post-collisional settings; dash-dot lines enclose continental arc compositions, and dashed lines enclose oceanic arc data.

The high enrichment of LIL elements combined with high MgO and compatible element contents characteristic of lamproites (Fig. 9.19b) point to low degrees of melting in a metasomatized SCLM source. The ubiquitous negative Nb anomaly (in contrast to kamafugites) suggests that earlier episodes of subduction have contributed to the metasomatic enrichment of the lithosphere. Some authors (e.g. Gao et al., 2007; Guo et al., 2006; Altherr et al., 2004) identify subducted oceanic sediment as the key component in lamproite magma genesis, supposedly added to the SCLM by low-degree partial melts derived from the descending slab. Experimental studies suggest that – as for the potassic volcanics of the Western Rift of East Africa – the source must have contained a potassium-rich residual mineral such as phlogopite or amphibole (Edgar and Vukadinovic; 1992), perhaps as a component of metasomatic veins. The occurrence of diamond xenocrysts in some lamproites indicates derivation from considerable depth in the lithosphere (Fig. 9.23).

Lamprophyres

> *'Lamprophyres are as diverse genetically as they are compositionally – differing sources and/or melting conditions can apply even to different examples of one branch within a single igneous complex.'* Rock (1987)

The term 'lamprophyre' embraces such a wide range of magma type and tectonomagmatic setting (Box 9.6) that no single magma genesis model can be expected to account for all examples. It is probably true to say that lamprophyres – though among the most widespread of alkali rocks – are also the least understood in petrogenetic terms.

REVIEW – THE SIGNIFICANCE OF ALKALI IGNEOUS MAGMATISM

Alkali igneous rocks are notable for their wide diversity of composition, both mineralogical (Tables 9.1 and 9.3) and geochemical (Figs. 9.1a and 9.19). Silica-undersaturation, high alkali content and strong enrichment in

incompatible elements may lead to the presence of unusual minerals such as sodalite or eudialyte. Notable characteristics of alkali rocks include the following:

- The diversity in alkali rock composition straddles the divisions between silica-undersaturated and oversaturated, between metaluminous and peralkaline, between sodic, potassic and ultrapotassic, and between silicate and carbonate mineralogy.
- Some alkali magmas like leucite nephelinite and natrocarbonatite have remarkably low viscosity.
- Alkali basalts and related alkali lavas occur on ocean islands. In Hawai`i they make up the pre-shield stage (predating the tholeiitic shield forming the bulk of the island), the post-caldera stage and the post-erosional stage. Many smaller islands and seamounts consist entirely of alkali basalts and their derivatives.
- Large volumes of alkali volcanic rocks are associated with active continental rifts like the East African rift system, where they commonly form a bimodal population (Fig. 9.13). Correlated uplift, extension, rifting, alkali volcanism (Fig. 9.3) and a regional negative Bouguer anomaly (Fig. 9.14) here suggest the presence of one or more hot, buoyant mantle plumes invading and thinning the continental lithosphere.
- Carbonatites are associated with many volcanic centres in East Africa. Some may be the product of melt immiscibility in an ascending parental silicate-carbonate magma. It is unclear how natrocarbonatite at Oldoinyo Lengai relates genetically to the more common calcic or magnesian carbonatites.
- Continental alkali basalts are closely similar geochemically to those erupted on oceanic islands. Enrichment in HITE may be explained here by low degrees of decompression melting constrained by thick lithosphere. Potassic magmas showing the greatest HITE enrichment (kamafugite, kimberlite, lamproite) are however confined to continental provinces and probably involve melting of metasomatized SCLM.
- Shoshonites correlate with back-arc extension in both oceanic and continental magmatic arcs. They are also associated with lamproites in post-collisional extensional settings. Subducted ocean sediment may play a part in their magma genesis.
- Kimberlites are derived from greater depths within the subcontinental mantle than any other magma type. Despite their minute aggregate volume, they are uniquely valuable in shedding light on the deeper regions of the sub-continental lithosphere.

EXERCISES

9.1 Select appropriate root-names for fine-grained rocks with the following compositions:
- (a) 29 % sodic plagioclase, 40% alkali feldspar, 15% nepheline, 12% aegirine–augite and 4% opaques by volume;
- (b) 45.0% SiO_2, 4.5% Na_2O, 2.5% K_2O and LOI 2.5% with 20% olivine in the norm;
- (c) 52.35% SiO_2, 4.05% Na_2O, 2.98% K_2O volatile-free;
- (d) 48.9% SiO_2, 4.50% Na_2O, 2.09% K_2O volatile-free;
- (e) a dyke rock with phenocrysts of kaersutite and titanian augite (Fig. 2.1.1 caption) in a groundmass of titanian augite, analcite and glass.

9.2 Outline the difference between:
- (a) urtite and melteigite;
- (b) type I and type II kimberlites;
- (c) post-caldera and post-erosion stages of ocean-island magmatism;
- (d) essexite and monzonite;
- (e) syenite and sövite.

9.3 (a) Calculate the compositions (in mass % CaO, MgO, N a_2O, Al_2O_3 and SiO_2) of the two ternary eutectic melts E_1 and E_2 in Fig. 9.7b. E_1 is 45 °C hotter than E_2; explain what prevents a cooling melt of composition E_1 evolving by fractional crystallization to E_2. (b) Trace the evolution of melt *y* in Fig. 9.7b as crystallization proceeds. If E_1 can be described as a 'phonolite' eutectic, and E_2 as a

'rhyolite' eutectic, what rock name most aptly summarizes the residual melt produced by crystallizing melt *y*?

9.4 Which of the analyses given in Table 9.1 represent primary melts, and why?

9.5 Estimate the relative proportions by mass of the immiscible melts m_1 and m_2 into which melt M in Fig. 9.21 will exsolve at 2.5 GPa and 1250 °C under CO_2-saturated conditions.

Appendix A

Mineral identification using a polarizing microscope

INTRODUCTION

Mineral identification is a bit like medical diagnosis: initial suspicions are followed up by further tests. For a student who is new to microscope work, it is best to adopt a systematic approach to ensure that key observations are not overlooked. Fig. A1 summarizes a general procedure that is recommended for *each unknown mineral* in a thin section:

1 observations in plane-polarized light;
2 observations between crossed polars (parallel light);
3 when necessary, observations between crossed polars using convergent light.

More experienced readers, having assimilated a repertoire of key mineral properties, can devise short cuts based on the most diagnostic features.

Box A1 summarizes the main igneous and secondary minerals in terms of two key diagnostic properties:

- minerals are grouped according to dominant **body colour** in plane-polarized light (left to right);
- within each group, minerals are positioned on a scale of birefringence, as indicated by their **interference colours**[1] (top to bottom) see Plate 1.

Tentative identifications may then – where necessary – be checked against mineral data given elsewhere in this book:

Pyroxenes:	Box 2.1 (Ca–Mg–Fe pxs);
	Box 2.2 (augite *versus* olivine);
	Box 4.2 (opx *versus* cpx);
	Box 4.5 (exsolution textures);
	Box 9.2 (sodic pyroxenes).
Olivine:	Box 2.2 (augite *versus* olivine).
Feldspars:	Box 4.1 (plag determination);
	Box 6.1 (volcanic feldspars);
	Box 8.1 (plutonic feldspars).
Foids & melilite:	Box 9.1.
Amphiboles:	Box 9.2 (sodic pyroxenes);
	Box 9.4 (sodic amphiboles).
Al minerals in granites:	Table 8.2.1.
Spinel:	Box 5.1.
Garnet:	Box 5.2.

[1] Bear in mind that interference colour depends not only on the birefringence of the mineral but also on the orientation of the particular crystal being examined. Estimation of birefringence should always be based on the highest-order interference colour observed from several different crystals (Fig. A1).

Igneous Rocks and Processes: A Practical Guide, 1st edition. By Robin Gill. Published 2010 by Blackwell Publishing

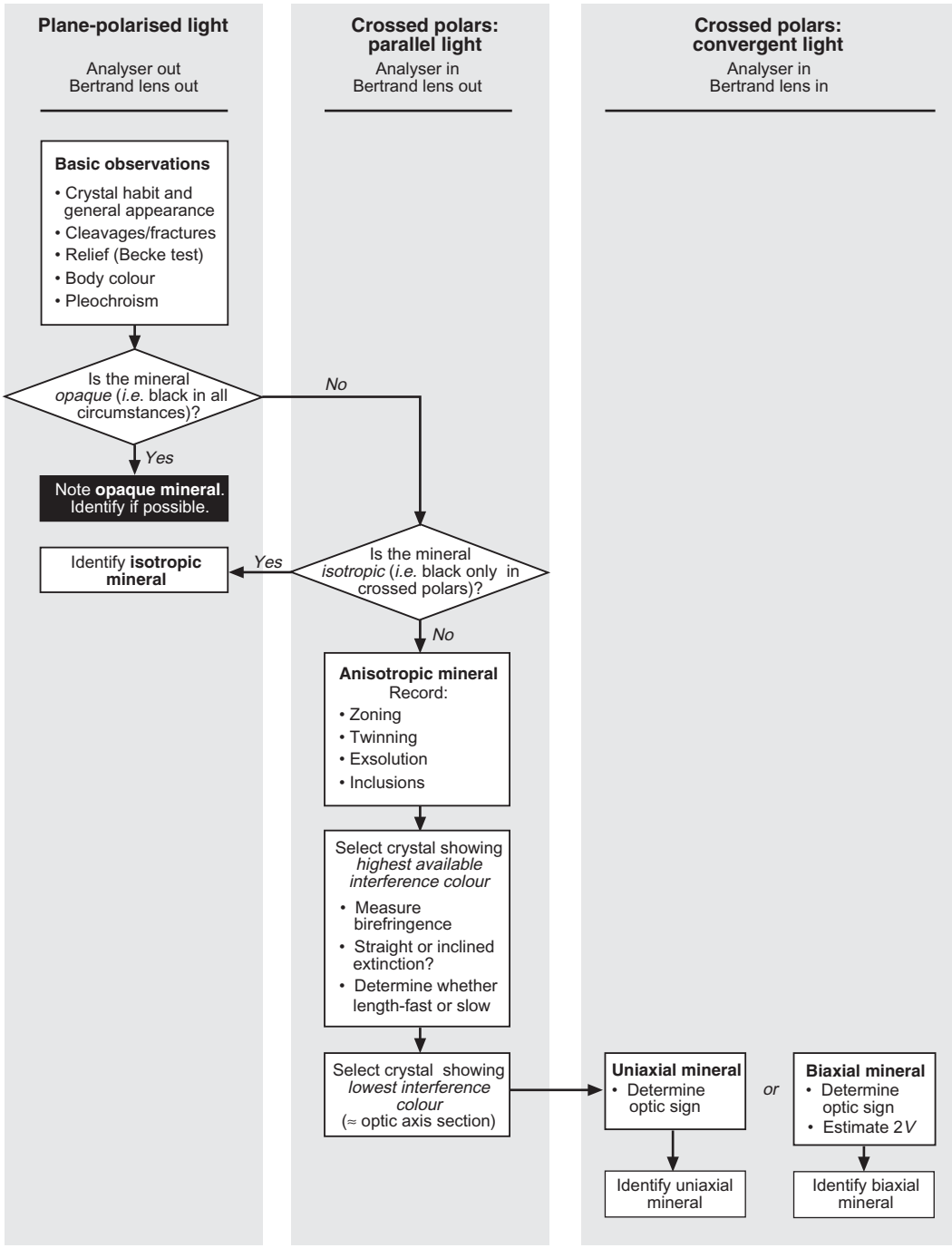
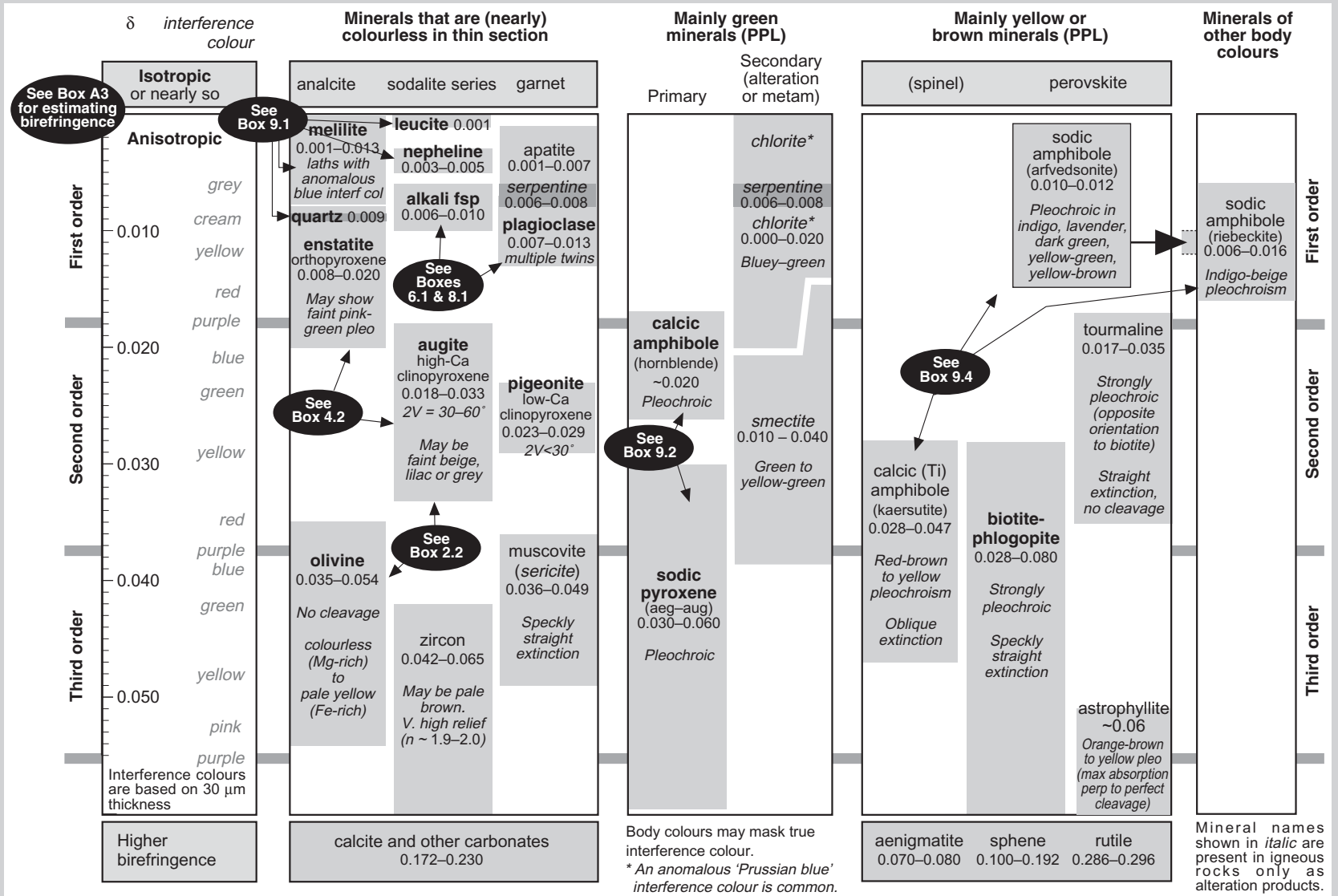


Fig. A1 A systematic procedure for mineral identification in thin section.

Box A1 A simplified scheme of mineral identification for common igneous minerals

Minerals are grouped horizontally into four **body colour** groupings. Each shaded rectangle represents the range of birefringence (δ) characteristic of the mineral concerned. Isotropic minerals are shown in boxes at the top; minerals with unusually high birefringence are shown in boxes at the bottom. Mineral names shown in **bold** signify major rock-forming minerals; *italicized* names indicate secondary (alteration) minerals. The black ellipses reference boxes that deal with more advanced techniques required to distinguish between similar minerals.



Alternatively, reference may be made to a mineralogy text such as Deer et al. (1992) or Gribble and Hall (1992).

OBSERVATIONS IN PLANE-POLARIZED LIGHT

Observations made at this stage include:

1 The *crystal habit* of the mineral:
- is it **euhedral**, **subhedral** or **anhedral**?
- Are the crystals **equant**, elongated, tabular, **acicular**, fibrous, **prismatic**, platy, square or six-sided?[2]
- What is the average grain size of the mineral?
- Is it a phenocryst or a groundmass mineral?

2 The *cleavage(s)* exhibited by the mineral:
- Is there just one cleavage direction or are there two or more?
- Different grains of the same mineral may show different cleavages; e.g., basal sections of mica show no cleavage, whereas sections perpendicular to the sheets show a single strong cleavage. It is equally relevant to note *absence* of regular cleavage: the irregular fractures seen in olivine, for example, are an important diagnostic feature.

3 The mineral's *refractive index* (RI). RI may be estimated by combining two simple tests, both of which use the mounting resin (RI = 1.54) as a reference material:

(**a**) The Becke test: indicates whether the mineral's refractive index is greater than or less than that of the resin (see Box A.2).

(**b**) The mineral's *relief:* A crystal whose features or surface irregularities stand out strongly in plane-polarized light (PPL) is said to have *high relief*, indicating that its refractive index differs markedly from that of the resin. A mineral that appears flat and featureless – *low relief* – has an RI close to that of the resin (e.g. quartz, RI ~ 1.55). The ranges of RI that each implies are outlined in Table A1. Note that *high relief* implies that the mineral's RI *exceeds* that of resin.

4 The mineral's *body colour:* its colour when viewed in PPL.[3] Even quite faint body colour may have diagnostic value, e.g. the pale beige colour of augite that often helps to distinguish it from colourless olivine.

A mineral that looks black in PPL regardless of orientation (unable to transmit light of any wavelength through its 30 μm thickness) is described as *opaque*. Opaque minerals consist of oxides (magnetite, chromite, ilmenite, hematite) or sulphides (pyrite, chalcopyrite, pyrrhotite, galena) of transition metals; they are usually indistinguishable from each other in transmitted light. *Opaque* should not be confused with *isotropic* (black *only* between crossed polars – see Table A2).

5 *Pleochroism:* the mineral's body colour changes, or varies in intensity, as the stage is rotated. Pleochroism provides an invaluable diagnostic tool for certain coloured anisotropic minerals (biotite, Plate 8.10; tourmaline, Plate 8.4; aegirine–augite, hornblende and riebeckite, Plate 9.18; titanian augite and enstatite show less intense but often distinctive pleochroism).

Coloured minerals belonging to the cubic crystal system (e.g. spinel, coloured varieties of garnet) are non-pleochroic. A pleochroic mineral may appear non-pleochroic in some sections: e.g. biotite shows no pleochroism when viewed in a basal section.

[2] Unless the mineral forms *regular* hexagons, it is best to avoid the adjective 'hexagonal', because crystals may exhibit six-sided cross-sections without belonging to the hexagonal crystal system (e.g. amphiboles).

[3] Do not confuse **body colour** with **interference colour** (discussed below).

Box A2 The Becke test

This simple test allows us to determine whether a mineral's refractive index (RI) is greater or less than that of the mounting resin (Canada balsam or epoxy resin with an RI of 1.54). There are three conditions for successful use:

1 select a grain of the mineral to be identified that is adjacent to resin rather than to neighbouring minerals; a grain at the edge of the thin section is often used;
2 focus the microscope on the selected grain boundary using a medium- or high-power objective;
3 reduce the illumination by partially closing the sub-stage diaphragm.

A diffuse bright line will be seen along the selected boundary, formed of light refracted by the difference in RI (not distinguishable under full illumination). The movement of this bright line should be observed as the microscope is gradually defocused by *increasing the distance* between the objective and the slide, either by raising the objective (in older microscopes) or by lowering the stage assembly; the fine-focus knob should be used if available. The bright band will be seen to migrate *into the material with the higher RI* (Fig. A2.1): if the mineral's RI is greater than 1.54, the bright band will migrate inward into the mineral (Fig. A2.1a); if it is lower than 1.54, the bright line will migrate outward into the adjacent resin (Fig. A2.1b).

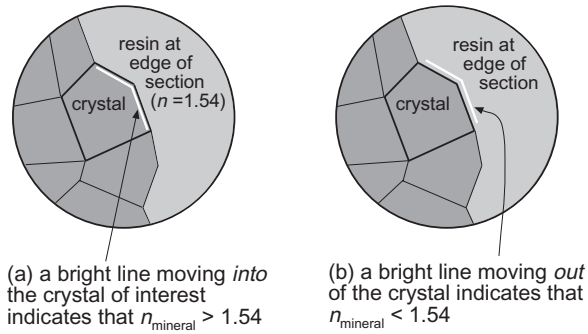


Fig. A2.1 Use of the Becke bright line to determine a mineral's refractive index $n_{mineral}$ relative to that of the mounting resin (n_{resin} = 1.54) at the edge of the thin section. Both diagrams show the effect of slightly *increasing the stage–objective distance* from the focus position. (a) $n_{mineral} > n_{resin}$; (b) $n_{mineral} < n_{resin}$.

Table A1 Low and high relief.

Range of RI	How relief is described	Examples
1.40–1.50	moderate, negative	analcite, sodalite (feldspathoids)
1.50–1.54	low, negative	alkali feldspar, albite, nepheline
1.54–1.58	low, positive	quartz, calcic plagioclase
1.58–1.67	moderate, positive	tourmaline, apatite
1.67–1.76	high	augite, epidote, garnet (pyrope)
>1.76	very high	sphene

After Gribble and Hall (1992).

Table A2 Four reasons why a mineral may appear black in thin section.

Black in PPL	Black in crossed polars	Reason for black appearance
Yes – the mineral is opaque.		No light passes through crystal.
No	The (non-opaque) mineral is *isotropic**.	Same RI for both rays ∴ no phase difference ∴ destructive interference.
No	The (anisotropic) mineral happens to be in an *extinction position*.	Mineral vibration directions happen to lie parallel to those of polarizer and analyzer ∴ no light passes through analyzer.
No	The (anisotropic) mineral is being viewed down an *optic axis*.	Same RI for both rays (in this section) ∴ no phase difference ∴ destructive interference.

* Isotropic materials include volcanic glass, crystals belonging to the cubic system, amorphous minerals (e.g. agate) and mounting resin.

OBSERVATIONS IN CROSSED POLARS

Crossed polars used with parallel light

'Crossed polars' (XP[4] as distinct from PPL) provides an invaluable means for examining anisotropic minerals: by studying the interference colours obtained, the user can quickly estimate a mineral's birefringence, a key diagnostic property (see Box A1).

The following observations are among those made in crossed polars:

6 Is the mineral **isotropic**? Because no phase difference develops between the two rays, an isotropic mineral appears black in all sections when viewed in crossed polars. The few isotropic crystalline minerals found in igneous rocks are listed at the top of Box A1; most are mutually distinguishable by colour or refractive index.

Before describing a crystal as isotropic, it is important to check other possible reasons for appearing black (Table A2). Isotropic appearance may also be obtained where a mineral grain has been plucked out during section preparation and replaced by mounting resin.

7 *Internal crystal structures* are often visible in crossed polars. Diagnostic ones include:

- twinning, e.g. the multiple twinning of plagioclase (Fig. 4.1.1), the simple twinning of sanidine (Fig. 6.1.1), the tartan twinning of microcline and anorthoclase (Fig. 8.1.1) and the complex multiple twinning in leucite (Plate 9.8);
- exsolution lamellae (e.g. pyroxenes in gabbros – Plates 4.7 and 4.8).

Other internal features such as compositional **zoning** – often revealed by a change in extinction angle from crystal core to rim (Plate 6.2) – may not assist in mineral identification but should be recorded.

The extent of optically continuous **oikocrysts** in ophitic and poikilitic textures (Plates 4.1, 4.2, 4.3) can also be noted in crossed polars.

8 Some properties need to be measured on a *maximum interference colour* section of the mineral, i.e. the α–γ section. The thin section should be examined carefully to identify those grains of the mineral of interest that exhibit the highest **relative retardation**. The following measurements should be based on those crystals alone:

- Estimate the mineral's birefringence δ by comparing the interference colour of the crystal with the Michel–Levy chart (Plate 1), assuming a section thickness $t = 30\,\mu m$. It is vital to recognize which order the interference colour belongs to (see Box A3).
- Determine whether crystals exhibit straight or oblique extinction (see Box A1) relative to crystal faces or cleavage traces. This test discriminates between orthopyroxene and clinopyroxene, for which this section is the most appropriate to use (Box 4.2).

[4] The term 'cross-polarized light' (or 'XPL'), used in a few geology texts (e.g. MacKenzie et al., 1982), is best avoided as it is based on a misunderstanding of simple physical optics.

Box A3 Two alternative ways to determine the order of an unknown interference colour

1 Examine parts of the crystal where it has become thinned during preparation, either at its edge or along internal cracks (e.g. Plate 4.8 – the yellow and white areas in the crystal with the predominantly blue-purple interference colour). Here it is often possible to trace (and count) the orders down to the distinctive grey of first order.
2 With the mineral grain in the field of view, insert a quartz wedge into the microscope's accessory slot. If this results in a high-order interference colour, rotate the stage through 90°. Carefully slide the wedge in or out until a dark fringe indicates where the wedge is exactly compensating the relative retardation of the mineral crystal. Removing the thin section should restore the original interference colour – now due to the wedge, not the mineral. Count down the orders of colour as the wedge is slowly retracted.

- It is occasionally useful (e.g. in distinguishing between green alkali pyroxene and hornblende) to determine whether a crystal is 'length-**slow**' (i.e. the crystal is elongated parallel to the higher refractive index) or 'length-fast'. The procedure is described in Box 9.2.

Sometimes it is necessary to select other specific crystal sections for particular measurements, such as the estimation of plagioclase composition (see Box 4.1).

Crossed polars used with convergent light

Most minerals found in igneous rocks can be identified using just the PPL and XP properties listed above. Occasionally (e.g. in distinguishing between sanidine, quartz and nepheline) it is also helpful to determine whether a mineral is *uniaxial* or *biaxial* (Fig. A2), and to establish its *optic sign*. These observations require the use of the polarizing microscope in its 'conoscopic' or convergent-light mode.[5]

Prior to observing a mineral in convergent light, select a crystal that maintains the *lowest interference colour* as the stage is rotated in parallel light: this section will be nearly perpendicular to an optic axis.

[5] The microscope is focused on the crystal of interest under high power, the analyzer is introduced, the substage condenser is racked up (or a supplementary converging lens is introduced), and the Bertrand lens is deployed.

Uniaxial minerals

Uniaxial minerals possess one dominant symmetry axis (triad, tetrad or hexad), and their refractive properties are summarized by an ellipsoidal **indicatrix** having rotational symmetry about this axis, as shown in Fig. A2b. The indicatrix has one circular section. Two principal refractive indices specify the optical properties of a uniaxial mineral (see caption to Fig. A2).

When viewed down the optic axis *in convergent light*, a uniaxial mineral shows a distinctive dark cross (Fig. A3a) that persists as the stage is rotated; if the optic axis is slightly oblique to the microscope axis, the centre of the cross is eccentric (as shown here) and moves in a circle when the stage is rotated, but the cross neither rotates nor breaks up.[6] Concentric interference-colour fringes show increasing **relative retardation** from the centre of the cross to edge of the field of view; with low-birefringence minerals like feldspathoids and quartz, only first order colours will be seen. These features constitute what is called the *interference figure* of a uniaxial mineral, and serve – especially the persistent cross – to distinguish it from biaxial minerals (cf. Fig. A5 showing a biaxial figure). Figure A3b shows how the interference figure relates to the indicatrix: the centre of the cross represents rays moving parallel to the optic axis,

[6] If the optic axis is still more oblique, the centre of the cross may lie outside the field of view and individual limbs of the cross sweep across as the stage is rotated.

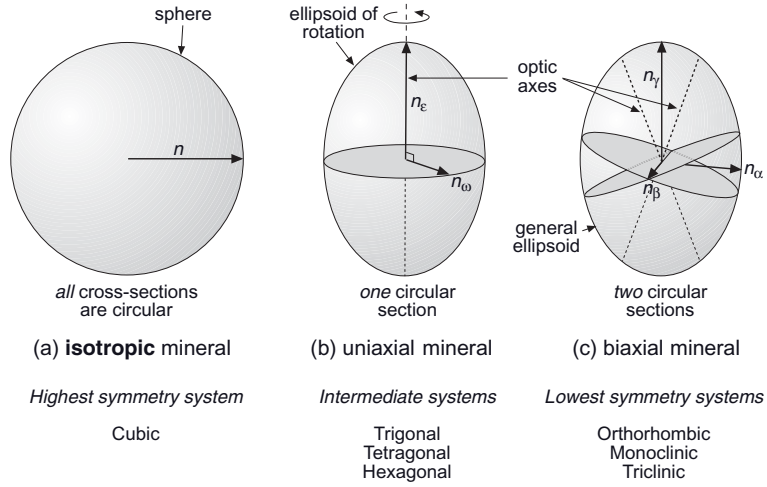


Fig. A2 Figures illustrating how refractive index *n* varies with the vibration direction of transmitted light in (a) isotropic, (b) uniaxial and (c) biaxial crystals; the ellipticity of uniaxial and biaxial **indicatrices** has been exaggerated for clarity. The number of '*n*-arrows' indicates how many principal refractive indices are needed to specify the refractive behaviour of each crystal:

	Principal refractive indexes	Circular sections
• isotropic crystal:	n	All sections are circular
• uniaxial crystal:	n_ω (ordinary wave) n_ε (extraordinary wave)	One
• biaxial crystal	n_α (minimum RI) n_β (intermediate RI*) n_γ (maximum RI)	Two

*Foreshortened by perspective in Fig. A2c.

Each circular cross-section, perpendicular to an optic axis, indicates a plane in which the crystal appears isotropic.

and the colour fringes indicate the increasing relative retardation experienced by the more oblique rays that emerge in the outer parts of the field of view.

The indicatrix of a uniaxial mineral may either have a rugby ball shape (prolate ellipsoid, $n_\varepsilon > n_\omega$), or it may be flattened (oblate ellipsoid, $n_\varepsilon < n_\omega$). These shapes are codified by the optic sign: the rugger ball shape, illustrated by the indicatrix of quartz, is said to have positive sign, while the oblate ellipsoid, characteristic of nepheline and calcite, has negative sign. The method for determining the optic sign of a uniaxial mineral is described in Box 9.1.

Biaxial minerals

Most rock-forming minerals – belonging to the orthorhombic, monoclinic and triclinic crystal systems (Fig. A2) – have biaxial optics. The biaxial **indicatrix** is a general ellipsoid having three perpendicular semi-axes of different lengths as shown in Figs. A2c and A5b, representing three principal refractive indices: the notation used is shown in the caption to Fig. A2. Any such ellipsoid has 2 circular sections, marking 2 sections in which the crystal appears isotropic. The two lines perpendicular to these circular sections are the two *optic axes* (hence 'biaxial'). The plane in which they lie is called the *optic axial plane* (OAP).

For a biaxial crystal whose OAP is near-vertical and runs parallel to the polarizer or analyser directions, the isogyres[7] form a cross that differs little from a uniaxial optic axis

[7] As in a uniaxial figure, the isogyres mark points in the figure where the mineral's vibration directions are parallel to those of the analyzer and polarizer.

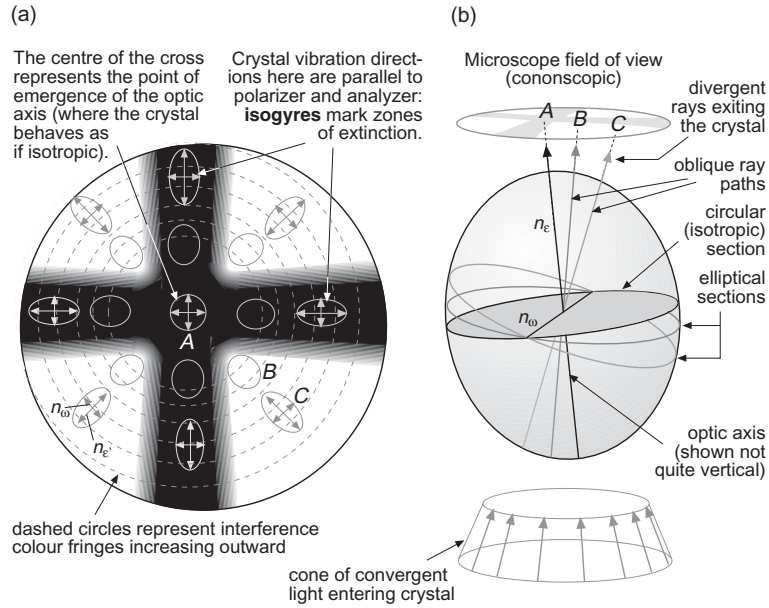


Fig. A3 (a) Slightly off-centre optic-axis figure of a uniaxial mineral (using high power, crossed polars, convergent light). Dashed circles represent colour fringes (RR increasing radially outwards). The grey arrows and ellipses have been added to indicate the vibration directions of rays emerging at the points concerned and the refractive indices they encounter. The circle at *A* marks the emergence point of rays travelling along the optic axis and experiencing isotropic behaviour (two RIs of equal value). *B* and *C* mark emergence points of rays of increasing obliquity to the optic axis, to which the crystal appears increasingly anisotropic. (b) how the interference figure can be understood in terms of the uniaxial indicatrix. The field of view when using convergent light is a 'directions image'. The black line pointing to *A* represents the optic axis lying perpendicular to the circular (isotropic) section; the optic axis is not quite vertical, reflecting the slightly off-centre interference figure in (a). Oblique rays *B* and *C* are perpendicular to elliptic sections of the indicatrix, representing anisotropic behaviour. **Relative retardation** and interference colour increase from A to C.

figure (cf. Fig. A3). The key distinction is that, when the stage is rotated 45° from this position, the isogyres of a biaxial mineral *separate* and form two hyperbolae as shown in Fig. A5a. If a low-**RR** section was selected before switching to convergent light, the interference figure may be less symmetric than in Fig. A5a, and indeed it is possible that only one isogyre will be seen; in either case the interference figure with its curved dark isogyres is readily distinguished from the uniaxial case.

The apex of each hyperbola represents one of the two optic axes (Fig. A5). If two isogyres are visible, the distance between them at maximum separation provides an estimate of the 2*V* angle. In a symmetric case like Fig. A5a, the isogyres lie at the very edge of the field of view when $2V \sim 60°$, and this pro-

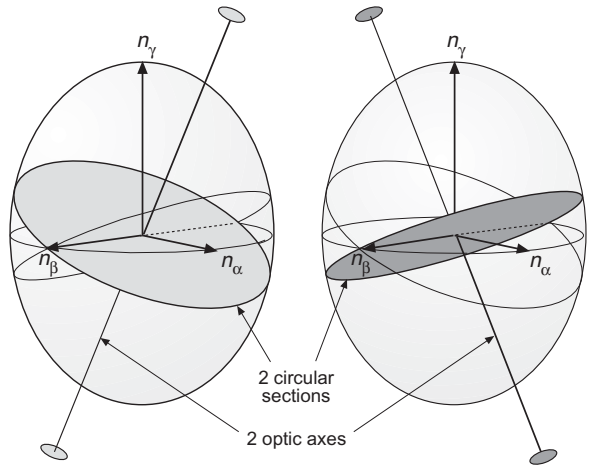


Fig. A4 The two circular (isotropic) sections and two optic axes of a biaxial indicatrix.

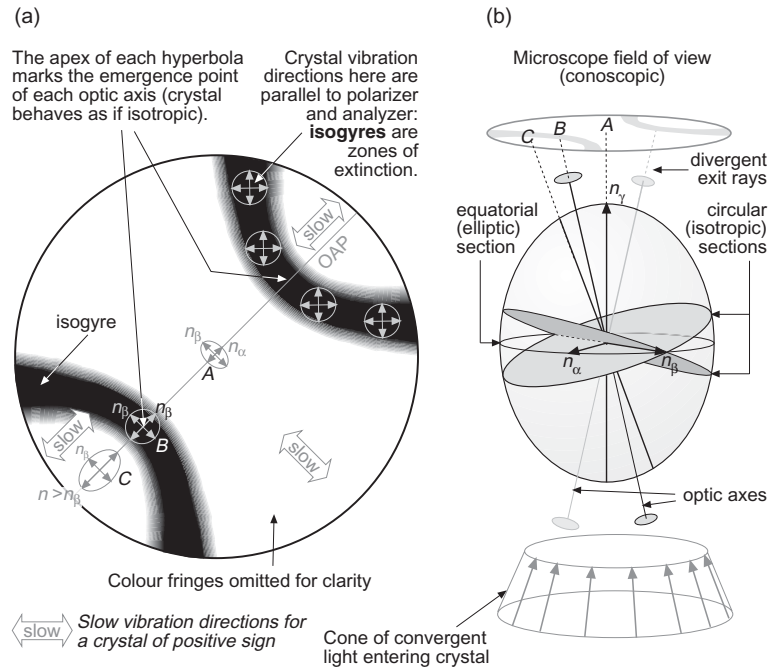


Fig. A5 (a) the separated isogyres of a biaxial interference figure of moderate $2V_\alpha$, shown for a crystal whose optic axial plane (OAP) is at 45° to the polars (high power, crossed polars, convergent light). The grey arrows and ellipses have been added to show the vibration directions and relative refractive indices for three rays emerging at *A*, *B* and *C* – see (b). (b) how the interference figure can be understood in terms of the biaxial indicatrix. *A*, *B* and *C* represent rays travelling along a line bisecting the two optic axis (the 'acute bisectrix'), along an optic axis, and along a more oblique direction. The optic axes are shown with the same symbolism as used in Fig. A4.

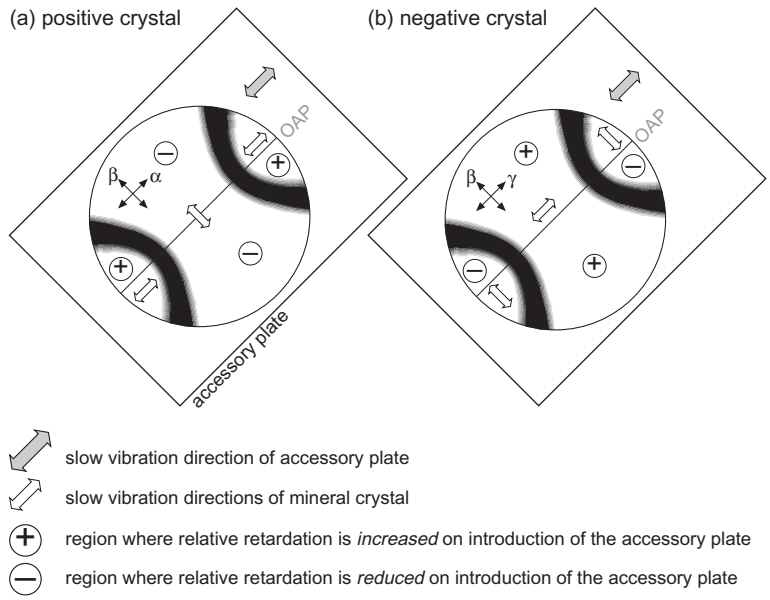


Fig. A6 Determining optic sign in a biaxial mineral. (a) Changes to the interference colour seen in each domain of the interference figure of a *positive* crystal when an accessory plate is introduced. (b) Corresponding changes for a biaxial *negative* crystal. α, β and γ are the vibration directions relating to the minimum (n_α), intermediate (n_β) and maximum (n_γ) RIs.
Hint: As with uniaxial minerals (Box 9.1), the change in relative retardation seen in the SW quadrant on inserting the accessory plate reflects the optic sign of the mineral.

vides a rough calibration for visual estimation of lower $2V$ values.

The optic sign of a biaxial mineral is defined in a different way from the uniaxial case. The sign can be determined in an interference figure like Fig. A5a by inserting an accessory plate (typically the sensitive tint plate) into the slot and observing how the interference colours change (Fig. A6). Where the slow direction of the plate is superimposed on the slow direction of the mineral, relative retardation is reinforced and a higher interference colour is seen; note that the slow/fast directions change in passing across the isogyres. Where the plate slow direction is superimposed on the mineral's fast direction, compensation occurs, relative retardation diminishes and a lower interference colour is seen.

Appendix B

Petrographic calculations

SIMPLIFIED CIPW NORM CALCULATIONS

Stages of **CIPW norm** calculation

As outlined in Box 2.4, norm calculation[1] consists of five stages, all of which (except Stage 1) may be carried out using a photocopy of the pro forma shown in Table B1:

1 Recalculating the analysis to be volatile-free

See Box 1.3

2 Transforming the analysis to molecular proportions

Divide the weight per cent figure for each oxide (i.e. g oxide per 100 g of rock) by the relative molecular mass (RMM) for the oxide concerned to express the analysis in the number of **moles** of each oxide per 100 g of sample.

3 Allotment of oxides other than SiO_2

One then follows a sequence of calculations (each involving only simple arithmetic) in which each oxide is allotted in turn to appropriate mineral molecules (as set out in Table 2.3 in Chapter 2). When carried out on paper, *entries in the table should initially be made only in pencil, to allow correction later.* Accessory minerals such as apatite and ilmenite, being easy to determine, are by convention calculated first. Then one calculates provisional amounts of orthoclase, albite and anorthite: the amount of each is determined by the amount of the *least abundant* constituent remaining from previous allotments. Next, the amounts of high-Ca pyroxene (HCP; diopside) and low-Ca pyroxene (LCP; enstatite[2]) are determined. If any Al_2O_3, CaO or Na_2O are left over (not usual), they are assigned to corundum, wollastonite and acmite (sodic pyroxene) respectively.

4 Allotment of SiO_2: quartz or silica-deficient minerals?

The provisional allotments carried out in (2) have formed the silica-saturated minerals feldspar and pyroxene, regardless of the amount of silica actually available. The next, very important stage is to allot the available SiO_2. If, after these SiO_2 allotments, an excess of SiO_2 remains, it is assigned to quartz, and the allotting process is complete. If, conversely there is *insufficient* SiO_2 available to form all of the saturated minerals calculated in (3), one must substitute SiO_2-undersaturated minerals in place of enstatite and feldspar. First, MgO and FeO (with MnO) are re-assigned from enstatite to olivine until the silica deficit has been cancelled out. If this adjustment still leaves a deficit, however, albite must be recal-

[1] All calculations at this stage should be carried out (and written down) to four decimal places; when a spreadsheet is used for the calculation, the cells should – for clarity – be formatted to show four decimal places for molar data, and two decimal places for mass % data.

[2] Referred to in the original CIPW scheme by the now-obsolete name 'hypersthene'.

Igneous Rocks and Processes: A Practical Guide, 1st edition. By Robin Gill. Published 2010 by Blackwell Publishing

Table B1 Worksheet for the manual calculation of a simplified norm. An electronic version (which can be used as a template for spreadsheet calculations) is available as a MS Excel® document at www.blackwell.. . . . / . Enter the volatile-free rock analysis in the first row.

	SiO_2	TiO_2	Al_2O_3	Fe_2O_3	FeO+MnO	MgO	CaO	Na_2O	K_2O	P_2O_5	Σ analysis	
Mass % anal												
Approx RMM	60	80	102	160	72	40	56	62	94	142		
Moles/100g												
					Φ =						Multiply by RMM	**Norm** Mass %
					μ =							
q											60	
or											556	
ab (Plag)											524	
an (Plag)											278	
ne											284	
lc											436	
c											102	
ac											462	
D_i											224*	
wo											116	
En											108*	
Ol											156*	
mt											232	
he											160	
il											152	
ap											328	
Σ column												

W =

H = | *W* − *S* = | *X* = | *X* − *S* =

N.B.*Carry out all molar calculations to four decimal places.* For relevant mineral formulae, see Table 2.3(b) in Chapter 2.

* These values are approximations applicable to basic rocks ($\mu < 0.5$); values for more evolved rocks are given in the text, as are exact solutions.

culated to nepheline and, if necessary, orthoclase to leucite.

The key purpose of the norm in this book is to express the degree of silica-saturation of an igneous rock in the same way that Nature does it, in terms of minerals such as quartz, enstatite, olivine and nepheline, emphasizing the significance of these key minerals when they occur naturally (i.e. modally).

5 Calculation of the mass % norm

Following Cross, Iddings, Pirsson and Washington, the norm is expressed in *percentages by mass* of the constituent minerals (though a 'molar norm' would be more convenient to use). The final stage of calculation is therefore to multiply the amount of each normative mineral by the appropriate molecular mass as given in Table B1.

Calculation Procedure

The simplified procedure outlined below disregards MnO (assumed to be already incorporated in 'FeO'), and treats (FeO + MgO) as a single entity Φ once the FeO-bearing accessory minerals have been calculated.[3]

1 Enter the volatile-free oxide analysis in line 2 of the table and convert it to molecular proportions by dividing each entry by the relative molecular mass immediately below it (line 3). Enter the results in line 4 (mol/100 g).

2a The nominal formula for apatite ($Ca_5[PO_4].3[OH,F]$) may be expressed in anhydrous oxide terms approximately as $3.33CaO.\ P_2O_5$. Thus for every molecule of P_2O_5 in the oxide analysis, one molecule of apatite will appear in the norm, and this will 'use up' 3.33 molecules of CaO.

In the P_2O_5 column of the *ap* line of the table, enter the molecular amount of P_2O_5 (from line 4).[4] Multiply this number by 3.33 and enter in the CaO column of the *ap* line.

2b The formula for ilmenite $FeTiO_3$ may be written in the form $FeO.TiO_2$. TiO_2 is usually less abundant than FeO, and the molar amount of TiO_2 will therefore determine the amount of ilmenite in the norm, with some FeO left over. Enter the moles of TiO_2 in the *il* line under 'TiO_2', and enter the *same number* in the *il* line under 'FeO'; this represents the amount of FeO reserved for ilmenite, which is no longer available for forming other mineral molecules.

3a Transfer the moles of K_2O to the line '*or*' to indicate the amount of orthoclase present. Enter the same number in the *or* line under $A1_2O_3$. This amount of Al_2O_3 is now reserved for orthoclase, and must not be assigned to other molecules.

3b If the moles of Al_2O_3 remaining exceed Na_2O, transfer the moles of Na_2O to the *ab* line to make albite; write the same number under Al_2O_3.

If the remainder of Al_2O_3 from 3a is *less* than Na_2O, the amount of albite present is determined by the Al_2O_3 available; enter this number under Al_2O_3 and Na_2O; Al_2O_3 is now used up, and the excess Na_2O is used to make acmite (see 4a).

3c If 3a and 3b leave a residue of Al_2O_3, it is allotted with an equal molar proportion of CaO to make anorthite *an*: write the residue of Al_2O_3 on the *an* line under Al_2O_3 and under CaO.

3d If 3c uses all the available CaO, leaving an excess of Al_2O_3, this is entered as corundum (*c*).[5] This is a symptom of highly aluminous modal minerals such as muscovite.

4a If an excess of Na_2O remains from 3b, it is allotted to an equal proportion of Fe_2O_3 to make acmite (*ac*).

4b If, as usually happens, an excess of Fe_2O_3 remains after 4a, it is allotted with an equal number of moles of FeO to make magnetite (*mt*).

4c If 4b leaves an excess of Fe_2O_3, or if all FeO has been used in making ilmenite, assign Fe_2O_3 to hematite (*he*).

[3] The full norm calculation procedure is described in Cox et al. (1979).

[4] At the end of the calculation, all the allotments in a particular column must add up to the original molecular proportion of the oxide concerned. That is, the totals in the bottom line of the table must agree with the entries in line 4.

[5] At this stage, all of the separate entries under Al_2O_3 should add up to the Al_2O_3 entry in line 4.

5a The remaining FeO is added to MgO and the total entered in the Φ ('phi') box. This is used in calculating the ferromagnesian silicates. (This is a simplification: the original CIPW scheme treats FeO and MgO separately throughout, reporting olivine separately as fo and fa, for example.)

5b Calculate $\mu = \text{MgO}/\Phi$ where MgO is the molar MgO used in step 5a. (This parameter is used in the final step of the norm calculation.)

6a If CaO remains after 3c, it is allotted with an equal amount of Φ to make diopside (high-Ca pyroxene).

6b If 6a leaves an excess of CaO, it is allotted to wollastonite (wo).

6c If 6a leaves an excess of Φ, it is allotted to enstatite.

That completes the allotment of oxides other than SiO_2: for all oxides except SiO_2, the entry in the 'Column sum' box at the bottom of the table should equal that in the 'moles/100 g' box near the top. The proportions of enstatite, albite and orthoclase (and in extreme cases other minerals) are however dependent upon there being a sufficient amount of SiO_2 available to satisfy their formulae. This test is applied, and the necessary adjustments made, in the sections 7a–7e following.

7a Using the mineral formulae given in Table 2.3, allocate SiO_2 to the silicate minerals which have been established provisionally in items 2 to 6c. Enter (in pencil) the amount of SiO_2 required for each mineral on the appropriate line under SiO_2. Add up the total moles of SiO_2 which these allocations will require. Call it '*W*' and enter it in the *W* box on the form.

7b Call the total SiO_2 available '*S*' (see line 4). If *S* is *greater than W*, an excess of SiO_2 exists, and the difference should be entered as quartz (*q*). In this case, proceed directly to item 8.

7c If *S* is *less than W*, there is a *deficiency* in SiO_2, and the amount of enstatite (LCP) calculated in 6c must be amended. Call the original amount of SiO_2 allocated to enstatite '*E*'. $(W - E)$ is the total SiO_2 requirement if enstatite is disregarded. If all the enstatite were transformed to olivine (which has half the silica requirement of enstatite), the total silica requirement would become $(W - E) + 0.5E = W - 0.5E$.

Thus, if:

$$W - S \leq 0.5E \qquad \text{[B1]}$$

the silica deficiency will be eliminated by transforming part or all of the enstatite into olivine. The required adjustments are then:

$$\begin{aligned}\text{Revised amount of enstatite} &= E' \\ &= E - 2(W - S)\end{aligned} \qquad \text{[B2]}$$

Enter this number E' on the enstatite line under SiO_2 and under Φ in place of the old values. The remaining Φ is entered on the olivine line:

$$\text{Amount of olivine} = E - E' \qquad \text{[B3]}$$

The amount of SiO_2 allocated to olivine is *half* of this number; enter this on the olivine line under SiO_2.

Then proceed directly to item 8.

If $W - S > 0.5E$, *all* of the enstatite must be transformed into olivine, and further steps taken to meet the remaining SiO_2 deficiency, the first being to transform albite into nepheline.

7d The new silica requirement, once some or all of the enstatite has been replaced by olivine, is $X = W - 0.5E$. (Though enstatite has now been eliminated from the norm, the quantity *E* calculated in 7c is still relevant in the calculations).

Let the provisional amount of Na_2O in albite calculated in 3b be called '*A*'. $X - 6A$ would be the new SiO_2 requirement if albite were disregarded. If we transformed all the albite into nepheline, the new SiO_2 requirement would become $(X - 6A) + 2A = (X - 4A)$.

Thus, if:

$$S \geq X - 4A \qquad \text{[B4]}$$

the silica deficiency will be eliminated by transferring all or part of the albite into nepheline. The required adjustments are then:

Revised amount of Na_2O in albite = A' = $A - 0.25\,(X - S)$ [B5]

Amount of Na_2O in nepheline = N = $0.25\,(X - S)$ [B6]

Now proceed directly to item 8.

If $S < X - 4A$, *all* of the albite must be transformed into nepheline, and yet further steps taken to reduce the silica requirement.

7e If step 7d leaves a silica deficiency, orthoclase may be recalculated to leucite. It is very unusual for a silica deficiency to persist after this step.

8 All the SiO_2 allotments are now complete. The final step, having checked that the totals in each column add up to the amount of each oxide available in line 4, is to convert the molecular norm into mass % form. For each mineral, take the moles of any constituent which is present in the formula as a *single* molecule (e.g. for feldspar use K_2O or Al_2O_3, not SiO_2; for olivine use SiO_2, not Φ), and multiply it by the molecular weight given in the penultimate column, entering the result in the final column.

For the *ferromagnesian minerals* diopside, enstatite and olivine, the mineral RMM values used here depend on their MgO/FeO ratio. A simple approximation is to use the following values:

	Less evolved rocks ($\mu > 0.5$)	**More evolved rocks ($\mu < 0.5$)**
Diopside	224	240
Enstatite	108	124
Olivine	156	188

The accurate solution is to use the equations:

	Equation for mineral RMM
Diopside	RMM = 216 × μ + 248 × (1 − μ)
Enstatite	RMM = 100 × μ + 132 × (1 − μ)
Olivine	RMM = 140 × μ + 204 × (1 − μ)

9 Calculate the total of normative mineral percentages and compare with the volatile-free analysis total. If the exact RMM values for Di, En and Ol have been used, the norm total should agree with the analysis within ± 0.05%; if approximate RMM values have been used, agreement should usually be within ± 0.50%. A larger discrepancy may indicate a calculation error.

PLOTTING DATA IN TERNARY AND QUATERNARY DIAGRAMS

Fig. 8.1 illustrates the kind of diagram recommended by International Union of Geological Sciences (**IUGS**) for defining the composition ranges covered by various plutonic rock names. It is a **ternary** diagram in which the relative proportions of three minerals in a rock are plotted to see which name is applicable: in this example the three minerals are quartz (Q), alkali feldspar (A) and plagioclase feldspar (P). The mineralogical composition of a rock is determined by point-counting a thin section as described in Chapter 1 (see 'Classification by mineral proportions – colour index') and thus the percentages obtained are *volume percentages* rather than mass percentages.

Data points in ternary graphs may be plotted using special triangular graph paper as illustrated in Fig. B1a. Table B2 gives an illustrative modal composition of a granite for explaining the plotting process. Attempting to plot the percentages of quartz, alkali feldspar and plagioclase (column 1 of Table B2) *directly* leads to three separate lines that together form a triangle (shaded in Fig. B1b; the size of the triangle obtained is related to the total percentage of the other minerals in

Table B2 Recalculation of a rock mode for plotting in a ternary diagram.

	All minerals *(volume %)*	**Felsic minerals *(rel. volume %)***	
quartz	24	**Q**	31
alkali feldspar	33	**A**	43
plagioclase	20	**P**	26
hornblende	5		
biotite	11		
opaques	5		
accessories	2		
total	100		
total of felsic minerals	77		100

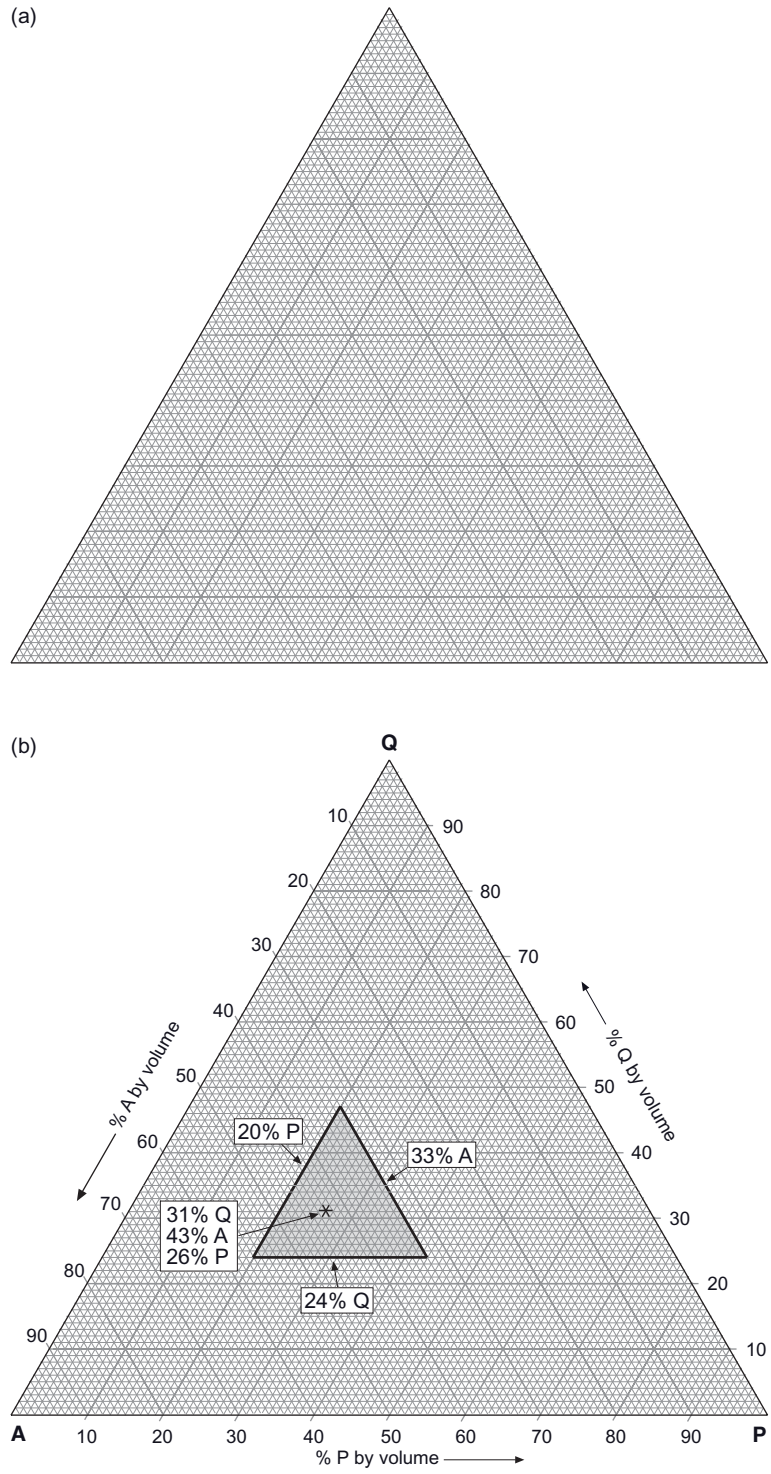


Fig. B1 (a) Example of ternary graph paper scaled to a 10 cm side; graduations divide each side into 100 equal parts. Proprietary versions are available from specialist stationers. (b) Ternary QAP plot (cf. Figs. 6.1 and 8.1) of the illustrative granite mode in Table B2; Q represents quartz, A represents alkali feldspar and P represents plagioclase (see Figs. 6.1.1 and 8.1.1).

the rock (hornblende etc.) not represented in Fig. B1(b). For the rock to appear as a single point in Fig. B1(b), it is necessary to scale up the quartz, alkali feldspar and plagioclase percentages so that (as Q, A and P in column 2 of Table B1) they add up to 100% on their own. Note that the 3 felsic minerals constitute 77% of the mode; scaling up is achieved by multiplying each one by the factor 100/77 (or dividing by 0.77). The values so obtained are shown in column 2 of Table B2 and they plot as the star in Fig. B1(b).

The same procedure is used to plot ternary variation diagrams from norms or other data.

It is also possible to visualize – in principal – plotting chemical or mineralogical data in three-dimensional quaternary (i.e. 4-component) diagrams having the form of a regular tetrahedron, though representing such plots on a two-dimensional page raises obvious practical challenges. An example of such a quaternary diagram is shown in the inset in Fig. 4.1. The solution often adopted is to **project** coordinates that plot in the interior volume of such a figure on to one of the two-dimensional faces (e.g. Fig. 9.21). The calculation in Exercise B2 illustrates the simplest form of such projection. Other ways of projecting in quaternary systems are described by Cox et al. (1979).

MIXING CALCULATIONS

It is often helpful to test a petrological hypothesis using a numerical model. One example is testing whether the composition of a given hybrid sample (analysis 'A') could be the result of the bulk assimilation of typical wall-rock (analysis 'B') by a magma represented by rock analysis 'C'. This possibility can be tested using a simple mixing equation:

$$C_i^{\mathrm{A}} = C_i^{\mathrm{B}} x^{\mathrm{B}} + C_i^{\mathrm{C}} x^{\mathrm{C}} \qquad [\mathrm{B7}]$$

where C_i^{A} represents the concentration (mass %) of species i (e.g. MgO) in analysis A, C_i^{B} represents its concentration in wall-rock B, and x^{B} represents the mass proportion of wall-rock B assimilated by melt C ($0 < x^{\mathrm{B}} < 1.00$, $x^{\mathrm{B}} + x^{\mathrm{C}} = 1.00$.). An example of using this calculation is given in Exercise 8.5 at the end of Chapter 8. The equation can be used to estimate how much of a given potential contaminant is needed to account for the composition of a hybrid rock (solving for x^{B}).

Other instances where the mixing equation (which need not be confined to mixtures of just two components) are *(i)* assessing the effects of olivine accumulation at the base of a komatiite flow and *(ii)* calculating the change of melt composition when 20% plagioclase (of specified composition) is crystallized from a parent melt. In the latter case where a component is being subtracted, the equation needs to be formulated in terms of mixing plagioclase with the residual melt to recreate the initial melt:

$$C_i^{\text{parental melt}} = C_i^{\text{residual melt}} x^{\text{residual melt}} + C_i^{\text{plagioclase}} x^{\text{plagioclase}} \qquad [\mathrm{B8}]$$

Such calculations can be repeated for a number of major elements. Computer programs are available which use a range of different major elements to calculate a least-squares best fit mixture (of residual melt and several fractionating minerals) to match the observed composition of the candidate parental melt.

EXERCISES

B1. Calculate simplified CIPW norms for the following rock analyses (volatile-free):

	a	b	c
SiO_2	56.9	75.4	48.57
TiO_2	0.75	0.11	1.18
Al_2O_3	19.70	13.72	17.40
Fe_2O_3	2.80	0.29	1.33
FeO+MnO	2.20	0.82	8.69
MgO	1.31	0.12	8.71
CaO	2.36	0.49	11.50
Na_2O	7.95	4.05	2.40
K_2O	5.45	4.40	0.25
P_2O_5	0.18	0.03	0.10

B2. Plot on Fig. B1(a) the following modal composition of a plutonic rock: plagioclase 38%, orthopyroxene 30%, clinopyroxene 21%, olivine 4%, opaques and accessories 7%. Devise an appropriate rock name using Fig. 4.1.

B3. Explain which normative minerals are ruled out if the following normative minerals are present?
enstatite (En);
corundum (c);
olivine (Ol).

Appendix C

Symbols, units and constants used in this book

The units given below are SI units (http://physics.nist.gov/cuu/Units/). Some older publications may give the same quantities in traditional units (e.g. viscosity in poise); for on-line conversion to SI, visit http://www.megaconverter.com/Mega2/index.html.

A atomic **mass number** of an isotope = $Z + N$

An_{65} (e.g.) symbol representing a plagioclase solid solution consisting of 65 molar % of the anorthite ($CaAl_2Si_2O_8$) end-member and 35 molar % of albite ($NaAlSi_3O_8$)

C number of **components** in a system at equilibrium (Phase Rule, Box 3.3)*

C_i^a the concentration of species i in phase (mineral, melt …) a, in mass % unless otherwise indicated

c speed of light (= $2.998 \times 10^8\,m\,s^{-1}$ *in vacuo*)

D_i bulk distribution coefficient for the element i in a specified mix of minerals*

F melt fraction during partial melting or fractional crystallization (between 0.0 and 1.0)*

f number of degrees of freedom (variance) associated with an equilibrium (Phase Rule, Box 3.3)*

Fo_{90} symbol representing an olivine solid solution consisting of 90 molar % of forsterite (Mg_2SiO_4) and 10 molar % of fayalite (Fe_2SiO_4)

G crystal growth rate (units unspecified)

*dimensionless quality

Igneous Rocks and Processes: A Practical Guide, 1st edition. By Robin Gill. Published 2010 by Blackwell Publishing

g acceleration due to gravity (= $9.81\,m\,s^{-2}$)

h depth, in km

K_i^A **partition coefficient** describing the distribution of element i between melt and mineral A (see Box 2.7)*

M colour index (Fig. 1.3b)

N crystal nucleation rate (units unspecified) *or* neutron number of an isotope (according to context)

n refractive index in general, or of an isotropic material (e.g. glass)*

n_α the lowest refractive index of a biaxial mineral (see Fig. A2)*

n_β refractive index of a biaxial mineral for a ray vibrating in the β direction (see Fig. A2)*

n_γ the highest refractive index of a biaxial mineral (see Fig. A2)*

n_ε the refractive index for the extraordinary ray in a uniaxial mineral (see Fig. A2)*

n_ω the refractive index for the ordinary ray in a uniaxial mineral (see Fig. A2)*

$n+$ nominal cation charge* (Box 2.7) in atomic charge units

P load pressure, in pascals (Pa), megapascals (MPa = 10^6 Pa) or gigapascals (GPa = 10^9 Pa)

P_{H_2O} **partial pressure** of water, in same units as P

P_m magma pressure, in same units as P

r ionic radius (Box 2.7), in pm (picometres = 10^{-12} m)

r_x radius of a spherical particle (or linear size of an equant crystal) used in Stokes' equation, in m

t thickness of a crystal section (or path-length through it), in m

T temperature, in °C or kelvins (K)

T_p potential temperature, in °C

v_t	terminal velocity (see **Stokes' Law**) in $m\,s^{-1}$		molar proportions of its end-members*
x^A	mass fraction of mineral A in a solid assemblage undergoing partial melting.	x^a	the mass proportion ($0 < x^a < 1.00$) of component (e.g. mineral) *a* in a mixture
X	(a) composition in general terms; (b) composition of a mineral expressed in	Z	atomic number*

Greek and other symbols (in Greek alphabetic order)

α	alpha	the vibration direction experiencing the *lowest* refractive index in a biaxial crystal (see Fig. A2)
β	beta	the vibration direction perpendicular to both α and γ in a biaxial crystal (see Fig. A2)
γ	gamma	the vibration direction experiencing the *highest* refractive index in a biaxial crystal (see Fig. A2)
δ	delta	the birefringence of an anisotropic mineral = $n_{maximum} - n_{minimum}$
δ^{18}**O**		$^{18}O/^{16}O$ ratio in a mineral or rock, expressed as the positive or negative deviation 'per mil' (‰ = parts per thousand) from the $^{18}O/^{16}O$ value in a reference material (see Glossary)
ΔT	delta-*T*	degree of supercooling (= $T - T_{solidus}$) in °C – see Box 2.3
ε	epsilon	the extraordinary ray vibration direction parallel to the symmetry axis of a uniaxial crystal (Fig. A4)
η	eta	melt viscosity, in $N\,s\,m^{-2} = kg\,m^{-1}\,s^{-1}$
κ	kappa	tensile strength of country rock, in Pa
λ	lamda	wavelength, given in metres (m), micrometres (μm = 10^{-6} m), or picometres (pm = 10^{-9} m)
μ	mu	the molar ratio MgO/Φ in the norm calculation (Appendix B)
ν	nu	frequency of light, in Hz = s^{-1}
ρ	ro	density, in kg dm^{-3}
ρ_m		density of melt, in kg dm^{-3} = g cm^{-3}
ρ_x		density of a suspended crystal, in kg dm^{-3} = g cm^{-3}
σ_1	sigma-1	maximum principal compressive stress, in Pa
σ_2		intermediate principal compressive stress, in Pa
σ_3		least principal compressive stress, in Pa
ϕ	phi (l.c.)	number of phases participating in an equilibrium (Box 3.3)*
Φ	phi (cap)	= molar MgO + FeO (after calculation of Fe oxides minerals) in the calculation of a simplified norm (Appendix B)
ω	omega	the ordinary ray vibration direction, perpendicular to the symmetry axis of a uniaxial crystal (Fig. A4)
‰	per mil	See δ^{18} **O** above

Glossary

a'a Hawaiian term (pronounced 'ah-ah') describing basaltic lava with a very rough, clinkery or rubbly fragmented surface.

accumulation the concentration of crystals of one or more minerals near to the base of a magma chamber (or a thick lava flow) to form a **cumulate**.

acicular needle-shaped crystal habit (from Latin for an ornamental pin).

acid, acidic describes a magmatic rock containing quartz, or a melt sufficiently SiO_2-rich to crystallize quartz.

adakite an andesite or dacite lava characterized by Na_2O >3.5%, low **HREE** and yttrium ($Y \leq 18$ **ppm**) and consequently a high La/Yb ratio, with a positive Sr anomaly in a **primitive-mantle**-normalized diagram (Fig. 6.15b) and Sr/Y >4.

adiabatic, adiabat describes a process, e.g. expansion or contraction, in which a body of rock exchanges no heat with its surroundings. Work done, e.g. on expanding, draws on internal energy and thus causes temperature to change. An adiabat is an ascent path in a P–T diagram representing the temperature change during such a process (e.g. Fig. 2.17).

AFC (crustal) **A**ssimilation with **F**ractional **C**rystallization, a mechanism in which assimilation of crustal wall-rocks by an evolving magma is assisted by the release of **latent heat** during fractional crystallization.

alkali prefix specifying a category of rocks containing high total alkali contents in a **TAS plot** (those above the lines X–Y or X–Z in Fig. 1.5). **IUGS** defines alkali rocks as those containing either (ii) modal or normative **foids**, and/or (iii) alkali pyroxenes or amphiboles. Cf. **subalkali** and **tholeiitic**.

alkali feldspar term embracing all feldspars whose compositions lie between $KAlSi_3O_8$ (orthoclase) and $NaAlSi_3O_8$ (albite), including perthites (Box 8.1).

alkaline ('alkalic' in N. America) older forms of **alkali**.

alteration a process in which one or more **primary** igneous minerals (e.g. olivine) are converted into secondary **hydrous** minerals (e.g. serpentine) that are more stable under **hydrothermal** conditions.

amphibolite (a) a mafic metamorphic rock consisting essentially of hornblende and plagioclase. (b) a facies of regional metamorphism.

a.m.u. atomic mass unit; scale of relative atomic masses in which $^{12}C = 12.0000$.

amygdale, -dule a **vesicle** in a volcanic rock that has been filled with post-magmatic **hydrothermal** minerals. From the Greek for 'almond'.

analyser sheet of Polaroid™ located above the objective lens whose vibration direction is oriented perpendicular to that of the **polarizer**. The analyser may be removed (**PPL**) or inserted (**XP**) according to the task in hand.

anatexis partial melting of a crustal rock under high-grade metamorphic conditions.

anhedral describes a mineral grain showing no regular crystal form (Greek: 'no sides').

anhydrous describes a mineral or other material that contains no water (Greek: 'no water').

anisotropic (optics) describes a mineral whose refractive index and other properties vary according to crystallographic direction.

Igneous Rocks and Processes: A Practical Guide, 1st edition. By Robin Gill. Published 2010 by Blackwell Publishing

ankaramite a basaltic rock having a high content of olivine *and* pyroxene **phenocryst**s (after Ankaramy in Madagascar).

antiperthite sodium-rich feldspar containing exsolution lamellae of K-rich feldspar (cf. **perthite**).

aphanitic describes a rock or groundmass whose crystalline constituents are too fine-grained to be discernable with the naked eye (Greek: 'not visible').

aphyric non-porphyritic.

aplite vein or other intrusive body of granitic rock consisting of light-coloured minerals with a fine-grained **phaneritic** texture.

apophysis (plural –yses) irregular small offshoot or vein, branching into the wall-rocks from the margin of a dyke or other minor intrusion.

ash name for pyroclasts with diameter <2 mm.

aspect ratio the thickness:length ratio used to characterise the geometry of lavas, **pyroclastic** flow deposits and granite plutons.

atomic number the number Z of protons in the nucleus, identifying a particular element; numerically equal to (a) the charge on the nucleus in atomic charge units, and (b) the number of electrons in the neutral atom.

atomic proportions the relationship (e.g. the ratio) between two or more elements, expressed in terms of the *numbers of atoms* rather than their mass proportions. Numerically the same as the **molar proportions** of the corresponding oxides.

autobrecciation the fragmentation of the rigid outer skin of a lava flow arising from stress associated with continued flow in the interior.

autolith a **cognate** inclusion in an igneous rock.

balsam (Canada balsam) optical cement with RI = 1.54 (similar to optical glass) historically used in thin section preparation; epoxy resin is more common today.

bar obsolete unit of pressure ≈ 1 atmosphere. 1 bar = 0.1 MPa = 10^5 Pa.

basic describing a rock whose SiO_2 content lies between 45% and 52%.

batholith large-scale intrusive body (100–10,000 km^2 in outcrop) comprising a number of individual granitoid plutons (Greek: 'depth rock').

bimodal describes an igneous rock suite consisting of basic and acidic (or melanocratic and leucocratic) rock types, with intermediate rock types under-represented (e.g. Figs. 6.22 and 9.13).

binary a **system** or **phase diagram** embracing mixtures or solutions of *two* pure **component**s; e.g. Mg_2SiO_4–Fe_2SiO_4.

body colour the colour of a mineral under the microscope, seen in plane-polarized light. Cf. **pleochroism**, **interference colour**.

Bouguer anomaly the gravity variation observed along a measured traverse, corrected for factors such as latitude, elevation and terrain.

brittle describes mechanical behaviour in which a material fractures under stress rather than changing shape continuously. Cf. **ductile**.

bulk analysis a geochemical analysis of powder prepared by crushing a complete rock sample (after removal of weathered surface, veins, etc.). Cf. **mineral analysis**.

calc-alkaline (-ic) ambiguous term (see Sheth et al., 2002; Arculus, 2003) for rock suites showing negligible iron-enrichment (Fig. 6.8); broadly synonymous with the medium- and high-K associations in Figs. 1.6 and 6.11.

caldera surface depression (>1 km in diameter and usually bounded by ring-fault scarps) due to subsidence of the roof of an underlying magma chamber. Often the result of one or more large-scale ignimbrite eruptions. Latin: *caldaria* = 'boiling pot'.

carbonatite an igneous-textured rock consisting mainly of carbonate minerals believed to have crystallized from a molten-carbonate magma.

cauldron a **caldera** exhumed to a level at which most of the eruptives have been removed by erosion, and older volcanic or sedimentary units below the caldera floor are now exposed (adapted from Cole et al., 2005).

cauldron subsidence foundering of a large crustal block bounded by ring faults, with complementary rise of magma to form ring intrusions and/or a roof intrusion (Fig. 8.9b).

chalcophile class of chemical elements that partition readily into sulphide materials (Greek: 'copper-liking') rather than silicates. Cf. **lithophile**.

charge in a phase equilibrium experiment, the material being experimented on (usually sealed in a Au or Pt capsule); normally prepared by mixing synthetic oxide gels in pre-determined proportions, but during the experiment it will consist of crystals and/or melt, and after **quench**ing of crystals and/or glass.

charnockite a granitic rock characteristic of high-grade and AMC terrains in which the principal mafic mineral is orthopyroxene. Named

after the 17th century founder of Calcutta, Job Charnock, whose gravestone is carved from rock of this type.

chondrite the most abundant class of stony **meteorite**, most of which are characterized by mm-scale spheroidal assemblages of crystals and glass called chondrules.

chromitite an **ultramafic** rock consisting essentially of chromite (chrome spinel – Fig. 5.1.1); forms layers in many layered mafic intrusions.

CIPW norm synonym for the **norm** calculation devised by the early 20th century petrologists W Cross, J P Iddings, L V Pirsson and H S Washington.

cognate describes an inclusion (**autolith**) that is genetically related to the host igneous rock (e.g. a cumulate block).

colour index the **modal** percentage (by volume) of **mafic** minerals in a rock (see Fig. 1.3b).

comb layering layers made up of elongated crystals (e.g. plagioclase, hornbende) oriented perpendicular to the plane of layering (cf. **orbicular**).

compatible element An element whose cations are readily incorporated into the cation sites of one or more crystallizing minerals (see Box 2.5). Compatible elements and host minerals are mutually selective: e.g. Ni is accepted in olivine (and to some extent pyroxene) crystals but not feldspar.

component one of the basic chemical constituents of a rock, **phase** or **system**, formulated in such a way as to minimize their number [e.g. for most purposes the components of olivine are defined as Mg_2SiO_4 + Fe_2SiO_4 (= 2 components), not MgO + FeO + SiO_2 (= 3 components) or Mg + Fe + Si + O (= 4 components)]. For clarity, components are represented in this book by formulae rather than end-member names.

composition plane the boundary between neighbouring **twin** domains in a crystal.

continental flood basalts (CFBs) continental volcanic provinces characterized by the eruption of thick successions of extensive tabular basaltic lavas; continental examples of **large igneous provinces**.

cooling unit package of lava flows or PDCs emplaced in a sufficiently short interval to cool as a single entity (often indicated by a common jointing pattern).

corona (texture) a reaction rim between two adjacent crystals (e.g. olivine and plagioclase in gabbros) reflecting grain-boundary reactions at sub-**solidus** temperatures (Latin: 'wreath' or 'crown').

cotectic a curvilinear boundary in a phase diagram where two or more minerals are in equilibrium with melt.

coulée an elongated lava dome, or a lobe of lava on a exogenous dome (see Fig. 6.3e and Fig. 9.10).

crystal a state of matter in which atoms, ions or molecules are arranged in a regularly repeated three-dimensional structure, whose symmetry bestows on minerals certain well defined compositional and optical characteristics.

cumulate describes a plutonic rock in which one or more **cumulus** minerals have been concentrated by unspecified crystal sorting processes during slow cooling of a magma chamber. Cumulate rocks often exhibit igneous **layering**.

cumulus describes an early-formed mineral or crystal that accumulates – becomes concentrated – on the floor of a crystallizing magma chamber. As used in this book, the term carries no implication as to mechanism of concentration.

cuspate shape bounded by concave surfaces that meet at pointed terminations.

$$\delta^{18}O = 1000 \times \frac{\left(^{18}O/^{16}O\right)_{sample} - \left(^{18}O/^{16}O\right)_{standard}}{\left(^{18}O/^{16}O\right)_{standard}} ‰;$$

the symbol '‰' ('per mil') is an abbreviation for 'parts per thousand'. 'Standard' in this formula refers to an international reference material (usually 'standard mean ocean water') measured in the same laboratory. The purpose of using $\delta^{18}O$ is to minimize inter-laboratory errors in measuring small differences in $^{18}O/^{16}O$ ratio of 1% or less.

decompression melting melting caused by mantle upwelling to depths shallow enough for the mantle **solidus** to be crossed (see Fig. 2.17). No rise of temperature is required.

dehydration reaction in which a **hydrous** mineral (one containing OH, e.g. amphibole) breaks down into an **anhydrous** mineral (e.g. pyroxene) plus a hydrous (H_2O) fluid.

dendritic describes a crystal that has adopted a branching habit (Greek *dendron* = 'tree') – see Plate 5.11.

dense rock equivalent (DRE) A basis for reporting the volume of a pyroclastic deposit by recalculating to the magma volume prior to inflation (*i.e.* with zero vesiculation). The formula used

is: $\text{volume}_{DRE} = \text{volume}_{measured} \times \rho/2.5$ where ρ = density of the tephra in g cm^{-3}.

depleted, depletion *rock (or magma source)*: having a **normalized** concentration of incompatible elements lower than in comparable rock types (see Chapter 2); *element:* present in a rock at a lower **normalized** concentration than comparable elements (e.g. Nb in subduction-related volcanics).

deuteric describes alteration by late-stage magma-derived fluids (Greek: 'secondary')

diapir up-welling cylindrical or mushroom-like plume of buoyant material (Greek: 'to pierce').

diatreme a breccia-filled sub-volcanic vent or pipe ('carrot-shaped vertical intrusion' – Mitchell, 1986) drilled through near-surface country rocks by explosive gas-rich **silica-undersaturated** magmas such as kimberlite and melilitite (Box 9.7).

ductile mechanical behaviour in which a material deforms (changes shape) irreversibly without cracking. Cf. **brittle**.

dyke a parallel-sided minor intrusion that cross-cuts the fabric of the host rocks.

eclogite a coarse-grained metamorphic rock consisting of garnet and **omphacite** pyroxene – the mineral assemblage adopted by basaltic rock at high (mantle) pressures.

effective viscosity loose term used to describe the resistance to flow in fluids that exhibit a finite yield strength (i.e. not strictly **viscous**).

effusion rate the volume rate of lava production at a vent, in units such as $m^3 s^{-1}$.

effusive describes eruptions characterized by passive emission of lava (cf. **explosive**).

electron microprobe an analytical instrument in which a mineral crystal in a rock section is bombarded by a fine beam of high-energy electrons; elements present emit characteristic X-rays with intensities proportional to their concentration, allowing μm-scale *in situ* chemical analysis.

***en echelon* dykes** parallel dykes that are longitudinally offset like the edges of shingles on a roof.

end-member one of the pure ingredients that are mixed together in a **solid-solution** mineral series such as plagioclase, which is made up of the end-members albite ($NaAlSi_3O_8$) and anorthite ($CaAl_2Si_2O_8$).

equant equi-dimensional, of equal size in all directions.

equilibrium *chemical:* two **phases** A and B in mutual contact are said to be in chemical equilibrium with each other if, for every chemical **component** common to both, the rate at which the component passes from A to B is exactly matched by the rate at which it passes from B to A, so that the overall chemical compositions of A and B remain unchanged. The two phases need *not* have the same composition.

thermal: two phases in intimate contact are said to be in thermal equilibrium if they have the same temperature.

equilibrium crystallization a crystallization process in which ideally all crystals of a given mineral, regardless of when they formed, have a uniform composition which changes with falling temperature, so as to remain in continuous chemical and thermal equilibrium with the evolving melt. Cf. **fractional crystallization**.

euhedral describes the shape of a crystal that is completely bounded by its characteristic crystal faces, showing perfect or near-perfect crystal form (= idiomorphic) (Greek: 'well sided').

eutaxitic foliation caused by sub-parallelism of lensoid pumice lapilli in a **welded lapilli tuff** (Greek: 'well arranged').

eutectic a point in a **phase diagram** (e.g. E in Fig. 2.2) marking the lowest point on the **liquidus**, at the point where it meets the **solidus**. It indicates the *composition* of the final melt formed during crystallization, and of the first melt to form during melting. It also marks the *temperature* at which a melt becomes entirely crystallized during cooling, and at which melting begins during heating (Greek: 'easily melting').

evolved describes a magma or rock composition having relatively low MgO content and/or high SiO_2 content, suggesting that it has undergone a significant degree of fractional crystallization. Cf. **primitive**.

explosive eruption one involving the explosive release of pressurized gas and dominated by production of pyroclastic material (cf. **effusive**).

exsolve, exsolution the separation of a **supersaturated** solute to form a new phase, either crystalline, gaseous or – in special cases – liquid. In crystals, this process usually produces exsolution lamellae or blebs (e.g. Plate 4.7 and Fig. 8.1.1c in Box 8.1).

extinction angle the angle measured (by stage rotation) between an extinction position of a crystal and some reference feature of the crystal e.g. a face, a cleavage trace (pyroxene) or a **twin composition plane** (plagioclase).

extract denotes the overall composition of solid material separating from a melt when *several* minerals crystallize together, taking account of individual mineral compositions and their relative proportions.

fast (optical) in a general cross-section of a birefringent mineral, the vibration direction having the lower RI is the 'fast' direction. Cf. **slow**.

feldspathoid (abbreviated by IUGS to '**foid**') see Box 9.1.

felsic class of minerals including feldspars, feldspathoids and silica minerals such as quartz. Also describes rocks that are rich in such minerals (see Fig. 1.3).

fenite quartzo-feldspathic alkali-metasomatized contact-rocks rich in K-feldspar and sodic pyroxenes or amphiboles, found bordering many intrusive carbonatites.

ferromagnesian category of minerals rich in ferrous iron and magnesium, including olivine, pyroxene, amphibole, biotite and **phlogopite**.

fertile describes a mantle peridotite that has not experienced previous episodes of melting.

fiamme sub-parallel, lensoid pumice lapilli (Table 7.2) or smaller clasts in a **welded** (eutaxitic) **lapilli-tuff** (Italian: 'flames').

fine-grained see Fig.1.3a.

flow field 'a tangle of (lava) flows from a single eruptive episode' (Francis and Oppenheimer, 2004).

fluid *Physics:* a general term embracing states of matter capable of flow, i.e. liquids and gases. *Geology:* refers to hydrous or other volatile-rich fluids, whether in liquid, gas or supercritical state.

foid abbreviation for **feldspathoid** (Le Maitre, 2002). See Box 9.1.

fractional crystallization an idealized crystallization process in which early fractions of crystals are isolated from later fractions of melt; circumstances (e.g. rapid cooling) inhibit interaction between early-formed crystals and later fractions of melt. Cf. **equilibrium crystallization**.

gabbroic an adjective embracing gabbro-like coarse-grained rocks such as anorthosite and norite, in addition to gabbro *sensu stricto*.

geotherm a model curve, estimated from surface heat flow measurements, indicating how temperature increases with depth within the Earth.

geothermometer a temperature-dependent equilibrium between two coexisting solid-solution minerals which, when calibrated by laboratory experiments at controlled temperatures, can be used to estimate the temperature of crystallization of a natural rock from the measured compositions of relevant minerals; e.g. the pyroxene **solvus** shown in Fig. 4.5.2.

glomeroporphyritic porphyritic texture in which **phenocryst**s occur in clusters.

granitoid field name for all coarse-grained rocks consisting of quartz, alkali feldspar and plagioclase in any proportions.

granophyre (porphyritic) granitoid whose groundmass exhibits a micrographic texture between K-feldspar and quartz (see Plate 8.3).

gravity-stratified superseded description of **modally graded** layers (Fig. 4.7b,c).

greenstone; – belt field term for basic volcanic rocks metamorphosed in greenschist facies, having a greenish hue on account of secondary chlorite, hornblende and epidote; an elongated, folded belt of such rocks (with metasediments).

groundmass **interstitial** material surrounding the **phenocryst**s in a porphyritic rock.

hawaiian describes the least explosive style of volcanic eruption, characterised by mild fire-fountaining of low-viscosity basalt magma.

HCP abbreviation for high-Ca pyroxene (Fig. 2.1.1).

heterogeneous nucleation describes nucleation and growth of one mineral on a crystal of another, or on some other solid substrate.

HFS elements (HFSE) high field strength elements, a sub-group of **incompatible elements**. See Box 2.7.

high-alumina basalt (HAB) currently defined as any basalt with $(Al_2O_3)_{vol\text{-}free} > 16\%$ (Le Maitre, 2002). Though used by some as a synonym for calc-alkaline basalt, HABs may in fact be **sub-alkali**, calc-alkaline *or* alkali basalts.

HITE highly incompatible **trace element** (e.g. Rb, Ba, Th, Nb).

hot spot 'any localized occurrence of anomalous (usually intraplate) magmatism not easily explained by plate tectonic processes' (Fitton, 2007). Only a minority of hot spots are associated with mantle **plumes**.

HREE refers to the 'heavy' (i.e. high-*Z*) rare earth elements Gd – Lu (see Fig. 2.7.2).

hyalo- IUGS prefix indicating the presence of glass in an igneous rock (e.g. Plate 9.3).

hyaloclastite **pyroclastic** deposit consisting of shattered fragments of volcanic glass formed by subaqueous **quench**ing of (usually basaltic) melt (Greek: 'glassy-fragment').

hydrolysis a chemical reaction involving breakdown of the water molecule, one fragment becoming one of the reactants, e.g. H^+ in reaction 8.1.

hydrothermal describes a category of late- and post-magmatic processes involving water at elevated temperatures (typically 150–500 °C); e.g. alteration, mineralization.

hydrous describes a mineral (e.g. mica, amphibole) that contains structural water or hydroxyl (OH), or a fluid that consists mainly of H_2O.

hypabyssal describes intrusive rocks emplaced at relatively shallow depth. Cf. **plutonic**.

hypersolvus the region of homogeneous solid solution above a solvus in a phase diagram (e.g. Fig. 8.12a); a granite containing single homogeneous alkali feldspar (crystallized under low P_{H_2O} conditions) that has subsequently exsolved into **perthite**.

hypersthene obsolete name for orthopyroxene solid solutions in the range $En_{50–70}$ (see Box 2.1 for current nomenclature).

hypersthene-normative obsolete description of a rock whose **norm** contains orthopyroxene. 'Enstatite-normative' is now preferred (Table 2.3).

iddingsite informal name for a reddish brown composite alteration product of olivine, consisting of goethite/hematite, chlorite and **smectite**.

idiomorphic see **euhedral** (Greek: 'having own shape').

ignimbrite a deposit (usually of massive **lapilli-tuff**) resulting from the passage of a pumiceous **pyroclastic density current**.

immobile identifies a group of elements whose concentrations are least affected by **hydrothermal alteration**.

incompatible element a **trace element** whose large ionic radius or high ionic charge causes it to be excluded from **phenocryst** minerals, so that its concentration builds up in residual melt fractions (Box 2.7). The major elements K, Ti and P often behave as incompatible elements.

incongruent melting melting of a mineral where a new mineral is formed in addition to melt: mineral A → melt + mineral B; the converse of the reaction relationship discussed in Box 4.3. One mineral that melts incongruently (at atmospheric pressure) is enstatite: $Mg_2Si_2O_6$ (En) → melt + Mg_2SiO_4 (Fo) – see Fig. 4.3.1.

indicatrix a hypothetical three-dimensional figure (Fig. A2) indicating how refractive index varies with the vibration direction of transmitted light in an anisotropic crystal.

initial isotope ratio the initial **radiogenic**-isotope ratio, e.g. the initial Sr isotope ratio $(^{87}Sr/^{86}Sr)_0$, inherited by a magmatic rock from its magma source, prior to the growth with time of the daughter isotope (^{87}Sr) resulting from *in situ* decay of the parent nuclide (^{87}Rb). Determined from the *y*-intercept of an **isochron plot** (see Fig. 8.21a) or by calculated age correction.

intercumulus describes a melt that fills pore spaces between **cumulus** minerals, or a mineral that has crystallized from such a melt (e.g. Plate 5.2).

interference colour (synonym 'polarization colour') the colour a crystal appears to have when viewed between crossed polars. In principle unrelated to body colour, though a strong body colour may distort interference colour.

intergranular texture in which equant olivine and pyroxene crystals fill spaces within a framework formed by tabular plagioclase crystals.

intersertal texture in which glass fills the spaces within a framework of tabular plagioclase crystals.

interstitial material found in the interstices of a rock, i.e. in the spaces between earlier-formed crystals (Greek: 'standing between').

invariant describes a chemical equilibrium which can tolerate no variation in applied conditions – see Box 3.3.

invert, inversion recrystallize (-ation of) a mineral from a structure stable at high temperatures into a low-temperature form.

inverted pigeonite pigeonite that has **inverted** from its original **monoclinic** crystal structure into orthorhombic enstatite (Box. 4.5).

isochemical describes a process that causes no change in rock composition.

isochron plot a plot of the **radiogenic** isotope ratios of a range of cogenetic samples (whole rocks or minerals) from which their common age may be determined. It shows the abundance of the daughter isotope (e.g. ^{87}Sr) in each sample ratioed to a reference non-**radiogenic** isotope (e.g. ^{86}Sr), plotted against the abundance of the parent nuclide (e.g. ^{87}Rb) ratioed to the same reference daughter isotope (Fig. 8.21a).

isomorphous series a mineral (e.g. olivine) whose composition may vary without change in crystal symmetry (Greek: 'same shape'), forming a **solid solution series**.

isotherm, -al describes a line of (or process at) constant temperature in a **phase diagram**.

isotope, –ic refers to atoms of an element that differ in the number of neutrons in the nucleus (N). Individual isotopes are identified by their **mass number**s, e.g. ^{87}Sr.

isotropic (optics) describes a mineral or other substance with uniform refractive index (independent of crystal orientation) and with zero **birefringence**. Includes crystalline minerals of the cubic system, volcanic and synthetic glass, liquids, **balsam** or epoxy resin (e.g. filling a void in the slide) (Greek: 'equal' + 'turn').

IUGS The International Union of Geological Sciences, whose *Subcommission on the Systematics of Igneous Rocks* has defined current conventions on igneous nomenclature (see Le Maitre, 2002).

juvenile describes samples of an erupting magma, as opposed to solid material derived from earlier eruptions.

K-feldspar term embracing all K-rich members of the **alkali feldspar** series (sanidine, microcline, orthoclase) but excluding perthite.

kamafugite ultrabasic ultrapotassic volcanic rock (Box 9.8)

kb, kbar = kilobar = 1000 **bar**, 1 kb = 0.1 GPa.

laccolith a concordant sheet intrusion that has a flat floor and a domed roof (Greek: 'reservoir' + 'rock').

lamination (meaning applied only to igneous rocks) sub-parallelism of platy plagioclase laths in a plagioclase-rich cumulate rock, probably as a result of depositional processes.

lamprophyre a class of porphyritic mafic dyke rocks having phenocrysts solely of mafic minerals (augite, hornblende, biotite) (Greek: 'glistening' and **porphyritic**). See Box 9.6.

lapilli pyroclasts with diameters in the range 2–64 mm.

lapilli-tuff **tuff** containing both lapilli (Table 7.2) and **ash**.

large igneous province (LIP) a large-volume volcanic province (or its hypabyssal feeder dyke swarm) that testifies to the surface eruption in a relatively short time span (commonly no more than 0.5–2 Ma) of mainly basaltic magma exceeding 1×10^6 km^3 in total volume. Cf. **continental flood basalts**, **oceanic plateau**.

latent heat heat released when a melt crystallizes, or absorbed when a crystalline solid melts.

layering, layered variation, with **structural height** in an intrusion, of the relative proportions of cumulus minerals ('modal layering'), of their compositions ('cryptic layering') or their identity ('phase layering').

LCP abbreviation for low-Ca pyroxene, embracing orthopyroxenes and pigeonite (Fig. 2.1.1).

leuco- prefix applied to a rock name to denote a lower proportion of dark minerals than the rock type normally contains (Greek: light colour). E.g. leucogabbro. See Le Maitre (2002) Tables 2.7 and 2.8.

leucocratic describes the composition of a rock whose **colour index** is less than 35 volume % as in Fig. 1.3(b) (Greek: light colour-dominant).

Lever Rule see Box 3.2.

LIL elements (LILE) large-ion **lithophile** elements, a sub-group of **incompatible elements** (Box 2.7).

LIP see **large igneous province.**

liquidus *either* the highest temperature at which a melt of a given composition can equilibrate with crystals, *or* a line in T–X space showing how that temperature varies with melt composition (e.g. Fig. 3.1.1), *or* a line in P-T space showing how that temperature varies with pressure (e.g. Fig. 2.17).

lithic term describing pyroclastic ejecta or debris consisting of dense solid rock (= products of earlier eruptions, or material torn from the vent wall), as distinct from **juvenile** magmatic products of an eruption in progress.

lithophile element class of elements that reside preferentially in **silicate** melts and minerals (Greek: 'rock-liking'), rather than in sulphide minerals (**chalcophile** elements) or metallic materials (*siderophile* elements).

lopolith describes a large intrusion that is saucer-shaped, with concave-upward floor and relatively flat roof (Greek: 'basin' + 'rock').

loss-on-ignition (LOI) a simple method to measure the total volatile content of a rock or mineral sample: a weighed sample is ignited at 1000+ °C in air for 30 minutes and re-weighed on cooling to determine the mass of volatiles lost.

LREE refers to the 'light' (i.e. low-Z) rare earth elements La–Sm (see Fig. 2.7.2).

Ma ('Mega annum') informal but widely used unit of geological time = 10^6 years.

maar explosion crater from a **phreatomagmatic** eruption, often filled with water and/or alluvium.

macro-rhythmic a relatively thick (>5 m) rhythmically repeated set of cumulate layers (Irvine, 1982).

mafic category of minerals rich in magnesium (Mg) and iron (Fe), also known as **ferromagnesian** minerals. Also used of rocks that are relatively rich in such minerals (see Fig. 1.3b).

magma term embracing all molten and partially molten rocks, including melt, crystal and gaseous phases.

magnesian describes a melt or mineral crystal that is rich in magnesium relative to iron, i.e. has a high MgO/(MgO + ΣFeO) value.

major element a chemical element present in a rock/mineral sample with a concentration exceeding 0.1 mass % (contributing significantly to the analysis total). In silicate analyses, major elements are presented in oxide form (in mass % of each oxide).

mass number the integer A for an isotope, representing the sum of the **atomic number** Z and the neutron number (N).

mass %, mass percent percentage of an element or oxide in a mineral or rock expressed in terms of mass (i.e. g of element or oxide per 100 g sample). Alternatively known as weight %.

medium-grained see Fig.1.3(a).

mela- prefix applied to a rock name to denote a higher proportion of dark minerals than the rock type normally contains (Greek: dark colour). E.g. **melanephelinite**. See Le Maitre (2002) Tables 2.7 and 2.8.

melanocratic describes the composition of a rock whose **colour index** lies between 65 and 90 volume % as in Fig. 1.3(b) (Greek: dark colour-dominant).

melt the liquid phase in a magma (Fig. 1.1) or an experimental **charge** (Cf. **magma**).

melt inclusion small glass inclusion within a **phenocryst** preserving a sample of the melt composition (particularly volatile content) from which the phenocryst crystallized prior to eruption – see Box 1.4 and Plate 6.11.

melting column basalts and other mantle-derived mafic magmas are products of melting over a range of depths (Fig. 2.17). The vertical path from beginning of melting to where melt segregates and escapes to the surface is called the melting column.

mesocratic describes the composition of a rock whose **colour index** lies between 35 and 65 volume % (Fig. 1.3b). (Greek: 'between' and 'dominating'.)

metaluminous describes rocks in which $([Na_2O]_{mol} + [K_2O]_{mol}) < [Al_2O_3]_{mol} < ([Na_2O]_{mol} + [K_2O]_{mol} + [CaO]_{mol})$; i.e.. rocks which are neither **peralkaline** nor **peraluminous**. See Fig. 8.14.

metasomatic, -ism form of metamorphism in which chemical components are introduced into (or leached from) a rock by passage of a **fluid**.

metastable an unstable state (e.g. a mineral assemblage) preserved owing to the slowness of the reactions that lead to the stable state.

meteoric describes fluids derived ultimately from atmospheric precipitation.

meteorite a fragment of solid solar system debris that survives the high temperatures of atmospheric entry and lands as a recoverable sample on the Earth's surface.

Mg number $= \left[\dfrac{100\ \mathrm{Mg}}{\mathrm{Mg} + \mathrm{Fe}^{2+}}\right]$ in **atomic proportions**

$= \dfrac{100 \times (\mathrm{MgO}/40.32)}{(\mathrm{MgO}/40.32) + (\mathrm{FeO}/71.85)}$ where 'MgO' etc. represents **mass %** oxide in the major element analysis of an igneous rock or mineral sample (40.32 and 71.85 are **RMM** values for MgO and FeO). Where a rock analysis gives only total iron (as ΣFeO), actual FeO may be approximated using FeO ≈ 0.9 ΣFeO.

microlite very small elongate crystal (large enough to exhibit birefringence) in a volcanic rock, typically of feldspar.

microperthite **perthite** whose exsolution texture is visible only under the miroscope.

microphenocryst a **phenocryst** too small to be seen by the naked eye (after Shelley, 1992).

mineral analysis chemical analysis of a mineral in a rock, performed either on a mineral separate, or on an individual crystal of the mineral (e.g. a **phenocryst**), or on a part of such a crystal (e.g. if **zoned**). See electron microprobe.

mingling the mixing together – without complete homogenization – of magmas of contrasted composition or vesicularity.

miscibility gap compositional range within a **solid solution series** where no homogeneous crystal is stable: compositions here consist of two-phase mixtures. The mutual solubility of end-members is strongly temperature-dependent, as shown by the **solvus** curve (Fig. 4.5.2a).

mobile refers to the susceptibility of an element to partial solution in hot aqueous fluids during **alteration**, which may affect the element's concentration in a partially altered rock or mineral

sample or in fluids derived from slab dehydration. See Box 2.6.

mode, modal the actual mineralogical constitution of a rock, expressed as the volume percentages of the various minerals present as determined by quantitative petrographic analysis ('point-counting' – see Chapter 1) of a thin section. Cf. **norm**.

mole, –ar that amount of a chemical compound whose mass, when expressed in grammes, is numerically equal to the compound's **RMM**. The number of moles may be calculated by dividing the mass of the compound present (in grammes) by its **RMM**. Molar concentrations are those expressed in relative numbers of moles.

molar proportions the relationship (e.g. the ratio) between two or more oxides or end-members, expressed in terms of the *numbers of moles* rather than mass proportions. Numerically the same as the **atomic proportions** of the corresponding metals.

mol % molar percentage. Conventional way of expressing the composition of a mineral solid solution in terms of its end-members (e.g. Fo_{85}). Cf. **mass %.**

monoclinic class of crystals (e.g. clinopyroxene) whose structure is characterized by one (2-fold) axis of rotational symmetry.

monogenetic describes a volcano produced by a single eruptive episode.

norm, normative the major element composition of a rock re-calculated as mass percentages of a restricted number of standardized anhydrous ('normative') minerals. Cf. **mode**.

normal zoning secular radial **zoning** in which the outer portions of the crystal have a lower-temperature composition than the core. Usually reflects progressive change of melt composition during growth of the crystal.

normalized a chemical rock analysis or element concentration expressed as the ratio $(C_{element})^{rock}/(C_{element})^{reference\ composition}$, where 'reference composition' usually refers to '**primitive mantle**' or average MORB (Box 2.7).

oceanic plateau an extended region of anomalously thick oceanic crust, an oceanic example of a **large igneous province**.

obsidian jet-black, aphyric volcanic glass, usually (though not always) rhyolitic in composition.

ocelli centimetre-scale globular, felsic or carbonate segregations suggesting melt immiscibility (Latin: 'little eyes').

oikocryst a host crystal that has grown around other crystals in **poikilitic** or **ophitic** texture.

olivine-phyric (e.g.) describes a porphyritic (phyric) rock containing (e.g.) olivine **phenocryst**s.

omphacite Na–Al clinopyroxene (Fig. 9.2.1) characteristic of **eclogite**.

ophiolite variable though distinctive assemblage of rocks (see Box 5.3) found in collisional orogens; believed to represent slice of oceanic lithosphere. (Greek: 'snake rock'.)

ophitic a class of **poikilitic** texture in gabbros, dolerites and a few basalts in which smaller euhedral plagioclase crystals are enclosed by larger, **optically continuous** anhedral augite crystals (Greek: 'snake-like' referring to mottled surface).

optically continuous the property, possessed by different parts of a large single crystal when viewed in crossed polars, of extinguishing at the same stage-orientation (even when appearing unconnected to each other in the plane of the section – see Plate 8.3).

orbicular layering radial variant of comb layering, probably due to **heterogeneous** nucleation on solid inclusions within a magma body.

orthorhombic class of crystals (e.g. orthopyroxene) whose structure is has three perpendicular (2-fold) axes of rotational symmetry; higher symmetry than monoclinic.

oscillatory zoning repetitive pattern of radial **zoning** in a crystal: a scan of composition from core to rim reveals alternating high- and low-temperature zones (Fig. 6.6). May be detected optically (e.g. in plagioclase) by bands of varying **extinction angle**.

pahoehoe Hawaiian term (pronounced 'pah-ho-eh-ho-eh') describing basaltic lava with a smooth or wrinkled surface.

pargasite $\{NaCa_2(Mg,Fe)_4Al[Si_6Al_2O_{22}](OH)_2\}$ a variety of hornblende that resists dehydration to higher temperatures than others.

partial pressure the effective pressure exerted by a single volatile component (e.g. P_{H_2O}) of a magma. If partial pressure < load pressure, the component is entirely dissolved in the magma; when partial pressure ≥ load pressure, a separate gaseous phase forms.

partition coefficient see Box 2.7.

pegmatite, -itic a facies of plutonic rock that is notably coarser-grained than the host; forms veins or pockets within an intrusion, but may extend into surrounding country rocks.

pelite metamorphosed argillaceous sedimentary rock, containing Al-rich minerals like muscovite (after original clay minerals).

pelletal lapilli spheroidal lapilli in diatreme-facies kimberlite consisting of primary crystals and accidental lithic clasts enveloped by a thin rim of kimberlite groundmass material.

peralkaline describes (acmite-normative) rocks in which $([Na_2O]_{mol} + [K_2O]_{mol})/[Al_2O_3]_{mol} > 1.00$.

peraluminous describes rocks in which $[Al_2O_3]_{mol}/([CaO]_{mol} + [Na_2O]_{mol} + [K_2O]_{mol}) > 1.00$. Such rocks are corundum-normative. See Fig. 8.14. Cf. **metaluminous**.

peridotite see Fig. 5.1.

perlitic cracks spheroidal contraction cracks (hand specimen or thin section) in glassy rocks, particularly rhyolite.

perthite crystal of potassium-rich feldspar containing exsolution lamellae of sodium-rich feldspar (cf. **antiperthite**). See Fig. 8.1.1(c). Typically visible only under the microscope (**microperthite**).

PGE abbreviation for the Platinum-Group Elements (Ru, Rh, Pd, Os, Ir and Pt).

phaneritic describes a rock in which the crystals of all the main minerals can be seen by the naked eye (Greek: 'visible').

phase (chemical) a domain in a solid or partially molten rock which has uniform physical and chemical characteristics that distinguish it from other parts of the rock. Each mineral, melt , or gas present (as bubbles) constitutes a separate chemical *phase*. Solid phases are identified in this book by mineral names rather than formulae.

phase diagram a diagram showing (a) the limits of stability of various **phases** (minerals, melt) as a function of temperature, pressure and/or composition, and (b) which phases may co-exist in mutual equilibrium under various conditions.

phenocryst a crystal significantly larger than groundmass crystals, whose relative size and **euhedral** shape indicate that it formed early in the magma's crystallization history. The term embraces any smaller euhedral crystals that have been enclosed by larger phenocrysts (Cox et al., 1979, p 179). (Greek: 'shining crystal')

phlogopite mica with approximate composition $K_2Mg_6[Si_6Al_2O_{20}](OH,F)_4$ forming the magnesian end-member of the biotite series.

phonolite fine-grained rock or consisting essentially of alkali feldspar and feldspathoid (Fig. 9.n); highly evolved, **silica-undersaturated** magma (Fig. 1.5).

phreatic describes a steam explosion due to interaction between *hot rock* and groundwater, forming a tuff ring of country rock ejecta (Greek: 'a well').

phreatomagmatic describes the explosive interaction between *magma* and groundwater, forming a tuff ring of juvenile and country-rock ejecta. Cf. **maar, phreatic**.

phyric US synonym for **porphyritic** (i.e. containing **phenocryst**s). 'Olivine-phyric' signifies the presence of olivine phenocrysts (for example).

picrite a basaltic rock unusually rich in olivine crystals (from the Greek: 'bitter', an obscure reference to high MgO content).[1]

plagioclase feldspar series comprising solid solution between the end-members $NaAlSi_3O_8$ and $CaAl_2Si_2O_8$ – see Fig. 3.4.

pleochroic halo halo surrounding a U, Th-rich mineral inclusion, where the host mineral (typically cordierite or biotite (see Plate 8.10) shows exaggerated **pleochroism** owing to radiation damage.

pleochroism the property of an anisotropic crystal to change its body colour according to the vibration direction of the polarized light passing through it. (Greek: 'more colours'.)

plume, mantle plume a mushroom-shaped convective feature consisting of hot buoyant mantle believed to well up – and promote melting – beneath a hot spot (Fig. 2.18b). Some petrologists question the existence of plumes in the face of seismic evidence.

plumose made of numerous fine curvilinear filaments like a feather (see Plate 5.10).

pluton a large-scale intrusive body of unspecified shape emplaced at depth.

plutonic describes intrusive rocks originally emplaced at, or magmatic processes occurring at, considerable depth below the surface. Unfortunately used in the IUGS nomenclature as a synonym for **coarse-grained** (Le Maitre, 2002, p3).

poikilitic texture in which many small crystals of one mineral (or several minerals) are enclosed by fewer, larger crystals of another (Greek: 'mottled'). Cf. **ophitic**.

polarizer sheet of Polaroid™ located below the stage and having an 'E–W' vibration direction. The polarizer is always in place. Cf. **analyser**.

polyhedral term used to distinguish the regular habit of olivine in **picrites** from the skeletal form

[1] Historically the term **picrite** has sometimes been broadened to include **ankaramite**.

of olivine seen in upper portions of **komatiite** lavas. Also used (confusingly) to describe the jointing seen in the upper parts of many komatiite lavas (Greek: 'multi-sided').

polymerized describes the connectiveness of the negatively charged Si–O–Si framework in a silicate melt or crystal, whether consisting of small silicate anions ('relatively unpolymerized') in a low-viscosity komatiite melt at one extreme, or of large 3D silicate networks ('highly polymerized') in acidic melts such as rhyolite at the other (Box 6.3).

porphyritic igneous texture in which larger, euhedral, *early-formed* crystals (**phenocrysts**) are surrounded by a matrix of smaller crystals that evidently crystallized later. (Greek: 'purple', the colour of the original Egyptian porphyry widely used as ornamental stone.)

porphyroblast a crystal in a metamorphic rock that is large in relation to the grain size of the rock matrix.

PPL abbreviation for plane-polarized light, a configuration of the polarizing microscope in which the **analyser** is removed.

ppm. parts per million (of element by mass); 1000 ppm is equivalent to 0.1 mass % (of element, not oxide).

precision refers to the closeness of agreement between repeated determinations of the same element in the same sample by the same method; a statement of the magnitude of random error associated with an analysis. A *precise* analysis is one with a *small* random error. Precision may be expressed quantitatively in terms of standard deviation or variance.

primary *of a mineral:* an igneous mineral that has crystallized from a melt (cf. **secondary**); *of a melt or magma:* having a bulk composition (especially **Mg number** > 65) consistent with direct derivation from (and equilibrium with) upper mantle peridotite, without intervening fractional crystallization. See Box 9.5.

primitive (magma) least fractionated.

– mantle a hypothetical mantle composition representing the average composition of the mantle soon after Earth formation: a model composition calculated from chondrite **meteorite** analyses (Sun and McDonough, 1989).

primitive a magma or rock composition relatively rich in MgO and/or poor in SiO_2, suggesting the magma has undergone little fractionation since the melting event by which it was formed. Cf. **evolved**.

prismatic describes a cleavage, face or cross-section parallel to a crystal's axis of elongation (strictly the *z* crystallographic axis).

projection technique of representing *n*-dimensional coordinates in (*n*–1)-dimensional form or diagram; e.g. a trend of data points within a quaternary (4-component 3D) diagram can be represented (imperfectly) by projecting them on to one of its ternary faces. Imagine the shadows cast by the points on the face concerned when a point source of light shines from the point in space from which projection is made (usually an apex of the 3D tetrahedron).

pseudomorph (Greek: 'false shape') the outline of an alteration product that retains the recognizable shape of the **primary** mineral it has replaced.

pumice microvesicular, low-density volcanic 'foam' formed by decompression of volatile-rich, **evolved** magma.

pyroclast, pyroclastic a clast of hot juvenile volcanic material fragmented during eruption by the explosive force of decompressed volcanic gas, or by collapse of a lava dome (Greek: 'fiery fragment'). An eruption whose main product is pyroclastic deposits.

pyroclastic density current (PDC) an incandescent, ground-hugging cloud of pumice (or lithic material) and ash that flows rapidly down the flanks of an erupting volcano, following collapse of an eruption column or a perched lava dome.

pyroxenite a coarse-grained **ultramafic** rock consisting essentially of pyroxenes, with less than 40% olivine (Fig. 5.1).

qualifier an adjective, mineral name or chemical descriptor placed in front of the **root name**, which highlights textural, mineralogical or chemical attributes of a particular specimen (e.g. ***poikilitic*** gabbro, *olivine* basalt, *low-K* tholeiite).

quartz one of several crystalline minerals having the composition SiO_2. Cf. **silica**.

quaternary describes a system (or phase diagram) consisting of four independent chemical **components** (cf. **binary**, **ternary**). A quaternary diagram is a hypothetical regular tetrahedron in which the relative proportions of four quantities (each represented by one apex) can be presented in 3 dimensions, provided that they sum to 100%.

quench, –ed, –ing the chilling of an experimental **charge** rapidly to room temperature in order to

ensure that the **phases** in equilibrium at the temperature of the experiment are preserved, and do not recrystallize to other phases during slow cooling. Also refers to glass and other natural textures (e.g. spinifex) related to very rapid cooling.

radiogenic, – isotope a stable daughter isotope formed by a radioactive decay reaction. Its abundance increases directly with time and in proportion to the parent:daughter isotope ratio of the material in which it resides. Radiogenic isotope abundance is normally ratio-ed to a stable non-radiogenic isotope of the same element (e.g. $^{87}Sr/^{86}Sr$).

RAM Relative Atomic Mass (or 'atomic weight') of an element: the mass of an atom expressed on a scale in which $^{12}C = 12.0000$.

rapakivi variety of granitoid in which large, often rounded orthoclase crystals are mantled by plagioclase (Finnish: 'rotten stone').

rare earth element (REE) series of **trace elements** from lanthanum (La, $Z = 57$) to lutetium (Lu, $Z = 71$) – see Fig. 2.7.2 – whose geochemical properties vary smoothly from one element to the next. More in Box 6.6.

refractory an element or compound that melts only at a very high temperature.

relative retardation (RR) $= t\,(n_1 - n_2)$ expressed in nm; a numerical scale of interference colours obtained when light passes through a crystal section of thickness t and birefringence $(n_1 - n_2)$. Also known as optical path difference.

resorption partial re-dissolving of a phenocryst into melt, resulting in a rounded or embayed outline and/or **sieve texture**.

reverse zoning secular radial **zoning** in which the outer portions of the crystal have a higher temperature composition than the core. Usually reflects mixing between host magma and more **primitive** magma during crystal growth.

rhythmic layering systematic recurrence of distinctive layers or sequences of layers (Irvine, 1982).

ring dyke a late arcuate intrusive sheet, partially or wholly surrounding a pluton, usually with steeply outward-dipping contacts.

RMM Relative Molecular Mass (or molecular 'weight') of a compound: the sum of the **RAM**s of all of the constituent elements, weighted according to the number of atoms of each shown in the formula. Thus the RMM of $Na_2O = (23 \times 2) + 16$. RMM is expressed in atomic mass units or in g mole^{-1}.

root name the basic rock name derived from the essential minerals (e.g. **trachyte**).

RR see **relative retardation.**

salic category of CIPW normative minerals comprising quartz, feldspars and feldspathoids. Sometimes also used to describe igneous rocks with norms rich in such minerals (cf. **felsic** which refers to modal composition). Antonym: femic.

saturated said of a melt containing in dissolved form the maximum possible amount (at the temperature in question) of a particular mineral component, and therefore capable of coexisting stably with the crystalline mineral. See also **silica-oversaturated**.

schlieren streaky concentrations of coarser crystals of mafic and other minerals, e.g. in granites (German: to slip [of knot or rope]).

SCLM sub-continental lithospheric mantle.

scoria pyroclasts (typically lapilli-grade – Table 7.2) consisting of highly vesicular basalt or andesite.

scoria cone conical form of **pyroclastic** fall deposit consisting of **scoria** surrounding the vent of a **strombolian** eruption.

secondary used of post-magmatic minerals and processes in which original magmatic minerals are replaced by lower-temperature minerals, usually **hydrous** ones more stable under **hydrothermal** conditions.

sector zoning non-radial form of **zoning** (common in clinopyroxene) in which a crystal is divided into four quadrants whose composition and optical properties are identical for opposed quadrants but differ between the adjacent quadrants.

seriate texture resembling porphyritic but displaying a continuum of crystal size from the largest **phenocryst** to the finest groundmass crystal.

sericite, sericitized colourless alteration product, mainly comprising finely divided muscovite, replacing feldspars and foids.

serpentinite rock name for a peridotite that has been almost entirely altered to serpentine minerals. Relics of olivine or pyroxene may be present as well as chromite or chrome spinel.

sheeted dyke swarm A dyke swarm so dense that negligible country rock is found between neighbouring dykes and many dykes intrude into other dykes; characteristic of oceanic spreading centres.

shield volcano a volcano with gently sloping, upward-convex sides consisting of basaltic lavas.

shoshonite mildly potassic trachyandesite (Figs. 6.11 and 9.2). Plagioclase-phyric fine grained mesocratic rock with olivine, HCP, LCP, magnetite, hornblende and/or biotite.

sialic describes rocks rich in $\underline{Si}O_2$ and $\underline{Al}_2O_3$ (e.g. continental crust)

sieve texture a high density of **melt inclusions** in a phenocryst (especially of plagioclase) giving a sieve-like appearance (Plate 6.7); may reflect resorption during decompression.

significant figures the number of digits given for an analytical result; e.g. the statement 'Nb = 1.645 ppm' records a concentration of niobium to four significant figures. Good practice requires the significant figures quoted to be matched to the precision of the analysis: 1.645 implies a precision of roughly ± 0.003, whereas 1.6 implies ± 0.3.

silica silicon dioxide, SiO_2. In petrology, silica refers specifically to the chemical **component** SiO_2, *not* the mineral **quartz** (a rock with a silica content of 65% may contain only 10% quartz).

silica-oversaturated describes a rock or melt composition whose norm contains enstatite[2] and quartz.

silica-saturated describes a rock or melt composition whose norm contains enstatite ± olivine but no quartz or feldspathoid.

silica-undersaturated describes a rock or melt composition whose norm contains olivine and nepheline but no enstatite or quartz.

silicate a chemical compound in which silicon is combined with oxygen and various metals (e.g. the olivine *forsterite* Mg_2SiO_4). Silicates may occur in molten, crystalline and amorphous (glassy) states.

silicic ill-defined adjective describing rocks with a high SiO_2 content or containing quartz; broadly synonymous with acidic.

slow (**optics**) vibration direction having the higher refractive index; a higher RI means a slower speed of light.

smectite group of clay minerals (hydrous sheet silicates) that occur as a green, fine-grained alteration or weathering product in igneous rocks.

sodic plagioclase plagioclase containing more albite than anorthite ($An_{<50}$).

solid solution a mineral consisting of two or more chemical compounds (**end-members**) intermixed on the atomic scale; may be *complete solid solution* such as olivine, whose crystals allow the compounds to be mixed together in any proportions like two fully miscible liquids, or *partial solid solution* such as alkali feldspar, whose crystals accommodate only a limited range of intermixing (see **miscibility gap**).

solid solution series the entire range of compositions encompassed by **solid solutions** formed by mixing two (or more) specific **end-members**. Cf. **isomorphous series**.

solidus *either* the temperature at which a solid (or a mixture of solids) of a given composition begins to melt, *or* a line in T–X space showing how that temperature varies with composition (e.g. Fig. 3.4), *or* a line in P–T space showing how that temperature varies with pressure (e.g. Fig. 2.17).

solvus a curve in a phase diagram (e.g. Figs. 4.5.2 & 9.21) defining the extent of partial miscibility between two **end-members**, the **miscibility gap** between them, and the compositions of coexisting phases (e.g. as a function of temperature).

spherulite organized aggregate of acicular microcrystals emanating from a point or line (after Fowler et al., 2002), usually due to devitrification of glass. Hence spherulitic.

spidergram alternative name for an incompatible element enrichment diagram like Fig. 2.16.

spilite rock produced by intense greenschist-facies sea-floor metamorphism of basalt. Albite replaces calcic plagioclase, and glassy pillow rims and olivine crystals are transformed into chlorite; actinolite and epidote are also common. Voids are filled with calcite.

SSZ abbreviation for Supra-Subduction Zone, embracing magmatic processes at all convergent plate margins.

Stokes' Law an equation relating the settling velocity[3] v_t of a solid particle (e.g. a crystal) of radius r_x and density ρ_x in a fluid (e.g. melt) of density ρ_m and viscosity η:

$$v_t = \frac{2gr_x^2(\rho_x - \rho_m)}{9\eta}$$

stratovolcano a large, relatively steep-sided volcanic edifice constructed of alternating lavas and volcaniclastic (including pyroclastic) beds.

[2] 'Enstatite' refers to low-Ca pyroxene according to modern mineralogical usage (Deer et al., 1992). Enstatite in a norm here means the same as hypersthene-normative in older literature (see Box 2.1).

[3] A particle initially at rest accelerates until frictional drag balances out gravitational acceleration, resulting in a steady-state or 'terminal' velocity v_t.

strombolian describes a mildly explosive eruption of basaltic/andesitic magma; repeated explosions eject glowing **scoria** clasts that build a **scoria cone** around the vent.

structural height a reference scale of relative height (perpendicular to modal layering if tilted) above the lowest exposed level of cumulates in a layered intrusion.

subalkali denotes magma series characterized by lower total alkali contents, as defined on a TAS diagram (Fig. 1.5). Cf. **alkali(-ne)** and **tholeiitic**.

subhedral describes a mineral exhibiting recognizable though imperfect crystal form.

subsolvus describes a granite or syenite in which the alkali feldspars are present as separate Na and K feldspar crystals, having crystallized under high P_{H_2O} conditions.

supercooling, -ed describes a melt that remains metastably molten when its temperature falls below the equilibrium **liquidus** temperature. Supercooling is a pre-requisite for crystal nucleation to occur. The amount of supercooling is usually expressed as $\Delta T = T_{liquidus} - T_{actual}$ in °C. Cf. **supersaturated**.

superheated describes a melt whose actual temperature exceeds its liquidus temperature.

supersaturated describes a solution or melt containing a concentration of a particular solute that is higher than its saturation concentration under the prevailing conditions (e.g. temperature, pressure).

surtseyan describes an explosive eruption arising from interaction between ascending magma and sea or lake water.

symplectite a microscopic 'wormy' intergrowth formed at the interface between two minerals (Plates 4.10 and 4.11), by reaction either in solid state or with residual melt or fluid.

system (chem) a specified region of compositional space on which attention is focussed. 'The system Mg_2SiO_4–Fe_2SiO_4' refers to all compositions (whether melt, solid solution or mechanical mixture) that can be formed by mixing Mg_2SiO_4 and Fe_2SiO_4 in varying proportions under various conditions.

TAS plot abbreviation for the total alkalis–silica [$(Na_2O + K_2O)$ *versus* SiO_2] variation diagram – see Figs. 1.6 and 2.1.

tephra a collective term embracing all kinds of unconsolidated pyroclastic deposit (Greek: 'ashes'); some volcanologists reserve the term for pyroclastic fall deposits (e.g. Oppenheimer and Francis, 2005).

ternary describes a system (or phase diagram) consisting of three chemical components (cf. **binary**). A ternary diagram is an equilateral triangle in which the relative proportions of three quantities (each represented by one apex) can be presented in 2 dimensions, provided that they sum to 100%.

tholeiite (-ic basalt) a subalkali basalt (name derived from Tholey in the Saar region of Germany) containing low-Ca pyroxene, or with enstatite in the norm.

tholeiitic refers to magmas of **subalkali** affinity characterized by **normative** enstatite.

tie line an **isothermal** line in a phase diagram joining two immiscible phases coexisting in mutual equilibrium.

trace element a chemical element generally present in a rock/mineral sample at a concentration below 0.1 mass %. Reported in silicate analyses in parts per million (ppm) by mass (= $\mu g\,g^{-1}$) of the *element*.

trachyte fine-grained alkaline igneous rock consisting of alkali feldspar (Fig. 9.1); an evolved alkaline magma that is neither strongly **silica-oversaturated** or **-undersaturated** (Fig. 1.5).

trachytic texture Groundmass texture in which feldspar microlites or laths are aligned in a swirly flow pattern.

transitional basalt a basalt whose composition lies close to the boundary line between alkali basalt and tholeiitic basalt (Fig. 2.1).

triclinic class of crystals whose structure has no axes of rotational symmetry: lowest-symmetry crystal system.

trondhjemite leucocratic variety of tonalite (Fig. 8.1) containing biotite. Derived from old name for Trondheim, Norway.

TTG abbreviation for the '**trondhjemite**-tonalite-granodiorite' suite prevalent among magmatic protoliths of Archaean gneisses.

tuff a consolidated pyroclastic deposit with ash > 75%.

twin, –ned, –ning A crystal comprising two or more parts whose crystal lattices have different orientations related through a symmetry operation (such as a mirror plane ('twin plane') or a rotation axis ('twin axis')) is said to be twinned. Twinning is usually detected by difference in extinction angle in crossed polars (see Fig. 8.1.1).

two-phase field a field in a binary phase diagram delineating a range of compositions that can exist only as mixtures of two immiscible phases (crystal-melt or crystal-crystal).

ultrabasic a class of igneous or metamorphic rocks having (volatile-free) SiO_2 contents less than 45 mass %. See Fig. 1.3c.

ultramafic class of rocks having mafic mineral contents exceeding 90% by volume (i.e. colour index ≥ 90). See Fig. 1.3b.

ultrapotassic describes a class of rare igneous rocks in whose **whole-rock** analyses $K_2O > 2 \times Na_2O$ in mass % (Foley et al., 1987).

underplating the density-controlled accumulation of basaltic magma near the base of the continental crust during a major magmatic episode.

unmixing see **exsolution**.

unsteady describes a pyroclastic density current having a flow regime fluctuating with time.

uralite informal name for a bluey-green secondary amphibole occurring as an alteration product of pyroxenes, either as a single crystal or as a fibrous aggregate (see Deer et al., 1992).

vapour (N Am: vapor) a substance in the gaseous state.

variation diagram a diagram showing the correlation between the concentrations of two or more chemical components in a suite of related igneous rock (or mineral) samples (e.g. Fig. 3.10).

vermicular describes a worm-like intergrowth of two or more minerals.

vesicle a spherical or rounded void in a volcanic rock, representing a gas bubble formed when the rock was molten (from the Latin for 'blister'). Hence vesicular. See also **amygdale**.

viscosity, viscous *informally:* describes a melt's (or any **fluid**'s) capacity to resist flow. *formal usage:* a viscous fluid is one that develops a velocity gradient proportional to the shear stress applied to it. Viscosity is the ratio: applied shear stress / velocity gradient.

VMS deposit volcanogenic massive sulphide deposit.

volatile *adjective:* forming a gas at a relatively low temperature. *noun:* one of several chemical components of igneous melts that may be lost as a gas during decompression (which promotes 'degassing') or during crystallization: includes H_2O (usually dominant), CO_2, SO_2, H_2S, HCl and HF.

volcanic describes igneous processes occurring on the Earth's surface. A volcanic *rock* is an igneous rock emplaced by surface eruption (Cf. Le Maitre, 2002, p3). The term derives from the name of the Roman god of fire, Vulcan.

Wadati-Benioff zone the dipping zone of earthquake foci that delineates the upper surface of a subducting slab (see Fig. 6.13).

weight percent obsolete term still widely used to represent the mass percentage of an element or oxide in a mineral or rock (i.e. g of element or oxide per 100 g of sample).

welding, welded sintering and compaction of hot pumice clasts and glass shards in an ignimbrite or (more rarely) a proximal fall deposit, to form a planar fabric of **fiamme**.

whole-rock analysis see **bulk analysis**.

xenolith fragment of pre-existing, unrelated solid rock mechanically incorporated into a magma (Greek: 'foreign stone'). Cf. **autolith**.

XP abbreviation for 'crossed polars', a configuration of a polarizing microscope with both **polarizer** and **analyser** inserted.

yield strength the critical shear stress that has to be applied to a melt or ductile solid before it will begin to flow or deform. If a melt has a significant yield strength, crystals may remain in suspension and not sink according to Stokes' law.

zoning, zoned describes a crystal, typically a **phenocryst**, that exhibits systematic chemical and optical heterogeneity. See **normal –, oscillatory –, reverse –, sector –**.

Answers to exercises

CHAPTER 1

1.1 Of the terms given, *fine-grained* is the appropriate description (based on a *groundmass* grain-size < 1 mm in Fig. 1.3a). A more complete description would be 'porphyritic with a fine-grained groundmass'.

1.2

(a) Quantitatively, the rock SiO_2 content is given by the weighted mean of the mineral SiO_2 contents [= (40 × 51.3 + 55 × 50.9 + 5 × 55.1)/100]. Without doing the calculation, one can see merely by inspection that the SiO_2 content of the rock must lie between 50.9 and 55.1%, therefore it *does not qualify* as ultrabasic (requires SiO_2 < 45%; Fig. 1.3c).

(b) Mafic minerals make up 40 + 55 = 95%; a rock with this colour index *can* be described as ultramafic (Fig. 1.3b).

(c) The colour index is *too high* for melanocratic, but (d) is *right* for holomelanocratic (Fig. 1.3b).

1.3 Analyses can be plotted in Figs. 1.4 and 1.5 by adding Na_2O and K_2O and plotting the sum against SiO_2 content. The co-ordinates (x, y) are *A* (48.30, 4.25), *B* (56.29, 5.32), *C* (55.59, 13.53).

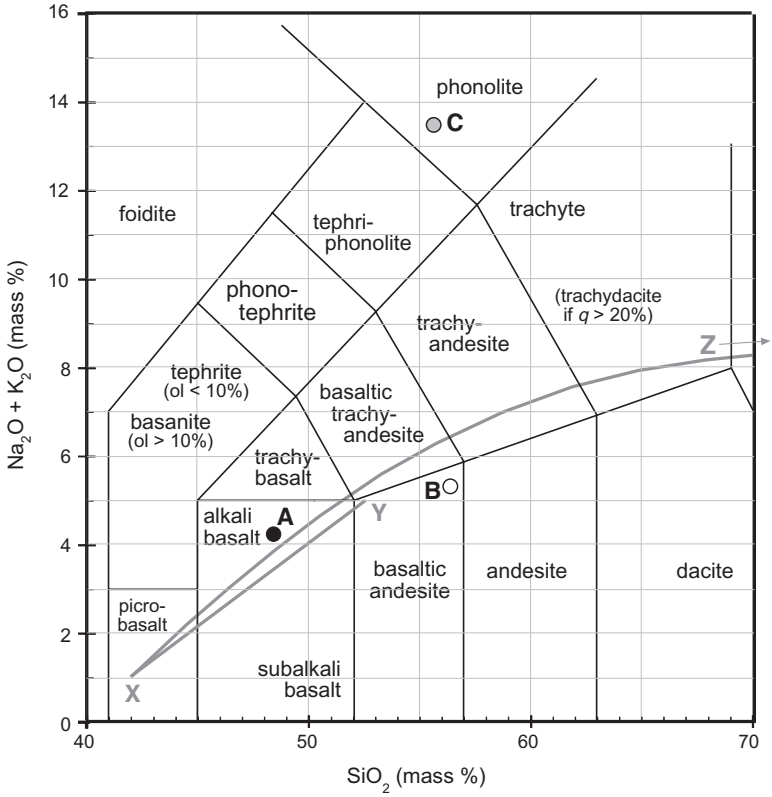


Fig. EA1

A falls in the field of basalt in Fig. 1.4 (in the *alkali basalt* division in Fig. 1.5).

B lies in the basaltic andesite field of Fig. 1.4. Plotting in Fig. 1.6 identifies it as a *high-K basaltic andesite*.

Owing to its extremely high total alkali content, *C* falls in the *phonolite* field of Fig. 1.4.

1.4 See Table 1.1

(a) biotite trachyte;
(b) tephrite;
(c) quartz latite;
(d) olivine nephelinite;
(e) hornblende andesite (the presence of quartz would make this hornblende dacite).

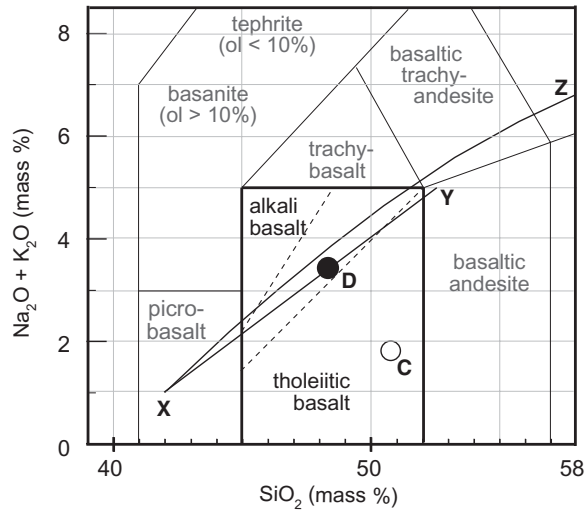


Fig. EA2

CHAPTER 2

2.1 Basalt C has a SiO_2 content of 50.77% and $Na_2O + K_2O$ = 1.82%. The analysis plots well inside the subalkali (or tholeiitic) field in Fig. EA2. Analysis D (SiO_2 = 48.18%, $Na_2O + K_2O$ = 3.43%) plots on the dividing line X–Y between alkali and subalkali basalts, and slightly below the line X–Z; its composition is best described as transitional.

2.2 As the table below (Table EA1) shows, analysis C is enstatite- and quartz-normative and can be described in normative terms as a quartz tholeiite (consistent with its position in the subalkali field above). The norm of analysis D contains olivine in place of low-Ca pyroxene; with only 0.5% nepheline it barely counts as an alkali basalt and is best described as transitional, in keeping with its coordinates in the TAS plot (exercise 2.1).

	Analysis C		Analysis D	
(a) Oxide analysis	**mass %**	**mol/100 g**	**mass %**	**mol/100 g**
SiO_2	50.77	0.8449	48.18	0.8018
TiO_2	0.67	0.0084	1.9	0.0238
Al_2O_3	18.97	0.1861	15.06	0.1477
Fe_2O_3	1.55	0.0097	1.87	0.0117
FeO	7.95	0.1106	9.55	0.1329
MnO	0.19	0.0027	0.19	0.0027
MgO	6.32	0.1567	6.97	0.1729
CaO	11.8	0.2104	12.15	0.2167
Na_2O	1.69	0.0273	2.76	0.0445
K_2O	0.13	0.0014	0.67	0.0071
P_2O_5	0.03	0.0002	0.29	0.0020
Total	100.07		99.59	

Continued

(b) Norm	mol/100 g	mass %	mol/100 g	mass %
Q	0.0540	3.24		
C				
or	0.0014	0.77	0.0071	3.96
ab	0.0273	14.30	0.0427	22.39
an	0.1574	43.79	0.0961	26.73
ne			0.0018	0.52
ac				
ns				
di	0.0523	11.93	0.1138	25.91
en	0.1996	22.38		
ol			0.0796	13.01
mt	0.0097	2.25	0.0117	2.71
il	0.0084	1.27	0.0238	3.61
ap	0.0002	0.07	0.0020	0.67
Total		100.00		99.51

2.3 Primitive mantle-normalized incompatible element data are calculated by dividing the concentrations given in Table 2.5 by the corresponding concentrations for primitive mantle. The primitive mantle data and the normalized results are given below (note the number of significant figures recorded here for each element – reflecting the precision of the analysis – corresponds to that in the original analysis).

	Primitive mantle	Normalized analyses	
		A	B
Rb	0.635	4.3	20
Ba	6.989	4.2	57.6
Th	0.085	3	27.2
Nb	0.713	0.29	35
K*	0.03	4.3	22.3
La	0.687	1.62	32.6
Ce	1.775	1.60	24.6
Sr	21.1	5.7	21.8
P*	0.022	1.4	13.2
Nd	1.354	2.19	18.1
Zr	11.2	1.71	9.8
Sm	0.444	2.39	11.6
Ti*	0.217	3.1	8.76
Gd	0.596	2.55	
Tb	0.108		8
Y	4.55	2.92	6.4
Yb	0.493	2.86	5.09
Lu	0.074	2.7	

* Primitive mantle figure given is in mass % oxide.

The data are plotted in a graph with elements arranged in order on the category (x) axis, and the normalized analysis plotted on a logarithmic y axis, either by calculating logs or by using log-linear graph paper (see Fig. EA3 below); where an element is omitted owing to the analytical method used (Gd, Tb), the line is drawn directly between the neighbouring elements. Analysis A has a marked negative Nb anomaly, identifying it as subduction-related, superimposed on a relatively flat, depleted pattern; it has much in common with the South Sandwich Islands low-K tholeiite in Fig. 2.16c.

2.4 $\Sigma Fe_2O_3 = Fe_2O_3 + (1.11 \times FeO) = 1.56 + (1.11 \times 9.8) = 12.44$ mass % (Box 2.6).

$$\Sigma FeO = FeO + (Fe_2O_3 \div 1.11)$$
$$= 9.8 + (1.56 \div 1.11) = 11.53 \text{ mass \%}.$$

NB These two numbers are two alternative ways of representing the *same* total iron content. They differ because of the different number of oxygen atoms associated with each Fe atom in each oxide formula. In FeO, each Fe has one oxygen attached whereas in Fe_2O_3 each Fe is associated with 1.5 oxygen atoms. The factor 1.11 is the ratio of $RMM_{FeO1.5}$ (or $RMM_{Fe2O3} \div 2$) to RMM_{FeO} = (159.7 ÷ 2): 71.85.

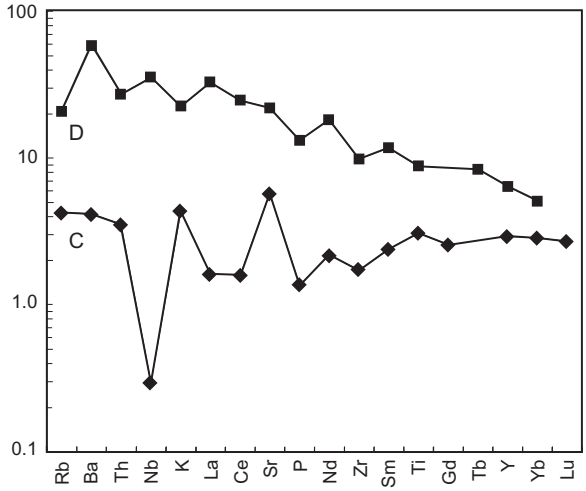


Fig. EA3

CHAPTER 3

3.1 The formulae of diopside and anorthite can be re-written in the form $CaO.MgO.2SiO_2$ and $CaO.Al_2O_3.2SiO_2$ respectively, indicating the proportions in which the oxides are combined in each mineral. The clearest way to set out the calculation is as follows):

Oxide:	**MgO**	**Al_2O_3**	**SiO_2**	**CaO**	**Total**
RMM:	**40.32**	**101.96**	**60.09**	**56.08**	
Diopside					
Proportions of oxides	1		2	1	
Mass of *n* moles	40.32		120.18	56.08	216.58
Mass % of each oxide*	18.62		55.49	25.89	100.00
Anorthite					
Proportions of oxides		1	2	1	
Mass of *n* moles		101.96	120.18	56.08	278.22
Mass % of each oxide		36.65	43.20	20.16	100.00

* e.g. 18.62 = 100 × 40.32/216.58

3.2

	MgO	**Al_2O_3**	**SiO_2**	**CaO**	**Totals**
0.26*anorthite	0.00	9.53	11.23	5.24	26.00
0.74*diopside	13.78	0.00	41.06	19.16	74.00
Composition of melt *n*	**13.78**	**9.53**	**52.29**	**24.40**	100.00
0.41*anorthite	0.00	15.03	17.71	8.26	41.00
0.59*diopside	10.98	0.00	32.74	15.28	59.00
Composition of eutectic E	**10.98**	**15.03**	**50.45**	**23.54**	100.00

3.3 (a) Olivine begins to crystallize at about 1430 °C (interpolating contours on the liquidus surface). (b) The distances *y*–*z* and *y*–Fo in Fig. 3.3 are 12.0 and 55.0 mm respectively. The composition *y* can be considered to consist of 100 × 12.0/(12.0 + 55.0) = 17.9% of Fo crystals and 100 × 55/(55 + 12) = 82.1% melt *z*. Therefore 17.9 mass % of melt *y* must crystallize (as olivine) before reaching the cotectic at *z* where anorthite appears at ~1285 °C.

3.4 Extend the line at *m* vertically downward. (a) 1700 °C: the horizontal distance from the line (= overall composition of melt + crystals) to the solidus is 18.0 mm and that from line to liquidus is 11.5 mm. The percentage of melt (by mass) = 100 × 18.0/(18.0 + 11.5) = 61% therefore 39% has crystallized. (b) 1600 °C: the corresponding lengths are 8.5 and 24.0 mm. The mass % melt is 100 × 8.5/(8.5 + 24.0) = 26% therefore 74% has crystallized. (c) 1550 °C: 2.5 and 30.00 mm: 7.7% melt remains therefore 93% has crystallized. Olivine compositions are 83.5, 73 and 63 % Fo by weight. Expressing 83.5 mass % in molar terms

$$= \frac{(83.5/40.32)}{(83.5/40.32)+(16.5/71.85)} = Fo_{90}$$

The corresponding compositions at 1600 °C and 1550 °C are Fo_{83} and Fo_{75}.

3.5

(a) The distances Z–extract and extract––Y in Fig. 3.10(f) measure 13.5 and 8.5 mm respectively. Using the Lever Rule (Box 3.2), the percentage of Y in the extract = 100 × 8.5/(8.5 + 13.5) = 39%. The percentage of Z = 100 × 13.5/(13.5 + 8.5) = 61%.

(b) The initial melt m_0 can be regarded as consisting of 'extract (Z + Y)' and residual melt m_1. The chords extract – m_0 and m_0 – m_1 measure 13.0 and 4.0 mm respectively. m_0 therefore consists of 100 × 4.0/(13.0 + 4.0) = 24% extract and 100 × 13.0/(13.0 + 4.0) = 76% melt. The composition m_1 is therefore reached when 24% of melt m_0 has crystallized as Z + Y and 76 mass % of melt remains.

(c) The chords extract – m_0 and m_0 – m_5 measure 13.0 and 13.5 mm respectively. m_0 can therefore be divided into 100 × 13.5/(13.0 + 13.5) = 51% extract and 100 × 13.0/(13.0 + 13.5) = 49% melt. The composition m_5 is therefore reached when 51% of melt m_0 has crystallized as X + Y and 49 mass % of melt remains.

CHAPTER 4

4.1 Refer to Fig. 4.1.

(a) Roughly equal amounts of opx and cpx with less than 65% plag make this a *gabbronorite*; opaques are accessory so are not mentioned in the name.

(b) plag is over 65% of the rock, making this a *leucotroctolite*.

(c) an opx-plagioclase plutonic rock is called a *norite*; according to current usage (Fig. 4.1 caption) this term applies even when the plagioclase is not calcic (in this case An_{45}); the amount of cpx present is below 5%, within the field of norite in Fig. 4.1.

(d) the larger proportion of augite makes this a *clinopyroxene* (or *augite*) *norite* (Fig. 4.1).

(e) plagioclase + augite suggests gabbro, but note that the plagioclase is andesine (An_{45}), so that this rock is more appropriately called a diorite (in full, *hornblende gabbro*).

(f) analcite – a feldspathoid – makes this an *alkali gabbro* (or analcite gabbro).

4.2

(a) From equation 3.3.1 in Box 3.3, the Phase Rule for *T*–*X* diagrams is $\phi + f = C + 1$. Point R lies at the junction between the 'melt + Fo' and 'melt + En' fields, indicating that 3 phases are in equilibrium (melt, forsterite and enstatite) so $\phi = 3$. As all phases in this system are combinations of 2 components Mg_2SiO_4 and SiO_2, $C = 2$. Hence $3 + f = 2 + 1$ and $f = 0$ (an invariant condition). The arithmetic is identical for point E (the phases in equilibrium with melt here are enstatite and a silica mineral).

(b) Unlike melt m_a, melt m_b lies to the *right* (forsterite-rich side) of the $Mg_2Si_2O_6$ composition in Fig. 4.3.1a: a line projected vertically downward from m_b intersects the En + Fo sub-solidus field. This factor, together with the higher temperature, means that melt m_b will crystallize more olivine than m_a in fractionating to R. The melt composition will (like m_a) arrive at R, but here the melt remaining will be subordinate in amount to olivine and it will be used up in the melt + olivine reaction, leaving a solid mixture of enstatite and excess forsterite (as opposed to excess melt in the case of m_a).

4.3 This is an application of the mixing equation given in equation B7 of Appendix B; the *C* terms in the equation refer here to the oxide concentrations, and the x terms refer to the proportions in which the olivine and basaltic matrix are mixed. For example, the SiO_2 content of the cumulate (mixture) is calculated as 0.7 × 48.18 + 0.3 × 39.58 = 42.16

%. The same weighted mean is calculated for each of the major element oxides in the table below.

	D	Olivine	Cumulate
SiO_2	48.18	39.58	42.16
TiO_2	1.9		0.57
Al_2O_3	15.06		4.518
Fe_2O_3	1.87		0.561
FeO	9.55	16.63	14.506
MnO	0.19		0.057
MgO	6.97	43.66	32.653
CaO	12.15		3.645
Na_2O	2.76		0.828
K_2O	0.67		0.201
P_2O_5	0.29		0.087
Total	99.59	99.87	99.786

CHAPTER 5

5.1 The Fo_x notation expresses in molar proportions the ratio 100 × MgO/(MgO + FeO) for the olivine. The first step is to calculate the relative molecular masses for FeO and MgO. The second is to divide the mass % values for these oxides by the relevant RMM to determine the number of moles of each oxide per 100 g of olivine:

	RMM	Analysis ÷ RMM	
SiO_2			
FeO	55.85 + 16.00	13.97 ÷ 71.85 = 0.1944	100 × MgO/(MgO + FeO)
MnO			= 100 × 1.1327/(1.1327 + 0.1944) = 85.35
MgO	24.32 + 16.00	45.67 ÷ 40.32 = 1.1327	
CaO			

The number of moles of each oxide per 100 g of olivine can then be plugged into the formula as shown in the right-hand box. Note that no calculations are required for oxides other than FeO and MgO.

5.2 Fo_{88} signifies an olivine consisting of 88 mole % Mg_2SiO_4 and (100 – 88) = 12 mole % Fe_2SiO_4. The atomic $(Fe^{2+}/Mg)_{olivine}$ ratio therefore = 12 ÷ 88 = 0.136. Therefore

$$\left(\frac{Fe^{2+}}{Mg}\right)_{melt} = \frac{(Fe^{2+}/Mg)_{olivine}}{0.3} = \frac{0.136}{0.3} = 0.453 = \frac{0.453}{1.00}$$

The Mg number for a melt in equilibrium with Fo_{88} is calculated as follows:

$$\text{Mg \#} = \frac{100 \times 1.00}{(1.00 + 0.453)} = 68.8$$

Since Fo_{88} is the least magnesian limit of the range of mantle olivine composition, Mg # = 68.8 represents the least magnesian melt that can coexist with mantle olivine, according to equation 5.1.

5.3 (a) 'FeO' for use in calculating Mg number = 0.9 × ΣFeO = 0.9 × 10.46 = 9.41%.

$$\text{Mg number} = \frac{100 \times (7.56/40.32)}{(7.56/40.32 + 9.41/71.85)} = 58.88$$

This value is much less than the critical value of 68 and therefore this basalt does not qualify as a primary melt: it has evidently experienced fractional crystallization between melting and eruption.

(b) For the subalkali (tholeiitic) basalt, 'FeO' for use in calculating Mg number = 0.9 × ΣFeO = 0.9 × 11.18 = 10.06%.

$$\text{Mg } \# = \frac{100 \times (9.74/40.32)}{(9.74/40.32 + 10.08/71.85)} = 63.30$$

For the alkali basalt, 'FeO' for use in calculating Mg number = 0.9 × ΣFeO = 0.9 × 12.44 = 11.20%.

$$\text{Mg number} = \frac{100 \times (11.36/40.32)}{(11.36/40.32 + 11.20/71.85)} = 64.39$$

Neither Mg number value qualifies as a primary melt. However the values are quite similar, suggesting the two melts have fractionated to similar degrees.

5.4 ΣFeO for analysis 6 in Table 2.4 = 8.53 %. Multiply by 0.9 to estimate FeO = 7.68 %.

$$\text{Mg number} = \frac{100 \times (6.34/40.32)}{(6.34/40.32 + 7.68/71.85)} = 59.5$$

This low-K tholeiite is too magnesian to have originated by hydrous partial melting of subducted oceanic crust, according to the experiments of Helz.

CHAPTER 6

6.1

(a) Recalculating plagioclase, alkali feldspar and quartz alone to a total of 100% gives 54% plag, 10% alkali feldspar and 36% quartz by volume. These coordinates fall in the *dacite* field in Fig. 6.1b.

(b) Using the correction factor given in Box 1.3, recalculate the analysis volatile-free. The correction factor is 1.026; the volatile-free values are SiO_2 = 52.8, Na_2O = 2.6%, K_2O = 1.03%, $Na_2O + K_2O$ = 3.59%. These coordinates plot just inside the *basaltic andesite* field in Fig. 6.1a.

(c) The LOI is too low to make a significant difference to the SiO_2 and K_2O data so no correction is necessary. In Fig. 6.1a the SiO_2 plots in the andesite field. Fig. 6.11 shows it to be a *high-K andesite*.

(d) No volatile correction is necessary. ΣFeO/MgO = 1.43, placing this analysis in the *calc-alkaline* and '*loFe*' fields in Fig. 6.8b. Alternatively 100 × ΣFeO/(ΣFeO + MgO) = 58.8, placing this analysis in *calc-alkaline* and '*loFe*' categories in Fig. 6.8c.

6.2

(a) SiO_2 (volatile-free) is greater (dacite) or less (andesite) than 63% (Fig. 6.1a).

(b) $Na_2O + K_2O$ (volatile-free) lies above the andesite/trachyandesite line in Fig. 6.1a).

(c) K_2O (volatile-free) lies above the BA/shoshonite boundary line in Fig. 6.11.

(d) the population of analyses should plot below or above the heavy dashed line in Fig. 6.7b or the heavy dashed curve in Fig. 6.7c.

(e) for a calc-alkaline dacite Sr/Y < 40 whereas for an adakite Sr/Y > 40 (as well as SiO_2 > 56%, Na_2O > 3.5% and HREE < 3 x primitive mantle (Fig. 6.15b).

(f)

	boninite	low-K basalt
SiO_2	>53%	<52%
MgO	8% < boninite < 24%	usually <8.0%
TiO_2	<0.5%	>0.5%
REE*	all REE_N < 1.0	$LREE_N < HREE_N$
Fig. 6.14(b)	U-shaped pattern	

* The subscript 'N' denotes normalization to primitive mantle.

(g) 'Rhyolite … is distinguished from dacite by the dominance of alkali feldspar over plagioclase, and often by the glassy nature of the groundmass, emphasized by such features as perlitic cracks (Fig. 6.2) and spherulites (Plate 6.9).'

6.3 Dividing the ppm data by the MORB normalizing factors given in the caption to Fig. 6.25 gives a plot as opposite:

(a) The negative Nb anomaly h_1 (the factor by which the real Nb value falls short of the interpolated value, ~1.5 x) for the Yellowstone rhyolite is much smaller than that for the Taupo rhyolite (h_2~ 8 x) and the SSZ patterns shown in Fig. 6.25, suggesting a magma source only slightly affected by subduction processes. Yellowstone volcanism occurred in a

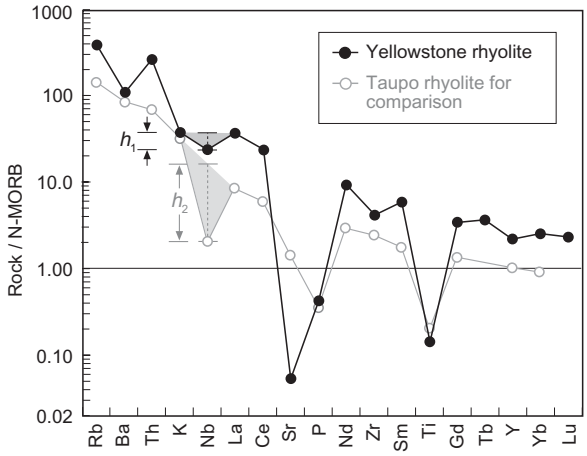


Fig. EA4

continental extension environment (periphery of the Basin and Range) with the possible involvement of a mantle plume (Fig. 2.16). The small negative Nb anomaly h_1 may simply reflect contamination by subduction-derived continental crust.

(b) The large negative spike at P is likely to be due to fractionation of apatite during the fractional crystallization of the rhyolite's parent magma.

CHAPTER 7

7.1 The rock consists chiefly of crystal fragments and glass shards, so is a *crystal-vitric tuff*. The field of view (given in caption) is 1.3 mm, so the larger crystals and shards are < 0.25 mm in size and fall within (coarse) ash grade (Table 7.2). The largest crystal (bottom right) is only partially in view but cannot exceed 2 mm.

7.2 *lapilli tuff and ignimbrite*

Lapilli tuff is a *descriptive* field term for a pyroclastic rock consisting of lapilli and lithified ash.

Ignimbrite is the *conceptual* term for the deposit formed by a pumiceous PDC. An ignimbrite could be described in the field as a pumiceous lapilli tuff.

plinian and vulcanian

A plinian eruption is a *sustained eruption* with a *high eruption column* (>15 km – see Fig. 7.4c) producing copious volumes of pumice which is deposited initially as pumice fall over a wide area, after which column collapse leads to the formation of PDCs that deposit ignimbrite.

A vulcanian eruption is on a smaller scale with a *lower eruption column* (<15 km – see Fig. 7.4a); it is marked by an *irregular series of discrete explosions* that clear the vent and erupt lithics and small volumes of juvenile pyroclastics, mostly in the form of breadcrust bombs and thinly bedded fall deposits.

pumice-rich PDC and ignimbrite

A pumiceous pyroclastic density current is a *phenomenon* associated with plinian eruptions at the column-collapse stage;.

An ignimbrite is the *deposit* formed by a pumiceous PDC.

resurgent dome and lava dome

A resurgent dome represents the non-eruptive *structural up-doming* of a caldera floor some time after the end of a caldera-forming eruption (Fig. 7.19c).

A lava dome forms when *viscous* (evolved), relatively *volatile-poor magma* is erupted; this may occur in the crater (Fig. 7.4f) or caldera (Fig. 7.20b) formed by an earlier explosive eruption from the same vent, or may be independent of earlier activity.

column collapse, dome collapse and sector collapse

Column collapse refers to the *gravitational collapse of an initially buoyant eruption column* (ash cloud), for example during a sustained plinian eruption (Fig. 7.6b); the product is one or more PDCs that deposit ignimbrites (in the plinian example) or other current deposits.

Dome collapse refers to the failure of part of a tumescent lava dome; in the case of a perched dome, the typical product is a nuée ardente (block-and-ash current – see Fig. 7.14) and associated hot deposits.

Sector collapse refers to the gravitational failure of a volcanic edifice, part of which

slides and breaks up; the product usually takes the form of a cold debris avalanche (Fig. 7.16).

caldera and crater

A caldera is a depression resulting from the *structural subsidence of a magma chamber roof* by down-faulting across arcuate ring faults (Fig. 7.19), following the rapid eruption of magma from a high-level magma chamber (or by draining away of magma into an associated plumbing system in the case of large basalt volcanoes).

A crater is a funnel-shaped depression formed by the *explosive ejection of material as a result of volcanic or hydrovolcanic processes*.

lahar and debris avalanche

A lahar is a *volcano-related mudflow* caused by the mixing of water (snow-melt, etc) and volcanic ash on a volcanic edifice.

A debris avalanche is a cold *dry, lithic-dominated density current* caused by the gravitational failure of part of a volcanic edifice (Fig. 7.16).

7.3

	(a) Description	(b) Inferred process
5.	lapilli-tuff showing eutaxitic (welding) texture	Welded ignimbrite deposited by PDC under conditions favouring increased discharge rate, perhaps as a result of vent widening.
4.	lapilli-tuff rich in lithics	May represent explosive vent widening (Table 7.3).
3.	(pumice) lapilli-tuff	Ignimbrite deposited by PDC during initial collapse of non-buoyant plinian column (Fig. 7.6b).
2.	pumice lapilli	Pumice-fall bed formed during buoyant stage of an evolving plinian column (Fig. 7.6a).
1.	(pumice) lapilli-tuff	Weathered top suggests part of an older eruptive cycle. Ignimbrite related to collapse of plinian eruption column.

CHAPTER 8

8.1

(a) Recalculating plagioclase, alkali feldspar and quartz alone to a total of 100% gives 50% plag, 35% alkali feldspar and 15% quartz by volume. These coordinates fall in the *quartz monzonite* field in Fig. 8.1.
(b) Plots in the granite field, but medium grain-size leads to the name biotite microgranite.
(c) Arfvedsonite (alkali) granite.

8.2

(a) In granite, plagioclase makes up *< 65 % by volume* of the overall feldspar content (graduations along bottom of Fig. 8.1), whereas in granodiorite *plag > 65%*.
(b) In granite, quartz makes up *more than 20%* of the felsic minerals by volume; in quartz monzonite it is *less than 20%*.
(c) Tonalite is a *mesocratic* coarse-grained igneous rock consisting essentially of plagioclase and quartz; trondhjemite is similar but *leucocratic*.
(d) Diorite and anorthosite both plot near the P apex of Fig. 8.1; anorthosite is a hololeucocratic rock (colour index < 10%) whereas diorite is *meso- or melanocratic*.
(e) Mangerite is an enstatite monzonite.
(f) S-type granites (Box 8.3) are usually peraluminous and contain key aluminous minerals such as muscovite, tourmaline and cordierite, suggesting derivation from a metasedimentary protolith, whereas A-type granites are metaluminous or peralkaline; their mafic minerals include biotite, aegirine (alkali pyroxene) and arfvedsonite (alkali amphibole).

8.3 The values of $(Na_2O + K_2O)/Al_2O_3$ and $Al_2O_3/(Na_2O + K_2O + CaO)$ *in molar units* for the 8 analyses in Table 8.3 are as given below in. E.g. for analysis 1, $[(Na_2O + K_2O)/Al_2O_3]_{mol}$ = (3.59/61.98 + 1.51/94.2)/(17.29/101.96) = 0.434.

Analysis	1	2	3	4	5	6	7	8
$(Na_2O + K_2O)/Al_2O_3$	0.434	0.483	0.561	0.745	0.792	**1.092**	0.663	0.595
$Al_2O_3/(Na_2O + K_2O + CaO)$	0.848	0.976	0.896	**1.027**	**1.155**	0.872	**1.173**	0.940
	met	met	met	peralum	peralum	peralk	peralum	met

If $(Na_2O + K_2O)/Al_2O_3$ exceeds 1.0, the rock is peralkaline. If $Al_2O_3/(Na_2O + K_2O + CaO)$ exceeds 1.0, the rock is peraluminous. If neither ratio exceeds 1.0, the rock is metaluminous.

8.4 Recalculating the data volatile-free leads to the following compilation:

Analysis	1	2	3	4	5	6	7	8
Y/ppm	18	7	26	8	22	63	56	31
Nb/ppm	7	5	8	9	11	23	42	20
Y+Nb/ppm	26	12	34	17	33	86	98	51
Rb/ppm	90	50	136	159	238	152	2	101

The data plot in Fig. 8.19 as shown in Fig. EA5. Note that the plagiogranite, collected at 45°N on the Mid-Atlantic Ridge, plots within the 'anomalous ridge segment' field in (a).

8.5 This calculation uses the mixing equation:

$$C_i^{\text{mix}} = C_i^{\text{A}} x^{\text{A}} + C_i^{\text{B}} x^{\text{B}} + \ldots \quad \text{(Appendix B)}$$

where C_i^{mix} is the concentration of species i (Th, Nb or K) in the contaminated basalt melt, C_i^{A} is its concentration in the uncontaminated basalt A, C_i^{B} is its concentration in the granite contaminant B, x^{B} is the mass proportion of contaminant B assimilated into the contaminated melt, and $x^{\text{A}} = 1 - x^{\text{B}}$. It is simplest to use trace element concentrations in their primitive-mantle normalized form (divide the ppm in Tables 2.4 and 8.4 by the primitive mantle ppm given in Table 2.4). Applying the above equation to the normalized values (which are shown in the following table in italics):

	Etendeka basalt	I-type granite	95% basalt 5% granite	90% basalt 10% granite	80% basalt 20% granite
Th_N	*48.7*	*199.4*	56.3	63.8	78.9
Nb_N	*39.7*	*12.7*	38.3	37.0	34.3
K_N	*49.0*	*140.4*	53.6	58.2	67.3

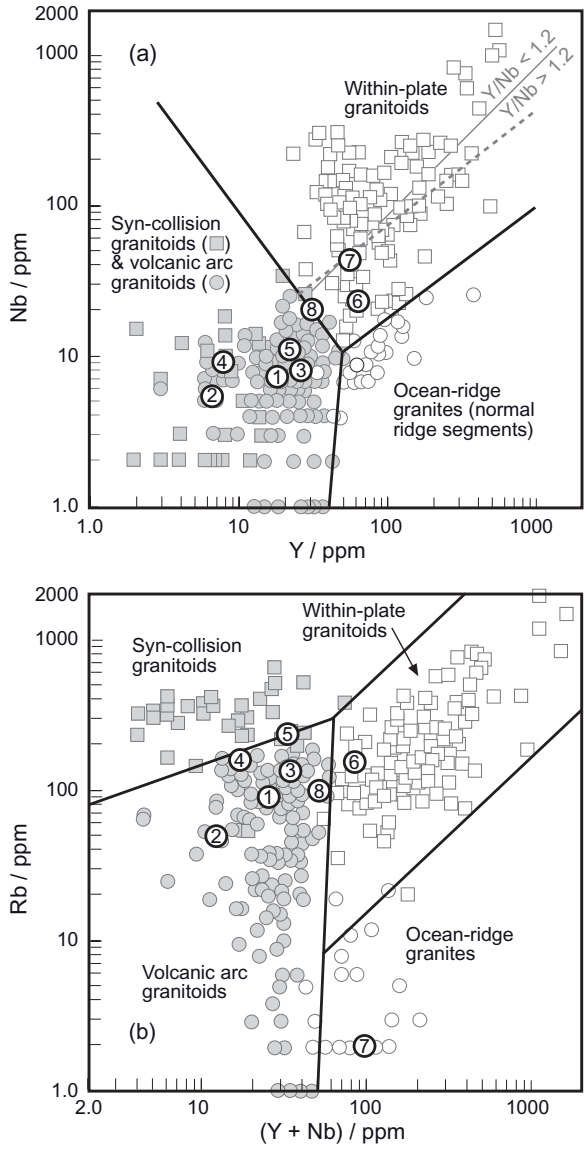


Fig. EA5

The results are plotted in the graph overleaf (Fig. EA6). Note that as the proportion of assimilant increases, the negative Nb anomaly becomes more pronounced, because Nb is

reduced slightly but mainly because Th and K are elevated by assimilation.

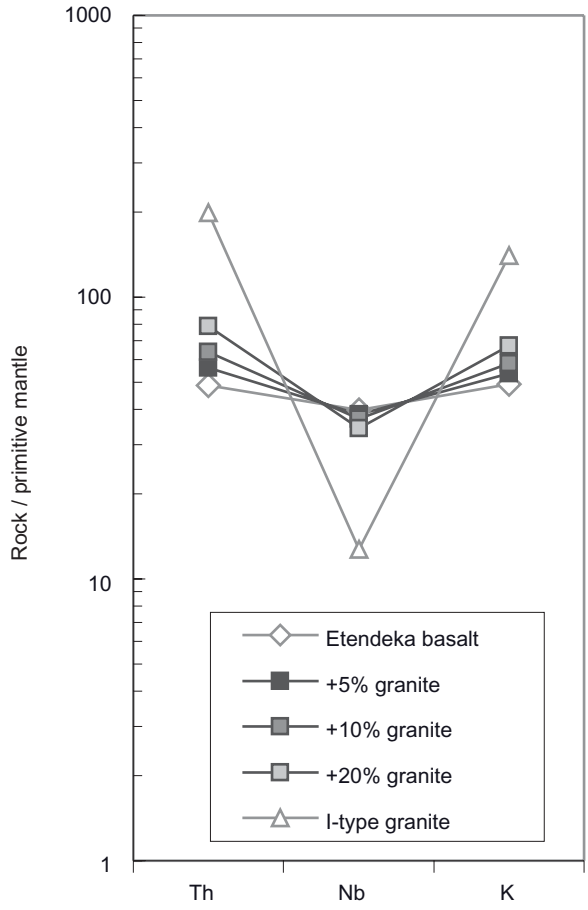


Fig. EA6

CHAPTER 9

9.1

(a) 29% plagioclase, 40% alkali feldspar and 15% nepheline add up to 84% felsic minerals. Dividing each by 84/100 = 0.84 gives 35% plagioclase, 48% alkali feldspar and 18% nepheline. This composition plots in the tephritic phonolite field in Fig. 9.1(b).

(b) Correcting for volatiles (assume an analysis total of 100%) means multiplying each percentage by 100/(100 – 2.5) = 1.025, giving SiO_2 = 46.15%, Na_2O = 4.62% and K_2O = 2.56% volatile-free. With $Na_2O + K_2O$ = 7.18%, this plots in the basanite-tephrite field in Fig. 9.1a. As normative olivine exceeds 10%, the rock is a basanite.

(c) 52.35% SiO_2, 4.05% Na_2O, 2.98% K_2O volatile-free gives $Na_2O + K_2O$ = 7.03% which places the analysis in the basaltic trachyandesite field in Fig. 9.1a. As $Na_2O - K_2O < 2.0$, the rock qualifies as shoshonite in Fig. 9.2.

(d) 48.9% SiO_2, 4.50% Na_2O, 2.09% K_2O volatile-free gives ($Na_2O + K_2O$ = 6.60%) which plots in the trachybasalt field in Fig. 9.1a. As $Na_2O - K_2O > 2.0$, the rock is a hawaiite.

(e) a dyke rock with phenocrysts of mafic minerals alone is called a lamprophyre (Box 9.6). Table 9.6.1 provides the varietal name monchiquite for this rock.

9.2

(a) urtite and melteigite are respectively leucocratic and melanocratic varieties of ijolite (Fig. 9.5);

(b) Type I and type II are classes of S. Africa kimberlites that have (type I) high Nb contents and OIB-like Sr isotope ratios, and (type II) negative Nb anomalies and more radiogenic Sr, believed to reflect different types of metasomatism of SCLM;

(c) The post-caldera stage of Hawaiian volcanism consists of a thin capping of alkali basalts, ankaramites, hawaiites, etc. erupted after the collapse of a summit caldera at the close of the shield-building stage of development; the post-erosional stage follows these after a 1–2 Ma hiatus, and consists of alkali basalts, basanites and nephelinites (Fig. 9.8).

(d) Both are coarse-grained alkali rocks: essexite is a nepheline-bearing gabbro consisting of calcic plagioclase + cpx + nepheline + alkali feldspar; monzonite is a mesocratic rock consisting essentially of sodic plagioclase and alkali feldspar in roughly equal proportions.

(e) both are coarse-grained igneous rocks: syenite is a leucocratic silicate rock consisting mainly of alkali feldspar, whereas sövite is a calcite-rich carbonatite.

9.3 (a) Reading off Fig. 9.7b, E_1 and E_2 can be expressed in terms of the following approximate mineral proportions (mass %):

	Diopside %	Nepheline %	Quartz %
E_1	15	66	19
E_2	2	36	62

The calculation below is most easily carried out in a spreadsheet. The first three blocks recalculate the formula of each mineral into mass percentages of the constituent oxides. The 4th and 5th blocks calculate the compositions of E_1 and E_2 as weighted means of these idealized mineral analyses.

Diopside		**$CaO.MgO.2SiO_2$**		
	RMM	**Mol props**	**Mass props**	**Mass %**
SiO_2	60.09	2	120.18	55.49
Al_2O_3	101.96		0	0.00
MgO	40.32	1	40.32	18.62
CaO	56.08	1	56.08	25.89
Na_2O	61.98		0	0.00
			216.58	100.00

Nepheline		**$Na_2O.Al_2O_3.2SiO_2$**		
	RMM	**Mol props**	**Mass props**	**Mass %**
SiO_2	60.09	2	120.18	42.30
Al_2O_3	101.96	1	101.96	35.89
MgO	40.32		0	0.00
CaO	56.08		0	0.00
Na_2O	61.98	1	61.98	21.81
			284.12	100.00

Quartz		**SiO_2**		
	RMM	**Mol props**	**Mass props**	**Mass %**
SiO_2	60.09	1	60.09	100.00
Al_2O_3	101.96		0	0.00
MgO	40.32		0	0.00
CaO	56.08		0	0.00
Na_2O	61.98		0	0.00
			60.09	100.00

E_1	Diop × 0.15	Neph × 0.66	Quartz × 0.19	
SiO_2	8.32	27.92	19.00	55.24
Al_2O_3	0.00	23.68	0.00	23.68
MgO	2.79	0.00	0.00	2.79
CaO	3.88	0.00	0.00	3.88
Na_2O	0.00	14.40	0.00	14.40
				100.00

Continued

E_2	Diop × 0.02	Neph × 0.36	Quartz × 0.62	
SiO_2	1.11	15.23	62.00	78.34
Al_2O_3	0.00	12.92	0.00	12.92
MgO	0.37	0.00	0.00	0.37
CaO	0.52	0.00	0.00	0.52
Na_2O	0.00	7.85	0.00	7.85
				100.00

Fractional crystallization causes a melt to evolve in composition as temperature *falls*. A cooling melt of eutectic composition E_1 is prevented from evolving to E_2 by the higher liquidus temperature at S (~1140 °C).

(b) Crystallization of pure diopside from melt *y* will drive the residua melt directly down the 'thermal divide' to the saddle 'S' on the cotectic between the diopside and albite fields. Albite will therefore begin to crystallize alongside diopside. Since diopside, S and albite are colinear in this diagram, the melt cannot evolve toward either E_1 or E_2. The residual melt composition will therefore remain fixed at S until crystallization is complete. The albite-rich composition containing neither nepheline nor quartz corresponds to trachyte.

9.4 The criteria for primary melt are Mg# > 65 and Ni > 250 ppm. (Box 9.5). The data are calculated from Table 9.5 as below (first dividing FeO and MgO % by their RMMs to convert to molar proportions):

	1	**2**	**3**	**4**	**5**	**6**	**7**	**8**
ΣFeO	11.17	6.00	11.46	8.93	9.11	6.51	6.41	3.41
0.9xΣFeO*	10.05	5.40	10.31	8.04	8.20	5.86	5.77	3.07
/71.85	0.1399	0.0752	0.1435	0.1119	0.1141	0.0815	0.0803	0.0427
MgO	8.64	7.95	5.39	3.8	2.84	2.89	0.36	0.4
/40.32	0.2143	0.1972	0.1337	0.0942	0.0704	0.0717	0.0089	0.0099
Mg #	60.5	**72.4**	48.2	45.7	38.2	46.8	10.0	18.8
Ni/ppm	112	233	14	2	4	9.43		5

* To correct ΣFeO to FeO.

Only analysis 2 (Gaussberg lamproite, Antarctica) qualifies as primary on grounds of Mg number. Its Ni content (even corrected for volatile content → 236 ppm.) is slightly too low.

9.5 Measuring Fig. 9.21 with a ruler, distance m_1–M is 13.5 mm and distance M–m_2 is 23.5 mm. Using the Lever Rule (Box 3.2), it is clear that m_1 predominates: the mass ratio m_1/m_2 = 23.5/13.5 = 1.74 so the mass percentage of m_1 in M is 100 × 23.5/(13.5 + 23.5) = 63.5% (m_2 = 36.8%).

APPENDIX B

B1. The results are summarized in the table opposite. A PDF file giving the workings can be viewed at www.wiley.com/go/gill/igneous

	a	b	c
q		33.31	
or	32.24	26.03	1.49
ab	34.75	34.23	20.24
an	1.93	2.43	35.95
ne	17.57		
lc			
c		1.39	
ac			
Di	6.94		16.51
wo			
En		1.39	7.57
Ol	0.43		13.38
mt	4.06	0.42	1.93
he			
il	1.43	0.21	2.25
ap	0.42	0.07	0.23
total	99.76	99.48	99.57

B2. The calculations are tabulated below. As only a trace of olivine is present, the composition is most appropriately plotted in the plag–opx–cpx face of the tetrahedron; the coordinates are shown as a filled circle (labelled 'Ex B2') in Fig. 4.1.

	Original mode (volume %)	Plag, opx, cpx (rel. volume %)
plag	38	43
opx	33	37
cpx	18	20
ol	4	
opaques & acc	7	
total	100	
Plag + opx + cpx	89	100

Note that this composition actually plots within the interior of the quaternary plag–opx–cpx–olivine figure in Fig. 4.1 (albeit close to face A). Eliminating olivine as above is exactly equivalent to **projecting** the quaternary coordinates on to face A from the olivine apex: imagine placing a point source of light at the olivine apex, and observing where it casts a shadow of the quaternary composition on face A.

B3.

(a) *nepheline* is only calculated once all of the enstatite has been converted to olivine.
(b) *diopside*: corundum only appears when Al_2O_3 exceeds that required for all feldspars: in these circumstances no CaO remains after calculating anorthite, so no Di can form.
(c) *quartz*: olivine is only calculated in the norm when there is insufficient SiO_2 present to meet the requirements of enstatite (En); in these circumstances no quartz is possible.

Bibliography

Aitken, B. G. & Echeverria, L. M. (1984). Petrology and geochemistry of komatiites and tholeiites from Gorgona Island, Colombia. *Contributions to Mineralogy and Petrology* **86**, 94–105.

Alabaster, T., Pearce, J. A. & Malpas, J. (1982). The volcanic stratigraphy and petrogenesis of the Oman ophiolite complex. *Contributions to Mineralogy and Petrology* **81**, 168–183.

Altherr, R., Meyer, H. P., Holl, A., Volker, F., Alibert, C., McCulloch, M. T. & Majer, V. (2004). Geochemical and Sr–Nd–Pb isotopic characteristics of Late Cenozoic leucite lamproites from the East European Alpine belt (Macedonia and Yugoslavia). *Contributions to Mineralogy and Petrology* **147**, 58–73.

Andersen, J. C. Ø., Rasmussen, H., Nielsen, T. F. D. & Rønsbo, J. G. (1998). The Triple Group and the Platinova gold and palladium reefs in the Skaergaard Intrusion: stratigraphic and petrographic relations. *Economic Geology* **93**, 488–509.

Andersen, J. C. Ø. (2006). Postmagmatic sulphur loss in the Skaergaard Intrusion: implications for the formation of the Platinova Reef. *Lithos* **92**, 198–221.

Anderson, E. M. (1938). The dynamics of the formation of cone-sheets, ring-dykes, and cauldron-subsidences. *Royal Society of Edinburgh Proceedings* **56**, 128–157.

Anderson, T. & Flett, J. S. (1903). Report on the eruptions of the Soufrière in St Vincent, in 1902 and on a visit to Montagne Pelée, in Martinique: Part 1. *Philosophical Transactions of the Royal Society* **A200**, 353–553.

Annen, C., Blundy, J. & Sparks, R. S. J. (2006). The genesis of intermediate and silicic magmas in deep crustal hot zones. *Journal of Petrology* **47**, 505–539.

Annen, C., Scaillet, B. & Sparks, R. S. J. (2006). Thermal constraints on the emplacement rate of a large intrusive complex: The Manaslu leucogranite, Nepal Himalaya. *Journal of Petrology* **47**, 71–95.

Arculus, R. J. (2003). Use and abuse of the terms calcalkaline and calcalkalic. *Journal of Petrology* **44**, 929–935.

Arculus, R. J. (2004). Evolution of arc magmas and their volatiles. In: Sparks, R. S. J. & Hawkesworth, C. J. (eds.) *The state of the planet: frontiers and challenges in geophysics*. Washington DC: American Geophysical Union, **150**, 95–108.

Arculus, R. J. & Wills, K. J. A. (1980). The petrology of plutonic blocks and inclusions from the Lesser Antilles island arc. *Journal of Petrology* **21**, 743–799.

Arndt, N., Ginibre, C., Chauvel, C., Albarède, F., Cheadle, M., Herzberg, C., Jenner, G. & Lahaye, Y. (1997). Were komatiites wet? *Geology* **26**, 739–742.

Arndt, N. T., Lesher, C. M., Houlé, M. G., Lewin, E. & Lacaze, Y. (2004). Intrusion and crystallization of a spinifex-textured komatiite sill in Dundonald Township, Ontario. *Journal of Petrology* **45**, 2555–2571.

Arndt, N. T., Naldrett, A. J. & Pyke, D. R. (1977). Komatiitic and iron-rich tholeiitic lavas of Munro Township, northeast Ontario. *Journal of Petrology* **18**, 319–369.

Arndt, N. T. & Nisbet, E. G. (1982). *Komatiites*. London: Allen and Unwin.

Ashwal, L. D. (1993). *Anorthosites*. Berlin: Springer-Verlag.

Atherton, M. P. & Ghani, A. A. (2002). Slab breakoff: a model for Caledonian, Late Granite syn-collisional magmatism in the orthotectonic (metamorphic) zone of Scotland and Donegal, Ireland. *Lithos* **62**, 65–85.

Atherton, M. P. & Petford, N. (1993). Generation of sodium-rich magmas from newly underplated basaltic crust. *Nature* **362**, 144–146.

Atherton, M. P. & Sanderson, L. M. (1985). The chemical variation and evolution of the super-units of the segmented Coastal Batholith. In: Pitcher, W. S., Atherton, M. P., Cobbing, E. J. & Pankhurst, R. J. (eds.) *Magmatism at a plate edge – the Peruvian Andes*. Glasgow: Blackie, 208–227.

Ayres, M. & Harris, N. (1997). REE fractionation and Nd-isotope disequilibrium during crustal anatexis: constraints from Himalayan leucogranites. *Chemical Geology* **13**, 249–269.

Bachmann, O. & Bergantz, G. (2008). The magma reservoirs that feed supereruptions. *Elements* **4**, 17–21.

Bachmann, O., Dungan, M. A. & Lipman, P. W. (2002). The Fish Canyon magma body, San Juan Volcanic Field, Colorado: rejuvenation and eruption of an upper-crustal batholith. *Kournal of Petrology* **43**, 1469–1503.

Bacon, C. R., Sisson, T. W. & Mazdab, F. K. (2007). Young cumulate complex beneath Veniaminof caldera, Aleutian arc, dated by zircon in erupted plutonic blocks. *Geology* **35**, 491–494.

Bailey, D. K., Garson, M., Kearns, S. & Velasco, A. P. (2005). Carbonate volcanism in Calatrava, central Spain: a report on the initial findings. *Mineralogical Magazine* **69**, 907–915.

Bailey, J. C., Sørensen, H., Andersen, T., Kogarko, L. N. & Rose-Hansen, J. (2006). On the origin of microrhythmic layering in arfvedsonite lujavrite from the Ilímaussaq alkaline complex, South Greenland. *Lithos* **91**, 301–318.

Bailey, K., Kearnsi, S., Mergoil, J., Daniel, J. M. & Paterson, B. (2006). Extensive dolomitic volcanism through the Limagne Basin, central France: a new form of carbonatite activity. *Mineralogical Magazine* **70**, 231–236.

Baker, B. H. (1987). Outline of the petrology of the Kenya Rift alkaline province. In: Fitton, J. G. & Upton, B. G. J. (eds.) *Alkaline igneous rocks*. London: Geological Society of London Special Publication **30**, 293–311.

Baker, J., Snee, L. & Martin, M. (1996). A brief Oligocene period of flood volcanism in Yemen: implications for the duration and rate of continental flood volcanism at the Afro-Arabian triple junction. *Earth and Planetary Science Letters* **138**, 39–55.

Baker, J. A., Macpherson, C. G., Menzies, M. A., Thirlwall, M. F., Al-Kadasi, M. & Mattey, D. P. (2000). Resolving crustal and mantle contributions to continental flood volcanism, Yemen: constraints from mineral oxygen isotope data. *Journal of Petrology* **41**, 1805–1820.

Baker, M. B. & Beckett, J. R. (1999). Origin of abyssal peridotites: a reinterpretation of constraints based on primary bulk compositions. *Earth and Planetary Science Letters* **171**, 49–61.

Baranzangi, M. & Isacks, B. L. (1971). Spatial distribution of earthquakes and subduction of the Nazca plate beneath South America. *Geology* **4**, 686–692.

Barberi, F., Santacroe, R. & Varet, J. (1982). Chemical aspects of rift magmatism. In: Pálmason, G. (ed.) *Continental and oceanic rifts: final report of Inter-Union Commission on Geodynamics Working Group 4, Continental and Oceanic Rifts*. Washington DC: American Geophysical Union: Geodynamics Series, **8**, 223–258.

Barclay, J., Carroll, M. R., Houghton, B. F. & Wilson, C. J. N. (1996). Pre-eruptive volatile content and degassing history of an evolving peralkaline volcano. *Journal of Volcanology and Geothermal Research* **74**, 75–87.

Barnes, S. J. (2004). Introduction to nickel sulfide orebodies and komatiites of the Black Swan area, Yilgarn Craton, Western Australia. *Mineralium Deposita* **39**, 679–683.

Barsdell, M., Smith, I. E. M. & Sporli, K. B. (1982). The origin of reversed geochemical zoning in the northern New Hebrides volcanic arc. *Contributions to Mineralogy and Petrology* **81**, 148–155.

Basaltic Volcanism Study Project. (1981). *Basaltic volcanism on the terrestrial planets*. New York: Pergamon Press.

Bateman, P. C. & Chappell, B. W. (1979). Crystallization, fractionation, and solidification of the Tuolumne Intrusive Series, Yosemite National Park, California. *Bulletin of the Geological Society of America* **90**, 465–482.

Beard, J. S. & Borgia, A. (1989). Temporal variation of mineralogy and petrology in cognate gabbroic enclaves at Arenal Volcano, Costa Rica. *Contributions to Mineralogy and Petrology* **103**, 110–122.

Becker, M. & Le Roex, A. P. (2006). Geochemistry of South African on- and off-craton, Group I and Group II kimberlites: petrogenesis and source region evolution. *Journal of Petrology* **47**, 673–703.

Beckinsale, R. D. (1981). Granite magmatism in the tin belt of south-east Asia. In: Atherton, M. P. & Tarney, J. (eds.) *Origin of granite batholiths – geochemical evidence*. Nantwich: Shiva Publishing Ltd, 34–44.

Beckinsale, R. D., Sanchez-Fernandez, A. W., Brook, M., Cobbing, E. J., Taylor, W. P. & Moore, N. D. (1985). Rb-Sr whole-rock isochron and K-Ar age determinations for the Coastal Batholith of Peru. In: Pitcher, W. S., Atherton, M. P., Cobbing, E. J. & Pankhurst, R. J. (eds.) *Magmatism at a plate edge – the Peruvian Andes*. Glasgow: Blackie, 177–207.

Bedard, J. H. (2005). Partitioning coefficients between olivine and silicate melts. *Lithos* **83**, 394–419.

Belkin, H. E., De Vivo, B., Torok, K. & Webster, J. D. (1998). Pre-eruptive volatile content, melt-inclusion chemistry, and microthermometry of interplinian Vesuvius lavas (pre-AD1631). *Journal of Volcanology and Geothermal Research* **82**, 79–95.

Bell, J. D. (1976). The Tertiary intrusive complex on the Isle of Skye. *Proceedings of the Geologists' Association* **87**, 247–271.

Bell, K., Castorina, F., Rosatelli, G. & Stoppa, F. (2006). Plume activity, magmatism, and the geodynamic evolution of the Central Mediterranean. *Annals of Geophysics* **49**, 357–371.

Beresford, S., Cas, R., Lahaye, Y. & Jane, M. (2002). Facies architecture of an Archean komatiite-hosted Ni-sulphide ore deposit, Victor, Kambalda, Western Australia: implications for komatiite lava emplacement. *Journal of Volcanology and Geothermal Research* **118**, 57–75.

Beresford, S. W. & Cas, R. A. F. (2001). Komatiitic invasive lava flows, Kambalda, Western Australia. *Canadian Mineralogist* **39**, 525–535.

Bickle, M. J. (1986). Implications of melting for stabilisation of the lithosphere and heat loss in the Archaean. *Earth and Planetary Science Letters* **80**, 314–324.

Bickle, M. J., Nisbet, E. G. & Martin, A. (1994). Archean Greenstone Belts Are Not Oceanic-Crust. *Journal of Geology* **102**, 121–138.

Blake, D. H., Elwell, R. W. D., Gibson, I. L., Skelhorn, R. R. & Walker, G. P. L. (1965). Some relationships resulting from the intimate association of acid and basic magmas. *Quarterly Journal of the Geological Society of London* **121**, 31–49.

Blake, S. & Argles, T. (2003). *Growth and destruction: continental evolution at subduction zones. Course S339 Understanding the Continents Block 3, 153 pp*. Milton Keynes: The Open University.

Blundy, J. & Cashman, K. (2001). Ascent-driven crystallisation of dacite magmas at Mount St Helens, 1980–1986. *Contributions to Mineralogy and Petrology* **140**, 631–650.

Blundy, J. & Cashman, K. (2005). Rapid decompression-driven crystallization recorded by melt inclusions from Mount St. Helens volcano. *Geology* **33**, 793–796.

Blundy, J., Cashman, K., Rust, A. & Melnik, O. (2008). *Textural and chemical consequences of post-eruptive pressure changes at Mount St. Helens volcano (abstract)*. In: Troll, V. (ed.) *Volcanic and Magmatic Studies Group Meeting*. Dublin.

Blundy, J., Cashman, K. V. & Humphreys, M. (2006). Magma heating by decompression-driven crystallization beneath andesite volcanoes. *Nature* **443**, 76–80.

Blundy, J. & Wood, B. (2003). Partitioning of trace elements between crystals and melts. *Earth and Planetary Science Letters* **210**, 383–397.

Bodinier, J. L., Menzies, M. A. & Thirlwall, M. F. (1991). Continental to oceanic mantle transition – REE and Sr-Nd isotopic geochemistry of the Lanzo Lherzolite Massif. In: Menzies, M. A., Dupuy, C. & Nicolas, A. (eds.) *Orogenic lherzolites and mantle processes. Special volume of the Journal of Petrology 1991*. Oxford, 191–210.

Bolle, O., Demaiffe, D. & Duchesne, J. C. (2003). Petrogenesis of jotunitic and acidic members of an AMC suite (Rogaland anorthosite province, SW Norway): a Sr and Nd isotopic assessment. *Precambrian Research* **124**, 185–214.

Bott, M. H. P. (1974). The geological interpretation of a gravity survey of the English Lake District and the Vale of Eden. *Journal of the Geological Society of London* **130**, 309–331.

Bottinga, Y. & Weill, D. F. (1970). Densities of liquid silicate systems calculated from partial molar volumes of oxide components. *American Journal of Science* **269**, 169–182.

Boudier, F. & Nicolas, A. (1995). Nature of the Moho transition zone in the Oman Ophiolite. *Journal of Petrology* **36**, 777–796.

Bowen, N. L. (1915). The crystallization of haplobasaltic, haplodioritic and related magmas. *American Journal of Science (4th series)* **40**, 161–185.

Bowen, N. L. (1922). The reaction principle in petrogenesis. *Journal of Geology* **30**, 177–198.

Bowen, N. L. (1928). *The evolution of the igneous rocks*. Princeton NJ: Princeton University Press (republished by Dover Publications Inc in 1956).

Bowen, N. L. & Anderson, O. (1914). The binary system MgO-SiO_2. *American Journal of Science (4th series)* **37**, 487–500.

Bowen, N. L. & Schairer, J. F. (1932). The system FeO-SiO2. *American Journal of Science (4th series)* **24**, 177–213.

Bowen, N. L. & Schairer, J. F. (1935). The system MgO-FeO-SiO_2. *American Journal of Science (5th series)* **29**, 151–217 (an annotated extract is printed in Morse, 1980, pp 1437–1959).

Branney, M. J. & Kokelaar, P. (1992). A reappraisal of ignimbrite emplacement: progressive aggradation and changes from particulate to non-particulate flow during emplacement of high-grade ignimbrite. *Bulletin of Volcanology* **54**, 504–520.

Branney, M. J. & Kokelaar, P. (2002). *Pyroclastic density currents and the sedimentation of ignimbrites*. London: Geological Society Memoir No **27**, 143 pp.

Brooker, R. A. (1998). The effect of CO_2 saturation on immiscibility between silicate and carbonate liquids: an experimental study. *Journal of Petrology* **39**, 1905–1915.

Brown, G. M. (1956). The layered ultrabasic rocks of Rhum, Inner Hebrides. *Philosophical Transactions of the Royal Society of London, series B* **240**, 1–53.

Brown, M. (2007). Crustal melting and melt extraction, ascent and emplacement in orogens: mechanisms and consequences. *Journal of the Geological Society of London* **164**, 709–730.

Bryant, J. A., Yogodzinski, G. M., Hall, M. L., Lewicki, J. L. & Bailey, D. G. (2006). Geochemical constraints on the origin of volcanic rocks from the Andean Northern Volcanic Zone, Ecuador. *Journal of Petrology* **47**, 1147–1175.

Buddington, A. F. (1959). Granite emplacement with special reference to North America. *Geological Society of America Bulletin* **70**, 671–747.

Bühn, B. & Rankin, A. H. (1999). Composition of natural, volatile-rich Na-Ca-REE-Sr carbonatitic fluids trapped in fluid inclusions. *Geochimica Et Cosmochimica Acta* **63**, 3781–3797.

Burnham, C. W. (1997). Magmas and hydrothermal fluids. In: Barnes, H. L. (ed.) *Geochemistry of hydrothermal ore deposits*. New York: J. Wiley. 3rd edn, 63–123.

Calzia, J. P. & Rämö, O. T. (2005). Miocene rapakivi granites in the southern Death Valley region, California, USA. *Earth-Science Reviews* **73**, 221–243.

Campbell, I. H. & Taylor, S. R. (1983). No water, no granites – no oceans, no continents. *Geophysical Research Letters* **10**, 1061–1064.

Caress, D. W., McNutt, M. K., Detrick, R. S. & Mutter, J. C. (1995). Seismic Imaging of Hotspot-Related Crustal Underplating Beneath the Marquesas Islands. *Nature* **373**, 600–603.

Carmichael, I. S. E. (1964). The petrology of Thinmuli, a Tertiary volcano in eastern Iceland. *Journal of Petrology* **5**, 453–460.

Carmichael, I. S. E., Turner, F. J. & Verhoogen, J. (1974). *Igneous petrology*. New York: McGraw Hill.

Castro, J. M., Beck, P., Tuffen, H., Nichols, A. R. L., Dingwell, D. B. & Martin, M. C. (2008). Timescales of spherulite crystallization in obsidian inferred from water concentration profiles. *American Mineralogist* **93**, 1816–1822.

Cawthorn, R. G. (ed.) (1996). *Layered Intrusions*. Amsterdam: Elsevier.

Cawthorn, R. G. & Walraven, F. (1998). Emplacement and crystallization time for the Bushveld Complex. *Journal of Petrology* **39**, 1669–1687.

Chambers, A. D. & Brown, P. E. (1995). The Lilloise Intrusion, East Greenland – Fractionation of a Hydrous Alkali Picritic Magma. *Journal of Petrology* **36**, 933–963.

Chappell, B. W. & White, A. J. R. (1974). Two contrasting granite types. *Pacific Geology* **8**, 173–174.

Charlier, B. L. A., Wilson, C. J. N., Lowenstern, J. B., Blake, S., Calsteren, P. W. V. & Davidson, J. P. (2005). Magma generation at a large, hyperactive silicic volcano (Taupo, New Zealand) revealed by U–Th and U–Pb systematics in zircons. *Journal of Petrology* **46**, 3–32.

Chorowicz, J. (2005). The East African rift system. *Journal of African Earth Sciences* **43**, 379–410.

Christensen, U. (1998). Fixed hotspots gone with the wind. *Nature* **391**, 739–740.

Christiansen, R. L. (2001). *Geology of Yellowstone National Park – The Quaternary and Pliocene Yellowstone plateau volcanic field of Wyoming, Idaho and Montana*.

Christiansen, R. L., Foulger, G. R. & Evans, J. R. (2002). Upper-mantle origin of the Yellowstone hotspot. *Geological Society of America Bulletin* **114**, 1245–1256.

Claeson, D. T. & Meurer, W. P. (2004). Fractional crystallization of hydrous basaltic 'arc-type' magmas and the formation of amphibole-bearing gabbroic cumulates. *Contributions to Mineralogy and Petrology* **147**, 288–304.

Clague, D. A. (1987). Hawaiian alkaline volcanism. In: Fitton, J. G. & Upton, B. G. J. (eds.) *Alkaline igneous rocks*. London: Geological Society of London Special Publication **30**, 227–252.

Clemens, J. D. & Petford, N. (1999). Granitic melt viscosity and silicic magma dynamics in contrasting tectonic settings. *Journal of the Geological Society of London* **156**, 1057–1060.

Clift, P. & Vannucchi, P. (2004). Controls on tectonic accretion versus erosion in subduction zones: implications for the origin and recycling of the continental crust. *Reviews of Geophysics* **42**, doi:10.1029/2003RG000127.

Clough, C. T., Maufe, H. B. & Bailey, E. B. (1909). The cauldron-subsidence of Glen Coe, and the associated igneous phenomena. *Quarterly Journal of the Geological Society of London* **65**, 611–678.

Cobbing, E. J. (1999). The Coastal Batholith and other aspects of Andean magmatism in Peru. In: Castro, A., Fernández, C. & Vigneresse, J. L. (eds.) *Understanding granites: integrating new and classical techniques*. London: Geological Society of London Special Publication **168**, 111–122.

Coffin, M. F. & Eldholm, O. (1994). Large igneous provinces: crustal structure, dimensions, and external consequences. *Reviews of Geophysics* **32**, 1–36.

Coffin, M. F., Pringle, M. S., Duncan, R. A., Gladczenko, T. P., Storey, M., Müller, R. D. & Gahagan, L. A. (2002). Kerguelen hotspot magma output since 130 Ma. *Journal of Petrology* **43**, 1121–1139.

Cole, J. W., Milner, D. M. & Spinks, K. D. (2005). Calderas and caldera structures: a review. *Earth-Science Reviews* **69**, 1–26.

Coleman, D. S. & Glazner, A. F. (1997). The Sierra Crest magmatic event: rapid formation of juvenile crust during the Late Cretaceous in California. *International Geology Review* **39**, 768–787.

Coleman, R. G. & Peterman, Z. E. (1975). Oceanic plagiogranite. *Journal of Geophysical Research* **80**, 1099–1108.

Coltice, N., Phillips, B. R., Bertrand, H., Ricard, Y. & Rey, P. (2007). Global warming of the mantle at the origin of flood basalts over supercontinents. *Geology* **35**, 391–394.

Coltorti, M., Alberti, A., Beccaluva, L., Dossantos, A. B., Mazzucchelli, M., Morais, E., Rivalenti, G. & Siena, F. (1993). The Tchivira-Bonga Alkaline-Carbonatite Complex (Angola) – Petrological Study and Comparison With Some Brazilian Analogs. *European Journal of Mineralogy* **5**, 1001–1024.

Conrad, W. K. & Kay, R. W. (1984). Ultramafic and mafic inclusions from Adak Island: crystallisation history, and implications for the nature of primary magmas and crustal evolution in the Aleutian Arc. *Journal of Petrology* **25**, 88–125.

Conticelli, S. & Peccerillo, A. (1992). Petrology and geochemistry of potassic and ultrapotassic volcanism in central Italy – petrogenesis and inferences on the evolution of the mantle sources. *Lithos* **28**, 221–240.

Coogan, L. A., Thompson, G. & MacLeod, C. J. (2002). A textural and geochemical investigation of high level gabbros from the Oman ophiolite: implications for the role of the axial magma chamber at fast-spreading ridges. *Lithos* **63**, 67–82.

Courtillot, V. E. & Renne, P. R. (2003). On the ages of flood basalt events. *Comptes Rendus Geosciences* **335**, 113–140.

Cox, K. G., Bell, J. D. & Pankhurst, R. J. (1979). *The interpretation of igneous rocks*. London: George Allen and Unwin.

Cox, K. G., Price, N. B. & Harte, B. (1988). *An introduction to the practical study of crystals, minerals and rocks*. London: McGraw-Hill. Revised 1st edn.

Crawford, A. J. (ed.) (1989). *Boninites and related rocks*. London: Unwin Hyman.

Crisp, J. (1984). Rates of magma emplacement and volcanic output. *Journal of Volcanology and Geothermal Research* **20**, 177–211.

Cross, W., Iddings, J. P., Pirsson, L. V. & Washington, H. S. (1902). A quantitative chemicomineralogical classification and nomenclature of igneous rocks. *Journal of Geology* **10**, 555–690.

Cruden, A. R. (1998). On the emplacement of tabular granites. *Journal of the Geological Society of London* **155**, 853–862.

Cruden, A. R., Tobisch, O. T. & Launeau, P. (1999). Magnetic fabric evidence for conduit-fed emplacement of a tabular intrusion: Dinkey Creek pluton, central Sierra Nevada batholith, California. *Journal of Geophysical Research* **104**, 10511–10530.

Danyushevsky, L. V., Eggins, S. M., Falloon, T. J. & Christie, D. M. (2000). H_2O abundance in depleted to moderately enriched mid-ocean ridge magmas; Part I: incompatible element behaviour, implications for mantle storage, and origin of regional variations. *Journal of Petrology* **41**, 1329–1364.

Davies, J. H. & Stevenson, D. J. (1992). Physical model of source region of subduction zone volcanics. *Journal of Geophysical Research* **97**, 2037–2070.

Davis, B. K. & McPhie, J. (1996). Spherulites, quench fractures and relict perlite in a Late Devonian rhyolite dyke, Queensland, Australia. *Journal of Volcanology and Geothermal Research* **71**, 1–11.

Davison, I., Al-Kadasi, M., Al-Khirbash, S., Al-Subbary, A. K., Baker, J., Blakey, S., Bosence, D., Dart, C., Heaton, R., McClay, K., Menzies, M., Nichols, G., Owen, L. & Yelland, A. (1994). Geological evolution of the southeastern Red Sea rift margin, Republic of Yemen. *Geological Society of America Bulletin* **106**, 1474–1493.

Dawson, J. B. (1962). The geology of Oldoinyo Lengai. *Bulletin Volcanologique* **24**, 348–387.

De Graff, J. M. & Aydin, A. (1987). Surface morphology of columnar joints and its significance to mechanics and direction of joint growth. *Geological Society of America Bulletin* **99**, 605–617.

De Paolo, D. J. (1981). Trace element and isotopic effects of combined wallrock assimilation and fractional crystallisation. *Earth and Planetary Science Letters* **53**, 189–202.

de Silva, S. L. (1989). Altiplano-Puna volcanic complex of the central Andes. *Geology* **17**, 1102–1106.

de Wit, M. J. (1998). On Archaean granites, greenstones, cratons and tectonics: does the evidence demand a verdict? *Precambrian Research* **91**, 181–226.

Debon, F., Le Fort, P., Sheppard, S. M. F. & Sonet, J. (1986). The four plutonic belts of the Transhimalaya-Himalaya: a chemical, mineralogical, isotopc and chronological synthesis along a Tibet-Nepal section. *Journal of Petrology* **27**, 219–250.

Deer, W. A. & Abbott, D. (1965). Clinopyroxenes of the gabbro cumulates of the Kap Edvard Complex, East Greenland. *Mineralogical Magazine* **34**, 177–193.

Deer, W. A., Howie, R. A. & Zussman, J. (1992). *An introduction to the rock-forming minerals*. Harlow: Longman. 2nd edn.

Defant, M. J. & Drummond, M. S. (1990). Derivation of some modern arc magmas by melting of young subducted lithosphere. *Nature* **347**, 662–665.

Dempster, T. J., Preston, R. J. & Bell, B. R. (1999). The origin of Proterozoic massif-type anorthosites: evidence from interactions between crustal xenoliths and basaltic magma. *Journal of the Geological Society of Londion* **156**, 41–46.

Déruelle, B., Ngounouno, S. & Demaiffe, D. (2007). The 'Cameroon Hot Line' (CHL): a unique example of active alkaline intraplate structure in both oceanic and continental lithospheres. *Comptes Rendus Geoscience* **339**, 589–600.

Devine, J. D. (1995). Petrogenesis of the basalt-andesite-dacite association of Grenada, Lesser Amtilles island arc, revisited. *Journal of Volcanology and Geothermal Research* **69**, 1–33.

Dick, H. J. B., Fisher, R. L. & Bryan, W. B. (1984). Mineralogic variability of the uppermost mantle along mid-ocean ridges. *Earth and Planetary Science Letters* **69**, 88–106.

Dick, H. J. B., Lin, J. & Schouten, H. (2003). An ultraslow–spreading class of ocean ridge. *Nature* **426**, 405–412.

Dickinson, W. R. (1975). Potash-depth (K-h) relations in continental margin and intra-ocean magmatic arcs. *Geology* **3**, 53–56.

Dilek, Y. (2003). Ophiolite concept and its evolution. In: Dilek, Y. & Newcomb, S. (eds.) *Ophiolite concept and the evolution of geological thought*. Boulder CO: Geological Society of America, **Special Paper 373**, 1–16.

Dixon, J. E., Stolper, E. M. & Holloway, J. R. (1995). An experimental study of water and carbon dioxide solubilities in mid ocean ridge basaltic liquids .1. Calibration and solubility models. *Journal of Petrology* **36**, 1607–1631.

Donaldson, C. H. (1976). An experimental investigation of olivine morphology. *Contributions to Mineralogy and Petrology* **57**, 187–213.

Donaldson, C. H. (1982). Spinifex-textured komatiites: a review of textures, compositions and layering. In: Arndt, N. T. & Nisbet, E. G. (eds.) *Komatiites*. London: Allen and Unwin, 213–244.

Dowling, S. E., Barnes, S. J., Hill, R. E. T. & Hicks, J. D. (2004). Komatiites and nickel sulfide deposits of the Black Swan area, Yilgarn Craton, Western Australia. 2: geology and genesis of the ore bodies. *Mineralium Deposita* **39**, 707–728.

Downes, H. (1984). Sr and Nd isotope geochemistry of coexisting alkaline magma series, Cantal, Massif Central, France. *Earth and Planetary Science Letters* **69**, 321–334.

Downes, H., Balaganskayab, E., Bearda, A., R., L. & Demaiffe, D. (2005). Petrogenetic processes in the ultramafic, alkaline and carbonatitic magmatism in the Kola Alkaline Province: a review. *Lithos* **85**, 48–75.

Dowty, E. (1980). Crystal growth and nucleation theory and the numerical simulation of igneous crystallization. In: Hargraves, R. B. (ed.) *Physics of magmatic processes*. Princeton NJ: Princeton University Press., 419–485.

Drummond, M. S., Defant, M. J. & Kepezhinskas, P. K. (1996). Petrogenesis of slab-derived trondjemite-tonalite-dacite/adakite magmas. *Transactions of the Royal Society of Edinburgh: Earth Sciences* **87**, 205–215.

Dunbar, N. W. & Hervig, R. L. (1992). Petrogenesis and volatile stratigraphy of the Bishop Tuff: evidence from melt inclusion analysis. *Journal of Geophysical Research* **97** (**B11**), 15129–15150.

Dunbar, N. W. & Kyle, P. R. (1993). Lack of volatile gradient in the Taupo plinian-ignimbrite transition: evidence from melt inclusion analysis. *American Mineralogist* **78**, 612–618.

Dungan, M. A., Wulff, A. & Thompson, R. (2001). Eruptive stratigraphy of the Tatara–San Pedro Complex, 36°S, Southern Volcanic Zone, Chilean Andes: reconstruction method and implications for magma evolution at long-lived arc volcanic centers. *Journal of Petrology* **42**, 555–625.

Eales, H. V. & Cawthorn, R. G. (1996). The Bushveld Complex. In: Cawthorn , R. G. (ed.) *Layered Intrusions*. Amsterdam: Elsevier, 181–229.

Ebinger, C. J. & Sleep, N. H. (1998). Cenozoic magmatism throughout east Africa resulting from impact of a single plume. *Nature* **395**, 788–791.

Eby, G. N. (1990). The A-type granitoids: a review of their occurrence and chemical characteristics and speculations on their petrogenesis. *Lithos* **26**, 115–134.

Edgar, A. D. & Vukadinovic, D. (1992). Implications of experimental petrology to the evolution of ultrapotassic rocks. *Lithos* **28**, 205–220.

El Hinnawi, E. E. (1965). Petrochemical character of African volcanic rocks, Part III: central Africa. *Neues Jahrbuch für Mineralogie Abhandlungen* **103**, 126–146.

Elliott, T., Plank, T., Zindler, A., White, W. & Bourdon, B. (1997). Element transport from slab to volcanic front at the Mariana arc. *Journal of Geophysical Research-Solid Earth* **102**, 14991–15019.

Elliston, J. N. (1984). Orbicules: an indication of the crystallisation of hydrosilicates, I. *Earth-Science Reviews* **20**, 265–344.

Elsdon, R. (1971). Clinopyroxenes from the Upper Layered Series, Kap Edvard Holm, East Greenland. *Mineralogical Magazine* **38**, 49–57.

Elthon, D. (1991). Geochemical evidence for formation of the Bay of Islands ophiolite above a subduction zone. *Nature* **354**, 140–143.

Emeleus, C. H. & Bell, B. R. (2005). *The Palaeogene volcanic districts of Scotland*. Nottingham: British Geological Survey.

Emeleus, C. H., Cheadle, M. J., Hunter, R. H., Upton, B. G. J. & Wadsworth, W. J. (1996). The Rum layered suite. In: Cawthorn, R. G. (ed.) *Layered intrusios=ns*. Amsterdam: Elsevier, 403–439.

Emeleus, C. H. & Upton, B. G. J. (1976). The Gardar period in southern Greenland. In: Escher, A. & Watter, W. S. (eds.) *Geology of Greenland*. Copenhagen: Geological Survey of Greenland, 152–181.

England, R. W. (1992). The genesis, ascent and emplacement of the Northern Arran Granite, Scotland: implications for granite diapirism. *Geological Society of America Bulletin* **104**, 606–614.

Ernst, R. E., Head, J. W., Parfitt, E., Grosfils, E. & Wilson, L. (1995). Giant radiating dyke swarms on Earth and Venus. *Earth-Science Reviews* **39**, 1–58.

Evans, D. J., Rowley, W. J., Chadwick, R. A. & Millward, D. (1993). Seismic reflections from within the Lake District batholith, Cumbria, northern England. *Journal of the Geological Society of London* **150**, 1043–1046.

Ewart, A. (1979). A review of the mineralogy and chemistry of Tertiary-Recent dacitic, latitic, rhyolitic, and related salic volcanic rocks. In: Barker, F. (ed.) *Trondhjemites, dacites and related rocks*. Amsterdam: Elsevier, 13–121.

Ewart, A. (1982). The mineralogy and petrology of Tertiary–Recent orogenic volcanic rocks, with special reference to the andesitic–basalt composition range. In: Thorpe, R. S. (ed.) *Andesites: Orogenic Andesites and Related Rocks*. Chichester, UK: J. Wiley, 26–87.

Ewart, A., Marsh, J. S., Milner, S. C., Duncan, A. R., Kamber, B. S. & Armstrong, R. A. (2004a). Petrology and geochemistry of early Cretaceous bimodal continental flood volcanism of the NW Etendeka, Namibia. Part 1: Introduction, mafic lavas and re-evaluation of mantle source components. *Journal of Petrology* **45**, 59–105.

Ewart, A., Marsh, J. S., Milner, S. C., Duncan, A. R., Kamber, B. S. & Armstrong, R. A. (2004b). Petrology and geochemistry of early Cretaceous bimodal continental flood volcanism of the NW Etendeka, Namibia. Part 2: Characteristics and petrogenesis of

the high-Ti latite and high-Ti and low-Ti voluminous quartz latite eruptives. *Journal of Petrology* **45**, 107–138.

Feeley, T. C. & Davidson, J. P. (1994). Petrology of calc-alkaline lavas at Volcan Ollagüe and the origin of compositional diversity at central Andean stratovolcanoes. *Journal of Petrology* **35**, 1295–1340.

Fenner, C. N. (1931). The residual liquids of crystallizing magmas. *Mineralogical Magazine* **22**, 539–560.

Fink, J. H., Malin, M. C. & Anderson, S. W. (1990). Intrusive and extrusive growth of the Mount St Helens lava dome. *Nature* **348**, 435–437.

Fisher, R. V. (1966). Mechanism of deposition from pyroclastic flows. *American Journal of Science* **264**, 350–363.

Fitton, J. G. (1987). The Cameroon line, West Africa: a comparison between oceanic and continental alkaline volcanism. In: Fitton, J. G. & Upton, B. G. J. (eds.) *Alkaline Igneous Rocks*. London: Geological Society Special Publication **30**, 273–291.

Fitton, J. G. (2007). The OIB paradox. In: Foulger, G. R. & Jurdy, D. M. (eds.) *Plates, plumes and planetary processes*: Geological Society of America, **430**, 387–412.

Fitton, J. G. & Godard, M. (2004). Origin and evolution of magmas on the Ontong Java Plateau. In: Fitton, J. G., Mahoney, J. J., Wallace, P. & Saunders, A. D. (eds.) *Origin and Evolution of the Ontong Java Plateau*: Geological Society of London Special Publication **229**, 151–178.

Fodor, R. V. & Galar, P. (1997). A view into the subsurface of Mauna Kea volcano, Hawaii: crystallization processes interpreted through the petrology and petrography of gabbroic and ultramafic xenoliths. *Journal of Petrology* **38**, 581–624.

Foley, S. F., Venturelli, G., Green, D. H. & Toscani, L. (1987). The ultrapotassic rocks: characteristics, classification, and constraints for petrogenetic models. *Earth-Science Reviews* **24**, 81–134.

Foley, S. F. & Jenner, G. A. (2004). Trace element partitioning in lamproitic magmas – the Gaussberg olivine leucitite. *Lithos* **75**, 19–38.

Foster, J. G., Lambert, D. D., Frick, L. R. & Maas, R. (1996). Re-Os isotopic evidence for genesis of Archaean nickel ores from uncontaminated komatiites. *Nature* **382**, 703–706.

Fowler, A. D., Berger, B., Shore, M., Jones, M. I. & Ropchan, J. (2002). Supercooled rocks: development and significance of varioles, spherulites, dendrites and spinifex in Archaean volcanic rocks, Abitibi Greenstone belt, Canada. *Precambrian Research* **115**, 311–328.

Fowler, C. M. R. (2005). *The solid Earth: an introduction to global geophysics*. 2nd edition. Cambridge: Cambridge University Press. 2nd edn.

Fowler, M. B. & Henney, P. J. (1996). Mixed Caledonian appinite magmas: implications for lamprophyre fractionation and high Ba-Sr granite genesis. *Contributions to Mineralogy and Petrology* **126**, 199–215.

Francalanci, L., Tommasini, S., Conticelli, S. & Davies, G. R. (1999). Sr isotope evidence for short magma residence time for the 20th century activity at Stromboli volcano, Italy. *Earth and Planetary Science Letters* **167**, 61–69.

Francis, E. H. (1982). Magma and sediment-I: emplacement mechanism of late Carboniferous tholeiite sills in northern Britain. *Journal of the Geological Society of London* **139**, 1–20.

Francis, P. & Oppenheimer, C. (2004). *Volcanoes*. Oxford: Oxford University Press. 2nd edn.

Fretzdorff, S., Livermore, R. A., Devey, C. W., Leat, P. T. & Stoffers, P. (2002). Petrogenesis of the back-arc east Scotia Ridge, South Atlantic Ocean. *Journal of Petrology* **43**, 1435–1467.

Frey, F. A., Chappell, B. W. & Roy, S. D. (1978). Fractionation of rare-earth elements in the Tuolumne Intrusive Series, Sierra Nevada Batholith, California. *Geology* **6**, 239–242.

Friend, C. R. L. (1981). Charnockite and granite formation and influx of CO_2 at Kabbaldurga. *Nature* **294**, 550–552.

Frost, B. R., Barnes, C. G., Collins, W. J., Arculus, R. J., Ellis, D. J. & Frost, C. D. (2001). A geochemical classification for granitic rocks. *Journal of Petrology* **42**, 2033–2048.

Frost, C. D., Frost, B. R., Chamberlain, K. R. & Edwards, B. R. (1999). Petrogenesis of the 1.43 Ga Sherman batholith, SE Wyoming, USA: a reduced, rapakivi-type anorogenic granite. *Journal of Petrology* **40**, 1771–1802.

Furukawa, Y. (1993). Magmatic processes under arcs and formation of the volcanic front. *Journal of Geophysical Research* **98**, 8309–8319.

Gallo, F., Giammetti, F., Venturelli, G. & Vernia, L. (1984). The kamafugitic rocks of San Venanzo and Cuppaello, central Italy. *Neues Jahrbuch für Mineralogie Monatshefte* **Jahrgang 1984**, 198–210.

Gao, Y., Hou, Z., Kamber, B. S., Wei, R., Meng, X. & Zhao, R. (2007). Lamproitic rocks from a continental collision zone: evidence for recycling of subducted Tethyan oceanic sediments in the mantle beneath southern Tibet. *Journal of Petrology* **48**, 729–752.

Garuti, G., Fershtater, G., Bea, F., Montero, P., Pushkarev, E. V. & Zaccarini, F. (1997). Platinum-group elements as petrological indicators in mafic- ultramafic complexes of the central and southern Urals: Preliminary results. *Tectonophysics* **276**, 181–194.

Geist, D., Howard, K. A. & Larson, P. (1995). The Generation of Oceanic Rhyolites By Crystal Fractionation – the Basalt-Rhyolite Association At Volcan-Alcedo, Galapagos-Archipelago. *Journal of Petrology* **36**, 965–982.

Gerlach, T. M., Westrich, H. R. & Symonds, R. B. (1997). Preeruption vapor in magma of the climactic Mount Pinatubo eruption: source of the giant stratospheric sulfur dioxide cloud. In: Newhall, C. G. &

Punongbayan, R. S. (eds.) *Fire and Mud – Eruptions and lahars of Mount Pinatubo, Philippines*. Quezon City *and* Seattle: Philippine Institute of Volcanology and Seismology *and* University of Washington Press, 415–420.

Gibb, F. G. F. & Henderson, C. M. B. (2006). Chemistry of the Shiant Isles Main Sill, and wider implications for the petrogenesis of mafic sills. *Journal of Petrology* **47**, 191–230.

Gill, J. B. (1981). *Orogenic andesites and plate tectonics*. Berlin: Springer-Verlag.

Gill, R. (1996). *Chemical fundamentals of geology*. London: Chapman and Hall. 2nd edn.

Gill, R. (ed.) (1997). *Modern analytical geochemistry*. Harlow: Longman.

Gill, R. & Thirlwall, M. (2003). *Tenerife, Canary Islands*. London: Geologists' Association Guide No. 49.

Gill, R. C. O. (1973). Mechanism for the salic magma bias of continental alkaline provinces. *Nature phys. Sci.* **242**, 41–42.

Gill, R. C. O., Aparicio, A., El Azzouzi, M., Hernandez, J., Thirlwall, M. F., Bourgois, J. & Marriner, G. F. (2004). Depleted arc volcanism in the Alboran Sea and shoshonitic volcanism in Morocco: geochemical and isotopic constraints on Neogene tectonic processes. *Lithos* **78**, 363–388.

Gillepsie, M. R. & Styles, M. T. (1999). BGS rock classification scheme. Volume 1: Classification of igneous rocks. Research Report RR 99–06. Keyworth, Nottingham, UK: British Geological Survey, 52 pp.

Giordano, D., Polacci, M., Longo, A., Papale, P., Dingwell, D. B., Boschi, E. & Kasereka, M. (2007). Thermo-rheological magma control on the impact of highly fluid lava flows at Mt. Nyiragongo. *Geophysical Research Letters* **34**.

Glazner, A. F. & Bartley, J. M. (2006). Is stoping a volumetrically significant pluton emplacement process? *Geological Society of America Bulletin* **118**, 1185–1195.

Goldschmidt, V. M. (1937). The principles of distribution of chemical elements in minerals and rocks. *Journal of the Chemical Society of London* **140**, 655–673.

Goodrich, C. A. (2003). Petrogenesis of olivine-phyric shergottites Sayh Al Uhaymir 005 and elephant moraine A79001 lithology A. *Geochimica Et Cosmochimica Acta* **67**, 3735–3772.

Gorring, M. L. & Naslund, H. R. (1995). Geochemical reversals within the lower 100 M of the Palisades Sill, New Jersey. *Contributions to Mineralogy and Petrology* **119**, 263–276.

Gottschalk, M. (1997). Internally consistent thermodynamic data for rock-forming minerals in the system SiO_2-TiO_2-Al_2O_3-Fe_2O_3-CaO-MgO-FeO-K_2O-Na_2O-H_2O-CO_2. *European Journal of Mineralogy* **9**, 175–223.

Green, T. H., Blundy, J. D., Adam, J. & Yaxley, G. M. (2000). SIMS determination of trace element partition coefficients between garnet, clinopyroxene and hydrous basaltic liquids at 2–7.5 GPa and 1080–1200 degrees C. *Lithos* **53**, 165–187.

Greene, A. R., DeBari, S. M., Kelemen, P. B., Blusztajn, J. & Clift, P. D. (2006). A detailed geochemical study of island arc crust: the Talkeetna Arc section, south-central Alaska. *Journal of Petrology* **47**, 1051–1093.

Gribble, C. D. & Hall, A. J. (1992). *Optical Mineralogy – principles and practice*. London: UCL Press.

Grocott, J., Garde, A. A., Chadwick, B., Cruden, A. R. & Swager, C. (1999). Emplacement of rapakivi granite and syenite by floor depression and roof uplift in the Palaeoproterozoic Ketilidian orogen, South Greenland. *Journal of the Geological Society of London* **156**, 15–24.

Grout, F. F. (1945). Scale models of structures relating to batholiths. *American Journal of Science* **243A**, 260–284.

Grove, T. L., Chatterjee, N., Parman, S. W. & Médard, E. (2006). The influence of H_2O on mantle wedge melting. *Earth and Planetary Science Letters* **249**, 74–89.

Grove, T. L., Gerlach, D. C. & Sando, T. W. (1982). Origin of calc-alkaline series lavas at Medicine Lake volcano by fractionation, assimilation and mixing. *Contributions to Mineralogy and Petrology* **80**, 162–180.

Grove, T. L. & Parman, S. W. (2004). Thermal evolution of the Earth as recorded by komatiites. *Earth and Planetary Science Letters* **219**, 173–187.

Gudmundsson, A. (2007). Infrastructure and evolution of ocean-ridge discontinuities in Iceland. *Journal of Geodynamics* **43**, 6–29.

Guest, J. E., Cole, P. D., Duncan, A. M. & Chesteer, D. K. (2003). *Volcanoes of southern Italy*. London: Geological Society of London.

Guo, Z.-F., Wilson, M., Liu, J.-Q. & Mao, Q. (2006). Post-collisional, potassic and ultrapotassic magmatism of the Northern Tibetan plateau: constraints on characteristics of the mantle source, geodynamic setting and uplift mechanisms. *Journal of Petrology* **47**, 1177–1220.

Gust, D. A., Arculus, R. J. & Kersting, A. B. (1997). Aspects of magma sources and processes in the Honshu arc. *Canadian Mineralogist* **35**, 347–365.

Gutscher, M.-A., Maury, R., Eissen, J.-P. & Bourdon, E. (2000). Can slab melting be caused by flat subduction? *Geology* **28**, 535–538.

Haerderle, M. & Atherton, M. P. (2002). Shape and intrusion style of the Coastal Batholoth, Peru. *Tectonophysics* **345**, 17–28.

Hammer, J. E. (2006). Interpreting inclusive evidence. *Nature* **439**, 26–27.

Harris, N., Ayres, M. & Massey, J. (1995). Geochemistry of granitic melts produced during the incongruent melting of muscovite – implications for the extraction of himalayan leukogranite magmas. *Journal of Geophysical Research-Solid Earth* **100**, 15767–15777.

Hatton, C. J. (1995). Mantle plume origin for the Bushveld and Ventersdorp magmatic provinces. *Journal of African Earth Sciences* **21**, 571–577.

Hay, D. E. & Wendlandt, R. F. (1995). The origin of Kenya rift plateau-type flood phonolites: results of high-pressure/high-temperature experiments in the systems phonolite-H_2O and phonolite-H_2O–CO_2. *Journal of Geophysical Research* **100**, 401–410.

Helz, R. T. (1976). Phase relations of basalts in their melting range at P_{H20} = 5 Kb – Part II: Melt compositions. *Journal of Petrology* **17**, 139–193.

Herzberg, C., Gasparik, T. & Sawamoto, H. (1990). Origin of mantle peridotite: constraints from melting experiments to 16.5 GPa. *Journal of Geophysical Research* **95**, **15**, 779–803.

Herzberg, C. & O'Hara, M. J. (1998). Phase equilibrium constraints on the origin of basalts, picrites, and komatiites. *Earth-Science Reviews* **44**, 39–79.

Herzberg, C. & O'Hara, M. J. (2002). Plume-associated ultramafic magmas of Phanerozoic age. *Journal of Petrology* **43**, 1857–1883.

Hess, H. H. (1938). A primary peridotite magma. *American Journal of Science, Series 5* **35**, 321–344.

Hibbard, M. J. (1981). The magma mixing origin of mantled feldspars. *Contributions of Mineralogy and Petrology* **76**, 158–170.

Hildreth, W., Halliday, A. N. & Christiansen, R. L. (1991). Isotopic and chemical evidence concerning the genesis and contamination of basaltic and rhyolitic magma beneath the Yellowstone Plateau Volcanic Field. *Journal of Petrology* **32**, 63–138.

Hildreth, W. & Wilson, C. J. N. (2007). Compositional zoning of the Bishop Tuff. *Journal of Petrology* **48**, 951–999.

Hill, R. E. T., Barnes, S. J., Gole, M. J. & Dowling, S. E. (1994). The volcanology of komatiites as deduced from field relationships in the Norseman-Wiluna greenstone belt, Western Australia. *Lithos* **34**, 159–188.

Hirose, K. & Kushiro, I. (1993). Partial melting of dry peridotites at high pressures: Determination of compositions of melts segregated from peridotite using aggregates of diamond. *Earth and Planetary Science Letters* **114**, 477–489.

Holder, M. A. (1979). An emplacement mechanism for post-tectonic granites and its implications for the geochemical features. In: Atherton, M. P. & Tarney, J. (eds.) *Origins of batholiths*. Nantwich: Shiva, 117–126.

Holloway, J. R. & Burnham, C. W. (1972). Melting relations of basalt with equilibrium water pressure less than total pressure. *Journal of Petrology* **13**, 1–29.

Holloway, J. R. & Wood, B. J. (1988). *Simulating the Earth – experimental geochemistry*. London: Unwin Hyman.

Holm, P. M., Gill, R. C. O., Pedersen, A. K., Hald, N., Larsen, J. G., Nielsen, T. F. D. & Thirlwall, M. F. (1993). The picritic Tertiary lavas of West Greenland: contributions fom 'Icelandic' and other sources. *Earth and Planetary Science Letters* **115**, 227–244.

Holmes, A. (1928). *The nomenclature of petrology, with reference to selected literature*. London: Murby. 2nd edn.

Holness, M. B. (2005). Spatial constraints on magma chamber replenishment events from textural observations of cumulates: the Rum Layered Intrusion, Scotland. *Journal of Petrology* **46**, 1585–1601.

Holten, T., Jamtveit, B., Meakin, P., Cortini, M., Blundy, J. & Austrheim, H. (1997). Statistical characteristics and origin of oscillatory zoning in crystals. *American Mineralogist* **82**, 596–606.

Holtz, F., Johannes, W., Tamic, N. & Behrens, H. (2001). Maximum and minimum water contents of granitic melts geneated in the crust: a re-evaluation and implications. *Lithos* **56**, 1–14.

Hunter, R. H. & Sparks, R. S. J. (1987). The differentiation of the Skaergaard intrusion. *Contributions to Mineralogy and Petrology* **95**, 451–461.

Huppert, H. H., Sparks, R. S. J., Turner, J. S. & Arndt, N. T. (1984). Emplacement and cooling of komatiite lavas. *Nature* **309**, 19–22.

Husch, J. M. (1990). Palisades Sill – Origin of the Olivine Zone By Separate Magmatic Injection Rather Than Gravity Settling. *Geology* **18**, 699–702.

Hutton, D. H. W. (1982). A tectonic model for the emplacement of the Main Donegal Granite, NW Ireland. *Journal of the Geological Society of London* **139**, 615–631.

Hutton, D. H. W. (1988). Granite emplacement mechanisms and tectonic controls: influences from deformation studies. *Transactions of the Royal Society of Edinburgh: Earth Sciences* **79**, 245–255.

Ikeda, S., Toriumi, M., Yoshida, H. & Shimizu, I. (2002). Experimental study of the textural development of igneous rocks in the late stage of crystallization: the importance of interfacial energies under non-equilibrium conditions. *Contributions to Mineralogy and Petrology* **142**, 397–415.

Ildefonse, B., Blackman, D. K., John, B. E., Ohara, Y., Miller, D. J., MacLeod, C. J. & Party, I. O. D. P. E. S. (2007). Oceanic core complexes and crustal accretion at slow-spreading ridges. *Geology* **35**, 623–626.

IMA. (1997). Nomenclature of amphiboles: report of the Subcommittee on Amphiboles of the International Mineralogical Association, Commission on New Minerals and Mineral Names. *Mineralogical Magazine* **61**, 295–321.

Inger, S. & Harris, N. (1993). Geochemical constraints on leucogranite magmatism in the Langtang valley, Nepal Himalaya. *Journal of Petrology* **34**, 345–368.

Ingle, S. & Coffin, M. F. (2004). Impact origin for the greater Ontong-Java Plateau? *Earth and Planetary Science Letters* **218**, 123–134.

Ingram, G. M. & Hutton, D. H. W. (1994). The Great Tonalite Sill – Emplacement Into a Contractional Shear Zone and Implications For Late Cretaceous to Early Eocene Tectonics in Southeastern Alaska and British-Columbia. *Geological Society of America Bulletin* **106**, 715–728.

Irvine, T. N. (1974). Petrology of the Duke Island ultramafic complex, southeastern Alaska. *Geological Society of America Memoir* **138**, 240 pp.

Irvine, T. N. (1982). Terminology for layered intrusions. *Journal of Petrology* **23**, 127–162.

Irvine, T. N., Anderson, J. C. Ø. & Brooks, C. K. (1998). Included blocks (and blocks within blocks) in the Skaergaard intrusion: geologic relations and the origins of rhythmic modally graded layers. *Geological Society of America Bulletin* **110**, 1398–1447.

Irvine, T. N. & Baragar, W. R. A. (1971). A guide to the chemical classification of the common volcanic rocks. *Canadian Journal of Earth Sciences* **8**, 523–548.

James, D. E. (1981). The combined use of oxygen and radiogenic isotopes as indicators of crustal contamination. *Annual Reviews of Earth and Planetary Sciences* **9**, 311–344.

Jang, Y. D., Naslund, H. R. & McBirney, A. R. (2001). The differentiation trend of the Skaergaard intrusion and the timing of magnetite crystallization: iron enrichment revisited. *Earth and Planetary Science Letters* **189**, 189–196.

Jeffreys, H. (1938). A note on fracture mechanisms. *Royal Society of Edinburgh Proceedings* **56**, 158–163.

Jenner, G. A., Dunning, G. R., Malpas, J., Brown, M. & Brace, T. (1991). Bay of Islands and Little Port complexes, revisited: age, geochemical and isotopic evidence confirm suprasubduction-zone origin. *Canadian Journal of Earth Sciences* **28**, 1635–1652.

Johnson, S. E., Fletcher, J. M., Fanning, C. M., Vernon, R. H., Paterson, S. R. & Tate, M. C. (2003). Structure, emplacement and lateral expansion of the San Jose Tonalite pluton, Peninsular Ranges batholith, Baja California, Mexico. *Journal of Structural Geology* **25**, 1933–1957.

Jonasson, K. (1994). Rhyolite Volcanism in the Krafla Central Volcano, Northeast Iceland. *Bulletin of Volcanology* **56**, 516–528.

Kampunzu, A. B., Bonhomme, M. G. & Kanika, M. (1998). Geochronology of volcanic rocks and evolution of the Cenzoic western branch of the East African Rift System. *Journal of African Earth Sciences* **26**, 441–461.

Kaneko, T., Wooster, M. J. & Nakada, S. (2002). Exogenous and endogenous growth of the Unzen lava dome examined by satellite infrared image analysis. *Journal of Volcanology and Geothermal Research* **116**, 151–160.

Karson, J. A. & Curtis, P. A. (1989). Tectonic and magmatic processes in the Eastern Branch of the East African Rift and implications for magmatically active continental rifts. *Journal of African Earth Sciences* **8**, 431–453.

Kay, R. W. (1978). Aleutian magensian andesites: melts from Pacific ocean crust. *Journal of Volcanology and and Geothermal Research* **4**, 117–132.

Kebede, T. & Koeberl, C. (2003). Petrogenesis of A-type granitoids from the Wallagga area, western Ethiopia: constraints from mineralogy, bulk-rock chemistry, Nd and Sr isotopic compositions. *Precambrian Research* **121**, 1–24.

Kelemen, P. B., Rilling, J. L., Parmentier, E. M., Mehl, L. & Hacker, B. R. (2003). Thermal structure due to solid-state flow in the mantle wedge beneath arcs. In: Eiler, J. M. (ed.) *Inside the subduction factory*. Washington, D.C.: American Geophysical Union Geophysical Monograph **138**, 293–311.

Kelley, K. A., Plank, T., Grove, T. L., Stolper, E. M., Newman, E. & Hauri, E. (2006). Mantle melting as a function of water content beneath back-arc basins. *Journal of Geophysical Research* **111**, B09208 doi:09210.01029/02005JB003732, 002006.

Kelley, S. P. (2007). The geochronology of large igneous provinces, terrestrial impacts craters, and their relationship to mass extinctions on Earth. *Journal of the Geological Society* **164**, 923–936.

Kennedy, G. C. (1955). Some aspects of the role of water in rock melts. *Crust of the Earth: a symposium*.**62**: Geological Society of America Special Paper, 489–503.

Kerr, A. C. & Arndt, N. T. (2001). A note on the IUGS reclassification of the high-Mg and picritic volcanic rocks. *Journal of Petrology* **42**, 2169–2171.

Kerr, A. C., Marriner, G. F., Arndt, N. T., Tarney, J., Nivia, A., Saunders, A. D. & Duncan, R. A. (1996). The petrogenesis of komatiites, picrites and basalts from the Isle of Gorgona, Colombia; new field, petrographic and geochemical constraints. *Lithos* **37**, 245–260.

Kil, Y. & Wendlandt, R. F. (2004). Pressure and temperature evolution of upper mantle under the Rio Grande Rift. *Contributions to Mineralogy and Petrology* **148**, 265–280.

Kilburn, C. J. & McGuire, W. J. (2001). *Italian volcanoes*. Harpenden: Terra Publishing.

Kilpatrick, J. A. & Ellis, D. J. (1992). C-type magmas: igneous charnockites and their extrusive equivalents. *Transactions of the Royal Society of Edinburgh: Earth Sciences* **83**, 155–164.

Kjarsgaard, B. & Peterson, T. (1991). Nephelinite-carbonatite liquid immiscibility at Shombole volcano, East Africa: Petrographic and experimental evidence. *Mineralogy and Petrology* **43**, 293–314.

Klaudius, J. & Keller, J. (2006). Peralkaline silicate lavas at Oldoinyo Lengai, Tanzania. *Lithos* **91**, 173–190.

Klingelhöfer, F., Minshull, T. A., Blackman, D. K., Harben, P. & Childers, V. (2001). Crustal structure of Ascension Island from wide-angle seismic data:

implications for the formation of near-ridge volcanic islands. *Earth and Planetary Science Letters* **190**, 41–56.

Kogarko, L. N., Williams, C. T. & Woolley, A. R. (2006). Compositional evolution and cryptic variation in pyroxenes of the peralkaline Lovozero intrusion, Kola Peninsula, Russia. *Mineralogical Magazine* **70**, 347–359.

Kokelaar, B. P. & Moore, I. D. (2006). *Glencoe caldera volcano, Scotland*. Nottingham: British Geological Survey.

Kokfelt, T. F., Hoernle, K., Hauff, F., Fiebig, J., Werner, R. & Garbe-Schonberg, D. (2006). Combined trace element and Pb-Nd-Sr-O isotope evidence for recycled oceanic crust (upper and lower) in the Iceland mantle plume. *Journal of Petrology* **47**, 1705–1749.

Kopylova, M. G., Russell, J. K. & Cookenboo, H. (1998). Petrology of peridotite and pyroxenite xenoliths from the Jericho Kimberlite: implications for the thermal state of the mantle beneath the Slave craton, northern Canada. *Journal of Petrology* **40**, 79–104.

Kuno, H. (1960). High-alumina basalt. *J. Petrology* **1**, 121–145.

Kurth–Velz, M., Sassen, A. & Galer, S. J. G. (2004). Geochemical and isotopic heterogeneities along an island arc–spreading ridge intersection: evidence from the Lewis Hills, Bay of Islands Ophiolite, Newfoundland. *Journal of Petrology* **45**, 635–668.

Lacroix, A. (1904). *La Montagne Pelée et ses éruptions*. Paris: Masson et Compagnie.

Lahaye, Y., Barnes, S. J., Frick, L. R. & Lambert, D. D. (2001). Re-Os isotopic study of komatiitic volcanism and magmatic sulfide formation in the southern Abitibi greenstone belt, Ontario, Canada. *Canadian Mineralogist* **39**, 473–490.

Lallemand, S., Heuret, A. & Boutelier, D. (2005). On the relationships between slab dip, back-arc stress, upper plate absolute motion, and crustal nature in subduction zones. *Geochemistry, Geophysics, Geosystems* **6**, doi:10.1029/2005GC000917.

Larsen, L. M. & Sørensen, H. (1987). The llimaussaq intrusion – progressive crystallization and formation of layering in an agpaitic magma. In: Fitton, J. G. & Upton, B. G. J. (eds.) *Alkaline igneous rocks*. London: Geological Society of London Special Publication **30**, 473–488.

Larsen, L. M., Watt, W. S. & Watt, M. (1989). Geology and petrology of the lower Tertiary plateau basalts of the Scoresby Sund region, East Greenland. *Geological Survey of Greeland Bulletin* **157**, 1–164.

Lassiter, J. C., Hauri, E. H., Reiners, P. W. & Garcia, M. O. (2000). Generation of Hawaiian post-erosional lavas by melting of a mixed lherzolite/pyroxenite source. *Earth and Planetary Science Letters* **178**, 269–284.

LaTourrette, T., Hervig, R. L. & Holloway, J. R. (1995). Trace-Element Partitioning Between Amphibole, Phlogopite, and Basanite Melt. *Earth and Planetary Science Letters* **135**, 13–30.

Le Bas, M. J. (1977). *Carbonatite-nephelinite volcanism*. London: Wiley-Interscience.

Le Bas, M. J. (2000). *IUGS* rclassification of the high-Mg and picritic volcanic rocks. *Journal of Petrology* **41**, 2467–2470.

Le Maitre, R. W. (1962). Petrology of volcanic rocks, Gough Island, South Atlantic. *Geological Society of America Bulletin* **73**, 1309–1340.

Le Maitre, R. W. (1976). The chemical variability of some common igneous rocks. *Journal of Petrology* **17**, 589–637.

Le Maitre, R. W. (2002). *Igneous rocks – a classification and glossary of terms. Recommendations of the IUGS subcommission on the Systematics of Igneous Rocks*. Cambridge: Cambridge University Press. 2nd edn.

Le Roex, A. P. (1985). Geochemistry, mineralogy and magmatic evolution of the basaltic and trachytic lavas from Gough Island, South Atlantic. *Journal of Petrology* **26**, 149–186.

Le Roex, A. P., Bell, D. R. & Davis, P. (2003). Petrogenesis of group I kimberlites from Kimberley, South Africa: evidence from bulk-rock geochemistry. *Journal of Petrology* **44**, 2261–2286.

Le Roex, A. P., Watkins, R. T. & Reid, A. M. (1996). Geochemical evolution of the Okenyenya sub-volcanic ring complex, northwestern Namibia. *Geological Magazine* **133**, 645–670.

Leat, P. T. (2008). On the long-distance transport of Ferrar magmas. In: Thomson, K. & Petford, N. (eds.) *Structure and Emplacement of High-Level Magmatic Systems*. London: Geological Society Special Publication **302**, 45–61.

Lee, C. A. (1996). A review of mineralization in the Bushveld Complex and some other layered intrusions. In: Cawthorn, R. G. (ed.) *Layered Intrusions*. Amsterdam: Elsevier, 103–145.

Lin, S.-C., Kuo, B.-Y., Chiao, L.-Y. & van Keken, P. E. (2005). Thermal plume models and melt generation in East Africa: a dynamic modeling approach. *Earth and Planetary Science Letters* **237**, 175–192.

Lindsay, J. M., Trumbull, R. B. & Siebel, W. (2005). Geochemistry and petrogenesis of late Pleistocene to Recent volcanism in southern Dominica, Lesser Antilles. *Journal of Volcanology and Geothermal Research* **148**, 259–294.

Lindsley, D. H. (1983). Pyroxene thermometry. *American Mineralogist* **68**, 477–493.

Lindsley, D. H. & Andersen, D. J. (1983). A two-pyroxene thermometer. *Proceedings of the Thirteenth Lunar and Planetary Science Conference. Journal of Geophysical Research* **88 Supplement**, A887–A906.

Lofgren, G. (1980). Experimental studies on the dynamic crystallization of silicate melts. In: Hargraves, R. B. (ed.) *Physics of magmatic processes*. Princeton NJ: Princeton University Press., 487–551.

Longhi, J. (2005). A mantle or mafic crustal source for Proterozoic anorthosites? *Lithos* **83**, 183–198.

Longhi, J., van der Auwera, J., Fram, M. S. & Duchesne, J.-C. (1999). Some phase equilibrium constraints on the origin of Proterozoic (massif) anorthosites and related rocks. *Journal of Petrology* **40**, 339–362.

Lowenstern, J. B. & Hurwitz, S. (2008). Monitoring a supervolcano in repose: heat and volcanic flux at the Yellowstone caldera. *Elements* **4**, 35–40.

Lyle, P. (2000). The eruption environment of multitiered columnar basalt lava flows. *Journal of the Geological Society* **157**, 715–722.

Maaløe, S., James, D., Smedley, P., Petersen, S. & Garmann, L. B. (1992). The Koloa volcanic suite of Kauai, *Hawaii. Journal of Petrology* **33**, 761–784.

Macdonald, G. A. (1967). Forms and structures of extrusive basaltic rocks. In: Hess, H. H. & Poldervaart, A. (eds.) *Basalts: the Poldervaart treatise on rocks of basltic composition*. New York.: Interscience, **Vol 1**, 1–61.

Macdonald, G. A. & Katsura, T. (1964). Chemical composition of Hawaiian lavas. *Journal of Petrology* **5**, 82–133.

Macdonald, R., Hawkesworth, C. J. & Heath, E. (2000). The Lesser Antilles volcanic chain: a study in arc magmatism. *Earth-Science Reviews* **49**, 1–76.

Macdonald, R., Navarro, J. M., Upton, B. G. J. & Davies, G. R. (1994). Strong compositional zonation in peralkaline magma: Menengai, Kenya rift valley. *Journal of Volcanology and Geothermal Research* **60**, 301–325.

Macdonald, R., Rogers, N. W., Fitton, J. G., Black, S. & Smith, M. (2001). Plume-lithosphere interactions in the generation of the basalts of the Kenya Rift, East Africa. *Journal of Petrology* **42**, 877–900.

Macdonald, R. & Upton, B. G. J. (1993). The Proterozoic Gardar rift zone, south Greenland: comparisons with the East African Rift System. In: Pritchard, H. M., Alabaster, T., Harris, N. B. W. & Neary, C. R. (eds.) *Magmatic Processes and Plate Tectonics*. London: Geological Society of London Special Publication 76, 427–442.

MacGregor, I. D. (1974). The system MgO–Al_2O_3–SiO_2: solubility of Al_2O_3 in enstatite for spinel and garnet peridotite compositions. *American Mineralogist* **59**, 110–119.

MacKenzie, W. S., Donaldson, C. H. & Guilford, C. (1982). *Atlas of igneous rocks and their textures*. Harlow: Longman.

Macpherson, C. G., Dreher, S. T. & Thirlwall, M. F. (2006). Adakites without slab melting: high pressure differentiation of island arc magma, Mindanao, the Philippines. *Earth and Planetary Science Letters* **243**, 581–593.

Macpherson, C. G. & Hall, R. (2001). Tectonic setting of Eocene boninite magmatism in the Izu-Bonin-Mariana forearc. *Earth and Planetary Science Letters* **186**, 215–230.

Mahoney, J. J. & Coffin, M. F. (eds.) (1997). *Large Igneous Provinces: continental, oceanic, and planetary flood volcanism*. Washington: American Geophysical Union.

Malpas, J. (1978). Magma generation in the upper mantle, field evidence from ophiolite suites, and application to the generation of oceanic lithosphere. *Philosophical Transactions of the Royal Society of London A* **288**, 527–546.

Mariita, N. O. & Keller, G. R. (2007). An integrated geophysical study of the northern Kenya rift. *Journal of African Earth Sciences* **48**, 80–94.

Martel, C., Pichavant, M., Bourdier, J. L., Traineau, H., Holtz, F. & Scaillet, B. (1998). Magma storage conditions and control of eruption regime in silicic volcanoes: experimental evidence from Mt. Pelee. *Earth and Planetary Science Letters* **156**, 89–99.

Martin, H. (1986). Effect of steeper Archaean geothermal gradient on geochemistry of subduction-zone magmas. *Geology* **14**, 753–756.

Martin, H. (1999). Adakitic magmas: modern analogues of Archean granitoids. *Lithos* **46**, 411–429.

Martinez, F., Okino, K., Ohara, Y., Reysenbach, A.-L. & Goffredi, S. K. (2007). Back-arc basins. *Oceanography* **20**, 116–127.

Mathison, C. I. & Ahmat, A. L. (1996). The Windimurra Complex, Western Australia. In: Cawthorn, R. G. (ed.) *Layered Intrusions*. Amsterdam: Elsevier, 485–510.

McBirney, A. R. (1996). The Skaergaard Instrusion. In: Cawthorn, R. G. (ed.) *Layered Intrusions*. Amsterdam: Elsevier, 147–180.

McBirney, A. R. & Naslund, H. R. (1990). The differentiation of the Skaergaard intrusion. *Contributions to Mineralogy and Petrology* **104**, 235–247.

McCallum, I. S. (1996). The Stillwater Complex. In: Cawthorn, R. G. (ed.) *Layered intrusions*. Amsterdam: Elsevier, 441–483.

McHone, J. G. (2000). Non-plume magmatism and rifting during the opening of the central Atlantic Ocean. *Tectonophysics* **316**, 287–296.

McKenzie, D. & Bickle, M. J. (1988). The volume and composition of melt generated by the extension of the lithsophere. *Journal of Petrology* **29**, 625–679.

McLelland, J. M., Bickford, M. E., Hill, B. M., Clechenko, C. C., Valley, J. W. & Hamilton, M. A. (2004). Direct dating of Adirondack massif anorthosite by U-PbSHRIMP analysis of igneous zircon: Implications for AMCG complexes. *Geological Society of America Bulletin* **116**, 1299–1317.

Mechie, A., Keller, G. R., Prodehl, C., Khan, M. A. & S. J., G. (1997). A model for the structure, composition and evolution of the Kenya rift. *Tectonophysics* **278**, 95–119.

Mehnert, K. R. (1968). *Migmatites and the origin of granitic rocks*. Amsterdam: Elsevier Publishing.

Mercalli, G. (1907). *I vulcani attivi della Terra*. Milan: Ulrico Hoepli.

Mitchell, R. H. (1986). *Kimberlites – mineralogy, geochemistry and petrology*. New York: Plenum Press.

Mitchell, R. H. (2005). Carbonatites and carbonatites and carbonatites. *Canadian Mineralogist* **43**, 2049–2068.

Mitchell, R. H. & Bergman, S. C. (1991). *Petrology of lamproites*. New York: Plenum Press 441 pp.

Mitchell, R. H. & Dawson, J. B. (2007). The 24th September 2007 ash eruption of the carbonatite volcano Oldoinyo Lengai, Tanzania: mineralogy of the ash and implications for formation of a new hybrid magma type. *Mineralogical Magazine* **71**, 483–492.

Miyashiro, A. (1974). Volcanic rock series in island arcs and active volcanic margins. *American Journal of Science* **274**, 321–355.

Miyashiro, A. (1978). Nature of alkalic volcanic rock series. *Contributions to Mineralogy and Petrology* **66**, 91–104.

Molyneux, S. J. & Hutton, D. H. W. (2000). Evidence for significant granite space creation by the ballooning mechanism: The example of the Ardara pluton, Ireland. *Geological Society of America Bulletin* **112**, 1543–1558.

Moore, J. G. & Lockwood, J. P. (1973). Origin of comb layering and orbicular structure, Sierra Nevada batholith, California. *Bulletin of the Geological Society of America* **84**, 1–20.

Moores, E. M. (1982). Origin and emplacement of ophiolites. *Reviews of Geophysics and Space Physics* **20**, 735–760.

Moores, E. M., Kellogg, L. H. & Dilek, Y. (2000). Tethyan ophiolites, mantle convection, and tectonic 'historical contingency': a resolution of the ophiolite conundrum. In: Dilek, Y., Moores, E., Elthon, D. & Nicolas, A. (eds.) *Ophiolites and oceanic crust: new insights from field studies and the Ocean Drilling Program*: Geological Society of America Special Paper, **349**, 3–20.

Morimoto, N., Fabries, J., Ferguson, A. K., Ginzburg, I. V., Ross, M., Seifert, F. A. & Zussman, J. (1988). Nomenclature of pyroxenes. *Mineralogical Magazine* **52**, 535–550.

Morse, S. A. (1970). Alkali-feldspars with water at 5 kb pressure. *Journal of Petrology* **11**, 1–20.

Morse, S. A. (1980). *Basalts and phase diagrams*. New York: Springer-Verlag.

Myers, J. S. (1975). Igneous stratigraphy of Archaean anorthsite at Majorqap qâva, near Fiskenæsset, South-West Greenland. *Report of the Geological Survey of Greenland* **75**, 77–80.

Myers, J. S. (1981). The Fiskenaesset anorthosite complex – a stratigraphic key to the tectonic evolution of the West Greenland Gneiss Complex 3000–2800 m.y. ago. In: Glover, J. E. & Groves, D. I. (eds.) *Archaean Geology – second international symposium, Perth 1980.*: Geological Society of Australia,7, 351–360.

Myers, J. S., Gill, R. C. O., Rex, D. C. & Charnley, N. (1993). The Kap Gustav Holm Tertiary Plutonic Centre, East Greenland. *Journal of the Geological Society of London* **150**, 259–275.

Nakajima, J., Matsuzawa, T., Hasegawa, A. & Zhao, D. P. (2001). Three-dimensional structure of V_p, V_s, and V_p/V_s beneath northeastern Japan: implications for arc magmatism and fluids. *Journal of Geophysical Research-Solid Earth* **106**, 21843–21857.

Nelson, S. T. & Montana, A. (1992). Sieve-textured plagioclase in volcanic rocks produced by rapid decompression. *American Mineralogist* **77**, 1242–1249.

Nesbitt, R. W. (1971). Skeletal crystal forms in the ultramafic rocks of the Yilgarn Block, Western Australia: evidence for an Archaean ultramafic liquid. *Geological Society of Australia Special Publication* **3**, 331–347.

Nicholson, H., Condomines, M., Fitton, J. G., Fallick, A. E., Gronvold, K. & Rogers, G. (1991). Geochemical and Isotopic Evidence For Crustal Assimilation Beneath Krafla, Iceland. *Journal of Petrology* **32**, 1005–1020.

Nicolas, A., Boudier, F. & Ildefonse, B. (1994). Evidence from the Oman ophiolite for active mantle upwelling beneath a fast-spreading ridge. *Nature* **370**, 51–53.

Nielsen, T. F. D. (2004). The shape and volume of the Skaergaard Intrusion, Greenland: implications for mass balance and bulk composition. *Journal of Petology* **45**, 507–530.

Nielsen, T. F. D. (2006). A world class deposit in the Skaergaard intrusion. Copenhagen: Geological Survey of Denmark and Greenland (Greenland Mineral Resources, Fact Sheet No 13 www.geus.dk/minex/go_fs13.pdf).

Nielsen, T. F. D., Andersen, J. C. Ø. & Brooks, C. K. (2005). The Platinova Reef of the Skaergaard Intrusion. In: Mungall, J. E. (ed.) *Exploration for Platinum-Group Element Deposits*. Ottawa: Mineralogical Association of Canada,35, 431–455.

Nisbet, E. G., Cheadle, M. J., Arndt, N. T. & Bickle, M. J. (1993). Constraining the potential temperature of the Archaean mantle: a review of the evidence from komatiites. *Lithos* **30**, 291–307.

Nixon, G. T. & Pearce, T. H. (1987). Laser-interferometry study of oscillatory zoning in plagioclase: the record of magma mixing and phenocryst recycling in calc-alkaline magma chambers, Iztaccíhuatl volcano, Mexico. *American Mineralogist* **72**, 1144–1162.

Norton, G. & Pinkerton, H. (1997). Rheological properties of natrocarbonatite lavas from Oldoinyo Lengai, Tanzania. *European Journal of Mineralogy* **9**, 351–364.

Nutman, A. P., Bennett, V. C., Friend, C. R. L. & Norman, M. D. (1999). Meta-igneous (non-gneissic) tonalites and quartz-diorites from an extensive ca.

3800 Ma terrain south of the Isua supracrustal belt, southern West Greenland: constraints on early crust formation. *Contributions to Mineralogy and Petrology* **137**, 364–388.

Nutman, A. P., McGregor, V. R., Friend, C. R. L., Bennett, V. C. & Kinny, P. D. (1996). The Itsaq Gneiss Complex of southern west Greenland; The world's most extensive record of early crustal evolution (3900–3600 Ma). *Precambrian Research* **78**, 1–39.

Nyblade, A. A., Owens, T. J., Gurrola, H., Ritsema, J. & Langston, C. A. (2000). Seismic evidence for a deep upper mantle thermal anomaly beneath east Africa. *Geology* **28**, 599–602.

O'Halloran, D. A. (1985). Ras ed Dom migrating ring complex: A-type granites and syenites from the Bayuda Desert, Sudan. *Journal of African Earth Sciences* **3**, 61–75.

O'Hara, M. J., Richardson, S. W. & Wilson, G. (1971). Garnet-peridotite stability and occurrence in crust and mantle. *Contributions to Mineralogy and Petrology* **32**, 48–68.

Oberthur, T., Davis, D. W., Blenkinsop, T. G. & Hohndorf, A. (2002). Precise U-Pb mineral ages, Rb-Sr and Sm-Nd systematics for the Great Dyke, Zimbabwe – constraints on late Archean events in the Zimbabwe craton and Limpopo belt. *Precambrian Research* **113**, 293–305.

Osborne, E. F. & Tait, D. B. (1952). The system diopside–forsterite–anorthite. *American Journal of Science* **Bowen Volume**, 413–433.

Panza, G. F. & Suhadolc, P. (1990). Properties of the lithosphere in collisional belts in the Mediterranean – a review. *Tectonophysics* **182**, 39–46.

Parman, S., Dann, J., Grove, T. L. & de Wit, M. J. (1997). Emplacement conditions of komatiite magmas from the 3.49 Ga Komati Formation, Barberton Greenstone Belt, South Africa. *Earth and Planetary Science Letters* **150**, 303–323.

Paterson, S. R. & Vernon, R. H. (1995). Bursting the bubble of ballooning plutons – a return to nested diapirs emplaced by multiple processes. *Geological Society of America Bulletin* **107**, 1356–1380.

Peacock, M. A. (1931). Classification of igneous rock series. *Journal of Geology* **39**, 54–67.

Peacock, S. M., Rushmer, T. & Thompson, A. B. (1994). Partial melting of subducting oceanic crust. *Earth and Planetary Science Letters* **121**, 227–244.

Pearce, J. A. (1983). Role of the sub-continental lithosphere in magma genesis at active continental margins. In: Hawkesworth, C. J. & Norry, M. J. (eds.) *Continental basalts and mantle xenoliths*. Nantwich: Shiva, 230–249.

Pearce, J. A., Baker, P. E., Harvey, P. K. & Luff, I. W. (1995). Geochemical evidence for subduction fluxes, mantle melting and fractional crystallization beneath the South Sandwich-Island Arc. *J. Petrol.* **36**, 1073–1109.

Pearce, J. A., Harris, N. B. W. & Tindle, A. G. (1984). Trace element discrimination diagrams for the tectonic interpretation of granitic rocks. *Journal of Petrology* **25**, 956–983.

Pearce, J. A. & Parkinson, I. J. (1993). Trace element models for mantle melting: application to volcanic arc petrogenesis. In: Prichard, H. M., Alabaster, T., Harris, N. B. W. & Neary, C. R. e. (eds.) *Magmatic Processes and Plate Tectonics*. London: Geological Society of London Special Publication **76**, 373–403.

Pearce, J. A. & Peate, D. W. (1995). Tectonic implications of the composition of volcanic arc magmas. *Ann. Rev. Earth Planet. Sci.* **23**, 251–285.

Peate, I. U., Baker, J. A., Al-Kadasi, M., Al-Subbary, A., Knight, K. B., Riisager, P., Thirlwall, M. F., Peate, D. W., Renne, P. R. & Menzies, M. A. (2005). Volcanic stratigraphy of large-volume silicic pyroclastic eruptions during Oligocene Afro-Arabian flood volcanism in Yemen. *Bulletin of Volcanology* **68**, 135–156.

Peccerillo, A. & Taylor, S. R. (1976). Geochemistry of Eocene calc-alkaline volcanic rocks from the Kastamonou area, northern *Turkey. Contributions to Mineralogy and Petrology* **58**, 63–81.

Petford, N. & Atherton, M. (1996). Na-rich partial melts from newly underplated basaltic crust: the Cordillera Blanca Batholith, Peru. *Journal of Petrology* **37**, 1491–1521.

Petford, N., Atherton, M. P. & Halliday, A. N. (1996). Rapid magma production rates, underplating and remelting in the Andes: isotopic evidence from northern-central Peru (9–11°S). *Journal of South American Earth Sciences* **9**, 69–78.

Petford, N., Cruden, A. R., McCaffrey, K. J. W. & Vigneresse, J.-L. (2000). Granite magma formation, transport emplacement in the Earth's crust. *Nature* **408**, 669–673.

Petford, N., Kerr, R. C. & Lister, J. R. (1993). Dike transport of granitoid magmas. *Geology* **21**, 845–848.

Petterson, M. G. & Treloar, P. J. (2004). Volcanostratigraphy of arc volcanic sequences in the Kohistan arc, North Pakistan: volcanism within island arc, back-arc-basin, and intra-continental tectonic settings. *Journal of Volcanology and Geothermal Research* **130**, 147–178.

Pitcher, W. S. (1982). Granite type and tectonic environment. In: Hsü, K. J. (ed.) *Mountain building processes*. London: Academic Press, 19–40.

Pitcher, W. S. (1997). *The nature and origin of granite*. London: Chapman & Hall. 2nd edn.

Pitcher, W. S., Atherton, M. P., Cobbing, E. J. & Pankhurst, R. J. (1985). *Magmatism at a plate edge – the Peruvian Andes*. Glasgow: Blackie.

Pitcher, W. S. & Bussell, M. A. (1985). Andean dyke swarms: abdesite in synplutonic relationship with tonalite. In: Pitcher, W. S., Atherton, M. P., Cobbing, E. J. & Pankhurst, R. J. (eds.) *Magmatism at a*

plate edge – the Peruvian Andes. Glasgow: Blackie, 102–107.

Platz, T., Foley, S. F. & André, L. (2004). Low-pressure fractionation of the Nyiragongo volcanic rocks, Virunga Province, D.R. Congo. *Journal of Volcanology and Geothermal Research* **136**, 269–295.

Polacci, M., Cashman, K. V. & Kauahikaua, J. P. (1999). Textural characterization of the pahoehoe-a`a transition in Hawaiian basalt. *Bulletin of Volcanology* **60**, 595–609.

Poli, S. & Schmidt, M. W. (2002). Petrology of subducted slabs. *Annual Review of Earth and Planetary Sciences* **30**, 207–235.

Pons, J., Barbey, P., Nachit, H. & Burg, J. P. (2006). Development of igneous layering during growth of pluton: The Tarcouate Laccolith (Morocco). *Tectonophysics* **413**, 271–286.

Prendergast, M. D. (2003). The nickeliferous Late Archean Reliance komatiitic event in the Zimbabwe craton-magmatic architecture, physical volcanology, and ore genesis. *Economic Geology* **98**, 865–891.

Price, R. C., Gamble, J. A., Smith, I. E. M., Stewart, R. B., Eggins, S. & Wnight, I. C. (2005). An integrated model for the temporal evolution of andesites and rhyolites and crustal development in New Zealand's North Island. *Journal of Volcanology and Geothermal Research* **140**, 1–24.

Pyke, D. R., Naldrett, A. J. & Eckstrand, O. R. (1973). Archean ultramafic flows in Munro Township, Ontario. *Geological Society of America Bulletin* **84**, 955–978.

Radice, B. (ed.) (1963). *The letters of the Younger Pliny*. London: Penguin.

Raedeke, L. D. & McCallum, I. S. (1984). Investigations of the Stillwater Complex: Part II. Petrology and petrogenesis of the Ultramafic Series. *Journal of Petrology* **25**, 395–420.

Ramberg, H. (1981). *Gravity, deformation, and the earth's crust: in theory, experiments, and geological application*. London: Academic Press. 2nd edn.

Read, H. H. (1957). *The granite controversy*. London: Murby.

Reed, M. H. (1997). Hydrothermal alteration and its relationship to ore fluid composition. In: Barnes, H. L. (ed.) *Geochemistry of hydrothermal ore deposits*. New York: J. Wiley. 3rd edn, 303–365.

Reid, J. B., Murray, D. P., Hermes, O. D. & Steig, E. J. (1993). Fractional crystallization in granites of the Sierra-Nevada – how important is it? *Geology* **21**, 587–590.

Renner, R., Nisbet, E. G., Cheadle, M. J., Arndt, N. T., Bickle, M. J. & Cameron, W. E. (1994). Komatiite flows from the Reliance Formation, Belingwe Belt, Zimbabwe: I. petrography and mineralogy. *Journal of Petrology* **35**, 361–400.

Ribe, N. M. & Christensen, U. R. (1999). The dynamical origin of Hawaiian volcanism. *Earth and Planetary Science Letters* **171**, 517–531.

Richter, F. M. (1988). A major change in the thermal state of the Earth at the Archaean-Proterozoic Boundary: consequences for the nature and preservation of continental lithosphere. *Journal of Petrology* **Special Lithosphere Issue**, 39–52.

Roach, T. A., Roeder, P. L. & Hulbert, L. J. (1998). Composition of chromite in the upper chromitite, Muskox layered intrusion, Northwest Territories. *Canadian Mineralogist* **36**, 117–135.

Rock, N. M. S. (1977). The nature and origin of lamprophyres: some definitions, distinctions, and derivations. *Earth-Science Reviews* **13**, 123–169.

Rock, N. M. S. (1987). The nature and origin of lamprophyres: an overview. In: Fitton, J. G. & Upton, B. G. J. (eds.) *Alkaline igneous rocks*. London: Geological Society of London, **30**, 191–226.

Roeder, P. L. & Emslie, R. F. (1970). Olivine-liquid equilibrium. *Contributions to Mineralogy and Petrology* **29**, 275–289.

Rogers, N., Macdonald, R., Fitton, J. G., George, R., Smith, M. & Barreiro, B. (2000). Two mantle plumes beneath the East African rift system: Sr, Nd and Pb isotopic evidence from Kenya Rift basalts. *Earth and Planetary Science Letters* **176**, 387–400.

Rogers, N. W. (2006). Basaltic magmatism and the geodynamics of the East African Rift System. In: Yirgu, G., Ebinger, C. J. & Maguire, P. K. H. (eds.) *The Afar Volcanic Province within the East African Rift System*. London: Geological Society of London, Special Publication **259**, 77–93.

Rosenberg, C. L., Berger, A. & Schmid, S. M. (1995). Observations from the floor of a granitoid pluton: inferences on the driving force of final emplacement. *Geology* **23**, 443–446.

Rosing, M. T., Bird, D. K., Sleep, N. H., Glassley, W. & Albarede, F. (2006). The rise of continents – an essay on the geologic consequences of photosynthesis. *Palaeogeography, Palaeoclimatology, Palaeoecology* **232**, 99–113.

Rothery, D. A. (2001). *Volcanoes*. London/Blacklick OH: Hodder/McGraw Hill.

Rüpke, L. H., Morgan, J. P., Hort, M. & Connolly, J. A. D. (2004). Serpentine and the subduction zone water cycle. *Earth and Planetary Science Letters* **223**, 17–34.

Sahama, T. G. (1974). Potassium-rich alkaline rocks. In: Sørensen, H. (ed.) *The Alkaline Rocks*. New York: J. Wiley.

Sajona, F. G., Maury, R. C., Bellon, H., Cotten, J., Defant, M. J. & Pubellier, M. (1993). Initiation of Subduction and the Generation of Slab Melts in Western and Eastern Mindanao, Philippines. *Geology* **21**, 1007–1010.

Saleeby, J. B. (1992). Age and Tectonic Setting of the Duke Island Ultramafic Intrusion, Southeast Alaska. *Canadian Journal of Earth Sciences* **29**, 506–522.

Salisbury, M. H. & N.I., C. (1978). The seismic velocity structure of a traverse through the Bay of Islands

Ophiolite Complex, Newfoundland, an exposure of oceanic crust and upper mantle. *Journal of Geophysical Research* **83**, 805–817.

Saxena, S. K. & Eriksson, G. (1983). Theoretical computation of minerals assemblages in pyrolite and lherzolite. *Journal of Petrology* **24**, 538–555.

Scarfe, C. M. (1977). Viscosity of a pantellerite melt at one atmosphere. *Canadian Mineralogist* **15**, 185–189.

Schairer, J. F. (1957). Melting relations of the common rock-forming oxides. *Journal of the American Ceramic Society* **40**, 215–235.

Schairer, J. F. & Yoder, H. S. J. (1960). The nature of residual liquids from crystallization, with data on the system nepheline–diopside–silica. *American Journal of Science* **258A**, 273–283.

Schmidt, M. W. & Poli, S. (1998). Experimentally based water budgets for dehydrating slabs and consequences for arc magma generation. *Earth and Planetary Science Letters* **163**, 361–379.

Scoates, J. S. (2000). The plagioclase-magma density paradox re-examined and the crystallization of Proterozoic anorthosites. *Journal of Petrology* **41**, 627–649.

Sdrolias, M., Roest, W. R. & Muller, R. D. (2004). An expression of Philippine Sea plate rotation: the Parece Vela and Shikoku Basins. *Tectonophysics* **394**, 69–86.

Seaman, S. J., Scherer, E. E. & Standish, J. J. (1995). Multistage magma mingling and the origin of flow banding in the Aliso lava dome, Tumacacori Mountains, southern Arizona. *Journal of Geophysical Research* **100**, 8381–8398.

Searle, M. & Cox, J. (1999). Tectonic setting, origin, and obduction of the Oman ophiolite. *Geological Society of America Bulletin* **111**, 104–122.

Searle, M. P. (1999). Emplacement of Himalayan leucogranites by magma injection along giant sill complexes: examples from the Cho Oyu, Gyachung Kang and Everest leucogranites (Nepal Himalaya). *Journal of Asian Earth Sciences* **17**, 773–783.

Self, S. & Blake, S. (2008). Consequences of explosive supereruptions. *Elements* **4**, 41–46.

Self, S., Keszthelyi, L. & Thordarson, T. (1998). The importance of pahoehoe. *Annual Review of Earth and Planetary Sciences* **26**, 81–110.

Self, S., Thordarson, T., Keszthelyi, L., Walker, G. P. L., Hon, K., Murphy, M. T., Long, P. & Finnemore, S. (1996). A new model for the emplacement of Columbia River Basalts as large, inflated pahoehoe lava flow fields. *Geophysical Research Letters* **23**, 2689–2692.

Shand, S. J. (1951). *Eruptive rocks*. London: Murby. revised 3rd ed.

Shaw, H. R. (1980). The fracture mechanisms of magma transport from the mantle to the surface. In: Hargraves, R. B. (ed.) *Physics of magmatic processes*. Princeton NJ: Princeton University Press, 201–264.

Shelley, D. (1992). *Igneous and metamorphic rocks under the microscope: classification, textures, microstructures and mineral preferred orientations*. London: Chapman and Hall.

Sheraton, J. W., Black, L. P. & Tindle, A. G. (1992). Petrogenesis of plutonic rocks in a Proterozoic granulite-facies terrane – the Bunger Hills, East Antarctica. *Chemical Geology* **97**, 163–198.

Sheraton, J. W. & Cundari, A. (1980). Leucitites from Gaussberg, Antarctica. *Contributions to Mineralogy and Petrology* **71**, 417–427.

Sheth, H. C., Torres-Alvarado, I. S. & Verma, S. P. (2002). What is the 'calc-alkaline rock series'? *International Geology Review* **44**, 686–701.

Shore, M. & Fowler, A. D. (1996). Oscillatory zoning in minerals: a common phenomenon. *Canadian Mineralogist* **34**, 1111–1126.

Shore, M. & Fowler, A. D. (1999). The origin of spinifex texture in komatiites. *Nature* **397**, 691–694.

Sisson, T. W. & Grove, T. L. (1993a). Experimental investigations of the role of water in calc-alkaline differentiation and subduction zone magmatism. *Contributions to Mineralogy and Petrology* **113**, 143–166.

Sisson, T. W. & Grove, T. L. (1993b). Temperature and H2O contents of low-MgO high-alumina basalts. *Contributions to Mineralogy and Petrology* **113**, 167–184.

Smith, D. K. & Cann, J. R. (1993). Building the crust at the Mid-Atlantic Ridge. *Nature* **365**, 707–715.

Smithies, R. H. (2000). The Archaean tonalite-trondhjemite-granodiorite (TTG) series is not an analogue of Cenozoic adakite. *Earth and Planetary Science Letters* **182**, 115–125.

Smithson, S. B. & Ramberg, I. B. (1979). Gravity interpretation of the Egersund anorthosite complex, Norway: its petrological and geothermal significance. *Geological Society of America Bulletin* **90**, 199–204.

Sobolev, A. V. & Chaussidon, M. (1996). H_2O concentrations in primary melts from supra-subduction zones and mid-ocean ridges: implications for H_2O storage and recycling in the mantle. *Earth and Planetary Science Letters* **137**, 45–55.

Sparks, R. S., Huppert, H. E., Koyaguchi, T. & Hallworth, M. A. (1993). Origin of modal and rhythmic igneous layering by sedimentation in a convecting magma chamber. *Nature* **361**, 246–249.

Sparks, R. S. J., Baker, L., Brown, R. J., Field, M., Schumacher, J., Stripp, G. & Walters, A. (2006). Dynamical constraints on kimberlite volcanism. *Journal of Volcanology and Geothermal Research* **155**, 18–48.

Sparks, R. S. J., Self, S. & Walkeer, G. P. L. (1973). Products of ignimbrite eruptions. *Geology* **1**, 115–118.

Steinberger, B. (2000). Plumes in a convecting mantle: models and observations for individual hotspots.

Journal of Geophysical Research (Solid Earth) **105**, 11127–11152.

Stevenson, C. T. E., Owens, W. H., Hutton, D. H. W., Hood, D. N. & Meighan, I. G. (2007). Laccolithic, as opposed to cauldron subsidence, emplacement of the Eastern Mourne pluton, N. Ireland: evidence from anisotropy of magnetic susceptibility. *Journal of the Geological Society* **164**, 99–110.

Stoiber, R. E. & Morse, S. A. (1994). *Crystal identification with the polarizing microscope*. Dordrecht: Kluwer.

Storey, B. C. & Kyle, P. R. (1997). An active mantle mechanism for Gondwana breakup. In: Hatton, C. J. (ed.) *Special Issue on the Proceedings of the Plumes, Plates and Mineralisation '97 Symposium*: South African Journal of Geology, **100**, 283–290.

Stripp, G. & Holness, M. (2006). Enigmatic late-stage textures in mafic cumulates: Skaergaard Intrusion, East Greenland (abstract). *Transactions of the American Geophysical Union* **87** (**Supplement V51B**), 1672.

Sun, C.-H. & Stern, R. J. (2001). Genesis of Mariana shoshonites: contribution of the subduction component. *J. of Geophys. Res. – Solid Earth* **106**, 589–608.

Sun, S.-s. & McDonough, W. F. (1989). Chemical and isotopic systematics of oceanic basalts: implications for mantle composition and processes. In: Saunders, A. D. & Norry, M. J. (eds.) *Magmatism in the ocean basins*: Geological Society of London Special Publication 42, 313–345.

Sylvester, P. J. (1989). Post-collisional alkaline granites. *Journal of Geology* **97**, 261–280.

Tarduno, J. A. (2007). On the motion of Hawaii and other mantle plumes. *Chemical Geology* **241**, 234–247.

Tatsumi, Y. & Eggins, S. (1995). *Subduction zone magmatism*. Cambridge, Mass: Blackwell Science.

Tatsumi, Y., Shukuno, H., Tani, K., Takahashi, N., Kodaira, S. & Kogiso, T. (2008). Structure and growth of the Izu-Bonin-Mariana arc crust: 2. Role of crust-mantle transformation and the transparent Moho in arc crust evolution. *Journal of Geophysical Research* **113**, B02203, doi:02210.01029/02007JB005121.

Taylor, B. (2006). The single largest oceanic plateau: Ontong Java-Manihiki-Hikurangi. *Earth and Planetary Science Letters* **241**, 372–380.

Taylor, G. K. (2007). Pluton shapes in the Cornubian Batholith: new perspectives from gravity modelling. *Journal of the Geological Society of London* **164**, 525–528.

Taylor, R. N., Nesbitt, R. W., Vidal, P., Harmon, R. S., Auvray, B. & Croudace, I. W. (1994). Mineralogy, chemistry, and genesis of the boninite series volcanics, Chichijima, Bonin Islands, Japan. *J. Petrol.* **35**, 577–617.

Taylor, S. R. (1982). *Planetary science: a lunar perspective*. Houston: Lunar and Planetary Institute.

Taylor, S. R. & McLennan, S. M. (1985). *The continental crust: its composition and evolution*. Oxford: Blackwell Scientific Publications.

Taylor, S. R. & McLennan, S. M. (1995). The geochemical evolution of the continental crust. *Reviews of Geophysics* **33**, 241–265.

Tegner, C. (1997). Iron in plagioclase as a monitor of the differentiation of the Skaergaard intrusion. *Contributions to Mineralogy and Petrology* **128**, 45–51.

Thompson, R. N. & Tilley, C. E. (1969). Melting and crystallization relations of Kilauean basalts of Hawaii. The lavas of the 1959–1960 Kilauea eruption. *Earth and Planetary Science Letters* **5**, 469–477.

Thomson, K. (2004). Sill complex geometry and internal architecture: a 3D seismic perspective. In: Breitkreuz, C. P., N. (ed.) *Physical Geology of High-Level Magmatic Systems*: Geological Society of London Special Publication **234**, 229–232.

Thomson, K. & Schofield, N. (2008). Lithological and structural controls on the emplacement and morphology of sills in sedimentary basins. In: Thomson, K. & Petford, N. (eds.) *Structure and Emplacement of High-Level Magmatic Systems*. London: Geological Society of London Special Publication **302**, 31–44.

Thorarinsson, S., Einarsson, T., Sigvaldason, G. & Elisson, G. (1964). The submarine eruption off the Vestmann Islands 1963–64. *Bulletin Volcanologique* **27**, 435–446.

Tilton, G. R., Bryce, J. G. & Mateen, A. (1998). Pb–Sr–Nd isotope data from 30 and 300 Ma collision zone carbonatites in northwest Pakistan. *Journal of Petrology* **39**, 1865–1874.

Tistl, M., Burgath, K. P., Höhndorf, A., Kreuzer, H., Muñoz, R. & Salinas, R. (1994). Origin and emplacement of Tertiary ultramafic complexes in northwest Colombia: evidence from geochemistry and K-Ar, Sm-Nd and Rb-Sr isotopes. *Earth and Planetary Science Letters* **126**, 41–59.

Tolstykh, N. D., Sidorov, E. G. & Kozlov, A. P. (2004). Platinum-group minerals in lode and placer deposits associated with the ural-alaskan-type Gal'moenan complex, Koryak-Kamchatka Platinum Belt, Russia. *Canadian Mineralogist* **42**, 619–630.

Tomkeieff, S. I., Walton, E. K., Randall, B. A. O., Battey, M. H. & Tomkeieff, O. (1983). *Dictionary of petrology*. New York.: Wiley.

Turco, E. & Zuppetta, A. (1998). A kinematic model for the Plio-Quaternary evolution of the Tyrrhenian–Apenninic system: implications for rifting processes and volcanism. *Journal of Volcanology and Geothermal Research* **82**, 1–18.

Turner, S., Arnaud, N., Liu, J., Rogers, N., Hawkesworth, C., Harris, N., Kelley, S., van Calsteren, P. & Deng, W. (1996). Post-collision, shoshonitic volcanism on the Tibetan Plateau: implications for convective thinning of the lithosphere and the source of ocean island basalts. *J. Petrol.* **37**, 45–71.

Tuttle, O. F. & Bowen, N. L. (1958). *Origin of granite in the light of experimental studies in the system $NaAlSi_3O_8$-$KAlSi_3O_8$-SiO_2-H_2O*.

Upton, B. G. J., Emeleus, C. H., Heaman, L. M., Goodenough, K. M. & Finch, A. A. (2003). Magmatism of the mid-Proterozoic Gardar Province, South Greenland: chronology, petrogenesis and geological setting. *Lithos* **68**, 43–65.

Upton, B. G. J., Parsons, I., Emeleus, C. H. & Hodson, M. E. (1996). Layered alkaline igneous rocks of the Gardar Province, South Greenland. In: Cawthorn, R. G. (ed.) *Layered Intrusions*. Amsterdam: Elsevier, 331–363.

Valbracht, P. J., Staudigel, H., Honda, M., McDougall, I. & Davies, G. R. (1996). Isotopic tracing of volcanic source regions from Hawaii: Decoupling of gaseous from lithophile magma components. *Earth and Planetary Science Letters* **144**, 185–198.

Van Kranendonk, M. J., Collins, W. J., Hickman, A. & Pawley, M. J. (2004). Critical tests of vertical vs. horizontal tectonic models for the Archaean East Pilbara granite-greenstone terrane, Pilbara craton, Western Australia. *Precambrian Research* **131**, 173–211.

Vernon, R. H. (1985). Possible role of superheated magma in the formation of orbicular granitoids. *Geology* **13**, 843–845.

Vernon, R. H. (1986). K-feldspar megacrysts in granites – phenocrysts, not porphyroblasts. *Earth-Science Reviews* **23**, 1–63.

Vernon, R. H. (2004). *A practical guide to rock microstructure*. Cambridge: Cambridge University Press.

Vigneresse, J. L. (1995). Control of granite emplacement by regional deformation. *Tectonophysics* **249**, 173–186.

Viljoen, M. J. & Viljoen, R. P. (1969). Evidence for the existence of a mobile extrusive peridotitic magma from the Komati Formation of the Onverwact Group. *Geological Society of South Africa Special Publication* **2**, 87–112.

Viljoen, R. P. & Viljoen, M. J. (1982). Komatiites – an historical review. In: Arndt, N. T. & Nisbet, E. G. (eds.) *Komatiites*. London: Allen and Unwin, 5–17.

Vogt, J. M. L. (1926). Magmas and igneous ore deposits. *Economic Geology* **21**, 207–233.

Wadsworth, W. J. (1961). The ultrabasic rocks of southwest Rhum. *Philosophical Transactions of the Royal Society, Series B* **244**, 21–64.

Wager, L. R. (1960). The major element variation of the Layered Series of the Skærgaard intrusion and a re-estimation of the average composition of the hidden layered Series and of the successive residual magma. *Journal of Petrology* **1**, 364–398.

Wager, L. R. & Brown, G. M. (1968). *Layered igneous rocks*. Edinburgh: Oliver and Boyd.

Wager, L. R., Brown, G. M. & Wadsworth, W. J. (1960). Types of igneous cumulates. *Journal of Petrology* **1**.

Wager, L. R. & Deer, W. A. (1939). Geological investigations in East Greenland, Part III. The petrology of the Skærgaard Intrusion, Kangerdlugssuaq, East Greenland. *Meddelelser om Grønland* **105**, 1–346.

Walker, G. P. L. (1965). Some aspects of Quaternary volcanism in Iceland. *Transactions of the Leicester Literary and Philosophical Society* **59**, 25–40.

Walker, G. P. L. (1973). Explosive volcanic eruptions – a new classification scheme. *Geologische Rundschau* **62**, 431–446.

Walker, G. P. L. (1980). The Taupo Pumice – Product of the Most Powerful Known (Ultraplinian) Eruption. *Journal of Volcanology and Geothermal Research* **8**, 69–94.

Walker, G. P. L. & Croasdale, R. (1972). Characteristics of some basaltic pyroclastics. *Bulletin Volcanologique* **35**, 303–317.

Wallace, P. J. (2002). Volatiles in submarine basaltic glasses from the North Kerguelen Plateau (ODP site 1140): implications for source region compositions, magmatic processes, and plateau subsidence. *Journal of Petrology* **43**, 1311–1326.

Wallace, P. J. (2005). Volatiles in subduction zone magmas: concentrations and fluxes based on melt inclusion and volcanic gas data. *Journal of Volcanology and Geothermal Research* **140**, 217–240.

Walter, M. J. (1998). Melting of garnet peridotite and the origin of komatiite and depleted lithosphere. *Journal of Petrology* **39**, 29–60.

Wenner, J. M. & Coleman, D. S. (2004). Magma mixing and Cretaceous crustal growth: Geology and geochemistry of granites in the Central Sierra Nevada Batholith, California. *International Geology Review* **46**, 880–903.

Wessel, P. & Lyons, S. (1997). Distribution of large Pacific seamounts from Geosat/ERS-1: Implications for the history of intraplate volcanism. *Journal of Geophysical Research-Solid Earth* **102**, 22459–22475.

West, H. B. & Leeman, W. P. (1993). The open-system geochemical evolution of alkalic cap lavas from Haleakala Crater, Hawaii, USA. *Geochimica Et Cosmochimica Acta* **58**, 773–796.

White, R. & McKenzie, D. (1989.). Magmatism at rift zones: the generation of volcanic continental margins and flood basalts. *Journal of Geophysical Research* **94**, 7685–7729.

White, R. S. (1993). Melt production rates in mantle plumes. *Philosophical Transactions of the Royal Society of London A* **342**, 137–153.

White, R. S., McKenzie, D. & O'Nions, R. K. (1992). Oceanic crustal thickness from seismic measurements and rare earth element inversions. *Journal of Geopysical Research* **97**, **19**,683–715.

White, R. V. & Saunders, A. D. (2005). Volcanism, impact and mass extinctions: incredible or credible extinctions? *Lithos* **79**, 299–316.

Whitney, J. A. (1988). The origin of granite: the role and source of water in the evolution of granitic

magmas. *Geological Society of America Bulletin* **100**, 1886–1897.

Williams-Jones, A. E. & Palmer, D. A. S. (2002). The evolution of aqueous-carbonic fluids in the Amba Dongar carbonatite, India: implications for fenitisation. *Chemical Geology* **185**, 283–301.

Wilson, A. H. (1996). The Great Dyke of Zimbabwe. In: Cawthorn, R. G. (ed.) *Layered Intrusions*. Amsterdam: Elsevier, 365–402.

Wilson, C. J. N. (2001). The 26.5 ka Oruanui eruption, New Zealand: an introduction and overview. *Journal of Volcanology and Geothermal Research* **112**, 133–174.

Wilson, C. J. N. (2008). Supereruptions and supervolcanoes: processes and products. *Elements* **4**, 29–34.

Wilson, J. R. & Larsen, S. B. (1985). Two-dimensional study of a layered intrusion: the Hyllingen Series, Norway. *Geological Magazine* **122**, 97–124.

Wilson, J. R. & Sørensen, H. S. (1996). The Fongen-Hyllingen layered intrusive complex, Norway. In: Cawthorn, R. G. (ed.) *Layered intrusions*. Amsterdam: Elsevier, 303–329.

Wilson, J. T. (1963). A possible origin of the Hawaiian islands. *Canadian Journal of Physics* **41**, 863–870.

Wilson, M. (1989). *Igneous petrogenesis*. London: Unwin Hyman.

Wilson, M. (1993). Magmatic differentiation. *Journal of the Geological Society of London* **150**, 611–624.

Wohletz, H. & McQueen, R. G. (1984). Experimental studies of hydromagmatic volcanism. In: *Geophysics Study Committee: Explosive volcanism: inception, evolution and hazards*. Washington DC: National Academy of Sciences, 158–169.

Woolley, A. R. (2001). *Alkaline rocks and carbonatites of the world*. London: The Geological Society.

Woolley, A. R. & Church, A. A. (2005). Extrusive carbonatites: a brief review. *Lithos* **85**, 1–14.

Wright, I. C., Gamble, J. A. & Shane, P. A. R. (2003). *Submarine silicic* volcanism of the Healy caldera, southern Kermadec arc (SW Pacific): I – volcanology and eruption mechanisms. *Bulletin of Volcanology* **65**, 15–29.

Wright, J. V., A. L., S. & Self, S. (1980). A working terminology of pyroclastic deposits. *Journal of Volcanology and Geothermal Research* **8**, 315–336.

Wyllie, P. J. (1981). Plate tectonics and magma genesis. *Geologische Rundschau* **70**, 128–153.

Yamazaki, T., Seama, N., Okino, K., Kitada, K. & Naka, J. (2003). Spreading process of the northern Mariana Trough: Rifting-spreading transition at 22°N. *Geochemistry Geophysics Geosystems* **4**.

Yang, Y. & Morse, S. A. (1992). Age and Cooling History of the Kiglapait Intrusion From an Ar- 40/ Ar-39 Study. *Geochimica Et Cosmochimica Acta* **56**, 2471–2485.

Yardley, B. W. D. (1989). *An introduction to metamorphic petrology*. Harlow: Longman.

Yoder, H. S. J. (1976). *Generation of basaltic magmas*. Washington DC: National Academy of Sciences.

Yoder, H. S. J. & Tilley, C. E. (1962). Origin of basalt magmas: an experimental study of natural and synthetic rock systems. *Journal of Petrology* **3**, 342–532.

Yuan, H. & Dueker, K. (2005). Teleseismic P-wave tomogram of the Yellowstone plume. *Geophysical Research Letters* **32**, doi:10.1029/2004GL022056.

Zaitsev, A. N. & Keller, J. (2006). Mineralogical and chemical transformation of Oldoinyo Lengai natrocarbonatites, Tanzania. *Lithos* **91**, 191–207.

Zellmer, G. F., Hawkesworth, C. J., Sparks, R. S. J., Thomas, L. E., Harford, C. L., Brewer, T. S. & Loughlin, S. C. (2003). Geochemical evolution of the Soufrière Hills Volcano, Monserrat, Lesser Antillerr volcanic arc. *Journal of Petrology* **44**, 1349–1374.

Zeng, L. S., Saleeby, J. B. & Ducea, M. (2005). Geochemical characteristics of crustal anatexis during the formation of migmatite at the Southern Sierra Nevada, California. *Contributions to Mineralogy and Petrology* **150**, 386–402.

Zhang, Y. X. & Xu, Z. J. (2008). 'Fizzics' of bubble growth in beer and champagne. *Elements* **4**, 47–49.

Index

Terms printed here in **bold** are defined in the Glossary. Integer numbers below refer to page numbers. Decimal numbers in *italics* refer to figures and those in **bold** to colour plates.

α–γ section 98, *4.2.1*, 352–3
A-type granitoid 269, 272–3, 276–7, *8.19*, *8.20*, 285–8
a′a 24, *2.2c*
Abitibi (Canada) 157
accessory mineral 9
accretionary fore-arc 186
accretionary lapilli *7.15b*, 233
accretionary prism 186, *6.13*
accumulation 85
achondrite 58
acid, –ic *1.3c*, 8, 291
acmite 37, 269
active continental margin volcanism 58
adakite *6.15*, 196, 204–6, 279–80, *8.20*
adcumulate 117, 136, 158
adiabat 61
— ic expansion 61
— ic upwelling 61, *2.18*, *6.19*
Adirondacks (New York) *4.13*, 124
aegirine *9.2.1*, 296
aegirine-augite (pyroxene) 269, 296–7, 311, **9.7**, **9.8**
Aeolian arc (Italy) 327–30, *9.17*, 343
Afar (Ethiopia) *9.3*
— plume 339
AFC: see assimilation with fractional crystallization
AFM plot *6.8a*, 180–2
Afro-Arabian flood basalt 197, *6.22*
age-progressive island chains 337
agpaitic 311
aillikite (lamprphyre) 325
Al_2O_3 85, *3.10*, *6.9*, 183–4
Alaska 195
Alaska-type ultramafic bodies 141, *5.4*
albite 11, 37
Aleutian arc (Alaska etc) 123, *6.2.1*, 186, *6.12*, 195–6, 270
Alexo (Canada) 155, 157
alkali *1.5*, 16
— basalt 21, *2.1*, 22–3, 299, *9.11*, 338
— **feldspar** 162–5, *6.1.1*, *6.7*, *8.1*, 243–5, *8.1.1*, 309, **8.3**, 263
— granite 123, *8.1*, 242–3
— lamprophyre *9.6.1*, 324–5
— picrite 308
— rhyolite *1.5*, 167, *9.1a*, 323
— rocks Ch 9
— trachyte *9.1b*
alkalic 291
alkaline 291
alkalinity 298–9
almandine (garnet) *5.2.1*
alnöite (lamprphyre) 325
Alps 146, 329–30
alteration, **altered** 3, 14, 16, 30, 35, **2.3**, **2.7–2.9**, 119, **4.12**, 134, **5.10**, **8.1**, **8.3**, **9.2**, **9.4**, **9.15**, 325
— basalt 201–2
Altiplano 196
aluminous minerals 268–9, 285
aluminous phase (in mantle) 132
alvikite 305
AMC (anorthosite-mangerite-charnockite) suite 124, 279–80, *8.20c*, 288
amphibole 63, *6.2.1*, *6.5*, **6.6**, **8.1**, **9.18**
amphibolite facies 202
AMS: see anisotropy of magnetic anisotropy
amygdale amygdaloidal 30, *2.8b*
An number 11
analcite (foid) 292–3
anatexis 162, 207, 251–2, 273, 280
andalusite 268–9
Andes *6.21*
andesine 11
andesite 12, *1.4*, 151, Ch 6, 161–2, 168, *6.1*, **6.1**, **6.2**, **6.3**, *6.15*, 236, *8.10c*, *8.20*
anhydrous minerals 35, 171
anisotropy of magnetic anisotropy (AMS) 250
ankaramite 21, **2.3**, **2.4**, **2.5**
ankerite 302
anomalous interference colour 292, **9.9**, **9.10**
anomalous interference colour 349, **9.9**, **9.10**
anorogenic granitoid 269, 273
anorthite (feldspar) 11, 269
anorthoclase (feldspar) 164–5, *8.1.1*, 310, **9.5**, **9.6**
anorthosite *4.1*, 95, 119, 123–8, *4.14*, *4.15*, *4.16*, **4.13**, 279–80
anorthosite problem 123

antiperthite 243–5, *8.1.1*, *8.12*
apatite 175, 281
aphanitic texture 34
aphyric texture 34, 76, 189
aplite *8.13b*, 265–6
apophysis -ses *4.3c*, 257
appinite 249, 258–60
arc crust 198, *6.23*, *6.24*
arc-trench gap 188–9
Archaean anorthosite 124–7, *4.14*
arcuate intrusion 248, *8.5b*
Ardara pluton (Ireland) **8.1**, *8.9d*, 255
Ardnamurchan Central Complex (Scotland) 258
Arequipa segment (Peru) 271
arfvedsonite (amphibole) 269, 306, *9.4.1*, 309, **9.21**, **9.22**
Armykon Hill (Tanzania) **9.10**
Ascension Island *2.13*, 275
aseismic ridge 195–6
ash 28, 212–4, 219, *7.5*
aspect ratio 24, 16, 250
assimilation 258, 282–4
— with fractional crystallization (AFC) 89, 207, 282–4
asthenosphere 60–1
augite 8, 20, 22–3, *2.1.1*, 30, **2.3**, **2.5**, 262
Austral Volcanic Zone (Andes) *6.12*, *6.21*
autolith 256
AVZ: see Austral Volcanic Zone
axial magma chamber 41, 138–9, 143
back-arc basin 57, *6.18*, *9.17*, 343
— extension 192–5, *6.18*
back-veining 257–8, *8.10c*
Baikal Rift *2.12*, 54
ballooning *8.9d*, 254–5, 260
Bandelier tuff *6.14*, *7.11e*
Barberton (S. Africa) 150, 155, *5.12*
basalt 8, 9, 12, *1.4*, Ch 2, 20, 198, 236, 299
— tetrahedron *2.11*, 313–6, *9.7a*
basaltic achondrite 58
basaltic andesite *1.4*, *6.1*, 164, 168, **6.3**
basaltic komatiite 150
basanite 12, *1.4*, *9.1a*,*b*, 294–5, 299, 312, 317–9, *9.8*, *9.11*, 329
base surge *7.9a*, 230–3, *7.15a*
basic *1.3c*, 8, 21
Basin and Range province *2.12*, 54, *6.12*, 197, 322
bastite 135
batholith 65, 248–51, *8.7*
— geometry 248–50, *8.7*
— s of Western USA *8.6*
Bay of Islands ophiolite (Newfoundland) *4.13*, 136, *5.3.2*
Becke test 351
Belingwe greenstone belt (Zimbabwe) 151, 155–6, *5.12*, *5.13*
bell-jar intrusion *8.9b*, 253–4
benmoreite *9.1a*, 297, 323
Benue Trough (Nigeria) 326, *9.16*
Bertrand lens 293
beryl 265–6
biaxial (optics) *A1*, 353–7, *A2*, *A4*, *A5*, *A6*
Big Feldspar Dykes 326
bimodal suite 196–8, *6.22*, 207, 318, 321, *9.12*, *9.13*
binary phase diagram 69
biological extinctions 54
biotite 95, 162, 166–7, **6.6**, **6.8**, 243, **8.1**, **8.2**, **8.10**, 262, 267, 311, 325, **9.15**
birefringence 30, 98, 180, **6.9**, **9.7**
Bishop Tuff (California) 237, *6.14*
black smoker 46
bleb 256
block 219
— -and-ash flow 229–30, *7.14*, *7.16*
blocky lava 169, *6.3a*
body colour 347–50
bolide impact 54
bomb 219, 223, *7.9a*
Bonin Islands **6.4**, 206
boninite 137, 165–8, *6.12*, **6.4**, **6.5**, *6.15*, 206
border zone 135
Bouguer gravity anomaly 55, 128, *4.16b*, 186, *6.13a*, 246, *8.4a*, 321–2, *9.14*
Boulder batholith (Montana) *8.6*
Bouvet Island *6.12*
Bowen N.L. 77, 80, 112–3, 148, 178
bowlingite 30
bread-crust bomb 214–5, *7.4b*
brittle 24, 26, 252–4, 257–8
bronzitite *5.2*
bubble nucleation *7.1*
Buddington A.F. 251
Bufumbira (Uganda) **9.9**
bulk analysis 3
bulk distribution coefficient 334
buoyancy 288
Burro Mt (California) *4.13*
Bushveld complex (S. Africa) 103–4, *4.13*, 135–6, *5.2*
bytownite 11

C-type granitoid 280, 288
calc-alkali -ic, -ine 180–4, *6.8*, *6.9*, 189
— basalt 44–5
— lamprophyre 324–5, *9.6.1*
calcic plagioclase 8, 20
calcite 302, 324
caldera 236–8, *7.19*, *7.20*, *9.10*, 318–9
Caledonian granites 249
Cameroon Line 326, *9.16*, 341
Campanian Province (Italy) 329, *9.17*
camptonite (lamprphyre) 325
Cañadas caldera (Tenerife) 318–9, *9.10*
Canary Islands **9.11**
cancrinite (foid) 292–3, 310, **9.17**
Cantal volcano (France) 88, *3.11*, **9.12**
CaO 85, *3.10*
carbonate 324
carbonatite 5, 298–303, *9.6*, 307–8, 317, 322–3, 339–40, *3.21*
carbonized wood *7.11c*
Carnegie Ridge *6.21*
Cascade Range (NW USA) *6.2.1*, 185, *6.12*, 195–6, 329–30
cassiterite 265–6
catapleite (mineral) 311
cauldron subsidence 248, *8.9b*, 253–4
Ce/Yb ratio 343, *9.24*

Central Atlantic Magmatic Province (CAMP) *2.15*, 54
Central Volcanic Zone (Andes) *6.12*, 195, *6.21*
CFB: see continental flood basalt
chalcophile 157
charnockite 124, *4.16*, 245–6, *8.2*, 276–7, *8.20c*, 288
chemical analysis 4
chemical gradient 111
Chile *6.16*
chilled margin 98, *4.3b*
chlorite 9, 63, 94, 162, 202, 267
chrome-diopside 142, **5.4**
chromite 115, 126–7, 133, *5.1.1*, 158, **5.9**, **5.11**
chromitite 115, 135, *5.2*, 137, 141
cinder cone: see scoria cone
CIPW norm 37–40, 268–9, 293–4, 313–6, *9.7*, Appendix B
cleavage 30, 350
clinoenstatite 166, **6.4**, **6.5**
clinopyroxene 22–3, 98, 175, **6.5**
CO_2 *3.21*, 340
coarse-grained *1.3a*
Coastal Batholith of Peru *6.21*, 249, 270–2, *8.16*
Coastal Range batholith (British Columbia) *8.6*
cock's tail *7.9a*, 223
Cocos Plate *6.21*, 204
Cocos Ridge *6.21*
cognate cumulate 142
— inclusions 256
Colombia 141
colonnade 26, *2.3*
Colorado Plateau *6.12*
colour index 6, *1.3b*, 131
Columbia River 26
column collapse 220, *7.6b*
columnar jointing 26, *2.3*, 98, 225, *7.11e*
comb layering 118, 256–7
compatible element 49–51, *6.6.1*
complex multiple twinning *6.1.1*, 244–5, *8.1.1*, 292–3, 310, **9.6**, **9.8**, **9.9**, **9.16**
component 68
composite sill, dyke 103, 324
composition 3
composition plane *4.1.2*
compositional banding 147
compressible, -ility 60, 156
concordant 99
Condoto intrusion *5.4*
conductive geotherm *2.17*, *5.5*
cone sheet *4.3e*, 102, *4.6a*
continental arc 195–6, *6.20*, *6.21*, 248–9, *8.6*
continental crust 91, 189, 195, 280–8
continental flood basalt (**CFB**) province 52–4, *2.15*, 63
continental suture zone 139, 146, 189, 248–50, *8.17*
continuous reaction series 113
convection current 110–5, *4.9*
convective geotherm *2.17*
convergent light 347–8, 353–7
convergent plate margin 180
Cook inlet (Alaska) *6.12*, 195
Coppermine volcanics (NWT Canada) 4.13
cordierite 268–9
Cordillera Blanca batholith (Peru) 255, *8.16*, 270–2, *8.20c*, 284
Cordilleran granitoids 282–4, *8.20*
core-and-mantle microstructure 119, **4.13**
corner flow *6.24*, 202
corona texture 118
corundum-normative 268–9
Costa Rica 196
cotectic 75, *3.3*, *3.7*, 85, *5.4.1*, 263, 313, *9.7b*
coulée 167, *6.3f*, *3.10*, 319
Cr 319
crater 239
Crater Lake (Oregon) 237, *7.20a*
craton *9.3*, 323–6, *9.15*, 326, *9.16*, 328–9, *9.23*
crescumulate texture 118, **4.6**
critical plane of silica undersaturation 313–6, *9.7a*
cross-hatched multiple twinning *6.1.1*, *8.1.1*, **9.6**, **9.16**
cross-laminated 231
cross-stratified 109, *4.9*, 256
crossed polars 347–8, 352–7
crushing 3
crustal assimilation / contamination *3.11*, *3.12*, 87–91, *3.4.2*, 204, 341
crustal melting 203
crustal thickness 196
cryptic layering 108, *4.8*, 110, *4.9*
cryptodome 169
crystal 2
— accumulation 17
— content 171
— growth rate (*C*) 32, *2.3.1*, 257, 262
— habit 350
— tuff 235
— -mush 128
— -vitric tuff **7.1**, 235–6
crystallization path 71
cumulate (rock) 15, 17, 76, *3.8*, 93, 107–15, 138–9. 189, 256, 308–9
— texture 116, **4.4**, **5.1**, **5.2**
— xenolith 123, 189
cumulus (mineral) 77, 83, 107–15, *4.8*, *5.2*
Cupaello (Italy) 329–33, *9.17*, *9.19*
cuspate glass shard 235, **7.1**
cuspate intrusive margin 258
CVZ: see Central Volcanic Zone

^{TM18}**O** 89
dacite 12, *1.4*, Ch 6, 162, 168, *6.1*, *6.3c*, *6.5*, **6.6**, *6.15*, *7.4c*,*f*, 219, 236, 280
damkjernite (lamprphyre) 325
debris avalanche 231, *7.16*
Deccan 26, 52, *2.15*
decompression 175, 178, 210
— **melting** *2.18*, 202, 341
deep-sea sediment 201–2
deflation 225
degassing 16, 29, 175, 228, 239
degrees of freedom 74
dehydration 167, *6.2.2*, *6.24*, 202
— melting 286, *8.4.1*
dendrite -itic habit 152, *5.10*, **5.9**, **5.11**

dense rock equivalent (**DRE**) 186, 225
density 102, 110, 202–3, *6.5.1*, 246–8, *8.4*, *9.14*, 322
— current 110
— filter 202, 322
depleted (mantle) 143, 200
depth 332
deuteric alteration 35
devitrification *2.9b*, 32, 179–80, **6.9**
diabase see dolerite 93
diamond 328–31, *9.18*, 341–2, *9.22*, *9.23*
diapir diapiric 246, *8.9c*, 254
diatreme 302, 305, *9.7.1*, 328–9
— facies (kimberlite) 328–9
differentiated sill 103
dike: see dyke
diopside 132
diorite 93, 108, *8.1*, 242–3, *8.1*, 249, 258, 276–7
discontinuous reaction series 113
dispersal index *D* km^2 221, *7.8*
divariant 74, 78
dolerite 93
dolomite 302
dome: see lava dome
Donegal Main Granite (Ireland) *8.9f*, 255–6
double-diffusive convection *4.9*
downgoing slab 198, *6.23*
downsag caldera 237
DRE: see dense rock equivalent
dry liquidus 177, *6.4.1*
dry solidus 177, *6.4.1*
ductile 24, 26, 225, 254
Duke Island 136, 141
dunite 131, *5.1*, *5.2*, *5.4*, 142–5, 147
dyke 95, *4.5a*
— swarm 98, *4.3a*, 138, *5.3.1*, *9.15*, 323

E-MORB 42
EARS: see E. African rift system
earthquake *6.13*, *9.17*
East African Rift System (EARS) *2.12*, *9.3*, 319–22, *3.11*, *3.12*, *3.13*
East Greenland 26, *4.3a-c*, 130
East Pacific Rise 41
East Pacific Rise 197
East Scotia Ridge *2.12*, *6.12*
eclogite 142, 199–202, *6.24*, *6.25*, 204, 328
Ecuador 196
edifice instability 233
effusion rate 26, 28
effusive eruption 170–1, 175, 209, *7.10*, 239
electron microprobe **2.10**, 183, *9.18*
embayment **6.7**, **6.9**, 310, **9.5**
en echelon fracture 102
enclave **8.9**, 256, *8.10a*, 261
end-member 11, 77
enderbite *8.2*
endogenous growth (of lava dome) 169, *6.3b*, 176, 230
Ennerdale Granophyre (UK) 246–7
enstatite *2.1*, 39, 42, 118, 120–1, **4.8**, 132, 136, **5.1**, **6.4**, **6.5**, 330
entablature 26, *2.3*
epigranite 260
equilibrium 68, 72
— **crystallization** 78–9, *3.5*
erosion 110, 146
—-al fore-arc 186
eruption column 218
Eskdale Granite (UK) 246–7
essential mineral 9
essexite 303–4, *9.4*
Etendka flood basalt province *2.15*, 54, *2.16*
Ethiopian Rift *9.3*, *9.13*, 338
Eu (europium) *8.23*, 284–5, 287, *8.5.1*
eucrite (basaltic achondrite) 58
eudialyte 309, 311, **9.21**, **9.22**
eutaxitic texture 225, *7.11d*, **7.3**
eutectic *3.1.1*, 69, *3.2*, 71, *3.3*, *4.3.1*, 144, *5.4.1*, *9.7b*, 313, 345
evolved 11, 42, 48, 76, 318
excess water 177
exogeneous growth (of lava dome) 169, *6.3e*, 176, *9.10*, 319
experimental charge 68
experimental petrology 67
explosive efficiency *7.10*, 224
explosive eruption 175, 209, 239
exsolution lamellae 95, **4.7–4.9**
exsolve, exsolution 29, 118, 120–1, **4.7–4.9**, 263–4, *8.12*, 352
extensional collapse (of orogen) 329–31
extinction angle 96–7, *4.1.2*, 352
extract *3.10*, 87
extraterrestrial basalts 58

fall deposit 219–21
Farallon plare 54
fast vibration direction 96–7
fayalite (olivine) 10, 305, 309
Fe_2O_3 46–7
Fe-number *8.15*, 270
Fe-Ti oxides 166, 175, 281
feeder dyke (system) *8.7b*, 255
feldspar 96–7, 164–5, *6.1.1*, 244–5, *8.1.1*, **4.1–4.5**, **5.2**, **6.1**, **6.2**, **6.6**, **6.7**, **6.9**, **6.10**, **8.1**, **8.3**, **8.6**, **8.7**, **8.8**, **9.**, **9.6**, **9.11**, **9.12**, **9.14**, **9.16**
feldspar-free rocks 299
feldspathoid 39–40, 291–3, **9.5**, **9.7**, **9.8**, **9.13**, **9.15**, **9.17**
felsic 6, *1.3b*, 292
fenite fenitization *9.6*, 307, 340
Fenner trend 180
FeO 46–7
Ferrar dolerites (LIP) *2.15*, *4.3d*
— sill complex 99
ferric 4
ferroaugite *2.1.1*
ferrodiorite 108
ferromagnesian 6, *1.3*
ferrosilite *2.1.1*
ferrous 4
fertile (mantle) 142, *5.4.1*, 144–5, 154
fiamme 225, *7.11d*, 236
fine-grained *1.3a*, 8
fire fountain 214, *7.3a*,*b*, 318–9
Fish Canyon Tuff (Colorado) 237

Fiskenaesset anorthosite (W. Greenland) *4.13*, 124, 126–7
flank eruption 238
flat-ramp-flat (sill) *4.4b*
flat-slab zone 195, *6.21*
flexural monocline 130
flow banding 170, *6.3g*, *6.4*
flow field 26
flow foliation 171
fluid 35
fluorite 267, 303, **9.4**
foid: see feldspathoid
foidite (fine-grained rock) *1.4*, *9.1b*, 294–5
foidolite (coarse-grained rock) *9.4*
foliation 140–1, *5.3*, 225, *8.9d*,*f*, 254–5, 260–1, *8.11*
forceful emplacement 255
fore-arc basin 186, *6.13*
fore-arc high 186, *6.13*
formula calculation (mineral) 11
forsterite 10
fountaining 31, 210, *7.3a*,*b*, 212
fractional crystallization 5, *3.1*, 79–80, *3.5*, *3.8*, 83, 88, 201, 280–8, 332–3
fragmentation horizon *7.1*
fragmentation index *F* % 221, *7.8*
funnel-shaped pluton 103

gabbro Ch 4, 93, *4.1*, 249
gabbroic 93
gabbronorite *4.1*, 95
Galapagos 161, *6.12*, *6.21a*, 196–7, 207
Gardar alkali province (S. Greeland) 123, 309, *9.15*, 322–6
garnet 11, 50, 132, 158, **5.5**, 162, **6.8**, 204–6, *6.6.1*, 268–9, 284–5, 333
— lherzolite 142, *5.5*, **5.5**, 205, 317, 341–2, *9.22*
— peridotite 59, *5.5*, **5.5**
gas bubbles 210
Gaussberg lamproite (Antarctica) 312, 333, *9.19*
geochemical analysis 3, 5, 13, *1.2*
geochemical qualifier 16, 18, *6.8b-c*, *8.14*, *8.19*, *9.8.1*, *9.24*
geotherm 59–63
geothermal gradient 142, 155
geothermometer 121, *9.22*, 342
giant dyke 103, 123
glass 13, 162, 165, **6.9–6.11**, 234
Glass Mountain coulée (California) *6.3e*, 180
Glencoe (Scotland) 248–9, *8.5a*, 270
glomerocryst 34, **2.10**
glomeroporphyritic 34, **2.3**, **2.4**
Gorgona Island (Colombia) 148–52, 155, *5.12*, *5.13*
Gough Island 85–7, *3.10*
graben 319–22, *9.11*
grain boundary 147
grain size 5, *1.3*, 32, 116
grain-boundary re-adjustment 136
granite Ch 8, *8.1*, 242–3, **8.2**, **8.4**, **8.6**, **8.7**, **8.9**, 276–7, 323
— -greenstone terrain 151, *5.6.1*
granitic 241
granitization 251
granitoid Ch 8
granodiorite *8.1*, 242–3, 249–52, 256, 276–9
granophyre **8.3**, 263
gravity anomaly 55, 128, *4.16b*, 186, *6.13a*, 246, *8.4a*, 250, 255, 309, 321–2, *9.14*
Great Dyke (Zimbabwe) 103–4, *4.13*, 136, *5.2*
Great Tonalite Sill (Alaska) 249
greenstone belt 150–1, 157
Gregory Rift *9.3*, 319–322, *9.11*, *9.12*, *9.14*
gregoryite (mineral) 302
greisen 267
Grønnedal-Íka complex (S. Greenland) *9.15*, **9.14**, **9.15**, **9.17**
groundmass 2, *1.1*, 6, 32, *2.10*
Group I kimberlite 342
Group II kimberlite 343
growth rate: see crystal growth rate

H_2O and melt evolution 182–4, *6.9*, *6.10*
H_2O content 189, *6.14*
H_2O flux 199, *6.24*
H_2O-saturated solidus *6.4.1*, 252, 263
H_2O-undersaturated conditions 177, 252, 262, 285–6, *8.4.1*
half-graben 319–22, *9.11*
hand-specimen mineral ID 243
harzburgite 132, *5.1*, 135, *5.2*, 140, *5.3*, 142–5, 328
Hawai`i 26, **2.1**, **2.6**, 316–7, *9.8*, *9.19*
hawaiian eruption 24, 31, 210, 212, *7.3a*,*b*, 214, 221, *7.8*
hawaiite *9.1a*, 318, **9.11**
HCP: see high-Ca pyroxene
heat flow 55, 59, *6.13*
Hebrides 26
hedenbergite (pyroxene) *2.1.1*, *9.2.1*, 309
hercynite (spinel) 133, *5.1.1*
Hess H.H. 148
heterogeneous nucleation 257, 263
HFSE 200–1, 273
— depletion 200–1
Hidden Zone (Skærgaard) 108–9, *4.8*, *4.9*
hiFe magma lineage *6.8b*,*c*, 182
high field strength element (HFSE) 49–51, *2.7.1*, 55, *2.16*, 190–2, *6.15*, 199–201, *6.25*, 206
High Himalaya leucogranites *8.17*, 285–6, *8.20a*, *8.4.1*, 285–6
high-alumina basalt 57
high-Ca pyroxene (HCP) 8, 22–3, *2.1.1*, 42, 120–1
high-K arc basalt 57
high-K series *1.6*, 57, 327–30
high-volcanic-output rifts *9.13*
highly incompatible trace element (HITE) 317, 332, 335
Hikurangi Plateau 52, *2.15*
hinge-line 193, *6.19*
HITE: see highly incompatible trace element
Hoggar 338
holocrystalline **2.2**
hololeucocratic *1.3b*
holomelanocratic *1.3b*

homogeneous gabbro 110
homogeneous nucleation 257
Honolulu volcanics 317
hornblende 95, 134, 141, *5.4*, 158, 162, 166–7, 175–6, *6.5*, **6.6**, 243, **8.1**, 256, 258, 262, 267, 270, 288, 308–11, 325
hornblende gabbro 123
hornblendite *5.1*, 147, 249
hot spot 41, *2.12*, 47, 335
HREE 51, 205, *6.6.1*, 333
hummocky terrain 233, *7.17*
Huoshi (Mariana arc, Japan) 312, *9.19*
hyaline, **hyalo-** *1.3a*
hyaloclastite 24, 27, *2.4*
hybabyssal kimberlite **9.1**
hydrolysis 266
hydrothermal 9, 14, 16, 35, 58, 266
— alteration 266–7
— metamorphism 35
hydrous fluid 201–2
hydrous magma 141, 184, *6.10*, 2.6
hydrous mineral 35, 63, 141, 166–7, *6.2.2*
hydrovolcanic eruption 204, 222–4, *7.9*
hypabyssal facies (kimberlite) 328–9, *9.7.1*
hypersolvus granite/syenite 264, 273, **9.14**, 310
hypersthene 22, *2.1.1*
— **-normative** 36

I-type granitoid 272–3, 276–7
IAT: see island arc tholeiite
Iceland 48–52, *2.14*, 161, 196–7, 206–7, *9.9*, 317–8, 337–8, *9.20*
icelandite 181–2, 207
ICP-AES 4
Idaho batholith (Idaho) *8.6*
iddingsite 20, 30, **2.3**, **2.7**, **2.9**, 94, 162
igneous **lamination** 110, 117, **4.5**, 260, 308, **9.14**
igneous **layering** 93, 103–15, *4.7*, *4.8*, *4.9*, 308–9
ignimbrite 171, 196–7, 214, 220, 225–9, *7.11b-e*, *7.12*, **7.2**, **7.3**, 236, 249
ijolite 303–4, *9.4*, *9.5*
Ilímaussaq complex (S. Greenland) 309, *9.15*, **9.21**, **9.22**
immiscible melts 324, *9.23*, 39–401, 345
in situ crystallization 111, *4.9*
incompatible element 41, 49–51, 54–8, *2.16*, 189, 195, 199–201, *6.25*, 204–5, 266–7, *8.20*, 281–8, 285, 309, *3.19*, 339
incongruent melting 112–3, *4.5.1*, 120, 316, *9.7c*
indicatrix (optics) 354–5, *A2-A5*
Indonesia 186, *6.12*
inflation 26, *8.9e*, 255
initial Sr-isotope ratio *3.4.2*, 90–1
intercumulus 107, 110, 117, 135
interfacial angle 147
interfacial energy 34
interference colour 293, 347–9, 352–3
interference figure (optics) 293, 353, *A3*, *A5*, *A6*
intergranular texture 34
intermediate *1.3c*, 8
intersertal texture 33, **2.3**
interstitial melt 95, 107, **5.9–5.11**, 263
intracaldera-facies ignimbrite *7.19*
intracontinental rift basalts 54–5
intraplate granitoids 274–5, 285–8, *8.18*
intrusion breccia 257–8, *8.10b*
invariant 74, *4.3.1*, 113
inverse grading (of pumice) 225, *7.12*
invert inversion 120–1, *4.5.1*, 244–5, *8.1.1*
inverted pigeonite *4.8*, 118, 120–1, **4.7**
ionic solute 266–7
ionic strength 46
iron-enrichment *6.3a*, 180
island arc 63, 185–95, *6.12*, *6.13*, *6.15*, *6.16*, *6.17*, *6.18*, *6.19*
— basalt *2.18*
— (IAT) 55, 189
isobaric 175
isochron *8.21*
isogyre (optics) 354–6, *A3*, *A5*, *A6*
isopach *7.8*
isostacy 196
isotherm 313, *9.7b*,*c*, *9.21*
isotropic (optics) 292–3, 348–50, *A1*, 352
Italy 327–30, *9.17*
IUGS 8, *1.4*, 14, *2.1*, *4.1*, 162, *6.1*, 219, 241, 291, 294, 302, 305, *9.1*
Izu-Bonin-Mariana (IBM) arc 185, 188, *6.12*, 192–5, *6.18*, 329–30

Jacupiranga complex (Brazil) 308
Japan arc *6.12*, *6.16*
Jemez Mts (New Mexico) *7.11e*
Jericho kimberlite (Canada) *9.22*
jointing 26, *2.3*, 98
jotunite *4.16a*, *8.2*
Juan de Fuca plate 195–6, *6.21*
juvenile tephra 215, 219
K_2O 4, *6.14*

— versus SiO_2 plot 6.11
K-feldspar megacryst 261–2, *8.11*, **8.8**, **8.9**
K-*h* relationship 190–2, *6.16*
K-richterite (amphibole) 298, 306, 330
Kaapval craton (South Africa) 151
kaersutite 95, 306, *9.4.1*, 308, 325
kakortokite 309, **9.21**
kalsilite (foid) 292–3, 297
kalsilitite (rock) 298–9
kamafugite 299, 322, 329–1, *9.8.1*
Kambalda (Australia) 157
Kamchatka arc *6.12*, *6.16*
Kao diatreme (S. Africa) **9.2**
Kap Edvard Holm intrusion (E. Greenland) *4.2*
Karakorum batholith 248, *8.17*, 272–4
Karoo province (southern Africa) 26
Kenya 54, *2.16*, 63
Kenya plume 339
Kenya Rift Valley *9.11*, *9.12*, 319–22, *9.14*, *9.19*

Kerguelen Plateau 52, *2.15*
kersantite (lamprphyre) 325
Kilauea (Hawaii) 212, 238
Kilimanjaro (Tanzania) *9.3*, 319
kimberlite 142, 291, 299, 328–9, **9.1**, **9.2**, 341–3, *9.22*, *9.23*
Kohistan arc section (Himalaya) 189, 273, *8.17*
komatiite 148–57, *5.5.1*, *5.7*, *5.8*, *5.9*, *5.11*, **5.9–5.11**
Krakatau (Indonesia) 234, 237
Kurile arc *6.12*, *6.16*, 270

La/Yb ratio 284
Laacher See (Germany) 209
labradorite 9, 11
Lac St Jean anorthosite (Canada) 123, *4.15*
laccolith 255, 274
lahar 233, *7.16*
Laki fissure zone 48, 317, *9.9*
laminar flow 225, 310
lamination: see igneous lamination
lamproite 291, 299, **9.3**, 312, 330–1, *9.8.1*, 344
lamprophyre 258–60, 323–5, *9.6.1*, 344
lapilli 28, 212–4, 219, *7.5*
— ash 221
— **tuff** **6.7**, **7.2**, **7.3**, 214, *7.5*, 221, 225–9, *7.11d*, 236
— -stone *7.5*
large igneous province (LIP) 44–5, 52–4, *2.15*, 63, 137, 122–3, 128, 161, 207
large-ion lithophile element (**LILE**) 49–51, *2.7.1*, *2.16*, 55, 190–2, *6.15*, 199–201, *6.25*
larvikite 303
late-stage processes 266–7, *8.13*
latent heat 89, 156, 175
latite 12, 162, *6.3g*, *9.1b*, 296–7, 329–30
lava 3
— dome 169, *6.3b*, *6.5*, *7.4f*, 230, 238, *7.20b*, 299, *9.10*
— fountaining 31, 210, *7.3a*,*b*, 212
— lake 212, *7.3b*, 300
— spine 169, *6.3c*
— tube, tunnel 26, 212
Layered Series 108–15
layering: see igneous latering
LCP: see low-Ca pyroxene
least principal stress *4.5*
length-fast (optics) 96–7, 297, 353
Lesser Antilles 123, *6.12*, 189, 192, *6.17*, 270
leucite (foid) 292–3, 297, **9.8**, 310, 316, *9.7c*, 330
Leucite Hills (Wyoming) *9.8.1*, 330
leucitite (rock) 12, 298–9, 329
leuco- 242, 305
leucocratic 7, *1.3b*
leucogabbro 124–8, *4.6.3b*
leucogranite *8.20c*, 285
leucogranodiorite 271–2
leuconorite 124–8
leucosome 252
leucotroctolite 124–8
Lever Rule 72–3. *3.2.1*
Lherz peridotite (Pyrenees) *4.13*, 146–7
lherzolite 131, *5.1*, 143–6, 328, 338–9
LILE/HFSE ratio 190, 339
LILE/REE ratio 190
Lilloise intrusion (E. Greenland) 308
lineation 141, 260–1
LIP: see large igneous province
Lipari *6.3d*
liquid line of descent (LLD) 75
liquidus *2.17*, *3.1.1*, 69–70, *5.12*, *6.5*, 177
lithic clast 214–5, 225
lithic tuff 236
lithosphere 155, *5.12*
lithospheric mantle: see mantle lithosphere
lithospheric thinning *9.14*, 322, 341
Ljugaren granite (Sweden) 249
LLD: see liquid line of descent
loFe magma lineage *6.8b*,*c*, 182
Loihi seamount 316–7, *9.8*, 335–7
Long Valley caldera (California) 238
lopolith 103–4, 255, 308
loss-on-ignition 15
Lovozero intrusion (Kola, NW Russia) 308
low-Ca pyroxene (LCP) 22–3, *2.1.1*, 39, 42, 120–1, 142
low-grade metamorphism 16, 35
low-K tholeiite 52, 55, *2.16*, 57, 189, 198
Lower Zone (Skærgaard) 108, *4.8*
LREE *6.6.1*
lujavrite (rock) 309
lunar anorthosite 128, *8.5.1*
lunar basalt 58, *8.5.1*

maar 24, *7.9b*, 224
Macdonald and Katsura *1.5*, 17, 42
Mackenzie dyke swarm (Canada) 98, *4.13*
macro-rhythmic layering 115, 135, 158, 309, **9.21**
macrocryst (kimberlite, etc) 310, **9.1**, **9.2**, 328–9
mafic 6, *1.3b*
magma 2, *1.1*
— chamber 3
— composition 16
— differentiation Ch 3, 65
— mingling 171, 258, *8.10c*
— **mingling** 258
— ocean (Moon) 128
— pressure 99–102, *4.5*, *4.6*, 169, 214–5, 255
— tube *4.4a*
magnetic anomaly 309
magnetite 133, *5.1.1*, 167, *6.2.2*, 182–5, *6.9*, *6.10*
major element 4
Majorqap Qâva (Fiskenaesset) 126–7
malignite 305, *9.5*
mangerite 124, 245–6, *8.2*, 279–80
Manihiki Plateau 52, *2.15*
mantle bedding 221, *7.7a*, *7.11a*
mantle lithosphere 146
mantle olivine *5.6*, **5.3–5.7**, 319
mantle plume 61–3, *2.18*, 104, 122, 157, 337–9
mantle wedge *2.18*, 63, *6.13*, 198–202, *6.23*, *6.24*

mantle xenoliths 141–6, **5.3**, **5.4**, **5.5**, 302, 317, 319, 323, 328, 339–42, *9.22*
Marginal Border Series (Skærgaard) *4.8*, *4.9*
Mariana arc 186, *6.12*, 189
Masaya (Nicaragua) 238
maskelynite **2.10**
mass % 10
massif-type anorthosite 4.14, 124–8
massive volcaniclastic kimberlite (MVK) **9.2**, 328–9
Mauna Kea (Hawaii) 212
Mauna Loa (Hawaii) 212, 238
mechanical boundary layer 61, *2.18b*
Medicine Lake (California) *6.3e*, 180
medium-grained *1.3a*
medium-K *1.6*
— arc basalt *55*–6, *2.16*
meFe magma lineage *6.8b*,*c*, 182
megablock 233, *7.17*
megacryst -ic 124, *4.6.3a*, 8.1.1, 326
mela- 305
mélange 186
melanite (garnet) *5.2.1*, 304
melanocratic 7, *1.3b*
melanosome 252
melilite (mineral) 292–3, 325, **9.9**, **9.10**
melilitite (rock) 294–5, 299, *9.11*, **9.9**, **9.10**, *9.23*
melt 2, *1.1*, *5.4.1*
— composition 83
— evolution path *5.4.1*
— **inclusion** 16, 178, **6.7**, **6.11**, 189, *6.14*
— production rate 41, 52
melteigite 304–5, *9.5*
Mercalli Giuseppe 212
Merensky Reef (Bushveld) 115
mesocratic 7, *1.3b*
mesosome 252
metabasalt 42
metaluminous 268–9, *8.14*, 304, 311
metasomatism 200–1, 334, 342–4
metastable, i. 32, 118, 121
meteoric water 35, 224, 239
Mg number *5.1.1*, 143–6, 204–6, 319, 333
MgO 85, 90, *3.10*, 92, 166, 183, *6.9*
miarolitic cavity 260
mica schist *8.20a*, 285–6
Michel-Levy chart Plate **1**
micro- 242
microcline (feldspar) *8.1.1*, 310, **9.16**
microdiorite 242, 249, *8.10d*, **8.9**
microgabbro (IUGS) 93
micrographic texture 263, **8.3**
microlite (crystals) 175, 180, **6.10**, 234, *7.18b*
microperthite 263–4
microphenocryst 21, **2.2**, *2.10*, 180
microsyenite *8.10c*
Mid-Atlantic Ridge 41, *2.16*
mid-ocean ridge basalt (MORB) 41–6, *2.16*, *2.18*, 147, 199–201, *6.25*, 280–1
Middle Zone (Skærgaard) 108, *4.8*
Midland Valley of Scotland 341
migmatite 251–2, *8.8*
mildly potassic rocks 296–7, *9.2*
mineral 3
mineral identficiation 22–3, *2.1.1*, 96–7, *4.1.1*, *4.1.2*, 164–5, *6.1.1*, 244–5, *8.1.1*, 292–3, *9.1.1*, 296–7, *9.2.1*, 306, *9.4.1*, 310, 347–57
mineral inclusion 261
mineralization 267
minette (lamprphyre) 325
mingling 258
miscibility gap 22, 120–1, 340
Misenum (Italy) 215
mixing calculation 364
Miyashiro *1.5*, 17
moat *7.19*, 238, *7.20b*
móberg 48, *2.14*
mobile element 14, 35, 46, 51
modal layering 108, 110–5, *4.9*, *4.6.3c*, 256
mode, **modal** proportions *4.1*, 132, *5.1*, 161, *6.1b*, 241, *8.1*, *9.1b*, 294
Moho 138–9
mole molar 10, 38–40,143, *8.14*
monazite 265–6
monchiquite (lamprphyre) 325
monoclinic 22, *6.1.1*, 244–5, *8.1.1*
monogenetic 214
monzodiorite *8.1*, 243–4
monzonite *8.1*, 243–4, 262–3, 303–4, *9.4*
MORB reservoir 200
MORB-normalized plot 199–201, *6.25*
MORB-normalizing values *6.25*
MORB: see mid-ocean ridge basalt
Mt Cameroon 326
Mt Kenya *9.3*, 319
Mt Pelée 169, *6.14*, 229–30, *7.14a*
Mt St Helens (Washington) *6.3c*, 175–6, *6.5*, *6.14*, *7.4c*,*e*,*f*
mugearite *9.1a*, 297, 312, 318, 323
Mull 26, *2.3*, **6.10**, **8.3**
multiple twinning 96–7, 118, *6.1.1*, **9.8**, **9.16**
Munro Township (Canada) 150, *5.8*, **5.9–5.10**
muscovite 243, **8.4**, 267–9, 285–6, *8.4.1*
Muskox intrusion (Canada) *4.13*, 133

N-MORB 41, 44–5, *55*, *2.16*
N:G ratio 262, 266
Nain anorthosite (Labrador) *4.13*
Naples 209, 215
natrocarbonatite 301–3, **9.4**, **9.19**, **9.20**
naujaite 309, **9.22**
Nauru Basin 52, *2.15*
Nazca plate 195–6, *6.21*, 204
Nb 190, 302, 339
— anomaly 58, 190–2, *6.15*, 200–1, *6.25*, 334, 343
negative (optic sign) 293
neoblast 147, **5.8**
neovolcanic zone (Iceland) *9.9*
nepheline (foid) 6, 36–40, 292–3, *9.1b*, 309–10, **9.5**, **9.7**, **9.15**, **9.17**

— syenite 123, 304–5, 309, **9.15**, **9.17. 9.21**, **9.22**
nephelinite (rock) 12, 36, *2.11*, 37, *9.1b*, *299*, **9.7**, 300–1, 312, 317, 320–2, *9.8*, *9.11*, *9.23*
net-vein 257–8, *8.10b*
New Guinea *6.12*
New Zealand *6.12*
Ni 104, 115, 127, 319
non-eruptive fissure 52
norite *4.1*, 94–5, 123, *5.2*, 137
norm 37–40, 268–9, 293–4, 313–6, *9.7*, Appendix B
normal zoning 178, 310
North Arran granite 249, 254
North Atlantic Volcanic Province (NAVP) *2.15*
North Himalayan plutonic belt 274
Northern Volcanic Zone (Andes) *6.12*, *6.21*
nosean (sodalite) **9.8**, **9.13**
nucleation 32, *2.3.1*, 111, 175, 257, 266
nucleation rate (*N*) 257, 262, 266
nuée ardente 229–30, *7.14a*, *7.16*
NVZ: see Northern Volcanic Zone
nyerereite (mineral) 902–3, **9.4**
Nyiragongo (DR Congo) 300, 312, *9.3*, 333, *9.19*

oblique extinction 98
obsidian 164–5, 179–80, *6.3d*
ocean-island basalt (OIB) 44–5, 46–52, *2.16*, *2.18*, 285, 317, *9.8*, *9.19*
ocean-ridge granite *8.19*
oceanic geotherm 59–63, *2.17*, *2.18*
oceanic lithosphere *2.18*
oceanic plagiogranite: see plagiogranite
ocelli 324, 340
off-rift alkali basalt (Iceland) *9.9*, 317–8
ogive 169, *6.3f*
OIB: see ocean-island basalt
oikocryst **4.1**, *4.11*, **4.9**, 136, 158, **5.1**, 175, 309, **9.22**, 352
Oldoinyo Lengai (Tanzania) 300–2, *9.3*, **9.4**, **9.19**, **9.20**
oligoclase (plagioclase) 11, 263
olivine 10, 30, 39, **2.1–2.5**, **2.7–2.9**, **2.10**, 112–3, 132, 143–6, **4.3–4.5**, **4.12**, *5.6*, **5.1–5.11**, 150–4, *5.9*, *5.11*, 166, **6.3**, **9.1–9.2**, **9.9**, **9.10**
— basalt 9, 23, **2.1**
— fractionation 155
— gabbro 9
— melilitite **9.9**, **9.10**
— tholeiite 21, **2.1**, **2.2**, *6.10*
olivine-phyric **2.1**, **2.3**
Ontong Java Plateau 44–5, 52–4, *2.15*, *2.16*
opaque (optics) 248, 350–2
opdalite *8.2*
ophiolite 42, 119, *4.13*, 137–41, 244, *8.17*
ophitic texture 34, 116, *4.11*, **4.1**
optic sign 293, A1, 353–7, *A6*
optically continuous 35, 263, **8.3**, 325
Öræfajökull (Iceland) *9.9*, 317–8
orbicular texture 256–7, **8.5**
order of interference colour 353
orthoclase 37, **8.7**
orthocumulate 117, **4.4**
orthopyroxene 22–3, 98, 165–7, 175, 245, *8.2*
orthopyroxene-bearing granitoids *8.2*
orthorhombic 22
oscillatory zoning 162, 176–8, *6.6*, **6.1**, **6.2**, **6.6**, **9.11**, 310
Oslo alkali province 323
outflow-facies ignimbrite *7.19*
overgrowth 262, **8.6**, **8.7**
oxide 4
oxygen isotopes 89, *3.12*

P_{H2O} 177, *6.4.1*, 260, 286, 316
P-T-t path *8.4.1*
P-T-X diagram 69
pahoehoe 24. *2.2a*, 300–3, **9.20**
— toe 24, *2.2b*, *2.5*, 99, **9.20**
palagonite 27
Pantelleria (Italy) 327–30, *9.17*
pantellerite 327–30, *9.17*
Paraná-Etendeka flood basalt 197
pargasite (amphibole) *6.24*, 202–3, *6.6.1*
partial melting 59, 61, 65, *3.1*, 142, 144–5, *5.4.1*, 198–9, *6.24*, 199–202, *6.25*, 207, 280–8, 332–5, *9.9.1*, 342–3
partial melting equation 334–5
partition coefficient 50, 2.5, *6.6.1*, 334
pegmatite 103, 141, *8.13a*, 265–6
pelagic sediment *5.3.1*
Pele's hair 31, *2.9a*, 212
Peléan activity 230
pelite 285–6
pelletal lapilli **9.2**, 328–9
Peninsula Ranges batholith (California-Mexico)
peralkaline 9
peralkaline 268–9, *8.14*, 304, 311
peraluminous 268–9, *8.14*, 285
peridotite 59, 131, *5.1*, *5.2*
perlitic crack *6.2*, 180, **9.5**
permissive emplacement 254, 271
perovskite (mineral) 310, **9.9**, 325
perthite 244–5, *8.1.1*, 263–4, *8.12*, 304, **9.14**, **9.16**
Peruvian coastal batholith *6.21*
petrography -ic 3, 161, 241
petrological Moho 138–40
PGE 104, 115, 137, 141, 157–8
*p*H 267
phaneritic texture 266
phase 65, 69
— **diagram** 66, *3.1.1*
— equilibrium experiments 67
— layering 108, *4.8*, 110, *4.9*
— Rule 74
phenocryst 2, *1.1*, 32, **2.3**, **2.7**, **2.8**, **2.9**, *2.10*, 261
Philippines arc *6.12*, *6.16*, 270

phlogopite 134, 202, 298, **9.1**, **9.3**, 325, 328, 330, 343
phonolite 12, *1.4*, 209, 219, 236, *9.1*, 295–6, 301, 312, 318–22, *9.10*, *9.11*, **9.5**, **9.7**, **9.8**, **9.12**
phonotephrite *1.4*, *9.1a*
phreatic explosion 224
phreatomagmatic eruption 224
phyric (e.g. olivine-phyric) 12, 21, 32
picrite 21, 136, 148–52, *5.5.1*, *5.5.2*
picrobasalt 85
pigeonite *2.1.1*, 42, **2.10**
Pilbara craton (Austraia) 151, *5.6.1*
pillow lava 24, 26, *2.4*, *2.5*, 138, *5.3.1*, 154, *7.10*
Pinatubo (Philippines) *6.14*, *7.4d*
pipe vesicle, – amygdale 30, *2.8b*
pirssonite **9.4**
Pitcher W.S. 251
pitchstone 180, **6.10**
plagioclase *6.1b*, *8.1*, 243–6, *8.1.1*, 256, 284–5
— composition 96–7, *4.1.2*
— flotation 114
— series *3.4*, 77–80, 164–5
— twinning *6.1.1*
— -phyric 175, **6.1**, **6.2**, **6.6**
plagiogranite 244, 275–7, *8.19*, 280–2, *8.20*
plane of silica saturation 313–6, *9.7a*
plane-polarized light 347–51
Platinova Reefs *4.8*, 115
pleochroic halo **8.2**, **8.10**, 268–9
pleochroism 98, **8.4**, **8.10**, **9.18**, 348–50
pleonaste (spinel) 133, *5.1.1*
plinian eruption 214–9, *7.4c*,*d*, *7.6*, *7.7*, 221, *7.8*, 299, 318–9
Pliny 215
plume 61–3, *2.18*, 104, 122, 157
— head 337, *9.20*
plumose habit **5.10**, **5.11**
pluton 103–4, 245–56
plutonic viii, 8, 16–7, Ch 4, *4.1*, 131–14, *5.1*, Ch 8, 303–9, *9.4*
poikilitic texture 116, *4.11*, 175
poikilophitic texture 116, **4.3**
point counting 6
polarization colour: see interference colour
polybaric 175
polygonal texture 118, 136, 147
polyhedral olivine 148–50, *5.8*, *5.9*, *5.11*, 158
polymerized, -zation 33, 167–71, 266, 300
polysynthetic twinning *6.1.1*, *8.11*
porphyritic texture 12, 32, *2.10*, 310
porphyroblast 261
porphyroclast -ic texture 147, **5.8**
porphyry copper 267
positive (optic sign) 293
post-caldera stage 317, *9.8*, 335–7
post-collisional 329–31, 343–4, *9.24*
post-erosional stage 317, *9.8*, 335–7
post-magmatic mineral 9
post-magmatic process 3
post-tectonic granitoid 261
potassic volcanism 297, 299, 322
potassium see high-K etc. 17, *1.6*, 41
potential temperature 61, 155–6, *5.12*, *5.13*
ppb 4
PPL 350–1
ppm 4
pre-eruption volatile content *6.14*, *7.13*
pre-shield stage 316, *9.8*
precision 44
pressure 2, 16, 29, *2.17*, 59–63, 99–102, *4.5*, *4.6*, *5.5*, 142, *5.4.1*, 155–7, *5.12*, *6.5*, *6.7*, 170–1, 175–6, 179, 182–4, *6.9*, *6.10*, *6.2.2*, *6.4.1*, *7.1*, 224, 236, 260, 286, *8.4.1*, 313–6, 332–3, *9.18*
primary melt/basalt 143–6, 154, 319–20, 345
primitive 11, 198
— magma 198
— **mantle** 50–1
progressive aggradation (of ignimbrite) 225–8, *7.12b*
projection in phase diagram 364
protogranular texture 147, **5.3–5.7**, 158
pseudoleucite (alteration product) 311, 316
pseudomorph 35, **2.9**, 311
pumice 203, 214–9, *7.18*, 234–6
Pyrenees 146
pyrochlore (mineral) 265–6, 302
pyroclast -ic 175, 219
— grade 219
— nomenclature *7.5*
pyroclastic breccia *7.5*
pyroclastic current deposit 219–21, *7.7b*, *7.11b-e*
pyroclastic density current 214, *7.4a*,*e*, 219, *7.6b*, 225–33, *7.14*, *7.15a*, 236
pyroclastic fall deposit *2.6b*, 219–21, *7.7a*, *7.11a*
pyrope 132, *5.2.1*
pyroxene 8, 11, 22–3, 30, 98, **4.1– 4.9**, **5.1.–5.5**, **5.9–5.11**, 120–1, **6.4–6.5**, 162, 243, 296–7, **9.7**, **9.8**, **9.15**
— quadrilateral *2.1.1*, *4.2*, **4.5.2**
pyroxenite *5.1*, 135, *5.2*, 142, 147, 337–8

QAP diagram *6.1b*, *8.1*
QAPF diagram 293, *9.1b*, *9.4*
qualifier 8, 10
quartz 6, *2.11*, 37, 95, 175–6, 179, **6.9**, *8.1*, 243, 263, **8.3**, 267, 293
— diorite 276–7
quartzo-feldspathic 251, 279
quaternary diagram 362–4
quench, -ed, -ing 68, 84, 183, *9.18*
Quernertoq rapakivi granite (S. Greenland) 249

radiogenic isotopes *3.11*, *3.12*, 87–91
rapakivi granite 124
rapakivi texture **8.7**, 262–3
rare earth elements (**REE**) 45, 49–51, *6.15*, 199–20, *6.25*, 204–6, *6.6.1*, *8.5.1*, 287, 302

Ras ed Dom ring complex (Sudan) 254, *8.18*, 257, 274–5
reaction point 75, *4.3.1*, 113
Reaction Principle 77, 110, 112–3
reaction rim 262–3
reaction texture 118, 262
Read H.H. 251, 280
REE: see rare earth element
reef 114
refractive index (RI) 32, 350–1, *A2.1*
refractory *59*
relative molecular mass (**RMM**) 38–40, 145
relative retardation 352–3
relief (optical) 269, 348, 350–1
Residua system *9.7c*
residual gravity anomaly *8.7a*
residual mantle 143
resorb **resorption** 176, 178–9, 310
resurgent dome *7.19*, 238, *7.20b*
Réunion 26
reversal (cryptic layering) 136
Reykjanes peninsula 317–8, *9.9*, 337, *9.20*
Rhine rift *2.12*, *54–5*
rhyolite 12, *1.4*, Ch 6, 162, *6.1*, 168, *6.3f*, **6.9**, *6.15*, 196–8, 206–7, 219
rhythmic layering: see modal layering
richterite 306, *9.4.1*
riebeckite (amphibole) 269, 306, *9.4.1*, 311, **9.18**
ring dyke *4.3f*, 102, *4.6b*
ring fault (caldera) 170, *7.19*, 238, *7.20b*, 254
ring intrusion 248–9, *8.5*, *8.9b*, *9.6*, 307
Ring of Fire 185
Rio Grande rift (USA) *2.12*, 54, *5.1*, 322
RMM 38–40, 46, *8.14*, 269, 311
Roeder and Emslie 143
Rogaland igneous complex *4.13*, 125–8, *4.15*
roll-back *6.19*
Roman Province (Italy) 329, *9.17*
roof subsidence 103
roof-cumulate 128
root name 8, 9, 10
ropy pahoehoe 24, 303
rosette jointing *2.3*
Rum (Hebrides) 104, *4.7a*, *4.7f*, *4.7g*, *4.13*, 135–6

ΣFe_2O_3 46–7, 146
ΣFeO 44–7, 146, 168, *6.9*
ΣFeO/MgO ratio *6.8*
S-type granitoid 269, 272–3, 276–7
salic 292, 341
saline salinity of fluid 267
San Andreas Fault *6.12*
San Juan volcaic field *6.12*, 237–8
San Venanzo (Italy) 329, *9.17*
Sandwich horizon (Skærgaard) *4.8*
Sangihe arc (Indonesia) *6.16*
sanidine 164–5, 167, *6.2.2*, **6.10**, *8.1.1*, 297, **9.12**
sannaite (lamprophyre) 325
saturated 71
saucer-shaped 99
schlieren 256
SCLM: see sub-continental mantle lithospere
scoria *2.2e*, *2.6b*, 28, **5.3**, 212–4, 219
— cone *2.6a*, 169, 212–4. 299, 326
seawater 42
secondary 9, 15, 16
sector collapse 233
seismic Moho 138–9, *5.3*
seismic reflection profile *5.3.1b*, 189, 246, *8.4c*
seismic tomography 199, *6.24*, 202, 207, 338
Semail ophiolite (Oman) 119, 136, 138, *5.3.2*, 140, *5.3*
sensitive tint (optics) 96, 293
seriate texture 12, **2.3**, *2.10*, 175, **6.1**, **6.6**, 310, **9.7**
sericite 20, 94, 162, 243, **8.1**, 266, 292, **9.15**
serpentine (mineral) 20, 30, 63, *2.8*, 94, 135, *5.3.1a*, 162, 328
serpentinite (rock) 135
serpentinization **2.8**, **5.9–5.11**
Shap granite **8.9**
sheared serpentinite *5.3.1a*
sheared texture 158, **5.8**
sheet intrusion 246–7, *8.3a*, *8.4c*, 250
sheeted dyke swarm 138, *5.3.1*
shelly pahoehoe 24
shergottite 58, **2.10**
shield geotherm 9.22, 345
shield volcano 26, 48, 210, *7.2a*, 214
shield-building stage 316–7, *9.8*, 335
shonkinite 305, *9.5*
shoshonite-latite *1.6*, 57, 185, *6.11*, *6.18*, 194, 297, *9.2*, 312, 329–30, *9.19*, 343–4, *9.24*
sialic crust 161, 288–9
Siberian 'Traps' *2.15*
Siberian platform 141
siderite 302
sideromelane 32
Sierra Nevada batholith (California) *8.6*, 250, *8.20*, 282–4, *8.22*
sieve texture 179, **6.7**
significant figures 44, *8.19*
silica 4
silica-oversaturated 6, *2.11*, 36, 38–9
silica-saturated *2.11*, 36, *9.11*, *9.12*
silica-undersaturated 6, *2.11*, 36, 39–40, 292–3, *9.11*, *9.12*, 322, 332
silicate 4
silicic 8
sill 99, *4.3d*, *4.5b*, *8.9e*, 255
simple twin 165,, **9.12**, **9.13**
SiO_2 5, 131, 166, 204–6, 285, *9.18*
size-graded layering 108
Skærgaard intrusion (E. Greenland) *4.2*, *4.7b-e*, *4.7h*, *4.8*, *4.9*, 136
skeletal texture *5.9*, **5.9–5.11**, **6.10**
Skye (Hebrides) 26
skylight 26, **2.6**
slab dip 195, *6.21*
slab roll-back 193–4, *6.19*
slab-derived component 200–2, *6.25a*
slow vibration direction (optics) 96–78, 353
slumping 110, *4.7f*
Sm (samarium) 206
smectite 20

Snaefellsnaes peninsula (Iceland) 48, *9.9*, 317–8, 337–8, *9.20*
sodalite (foid) 292–3, **9.8**, **9.13**, **9.22**
sodalitolite (rock) 309
sodian augite *9.2.1*
sodic amphibole 291, 306, 311
sodic pyroxene 291–7, *9.2.1*, **9.7**, **9.8**, **9.15**, 311
solid solution 10, 77, *6.1.1*, *8.1.1*
solidification front 111, *4.9*
solidus *59*, *2.17*, *2.18*, *3.1.1*, 69–70, 121, *5.5*, *5.12*, 175–7, *6.5*
Solomon Islands arc 270
solubility 30
solvus 22, 120–1, *4.5.2*, 244–*5*, *8.1.1*, 263–4, *8.12*, *9.21*, 340
sorting 220, *7.7*, 225
Soufrière Hills (Montserrat) front cover, 169, *6.3b*, 215, *7.4a*, 230
South Sandwich Islands (SSI) *2.12*, *6.12*, 189, 200–1, *6.25a*
South Tibetan Detachment (STD) 274, *8.17*
Southern Volcanic Zone (Andes) *6.12*, 195–6, *6.21*
sövite 305, 308, 340
space problem 251–*5*, *8.9*
spatter cone *7.3a*, 901, **9.19**
spessartite (lamprophyre) 325
sphene **9.7**
spherulite –ic 12, 31–2, *2.9b*,*c*, 162, *6.2*, 180
spidergram 51, *2.16*, 57, *6.15*, *8.19*, 333–8
spilite 42
spinel 132–3, *5.1.1*, 142, *5.5*, **5.8**, 158, 169, *6.3c*
— lherzolite 142, *5.5*, **5.3**, **5.4**, **5.6–5.8**, 147, 317
spinifex texture 148–54, *5.7*, *5.8*, *5.9*, *5.10*, *5.11*, 158, **5.9**, **5.10**, **5.11**
spinifex zone *5.11*
spodumene 265–6
Sr-isotope ratio 87–91, *8.21*, 282–5
Sr/Y ratio 204–6, 279, 284
SSZ: see supra-subduction zone
St Paul's Rocks *2.12*
stable isotopes 90–1
Staffa *2.3*
standard model (of ignimbrite emplacement) 225–8, *7.12a*
starting plume 63, 206
Stillwater intrusion, Montana 104, *4.13*, **4.9**, **5.1**, **5.2**, 135–6, *5.2*
stock 246, 249
Stokes' Law 110, 114
stoped, stoping *8.3b*, *8.9a*, 252–3, 258
straight extinction 98
strain marker 255–6
stratovolcano 151, 188, 210, *7.2b*, 214, 300, 328
streaky pumice 171
stress trajectory *4.6*
Stromboli (Aeolian Island, Italy) *2.16*, 57, 327–30, *9.17*, *9.19*
strombolian eruption 24, 28, 212–4, *7.3c*,*d*, 221, *7.8*, *7.10*, 301, 328
structural caldera margin *7.19*, 238
sub-continental mantle lithosphere (SCLM) 333, 341–3, *9.23*
sub-ophitic texture 116, **4.2**
sub-plinian eruption 214, 221, *7.8*
sub-solidus 121
subalkali *1.5*, 16, *2.1*
— basalt 22, 37
subducting slab 198, *6.23*
subduction 63
— zone 185–96
— -related basalts 55–8
— -related magmas 185, 327–30, 334
subgrain 119, **4.13**
submarine basalt 13
subsolvus granitoid **8.2**, 309
Sulawesi arc (Indonesia) *6.16*
sulfide: see sulphide
sulphide 115, 157, 258
super-eruption 237
supercooling -ed 32, *2.3.1*, 118, 263
superheating -ed 257, 300
supersaturated *7.1*
supra-subduction zone magma 57, 161
surge deposit 230–3, *7.15a*
surtseyan eruption *7.8*, 223, *7.9a*, *7.10*
SVZ: see Southern Volcanic Zone
swallowtail termination **5.9**, **6.3**
syenite *8.1*, 243–4, *9.4*, 275, 304–5, 323, **9.14**, **9.15**, **9.16**, **9.17**, **9.18**
sylvite (mineral) 303
symplectite texture 119, **4.10**, **4.11**
syn-collision granitoid *8.19*
syn-tectonic granitoid 260, 8.11
synkinematic intrusion *8.9f*, 255–6
synplutonic dyke 249, 258, *8.10d*, 270
system 67
— $CaMgSi_2O_6$–$CaAl_2Si_2O_8$ *3.1.1*, *3.2*, 68–72
— $CaMgSi_2O_6$–$CaAl_2Si_2O_8$–Mg_2SiO_4 *3.3*
— $CaMgSi_2O_6$–Mg_2SiO_4–$NaAlSiO_4$–SiO_2 313, *9.7b*
— $CaMgSi_2O_6$–$NaAlSi_3O_8$–$CaAl_2Si_2O_8$ *3.7*, *3.8*, 80–4
— $CaMgSi_2O_6$–$NaAlSiO_4$–SiO_2 313, *9.7b*
— Mg_2SiO_4–Fe_2SiO_4 *3.6*
— $NaAlSi_3O_8$–$CaAl_2Si_2O_8$ *3.4*, 77–80, *3.5*
— SiO_2–$NaAlSiO_4$–$KAlSiO_4$ *9.7c*, 316

T-X diagram 68, *3.1.1*, *3.2*, *3.4*
tabular pluton *8.9e*
talc 135
Talkeetna arc section (Alaska) 189
Tanzanian craton *9.3 (inset)*, 322–3, *9.16*
Tarçouate Laccolith (Morocco) 256
'tartan' twinning *6.1.1*, *8.1.1*, 352
TAS plot, diagram 5, *1.2*, *1.4*, *1.5*, 41, *3.1*, 149, *5.5.1*, *5.5.2*, 161–2, *6.1*, *9.1*, *9.6.1*
Tasman orogenic zone 272
Tatara/San Pedro volcano (Chile) *180–2*, *6.8*, *6.9*
Taupo (New Zealand) *6.12*, *6.14*, *7.8*, *7.11c*
— ignimbrite *7.11c*
Tchivira ring complex (Angola) 307, *9.6*
tectonite 138–40

Teide (Tenerife) 318–9
Tenerife 209, 318–9. *9.10*, *9.19*
tensile strength 99
tephra 175
— fingers 223, *7.9a*
tephriphonolite *1.4*, *9.1a*
tephrite 12, *1.4*, *9.1*, 294–5, 299, 312
ternary diagram 72–7, *3.3*, 80–4, *3.7*, *3.8*, *4.3.1b*, 112–3, 144–5, *5.4.1*, 178–9, *6.7*, *9.7b*,*c*, 313, 316, 362–4, *B1*
ternary eutectic *3.3*, 76
terrane accretion 141, 189
textural equilibration 118
theralite 303–4
thermal boundary layer 60–2, *2.17*
thermal divide *9.7a*,*b*, 315–6
thermal erosion 157
thermal minimum *9.7c*
thin section Appendix A
Thingmuli (Iceland) 180–4, *6.8*, *6.9*
tholeiite tholeiitic basalt 21, 22, 35–41, 151, *6.10*
tholeiitic trend 180, *6.8a*
three-phase triangle *3.8*, 82
Ti 206
Tibesti 338
Tibet 272–4, *8.17*, 329–30, 344
tie-line 71, 77–8, *3.4*, *3.8*, 82, 244–5, *8.1.1*, *9.21*, 340
tin-tungsten-moly ore bodies 267, 272–3, *8.3.1*
TiO_2 166
titanian augite *2.1.1*, 42, 95, 325
Toba (Indonesia) 234
tonalite *8.1*, 242–3, 271–2, 276–9
Tonga-Kermadec arc 186, *6.12*, 189
topaz 265–9
topographic caldera margin *7.19*, 238
topographic swell *9.3*, 335, 337–9
Toro-Ankole volcanic province *9.3*, 330–1
total alkalis 5
total iron oxide 46–7
tourmaline 243, **8.4**, 265–9
trace element 4, 42
trachyandesite *1.4*, 164, *9.1*, 295–6, 329–30
trachybasalt 12, *1.4*, 164, *9.1a*, 294–5, 329–30
trachydacite *9.1a*
trachyte 12, *1.4*, 85, *3.10*, 162, 209, 236, *9.1*, 295–6, 312, 318, *9.11*, 323
trachytic texture 310, **9.12**
Trans-Himalayan batholith 248, *8.17*, 272–4
transgressive 99
transitional *1.5*
transitional basalt 41, *9.11*
trap topography *2.2d*, 26
trapdoor caldera 237
triclinic 165, *6.1.1*, 244–5, *8.1.1*
tridymite 175
triple junction (grain boundary) 142, **5.6**, 147
trivariant 76
troctolite *4.1*, 95, 119. 123–8, 140
trondhjemite 206, 242–3, 278–9
Troodos ophiolite (Cyprus) 139, *5.3.2*, 206
trough bands *4.7e*, 110, 256
TTG (tonalite-trondhjemite-granodiorite) suite 278–80, *8.20*, 284–5, *8.23*
tuff 214, *7.5*, 235–6
— ring 302
tuffisitic kimberlite: see massive volcaniclastic kimberlite
Tuolumne pluton (Sierra Nevada) 276–7
twin twinning 98, *6.1.1*, 176, 262, **9.6**, **9.9**, **9.16**, 348, 352
two-mica (leuco) granite 243, **8.2**, 274
two-phase field 71–2, *3.2.1*, *4.3.1*
type mineral 9
Tyrrhenian Sea back-arc basin *9.17*, 343

ultrabasic *1.3c*, 8, 59, Ch 5
ultramafic *1.3b*, Ch 5, *5.1*
— cumulate *5.3.1*
— lamprophyre 323–5, *9.6.1*
— tectonite 138–9
ultraplinian eruption 221, *7.8*
ultrapotassic rocks 297, 299, 327, 330–1, *9.8.1*
ulvöspinel 133
umbrella 215–8
umbrella pine 215, *7.4g*
underplating 47, 207, 284–8
uniaxial (optics) 293, *A1*, 353–7, *A2*, *A3*
univariant 74, 78, *4.3.1*, 113
unmixing 118, 120–1, **4.7–4.9**
uplift 146
Upper Border Series (Skærgaard) *4.8*, *4.9*
Upper Zone (Skærgaard) 108, *4.8*
upwelling: see asthenosphere upwelling
uralite 20, 30, 94, 162, 243
Urals (Russia) 141
urtite 304–5, *9.5*

Valles caldera (New Mexico) 170, **6.7**, 238, *7.20b*
Vanuatu **2.5**, *6.12*, **6.3**
variance 74
variation diagram 5, *1.2*, *1.4*, *1.5*, *1.6*, 73, 85, *3.10*, 183–4, *6.9*
variole 32
vertical grading 225, *7.12*
vesicle vesicular 2, *1.1*, 12, 16, 24, 29–30, **2.3**, *2.7*, *2.8a*, 203, *7.18*, 234, **9.11**
vesiculation horizon *7.1*
Vestmannaeyjar (Iceland) *9.9*, 318, 337–8, *9.20*
Vesuvius (Italy) 212, 215, *9.17*
vibration direction 96–7
viscosity 169–71, 210
vitric tuff 235
VMS: see volcanogenic massive sulphide
vogesite (lamprphyre) 325
volatile (content, pressure) 3, 15, 29, 171, 175, 189–90, 198–202, 258, 324–5
— -free 15, 38
volcanic viii, 8, 16–7, Ch 2, *2.1*, Ch 6, *6.1*, 291–303, *9.1*
volcanic-arc granitoid *8.19*
volcanogenic massive sulphide (VMS) 58

vug 260
vulcanian eruption *7.2c*, *7.4a*, 214–5
Vulcano (Aeolian Islands, Italy) *7.2c*, *7.4b*, 327–30, *9.17*

Wadati-Benioff seismic **zone** 188–90, *6.13*, *9.17*, 343
Walker G.P.L. 221
water and melt evolution 175–7, 182–4, *6.9*, *6.10*, 288
water-saturated solidus *6.4.1*, 252, 263, 266
water-undersaturated conditions 177, 252, 262, 266, 285–6, *8.4.1*
water:rock ratio 267
weathering -ed 3, 165, *6.3f*
websterite 132, *5.1*
wedge component 200–1
wedge depletion 201
wehrlite 132, *5.1*, 140, *5.3*, *5.4*
weight percent *1.1*, 4
welded lapilli tuff *7.11d*, 236
welded, **welding** 12, 171–5, **7.3**, *7.11d*,*e*, 236
Wesselton kimberlite (S. Africa) **9.1**, 333, *9.19*
Western Red Hills centre (Skye) 248, *8.5b*, 254, 257
Western Rift (E. Africa) *9.3*, *9.13*, 322
whole-rock analysis 2, *1.1*, 3
within-plate granitoid *8.19*
wyomingite (lamproite) 330

xenocryst 1
xenolith 17, 59
XRFS 4

Y (yttrium) 205
Y/Nb ratio *8.19*, 285–8
Yellowstone (Wyoming) *2.12*, *2.15*, 197–8
— hotspot / plume 198, 207
Yemen 89, *6.12*, *6.22*, 207
yield strength 169–71, 209
Yoder and Tilley 59, 182–4, *6.10*, 311–6

zeolite 325
zircon (mineral) 311
zoned pegmatite 266
zoned ultramafic intrusion 141
zoning, **zoned** 33, **2.5**, 65, *3.5*, 80, 83, 116, 126–7, 176, **6.1**, **6.2**, **6.6**, 352
Zr 92, 190, 206, 311
Zr-Nb ore bodies 267
Zr/Sm ratio 206
Zr/Ti ratio 206